



PHYSICAL CHEMISTRY 2014

12th International Conference
on Fundamental and Applied Aspects of
Physical Chemistry

The Conference is dedicated to the
25. Anniversary of the Society of Physical Chemists of Serbia

September 22-26, 2014
Belgrade, Serbia



PHYSICAL CHEMISTRY 2014

12th International Conference
on Fundamental and Applied Aspects of
Physical Chemistry

Proceedings
Volume I

The Conference is dedicated to the
25. Anniversary of the Society of Physical Chemists of Serbia

September 22-26, 2014
Belgrade, Serbia

ISBN 978-86-82475-30-9

Title: PHYSICAL CHEMISTRY 2014 (Proceedings)

Editors: Ž. Čupić and S. Anić

Published by: Society of Physical Chemists of Serbia, Studenski trg 12-16, 11158, Belgrade, Serbia

Publisher: Society of Physical Chemists of Serbia

For Publisher: S. Anić, President of Society of Physical Chemists of Serbia

Printed by: “Jovan” Printing and Publishing Company; 200 Copies;

Number of pages: 6+ 441; **Format:** B5; Printing finished in September 2014.

Text and Layout: “Jovan”

Neither this book nor any part may be reproduced or transmitted in any form or by any means, including photocopying, or by any information storage and retrieval system, without permission in writing from the publisher.

200 - Copy printing

CONTENTS

Volume 1

Organizers	IV
Committees	V
Sponsors	VI
Plenary lectures	1
Chemical Thermodynamics	47
Spectroscopy, Molecular Structure, Physical Chemistry of Plasma	113
Kinetics, Catalysis	205
Nonlinear Dynamics	317
Electrochemistry	365

PHYSICAL CHEMISTRY 2014

*12th International Conference on
Fundamental and Applied Aspects of
Physical Chemistry*

*Organized by
The Society of Physical Chemists of
Serbia*

*in co-operation
with_*

Institute of Catalysis Bulgarian Academy of Sciences

*Boreskov Institute of Catalysis of Siberian Branch of the Russian Academy
of Sciences*

Faculty of Physical Chemistry, University of Belgrade, Serbia

*Institute of Chemistry Technology and Metallurgy,
University of Belgrade, Serbia*

Vinča Institute, University of Belgrade, Serbia

Institute of General and Physical Chemistry, Serbia

Faculty of Pharmacy, University of Belgrade, Serbia

International Organizing Committee

Chairman: S. Anić (Serbia)
Vice-chairman: M. Gabrovska (Bulgaria)
V. A. Sadykov (Russia)

Members:

N. Cyjetičanin (Serbia), S. N. Blagojević (Serbia), M. Daković (Serbia), T. Grozdić (Serbia), D. Jovanović (Serbia), M. Kuzmanović (Serbia), D. Marković (Serbia), J. Marković-Dimitrić (Serbia), B. Milosavljević (USA), M. Mojović (Serbia), N. Ostrovski (Serbia), I. Pašti (Serbia), M. Petković (Serbia), A. Popović-Bjelić (Serbia), B. Simonović (Serbia), D. Stanisavljev (Serbia), B. Šljukić (Serbia), N. Vukelić (Serbia), V. Vukojević (Sweden)

International Scientific Committee

Chairman: Ž. Čupić (Serbia)
Vice-chairmans: V. N. Parmon (Russia)
S. Rakovsky (Bulgaria)

Members:

B. Adnađević (Serbia), S. Anić (Serbia), A. Antić-Jovanović (Serbia), G. Bačić (Serbia), A. Kellarakis (Greece), R. Cervellati (Italy), V. Dondur (Serbia), Ivan Gutman (Serbia), S. D. Furrow (USA), K. Hedrih (Serbia), M. Jeremić (Serbia), A. V. Knyazev (Russia), Lj. Kolar-Anić (Serbia), V. Kuntić (Serbia), Z. Marković (Serbia), S. Mentus (Serbia), Š. Miljanić (Serbia), M. Perić (Serbia), M. Plavšić (Serbia), D. M. F. Santos (Portugal), G. Schmitz (Belgium), I. Schreiber (Czech), P. Sevcik (Slovakia), B. C. Simionescu (Romania), N. Stepanov (Russia), D. Todorović (Serbia), M. Trtica (Serbia), V. Vasić (Serbia), D. Veselinović (Serbia)

Local Executive Committee

Chairman: S. Blagojević
Vice-chairmans: A. Ivanović-Šašić

Members:

P. Banković, N. Bošnjaković, J. Dostanić, A. Đerić, A. Ignjatović, A. Jović, N. Jović-Jovičić, D. Lončarević, J. Krstić, J. Maksimović, V. Marković, M. Milenković, S. Maćešić, V. Marković, B. Nedić, N. Potkonjak, D. Ranković, M. Stević, M. Žunić, M. Ristić,

SPONSORS

Ministry of Science and Technological Development

University of Belgrade, Belgrade

Institute of General and Physical Chemistry, Belgrade

Analysis DOO, Belgrade

PLENARY SECTION

MULTIDISCIPLINARY CHARACTER OF PHYSICAL CHEMISTRY: FROM MATERIAL SCIENCE TO QUANTUM CHEMISTRY AND BACK

M. Perić

Faculty of Physical Chemistry, University of Belgrade, Studentski trg 12–16, 11000 Belgrade, Serbia

ABSTRACT

During plasma electrolytic oxidation of aluminum two broad emission peaks with clearly pronounced structure, extending from 18200 to 18800 and from 19000 to 19700 cm^{-1} , were detected. Based on comparison with the results of high-resolution spectroscopic measurements the spectra were assigned to $\nu' - \nu'' = -1$ and -2 band sequences of the $B^2\Sigma^+ \rightarrow X^2\Sigma^+$ electronic transition of AlO. Employing tools of quantum mechanics/chemistry the measured intensity distributions were utilized to estimate the plasma temperature.

INTRODUCTION

In the present study we illustrate on a concrete example the multidisciplinary character of contemporary physicochemical investigations. We focus attention to the process of plasma electrolytic oxidation (PEO) of aluminium, serving to obtain a material of favourable physical and chemical properties.

Aluminium is a relatively soft, durable, lightweight, ductile, malleable and conductive metal, not soluble in water. Due to its favourable physical properties and its ability to resist corrosion Al is the most widely used non-ferrous metal. It is usually alloyed (with Cu, Zn, Mg, Mn, and Si), which markedly improves its mechanical properties. Al and its alloys are vital to the aerospace industry and are important in other areas of transportation, as well as in construction, production of household items, in electronics etc.

Corrosion resistance of aluminium is based on forming of a thin surface layer of aluminium oxide when the metal is exposed to air, effectively preventing further oxidation. This corrosion resistance can be improved by increasing the thickness of Al_2O_3 layer by means of various procedures. One of the most important is that one considered in the present study.

PEO is a process based on anodizing of lightweight metals (aluminum, titanium, magnesium, zirconium, etc.) or metallic alloys above the dielectric breakdown voltage of the anodic oxide films. During the PEO process, numerous transient short-lived discharges are generated over the coating surface, accompanied by light emission and gas evolution. Due to increased

local temperature and pressure, at the discharge sites are induced plasma-chemical, thermal, and anodic oxidation processes, which modify the structure, composition, and morphology of such oxide coatings. Thick, highly crystalline oxide coatings formed by the PEO process have excellent wear, friction, corrosion, electrical and thermal properties. The morphology and composition of obtained oxide coatings, and particularly of their change in course of the PEO process, can be characterized by means of scanning electron microscopy and X-ray diffractometry. The most efficient tool for studying micro-discharge phenomena has become optical emission spectroscopy. Measuring intensities of atomic and ionic spectral lines as well as of molecular bands, one can extract information on important parameters like local plasma temperature and electron density.

EXPERIMENTAL

The experimental set-up was described in one of our previous studies [1]. We repeat here only the key points. High purity cold-rolled Al samples of dimensions 25 mm × 10 mm × 0.25 mm were used as starting material. The oxidation process was carried out in an electrolytic cell with flat glass windows. Platinum wires were used as cathodes. The anodization was conducted under a constant current density in 0.01 M citric acid. Spectral characterization of PEO was performed utilizing a spectrograph system based on the Intensified Charge Coupled Device (ICCD) camera intended for time-resolved measuring of very weak light intensity in a wide range of wavelengths. The optical detection system consisted of a large-aperture achromatic lens, a Hilger spectrograph with diffraction grating 1200 grooves/mm and a very sensitive PI-MAX ICCD cooled camera with high quantum efficiency. The optical-detection system was calibrated using a standard tungsten strip lamp (OSRAM Wi-17G). The obtained spectra were adjusted to the spectral response of the measuring system.

RESULTS AND DISCUSSION

In our recent study on Al [1] we recorded an emission spectrum dominated by two broad peaks with clearly pronounced structure, extending from roughly 18200 to 18800 cm^{-1} and 19000 to 19700 cm^{-1} , i.e. in the region where the appearance of the bands of the $B^2\Sigma^+ \rightarrow X^2\Sigma^+$ transition of AlO was expected [2,3] (Fig. 1).

The three lowest-lying doublet electronic states of AlO are $X^2\Sigma^+$, $A^2\Pi$, and $B^2\Sigma^+$ ([2–4]. The green $B^2\Sigma^+ - X^2\Sigma^+$ system, appearing in the wavelength range 541–433 nm, is described in detail by Pearse and Gaydon [2]. Molecular parameters for the electronic states in question are collected by Huber and Herzberg [3]. The third comprehensive source of newer literature

data on the AlO spectra is the benchmark *ab initio* theoretical study by Zenouda et al [4].

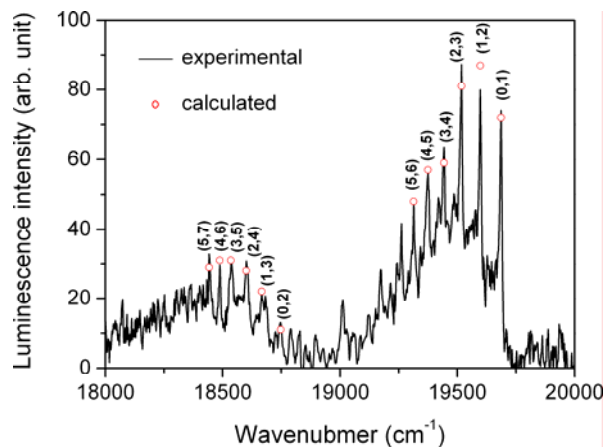


Figure 1. Emission spectrum recorded during PEO of Al. The peaks are assigned to $v'-v'' = -1, -2$ sequences of the $B^2\Sigma^+ \rightarrow X^2\Sigma^+$ system of AlO.

Measured electronic-vibration terms are usually represented by

$$\frac{E_{v'v''}}{hc} \equiv \tilde{\nu}^{v'v''} = T_e + \left(v' + \frac{1}{2}\right) \tilde{\nu}' - \left(v' + \frac{1}{2}\right)^2 (\omega_e x_e)' + \left(v' + \frac{1}{2}\right)^3 (\omega_e y_e)' + \dots$$

$$- \left(v'' + \frac{1}{2}\right) \tilde{\nu}'' + \left(v'' + \frac{1}{2}\right)^2 (\omega_e x_e)'' - \left(v'' + \frac{1}{2}\right)^3 (\omega_e y_e)'' + \dots \quad (1)$$

where T_e is the electronic term value and $\tilde{\nu}$ is the vibrational wave number. $(\omega_e x_e)$ and $(\omega_e y_e)$ are experimentally determined anharmonicity parameters expressed in cm^{-1} .

The rotational levels of both $X^2\Sigma^+$ and $B^2\Sigma^+$ electronic states consist of pairs of close-lying sub-levels characterized by the same value of the quantum number N and by $J = N \pm 1/2$ [Hund's case (b)]. The splitting is caused by the spin-rotation coupling, and it cannot be observed in our experiments. The selection rule for rotational transitions when both electronic states are of Σ symmetry is $J' = J'' + 1$ („R branch“) and $J' = J'' - 1$ („P branch“). When $B' < B''$, as in the present case, the band heads appear at a wave number higher than that of the band origin, $\tilde{\nu}_0$, i.e. at the „violet

side“ with respect to $\tilde{\nu}_0$. The band is „shaded“ („degraded“) towards the red

The term difference between the band head and origin in the R branch is

$$\tilde{\nu}_h - \tilde{\nu}_0 = 2B' + \frac{(3B' - B'')^2}{4(B' - B'')} \quad (2)$$

In order to assign the observed spectral features in the spectrum shown in Fig. 1, we constructed a Deslandres table for the $B^2\Sigma^+ - X^2\Sigma^+$ system of AlO. We used for that the band origins published by Saksena *et al.* [5]. Using the rotational constants from that reference, $B'' = 0.64165$ and $B' = 0.60897$, and Eq. (2), we estimated that the position of the band head with respect to the band origin is about 12 cm^{-1} blue-shifted. The results of our study match very reasonably the $\nu' - \nu'' = -1$ and -2 sequences of the $B^2\Sigma^+ - X^2\Sigma^+$ system.

The intensity of the spectral band appearing as a consequence of the transition between the vibrational level ν' of the electronic state e' and the vibrational level ν'' of the electronic state e'' is determined by the formula

$$I_{e'\nu', e''\nu''} \propto N_{\nu'} (E_{\nu'e'} - E_{e''\nu''})^4 |\bar{R}^{e'\nu', e''\nu''}|^2 e^{-\frac{E_{\nu'e'} - E_{e''\nu''}}{kT}} \quad (3)$$

where $E_{\nu'e'}$ and $E_{e''\nu''}$ are the energies of these two states, $N_{\nu'}$ is the number of molecules in the upper state, k Boltzmann constant, and T the temperature. The quantity $\bar{R}^{e'\nu', e''\nu''}$ is the vibrational transition moment (*VTM*). Its g -component, where $g = x, y$ or z (molecular axis), is defined as

$$R_g^{e'\nu', e''\nu''} \equiv (VTM)_g^{e'\nu', e''\nu''} = (R_g^{e', e''})_{r=r_0} \langle \nu' | \nu'' \rangle + \left(\frac{dR_g^{e', e''}}{dr} \right)_{r=r_0} \langle \nu' | (r - r_0) | \nu'' \rangle + \dots; \quad (4)$$

$$\langle e' | \hat{\mu}_g | e'' \rangle \equiv R_g^{e', e''} \quad (5)$$

is the electric transition moment; In Eq. (5) $\hat{\mu}_g$ is the g -component of the electric dipole operator, and the integration is only carried out over electronic variables. The electric transition moment is a function of the bond length, r , and Eq. (4) represents this quantity as a Taylor expansion in the vibrational coordinate $(r - r_e)$, where r_e is the equilibrium bond length. The square of the scalar product $\langle \nu' | \nu'' \rangle$ from Eq. (4),

$$(FCF)^{e'\nu', e''\nu''} = \langle \nu' | \nu'' \rangle^2 = \left[\int \psi_{\nu'}^* \psi_{\nu''} d\tau_{\nu} \right]^2, \quad (6)$$

is the Franck–Condon factor (*FCF*). In the Franck–Condon (F–C) approximation we neglect the second term on the right-hand side of Eq. (4), i.e. we assume the electric transition moment to be constant. The magnitude

of $|VTM|^2$ or (sometimes significantly less reliably) FCF determines the intensity distribution within a (rotationally unresolved) band system.

Since the wave number differences between all bands we used in the present study for determination of temperature, namely the members of the band sequences $\nu' - \nu'' = -1, -2$, are negligibly small compared to the energy of the electronic transition, the quantity $E_{\nu'e'} - E_{\nu''e''}$ can in Eq. (3) be assumed constant and then the number of the molecules in the upper state is

$$N_{\nu'} \propto \frac{I_{e'\nu',e''\nu''}}{|\bar{R}^{e'\nu',e''\nu''}|^2}. \quad (7)$$

Assuming a partial local thermal equilibrium of the system, the ratio of the number of molecules $N_{e'\nu'}$ in the vibrational state ν' and in the lowest vibrational state $\nu' = 0$ of the same electronic species, $N_{e'0}$ is determined by

$$\frac{N_{e'\nu'}}{N_{e'0}} = e^{-\frac{E_{e'\nu'} - E_{e'0}}{kT}}. \quad (8)$$

Combining the formulae (3) and (8), we obtain for the sequence $\nu' - \nu'' = -\Delta\nu$

$$\ln \left(\frac{\frac{I_{e'\nu',e''\nu'+\Delta\nu}}{|\bar{R}^{e'\nu',e''\nu'+\Delta\nu}|^2}}{\frac{I_{e'0,e''\Delta\nu}}{|\bar{R}^{e'0,e''\Delta\nu}|^2}} \right) = - \left(\frac{E_{e'\nu'} - E_{e'0}}{k} \right) \frac{1}{T}. \quad (9)$$

In the F-C approximation, on the left hand side of Eq. (9) $|VTM|^2$ are replaced by FCF . We use Eq. (9) to determine the plasma temperature.

Thus, for determination of the plasma temperature we need the $FCFs$ and/or $VTMs$. In order to calculate these quantities we have to solve the vibrational Schrödinger equation for two electron states in question and to use the so obtained wave functions to compute the required quantities. If one wishes to avoid *ab initio* calculations of the potential energy curves for the electronic states in question, one has first to find a way how to extract the potential energy function that, combined with the corresponding kinetic energy operator, gives the energy eigenvalues as close as possible to those presented by Eq. (1). We have solved this problem combining the quantum-mechanical perturbative and variational approaches.

We assume the potential energy curve for vibrations in the form

$$V' = \frac{1}{2} k_3 x^2 + k_3 x^3 + k_4 x^4 + \dots; \quad (10)$$

where $x \equiv (r - r_e)$. Applying the perturbation theory we can relate the force constants $k, k_3, k_4 \dots$ to the coefficients in the expansion (1) [6]. E.g.,

$$k = \mu\omega^2 = 4\mu\pi^2 c^2 \tilde{\nu}^2, \quad k_3^x = \frac{2}{\sqrt{15}} \frac{\mu^{3/2} \omega^2}{\hbar} \sqrt{(\omega_e x_e) \hbar c}, \quad (11)$$

where μ is the reduced mass. In variational calculations of *FCFs* and *VTMs* the following procedure is applied: The potential energy curves are fitted to a polynomial of the type (10). An electronic state (typically ground state) is chosen as the referent one. The basis functions (being the eigenfunctions of a suitably chosen harmonic oscillator) are centered with respect to its equilibrium bond length, r_e . Then the potential energy curve of the other state as well as the bond-length dependence of the electric transition moment (if it is taken into account) are transformed into the polynomial series in the same variable as for the reference state. This enables very simple calculation of the *FCFs* and *VTMs*.

Table 1. $v' - v'' = -1$ and -2 sequences of the $B^2\Sigma^+ \rightarrow X^2\Sigma^+$ system of AlO. *T*: Band positions measured in our study [1]. *FCF*: Franck–Condon factors computed in the present study by employing molecular parameters from Ref. 5. *VTM* (squared) computed using molecular parameters from Ref. 5 and *ab initio* computed electric transition moment function [4]. *I*: Measured band intensities (in arbitrary units).

v', v''	<i>T</i>	<i>FCF</i>	<i>VTM</i> ²	<i>I</i>	<i>I/FCF</i>	<i>I/VTM</i> ²
0,1	19680	.235	.112	74	315→1.00	660→1.00
1,2	19590	.3315	.1545	81	244→.77	524→.79
2,3	19510	.357	.162	86	241→.76	530→.80
3,4	19435	.352	.155	63	179→.57	406→.62
4,5	19365	.340	.1445	56	165→.52	388→.59
5,6	19305	.332	.1355	47	141→.45	347→.53
0,2	18730	.0354	.0151	11	311→1.00	728→1.00
1,3	18660	.0806	.0334	20	248→.80	599→.82
2,4	18590	.124	.0496	30	242→.78	605→.83
3,5	18530	.160	.0618	30	187→.60	485→.67
4,6	18475	.189	.0695	30	159→.51	432→.59
5,7	18430	.208	.0725	31	149→.48	427→.59

We calculated the *FCFs* and *VTMs* for the $B^2\Sigma^+ - X^2\Sigma^+$ using a set of experimentally derived molecular parameters [5] and the *ab initio* computed electronic transition function [4]. The computed *FCFs* and squared *VTMs* (in atomic units) are presented in Table 1 and Fig. 2(a). In the last two columns in Table 1 are given the ratios of the measured intensity of bands and the computed *FCFs* and squared *VTMs*. These numbers should be proportional to the population of the vibrational levels of the $B^2\Sigma^+$ state. If

our approach is correct, they should be equal for the transitions $\nu' - \nu'' = -1$ and $\nu' - \nu'' = -2$ with the same quantum number ν' . We find the agreement between both sets of results satisfactory. In Table 1 are also presented the values for I/FCF and $I/|VTM|^2$ normalized to one for the $\nu', \nu'' = 0, 1$ and $0, 2$ transitions. These numbers should correspond to relative population of the excited vibrational ν' levels with respect to the $\nu' = 0$ one, $N_{e'\nu'} / N_{e'0}$.

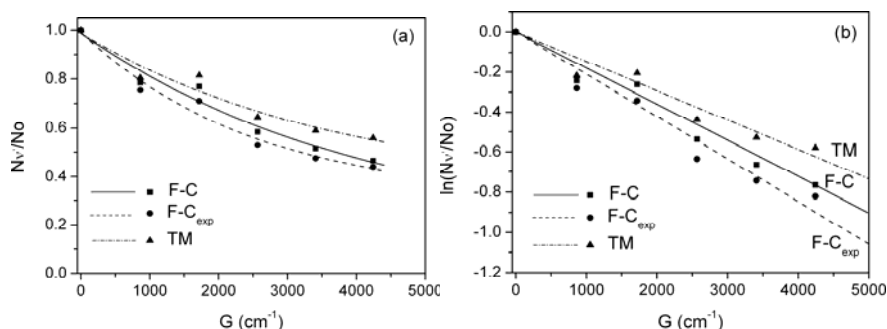


Figure 2. (a) Computed relative population of $\nu' = 0-5$ vibrational levels (from left to right) of the $B^2\Sigma^+$ electronic state of AlO. Measured intensity distributions within recorded band progressions are combined with the $FCFs$ (F-C) and $VTMs$ (TM) calculated in our study, as well as with the $FCFs$ (FCF_{exp}) published in Ref. 7. (b) Logarithm of the relative population of $\nu' = 1-5$ vibrational levels as function of the corresponding term values.

From these results we can extract the value for the mean temperature of our plasma. In Fig. 2b are displayed the values for $\ln(N_{e'\nu'} / N_{e'0})$ as functions of the vibrational term values (G) of the $B^2\Sigma^+$ state. A third set of results (FCF_{exp}), obtained by using the F-C factors published by Londhe et al. [7], is also presented. In spite of some deviations of the points from the straight lines, one can extract quite unambiguously three temperature values: $T \approx 8000$ K (FCF data), $T \approx 6800$ K (FCF_{exp} data), and $T \approx 9400$ K (VTM data). Note that the neglect of variation of the electric TM on the bond length causes a decrease of estimated temperature of almost 1500 K. We found it correct to conclude that the temperature of our plasma is $T = 8000 \pm 2000$ K. In Fig. 1 we present the intensity distribution simulated by employing the temperature value of 8000 K and the $FCFs$ computed in the present study (circles), i.e. combining $T = 9400$ K with the the $VTMs$.

Let us note that the above vibrational temperatures are very similar to the temperature we obtained very recently (unpublished results) employing several atomic lines of Al. This is an indication that the concept of “partial

local thermal equilibrium” can be extended such that we can speak about “local thermal equilibrium” that involves different excitation modes.

CONCLUSION

The present study started in the field of material science. The main goal was protecting of valve metals (concretely aluminium) from corrosion by means of oxide films, through the process of PEO. The morphology of the material was investigated using special electronics, optics, microscopy and crystallography. In order to obtain information about the processes that took place, emission spectra were recorded. Their assignment was carried out by tolls of atomic and molecular spectroscopy. The methods of quantum mechanics and the results of *ab initio* quantum chemical calculations were used for estimation of plasma parameters like temperature. Plasma composition was calculated in order to understand the appearance of the spectra measured and the characteristics of the system they originate from. It turned out that the systems we are dealing with can serve as a source of new spectroscopic information, and that the results of combined spectroscopic, quantum chemical, and statistical mechanical investigations can be used for monitoring the processes of material protecting.

ACKNOWLEDGEMENT

This work was supported by the Ministry for Education, Science and Technological Development of the Republic of Serbia (Grant no. 172040).

REFERENCES

- [1] S. Stojadinović, M. Perić, M. Petković, R. Vasilić, B. Kasalica, I. Belča and J. Radić-Perić, *Electrochim. Acta*, 2011, 56, 10122–9.
- [2] R.W.B. Pearse, A.G. Gaydon, *The Identification of Molecular Spectra*, Chapman and Hall, London, 1976.
- [3] K. P. Huber, G. Herzberg, *Molecular Spectra and Molecular Structure IV. Constants of Diatomic Molecules*, Van Nostrand, New York, 1979.
- [4] C. Zenouda, P. Blottiau, G. Chambaud, P. Rosmus, *J. Mol. Struct. (Theochem)*, 1999, 458, 61–72.
- [5] M.D. Saksena, M.N. Deo, K. Sunanda, S.H. Behere, C.T. Londhe, *J. Mol. Spectrosc.*, 2008, 247, 47–56.
- [6] R. Ranković, S. Stojadinović, M. Sarvan, B. Kasalica, M. Krmar, J. Radić-Perić, M. Perić, *J. Serb. Chem. Soc.*, 2012, 77, 1483–1528.
- [7] C.T. Londhe, K. Sunanda, M.D. Saksena and S.H. Behere, *J. Mol. Spectrosc.*, 2010, 263, 178–182.

COMPLEX MACROMOLECULAR ARCHITECTURES: CHALLENGES, STRATEGIES, APPLICATIONS

Bogdan C. Simionescu^{1,2}

¹*"Petru Poni" Institute of Macromolecular Chemistry, Iasi, Romania*

²*Department of Natural and Synthetic Polymers, "Gh. Asachi" Technical
University of Iasi, Romania*

ABSTRACT

Nowadays, the increased demand for a high life quality requires the development of materials and devices with high performances. The control of polymer functionality, polymer composition and polymer topology provides an opportunity to prepare polymeric materials for a large variety of applications in advanced domains. Fortunately, the design and even fabrication of tailor-made complex, multifunctional materials became a reality due to the last achievements in controlled polymer synthesis, chemistry, physics, biology, characterization and simulation/predicting tools improvement. To design and control the nanoscale organization of macromolecular materials to achieve novel functionality is no more a far goal, but remains a scientific challenge. Specific, efficient strategies for the generation of complex macromolecular architectures were developed in the last years, based on the use of functional organic compounds, including macromolecules, and architectural polymers as *bricks* in combination with old and new "building" alternatives.

The presentation will review the evolutions in polymer science, as exemplified by some literature and original data. The main included subjects refer to:

- controlled synthesis of block copolymers, considering the structure-properties-application relation
- combination of common polymer synthesis/modification techniques and self-assembling or complexation processes to develop multifunctional nanomaterials (i.e. nanovesicles, nanoparticles, cyclodextrines-based supramolecular architectures) with application in advanced domains (mainly biomedicine, electronics)
- preparation and application of hyperbranched polymers
- formation of programmable, complex assemblies intermediated by DNA control of material architecture and functions through stable, specific, and reversible molecular recognition.

All are pointing on the facilities offered by the new synthesis strategies in macromolecular chemistry to achieve the increased beneficiary requirements for high quality and multifunctionality of polymer-based products, conditioned by a rational design of the intermediates, product (no matter the macromolecular architecture complexity) and preparative protocols included therein.

SOME UNRESOLVED PROBLEMS AND VARIATIONS WITH THE BRIGGS-RAUSCHER OSCILLATING REACTION

S. Furrow

*Chemistry Department emeritus, Pennsylvania State University, Berks
College, Tulpehocken Rd., P.O. Box 7009, Reading, PA, 19610, USA*

ABSTRACT

The Briggs-Rauscher oscillating reaction has been known for over forty years, yet the underlying mechanism has not been fully resolved. The original skeleton mechanism drew heavily on the accepted mechanism for the Belousov-Zhabotinsky oscillator with pertinent H₂O₂-iodine species reactions added, but good agreement between experimental and simulated reactions has been lacking. The Bray-Liebhafsky oscillator can be considered a subset of the Briggs-Rauscher. Mechanisms for those two reactions have been developed more or less independently and some reactions are not shared between the two simulated systems. A different approach to modeling the Briggs-Rauscher reaction depends on adapting recent Bray-Liebhafsky steps. If the Briggs-Rauscher simulation was robust, it would open the way for explanation of some complex behavior including sudden transitions after oscillations cease, consecutive oscillations, and strong effects of very small amounts of additives.

INTRODUCTION

The Briggs-Rauscher (BR) chemical oscillator [1], consisting of acidic iodate, potassium iodate, manganous sulfate, malonic acid, and hydrogen peroxide has been known for over forty years, yet a robust mechanism remains elusive.

The BR oscillator is related to two other oscillating reactions: the Bray-Liebhafsky (BL) oscillating reaction, which typically runs at elevated temperature (50 – 70 °C) [2, 3], and consists of acidic iodate and hydrogen peroxide; and the Belousov-Zhabotinsky oscillating reaction (BZ) [4, 5] nominally containing sulfuric acid, potassium bromate, cerium (IV) sulfate catalyst, and malonic acid. Many substitutions are possible for the catalyst and the organic substrate.

The BL reaction [2, 3] (1921, 1931) was the first reported homogeneous oscillator. It attracted little attention, partly because of the suspicion that the phenomena was caused by some physical process, such as iodine or oxygen escape. It was widely believed that chemical oscillations were impossible. Only about a half dozen papers were published on the topic in the next 40 years.

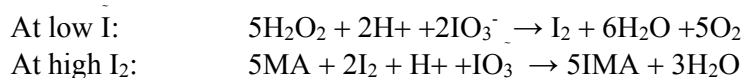
The BZ reaction [4](1958) had an inauspicious beginning as attempts by Boris Belousov to publish were initially rejected. Several years later, Anton Zhabotinski [5] carried out numerous investigations, and made some changes in the recipe. He published his work in 1964 (in a physics journal) and had no problem with the reviewers.

The recipe eventually made its way to the University of Oregon, where Field, Korosand Noyestook up the interpretation challenge, and published the FKN mechanism for the reaction in 1972 [6]. That mechanism remains the basis for extended versions. The BZ system now refers to a whole series of related oscillators. Several thousand papers have been published on various aspects of the reaction.

The mechanism involves overall reduction of bromate, oxidation of malonic acid, and periodic oxidation and reduction of cerium and bromine intermediates. A key feature is the autocatalytic increase in HOBrO when $[Br^-]$ is low.

In 1973, Briggs and Rauscher [1] combined components from the BL reaction and the BZ reaction, using $HClO_4$ or H_2SO_4 , KIO_3 , $MnSO_4$ or $Ce_2(SO_4)_3$, MA, and H_2O_2 . In 1982 two groups published very similar skeleton mechanisms to explain the reaction [7, 8]. The steps were essentially the same, although several of the assumed rate constants were different. See Table 1.

The starred reactions are analogous to the bromine reactions in the BZ mechanism.



The mechanism produced oscillations, but several problems soon surfaced. If the unknown rate constants were adjusted to give the correct frequency,

the $[I_2]$ amplitude was incorrect. The value for low $[I_2]$ was much lower in the simulation than in the experiment.

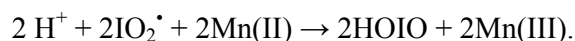
Table 1. Briggs-Rauscher skeleton model reactions

Reaction	Rate const. [7]	Rate const. [8]
* $H^+ + IO_3^- + I^- \rightarrow HOIO + HOI$	1.4×10^3	1.4×10^3
* $HOIO + H^+ + I^- \rightarrow 2HOI$	2×10^9	2×10^{10}
* $HOI + H^+ + I^- \leftrightarrow I_2 + H_2O$	$3.1 \times 10^{12}; 2.2$	$3.1 \times 10^{12}; 2.2$
* $2 HOIO \rightarrow H^+ + IO_3^- + HOI$	45.3	6×10^5
* $MA \leftrightarrow enol$	$3.9 \times 10^{-3}; 91$	40; 1.0
* $enol + I_2 \rightarrow IMA + H^+ + I^-$	9.1×10^5	1.0×10^4
$HOI + H_2O_2 \rightarrow H^+ + I^- + H_2O + O_2$	37	37
* $H^+ + IO_3^- + HOIO \leftrightarrow 2IO_2^\bullet + H_2O$	1.516×10^4	7.3×10^3
* $2IO_2^\bullet + 2Mn(II) \rightarrow 2HOIO + 2Mn(III)$	1.0×10^4	1.0×10^4
$Mn(III) + H_2O_2 \rightarrow Mn(II) + H^+ + HOO^\bullet$	3.2×10^4	3.2×10^4
$2 HOO^\bullet \rightarrow H_2O_2 + O_2$	7.5×10^5	7.5×10^5

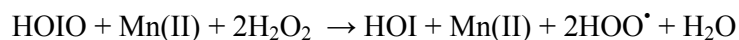
The experimental reaction rate for $2 HOIO \rightarrow H^+ + IO_3^- + HOI$ is much slower than assumed in the model [9, 10, 11]. The subsystems, $H_2O_2 - IO_3^- - Mn^{2+}$ - acid and $H_2O_2 - IO_3^-$ - acid are incorrectly modeled. Furthermore, there is no independent evidence for the reaction



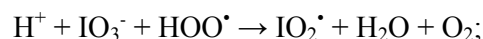
There is also no independent evidence for the following reaction.



To bypass the latter two difficulties, the following composite reaction was introduced [12]:



This allowed reduction of iodate by HOO^\bullet :



$H^+ + IO_3^- + HOIO \rightarrow 2IO_2^\bullet + H_2O$ was omitted as a radical source.

The mechanism for radical production remains unsolved. The reaction $H^+ + Mn(II) + H_2O_2 \rightarrow Mn(III) + HOO^\bullet$ is much too slow.

The mechanism can be simplified because the BR can run without a metal catalyst[1]. See Figure 1. The iodine production mode seems to involve radicals from an unknown source.

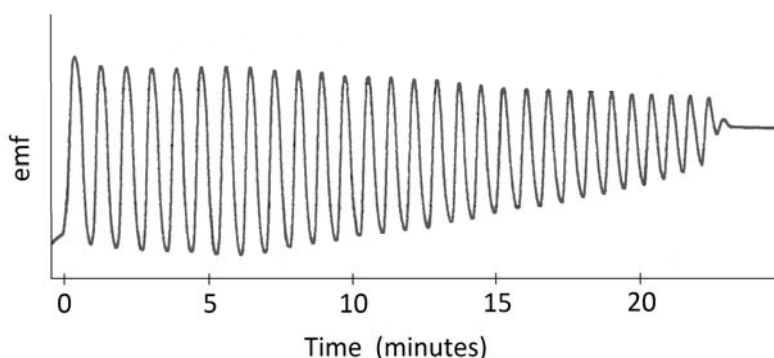


Figure 1. BR oscillations with no catalyst. [HClO₄] 0.10M, [KIO₃] 0.0033M, [H₂O₂] 2.0M, [MA] 0.0035M [13].

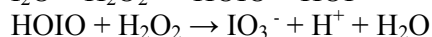
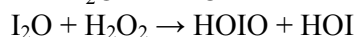
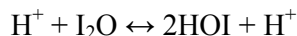
Bypassing for now the role of the metal catalyst, one can compare the BR system (no catalyst) with the BL system. It is possible to run the BL system at room temperature with very long periods [2, 14].

Table 2. Comparison of BR and BL systems.

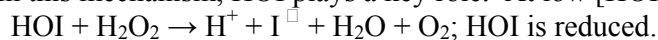
	BR no catalyst [13] 25°C	BL 60 °C [15]	BL 25 °C [14]
[HClO ₄]	0.10M	0.063M	0.030M
[KIO ₃]	0.0060M	0.10M	0.030M
[H ₂ O ₂]	1.5M	0.05M	0.16M
[MA]	0.0050M	0	0

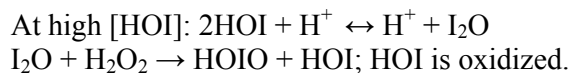
Schmitz [16] has published a non-radical mechanism for BL which agrees rather well with experiment. Values of rate constants are also given for 25°C.

The steps are the same as in Table 1, omitting the reactions of MA and Mn(II), and including the following non-radical iodine oxidation steps.



In this mechanism, HOI plays a key role. At low [HOI]:





It was recently shown [17] that reduction of iodate by hydrogen peroxide follows very different pathways at low $[\text{H}_2\text{O}_2]$ (BL conditions) compared to high $[\text{H}_2\text{O}_2]$ (BR conditions). A more complete account of application of this pathway to the BR will be given by Schmitz at this conference[18].

COMPLEX BEHAVIOR

The ending mode of the BR system depends on the initial conditions, but especially on the ratio of $[\text{MA}]$ to $[\text{IO}_3^-]$ [19]. When that ratio is high ($> 2:1$), the oscillations (state O) end in a state of low $[\text{I}_2]$ and low $[\text{I}^-]$ (state I). Eventually, there is a sharp transition to high $[\text{I}_2]$ and $[\text{I}^-]$ (state II). When the ratio is low, there is an immediate transition from oscillations to state II. See Figure 2 [20].

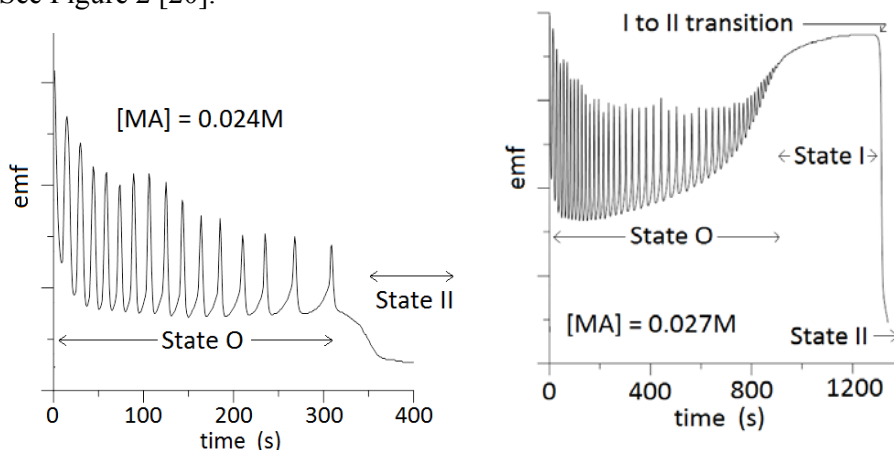


Figure 2. Transitions to state II, depending on concentration. $[\text{HClO}_4]$ 0.10M, $[\text{KIO}_3]$ 0.020M, $[\text{MnSO}_4]$ 0.0050M, $[\text{H}_2\text{O}_2]$ 1.2M.

It is believed that the $\text{I} \rightarrow \text{II}$ transition is due to autocatalytic decomposition of diiodomalonic acid (I_2MA) [19, 21]. Radicals generated by $\text{H}_2\text{O}_2 + \text{I}^-$ [22] may be a factor in the autocatalysis. Under certain conditions (very low $[\text{IO}_3^-]_0$), the $\text{I} \rightarrow \text{II}$ transition may repeat, with diminishing sharpness and amplitude. See Figure 3.

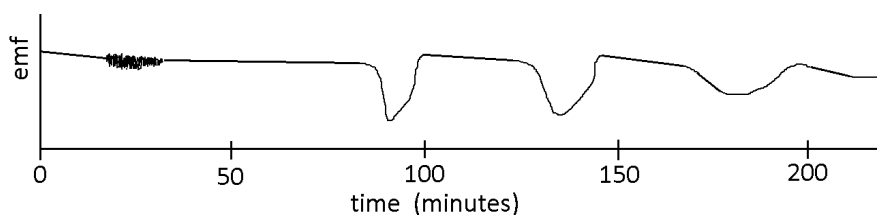


Figure 3. Consecutive oscillations at low [iodate]. $[\text{HClO}_4]$ 0.015M, $[\text{KIO}_3]$ 0.0033M, $[\text{MnSO}_4]$ 0.0020M, $[\text{MA}]$ 0.0066M, $[\text{H}_2\text{O}_2]$ 1.5M.

Near the critical ratio which defines whether state I or state II prevails, the system is very sensitive to stirring. For otherwise identical conditions, fast stirring leads to state $\text{O} \rightarrow \text{II}$; slow stirring leads to $\text{O} \rightarrow \text{I} \rightarrow \text{II}$.

Certain additives in millimolar concentrations stop oscillations for times dependent on additive concentrations. Cervellati *et al.* [23] have used this effect to classify the antioxidant effectiveness of various diphenols and natural products.

More than one organic substrate may lead to consecutive oscillations. Under certain conditions, each substrate may oscillate in turn. Many pairs, such as acetone – MA, [24], MA – MeMA, iodomalonic acid (IMA) – MA, IMA – MeMA, etc. [13], demonstrate this phenomenon. Under limited conditions, three sets of oscillations occur. See Figure 4.

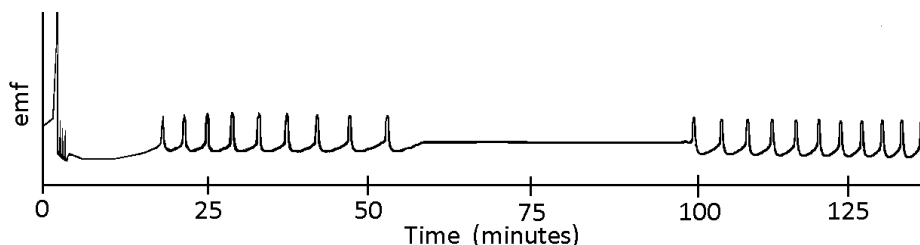


Figure 4. Consecutive oscillations with three substrates. $[\text{HClO}_4]$ 0.10M, $[\text{KIO}_3]$ 0.020M, $[\text{MnSO}_4]$ 0.010M, $[\text{H}_2\text{O}_2]$ 1.5M, [phenylmalonic acid] 0.0018M, [MeMA] 0.0058M, [acetone] 0.69M.

The gap between successive oscillations is probably due to relatively high $[\text{I}^-]$ from decomposition of one of the iodoproducts.

Phenol as an additive leads to complex behavior both in batch systems and in flow systems [13, 25]. See Figures 5 and 6. This phenomenon remains unexplained.

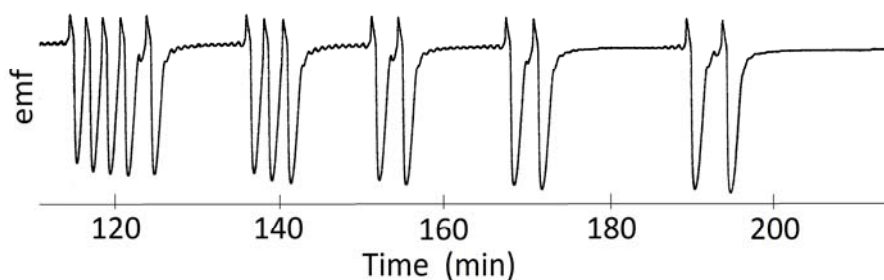


Figure 5. Emf (iodide electrode) vs. time. Bursting phenomena – BR with phenol; $[\text{HClO}_4] = 0.10 \text{ M}$; $[\text{KIO}_3] = 0.020 \text{ M}$; $[\text{MnSO}_4] = 0.0020 \text{ M}$; $[\text{MeMA}] = 0.032 \text{ M}$; $[\text{H}_2\text{O}_2] = 1.20 \text{ M}$; $[\text{phenol}] = 3.0 \times 10^{-5} \text{ M}$.

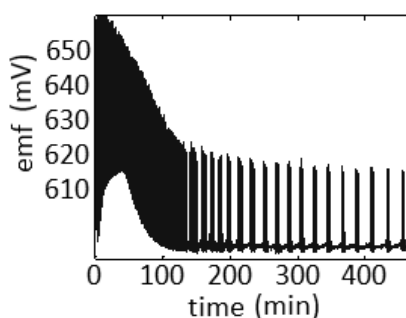


Figure 6. Emf (Pt electrode) vs. time. Flow system with sustained bursts. (High $[\text{I}^-]$, decreasing emf.) Initial concentrations: same as Figure 5.

CONCLUSIONS

The BR mechanism based on the BZ mechanism is inadequate to describe the basic BR oscillations. Basing the mechanism on the BL mechanism (without catalyst) is promising. With the basic BR mechanism in place, it should be feasible to explain other phenomena such as the sudden

transition to high [iodide], consecutive oscillations with several substrates, and bursting phenomena with phenol.

REFERENCES

- [1] T. S. Briggs, W. C. Rauscher, *J. Chem. Educ.*, 1973, 50, 496.
- [2] W. C. Bray, *J. Amer. Chem. Soc.* 1921, 43, 1262-1267.
- [3] W. C. Bray, H. A. Liebafsky, *J. Am. Chem. Soc.* 1931, 53, 38-48.
- [4] B. Belousov, *Sbornik ReforatorovpoRadiatsionneMeditsine, Medgiz, Moscow*, 1958, 145.

- [5] A.Zhabotinskii, *Biophysicka*, 1964, 9, 306-311.
- [6] R. Field, E. Koros, R. M. Noyes, *J. Am. Chem. Soc.*, 1972, 94, 8649-8664.
- [7] R. M. Noyes, S. D. Furrow, *J. Am. Chem. Soc.* 1982, 104, 45-48.
- [8] P. DeKepper, I. R. Epstein, *J. Am. Chem. Soc.* 1982, 104, 49-55.
- [9] Z. Noszticzius, E. Noszticzius, Z. A. Schelly, *J. Phys. Chem.*, 1983, 87, 510.
- [10] S. Furrow, *J. Phys. Chem.*, 1987, 91, 2129-2135.
- [11] G. Schmitz, S.D. Furrow, *Int. J. Chem. Kinet.*, 2013, 87, 2121.
- [12] S. D. Furrow, R. Cervellati, G. Amadori, *J. Phys. Chem. A*, 2002, 106, 5841.
- [13] S. D. Furrow, unpublished data.
- [14] G. Schmitz, S. D. Furrow, unpublished data.
- [15] H. A. Liebhaftsky, L. S. Wu, *J. Am. Chem. Soc.* 1974, 96, 7180.
- [16] (a) G. Schmitz, *Phys. Chem. Chem. Phys.*, 2010, 12, 6605; (b) G. Schmitz, *Phys. Chem. Chem. Phys.*, 2011, 13, 7102-7111.
- [17] G. Schmitz, S. D. Furrow, *Phys. Chem. Chem. Phys.*, 2012, 14, 5717-23.
- [18] G. Schmitz, S. D. Furrow, "Iodine Inorganic Reactions in Acidic Solutions and Oscillating Reactions", *Physical Chemistry 2014*, Belgrade.
- [19] V. K. Vanag, *J. Chem. Biochem. Kinet.* 1992, 2, 75-83.
- [20] R. Cervellati, E. Greco, private communication.
- [21] S. D. Furrow, R. Cervellati, E. Greco, *Z. Naturforsch.* 2012, 67b, 1-9.
- [22] M. C. Milenković, D. R. Stanisavljev, *J. Phys. Chem. A*, 2012, 116, 5541-5548.
- [23] R. Cervellati, S. D. Furrow, *Russ. J. Phys. Chem. A*, 2013, 87, 2121-2126, and references therein.
- [24] D. O. Cooke, *Int. J. Chem. Kinetics*, **1982**, 14, 1047.
- [25] Ž. Čupić, Lj. Kolar-Anić, S. Anić, S. Maćešić, J. Maksimović, M. Pavlović, M. Milenković, I. N. Bujanja, E. Greco, S. D. Furrow, R. Cervellati, *Helv. Chim. Acta*, 2014, 97, 321-333. Figure 6 is an unpublished plot from the Belgrade group.

STOICHIOMETRIC NETWORKS AND DYNAMICAL INSTABILITIES IN A MODEL OF THREE WAY CATALYTIC CONVERTER

O. Hadač, M. Kohout and I. Schreiber

*Department of Chemical Engineering, Institute of Chemical Technology,
Prague, Technická 5 166 28 Praha 6, Czech Republic.
(igor.schreiber@vscht.cz)*

ABSTRACT

This paper presents stability analysis of the reaction network corresponding to the mechanism of simultaneous oxidation of carbon monoxide CO, unburned hydrocarbons represented by acetylene C₂H₂ and reduction of nitrogen oxides NO_x, taking place in the three-way catalytic converter used in cars to remove noxious components from exhaust gases. We use stoichiometric network analysis as a method for decomposing the entire mechanism into irreducible subnetworks (extreme currents) and examining stability of corresponding steady states. This method allows for indication of those subnetworks, which may within a range of control parameters display instabilities leading to oscillations. Within those subnetworks the major positive and negative feedbacks are used to explain the oscillatory dynamics in chemical terms.

INTRODUCTION

Nonlinear dynamical effects in catalytic reactors including spatiotemporal patterns have been a subject of considerable research activity within past two decades, see, e.g. [1]. Multiple steady states and waves have been examined both theoretically and experimentally in a number of studies, most notably dynamics observed on the surface of a single Pt crystal [2]. Oscillations and patterns in heterogeneous reactors with supported catalyst are of great practical interest and have been also extensively studied [3]. This work focuses on exploring oscillatory instabilities in a three-way catalytic converter (TWC). This is the most common reactor for detoxification of automobile exhaust gases [4]. In the TWC, carbon monoxide, hydrocarbons and nitrogen oxides are converted into carbon dioxide, nitrogen and water vapor, respectively. The detailed TWC mechanism involving adsorption, desorption, surface reaction and gas-surface reaction steps in the Pt/Rh/CeO₂/γ-Al₂O₃ converter [5-7] was partly analyzed with the use of the reaction network approach [8]. It is well known

that the catalytic oxidation of CO alone shows a broad variety of complex nonlinear dynamics including oscillations on a supported Pt catalyst, oscillations on CuO/Al₂O₃ and periodic and chaotic behavior on Pt/Al₂O₃ pellets. Adding two more catalytic processes raises a question to what extent their interaction gives rise to new instabilities and pattern formation.

Generally, chemistry of catalytic converters is complex, heterogeneous reaction mechanisms include many positive and negative feedback loops and consequently reaction network theories may be conveniently applied. In this work, methods of stoichiometric network analysis (SNA) [9] are employed. The SNA provides a natural way of decomposing the entire chemical network into elementary subnetworks and identify those among them that are potentially a source of dynamical instabilities [10]. The TWC reaction mechanism [5-7] examined in this work can be intuitively decomposed into three subsystems -- CO oxidation, C₂H₂ oxidation (a prototypical hydrocarbon), and NO_x reduction. However, such a decomposition is not useful in finding whether there are dynamical instabilities. Based on a systematic analysis employing the SNA, Marek *et al.* [8] identified possible sources of oscillatory behavior in the CO oxidation subsystem of the TWC mechanism while Hadac *et al.* [11] examined dominant subnetworks inducing instabilities occurring due to synergy between the pairs of the three intuitive subsystems, as well as those accounting for instabilities in the entire TWC network. Below these dominant subnetworks are used to elucidate bifurcation diagrams for a lumped TWC model.

STOICHIOMETRIC NETWORK ANALYSIS

A chemical network is a set of n chemical species and m chemical reactions with known kinetics. The time evolution in a spatially homogeneous system at constant temperature is based on mass balance equations that may be written in a compact form as

$$\frac{dc}{dt} = Nr(c) \quad (1)$$

where c is the n -vector of concentrations of the species, $r(c)$ is the m -vector of the rate laws and N is the stoichiometric matrix. The Eq. (1) may be readily accommodated to represent a flow system provided that N and r involve pseudoreactions corresponding to inflows and outflows (zero and first order terms, respectively). According to the stoichiometric network analysis, stability of steady states of Eq. (1) can be conveniently analyzed by determining the structure of the

null space of N using convex analysis and examining the Jacobi matrix upon reformulating the system in terms of convex parameters [9].

Table 1. Detailed reaction mechanism of the TWC; * represents a noble metal (Pt) catalytic site and s indicates an oxygen storing (Ce) site).

No. Reaction	Reaction rate
1 $\text{CO} + * \rightleftharpoons \text{CO}^*$	$\mathcal{R}_1 = k_1^f L_{\text{NM}} c_{\text{CO}} \theta_* - k_1^b L_{\text{NM}} \theta_{\text{CO}^*}$
2 $\text{O}_2 + 2* \rightarrow 2\text{O}^*$	$\mathcal{R}_2 = k_2 L_{\text{NM}} c_{\text{O}_2} \theta_*$
3 $\text{CO}^* + \text{O}^* \rightarrow \text{CO}_2 + 2*$	$\mathcal{R}_3 = k_3 L_{\text{NM}} c_{\text{CO}^*} \theta_{\text{O}^*}$
4 $\text{CO} + \text{O}^* \rightleftharpoons \text{OCO}^*$	$\mathcal{R}_4 = k_4^f L_{\text{NM}} c_{\text{CO}} \theta_{\text{O}^*} - k_4^b L_{\text{NM}} \theta_{\text{OCO}^*}$
5 $\text{OCO}^* \rightarrow \text{CO}_2 + *$	$\mathcal{R}_5 = k_5 L_{\text{NM}} \theta_{\text{OCO}^*}$
6 $\text{C}_2\text{H}_2 + * \rightleftharpoons \text{C}_2\text{H}_2^*$	$\mathcal{R}_6 = k_6^f L_{\text{NM}} c_{\text{C}_2\text{H}_2} \theta_* - k_6^b L_{\text{NM}} \theta_{\text{C}_2\text{H}_2^*}$
7 $\text{C}_2\text{H}_2^* + 2* \rightleftharpoons \text{C}_2\text{H}_2^{**}$	$\mathcal{R}_7 = k_7^f L_{\text{NM}} \theta_{\text{C}_2\text{H}_2^*} \theta_*^2 - k_7^b L_{\text{NM}} \theta_{\text{C}_2\text{H}_2^{**}}$
8 $\text{C}_2\text{H}_2^* + 3\text{O}^* \rightarrow 2\text{CO}^* + \text{H}_2\text{O} + 2*$	$\mathcal{R}_8 = k_8 L_{\text{NM}} \theta_{\text{C}_2\text{H}_2^*} \theta_{\text{O}^*}^3$
9 $\text{C}_2\text{H}_2^{**} + 3\text{O}^* \rightarrow 2\text{CO}^* + \text{H}_2\text{O} + 4*$	$\mathcal{R}_9 = k_9 L_{\text{NM}} \theta_{\text{C}_2\text{H}_2^{**}} \theta_{\text{O}^*}^3$
10 $\text{C}_2\text{H}_2 + \text{O}^* \rightleftharpoons \text{C}_2\text{H}_2\text{O}^*$	$\mathcal{R}_{10} = k_{10}^f L_{\text{NM}} c_{\text{C}_2\text{H}_2} \theta_{\text{O}^*} - k_{10}^b L_{\text{NM}} \theta_{\text{C}_2\text{H}_2\text{O}^*}$
11 $\text{C}_2\text{H}_2\text{O}^* + 2\text{O}^* \rightarrow 2\text{CO}^* + \text{H}_2\text{O} + *$	$\mathcal{R}_{11} = k_{11} L_{\text{NM}} \theta_{\text{C}_2\text{H}_2\text{O}^*} \theta_{\text{O}^*}^2$
12 $\text{O}_2 + 2s \rightarrow 2\text{O}^s$	$\mathcal{R}_{12} = k_{12} L_{\text{OSC}} c_{\text{O}_2} \xi_s$
13 $\text{CO}^* + \text{O}^s \rightarrow \text{CO}_2 + * + s$	$\mathcal{R}_{13} = k_{13} L_{\text{NM}} c_{\text{CO}^*} \xi_{\text{O}^s}$
14 $\text{C}_2\text{H}_2^* + 3\text{O}^s + * \rightarrow 2\text{CO}^* + \text{H}_2\text{O} + 3s$	$\mathcal{R}_{14} = k_{14} L_{\text{NM}} \theta_{\text{C}_2\text{H}_2^*} \xi_{\text{O}^s}^3$
15 $\text{CO}_2 + \gamma \rightleftharpoons \text{CO}_2^\gamma$	$\mathcal{R}_{15} = k_{15}^f L_{\text{SUP}} c_{\text{CO}_2} \delta_\gamma - k_{15}^b L_{\text{SUP}} \delta_{\text{CO}_2^\gamma}$
16 $\text{NO} + * \rightleftharpoons \text{NO}^*$	$\mathcal{R}_{16} = k_{16}^f L_{\text{NM}} c_{\text{NO}} \theta_* - k_{16}^b L_{\text{NM}} \theta_{\text{NO}^*}$
17 $\text{NO}^* + * \rightarrow \text{N}^* + \text{O}^*$	$\mathcal{R}_{17} = k_{17} L_{\text{NM}} \theta_{\text{NO}^*} \theta_*$
18 $\text{NO}^* + \text{N}^* \rightarrow \text{N}_2\text{O}^* + *$	$\mathcal{R}_{18} = k_{18} L_{\text{NM}} \theta_{\text{NO}^*} \theta_{\text{N}^*}$
19 $\text{N}_2\text{O}^* \rightarrow \text{N}_2\text{O} + *$	$\mathcal{R}_{19} = k_{19} L_{\text{NM}} \theta_{\text{N}_2\text{O}^*}$
20 $\text{N}_2\text{O}^* \rightarrow \text{N}_2 + \text{O}^*$	$\mathcal{R}_{20} = k_{20} L_{\text{NM}} \theta_{\text{N}_2\text{O}^*}$
21 $\text{N}^* + \text{N}^* \rightarrow \text{N}_2 + 2*$	$\mathcal{R}_{21} = k_{21} L_{\text{NM}} \theta_{\text{N}^*}^2$
22 $\text{NO} + \text{O}^* \rightleftharpoons \text{NO}_2^*$	$\mathcal{R}_{22} = k_{22}^f L_{\text{NM}} c_{\text{NO}} \theta_{\text{O}^*} - k_{22}^b L_{\text{NM}} \theta_{\text{NO}_2^*}$
23 $\text{NO}_2^* \rightleftharpoons \text{NO}_2 + *$	$\mathcal{R}_{23} = k_{23}^f L_{\text{NM}} \theta_{\text{NO}_2^*} - k_{23}^b L_{\text{NM}} c_{\text{NO}_2} \theta_*$

In the first step the set of steady state reaction rate vectors corresponding to extreme (or elementary) subnetworks is found. Any steady state reaction rate vector in the chemical network can be obtained as a linear combination of the rate vectors of the extreme subnetworks, which in geometrical terms are edges of an open convex cone in the nonnegative orthant of the null space. Certain k-tuples of the edges span faces of the cone constituting thus a natural hierarchy of increasingly complex subnetworks.

In the second step linear stability analysis is applied to edges/faces to reveal mechanistic sources of multiple steady states or oscillatory behavior. The stability of a subnetwork is indicated by principal subdeterminants of a matrix closely related to the Jacobi matrix. Of particular interest are oscillatory instabilities occurring via Hopf bifurcation. Namely, the subnetworks accounting for oscillations can be used to classify the chemical mechanism according to the arrangement of positive and negative feedback loops and to determine the role of species in the oscillations [12]. Specifically, at the Hopf bifurcation, various methods can be applied to determine the role, for example, by calculating mutual phase shifts of chemical species [10], which can be calculated from the eigenvectors associated with the pair of pure imaginary eigenvalues of the Jacobi matrix. Of interest here are three types of species playing an essential role in the oscillations: type X is the autocatalytic species that appears in the autocatalytic loop; type Z provides negative feedback controlling the oscillations and type Y that removes the type X species from the autocatalytic cycle.

LUMPED MODEL OF TWC

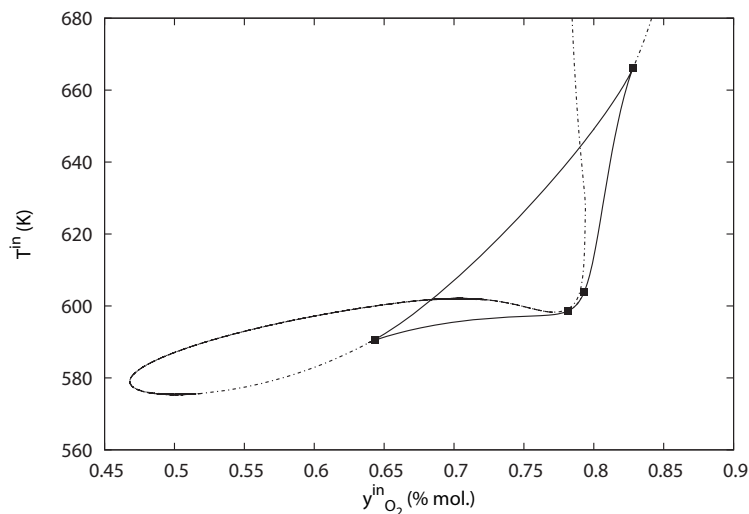
The model conforming with Eq. (1) is describing a simplified situation where the catalytic converter is treated as an ideally mixed isothermal system. Thus spatial distribution along the converter is neglected (transport phenomena in longitudinal direction are assumed fast). On the other hand, mass transfer from the gas phase onto the catalytic surface is included in the model. Input parameters of this lumped model are: inflow rate, inflow concentrations of reactants, inflow temperature, the loading of the catalyst with noble metal L_{NM} and the loading with oxygen storing cerium L_{OSC} . The inflow concentration of oxygen and inflow temperature are chosen as bifurcation parameters and continuation techniques [13] are used to construct a bifurcation diagram showing parameter regions where oscillations, multiple steady states and excitable steady states occur.

RESULTS AND DISCUSSION

The overall TWC mechanism can be intuitively decomposed into two subsystems: the mechanism combining oxidations of CO and C_2H_2 , and mechanism of simultaneous CO oxidation and NO_x reduction. These simplified cases result from assuming that either NO_x or hydrocarbons are absent from the inlet gas stream, respectively. Our primary goal is to examine to what extent the instabilities in these major subsystems differ and how is this difference reflected in the dynamics under the CFR conditions. Both subsystems are examined in detail using the SNA elsewhere [11], here we focus on the relation between bifurcation behavior of the model and the oscillatory subnetworks found by the SNA for the case of oxidation of CO and C_2H_2 .

Fig. 1 shows the bifurcation diagram in the parameter plane of the inlet molar fraction of oxygen $y_{O_2}^{in}$ and the inlet temperature T^{in} for the lumped system. We use $L_{NM} = 40 \text{ mol m}^{-3}$, $L_{OSC} = 20 \text{ mol m}^{-3}$. The closed bow-shaped curve of the saddle-node bifurcations encloses a region of multiple steady states.

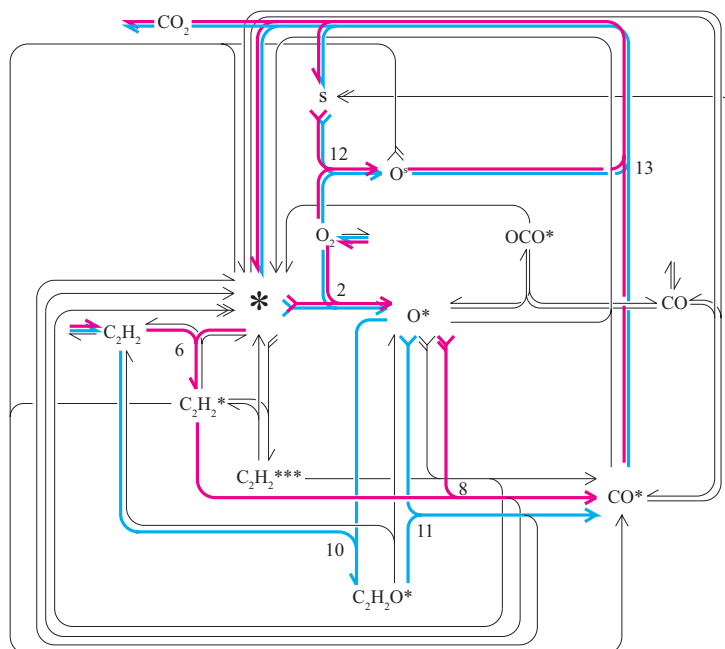
Figure 1. Bifurcation diagram for CO and C_2H_2 oxidation in the parameter plane $y_{O_2}^{in} - T^{in}$; full-line -- curve of saddle-node bifurcation, dashed line -- curve of Hopf bifurcation.



The stoichiometric amount of oxygen required for complete removal of CO_2 and C_2H_2 corresponds to $y_{\text{O}_2}^{\text{in}} = 0.78$ mol %, which is dividing the region into sub- and superstoichiometric domains. In addition, the Hopf bifurcation curves terminating at the saddle-node bifurcation mark two regions of stable oscillatory dynamics outside the multiple steady state region and two subregions of a unique stable steady state within the multiple steady state region. The dynamics within these two subregions is excitable, i.e., a small but finite perturbation of the steady state causes a large excursion before returning to the steady state. There is bistability elsewhere in the region of the multiple steady states. Remarkably, the two regions of stable oscillations are distinguished by occurring in the sub- and superstoichiometric regions. The same observation holds for the excitability, whereas the region of bistability falls within the substoichiometric domain.

These observations can be explained by using the SNA. The CO & C_2H_2 network with the two embedded oscillatory subnetworks can be conveniently represented by the network diagram shown in Fig. 2. Here each reaction along with stoichiometry and reaction orders is displayed as a multi-tail/multi-head arrow with the number of feathers/barbs indicating stoichiometric coefficients of reactants/products and, additionally, the number of left feathers indicate the reaction order of the corresponding reactant. In the substoichiometric region the dominant process is as follows: upon adsorption of oxygen on Pt sites the gaseous C_2H_2 reacts with O^* and the intermediate species C_2H_2^* is successively oxidized to CO^* and CO_2 via steps 11 and 13 that involve oxygen adsorbed both on Pt and Ce sites. The hydrocarbon in the gas interacts with the adsorbed oxygen - a process known as Eley-Rideal mechanism. A detailed analysis of the role of species [11] further reveals that the autocatalytic cycle is formed by linking three type X species: $*$, O^* and CO^* , while the negative feedback is provided by the flow-controlled availability of oxygen (type Z species) and C_2H_2 plays the role of the exit species (type Y). In the superstoichiometric region there is a different source of the oscillatory instability. Here the dominant process involves adsorption of both O_2 and C_2H_2 on Pt sites prior their interaction. More specifically, the autocatalytic loop includes the species $*$, C_2H_2^* and CO^* via the steps 6, 8 and 13. As in the previous case, this necessitates the involvement of Ce site used in step 13. This type of interaction is known as Langmuir-Hishelwood mechanism. When compared, the roles of the negative feedback species and the exit species in the two subnetworks are exchanged, here C_2H_2 (type Z) is controlling the oscillations via step 6 and O_2 (type Y) removes $*$ from the autocatalytic cycle via the exit reaction 2.

Figure 2. Stoichiometric network of CO & C₂H₂ oxidation subsystem. Blue line - dominant substoichiometric oscillatory subnetwork, red line - dominant superstoichiometric oscillatory subnetwork.



CONCLUSIONS

A systematic approach combining stability analysis of complex reaction networks and reactor dynamics was applied to a cross-flow catalytic tubular reactor for removal of noxious components from exhaust gases with the use of a detailed kinetic scheme of simultaneous oxidations of carbon monoxide and acetylene (a representative hydrocarbon) and reduction of nitrogen oxides. To demonstrate various possibilities for oscillatory instabilities, the system was simplified to a lumped model by neglecting longitudinal transport. The mechanism was split into CO & C₂H₂ and CO & NO_x subsystems. Only the former is analyzed here using the stoichiometric network analysis to identify positive and negative feedbacks that cause oscillations of reaction components in the lumped model. These results were used to explain the structure of the bifurcation

diagrams obtained by numerical continuation. In particular, regions of oscillatory dynamics are understood in terms specific subnetworks involving certain species that play crucial role in the alternating dominance of positive and negative feedback during oscillations. The occurrence of bistability/excitability of steady states is also readily explained by permanent/transient dominance of the corresponding positive or negative feedback loops.

ACKNOWLEDGEMENT

This work was supported by the grant GACR 209/09/2091.

REFERENCES

- [1] M. Sheintuch, N.I. Jaeger (Eds), *Spatiotemporal Catalytic Patterns*, Catalysis Today, 2001, 70, 285–426.
- [2] R. Imbihl, G. Ertl, *Chemical Reviews*, 1995, 95, 697–733.
- [3] M. M. Slinko, *Catalysis Today*, 2010, 154, 38-45.
- [4] R. M. Heck, J. Wei, J. R. Katzer, *AIChE Journal*, 1976, 22, 477–484.
- [5] R. H. Nibbelke, A. J. Nievergeld, J. H. Hoebink, G. B. Marin, *Applied Catalysis B: Environmental*, 1998, 19, 245–259.
- [6] J. M. Harmsen, J. H. Hoebink, J. C. Schouten, *Chemical Engineering Science*, 2001, 56, 2019–2035.
- [7] J. M. Harmsen, J. H. Hoebink, J. C. Schouten, *Catalysis Letters*, 2001, 71, 81–90.
- [8] M. Marek, M. Schejbal, P. Kočí, V. Nevorál, M. Kubíček, O. Hadač, I. Schreiber, *Chaos*, 2006, 16, 1–13.
- [9] B. L. Clarke, *Stability of complex reaction networks*. *Advances in Chemical Physics*, 1980, 43, 1–278.
- [10] J. Ross, I. Schreiber, M. O. Vlad, *Determination of Complex Reaction Mechanisms*, Oxford University Press, New York, 2006.
- [11] O. Hadač, I. Schreiber, to be submitted to *Journal of Physical Chemistry*, 2014.
- [12] M. Eiswirth, A. Freund, J. Ross. *Mechanistic classification of chemical oscillators and the role of species*. *Advances in Chemical Physics*, 1991, 80, 127–199.
- [13] M. Kohout, I. Schreiber, M. Kubíček, *Computers & Chemical Engineering*, 2002, 26, 517–527.

ORIGIN OF CHIRALITY OF BIOMOLECULES

I. Gutman

¹ *Faculty of Science, University of Kragujevac.*

ABSTRACT

It is not known why living organisms on the Earth contain (almost exclusively) L-amino acids and D-sugars, and why not D-amino acids and L-sugars, i.e., why biomolecules are homochiral. This puzzle, in an obvious manner related to the origin of life, attracts the attention of scientists since the times of Pasteur (1860s). Recent experimental and theoretical findings, relevant for this matter will be outlined. As a kind of surprise, earlier attempts to rationalize homochirality by parity non-conservation in weak interactions combined with amplification by convenient kinetic models, appear to be a dead-end. Another, simple, logical, and experiment-based explanation is envisaged.

NMR IN BIOMEDICINE: FROM IMAGING TO METABOLOMICS

S. Macura

*Department of Biochemistry and Molecular Biology
Mayo College of Medicine, Mayo Clinic
Rochester, Minnesota, 55905, USA*

ABSTRACT

The role of (physical) chemistry in understanding the living things was recognized long time ago [1] and many physicochemical methods play crucial role in medical practice and research today. One such method, is nuclear magnetic resonance (NMR), which became indispensable tool in medical practice mostly through magnetic resonance imaging (MRI). However, the versatility and its noninvasive character make the application of NMR much broader. Many diseases and disorders could be identified at the molecular level, therefore in vivo measurement of diffusion, perfusion, pH, oxygenation level, metabolite concentration etc., is of a great value for medical diagnostics and research. In this presentation the application of NMR in biomedical research is illustrated through various examples from MRI of rodent organs [2] via MRS (NMR spectroscopy) of mouse brain [3], MRM (NMR microscopy) of pathology specimens [4] to NMR metabolomics of tissue extracts and body fluids [5].

REFERENCES

- [1] J. J. Abel, 'Experimental and Chemical Studies of the Blood with an Appeal for More Extended Chemical Training for the Biological and Medical Investigator', *Science* (6 Aug 1915), 42, 176. ("As soon as we touch the complex processes that go on in a living thing, be it plant or animal, we are at once forced to use the methods of this science [chemistry]. [...] For the further analysis of these phenomena which are in flux and flow, the investigator must associate himself with those who have labored in fields where molecules and atoms, rather than multicellular tissues or even unicellular organisms, are the units of study.")
- [2] Denic A, Macura SI, Mishra P, Gamez JD, Rodriguez M, Pirko I. *Neurotherapeutics*. 2011 Jan; 8(1):3-18.
- [3] 19. Lee MR, Denic A, Hinton DJ, Mishra PK, Choi DS, Pirko I,

- Rodriguez M, Macura SI, *Bioanalysis*. 2012 Jul; 4(14):1787-804.
- [4] Macura S, Mishra PK, Gamez JD, Pirko I., *Mag. Res. Med.*, 71:1989–1994 (2014)
- [5] Nemutlu E, Juranic N, Zhang S, Ward LE, Dutta T, Nair KS, Terzic A, Macura S, Dzeja PP., *Anal Bioanal Chem*. 2012 May; 403(3):697-706.

NUCLEATION RATE SURFACES AS A NEW TOOL FOR ADVANCED MATERIAL DESIGN

M. P. Anisimov

*Nanoaerosol Research Laboratory, FSBSI Technological Design
Institute of Scientific Instrument Engineering SB RAS (TDISIE SB RAS,
anisimovmp@mail.ru), 41 Russkaya Street, 630058, Novosibirsk, Russia.*

ABSTRACT

One can find in scientific literature a pretty fresh idea of the nucleation rate surfaces design over the diagrams of phase equilibria. That idea looks like profitable for the nucleation theory development and for various practical applications where predictions of theory have no high enough accuracy for today. The common thermodynamics has no real ability to predict parameters of the first order phase transition. Kinetics of that transition is complicate problem as well. It is known widely that many-body problem has no exact solution. The usual way of any theory is to reduce the many-body problem to one body in some field. The features of one body and the field are adjusted usually to get the reasonable compliance to the empirical results. Relation of the theoretical and empirical results is not good enough in case of the Nucleation Theory.

Nucleation experiment can be provided in very local nucleation conditions even the nucleation takes place from the critical conditions down to the absolute zero temperature limit and from zero nucleation rates at phase equilibria up to the spinodal conditions. Theory predictions have low reliability as a rule. It is well known that any phase diagram has several lines of phase equilibria. It is easy to show that each line of phase equilibria generates the nucleation rate surface in space of nucleation process parameters. It means that one has multi sheet nucleation rate surfaces in the common case. Each nucleation rate surface is related to one phase state generation, or it is related to a single channel of nucleation. Semiempirical design of the nucleation rate surfaces over diagrams of phase equilibria have a potential ability to provide a reasonable quality information on nucleation rate for each channel of nucleation. Consideration and using of the nucleation rate surface topologies to optimize synthesis of a given phase of the target material can be available when data base on nucleation rates over diagrams of phase equilibria will be created.

INTRODUCTION

One reason for nucleation theory problem is the application of inconsistent assumptions that are used to interpret the experimental results. The most experimental data on vapor nucleation are interpreted as a one-surface (one nucleation channel) approximation of a nucleation theory. However, two or more nucleation channels are really present in most systems as it was recently reported by Anisimov et al [1].

We need to admit now that agreement between experimentally measured vapor nucleation rates and current theoretical predictions exists for only a limited number of systems. It was found long ago that the lines of phase equilibria are continued by line of unstable equilibria for metastable systems. Vortisch et al. concluded [2] retrospectively that “the temperatures and compositions leading to a given nucleation rate roughly follow the melting curve.” That kind of empirical result initiated the two-sheet vapor nucleation rate surface design (Figure 1) twenty years ago in the vicinity of the triple point [3].

EXPERIMENTAL

To empirically detect a single nucleation channel one needs to have the appropriate measuring system, but these kinds of systems are not currently under active development. The semiempirical approach permits the prediction of a realistic topology for the nucleation rate surface. That topology can be designed over the phase equilibria diagrams [1]. One needs at least several experimental points on the nucleation rate surface and the phase diagram to effectively develop these surfaces [4].

A short history of semiempirical design of the nucleation rate surfaces over phase equilibrium diagrams will be presented. This approach involves a simple idea developed by Anisimov et al. [1], that nucleation rate surfaces arise up from the phase equilibria lines. It means that each line of the real and metastable phase equilibria produces two nucleation rate surfaces (for two areas of the adjacent metastable states).

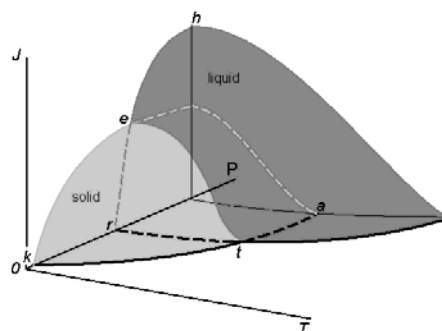


Figure 1. Nucleation rate, J , surface topology for triple point vicinity.

Vapor-solid (light grey) and vapor-liquid (dark grey) nucleation separately. T is temperature; P is pressure; kta is line of vapour-solid and rtc is vapour-liquid equilibria; t is triple point; c is critical one

Both surfaces reflect the nucleation kinetics for each of two metastable phases that can be joined by an equilibrium line.

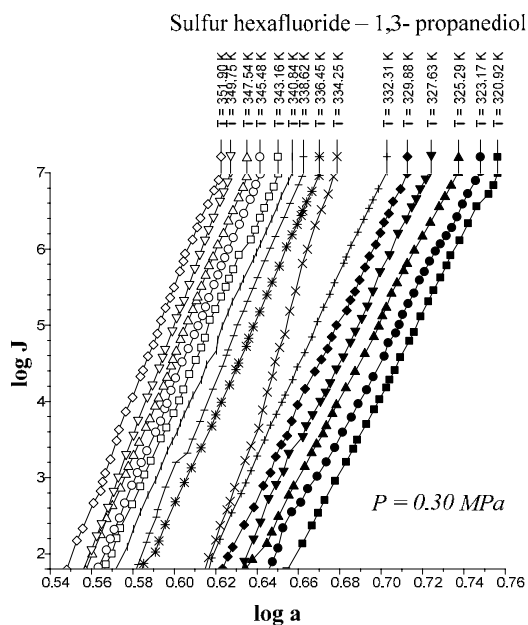


Figure 2. Sulfur hexafluoride – 1,3- propanediol nucleation at pressure of 0.30 MPa.

Experimental detection of nucleation rate for each of two individual vapor nucleation rate channels, which are generating two single nucleation rate surfaces for vicinity of the triple point, one can see in article [5]. That result is unique to the present time. However, the most experimental data are interpreted in the one-surface (one channel) approximation. The theory not yet adequately developed to accurately predict two-channel nucleation unfortunately.

RESULTS AND DISCUSSION

Empirical studies of vapor nucleation are of significant interest as this is a fundamentally important problem of the first-order phase formation kinetics description. The current technical level of research for the study of aerosol formation is of fairly high quality, but there is no theory that is suitable for quantitative prediction of the experimental vapor nucleation rates. In the common case, the theory of phase transitions cannot predict the phase transition parameters such as pressure and temperature for nowadays.

Theory involves a number of assumptions to describe small clusters [6]. Further, when the size dependencies of the surface tension and density of nuclei were taken into account [7] and the inherent degrees of freedom were used to calculate the statistical sum for a nascent cluster [8], agreement between theoretical and experimental results get worse. Semiempirical design over diagram of phase equilibria is applied for metastable volume construction [1]. That way has a considerable potential in the nucleation rate description.

A Laminar Flow Diffusion Chamber [9] is widely used for nucleation rate measurements of vapor-gas systems. A simple relation [10] can be used as criterion, A , to detect a nucleation rate surface singularity which is initiated by phase transitions of the first order for the surface section at $J(T,S) = \text{constant}$:

$$\left(\frac{\partial \ln J}{\partial T}\right)_{S,P_1\dots P_n} + \left(\frac{\partial \ln J}{\partial \ln S}\right)_{T,P_1\dots P_n} \left(\frac{\partial \ln S}{\partial T}\right)_{J,P_1\dots P_n} = A.$$

The criterion value, A , is equal to zero if the vapor nucleation rate surface $J = J(T,S)$ has no singularities. Here S and P_i are vapor supersaturation and partial pressure of component i at temperature T of system respectively. Singularity in the nucleation rate surface breaks the local condition for surface continuity and monotony. Criterion, A , is deviating from zero value in that case. The A -criterion provides a sensitive tool for the detection of singularities in nucleation rate surfaces.

Clear singularities presence was found for data in Figures 2&3. These singularities can be attributed to unknown earlier phase transitions of the first order in the vicinity of critical line of binary (vapor-gas) systems. The phase transition temperature clearly decreases with a rise in sulfur hexafluoride pressure (P). Presumably the sulfur hexafluoride concentration in a condensed solutions increases proportionally to the total pressure. Mole fraction of sulfur hexafluoride grows up in a critical embryo composition. Naturally for that trend that phase transitions in subcritical conditions, which are higher a sulfur hexafluoride critical temperature, are shifting down to critical point temperature. New phase transitions of the first order probably produce surface. It needs to get more data to reveal the real topology of the phase transition surface.

That surface involves critical points of gas and vapor, jointed by critical line for sulfur hexafluoride and propanediol system in the present case. A vapor-gas as binary system has a three dimensional volume of metastable states, which is bounded by surfaces of phase equilibria and

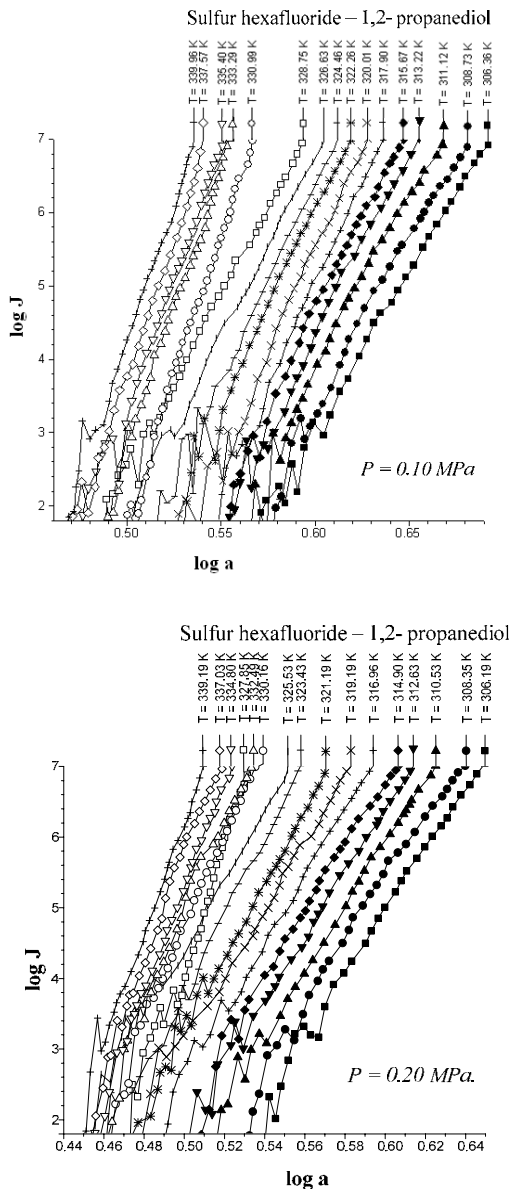


Figure 3. Sulfur hexafluoride – 1,2- propanediol nucleation rates at total pressures of 0.10 and 0.20 MPa. These surfaces are jointed along the critical line of binary system which can be calculated using one of the correlations [11]. The glycerine vapor activities (a) on nucleation temperatures (T) for two

levels of the nucleation rates (J) are presented in article [9] for a total pressure 0.10 MPa. The same shapes are appeared for total pressure of 0.20 MPa. The clear discontinuities, which are produced by melting points, can be seen for all cases.

Let look the reasons for these discontinuities. In our experiments we have transition from a nucleation rate surface of one phase to other. In common case nucleation rates can be expressed such as $J = B \exp(-\Delta G/kT)$. In that equation $\Delta G = n^*(\mu_{cond} - \mu_{vapor}) + f$; where n^* is number of molecules in the critical embryos; $\mu_{cond} - \mu_{vapor}$ is a chemical potential difference for the condensed phases and vapor for the macro-scale samples; f is an excess energy of a critical embryo comparing with n^* molecules in a bulk condensed phase (presumably $\frac{\partial f}{\partial T}$ has a discontinuity at conditions of the phase transition);

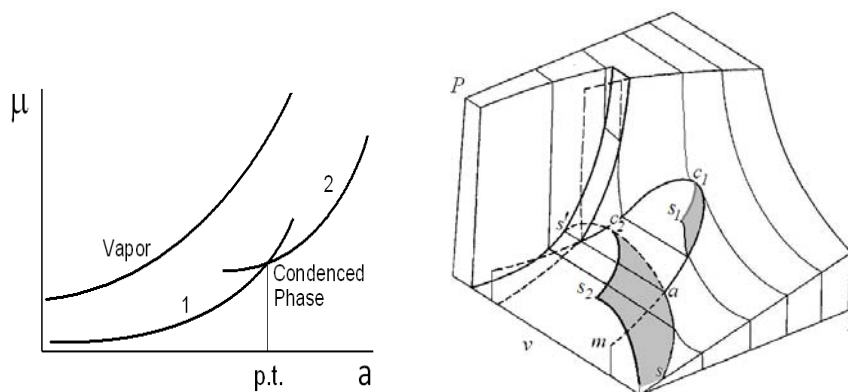


Figure 4. Schematic presentation of a chemical potentials, μ , on vapor activity (a) for the condensed phases of 1 and 2 (left). Pressure (P) - Temperature (T) - partial volume (v) diagram for a single component system with a line ($s'a$) of the triple points. Lines mac_1 and sac_2 are the vapour-liquid and vapour-solid binodals. c_1 and c_2 are critical points (right).

Partial derivative $\frac{\partial \mu_{cond}}{\partial T}$ is broken at conditions for a phase transition of the first order; μ_{vapor} is a continuous and monotonous function of temperature. The partial derivatives $\frac{\partial \Delta \mu}{\partial T}$ and $\frac{\partial f}{\partial T}$ are negative and positive quantities. In some cases their difference $(\frac{\partial \Delta \mu}{\partial T} - \frac{\partial f}{\partial T})$ as well as A -criterion can be equal

to zero. It means that a nucleation rate surface has a local continuity and monotony in that case. Figures 2&3 illustrate an impact of a critical embryo phase change on the nucleation rate surface topology.

It may be that there is a sufficient experimental variation in the nucleation rate measurements which is preventing the detection of this kind of nucleation event. A major problem in detection of the nucleation rate surface singularities is the random error inherent in any experimental data. This problem exists even one has experimental results of relatively high accuracy as it is shown by Anisimov [7]. A conceptual problem in vapor-gas to liquid (or solid phase) nucleation is its treatment of the nucleation as a single component problem instead as a two component system. Results of the present research illustrate clearly that gases can generate a phase transitions in a condensed state of matter. It has led conclusion that gas can be involved in the critical embryos and any vapor-gas system nucleation should be considered in an approximation of binary solution. A direct mass spectrometric measurements show the presence of the carrier gas in the critical cluster under some nucleation conditions for example in a monosilane-argon system [12].

CONCLUSION

It can be concluded that a conceptual problem in vapor-gas to liquid (or solid phase) nucleation is its treatment of the nucleation as a single component problem instead of a two component approximation. Results of the present research illustrate clearly that gases can generate a phase transitions in a condensed state of matter in the critical line vicinity. Gas can be involved in the critical embryos and any vapor-gas system nucleation should be considered in an approximation of binary solutions. A direct mass spectrometric measurements show the presence of the carrier gas in the critical cluster under some nucleation conditions, for example, in a monosilane - argon system [12]. Several contemporary achievements are collected in the present review. It is clear that idea of a semiempirical design of the nucleation rate surfaces is promising tool for the advanced material synthesis. One can easily see that idea of semiempirical design of the nucleation rate surfaces will get development in the nearest future. The data base file of the algorithms of that kind of activities, the digital information on nucleation rates, equations of states, phase equilibria diagrams, binodal and spinodal conditions, *etc* will be intensively collected without doubt. Time when soft to the nucleation rate surface design will be available for each scientist and engineer is approaching. It means that knowledge on nucleation will get position of powerful tool which is effective in scientific research and industrial applications.

ACKNOWLEDGEMENT

The research is supported by the Russian Ministry for Science and Education through the grant of RSCF No 14-13-00836.

REFERENCES

- [1] M. P. Anisimov, M. P., Hopke, P. K., *et al.*, J. Chem. Phys., 1998, 109(4), 1435-1444.
- [2] H. Vortisch, B. Kramer, *et al.*, Phys. Chem. Chem. Phys. 2000, 2, 1407-1413.
- [3] M. P. Anisimov, J. Aerosol Sci. Metastable vapor states diagram. 1990, 21, suppl.1, 23-25.
- [4] Anisimova, L., Hopke, P. K., *et al.*, J. Colloid Interface Sci., 2005, 290, 107-116.
- [5] L. Anisimova, P. K. Hopke, and J. Terry, J. Chem. Phys. 2001, 114(22), 9852-9855.
- [6] M. P. Anisimov, M. P., Hopke, P. K., *et al.*, J. Aerosol Sci., 2009, 40, 733-746.
- [7] M. P. Anisimov, Russian Chem. Rev., 2003, 72(7) 591-628.
- [8] J. Lothe and G. Pound, J. Chem. Phys., 1966, 45, 630-634.
- [9] M.P. Anisimov, A.G. Nasibulin, J.A. Koropchak, L.V. Timoshina, J Chem. Phys. 1998, 109(22), 10004-10010.
- [10] M.P. Anisimov, A.G. Nasibulin, & S.D. Shandakov, J. Chem. Phys., 2000, 112, 2348.
- [11] R. C. Reid, J. M. Prausnitz, and T. K. Sherwood, *The Properties of Gases and Liquids* (McGraw-Hill, New York, 1977).
- [12] R. G. Sharafutdinov, A. E. Zarvin, *et al.*, Technical Physics Letters, 1999, 25(21), 47.

SOFT NANOTECHNOLOGY: THE BACKSTAGE

A. Kelarakis

*Centre for Materials Science, School of Forensic and Investigative Sciences,
University of Central Lancashire, Preston PR12HE, UK
(akelarakis@uclan.ac.uk)*

ABSTRACT

Recent advances in nanotechnology raise the prospect for the development of a new generation of highly adaptive materials that can simultaneously assume a variety of functions. While nature has set the bar too high by optimizing a large number of self-sustained nanostructures, it remains an open challenge for the scientific community to identify and accomplish realistic targets in that direction. To that end, engineering principles and mature scientific concepts adopted by related disciplines can safe-guide our efforts to gain control over the nanoworld in a socially and environmentally responsible manner.

INTRODUCTION

A remarkably diverse range of naturally and biologically occurring nanostructures has reached multi-level functionality, optimised structural organization and artistic perfection. Living organisms rely on strictly prescribed biosynthetic pathways to generate nanostructures that are able to rapidly and errorless store, encode, and decode information [1]. Moreover, finely tuned molecular and supramolecular assembly mechanisms allow self-replication, protein folding, formation of phospholipid bilayers cells, ligand-receptor binding, etc. [2].

In the manufactured world however, nanotechnology still faces major challenges. This is not surprising given that nanotechnology relies on material engineering at a scale many orders of magnitude smaller than a human eye can discern. First, one needs to create reliable tools able to handle nanosized objects. Second, one needs to develop techniques to monitor the processing in the nanoscale. But even if both requirements are to be fulfilled, the ultimate challenge is to identify the environmentally conscious shortcut that leads to nanostructured materials with optimum performance. But, what is their optimum performance? What are the risks and the ethical concerns associated to nanotechnology?

As the early overdose of enthusiasm around nanotechnology slowly and steadily gives its place to a mature understanding about its realistic

potential, we become to witness significant advances in the field. And as a breath of new physical phenomena is revealed in the limit of nano confinement, important applications are now realized for the first time. Below we highlight certain aspects that are central for the progression of nanotechnology towards a field of continuous innovation and scientific advancement.

DISCUSSION

Copolymer self-assembly

By design, block copolymers and peptide/polymer conjugates are formed when two chemically dissimilar chains are covalently attached to each other and are, therefore, forced to coexist in the same macromolecule. It is exactly this internal incompatibility that actually provides a platform for structuring nanomaterials with tuneable morphologies. In selective solvents, block copolymers spontaneously generate well-defined spherical, cylindrical or vesicular micelles, in a manner that critically depends upon the chemical nature of the repeating units, the chain length of the blocks and the macromolecular architecture [3].

In melt, the thermodynamic incompatibility of the two blocks gives rise to phase separation on a molecular level. The nanostructure morphology, thus obtained, reflects the interplay between the minimization of the interfacial energy between the two blocks (that causes deviations from an ideal coiled conformation) and the entropic penalty associated with substantial chain stretching. By increasing the volume fraction of one phase we successively obtain spheres, cylinders, gyroid, lamella and, ultimately, inverse gyroid, cylinders and spheres. Suffice to say that incorporation of nanoparticles significantly modifies and further enriches the phase diagrams of block copolymers [4].

Polymer nanocomposites

Polymer nanocomposites combine the processibility and flexibility of polymer matrices with desired properties endowed by the dispersed nanoparticles (silica, titania, clay, carbon nanotube-CNT, graphene, etc). For example, incorporation of clay platelets improve the barrier properties in polymers used for food packaging or bottling, hydroscopic particles enhance the water retention in membranes, silver nanoparticles afford antimicrobial activity, CNTs impart electrical conductivity in, otherwise insulating, materials. Oftentimes, those desired improvements are supplemented by substantial mechanical reinforcement.

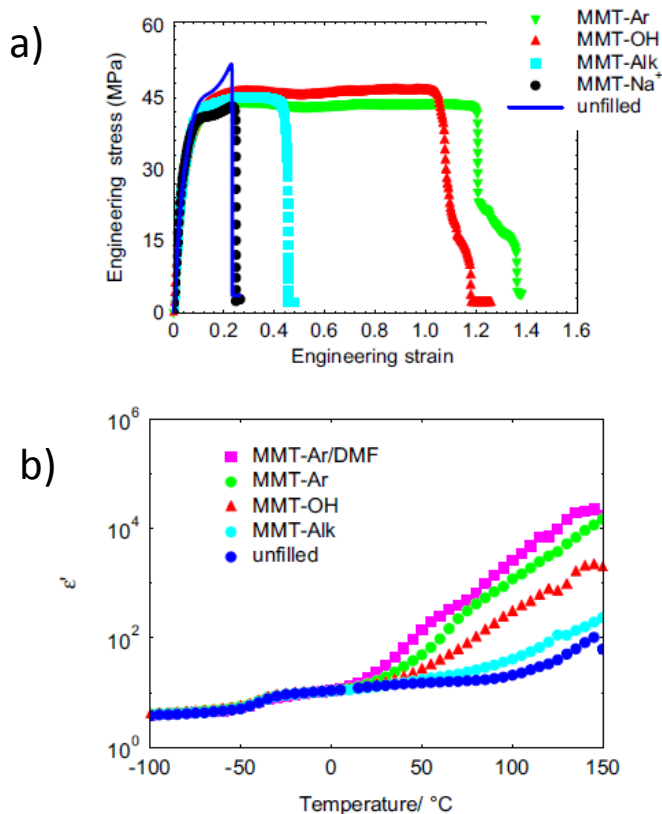


Figure 1. PVDF-HFP copolymer (blue) and corresponding nanocomposites based on different types of clays (clay content 5 wt%); a) Uniaxial deformation at room temperature. b) Real part of dielectric permittivity at 1Hz. Reprinted with permission from Reference 7, Copyright 2010, Elsevier Ltd., Oxford, U.K.

The main difference between nanocomposites and conventional composites (microcomposites) is that dispersion in the nanoscale can only be achieved in the presence of favorable particle-matrix interactions that are able to overcome the strong particle-particle attractions. To that end, covalent or non-covalent functionalization of the nanoparticles is oftentimes necessary to promote dispersion in polymeric matrices [5].

Local dynamics in the vicinity of the organic/inorganic interface can be understood in terms of confinement of the polymer chains. Oftentimes, the

hybrid morphology depends on the processing conditions and the nanoparticles might be kinetically locked in a system that is far from a thermodynamic equilibrium. Moreover, nanofillers might disturb polymer crystallization [6] or, oppositely, they can act as nucleating agents. In certain hybrids, nanoparticles are known to preferentially stabilize one phase at the expense of another. For example, clay, CNT, graphene, etc tend to promote the evolution of the piezoelectric β phase of poly(vinylidene fluoride) instead of the commonly encountered, albeit inert, α phase [7]. Within this framework, addition of organically modified clays to poly(vinylidene fluoride-co-hexafluoropropylene), gives rise to nanocomposites that exhibit significant increases in elongation to failure compared to the neat copolymer (Figure 1a). In addition, their dielectric permittivity is substantial higher over a wide temperature range (Figure 1b).

In case of immiscible polymer blends, selective localization of nanoparticles to the organic/inorganic interphase or preferential enrichment of one component results in a significant emulsifying effect. The underlying mechanism might be kinetic (by preventing the coalescence of the suspended droplets) or thermodynamic (by lowering the free energy of mixing for the two phases) in origin [8].

Nanostructured coatings

Coating strategies (such as spraying, dip and spin coating, sol-gel, chemical vapor deposition, inject printing, etc.) are widely explored to generate aesthetic finishes and smart surfaces [9]. It is instructive to note that nanostructured coatings do not necessarily contain functional nanoparticles. For example, topographical features resolved in the nanoscale can be induced simply by coating a surface with a phase separated polymer. The surface topography mirrors the complex nature of the polymer, so that the roughness might be adjusted by regulating the chemical composition of the deposited layer (Figure 2).

Layer by layer assembly is a popular strategy for advanced coating that relies on the successive deposition of opposing charged nanomaterials. Strong electrostatic and hydrophobic interactions allow the build-up of stable coatings that resist detachment even under harsh conditions. Systematic investigations focus on the incorporation of nanoparticles to ultrathin formulations to afford mechanical, scratch and crack resistance, protection against corrosion and photodegradation, antimicrobial and biocatalytic properties, stimuli responsive wetting behavior, improved

color retention, self-cleaning, antireflection and antifogging performance and fire retardancy.

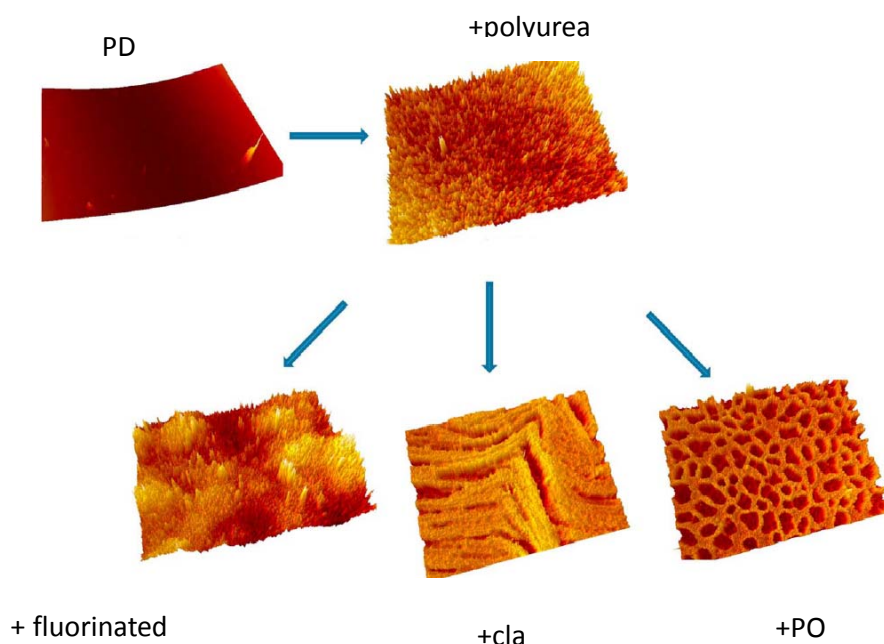


Figure 2. 3-D profilometer images of solvent cast samples based on polydimethylsiloxane (PDMS). Reprinted with permission from Reference 10, Copyright 2010, Elsevier Ltd., Oxford, U.K.

Biomimetic approaches-Hierarchical organization

Engineering approaches inspired and extracted by the anatomical characteristics of natural organisms are common to nanotechnology. Particular emphasis is given to artificial photosynthesis, tissue engineering and controlled mineralization. Those approaches underscore the prominent role of hierarchical organization across various length scales as a key factor for the development of high performance materials. The lotus leaf is a classic example of a super-hydrophobic surface, exhibiting remarkable characteristics stemming directly from its multilevel surface roughness. Capitalizing on this concept, a wide spectrum of materials with advanced wetting performance has been fabricated (Figure 3). Likewise, by

reformulating the iridescent butterfly wings, scientists create synthetic replicas with impressive light-reflective patterns and color displays.

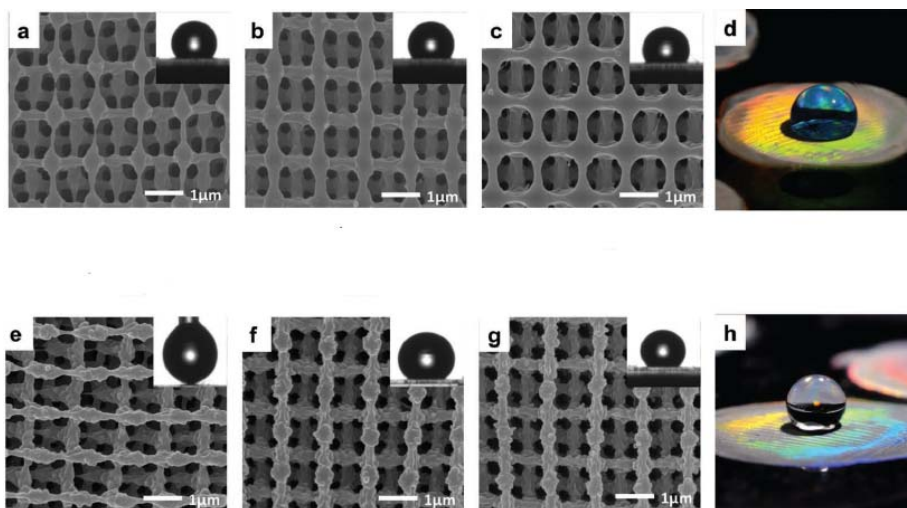


Figure 3. Water wetting behavior of fluorosilane-treated epoxy-POSS diamond structures; (a-d) smooth surfaces and (e-h) rough surfaces. Reprinted with permission from reference 11, Copyright 2012 John Wiley & Sons, Inc.

The bone is a vital nanostructured material that shows seven distinct levels of hierarchy starting from a very specific amino acid sequence, to form peptides that are coiled to produce tropocollagen, and then assembled to give collagen fibrils that, in turn, are organized and packed to larger assemblies. Remarkably, the mechanical properties of the bone are several orders of magnitude stronger compared to its constituents, by virtue of its hierarchical architecture. The intrinsic toughness of the bone involves energy dissipation mechanism at all scales including molecular uncoiling, interfibrillar sliding, microcracking and collapse of sacrificial bond [12].

Material properties in the nanoscale limit

It is now well established that many types of materials behave in a fundamentally different manner when they approach their nanoscale limit. For example, gold is typically considered as inert metal but its nanoparticles actually exhibit remarkable catalytic performance for challenging reactions. This behavior is directly related to the presence of exposed atoms at the corners of gold nanocrystals. Moreover, the optical properties of colloidal gold largely vary with the size of the suspended nanoparticles, an effect that allows the development of advanced sensors.

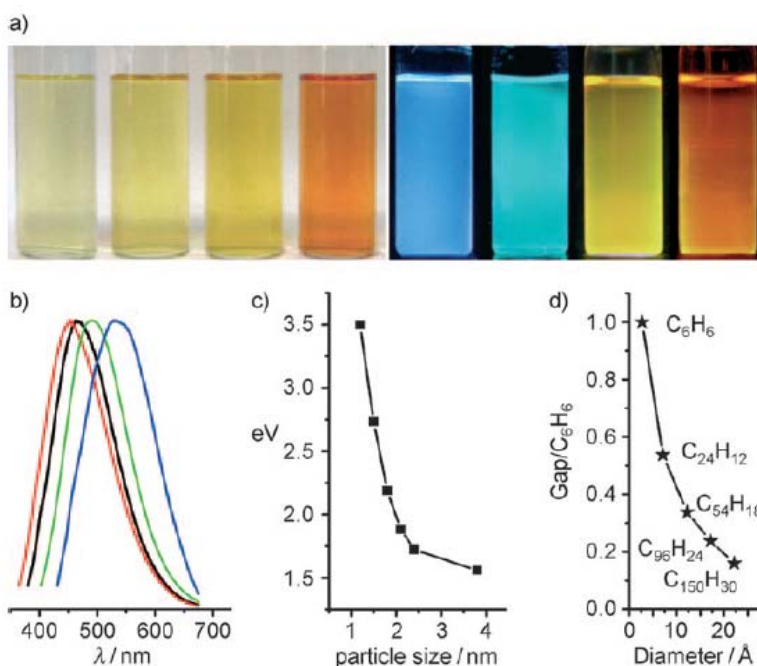


Figure 4. a) Typical sized graphene dots optical images illuminated under white (left; daylight lamp) and UV light (right; 365 nm), b) PL spectra of typical sized dots: the red, black, green, and blue lines are the PL spectra for blue-, green-, yellow-, and red-emission gC-dots, respectively, c) relationship between the dot's size and the PL properties, d) HOMO-LUMO gap dependence on the size of the fragment. Reprinted with permission from reference 13, Copyright 2010 John Wiley & Sons, Inc.

Graphite is a common brittle material, but a single layer of graphene is highly flexible. Although an ideally π -conjugated monolayer of graphene has zero band gap and is not photoactive, its nanofragments (otherwise known as graphene dots) exhibit characteristic, excitation wavelength dependent, photoluminescence properties (Figure 4) [13]. Likewise, semiconductor nanocrystals, commonly referred as quantum dots, show electronic properties (such as band gap) that are determined by their size and shape. Those novel nanomaterials are actively explored for applications such as diagnostics, therapeutics, bioimaging, photocatalysts, multicolour printing, etc.

CONCLUSION

Nanotechnology is a rapidly emerging field of continuous innovation that has already contributed significant scientific advances and cutting-edge applications in electronics, medicine, energy production, etc. Nanotechnology should not be considered as a mere adaptation of conventional engineering at a lower scale, given that materials in their nanolimit oftentimes exhibit unexpected behavior, thoroughly inaccessible at higher scales.

REFERENCES

- [1] Y. Sasai, *Nature*, 2013, 493, 318-326.
- [2] G.M. Whitesides, B. Grzybowski, *Science*, 2002, 295, 2418-2421.
- [3] C. Booth, D. Attwood, *Macromol. Rapid Commun.*, 2000, 21, 501-527.
- [4] M.C. Orilall, U. Wiesner, *Chem. Soc. Rev.*, 2011, 40, 520-535.
- [5] *Hybrid Nanocomposites for Nanotechnology*, ed. L. Merhari, Springer, 2009.
- [6] A. Kelarakis, E.P. Giannelis, *Polymer*, 2011, 52, 2221-2227.
- [7] A. Kelarakis, S. Hayrapetyan, S. Ansari, J. Fang, L. Estevez, E. P. Giannelis, *Polymer*, 2010, 51, 469-474.
- [8] A. Kelarakis, E.P. Giannelis, K. Yoon, *Polymer*, 2007, 48, 7567-757.
- [9] J. Fang, A. Kelarakis, L. Estevez, Y. Wang, R. Rodriguez, E. P. Giannelis, *J. Mater. Chem.*, 2010, 20, 1651-1653.
- [10] J. Fang, A. Kelarakis, D. Wang, E.P. Giannelis, J.A. Finlay, M.E. Callow, J.A. Callow, *Polymer*, 2010, 51, 2636-2642.
- [11] J. Li, G. Liang, X. Zhu, S. Yang, *Adv. Funct. Mater.*, 2012, 22, 2980-2986.
- [12] R. O. Ritchie, *Nature Materials*, 2011, 10, 817-822.
- [13] H. Li, X. He, Z. Kang, H. Huang, Y. Liu, J. Liu, S. Lian, C. H. A. Tsang, X. Yang, S.-T. Lee, *Angew. Chem., Int. Ed.* 2010, 49, 4430-4434.

CHEMICAL
THERMODYNAMICS

HETEROGENEOUS DESIGN: MULTICOMPONENT SYSTEMS ENGINEERING BY MEANS OF EQUATIONS FOR THE HOMOGENEOUS REGIONS BORDERS

V. Lutsyk^{1,2}

¹ *Institute of Physical Materials Science, Siberian Branch of the RAS, 6, Sahyanova st., Ulan-Ude, 670047 Russia (vluts@ipms.bsnet.ru)*

² *Buryat State University, 24a, Smolina st., Ulan-Ude, 670000 Russia*

ABSTRACT

Novel technique of phase diagram (PD) assembling and the appropriate software make possible to obtain the space models of T-x-y or T-x-y-z diagrams of different topology. They help to understand a sophisticated geometrical structure of PD. Kinematical method of surfaces description was chosen as the most effective one on this stage. In the case of T-x-y diagram, any surface is presented as the pseudo-ruled one, that is, a space curve, given by the interpolation polynomial, moves along the analogously given directing curves. Within a T-x-y-z diagram a hypersurface is forming when the originating curve moves along the directing surfaces. Such method permits to simulate the phase regions boundaries of any complexity using the minimum of initial experimental or calculated data. 3D computer models, except visualization of projections and sections, are able to show incorrect elements of PD and to detect the effects of three-phase reaction type changing. PD space models are used as an effective instrument for the heterogeneous design (HD) and for the imitation of physics-chemical analyses tasks.

INTRODUCTION

A variety of science-funding agencies are working to halve the time it takes for newly discovered materials to reach the market. The vision and goals of their effort are presented in the white paper “Materials Genome Initiative for Global Competiveness” [1].

There is an opinion that Prof. Aourag is the founder of this concept and the idea of materials genome project was first launched in Oran, Algeria in 2007 [2].

An important part of the similar research was made in Ulan-Ude, Russian Federation at the Institute of Physical Materials Science of the Siberian Branch of the Russian Academy of Sciences by the projects of the Russian Foundation for Basic Research 98-03-32844 “The design of the

microstructures of multicomponent materials according to the equations of the boundaries of single-phase regions” (1998-2000) and 01-03-32906 “The genotype of heterogeneous material (boundary of concentration domains with the unique schemes of phase transformations and thermodynamically unstable fragments of phase fields in the multidimensional diagrams of the known and forecasted topological types)” (2001-2003) [3-8].

The searching of the effective technologies of PD assembling have been carried out: 1) approximating technique (Fig. 1-2) for the of surfaces of T-x-y and hypersurfaces of T-x-y-z diagrams; 2) ideology of software creation – a) unique PD model, b) reducible PD model, c) editors and designers of PD; 3) principles of PD assembling – a) from (hyper)surfaces, b) from phase regions. As experimental studies and thermodynamic calculation do not guarantee the sufficient conditions to make a PD the real working tool for materials science, then the assembling of multi-dimensional PD from the corresponding (hyper) surfaces or the phase regions is required. At that the first version of assembly makes it difficult to use PD for the mass balances analyses, whereas by the PD installation of the phase regions much more possibilities have been appeared, up to the interpretation of the genotype of the heterogeneous material (Fig. 3-6).

Three different variants of the surface (hypersurface) approximation were used: 1) additive contour is filled by the triangular tiles (Fig.1, a); 2) originating line M_1M_2 moves along the directing ones $A_{00}A_{01}...A_{0k}$, $A_{10}A_{11}...A_{1k}$, ..., $A_{m0}A_{m1}...A_{mk}$ (Fig. 1, b); 3) minimal area for the arbitrary taken contour is used (c).

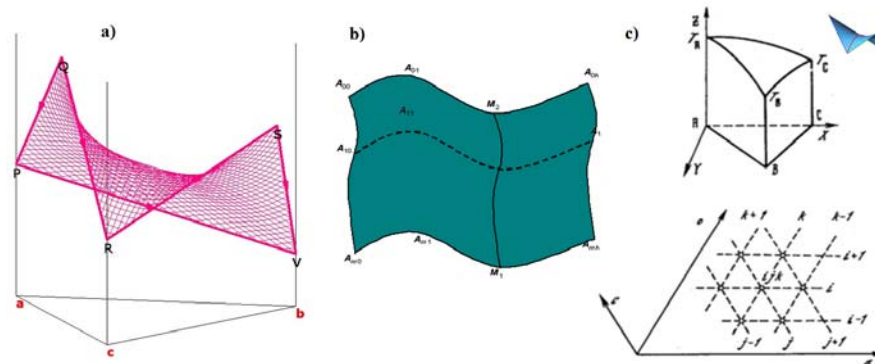


Figure 1. Three variants of a surface approximation.

For the surface with a cut (or hole) forming two different technologies were elaborated (Fig. 2): by the assembling of 4 fragments - $Ae_{AB}(e_{AB}[e_{AB},E])(A[A,e_{AC}])$, $(A[A,e_{AC}])k_1k_2([A,e_{AC}]e_{AC})$, $k_1(e_{AB}[e_{AB},E])([e_{AB},E]E)k_2$, $([A,e_{AC}]e_{AC})([e_{AB},E]E)Ee_{AC}$ (Fig. 2, b), and by a

template method (Fig. 2, c) with addition of directing curves $k_1k_4mk_3k_2$ and $k_1k_5nk_6k_2$ (Fig. 2, d).

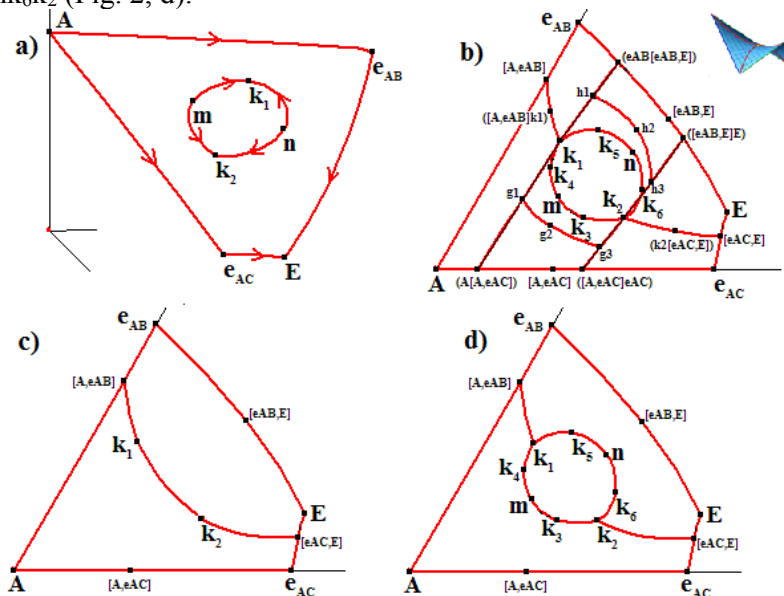


Figure 2. Different techniques for the surface forming.

PHASE DIAGRAM AS A TOOL OF MATERIAL SCIENCE

Three principal discoveries were obtained to use the computer space model of PD for the data mining of its content: 1) crystals with different dispersity competition in the invariant reactions (Fig. 3); 2) three 2-wing ruled surfaces existence for the reaction type changing in the 3-phase region (Fig. 4); 3) concentration fields with the unique crystallization scheme and with the unique set of the microconstituents (Fig. 6).

Field $Ae_{AB}FS$ within PD with an incongruent compound $R=A_3C$ (Fig. 3, e, g) consists of fragments $e_{AB}FK$, $Ae_{AB}K$, ASK with the microstructures $M+A^e$, $M+A^e+A^1$, $M+A^1$, where $M=R^Q+B^Q+B^e$. Vertical mass balances for the compositions 3, K, 7, N are shown on the Fig. 3 (a-d).

Horizontal mass balances (Fig. 3, h, i) at two isothermal equilibria permit to investigate the results of the primary crystals A^1 and the eutectical crystals A^e competition in the invariant reaction. Both of them are given for the same isopleth UH at $T_Q+\delta$ and $T_Q-\delta$.

For the first time the «remarkable» lines AF ($A^e=A^Q$), $e_{AB}S$ ($A^1=A^Q$), WQ ($A^1=A^e$) and the point V ($A^1=A^e=A^Q=A^r$) with the specific mass balances, where found, where r – the remains of crystals mass after the invariant reaction $L+A^Q=B^Q+R^Q$. Contrary to 3-dimensional field QFS , 2-

dimensional field QF differs by the reaction $L^1 \rightarrow A^1$ absent. However, according to the competition of crystals A^1 and A^e , both fields have the same microstructures. As a result the 1-dimensional concentration field QF belongs to the 2-dimensional concentration field ($QF \in QFS$) and isn't the unique one.

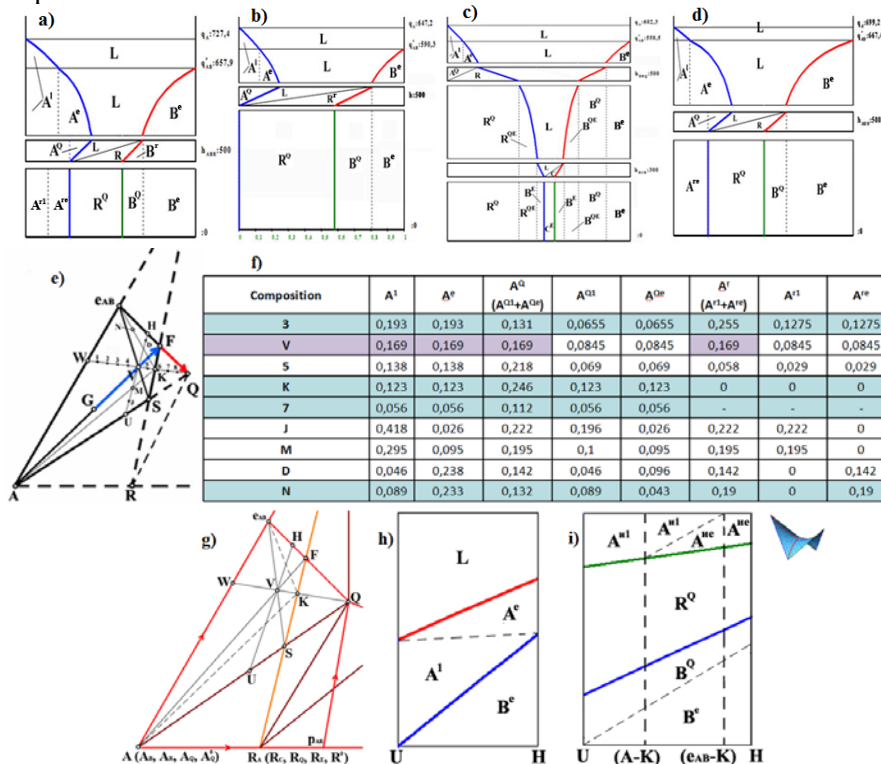


Figure 3. Investigation of the concentration field with the primary crystals A^1 and eutectical crystals A^e competition in the invariant reaction.

Two-phase reaction surfaces in the region $A+B+C$ (at the mass increment sign change for the third phase in the process of heterogeneous material cooling) were investigated (Fig. 4, a-b). Isothermity of 3-phase transformation in accordance with A. Storonkin condition [9] has been confirmed by the mass balances - (Fig. 4, c-f).

PHASE DIAGRAMS SIMULATORS

A kind of the training software allows to create the PD computer model and then to construct vertical and horizontal sections with the decoding of intersected surfaces and phase regions, to calculate the mass balances, to

generate the spectra of thermal and X-ray phase analyses for a given composition. A user assumes the PD topology (Fig. 5, a-c) by means of the binary systems information, and then determines all geometrical elements by means of minimal number of experiments.

Main destination of PD computer model – to solve practical problems, beginning from correct and compact representation of the experimental information and finishing the calculation of formed in the system microconstituents of the phases assemblages.

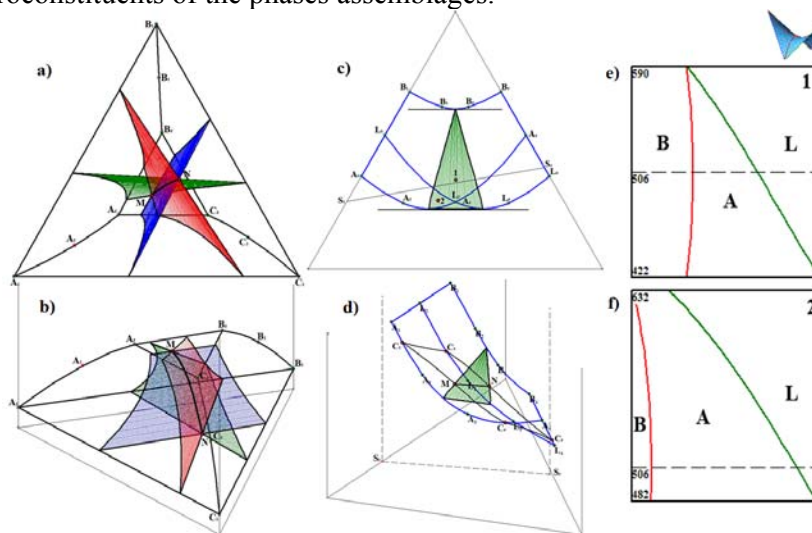


Figure 4. Common case of the 3 two-wing ruled surfaces of the 2-phase reactions the region $A+B+C$ and the confirming mass balances.

Diagram of vertical mass balances give a possibility to follow the changing of phase's mass fraction for any composition within the temperature interval. Horizontal mass balances diagrams help to show the phase portions in vertical sections MN at given temperatures (Fig. 5, d).

It is possible to generate a thermogram prototype for any composition (Fig. 5, e). The peak height of the DTA signal represents the phase with the maximal increase or decrease of mass portion in the corresponding temperature interval. Not gear but rectangular peak corresponds to the invariant regrouping of masses on the horizontal plane.

The melt presence is showed by the elevated level of electrical conductivity. For generation of X-ray spectra the training software has been fitted by the data base with characteristics of initial components A, B, C and corresponding compounds (with their allotropies).

MATERIAL’S GENOTYPE DECODING

Computer model of PD helps to design the microstructure of heterogeneous material and to decipher its genotype [3-8]. Investigation of 52 concentration fields of CaO-Al₂O₃-SiO₂ system (Fig. 6), that belong to the primary crystallization of component C(CaO) and neighbor compounds C₃S≡R1 and C₃A≡R6 (19 two-, 21 one- and 12 zero-dimensional fields) reveals that there are 18 fields (12 one-dimensional and 6 zero-dimensional) without the unique set of microconstituents.

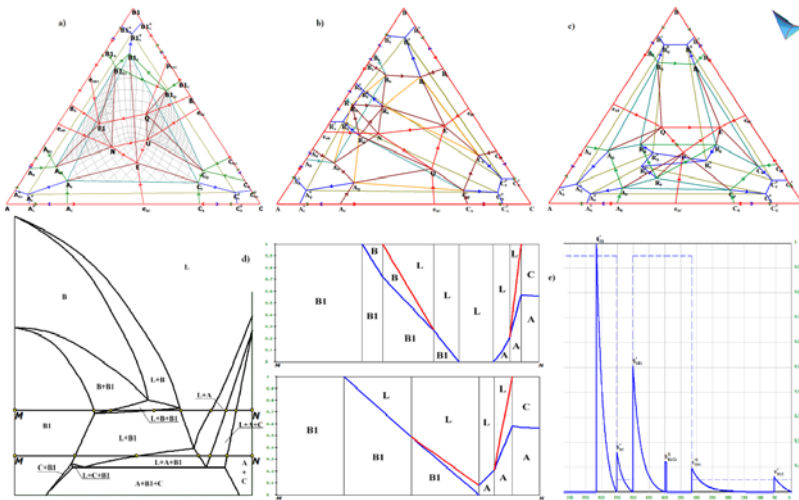


Figure 5. PD with component B allotropy (a), decomposing A_mB_n (b) and incongruently melting A_mB_nC_k (c) compounds. Horizontal mass balances for PD (a) within the isopleth B-AC (d). DTA and electroconductivity spectra for the composition on the liquidus curve e_{BC}U (a) imitation (e).

As an example a two-dimensional field Q₂-8-9 within a subsystem R₂R₆R₇ (R₇=C₁₂A₇, R₂=C₂S) is shown (Fig. 6, a). Vertical line in the mass centre G intersects the phase regions L+R₁, L+R₁+R₂, L+R₂+R₆, R₂+R₆+R₇, two planes of four-phase regrouping of phases (at the temperature of invariant points Q₂ and Q₃).

The composition of melt changes along the extension of segment R₁-G₁ to liquidus line e₁Q₂ when the point G passes through the region L+CaO. Then mass center G falls into phase regions L+R₁+R₂ and L+R₂+R₆ (with the reaction Q₂: L^{Q₂}+R₁→R₂^{Q₂}+R₆^{Q₂} between them) and the melt moves along the liquidus curves e₁Q₂ and Q₂Q₃.

Solidification finishes on the subsolidus simplex R₂R₆R₇ at the temperature of point Q₃. The diagram of vertical mass balance (Fig. 6, b) confirms the

phase reactions $L \rightarrow R_1^{R1}$, $L^{e1} \rightarrow R_1^{R2} + R_2^{R1}$, $L^{Q2} + R_1 \rightarrow R_2^{Q2} + R_6^{Q2}$, $L^{en} \rightarrow R_2^{R6,en} + R_6^{R2,en}$, $L^{Q3} + R_6 \rightarrow R_2^{Q3} + R_7^{Q3}$ with the forming of microconstituents R_2^{R1} , R_2^{Q2} , R_6^{Q2} , $R_2^{R6,en}$, $R_6^{R2,en}$, R_2^{Q3} , R_7^{Q3} . Since the solidification finishes on the simplex $R_2R_6R_7$, then the crystals R_1^{R1} and R_1^{R2} are absent as the microconstituents (they are expended during quasiperitectic reaction Q_2).

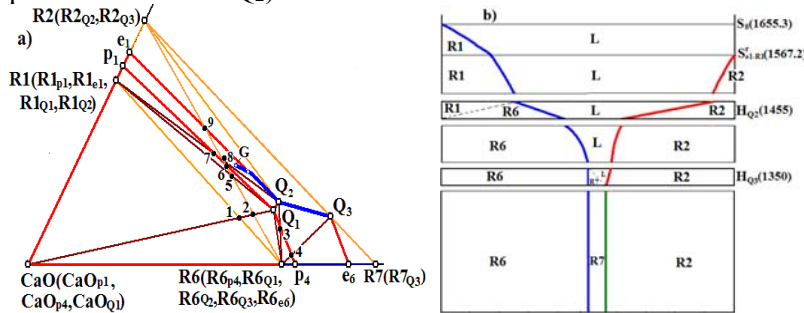


Figure 6. Trajectory G-1-2-3- Q_2 (a) for liquid phase and mass balances (b) in the process of solidification for composition G ($R_1 \equiv C_3S$, $R_2 \equiv C_2S$, $R_6 \equiv C_3A$, $R_7 \equiv C_{12}A_7$).

CONCLUSION

When the phase regions are projecting on the concentration simplex, the latter is dividing into the concentration fields with the individual set of phase reactions and appropriate microstructures. Then the fields, which belong to the 3-phase regions, are dividing additionally by the surfaces of 2-phase reaction into the fragments with the different dynamics of phase masses increment. Every 3-phase region has 1-3 these surfaces of 2-phase reactions, and the sections of them are to be fixed on the isopleths and on the isothermal cuts. Analogously in the fields, connected with the invariant phase reactions, the domains with different results of the large and small crystals competition are allocated too. This thrice-repeated segmentation of concentrations space forms a genotype of multicomponent material.

PD computer models are using to study salt systems with an idea to design the materials for molten salt reactor [8]. Fluoride systems have been described as one of the possible fuels for molten salt reactor application. Besides the lowest melting point another criterion is the same important for the salt fuel: a concentration of fissile material. To optimize the molten salt fuel parameters the computer models of fluoride systems are to be built. To ensure reliable exploitation of new generation reactor, exhaustive information is to be used about the chemical processes and equilibria in the fluoride-chloride reciprocal systems.

The PD of multi-component systems (MCS) are the fundamental theoretical base for elaboration of many materials. The limited information about the MCS properties and the behavior, as the projections and sections calculated or constructed according to the experimental data are usually used. Their application becomes more effective after assembling of PD computer models. This development is based on the unique new technology of the space models design for the multi-dimensional PD MCS from the totality of all its geometric elements with different dimensions.

Space models are assembling for the multi-dimensional PD to design the microstructures in multi-component alloys, ceramics and composite materials. The approximation of specified contour by the minimal surface (soap film) could strengthen the possibilities of PD computer models. It is provided also the proto-typing by a 3D printer the so-called exploded phase regions with the mapping by laser beam inside the transparent phase region of such important special features of interaction of components as change of the phase reaction type, laws governing the tie-lines arrangement, the trajectory of phases, the formation of concentration fields at the expense of the competitive participation in the invariant reactions of the crystals with different dispersion.

ACKNOWLEDGEMENT

This work was partially supported by the Russian Foundation for Basic Research (projects 14-08-00453 and 14-08-31468).

REFERENCES

- [1] L. Kaufman, J. Ågren, *Scripta Materialia*, 2014, 70, 3–6.
- [2] H. Aourag, *AIP Conf. Proc.*, 2008, 48, 1047.
- [3] V. Lutsyk in: *Phase Diagrams in Materials Science*, T. Ya. Velikanova (Ed.), Materials Science International Services, GmbH, Stuttgart, 2004, 304-306.
- [4] V. I. Lutsyk, *Bulletin Buryat Scientific Centre SB RAS*, 2012, 1(5), 78-97. (In Russian)
- [5] V. I. Lutsyk, E. R. Nasrulin, *Crystallography Reports*, 2012, 57(7), 106-110.
- [6] V. Lutsyk, A. Zelenaya, *Solid State Phenomena*, 2013, 200, 73-78.
- [7] V. Lutsyk, A. Zelenaya, M. Parfenova, *Advanced Materials Research*, 2013, 704, 173-178.
- [8] V. Lutsyk, A. Zelenaya, Dai YaZhou. *Advanced Materials Research*, 2013, 704, 349-352.
- [9] A. Storonkin, *Russian J. Phys Chem*, 1971, 45, 1210-1213.

CHEMICAL THERMODYNAMICS OF COMPLEX OXIDES

A. V. Knyazev, N. N. Smirnova and S. S. Knyazeva

*Chemistry Department, Lobachevsky State University of Nizhni Novgorod
Gagarin Av. 23/2, 603950, Nizhni Novgorod, Russia
(knyazevav@gmail.com).*

ABSTRACT

The present work presents the results of investigating complex oxides obtained in thermodynamic field over the past few years. There is realized crystal chemistry systematization of studied compounds. The temperature dependences of heat capacities at constant pressure for more than 50 compounds in a temperature interval from 7 to 350 K were studied in an adiabatic vacuum calorimeter. The description of transitions in compounds was made by means of McCallaf–Vestrum classification of physical transitions. The standard enthalpies of formation at $T = 298.15$ K of 250 inorganic compounds were determined first by the method of reaction calorimetry. Several mathematical models having a predictive power and describing the behavior of compounds in “precipitate–solution”, “crystal–liquid” and “individual phase–solid solution” systems were suggested.

INTRODUCTION

Since the inception of chemical thermodynamics one of the most important tasks of this science is to determine the standard thermodynamic functions of individual substances. Such data are required primarily for calculating equilibrium chemical reactions at various temperatures and pressures. In this case the limiting factor in such calculations is usually relatively low accuracy in determining the enthalpy of a chemical reaction, which is calculated as the algebraic sum of the enthalpies of formation of the reactants. In the measurements of entropy admissible large errors, particularly when it comes to reactions involving condensed substances. Therefore, determination of standard enthalpies of formation and absolute entropies of individual substances is necessary and important task of chemical science and technology. The thermodynamic functions of compounds allow to predict the behavior of phases in different geological and technological conditions.

EXPERIMENTAL

The synthesis of the complex was carried out by three various methods:

(1) solid state reactions and reactions in melt in a temperature range from 500°C to 1300°C; (2) reactions under hydrothermal conditions; and (3) precipitation reactions from solutions. Using the first method we synthesized compounds with frame structure. But our studies show that, the most universal method of producing mineral-like compounds is the synthesis under hydrothermal conditions. It is significant that the second method is optimal for the synthesis of compounds with layer and isle structure. Precipitation reaction, in other words the third method is the most suitable one for compounds with isle and rare layer structure and having solubility in neutral solutions more than 10^{-4} mol/l. The techniques, developed by us, allowed obtaining in total of more than 400 compounds and more than half of them were prepared and identified for the first time.

For structural investigations and confirming phase individuality, X-ray diffraction patterns of all samples were recorded on a Shimadzu X-ray diffractometer XRD-6000 (CuK_α radiation, geometry $\theta-2\theta$) in the 2θ range from 10° to 120° with scan increment of 0.02° . The low-temperature and high-temperature X-ray diffraction were carried out on a Shimadzu X-ray diffractometer XRD-6000 using Attachment TTK-450 (Anton Paar) and Sample Heating Attachment HA-1001 (Shimadzu) respectively.

To measure the heat capacity of the tested substances in the range from 7 to 350 K a BKT-3.0 automatic precision adiabatic vacuum calorimeter with discrete heating was used. The calorimeter was tested by measuring the heat capacity of highpurity copper and reference samples of synthetic corundum and K-2 benzoic acid. The analysis of the results showed that measurement error of the heat capacity of the substance at helium temperature was within $\pm 2\%$ ($5 < T < 20$ K), then it decreased to $\pm 0.5\%$ as the temperature was rising to 40 K, and was equal to $\pm 0.2\%$ at $T > 40$ K. Temperatures of phase transitions can be determined with the error of ± 0.02 K.

To measure the heat capacity of the sample between 330 and 650 K an automatic thermoanalytical complex (ADKTTM) –a dynamic calorimeter operating by the principle of triple thermal bridge – was used. The data on the heat capacity of the objects under study were obtained in the range from 330 to 650 K at the average rate of heating of the calorimeter and the substances of 0.0333 K/s.

The experimental thermochemical data set was obtained using a modified Skuratov calorimeter.

Thermal behavior was carried out with DSC Labsys from Setaram in a platinum crucible ranging from 293 to 1173 K (heating rate 0.167 K/s).

RESULTS AND DISCUSSION

Realized crystal chemistry systematization of studied compounds allows concluding that the element with the highest oxidation number determines the forming structure, as usual for majority others complex compounds. We could sort all the compounds into three types according to structural features, that is, compounds with frame, layer and isle structures.

A sufficiently important task of the work was the estimating thermodynamic functions of the compounds with the purpose of describing processes with their participation and detecting criteria of their stability. For this purpose we choose the thermochemical schemes. As solvents concentrated nitric, hydrochloric, hydrofluoric and sulphuric acids were used. It was caused by good solubility of compounds under investigations in their solutions. The enthalpies of formation of about 250 inorganic compounds containing uranium were experimentally determined for the first time using a reaction adiabatic calorimeter. In Table 1 there are represented thermodynamic functions of formation for some compounds.

The temperature dependences of heat capacities at constant pressure for more than 50 compounds in a temperature interval from 7 to 350 K were studied in an adiabatic vacuum calorimeter. The obtained data allowed describing possible phase transitions and calculating absolute entropies of formation of the compounds. It is significant to note that heat capacities at constant pressure of the majority complex oxides monotonously grow with rising temperature without any visible anomalies. On the contrary, the physical transitions are observed in uranylcarbonates, uranylsulfates, several tungstates and spinels (Table 2). The description of transitions was made by means of McCallaf–Vestrum classification of physical transitions. According to this classification phenomenological all phase transitions in solids can be categorized into seven types (I, 2I, 3I, 2N, 3N, G, H).

The most widespread type of transitions in the layered compounds is isothermal (I) transitions connected with polymorphic transitions in the crystal. The polymorphism is caused by possible shifts or rotations of layers relatively to each other in the crystalline structure. Isothermal transitions are seen as “peaks” on the curve of heat capacity; the area of “peaks” is numerically equal to the enthalpy of phase transition. The physical transitions, which are more rarely met with, are H-transitions and they are observed as “humps” on the curve of heat capacity. According to physical point of view the given anomaly may be connected with “defreezing” of rotations around M–OH₂ bond in structures of the appropriate crystallohydrates.

The compounds Na₄UO₂(CO₃)₃ and K₂Fe₂Ti₆O₁₆ show the G-type (glass-like) of physical transitions (Table 2). The nature of this anomaly is,

probably, related to the presence of cation–cation interactions in the structure of this compound that is confirmed by us using Voronoi–Dirihle calculations of polyhedra with program complex TOPOS.

Table 1. Standard thermodynamic functions of some studied compounds [1-10.

Compound	$-\Delta_f H^\circ(298)$ (kJ/mol)	$S^\circ(298)$ (J/(mol·K))	$-\Delta_f S^\circ(298)$ (J/(mol·K))	$-\Delta_f G^\circ(298)$ (kJ/mol)
Uranium- and thorium-containing compounds				
Ba ₂ SrUO ₆	2940 ± 9	287.5 ± 0.9	558.6 ± 1.1	2774 ± 9
UO ₂ (BO ₂) ₂	2543 ± 4	174.2 ± 0.5	502.8 ± 0.7	2393 ± 4
Li(UO ₂ BO ₃)	2273 ± 4	178.7 ± 0.5	419.1 ± 0.7	2148 ± 5
Na(UO ₂ BO ₃)	2258 ± 4	167.2 ± 0.5	452.7 ± 0.7	2123 ± 5
Ca(UO ₂ BO ₃) ₂	4491 ± 8	291.8 ± 0.9	887.1 ± 1.1	4227 ± 9
Na ₄ (UO ₂ (CO ₃) ₃)	4010 ± 8	451.3 ± 1.4	949.0 ± 1.5	3727 ± 9
K ₃ Na(UO ₂ (CO ₃) ₃)	4001 ± 9	485.0 ± 1.5	955.5 ± 1.6	3716 ± 9
K ₄ (UO ₂ (CO ₃) ₃)	4030 ± 9	447.8 ± 1.3	1006.1 ± 1.4	3730 ± 9
Ca(UO ₂ SiO ₃ OH) ₂ ·5H ₂ O	6781 ± 10	727.3 ± 2.2	1978.6 ± 2.3	6191 ± 10
Mn(UO ₂ (SO ₄) ₂)·5H ₂ O	4422 ± 5	607.3 ± 1.8	1728.4 ± 1.9	3907 ± 5
Fe(UO ₂ (SO ₄) ₂)·5H ₂ O	4285 ± 5	574.6 ± 1.7	1757.2 ± 1.8	3761 ± 5
Co(UO ₂ (SO ₄) ₂)·5H ₂ O	4239 ± 5	600.7 ± 1.8	1734.0 ± 1.9	3722 ± 5
Ni(UO ₂ (SO ₄) ₂)·5H ₂ O	4249 ± 5	581.4 ± 1.7	1753.1 ± 1.8	3727 ± 6
Cu(UO ₂ (SO ₄) ₂)·5H ₂ O	4114 ± 5	514.2 ± 1.5	1823.8 ± 1.6	3570 ± 5
Zn(UO ₂ (SO ₄) ₂)·5H ₂ O	4330 ± 5	477.1 ± 1.4	1869.2 ± 1.5	3773 ± 5
KTh ₂ (PO ₄) ₃		336.2 ± 1.3	1186.3 ± 1.4	
Titanium- and vanadium-containing compounds				
Li _{4/3} Ti _{5/3} O ₄	2050 ± 10	108.8 ± 0.5	391.5 ± 0.6	1933 ± 10
K ₂ Fe ₂ Ti ₆ O ₁₆		457.2 ± 2.3	1542.9 ± 2.9	
(UO ₂) ₂ V ₂ O ₇	3936 ± 12	356.0 ± 1.1	930.0 ± 1.2	3658 ± 12
Pb ₅ (VO ₄) ₃ Cl	3669 ± 15	643.0 ± 0.8	1109.5 ± 0.9	3338 ± 16
Tungsten- and antimony-containing compounds				
LiVWO ₆		174.1 ± 1.5	532.1 ± 1.6	
NaVWO ₆		184.7 ± 1.5	543.6 ± 1.6	
KSbWO ₆		205.9 ± 1.5	552.6 ± 1.7	
RbNbWO ₆		222.9 ± 1.5	538.5 ± 1.6	
CsTaWO ₆		221.7 ± 1.5	553.2 ± 1.7	
Co _{7/3} Sb _{2/3} O ₄		153.4 ± 0.5	357.5 ± 0.6	

Thus, the calorimetric methods allowed estimating all necessary thermodynamic functions of some inorganic compounds.

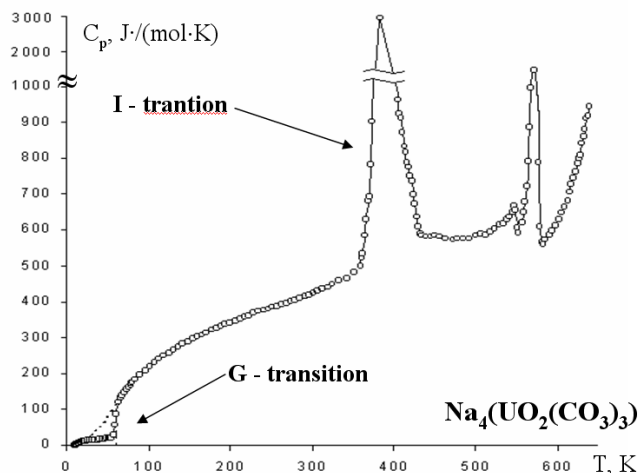


Figure 1.
Temperature
dependence of heat
capacity of
 $\text{Na}_4(\text{UO}_2(\text{CO}_3)_3)$.

Table 2. Thermodynamic characteristics of physical transitions in compounds.

Compound	Phase transition	T_{tr} , K	$\Delta_{tr}H^\circ$ (kJ/mol)	$\Delta_{tr}S^\circ$ (J/(mol·K))
$\text{Na}_4(\text{UO}_2(\text{CO}_3)_3)$	G	60.5	1500 ± 3	33.0 ± 1.0
	I	386	50200 ± 200	$130. \pm 3.0$
$\text{K}_3\text{Na}(\text{UO}_2(\text{CO}_3)_3)$	I	395	800 ± 100	2.00 ± 0.02
$\text{K}_4(\text{UO}_2(\text{CO}_3)_3)$	I	403	6900 ± 100	17.1 ± 0.5
$\text{Mn}(\text{UO}_2(\text{SO}_4)_2) \cdot 5\text{H}_2\text{O}$	H	176	510 ± 3	2.90 ± 0.02
	I	238	190 ± 3	0.80 ± 0.02
$\text{Fe}(\text{UO}_2(\text{SO}_4)_2) \cdot 5\text{H}_2\text{O}$	H	182	200 ± 3	1.10 ± 0.02
$\text{Co}(\text{UO}_2(\text{SO}_4)_2) \cdot 5\text{H}_2\text{O}$	I	237	1920 ± 3	8.10 ± 0.02
$\text{K}_2\text{Fe}_2\text{Ti}_6\text{O}_{16}$	G	72	-	-

When studying isomorphism, one needs to know not only the type of solid solution and the miscibility regions but also the energy parameters of this phenomenon. Provided that the thermodynamic functions of mixing are known, one can answer many questions concerning the character of the solid solution formation and the thermodynamic stability regions of the solutions.

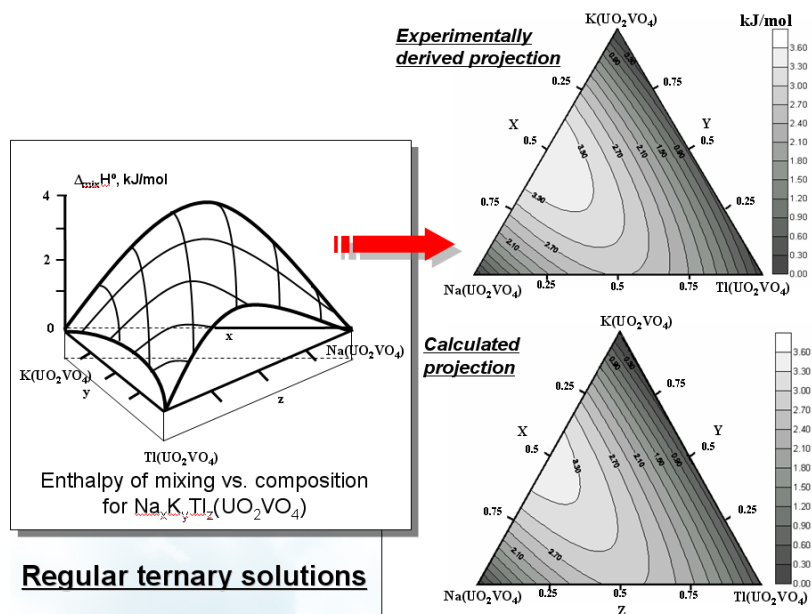


Figure 2. Calculated and experimentally derived projections of enthalpy of mixing surfaces for $\text{Na}_x\text{K}_y\text{Tl}_z(\text{UO}_2\text{VO}_4)$.

Objects of our investigations are two solid solution systems $\text{Na}_x\text{K}_y\text{Tl}_z\text{VUO}_6$ [11] and $\text{Mg}_x\text{Mn}_y\text{Co}_z\text{UO}_2(\text{SO}_4)_2 \cdot 5\text{H}_2\text{O}$ [12]. For the first system the compositional dependence of the enthalpy of mixing can be described by Prigogin's regular model [46]. In terms of this model, a maximum of the enthalpy of mixing surface should occur in the vicinity of one of the binary systems, which is precisely observed in our case. The second system can be described by a subregular model. The above-mentioned regular model is inapplicable for this system. Therefore, we advanced a theoretical subregular solutions model for ternary systems. In terms of this model, the maximal value of the enthalpy of mixing is observed for random concentrations of the three components. In this connection, the enthalpy of mixing should be presented as a function of composition in the form of four summands. Three summands describe the behavior of the function near binary systems, and the fourth summand, in the central portion of the diagram.

The search for new forms of radionuclide binding capable to restrict their migration in the environment stimulates studying the state of poorly soluble uranium compounds in aqueous solutions. In this connection, it is extremely important to explore their behaviour in water solutions. The quantitative physicochemical model describing heterogeneous system “precipitate–aqueous solution”, represented by the following block diagram, is offered (Fig. 3) [13].

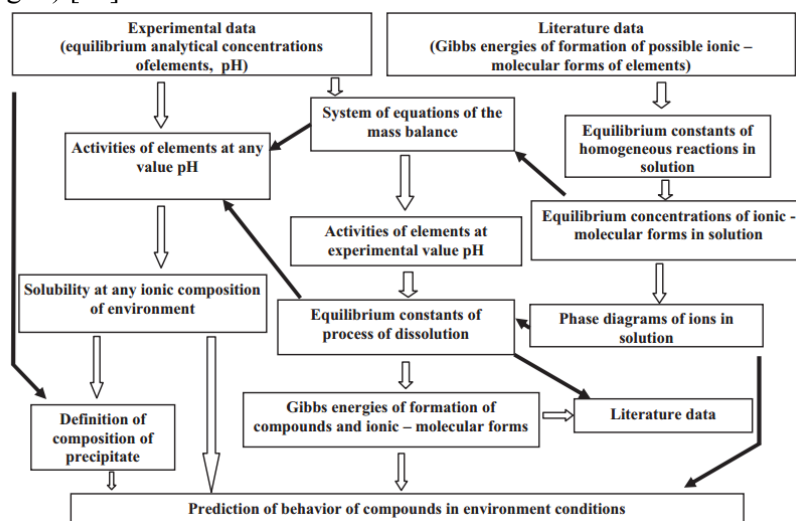


Figure 3. Scheme of investigating heterogeneous systems “precipitate–solution”.

CONCLUSION

The techniques for the synthesis of individual compounds and solid solutions were developed, more than half of which were obtained and identified for the first time. The standard enthalpies of formation at $T=298.15$ K of 250 inorganic compounds were determined first by the method of reaction calorimetry. The heat capacity at constant pressure of more than 50 compounds was studied also first by adiabatic vacuum calorimetry. The standard entropies and Gibbs functions of formation at $T=298.15$ K were calculated as well. All the results were discussed and tabulated and those made up the foundation of thermodynamics of the given class of inorganic compounds. The polyphase equilibria “precipitate–solution”, “crystal–liquid” and “individual phase–solid solution” of several compounds was investigated and mathematical models of their behaviour under corresponding conditions based on the equations of equilibrium thermodynamics were made.

ACKNOWLEDGEMENT

The work was performed with the financial support of the Russian Foundation of Basic Research (Project Number 13-03-00152).

REFERENCES

- [1] N.V. Karyakin, N.G. Chernorukov, A.V. Knyazev, M.A. Knyazeva, A.V. Markin, E.V. Zamkovaya, *Russ. J. Phys. Chem.*, 2005, 79, 1560–1564.
- [2] N.G. Chernorukov, N.N. Smirnova, A.V. Knyazev, M.N. Marochkina, T.A. Bykova, A.V. Ershova, *Russ. J. Phys. Chem.*, 2006, 80, 37–41.
- [3] A.V. Knyazev, M. Maćzka, N.Yu. Kuznetsova, J. Hanuza, A.V. Markin, *Journal of Thermal Analysis and Calorimetry*, 2009, 98, 843-848.
- [4] Knyazev A.V., Maćzka M., Smirnova N.N., Macalik L., Kuznetsova N.Yu., Letyanina I.A., *Journal of Solid State Chemistry*, 2009, 182, 3003-3012.
- [5] Knyazev A.V., Bulanov E.N., Smirnova N.N., Kuznetsova N.Yu., Letyanina I.A., Pryamova E.D., *Thermochimica Acta*, 2011, 515, 79-83.
- [6] Knyazev A.V., Tananaev I.G., Kuznetsova N.Yu., Smirnova N.N., Letyanina I.A., Ladenkov I.V., *Thermochimica Acta*, 2010, 499, 155-159.
- [7] A.V. Knyazev, N.Yu. Kuznetsova, N.G. Chernorukov, I.G. Tananaev, *Thermochimica Acta*, 2012, 532, 127-133.
- [8] Knyazev A.V., Chernorukov N.G., Letyanina I.A., Zakharova Yu. A., Ladenkov I.V., *Journal of Thermal Analysis and Calorimetry*, 2013, 112, 991-996.
- [9] A.V. Knyazev, N.N. Smirnova, M.E. Manyakina, A.N. Shushunov, *Thermochimica Acta*, 2014, 584, 67-71.
- [10] A.V. Knyazev, N.N. Smirnova, M. Maćzka, K. Hermanowicz, S.S. Knyazeva, I.A. Letyanina, M.I. Lelet, *The Journal of Chemical Thermodynamics*, 2014, 74, 201-208.
- [11] N.G. Chernorukov, A.V. Knyazev, R.A. Vlasov, E.N. Bulanov, *Russ. J. Inorg. Chem.*, 2005, 50, 1463–1471.
- [12] N.G. Chernorukov, A.V. Knyazev, R.A. Vlasov, Yu.S. Sazhina, *Russ. J. Inorg. Chem.*, 2004, 49, 978–983.
- [13] N.G. Chernorukov, O.V. Nipruk, A.V. Knyazev, E.Yu. Pegeeva, *Russ. Radiochem.*, 2004, 46, 452–456.

TERT-BUTYL CHLORIDE AS A PROBE OF THE SOLVOPHOBIC EFFECTS

I. Sedov¹, M. Stolov¹ and B. Solomonov¹

¹*Chemical Institute, Kazan Federal University, Kazan, Russia.
(igor_sedov@inbox.ru)*

ABSTRACT

Relationships between the Gibbs free energy and enthalpy of solvation of tert-butyl chloride in various protic solvents are considered in order to compare the strength of the solvophobic effects from solvent to solvent. The values of thermodynamic functions of solvation are determined experimentally using titration calorimetry and gas chromatographic headspace analysis techniques. Positions of the data points on the $\Delta_{solv}G$ vs $\Delta_{solv}H$ plot indicate that the solvophobic effects take place in various mono- and dihydric alcohols, acetic acid, and acid amides. The excess positive contribution into free energy of solvation of tert-butyl chloride in self-associated solvents is used to characterize their strength quantitatively. It is shown that the solvophobic effects are stronger the larger is the concentration of the hydrogen bonds in a solvent.

INTRODUCTION

The solvophobic effects is a term used to describe a more general phenomenon than the hydrophobic effect in water. These effects take place in various solvents, the molecules of which can form hydrogen bonds with each other. Examples of such solvents are polyhydric and monohydric alcohols, formamide, hydrazine etc. The typical manifestations of the solvophobic effects are low solubility of apolar solutes, low entropy and large heat capacity change upon dissolution, micellization of amphiphilic compounds.

In our earlier works [1–3], we investigated the impact of these effects on the thermodynamic functions of solvation in various solvents. We have shown that the relationship of magnitudes of the Gibbs free energy and enthalpy of solvation is useful for qualitative identification and quantitative description of the solvophobic effects. Experimental values of thermodynamic functions are necessary for such analysis. Since alkanes are the least polar organic molecules and cannot form hydrogen bonds with other species, we have studied them in the first place. However, it is very difficult to measure

accurately the enthalpies of solution and activity coefficients of alkanes in many of self-associated solvents due to their poor solubility. Monohalogenated alkanes are also low polar compounds that are not likely to form hydrogen bonds, but have significantly lower volatility than alkanes and therefore are more convenient to study calorimetrically. Thus, we have chosen 2-chloro-2-methylpropane (tert-butyl chloride) as a probe of the solvophobic effect. Tert-butyl chloride is a model compound to study the nucleophilic substitution reactions. The influence of solvent on their rate was a subject of several studies [4,5], for which the values of excess thermodynamic functions in dilute solutions were determined. The enthalpies of solution of tert-butyl chloride have been reported in the works of Albuquerque et al. [6] along with several other monohalogenated hydrocarbons (2-bromo-2-methylpropane, 2-chloro-2-methylbutane, and 3-chloro-3-methylpentane) in mono- and dihydric aliphatic alcohols. We compare their values with our own experimental data for the same systems.

EXPERIMENTAL

Enthalpies of solution $\Delta_{soln}H$ were measured at $T = 298.15$ K by calorimetric titration method using TAM III solution calorimeter. A correction was made to take into account partial evaporation of the solute to the headspace of the calorimetric vessel. Automated static headspace GC analysis was used to measure limiting activity coefficients γ_{∞} of tert-butyl chloride in various solvents. They were converted into the Gibbs free energies of solvation using a formula $\Delta_{solv}G = RT \ln \gamma_{\infty} - \Delta_{vap}G$.

RESULTS AND DISCUSSION

We have considered [3] the relation between the Gibbs free energy and enthalpy of solvation for solutes and solvents from different classes of organic compounds with different structure, polarity, molecular size and shape. A linear correlation between $\Delta_{solv}G$ and $\Delta_{solv}H$ for 978 solutions in aprotic solvents is given by equation $\Delta_{solv}G = 0.627\Delta_{solv}H + 16.3$ (1). For solutions in self-associated solvents, the deviations from this correlation to the side of more positive Gibbs free

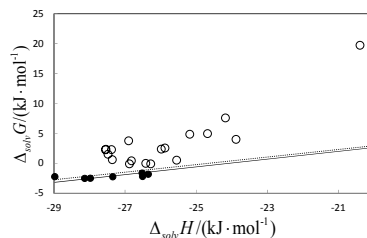
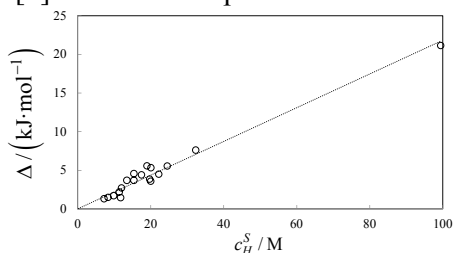


Figure 1. Gibbs free energies vs enthalpies of solvation of tert-butyl chloride in various aprotic (filled circles) and self-associated (empty circles) solvents at 298 K

energies are observed due to the solvophobic effect. The magnitude of the deviation can be interpreted as a quantitative measure of this effect.

In Figure 1, the Gibbs free energies of solvation are plotted versus enthalpies of solvation. Literature data [6] for the enthalpies of solvation in water and n-alkanols were used, other values are experimental. The dotted line corresponds to the linear correlation (1) that exists for solutions in non-associated solvents. Indeed, the filled circles on the plot, which correspond to the



thermodynamic functions of solvation of tert-butyl chloride in aprotic solvents (n-heptane, n-octane, cyclohexane, benzene, tert-butyl chloride, ethylene chloride, ethyl acetate) fall on this line (the deviation is no more than $1.0 \text{ kJ}\cdot\text{mol}^{-1}$, mostly to the side of lower Gibbs free energies).

Figure 2. The strength of the solvophobic effect as characterized by the values of Δ against the average concentration of hydrogen bonds in various solvents

Since the coefficients in correlation equations for various solutes are a little different, we have chosen a “baseline” specific to solvation of tert-butyl chloride in order to fit the experimental values in aprotic solvents the best. The resulting equation is $\Delta_{\text{sol}v}G = 0.647\Delta_{\text{sol}v}H + 15.6$ (2), solid line in Figure 1. The values of the deviation $\Delta = \Delta_{\text{sol}v}G - 0.647\Delta_{\text{sol}v}H - 15.6$ from line (2) for self-associated solvents are given in Table 1. In Figure 2, these values are plotted against the concentration of hydrogen bonds in corresponding solvents c_H^S .

CONCLUSION

Table 1. The strength of the solvophobic effect in solutions of tert-butyl chloride in various solvents

Solvent	$\Delta/(\text{kJ}\cdot\text{mol}^{-1})$	Solvent	$\Delta/(\text{kJ}\cdot\text{mol}^{-1})$
Hexanol-1	1.3	Acetic acid	4.4
Propanol-2	1.4	Methanol	4.5
Pentanol-1	1.5	N-methylformamide	4.6
Butanol-1	1.7	Butanediol-1,3	5.3
2-methoxyethanol	2.2	Propanediol-1,2	5.5
Propanol-1	2.7	Diethylene glycol	5.6
Butanediol-1,2	3.6	Ethenediol-1,2	7.6
Ethanol	3.7	Water	21.1
Triethyleneglycol	3.7		
Butanediol-2,3	3.9		

The increase in the Gibbs energy of solvation is due to a large negative entropy of creating a cavity in self-associated solvents. This contribution appears to grow up if the concentration of hydrogen bonds in the solvent grows up. Thus, we can qualitatively characterize the strength of the solvophobic effect using the number of hydrogen bonds in the unit volume of a solvent, which is easy to estimate from its structural formula and experimental density. From the considered alcohols, the solvophobic effect is the strongest in ethylene glycol. There should be a very limited number of individual solvents in which the solvophobic effect is at least as strong as in ethylene glycol, because such solvents should have very high concentration of H-bonds in the liquid phase. One of such solvents is trihydric alcohol glycerol, and another is formamide [1]. Finally, there is likely no solvent with the solvophobic effect stronger than the hydrophobic effect in water with its extremely small molecular volume.

The solvophobic effects are also present in solvent mixtures with cross- and self-association of components. Molecular probes such as tert-butyl chloride can be useful to estimate their strength in just two thermodynamic experiments.

ACKNOWLEDGEMENT

This work was supported by RFBR (project No. 12-03-00549-a).

REFERENCES

- [1] I.A. Sedov, M.A. Stolov, B.N. Solomonov, *J. Chem. Thermodyn.* 2013, 64, 120.
- [2] I.A. Sedov, M.A. Stolov, B.N. Solomonov, *Fluid Phase Equilibria*, 2013, 354, 95.
- [3] I.A. Sedov, M.A. Stolov, B.N. Solomonov, *J. Phys. Org. Chem.* 2011, 24, 1088.
- [4] J.J. Gajewski, *J. Am. Chem. Soc.* 2001, 123, 10877.
- [5] M.H. Abraham, P.L. Grellier, A. Nasehzadeh, R.A.C. Walker, *J. Chem. Soc. Perkin Trans.* 1998, 2, 1717.
- [6] L.M.P.C. Albuquerque, M.L.C.J. Moita, M.N. Simões, R.M.C. Gonçalves, *Thermochim. Acta*, 1996, 275, 67.

CALORIMETRIC INVESTIGATION OF RIBOFLAVIN AND CYANOCOBALAMIN

A.S. Plesovskikh, A.V. Knyazev, E.V. Gusarova and S.S. Knyazeva

*Chemistry Department, Lobachevsky State University of Nizhni Novgorod
Gagarin Av. 23/2, 603950, Nizhni Novgorod, Russia (28_stasy@bk.ru)*

ABSTRACT

The temperature dependences of heat capacity of riboflavin ($C_{17}H_{20}N_4O_6$) and cyanocobalamin ($C_{63}H_{89}CoN_{14}O_{14}P$) have been measured for the first time in the range from 7 to 330 K and from 6 to 343 K respectively. The experimental data were used to calculate standard thermodynamic functions, namely the heat capacity, enthalpy $H^\circ(T) - H^\circ(0)$, entropy $S^\circ(T) - S^\circ(0)$ and Gibbs function $G^\circ(T) - H^\circ(0)$, for the range from 0 to 330 K. The value of the fractal dimension D in the function of multifractal generalization of Debye's theory of the heat capacity of solids was estimated and the character of heterodynamics of structure was detected. In a calorimeter with a static bomb and an isothermal shield, the energy of combustion of the riboflavin and cyanocobalamin have been measured at 298.15 K. The enthalpy of combustion $\Delta_c H^\circ$ and the thermodynamic parameters $\Delta_f H^\circ$, $\Delta_f S^\circ$, $\Delta_f G^\circ$ and of reaction of formation of the riboflavin and cyanocobalamin from simple substances have been calculated. For the tested substances using differential scanning calorimetry were determined by the decomposition temperatures.

INTRODUCTION

Riboflavin (vitamin B_2) and cyanocobalamin (vitamin B_{12}) are water-soluble B vitamins. Riboflavin (PubChem CID: 493570) is an easily absorbed colored micronutrient with a key role in maintaining health in humans and animals. It is the central component of the cofactors flavin adenine dinucleotide (FAD) and flavin mononucleotide (FMN), and is therefore required by all flavoproteins. Various biotechnological processes have been developed for industrial scale riboflavin biosynthesis using different microorganisms.

Vitamin B_{12} (PubChem CID: 5479203) is a water-soluble vitamin with a key role in the normal functioning of the brain and nervous system, and for the formation of blood. The cyanocobalamin form of B_{12} does not occur in nature normally, but is a byproduct of the fact that other forms of B_{12} are avid binders of cyanide ($-CN$) which they pick up in the process of activated

charcoal purification of the vitamin after it is made by bacteria in the commercial process. Since the cyanocobalamin form of B₁₂ is easy to crystallize and is not sensitive to air-oxidation, it is typically used as a form of B₁₂ for food additives and in many common multivitamins.

This work is a systematic study of vitamins B. The goals of this work include calorimetric determination of the standard thermodynamic functions of the vitamins with the purpose of describing biochemical and industrial processes with their participation.

EXPERIMENTAL

Riboflavin and cyanocobalamin were purchased from Fluka. For phases identification, an X-ray diffraction patterns of the vitamin B₂ and B₁₂ samples were recorded on a Shimadzu X-ray diffractometer XRD-6000 (CuK α radiation, geometry θ -2 θ). The X-ray data and estimated impurity content (0.1 wt %) in the substance led us to conclude that the samples studied were an individual crystalline compounds.

To measure the heat capacity of the tested substances in the range from 6 to 330 K a BKT-3.0 automatic precision adiabatic vacuum calorimeter with discrete heating was used. The calorimeter design and the operation procedure were described earlier [1]. The analysis of the results showed that measurement error of the heat capacity of the substances at helium temperatures was within $\pm 2\%$, then it decreased to $\pm 0.5\%$ as the temperature was rising to 40 K, and was equal to $\pm 0.2\%$ at $T > 40$ K.

The energy of combustion, $\Delta_c U$, of riboflavin and cyanocobalamin were measured in a calorimeter (V-08) with a static bomb and an isothermal shield. The calorimeter design, the procedure of measuring the energies of combustion and the results of calibration and testing are given elsewhere [2]. It should be noted that while checking the calorimeter by burning succinic acid, prepared at D.I. Mendeleev Research Institute of Metrology. For complete combustion of samples we used paraffin as an auxiliary substance. Thermal analysis was carried out with a Setaram Labsys differential scanning calorimeter in an argon atmosphere at a heating rate of $0.0833 \text{ K}\cdot\text{s}^{-1}$.

RESULTS AND DISCUSSION

The experimental values of the molar heat capacity of riboflavin over the range from 6 to 322 K are presented in Figure 1. Experimental values were obtained in two series of experiments. The experimental points in temperature intervals 20-322 K (vit. B₂) and 6-350 K (vit. B₁₂) were fitted by means of the least-squares method and polynomial equations of versus temperature have been obtained. The heat capacity for both substances

gradually increases with rising temperature and does not show any peculiarities.

From the experimental values in the range 20–40K the value of the fractal dimension D was evaluated from the experimental data on the temperature-dependent heat capacities from a slope of the corresponding rectilinear sections of the plot $\ln C_v$ versus $\ln T$ [3]. Was found that in the range 20–40 K, $D=2$ K for riboflavin and $D=1.8$ K for cyanocobalamin. The D -value points to the layer structure of compounds. To calculate the standard thermodynamic functions of compounds, heat capacity values of it were extrapolated from the starting temperature of the measurement (approximately 7 K) to 0 K by Debye's function of heat capacity.

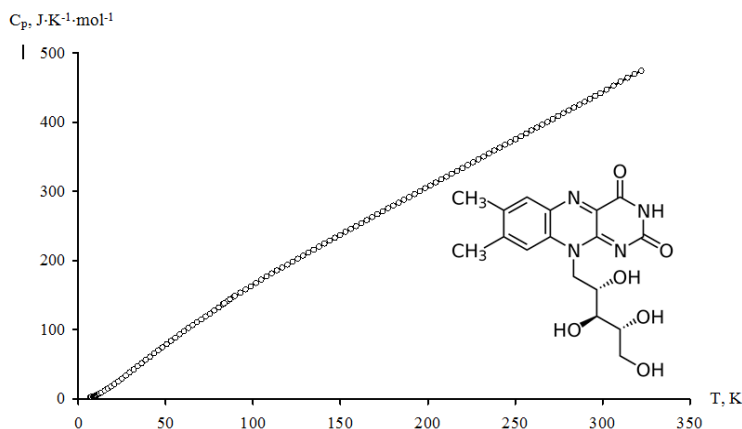
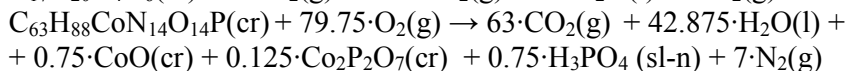
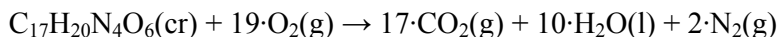


Figure 1. Temperature dependence of heat capacity of riboflavin [4].

In a calorimeter with a static bomb and an isothermal shield, the energy of combustion of the riboflavin and cyanocobalamin have been measured at 298.15 K. The data on the enthalpy of combustion of the crystalline vitamins were used to estimate enthalpy of combustion and formation. We have established the combustion reactions.



From the absolute value of the entropy of the riboflavin, carbon in the form of graphite, gaseous hydrogen, oxygen and nitrogen the standard entropy of formation $\Delta_f S^\circ$ of riboflavin at $T = 298.15\text{K}$ was calculated by methods described earlier [5]. The standard entropy of formation $\Delta_f S^\circ$ of cyanocobalamin was calculated similarly. The Gibbs function of formation $\Delta_f G^\circ$ of the riboflavin and cyanocobalamin were evaluated from the $\Delta_f H^\circ$ and $\Delta_f S^\circ$ values (Table 1).

Thermal analysis made it possible to establish some peculiarities of processes taking place in the compound under investigation during heating. DSC curve of riboflavin has the endothermic effect at 571 K. This effect is connected with melting and decomposition of compound. DSC curve of cyanocobalamin has the endothermic effects at 504, 522, 530 K. These effects are connected with the decomposition of ligands coordinated to the cobalt atom.

Table 1. Standard thermodynamic functions of vitamins [4, 6].

Compound	$-\Delta_c H^\circ$ (kJ·mol ⁻¹)	$-\Delta_f H^\circ(298)$ (kJ/mol)	$-\Delta_f S^\circ(298)$ (J/(mol·K))	$-\Delta_f G^\circ(298)$ (kJ/mol)
C ₁₇ H ₂₀ N ₄ O ₆	8116 ± 13	1432 ± 13	1961 ± 3	847 ± 14
C ₆₃ H ₈₉ CoN ₁₄ O ₁₄ P	33461 ± 14*	5015 ± 15*	7281 ± 5	2844 ± 15*

* new data

CONCLUSION

The general aim of these investigations was to report the results of the thermodynamic study of the riboflavin and cyanocobalamin. The heat capacities of these vitamins are measured over a wide temperature range from, the thermodynamic functions are calculated and the fractal dimensions D are evaluated. Thermochemical parameters of formation are determined by combining the data obtained by using combustion calorimetry and heat capacity measurements.

ACKNOWLEDGEMENT

The work was performed with the financial support of the Russian Foundation of Basic Research (Project Number 13-03-00152).

REFERENCES

- [1] R.M. Varushchenko, A.I. Druzhinina, E.L. Sorkin, *J. Chem. Thermodyn.*, 1997, 29, 623–637.
- [2] B.V. Lebedev, E.G. Kiparisova, *Russ. J. Phys. Chem.*, 1996, 70, 1253–1259.
- [3] T.S. Yakubov, *Dokl. Academy of Science*, 1990, 310, 145–150.
- [4] A.V. Knyazev, I.A. Letyanina, A.S. Plesovskikh, N.N. Smirnova, S.S. Knyazeva, *Thermochimica Acta*, 2014, 575, 12–16.
- [5] B.V. Lebedev, *Thermochimica Acta*, 1997, 297, 143–149.
- [6] A.V. Knyazev, N.N. Smirnova, A.S. Plesovskikh, A.N. Shushunov, S.S. Knyazeva, *Thermochimica Acta*, 2014, 582, 35–39.

CALORIMETRIC INVESTIGATION OF SOME SPINELS

S.S. Knyazeva¹, N.G. Chernorukov¹ and M. Mączka²

¹*Chemistry Department, Lobachevsky State University of Nizhni Novgorod
Gagarin Av. 23/2, 603950, Nizhni Novgorod, Russia (bess1706@rambler.ru)*

²*Institute of Low Temperature and Structure Research, Polish Academy of
Sciences, P.O. Box 1410, 50-950, Wrocław, Poland.*

ABSTRACT

The temperature dependences of heat capacity of $\text{Li}_{4/3}\text{Ti}_{5/3}\text{O}_4$ and $\text{Co}_{7/3}\text{Sb}_{2/3}\text{O}_4$ have been measured for the first time in the range from 6 to 330 K by precision adiabatic vacuum calorimetry. The experimental data were used to calculate standard thermodynamic functions, namely the heat capacity, enthalpy $H^\circ(T) - H^\circ(0)$, entropy $S^\circ(T) - S^\circ(0)$ and Gibbs function $G^\circ(T) - H^\circ(0)$, for the range from 0 to 330 K.

INTRODUCTION

Materials with the spinel structure have been extensively studied for a range of applications including their use as inorganic pigments [1], component of Mixed-Oxide (MOX) fuel for atomic energy [2], ion conductors, Li-battery electrodes, and for production of heat-insulated materials and materials for microelectronics [3]. The spinel structure type is also represented in a wide range of natural occurrences by the mineral form of magnetite, hetaerolite, hausmannite, chromite, trevorite and others [4]. Recently lithium insertion oxides like $\text{Li}_{4/3}\text{Ti}_{5/3}\text{O}_4$ have acquired considerable attention as alternative anode to carbon/graphite in rechargeable lithium-ion batteries. The $\text{M}_{7/3}\text{Sb}_{2/3}\text{O}_4$ ($M = \text{Ni}, \text{Co}$) compounds display interesting magnetic properties. In fact, depending on the M ion this system can be considered as a candidate to magnetic storage devices.

The ideal spinel structure has cubic symmetry (space group Fd3m) and crystal chemistry formula $\text{M}^{[4]}\text{A}_2^{[6]}\text{X}_4^{[4]}$. M atoms are located in tetrahedral positions 8a, while A atoms are located in octahedral positions 16d. X atoms of 32e position form compact layer. Typically X is O^{2-} but X may also be an anion such as S^{2-} , Se^{2-} , Cl^- or F^- .

The goals of this work include calorimetric determination of the temperature dependences of the heat capacity of $\text{Li}_{4/3}\text{Ti}_{5/3}\text{O}_4$ and $\text{Co}_{7/3}\text{Sb}_{2/3}\text{O}_4$ from 6 to 330 K, detection of the possible phase transitions, and calculation of the standard thermodynamic functions in the range from 0 to 330 K.

EXPERIMENTAL

The compounds were prepared by the solid-state reactions. Cobalt antimony oxide (lithium titanium oxide) was prepared by the solid-state reaction between antimony (III) oxide and cobalt sulfate heptahydrate (titanium oxide and lithium carbonate). The synthesis was performed in a porcelain crucible, into which the reaction mixture with the atomic ratio $7\text{Co} : 2\text{Sb}$ ($4\text{Li} : 5\text{Ti}$) was loaded. The mixture was calcined at 1173 K for 50 h, undergoing regrinding every 10 h.

To measure the heat capacity of the tested substances in the range from 5 to 340 K a BKT-3.0 automatic precision adiabatic vacuum calorimeter with discrete heating was used. The calorimeter was tested by measuring the heat capacity of high-purity copper and reference samples of synthetic corundum and K-2 benzoic acid. The analysis of the results showed that measurement error of the heat capacity of the substance at helium temperatures was within $\pm 2\%$, then it decreased to $\pm 0.5\%$ as the temperature was rising to 40 K, and was equal to $\pm 0.2\%$ at $T > 40$ K.

RESULTS AND DISCUSSION

The experimental values of the molar heat capacity of $\text{Co}_{7/3}\text{Sb}_{2/3}\text{O}_4$ over the range from 6 to 337 K are presented in Figure 1a. The heat capacity of this substance in intervals from 6 to 55 and from 70 to 327 K gradually increases with rising temperature and does not show any peculiarities, but from 55 to 70 K there is seen an anomalous heat capacity [5]. The calculations of $H^\circ(T) - H^\circ(0)$ and $S^\circ(T) - S^\circ(0)$ were made by the numerical integration of $C_p^\circ = f(T)$ and $C_p^\circ = f(\ln T)$ curves, respectively, and the Gibbs function $G^\circ(T) - H^\circ(0)$ was estimated from the enthalpies and entropies at the corresponding temperatures. The absolute entropies of compounds and the corresponding simple substances were used to calculate the standard entropy of formation of the compound under study at 298.15 K. Received values of standard enthalpies and entropies of formation were used to calculate the standard Gibbs function of formation $\text{Li}_{4/3}\text{Ti}_{5/3}\text{O}_4$ at 298K by Gibbs–Helmholtz equation. The transition temperature of the sample under study $T_\pi = 60.3 \pm 0.1$ K was estimated as the temperature of maximal heat capacity value within the temperature interval of the transition. The standard enthalpy and entropy of phase transition are $\Delta_{\text{tr}}H^\circ = 15.8 \pm 0.5$ J/mol and $\Delta_{\text{tr}}S^\circ = 0.258 \pm 0.007$ J/(mol·K). According to the work [6], magnetization measurements of the $\text{Co}_{7/3}\text{Sb}_{2/3}\text{O}_4$ compounds revealed the presence of a spin-glass transition, which should be a result of the competition between several magnetic interactions depending on the Co^{2+} site occupation. It should be noted that

the spinel, containing d-metals in their composition, often observed transitions at temperatures below 70 K.

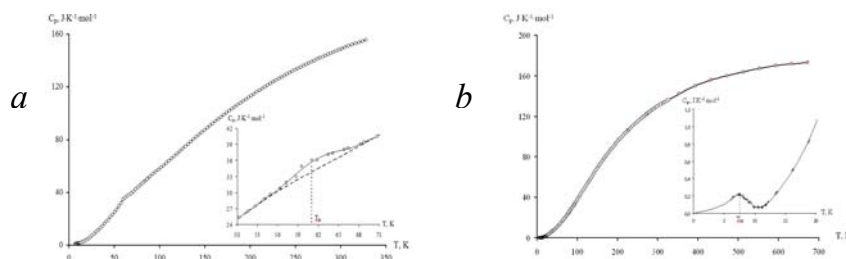


Figure 1. Temperature dependences of the heat capacities of the compounds: a) $\text{Co}_{7/3}\text{Sb}_{2/3}\text{O}_4$; b) $\text{Li}_{4/3}\text{Ti}_{5/3}\text{O}_4$.

There are at least two factors related to the spin-glass transition: (a) a competition between the diamagnetic Sb^{5+} and the ferromagnetic Co^{2+} ions both occupying the same crystallographic site; (b) the different crystallographic sites occupied by the Co^{2+} ions, as we observe in the structural analysis. It is believed that there are several possible magnetic interactions that could contribute to the spin-glass transition. Firstly, the spin-glass transition could be related to diamagnetic and ferromagnetic interactions between the Sb^{5+} and Co^{2+} ions. Also, the spin-glass behavior could be attributed to antiferromagnetic interaction between the Co^{2+} ions in the octahedral–octahedral or tetrahedral–tetrahedral sites or the ferromagnetic interaction between Co^{2+} ions in the octahedral–tetrahedral sites. In this sense, the magnetic frustration in the spinel structure could be a consequence of the competition among these magnetic interactions.

The heat capacity of $\text{Li}_{4/3}\text{Ti}_{5/3}\text{O}_4$ in interval from 12 to 670 K gradually increases with rising temperature and does not show any peculiarities, but over the range from 6 to 12 K there is seen an anomalous heat capacity (Fig. 1b) [7]. The transition temperature of the sample under study $T_{\pi} = 7.5 \pm 0.1$ K was estimated as the temperature of maximal heat capacity value within the temperature interval of the transition.

The absolute entropies of compounds and the corresponding simple substances were used to calculate the standard entropy of formation of the compound under study at 298.15 K. Received values of standard enthalpies and entropies of formation were used to calculate the standard Gibbs function of formation $\text{Li}_{4/3}\text{Ti}_{5/3}\text{O}_4$ at 298K by Gibbs–Helmholtz equation (table 1).

Table 1. Standard thermodynamic functions of studied compounds.

Compound	$-\Delta_f H^\circ(298)$ (kJ/mol)	$S^\circ(298)$ (J/(mol·K))	$-\Delta_f S^\circ(298)$ (J/(mol·K))	$-\Delta_f G^\circ(298)$ (kJ/mol)
$\text{Li}_{4/3}\text{Ti}_{5/3}\text{O}_4$	2050 ± 10	108.8 ± 0.5	391.5 ± 0.6	1933 ± 10
$\text{Co}_{7/3}\text{Sb}_{2/3}\text{O}_4$		153.4 ± 0.5	357.5 ± 0.6	

CONCLUSION

Thermodynamic studies were performed for two compounds with spinel structure in a wide temperature range. Much attention is paid to the low-temperature phase transitions. Transition mechanism is proposed on the basis of spectroscopic studies.

ACKNOWLEDGEMENT

The work was performed with the financial support of the Russian Foundation of Basic Research (Project Number 13-03-00152).

REFERENCES

- [1] A.V. Knyazev, M. Mączka, E.N. Bulanov, M. Ptak, S.S. Belopolskaya, *Dyes and Pigments*, 2011, 91, 286-293.
- [2] R.P.C. Schram, F.C. Klaassen, *Progress in Nuclear Energy*, 2007, 49, 617-622.
- [3] H. Shiiba, M. Nakayama, M. Nogami, *Solid State Ionics*, 2010, 181, 994-1001.
- [4] H. Sawada, *Materials Research Bulletin*, 1996, 31, 361-366.
- [5] A.V. Knyazev, N.N. Smirnova, M. Mączka, K. Hermanowicz, S.S. Knyazeva, I.A. Letyanina, M.I. Lelet, *The Journal of Chemical Thermodynamics*, 2014, 74, 201-208.
- [6] M. S. L. Brito, M. T. Escote, C. O. P. Santos, P. N. Lisboa-Filho, E. R. Leite, J. B. L. Oliveira, L. Gama, E. Longo, *Mat. Chem. Phys.*, 2004, 88, 404-409.
- [7] A.V. Knyazev, N.N. Smirnova, M. Mączka, S.S. Knyazeva, I.A. Letyanina, *Thermochimica Acta*, 2013, 559, 40-45.

THE VOLUME OF METASTABLE STATES FOR BINARY SYSTEM UNDER NUCLEATION

M. P. Anisimov and N. T. Tukubaev

*Nanoaerosol Research Laboratory, FSBSI Technological Design
Institute of Scientific Instrument Engineering SB RAS (TDISIE SB RAS,
anisimovmp@mail.ru), 41 Russkaya Street, 630058, Novosibirsk, Russia*

ABSTRACT

Any metastable state volume for binary system is restricted by the critical condition line and by the surfaces of phase equilibria and spinodal conditions which are jointed by the critical line. The real state equations can be used to found all these boundaries. In the most cases the equation of real states can not be found and the equation for ideal system should be used. The accuracy of the ideal system approximation was estimated in the present research by a direct comparison with the calculation results on the base of equation of states for a real system.

INTRODUCTION

Nucleation rate measurements along the critical line of a binary system is problem which has no real solution up-to now. It is easy to show, for example [1], that any metastable volume for binary system is restricted by the critical conditions, by the surfaces of phase equilibria and spinodal conditions. Let show briefly the main points which should be taken into account to design of a volume of metastable states for a simplified binary system. For simplicity let take a vapor-gas system. The surface of the vapor-liquid equilibria (dark grey color, see Figure 1), contour $Ba_2a_1b_1$, and spinodal states surface, $a_3a_1b_1b_3$ (light grey one) which are bounding a volume of metastable states are shown schematically in Figure 1.

The real topology of the metastable volume needs to be measured empirically. The low as well as high (at least elevated) pressures are used in several research groups. But there are no systematic measurements to clarify the geometry of a volume of metastable states. Some time ago the flow diffusion was developed [2]. It looks that the chamber can be modified for measurements at the high pressures. We did a scheme, created and tested of the High Pressure (up-to 200 bar) Aerosol Counter recently which can be incorporated into the Flow Diffusion Chamber for the High Pressure measurements.

Well known that any critical conditions are the locus of the second order phase transitions (line a_1b_1 in Figure 1) where zero rate of nucleation is appeared.

No nucleation at conditions of phase transition of the second order can rise [3]. Several approximations are created to calculate the line of the critical conditions for binary systems [4]. It is obvious that one should solve a set of equations for real vapor-gas system to calculate the nucleation conditions at a High Pressure Flow Diffusion Chamber (HPFDC).

High pressure measurements, at several hundred bars at least, is actual problem for empirical detection of volume for the system metastable states as well as for measurements of the four-dimensional nucleation rate volume and topologies of the nucleation rate surfaces at constant temperatures or/and pressures. These kinds of measurements nobody did up to now, even these data are very helpful for development of the Nucleation Theory.

HPFDC has chance to give a direct answer on the nucleation data discrepancy nature revealed, for example, by Brus et al. [5]. It is very reasonable to use the real gas equation of state to describe a heat-mass transfer for the nucleation conditions in the laminar axial vapour-gas flow at elevated pressures. The empirical data approximation for compressibility $Z(\omega, \tau)$ of nonideal (real) gas [6] is used, where:

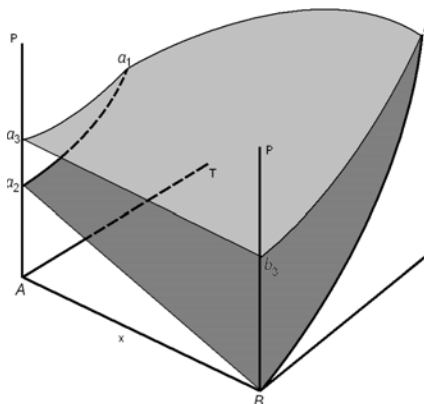


Figure 1. Schematic presentation of the metastable volume in the parameters space

$$\begin{aligned}
 Z(\omega, \tau) = & 1 + a_1(e^\tau - 1 - \tau)(\omega_{tr} - \omega)^2(4\omega - \omega_{tr})\omega - a_2\omega(e^{-\tau} - 1) \\
 & - a_3\omega(e^{-3\tau} - 1) - a_4\omega\tau \\
 & + a_5(e^{3\tau} - 1 - 3\tau)(\omega_{tr} - \omega)^4(6\omega - \omega_{tr})\omega \\
 & + a_6(e^{6-\tau} - 6\tau)(\omega_{tr} - \omega)^3(3\omega - \omega_{tr})\omega^2 + a_7 \frac{\omega}{(1 - Z_c\omega)} \\
 & + a_8 \frac{\omega^2}{(1 - Z_c\omega)^2} + a_9 \frac{\omega^3}{(1 - Z_c\omega)^3} + a_{10} \frac{\omega^4}{(1 - Z_c\omega)^4}
 \end{aligned}$$

Steady state axisymmetric motion of a laminar flow of viscous gas is described by a system of equations for boundary layer and equation of state, which in the cylindrical coordinates can be presented such as:

$$P = \rho R_g T Z(\omega, \tau) \quad (1)$$

$$2 \cdot \pi \cdot \int_0^R r \cdot \rho \cdot u dr = Q, \quad (2)$$

$$\rho \cdot u \frac{\partial u}{\partial x} = -\frac{\partial P}{\partial x} + \frac{1}{r} \frac{\partial}{\partial x} \cdot (r \cdot \eta \cdot \frac{\partial u}{\partial r}), \quad (3)$$

$$\rho \cdot u \cdot C_p \frac{\partial T}{\partial x} - u \frac{\partial P}{\partial x} - \eta \cdot \left(\frac{\partial u}{\partial r}\right)^2 - \frac{1}{r} \cdot (r \cdot \lambda \frac{\partial T}{\partial r}) = 0. \quad (4)$$

$$\rho \cdot u \cdot \frac{\partial C(x,r)}{\partial x} = \frac{1}{r} \frac{\partial}{\partial x} \left(r \cdot \rho \cdot d(T) \cdot \frac{\partial C(x,r)}{\partial x} \right) \quad (5)$$

where P is pressure of gas, $Z(\omega, \tau)$ is gas compressibility and Z_c is a critical one; ω and τ are reduced density and temperature defined by ratios $\omega = \rho/\rho_c$ and $\tau = T/T_c$; ρ_c and T_c are critical density and temperature; $a_1 - a_{10}$ are gas empirical coefficients; $\omega_{tr} = \rho_{tr}/\rho_c$ is a reduced density at triple point; x is the axial coordinate of cylindrical tubing, r is the radial coordinate, $u(x,r)$ is a radial gas velocity distribution, T is the temperature, ρ is the density of the gas, λ η are thermal conductivity and viscosity coefficients of gas, respectively, C_p is the heat capacity, R_g is the universal gas constant, R is the radius of the tube, Q is the mass flow rate of gas; $C(x,r)$ is the concentration of substance; $d(T)$ is the vapor-gas diffusion coefficient.

The equations (1–5) have the well known physical sense. The boundary conditions for system of equations (1)–(5) are set as follows.

$$\text{Along the axis: } \frac{\partial u}{\partial r}(0, x) = 0, \quad \frac{\partial T}{\partial r}(0, x) = 0, \quad \frac{\partial C}{\partial r}(0, x) = 0. \quad (6)$$

$$\text{At the wall: } u(R, x) = 0, \quad T(R, x) = T_w(x), \quad C(R, x) = C[T_w(x)] \quad (7)$$

At the entrance of the tube:

$$T(r, 0) = T_0(r), \quad u(r, 0) = u_0(r), \quad P(r, 0) = P[T_0(r)], \quad C(r, 0) = C(T_{sat}),$$

where $T_w(x)$ is the tubing wall temperature, $T_0(r)$ is the initial temperature profile of the flow at the tubing entrance, T_{sat} is the saturation temperature, $u_0(r)$ is the initial profile of the flow velocity at the tubing opening. The vapor supersaturation and temperature fields can be found following article by Voevodin&Goncharova [7].

Assuming that the velocity at the opening of the tube has a parabolic profile corresponding to the mass flow rate Q_0 , one can get

$$u_0(r) = \frac{2Q_0}{\pi R^2} \left(1 - \frac{r^2}{R^2} \right),$$

Using the continuity equation, it is easy to get: $\rho u = \rho_0 u_0 \equiv b_0(r)$.

The boundary conditions for the parameters are similar to velocities one. To find them one can use the mass flow that does not depend on x , related equation and get the ratio. The flow speed at every step, the temperature, and the density can be calculated by such a way. Viscosity and thermal conductivity depends on the temperature, an iterative process is used to nonlinearity disclosure for each step. The approximation of equations on r , and using a tridiagonal run of linear equations by the Thomas algorithm [8]. Then the concentration C can be calculated.

CONCLUSIONS

A difference of the ideal and real state equations using is found and discussed. Deviation of the nucleation rates for ideal and real gas approximations is found numerically. A threshold for the ideal state equation using is found for case of glycerol-carbon dioxide system. It can be seen easily on the result of our computer estimations that ideal gas model produces a nucleation rate overestimation more than 100 decimal orders of magnitude against the real gas state equation applied for case of the total pressure near 100 bar and nucleation temperature $T = 350$ K for nucleation of glycerol-carbon dioxide system. One can conclude that ideal gas model can be used for pressures not more than 10 bar.

REFERENCES

- [1] M. P. Anisimov, P. K. Hopke. J. Phys. Chem. B, 2001, 105(47), 11817-11822.
- [2] M.P. Anisimov, History of the Flow Diffusion Chamber Development. In Aerosol Science and Technology: History and Reviews. Ed. D. S. Ensor. RTI Press. Research Triangle Park, NC, USA. 2011, 457-469.
- [3] J. I. Frenkel, A Kinetic Theory of Liquids, Oxf. Univ. Press, 1946.
- [4] R. C. Reid, J. M. Prausnitz, T. K. Sherwood, The Properties of Gases and Liquids, McGraw-Hill, New York, 1987
- [5] D. Brus, A. Hyvarinen, V. Zdimal, & H. Lihavainen, J. Chem. Phys., 2005, 122, 214506 – 1514.
- [6] A. B. Kaplun, & A. B. Meshalkin, 2003, The Russian Academy Reports, 392(1), 48-53.
- [7] A. F. Voevodin, O. H. Goncharova, Matem. Mod., 2001, 13(5), 90–96.
- [8] S. D. Conte, and C. de Boor, Elementary Numerical Analysis. McGraw-Hill, New York, 1972.

THERMODYNAMIC AND THERMOPHYSIC INVESTIGATION OF APATITE BINARY SYSTEMS

E.N. Bulanov, V.J. Korokin, and A.G. Blokhina

*Chemistry Department, Lobachevsky State University,
23, Gagarin av., 603950 Nizhni Novgorod, Russia*

ABSTRACT

Compounds in three binary apatite systems $Pb_5(PO_4)_3F - Pb_5(PO_4)_3Cl$, $Pb_5(PO_4)_3Cl - Pb_5(VO_4)_3Cl$, and $Ca_5(PO_4)_3Cl - Pb_5(PO_4)_3Cl$ are synthetic analogues of natural minerals. Phase diagrams of those systems were plotted on the basis of thermodynamic modeling and experimental data. Calculation of the thermal expansion coefficients of the compounds were used to discover features of isomorphic substitution in the systems under study.

INTRODUCTION

Apatites are one of the most broadest mineral family [1]. This fact is made possible by different isomorphic substitutions in the chemical composition of the apatites. In the common case, the general formula of the apatites may be represented as follows: $M_5(AO_4)_3L$, where M – mono-, di-, tris- and tetravalent cations and their combinations; A – atoms, which can form tetrahedra as coordination polyhedra; L – is the position for halogen and different groups of atoms such as OH, CO_3 and others. Moreover, in all of the positions various types of defect can be observed. Apatites have high isomorphic capacity, which causes necessity of investigation not only individual compounds, but various binary systems. We investigated phase diagrams of three binary systems: $Pb_5(PO_4)_3F - Pb_5(PO_4)_3Cl$ (I) [2], $Pb_5(PO_4)_3Cl - Pb_5(VO_4)_3Cl$ (II) [3], and $Ca_5(PO_4)_3Cl - Pb_5(PO_4)_3Cl$ (III) [4] on the basis of thermodynamic modeling and experimental data. Moreover, for hexagonal modifications of all compounds and solid solutions of aforementioned systems high-temperature XRD investigations were done.

EXPERIMENTAL

Samples of individual compounds and solid solutions were synthesized *via* solid-state reactions between diammonium hydrophosphate, nitrates and halogenates of calcium and lead. The phase individuality of synthesized compounds was monitored by X-ray diffraction. X-ray diffraction patterns were recorded on a XRD-6000 Shimadzu diffractometer (CuK_α radiation, geometry θ -2 θ) in the 2 θ range from 10° to 120° with scan increment of

0.02°. High-temperature X-ray diffraction experiments in the range from 298 to 1173 K were carried out on the same diffractometer with increments of 0.02° ranging from 10° to 60° using an HA-1001 Shimadzu attachment. Thermal experiments were carried out on a LABSYS Setaram differential scanning calorimeter at a heating rate of 10 K/min in an argon atmosphere. The samples were enclosed in platinum crucibles. The experimental thermochemical data set was obtained using a modified Skuratov calorimeter. Calorimetric experiments were carried out in order to calculate standard enthalpies of formation and enthalpies of mixing and to elucidate the isomorphous miscibility model. Inspection of the resulting values shows that the enthalpy of mixing as a function of composition is fitted by a second-order polynomial for all systems, in agreement with the regular solid solutions model. In calculating solidus and liquidus temperatures for phase diagrams, we used the general form of the Clausius–Clapeyron equation:

$$\ln \frac{x_l \cdot \gamma_l}{x_c \cdot \gamma_c} = -\frac{\Delta_{fus} H^\circ}{R} \left(\frac{1}{T} - \frac{1}{T_{liq}} \right) \quad (1)$$

because regular liquid and solid solutions are characteristic of the system under study, as shown by thermochemical studies [2-4]. Equation (1) for a binary system may be represented by the system of equations [5]

$$\begin{cases} \ln x_{l,1} + \frac{\Omega_l \cdot (1-x_{l,1})^2}{RT} - \ln x_{c,1} - \frac{\Omega_c \cdot (1-x_{c,1})^2}{RT} = -\frac{\Delta_{fus,1} H^\circ}{R} \left(\frac{1}{T} - \frac{1}{T_{liq,1}} \right) \\ \ln x_{l,2} + \frac{\Omega_l \cdot (1-x_{l,2})^2}{RT} - \ln x_{c,2} - \frac{\Omega_c \cdot (1-x_{c,2})^2}{RT} = -\frac{\Delta_{fus,2} H^\circ}{R} \left(\frac{1}{T} - \frac{1}{T_{liq,2}} \right) \end{cases} \quad (2)$$

System (2) was used to calculate the thermodynamic parameters of the liquid (Ω_l) and the crystal (Ω_c) and the enthalpies of melting of the first component and the second component ($\Delta_{fus,1} H^\circ$, $\Delta_{fus,2} H^\circ$). This solved the inverse problem; that is, simulation was based on experimentally derived data on phase boundaries [5]. The values obtained in this way were used to construct the plots of the Gibbs energies versus composition for a liquid and a crystal and the phase diagrams (Fig. 1).

RESULTS AND DISCUSSION

It was observed that systems I and II have complete solid miscibility. System III due to the formation of the individual compound with the composition $\text{Ca}_7\text{Pb}_3(\text{PO}_4)_6\text{Cl}_2$ should be considered as combination of two binary systems $\text{Pb}_{10}(\text{PO}_4)_6\text{Cl}_2 - \text{Ca}_7\text{Pb}_3(\text{PO}_4)_6\text{Cl}_2$ and $\text{Ca}_7\text{Pb}_3(\text{PO}_4)_6\text{Cl}_2 - \text{Ca}_{10}(\text{PO}_4)_6\text{Cl}_2$.

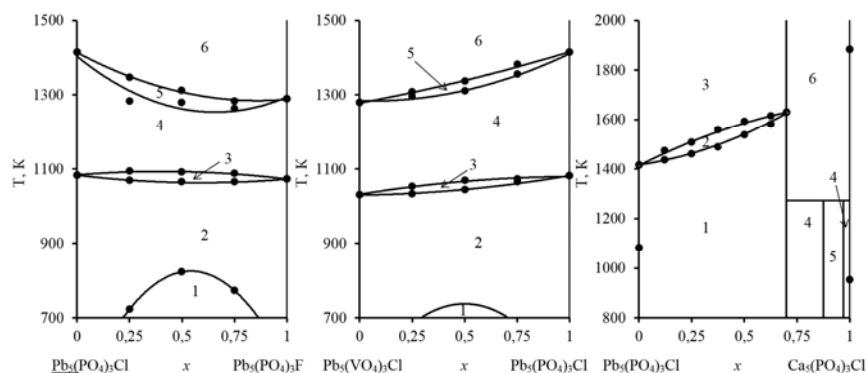


Figure 1. Phase diagrams for binary apatite systems. For $\text{Pb}_5(\text{PO}_4)_3\text{F}$ - $\text{Pb}_5(\text{PO}_4)_3\text{Cl}$ and $\text{Pb}_5(\text{PO}_4)_3\text{Cl}$ - $\text{Pb}_5(\text{VO}_4)_3\text{Cl}$: 1) mixture of solid solutions, (2) solid solution (the hexagonal phase), (3) mixture of two phases of solid solutions, (4) solid solution (the monoclinic phase), (5) solid solution (monoclinic phase) + liquid, and (6) liquid. For $\text{Ca}_5(\text{PO}_4)_3\text{Cl}$ - $\text{Pb}_5(\text{PO}_4)_3\text{Cl}$: (1) solid solutions of the $\text{Pb}_{10}(\text{PO}_4)_6\text{Cl}_2$ – $\text{Ca}_7\text{Pb}_3(\text{PO}_4)_6\text{Cl}_2$ system, (2) solid solutions of the $\text{Pb}_{10}(\text{PO}_4)_6\text{Cl}_2$ – $\text{Ca}_7\text{Pb}_3(\text{PO}_4)_6\text{Cl}_2$ system + liquid, (3) liquid, (4) solid solutions of the $\text{Ca}_7\text{Pb}_3(\text{PO}_4)_6\text{Cl}_2$ – $\text{Ca}_{10}(\text{PO}_4)_6\text{Cl}_2$ system, (5) mixture of solid solutions of the $\text{Ca}_7\text{Pb}_3(\text{PO}_4)_6\text{Cl}_2$ – $\text{Ca}_{10}(\text{PO}_4)_6\text{Cl}_2$ system, (6) decomposition products of compounds solutions of the $\text{Ca}_7\text{Pb}_3(\text{PO}_4)_6\text{Cl}_2$ – $\text{Ca}_{10}(\text{PO}_4)_6\text{Cl}_2$ system.

All of the diagrams have a lens form and solid solutions in all studied systems can be described with the regular model. A deviation scope from the idealness in the systems is determined by an equivalence of the replaceable positions in the apatite structure. $\text{Pb}_{10}(\text{PO}_4)_6\text{Cl}_2$ – $\text{Ca}_7\text{Pb}_3(\text{PO}_4)_6\text{Cl}_2$ system is characterized by small relative difference of ionic radii of substituted atoms (~14%). In addition, the substitution progresses in one crystallographic position. Therefore a small deviation from the idealness occurs. In $\text{Pb}_{10}(\text{PO}_4)_6\text{Cl}_2$ – $\text{Pb}_{10}(\text{VO}_4)_6\text{Cl}_2$ system in spite of ~100 % relative difference in ionic radii P and V atoms there is a small deviation from the idealness too because of the identity of their crystallographic positions. Situation in $\text{Pb}_{10}(\text{PO}_4)_6\text{F}_2$ – $\text{Pb}_{10}(\text{PO}_4)_6\text{Cl}_2$ system is more complicated due to big relative difference of halogen ionic radii and an effect of isodimorphism that means a substitution in different crystallographic positions. High-temperature XRD investigations of hexagonal modifications of apatites in temperature range 298-973 K [6] shown the following facts. In case of $\text{Pb}_5(\text{PO}_4)_3\text{F}_x\text{Cl}_{1-x}$ system it can be seen that in the range of $0 < x <$

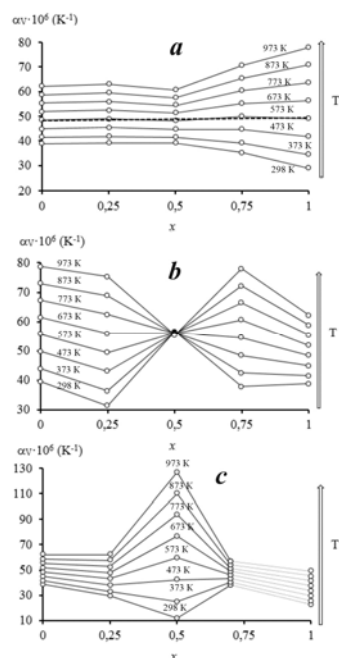


Figure 2. Thermal-composition dependencies of volume thermal expansion coefficient for $\text{Pb}_5(\text{PO}_4)_3\text{F}-\text{Pb}_5(\text{PO}_4)_3\text{Cl}$ (**a**), $\text{Pb}_5(\text{PO}_4)_3\text{Cl}-\text{Pb}_5(\text{VO}_4)_3\text{Cl}$ (**b**) $\text{Ca}_5(\text{PO}_4)_3\text{Cl}-\text{Pb}_5(\text{PO}_4)_3\text{Cl}$ (**c**) systems.

0.5 volume thermal expansion coefficient doesn't depend on the composition for all temperatures (Fig. 2a). At the 573 K volume thermal expansion coefficient doesn't depend on the composition of the solid solution. In the case of $\text{Pb}_5(\text{PO}_4)_3\text{Cl} - \text{Pb}_5(\text{VO}_4)_3\text{Cl}$ (Fig. 2b) there is the independence of the volume thermal expansion coefficient from the temperature in the solid solution with equimolar ratio of substituted atoms (P and V). $(\text{Ca}_x\text{Pb}_{1-x})_5(\text{PO}_4)_3\text{Cl}$ system is characterized by the strong temperature dependence of volume thermal expansion coefficient in the case of equimolar ratio of substituted atoms (Ca and Pb) (Fig. 2c).

CONCLUSION

Phase diagram of investigated binary apatite systems may be used in geochemical investigations of apatite minerals. In addition, that information coupled with data on the thermal expansion may be very useful for the creation of apatite-based functional materials.

ACKNOWLEDGEMENT

This work was partially supported by the Russian Fund of the Basic Research (research project No. 14-03-31234 мол-а).

REFERENCES

- [1] M. Pasero, A. R. Kampf, C. Ferraris, I. V. Pekov, J. Rakovan, T.J. White, *European Journal of Mineralogy*, 2010, 22, 163-179.
- [2] A.V. Knyazev, N.G. Chernorukov, E.N. Bulanov. *Thermochimica Acta*, 2011, 513, 112-118.
- [3] N.G. Chernorukov, A.V. Knyazev. E.N. Bulanov. *Russian Journal of Inorganic Chemistry*, 2010, 55(9), 1463-1470.
- [4] A.V. Knyazev, N.G. Chernorukov, E.N. Bulanov. *Thermochimica Acta*, 2011, 526, 72-77.
- [5] R. Lyupis. *Chemical Thermodynamics of Materials*, Moscow, 1989.
- [6] A.V. Knyazev, N.G. Chernorukov, E.N. Bulanov. *Materials Chemistry and Physics*, 2012, 132, 773-781.

EVALUATION OF THERMODYNAMIC PROPERTIES ON UNSTABLE STEAM

H.Serizawa¹, T. Osawa², Y. Ohishi³ and Y. Kaji¹

¹*Tokai Research and Development Center, (Nuclear Science Research Institute), Japan Atomic Energy Agency (JAEA), 2-4 ShiraneShirakata, Tokai-mura, Naka-gun, Ibaraki, 319-1195, Japan*

²*Quantum Beam Science Center, Japan Atomic Energy Agency (JAEA), Shirakata Shirane 2-4, Tokai-mura, Naka-Gun, Ibaraki, 319-1195, Japan*
³*Graduate School of Engineering, Osaka University, 2-1 Yamada-oka, Suita, Osaka 565-0871, Japan*

ABSTRACT

When the steam is in unstable state, the activity of oxygen in the gas phase increases drastically. We propose here a new thermodynamic model using the concept of partial equilibrium to explain the behavior of metal/steam oxidizing reaction.

INTRODUCTION

Researchers who analyze the metal corrosion by steam generally consider that the metal oxidation in humid environment is caused by the direct reaction between H₂O and metal [1-3]. In the previous studies, H₂O in the gas phase is considered to be in equilibrium state. Quadackers and Zurek assumed that H₂O decomposed into H₂ and O₂ to reach the equilibrium state at the temperature in the evaluation of the partial pressure of O₂ in the steam [1]. However, it is a question that such kind of gaseous equilibrium is attained easily. Of course, the catalytic decomposition must occur on the surface of the metal and the wall of the reaction chamber. Uetsuka *et al.* examined the critical steam supply rate necessary for steam starvation [3]; they showed that the oxidation of the metal is suppressed, when the flow rate was extremely decreased. Though the physical meaning of the word, "starvation", is not clear, their research implies that the corrosion by steam in the closed system is different from that in an open system (gas flow system) which means that the equilibrium in the gas phase is not attained in the gas flow system. It should be noted that the decomposition of the introduced gas is suppressed when the reaction proceeds in the open system [4-11]. Therefore, it is meaningful to clarify the state of unstable steam to analyze the oxidation reaction in the gas flow system. In this investigation, we clarified thermodynamic properties of the steam which is not in equilibrium state by introducing a novel idea of the partial equilibrium.

MODELING & THERMODYNAMICS

We model the reaction between a metal and flowing steam under the condition that oxide layer is formed preferentially. Generally, the growth rate of the oxide layer on the metal surface depends on the corrosion mechanism. In the case of Fe-Cr, alloy, Yamauchi et al. suggested that a formation and evaporation of Cr_2O_3 is the primary factor of the deterioration of surface scale [12]. Whereas, in the case of the Zr alloy, the

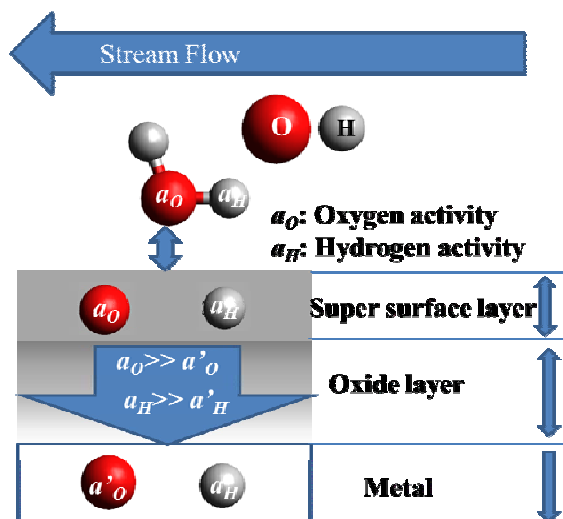
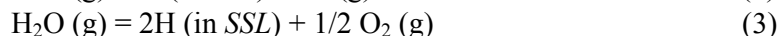


Figure 1. Model of the reaction between Steam and metal

phase to *SSL* is much faster than that from *SSL* to metal through under oxide layer, which means that the activities of oxygen and hydrogen in *SSL* is equal to that in the gas phase. The figure shows that the diffusion in the oxide layer is induced by the difference in the oxygen activities in the *SSL* and metal phase.

When a metal is brought into contact with steam, following three reactions are possible.



Reaction (1) shows the dissociation of steam into H_2 and O_2 catalyzed by the metal surface or the wall of the reaction chamber. Reaction (2) and (3) represent dissolution of the oxygen and hydrogen into *SSL*, respectively. If equilibrium is attained, H_2O , O_2 , and H_2 coexist in the gas phase; the partial pressure of each gas is uniquely determined by the equilibrium constant of (1) as a function of temperature. However, when the steam is flowed over the

Zr alloy/ H_2O reaction obeys parabolic kinetics, which shows that the oxygen diffusion process is the rate-controlling step [13]. Thus, it is clear that the corrosion reactions described above are greatly affected by the activity of oxygen in the gas phase or partial pressure of O_2 . The model is given in Fig. 1. A distinctive feature of the model is a Super-Surface-Layer (*SSL*) virtually arranged on the surface of oxide layer. We assume here that the mobility of oxygen and hydrogen from gas

metal, the dissociation of steam might be suppressed to a great extent just like the case of ammonia stream [6, 11]. In the case of the gas flow system, the system should tend to differ from equilibrium because of the entropy produced by the continuous introduction of steam. Therefore, a partial pressure of O₂ in the gas phase cannot be obtained with an equilibrium constant *K_p* of reaction (1). However, according to our model, equilibrium of reaction (2) is attained between the gas phase and *SSL*, which is the concept of a partial equilibrium. In such a series of relations given below must hold:

$$\mu(\text{H}_2\text{O}) = \mu(\text{O in SSL}) + \mu(\text{H}_2) \tag{4}$$

$$\mu(\text{H}_2\text{O}) = \Delta G_f^0(\text{H}_2\text{O}) + RT \ln(P_{\text{H}_2\text{O}}) \tag{5}$$

and

$$\mu(\text{H}_2) = \mu^0(\text{H}_2) + RT \ln(P_{\text{H}_2}) \tag{6}$$

where μ , T , $P_{\text{H}_2\text{O}}$, P_{H_2} , and $\Delta G_f^0(\text{H}_2\text{O})$ denote chemical potential, temperature, partial pressures of steam and H₂, and the standard free energy of formation of H₂O, viz. the difference in free energies of H₂O, O₂ and H₂ at 1 atm pressure. Since the pressure of flowing steam is considered to be equal to atmospheric pressure, it is reasonable to assume that gases behave ideally. Substituting Eqs. (5) and (6) into (4), we get

$$\mu(\text{O in SSL}) = \Delta G_f^0(\text{H}_2\text{O}) + RT \ln(P_{\text{H}_2\text{O}}/P_{\text{H}_2}) \tag{7}$$

Since the gas phase is in equilibrium with *SSL*, Eq. (7) indicates that $\mu(\text{O})$ in the gas phase increases as increasing the value of $P_{\text{H}_2\text{O}}/P_{\text{H}_2}$. $\mu(\text{O})$ is related to an oxygen activity, a_{O} , by the relation, $\mu(\text{O}) = RT \ln(a_{\text{O}})$. Thus, $a_{\text{O}} = \exp(\Delta G_f^0(\text{H}_2\text{O})/RT) \Gamma_{\text{O}}$ where denote $P_{\text{H}_2\text{O}}/P_{\text{H}_2}$ as Γ_{O} .

RESULTS AND DISCUSSION

The activity of oxygen calculated by Eq. (8) at 1273 K is given in Fig. 2. The figure indicates that the value of a_{O} varies drastically depending on the value of the oxidation potential. As described above, the value of Γ_{O} is the function of $P_{\text{H}_2\text{O}}$ and P_{H_2} . When the steam pass through the hot zone of the reaction system, H₂ and O₂ gases are

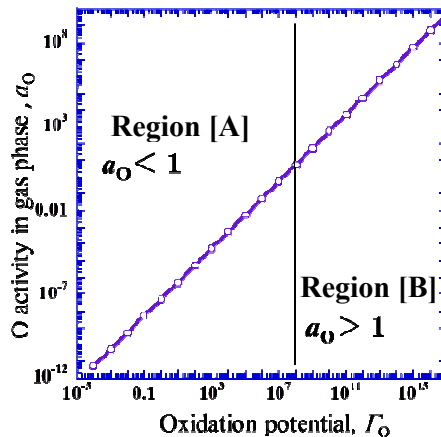


Figure 2 Relationship between oxidation potential and the activity of oxygen in the gas phase.

generated by a dissociation reaction shown by (1). Generally to say, the equilibrium is not attained in such gas flowing system. Thus the activity of oxygen in the flowing gas phase should be larger than that of oxygen in O_2 in equilibrium with H_2O and H_2 in a closed system. The dissociation rate of steam varies largely depending on the amount of introduced gas or flow rate. When the flow rate is decreased extremely, the system can be regarded as closed system; the dissociation rate of reaction (1) increases, which means that the value of Γ_O decreases. The decrease of Γ_O implies that the suppression of the oxidation of the metal coexists in the reaction system. Though Uetsuka *et al.* blame steam starvation for suppression of oxidation reaction [3], our thermodynamic consideration indicates that the suppression is because of the increase in the dissociation rate followed by the decrease in the activity of oxygen in the gas phase. The results of experimental work on Fe-Cr alloy indicate that the scale thickness formed by the reaction of the metal and Ar- H_2O mixed gas changes depending on the gas flow rate; the faster the flow rate, the faster the growth of the scale on the surface of the metal [14], which coincides our result of thermodynamic consideration.

CONCLUSION

It was established that the activity of oxygen in H_2O - O_2 - H_2 mixed gas phase changes depending on the oxidation potential. When the equilibrium of the system is not attained, we strongly recommend that the valuation activity of oxygen in gas phase should be taken into account.

REFERENCES

- [1] W.J. Quadackers, J. Zurek, SHREIR'S CORROSION, Elsevier B. V., The Netherlands, 2010, pp. 407.
- [2] N.W.G.o.F. Safety, in: O.F.E.C.-O.A.D. NUCLEAR ENERGY AGENCY (Ed.), 2009.
- [3] H. Uetsuka, T. Otomo, J. Nucl. Sci. Technol., 1989, 26.
- [4] M. Katsura, et al., J. Nucl. Mater., 1998, 839, 258-263.
- [5] T. Nakagawa et al. J. Nucl. Mater., 1997, 247, 127.
- [6] H. Serizawa, F. Fukkuda, M. Katsura, J. Alloys Comp., 1996, 232, 274.
- [7] H. Serizawa, F. Fukuda, M. Katsura, J. Alloys Comp., 1995, 223, 39.
- [8] M. Katsura, H. Serizawa, J. Alloys Comp., 1993, 196, 191.
- [9] M. Katsura, M. Miyake, H. Serizawa, J. Alloys Comp., 1993, 193, 101.
- [10] M. Katsura, H. Serizawa, J. Alloys Comp., 1992, 187, 389.
- [11] M. Katsura, J. Alloys Comp., 1992, 182, 91.
- [12] A. Yamauchi et al., Oxidation of Metals, 2003, 59, 517.
- [13] V.F. Urbanic, T.R. Heidrick, J. Nucl. Mater., 1978, 75, 251.
- [14] J. Zurek et al., Oxidation of Metals, 2005, 63, 401.

SOLUBILITY DETERMINATIONS OF $K_2HPO_4 \cdot 3H_2O(cr)$ AT TEMPERATURE 298.15 K BY THE ISOPIESTIC METHOD

D. Ž. Popović, J. M. Miladinović, and S. R. Grujić

*Faculty of Technology and Metallurgy, University of Belgrade, Karnegijeva
4, 11 000 Belgrade, Serbia,*

ABSTRACT

Phosphates are of great relevance for numerous physiological reactions as well as for a large number of industrial and agricultural applications. The trihydrate $K_2HPO_4 \cdot 3H_2O(cr)$ is the thermodynamically stable solid phase at temperature 298.15 K in contact with a saturated aqueous solution. Due to wide variations in reported solubility of this solid in literature, the isopiestic method was used in attempt to unambiguously determine the molality of K_2HPO_4 aqueous saturated solution and appropriate osmotic coefficient at $T = 298.15$ K, together with solubility product and Gibbs energy of solution.

INTRODUCTION

The potassium salts of phosphoric acid have considerable commercial and practical importance. Phosphates are contained in food, soft-drinks, anticorrosion liquids and paper while another important usage of phosphates is as mineral fertilizers. Despite their significance, a certain differences in evaluated thermodynamic values among its published thermodynamic database gives the risk of introducing inconsistencies into thermodynamic modeling calculations. A solid phase, $K_2HPO_4 \cdot 3H_2O(cr)$ is the thermodynamically stable form at 298.15 K (see Figure 1). Recently, we

reported the results of molality determination for the saturated solution in contact with metastable $K_2HPO_4 \cdot xH_2O(cr)$ at $T = 298.15$ K being $m < 10.6$ mol·kg⁻¹[2]. Now, the isopiestic determinations on solubility have been repeated, and lower molality value

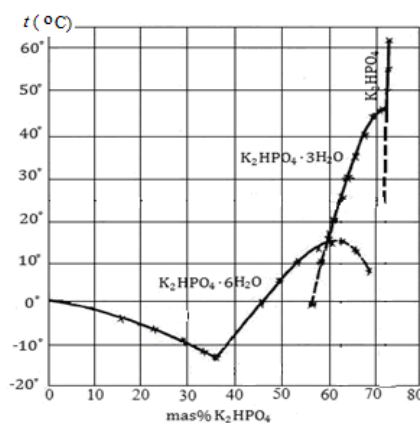


Figure 1. Solubility of K_2HPO_4 in water [1].

for aqueous saturated $\text{K}_2\text{HPO}_4(\text{aq})$ solution obtained by the isopiestic method with $\text{CaCl}_2(\text{aq})$ as a reference solution.

The isopiestic method is one of the most accurate methods for solubility determinations that have an additional advantage: solvent activity can be simultaneously determined for the saturated solution. Its basic features are as follows: physically isolated samples of solutions of two or more compounds, of known initial masses and known initial molalities, are allowed to equilibrate isothermally, through a common vapor phase. At isopiestic equilibrium, all of the solutions have the same solvent activities. Then, by equilibrating the samples with a referent solution whose solvent activities are accurately known as a function of molality, the solvent activities of the other solutions can be determined. In solubility determinations, by adding a reservoir cup containing saturated solution and excess crystals to the chamber during the equilibrations, the solubility of the solute can be determined. If the test solution is initially below saturation, then solvent will be transported from it to the reservoir cup; some of the crystals in the reservoir cup will dissolve to maintain saturation. Similarly, if the test solution is initially supersaturated, solvent will be transported to it from the reservoir cup and more crystals will grow in the reservoir cup to maintain saturation. Since no crystals are present in the sample cups, their molality at saturation can be determined simply by weighing. If these samples are also simultaneously equilibrated with a standard electrolyte whose water activities are accurately known as a function of molality, then the molality and the solvent activity of the saturated solution are determined.

EXPERIMENTAL

The isopiestic apparatus and experimental procedure in this work are the same as those previously described[3]. The stock solution of $\text{K}_2\text{HPO}_4(\text{aq})$ was prepared from anhydrous K_2HPO_4 (Merck Suprapure grade, mass fraction 0.9999) and double-distilled, deionized water. The molality of $\text{K}_2\text{HPO}_4(\text{aq})$ was determined gravimetrically by adding NH_4Cl and MgCl_2 when HPO_4^{2-} was precipitated as MgNH_4PO_4 and then calcined at $T = 1273$ K to form $\text{Mg}_2\text{P}_2\text{O}_7(\text{s})$. The resulting average molality is (7.7274 ± 0.0022) $\text{mol} \cdot \text{kg}^{-1}$. The reference $\text{CaCl}_2(\text{aq})$ stock solution was prepared from $\text{CaCl}_2 \cdot 4\text{H}_2\text{O}(\text{s})$ (Merck Suprapure grade, mass fraction 0.99995) and double-distilled, deionized water. The molality of this solution is determined by conversion of samples to anhydrous $\text{CaSO}_4(\text{s})$ and heating the residues at $T = (673 \text{ to } 973)$ K. The resulting average molality from this analysis was (5.8142 ± 0.0012) $\text{mol} \cdot \text{kg}^{-1}$. Crystals were prepared in a following manner: a mixture of double-distilled, deionized water and

$\text{K}_2\text{HPO}_4(\text{cr})$ was heated to 343 K until saturation was achieved and then supernatant was cooled to room temperature to yield a saturated solution plus crystals. Solubility experiment was performed with cumulative equilibration periods ranging from 5 to 25 days. The results from these isopiestic solubility measurements are reported in Table 1.

RESULTS AND DISCUSSION

The osmotic coefficients of the saturated $\text{K}_2\text{HPO}_4(\text{aq})$ solution at $T = 298.15$ K, ϕ_{sat} , were calculated from the following fundamental equation for isopiestic equilibrium:

$$\phi_{\text{sat}} = m_{\text{R}} \phi_{\text{R}} / m_{\text{sat}} \quad (1)$$

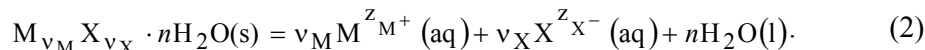
where m_{sat} and m_{R} are the equilibrium molalities of the saturated solution and referent solution, respectively and ϕ_{R} is the osmotic coefficient of the referent solution, calculated using the Extended Pitzer equation with an alternate form of expression for the ionic strength dependence of the third virial coefficient, proposed by Pitzer *et al.*[4].

Table 1. Experimental isopiestic equilibrium molalities, m_{sat} , and osmotic coefficients, ϕ_{sat} , for saturated $\text{K}_2\text{HPO}_4(\text{aq})$ solution in equilibrium with $\text{K}_2\text{HPO}_3 \cdot 3\text{H}_2\text{O}(\text{cr})$ vs. $\text{CaCl}_2(\text{aq})$ reference solution, R, at $T = 298.15$ K.

$m_{\text{sat}}(\text{K}_2\text{HPO}_4)$	ϕ_{sat}	$m_{\text{R}}(\text{CaCl}_2)$	ϕ_{R}	cumulative equilibrium periods (days)
9.7740±0.0081	1.2156	4.7742±0.0007	2.4887	5
9.7924±0.0063	1.2157	4.7796±0.0022	2.4908	12
9.7408±0.0023	1.2124	4.7576±0.0027	2.4824	13
9.7421±0.0044	1.2131	4.7595±0.0032	2.4831	19
9.7457±0.0039	1.2129	4.7600±0.0044	2.4833	25

We can adopt that the mean value of solubility represents the average of last 3 equilibrations where the assigned uncertainty is the 95-% confidence limit: $m_{\text{sat}} = (9.7429 \pm 0.012) \text{ mol} \cdot \text{kg}^{-1}$. The average molality value of the referent solution is: $m_{\text{R}} = (4.7590 \pm 0.0062) \text{ mol} \cdot \text{kg}^{-1}$ with the same confidence limit. The osmotic coefficient of the saturated $\text{K}_2\text{HPO}_4(\text{aq})$ solution can be calculated as $\phi_{\text{sat}} = 1.2128$. If we compare this value to the osmotic coefficient obtained by the Extended Pitzer equation and parameters of $\text{K}_2\text{HPO}_4(\text{aq})$, valid up to $m = 9.2723 \text{ mol} \cdot \text{kg}^{-1}$, at $T = 298.15$ K from the paper of Popović *et al.*[2] we obtain $\phi_{\text{sat}} = (1.2129 \pm 0.0041)$ that represents an excellent agreement. Activity of solvent is defined as: $\ln a_{\text{w}} = -\nu m M_{\text{w}} \phi$ where $\nu = 3$, is the stoichiometric ionization number of electrolyte

K_2HPO_4 and $M_w = 0.0180153 \text{ g}\cdot\text{mol}^{-1}$, is the molar mass of water. For the saturated solution $a_{w,\text{sat}} = (0.5280 \pm 0.0012)$ where the 95-% confidence limit uncertainty is based on the standard error of the osmotic coefficient fit multiplied by 1.96, and mean ionic activity coefficient is $\gamma_{\pm,\text{sat}} = (0.2301 \pm 0.0064)$. The reaction describing equilibrium between $K_2HPO_3 \cdot 3H_2O(\text{cr})$ and its saturated solution is:



The standard thermodynamic solubility product K_{sp} defined as:

$$K_{\text{sp}} = v_M^{v_M} v_X^{v_X} \left(m_{\text{sat}} / m^0 \right)^v \gamma_{\pm,\text{sat}}^v a_{w,\text{sat}}^v = 4 \left(m_{\text{sat}} / m^0 \right)^3 \gamma_{\pm,\text{sat}}^3 a_{w,\text{sat}}^3 \quad (3)$$

yields $K_{\text{sp}} = (6.6340 \pm 0.555)$ while Gibbs energy of solution can be calculated according to: $\Delta_{\text{sol}} G_m^0(K_2HPO_4 \cdot 3H_2O, \text{cr}, 298.15 \text{ K}) = -RT \ln K_{\text{sp}}$ that gives $\Delta_{\text{sol}} G_m^0(K_2HPO_4 \cdot 3H_2O, \text{cr}, 298.15 \text{ K}) = -(4.691 \pm 0.207) \text{ kJ}\cdot\text{mol}^{-1}$.

CONCLUSION

The isopiestic method used in determination of the molality of K_2HPO_4 aqueous saturated solution in equilibrium with $K_2HPO_3 \cdot 3H_2O(\text{cr})$ at $T = 298.15 \text{ K}$, yields $m_{\text{sat}} = (9.7429 \pm 0.012) \text{ mol}\cdot\text{kg}^{-1}$. The standard thermodynamic solubility product is $K_{\text{sp}} = (6.6340 \pm 0.555)$ and Gibbs energy of solution $\Delta_{\text{sol}} G_m^0(K_2HPO_4 \cdot 3H_2O, \text{cr}, 298.15 \text{ K}) = -(4.691 \pm 0.207) \text{ kJ}\cdot\text{mol}^{-1}$.

ACKNOWLEDGEMENT

This work was supported by the Ministry of Education, Science and Technological Development of the Republic of Serbia (Grants no. 172063).

REFERENCES

- [1] Gmelin Handbook of Inorganic and Organometallic Chemistry, 8th edition, Phosphorus (System-Nr. 16) Springer, 1965.
- [2] D. Popović, J. Miladinović, M. Todorović, M. Zrilić, Joseph A. Rard, J. Solution Chem., 2011, 40, 907-920.
- [3] V. Pavićević, R. Ninković, M. Todorović, J. Miladinović, Fluid Phase Equilibr., 1999, 164, 275-284.
- [4] K. Pitzer, P. Wang, J. A. Rard, S. Clegg, J. Solution Chem., 1999, 28, 265-282.

THE INFLUENCE OF INTERACTIONS ON ACTIVITY COEFFICIENTS OF TERNARY AQUEOUS SOLUTIONS OF K_2HPO_4 WITH KCl , KBr AND KNO_3 AT $T = 298.15$ K

D. Ž. Popović¹, J. M. Miladinović¹, Z. P. Miladinović² and S. R. Grujić¹

¹*Faculty of Technology and Metallurgy, University of Belgrade, Karnegijeva 4, 11 000 Belgrade, Serbia,*

²*Institute of General and Physical Chemistry, Studentski trg 12–16, 11 000 Belgrade, Serbia.*

ABSTRACT

Experimental results on isopiestic measurements for three ternary aqueous solutions of K_2HPO_4 with KCl , KBr and KNO_3 at $T = 298.15$ K were modeled with the Clegg–Pitzer–Brimblecombe equation based on mole–fraction–composition scale yielding appropriate mixing parameters, for the estimation of thermodynamic activities of solute components. The results for mean ionic activity coefficients of electrolytes in ternary solutions calculated this way are showing specific behavior depending on total ionic strength and ionic strength fractions of electrolytes. The activity coefficients of KCl in $\{yKCl+(1-y)K_2HPO_4\}(aq)$ and of KBr in $\{yKBr+(1-y)K_2HPO_4\}(aq)$ are changing consistently from the ionic strength and their ionic strength fractions contrary to activity coefficients of KNO_3 in $\{yKNO_3+(1-y)K_2HPO_4\}(aq)$.

INTRODUCTION

Despite the importance, thermodynamic properties of phosphate solutions and their mixtures with other electrolytes are poorly investigated. Therefore, the newest experimental results[1-3] on such mixtures, in ionic strength range $I = (0.5–6.0) \text{ mol}\cdot\text{kg}^{-1}$, were treated by widely applicable mole–fraction composition scale model of the Clegg–Pitzer–Brimblecombe (CPB)[4] (giving standard deviation of the fit of order 10^{-3}) to investigate activity coefficients of electrolytes.

Mole fractions are calculated on the basis of complete dissociation of all salts present, thus the mole fraction x_j of species j is given by $x_j = n_j / \sum_i n_i$ where n_i is the number of moles of all the species i , including cations, anions and solvent. In the systems of interest, $\{yKCl+(1-y)K_2HPO_4\}(aq)$, $\{yKBr+(1-y)K_2HPO_4\}(aq)$ and $\{yKNO_3+(1-y)K_2HPO_4\}(aq)$ where y is the ionic strength fraction of electrolyte, if m_1 is the molality of electrolyte of the type 1:1 and m_2 , molality of K_2HPO_4 , in ternary solution, then the ionic strength is $I = m_1 + 3m_2$ and $y = m_1 / (m_1 + 3m_2)$. In this case, $\sum_i n_i =$

$2m_1+3m_2+(1/M_1)$ where $1/M_1= 55.5084 \text{ mol}\cdot\text{kg}^{-1}$. Therefore, if ternary solution contains cation M and anions X, Y then: $x_M = (m_1+2m_2)/\sum_i n_i$; $x_X = m_1/\sum_i n_i$; $x_Y = m_2/\sum_i n_i$ and for solvent $x_1 = (1/M_1)/\sum_i n_i$. The equations for activity coefficients of cation M and anion X, according to the CPB model, are as follows:

$$\begin{aligned} \ln \gamma_{x,M} = & -z_M^2 A_x \left[(2/\rho) \ln(1 + \rho I_x^{1/2}) + I_x^{1/2} \left\{ 1 - (2I_x/z_M^2) \right\} / (1 + \rho I_x^{1/2}) \right] \\ & + x_X B_{MX} g(\alpha_{MX} I_x^{1/2}) + x_Y B_{MY} g(\alpha_{MY} I_x^{1/2}) \\ & - x_M x_X B_{MX} \left[z_M^2 g(\alpha_{MX} I_x^{1/2}) / (2I_x) + \left\{ 1 - z_M^2 / (2I_x) \right\} \exp(-\alpha_{MX} I_x^{1/2}) \right] \\ & - x_M x_Y B_{MY} \left[z_M^2 g(\alpha_{MY} I_x^{1/2}) / (2I_x) + \left\{ 1 - z_M^2 / (2I_x) \right\} \exp(-\alpha_{MY} I_x^{1/2}) \right] \\ & + x_1 E_X \left[(z_M + z_X) / z_X W_{1,MX} - \left\{ 0.5z_M + (1/F) \right\} (z_M + z_X) / z_M z_X W_{1,MX} \right] \\ & + x_1 E_Y \left[(z_M + z_Y) / z_Y W_{1,MY} - \left\{ 0.5z_M + (1/F) \right\} (z_M + z_Y) / z_M z_Y W_{1,MY} \right] \\ & + x_1 x_X \left[(z_M + z_X)^2 / (z_M z_X) U_{1,MX} - 2x_M (z_M + z_X)^2 / (z_M z_X) U_{1,MX} \right] \\ & + x_1 x_Y \left[(z_M + z_Y)^2 / (z_M z_Y) U_{1,MY} - 2x_M (z_M + z_Y)^2 / (z_M z_Y) U_{1,MY} \right] \\ & - 2x_X x_Y W_{MXY} - 4x_X x_Y \left\{ x_X / v_{X(M)} - x_Y / v_{Y(M)} \right\} U_{MXY} \\ & - 8x_1 x_X x_Y Q_{1MXY} - 0.5 \left[E_X (z_M + z_X) / z_X W_{1,MX} + E_Y (z_M + z_Y) / z_Y W_{1,MY} \right] \end{aligned} \quad (1)$$

$$\begin{aligned} \ln \gamma_{x,X} = & -z_X^2 A_x \left[(2/\rho) \ln(1 + \rho I_x^{1/2}) + I_x^{1/2} \left\{ 1 - (2I_x/z_X^2) \right\} / (1 + \rho I_x^{1/2}) \right] \\ & + x_M B_{MX} g(\alpha_{MX} I_x^{1/2}) - x_M x_X B_{MX} \left[z_X^2 g(\alpha_{MX} I_x^{1/2}) / (2I_x) + \left\{ 1 - z_X^2 / (2I_x) \right\} \exp(-\alpha_{MX} I_x^{1/2}) \right] \\ & - x_M x_Y B_{MY} \left[z_X^2 g(\alpha_{MY} I_x^{1/2}) / (2I_x) + \left\{ 1 - z_X^2 / (2I_x) \right\} \exp(-\alpha_{MY} I_x^{1/2}) \right] \\ & + x_1 \left[(z_M + z_X) / z_M W_{1,MX} - \left\{ 0.5z_X + (1/F) \right\} \left\{ E_X (z_M + z_X) / z_M z_X W_{1,MX} + E_Y (z_M + z_Y) / z_M z_Y W_{1,MY} \right\} \right] \\ & + x_1 x_M \left[(z_M + z_X)^2 / (z_M z_X) U_{1,MX} - 2 \left\{ x_X (z_M + z_X)^2 / (z_M z_X) U_{1,MX} + x_Y (z_M + z_Y)^2 / (z_M z_Y) U_{1,MY} \right\} \right] \\ & + 2 \left\{ x_Y W_{MXY} - x_X x_Y W_{MXY} \right\} + 2 \left\{ x_Y \left\{ 2x_X / v_{X(M)} - x_Y / v_{Y(M)} \right\} U_{MXY} - 2x_X x_Y \left\{ x_X / v_{X(M)} - x_Y / v_{Y(M)} \right\} U_{MXY} \right\} \\ & + 4x_1 \left\{ x_Y Q_{1MXY} - 2x_X x_Y Q_{1MXY} \right\} - \left[\left\{ 1 - 0.5E_X \right\} (z_M + z_X) / z_M W_{1,MX} - 0.5z_X E_Y (z_M + z_Y) / z_M z_Y W_{1,MY} \right] \end{aligned} \quad (2)$$

The B_{MX} and B_{MY} parameters with their corresponding α values represent long-range forces, while $W_{1,MX}$, $W_{1,MY}$ and $U_{1,MX}$, $U_{1,MY}$ in the above equations formally represent short-range forces. These parameters are valid for the pure electrolyte solutions as mixture constituents. Parameters W_{MXY} , U_{MXY} and Q_{1MXY} represent ionic and ion–solvent interactions in the mixed solution. Ionic strength on the mole fraction scale, I_x , is related to ionic strength molality scale, I , by: $I_x = I / \sum_i n_i$. z_j is the valence (with sign) of ion j where $j \equiv M, X$ or Y and v_j denotes the number of ions of type j formed by the stoichiometric dissociation of one molecule of the electrolyte. A_x is the Debye–Hückel limiting laws slope on the mole fraction scale for water and ρ is a dimensionless parameter related to the distance of closest approach. Quantities E_a , F , and $v_{a(c)}$ are defined as: $E_a = x_a z_a / (\sum_a x_a z_a)$, $F = 1 / [1/2(\sum_a x_a z_a + \sum_c x_c z_c)]$ and $v_{a(c)} = z_c / (z_c + z_a)$ while function $g(x)$ as $g(x) = 2[1 - (1+x)\exp(-x)]/x^2$. The mean activity coefficient $\gamma_{x,\pm}$ (infinite dilution

reference state) on the mole fraction-composition scale is related to the mean activity coefficient on the molality scale by $\ln \gamma_{\pm} = \ln \gamma_{x,\pm} + \ln x_1$.

RESULTS AND DISCUSSION

It is assumed that phosphate ions, present in all ternary solution belong to the group of structure makers and their influence on activity coefficient values is weaker comparing to other present ions. On the other hand, ions like $\text{K}^+(\text{aq})$, $\text{Cl}^-(\text{aq})$, $\text{Br}^-(\text{aq})$ and $\text{NO}_3^{2-}(\text{aq})$ are solution structure breakers that destabilize the structure intensifying ion-ion interactions except for $\text{NO}_3^{2-}(\text{aq})$ who's solutions are having more pronounced ion-solvent interactions.

Calculated values of mean ionic activity coefficients of electrolytes, by the CPB model, versus ionic strength fraction of electrolyte y , for different total ionic strengths of ternary solutions are illustrated in Figure 1. Activity coefficients of KCl (Fig. 1a) and KBr (Fig. 1b) increase with ionic strength fraction, y , of KCl and KBr in the systems $\{y\text{KCl}+(1-y)\text{K}_2\text{HPO}_4\}(\text{aq})$ and $\{y\text{KBr}+(1-y)\text{K}_2\text{HPO}_4\}(\text{aq})$, respectively. For the range of total ionic strength from 0.5 to 4.0 $\text{mol}\cdot\text{kg}^{-1}$ activity coefficients of KCl and KBr increase moderately with ionic strength fraction of KCl and KBr and then notably in

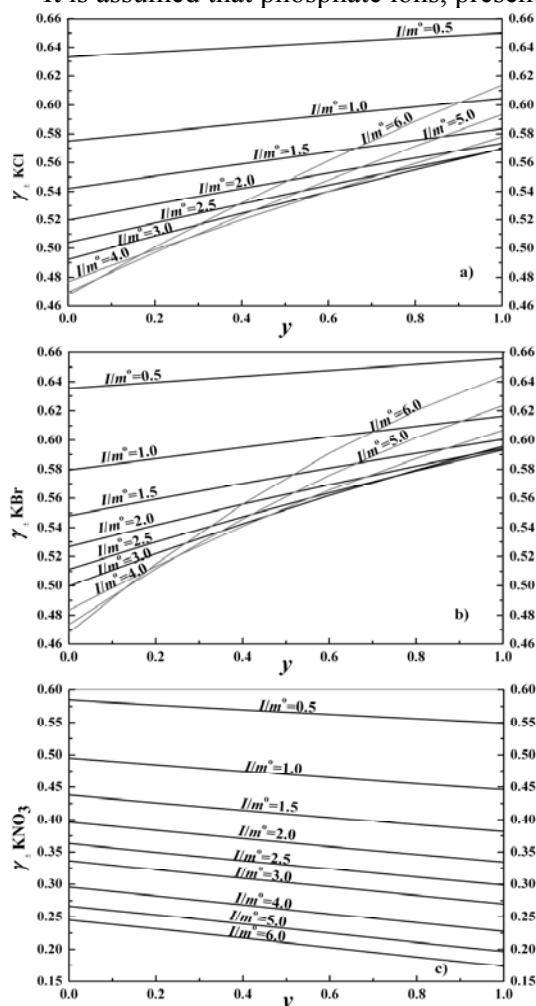


Figure 1. Mean ionic activity coefficient of electrolyte vs. ionic strength fraction, y , for different total ionic strengths of the mixed solution, I/m^0 ($m^0=1 \text{ mol}\cdot\text{kg}^{-1}$):
 a) of KCl in $\{y\text{KCl}+(1-y)\text{K}_2\text{HPO}_4\}(\text{aq})$
 b) of KBr in $\{y\text{KBr}+(1-y)\text{K}_2\text{HPO}_4\}(\text{aq})$

c) of KNO_3 in $\{y \text{KNO}_3 + (1-y) \text{K}_2\text{HPO}_4\}(\text{aq})$

the ionic strength range from 4.0 to 6.0 $\text{mol}\cdot\text{kg}^{-1}$, especially for the ionic strength fractions over $y = 0.2$. On the other hand, increasing of total ionic strength, from 0.5 to 4.0 $\text{mol}\cdot\text{kg}^{-1}$, has the effect of lowering of KCl and KBr coefficient values, but in the range from 4.0 to 6.0 $\text{mol}\cdot\text{kg}^{-1}$ values are ascending. It can be assumed that the changes in solution structure are appearing at ionic strength 4.0 $\text{mol}\cdot\text{kg}^{-1}$ and ionic strength fraction of $y = 0.2$. Unlike other two systems, activity coefficient of KNO_3 (Fig. 1c) monotonically decreases with total ionic strength and ionic strength fraction of KNO_3 .

Calculated values of K_2HPO_4 activity coefficients in the solutions with KCl and KBr increase with higher values of ionic strength fraction of 1:1 electrolyte and decrease with total ionic strength of both solutions in the range $I = (0.5-6.0) \text{mol}\cdot\text{kg}^{-1}$. In solution $\{y \text{KNO}_3 + (1-y) \text{K}_2\text{HPO}_4\}(\text{aq})$, activity coefficient of K_2HPO_4 decreases with both, total ionic strength and ionic strength fraction of KNO_3 .

CONCLUSION

The Clegg–Pitzer–Brimblecombe model was used in calculation of mean ionic activity coefficients of electrolytes in aqueous ternary solutions of K_2HPO_4 with KCl, KBr and KNO_3 at $T = 298.15 \text{ K}$. It was established that ion-ion and ion-solvent interactions in ternary systems have the same effects on activity coefficient values in ternary systems $\{y \text{KCl} + (1-y) \text{K}_2\text{HPO}_4\}(\text{aq})$ and $\{y \text{KBr} + (1-y) \text{K}_2\text{HPO}_4\}(\text{aq})$ contrary to coefficients in $\{y \text{KNO}_3 + (1-y) \text{K}_2\text{HPO}_4\}(\text{aq})$ at $T = 298.15 \text{ K}$.

ACKNOWLEDGEMENT

This work was supported by the Ministry of Education, Science and Technological Development of the Republic of Serbia (Grants no. 172063).

REFERENCES

- [1] D. Ž. Popović, J. Miladinović, M. D. Todorović, M. M. Zrilić, Joseph A. Rard, *J. Chem. Thermodyn.*, 2011, 43, 1877-1885.
- [2] D. Ž. Popović, J. Miladinović, Z. P. Miladinović, B. B. Ivošević, Joseph A. Rard, *J. Chem. Thermodyn.*, 2012, 55, 172-183.
- [3] D. Ž. Popović, J. Miladinović, Z. P. Miladinović, S. R. Grujić, M. M. Todorović, Joseph A. Rard, *J. Chem. Thermodyn.*, 2013, 62, 151-161.
- [4] S. L. Clegg, K. S. Pitzer and P. Brimblecombe, *J. Phys. Chem.*, 1992, 96, 9470-9479.

SPACE COMPUTER MODELS OF T-x-y DIAGRAMS Au-Bi-{Ag, Sb} FOR LEAD-FREE SOLDERS

V. Lutsyk^{1,2}, V. Vorob'eva¹ and S. Shodorova¹

¹*Institute of Physical Materials Science SB RAS, 6, Sahyanova st., Ulan-Ude, 670047 Russia (vluts@ipms.bscnet.ru)*

²*Buryat State University, 24a, Smolina st., Ulan-Ude, 670000, Russia*

ABSTRACT

On examples of systems Au-Bi-Sb and Ag-Au-Bi it is shown, how it is possible with a help of 3D computer models of T-x-y diagrams to carry out agreement of inconsistent data, to explain the unclear and incorrect fragments of phase diagrams. Publications, devoted to T-x-y diagrams of systems, intended for lead-free solders creation, are discussed.

INTRODUCTION

Space (3D) computer models of T-x-y diagrams are very useful when it is necessary to carry out an assessment and coordination of experimental and calculated sections and projections of phase diagrams, received from different sources [1], because each model is designed by data of the concrete source and it can reconstruct all published sections to compare isothermal sections and isopleths, designed by other authors.

Au-Bi-Sb SYSTEM

Results of experimental investigation and thermodynamic assessment by CALPHAD technology of the system Au-Bi-Sb=A-B-C with compounds R1=Au₂Bi, R2=AuSb₂ are published in [2,3]. The curve of solid solution Bi(Sb)=B(C) decomposition to Bi and Sb begins below 200°C in the binary system B-C [4] (Fig. 1,a). Obviously, that this curve gives the correspond surface in the ternary system (Fig. 1,h), because the trace of its section can be seen in the isopleths $z_{2(Bi)}=0.2$ (Fig. 1,b). However, the 2-phase region B+C is designated in this isopleths as the 3-phase region B+C+R2. Two-phase region (B(C)+R2) can be seen above it. Why phase regions, contained the compound AuSb₂=R2 with Au, adjoin to the binary system, formed by Bi and Sb? Maybe authors of [4] were mistaken in designations of these phase regions and the 2-phase region needs to be renamed to 1-phase (solid solution of Bi with Sb) and 3-phase region to 2-phase (decomposition of solid solution)? But then 1-phase region RHOMBO_A7=B(C) will be adjacent with 3-phase regions L+B(C)+R2 and B(C)+R1+R2 with breaking of the known law of adjoining phase regions.

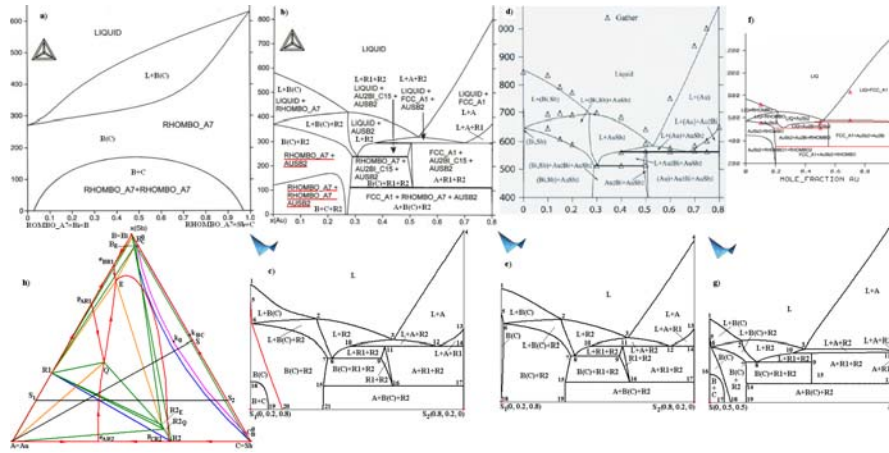


Figure 1. Binary system Bi-Sb [4] (a); isopleth $S_1(0, 0.2, 0.8)S_2(0.8, 0.2, 0)$: from [4] (b) and [2] (d), models by data [4] (c) and [2] (e); isopleth $S(0, 0.5, 0.5)$ -A: from [3] (f), model by data [3] (g), x-y projection (h).

To resolve this contradiction, it is possible to address to other publications devoted to this system. In the Atlas, intended for lead-free solders [4], when comparing the results presented in [2] and [3], the preference was given to the work [2]. However, the binary system B-C is considered in [2] at temperatures above 500 K that is above the binodal and the minimum temperature at which all isopleths are given is 400 K. The solid solution B(C) decomposition curve is absent in isopleths [2]. However, there is no contradiction also in designations of phase regions, because one-phase region B(C) adjoins directly to the system B-C, as, for instance, in the isopleth $z_{2(Bi)}=0.2$ (Fig. 1,d). And does the region of solid solution decomposition exist, which is given by the binodal in the binary system B-C? The trace of its section can be seen in isopleths as in [4] (Fig. 1,b), as in [3], and with the same inconsistent designations of phase regions (Fig. 1,g). To explain the reasons of contradictions when determining phase regions in [2] and in [3,4], three versions of the system Au-Bi-Sb T-x-y diagram computer models have been designed by data [2] (Fig. 1,e), [3] (Fig. 1,g), [4] (Fig. 1,c), depending on, whether really the solid solution decomposition in the binary system B-C takes place.

If "no", then isopleths in [2] (Fig. 1,d) are correct. They, as well as the corresponding to them computer model (Fig. 1,e) present borders of the solid solution B(C) region in the form of traces from the section of solidus and solvus surfaces (lines 5-6 and 6-18). They are located very close to a temperature axis, then it is badly visible, but they on isopleths are present.

If "yes" and the solid solution is decomposed in the system B-C, then the curve on T-x diagram, corresponding to it, gives a decomposition surface in

the ternary system. It is represented in isopleths [3] (Fig. 1,g) and [4] (Fig. 1,b). In that case the mistakes in designations of phase regions in these works are connected with that the lost of sections of solidus and solvus surfaces – curves 5-6, 6-18 (Fig. 1,g) and 5-6, 6-20 (Fig. 1,c) on the corresponding model isopleths. At the same time, it should be noted that solidus and solvus curves in the isopleth of [2] (Fig. 1,d) and corresponding curves 5-6 and 6-18 (Fig. 1,e) of the model isopleth can not pass very close to a temperature axis. They have to "be removed" from an axis "to make a space" for a trace from the section of the decomposition surface.

Au-Bi-Ag SYSTEM

In the paper [5], describing the system Ag-Au-Bi=A-B-C (Ag=Au=FCC_A1, Bi=Sb=RHOMBO_A7), decomposition of the compound $\text{Au}_2\text{Bi}=\text{R}$ in the binary system Au-Bi was not observed (its T-x diagram is shown up to the temperature 50°C) (Fig. 2, b). Later it was revealed [6], that the compound is decomposed at 110°C . These data as the most reliable, were selected for the Atlas [4] (Fig. 2, a).

However, in the isopleths [4,7,8], limited by temperatures 450 K [8] and 0°C [4], this compound is present at the lowermost phase regions. If the compound R in the binary system B-C is decomposed at 110°C why it does not decompose in the ternary system? More visually to show this contradiction, two versions of this system T-x-y diagram computer models have been constructed. In one version the compound decomposes, and then in the isopleth $z_{1(\text{Ag})}=0.2$ sections of corresponding ruled surfaces are borders of the closed 3-phase region A(B)+C+R on curves 7-8 and 6-8 (Fig. 2,e). In other version when the compound R does not decompose neither in the binary, nor in the ternary system, model isopleths (Fig. 2,f) are similar to isopleths [4] (Fig. 2,c) and [7] (Fig. 2,d).

RESULTS AND DISCUSSION

The analysis, which has been carried out by means of versions of the T-x-y diagrams space computer models of systems Au-Bi-{Sb, Ag}, constructed by data from various literature sources, showed that:

- 1) It is necessary to specify, whether there is on the Au-Bi-Sb system T-x-y diagram a region of decomposition of solid solution Bi(Sb) on Bi and Sb. Irrespective of it to correct the T-x-y diagram and its sections, the lost in [3] and [4] solidus and solvus surfaces have added.

- 2) After the adding of the lower temperature allotropy of the compound Au_2Bi in the ternary system Ag-Au-Bi the borders of phase regions with Au_2Bi and its sections are modified.

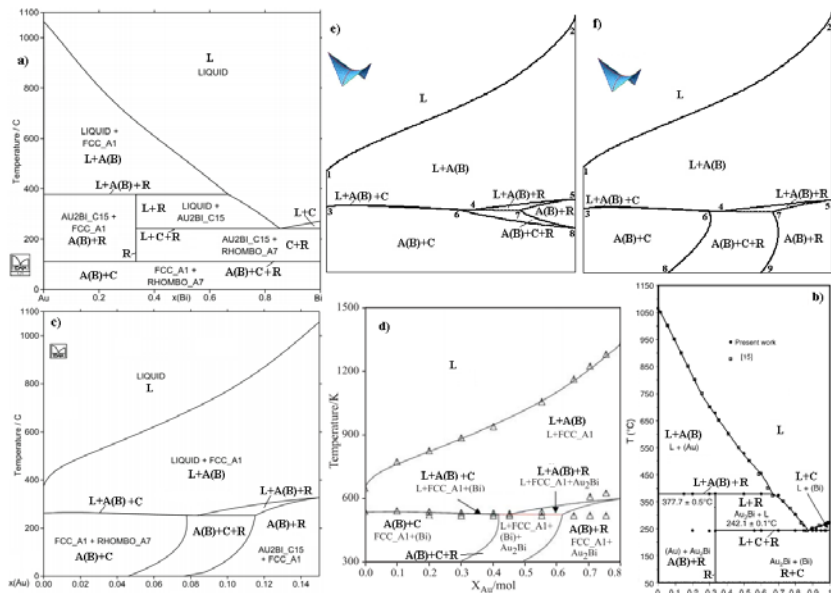


Figure 2. Binary system Au-Bi: [4] (a), [5] (b); isopleth $z_1(Ag)=0.2$: [4] (c), [7] (d), model with (e) and without (f) $R=Au_2Bi$ decomposition.

CONCLUSION

The 3D computer models of T-x-y diagrams constructed by calculated and experimental data of different authors, it is possible to apply to verification of sections and projections, to search of errors of calculations or incorrect interpretation of experiment.

ACKNOWLEDGEMENT

This work was partially supported by the Russian Foundation for Basic Research (projects 14-08-00453 and 14-08-31468).

REFERENCES

[1] V. I. Lutsyk, V. P. Vorob’eva, *Therm Anal Calorim*, 2010, 101, 1, 25.
 [2] J. Wang, F. G. Meng et al, *Electron. Mater.*, 2007, 36, 5, 568.
 [3] D. Manasijevića, D. Minićb et al, *Phys Chem Solids*, 2008, 69, 4, 847.
 [4] Atlas of Phase Diagrams for Lead-Free Soldering compiled by A. Dinsdale et al, COST 531, ESF, Brno, Czech Rep., 2008, Vol. 1.
 [5] E. Zoro, E. Dichi et al, *Alloys Compd.*, 2005, 400, 209.
 [6] C. Servant, E. Zoro et al, *CALPHAD*, 2006, 30, 443.
 [7] E. Zoro, C. Servant et al, *Therm Anal Calorim.*, 2007, 90, 2, 347.
 [8] E. Zoro, C. Servant et al, *CALPHAD*, 2007, 31, 89.

DEFINITION OF 3-PHASE REACTION TYPE CHANGING CONDITIONS IN SYSTEMS Cr-Zr-{Mo, W, V} BY MEANS OF THEIR T-x-y DIAGRAMS SPACE COMPUTER MODELS

V. Lutsyk^{1,2} and V. Vorob'eva¹

¹*Institute of Physical Materials Science, Siberian Branch of RAS, 6,
Sahyanova st., Ulan-Ude, 670047 Russia (vluts@ipms.bscnet.ru)*
²*Buryat State University, 24a, Smolina st., Ulan-Ude, 670000, Russia*

ABSTRACT

Three-dimensional (3D) computer models of the systems W-Zr-Cr, Mo-Zr-Cr and V-Zr-Cr T-x-y diagrams have been designed. The investigations of the possibilities for a eutectic-peritectic transition in the 3-phase regions have been carried out and the corresponding surfaces of two-phase reactions inside them have been constructed.

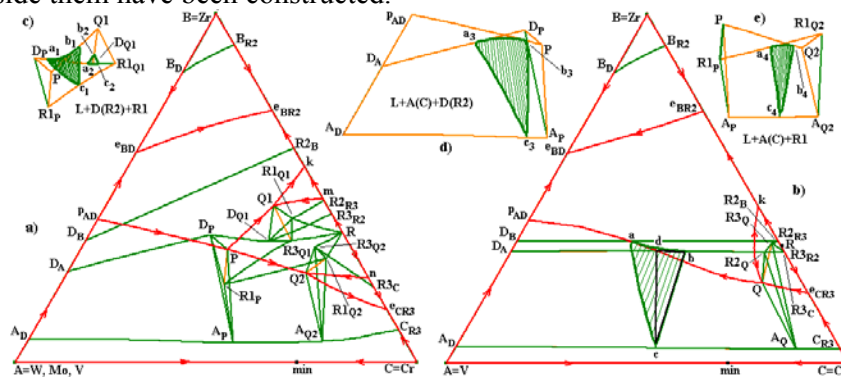


Figure 1. Projections of liquidus, solidus and connected with them ruled surfaces: the general prototype of the systems A-B-C=A-Zr-Cr, where A=W, Mo, V, with compounds D=A₂Zr and R=ZrCr₂ (a); the different version of the system V-Zr-Cr with the only invariant reaction without the high-temperature allotropy R1 of the compound ZrCr₂ (b); surfaces a_ib_ic_i, i=1, ..., 4 of 2-phase reactions in 3-phase regions L+D(R2)+R1 (c), L+A(C)+D(R2) (d), L+A(C)+R1 (e).

INTRODUCTION

Ternary systems on the basis of zirconium and chromium together with the tungsten and molybdenum (or vanadium) are characterized by experimentally fixed effects of the three-phase transformation type change [1]. Earlier it was shown that the special surface inside the 3-phase region,

on which 3-phase reaction temporary becomes a 2-phase one, in the presence of the third phase, corresponds to eutectic-peritectic transition [2]. The 3D computer model of T-x-y diagram is required for the surfaces of 2-phase reactions constructing. Its construction passes through some stages [3]. First the results of the analysis of the T-x-y diagram geometric structure are represented in the form of the scheme of uni- and invariant states (the Sheil scheme of phase reactions with attributed to 3-phase transformations the trajectories of a change in the concentration of each of three phases). Then the tabular scheme is transformed to the 3D form and further – to the prototype of the T-x-y diagram. The input of real coordinates (concentration, temperature) with the refinement of the curvature of lines and non-ruled surfaces (liquidus, solidus, solvus, etc) turns the prototype into the T-x-y diagram 3D model of real system.

GEOMETRICAL CONSTRUCTION OF THE SYSTEMS A-Zr-Cr, (A=W, Mo, V) T-x-y DIAGRAMS

Geometrical construction of the systems A-B-C=A-Zr-Cr (A=V, Mo, W) T-x-y diagrams is topologically equivalent (Fig. 1,a). Binary systems A-Cr form the continuous series of solid solutions with a minimum.

The incongruently melting compound $A_2Zr=D$ is formed in the binary systems by the peritectic reaction $L+A \rightarrow D$ (p_{AD}). The transformation of three-phase regions $L+D+B$ is fixed in the systems also. It is eutectic $L \rightarrow B+D$ ($n_{BD}=e_{BD}$ - $L \rightarrow Zr+V_2Zr$ and $L \rightarrow Zr+W_2Zr$) at $A=V, W$, and it is peritectic $L+D \rightarrow B$ ($n_{BD}=p_{BD}$ - $L+Mo_2Zr \rightarrow Zr$) at $A=Mo$.

The compound $ZrCr_2=R$ with 3 polymorphous modifications R1, R2, R3 is formed in the binary system B-C (Zr-Cr). The transition from the high-temperature modification R1 to the intermediate R3 occurs by the metatectic reaction $R1 \rightarrow R3+L$ (the points of liquidus m and n correspond to it), from R3 to low-temperature R2 – by the metatectic $L+R3 \rightarrow R2$ (k) and eutectoid $R3 \rightarrow C+R2$ reactions. Two eutectic reactions $L \rightarrow C+R3$ (e_{CR3}) and $L \rightarrow B+R2$ (e_{BR2}) are observed too.

Liquidus of the ternary systems A-B-C=A-Zr-Cr (A=V, Mo, W) consists of 6 primary crystallization surfaces: 1) Zr (B) – $Bp_{AD}e_{BR2}$; 2) the solid solution A(C) (C=Cr, A=V, W, Mo) – $An_{BD}PQ2e_{CR3}C$ and the solid solution D(R2) (the compound $D=A_2Zr$, the low-temperature polymorphous modification of the compound $R2=ZrCr_2$) – $p_{AD}n_{BD}PQ1ke_{BR2}$; 3) two polymorphous modifications of the compound $ZrCr_2$: the high-temperature R1 – $PQ1mnQ2$ and two fragments of the intermediate modification R3 – $kQ1m$ and $e_{CR3}Q2n$, where n_{BD} is the eutectic at $A=V, W$ and the peritectic at $A=Mo$ (Fig. 1,a).

Three invariant transformations occur in the systems with the tungsten and molybdenum: peritectic P: $L+A(C)+D(R2)\rightarrow R1$ and 2 quasi-peritectic Q1: $L+R1\rightarrow D(R2)+R3$, Q2: $L+R1\rightarrow A(C)+R3$. In contrast to the system with the tungsten, in this system the temperature Q2 is higher than Q1 (Table 1).

In system with vanadium the nature of invariant transformations is not accurately determined [1]. It is possible that they are differ with invariant reactions, when instead of the ternary peritectic P: $L+A(C)+D(R2)\rightarrow R1$ occurs quasi-peritectic reaction Q1: $L+R1\rightarrow A(C)+D(R2)$, and instead of the quasi-peritectic Q1: $L+R1\rightarrow D(R2)+R3$, the peritectic P: $L+R1+D(R2)\rightarrow R3$ has a place. But it is possible that in the system with vanadium the high-temperature polymorphous modification R1 does not participate in the invariant transformations, and one quasi-peritectic type invariant reaction Q: $L+R3\rightarrow A(C)+D(R2)$ takes a place only (Fig. 1,b).

Because of the geometric similarity of T-x-y diagrams it is possible first to design the general prototype, which qualitatively corresponds to the structure of diagrams, and then, introducing the experimental data of the concrete three systems A-B-C=A-Zr-Cr (A=V, Mo, W), to obtain 3D computer models of the T-x-y diagram of each system.

3-PHASE TRANSFORMATION TYPE CHANGING

During the experimental study of the systems A-B-C=A-Zr-Cr (A=W, Mo) it was noted that the peritectic reactions $L+D(R2)\rightarrow R1$ and $L+A(C)\rightarrow R1$ change by eutectic $L\rightarrow D(R2)+R1$ and $L\rightarrow A(C)+R1$ at the fall of temperature [1].

In contrast to them in the system with vanadium in both assumed cases with the different sets of invariant reactions the curve $p_{AD}Q$ and the surface abc of 2-phase reaction $L\rightarrow D(R2)$ in the presence of the solid solution $A(C)=V(Cr)$ corresponds to the changing of the type of the eutectic reaction $L\rightarrow A(C)+D(R2)$ to the peritectic $L+A(C)\rightarrow D(R2)$ one (Fig. 1, b). This surface is formed by horizontal (isothermal) generated lines inside a series of tie-triangles. In this case not one tie-triangle at the changing of the reaction type degenerates in the line (as about this it is written into [1] in connection with to the tie-triangle bdc), one its side crosses the point of intersection of the univariant lines of $p_{AD}Q$ and $D_A R2_Q$ projections on Fig. 1,b [1].

In the general prototype of the systems A-B-C=A-Zr-Cr (A=W, Mo, V) T-x-y diagram there are confirmed also the changes of the reactions type from $L+D(R2)\rightarrow R1$ to $L\rightarrow D(R2)+R1$, earlier discovered in [1], with further temperature falling to $L+R1\rightarrow D(R2)$, and also the changes of the reaction $L+A(C)\rightarrow R1$ to $L\rightarrow A(C)+R1$.

Surfaces $a_1b_1c_1$ and $a_2b_2c_2$ (Fig. 1,c) and $a_3b_3c_3$ (Fig. 1,d) correspond to these transitions. However, besides them the surface $a_4b_4c_4$ of the three-phase reaction type changing from $L+A(C)\rightarrow D(R2)$ to $L\rightarrow A(C)+D(R2)$ (Fig. 1,e) is discovered. It is analogous to the surface abc in the second version of the system V-Zr-Cr with one invariant reaction (Fig. 1, b) and it is absent in [1].

Table 1. Types and temperatures ($^{\circ}\text{C}$) of invariant reactions N_i of the systems $A-B-C=A-Zr-Cr$ ($A=W, Mo, V$)

A	N_1	N_2	N_3
W	P (1690)	Q1 (1560<T<1620)>Q2	Q2 (1590<T<1690)
Mo	P (~1850)	Q1 (1560<T<1620)<Q2	Q2 (~1600)
V	Q1 (1560)	P (~1600)	Q2 (1560<T<1620)
V		Q (1560)	

RESULTS AND DISCUSSION

The carried-out analysis of the geometrical structure of T-x-y diagrams of systems A-B(Zr)-C(Cr), where $A=W, Mo, V$, is fixed in the tabular and geometrical (Fig. 1,a) form. For the system with vanadium the surface of the 2-phase reaction of the crystallization of solid solution of vanadium with chrome V(Cr) in the 3-phase region $L+V(Cr)+VZr_2(ZrCr_2)$ is constructed and it is shown that the analogous surface must be, also, in the systems with tungsten and molybdenum.

CONCLUSION

It was established that the phase reaction type changing with the participation of liquid occurs in three 3-phase regions of systems A-B(Zr)-C(Cr), where $A=W, Mo, V$. Temperatures of such transitions are not constant, and their concentration borders are designated by the corresponding surfaces of two-phase reactions projecting.

ACKNOWLEDGEMENT

This work was partially supported by the Russian Foundation for Basic Research (projects 14-08-00453 and 14-08-31468).

REFERENCES

- [1] V. N. Yeremenko. Selected Works. Memories. On the Occasion of the Centenary of the Birth, Kiev, Ukraine, 2011 (In Russian).
- [2] V. P. Lutsyk, V. P. Vorob'eva, *Perspektivnye Materialy*, 2011, 13, 191 - 197 (In Russian).
- [3] V. I. Lutsyk, V. P. Vorob'eva, *Therm Anal and Calorim*, 2010, 101(1), 25 - 31.

COMPUTER MODELS OF T-X-Y DIAGRAMS OF NaCl-MgCl₂-UCl₃, NaCl-MgCl₂-PuCl₃, NaCl-UCl₃-PuCl₃ AND MgCl₂-UCl₃-PuCl₃ SYSTEMS

V. Lutsyk^{1,2}, A. Zelenaya¹, E. Nasrulin and A. Zyryanov¹

¹ *Institute of Physical Materials Science SB RAS, 6, Sahyanova st. 670047 Ulan-Ude, Russia (vluts@ipms.bscnet.ru)*

² *Buryat State University, 24a, Smolina st. 670000 Ulan-Ude, Russia.*

ABSTRACT

Computer models of phase diagrams of NaCl-MgCl₂-UCl₃, NaCl-MgCl₂-PuCl₃, NaCl-UCl₃-PuCl₃ and MgCl₂-UCl₃-PuCl₃ systems are elaborated. Their geometrical structures are discussed and an ability to use the templates of phase diagrams is demonstrated.

INTRODUCTION

The system with chlorides and fluorides of metals are characterized as a possible fuel for Molten Salt Reactors. The literature illustrates many variants of the potential fuel, as calculated by thermodynamic software and studied experimentally [1-4]. But the information about the structure of phase diagrams is limited by the visualization of liquidus surfaces and some sections. Whereas, a complete model of phase diagram is required for the obtaining of information about the existing phase equilibria and the sections decoding [5].

MODELS OF PHASE DIAGRAMS OF SYSTEMS UCl₃-NaCl-PuCl₃ AND UCl₃-MgCl₂-PuCl₃

Phase diagram of system UCl₃-NaCl-PuCl₃ (A-B-C) have two binary systems of eutectic type (NaCl-UCl₃ and NaCl-PuCl₃) and one system with continuous range of solid solution and minimum point (UCl₃-PuCl₃) on boundary. The system is characterized by the absence of three-phase transformations and the presence of minimum point on the monovariant liquidus line. The thermodynamically calculated coordinates of binary points (e_{AB} , e_{BC} , m) and ternary minimum point (e_{min}) [2] were used as the initial data for construction of a computer model.

Because the system has a continuous range of solid solutions, then the solidus and solvus surfaces with hypothetical values of binary points (a_B , c_B , a_B^0 , c_B^0) and ternary minimum point (a_{min}) are given from the UCl₃-PuCl₃ system. Thus, the model of phase diagram UCl₃-NaCl-PuCl₃ includes two

liquidus surfaces, solidus surface and solvus one, three ruled surfaces (Fig. 1). The line connecting points a_{\min} - e_{\min} - C_{\min} is a complex tie-line at the temperature of minimum point $T=722$. Point a_{\min} can be calculated as the intersection point of ray C_{\min} - e_{\min} with solidus curve a_B - c_B . The phase diagram contains one-phase region $A(C)$, 3 two-phase regions ($L+A(C)$, $L+B$, $A(C)+B$) and three-phase region ($L+A(C)+B$).

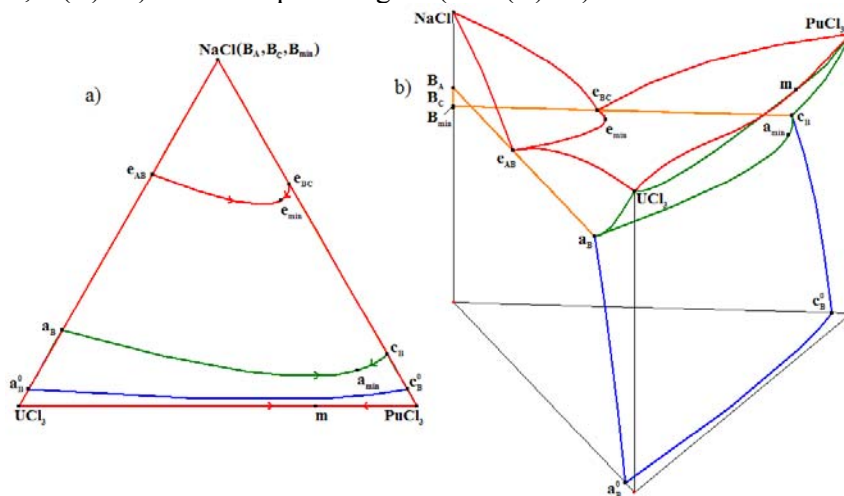


Figure 1. XY projection (a) and 3D model (b) of phase diagram of system UCl_3 - $NaCl$ - $PuCl_3$.

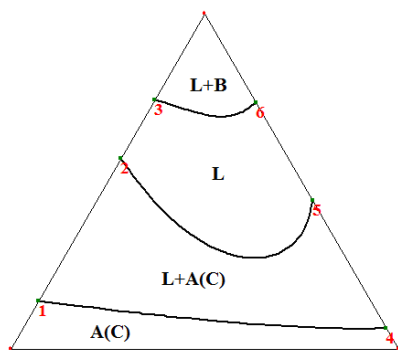


Figure 2. Horizontal section of UCl_3 - $NaCl$ - $PuCl_3$ system at $T=873K$.

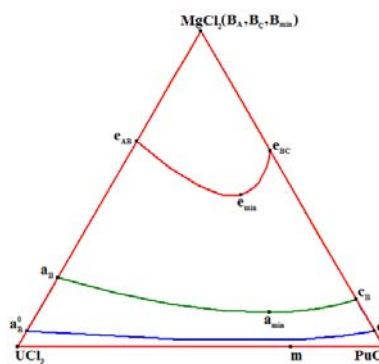


Figure 3. XY projection of phase diagram of UCl_3 - $MgCl_2$ - $PuCl_3$ system.

To validate the model, we compared the model section (Fig. 2) with the thermodynamically calculated section [2, p. 207].

The elaborated model was the template for construction of phase diagram of $\text{UCl}_3\text{-MgCl}_2\text{-PuCl}_3$ system (Fig. 3) having similar topological structure. For this purpose the coordinates of points on the surfaces contour were changed in the template.

MODELS OF PHASE DIAGRAMS OF SYSTEMS $\text{UCl}_3\text{-NaCl-PuCl}_3$ AND $\text{UCl}_3\text{-MgCl}_2\text{-PuCl}_3$

The phase diagram of system $\text{MgCl}_2\text{-NaCl-UCl}_3$ (A-B-C) includes two incongruently melting compounds $\text{R}_1=\text{NaMgCl}_3$, $\text{R}_2=\text{Na}_2\text{MgCl}_4$ (in binary system $\text{MgCl}_2\text{-NaCl}$). The system is characterized by a quasiperitectic transformation (Q: $\text{L}_Q+\text{MgCl}_2\rightarrow\text{R}_1+\text{UCl}_3$) and two eutectic ones (E_1 : $\text{L}_{\text{E}1}\rightarrow\text{R}_1+\text{R}_2+\text{UCl}_3$; E_2 : $\text{L}_{\text{E}2}\rightarrow\text{R}_2+\text{NaCl}+\text{UCl}_3$). There is a maximum point $[\text{E}_1, \text{E}_2]$ on the liquidus line E_1E_2 . The experimental [1] and thermodynamically calculated [2] coordinates of binary and ternary points are used as an initial data.

The computer model of phase diagram of $\text{MgCl}_2\text{-NaCl-UCl}_3$ system was elaborated on base of schema of mono- and invariant equilibria. It includes 5 liquidus surfaces, 14 ruled surfaces, 2 vertical planes (going through the UCl_3 and R_1 , R_2) and 3 horizontal planes at the temperatures of invariants points (Q, E_1 , E_2) (Fig. 4).

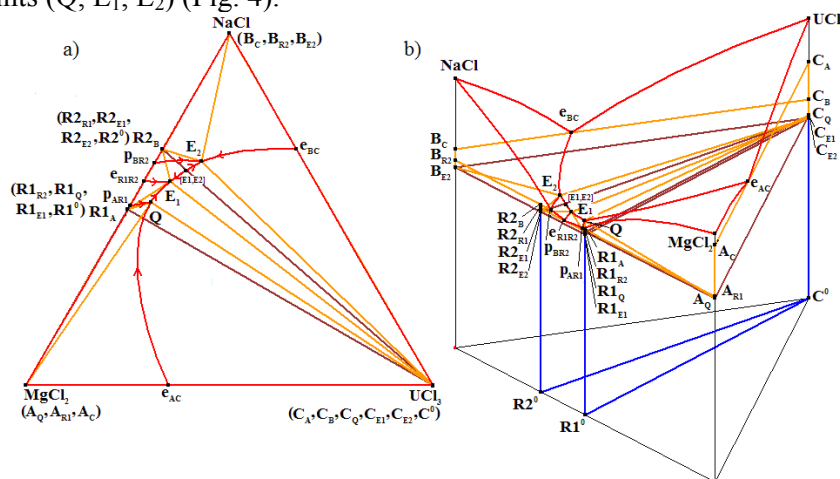


Figure 4. XY projection (a) and 3D model (b) of phase diagram of system $\text{MgCl}_2\text{-NaCl-UCl}_3$.

The phase diagram is formed by 7 two-phase regions (L+A , L+B , L+C , L+R_1 , L+R_2 , C+R_1 , C+R_2) and 10 three-phase regions (L+A+C , L+A+R_1 , L+B+C , L+B+R_2 , L+C+R_1 , L+C+R_2 , $\text{L+R}_1+\text{R}_2$, A+C+R_1 , B+C+R_1 , $\text{C+R}_1+\text{R}_2$).

The elaborated model was the template for construction of phase diagram of $\text{MgCl}_2\text{-NaCl-PuCl}_3$ system, which is characterized by a eutectic transformation ($E: L_E \rightarrow R_2 + \text{NaCl} + \text{PuCl}_3$) and two quasiperitectic ones ($Q_1: L_{Q_1} + \text{MgCl}_2 \rightarrow R_1 + \text{PuCl}_3$; $Q_2: L_{Q_2} + R_1 \rightarrow R_2 + \text{PuCl}_3$). The transformation on the plane at point Q_2 is degenerated (point Q_2 arranges on line $\text{PuCl}_3\text{-}R_2$ into the projection). The point's coordinates on contour surfaces and the configuration of horizontal plane at point Q_2 are changed in the template for construction of new phase diagram (Fig. 5).

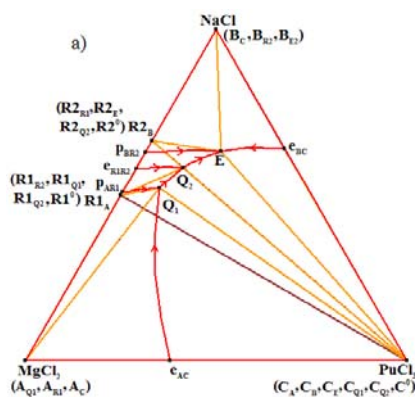


Figure 5. XY projection of phase diagram $\text{MgCl}_2\text{-NaCl-PuCl}_3$.

CONCLUSION

The using of computer templates useful for simulation of phase diagrams of chloride systems having similar topological structure. The elaborated models are used not only to visualize the phase diagram structure, but they are the source of information about the crystallization stages and microstructure formation (with the opportunity of qualitatively and quantitatively estimation of phases relationship for a given composition).

ACKNOWLEDGEMENT

This work was partially supported by the Russian Foundation for Basic Research (projects 14-08-00453 and 14-08-31468).

REFERENCES

- [1] P. Chartrand, A. D. Pelton, Metallurgical and materials transactions A, 2001, 32A, 1361-1383.
- [2] O. Beneš, R. J. M. Konings, Journal of Nuclear Materials, 2008, 375, 202-208.
- [3] V. Trnovcova, L.S. Garashina, A. Skubla, P.P. Fedorov, R. Cicka, E. A. Krivandina, B. P. Sobolev, Solid State Ionics, 2003, 157, 195-201.
- [4] L. Bulavin, Yu. Plevachuk, V. Sklyarchuk, I. Shtablavyy, N. Faidiuk, R. Savchuk, Journal of Nuclear Materials, 2013, 433, 329-333.
- [5] R. N. Savchuk, N. V. Faidyuk, A. O. Omelchuk, V. I. Lutsyk, A. E. Zelenaya, Russian Journal of Inorganic Chemistry, 2014, 59.

PHASE DIAGRAM OF THE SELECTED AQUEOUS TWO-PHASE SYSTEMS BASED ON IONIC LIQUIDS

A. Dimitrijević and T. Trtić-Petrović

Laboratory of Physics, Vinča Institute of Nuclear Sciences, University of Belgrade, P.O. Box 522, Belgrade, Serbia. (daleksandra@vinca.rs)

ABSTRACT

Liquid-liquid equilibrium data have been reported for aqueous two-phase systems formed by imidazolium-based ionic liquids, 1-hexyl-3-methylimidazolium chloride, and 1-butyl-3-methylimidazolium dicyanamide, with inorganic salts, K_2HPO_4 and K_3PO_4 . The binodal curves were fitted to a three parameter equation and the tie line length was calculated.

INTRODUCTION

Aqueous two-phase systems (ATPSs) exploit the incompatibility between aqueous solutions forming two phases [1]. ATPSs have consisted of two mutually incompatible salts or polymer, one of them kosmotropic or water-structuring, and the other chaotropic or water-destructuring, in the presence of water. Each phase contains mainly one of the compounds and a small amount of the other [2]. In the recent years, ionic liquids (ILs) have shown to be an attractive alternative to polymers in the formation of ATPSs due to their potential use as green solvents and as possible replacement for traditional volatile organic compounds [3].

Ionic liquids are salts with their ions poorly coordinated and which are liquid at temperatures below 100°C. As a new kinds of green solvents, ILs have unique properties such as negligible vapor pressure, wide liquid temperature range, non-flammability, enhanced thermal and chemical stability, tunable chemical structures, good electrical conductivity and improved solvation ability for a large matrix of compounds [3]. This makes ILs attractive as novel extractants for various metal ions and organic compounds (e.g., amino acids, dyes, proteins) [4].

Gutowski et al. demonstrated that addition of inorganic salt to aqueous solutions of ionic liquids can also cause liquid-liquid demixing and induce the formation of ATPSs.[5]

The phase diagram, comprised binodal curve and tie-lines, provides information about: the concentration of phase forming components required to form two phases, the concentration of phase components in top and bottom phases and the ratio of phase volume. Coordinates for all potential

systems will lie on a tie line, which connects two nodes on the binodal and represents the final concentration of phase components in top and bottom phases. Moving along the tie line coordinates, the systems denoted will have different total compositions and volume ratios, but with the same final concentration of phase components in the top and bottom phases. [4]

The aim of this study was forming of phase diagrams for two targeted hydrophilic ILs and determination of their tie lines. These results represent the first step of applying ATPS for extraction.

EXPERIMENTAL

The ionic liquids used in this work were 1-hexyl-3-methylimidazolium chloride, [C₆mim]Cl and 1-butyl-3-methylimidazolium dicyanamide, [C₄mim][N(CN)₂] with a stated purity of >99 wt % and supplied by Iolitec. Inorganic salts, 30 % solution of K₂HPO₄ or K₃PO₄ in deionized water.

The phase diagram was determined by the cloud-point method at room temperature. A known amount of IL was weight into a test tube and an appropriate volume of the salt was added dropwise into the test tube while shaking. By appearance of turbidity, the total mass of the added salt was calculated. The weight percentages of both ILs and salt were calculated by measuring the weights of both ILs and the salt. The sequential addition of water and salt was repeated until sufficient data points for constructing the phase diagram were obtained [6]. The binodal curve was fitted applying following equation:

$$\ln Y = A + BX^3 + CX^{0.5} \quad [1]$$

where Y and X are the concentrations (in w/w%) of IL and salt, respectively [7]. The fitting was performed using “Tablecurve 5.01” program.

The tie lines were experimentally determined through the relationship between the weight of the top phase and the overall weight by lever-arm rule. The tie line length (TLL) for different salt and IL compositions were calculated according to:

$$TLL = \sqrt{(Y_T - Y_B)^2 + (X_T - X_B)^2} \quad [2]$$

The symbols T and B refer to the top (IL-rich) and bottom (salt-rich) phases.

RESULTS AND DISCUSSION

A sufficiently high concentration of inorganic salts added in an aqueous solution of hydrophilic IL can cause phase separation a salt-rich bottom phase which is in equilibrium with IL-rich top phase. The first step in designing of ATPS is forming of phase diagram for the investigated system. The experimental phase diagrams for two investigated IL/salt

systems ($[C_6mim]Cl/K_2HPO_4$ and $[C_4mim][N(CN)_2]/K_3PO_4$) are presented in Figure 1.

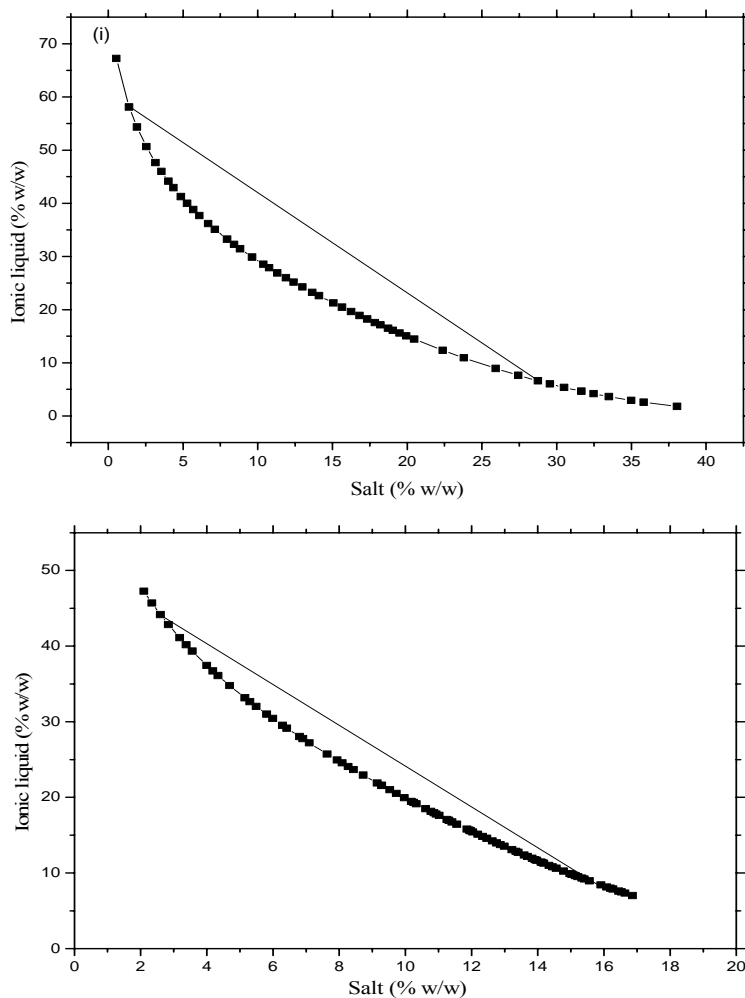


Figure 1. Phase diagrams of (i) $[C_6mim]Cl/K_2HPO_4$ and (ii) $[C_4mim][N(CN)_2]/K_3PO_4$ systems

The data were fitted according to the empirical relationships of Merchuk (Eq. 1), and the parameters for this equation as determined by least-squares regression of the cloud point data are shown in Table 1. Literature results confirmed that the method can satisfactorily correlate binodal curves and determined tie lines in these systems. TLL was experimentally determined for each system and given in Table 2.

Table 1. Correlation parameters used in Eq. 1 to describe the binodals.

System	A	B	C	R
[C ₆ mim]Cl/K ₂ HPO ₄	4.45364	-3.33576 10 ⁻⁵	-0.033085	0.99904
[C ₄ mim][N(CN) ₂]/K ₃ PO ₄	4.44272	-1.73984 10 ⁻⁴	-0.40424	0.99905

Table 2. Tie-line lengths for IL+Salt systems

System	IL	Salt	TLL
1 [C ₆ mim]Cl+K ₂ HPO ₄	27.5	17.6	45.129
2 [C ₄ mim][N(CN) ₂]	7.9	29.1	32.481

CONCLUSION

The phase diagrams of ATPS for two imidazolium-based ILs were determined by cloud point method at 298K. The binodal curves were fitted to the Merchuk equation, and tie-line lengths were determined. The results showed that the empirical equation is satisfactory for correlating the investigated systems [7]. It can be seen that [C₆mim]Cl/K₂HPO₄ system has greater ability to promote ATPS than [C₄mim][N(CN)₂]/K₃PO₄ system.

ACKNOWLEDGEMENT

We acknowledge the support to this work provided by the Ministry of Education and Science of Serbia through project *Physics and Chemistry with Ion Beams*, No. III 45006.

REFERENCES

- [1] J. A. Asenjo, B. A. Andrews, *Journal of Chromatography A*, 2011, 1218, 8826-8835.
- [2] F. J. Deive, A. Rodríguez, *The Journal of Chemical Thermodynamics* 2012, 54, 272-277.
- [3] S. Shahriari, C. M. Neves, M. G. Freire, J. o. A. Coutinho, *The Journal of Physical Chemistry B* 2012, 116, 7252-7258.
- [4] Z. Li, Y. Pei, H. Wang, J. Fan, J. Wang, *TrAC Trends in Analytical Chemistry* 2010, 29, 1336-1346.
- [5] K. E. Gutowski, G. A. Broker, H. D. Willauer, J. G. Huddleston, R. P. Swatloski, J. D. Holbrey, R. D. Rogers, *Journal of the American Chemical Society* 2003, 125, 6632-6633.
- [6] L. Sheikhan, M. Akhond, G. Absalan, *Journal of Environmental Chemical Engineering* 2014, 2, 137-142.
- [7] S. L. Mistry, A. Kaul, J. Merchuk, J. Asenjo, *Journal of Chromatography A* 1996, 741, 151-163.

SPECTROSCOPY,
MOLECULAR STRUCTURE,
PHYSICAL CHEMISTRY OF
PLASMA

STRUCTURAL AND VIBRATIONAL SPECTROSCOPY INVESTIGATION OF THE 4-(2,5-DI-2-THIENYL-1H- PYRROL-1-YL) BENZOIC ACID MOLECULE

M. Kurt¹, E. Babur Sas¹, M. Can², S. Okur³, S. Icli⁴ and S. Demic³

¹*Department of Physics, Ahi Evran University, Kırsehir, Turkey*

²*Department of Engineering Sciences, Faculty of Engineering, Izmir Katip Celebi University, Cigli, 35620 Izmir, Turkey*

³*Izmir Katip Çelebi University, Material Science and Engineering, Çiğli, Izmir, Turkey*

⁴*Ege University, Solar Energy Institute, 35040 Bornova, Izmir, Turkey*

ABSTRACT

The molecular structure and vibrations of 4-(2,5-di-2-thienyl-1H-pyrrol-1-yl) benzoic acid (tpba) were investigated by infrared spectroscopic techniques. FT-IR spectra were recorded in the solid phase. HOMO-LUMO analyses were performed. The theoretical calculations for the molecular structure and spectroscopic studies were performed with DFT (B3LYP) and 6-311G(d,p) basis set calculations using the Gaussian 09 program. After optimizing the geometry of the molecule, vibrational wavenumbers and fundamental vibrations wavenumbers were assigned on the basis of the total energy distribution (TED) of the vibrational modes calculated with SQM program. The results of theoretical calculations for the spectra of the title compound were compared with the observed spectra.

INTRODUCTION

The development of organic light-emitting diodes (OLEDs) has progressed due to their potential applications in many fields [1-3]. Multilayer OLEDs are known as one of the potential technologies for next-generation flat-panel display devices [3, 4]. In addition to many advantages of OLED displays, the investigators are focused on to improve performance and stability of OLED display.

In this work, the spectroscopic attitude of 4-(2,5-di-2-thienyl-1H-pyrrol-1-yl) benzoic acid (tpba) molecule was investigated. The structure of the molecule was optimized with DFT/B3LYP 6-311G(d,p). The vibration modes are assigned on the basis of TED computed by using SQM program [5].

RESULTS AND DISCUSSION

tpba molecule which has 37 atoms and 105 fundamental vibrational modes has C_1 symmetry. The optimized molecular structure, calculated and experimental IR spectra were given Fig. 1 and Fig. 2.

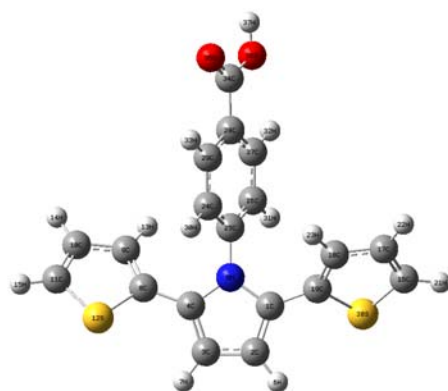


Figure 1. The optimized molecular structure of tpba

The ring C-C stretching vibrations occur between $1430\text{--}1625\text{ cm}^{-1}$. In the present work, aromatic C-C stretching vibrations were computed at $1594\text{--}1096$ and $1072\text{--}998\text{ cm}^{-1}$ by using B3LYP/6-311G(d,p) method and observed at $1610\text{--}1101$, 1043 , 1019 cm^{-1} in FT-IR. The main C-C stretching vibrations are computed at 1421 and 1538 cm^{-1} with the TED contribution 79% and 73% . The C-C stretching vibrations modes are contaminated other vibrations.

The vibrational bands of carboxylic acid of tpba contain the

C-O, C=O and O-H vibrational modes. The C=O stretching band of carboxylic acids appears strongly in the region between $1740\text{--}1660\text{ cm}^{-1}$ [9]. The C=O stretching mode is the strongest band in FT-IR. [12]. In this study, it is observed at 1674 cm^{-1} as a very strong band in FT-IR. The same band calculated as 1744 cm^{-1} with B3LYP/6-311G(d,p) method.

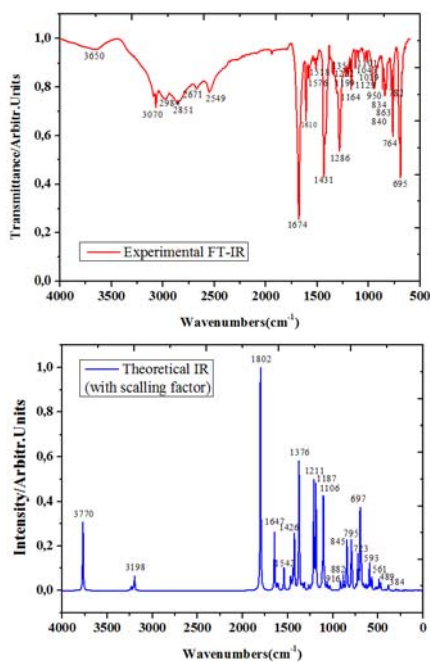


Figure 2. The calculated and experimental infrared spectra of tpba.

OH hydroxyl group which connects the molecules absorbs strongly in the region $3550\text{--}3200\text{ cm}^{-1}$ [10]. The O-H stretching vibration of tpba molecule was

calculated as 3647 cm^{-1} with B3LYP. These bands were observed at 3650 cm^{-1} in FT-IR. According to TED calculations the hydroxyl stretching vibrational mode is pure.

In-plane bending vibration of —OH group appears in the region of $1440\text{--}1260\text{ cm}^{-1}$ in the FT-IR spectrum [11]. Out-of-plane bending vibration appears in the region of $280\text{--}312\text{ cm}^{-1}$ for free —OH and in the region of $600\text{--}720\text{ cm}^{-1}$ for associated O—HO—H [13]. In-plane bending vibration calculated as 1331 cm^{-1} and observed as 1355 cm^{-1} as weak shoulder in the FT-IR. Out-of-plane bending vibration computed at 596 and 575 cm^{-1} .

The hetero aromatic structure shows the presence of C—H stretching vibrations as weak bands in the region $3000\text{--}3100\text{ cm}^{-1}$ [11]. For tpba molecule, the C—H stretching vibration computed in the range of $3089\text{--}3144\text{ cm}^{-1}$ with the B3LYP/6-311G(d,p) method were observed at 3070 cm^{-1} in FT-IR. The C—H in-plane bending vibration appears in the range of $1000\text{--}1300\text{ cm}^{-1}$ in the literature [14, 15]. The C—H in-plane bending vibrations observed in range of $1101\text{--}1222\text{ cm}^{-1}$ in FT-IR, were calculated in range of $1096\text{--}1225\text{ cm}^{-1}$ for tpba. The C—H out-

The HOMO and LUMO energy levels were calculated with TD-DFT/B3LYP/6-311G(d,p) method in DMSO, ethanol, water and gas phase.

of-plane bending vibration is shown in the range $800\text{--}950\text{ cm}^{-1}$ for aromatic compounds in the literature [14, 15]. These vibrations were calculated in range of $826\text{--}854$, $884\text{--}885$, and $956\text{--}968\text{ cm}^{-1}$ were observed in range of $834\text{--}950\text{ cm}^{-1}$ in FT-IR.

The C—N stretching vibration was assigned in the region $1382\text{--}1266\text{ cm}^{-1}$ for aromatic amines in the literature [16]. These vibrations were calculated at $1234\text{--}1272$, $1301\text{--}1327$ and 1380 cm^{-1} . The same vibration was observed at 1286 cm^{-1} in FT-IR. The PED of this vibration suggests that this is a mixed mode with C—C stretching vibration.

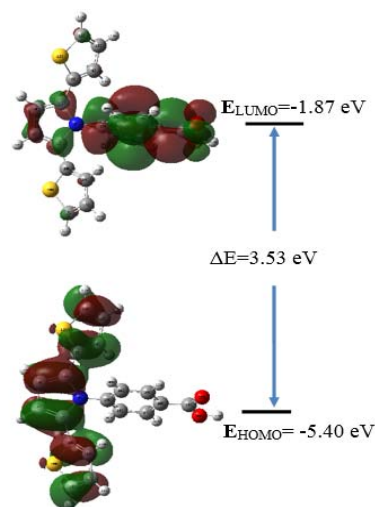


Figure 3. HOMO-LUMO orbitals of tpba for gas phase.

Plots of the HOMO and LUMO orbitals for the title molecule were shown for gas phase in Fig. 3. According to Fig. 3, HOMO orbitals are localized on the phenyl rings and nitrogen atom and LUMO orbitals are localized on the ring and carboxyl group of tpba.

The energy difference between H→L orbital is a critical parameter in determining molecular electrical transport properties because it is a measure of electron conductivity. The energy difference between HOMO and LUMO levels are 3.61 eV in DMSO and ethanol and 3.60 in water but it is 3.53 eV in gas phase for tpba.

ACKNOWLEDGEMENT

This work was supported by Ahi Evran University Scientific Project Unit (BAP) with, Project No: PYO. Fen-4003/2.13.003.

REFERENCES

- [1] M. Malagoli, M. Manoharan, B. Kippelen, J.L. Brédas, *Chem. Phys. Lett.*, 2002, 354, 283.
- [2] H. Kaji, T. Yamada, N. Tsukamoto, F. Horii, *Chem. Phys. Lett.*, 2005, 401, 246.
- [3] C.W. Tang, S. A. Van Slyke, *Appl. Phys. Lett.*, 1987, 51, 913–915.
- [4] C.W. Tang, S. A. Van Slyke, C.H. Chen, *J. Appl. Phys.* 1989, 65, 3610.
- [5] J. Baker, A.A. Jarzecki, P. Pulay, *J. Phys. Chem. A*, 1998, 102, 1412.
- [6] D. L. Vein, N. B. Colthup, W. G. Fateley, J. G. Grasselli, *The Handbook of Infrared and Raman Characteristic Frequencies of Organic Molecules*, Academic Press: San Diego, 1991.
- [7] A. Poiyamozhi, N. Sundaraganesan, M. Karabacak, O. Tanriverdi, M. Kurt, *J. Mol. Struct.*, 2012, 1024, 1–12.
- [8] M. Silverstein, F.X. Webster, *Spectroscopic Identification of Organic Compound*, sixth ed., John Willey & Sons, New York, 1998.
- [9] G. Varsanyi, *Vibrational Spectra of Benzene Derivatives*, Academic Press: New York, 1969.
- [10] Y. Shirota, K. Okumoto, H. Inada, *Synth. Met.*, 2000, 111, 387.
- [11] V. Krishnakumar, V.N. Prabavathi, *Spectrochim. Acta, Part A* 71 (2008) 449.
- [12] A. Altun, K. Golcuk, M. Kumru, *J. Mol. Struct.*, 2003, 637, 155.
- [13] K. Pihlaja, E. Kleinpeter (Eds.), *Carbon-13 Chemical Shifts in Structural and Stereochemical Analysis*, VCH Publishers, Deerfield Beach, 1994.

MODERN TENDENCIES IN VIBRATIONAL ANALYSIS OF MOLECULES

N. F. Stepanov and S.V. Krasnoshchekov

*Faculty of Chemistry, Moscow Lomonosov State University,
Moscow 119234, Russia*

ABSTRACT

The structure of energy spectra of vibrational states for polyatomic molecules depends strongly on the number of discrete vibrational states and their distance from the ground and corresponding dissociation states. Actually it is possible to approximately separate out the harmonic region nearby the bottom of the potential surface (at least for the semirigid molecules), the region nearby the dissociation limit where local modes are of essential importance, and the intermediate region which is characterized by the developed sets of polyads of vibrational states. The report will be mainly connected with this intermediate region [1, 2]. The theory of polyads is closely connected with the theory of resonance states. Any polyad is determined as a set of vibrational states characterized by one and the same polyad vector, composed of the so called polyad coefficients, and polyad (secondary) quantum number. The determination of these quantities and their relation to molecular structure is very important for vibrational spectra assignment and interpretation. That is why the polyad structure of vibrational spectra was actively discussed in recent years. The technique most suitable to the polyad description is based on the formalism of creation/annihilation operators and canonical van Vleck perturbation theory [3]. We discuss tendencies of the polyad theory development and some new techniques for solving the problem of polyad structure of vibrational spectra and constituent vibrational states. A very important tendency in molecular vibrational analysis is also connected nowadays with detection and treating resonance states of different types (not necessarily related to the polyads). The method based on canonical perturbation theory is developed for systematic identification of essential resonances. It is suitable for molecules of significant size and complexity as illustrated by several examples of molecules up to ten atoms.

REFERENCES

- [1] L. E. Fried and G. S. Ezra, *J. Chem. Phys.*, 1987, 86, 6270-6282.
- [2] M. E. Kellman, *J. Chem. Phys.*, 1990, 93, 6630-6635.
- [3] S. V. Krasnoshchekov and N. F. Stepanov, *J. Chem. Phys.*, 2013, 139, 184101-01 – 184101-16.

CARBOXYLATION OF SODIUM 2-NAPHTHOXIDE. REINVESTIGATION OF THE MECHANISM BY MEANS OF A META-HYBRID FUNCTIONAL

S. Marković¹, I. Đurović² and Z. Marković³

¹*Department of Chemistry, University of Kragujevac,
34000 Kragujevac, Serbia. (mark@kg.ac.rs)*

²*Faculty of Agronomy, University of Kragujevac,
32000 Čačak, Serbia.*

³*Department of Chemical-Technological Sciences, State University of Novi
Pazar, 36300 Novi Pazar, Serbia.*

ABSTRACT

The Kolbe-Schmitt reaction of sodium 2-naphthoxide was simulated using the M062X method. Kossugi's assumption that the NaONaph-CO₂ complex does not lead to the reaction products was confirmed. Instead, CO₂ performs electrophilic attacks at the positions 1, 3, and 6. Each reaction path proceeds via two transition states and two intermediates, leading to the major products: sodium 2-hydroxy-1-naphthoate and 3-hydroxy-2-naphthoate, and minor product sodium 6-hydroxy-2-naphthoate. Pathway 6 is both kinetically and thermodynamically unfavourable. Pathways 1 and 3 are competitive, where pathway 3 requires slightly higher activation energy, but yields the more stable product. These findings are in accord with the experimental results on the carboxylation reaction of sodium 2-naphthoxide.

INTRODUCTION

Aromatic hydroxy acids are of significant industrial importance. They can be prepared in the Kolbe-Schmitt reaction, which is a carboxylation reaction of alkali metal phenoxides (MOPh) and naphthoxides (MONaph). The mechanism of this reaction is still a vigorous research field. A mechanism of direct carboxylation has been supported by valuable experimental results, including the GC/MS analysis and CP-MAS NMR spectrum of the KOPh-¹³CO₂ complex [1, 2]. On the other hand, a mechanism involving initial formation of the MOPh-CO₂ or MONaph-CO₂ complex has been supported by numerous experimental and computational papers [3-5], and has become generally accepted.

Theoretical investigations of the mechanism of the Kolbe-Schmitt reaction of sodium 2-naphthoxide confirmed the initial formation of the NaONaph-CO₂ complex [6, 7]. It was shown that the carbon of the CO₂ moiety

performs an electrophilic attack at the naphthalene ring in the position 1, leading to the formation of sodium 2-hydroxy-1-naphthoate. Surprisingly, electrophilic attacks at the positions 3 and 6 were not revealed. The formation of sodium 3-hydroxy-2-naphthoate and sodium 6-hydroxy-2-naphthoate was explained by various rearrangements. In addition, this mechanism includes a reaction step with rather high activation energy.

It is worth pointing out that all computational investigations of the Kolbe-Schmitt reaction were performed by means of the B3LYP method. Since more sophisticated functionals are today available, the aim of this work is to reinvestigate the carboxylation reaction of NaONaph, in the light of the postulation of Rahim and Kossugi.

COMPUTATIONAL DETAILS

All geometry optimizations were performed using the Gaussian 09 program [8], at the M062X/LanL2DZ level of theory. This meta-hybrid functional proved to have excellent performance for main group chemistry [9]. The obtained geometries were verified to be minima (no imaginary frequencies), or maxima on the potential energy surface (one imaginary frequency). The transition states were additionally confirmed by performing the IRC (intrinsic reaction coordinates) calculations.

RESULTS AND DISCUSSION

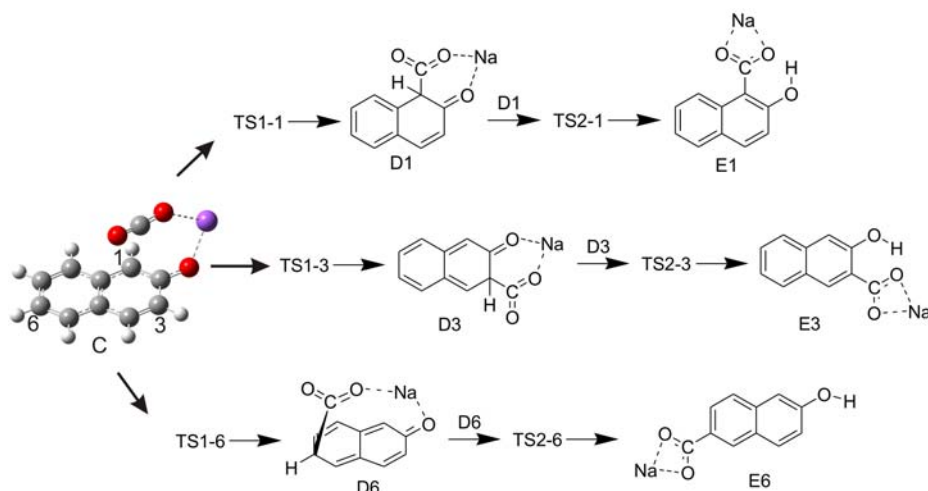


Figure 1. Proposed mechanism for the formation of sodium 2-hydroxy-1-naphthoate (E1), 3-hydroxy-2-naphthoate (E3), and 6-hydroxy-2-naphthoate (E6).

Our investigations with the M062X method demonstrated that NaONaph and CO₂ can spontaneously build two complexes: NaONaph-CO₂ (B in refs 6 and 7) and C (Figure 1), with the energetic stabilizations of 56.8 and 10.8 kJ/mol. While B can decompose under the experimental conditions, the CO₂ moiety in C takes perfect position for electrophilic attacks at all three sites (1, 3, and 6) of the ring. These attacks are realized via the transition states TS1, which lead to the formation of the new C-C bonds, and corresponding intermediates D. The next step of the reaction is bimolecular, implying that two D intermediates exchange the protons adjacent to the CO₂ groups. Our investigations showed that each pair of the D intermediates can exchange the protons (for example D1 and D3). In this paper only the results for the interactions between the pairs of the same D intermediates are presented (for example two molecules of D6). These bimolecular reaction steps require significantly lower activation energies (Table 1) in comparison to the monomolecular proton shift from C to O [4-7].

Table 1 and Figure 2:

Energetics of the examined pathways. ΔG_a^\ddagger and ΔG_r stand for activation free energies and reaction free energies. Dashed, solid, and dotted lines denote energy profiles for the reactions in the positions 1, 3, and 6.

Site	ΔG_a^\ddagger TS1	ΔG_a^\ddagger TS2	ΔG_r
1	6.1	76.5	-311.0
3	51.4	21.2	-400.6
6	105.0	67.3	-306.8

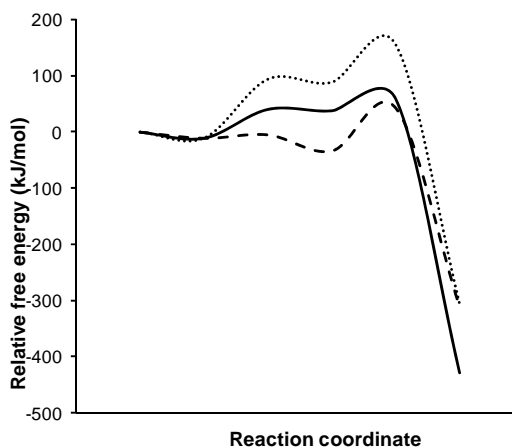


Table 1 and Figure 2 show the free energy values, calculated relative to that of the separated reactants. The carboxylation reaction in the position 6 is both kinetically and thermodynamically unfavourable. On the other hand, the pathways in the positions 1 and 3 are mutually competitive. The rate determining steps in the pathways 1 and 3 are the formation of TS2-1 and TS1-3, respectively. The ΔG_a^\ddagger value for TS1-3 is lower than ΔG_a^\ddagger value for TS2-1 (Table 1). However, Figure 2 demonstrates that TS1-3 and TS2-3 lie above TS1-1 and TS2-1. This finding is a consequence of the fact that TS1-3 is a late transition state, implying that its energy is only slightly higher than that of D3. On the other hand, E3 is significantly more stable than E6

and E1. In accord with these findings are the experimental results which show that at very low temperature (20 °C) only E1 is formed at low yield, whereas the yields of E3 and E6 increase with the increasing temperature. Thus, the main product is thermodynamically most stable E6.

CONCLUSION

Owing to experimental and computational results, a standpoint of the initial formation of the MOPh-CO₂ or MONaph-CO₂ complexes in the Kolbe-Schmitt reaction has become generally accepted. Our investigation of the carboxylation reaction of NaONaph performed by means of the M062X functional show that the NaONaph-CO₂ complex can be formed, but it cannot be further transformed to the reaction products. Using this method the transition states for direct carboxylation in all three positions (1, 3, and 6) were revealed. Pathway 6 is both kinetically and thermodynamically unfavourable. Pathways 1 and 3 are competitive, where pathway 3 requires slightly higher activation energy, but yields the more stable product. These findings are in accord with the postulation of Rahim and Kossugi.

ACKNOWLEDGEMENT

This work was partially supported by the Ministry for Science of the Republic of Serbia (Grants no. 172015 and 172016).

REFERENCES

- [1] M. A. Rahim, Y. Matsui, Y. Kosugi, *Bull. Chem. Soc. Jpn.* 2002, 75, 619 – 622.
- [2] Y. Kosugi, Y. Imaoka, F. Gotoh, M. A. Rahim, Y. Matsui, K. Sakanishi, *Org. Biomol. Chem.*, 2003, 1, 817 – 821.
- [3] M. Kunert, E. Dinjus, M. Nauck, J. Sieler, *Chem. Ber./Recueil*, 1997, 130, 1461 – 1465.
- [4] Z. Marković, S. Marković, N. Begović, *J. Chem. Inf. Model.*, 2006, 46, 1957 – 1964.
- [5] S. Yamabe, S. Yamazaki, *Theor. Chem. Acc.*, 2011, 130, 891 – 900.
- [6] Z. Marković, S. Marković, I. Đurović, *Monatsh. Chem.*, 2008, 139, 329 – 335.
- [7] S. Marković, I. Đurović, Z. Marković, 2008, *Monatsh. Chem.*, 139, 1169 – 1174.
- [8] Gaussian 09, Revision A.01, Gaussian Inc., Wallingford, CT, 2009.
- [9] Y. Zhao, G. D. Truhlar, *Acc. Chem. Res.*, 2008, 41, 157 – 167.

THEORETICAL STUDY OF ACID ACETYLATION OF DIMETHYLAMINE

S.C.Caglieri¹, M. Pagnan¹, and P.L.Zanel¹

¹*CIQA-Centro de Investigación y Transferencia en Ingeniería Química Ambiental. Universidad Tecnológica Nacional - Facultad Regional Córdoba. Avenida Cruz Roja Argentina esquina Maestro López. X5016ZAA. Córdoba, Argentina. (scaglieri@quimica.frc.utn.edu.ar)*

ABSTRACT

A theoretical study of acid acetylation of dimethylamine from the analysis of intermediate of the reaction was carried out. Geometries of all species involved in the reaction were made and identified. All of the geometry optimizations were performed by the method at the DFT with B3LYP level of theory and was adopted the 6-31+G* basis set. Energies were calculated using the MP2. The energy of activation for the reaction was 8.05 kcal/mol.

INTRODUCTION

The acetylation of amines is one of the most frequently used transformations in organic synthesis as it provides an efficient and inexpensive means for protecting amino groups in a multistep synthetic process.

Acetylation of amine is a nucleophilic substitution reaction. This reaction can be catalyzed by Brønsted acid. In the mechanism, the acetic anhydride first accepts a proton at the carbonyl oxygen and this change enhances the positive charge on the carbonyl carbon. This protonation facilitates the successive addition of amine at the position to form a tetrahedral intermediate, determining step of the rate of the reaction.

Computational method to study the reaction using acid catalysis [1] and an experimental work [2], agreed that this reaction takes place with the formation of a tetrahedral intermediate.

A theoretical study of acid acetylation of dimethylamine from the analysis of intermediate of the reaction was carried out. The reaction and the compounds studied are shown in Figure1.

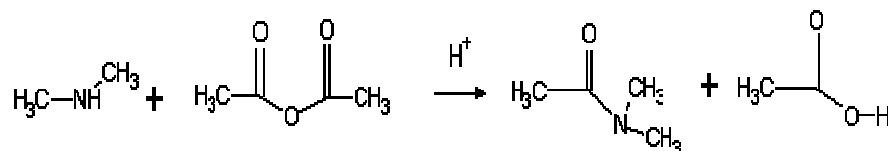


Figure 1. General Scheme of Acid Acetylation of Dimethylamine

THEORETICAL

Geometries of all species involved in the acetylation were made and identified. All of the geometry optimizations were performed by the method at the DFT - Density Functional Theory [3] with B3LYP level of theory and was adopted the 6-31+G* basis set.

Energies of all reactants and products and the energy of activation for the reaction were calculated using the MP2- 2nd order Mo/ller–Plesset method. Following the same procedure it was identified the geometric parameters and energy of intermediate. All the calculations were executed using Gaussian 09 [4] software package.

RESULTS AND DISCUSSION

Table 1 lists the geometric parameters, lengths and binding angles values, and energies of the reactants, obtained.

Table 1. Geometric Parameters Reactants

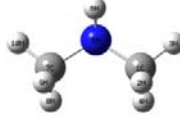
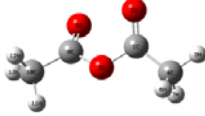
Reactants	Lengths (Å)	Angles (°)	Energies kcal/mol
 Dimethylamine	C-H = 1.12 C-N = 1.44 N-H = 1.00	C-N-C = 114.38 H ₃ -C-N = 108.78 H-N-C = 110.58	-5.69
 Acetic Anhydride	C ₁ -O ₂ = 1.22 C ₁ -C ₄ = 1.49 C ₁ -O ₃ = 1.39 C ₄ -H ₅ = 1.12	C ₁ -O ₃ -C ₈ = 121.83 O ₂ -C ₁ -C ₄ = 129.78 O ₂ -C ₁ -O ₃ = 118.05 C ₁ -C ₄ -H ₅ = 109.37	-131.71

Table 2 lists the geometric parameters, lengths and binding angles values, and energies of the products, obtained.

Table 2. Geometric Parameters Products

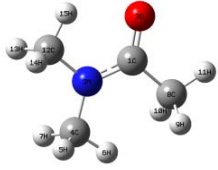

Products	Lengths (Å)	Angles (°)	Energies kcal/mol
 N,N Dimethylacetamide	$C_1-C_8 = 1.51$ $C_1-O = 1.25$ $C_1-N = 1.39$ $N-C_{12} = 1.43$ $N-C_4 = 1.43$	$C_8-C_1-N = 118.56$ $O-C_1-N = 120.48$ $C_1-N-C_{12} = 120.86$ $C_1-N-C_4 = 120.93$	-41.47
 Acetic Acid	$C-O_2 = 1.23$ $C-C = 1.49$ $C-O_3 = 1.36$ $H-O_3 = 0.97$ $C-H = 1.12$	$C-O-H = 109.76$ $O-C-O = 116.53$ $O_2-C-C = 129.27$ $O_3-C-C = 114.20$ $C-C-H_7 = 108.94$	-103.8

Figure 2 show the optimized structure of the intermediate and the Table 3 lists the geometric parameters, lengths and binding angles values, obtained. The calculations show 26.29 kcal/mol of energy for the tetrahedral intermediate and the activation energy was 8.05 kcal/mol.

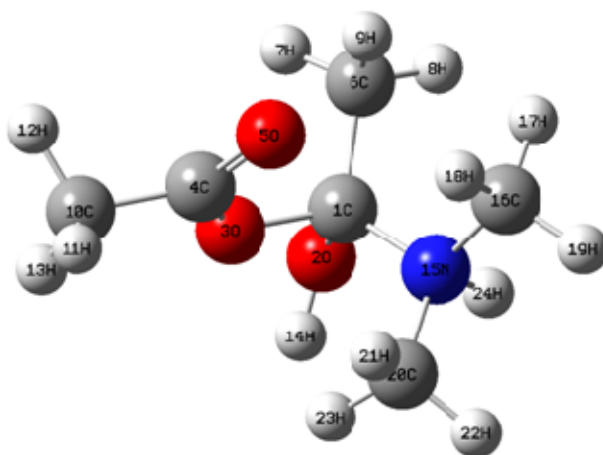
**Figure 2.** Tetrahedral Intermediate Structure

Table 3. Geometric Parameters Intermediate

Lengths	Å	Angles	°
r (C ₁ -O ₂)	1.41	θ (C ₁ -O ₂ -H ₁₄)	118.74
r (C ₁ -N)	1.50	θ (C ₁ -N-C ₁₆)	116.74
r (O ₂ -H ₁₄)	0.97	θ (N-C ₁ -O ₃)	113.26
r (C ₁ -C ₆)	1.53	θ (C ₆ -C ₁ -N)	116.22
r (C ₁ -O ₃)	1.47	θ (C ₁ -N-C ₂₀)	115.93
r (N-H ₂₄)	0.99	θ (N-C ₁ -O ₂)	112.02
r (C ₂₀ -N)	1.50	θ (N-C ₁₆ -H ₁₇)	108.98
r (C ₆ -H ₈)	1.11	θ (H ₇ -C ₆ -C ₁)	108.15

CONCLUSION

It was observed a marked consistency between the theoretical results and bibliographic data, which validates the use of theoretical methods DFT and PM2 as tools for kinetic studying the reaction of acetylation of dimethylamine

REFERENCES

- [1] H.G. Kruger, *J. Mol. Struct. (Theochem)*, 2002, 577, 281-285.
- [2] H.S. Prasad, G.R. Srinivasa, D. Channe Gowda, *Synth. Commun.*, 2005, 35, 1189-1195.
- [3] C. Lee, W. Yang, R.G. Parr, *Phys.Rev.B*, 1988, 37, 785-789.
- [4] Gaussian 09, Revision D.01, M. J. Frisch, G. W. Trucks, H. B. Schlegel, G. E. Scuseria, M. A. Robb, J. R. Cheeseman, G. Scalmani, V. Barone, B. Mennucci, G. A. Petersson, H. Nakatsuji, M. Caricato, X. Li, H. P. Hratchian, A. F. Izmaylov, J. Bloino, G. Zheng, J. L. Sonnenberg, M. Hada, M. Ehara, K. Toyota, R. Fukuda, J. Hasegawa, M. Ishida, T. Nakajima, Y. Honda, O. Kitao, H. Nakai, T. Vreven, J. A. Montgomery, Jr., J. E. Peralta, F. Ogliaro, M. Bearpark, J. J. Heyd, E. Brothers, K. N. Kudin, V. N. Staroverov, R. Kobayashi, J. Normand, K. Raghavachari, A. Rendell, J. C. Burant, S. S. Iyengar, J. Tomasi, M. Cossi, N. Rega, J. M. Millam, M. Klene, J. E. Knox, J. B. Cross, V. Bakken, C. Adamo, J. Jaramillo, R. Gomperts, R. E. Stratmann, O. Yazyev, A. J. Austin, R. Cammi, C. Pomelli, J. W. Ochterski, R. L. Martin, K. Morokuma, V. G. Zakrzewski, G. A. Voth, P. Salvador, J. J. Dannenberg, S. Dapprich, A. D. Daniels, Ö. Farkas, J. B. Foresman, J. V. Ortiz, J. Cioslowski, and D. J. Fox, Gaussian, Inc., Wallingford CT, 2009.

IR STUDY OF WATER COMPLEXES IN KBr MATRIX

I. Grinvald, I. Vorotyntsev, I. Kalagaev, A. Vorotyntsev and A. Petuhov

*Alekseev State Technical University
Minin street, 24, Nizhniy Novgorod, 603950, Russia*

ABSTRACT

The results of IR study of water complexes' formation in KBr matrix at room temperature are presented. There are considered a few systems: water-ammonia, water-carbon dioxide, water-alkali and water-alkali metal salt. The changes of spectra for components mixture give reliable evidence of the intermediates formation with hydrogen bond for the mentioned systems.

INTRODUCTION

The use of metal halide matrix for stabilization of intermediates is known quite a long time (see for an example [1]) and could be applied for IR study of labile complexes, since the matrix matter is in certain cases transparent in the IR range. The general aim of the recent work was to test the possibility of stabilization in KBr matrix and IR study of water containing intermediates at room temperature. We have considered the following systems: water-ammonia, water-carbon dioxide, water-alkali and water-alkali metal salt mixture.

EXPERIMENTAL TECHNIQUE

The sample preparation consists in the application of potassium bromide pallet as the matrix for the holding of unstable intermediates. Usually this technique is used for the recording of the IR spectra of solid waterless samples [2]. We have used similar method not only for crystal patterns, but also for gases and liquids. At the first step the KBr powder was milled separately on the sample to be investigated. Then the gas (ammonia or carbon dioxide) saturated the KBr powder, either together with the water vapour, or the gas passed preliminarily through the water layer. If the solid component (alkali or salt) was studied, the KBr powder was mixed with it and after that the water vapour saturated the KBr matter. For the IR experiments Fourier spectrometer IFS 1202 were used. The main parameters of measurements have been chosen as optimal for this instrument.

RESULTS AND DISCUSSION

We have considered the typical IR manifestation of molecular interaction: the appearing of new bands or the bands shift, which are caused owing to

complex formation. It was presumed that the water molecule plays in all the systems the role of a proton donor. This assumption can be taken as a good approximation for the investigated systems [3]. Ammonia-water system. In high frequencies IR region the new band at 3240 cm^{-1} was observed. We have assigned it to the hydrogen bond stretching in water - ammonia complex. It follows from the comparison with the spectra of KBr pallets, saturated by water or ammonia gas separately, since they have not shown the mentioned absorption (Figure 1, left side). On the Figure 1 and 2 by index "a" is labeled the spectrum of KBr pallets saturated by water vapour, by "b" – saturated by ammonium gas only and "c" – saturated by mix of components.

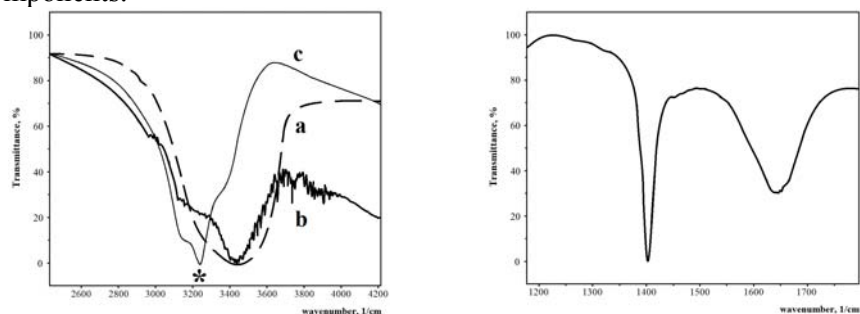


Figure 1. The spectra of KBr pallets saturated by ammonium and water

In the middle IR region we have observed a new band at 1401 cm^{-1} (Figure 1, right side), which is stronger than water bending band in the initial molecule, whereas the relative intensity of this vibration in complex should have been weaker. Besides the band at 1401 cm^{-1} locates close to the position of H-stretching in $(\text{NH}_4)^+$ containing compounds. Therefore we have assigned this band to the stretching vibration of the transferred hydrogen atom in the intermediate.

This assignment is verified by experiments with heavy water: in the middle IR range a new band at 1003 cm^{-1} was observed. Its position respectively to the band at 1401 cm^{-1} (in case of H_2O) is in accordance with the isotopic rule for hydrogen vibrations [4].

Carbon dioxide-water system. In case of carbon dioxide - water system we have observed the similar spectral picture. In the high frequencies IR region two new bands at 3120 and 2925 cm^{-1} are found to be (Figure 2, left side). In the middle IR region we have observed a new band at 1385 cm^{-1} , which are not found in the spectra of KBr pallets, saturated by H_2O or CO_2 separately (Figure 2, right side). This assignment is confirmed by the spectra of KBr pallets, saturated by carbon dioxide, passed through heavy water layer. In the middle IR-range new bands at 981 , 834 cm^{-1} were observed

instead the band at 1385 cm^{-1} . The position of these bands correlates well with the isotopic shift of hydrogen vibrations [4]. Therefore like for the ammonia-water system, we have assigned the mentioned bands to the hydrogen vibrations in different types of complexes: formed *via* hydrogen bond and owing to hydrogen atom transfer.

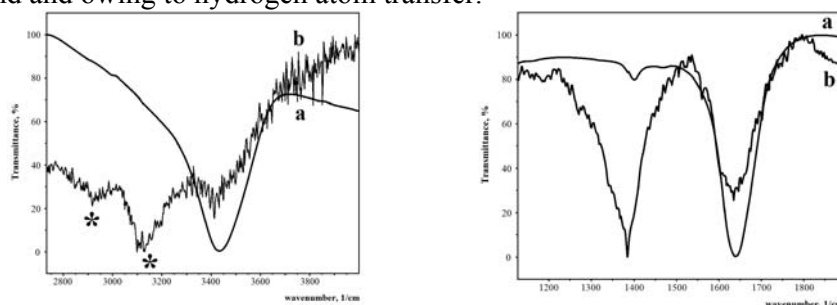


Figure 2. The spectra of KBr pallets saturated by CO_2 and water

Alkali -water system. Hereby the results for NaOH-water interaction are considered. The sample in this case was prepared by the following way: the KBr powder was mixed with the NaOH, and then this mixture was saturated by water vapour. The obtained pattern was pressed in pallet and its IR spectrum was registered. For this system we have observed the new bands in $3100\text{-}2300\text{ cm}^{-1}$ spectral region (Figure 3, spectrum “b”), which are not shown in the spectra of KBr pallets, containing NaOH (Figure 3, spectrum “a”) or saturated by water vapour. In the spectra of potassium bromide pallet with NaOH, saturated by heavy water vapour, a new strong band at 1815 cm^{-1} was detected. These data indicate on the formation of water-alkali complex in KBr matrix, owing to the interaction of water hydrogen atoms with the hydroxyl group of alkali molecule.

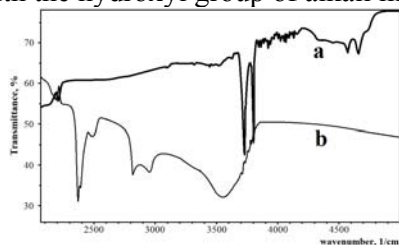


Figure 3. The spectra of KBr pallets containing alkali and water mixture

Alkali metal salt-water system. This kind of interaction is presented by Na_2CO_3 -water and NaNO_3 -water mixtures. The scheme of sample preparation in this case is the same, as for the previous system. In the Figure 4 the spectrum of KBr matrix, saturated by water vapour (spectrum “a”), the

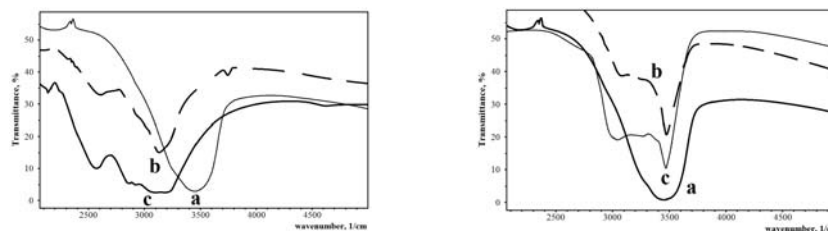


Figure 4. The spectra of KBr pellets containing alkali metal salt and water

spectra of Na_2CO_3 -water (left side) and NaNO_3 -water (right side) systems at ratio of components 1:1 (spectrum, labeled by “b”), 1:2 (spectrum labeled by “c”) are shown. For Na_2CO_3 the appearance of new bands at 2855 and 2569 cm^{-1} was observed. Besides OH stretching band shifts to 3160 cm^{-1} . At the saturation of KBr powder by heavy water the new bands at 2085 and 1855 cm^{-1} were detected. For NaNO_3 we have observed a few of overlapped bands in 3700-2800 cm^{-1} region, one of which at 3470 cm^{-1} locates close to the OH stretching position of water, and the others locate in 3300-2700 cm^{-1} range. For D_2O -salt interaction the bright band at 2315 cm^{-1} was found to be. The obtained data verify the formation of water-salt complexes in KBr matrix. We can assume that these complexes form due to the interaction of water hydrogen atoms with the oxygen atom of salt molecule.

CONCLUSION

The obtained results lead to the conclusion that the different types of complexes can exist in KBr matrix. These intermediates were fixed owing the appearance of new bands in high and middle IR regions, having a typical shift for D_2O systems. Therefore it is reasonable to assume that we have revealed the intermediates, forming due to the hydrogen bond and the hydrogen atom shift.

ACKNOWLEDGMENT

This work was supported by the Russian Foundation of Fundamental Research, grant 14-08-00898-a.

REFERENCES

- [1] H.Vancik, Pure & Appl. Chem., 1995, 67, 761-767.
- [2] A.L.Smith, Applied Infrared Spectroscopy, 1979, Wiley, 336p.
- [3] J.N.Jensen, A Problem-Solving Approach to Aquatic Chemistry, 2003, Wiley, 600p.
- [4] K.Nakamoto, Infrared and Raman Spectra of Inorganic and Coordination Compounds, 1986, Wiley, 245p.

**EUROPEAN PHARMACOPOEIA MONOGRAPHS ON
DERIVATIVE SPECTROPHOTOMETRY AND
CHITOSAN HYDROCHLORIDE:
INTER-LABORATORY VERIFICATION**

B. Marković¹, J. Ignjatović¹, V. Savić², M. Vujadinović³ and K.
Karljiković-Rajić³

¹*Department of Pharmaceutical chemistry (bojan@pharmacy.bg.ac.rs)*

²*Department of Pharmaceutical technology* ³*Department of Analytical
chemistry, University of Belgrade Faculty of Pharmacy,
Vojvode Stepe 450, 11221 Belgrade, Serbia.*

ABSTRACT

Interlaboratory verification of European pharmacopoeia monographs on derivative spectrophotometry (DS) method and chitosan hydrochloride was carried out on two generation of instruments (Cintra 20 and Evolution 300). Comparable results for DS method monograph were obtained only with smoothing point 7 and 2nd degree polynomial in Savitzky-Golay algorithm and also for evaluation with Medium digital indirect and Medium direct recording of digital spectra mode, since differences in percentages were within accepted criteria for assay in pharmaceutical method transfer ($\pm 3\%$). The difference for degree of deacetylation assessment of chitosan hydrochloride, via first derivative amplitude ¹D₂₀₂ determined on two instruments using 2nd degree polynomial and smoothing point 9 in Savitzky-Golay algorithm, was around 3% variation accepted for method transfer.

INTRODUCTION

Derivative spectrophotometry (DS) is one of the advanced modern spectrophotometric techniques, which consists in differentiation of zero-order spectra. Analytical advantage of derivative spectra originates from the fact that the derivative process discriminates in favor of sharp bands and against broad to an extent that increases with derivative order. Even if higher derivatives appear to improve resolution, the spectra obtained are also significantly distorted by noise. The objectives of this study were to evaluate, according to inter-laboratory verification, the effects of generating derivative spectra (instrumental and Savitzky-Golay algorithm parameters - smoothing points, polynomial degree and mode how derivative spectra are generated), for DS monograph since European Pharmacopoeia (EP) [1] prescribed instruments with analogue resistance-capacitance differentiation module or a digital

differentiator or another means of producing second-derivative spectra. Furthermore, degree of deacetylation assessment of chitosan hydrochloride via first derivative spectra was intended to evaluate criteria for method transfer.

EXPERIMENTAL

Absorption spectra of toluene in methanol (0.02 v/v %) as model system for DS monograph and series of N-acetylglucosamine (98%, Acros Organics) aqueous solutions (1.0-35.0 µg/ml) for standard curve as model for degree of deacetylation determination of chitosan hydrochloride via amplitude ${}^1D_{202}$, were recorded in 1cm quartz cells using UV-Vis spectrophotometers GBC Cintra 20 and Evolution 300.

Ten separately prepared solutions of toluene in methanol were obtained by transferring 20 µl of toluene into 100 ml volumetric flasks of different manufacturers and diluted with methanol to mark. Chitosan hydrochloride was prepared from 1 g chitosan (molecular weight 100 000-300 000 Acros Organics) by restricted addition of 30 ml 0.1M HCl and 65 ml of redistilled water (pH about 5.8) controlled with remained excess of base chitosan precipitate. The viscous salt solution was decanted and evaporated on warm plate (about 40°C) forming transparent film. For control of pH value of chitosan hydrochloride, Solution S was prepared by dissolving 0.1004 g in 10.00 ml of redistilled water with vigorous stirring for 20 min using a mechanical stirrer. The Test solution of chitosan hydrochloride for degree of deacetylation was prepared by dissolving 0.1274 g in redistilled water in 50 ml volumetric flask stirring vigorously, followed by dilution of 2.0 ml in 100 ml volumetric flask.

RESULTS AND DISCUSSION

The first introduction of Second derivative spectrophotometry appeared in British Pharmacopoeia (BP) 1988, addendum 1991, and up to BP 1998 for Resolution only descriptive requirement pro second-derivative spectrum of 0.02% v/v solution of toluene in methanol, was quoted for visibility of small peak between two large at about 261 nm and 268 nm. Since BP 2000, the figure of second-derivative spectrum has been initiated with defined amplitudes and the ratio A/B which is not less than 0.2. This version of DS monograph (BP 2000) has been transferred to EP Supplement 2001 of 3rd edition, but with diverse concentration of toluene in methanol solution of 0.02 g/l which remained up to EP 6. Prescribed mentioned concentration was changed to 0.02% v/v, in EP 6 and up to EP 8 [1], as originally introduced in BP. According to (Fig.1.) resolution between shoulder and

peak in zero-order spectrum (λ range 260-268 nm) corresponds with distinguished amplitudes. Slight amplitudes shifts recorded by digital methods on both instruments are presented in Table 1., along with A/B ratios. Both instruments compute digital derivative spectra from zero-order (there were no differences for two scan speeds 60 and 120 nm/min) using Savitzky-Golay algorithm. Using Evolution 300, direct digital spectra can be recorded with four smoothing values Low, Medium, High and Very high. To overcome the problem of different numerical values of absolute amplitudes recorded on various instruments, due to differences in Savitzky-Golay algorithm, EP monograph prescribed the absolute amplitude A/B ratio, and that could be an explanation why y-axis is not numerically defined.

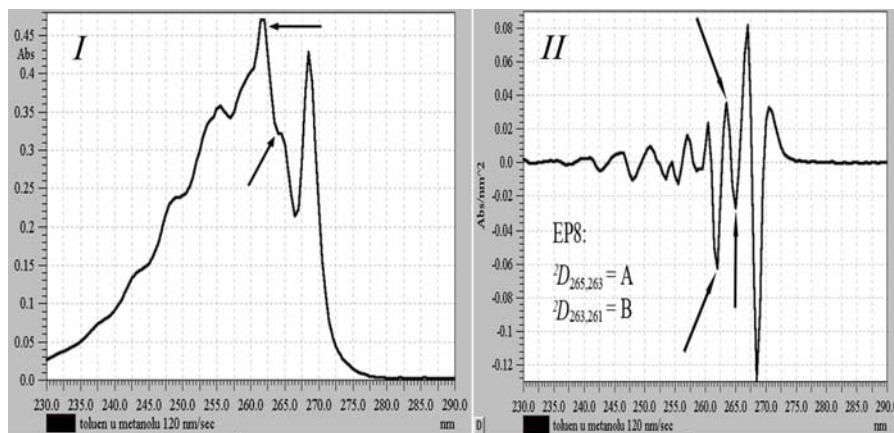


Figure 1. Absorption (*I*) and second-order derivative (*II*) spectra of 0.02% v/v solution of toluene in methanol.

The obtained results gave evidence for the comparison between two instruments applying smoothing points 5 and 7 (point 7 was superior with 2.08% and also it was possible to compare Medium digital ("indirect") with 1.53% and Medium direct with 0.86%) differences in percentages were within accepted criteria for assay in pharmaceutical method transfer as % difference between averages ($\pm 3\%$).

The absolute values of amplitudes A and B were higher applying advanced 4th and 6th degrees polynomial (Evolution 300) in comparison to second; the ratios of A/B increased from 0.5602 (2nd degree polynomial) to 0.6476 and 0.6176 with 4th and 6th, respectively.

The measured pH value 5.34, for Solution S prepared from obtained chitosan hydrochloride, was in the prescribed pH range 4.0 to 6.0. For optimal smoothing point 9 (with 2nd degree polynomial) from regression equation $y=0.0025x + 0.0001$ (Cintra20) degree of deacetylation was

93.92%, while 90.91% was obtained for Evolution 300 from equation $y=0.150x - 0.162$ using amplitude $^1D_{202}$ and $pH=4.56$ for diluted Test solution (required range 70.0–95.0%). The higher polynomial degrees caused unacceptable noise level. The difference was around 3% variation accepted for method transfer.

Table 1. Average values of amplitudes and A/B ratio for series of 10 solutions (n=10) analyzed on both instruments.

Instrument	GBC Cintra 20		TS Evolution 300			
	Derivative spectra	Digital algorithm	Digital algorithms		Direct recording	
smoothing / λ	5	7	5	7	„Medium indirect“	„Medium direct“
262	-0,0568	-0,0375	-0,7663	-0,4686	-0,4763	-0,4723
263,5	0,033	0,0198	0,4058	0,2515	0,2242	0,2196
265	-0,0245	-0,0116	-0,3283	-0,1519	-0,1661	-0,1634
A	0,0575	0,0314	0,7341	0,4034	0,3903	0,383
B	0,0898	0,0572	1,1721	0,7201	0,7005	0,6919
$X_{\text{average}}(A/B)$	0,6407	0,5488	0,6263	0,5602	0,5572	0,5535
Sd (A/B)	0,0065	0,0016	0,0096	0,0029	0,0031	0,0022

$X_{\text{average}}(A/B)$ is mean value; Sd (A/B) is standard deviation of A/B ratio

CONCLUSION

It was established that instrumental parameters, as well as derivatisation parameters such as smoothing points and polynomial degree should be included in EP monographs on derivative spectrophotometry method and on chitosan hydrochloride.

ACKNOWLEDGEMENT

This work was partially supported by the Ministry for Education, Science and Technological Development of the Republic of Serbia (Project no. TR34031).

REFERENCES

- [1] European Pharmacopoeia, Eight Edition, (EDQM), Council of Europe, Strasbourg, 2014.

FT-IR AND NMR SPECTROSCOPIC INVESTIGATION OF 12-OXO LITHOCHOLIC ACID DERIVATIVES

D.Škorić¹, B. Kordić¹, B.Jović¹ and J. Čanadi¹

¹ *Department of Chemistry, Biochemistry and Environmental Protection, University of Novi Sad Faculty of Sciences, 21000 Novi Sad, R. Serbia*

ABSTRACT

This paper reports the results of IR spectroscopic investigation of methyl-12-oxo lithocholate **1** and ¹H NMR spectroscopic investigation of sodium-12-oxo lithocholate **2**. The proton donor ability of hydroxyl group, as well as the proton acceptor properties of the carbonyl groups, of bile acid derivative was investigated by FT-IR. Data for correlation with Gutmann and Kamlet-Taft solvatochromic equations were obtained for eleven organic solvents. Micellization of 12-oxo lithocholic acid sodium salt was investigated by NMR spectroscopy. T1 relaxation time (spin-lattice relaxation time) was measured for the selected protons on this molecule in water. Relaxation time dependence from concentration indicated the critical micellar concentration (CMC) of 12 oxo-lithocholic acid sodium salt.

INTRODUCTION

Investigation of hydrogen bond interactions on oxo bile acid molecules as well as investigation of micellization of oxo bile acid sodium salts became very important due to the fact that these bile acid derivatives possess promotional action on the transport of drugs through biological membranes [1]. Formation constant (K) for hydrogen bond complex on hydroxyl group can be determined by FTIR spectroscopy employing Becker's method [2]. Investigation on formation constant of the hydrogen bond complex was carried out for 1,4-dioxane, tetrahydrofuran and acetonitrile as solvents. Positions, intensities and shapes of the specific absorption bands are usually influenced by polarity of solvent in which they were measured. Simply by recording these changes, such as band shifts etc., in different solvents it is possible to gain useful information about intermolecular interactions of investigated molecule. The linear correlation models that were used are Kirkwood-Bauer-Magat (Buckingham) equation, Gutman's acceptor number AN scale and Kamlet-Taft solvatochromic relationship [3]. Results were obtained for the following organic solvents: acetonitrile, tetrahydrofuran, diethylether, benzene, toluene, hexane, 1,4-dioxane, chloroform, dichloromethane, carbontetrachloride and 1,2-dichloroethane.

One of the main characteristics of oxo bile acids is micelle formation which occurs in water solutions of sodium salts of these compounds. Ability to form micelles is characterized by critical micellar concentration (CMC)[4]. NMR measurement of T1 relaxation time (spin-lattice relaxation) is convenient technique for micellization studies. T1 relaxation is in connection with molecular motion and with environment of measured nucleus, so the changes caused by micellization are simply monitored through T1 measurement. Micellization of some oxo bile acid sodium salts is already investigated with NMR technique [5].

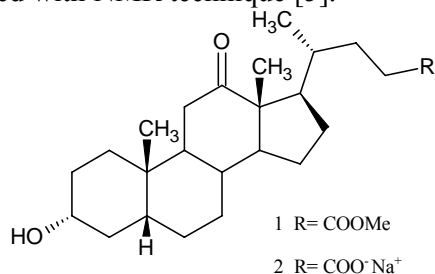


Figure 1. Structure of 12-oxo lithocholic acid methyl ester **1** and sodium salt **2**.

EXPERIMENTAL

Bile acid derivatives were prepared from deoxycholic acid using known synthetic procedures [6]. Hydrogen bond formation constants and spectroscopic parameters were investigated by IR in range of 3700-3200 cm^{-1} . Samples were placed in 1 cm (IR) UVIRASIL cells and the measurements were performed at temperature of 298 K. Solvent effects were investigated in range of carbonyl C=O vibration from 1800-1650 cm^{-1} . For all spectra, 50 scans were recorded and averaged with resolution of 2 cm^{-1} for each spectrum. Samples were placed in 0.512 mm path length NaCl cells and the measurements have been performed at 298 K.

NMR measurements were performed on a Bruker AC 250 spectrometer with frequency for ^1H nucleus of 250,13 MHz. For determination of T1 relaxation time standard inversion recovery experiment was used (180° - τ - 90° -AQC). Peak intensities for nine different interpulse delays τ (0.001, 0.01, 0.03, 0.07, 0.2, 0.3, 0.4, 0.8, 1.6 second) were determined. All NMR experiments were conducted at 298 K. Nine solutions in D_2O was prepared covering concentration range from 4mM to 40mM.

RESULTS AND DISCUSSION

FTIR hydrogen bond investigation showed that the strongest (highest value) constant of formation is for hydrogen bond complex of 12-oxo lithocholic

acid in form of methyl ester with acetonitrile. Tetrahydrofuran showed to be more potent proton acceptor than 1,4-dioxane, which is in seemingly contradiction with the fact that 1,4-dioxane has two proton acceptor atoms. On the basis of good correlation obtained in Gutman equation and magnitudes of parameter values for the LSER solvatochromic equation, it could be estimated that polarization effects and the possibility of solvent to donate hydrogen for hydrogen bonding contributes most to the shift of carbonyl band (Fig 3.).

Signal intensities from spectra obtained with inversion recovery Fig. 2. were used for calculation of T1 relaxation time for angular methyl group protons ($\delta_H=1.04$ ppm). After determination their T1 values for all solutions in used concentration range, T1 relaxation time was plotted as a function of concentration of oxo bile acid sodium salt as shown on Fig. 2. Inflection points on this function are indicating micellization, and CMC value is determined by arithmetic mean of the values of upper pseudo CMC (CMC') and lower pseudo CMC (CMC''). In this case there is two inflection points: one with the bigger difference in T1 relaxation time (30 ms) between 24mM and 28mM concentrations, determining them as CMC' and CMC'' and other with smaller difference in T1 relaxation time (20 ms) between 12mM and 16mM concentrations, respectively. Thus, two main CMC of 12-oxo lithocholic acid sodium salt are 14mM and 26mM.

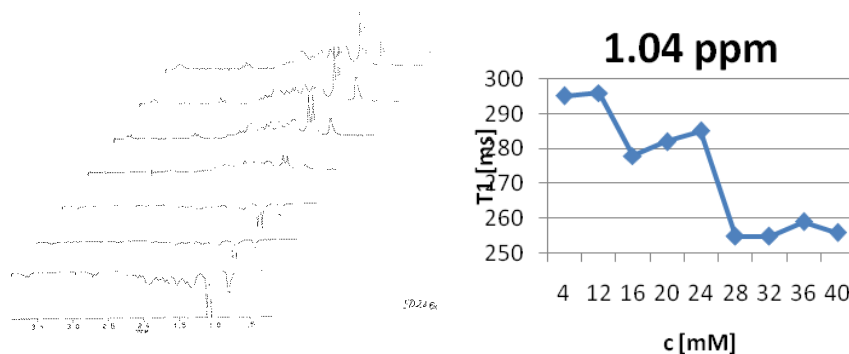


Figure 2. Seven of nine spectra obtained during inversion recovery experiment (*left*) and plot of T1 relaxation time as a function of concentration (*right*)

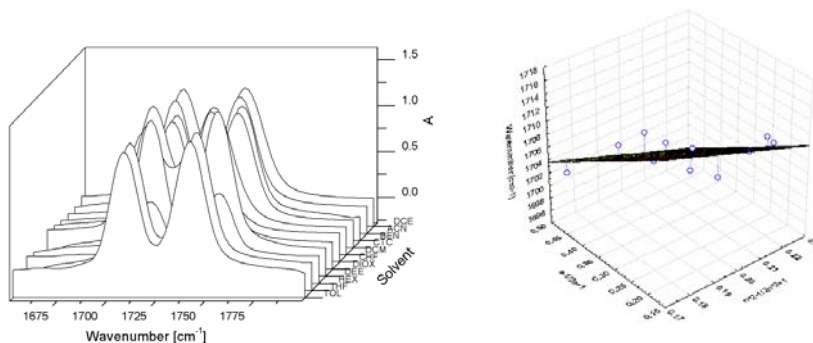


Figure 3. Shifts of carbonyl groups IR bands in different solvents (*left*) and the Kirkwood-Bauer-Magat correlation of carbonyl band position against refractive index and relative permittivity of solvent (*right*)

CONCLUSION

Based on the obtained data from FTIR measurements and the extracted correlations, it can be assumed that the both inductive and the steric effects play an important role in the stability of the investigated hydrogen bonded complexes. The two determined CMC values for the sodium salt of 12-oxo lithocholic acid can be explained with a complex micellization process, where primary micelles, which are first formed, rearrange in to secondary micelles.

ACKNOWLEDGEMENT

Financial support of AP of Vojvodina Republic of Serbia, contract No: 114-451-3690/2011-01 for IPA-CBC HUSRB/1002/214/193 project is gratefully acknowledged.

REFERENCES

- [1] M. Poša, K. Kuhajda, Journal of the Serbian Chemical Society, 2010, 75, 433-440
- [2] E. D. Becker, Spectrochim. Acta, 1961, 17, 436-447
- [3] B. Jovic, A. Nikolic, S. Petrovic, Journal of Molecular Structure, 2013, 1044, 140-143
- [4] M. Poša, Steroids, 2011, 76, 85-93
- [5] M. Poša, V. Guzsány, J. Csanádi, Colloids and Surfaces B: Biointerfaces, 2009, 74, 84-90
- [6] A. K. Batta, S. K. Aggarwal, G. Salen, S. Shefer, Journal of Lipid research, 1991, 32, 977-983

ENERGY REQUIREMENTS OF THE REACTIONS OF KAEMPFEROL AND SELECTED RADICAL SPECIES IN DIFFERENT MEDIA

J. M. Dimitrić Marković¹, Z.S. Marković², D. Milenković³ and J. Đorović³

¹ Faculty of Physical Chemistry University of Belgrade, Studentski trg 12-16, 11000 Belgrade, Republic of Serbia, markovich@ffh.bg.ac.rs

² Department of Bio-chemical and Medical Sciences, State University of Novi Pazar, Vuka Karadžića bb, Novi Pazar 36300, Republic of Serbia

³ Bioengineering Research and Development Center, 34000 Kragujevac, Republic of Serbia

ABSTRACT

Kaempferol, one of the most bioactive plant flavonoids was experimentally and theoretically (at M05-2X/6-311G(d,p) level of theory) investigated for its ability scavenge potentially highly damaging hydroxyl and superoxide anion radicals. Relating obtained hydroxyl radical activity sequence with kaempferol structural features it could be assumed that C4'-OH functional most probably renders it as hydroxyl radical scavenger while C5-OH group has more prominent role compared to *ortho*-hydroxy groups in B ring. However, kaempferol's activity towards superoxide anion radical implicate *ortho*-hydroxy groups in B ring as more relevant. Theoretical calculations point to HAT and SPLET mechanisms as operative for kaempferol in all solvents under investigations.

INTRODUCTION

Flavonoids are natural polyphenolic compounds reported to exert a wide range of positive health effects mainly arising from their antioxidant ability. The protective role of flavonoids is manifested in their capability to "sacrifice" first in the oxidative processes transforming free radicals into stable, deprotonated, forms. The inactivation of reactive radical species is related to flavonoid (ArOH) ability to transfer the phenolic H-atom ($1\text{H}^+/1\text{e}^-$) [1]. This transfer can be visualized through at least three mechanisms characteristic not only of flavonoids but phenolics generally: hydrogen atom transfer (HAT), sequential proton loss electron transfer (SPLET), and single electron transfer followed by proton transfer (SET-PT) [2]. Calculated energy requirements for each mechanism, BDE (bond dissociation enthalpy) (HAT), IP (ionization potential) and PDE (proton dissociation enthalpy) (SET-PT), and PA (proton affinity) and ETE (electron transfer energy)

(SPLET) may indicate, which radical scavenging mechanism is thermodynamically preferred and point out the active site for radical inactivation.

EXPERIMENTAL

DFT calculations The conformations of different kaempferol forms (neutral, radical, radical-cation, and anion) are fully optimized by the new local density functional method (M05-2X), developed by the Truhlar group [3] and 6-311G(d,p) basis set [4] implemented in the Gaussian 09 package.

The structures obtained on this way were verified by normal mode analysis to be minimum on the potential energy surface. No imaginary frequencies were obtained. The influence of water, dimethylsulfoxide (DMSO), ethanol and dimethylformamide (DMF) as solvents was approximated by a solute electron density (SMD) solvation model, the continuum solvation model based on the quantum mechanical charge density of a solute molecule interacting with a continuum description of the solvent. The vibrational frequencies were obtained from diagonalisation of the corresponding M05-2X Hessian matrices. The nature of the stationary points is determined by analyzing the number of imaginary frequencies: 0 for minimum and 1 for transition state. Mutual position of rings B and C was obtained by rotating around torsion angle τ (O1–C2–C1'–C2' atoms (Fig. 1). The torsion angle τ was scanned in steps of 10° without constraints on all other geometrical parameters. The effects of the torsion angles ω_1 (H–O5–C5–C6), ω_2 (H–O7–C7–C8), ω_3 (H–O3–C3–C2), and ω_4 (H–O4'–C4'–C3') were analyzed in order to determine the preferred relative positions of the rings B and C.

RESULTS AND DISCUSSION

The preferred mechanism of antiradical activity of kaempferol (Fig. 1, Table 1) can be estimated from ΔH_{BDE} , ΔH_{IP} , and ΔH_{PA} values. Namely, the lowest of these values indicates which mechanism is favorable and the preferred site of antiradical action can be estimated from the sum of enthalpies involved in a particular free radical scavenging mechanism (BDE for HAT; IP and PDE for SET-PT and PA and ETE for SPLET). Since the entropy factor is small, positive and nearly constant ($0.54\text{--}0.55 \text{ kJ K}^{-1} \text{ mol}^{-1}$), the sign of enthalpy change implies the same sign of free Gibbs energy change no matter the temperature value. On the basis of thermodynamical values in Table 1 it is clear that only HAT and SPLET are operative radical scavenging mechanisms of kaempferol in all solvents under investigations.

Table 1. Calculated reaction enthalpies (kJ/mol) for the reactions of kaempferol with hydroxyl radical, superoxide radical anion and peroxy radical

M05-2X/6-311G(d,p)										
Kaempferol	Water ($\epsilon=78.35$)					DMSO ($\epsilon=46.83$)				
	HAT	SET-PT		SPLET		HAT	SET-PT		SPLET	
	ΔH_{BDE}	ΔH_{IP}	ΔH_{PDE}	ΔH_{PA}	ΔH_{ETE}	ΔH_{BDE}	ΔH_{IP}	ΔH_{PDE}	ΔH_{PA}	ΔH_{ETE}
		99					242			
KOH-3 + ·OH	-148		-247	-127	-21	-139		-380	-219	80
KOH-4' + ·OH	-125		-223	-127	3	-119		-361	-230	111
KOH-5 + ·OH	-95		-194	-123	28	-76		-317	-207	131
KOH-7 + ·OH	-95		-194	-141	46	-91		-333	-245	153
		373					692			
KOH-3 + ·OO ⁻	66		-307	19	46	103		-588	-24	128
KOH-4' + ·OO ⁻	89		-284	19	70	123		-569	-36	158
KOH-5 + ·OO ⁻	118		-254	23	96	166		-526	-12	179
KOH-7 + ·OO ⁻	118		-254	5	114	151		-541	-50	201
		Ethanol ($\epsilon=24.85$)						DMF ($\epsilon=37.22$)		
		135						244		
KOH-3 + ·OH	-149		-284	-149	-1	-138		-383	-222	83
KOH-4' + ·OH	-128		-263	-151	23	-119		-363	-231	112
KOH-5 + ·OH	-95		-230	-144	49	-76		-320	-207	131
KOH-7 + ·OH	-97		-232	-165	68	-91		-335	-245	154
		454					697			
KOH-3 + ·OO ⁻	74		-379	12	62	103		-594	-28	131
KOH-4' + ·OO ⁻	96		-358	10	86	122		-575	-37	159
KOH-5 + ·OO ⁻	129		-325	17	112	166		-531	-13	179
KOH-7 + ·OO ⁻	127		-327	-5	131	150		-547	-51	201

The hydrogen atom is abstracted mainly from 3-OH group on the C ring when reaction takes place via HAT mechanism which confirms the role of the C3-OH group in antiradical mechanism of kaempferol. The 7-OH group in the ring A is dominant position for reaction via SPLET mechanism in all solvents. Examination of the reaction enthalpies for the reactions of kaempferol with hydroxyl radical shows that they are exothermic in all solvents. On the basis of the values in Table 1 it is clear that kaempferol reacts with hydroxyl radical via both, HAT and SPLET mechanisms in all solvents. For protic polar solvents (water and ethanol), HAT and SPLET are competitive mechanisms, while in other two aprotic polar solvents (DMSO and DMF), SPLET is the prevailing mechanism. In the reaction with superoxide anion radical kaempferol

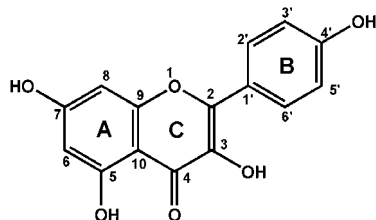


Figure 1.
Structure of kaempferol

undergoes SPLET mechanism which is dominant in all solvents while the reaction by HAT mechanism is endothermic in all solvents. Moreover, the aprotic polar solvents (DMF and DMSO) are more suitable medium for reactions of kaempferol with superoxide anion radical.

CONCLUSION

Reaction enthalpies and free energies, calculated using the M052X/6-311G(d,p) level of theory, of the individual steps of three possible radical scavenging mechanisms (HAT, SET-PT and SPLET) offer insight into the influence of the medium on the thermodynamically preferred mechanism as well as the preferred sites of the antiradical action. In protic polar solvents (water and ethanol) kaempferol reacts with hydroxyl radical *via* competitive HAT and SPLET mechanisms, while in aprotic polar solvents (DMSO and DMF) SPLET prevails. Preferred sites of action are C3-OH (via HAT) and C7-OH (via SPLET) functionals. Aprotic polar solvents (DMF and DMSO) are more favorable for the interaction with superoxide anion radical. In those solvents kaempferol undergoes SPLET mechanism.

ACKNOWLEDGEMENT

The authors acknowledge financial support of the Ministry of Science of the Republic of Serbia, grant No. 172015.

REFERENCES

- [1] J.S. Wright, E.R. Johnson, G.A. DiLabio J. Am. Chem. Soc.2001, 123(6),1173–1183.
- [2] J. M.Mayer, Annu Rev Phys Chem. 2004, 55, 363-390
- [3] Y. Zhao, D.G. Truhlar Theor Chem Acc.2008, 120, 215-241.
- [4] G. Shakila, S. Periandy, S. Ramalingam J. Atom. Mol. Optical Phys. 2011, 1-10.

COUPLED ELECTRON TRANSITIONS ABOVE THE CORE LEVEL THRESHOLD

A. Cholach and V. Tapilin

*Boreskov Institute of Catalysis, Novosibirsk 630090,
Prospekt Akademika Lavrentieva 5, Russian Federation*

ABSTRACT

Standard equipment for electron spectroscopy empowers fingerprinting the adsorbed layer at atomic-molecular level. The resource results from novel route for the primary electron energy dissipation through a set of shake-off and shake-up electron transitions, each coupled with the threshold core level excitation. Experimental evidence for the route is based on fine structures in extended Disappearance Potential Spectra from the Pt(100) single crystal fitting the valence state structures of adsorbed species and substrate atoms as well as plasmon excitations; in total over 20 peculiar satellites have been detected in conventional experimental conditions. Theoretical justification grounds on the mechanism which is a combination of well-known electron transitions. The phenomena signify fundamental regularity of electron-solid interaction disclosing the outer shell structure of near-surface atoms alike an Auger effect brings to light the inner shell structure.

INTRODUCTION

The resonant core level excitation makes a crucial impact on an atom and results in specific responses disclosing intrinsic properties of a system which part of that atom is. The following effects have been earlier detected under tunable synchrotron irradiation and became the basis of advanced techniques [1, 2]: a fine structure in extended and near above the threshold X-ray absorption spectra revealing the short-range atomic geometry and the density of vacant states, and being the grounds of EXAFS and XAS method, respectively; a fine structure in soft X-ray emission spectra near below the threshold disclosing the valence states of target atom and known as XES. Similar effects are discovered under electron impact as another source for the resonant core level excitation [3]: a fine structure in elastic scattering spectra above the threshold corresponding to valence state structures of adsorbed species and substrate atoms. In particular, the comparison between original Disappearance Potential Spectroscopy (DAPS) and reference Ultraviolet Photoelectron Spectroscopy (UPS) data has shown that a single or a set of satellites fits the valence state structure thus providing the molecular fingerprint of arbitrary adsorbed species. The same satellites

follows each threshold repeating assignment of the adsorbed layer and in total more 20 peculiar spectral features are detected for different species in conventional experimental conditions. The phenomena are regarded as a novel route for the primary electron energy dissipation named the Conjugate Electron Excitation (CEE). The present paper highlights experimental and theoretical CEE justification by confrontation with reference data and general concepts in the field of electron-solid interaction.

EXPERIMENTAL AND THEORETICAL

DAPS is based on the threshold core level excitation of target atoms by an electron beam of time-based energy. Whenever accelerating *potential* overcomes the core level energy a part of electrons *disappears* from elastic current providing the spectral dip. DAPS was used to trace the channels of electron consumption at the Pt(100)-(1x1) single crystal other than core level excitation [3]. The surface was controlled by Low Energy Electron Diffraction and Auger Electron Spectroscopy (AES). The Fermi level (E_F) \sim 314.8 eV corresponds to the Pt4d_{5/2} core level energy.

Density of States (DOS) for bulk Pt was calculated by Quantum Espresso package within a $12 \times 12 \times 12$ grid. The primary electron was described by the plane wave with $\vec{k}_{\parallel} = 0$ parallel to the surface [3].

RESULTS AND DISCUSSION

CEE includes a set of independent shake-off and shake-up electron transitions, each coupled with the threshold core excitation of target atom. The former transitions are sequential ionization of nearby valence states, while the latter are composed of multiple plasmon excitations and shifting the valence states of substrate atoms to E_F . Experimental evidence for CEE consists in continual satellites in DAPS spectra obtained from different adsorbed layers on the Pt(100) single crystal [3]. A certain satellite is a distinct peak of 1-2 eV base-width and coverage proportional intensity and localized at the respective valence state' ionization potential above the threshold. Fig. 1 (a) shows an example of fine spectral structure above Pt 4d_{5/2} corresponding to valence states of the adsorbed CO. Close similarity between experiment and theory in Fig. 1 (a) evidences that CEE affects the substrate atoms as well. Furthermore, nearly the same experimental spectral structure replicates right above E_F thus being close to theoretical spectra moved down by the Pt work function in Fig. 1 (b). The former transition corresponds to shake-off, while the latter to shake-up process consisted in shift the valence Pt DOS to E_F . In prospect, CEE empowers localization at the composite surface since satellites of the adsorbed particle accompany

threshold excitation of only that surface atom which is chemically bound to a given species, and core level energies are easily distinguishable. In addition to CEE of localized valence states, the collective excitations are also presented in Fig. 1 (b) as other satellites at surface $h\omega_s$ and bulk $h\omega_b$ plasmon energies above the threshold. In contrast to valence states, $h\omega_s$ disappears and $h\omega_b$ peak decreases on coverage due to screening effect by the adsorbed layer [3].

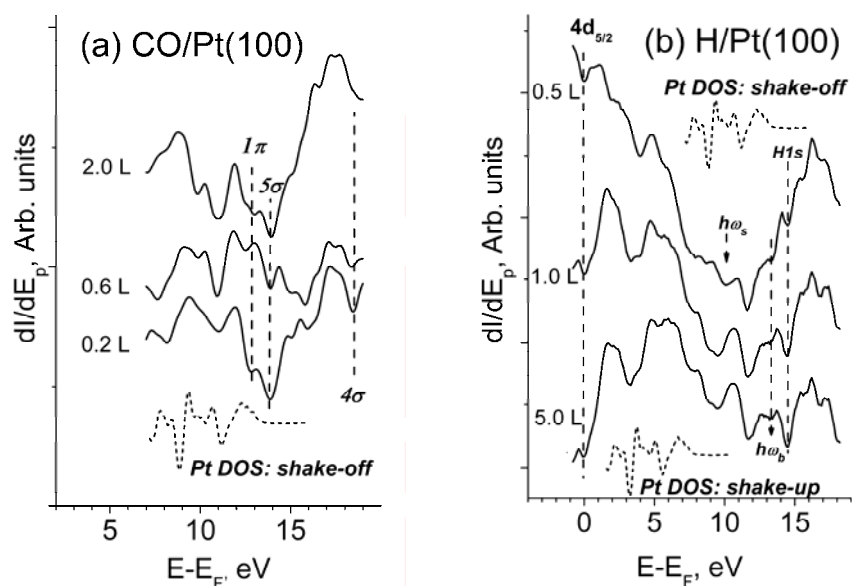


Figure 1. Satellite structures in theoretical (dashed curves) and experimental (solid curves) DAPS spectra for clean Pt(100) surface and after exposure of (a) CO and (b) H_2 at 300 K, respectively.

Theoretical CEE justification is grounded on its mechanism which is just a combination of well-known electron transitions [4]. Indeed, shake-up plasmon satellites are usual objects in X-ray Photoelectron and AES spectra. Ionization of the valence states comparable in efficiency for both, substrate atoms and adsorbed species is a basis of UPS. Satellite replicas above the thresholds conform to core levels identity regarding the threshold excitation. Therefore, CEE effect does not undermine the general concepts related to electron-solid interaction. Close similarity of satellite and valence state structures implies 1D density of vacant states at the vacuum level (infinite theoretically) to be an active spot for CEE electrons allocation. In turn, the one-dimensionality results from Rutherford relation [5] predicting effective electron-electron scattering for over small angles.

Above peculiarities give hope that CEE means the fundamental regularity of inelastic electron scattering by any adsorbed system and brings to light the outer shell structure of near-surface atoms like an Auger effect discloses the inner shell structure. Furthermore, CEE accentuates a strong community of substrate and adsorbate electronic structures and wave-corpucle dualism of electrons. CEE control is supposed to be a simple additional tool of any electron analyzer for fingerprinting the adsorbed layer at atomic-molecular level as alternative to XES, which requires a tunable synchrotron irradiation and fine analytical instrumentation [2]. Besides, elastic electron scattering basically provides the vacant states structure and geometrical parameters similar to XAS and EXAFS, respectively [6].

CONCLUSION

Routine equipment for electron spectroscopy empowers to fingerprint the adsorbed layer at molecular level. The resource results from novel route for primary electron energy dissipation through a set of shake-off and shake-up electron transitions, each coupled with the threshold core level excitation of target atom. A fine structure in elastic scattering spectra above the threshold fits the valence states of adsorbed species and substrate atoms as well as plasmon excitations. Experimental and theoretical evidence for the route is grounded on the large quantity of relevant satellites and on the mechanism consisted of well-known electron transitions, respectively. The conjugate electron excitation signifies the fundamental regularity of inelastic electron scattering by any adsorbed system and accentuates a strong community of substrate and adsorbate electronic structures.

ACKNOWLEDGEMENT

This work is supported by the Russian Foundation for Basic Research (Grant no. 14-03-00285).

REFERENCES

- [1] G. Bunker, Introduction to XAFS: A Practical Guide to X-ray Absorption Fine Structure Spectroscopy, Cambridge Univ. Press, 2010.
- [2] T. Schiros, K. J. Andersson, L. G. M. Pettersson, A. Nilsson, H. Ogasawara, J. Electron Spectrosc. Relat. Phenomena, 2010, 177, 85-98.
- [3] A. Cholach, V. Tapilin, J. Chem. Phys., 2013, 138, 104201-1-104201-7.
- [4] D. P. Woodruff, T. A. Delchar, Modern Techniques of Surface Science, Cambridge Univ. Press, 1994.
- [5] R. Feynman, Quantum Electrodynamics, Addison-Wesley, 1998.
- [6] M. L. den Boer, T. L. Einstein, W. T. Elam, R. L. Park, L. D. Roelofs, G. E. Laramore, Phys. Rev. Lett. 1980, 44, 496-499.

DEVELOPMENT OF LC-MS/MS METHOD FOR DETERMINATION OF ATORVASTATIN AND ITS METABOLITES IN BIOLOGICAL SAMPLES

M. Crevar Sakač¹, Z. Vujić¹ and V. Kuntić²

¹*Department of Pharmaceutical Chemistry, Faculty of Pharmacy, University of Belgrade, Vojvode Stepe 450, 11000 Belgrade – SERBIA*

²*Department of Physical Chemistry, Faculty of Pharmacy, University of Belgrade, Vojvode Stepe 450, 11000 Belgrade – SERBIA*

ABSTRACT

Analytical LC-MS/MS method was developed for determination of atorvastatin and its metabolites in rat blood plasma. Chromatographic separation was performed on C₁₈ analytical column and gradient mobile phase composed of acetonitrile and 0.1% acetic acid. Rosuvastatin was used as an internal standard (IS). Different Selected Reaction Monitoring (SRM) transitions were selected for every analysed compound in ESI+ interface. The method was validated over the concentration range 0.1–20 ng/mL for atorvastatin and atorvastatin-lactone and 0.5–20 ng/mL for *ortho*-hydroxyatorvastatin and *para*-hydroxyatorvastatin ($r^2 \geq 0.99$). This method demonstrated good precision, accuracy and stability of tested compounds.

INTRODUCTION

Atorvastatin belongs to group of statins, HMG-CoA reductase inhibitors, which are widely used for the treatment of hypercholesterolemia. Statins also have many beneficial pleiotropic effects such is their antioxidant activity. Atorvastatin is metabolized in liver to active metabolies, *ortho*-hydroxyatorvastatin (oOH-AT) and *para*-hydroxyatorvastatin (pOH-AT), and three corresponding inactive lactones [1]. HMG-CoA reductase inhibitory activity is mainly attributed to active metabolites [2]. The aim of this study was to establish LC-MS/MS method for monitoring changes in rat blood plasma concentration of atorvastatin, its active metabolites and inactive metabolite, atorvastatin-lactone (AT-L).

EXPERIMENTAL

Male Wistar albino rats, treated orally with Atorvastatin, were used for the experiment. Animal blood samples were collected directly from the heart in test tubes containing heparine and centrifuged at 3000 rpm for 15 min. All experimental procedures and protocols conformed to institutional guidelines

for the care and use of animals in research No 5/10 (Ethics Committee of the Faculty of Pharmacy, University of Belgrade). Samples were prepared by solid-phase extraction on OASIS® HLB SPE cartridges. The analytes were eluted with acetonitrile:ammonium acetate buffer (0.1M, pH 4.6, 95:5,v/v). Pure extracts were directly transferred to LC vials.

Method was validated in concentration range of 0.1-20 ng/mL for AT and AT-L and 0.5-20 ng/mL for oOH-AT and pOH-AT. Plasma samples as well as standard solutions were kept on ice to minimize possible interconversion of lactone and acid forms.

Analyses were carried out on a UHPLC–MS/MS system consisting of a Thermo ACCELA UHPLC (Thermo Scientific, MA, USA) coupled to a triple quad Mass Spectrometer Thermo TSQ Quantum Access Max (Thermo Scientific, MA, USA) with a heated electrospray ionization (HESI) interface operated in the positive mode. A ZORBAX Eclipse C₁₈ Analytical, 4.6×100 mm (3.5µm) column was used for the chromatographic separation. The column was kept at constant temperature at 25°C and autosampler tray was set at 4°C. The analytes were eluted by a gradient mobile phase system which consisted of acetonitrile and 0.1% CH₃COOH (Table 1). The flow rate was kept on 400 µL/min.

Table 1. Gradient mobile phase

t/min	%A	%B
0	65	35
4	65	35
4.5	80	20
7	80	20
7.05	65	35
8	65	35

A – acetonitrile, B – 0.1% glacial acetic acid

The MS detector was operated in the selected reaction monitoring (SRM) mode with SRM transitions selected: (m/z, Q1 → Q3, collision energy) of AT (m/z, 559.47 → 439.51, 22 eV); AT-L (m/z, 541.36 → 447.59, 19 eV); oOH-AT (m/z, 575.20 → 439.64, 20 eV); pOH-AT (m/z, 575.54 → 439.64, 20 eV) and IS (m/z, 482.25 with selected combination of two fragments to improve signal 257.72, 31 eV and 299.81, 35 eV).

Quality control samples at four concentration levels were used for determination of within-run and between-run accuracy and precision.

RESULTS AND DISCUSSION

Sample preparation

Plasma samples were mixed with ammonium acetate buffer, pH=4.6 (0.1M) in order to minimize possible interconversion between acid and lactone forms [3]. For SPE OASIS® HLB cartridges were chosen since they are acceptable for both, hydrophilic and lipophilic compounds. Washing cartridges was carried out with 1 mL water and 1 mL 5% acetonitrile which gave cleaner samples and better recoveries. Mixture of acetonitrile and ammonium acetate buffer, pH 4.6 (0.1 M; 95:5, v/v) used as eluent gave the highest recoveries.

LC-MS/MS conditions

Since *p*OH-AT and *o*OH-AT have the same fragmentation pattern, and because of possible acid-lactone interconversion, good chromatographic separation is essential. Gradient mobile phase was used in order to keep good separation in shorter time. The retention times of investigated compounds were (in minutes): 2.65 (*p*OH-AT), 3.97 (*o*OH-AT), 4.48 (AT) and 6.25 (AT-1) and 3.05 for IS.

Protonated molecular ion ($[M+H]^+$) was the major parent ion used to obtain the product ion spectra for all compounds. MS source parameters were optimized based on *p*OH-AT since its concentration in plasma is lower than other analytes.

Method validation

Validated method was linear within investigated concentration range ($r^2 \geq 0.99$). Within run and between run precision and accuracy were lower than 15% for all analysed samples. Calculated LOD was 0.1 and 0.13 ng/mL for *o*OH-AT and *p*OH-AT respectively and 0.05 ng/mL for AT and AT-L. Lowest concentration on calibration curve was LLOQ. Recoveries were between 57% and 75% for all analytes which is acceptable for bioanalytical methods. The specificity of the method was tested and no interfering peaks and no interfering matrix effect was found. Stability of analytes was tested (short term, freeze-thaw and long term). The obtained results were between 92 and 103% for all tested conditions which means that all analytes were stable at tested conditions. Chromatogram of a plasma sample taken from rats after six weeks of daily atorvastatin intake is shown on Figure 1. Chromatogram confirms possibility of detecting very low concentrations of all four components simultaneously in complex matrix: atorvastatin, its active and inactive metabolites by proposed analytical method.

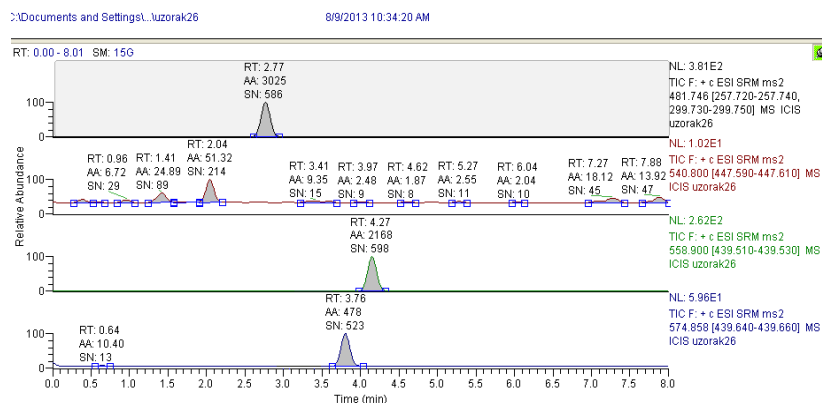


Figure 1. Chromatogram of a plasma sample taken from rats after six weeks of daily atorvastatin intake

CONCLUSION

During this study LC-MS/MS method for determination of atorvastatin, its active and inactive metabolites was optimized and validated. Comparing to previously published methods [4,5] the advantage of this method is determination of inactive lactone as well as active hydroxy metabolites, using SPE procedure instead of protein precipitation and short run time. Described method is sensitive, simple and reliable.

ACKNOWLEDGEMENT

This work was financially supported by a grant from the Ministry of Science and Environmental Protection, Republic of Serbia (Project numbers OI 172041).

REFERENCES

- [1] W. Jacobsen, B. Kuhn, A. Soldner, G. Kirchner, K.F. Sewing, P.A. Kollman, L.Z. Benet, U. Christians, *Drug. Metab. Dispos.*, 2000, 28, 1369-1378.
- [2] Parke-Davis, 2004, Product information: Lipitor (Atorvastatin Calcium), Parke-Davis (Division of Pfizer Inc.). Ann Arbor, MI, USA
- [3] M. Jemal, Y.O. Xia, *J. Pharmaceut. Biomed*, 2000, 22, 813-827.
- [4] J.S. Macwan, I.A. Ionita, M. Dostalek, F. Akhlaghi, *Anal. Bioanal. Chem.*, 2011, 400, 423-433.
- [5] P. Partani, S.M. Verma, S. Gurule, A. Khuroo, T. Monif, *Journal of Pharmaceutical Analysis*, 2014, 4(1), 26-36.

LASER DESORPTION/IONIZATION TIME-OF-FLIGHT MASS SPECTRA OF GADOLINIUM

J. Cvetičanin, M. Milošević and S. Veličković,

*VINČA Institute of Nuclear Sciences, University of Belgrade, P. O. Box 522,
11001 Belgrade, Serbia (vsuzana@vinca.rs)*

ABSTRACT

The laser desorption/ionization time-of-flight (LDITOF) mass spectra of the solution of Gd_2O_3 in HCl are reported. The results presented here illustrate the usefulness of the linear positive mode of LDI in the characterization of gadolinium metal ions. In addition, the laser desorption/ionization also leads to the formation of several ionic species containing gadolinium with oxygen and chlorine, which were detected in the negative linear mode. The ion signals are identified by both m/z values and distinctive isotope patterns.

INTRODUCTION

Lanthanide-doped nanomaterials may be applied in variety areas such as, solid-state lasers and displays, for lightening and fluorescence labeling [1, 2]. Among these materials, Gd_2O_3 nanoparticles are of particular importance due to their good chemical durability, thermal stability, low phonon energy, and easiness of doping with other lanthanide ions [3-5]. These particles may be used as contrast agents for medical magnetic resonance imaging [6, 7]. Recent experiments on the magnetic properties of Gd_2O_3 nanoparticles also showed that the particles exhibit paramagnetic rather than superparamagnetic behavior. [8]

Mass spectrometry is one of the most decisive analytical techniques for determination of metals, since it can determine the analyte using its mass to charge ratio. Also, mass spectrometric methods provide a unique experimental tool for the investigation of the conditions for obtaining the small-size metal clusters. Results have shown that inductively coupled plasma (ICP), induces a very “hard” ionization, and this ionization source may be used for detection of metal ions by ICP-MS. On the other hand, electrospray ionization (ESI) is a “soft” ionization; it cannot ionize metal ions themselves, even if they are dissolved in aqueous solution. However, it has been revealed that the ESI MS is suitable method for obtaining anionic lanthanide chloride clusters, $Ln_nCl_{3n+1}^-$, from $LnCl_3$ in isopropanol [9].

The focus of this work was to examine the ability of detection of Gd(II) and Gd(III) ions by a matrix assisted laser desorption/ionization time-of-flight mass spectrometry (MALDI-TOF-MS). Also, we studied the possibility of

obtaining heterogeneous clusters of gadolinium chloride, using a laser desorption ionization MS, where analytes loaded on a target plate can be ionized directly by laser radiation.

Matrix assisted laser desorption/ionization time-of-flight mass spectrometry has been extensively utilized for the analysis of large molecules [10, 11]. However, there are also reports of its use in the analysis of inorganic species [12 – 14].

EXPERIMENTAL

MALDI MS measurements were performed using Voyager-DE PRO, (AB Sciex, USA) mass spectrometer equipped with a TOF analyzer. In all cases 20 kV of total acceleration voltage and a delay time of 100 ns was used. The ions were detected in the linear mode. Instrument is equipped with nitrogen laser (337 nm, 2 ns pulse width), operating at 20.0 Hz which was used to produce laser desorption and ionization.

One micro liter of the solution of Gd_2O_3 in HCl was loaded in a well (i.e., sample spot) of a stainless steel MALDI target plate having 100 wells and allowed to dry. The target plate was inserted into the MALDI instrument. Laser desorption/ionization mass spectra acquired for this work were obtained from at least 300 laser pulses per spectrum and the recorded spectra of all the laser shots were summed.

RESULTS AND DISCUSSION

An example of a mass spectrum of gadolinium chloride obtained in the linear positive mode (without a matrix) by MALDI TOF is shown in Figure 1. Peaks detected from Figure 1 correspond to Gd^+ (expt 158.51, calcd 157.92 Da), Gd^{3+} (expt 52.64, calcd 52.64 Da), and $[Gd(H_2O)]^{3+}$ (expt 58.78, calcd 58.64 Da). Another peak of a relatively weak intensity at m/z 495.60 was assigned to protonated cluster ion $[Gd_2Cl_5]^+$ (calcd value at 494.69 Da).

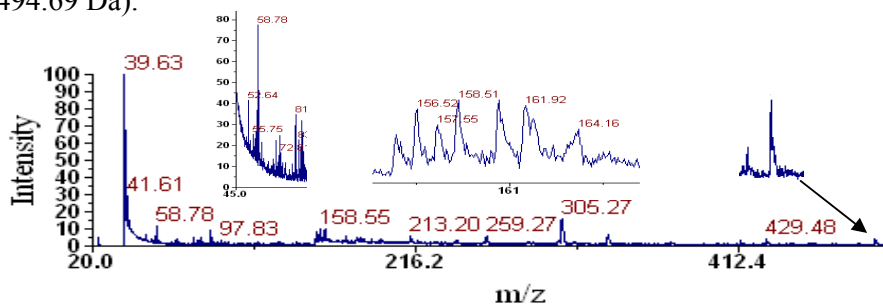


Figure 1. MALDI TOF mass spectrum of the solution of Gd_2O_3 in HCl obtained in the linear positive mode.

The formation of these positively charged ions in the mass spectra has been observed only after applying sufficiently high laser energy, of at least 2800 mW, to the solid sample of gadolinium chloride salt.

Obtained mass spectrum of the solution of Gd_2O_3 in HCl in the linear negative mode (without a matrix) is shown in Figure 2. The ion signals seen in the spectrum correspond to the following species: $[(Cl_2O_3)OH]^-$ (expt 134.99, calcd 134.92 Da), $[GdO_2]^-$ (expt 189.95, calcd 189.91 Da), $[GdClO_2(OH)]^-$ (expt 241.97 calcd 241.88 Da), $[GdCl_2O_2(OH)]^-$ (expt 276.99 calcd 276.85 Da), $[Gd(ClO_3)_3]^-$ (expt 406.12 calcd 406.78).

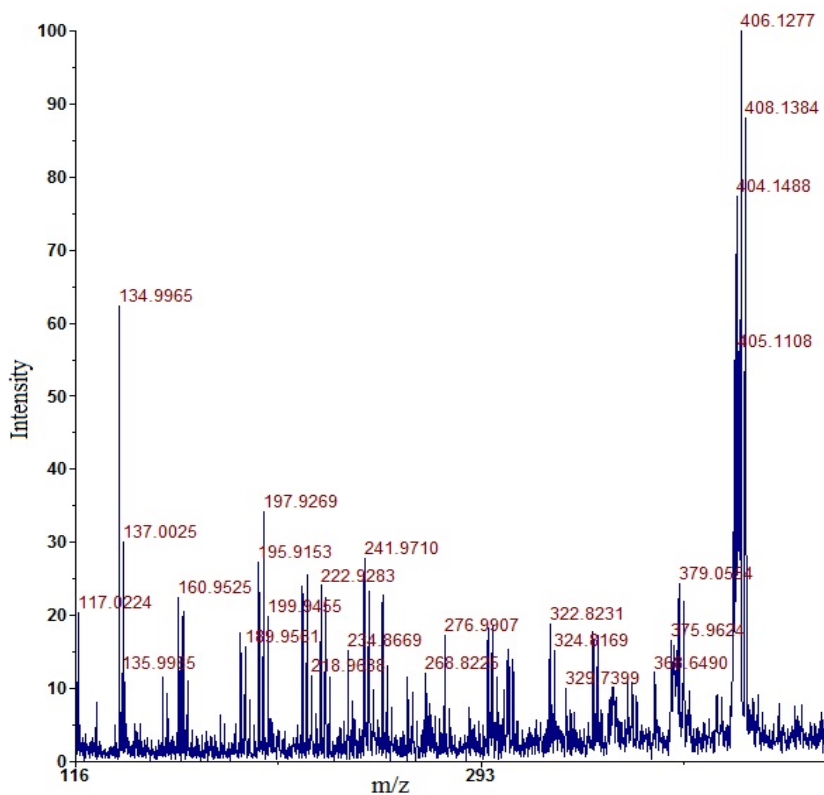


Figure 2. MALDI TOF mass spectrum of the solution of Gd_2O_3 in HCl obtained in the linear negative mode.

CONCLUSION

Preliminary results of an investigation of gadolinium salt in MALDI TOF system, which are the result of this work, have shown that gadolinium ions

can be observed when working in the linear positive mode, while linear negative mode give as a result different species of gadolinium with oxygen and chlorine. These results give promising ideas for further investigation of different lanthanide salts in MALDI TOF system.

ACKNOWLEDGMENT

The authors acknowledge the Ministry of Education and Science of the Republic of Serbia for financial support (Project No. 172019).

REFERENCES

- [1] W. O. Gordon, J. A. Carter, B. M Tissue, *J. Lumin.* 2004, 108, 339 - 342.
- [2] G. K. Liu, In *Spectroscopic Properties of Rare Earths in Optical Materials*; Liu, G. K., Jacquier, B., Eds.; Tsinghua University Press: Tsinghua, China, 2005; pp 1 - 94.
- [3] H. Guo, N. Dong, M. Yin, W. Zhang, L. Lou, S. Xia, *J. Phys. Chem. B*, 2004, 108, 19205 - 19209.
- [4] X. Chen, E. Ma, G. Liu, M. Yin, *J. Phys. Chem. C*, 2007, 111, 9638 - 9643.
- [5] X. Chen, E. Ma, G. Liu, *J. Phys. Chem. C*, 2007, 111, 10404 - 10411.
- [6] P. Caravan, J. Ellison, T. McMurry, R. Lauffer, *Chem.Rev.*, 1999, 99, 2293 - 2352.
- [7] P. Endres, T. Paunesku, S.Vogt, T. Meade, G. Woloschak, *J. Am. Chem. Soc.*, 2007, 129, 15760 - 15761.
- [8] M. Fortin, R. Petoral, F. Soderlind, A. Klasson, M. Engstrom, T. Veres, P. Kall, K. Uvdal, *Nanotechnology*, 2007, 18, 395501 - 3955009.
- [9] P. Rutkowski, M. Michelini, J. Gibson, *Phys. Chem. Chem. Phys.*, 2012, 14, 1965–1977.
- [10] K. Tanaka, H. Waki, Y. Ido, S. Akita, Y. Yoshida, T. Yoshida, *Rapid Commun. Mass Spectrom.* 1988, 2, 151–153.
- [11] R. Cramer, J. Gobom, E. Nordhoff, *Expert Rev. Proteomics* 2005, 2 , 407–420.
- [12] N. Dopke, P. Treichel, M. Vestling, *Inorg. Chem.*, 1998, 37, 1272-1277.
- [13] J. Zhang, V. Frankevich, R. Knochenmuss, S. Friess, R. Zenobi, *J Am Soc Mass Spectrom.*, 2003, 14, 42–50.
- [14] Z. Spalt, M. Alberti, E. Pena-Mendez, J. Havel, *Polyhedron*, 2005, 24, 1417–1424.

SPECTROSCOPIC CHARACTERIZATION OF THE PRODUCTS OF INTERACTION OF LACTIC ACID AND M(II) BIOMETAL IONS: Cu AND Co

N.S. Krstić, R.S. Nikolić, M.N. Stanković and M.G. Nikolić

Department of Chemistry, Faculty of Sciences and Mathematics, University of Niš, Višegradska 33, 18000 Niš, Serbia (nenad.krstic84@yahoo.com)

ABSTRACT

In the study was investigated products of interaction of M(II) biometal ions (Cu, Co) by UV/VIS, FTIR and ESI-MS spectroscopy with O-donor ligand, lactic acid, at molar, milimolar and micromolar level. Spectroscopic investigations showed that the lactic acid in the tested system behaves as a monodentate ligand, and comes to interact at all concentration levels.

INTRODUCTION

Lactic acid (2-hydroxypropanoic acid) (LA) is formed by fermentation of sugars and other carbohydrates action of anaerobic bacteria, as such, are found in milk and milk's products, and thus be inserted into the body with food. L-lactic acid is produced as a product of decomposition of glycogen in the muscles when they are under the same load. In the medicine it is used as a component of the Ringer's and Hartman's solution.[1] LA with M(II) metal ions, from the solutions of molar concentrations, depending on the conditions of complexation, can form a complex of the type $[ML]^+$, $[ML_2]$ and $[ML_3]^-$. [2]

Copper is a biogenic element found in numerous enzymes' systems. The Cu(II) ion (d^9 configuration) can give coordination compounds of various coordination and geometry through O, N, and S-donor atoms of different biomolecules and small molecules. This fact, together with its redox activity, is responsible for various roles of copper. [2, 3]

Cobalt as a micro-element has a role in the metabolism of proteins and amino acids as the constituent parts of metalloenzymes (methyltransferase and methionine transferase). [3] Via vitamin B₁₂, which plays an important role in the process of erythrocyte maturation, Co increases the use of iron in bone marrow cells. [4] The Co(II) ion (d^7 configuration) easily interacts with the parts of other molecules and builds complex particles with a coordination number 4, as well as the coordination number 6, via the O-, but also via the N-donor atom. [2, 3]

In the study was investigated products of interaction of M(II) biometal ions (Cu, Co) and lactic acid at molar, milimolar and micromolar level by UV/VIS, FTIR and ESI-MS spectroscopy.

EXPERIMENTAL

Ultraviolet-visible spectroscopy (UV/VIS). Model systems for the study of interaction of ligands and metals are obtained by mixing a solution of ligand and metal in a molar ratio of M:L=1:2, under the native pH value. The prepared model systems, were left to stand for 30 minutes, and thereafter were recorded on a UV/VIS spectrophotometer Shimadzu UV-1650 PC, in the wavelength range 190-800 nm.

Fourier Transform Infrared Spectroscopy (FTIR). The solid products of interaction M (II)-LA was obtained by mixing a solution of M(II) ions, and a ligand in a molar ratio of 1:2 in favor of the ligands, at room temperature, under conditions where the hydroxide is not precipitated, and separating by centrifugation after 7 days. FTIR spectra were recorded on a FTIR instrument Bomem MB-100 (Hartmann & Braun, Canada), with a DTGS/KBr (deuterated triglycine sulfate/KBr) detector, in a wave number area of the 4000-400 cm^{-1} .

Electrospray Ionisation Mass Spectrometry (ESI-MS). M(II)-LA interaction has been analyzed in concentration range from 1 to 10 $\mu\text{mol}/\text{dm}^3$ LA and M(II), in molar ratio from 1:9 to 9:1, using solvent MeOH:H₂O, 80:20 (v/v). ESI-MS analyses have been performed on LCQ DECA Ion Trap Spectrometer (Thermo Finnigan, USA), with optimization of working conditions for lactate anion m/z 89 as a monitoring ion, using LOOP-chromatogram method.[5]

RESULTS AND DISCUSSION

The changes in the UV/VIS spectra of the investigated model system M(II)-LA (λ_{max} , Abs., Δ) as compared to the solution of biometal ions show that there is interaction between the test O-donor ligand and the corresponding M(II) ion (Table 1).

Table 1. UV/VIS spectroscopic data of model system of M(II)-LA

System	λ_{maks} [nm]	Abs. [a.u.]	Δ [kJ/mol]
<i>Cu(II)-LA</i>	815,00	0,207	146,32
<i>Co(II)-LA</i>	510,00	0,055	233,83

In the FTIR spectra of the studied isolated solid product of interaction of the M(II)-LA, at milimolar concentration level, changes in the band position compared to the pure ligand was observed. Comparative presentation of

characteristic FTIR bands of pure lactic acid and products of interaction of studied systems, as well as the value of $\Delta\nu = \nu_{\text{asym}}(\text{COO}) - \nu_{\text{sym}}(\text{COO})$ based on what has been determined denticity of carboxyl group of lactic acid in the system with the Cu(II) and Co(II) ions, are given in Table 2.

Table 2. FTIR spectral data of LA and M(II)-LA systems

Band	LA [cm ⁻¹]	Cu(II)-LA [cm ⁻¹]	Co(II)-LA [cm ⁻¹]
$\nu(\text{OH}\cdots\text{O})$	2633		
$\nu(\text{OH})_{\text{COOH}}$	2500-3300		
$\nu(\text{OH})_{\text{OH}}$	3230-3350		
$\nu(\text{C}=\text{O})$	1733	1642*	1576*
$\nu(\text{C}-\text{O})$	1240	1385 [#]	1385 [#]
$\Delta\nu$	/	257	191
<i>ligand denticity</i>	/	<i>monodentate</i>	<i>monodentate</i>
		* $\nu_{\text{asym}}(\text{COO})$, # $\nu_{\text{sym}}(\text{COO})$	

Based on the data of Table 2, $\Delta\nu$ value, it can be concluded that the lactic acid in the system with investigated M(II) ions, acts as a monodentate ligand. [6, 7] Strength interaction, according to the position R-C-O---M vibrations in the FTIR spectrum is more pronounced for the system Co-LA. The study results of interaction between lactic acid and M(II) ions (Cu, Co), at the micro molar concentration level, were obtained by ESI-MS technique, through value of sub-integral area P_{LA} i $P_{\text{M(II)-LA}}$ of ESI-MS LOOP chromatograms, respectively calculating their relative differences ΔP , $\Delta P = \frac{P_{\text{LA}} - P_{\text{M(II)-LA}}}{P_{\text{M(II)-LA}}} \times 100\%$. [5] The values of investigate sub-integral areas of investigated binary systems and their ΔP values are shown in Table 3.

Table 3. The values of sub-integral areas and their ΔP values

	LA	Cu-LA	Co-LA
P [a.u.]	161,44	133,36	107,55
ΔP [%]	/	17,39	33,38

The area under the peaks in the LOOP chromatograms in the presence of investigated metal ions is lower than the analog area of the lactic acid without metal ions. It indicates that there is considerable interaction of M(II)-LA at the micro molar level and that is more pronounced in the system Co-LA.

CONCLUSION

UV/VIS studies have shown that the interaction occurs between the investigated biometal ions and lactic acid as ligand. Using FTIR characterization of isolated products of interaction of M (II)-LA was found that the LA acts as a monodentate ligand. Lower values of surface of ESI-MS LOOP chromatograms of the examined system of M(II)-LA in relation to the pure ligand (LA) indicating that the interaction between M(II) ions and lactic acid occurs at the micro molar level.

According to the position of R-C-O---M vibrations, and the results of ESI-MS examination of interactions Co-LA was more pronounced compared to the Cu-LA.

ACKNOWLEDGEMENT

This work was partially supported by the Ministry of Education, Science and Technological Development of the Republic of Serbia (Grants no. III45017 and TR34008).

REFERENCES

- [1] S. Spasić, Z. Jelić-Ivanović, V. Spasojević-Kalimanovska, Fundamentals of biochemistry, Belgrade, 2000. (in Serbian)
- [2] G. A. Lawrance, Introduction to coordination chemistry. John Wiley & Sons Ltd., Chichester, UK, 2010.
- [3] R. R. Crichton, Biological inorganic chemistry. An introduction, Elsevier, 2008.
- [4] M. Cakić, G. Nikolić, D. Cvetković, Lj. Ilić, Fe(III) complexes with oligosaccharides – antianemics. Leskovac, 2007. (in Serbian)
- [5] R. S. Nikolić, N. S. Krstić, G. M. Nikolić, G. M. Kocić, M. D. Cakić, D. H. Anđelković, Polyhedron, 2014, <http://dx.doi.org/10.1016/j.poly.2014.04.033>. (in press)
- [6] A. A. El-Asmy, E. M. Saad, M. S. El-Shahawi, Trans. Metal Chem., 1994, 19, 406-408.
- [7] R. Carballo, B. Covelo, S. Balboa, A. Castiñeiras, J. Niclós, Z. Anorg. Allg. Chem., 2001, 627, 948-954.

GENERATION OF GAS-PHASE LITHIUM CHLORIDE CLUSTER IONS BY LASER DESORPTION/IONIZATION MASS SPECTROMETRY

B. Pajkić¹, M. Milošević² and S. Veličković¹

¹*Department of Physical Chemistry, (vsuzana@vinca.rs)*

²*Department of Molecular Biology and Endocrinology,
University of Belgrade, VINČA Institute of Nuclear Sciences,
P. O. Box 522, 11001 Belgrade, Serbia*

ABSTRACT

Lithium heterogeneous clusters were generated from lithium chloride salt using laser desorption/ionization (LDI) on a commercial matrix assisted laser desorption ionization – time of flight (MALDI-TOF) mass spectrometric instrument. The generation of Li_nCl ($n=2-8$) clusters, has been successfully achieved in the positive mode when the initial salt concentrations were above approximately 10^{-3} M and after applying sufficiently high laser energy of 2.3 mW. These clusters can be obtained at higher concentration of LiCl, but the laser energy must be above 3.0 mW. Laser desorption/ionization also leads to the formation of several protonated lithium chloride cluster ions (Li_3ClH^+ , Li_7ClH^+), $\text{Li}_n(\text{H}_2\text{O})_2^+$ and $\text{Li}_n(\text{OH})_2^+$.

INTRODUCTION

Nonstoichiometric clusters of alkali atoms represent a challenge and new opportunity in chemistry because they can be used as building blocks for new cluster assembled materials [1]. To date, clusters of the type Li_nCl were formed by a thermal ionization mass spectrometry using triple filament ion source and by a thermal ionization source of modified design [2, 3]. Clusters of the type $(\text{LiCl})_n\text{Li}^+$ and $(\text{LiCl})_n\text{Cl}^-$ were obtained by a electrospray ionization and by fast-atom bombardment mass spectrometer [4].

Nonstoichiometric clusters are the rules rather than exceptions from such gas-phase techniques as laser vaporization. Matrix-assisted LDI, categorized as a “soft” ionization, is used frequently for the ionization of intact organic species. It should be noted that a laser ablation ionization MS and laser desorption/ionization MS can ionize directly analytes loaded on a target plate by laser light. Owing to the difference in excitation energy, laser ablation ionization is categorized as a “hard” ionization, whereas LDI is a “soft” ionization [5, 6].

In this work, we used laser desorption/ionization mode of MALDI-TOF mass spectrometer to produce lithium chlorides clusters. The factors that may influence the formation and abundances of lithium chloride cluster ions, including salt concentration, solvent choice, and the LDI instrumental conditions, have been investigated.

EXPERIMENTAL

LDI mass spectra were obtained using the commercial MALDI-TOF mass spectrometer (Voyager-DE PRO, AB Sciex, USA). The instrument was equipped with a nitrogen laser (337 nm) to desorb and ionize the samples, and video camera, allowing us to aim the laser at a specific spot within the area of the target. The accelerating voltage used was 19 kV. A stainless steel target was used as the MALDI substrate on which the samples are deposited. Mass spectra were obtained in the positive ion linear and reflectron mode. In general, 400 laser shots were averaged to generate a spectrum. Solutions were prepared by dissolving the lithium chloride salt in either pure methanol or in pure acetonitrile. A volume of 0.5 μl of the solution were deposited onto a sample plate and air-dried at room temperature.

RESULTS AND DISCUSSION

First, the effects of various concentrations of lithium chloride salt on the abundances of cluster Li_nCl^+ ions were investigated. LDI mass spectra of lithium chloride dissolved in methanol at concentrations of 10^{-5} M, 10^{-3} M, and 10^{-1} M is shown in Figure 1. In the mass spectra, the formation of positively charged clusters has been observed only after applying sufficiently high laser energy, of at least 2.3 mW.

The mass peaks at m/z 49.07, 56.10, 57.17, 58.11, 63.08, 69.11, 70, 71.20, 77.18, 85.24, 91.19 were assigned to Li_2Cl^+ , Li_3Cl^+ , Li_3ClH^+ , $\text{Li}_3(\text{H}_2\text{O})_2\text{H}^+$, Li_4Cl^+ , $\text{Li}_5(\text{OH})_2^+$, Li_5Cl^+ , Li_5ClH^+ , Li_6Cl^+ , $\text{Li}_7\text{ClH}^+/\text{Li}_7(\text{H}_2\text{O})_2$, Li_8Cl^+ cluster ions, respectively.

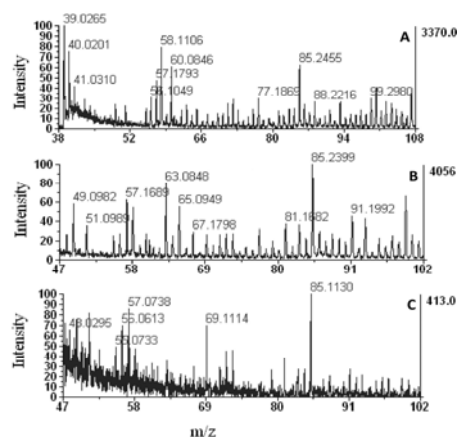


Figure 1. LDI mass spectra of the solution $\text{LiCl}/\text{CH}_3\text{OH}$ at following concentrations:

- A) 10^{-5} M;
 - B) 10^{-3} M;
 - C) 10^{-1} M
- (laser energy of 2.3mW)

Second, by comparing the mass spectra in Figure 2 and Figure 1B, it can be seen that the abundance of Li_nCl cluster ions is about 1.5 times higher for a solution lithium chloride in acetonitrile than for a solution of LiCl in methanol. The heterogeneous clusters of lithium, Li_nCl , can be obtained at the concentration of 10^{-1} M but the laser energy must be above 3.0 mW (Figure 3).

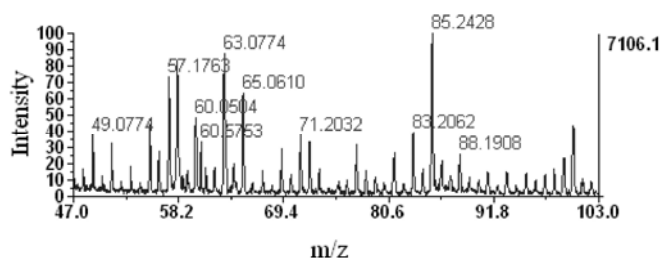


Figure 2.
LDI mass spectra
of the solution 10^{-3}
M $\text{LiCl}/\text{CH}_3\text{CN}$
(laser energy of 2.3
mW).

It should be noted that, earlier results have shown that the most prominent peaks were those of Li_2Cl^+ and Li_6Cl^+ clusters (the order intensity was $\text{Li}_2\text{Cl}^+ > \text{Li}_6\text{Cl}^+$). It has also been observed that Li_nCl^+ ions with an even number of lithium atoms (Li_2Cl^+ , Li_4Cl^+ , Li_6Cl^+) were higher than those with an odd number of lithium atoms (Li_5Cl^+ , Li_3Cl^+). In this work, the clusters with three and seven lithium atoms (Fig. 1A and 1C, m/z about 58 and 85) are more stable than clusters with even number of lithium atoms.

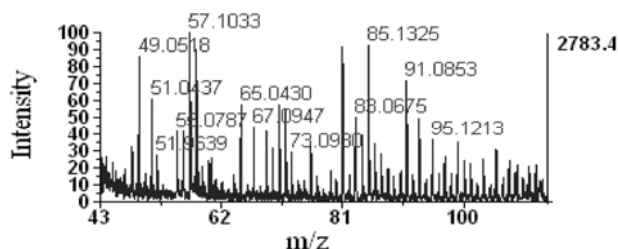


Figure 3. LDI mass
spectra of the solution
 10^{-1} M $\text{LiCl}/\text{CH}_3\text{OH}$
(laser energy of 3.0
mW).

However, for the concentration of 10^{-3} M of lithium chloride (Fig. 1B and Fig 2.) the clusters Li_2Cl^+ and Li_4Cl^+ were detected, but the order of the ion intensities was $\text{Li}_4\text{Cl}^+ > \text{Li}_2\text{Cl}^+$.

CONCLUSION

In this study the Li_nCl^+ ($n = 2 - 8$) cluster ions were produced using lithium chloride salt dissolved in either acetonitrile or methanol, when the salt concentrations were approximately 10^{-3} M, by the LDI mode of MALDI-TOF mass spectrometer. It was also found the positive correlation between the laser energies and the relative abundances of the cluster ions.

ACKNOWLEDGEMENT

This work was supported by the Ministry of Education and Science of the Republic of Serbia (Project No. 172019).

REFERENCES

- [1] Boldyrev, L. Wang, *J. Phys.Chem. A*, 2001, 105, 10759-10775.
- [2] S. Velickovic, V. Djordjevic, J. Cveticanin, J. Djustebek, M. Veljkovic, O. Neskovic. *Rapid Commun. Mass Spectrom.*, 2006, 20, 3151-3153.
- [3] S. R. Velickovic, J. B. Djustebek, F. M. Veljkovic, B. B. Radak, M.V.Veljkovic, *Rapid Commun. Mass Spectrom.*, 2012, 26, 1 - 6.
- [4] C. Javanaud and J. Eagles, *Organic Mass Spectrom*, 1983, 18, 93–98.
- [5] M Zoriy, A. Matusch, T. Spruss, J.S. Becker, *Int J Mass Spectrom*, 2007, 260, 102–106.
- [6] F. Aubriet, J. F. Muller , *J Am Soc Mass Spectrom*, 2008, 19, 488–501.

DEVELOPING OF ANALYTICAL METHOD FOR EXTRACTION OF BERYLLIUM IONS ON K-BIRNESSITE WITH LAYERED-STRUCTURE MATERIAL FORM (KBRLSM)

H. Ciftci¹, C. Er¹ and E. Aydin¹

¹*Ahi Evran University, Faculty of Science and Arts, Department of Chemistry, Kirsehir, TURKEY (harunciftci@yahoo.com)*

ABSTRACT

In the present work, we developed a separation and preconcentration method for Beryllium (Be) ions from water samples using K-birnessite with Layered-structure material form (KBRLSM). The experimental parameters that affected the extraction efficiency of the method such as pH, flow rate and volume of the sample solution, concentration of eluent, amount of adsorbent, and effect of common matrix ions were investigated and optimized. The adsorbed Be ions on KBRLSM were eluted with 5 mL of 1 mol L⁻¹ HNO₃ solutions and their concentrations were determined by High-Resolution Continuum Source Flame Atomic Absorption Spectrometry (HR-CS FAAS). The optimum pH value for quantitative sorption of Be ions was found between 7.0 and 8.5. The preconcentration factor was found as 100 for 500 mL aqueous solution containing 5 µg Be ions. The developed method was successfully applied to some water samples for separation of beryllium.

INTRODUCTION

Beryllium alloys are used in many applications because of their combination of elasticity, high electrical conductivity and thermal conductivity, high strength and hardness, nonmagnetic properties, as well as good corrosion and fatigue resistance [1]. Because of its low atomic number and very low absorption for X-rays, the oldest and still one of the most important applications of beryllium is in radiation windows for X-ray tubes [2]. Approximately 35 micrograms of beryllium is found in the human body, but this amount is not considered harmful. Beryllium is chemically similar to magnesium and therefore can displace it from enzymes, which causes them to malfunction. Chronic berylliosis is a pulmonary and systemic granulomatous disease caused by inhalation of dust or fumes contaminated with beryllium; either large amounts over a short time or small amounts over a long time can lead to this ailment. Symptoms of the disease can take

up to five years to develop; about a third of patients with it die and the survivors are left disabled [3]. The International Agency for Research on Cancer (IARC) lists beryllium and beryllium compounds as Category 1 carcinogens [4].

Therefore, the elimination and determination of Be ions from food, environmental by using removal and separation techniques are important to protect public health.

Separation and preconcentration procedures have a very important role for sample preparation, removing process and inorganic and organic trace analysis in environmental and analytical purposes. Separation procedures based on solid-phase extraction have been widely used to remove certain components of the sample, commonly toxic metal ions and/or harmful organic compounds from various samples [5]. A number of separation procedures for trace metals involving cloud point extraction (CPE), solid-phase extraction (SPE), co-precipitation and solvent extraction have been used in literature. For economic and environmental reasons, among these separation techniques, the SPE is not only the most promising for the recovery of metal ions from environmental samples when a suitable adsorbent but also an efficient and selective technique for analytical purposes [6].

Recently, there are increasing interest to layer-structure materials due to their potential applications such as adsorption, catalysis and ion-sieves [7]. Manganese oxides with layered-structure material forms are interesting materials because of their extremely high selective affinity for some atomic ionic such as Li^+ , Pb^{2+} and Be^{2+} [8]. Birnessite is a layer-structure manganese oxide with edge-sharing MnO_6 octahedra, and has been a subject of intensive investigations due to its ion exchange, sorption, and redox properties. MnO_6 layers of birnessite comprise edges having Mn(IV)O_6 octahedral, Mn(III)O_6 octahedral and cation vacancies [9]. The vacancies in the structure of birnessite commonly account for the negatively charged layer partially causing adsorption of heavy metals and other pollutants in contaminated water systems and soils [10].

In the present work, we have developed a separation and preconcentration method for beryllium ions from water samples using K-birnessite with Layered-structure material form (KBRLSM).

EXPERIMENTAL

The analysis was performed by ContrAA 300 a High Resolution-Continuum Source Flame Atomic Absorption Spectrometer (HR-CS AAS) (GLE, Berlin, Germany) equipped with a 50 mm burner head. All absorption lines

of elements in the spectral range of 185-900 nm can be analytically evaluated by using a Xe short-arc lamp as a continuum lamp source.

Synthesis of KBRLSM

KBRLSM was prepared according to study of Eren *et al* [10]. 2.85 g $\text{Mn}(\text{NO}_3)_2$ was dissolved in 450 cm³ distilled water. The 100 cm³ of a solution containing 1.1 g KMnO_4 and 0.8 g KOH was added from a fast-dripping burette. A dark Brown to black precipitate was formed immediately and the solution was stirred continuously for 1 h. After stirring, the suspension was settled for 30 min. Then the excess supernatant was removed and the concentrated suspension was centrifuged and washed several times with distilled water. The KBRLSM was treated with a 1 mol L^{-1} HCl solution for 1 day at room temperature, and then washed with distilled water, and dried at 70 °C.

Preparation of separation column

0.3 g of KBRLSM was packed into a glass column (100x 8 mm² i.d.) plugged with small portion of glass wool at both ends. Before each cycle, the column was preconditioned by passing the blank solutions in working pH. The sample solution was permitted to flow through the column under gravity.

Separation/Adsorption procedure

The proposed procedure was tested with model solutions. For the model solution; 2.5 mL of 2.0 mg L^{-1} Be^{+2} solutions and 2 mL of buffer solutions were added to a flask. Then, final volume was completed to 50 mL by deionized water. The column was preconditioned by passing the aqueous solutions of working pH through column and then, the model solution was passed through the column at a flow rate of 5 mL min^{-1} . Afterwards, the column was rinsed with 10 mL of water, and the retained Be ions on the KBRLSM were eluted with 5 mL of 1 mol L^{-1} HNO_3 solutions at a flow rate of 2.0 mL min^{-1} . The Be concentration in the eluate solution was determined by HR-CS FAAS. The recovery of the analyte was calculated from the ratio of the concentration found by FAAS.

RESULTS AND DISCUSSION

The effects of some experimental parameters such as pH of the sample solution, kind of elution agent, flow rate and volume of the sample, interfering ions and amount of the KBRLSM, etc. were optimized using column procedures. Optimized experimental parameters and analytical performance of methods were given in Table 1.

CONCLUSION

KBRLSM may be used for removing, separation and preconcentration of trace metals in analytical and environmental chemistry.

Table 1. Analytical performance and optimum condition of the proposed method for separation and determination of Be

pH	7.0-8.5
Amount of KBRLSM (mg)	300
Eluent volume, (2 mol L ⁻¹ HNO ₃)	5 mL
Elue flow rate (mL min ⁻¹)	2
Sample flow rate (mL min ⁻¹)	5
Maximum sample volume (mL)	500
Preconcentration factor	100
Linear range (mg L ⁻¹)	0.015-5.000
Correlation coefficient (R ²)	0.9993
Detection limit (µg L ⁻¹)	0.28
Precision (R.S.D, N=7) (%)	1.6

ACKNOWLEDGEMENT

This work was partially supported by Ahi Evran University-TURKEY (Grants no. *PYO-FEN.4003.12.002*).

REFERENCES

- [1] K.A. Walsh, Beryllium Chemistry and Processing. Vidal, EE. et al. Eds. (2009), Materials Park, OH:ASM International.
- [2] J. Hans-Dieter, J. Hans, eds. (1994). Concise Encyclopedia Chemistry. trans. rev. Eagleson, Mary. Berlin: Walter de Gruyter.
- [3] E. John. (2001). Nature's Building Blocks: An A–Z Guide to the Elements. Oxford, England, UK: Oxford University Press.
- [4] International Agency for Research on Cancer. 1993. Retrieved 18 September 2008.
- [5] H. Ciftci, Desalination, 2010, 256, 18-22.
- [6] H. Ciftci, M.M. Temuz, E. Ciftci., J. AOAC Int., 2013, 96, 875-879.
- [7] G. Centi, S. Perathoner, Micropor. Mesopor. Mat., 2008, 107, 3-15.
- [8] W. Zhao, Q.Q. Wang, F. Liu, G.H. Qiu, W.F. Tan, X.H. Feng, J. Soils Sediments., 2010, 10, 870-878.
- [9] C.L. Peacock, D.M. Sherman, Chem. Geol, 2007, 238, 94-106.
- [10] E. Eren, H. Gumus, A. Sarihan, Desalination, 2011, 279, 75–85.

ELECTROSPRAY IONIZATION MASS SPECTROMETRIC STUDY OF PYROGALLOL AUTOXIDATION IN WEAKLY ALKALINE AQUEOUS SOLUTIONS

G. M. Nikolić¹, A. M. Veselinović¹, M. M. Vujović², B. S. Milosavljević²
and Ž. J. Mitić¹

¹ *Department of Chemistry, Faculty of Medicine, University of Niš, Bulevar dr Zorana Đinđića 81, 18000 Niš, Serbia,*

² *Institute of Forensic Medicine, Bulevar dr Zorana Đinđića 81, 18000 Niš, Serbia.*

ABSTRACT

Autoxidation of pyrogallol in weakly alkaline aqueous solutions was studied by electrospray ionization mass spectrometry (ESI-MS). ESI-MS spectra revealed that complete degradation/transformation of pyrogallol was achieved after the 4 hour autoxidation at pH 8.5. Tartronic and glyceric acid were identified as the main degradation products of pyrogallol during its autoxidation.

INTRODUCTION

Pyrogallol moiety is an important part of many natural polyphenolic compounds and due to its ease of oxidation and autoxidation it may be regarded responsible to the great extent for their biological activities [1]. In order to gain better understanding of the autoxidation of such compounds, we already performed the spectrophotometric study of pyrogallol (1,2,3-trihydroxybenzene) autoxidation in weakly alkaline aqueous solutions by applying multivariate curve resolution-alternating least squares (MCR-ALS) method [2] and we concluded that purpurogallin was formed as a main autoxidation product of pyrogallol during the first hour at pH 8.0. UV/Vis spectrophotometric data also indicated further transformation of purpurogallin to another compound we were not able to identify.

However, UV/Vis spectrophotometry has no capability to detect possible formation of pyrogallol degradation products which do not absorb the radiation in the UV/Vis range. For that reason we decided to study the pyrogallol autoxidation in weakly alkaline aqueous solutions by using electrospray ionization mass spectrometry (ESI-MS) because it proved to be very useful for studying the degradation of various phenolic compounds in aqueous solutions [3,4].

EXPERIMENTAL

All chemicals used in this study were of analytical (p.a.) grade. Pyrogallol (Fluka, Germany) was used without additional purification since its purity was proved to be satisfactory by HPLC. Deionized, air saturated, water was used and 0.5 mmol dm⁻³ solutions of pyrogallol were prepared just before the use by dissolving the exactly weighed amount of pyrogallol. Autoxidation of pyrogallol was initiated by mixing pyrogallol solution with equal volume of ammonia buffer.

Shimadzu Liquid Chromatograph Mass Spectrometer LCMS 8030 with quadrupole detector was used for obtaining ESI-MS spectra. Direct infusion of sample into ESI source with mobile phase (50% aqueous methanol) at 200 μ L min⁻¹ flow rate was applied. ESI-MS spectra in the negative mode were recorded in the m/z range from 100 to 500. Typical ESI parameters were as follows: heating block temperature, 500°C; drying gas (N₂) flow rate, 15 L min⁻¹; sheath gas (N₂) flow rate, 3 L min⁻¹; capillary voltage, 4.5 kV; desolvation temperature, 230°C.

RESULTS AND DISCUSSION

ESI-MS spectrum of freshly prepared unbuffered pyrogallol solution is shown in Figure 1.

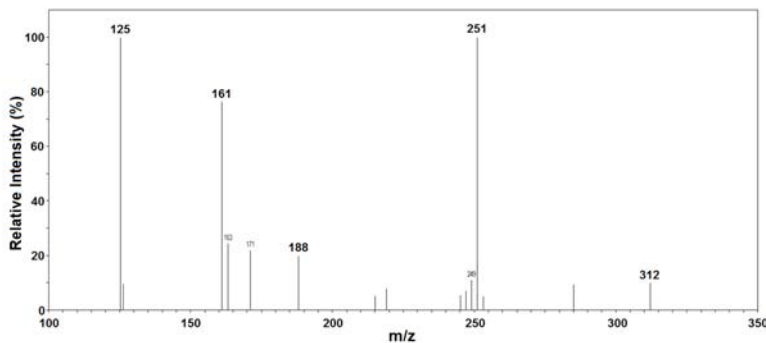


Figure 1. ESI-MS spectrum of freshly prepared unbuffered pyrogallol solution.

The most prominent peaks in mass spectrum of pyrogallol at 125 and 251 m/z belong to the mono-deprotonated anions of pyrogallol, [PG - H]⁻, and adduct formed by the hydrogen bonding between two pyrogallol molecules, [2PG - H]⁻, respectively. Intense peak at 161 m/z probably originates from the mono-deprotonated anion of adduct formed by the hydrogen bonding of two water molecules to the pyrogallol, [PG + 2H₂O - H]⁻. Two peaks with even m/z values at 188 and 312 m/z probably originate from the double

charged anions of adducts formed by the hydrogen bonding between three and five pyrogallol molecules, $[3PG - 2H]^{2-}$ and $[5PG - 2H]^{2-}$, respectively. Figure 2 displays ESI-MS spectrum of pyrogallol solution after prolonged autoxidation (4 hours) at pH 8.5.

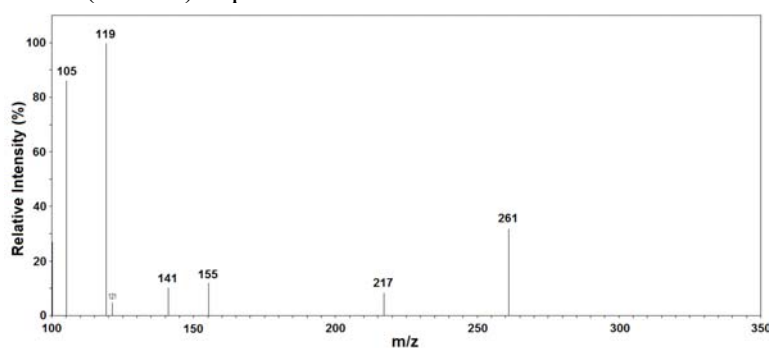


Figure 2. ESI-MS spectrum of pyrogallol solution after prolonged autoxidation (4 hours) at pH 8.5.

The most notable feature of the spectrum displayed in Figure 2 is the complete absence of peaks originating from various pyrogallol species which means that during the autoxidation for 4 hours at pH 8.5 complete degradation/transformation of pyrogallol was achieved. Most prominent peaks in the ESI-MS spectrum of autoxidized pyrogallol solution at 105 and 119 m/z probably originate from mono-deprotonated anions of carboxylic acids (tartronic and glyceric acid, respectively) formed by the degradation of pyrogallol. Hydroxylated carboxylic acids formation has been already demonstrated by ESI-MS during the catalytic degradation of phenol [3] and radiolytic degradation of gallic acid [4]. Formation of such products during the autoxidation of pyrogallol is not surprising because there is literature data that large quantity of very reactive superoxide anion radical ($O_2^{\cdot-}$) is produced during this process even at pH 7.9 [5]. Possible mechanism of formation of pyrogallol degradation products is shown in Figure 3.

The peaks at 141 and 155 m/z in the ESI-MS spectrum shown in Figure 2 probably originate from the mono-deprotonated anions of hydroxylated and methoxylated products of pyrogallol, respectively, (formation of methoxylated product is supposed to occur in the ESI source). Formation of purpurogallin quinone, which is the first oxidation product of purpurogallin formed during the initial autoxidation of pyrogallol [2], is indicated by the presence of the peak at 217 m/z which probably originates from its mono-deprotonated anion. The origin of the peak at 261 m/z is not clear at present.

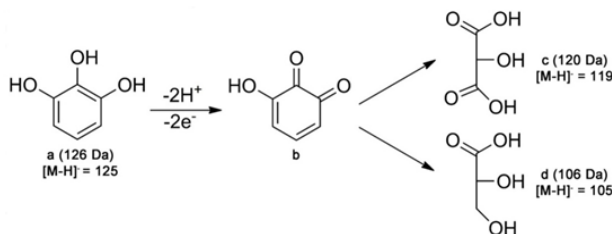


Figure 3. The possible mechanism of pyrogallol (a) degradation and formation of tartronic (c) and glyceric acid (d) via pyrogallol quinone (b) after prolonged autoxidation in aqueous solution for 4 hours at pH 8.5.

CONCLUSION

Prolonged autoxidation of pyrogallol in weakly alkaline aqueous solutions leads to the complete degradation/transformation of pyrogallol. By using electrospray ionization mass spectrometry (ESI-MS) tartronic and glyceric acid were identified as the main degradation products of pyrogallol during its autoxidation. ESI-MS spectra also indicated the formation of hydroxylated pyrogallol and purpurogallin quinone during this process.

ACKNOWLEDGEMENT

This work was partially supported by the Ministry of Education, Science and Technological Development of the Republic of Serbia (Grant no. 172044).

REFERENCES

- [1] S. Quideau, D. Deffieux, C. Douant-Casassus, L. Pouységu, *Angew. Chem. Int. Ed.* 2011, 50, 586-621.
- [2] A. M. Veselinović, R. S. Nikolić, G. M. Nikolić, *Cent. Eur. J. Chem.* 2012, 10, 1942-1948.
- [3] F. C. C. Moura, M. H. Araujo, I. Dalmázio, T. M. A. Alves, L. S. Santos, M. N. Eberlin, R. Augusti, R. M. Lago, *Rapid Commun. Mass Spectrom.* 2006, 20, 1859-1863.
- [4] R. P. Melo, J. P. Leal, M. L. Botelho, *Rapid Commun. Mass Spectrom.* 2011, 25, 218-222.
- [5] S. Marklund, G. Marklund, *Eur. J. Biochem.* 1974, 47, 469-474.

ANALYTICAL CAPABILITY OF PLASMA INDUCED BY IR TEA CO₂ LASER PULSES ON COPPER TARGET

M. Momčilović¹, D. Ranković², M. Kuzmanović², J. Ciganović¹,
M. Stoiljković¹, J. Savović¹ and M. Trtica^{1*}

¹*VINČA Institute of Nuclear Sciences, University of Belgrade, P.O.
BOX 522, 11001 Belgrade, Serbia*

¹*Faculty of Physical Chemistry, University of Belgrade,
P.O. BOX 276, 11001 Belgrade, Serbia*

ABSTRACT

Spatially-resolved time-integrated optical emission spectroscopy was applied for investigation of copper plasma produced by a nanosecond Infrared (IR) Transversely Excited Atmospheric (TEA) CO₂ laser, operating at 10.6 μm. The maximum intensity of emission, with sharp and well resolved spectral lines, and negligibly low background emission, was obtained from a plasma zone 8 mm from the target surface. The favorable signal to background ratio obtained in this plasma region, indicate possible analytical application of TEA CO₂ produced copper plasma. Detection limits of trace elements present in the Cu sample were in the order of 10 ppm.

INTRODUCTION

The plasma in LISPS (Laser-Induced Shock-Wave Plasma Spectroscopy) is generated by focusing of the laser beam onto the sample but at reduced gas pressures [1]. The created plasma, usually spherical in shape, emits from most of the volume intense and sharp spectral lines (mostly of the elements present in a target) with low background emission intensity. Good signal to background ratio, along with a linear relationship between spectral line intensity and elemental concentration in the sample, makes LISPS a suitable method for spectrochemical analysis [2,3].

Generation of copper target plasma, with low intensities of TEA CO₂ laser pulses was not reported in the literature until recently [4]. The aim of this investigation was to test the applicability of TEA CO₂ laser induced copper plasma under reduced air pressure for trace element spectrochemical analysis.

EXPERIMENTAL

Plasma was initiated by irradiation of a copper target with IR TEA CO₂ laser pulses. Typical output pulse energy was 150 mJ, and repetition rate during experiments was 1.5 Hz. The laser/optical pulse had a gain switched spike followed by a slowly decaying tail. Full width at half maximum of the spike was about 100 ns while the tail duration was ~2 μ s. The energy sustained in the initial spike was about 35% of the total irradiated laser energy.

Copper sample was placed in a glass vacuum chamber closed with NaCl and CaF₂ windows. Minimum air pressure during the experiments was ~0.1 mbar. Preparation of a target surface before irradiation was an essential process, because of high reflectivity of copper for CO₂ laser emission line(s). The enhancement of surface absorption was achieved by increasing the target surface roughness. The target surface was mechanically treated with 320-grit SiC abrasive paper. Such procedure created clearly visible scratches (1 to 6 μ m wide) on freshly prepared copper surface.

The optical emission from the plasma was viewed in the direction parallel to the target surface. By changing the position of plasma along the direction of a laser beam, while keeping the constant distance between focusing lens and a target, different parts of plasma were observed, i.e., a spatial plasma resolution was achieved. The horizontal part of the plume was projected by an lens on the entrance slit of a monochromator (Carl-Zeiss PGS2 dispersion 0.7 nm/mm). For the time-integrated spatially resolved measurements Apogee Alta F1007 CCD camera was used.

In this work we have used time-integrated space-resolved laser induced plasma spectroscopy (TISR-LIPS). TISR-LIPS was successfully applied for studying various laser induced plasma systems [5], and may be considered as similar to time-resolved spatially integrated emission spectroscopy. The method relies on the fact that intense plasma background spectral continuum emission is mostly emitted from a region close to the sample surface, while in further-out regions of the plasma the continuum emission is largely reduced. Thus, instead of time-gated detection the position-selective spectra were recorded. The time-integrated measurements provide average values in the different plasma spatial zones.

RESULTS AND DISCUSSION

The plasma was initiated by irradiation of a copper target with a fluence of ~8.6 J cm⁻² in air atmosphere at the pressure of 0.1 mbar. The plasma consisted of two clearly distinguished and spatially separated regions. The first region, close to the target surface (length about 5 mm), was characterized by a whitish color and is known as primary plasma. The

second region, also known as the secondary plasma, was larger in volume, had a hemispherical shape and intense green color, due to emission of the spectral lines of the target. The plasma expanded to a distance of about 15 mm from the surface.

Time-integrated emission spectra of trace elements present in the Cu sample are shown in Fig. 1. The sample was high purity Cu (99.9 %) with traces of Fe (60 ppm), Ca (50 ppm), Ag (50 ppm) and Mg (6 ppm). The spectrum consisted of well-resolved sharp emission lines, and low background emission intensity. Good signal to noise, and signal to background ratios were obtained. The estimated limits of detection (LOD) are presented in Table I. Limits of detection are calculated using the formula $LOD = 3 \times BEC \times RSD_B$ (BEC - background equivalent concentration, RSD_B - relative standard deviation of the background).

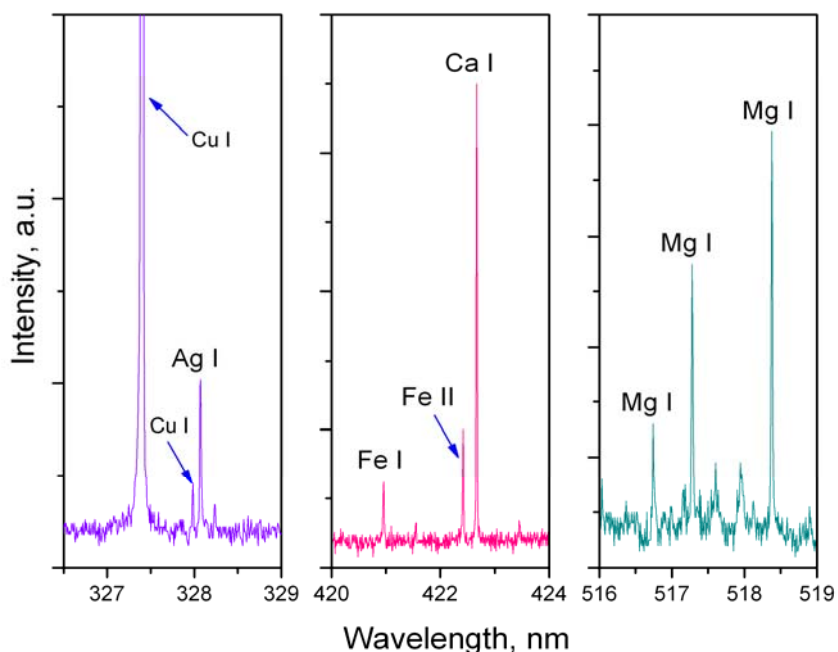


Figure 1. Time-integrated emission spectra of Fe, Ca and Mg obtained at a distance of 8 mm above the Cu surface.

Table 1. Estimated limits of detection.

Element	Wavelength, nm	LOD, mg/kg
Fe	422.42	10
Ca	422.67	4
Ag	328.07	5
Mg	518.36	1

CONCLUSION

The plasma was induced by irradiation of a copper target with 30 MW/cm² of TEA CO₂ laser peak intensity, in air at 0.1mbar. Time-integrated optical emission spectroscopy was applied for characterization of spatially-resolved plasma regions. The maximum intensity of Cu emission, and negligibly low background emission, was obtained from a plasma zone 8 mm above the target surface. Time-integrated emission spectra of Fe, Ca, Ag and Mg, which are the elements present in the copper sample as impurities, were used for evaluation of signal to background, and signal to noise ratio, and estimation of limit of detection. Detection limits in the order of 10 ppm imply that TEA CO₂ laser-induced copper plasma under 0.1 mbar air pressure could find analytical application.

ACKNOWLEDGEMENT

This work was supported by the Ministry of Education and Science of the Republic Serbia, project No. 172019.

REFERENCES

- [1] A.M. Marpaung, Koo H. Kurniawan, M.O. Tjia and K. Kagawa, J. Phys. D: Appl. Phys., 2001, 34, 758-771.
- [2] R. Hedwig, T.J. Lie, M.O. Tjia, K. Kagawa and Koo H. Kurniawan, Spectrochim. Acta B., 2003, 58, 531-542.
- [3] Koo H. Kurniawan, T. J. Lie, K. Kagawa and M.O. Tjia, Spectrochim. Acta B., 2000, 55, 839-848.
- [4] M. Momcilovic, M. Trtica, J. Ciganovic, J. Savovic, J. Stasic, M. Kuzmanovic, Appl. Surf. Sci., 2013, 270, 486-494.
- [5] A. Khumaeni, M. Ramli, Y. Deguchi, Y. Lee, N. Idris, K.H. Kurniawan, T.J.J Lie, K. Kagawa, Appl. Spectrosc., 2008, 62, 1344-1348.

THEORETICAL ANALYSIS OF Cu^+ AND Fe^{2+} COMPLEXES OF (*E*)-*N'*-[1-(2-HYDROXYPHENYL)ETHYLIDEN]ISONICOTINOYLHYDRAZIDE)

D. Dimic and M. Petkovic

*Faculty of Physical Chemistry, University of Belgrade,
Studentski Trg 12-16, P. O. Box 47, 11158 Belgrade, Serbia
dimicdusan@gmail.com*

ABSTRACT

Structures of Cu^+ and Fe^{2+} complexes with deprotonated (*E*)-*N'*-[1-(2-hydroxyphenyl)ethyliden]isonicotinoylhydrazide (HAPI) were optimized at CAM-B3LYP/cc-pVTZ level. Stability of complexes, harmonic vibrational frequencies and vertical electronic transitions of the three species are discussed with emphases on the changes that arise upon complex formation.

INTRODUCTION

Arylhydrazones present a class of compounds with interesting behavior. They exist in two conformations, E and Z (E isomer is more stable than Z isomer), and can undergo photoinduced isomerisation, which makes them interesting for photoswitching use. These molecules behave as tridentate ligands and use the phenolate O, the imine N and the carbonyl O donor atoms to form complexes [1]. Simunek and coworkers showed that complexes of (*E*)-*N'*-[1-(2-hydroxyphenyl)ethyliden]isonicotinoylhydrazide (HAPI) with iron have improved stability in plasma [2]. In this paper we investigated the stability, vibrational and electronic spectra of complexes of deprotonated E form of HAPI with Fe^{2+} and Cu^+ .

THEORETICAL METHODS

All of the calculations have been performed with the Gaussian 09 program package [3]. Density functional theory (DFT) with CAM-B3LYP functional [4,5] has been employed for electronic structure calculations in conjunction with Dunning's correlation-consistent basis set cc-pVTZ [6]. Solvent effects were modeled with the Polarizable Continuum Model (PCM). Vibrational frequencies were computed in harmonic approximation, and electronic spectra were computed for all species for eight transitions using the TDDFT approach.

RESULTS AND DISCUSSION

When dissolved in water, HAPI is deprotonated. Optimized geometries of deprotonated HAPI and its cuprous and ferrous complexes are shown in Figure 1.a)-c). Energies for Cu^+ and Fe^{2+} ions were also calculated in order to compare the stabilization effect upon complex building. The energy difference for cuprous complex when compared to separate cuprous ion and deprotonated HAPI is 74kcal/mol, and for ferrous complex is 75 kcal/mol. This has clearly showed that complexes are very stable in solution and that complex with Fe^{2+} is slightly more stable than the one with Cu^+ . The two rings of deprotonated HAPI are not coplanar with the N=N bond. On the other hand, the phenol/pyridine ring is in the in/out-of-plane position with respect to the hidrazone group for both complexes.

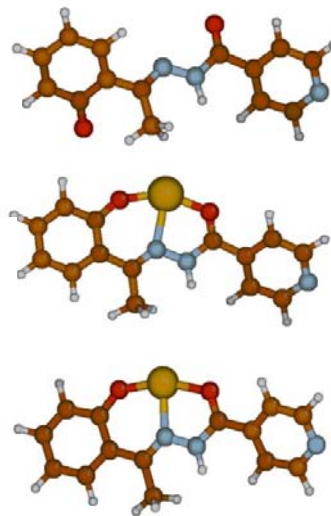


Figure 1. **Optimized geometries of a) deprotonated HAPI, b) cuprous complex and c) ferrous complex**

The differences in infrared (IR) spectra of these compounds are very evident because of strong bonds with metals that don't allow all of the vibrational modes to be active. These spectra are shown in Figure 2. The spectrum of deprotonated HAPI shows several very intensive peaks. One of the dominant peaks in vibrational spectrum of deprotonated HAPI belongs to the C=O stretching vibration (1744 cm^{-1}). This type of motion in the ferrous complex is identified in two modes at 1613 and 1653 cm^{-1} and for cuprous at 1620 and 1658 cm^{-1} . A decrease in dipole moment of the bond and limited freedom for vibration due to the presence of the transition metal cause a red shift of more 100 cm^{-1} . The IR spectrum of the ferrous complex has a distinctive peak at 1583 cm^{-1} which arises from coupled C-N stretching and N-H in-plane bending vibration. This peak in the spectrum of the cuprous complex is centered at 1571 cm^{-1} . This shift implies that the complex with Fe^{2+} is more rigid and more energy is needed for activation of this vibration. In the spectrum of deprotonated HAPI there is a peak at 1535 cm^{-1} from the phenol C-O vibration. This vibration is not observed in any of the complexes because of very strong bond between metal and oxygen. The vibrational modes of the two complexes are much more complex compared to the deprotonated HAPI.

They involve several groups that vibrate together, because of the very rigid bonds between donors and transition metals. These bonds act like a bridge between two rings.

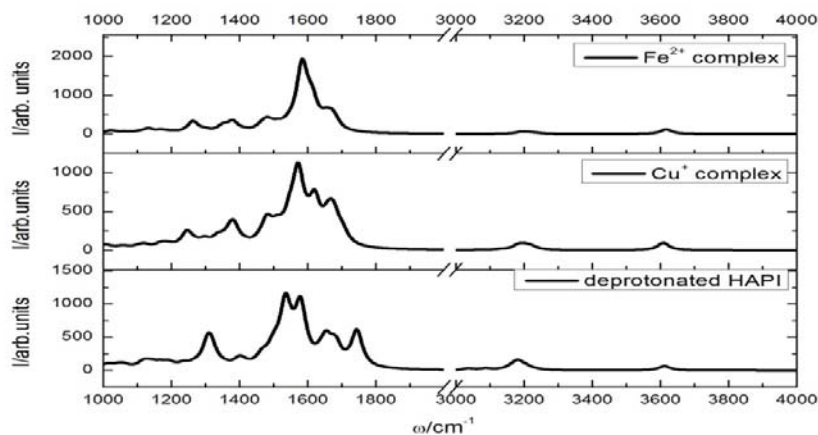


Figure 2. Infrared spectra of a) deprotonated HAPI, b) cuprous complex and c) ferrous complex

The results for electronic transitions of the three species are summarized in Table 1. The experimental spectrum of deprotonated HAPI is marked with three peaks at 288, 325 and 400 nm [1]. The results obtained for deprotonated HAPI showed good agreement for the first two transitions. The last one deviates from the experimental value, but this is probably due to the uncertainty of the method used and calculation of the energy difference between highest occupied orbital (HOMO) and lowest unoccupied orbital (LUMO).

Table 1. Electronic transitions for deprotonated HAPI, cuprous and ferrous complexes

	[nm]	Oscillatory strength	Assignment
Deprotonated HAPI	465	0.2041	HOMO → LUMO (91%)
	334	0.0804	HOMO → LUMO+2 (63%)
	292	0.1690	HOMO-2 → LUMO (81%)
Cuprous complex	381	0.2651	HOMO-1 → LUMO (49%)
			HOMO → LUMO (26%)
	318	0.0657	HOMO-2 → LUMO (16%)
			HOMO-1 → LUMO+4 (14%) HOMO → LUMO+4 (14%)
Ferrous complex	319	0.0818	HOMO-1 → LUMO (34%)
			HOMO → LUMO+1 (27%)
			HOMO-1 → LUMO+4 (22%)
	286	0.1027	HOMO-6 → LUMO (26%) HOMO-7 → LUMO (21%) HOMO-8 → LUMO (17%)

For the cuprous complexes, to the best of our knowledge there are no available experimental results, although a spectrum for the cupric complex

is given [1]. There are two distinct peaks at 320 and 400 nm. There is a difference of about 20 nm for the second peak, which is explained by the fact that the net charge of complex is different and not all of the solvent effects are accounted for in with the PCM model. A very broad peak around 320 nm is assigned to several transitions shown in Table 1. A more intense peak at 400 nm arises from the HOMO-1 \rightarrow LUMO and HOMO \rightarrow LUMO transitions. The peak intensities are well reproduced. Electronic spectrum of the ferric complex (not available for the ferrous complex) has two peaks at 280 nm (with higher intensity) and 370 nm. The experimental value of 280 nm could be assigned to the theoretical transitions at 286 nm, and the second value to that at 319 nm. The differences between these values are because of the net charge of molecule and solvent effects.

CONCLUSIONS

We investigated optimized geometries, vibrational and electronic properties of Cu^+ and Fe^{2+} complexes with deprotonated form of HAPI, a molecule that has great potential for molecular switches and iron regulation in human body. The ferrous complex is slightly more stable, since the bonds that connect two rings are more rigid, and affect vibrational motion. Normal mode analysis was limited to the C=O, N-H and C-O stretching modes that are responsible for the high intensity peaks in the IR spectra. The pronounced differences between vibrational spectra of deprotonated HAPI and its complexes result from the presence of three very strong bonds with the metal ions. Calculated electronic spectra are in very good agreement with experimental data, with two distinctive peaks for complexes and three for deprotonated HAPI.

ACKNOWLEDGMENT

We would like to thank to the Ministry of Education and Science of the Republic of Serbia for financial support under the project No. 172040

REFERENCES

- [1] K. J. Franz et al, *Inorg. Chem.*, 2014, 53, 1397-1405
- [2] T. Simunek *et al*, *Chem. Res. Toxicol*, 2011, 24, 290-302
- [3] Gaussian 09, Revision A.02, M. J. Frisch et al.
- [4] A. D. Becke, *J. Chem. Phys.*, 1993, 98, 5648
- [5] T. Yanai, D. Tew and N. Handy, *Chem. Phys. Lett.*, 2004, 393, 51-57
- [6] T.H. Dunning, *J. Chem. Phys.*, 1989, 90 1007

THEORETICAL STUDY OF SUBSTITUENT EFFECTS ON STRUCTURAL PROPERTIES OF ARYLAZO PYRIDONE DYES

J. Dostanić¹, D. Lončarević¹ and M. Zlatar²

¹University of Belgrade, Institute of Chemistry, Technology and Metallurgy,
Department of Catalysis and Chemical Engineering, Njegoševa 12,
Belgrade, Serbia. (jasmina@nanosys.ihtm.bg.ac.rs)

²University of Belgrade, Institute of Chemistry, Technology and Metallurgy,
Department of Chemistry, Njegoševa 12, Belgrade, Serbia.

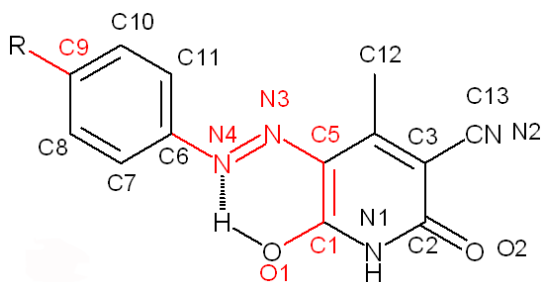
ABSTRACT

Quantum chemical calculations performed by the density functional theory (DFT) were used to determine the structural parameters of arylazo pyridone dyes. The influence of electronic effects of substituent in diazo moiety of dyes on their structure properties was studied and quantified using Hammett equation. The correlation between dye bond length and Hammett substituent constants σ_p gave us possibility to locate the most sensitive bond to substituent effects.

INTRODUCTION

The density functional theory is presently the most successful approach to compute the electronic structure of matter, in particular atoms, molecules, and the condensed phases. Using DFT method a great variety of molecular properties, such as molecular structures, vibrational frequencies, atomization and ionization energies, electric and magnetic properties, reaction paths, etc. could be predicted [1]. In this paper, the DFT method was used to determine structural parameters of substituted arylazo pyridone dyes (Scheme 1). The investigated dyes have the same benzene/pyridone skeleton, but different substituent group (R) in the benzene ring.

Arylazo pyridone dyes can exist as two tautomeric isomers, i.e. 6-hydroxy-2-pyridones (azo form) and



Scheme 1. Structure of arylazo pyridone dyes; R: OH, OCH₃, CH₃, H, Cl, Br, COOH, SO₃H, CH₃CO, CN, NO₂

pyridine-2,6 diones (hydrazone form). In water beside azo-hydrazone equilibrium, the dyes can co-exist in acid-base equilibrium. The influence of electron-donating and electron-withdrawing substituents on structural parameters of the most stable forms of arylazo pyridone dyes (azo, hydrazone and anionic) was also studied and quantified by means of Hammett equation.

EXPERIMENTAL

The investigated dyes were synthesized from the corresponding diazonium salts and 4-methyl-6-hydroxy-3-cyano-2-pyridone. A detailed procedure for dye synthesis and their structural characterization were given elsewhere [2-4]. All the DFT calculations have been carried out with the Gaussian 09, revision C.01 electronic structure program suite. The hybrid M06-2X density functional was used for geometry optimizations. An all-electron 6-31+G(d,p) basis set was used for all atoms. Analytical harmonic frequencies were calculated in order to ascertain that the optimized structures correspond to the minima on the potential energy surface.

RESULTS AND DISCUSSION

Geometry optimization for hydrazone, azo and anionic forms generated reliable minima structures as confirmed by the absence of imaginary force constant in vibrational analysis. Solvent was found to have negligible effects on the geometry of the investigated molecules. The results revealed that the pyridone and benzene fragments are completely planar with azo linkage in all forms. Concerning bond lengths, the attention was focused only to C6-N4, N3-N4, N3-C5, C1-C5, C1-O1 bonds and bond between benzene ring and substituent group, R-C9. The calculated bond lengths lie between the single and double bond, suggesting considerable electron-delocalization throughout the whole molecule.

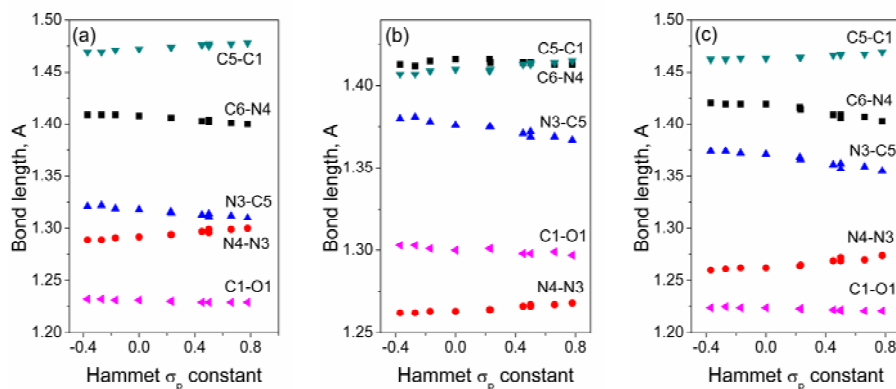


Figure 1. Bond lengths versus Hammett σ_p constants for (a) hydrazone form (b) azo form (c) anionic form of arylazo pyridone dyes.

The single-double bond character of C1-O1 bond is confirmation that lone pair of electrons of oxygen participate in the pyridone resonance structure. Considering anionic form of dyes with electron-donating group, the negative charge on oxygen atom in pyridone ring decreases conjugation between substituent and benzene ring and therefore lengthens the R-C9 bond. Opposite, negative charge on oxygen atom in anionic form of electron-withdrawing substituents increase conjugation between benzene ring and its substituent, leading to shortening of R-C9 bond length.

In order to determine how much is particular bond affected by substituents, the calculated bond lengths were correlated with Hammett σ_p constants (Fig. 1). The good linearity is observed for all bond lengths indicating that investigated bond lengths are affected by substituent effect, thus confirming electron-delocalization through whole dye molecule. The sensitivity of particular bond to substituent effect was determined from the slope of regression lines for each bond. Results from Fig. 2 indicate that N3-C5 bond is the most sensitive to

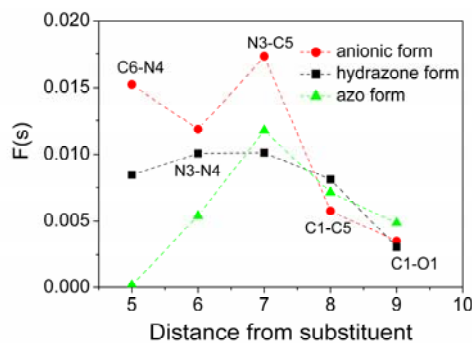


Figure 2. The sensitivity, $F(s)$ of the bond lengths to substituent electronic effects.

substituent electron effects, i.e. the substituents exert stronger effect on conjugation between N3-N4 bond and pyridone ring than on the conjugation between N3-N4 bond and benzene ring. Also, the conjugation is more affected by substituent effect in anionic form, than in azo and hydrazone form, which is probably a consequence of extra available electrons on oxygen atom in pyridone ring.

CONCLUSION

The results from this study showed that bond lengths are influenced by the type of substituents, showing a good correlation with Hammett σ_p constants. Substituents exerted stronger effect on the conjugation between azo bond and pyridone ring than on the conjugation between azo bond and the benzene ring. The obtained results indicate the position of active reaction center, thus facilitating the determination of complex reaction pathways that involve investigated dyes. Bond length in anionic form of dyes is more sensitive to substituent effect than other two forms, due to extra available lone pair on oxygen atom.

ACKNOWLEDGEMENT

This work was supported by the Ministry of Education, Science and Technological Development of the Republic of Serbia (Projects No. III 45001).

REFERENCES

- [1] R. G. Parr, W. Yang, Density-Functional Theory of Atoms and Molecules, OUP, Oxford, 1989.
- [2] D. Mijin, A. Marinković, Synthetic Communications, 2006, 36, 193-198.
- [3] J. M. Dostanić, D. R. Lončarević, P. T. Banković, O. G. Cvetković, D. M. Jovanović, D. Ž. Mijin, Journal of Environmental Science and Health, Part A, 2011, 46, 70-79.
- [4] G. S. Ušćumlić, D. Ž. Mijin, N. V. Valentić, V. V. Vajs, B. M. Sušić, Chemical Physics Letters, 2004, 397, 148-153.

DFT CALCULATIONS OF A $[\text{Cu}_2\text{tpmcGA}]^{3+}$ COMPLEX ION AS ACTIVE COMPONENT OF A VOLTAMMETRIC SENSOR FOR DETERMINATION OF GALLIC ACID

M. Milčić¹, B. B. Petković², D. Stanković¹ and S. P. Sovilj¹

¹Faculty of Chemistry, University of Belgrade, P.O. Box 118, 11158 Belgrade, Serbia

²Department of Chemistry, Faculty of Natural Sciences and Mathematics, University of Priština, Lole Ribara 29, 38220 Kosovska Mitrovica, Serbia (bedpet@orion.rs)

ABSTRACT

In our previous research we found that $[\text{Cu}_2\text{tpmc}](\text{ClO}_4)_4$ (*tpmc* = N,N',N'',N'''-tetrakis(2-pyridylmethyl)-1,4,8,11-tetraazacyclotetradecane) immobilized in PVC matrix and coated on graphite is efficient voltammetric sensor for determination of gallic acid in solution. We assumed that operation mechanism of this sensor is based on the gallic acid oxidation process at formed reversible $[\text{Cu}_2\text{tpmcGA}]^{3+}$ complex at the electrode surface. The present study examines possibility of formation of mixed ligand complex with $[\text{Cu}_2\text{tpmc}](\text{ClO}_4)_4$ and gallic acid (GA) through molecular modeling and DFT calculations. The optimized $[\text{Cu}_2\text{tpmcGA}]^{3+}$ complex ion structure is in the “unsymmetric chair” conformation with gallic acid acting as the bidentate bridging ligand between two copper(II) ions. Stability of $[\text{Cu}_2\text{tpmcGA}]^{3+}$ complex ion is examined using UB3LYP method and calculated energy of reaction suggested that gallic acid will have a very high preference for binding to $[\text{Cu}_2\text{tpmc}]^{4+}$ complex in aqueous solution.

INTRODUCTION

A number of dinuclear metal(II) complexes with *tpmc* and additional bidentate ligand are known [1, 2], but there is no evidence of dinuclear copper *tpmc* complex with GA. As we assume that reversible formation of this complex on the surface of the electrode membrane based on $[\text{Cu}_2\text{tpmc}](\text{ClO}_4)_4$ complex is sensitive to different concentration of GA in solution, the next step was to investigate formation possibility of proposed dinuclear copper *tpmc* complex with GA.

The determination of structural parameters obtained by molecular modeling is a powerful tool to add chemical and physical information to those

obtained by other techniques [3]. Taking it into account, we have studied a full optimization of all geometrical variables in order to provide an efficient approach to analysis of the configurationally and electronic parameters.

EXPERIMENTAL

Computation details: Based on Cambridge Structural Database search published in our previous paper [3] starting structures for optimization of different copper complexes with *tpmc* ligand were chosen. Geometries of all structures were fully optimized with DFT (Differential Function Theory) method, more specifically using unrestricted hybrid B3LYP functional. In all UB3LYP calculations standard Pople's basis set - 6-31G (d, p) – was used for nonmetallic atoms (O, N, C and H) and LanL2DZ basis set with Effective Core Potential (ECP) for copper atom. Global minima were found for every molecule in gas phase and were confirmed with frequency calculations. Solvation free energies (ΔG_{solv}) were calculated with new universal implicit solvent model SMD [4].

Reaction energies were calculated as a difference between ZPE corrected electronic energies of reaction products and reactants.

All DFT calculations were done with Gaussian09 program package [5].

RESULTS AND DISCUSSION

Results of the extensive CDS search [3] have shown that when forming dinuclear complexes with transition metal ions *tpmc* ligand can adopt three different conformations: “boat”, “symmetric chair” and “unsymmetric chair” conformation. Geometry optimization study on $[\text{Cu}_2\text{tpmcGA}]^{3+}$ complex ion with DFT method has shown that, independently of the starting geometry, optimized geometry is always in the “unsymmetric chair” conformation (Fig. 1) with gallic acid acting as the bidentate bridging ligand between two copper(II) ions.

In the optimized structure of $[\text{Cu}_2\text{tpmcGA}]^{3+}$ complex there are different geometries around two copper(II) ions. Geometry around first Cu(II) ion (labeled Cu1 in Fig. 1) is close to trigonal-bipyramidal geometry (τ parameters 0.81) with two nitrogen atoms from *tpmc* and the oxygen atom from gallic acid in equatorial position and other two nitrogen atoms from *tpmc* axial position. Ligating atoms around second copper ion (Cu2, Fig. 1) are arranged in square-pyramidal geometry (τ parameters 0.115) with three nitrogen atoms from *tpmc* and oxygen atom from gallic acid in in-plane position and fourth *tpmc* nitrogen atom in apical position.

Structure of optimized $[\text{Cu}_2\text{tpmcGA}]^{3+}$ complex ion is in agreement with other structures found in CSD. Namely, crystal structures of all dinuclear

copper(II) complexes with *tpmc* and another bidentate ligand (CO_3^{2-} [6], NO_3^- [6], HCOO^- [7], CH_3COO^- [7], succinato [8] and $\text{C}_6\text{H}_5\text{COO}^-$ [8]) are in “unsymmetric chair” conformation.

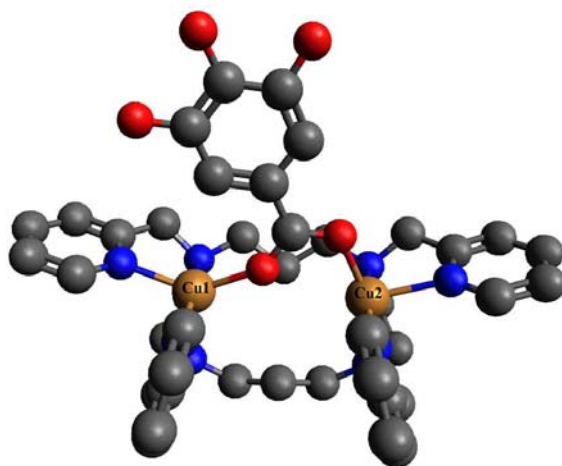
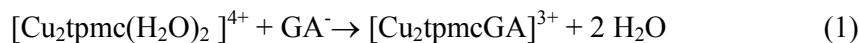


Figure 1. Optimized structure of $[\text{Cu}_2\text{tpmcGA}]^{3+}$ complex ion. Colors: yellow-copper; red-oxygen; blue-nitrogen; grey-carbon. Hydrogen atoms are omitted for clarity.

In order to obtain further insight in stability of $[\text{Cu}_2\text{tpmcGA}]^{3+}$ complex ion, energy of isodesmic reaction (1) in water solution is calculated using UB3LYP method. Solvation of molecules and ions participating in the reaction is simulated with SMD implicit solvation method [4].



Calculated value for the energy of reaction (1) is -10.4 kcal/mol in favor of $[\text{Cu}_2\text{tpmcGA}]^{3+}$ complex.

CONCLUSION

The present study is related to the possible explanation of the operating mechanism of the $[\text{Cu}_2\text{tpmc}](\text{ClO}_4)_4$ based voltammetric sensor for determination of gallic acid in solution and real samples. Based on gained results of molecular modeling and DFT calculations, it is clearly indicated that gallic acid will have a very high preference for binding to $[\text{Cu}_2\text{tpmc}]^{4+}$ complex in aqueous solution, and that at even very low concentration of gallic acid the $[\text{Cu}_2\text{tpmcGA}]^{3+}$ complex will be formed.

ACKNOWLEDGEMENT

Financial support for this study was granted by the Ministry of Science and Technological Development of the Republic of Serbia, Project Number 45022.

REFERENCES

- [1] G. Vučković, D. Opsenica, S. P. Sovilj, D. Poleti, M. Avramov-Ivić, J. Coord. Chem. 1997, 42, 241.
- [2] S. P. Sovilj, G. Vučković, K. Babić, N. Matsumoto, M. Avramov-Ivić, V. M. Jovanović, J. Coord. Chem. 1994, 31, 167.
- [3] B. B. Petković, M. Milčić, D. Stanković, I. Stambolić, D. Manojlović, V. M. Jovanović, S.P. Sovilj, Electrochim.Acta, 2013, 89, 680.
- [4] A. V. Marenich, C.J. Cramer, D. G. Truhlar, J. Phys. Chem. B, 2009, 113, 6378.
- [5] Gaussian 09, Revision D.01, M. J. Frisch, G. W. Trucks, H. B. Schlegel, G. E. Scuseria, M. A. Robb et al, Gaussian, Inc. Wallingford CT, 2009.
- [6] E. Asato, H. Toftlund, S. Kida, M. Mikurya, K. Murray, Inorg. Chim. Acta, 1989, 165, 207.
- [7] G. A. Bogdanović, Z. M. Miodragović, G. Vučković, R. Marković, A. Spasojević-de Bire, Synth. React. Inorg. Met-Org. Chem., 2001, 31, 1189.
- [8] G. Vučković, M. Antonijević-Nikolić, T. Lis, J. Mrozinski, M. Korabik, D. D. Radanović, J. Mol. Struct., 2008, 872, 135.

THEORETICAL INVESTIGATIONS ON THE STRUCTURAL ISOMERS OF STANNACYCLOPROPYLIDENOIDS AND PLUMBACYCLOPROPYLIDENOIDS

A. Azizoglu¹ and C. B. Yildiz^{1,2}

¹*Department of Chemistry, Faculty of Arts and Sciences, University of Balikesir, TR-10145 Balikesir, Turkey (azizoglu@balikesir.edu.tr)*

²*Department of Chemistry, Faculty of Arts and Sciences, University of Aksaray, TR-68100 Aksaray, Turkey*

ABSTRACT

The *ab initio* calculations at the MP2 level of theory using the 6-311+G(d,p) basis set have been carried out to investigate the isomeric structures, energies and properties of heavycyclopropylidenoids (C₂H₄XLiBr, X= Sn, or Pb). The theoretical calculations indicate that the inverted (**I**) forms of Ge, Sn, and Pb analogues are most stable than others, whereas the **C-Si** form are found to be more stable than the **I-Si** and **T-Si** forms for the Si analogue.

INTRODUCTION

Cyclopropylidenoids have been known as highly reactive carbon species in organic synthesis [1,2]. Heavycyclopropylidenoids (C₂H₄XLiBr), the Si, Ge, Sn, and Pb analogues of cyclopropylidenoids, are compounds in which heavy atoms (Si, Ge, Sn, and Pb) are replaced with the X atom. They are active intermediates in organosilicon reactions [3,4]. Despite the extensive experimental and computational studies on cyclopropylidenoids [5], only a few scientific works on silacyclopropylidenoids and germacyclopropylidenoids have been published so far [6,7]. However, there is no scientific work on the Sn and Pb analogues of cyclopropylidenoids.

It is necessary to be performed systematic theoretical study on all group 14 heavy analogues of cyclopropylidenoids to elucidate their structures, properties, and reactions. In the present paper we present the computational study of the geometries, electronic structures, and the stabilities of Si, Ge, Sn, and Pb analogues of cyclopropylidenoids.

EXPERIMENTAL

All calculations were performed with Gaussian 09W suite of program [8]. The structures were fully optimized at the MP2 level of theory with the

basis sets of 6-311+G(d,p) for H, C, Li, Br and LANL2DZ for Sn and Pb [9]. The optimized structures were determined as a minimum with no imaginary frequency. The energies reported herein include zero-point vibrational energy (ZPVE) corrections at the MP2/6-311+G(d,p) level.

RESULTS AND DISCUSSION

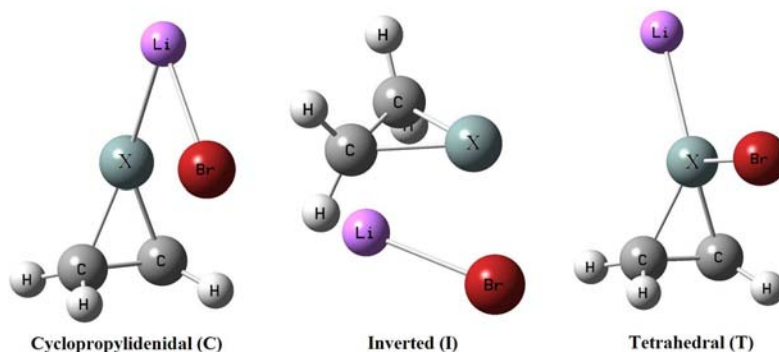


Figure 1. The illustration of C_2H_4XLiBr (where $X = Sn$ or Pb) complexes.

The structures of Si, Ge, Sn, and Pb analogues of cyclopropylidenoids have been calculated as low-spin (singlet) molecules (Figure 1). There is only a few theoretical data and no experimental data for the Si and Ge analogues of the title structures. We present in this study the first computational study of Sn and Pb analogues of cyclopropylidenoids. The findings reveal that the Si analogue of cyclopropylidenoids has three isomers cyclopropylidenoidal (**C-Si**), inverted (**I-Si**), and tetrahedral (**T-Si**) (Figure 1, $X = Si$) in accordance with previous study by Azizoglu et al [6]. The most stable isomer is determined to be the **C-Si** form. Furthermore, the Ge analogue of the cyclopropylidenoid has two constitutional isomers which are **C-Ge** and **I-Ge**. The **I-Ge** form is determined to be of lower energy than the **C-Ge** by 2.29 kcal/mol at the MP2/6311+G(d,p) level. On the other hand, the Sn analogue of the cyclopropylidenoid has three isomers and the **I-Sn form** is the most stable (Table 1). Similar to the results of the Ge analogue, we have also found that the **I-Pb** is energetically more stable than **C-Pb** by 15.08 kcal/mol including the zero-point vibrational energy at the MP2/6-311+G(d,p) level of theory. Their remarkable structural data are summarized in Table 1 and 2.

Table 1. Selected bond lengths (Å), ZPVE-corrected energies (E, *a.u.*), and frequency values for the Stannacyclopropylidenoid (C-Sn), Inverted (I-Sn), and Tetrahedral (T-Sn) forms.

	Stannacyclopropylidenoid	Inverted	Tetrahedral
Sn-Li	2.729	3.269	2.607
Sn-Br	2.924	2.889	2.573
Sn-C1	2.180	2.243	2.173
Sn-C2	2.180	2.243	2.173
C1-C2	1.505	1.523	1.505
E	-2661.785317	-2661.801123	-2661.757366
ν	-31.09	95.94	47.31

Table 2. Selected bond lengths (Å), ZPVE-corrected energies (E, *a.u.*), and frequency values for the silacyclopropylidenoidal (C-Pb) and Inverted (I-Pb), forms.

	Plumbacyclopropylidenoid	Inverted	Tetrahedral
Pb-Li	2.824	3.300	-
Pb-Br	3.051	2.978	-
Pb-C1	2.260	2.329	-
Pb-C2	2.260	2.329	-
C1-C2	1.492	1.511	-
E	-2661.870979	-2661.895021	-
ν	-76.50	64.85	-

CONCLUSION

The structural and electronic properties of the Si, Ge, Sn, Pb analogues of cyclopropylidenoids have been studied. Three isomers were determined for the Si and Sn analogues of the title structures. The **C-Si** form is the most stable for the Si analogue, whereas the **I-Sn** form has lower energy than other forms of the Sn analogue. On the other hand, the Ge and Pb analogues have two structural isomers (**C** and **I**) and the **C** forms of the title structures have higher energy than the **I** forms.

ACKNOWLEDGEMENT

This work was partially supported by the Scientific and Technological Research Council of Turkey (Grant no: TUBITAK TBAG-212T049).

REFERENCES

- [1] H. Siegel, *Top. Curr. Chem.*, 1982, 106, 55-78.
- [2] L. K. Sydnes, *Chem. Rev.*, 2003, 103, 1133-1150.
- [3] N. Sigal, Y. Apeloig, *J. Organomet. Chem.* 2001, 636, 148-156.
- [4] Y. Mizuhata, T. Sasamori, N. Tokitoh, *Chem. Rev.*, 2009, 109, 3479–3511.
- [5] A. Azizoglu, R. Ozen, T. Hokelek, M. Balci, *J. Org. Chem.*, 2004, 69, 1202-1206.
- [6] C. B. Yildiz, A. Azizoglu, *Struct. Chem.*, 2012, 33, 1777–1784.
- [7] C. B. Yildiz, A. Azizoglu, *Comp. Theor. Chem.*, 2013, 1023, 24–28.
- [8] Gaussian 09. Revision A02. Gaussian, Inc., Pittsburgh
- [9] W. J. Hehre, L. Radom, P. v. R. Schleyer, J. A. Pople, *Ab initio molecular orbital theory*. Wiley, New York, 1986.

COMPUTATIONAL STUDY ON THE ELECTRONIC AND STRUCTURAL PROPERTIES OF PLUMBAALLENES

A.Azizoglu¹ and C. B. Yildiz^{1,2}

¹*Department of Chemistry, Faculty of Arts and Sciences, University of Balıkesir, TR-10145 Balıkesir, Turkey (azizoglu@balikesir.edu.tr)*

²*Department of Chemistry, Faculty of Arts and Sciences, University of Aksaray, TR-68100 Aksaray, Turkey*

ABSTRACT

The DFT approach using the M052X functional and standard 6–311+G(d,p) basis set for H, B, C, Si, N, and O atoms and LANL2DZ for Pb atoms have been carried out with the help of relativistic effects to examine the structures, energies and properties of substituted (R= –BH₂, –CF₃, –CH₃, –CN, –NH₂, –OCH₃, –OH, –SiH₃, –H) plumbaallenes (**1–5**). The results show that the equilibrium geometries of **3** and **5** could not be obtained. The theoretical calculations show that the 1-plumbaallenes have lower energy than 2-plumbaallenes expect for the 1-plumbaallenes with the BH₂ substituent. Furthermore, the most bent allenic structures are determined to be 1,3-plumbaallenes.

INTRODUCTION

The chemistry of low-coordinated compounds with Si, Ge, Sn, and Pb atoms in organometallic chemistry have much interest for chemists in the last decades due to their unique structures. Several stable compounds with M=C or M=M (M stands for metal) double bond were identified: Si=C, Si=Si, Ge=C, Ge=Ge, Sn=C, Sn=Sn, and Pb=Pb [1–7].

Recently, 1- and 2-metalaallenes have been examined with computational methods by Apeloig et al. The theoretical results reveal that the pyramidalization at M of M–C–C or C–M–C increase from Si to Pb for the group of 14 elements. Moreover, 1-metalaallenes have lower energy than 2-metalaallenes due to the number of M=C bonds.

In order to understand the structural properties of plumbaallenes we have undertaken the computational study of all plumbaallenes substituted with R= –BH₂, –CF₃, –CH₃, –CN, –NH₂, –OCH₃, –OH, –SiH₃, –H using the M05-2X level of theory (Fig. 1).

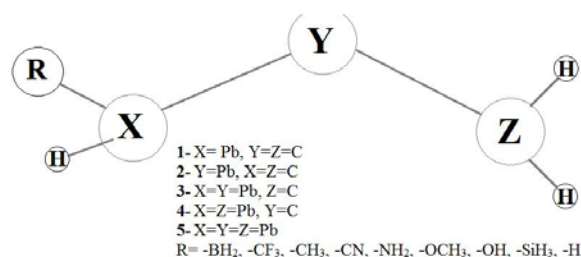


Figure 1. The illustration of plumballenes.

Two main questions that we wish to answer are the following:

1. What are the stabilization factors for plumballenes?
2. How do substituents affect the linearity of the plumballenes?

We believe that this study will be helpful for the experimental exploration of plumballenes.

THEORETICAL METHODS

All calculations were performed with Gaussian 09W suite of program [8]. The structures were fully optimized at the M05-2X level of theory with the help of relativistic effect [9]. The 6-311+G(d,p) is chosen as a basis set for the H, B, C, Si, N, and O atoms, whereas LANL2DZ for the Pb atom. The optimized structures were determined by the characterization of their Hessian matrix as a minimum (no imaginary frequency). The energies reported herein include the zero-point vibrational energy (ZPVE) corrections.

RESULTS AND DISCUSSION

First, we have carried out a series of geometry optimizations to find most stable plumballenes. For 1-plumballenes, 2-plumballenes, and 1,3-diplumballenes we obtained the equilibrium geometries, whereas for 1,2-diplumballenes and 1,2,3-triplumballenes the equilibrium geometries could not be detected. The calculated geometries are given in Table 1-3. The findings reveal that the plumballenes (**1**, **2**, and **3**) are predicted to be strongly bent and pyramidal at the Y atom (Fig.1). 1-plumballene (**1**) and 2-plumballene (**2**) were determined to be much bent allenic structures. On the other hand, 1,3-diplumballenes are even much more distorted with the XXY bond angle in the range from 119° to 142° (Table 3) at the M05-2X level of theory. For plumballenes, the degree of linearity at the Y atom increases along the series ($\mathbf{2} < \mathbf{1} < \mathbf{4}$).

As for the relative stability of 1-plumballenes and 2-plumballenes, two major factors exist: **1**) The bond numbers in the title structures (Pb=C and C=C): the substituted 2-plumballenes are generally less stable than 1-

plumbaallenes due to the number of Pb=C bonds. This bond makes the structures weaker [10]. **2)** The substituent effects on the structures: all the substituted 1-plumbaallenes have lower energy than 2-plumbaallenes except for the 1-plumbaallene with the BH₂ substituent. This is probably due to the electronegativity of the BH₂ substituent. Furthermore, the CN substituted 1-plumbaallenes and the OH, OCH₃ substituted 2-plumbaallenes could not be optimized on potential energy surface at the M05-2X level of theory.

Table 1. Selected optimized parameters for substituted 1-plumbaallenes. Bond lengths (Å), bond angles (°), vibration frequencies (cm⁻¹) and energies (*a.u.*).

	C1-C2	C2-Pb	Pb-R	Pb-C2-C1	ν	E
BH ₂	1.301	2.055	2.247	161.7	65.42	-107.285292
CF ₃	1.293	2.184	2.298	150.7	24.51	-418.990286
CH ₃	1.305	2.102	2.216	146.0	59.73	-121.167028
CN	-	-	-	-	-	-
H	1.302	2.108	1.759	147.5	189.82	-81.870713
NH ₂	1.307	2.195	2.064	134.1	78.18	-137.240929
OCH ₃	1.298	2.230	2.028	139.7	37.46	-196.407701
OH	1.298	2.227	2.036	139.1	74.61	-157.139375
SiH ₃	1.301	2.107	2.654	152.8	47.46	-372.558609

Table 2. Selected optimized parameters for substituted 2-plumbaallenes. Bond lengths (Å), bond angles (°), vibration frequencies (cm⁻¹) and energies (*a.u.*).

	C2-Pb	C1-Pb	C1-R	C1-Pb-C2	ν	E
BH ₂	1.964	1.990	1.487	170.9	76.59	-107.313589
CF ₃	1.968	1.956	1.461	160.1	23.32	-418.989529
CH ₃	1.988	2.010	1.504	147.8	54.71	-121.143583
CN	1.974	1.972	1.399	158.9	73.24	-174.129361
H	1.956	1.944	1.077	167.6	-142.53	-81.858282
NH ₂	1.962	1.970	1.419	167.2	-197.26	-137.193640
OCH ₃	-	-	-	-	-	-
OH	-	-	-	-	-	-
SiH ₃	1.965	1.960	1.836	166.0	41.84	-372.542589

Table 3. Selected optimized parameters for substituted 1,3-diplumbaallenes. Bond lengths (Å), bond angles ($^{\circ}$), vibration frequencies (cm^{-1}) and energies (*a.u.*).

	Pb3-C	Pb2-C	Pb2-R	Pb1-C-Pb2	ν	E
BH ₂	2.006	2.001	2.250	142.6	22.06	-72.547181
CF ₃	2.015	2.017	2.268	126.1	19.57	-384.247574
CH ₃	2.014	2.021	2.191	127.6	57.71	-86.430830
CN	2.019	2.019	2.198	124.2	40.72	-139.403827
H	2.014	2.014	1.746	128.4	66.80	-47.132172
NH ₂	2.028	2.062	2.036	116.2	38.67	-102.506221
OCH ₃	2.016	2.044	2.010	119.6	25.45	-161,668072
OH	2.016	2.042	2.016	119.8	44.70	-122.399003
SiH ₃	2.013	2.015	2.622	132.0	42.00	-337.819689

CONCLUSION

Different plumbaallenes have been investigated at the DFT level of theory using the M05-2X method. The equilibrium geometries of three plumbaallenes were determined on potential energy surface with the substituents -BH₂, -CF₃, -CH₃, -CN, -NH₂, -OCH₃, -OH, -SiH₃, -H. The 1-plumbaallenes are more stable molecules compared to their structural isomers of 2-plumbaallenes except for the isomer with the BH₂ substituent.

ACKNOWLEDGEMENT

This work was supported by the Scientific and Technological Research Council of Turkey (Grant no: TUBITAK TBAG-212T049).

REFERENCES

- [1] A. G. Brook, M. A. Brook, *Adv. Organomet. Chem.* 1996, 39, 71-158.
- [2] J. Escudie, C. Couret, H. Ranaivonjatovo, *Coord. Chem. Rev.* 1998, 178, 565-592.
- [3] R. Okazaki, R. West, R. *Adv. Organomet. Chem.* 1996, 39, 231-273
- [4] M. Weidenbruch, *Coord. Chem. Rev.* 1994, 130, 275-300
- [5] T. Tsumuraya, S. A. Batcheler, S. Masamune, *Angew. Chem., Int. Ed. Engl.* 1991, 32, 902.
- [6] P. P. Power, *Chem. Rev.* 1999, 99, 3463-3504.
- [7] K. M. Baines, W. G. Stibbs, *Coord. Chem. Rev.* 1995, 145, 157-200.
- [8] M.J. Frisch, et al., *Gaussian 09W Revision D.01*, Gaussian, Inc., Pittsburgh, 2009.
- [9] Y. Zhao, N. E. Schultz, and D. G. Truhlar, *J. Chem. Theory and Comput.*, 2006, 2, 364-382.
- [10] N. Sigal, Y. Apeloig, *Organometallics* 2002, 21, 5486-5493.

THE MOLECULAR STRUCTURE AND VIBRATIONAL SPECTRA OF N-(4-BROMO BENZOYL)-ANTHRANILIC ACID

A. Azizoglu¹ and I. Sen¹

¹*Department of Chemistry, Faculty of Arts and Sciences, University of Balikesir, TR-10145 Balikesir, Turkey (azizoglu@balikesir.edu.tr)*

ABSTRACT

The amide crystal N-(4-Bromobenzoyl)-anthranilic acid has been synthesized and characterized by the X-Ray, ¹H-NMR, ¹³C-NMR and IR techniques. The molecular geometry and vibrational frequency values in the ground state have been calculated using the HF and B3LYP level of theory with the 6-31G(d) and 6-31G+(d,p) basis sets. The calculated results show that the optimized geometry can well reproduce the crystal structure, and the theoretical vibrational frequencies and chemical shift values show good agreement with experimental values.

INTRODUCTION

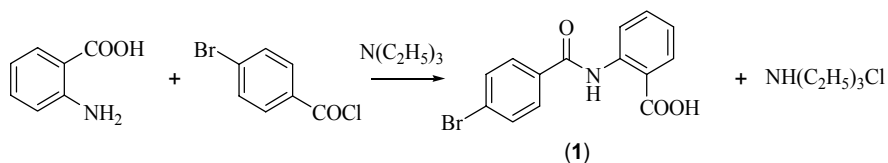
The amide bond structure of amide derivatives often plays a key role in molecular recognition events and biological activities [1]. Benzamide, the simplest aromatic carboxylic amide, is used in the synthesis of various organic compounds. Benzamide derivatives have therapeutic utility, particularly in the treatment of diabetes, obesity related conditions and disorders. It functions as fungicides in pharmacology and also has industrial applications [2].

In this context, we would like to report the preparation of N-(4-bromobenzoyl)-anthranilic acid crystal and its characterization with the help of elemental analysis and spectroscopic techniques (FT-IR, ¹H-NMR, and ¹³C-NMR). In addition, theoretical calculations have been performed using the Gaussian 03 program [3] at various levels of theory to investigate the structural and physical properties of title compound [4].

EXPERIMENTAL AND THEORETICAL METHODS

The calculations of geometrical parameters in the ground state were performed using the Gaussian 03 suite of programs at the HF and DFT levels with both the 6-31G(d) and 6-31G+(d,p) basis sets [3]. Initial geometry was generated from standard geometrical parameter.

N-(4-Bromobenzoyl)-anthranilic acid (**1**): A solution of anthranilic acid (10 mmol) in THF (50 ml) was added dropwise a THF solution of 4-bromo benzoyl chloride (10 mmol) at room temperature and then triethylamine (10 mmol) added. The reaction mixture was stirred for 15 h. It was poured and then 100 ml water was added. The crude product was crystallized from acetonitrile. Yield: 80 %; IR : ν 3317 (N-H), 3102 (Ar-H), 3024 (Ar-H), 2643 (OH-C=O), 1689 (C=O), 1661 (C=O, first amide band), 1585 (C=O, secondary amid band), 1485-1468 (C=C), cm^{-1} ; $^1\text{H-NMR}$ (400 MHz, $\text{DMSO-}d_6$): δ =12.2 (s, 1H, H₂, OH), 8.7 (t, 1H, H₁N, NH), 8.1-7.2 (m, 8H, Ar-H).



Scheme 1

RESULTS AND DISCUSSION

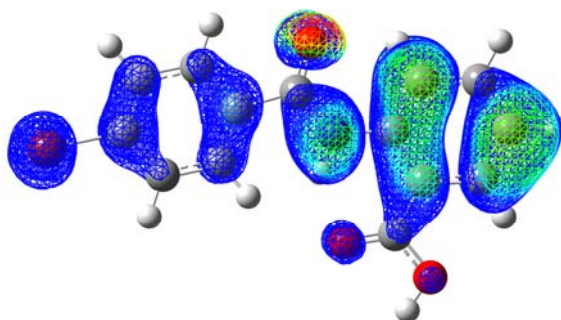
In order to obtain the spectroscopic signature of the title structure, we have performed the vibrational frequency calculations at different levels of theory. For comparison purposes, the experimental and theoretical frequencies are presented in Table 1. The structures show the presence of the N—H stretching vibrations experimentally 3317 cm^{-1} in accordance with computational calculations which is the characteristic region for ready identification of these structures. The stretching vibration of the C=O amide group occurs in the region $1661\text{--}1585\text{ cm}^{-1}$.

Table 1. The selected frequencies (cm^{-1}) of **1** calculated at HF and DFT levels with both the 6-31G(d) and 6-31G+(d,p) basis sets.

Exp.	HF/6-31G(d)	HF/6-31G+(d,p)	B3LYP/6-31G(d)	B3LYP/6-31G+(d,p)
742	765	764	760	735
865	860	855	862	859
1006	1007	1003	1010	1012
1168	1173	1170	1176	1166
1247	1232	1229	1277	1269
1311	1315	1313	1333	1324
1485	1523	1508	1470	1485
1533	1553	1544	1536	1527
1661	1670	1662	1665	1653
1689	1731	1720	1755	1729
3317	3855	3847	3482	3481
R^2	0,9937	0,9933	0,9988	0,9991

According to calculated correlation coefficient values, especially B3LYP/6-31G+(d,p) method is in a good agreement with the experimental values. As can be seen from R^2 values depicted in Table 1, we found a good agreement between theory and experiment.

Molecular electronic potential (MEP) map of **1** shown in Fig. 1, was calculated at the B3LYP/6-31+G(d,p) level. In this figure *blue* is partial negative (electron rich), and *red* is partial positive (electron deficient). On the other hand, the negative (red and yellow) and the positive (blue) regions in the MEP map are related to electrophilic reactivity and nucleophilic reactivity, respectively.

**Figure 1.** MEP map of **1** calculated at the B3LYP/6-31+G(d,p) level.

As can be seen in Fig.1 the negative region of the title structure was observed around the N atom, whereas a maximum positive region is localized on the carbonyl O atom.

CONCLUSION

Experimental and theoretical vibrational analyses of the N-(4-bromobenzoyl)-anthranilic acid have been performed for the first time. Calculated vibrational frequencies have been compared with those obtained from the experimental IR spectrum. Experimental fundamentals are found to have slightly better correlation for the DFT than for HF method.

ACKNOWLEDGMENT

The financial support of the TUBITAK (Scientific and Technological Research Council Turkey) and Balikesir University-BAP is gratefully acknowledged.

REFERENCES

- [1] R. Yamasaki, A. Tanatani, I. Azumaya, S. Saito, K. Yamaguchi, H. Kagechika, *Org. Let.*, 2003, 5, 8.
- [2] V. Krishnakumar, K. Murugeswari, N. Surumbarkuzhali, *Spectrochim. Acta A* 2013, 114, 410–420.
- [3] M.J. Frisch, et al., *Gaussian03W Revision C.02*, Gaussian Inc.: Wallingford, CT, 2004.
- [4] I. Sen, Doctoral thesis, The University of Balikesir, Graduate School of Natural and Applied Sciences, 2011.

BARRIER TO ROTATION AROUND THE C=C BOND AS A MEANS TO QUANTIFY PUSH-PULL EFFECT OF SELECTED 2-ALKYLIDENE-4-OXOTHIAZOLIDINES

A. Rašović¹, D.M. Minić², M. Baranac-Stojanović³, V.A. Blagojević²
and R. Marković^{1,3,†}

¹Center for Chemistry ICTM, University of Belgrade,
P. O. Box 473, 11000 Belgrade, Serbia (arasovic@chem.bg.ac.rs)

²Faculty of Physical Chemistry, University of Belgrade,
Studentski trg 12-16, 11001, Serbia

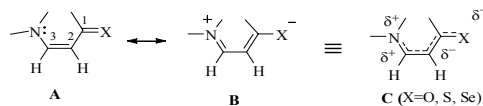
³Faculty of Chemistry, University of Belgrade,
Studentski trg 16, P. O. Box 158, 11001 Belgrade, Serbia

ABSTRACT

The configurational isomerization around the C=C double bond of (*E*)-(5-ethoxycarbonylmethyl-4-oxothiazolidin-2-ylidene) ethanthioamide **1** has been studied by the variable-temperature ¹H NMR dynamic spectroscopy. All relevant kinetic data, that is the Arrhenius parameters (activation energy E_a and frequency factor A) and thermodynamic activation parameters (ΔS^\ddagger , ΔH^\ddagger and ΔG^\ddagger) were determined and compared with the respective data for **2** and **3**. The ΔG^\ddagger values proved to be a good indicator of the strength of the *push-pull* character of the studied compounds.

INTRODUCTION

Numerous investigations of *push-pull* alkenes **A** have shown that donor-acceptor electronic interactions occurring via the C=C double bond (resonance structure **B** and hybrid structure **C** in Scheme 1) are the main factor responsible for the lowering of the rotational barrier around the C(2)=C(3) bond. In a fragment shown in Scheme 1, these electronic interactions increase in the order: O < S < Se [1,2].

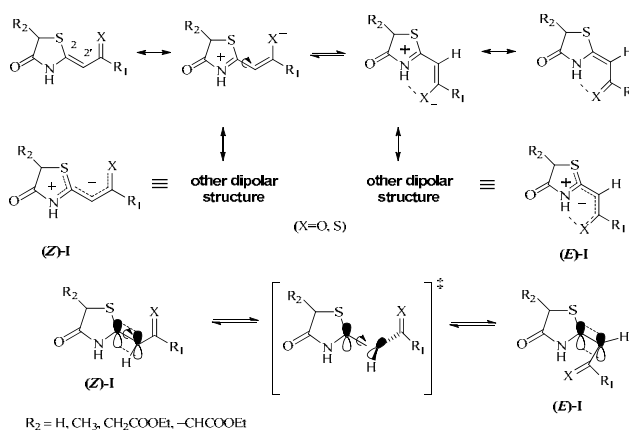


Scheme 1.

In the case of our stereodefined *push-pull* thiazolidine derivatives **I**, the above mentioned electronic interactions, occurring here between two

†1946-2012

electron -donors (-NH and -S-) and one electron-acceptor (R_1CX ; $R_1 = \text{Ph}$, OEt , NHPH ; $X = \text{O}$), have been evidenced by the facile Z/E configurational isomerization taking place spontaneously in solution, at room temperature (Scheme 2) [3,4]. Direction of this isomerization is dictated by the solvent polarity. Polar solvents break the intramolecular hydrogen bond in (E)-**1** and shift the equilibrium to the (Z)-**1**, by forming stable solvent-solute intermolecular interactions. On the other hand, in nonpolar solvents, the intramolecularly hydrogen bonded E isomer becomes the dominant species (Scheme 2).



Scheme 2.

EXPERIMENTAL

The (E)-(5-ethoxycarbonylmethyl-4-oxothiazolidin-2-ylidene)ethanthioamide (E)-**1** ($R_2 = \text{CH}_2\text{CO}_2\text{Et}$; $R_1 = \text{NH}_2$; $X = \text{S}$; Scheme 2) was synthesized according to the our reported procedure [5], including a slight modification [2]. Monitoring of the stereodynamic behaviour associated with the isomerization rate of (E)-**1** to (Z)-**1** has been done in $\text{DMSO-}d_6$ solutions at 298, 303 and 308 K. The ratios of the (E)-**1** versus (Z)-**1** isomers were calculated by the integration of the signals at δ 5.64 and δ 6.15 ppm, assigned to the $\text{C}(2')\text{-H}$ protons of the (E)-**1** and (Z)-**1**, respectively. The facile E to Z isomerization at 298 K is illustrated in Fig. 1 by the three ^1H NMR spectra recorded 5, 170 and 1380 minutes after the dissolution of **1** [2]. The variable-temperature ^1H NMR measurements were carried out on a Bruker AC-300 spectrometer. The total number of collected ^1H NMR spectral data at regular 5 min intervals was 135 (the time elapsed between two successive NMR spectra acquisitions was 4 min and 9.28 s). Typical conditions for ^1H NMR spectra were as follows: sixteen scans, spectral

width 10330 Hz with 65,536 data points, giving an acquisition time of 3.17 s.

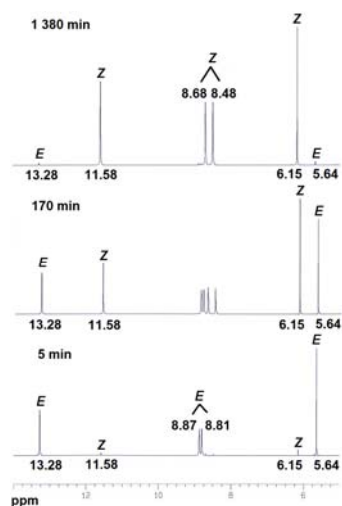
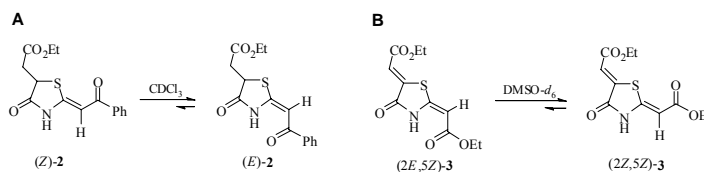
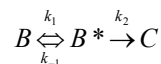


Figure 1. A part of ^1H NMR spectra ($\text{DMSO-}d_6$) of **1** recorded 5, 170 and 1380 min after the sample dissolution, at 298 K.

RESULTS AND DISCUSSION

To extend our knowledge on the solvent dependent Z/E configurational equilibrium of 2-alkylidene-4-oxothiazolidines and the strength of their *push-pull* character, we studied the isomerization of (*E*)-(5-ethoxycarbonylmethyl-4-oxothiazolidin-2-ylidene) ethanthioamide (*E*)-**1**. For this purpose, the variable temperature-NMR determination of the dynamics of the configurational isomerization of **1** has been done. The results are compared with those for (*Z*)-**2** and (*2E,5Z*)-**3** (Schemes 2 and 3, Table 1), previously reported by us [4].

The mechanism of the (*E*)-**1** \rightleftharpoons (*Z*)-**1** isomerization can be proposed, as follows:



Scheme 3.

Based on the steady state approximation and assuming that $k_{-1} < k_1$, reaction is further approximated to the first order reaction. The overall rate constant, k , is determined as the slope of the best straight line fitted through the first ten points, when $\ln[B/B_0]$ is plotted against time (t). The slope of the Arrhenius plot yields the energy of activation and the intercept at $1/T = 0$ yields the frequency factor A (Table 1). Thermodynamic activation parameter ΔS^\ddagger and ΔH^\ddagger of this transformation have been calculated from equations $A = (RT/hN_A)e^{\Delta S^\ddagger/R}$ and $\Delta H^\ddagger = E_a - RT$ (Table 1). The ΔG^\ddagger has been obtained by using the equation $\Delta G^\ddagger = \Delta H^\ddagger - T\Delta S^\ddagger$.

A comparison of ΔG^\ddagger values for the isomerization of **1-3**, determined at the same temperature conditions (Table 1), shows that the free energy of activation increases along the series **1** < **2** < **3**. This increase coincides with the decrease in their *push-pull* character, which has been shown by us to follow a decrease in the electron-accepting ability of substituents, in the order CSNH₂ > CPh > CO₂Et [6].

Table 1. The energy of activation E_a , the frequency factor A and the activation parameters for rotation around the C(2)=C(2') bond in 4-oxothiazolidines (*E*)-**1**, (*Z*)-**2** and (*2E*, *5Z*)-**3**

Entry	Compound	T [K]	E_a [kJ/mol]	$\ln A$ [s ⁻¹]	ΔH^\ddagger [kJ/mol]	ΔS^\ddagger [J/molK]	ΔG^\ddagger [kJ/mol]
1	(<i>E</i>)- 1	298	62.4	15.65	59.9	-123.1	96.6
2	(<i>Z</i>)- 2	298	41.8	6.91	39.3	-198.7	98.5
3	(<i>2E</i> , <i>5Z</i>)- 3	298	83.3	22.74	80.9	-64.7	100.2

CONCLUSION

This work shows the efficiency of experimentally determined rotational barrier (ΔG^\ddagger) around the C(2)=C(2') bond of selected 2-alkylidene-4-oxothiazolidines to quantify their *push-pull* effect. The *push-pull* character of the studied compounds decreases in the order (*E*)-**1** > (*Z*)-**2** > (*2E*, *5Z*)-**3**, following a decrease in the electron-accepting ability of substituents. The determined kinetic parameters indicated that the configurational isomerization (*E*)-**1** \rightleftharpoons (*Z*)-**1** followed the first order kinetics.

ACKNOWLEDGEMENT

This work was supported by the Ministry of Education, Science and Technological Development of the Republic of Serbia (project ID: 172020).

REFERENCES

- [1] E. Kleinpeter, A. Schulenburg, I. Zug, H. Hartmann, J. Org. Chem., 2005, 70, 6592-6602 and references therein.
- [2] A. Rašović, Ph.D. Dissertation, Belgrade University, 2010.
- [3] Z. Džambaski, M. Stojanović, M. Baranac-Stojanović, D. Minić, R. Marković, J. Serb. Chem. Soc., 2011, 76, 317-328 and references therein.
- [4] R. Marković, M. Baranac, N. Juranić, S. Macura, I. Cekić, D. Minić, J. Mol. Struct., 2006, 800, 85-92.
- [5] R. Marković, M. Baranac, Z. Džambaski, M. Stojanović, P. J. Steel, Tetrahedron, 2003, 59, 7803-7810.
- [6] M. Baranac-Stojanović, U. Klaumünzer, R. Marković, E. Kleinpeter, Tetrahedron, 2010, 66, 8958-8967.

KINETICS,
CATALYSIS

PROCESS DYNAMICS IN SLURRY POLYMERIZATION

N.M. Ostrovskii and L. Fekete

*Hipol a.d. (nikolaj.ostrovski@hipol.rs)
Gračački put b.b., 25250 Odžaci, Serbia*

ABSTRACT

The testing procedure of propylene polymerization catalyst is discussed. The reaction rate dynamics is analysed and contributions of feed flow, gas - liquid mass transfer, polymerization reaction and catalyst deactivation is estimated. It has been shown, that the reaction rate during first 20-30 minutes is much lower (3 to 7 times) than total monomer consumption. The method of kinetic experiments interpretation is proposed. It provides the estimation of mass-transfer coefficient, reaction rate constant, as well as parameters of active centres dynamics.

INTRODUCTION

Olefins polymerization is a non-stationary process by nature, because the rate of each process stage is changing with time [1]. The catalyst becomes part of the polymer, since the polymer “grows” on the surface of catalyst particle and encapsulates it. Figuratively, growing polymer particle can be imaged as a small pomegranate fruit (50-500 μm). Such a polymer “fruit” (macroparticle) consists of numerous “grains” (microparticles) with “seed” (catalyst crystallite) inside each grain [2].

Thus, the rate of polymerization depends on physical stages (mass transfer in growing particles and in solution), as well as on chemical stages (changes of active sites number). As distinct from other catalytic processes, it is rather difficult (if possible) to separate chemical and physical stages of reaction dynamics in polymerization kinetic experiments.

Because of polymer remains on a catalyst, the testing of polymerization catalyst is usually carried out in semi-batch reactor, and the rate of monomer absorption by catalytic suspension is considered as a rate of reaction. In fact, the rate of monomer consumption represents a total monomer flux, which becomes equal to the reaction rate only in quasi-steady state.

In this report the experimental procedure and mathematical model are presented that provide an interpretation of such a dynamic catalyst testing. The method enables to estimate the kinetic parameters of monomer dissolution, polymerization reaction and catalyst deactivation.

EXPERIMENTAL

Materials: Propylene, heptane, nitrogen, hydrogen, triethylaluminium (TEA) and the external donors were got from Hipol polypropylene plant and were used without additional purification. Propylene of polymerization grade was used, with at least 99.5 vol.% purity.

Pre-treatment of the reactor: The 3.7 L jacketed steel reactor was blown at 80 °C by repeated evacuation and flushing with nitrogen. The evacuated reactor was then charged with 1400 mL of heptane and stirred at 500 rpm. Then, the reactor jacket was connected to a water bath maintained at a constant temperature of 20 °C in order to prepare for prepolymerization.

Catalyst activation: The catalyst components were prepared in the glove box under purified nitrogen. The catalyst used was a commercially available $\text{TiCl}_4/\text{ID}/\text{MgCl}_2$ type of Ziegler–Natta catalyst (ID = internal donor). Triethylaluminium (TEA) was used as co-catalyst and cyclohexyl-methyl-dimethoxy-silane (donor C) or dicyclopentyl-dimethoxy-silane (donor D) as an external donor (ED). The dry catalyst (20 mg) was weighed into a vial. The required amount of TEA for molar ratio $\text{Al}/\text{Ti} = 500$ and ED for specified Si/Ti molar ratio were contacted in the presence of 100 mL of heptane in a burette. The catalyst was then transferred into the burette with TEA/ED complex. The resulting activated catalyst slurry was then injected into the reactor under vacuum. The quantity of added hydrogen was determined to obtain the desired melt flow index of polymer.

Prepolymerization: This procedure was typically performed during 30 minutes at 20 °C. It was started by injecting a fixed quantity of propylene from the inlet pipe into the reactor filled with slurry of activated catalyst.

Propylene polymerization: First, the reactor temperature was elevated up to 75 °C. Then, the mass flow meter (MFM, Bronkhorst Cori-Flow meter) was fully opened to start the charging of propylene into the reactor. This moment was taken as the start of polymerization. The polymerization temperature (70 °C) and pressure (1.0 MPa) usually were reached after 15–18 min. The propylene consumption was measured automatically by MFM during polymerization. After targeted polymerization time, the reaction was terminated by venting the reactor. The obtained product was filtered of, shortly dried under IR lamp and then dried under vacuum at 80 °C for 2 h.

RESULTS AND DISCUSSION

Propylene solubility in heptane

The solvent “heptane” consists of more than 20 C_7 -hydrocarbons. The propylene solubility in that mixture was calculated using Soave-Redlich-

Kwong equation of state [3], and then data were approximated by Henry-like equation (1):

$$C_m^* = H_m P_m^n, \quad H_m = H_m^o \exp(Q_m / RT) \quad (1)$$

where C_m^* – equilibrium concentration of propylene, g/g;

P_m – propylene partial pressure, bar; T – temperature, K;

Q_m – heat of dissolution; R – universal gas constant;

H_m – Henry coefficient for propylene; n – constant.

$$Q_m = 23.0 \text{ kJ/mole} \quad H_m^o = 4.5e-06 \text{ g/g bar}^n \quad n = 1.3.$$

The propylene solubility was verified in several experiments at different temperature and pressure, and the validity of eq. (1) was confirmed. Farther, eq. (1) was used for calculation of monomer equilibrium concentration.

Propylene dissolution dynamics

The propylene dissolution into heptane can control the overall process at the beginning of test, when its concentration in slurry-phase is low. That is why it was estimated in special experiments without catalyst. An example of experimental curve of propylene absorption by heptan is shown at Fig. 1.

The total propylene flow (W) was calculated by equation follows from Hagen-Poiseuille law:

$$W = \frac{k_h}{\sqrt{P_z}} \sqrt{P_z - P} \varphi(t), \quad \varphi(t) = \alpha (1 - \exp(-t/t_R)) \quad (2)$$

Propylene partial pressure in a gas phase ($P_m = P y_m$) and its concentration in liquid phase (C_m) depend on gas-liquid mass transfer and equilibrium conditions:

$$\frac{dP_m}{dt} = W \frac{RT}{MV_G} - \beta (C_m^* - C_m) RT \frac{V_L}{V_G}, \quad \frac{dC_m}{dt} = \beta (C_m^* - C_m) \quad (3, 4)$$

where W – propylene flow, g/min; k_h – constant (depends on apparatus);

$\varphi(t)$ – transient response function; P, P_z – current and desirable pressure;

t_R – time constant of regulator; M – molecular weight; V_L, V_G – volume of liquid and gas, L; β – mass transfer coefficient, min^{-1} .

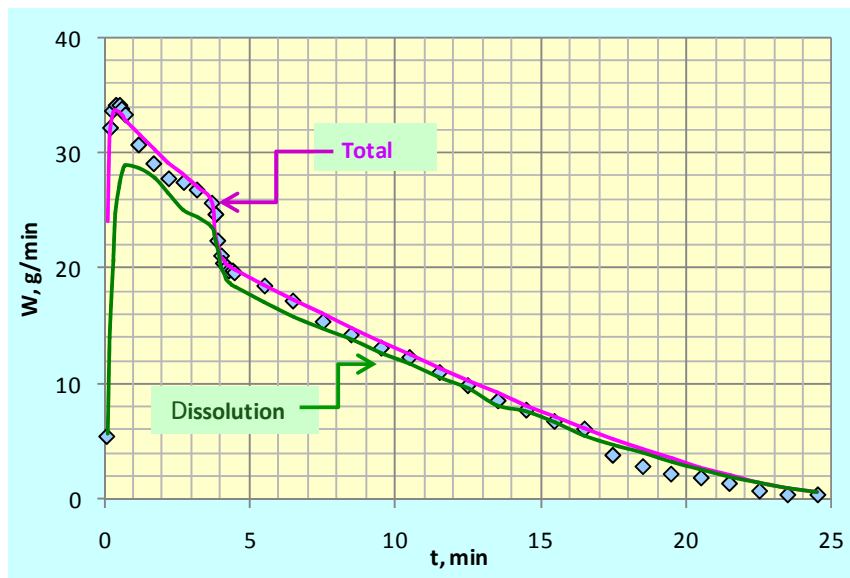


Figure 1. Propylene dissolution in heptane at $T = 70\text{ }^{\circ}\text{C}$ and $P = 10\text{ bar}$.
Points – experimental flow; Lines – calculated by model (1-4).

Two parameters in equations (2–4) were estimated from experiments on dissolution dynamics:

- apparatus constant $k_h = 55\text{-}60\text{ g/min}$,
- mass transfer coefficient $\beta = 0.5\text{-}0.7\text{ min}^{-1}$.

With these parameters the model fits excellent the experimental data for dynamics of flow rate – W (Fig. 1), total pressure – P (Fig. 2), and propylene amount in the reactor – G (Fig. 3).

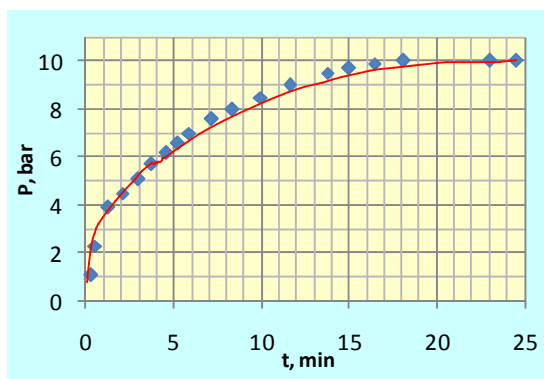


Figure 2. Total pressure dynamics during propylene dissolution in heptane.
Points – experimental data. Line – calculated by model (1–4).

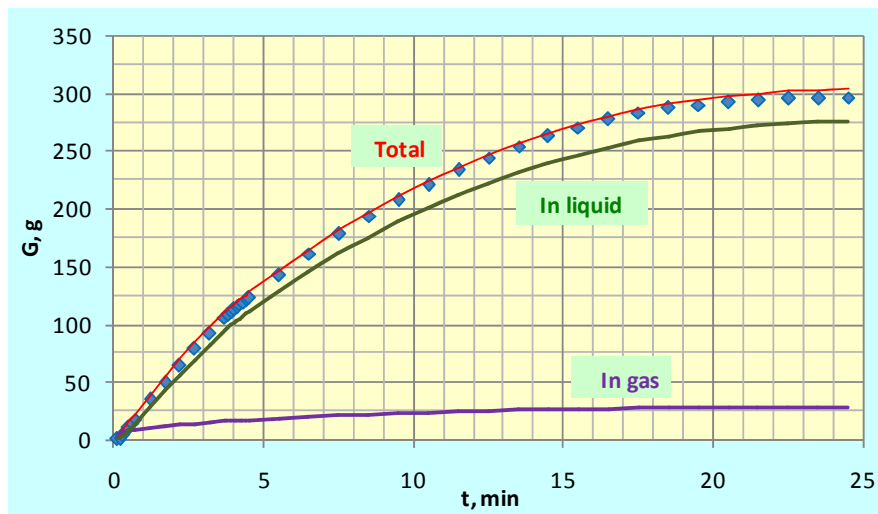


Figure 3. Propylene amount in the reactor.
Points – experimental data; Lines – calculated by model (1-4).

Propylene polymerization dynamics

In the presence of catalyst these flow rate constant (k_h) and mass transfer coefficient (β) should remain the same. Also the flow rate equation (2) and the equation for propylene in gas phase (3) are the same. The only equation for propylene concentration in liquid phase (4) must be modified by expressions for the reaction rate (R_p) and catalyst deactivation (da/dt):

$$\frac{dC_m}{dt} = \beta (C_m^* - C_m) - R_p, \quad (5)$$

$$R_p = k_p G_c C_m \psi a, \quad \psi = \frac{b_A C_A + b_H C_H}{(1 + b_A C_A + b_H C_H)^2} \quad (6)$$

$$\frac{da}{dt} = k_a C_A C_m a_i^0 \exp(-k_a C_A t) - k_d a + k_s (1 - a) \quad (7)$$

where R_p – reaction rate of polymerization, g/g min; a – relative activity; k_p – reaction rate constant; G_c – weight of the catalyst, g; ψ – cocatalyst and hydrogen function [4]; C_A, C_H – Al(Et)₃ and H₂ concentration in liquid, mole/L; b_A, b_H – their adsorption coefficients; k_a, k_d, k_s – rate constants of catalyst activation, deactivation, and self-regeneration.

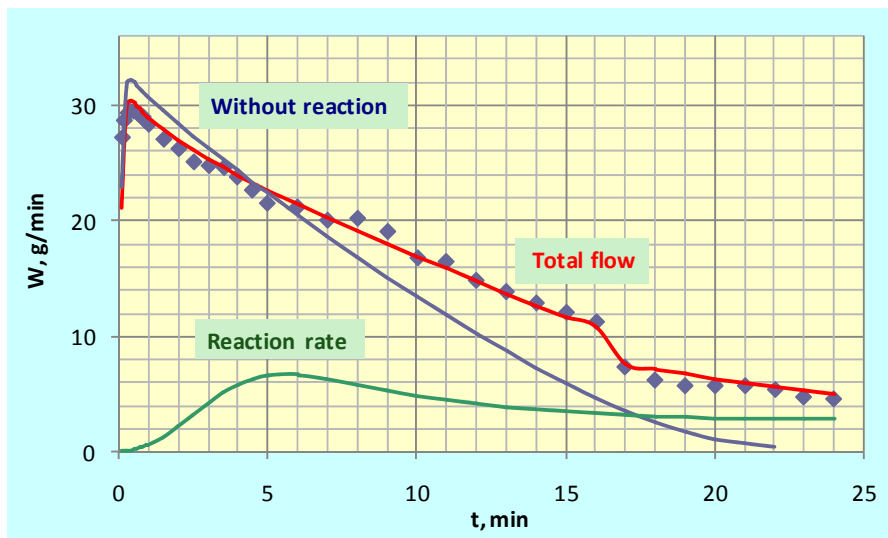


Figure 4. Propylene flow dynamics during polymerization at pressure growth period. Points – experimental flow; Lines – calculated by model (1–7).

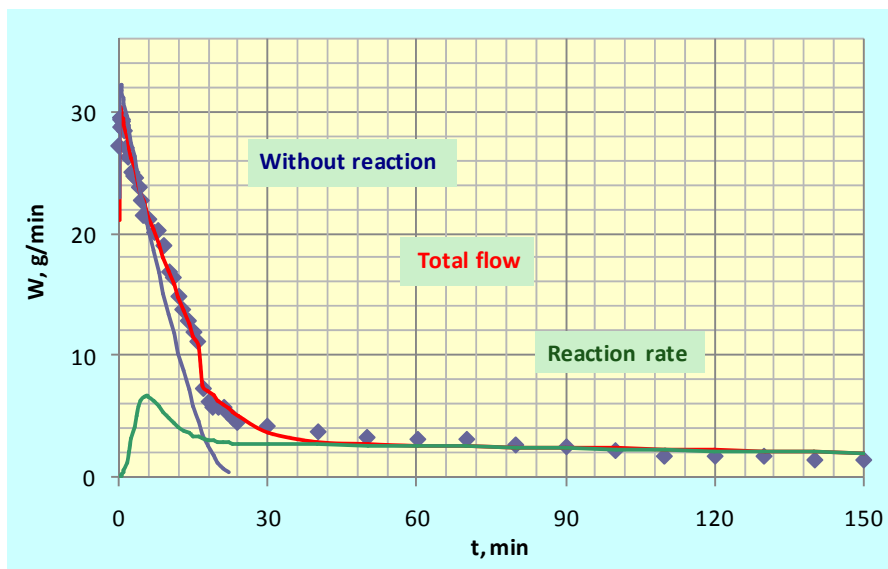


Figure 5. Propylene flow dynamics during polymerization for 2.5 hours. Points – experimental flow; Lines – calculated by model (1–7).

The set of equations (1–7) represents the complete model of polymerization process in laboratory reactor, which is non-stationary by nature. This model was used for the treating of experimental data. An example of propylene flow dynamics under reaction condition is shown in Fig. 4 (initial period of 25 min), and in Fig. 5 (total period of 2.5 hours). It is clearly seen that total flow and the reaction rate become equals each other only after 30–40 min, when the reaction becomes the rate limiting step.

The dynamics of propylene accumulation in the reactor is presented in Fig. 6. It shows that just that time (30–40 min) is necessary for propylene concentration in heptane (C_m) to reach its equilibrium value ($C_m^* = 0.26$ g/g = 4.4 mole/L), corresponding to $T = 70$ °C and $P_m = 9.4$ bar, and resulting in propylene total amount in the reactor of 270–275 g.

It is also seen from Figs. 4–6, that after 20 min, the amount of polymer increases with roughly constant rate of 7500–8800 kg/g cat. h. Finally, the specific catalyst activity (R_P / C_m) and propylene concentration in heptane, calculated by model, are shown in Fig. 7.

Because dissolution parameters (k_h, β) were determined prior to catalyst testing, the only reaction kinetic parameters (k_p, k_a, k_d, k_s) were calculated on the base of catalytic experiments presented in Figs. 4–6.

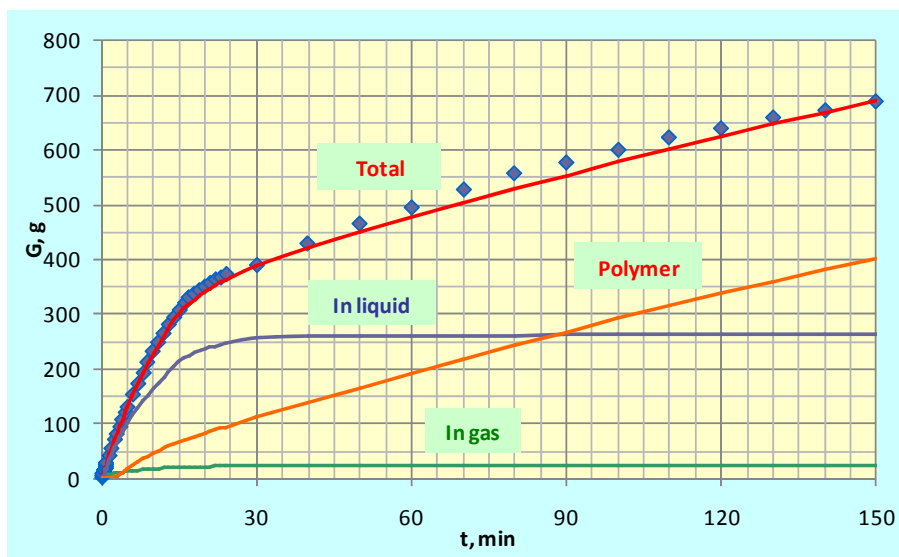


Figure 6. Propylene accumulation in the reactor during polymerization. Points – experimental data. Lines – calculated by model (1–7).

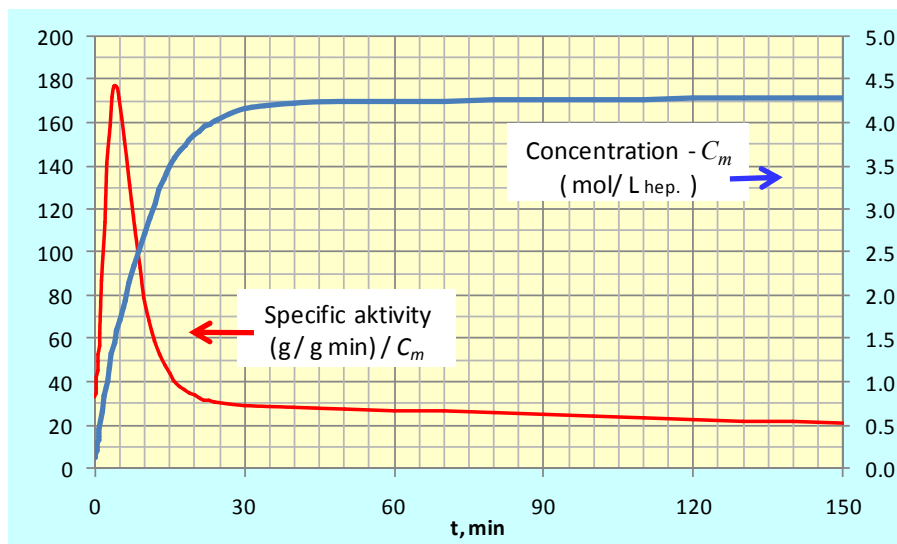


Figure 7. Specific catalyst activity and propylene concentration.
Lines – calculated by model (1–7).

Unfortunately, in the literature, extremely high monomer consumption at the beginning of test (Fig. 4) is often explained by complicated mechanism of active centres transformation.

CONCLUSION

The dynamics of catalytic polymerization in solvent (slurry process) depends considerably on monomer dissolution rate. It influences directly on catalyst activity that being determined in semi-batch reactor. The maximal monomer flux is observed at the beginning of test, and corresponds to monomer dissolution in solvent, but not to the rate of polymerization.

REFERENCES

- [1] T.F. McKenna, J.B.P. Soares, Chem. Eng. Sci., 2001, 56, 3931-3949.
- [2] N.M. Ostrovskii, F. Kenig, Chem. Eng. Journ., 2005, 107, 73-77.
- [3] R.C. Reid, J.M. Prausnitz, T.K. Sherwood, The Properties of Gases and Liquids. McGraw-Hill, 1977.
- [4] T. Keii, K. Soga, Catalytic polymerization of olefins. Elsevier, 1986.

OZONATION OF ALIPHATIC ALCOHOLS. KINETIC AND MECHANISMS

S. Rakovsky¹, M. Anachkov¹, D. Jovanovic² and G.E. Zaikov³

¹*Institute of Catalysis, Bulgarian Academy of Sciences, "11 Acad. G. Bonchev" str., 1113 Sofia Bulgaria*

²*University of Belgrade Institute of Chemistry, Technology and Metallurgy (I.Ch.T.M.) Center of Catalysis and Chemical Engineering, 11000 Belgrade, Republic of Serbia*

³*N.M. Emanuel Institute of Biochemical Physics, Russian Academy of Sciences, 4 Kosygin str., 119334, Moscow, Russia*

ABSTRACT

The mechanism of ozone reaction with alcohols in organic solvents is discussed in details, presenting the respective reaction schemes and the corresponding kinetic parameters are given and some thermodynamic parameters are also listed. The dependences of the kinetics and the mechanism of the ozonation reaction on the structure of the compounds, on the medium and on the reaction conditions are revealed. The various possible applications of alcohols ozonolysis are specified and discussed.

INTRODUCTION

The ozonolysis of alcohols is a promising process that takes place under mild conditions and yields products of a higher oxidation state than that of the starting compounds. It may find various applications in chemical and pharmaceuticals industries, fine organic synthesis, etc. [1, 2]. The widest application has been found for the oxidation of primary and secondary alcohols into their corresponding aldehydes and ketones. For example in the cases of the oxidation of open-chain and cyclic secondary alcohols the yield of ketones is within the range 57% up to 83% [3]. Moreover, the considered interactions are extremely important from an ecological point of view for the utilization and purification of industrial wastes. The importance of this process for theory and practice gave us an impetus to carry out systematic investigations [4-14]. The aim of the present paper is the precise determination of the rate constants of ozonolysis of some more widely occurring classes of studied organic compounds. Applying the activated complex method (ACT) [15] and collision theory (CT) [15] some investigations have also been carried out elucidating the structure of the transition state formed in the course of the reaction. Based on the correlation

between experimental and theoretical results for pre-exponent values in the Arrhenius equation the mechanism of ozone reactions with the open-chain and cyclic secondary alcohols have been established.

EXPERIMENTAL

Ozone has been obtained from dry oxygen by means of a silent discharge of 5-8 kV at an oxygen flow rate of 0.1 L/min. The ozone concentration, 10^{-5} - 10^{-3} M, has been measured spectrophotometrically in the wavelength region of 254-300 nm in a 5 cm quartz gas cell.

Methods

The UV, IR, ESR spectra were registered on standard equipment, as well as HPLC, and GC analyses.

Kinetic Measurements.

Static Method

Pure reagent or reagent solution was injected into thermostatic 1 cm quartz cuvette, containing a solution of ozone in CCl_4 , the time of mixing being less than 0.2 seconds [6].

Dynamic Method

The ozone was bubbled through a cylindrical glass reactor with inner diameter $\phi=1.7$ -3.7 cm and height 7-15 cm, supplied with porous glass grit-G2 at its bottom. The rate constants are calculated according to the mass and chemical reaction equilibrium equation - Eq. (1):

$$\omega([O_3]_o - [O_3]_g) = k[O_3]_l[RH] \quad (1)$$

where ω is the relative flow rate of ozone-oxygen gas mixture; $[O_3]_o$ and $[O_3]_g$ are the ozone concentrations at the reactor inlet and outlet, respectively, $[O_3]_l$ is ozone concentration in the solution; $[RH]$ is concentration of the reagent.

If in the case of a bimolecular reaction, in accordance with Henry's Law, $[O_3]_l$ is substituted with $\alpha[O_3]_g$, where α is Henry's coefficient, Eq. (1) can be transformed into Eq. (2) [1]:

$$k = \omega \cdot \Delta[O_3] / ([RH] \cdot \alpha[O_3]_g) \quad (2)$$

RESULTS AND DISCUSSION

A number of authors have tried to elucidate the kinetics and mechanism of the ozonolysis of alcohols and their application to the selective preparation of ketones and aldehydes in high yields under mild conditions [3, 16-23]. The basic concepts on such reactions are discussed in several references [1, 2, 4, 13-15]. It has been established that the rate constants of ethanol ozonolysis does not change when the hydroxyl group is deuterated [19] and its value is 4.17 times higher than that when the methylene group is deuterated [17-19]. The ratio between the relative reactivities of tertiary: secondary: primary alcohols is 1:12:241 according to reference [17], or 1:156:817 according to reference [24].

In this connection, we have carried out intensive experimental studies on the kinetics of ozonolysis of MeOH, *t*-BuOH, EtOH, *n*-PrOH, *n*-BuOH, *i*-PrOH, *s*-BuOH, *c*-HexOH both by the static and barbotage methods, the results of which are summarized in Figures 1-3 and Tables 1-3.

Figure 1 demonstrates the kinetic data of ozone consumption in solutions of methanol, ethanol and *iso*-propanol by means of the static method with time interval of mixing less than 0.2 seconds. It is seen that regardless of the type of alcohol being ozonized, the kinetic curves coincide with first-order rate law. With a view to more precise evaluation and comparison of the respective rate constants such concentrations of the respective alcohols have been selected, at which the rates of ozone consumption have close values. The kinetic curves of ozone reactions with MeOH, EtOH and *i*-PrOH gave the following values of the rate constants: 0.057, 0.17 and 1.13 $\text{M}^{-1}\cdot\text{s}^{-1}$, respectively.

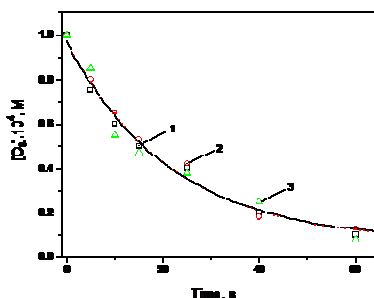


Figure 1. Kinetics of ozone consumption in the reaction of ozone with: 1 - methanol, 22°C, 0.74 M; 2 - ethanol, 3°C, 0.24 M; and 3 – *iso*-propanol, 3.5°C, 0.037 M.

The same values were also obtained by carrying out the reactions in a bubble reactor. The values of k are calculated on the basis of Equation 2 – the data are given in Table 2 and they are represented graphically in Figures 2 and 3.

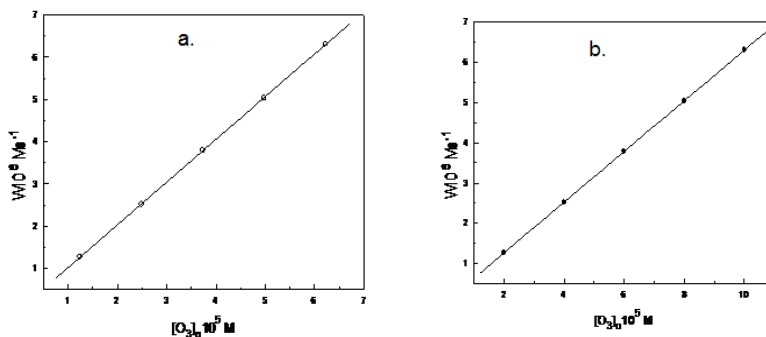


Figure 2. Dependence of the rate of ozone consumption on the ozone concentrations- (a) inlet $[O_3]_o$ and (b) outlet $[O_3]_g$, at MeOH concentration of 0.74 M.

Processing the data from Table 1 (down), columns 2, 3, and 5, based on Equation 2, yield the linear dependencies shown in Figure 2a and 2b. The dependence of the rate W on ΔO_3 has also been found out to be a linear one. The dependence of the rate W on the concentration of alcohol $[ROH]$ is a curve, which approaches a limit value at $W = 1.67 \cdot 10^{-5} \text{ M} \cdot \text{s}^{-1}$. The nonlinear character of this relationship is in accordance with the complexity of Equation 2 (see also Figure 3). In the case when $[ROH] \rightarrow \infty$, then we have $[O_3]_g \rightarrow 0$ and $\Delta O_3 \rightarrow [O_3]_o$. The values of k , calculated based on Equation 2 at each one of the points on the curve (Fig. 3), are equal to 0.057. Therefore the experimentally obtained linear dependences of W on $[O_3]_o$, $[O_3]_g$ and on $\Delta[O_3]$ as well as the profile of the curve in Figure 3 correspond to the mathematical description of ozonolysis in a barbotage reactor - Equation 2.

Judging from the analysis of the data obtained (Tables 2 and 3) it follows that the rate constant and the activation energies are strongly dependent on the alcohol structure. The interaction of ozone with MeOH possessing primary α -H atoms and with *tert*-BuOH having only primary C-H bonds has been found to be the slowest, and the value of k at 20 °C per one α -H atom in the first case is $1.62 \times 10^{-2} \text{ M}^{-1} \cdot \text{s}^{-1}$, and in the second case, related to one primary H atom, is $3.22 \times 10^{-3} \text{ M}^{-1} \cdot \text{s}^{-1}$. The difference in the values of these constants is due to the fact that while the OH group in MeOH directly affects the α -H atom, in the case of the *tert*-BuOH, which

does not possess any α -H atoms, the effect of the OH groups is transferred through one σ -bond and so it is considerably weaker.

Table 1. Kinetic parameters of ozone reaction with MeOH in carbon tetrachloride (CCl_4) and pure MeOH solutions: 22 °C, $\omega = 0.167 \text{ s}^{-1}$; $v = 1.67 \times 10^{-3} \text{ L/s}$, maximum rate of ozone inlet - $1.67 \times 10^5 \text{ M.s}^{-1}$

[MeOH], M	$[\text{O}_3]_0 \times 10^5, \text{ M}$	$[\text{O}_3]_g \times 10^5, \text{ M}$	$\Delta[\text{O}_3] \times 10^5, \text{ M}$	$W \times 10^6, \text{ M.s}^{-1}$	$k, \text{ M}^{-1} \cdot \text{s}^{-1}$
1	2	3	4	5	6
0	10	0	10	0	-
0.247	10	8.32	1.68	2.80	0.057
0.439	10	7.35	2.65	4.43	0.056
0.618	10	6.64	3.36	5.61	0.058
0.740	10	6.22	3.78	6.31	0.055
0.987	10	5.53	4.47	7.46	0.057
1.0	10	5.49	4.51	7.53	0.056
2.0	10	3.79	6.21	10.37	0.055
3.0	10	2.89	7.11	11.87	0.057
4.0	10	2.34	7.66	12.79	0.058
5.0	10	1.96	8.04	13.42	0.054
10.0	10	1.09	8.91	14.88	0.056
24.7	10	0.47	9.53	15.91	0.058
0.740	8	4.98	3.02	5.04	0.057
0.740	6	3.73	2.27	3.79	0.055
0.740	4	2.49	1.51	2.52	0.056
0.740	2	1.24	0.76	1.27	0.058

Table 2. Dependence of k on the temperature in °C for ozone reaction with three types of alcohols

$k, \text{ M}^{-1} \cdot \text{s}^{-1}$	0 °C	10 °C	20 °C	25 °C	30 °C
MeOH	0.008	0.021	0.049	0.072	0.108
<i>t</i> -BuOH	0.005	0.013	0.029	0.045	0.064
EtOH	0.14	0.28	0.54	0.74	1.10
<i>n</i> -PrOH	0.19	0.36	0.67	0.89	1.18
<i>n</i> -BuOH	0.15	0.30	0.56	0.76	1.10
<i>i</i> -PrOH	0.93	1.61	2.71	3.46	4.39
<i>s</i> -BuOH	0.88	1.54	2.58	3.29	4.18
<i>c</i> -HexOH	0.92	1.59	2.65	3.37	4.27

As a result of this, the reactivity of *tert*-BuOH becomes similar to that of methane and neopentane. The interactions of ozone with EtOH, *n*-PrOH, *n*-BuOH take place at higher rates and the values of k per one α -H atom amount to 0.27, 0.34 and 0.28, respectively.

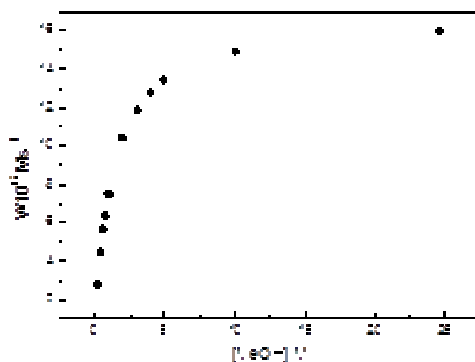


Figure 3. Dependence of the rate of ozone consumption on methanol concentration at $[O_3]_0 = 1.10^{-4}$ M (according to Equation 1).

The higher rates of the ozone reactions with these alcohols are associated with the presence of secondary α -H atoms in their molecules, which have lower bond energies than the primary ones. The enhanced reactivity of *n*-PrOH compared with that of EtOH could be assigned to the donor effect of the second CH_3 group while the donor effect of the C_2H_5 group in *n*-BuOH is weaker than that of the methyl group and therefore k is lower.

Table 3. Kinetic parameters of ozone reaction with some alcohols at 25°C

Param.	MeOH	<i>t</i> -BuOH	EtOH	<i>n</i> -PrOH	<i>n</i> -BuOH	<i>i</i> -PrOH	<i>s</i> -BuOH	<i>c</i> -HexOH
$k \times 10^2$, $M^{-1}.s^{-1}$	7.2	4.5	74	89	76	346	329	337
n , α -C-H	3	9 (β -C-H)	2	2	2	1	1	1
$k \times 10^2/n$, $M^{-1}.s^{-1}$	2.4	0.5	37	44	38	346	329	337
E_{as} , kcal/mol	13.9	13.7	10.9	10.1	10.4	8.5	8.5	8.4
$A \times 10^{-7}$, $M^{-1}.s^{-1}$	41	5.8	3.9	2.4	1.7	0.62	0.59	0.51

It has been found that the reactions of ozone with *i*-PrOH, *s*-BuOH and *s*-HexOH alcohols possessing *tert*-H atoms with the lowest bond energies is

the fastest with k equal to 2.71, 2.58 and 2.65, respectively, i.e., in fact they are almost the same.

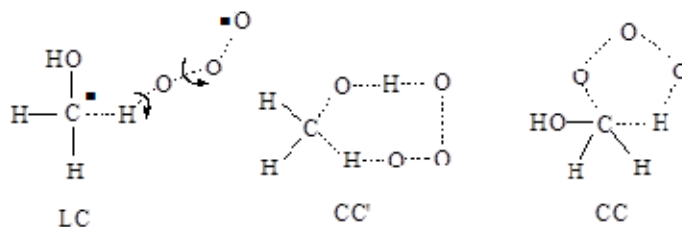


Figure 4. Structure of the probable activated complexes in the reaction of ozone with aliphatic alcohols: LC - linear with free fragment rotation and CC' and CC - cyclic complexes without free rotation.

The ratio between the reduced values of k at 25°C for methanol: ethanol: *sec.*butanol are 1:15:137. Simultaneously, the values of E_a decrease with the decrease of the α -H atoms bond energy (D) and their ratio is 1:0.78:0.61 (12, 15). This fact can be regarded as important evidence for the mechanism of α -C-H-atom abstraction by ozone.

The theoretical estimates of A were performed considering the two possible structures of the activated complex (AC): linear (LC) and cyclic (CC and CC') (Figure 4). The good agreement between the experimental data and theoretical estimates for A allows I'd rather AC structure and on this basis enables the selection of the most probable mechanism. Simultaneously the value of the pre-exponential factor was calculated by the collision method and by comparing its value with the one calculated based on the AC theory the steric factor $-p$ was determined [25-29]:

The pre-exponential factors for the reactions of ozone with alcohols, calculated according to the activated complex method (ACT) and collision theory (CT) are represented in Table 4.

An interesting fact is the good agreement between the values of A^{LC} and A^{CC} . The values of A^{CC} with the five- and seven-member cyclic form of AC are practically similar as they differ by not more than 1%. However the free rotation produces an increase in A^{LC}_{cal} by three orders of magnitude compared with that of A^{CC} . The steric factor has a value, which is in agreement with a liquid phase reaction. The ratio between the calculated and experimental values of A^{LC} , is increasing in the sequence primary: secondary: tertiary alcohols is 1:3.4:8.8, i.e., the coincidence in this sequence is decreasing. This is connected with the fact that E_{fr} is not zero and it is increasing with the changes in the alcohol structure in the same

sequence. It has been found that the values of $A_{\text{calc}}^{\text{LC}}$ and A_{obs} coincide when the values of rotation energy are those given in line 10 in Table 4. We have obtained the same values by means of the *MOPAC 6* software package and therefore the data on the free rotation energy (E_{fr}) in line 10 can also be considered as theoretically evaluated.

Table 4. The values of A calculated by ACT with LC and CC and by CT, the sums (R_{fr}) and energy (E_{fr}) of inner rotation, steric factors (p), VDW radii of the molecules (r) and the ratio between the calculated and experimental values of pre-exponentials $A_{\text{calc}}^{\text{LC}}/A_{\text{obs}}$

Param.	MeOH	EtOH	<i>n</i> - PrOH	<i>i</i> - PrOH	<i>n</i> - BuOH	<i>s</i> - BuOH	<i>t</i> - BuOH	<i>c</i> - HexOH
$A^{\text{CC}} \cdot 10^{-4}$, $\text{M}^{-1} \cdot \text{s}^{-1}$	52	8.3	3.7	3.5	2.4	2.2	6.3	1.6
$A^{\text{LC}} \cdot 10^{-4}$, $\text{M}^{-1} \cdot \text{s}^{-1}$	56	15	6.7	6.3	4.4	4.0	4.9	2.9
$F_{\text{fr}} \cdot 10^{-2}$	7.1	9.8	12	11	13.8	12.6	12.9	12.6
$A_{\text{calc}}^{\text{LC}} \cdot 10^{-7}$, $\text{M}^{-1} \cdot \text{s}^{-1}$	40	15	8.1	6.8	6.1	5.0	6.3	3.6
r , Å	2.24	2.57	2.91	2.88	3.13	3.23	3.13	3.23
$A^{\text{CT}} \cdot 10^{-11}$, $\text{M}^{-1} \cdot \text{s}^{-1}$	2.6	2.6	2.7	2.7	2.8	2.8	2.8	2.7
$p \cdot 10^5$	22	5.8	2.5	2.3	1.6	1.4	1.8	4.1
$A_{\text{calc}}^{\text{LC}}/A_{\text{obs}}$	1.0	3.8	3.4	11	3.1	8.3	1.1	7.2
E_{fr} , cal/mol	0	730	670	1368	701	1172	52	1081

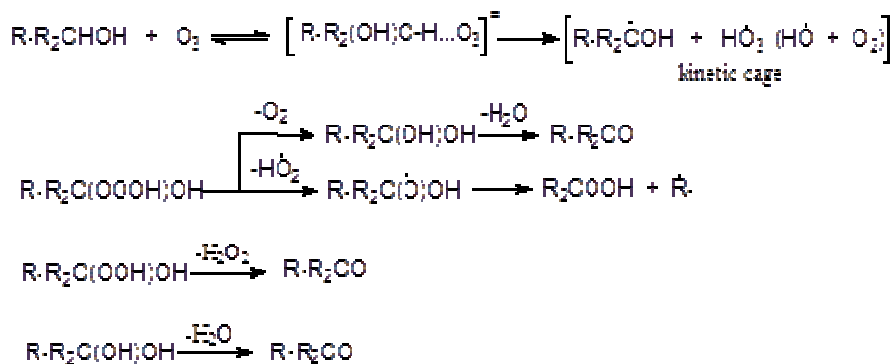
Note: ALC is the pre-exponential factor calculated with LC without free fragment rotation (it is absent at $E_{\text{fr}} \geq 4$ kcal); A_{CC} - calculated with CC; $A_{\text{calc}}^{\text{LC}}$ = at free fragment rotation, i.e., when $\exp(-E_{\text{fr}}/RT) = 1$ or $E_{\text{fr}} = 0$ kcal; A_{ct} - calculated according to the collision theory at 300 K and r - radius of the ozone molecule - 2Å; E_{fr} - the calculated values of the rotation energy at ratio of $A_{\text{calc}}^{\text{LC}}/A_{\text{obs}} = 1$.

The good agreement between $A_{\text{calc}}^{\text{LC}}$ and A_{obs} suggests that the ozone reaction with alcohols involves the formation of linear AC and abstraction of the α -H atom from the alcohol molecule.

The experimental and theoretical results conform well to Scheme 1.

Ozone attacks the α -H atom, forming a LC, which further undergoes decomposition into a radical (or ion) pair in one kinetic cage. The α -

hydroxy alcohol, α -hydroxyperoxy alcohol and α -hydroxytrioxy alcohol being unstable leave the cage and decompose rapidly to the corresponding aldehyde or ketone liberating water, hydroperoxide and oxygen or lead to the formation of hydroperoxy and alkoxy radicals. The latter species can further undergo monomolecular decomposition.



Scheme 1

CONCLUSION

The intensive experimental studies on the kinetics and mechanisms of ozonation of MeOH, *t*-BuOH, EtOH, *n*-PrOH, *n*-BuOH, *i*-PrOH, *s*-BuOH, *c*-HexOH by static and bubbling method were carried out. The wide theoretical investigations of the pre-exponential factors in the Arrhenius equation for all reactions are applied. It was established that the activation complex of the reactions has linear structure and the rate determined step is hydrogen abstraction. It was found that the reaction ability of alcohols depended on their structure and energy of α -C-H bonds, attached to the carbon atom where OH-groups are adjusted.

ACKNOWLEDGEMENT

This work was partially supported by Bulgarian Academy of Sciences, the Ministry for Science of the Republic of Serbia and Institute of Biochemistry of Russian Academy of Sciences (Projects in the frame equivalent exchange).

REFERENCES

- [1] S.D. Razumovskii, S.K. Rakovsky, D.M. Shopov, G.E. Zaikov, *Ozone and its Reactions with Organic Compounds*, Publishing House of the Bulgarian Academy of Sciences: Sofia, Bulgaria, 1983.
- [2] P.S. Bailey, In *Ozonation in Organic Chemistry*, Volume 2 - Nonolefinic Compounds; Academic Press: New York, NY, USA, 1982.
- [3] W.L. Waters, A.J. Rollin, C.M. Bardwell, J.A. Schneider, T.W. Aanerud, *J. Org. Chem.* 1976, 41, 889-896.
- [4] S.K. Rakovsky, D.R. Cherneva, *International Journal of Chemical Kinetics* 1990, 22(4), 321-329.
- [5] S.K. Rakovsky, D.R. Cherneva, D.M. Shopov, S.D. Razumovskii, *Communications of the Department of Chemistry, Bulgarian Academy of Sciences* 1976, 9(4), 711-716.
- [6] S.K. Rakovsky, D.R. Cherneva, *Oxidation Communications* 1989, 12(3), 108-117.
- [7] S.K. Rakovsky, L.G. Kulak, E.M. Kuramshin, S.S. Zlotsky, D.L. Rakhmankulov, *Communications of the Department of Chemistry, Bulgarian Academy of Sciences* 1989, 22(3), 722-733.
- [8] D.L. Rakhmankulov, S.S. Zlotsky, L.Z.; Rudnik, G.T. Teregulova, S.K. Rakovsky, *Communications of the Department of Chemistry, Bulgarian Academy of Sciences* 1989, 22(3), 652-664.
- [9] M.P. Anachkov, S.K. Rakovsky, A.K. Stoyanov, R.K. Fotty, *Thermochemica Acta* 1994, 237, 213-217.
- [10] S.K. Rakovsky, D.R. Cherneva, M. Deneva, *International Journal of Chemical Kinetics* 1995, 27(2), 153-162.
- [11] S.K. Rakovsky, D.R. Cherneva, M. Deneva, V.V. Ershov, *Oxidation Communications* 1997, 20(2), 169-176.
- [12] S.K. Rakovsky, R.A. Sheldon, F.V. Rantwijk, *Oxidation Communications* 1996, 19(4), 482-493.
- [13] G.E. Zaikov, S.K. Rakovsky, *Ozonation of Organic & Polymer Compounds*, iSmithers, Smithers Rapra, Shawbury, Shreswsbury, Shropshire, SY4 4NR, UK, 2009.
- [14] D. Popova, S. Rakovsky, M. Anachkov, *Oxidation Communications* 2007, 30(3), 529-534.
- [15] H. Eyring S.H. Lin; S.M. Lin, *Basic Chemical Kinetics*, Moskow, Mir, 1983 (In Russian).
- [16] E.T. Denisov, N.I. Mitskevich, V.E. Agabekov, *Mechanism of Liquid-Phase Oxidation of Oxygen Containing Compounds*, Science and Technique Publishing House, Minsk, 1975.
- [17] M. Whiting, A. Bolt, J. Parish, *Oxidation of Organic Compounds - III*, *Advances in Chemistry Series*, No. 77, ACS, Washington DC, USA, 1968.
- [18] D. Williamson, R.J. Cvetanovich, *Journal of American Chemical Society* 1970, 92, 2949-254.

- [19] A.Ya. Gerchikov, E.R. Kuznetsov, E.T. Denisov, *Kinetika i Kataliz* 1970, 15, 109-121.
- [20] V.V. Shereshovetz, N. Shafikov, V.D. Komissarov, *Kinetika i Kataliz* 1980, 21, 1596-1603.
- [21] N.Ya. Shafikov, A.A. Gusmanov, Yu.S. Zimin, V.D. Komissarov, *Kinetics and Catalysis* 2002, 43(6), 799-808.
- [22] A.Ya. Gerchikov, Yu.S. Zimin, N.V. Trukhanova, V.N. Evgrafov, *React.Kinet. Catal.Lett.* 1999, 68(2), 257-263.
- [23] A.A. Borodin, S.D. Razumovskii, *Kinetics and Catalysis* 2009, 50, 3385-3394.
- [24] E. Heinzle, H. Stockinger, M.; Stern, M. Fahmy, O.M. Kut, *Journal of Chemical Technology and Biotechnology* 1995, 62(3), 241-255.
- [25] V.N. Kondratiev, (Chief Editor), *Bond Energy, Ionization Potential and Electron Affinity*, [in Russian], Nauka Publishers: Moscow, 1974.
- [26] A.J. Gordon, R.A. Ford, *The Chemists Companion*, Mir, Moscow, 1976.
- [27] G. Eiring, Lin, S.G. Lin, S.M. Lin, *The Principles of Chemical Kinetics*, Mir, Moscow, 1983.
- [28] K. Karadakov, S.K. Rakovsky, *Calculation of Pre-exponents ver.1.0*, (Software) Copyright, 1987, based on the J. Howbert, Software: *The Molecular Animator*, vers. 1-3, Copyright, 1983.
- [29] W. Thiel, Software, IBM, Program MND0C, QCPE ver., Fachbereich Physikalische Chemie der Philipps-Universität, auf den Zähringen, D-3550, Marburg, Germany, based on M.Y.S. Dewar and W. Thiel, *Journal of the American Chemical Society* 1977, 99, 4899-4915.

SURFACE IMPERFECTIONS AND CATALYTIC ACTIVITY: THE QUANTITATIVE RELATIONSHIP

A. Cholach, N. Bulgakov, and V. Elokhin

*Boreskov Institute of Catalysis, Novosibirsk 630090,
Prospekt Akademika Lavrentieva 5, Russian Federation*

ABSTRACT

The total neighbors lost by adjacent atoms composing an adsorption site as compared with bulk atom are considered as a measure of local surface imperfection. Semi-empirical calculations have shown that surface defects provide the formation of weakly bound, but very inclined to hydrogenation state of atomic nitrogen that makes the grain boundary to be the center for sustained surface wave nucleation during NO+H₂ reaction on the Rh twin tip. In the same terms, an optimal site for catalytic NH₃ synthesis consisted of 2 and 3 Ru atoms is presumably characterized by 12 and 1 lost neighbors, respectively, whereas Rh is a poor catalyst in any case. The same approach can be applied to any other adsorption or catalytic processes exhibiting high surface sensitivity.

INTRODUCTION

Surface defects often play a crucial role in heterogeneous catalysis as the active centres for target reaction or for impurities accumulation [1]. For example, the wave nucleation during NO+H₂ reaction on monocrystalline Rh tip [2] and CO+O₂ reaction at Pt(110) and Pt(210) surfaces is truly governed by structural defects [3], while stabilization effect ~ 50-80 kJ/mole of low-coordinated sites at edges and corners of Pt nanoparticles against Pt(111) plane was reported for CH_n species [4]. Specific behaviour of surface imperfections is usually interpreted at qualitative level, and the lack of quantitative considerations has encouraged the present study highlighting a simple model for examination of surface defects as specific centres for adsorption and heterogeneous catalytic reactions.

THEORETICAL

Semi-empirical Method of Interacting Bonds (MIB) is used to examine thermodynamics of the adsorbed species [5]. The MIB does not predict coordination, bond angles and other particular features, but empowers perfect comparative accuracy. An equality of operating parameters, i.e.

identity of chemical bond nature in reference molecules and in a substance being examined is the only condition for high reliability of calculations [5].

RESULTS AND DISCUSSION

Numerical observation by Field Emission Microscopy (FEM) have found that the wave nucleation proceeds exactly at the grain boundary of Rh twin tip during sustained spatiotemporal oscillations in NO+H₂ reaction as shown in Fig. 1. The grain boundary is an extended surface defect whose atoms are slightly deepened into the bulk and thus enriched with nearest neighbours in comparison with smooth surface as schematically represented in Fig. 2. In order to perform the further quantitative analysis, a sum of nearest neighbors lost by adjacent atoms composing an adsorption site, or the Sum of Lost Bonds (SLB), in comparison with the bulk atom is considered as a measure of local surface imperfection.

Rh twin tip: $P_{\text{NO}} = 1.1 \cdot 10^{-5}$, $P_{\text{H}_2} = 1.3 \cdot 10^{-4}$ Pa; $T \sim 470$ K

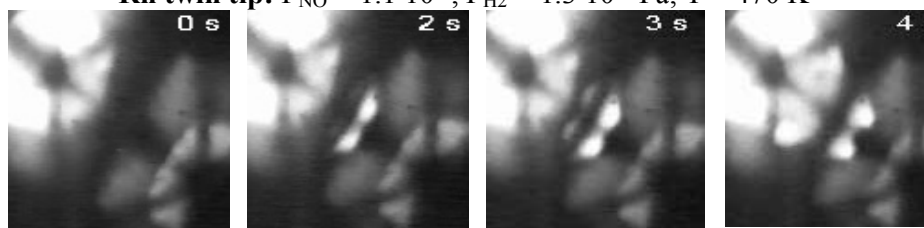


Figure 1. Screenshots of FEM images at indicated time points during the surface wave nucleation (from archive data of [2]).

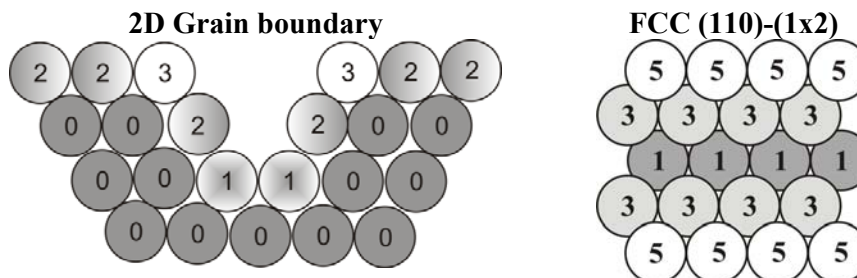


Figure 2. Number of neighbors lost by individual atoms at 2D grain boundary and FCC (110)-(1x2) plane.

\underline{N} species (adsorbed states are underlined hereinafter) dominate in the adsorbed layer under experimental conditions of NO+H₂ reaction, while \underline{NH} is a key intermediate enabling an oscillatory kinetic mode [5]. Fig. 3 shows the results of MIB calculations related to heats of reactions Q_N and Q_{NH} :



Q_N increases on SLB, whereas Q_{NH} shows an opposite behaviour in Fig. 3 where the grain boundary is indicated around (110)-(1x2) plane in Fig. 2 due to similar geometry. Fig. 3 means that \underline{N} at the grain boundary is weaker bound to surface, but much more disposed to reaction (2) thus providing the surface wave nucleation as well as the larger by 5-8 orders equilibrium \underline{NH} coverage against perfect terraces [5]. Just this peculiarity makes \underline{N} species to recombine and desorb at a particular spot between (111) terraces and (100) steps at the Rh(533) single crystal; the same reason determines difference between sites at stepped Rh surfaces [6].

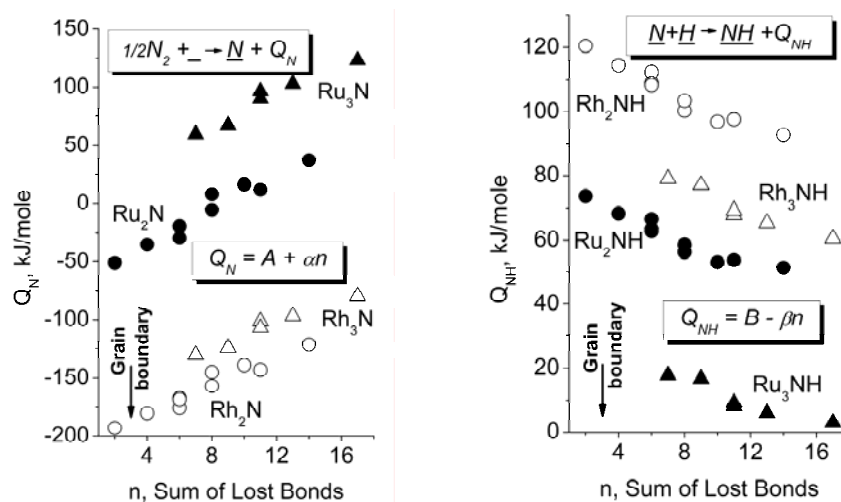


Figure 3. Heats of reactions (1) and (2) for 2-fold (circles) and 3-fold (triangles) bound \underline{N} at different sites of FCC planes, 0.5 ML coverage.

SLB model is further tried for examination the optimal structure of Rh and Ru as a catalyst for NH_3 synthesis assuming that activity is determined by equilibrium \underline{N} and \underline{H} coverage and the rate of reaction (2). Equilibrium and dynamic (2) gives maxima in \underline{NH} coverage and \underline{NH} rate at $K_N = (\alpha/\beta - 1)$ and $(\alpha - \gamma\beta)/(\alpha + \gamma\beta)$, respectively, where K_N is equilibrium constant for (1); α , β are slopes in Fig. 3; γ is a coefficient in relation for activation energy $E_2 \equiv C - \gamma Q_{NH} \equiv E_{2,0} + \gamma\beta n$, $0 \leq \gamma \leq 1$, and specifically $\gamma = 0.25$ corresponds to Semenov – Polanyi rule. Typical conditions of NH_3 synthesis $P_{N_2} \sim 10^5$ Torr and $T \sim 800$ K enable to estimate $K_{N,0} \sim 3.2 \cdot 10^{-2}$, including N_2 flux at sticking coefficient $s \sim 1$ and $k_{1,0} \sim 1.7 \cdot 10^{28}$ atoms/cm²s. The substitution of A , α , β from Fig. 3 and $K_{N,0}$ into equations for K_N then gives the prospective features of most active sites as $n = (RT \ln K_N / K_{N,0} - A) / \alpha$.

Table 1. Optimal SLB for NH₃ synthesis

	Dynamic \underline{NH} coverage				
	M ₂ N(H)		γ	M ₃ N(H)	
	Rh	Ru		Rh	Ru
α	6.06	7.51	-	5.23	6.64
A	-204.6	-65.0	-	-166	14.7
β	2.43	2.00	-	1.94	1.62
	37.3	11.6	0.25	35.9	1.1
n	36.6	11.2	1	35.1	0.7
	37.5	11.7	0	36.1	1.2
	Equilibrium \underline{NH} coverage				
n	38.0	12.6	-	36.8	2.4

Table 1. gives evidence that adsorption site of 3 Ru atoms should have ~ 1 SLB for non-equilibrium reaction (2), in line with “importance of C₇” sites at Fe single crystals [7]; and SLB about ~ 12 is a feature of site formed by 2 Ru atoms close to that at (110)-(2x1) plane, while Rh is an unpromising catalyst in any case due to unrealistic SLB values.

CONCLUSION

The sum of bonds lost by atoms of an adsorption site at clean surface, as compared to bulk atom, is considered as a measure of local imperfection. Surface defects provide the formation of weakly bound, but very inclined to hydrogenation state of atomic nitrogen that makes the grain boundary to be the center for surface wave nucleation during NO+H₂ reaction on Rh tip. In same terms, an optimal adsorption site for NH₃ synthesis consisted of 2 and 3 Ru atoms is characterized by 12 and 1 lost bonds, respectively, while Rh is a poor catalyst. Similar approach can be applied to any other adsorption or catalytic process exhibiting surface sensitivity.

ACKNOWLEDGEMENT

This work is supported by the Russian Foundation for Basic Research (Grants no. 12-03-00766 and 14-03-00285).

REFERENCES

- [1] F. Liu, H. He, Z. Lian, W. Shan, L. Xie, K. Asakura, W. Yang, H. Deng, J. Catal., 2013, 307, 340-351.
- [2] A. R. Cholach, M. F. H. Van Tol, B. E. Nieuwenhuys, Surf. Sci., 1994, 320, 281-294.
- [3] R. Imbihl, Surf. Sci., 2009, 603, 1671-1679.
- [4] F. Vines, Y. Lykhach, T. Staudt, M.P.A. Lorenz, C. Papp, H. P. Steinrueck, J. Libuda, K. M. Neyman, A. Goerling, Chem. – Eur. J., 2010, 16, 6530-6539.
- [5] A. R. Cholach, N. N. Bulgakov, Catalysis Letters, 2013, 143, 817-828.
- [6] F. Esch, A. Baraldi, C. Comelli, S. Lizzit, M. Kiskinova, P. D. Cobden, B. E. Nieuwenhuys, J. Chem. Phys., 1999, 110, 4013-4019.
- [7] D. R. Strongin, J. Carrazza, S.R. Bare, G.A. Somorjai, J. Catal., 1987, 103, 213-215.

PHOTOCATALYTIC ACTIVITIES OF NANODIMENSIONAL COBALT-FERRITE TYPE OF POWDERS IN THE DEGRADATION OF REACTIVE BLACK 5 DYE

K. Zaharieva¹, K. Milenova¹, Z. Cherkezova-Zheleva¹, A. Eliyas¹,
D. Jovanović² and I. Mitov¹

¹*Institute of Catalysis, Bulgarian Academy of Sciences,
Acad. G. Bonchev St., Block 11, 1113 Sofia, Bulgaria. (zzhel@ic.bas.bg)*

²*University of Belgrade, Institute of Chemistry, Technology and Metallurgy
Center of Catalysis and Chemical Engineering, Njegoseva 12,
Belgrade 11000, Serbia*

ABSTRACT

The photocatalytic activities of cobalt-ferrite type of powders, prepared by co-precipitation only or by combined co-precipitation and mechanochemical treatment, have been tested in the present research work. The oxidative photodegradation of model wastewater pollutant Reactive Black 5 dye under UV light irradiation, using nanosized cobalt-ferrite type of materials, has been investigated. The photocatalytic experiments established that the mechanochemically activated nano-dimensional cobalt-ferrite type of photocatalysts show higher photocatalytic activities than those of the co-precipitated ferrite type of samples. The degree of degradation of Reactive Black 5 dye varies within the range 61-99% for the studied nanostructured cobalt-ferrite type of photocatalysts.

INTRODUCTION

The synthetic dyes find wide applications in paper, textile, galvanic and printing industries and also in dyeing facilities [1]. In the textile industry the Reactive Black 5 dye has been used for the coloring of woollen, cotton and nylon fabrics extensively applicable in the everyday life of people. It is reported to have a toxic effect and to cause allergic reactions of respiratory tract [1]. The synthetic azo dyes having sulfo-functional group are highly soluble in water and they demonstrate a wide variety of colors. Most of the methods for discoloring wastewaters do not influence the structure of this dye and this could be due to the stability of benzene and naphthalene nuclei and presence of various substituents [2]. The photocatalytic degradation of Reactive Black 5 dye using different catalysts has been studied in previous works of researchers [3, 4] and other authors. The principal aim of the

present study was to investigate the photocatalytic activity of nanosized cobalt-ferrite type of materials by testing them in the reaction of Reactive Black 5 dye oxidative photodegradation under UV light irradiation. The photocatalytic properties of cobalt-ferrite type of photocatalysts prepared by different methods such as co-precipitation only or combination of co-precipitation and then mechanochemical activation are compared in order to select the most efficient procedure for the catalyst preparation designed for the degradation of Reactive Black 5 dye as model pollutant.

EXPERIMENTAL

The nanosized cobalt-ferrite type of samples, denoted as **Sample A** - $\text{Co}_{0.25}\text{Fe}_{2.75}\text{O}_4$, **Sample B** - $\text{Co}_{0.5}\text{Fe}_{2.5}\text{O}_4$, **Sample C** - $\text{Co}_{0.75}\text{Fe}_{2.25}\text{O}_4$ and **Sample D** - CoFe_2O_4 have been synthesized using co-precipitation only, while **Sample E** - $\text{Co}_{0.5}\text{Fe}_{2.5}\text{O}_4$, **Sample F** - CoFe_2O_4 have been obtained by co-precipitation, followed by mechanochemical activation as the methods, described for preparation in our previous investigations [5,6]. The structure and magnetic behaviour of cobalt-ferrite type of materials have been investigated by various physicochemical methods, such as X-ray diffraction analysis, Moessbauer and FTIR spectroscopy [5,6]. The textural characteristics of obtained ferrite type samples have also been measured. The photocatalytic degradation of Reactive Black 5 dye (RB5) under UV-light irradiation has been tested using polychromatic UV-A lamp (Sylvania BLB, 18 W) with wavelength range 315-400 nm and a maximum intensity at 365 nm. The degree of degradation of the model pollutant RB5 dye was measured by UV-Vis absorbance spectrophotometer CamSpec M501 in the wavelength interval from 200 to 800 nm. All photocatalytic experimental runs have been made at one and the same stirring rate - 400 rpm at room temperature. The adsorption-desorption equilibrium of the samples has been achieved in the dark for 30 min before switching on the UV irradiation lamp. A volume of 150 ml aqueous solution of RB5 (20 ppm concentration) was charged in a semi-batch reactor. An amount of 0.15g nanodimensional cobalt ferrite was added to the solution for the photocatalytic activity testing.

RESULTS AND DISCUSSION

The X-ray diffraction patterns of the synthesized cobalt-ferrite type of materials show the presence of a non-stoichiometric single ferrite phase $\text{Co}_x\text{Fe}_{3-x}\text{O}_4$ (PDF-22-1086; 75-0449) in case of samples **A** and **E**. The ferrite phase and additional amount of intermediate phases such as $\beta\text{-FeOOH}$ (PDF-75-1594) and iron-cobalt hydrotalcite (PDF-14-0191) have also been registered in XRD patterns of samples **B**, **C** and **D**. The **Sample F** contains

a non-stoichiometric spinel ferrite and cobalt iron phases [5, 6]. The mean crystallite size of the obtained cobalt-ferrite type of materials, calculated by the PowderCell software, is varying in the range 6-13 nm. The Moessbauer investigations established the superparamagnetic (SPM) behaviour of ferrite particles [5,6]. The photocatalytic activity results on the degree of oxidative conversion of RB5 dye under UV-light illumination, using the synthesized cobalt-ferrite type of photocatalysts, are represented in Figure 1.

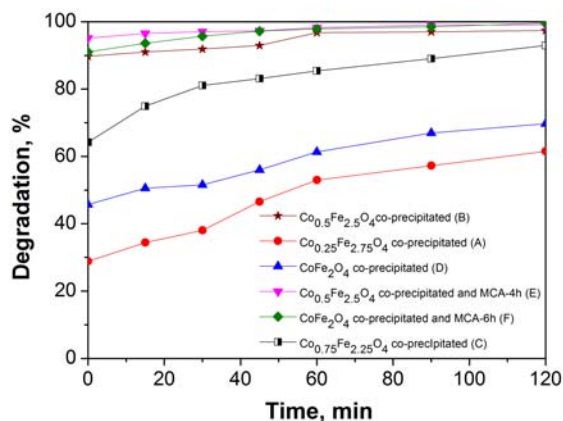


Figure 1. Degree of degradation of RB5 dye solution after 120 minutes of UV-light irradiation using different cobalt-ferrite type of photocatalysts.

As it can be seen, the degree of RB5 dye degradation varies between 61-99% depending on the used sample of cobalt ferrite. For the mechanochemically treated samples **E** and **F** the photodegradation process of the RB5 dye reached up to 99% manifesting the highest efficiency of these samples in the oxidative photocatalytic degradation of RB5 dye under UV-light irradiation. The samples **B** and **C** show slightly lower degrees of degradation of the dye (respectively 97% and 93% conversion) than that of the mechanochemically activated **E** and **F** samples, but yet higher in comparison to the co-precipitated **A** (61%) and **D** (70%). The higher degree of degradation of RB5 dye and also photocatalytic activity of mechanochemically treated samples **E** and **F** than the other cobalt ferrite-type materials is due to the presence of defects on inner surface of investigated photocatalysts induced by mechanochemical activation as method for preparation [7]. The changes in the photocatalytic activity of co-precipitated ferrite-type samples **A**, **B**, **C** and **D** could be attributed to the different degrees of incorporation of cobalt ions in magnetite host structure. The rate constants of nanosized cobalt-

ferrite catalysts are calculated by slopes of the $\ln(C/C_0) = f(t)$ dependences revealing first order reaction kinetics at low coverage. The photocatalytic activities of ferrite samples decrease in the order **Sample E** ($k=60.9 \times 10^{-3} \text{ min}^{-1}$) > **Sample F** ($k=53.4 \times 10^{-3} \text{ min}^{-1}$) > **Sample B** ($k=40.8 \times 10^{-3} \text{ min}^{-1}$) > **Sample C** ($k=26.8 \times 10^{-3} \text{ min}^{-1}$) > **Sample D** ($k=12.6 \times 10^{-3} \text{ min}^{-1}$) > **Sample A** ($k=9.8 \times 10^{-3} \text{ min}^{-1}$). The investigations established that the mechanochemically activated **Sample E** manifests the highest rate constant for photocatalytic degradation of RB5 dye under UV-light irradiation compared to the other samples. The co-precipitated **Sample B** shows the highest photocatalytic activity in comparison to the other three co-precipitated ferrite type of catalysts. The textural investigations of co-precipitated cobalt-ferrite type materials established that they are all mesoporous type of materials. The cobalt-ferrite type of samples, prepared by combined co-precipitation and mechanochemical activation, showed characteristic features of macroporous (or non-porous) materials. The co-precipitated **Sample C** - $\text{Co}_{0.75}\text{Fe}_{2.25}\text{O}_4$ shows the highest specific surface area $S_{\text{BET}} = 210 \text{ m}^2/\text{g}$ than the others cobalt-ferrite type materials.

CONCLUSIONS

The photocatalytic measurements confirmed that the obtained nanostructured cobalt-ferrite type of powders exhibit good photocatalytic efficiency in oxidative degradation of RB5 dye under UV-light irradiation. The combination of a co-precipitation procedure and mechanochemical treatment leads to obtaining superior performance ferrite materials with a higher photocatalytic activity, especially the **Sample E** - $\text{Co}_{0.5}\text{Fe}_{2.5}\text{O}_4$ ($60.9 \times 10^{-3} \text{ min}^{-1}$), than that of the co-precipitated nanodimensional cobalt-ferrite type of samples. The highest photocatalytic activity of **Sample E** is a result of appropriate preparation method, which leads to obtaining of single ferrite phase material and generation of defects revealing inner surface of catalyst. The mechanochemical activation improves the photocatalytic properties of nanosized cobalt ferrite-type samples revealing inner surface. The obtained results show that synthesized nanodimensional cobalt-ferrite type of materials could be successfully used to remove impurities containing RB5 dye from waters.

ACKNOWLEDGMENTS

The authors appreciate the financial support of the Bulgarian National Science Fund by Project DFNI-E01/7/2012 and Serbian Ministry of Education, Science and Technology Development by Project III 45001.

REFERENCES

- [1] M. S. Usha, B. Sasirekha, R. B. Bela, S. Devi, C. Kamalini, G. A. Manasa, P. M. Neha, *Journal of Chemical and Pharmaceutical Research*, 2011, 3 (6), 450-457.
- [2] M. Nisar, S. Nosheen, A. Noreen, I. Majeed, A. Saleem, M. Ahmad Sheikh, *African Journal of Environmental Science and Technology*, 2011, 5 (11), 916-923.
- [3] O. K. Mahadwad, P. A. Parikh, R. V. Jasra, C. Patil, *Bull. Mater. Sci.*, 2011, 34 (3), 551–556.
- [4] C. Tang, V. Chen, *Water Research*, 2004, 38, 2775–2781.
- [5] Z. Cherkezova-Zheleva, K. Zaharieva, B. Kunev, M. Shopska, I. Mitov, *Nanoscience and Nanotechnology* (Eds. E. Balabanova, E. Mileva), 2013, 13, 82-85.
- [6] K. Zaharieva, V. Rives, M. Tsvetkov, R. Trujillano, B. Kunev, I. Mitov, M. Milanova, Z. Cherkezova-Zheleva, *ICNN 2014: International Conference on Nanoscience and Nanotechnology*, Paris, France, 28-29 April, 2014, *International Science Index*, 2014, 8 (4), 991-992.
- [7] R. A. Buyanov, V.V. Molchanov, V.V. Boldyrev, *Catalysis Today*, 2009, 144, 212–218.

EFFECT OF Mg ADDITIVE ON THE STRUCTURE AND TEXTURE OF Ni/SiO₂ PRECURSORS OF VEGETABLE OIL HYDROGENATION CATALYSTS

M. Gabrovska*¹, D. Nikolova¹, M. Shopska¹, P. Tzvetkov², L. Spasov¹ and D. Simeonov²

¹*Institute of Catalysis, Bulgarian Academy of Sciences, Acad. G. Bonchev str., bl. 11, Sofia 1113, Bulgaria (margarita.gabrovska@abv.bg)*

²*Institute of General and Inorganic Chemistry, Bulgarian Academy of Sciences, Acad. G. Bonchev str., bl. 11, Sofia 1113, Bulgaria*

³*University of Belgrade, Institute of Chemistry, Technology and Metallurgy, Department of Catalysis and Chemical Engineering, Njegoševa 12, Belgrade 11000, Republic of Serbia*

ABSTRACT

The effect of Mg addition on the structure and texture of Ni/SiO₂ precursors synthesized using two types of different commercial silica gel, denoted as SIG-A and SIG-C, has been examined applying X-ray diffraction, Infrared spectroscopy, and N₂ physisorption techniques. It was found that modification by Mg brings about coexistence of Ni and Ni,Mg phyllosilicate phases, the latter being better crystallized in the MgNi/SIG-A sample. It was clarified that the MgNi/SIG-C sample is a promising material for vegetable oil hydrogenation catalysts due to its suitable pore system.

INTRODUCTION

Currently, metallic nickel (22–25 wt. % Ni) supported on different sources of silica, represents the main component of the commonly applied commercial catalyst for vegetable oil hydrogenation [1,2]. Despite intensive research activity in this field, the role of dopants on the structural and textural properties of the nickel catalyst precursors is scarcely discussed in the literature, particularly those, which might form compounds similar to that of the parent metal [3]. Therefore, the purpose of the present work was to study the effect of Mg additive on the structural and textural properties of Ni/SiO₂ systems by means of X-ray diffraction, Infrared spectroscopy, and N₂ physisorption techniques.

EXPERIMENTAL

Mg-modified samples were synthesized with identical composition (SiO₂/Ni=1.0 and Mg/Ni=0.1) by co-precipitation using aqueous solutions

of $\text{Ni}(\text{NO}_3)_2 \cdot 6\text{H}_2\text{O}$, $\text{Mg}(\text{NO}_3)_2 \cdot 6\text{H}_2\text{O}$, and Na_2CO_3 on SiO_2 supports. By analogy with non-modified Ni/SiO_2 samples, two types of commercial silica gel (SIG-A and SIG-C), differing in textural parameters, were applied as sources of silica support [4]. Detailed description of the preparation procedure is reported in our recent paper [5]. Powder X-ray diffraction (PXRD) patterns were recorded on a Bruker D8 Advance powder diffractometer employing CuK_α radiation. Infrared (IR) spectra within the range of $4000\text{--}400\text{ cm}^{-1}$ were recorded on a Nicolet 6700 FTIR spectrometer (Thermo Electron Corporation, USA) at 0.4 cm^{-1} resolution and 50 scans, using KBr pressed disk technique with sample concentration of $\sim 0.5\text{ wt. \%}$. Low-temperature N_2 sorption analyses were performed on a Sorptomatic 1990 (Thermo Finnigan) apparatus. Specific surface area (S_{BET}) and C constant values were calculated according to the BET method from the linear part of the N_2 adsorption isotherms. Mesopore volume (V_{meso}) data were acquired from isotherms adsorption branch by means of the Dollimore-Heal method. Micropore volume (V_{micro}) values were calculated using the Dubinin-Radushkevich method.

RESULTS AND DISCUSSION

Chrysotile, a monoclinic Mg-silicate ($\text{Mg}_3\text{Si}_2\text{O}_5(\text{OH})_4$) represents a group of polymorphous minerals with the same chemical composition but different crystal system, namely Lizardite, $\text{Mg}_3\text{Si}_2\text{O}_5(\text{OH})_4$ (hexagonal), Antigorite, $\text{Mg}_3\text{Si}_2\text{O}_5(\text{OH})_4$ (monoclinic), Pecoraite, $\text{Ni}_3\text{Si}_2\text{O}_5(\text{OH})_4$ (monoclinic), etc. Pecoraite is a nickel analogue of Chrysotile. Because of similar ionic radii, it is expected that Ni^{2+} ions (0.069 nm) may replace six-coordinated Mg^{2+} entities (0.074 nm) in hydrous Ni-Mg silicates, such as Nepouite, $(\text{Ni},\text{Mg})_3\text{Si}_2\text{O}_5(\text{OH})_4$ (orthorhombic). Nepouite and Pecoraite possess a layered structure that consists of a tetrahedral sheet joined to an octahedral one. In the octahedral sites, a complete solid solution is possible between divalent cations of Mg and Ni with a general formula $(\text{Mg},\text{Ni})_{3-x}\text{Si}_2\text{O}_5(\text{OH})_4$ [6].

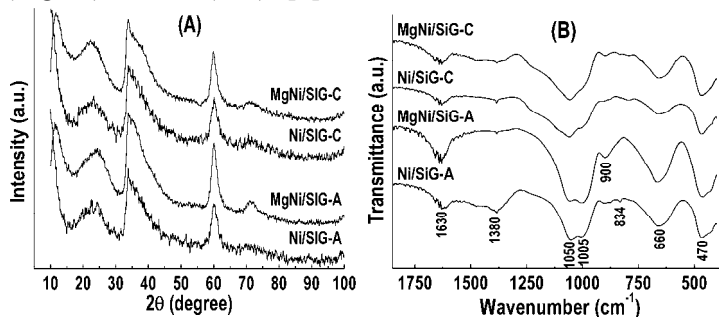


Figure 1.
PXRD
patterns
(A) and IR
spectra (B)
of the
precursors

PXRD patterns of the as-prepared non-modified samples (Fig. 1A) reveal the presence of a nickel silicate hydroxide (Pecoraite, $\text{Ni}_3\text{Si}_2\text{O}_5(\text{OH})_4$, JCPDS file 00-049-1859) phase [5]. Diffractograms of Mg-modified samples (Fig. 1A) manifest a simultaneous occurrence of the Pecoraite and Nepouite ($\text{Ni,Mg})_3\text{Si}_2\text{O}_5(\text{OH})_4$, JCPDS file 00-025-0524) phases. Because of turbostratic structure of the registered phases [7], the diffraction lines of all XRD patterns were not clearly organized however, they were better defined with the Mg-modified samples, particularly in MgNi/SIG-A.

IR spectra of the studied samples are displayed in the frequency range of $1800\text{--}400\text{ cm}^{-1}$ since variations in the absorption profiles characterizing the Ni-O-Si interactions are observed in this region (Fig. 1B). It can be seen that typical bands due to silica network are absent [5]. A doublet at 1050 and 1005 cm^{-1} , and a band at $\sim 660\text{ cm}^{-1}$ are related to the formation of Ni-phyllsilicate structure ($-\text{Si}-\text{O}-\text{Ni}-$), which cover the surface of the support particles [6,8]. The generation of a Ni-phyllsilicate phase is most significant in MgNi/SIG-A. A low intensity band at $\sim 900\text{ cm}^{-1}$ can be ascribed to the stretching vibrations of free Si-OH groups on the surface of the solids. Bands assigned to CO_3^{2-} anions ($\sim 1380\text{ cm}^{-1}$) and to bending vibrations at $\sim 1630\text{ cm}^{-1}$ of H_2O molecules were also detected [8,9]. Close inspection of the bands gives evidence for creation of different Ni^{2+} species on sample surfaces. A well expressed band at $\sim 1380\text{ cm}^{-1}$ and a weak one at $\sim 834\text{ cm}^{-1}$ in the IR spectrum of Ni/SIG-A are attributed to the presence of a basic nickel carbonate phase located on the surface of the Ni-phyllsilicate [5,10]. However, these bands were not registered with the MgNi/SIG-A sample proving the formation of a strongly bonded Ni,Mg-phyllsilicate phase.

Table 1. Textural characteristics of the precursors

Sample	S_{BET} (m^2/g)	V_{micro} (cm^3/g)	V_{meso} (cm^3/g)	d_{aver} (nm)	C
Ni/SIG-A	269	0.10	0.32	8.8	135
Ni/SIG-C	367	0.13	0.46	10.2	139
MgNi/SIG-A	341	0.13	0.35	9.2	186
MgNi/SIG-C	197	0.07	0.35	15.1	152

It is evident that modification by Mg causes an increase in S_{BET} for the MgNi/SIG-A sample (Table 1) in comparison with Ni/SIG-A due to formation of micropores (an increase in V_{micro}). On the contrary, S_{BET} for the MgNi/SIG-C solid diminishes considerably compared to Ni/SIG-C as a result of a two-fold decrease in V_{micro} . An increase of the C constant values observed with the Mg-containing samples was more pronounced for

MgNi/SIG-A which may be assigned to enhanced surface polarity [4] due to formation of mesoporous Ni,Mg phyllosilicate structures. The presence of Mg in the Ni/SiO₂ samples decreases the d_{aver} values in the following order: MgNi/SIG-C > Ni/SIG-C > MgNi/SIG-A >> Ni/SIG-A. It is known that a larger pore diameter permits faster diffusion of the reactants [1], thus higher values of d_{aver} for the MgNi/SIG-C sample may be a precondition for a higher reaction rate.

CONCLUSIONS

Based on characterization studies it may be summarized that magnesium addition to Ni/SiO₂ samples gives rise to formation of well-organized Ni and Ni,Mg phyllosilicate-type structures, which are more pronounced for MgNi/SIG-A. A considerable effect of magnesium is found on the texture of MgNi/SIG-C sample, which exhibits a smaller amount of micropores and a larger average pore diameter in comparison with other studied materials, thus improving the access of triacylglycerol molecules to the internal surface. One would expect an enhanced performance in the vegetable oil hydrogenation of the Mg-containing catalysts.

ACKNOWLEDGEMENT

This work was partially supported by the Ministry of Science of the Republic of Serbia (Grants no. III 45001).

REFERENCES

- [1] M. Balakos, E. Hernandez, *Catal. Today*, 1997, 35, 415-425.
- [2] J. Veldsink, M. Bouma, N. Schöön, A. Beenackers, *Catal. Rev. - Sci. Eng.*, 1997, 39, 253-318.
- [3] G. Babu, K. Ghuge, S. Rammohan, V. Krishnan, A. Bhat, *Catal. Lett.*, 1992, 15, 95-103.
- [4] D. Nikolova, J. Krstić, L. Spasov, D. Simeonov, D. Lončarević, Pl. Stefanov, D. Jovanović, *Russ. J. Phys. Chem. A*, 2011, 85, 2380-2385.
- [5] M. Gabrovska, J. Krstić, P. Tzvetkov, K. Tenchev, M. Shopska, N. Vukelić, D. Jovanović, *Russ. J. Phys. Chem. A*, 2011, 85, 2392-2398.
- [6] B. Reddy, R. Frost, M. Dickfos, *Spectrochim. Acta A*, 2009, 71, 1762-1768.
- [7] K. Ghuge, A. Bhat, G. Babu, *Appl. Catal. A: Gen.*, 1993, 103, 183-204.
- [8] J. Sohn, *Catal. Today*, 2002, 73, 197-209.
- [9] R. Lenza, W. Vasconcelos, *Mater. Res.*, 2001, 4, 189-194.
- [10] O. Solcova, D-C Uecker, U. Steinike, K. Jiratova, *Appl. Catal. A: Gen.*, 1993, 94, 153-160.
- [11] A. Lecloux, J. Pirard, *J. Colloid Interface Sci.*, 1979, 70, 265-281.

PHOTOCATALYTIC ACTIVITY OF PEG-MODIFIED CATALYSTS

D. Lončarević¹, J. Dostanić¹ and A. Radosavljević-Mihajlović²

¹*University of Belgrade, Institute of Chemistry, Technology and Metallurgy, Department of Catalysis and Chemical Engineering, Njegoševa 12, Belgrade, Serbia. (dloncarevic@nanosys.ihtm.bg.ac.rs)*

²*University of Belgrade, Institute of Nuclear Sciences Vinča, Laboratory for Material Science, P.O. Box 522, Belgrade, Serbia.*

ABSTRACT

This work is focused on the influence of polyethylene glycol (PEG) on structural, textural and photocatalytic properties of titanium dioxide (TiO₂) catalyst. Catalysts were synthesized by sol-gel method using PEG with different molecular weight (600 and 10000) as pore generating agent. The results showed that PEG enhances not only porous structure but also change anatase to rutile ratio. The photocatalytic activity of the synthesized catalyst was measured by decomposition of phenol. The order of catalyst photoactivity was: TiO₂/P600>TiO₂/P10000>TiO₂. The difference in catalyst photoactivity is attributed to their surface area and anatase fraction, rather than pore size.

INTRODUCTION

In the last decades photocatalysis became attractive method for the treatment of air and water pollution. The appliance of nanosized metal oxides, typically semiconductors, as photocatalyst has been studied intensively [1]. TiO₂ generate special interest as photocatalyst, due to its high photocatalytic activity, non-toxicity, chemical stability and low cost [2]. Among three distinct crystallographic forms (anatase, rutile and brookite), anatase is considered to be the most active phase, due to the lowest rate of electron/hole recombination [3]. Textural properties such as specific surface area, porosity and mean pore size are also of great importance and can be decisive factor for photocatalytic application [4]. The highly porous structure of catalyst is an imperative, since it offers a much larger number of catalytic sites than a dense structure.

Sol-gel method is one of the most used methods for the synthesis of solid inorganic materials [5]. The hydrolysis and polycondensation rate strongly affects the structure and properties of TiO_2 . One possibility to restrain the rapid hydrolysis and polycondensation is to use different organic additives during catalyst preparation [6]. Condensation process is accomplished by gelization, which is followed by calcination. Since calcination leads to decrease in catalyst porosity, organic templates, such as PEG [7] etc., are often used in order to retain the porous structure of the catalyst after calcinations.

This study investigates the influence of textural and structural parameters on photocatalytic activity of PEG-modified TiO_2 catalyst.

EXPERIMENTAL

TiO_2 catalysts were synthesized by sol-gel process. Briefly, 3.73 mL of titanium-tetraisoopropoxide was dissolved in 10 mL of anhydrous ethanol and 1.15 mL of diethanol amine at room temperature (solution A). Meanwhile, 35 mL of anhydrous ethanol was mixed with 3.75 mL of water (solution B). Solution A was subsequently added dropwise to solution B within 20 min. After that, 1.0 g of PEG was added to solution and stirred for another 40 min. The stabilized sol was aged for another 12 h at room temperature. The formed gel was then dried in an oven for 12 h at temperature of 80 °C, and calcined at 550 °C for 4 h. The control sample was prepared without the use of the template by the same sol-gel method.

Nitrogen adsorption-desorption isotherms were determined using nitrogen physisorption at -196 °C. Specific surface area (S_{BET}) and pore size (D_{max}) of the samples was calculated from the nitrogen adsorption isotherms according to the BET and BJH methods, respectively. Pore volume (V_{pore}) was determined by mercury intrusion porosimetry. Powder X-Ray diffraction patterns were measured on a diffractometer using Cu-K α radiation ($\lambda = 1.5418 \text{ \AA}$).

Photocatalytic tests were performed in an open cylindrical thermostated Pyrex cell (250 mL). The irradiation was performed using Osram Ultra Vitalux lamp (300 W), housed 50 cm above the top surface of the dye solution. Photocatalytic activity of catalysts was measured by decomposition of phenol in aqueous solution. Applied conditions used during photocatalytic tests were: solution volume: 150 mL, initial phenol concentration: $2.8 \times 10^{-5} \text{ mol/L}$, T: 30 °C, catalyst mass: 1.5 g. The concentration of phenol during catalytic tests was determined using UV-Vis spectrophotometer. The phenol removal, i.e. conversion efficiency, X, was determined using equation $X = (C_0 - C) / C_0$, where C_0 is the initial phenol concentration and C is the phenol concentration for the specified time.

RESULTS AND DISCUSSION

Table 1 presents textural and structural of the prepared catalyst. It can be seen that PEG-modified samples have noticeably larger pore volume and surface area than unmodified sample. The largest pore volume and specific surface is obtained for the sample TiO₂/P600, while sample TiO₂/P10000 has the largest pore diameter.

Table 1. Textural and structural properties of TiO₂ samples

Sample	S _{BET} [m ² /g]	D _{max} [nm]	V _{pore} [mm ³ /g]	Fraction of	
				Anatase	Rutile
				[%]	
TiO ₂	4.8	16.4	13	17.2	82.8
TiO ₂ /P600	28.3	15.7	125	74.2	25.8
TiO ₂ /P10000	14.4	18.3	97	45.8	54.2

Increasing molecular weight of PEG molecules led to higher pore diameter and smaller surface area. However, the samples didn't have the same porosity as it was expected. The difference in porosity indicates different stability of porous network during thermal treatment, which is a consequence of pore shrinkage.

The calculated weight fractions of the anatase and rutile phases for samples are presented in Table 1. The maximum rutile fraction was observed for the unmodified sample TiO₂, while PEG modified sample contain lower fraction of rutile phase. Among modified samples, sample TiO₂/P600 contain higher fraction of anatase phase then sample TiO₂/P10000.

The photocatalytic degradation of phenol was presented in Fig. 1. The results clearly indicate that PEG-modified samples exhibit significantly higher activity compared to the activity of the control unmodified sample. The increased activity of PEG-modified samples can be attributed to their higher surface area, pore volume and pore size. In addition, higher fraction of active anatase phase of PEG-modified samples additionally enhances their activity. Among modified samples, the sample TiO₂/P600 displayed significantly higher activity compared to the sample TiO₂/P10000. The

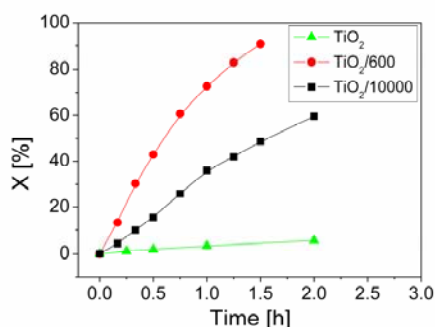


Figure 1. Photodegradation of phenol.

obtained results indicate that specific surface area and anatase to rutile ratio contribute more in determining photocatalytic efficiency, then pore size.

CONCLUSION

The results of this study illustrate the influence of PEG on textural, structural and photocatalytic properties of TiO₂ materials. The decomposition of PEG during thermal treatment led to generation of porous structure, thus improving the textural properties of samples. Also, PEG introduction changes anatase to rutile ratio. PEG-modified samples displayed significantly higher activity than unmodified sample. Among modified samples TiO₂/P600 showed higher activity than TiO₂/P10000. The difference in activity is attributed to the surface area and anatase to rutile ratio. Variation in pore size are found not to be decisive factor for photocatalytic efficiency.

ACKNOWLEDGEMENT

This work was supported by the Ministry of Education, Science and Technological Development of the Republic of Serbia (Projects No. III 45001).

REFERENCES

- [1] D. A. Tryk, A. Fujishima, K. Honda, *Electrochimica Acta*, 2000, 45, 2363-2376.
- [2] D. Beydoun, R. Amal, G. Low, S. McEvoy, *Journal of Nanoparticle Research*, 1999, 571, 439-458.
- [3] I. K. Konstantinou, T. A. Albanis, *Applied Catalysis, B: Environmental*, 2004, 49, 1-14.
- [4] Y. Chen, D. D. Dionysiou, *Applied Catalysis B: Environmental*, 2006, 69, 24-33.
- [5] C. Su, B-Y. Hong, C-M. Tseng, *Catalysis Today*, 2004, 96, 119-126.
- [6] S. J. Bu, Z. G. Jin, X. X. Liu, L. R. Yang, Z. J. Cheng, *Journal of the European Ceramic Society*, 2005, 25, 673-679.
- [7] B. Guo, Z. Liu, L. Hong, H. Jang, *Surface and Coatings Technology*, 2005, 198, 24-29.

CATALYTIC ACTIVITY OF PEROVSKITE TYPE OF OXIDES IN THE REACTION OF NITRIC OXIDE REDUCTION WITH CARBON MONOXIDE

D. Stoyanova¹, S. Petrović², P. Georgieva¹, A. Terlecki-Baricević² and D. Mehandjiev¹

¹*Institute of General and Inorganic Chemistry, BAS, 1113, Sofia, Bulgaria,
e-mail: dsto@svr.igic.bas.bg*

²*Department of Catalysis and Chemical Engineering, Institute of
Chemistry, Technology and Metallurgy, 11000 Belgrade, Serbia*

ABSTRACT

The catalyst samples under investigation have been prepared by the method of mixing in different ratios La_2O_3 , MgO , TiO_2 and Fe_2O_3 , followed by milling for 1 hour in a planetary ball mill and heating at temperature 1000°C for 10 hours. The samples have been characterized by chemical analysis, phase composition analysis and by XPS spectroscopy. Specific surface area of the samples is determined by BET single point method. Catalytic activity has been measured in the reaction of NO reduction with CO. The obtained results show that the perovskite structure of the precursor is of fundamental importance for this reaction as well as the inclusion of iron ions in it, which are involved in the formation of catalytically active sites (CAS).

INTRODUCTION

The application of oxides having a perovskite structure as catalyst precursors opens up an interesting possibility to develop highly active catalysts for various reactions. It has been shown in a previous work of some of the authors of the present one, that the perovskite type of oxides with the general formula LaMO_3 , in which M has been substituted respectively with Mg, Ti or Fe, catalyst samples can be prepared possessing some catalytic activity in regard to complete oxidation of methane [1]. At the same time it has been reported [2] that upon depositing palladium on the same type of perovskite – $\text{La}(\text{TiMg})\text{O}_3$ an efficient catalyst is obtained for reducing nitric oxide with carbon monoxide. For this reason the aim of the present work was to ascertain to what extent the inclusion of iron ions in this type of oxides with perovskite structure, such as $\text{La}(\text{TiMg})\text{O}_3$ for example, is leading to possible changes in the catalytic activity with respect to this specific reaction.

RESULTS AND DISCUSSION

The catalyst samples have been synthesized by mixing in various ratios La_2O_3 (99.99% purity), MgO (96.0%), TiO_2 (99.0%) and Fe_2O_3 (99.5 %), followed by milling for 1 hour in a planetary type of ball mill and calcination at temperature 1000°C in the course of 10 hours. The obtained catalyst samples are denoted as follows:

1 - $\text{LaTi}_{0.5}\text{Mg}_{0.5}\text{O}_3$ – TM (50:50); **2** - $\text{LaTi}_{0.4}\text{Mg}_{0.1}\text{Fe}_{0.4}\text{O}_3$ MF(10:40); **3** - $\text{LaTi}_{0.4}\text{Mg}_{0.4}\text{Fe}_{0.2}\text{O}_3$ - MF (40:20); **4** - $\text{LaTi}_{0.4}\text{Mg}_{0.5}\text{Fe}_{0.13}\text{O}_3$ - TF (40:13); **5** - $\text{LaTi}_{0.1}\text{Mg}_{0.5}\text{Fe}_{0.53}\text{O}_3$ -TF (10:53).

Table 1 lists the results from the chemical analysis of the samples, their specific surface area and the phase composition. All the catalyst samples reveal basically a well crystallized perovskite phase possessing orthorhombic structure. Moreover traces of the La_2O_3 phase are also observed, which has a higher content in the sample TF (10:53).

Table1. Chemical composition, phase composition and specific surface areas of the catalyst samples.

Catalyst sample notation	Chemical composition, at.%					Phase composition	Specific surface area, S (m^2/g)
	La	Ti	Mg	Fe	O		
TM(50:50)	20.0	10.0	10.0	-	60.0	Perovskite, La_2O_3	4.7
MF(10:40)	20.0	8.0	2.0	8.0	60.0	Perovskite	2.4
MF(40:20)	20.0	8.0	8.0	4.0	60.0	Perovskite	3.5
TF(40:13)	20.0	8.0	10.0	2.6	60.0	Perovskite, La_2O_3	3.3
TF(10:53)	20.0	2.0	10.0	10.6	60.0	Perovskite, La_2O_3	2.1

The data from the XPS analysis for the surface concentration of ions in the samples under investigation prove that the oxidation state of the lanthanum is La^{3+} . The surface concentration of this ion does not vary within a wide interval. As far as titanium is concerned its oxidation state is Ti^{3+} and its concentration is changing in accordance with the pre-set composition.

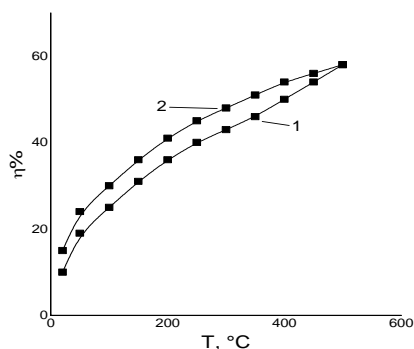


Figure 1. Conversion η (%) of NO – curve 1 and of CO - curve 2 as a function of the temperature for sample.

The same holds true also with respect to the concentration of magnesium, however it is interesting to note that its oxidation state, in view of the XPS data, is in fact Mg^0 , which is probably due to the greater mobility of the electrons in the considered systems. In regard to the iron ions state it was observed that Fe^{2+} ions are present in all the catalyst samples, while in the cases of the MF (40:20) samples and the TF (10:53) samples in addition to the Fe^{2+} ions also some Fe^{3+} ions have been detected. The recorded Moessbauer spectra confirm

the presence of Fe^{3+} ions in octahedral coordination, which fact is evidenced by the quadrupole doublet, characteristic of this state – the samples MF (10:40), MF (40:20) and TF (40:13), but in addition to this doublet a sextet is observed in the TF (10:53) sample, which gives evidence of different configuration of some specific Fe^{3+} ions [1]. Figure 1 illustrates the data on the catalytic activity of the initial TM (50:50) sample, which has not been doped with iron ions.

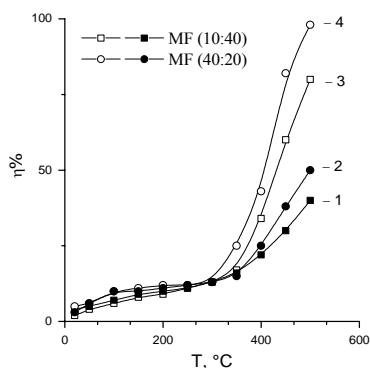


Fig. 2. Degree of conversion η (%) of CO (closed symbols) and NO (open symbols) depending on temperature.

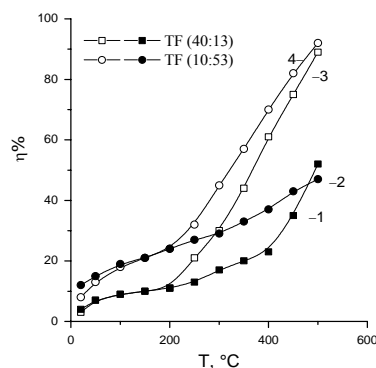


Fig.3. Degree of conversion η (%) of CO (closed symbols) and NO (open symbols) as a function of the temperature.

As it can be seen the course of the dependence: degree of conversion – temperature, both in regard to the nitric oxide, as well as in regard to the carbon monoxide, is one and the same. Upon increasing the temperature the

degree of conversion is growing up. In the case of carbon monoxide this degree is higher, which is most probably connected with the reduction on the surface of the catalyst sample. These dependences manifest quite a different course in the cases of the catalyst samples containing iron ions, represented in Figure 2 and Figure 3. The degrees of conversion for NO and CO over the catalyst samples of the MF series (MF (10:40) and MF (40:20)) - Fig. 2, starting from 20 °C and reaching 300°C, are coinciding in value, which fact is an indication that within this temperature interval only reduction of NO with CO is occurring. At temperature above 400°C there starts a sharp increase in the degree of conversion of NO, while this effect in regard to CO is a weak one. The difference with respect to degree of conversion (η) reaches 40%. The observed effect is even stronger in the case of the TF series of catalyst samples (Fig. 3). These differences show that in addition to the reduction of NO with CO there is a process of direct decomposition of the NO. In order to compare the magnitude of this effect Fig. 4 and Fig. 5 depict the dependences of the NO conversion degree, expressed by the amount of converted NO per one gram of the catalyst sample for one hour - I_g and the quantity of converted NO per unit of surface area for one hour - I_s . The same quantities are also given for comparison with the sample TM (50:50). It is obvious that at temperatures above 400°C in the case of MF samples and above 300°C for the TF samples there starts the occurrence of two reactions – reduction of NO with CO and decomposition of NO, whereupon the catalyst samples of the TF series manifest higher effectiveness in regard to the second reaction. The two reactions occurring on the surface of the catalyst samples can be expressed by the following scheme:



Therefore the inclusion of ions of the iron - Fe^{2+} and Fe^{3+} inside the structure of the perovskite leads to formation of new types of catalytically active sites (CAS), and after a certain temperature they activate the reaction (2).

The main components in these CAS are the Fe^{2+} ions and the Fe^{3+} ions, but it is also probable that the rest of the ions in the catalyst sample composition are also participating.

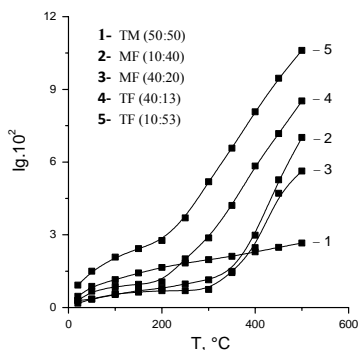


Fig.4. Intensity **I_g** for the conversion of **NO** as a function of the temperature.

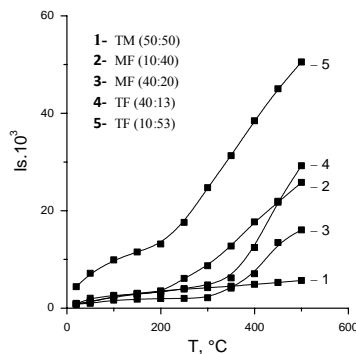


Fig.5. Intensity **I_s** for conversion of **NO** as a function of the temperature.

The most active is the TF (10:53) sample, where the content of Fe^{3+} is the highest, in accordance with the XPS data and it can be supposed that they are playing the most essential role in the catalytic process, described by equation (2). The direct decomposition of NO upon the same type of catalyst sample with perovskite structure, but having additionally palladium deposited on the surface was reported also in ref. [2], and it was assumed there that this fact is owing to the supported palladium ions.

CONCLUSION

Our experimental results show that the perovskite structure of the precursor underlies the basis of the occurring reaction of NO reduction with CO and the inclusion of iron ions in it, which leads to formation of specific catalytically active sites (CAS) for this reaction.

REFERENCES

- [1] S.Petrović, A. Terlecki-Baričević et al., Appl. Catal. B: Environmental, 2008, 79, 186-198.
- [2] M. Khristova, S. Petrovic et al., Centr. Eur. J. Chem., 2009, 7 (4), 857-863.

DIFFERENCES IN THE POTENTIAL ENERGY SURFACE FOR σ -BOND ACTIVATION OF n -C₃H₈ BETWEEN ON W-CENTER AND ON Rh-CENTER

Yo-ichi ISHIKAWA* and Nur Syuhada binti Che Yob

*Department of Chemistry and Materials Technology,
Kyoto Institute of Technology,
Matsugasaki, Sakyo-ku, Kyoto 606-8585 JAPAN*

ABSTRACT

DFT calculations were performed in order to investigate the three types of σ -bonds activation of n -C₃H₈ by coordinatively unsaturated transition metal centers, W(CO)₅ and Rh(Cp)(CO) (Cp = η^5 -C₅H₅). The theoretical results show that n -C₃H₈ coordinates to the coordinatively unsaturated site of W(CO)₅ and Rh(Cp)(CO) in a C-H η^2 -fashion with the small bond dissociation enthalpy (BDE) of *ca.* 30 kJ mol⁻¹. The C-H bond activation of propane does not seem to take place at room temperature because of the larger activation barrier of *ca.* 160 kJ mol⁻¹ and the instability of oxidative addition complex on W(CO)₅, which is quite distinct from Rh(Cp)(CO) with a high ability of σ -bonds activation. The activation energy for C-C bond-fission was higher than that for C-H bond-fission by *ca.* 130 kJ mol⁻¹ on both transition centers.

INTRODUCTION

The σ -bond activation such as C-H or C-C in alkanes on the transition metal center is an important step in many catalytic cycles and so far a number of experimental and theoretical studies have been carried out [1]. Especially a time-resolved infrared absorption spectroscopy in the gas phase has revealed the reaction mechanism and the potential energy surface from the coordination of alkane on the transition metal center to the bond-fission [2, 3]. In the case of tungsten center (W(CO)₅) an agostic complex was observed at room temperature without leading to a bond fission (a formation of oxidative addition complex) [2]. This agostic complex is regarded as a precursor of oxidative addition complex observed in the case of so-called late transition metal center (Rh or Ir) [3]. This agostic interaction is also considered to be associated not only to homogeneous chemical processes, e.g. oxidative addition and reductive elimination, but also to model surface chemistry for catalysis and synthesis.

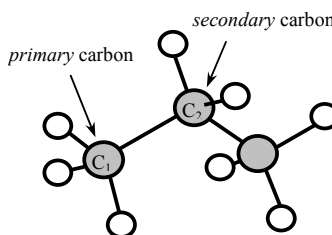
In this study, for the purpose of elucidating the difference in the ability of σ -

bond (*primary*-C-H, *secondary*-C-H, and C-C) activation between the transition metal centers ($W(CO)_5$ and $Rh(Cp)(CO)$), the potential energy surfaces (PESs) leading to bond activation of $n\text{-C}_3\text{H}_8$ on $W(CO)_5$ and on $Rh(Cp)(CO)$ were constructed.

COMPUTATIONAL METHODS

Hybrid DFT(B3LYP) calculations were used for all related transition-metal carbonyl compounds using the Gaussian 03W program. A basis set of 6-311+G(2d,p) functions on H, C, and O atoms and the LANL2DZ basis function with ECP on transition metal atoms were used in our calculations. This combination was chosen because it gave a reasonable optimized structure and vibrational frequency results for C-O stretching mode of some transition metal carbonyls [4].

For three types of σ -bond activation in $n\text{-C}_3\text{H}_8$ (Scheme 1; $p\text{-C-H} = C_1\text{-H}$, $s\text{-C-H} = C_2\text{-H}$, and C-C), the PES of singlet state for bond activation was constructed at B3LYP level. First, an agostic complex and an oxidative complex were optimized and then the transition state was searched using QST2 or QST3 method. After that, the transition state was confirmed by Intrinsic Reaction Coordinate method (IRC).



Scheme 1

RESULTS AND DISCUSSION

Figure 1 shows the optimized structures of agostic complex (Ag-C), transition state complex (TS-C), and oxidative addition complex (Ox-C) when $p\text{-C-H}$ of $n\text{-C}_3\text{H}_8$ coordinates on $W(CO)_5$. In Ag-C, $n\text{-C}_3\text{H}_8$ coordinates to the coordinatively unsaturated site of $W(CO)_5$ in η^2 -fashion and a W-C-H plane divides equally an angle of two neighbor equatorial-CO axes. Such a η^2 -Ag-C was also optimized for Rh case, which

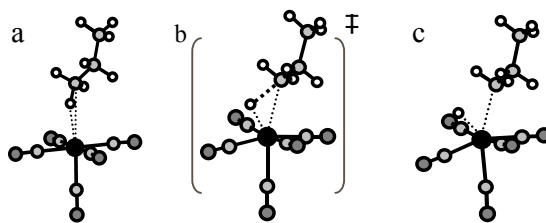


Figure 1. Optimized structures of agostic complex (a), transition state complex (b), and oxidative addition

Table 1. Differences in activated bond length $r(p\text{-C-H})$ between on W center and on Rh center.

Metal center	$r(\text{C-H}) / \text{\AA}$			
	$n\text{-C}_3\text{H}_8$	Ag-C	TS-C	Ox-C
$W(CO)_5$		1.12	2.01	2.33
$Rh(Cp)(CO)$	1.09	1.13	1.55	2.42

is similar to the previous calculation results [5, 6]. The calculated C-H bond length of each complex is shown in Table 1 as an index of bond activation, suggesting that C-H bond is required to be lengthened considerably for the bond activation on W center in comparison with Rh center.

Figure 2 shows the PESs of σ -bond activation on W center and on Rh center calculated at B3LYP level. The η^2 -C-C complex has been optimized neither on W nor Rh. In the both metal centers, the coordinated *p*-C-H and *s*-C-H in agostic fashion has a similar bond dissociation energy (BDE) of *ca.* 30 kJ mol⁻¹ and the position exchange energy between *p*-C-H and *s*-C-H was calculated to be about 20 kJ mol⁻¹.

The activation energy from Ag-C to Ox-C increases in order of *p*-C-H (*ca.* 150 kJ mol⁻¹ on W, *ca.* 50 kJ mol⁻¹ on Rh), *s*-C-H (*ca.* 170 on W, *ca.* 50 on Rh) and C-C (*ca.* 270 on W, *ca.* 180 on Rh) on the both metal centers. The calculation results support that the ability of σ -bond activation of Rh center is much higher than that of W center. This high ability is thought to result not from the initial agostic interaction (BDE) but from the small structural change required for the activation bond at the transition state.

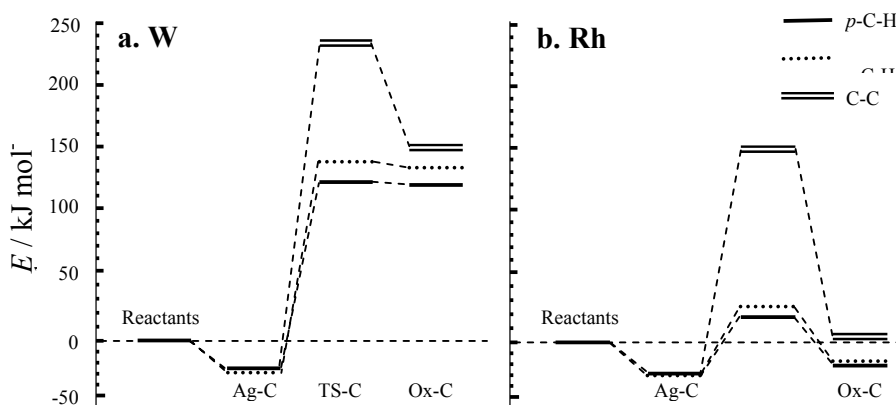


Figure 2. The potential energy surfaces (PESs) of σ -bond activation on W center ($W(CO)_5$) and on Rh center ($Rh(Cp)CO$) calculated at B3LYP level.

CONCLUSION

The calculated CO frequency shifts during the coordination of alkane support the formation of agostic complex on $W(CO)_5$ and that of oxidative addition complex on $Rh(Cp)(CO)$ in the gas phase at room temperature. The activation energy E_a becomes greater in order of *p*-C-H < *s*-C-H < C-C on both transition metals. The low regioselectivity is suggested by the small difference between $E_a(p\text{-C-H})$ and $E_a(s\text{-C-H})$ while the high stereoselectivity is expected by the large difference between $E_a(C\text{-H})$ and $E_a(C\text{-C})$. The high

activation energy for σ -bond activation on W-center is thought to be originated from the large distortion of coordinated alkane required at the transition state.

REFERENCES

- [1] N. Koga and K. Morokuma, *J. Phys Chem.*, 1990, 94, 5454-5462.; *Chem. Rev.*, 1991, 91, 823-842.
- [2] Y. Ishikawa, C. E. Brown, P. A. Hackett, and D. M. Rayner, *Chem. Phys. Lett.*, 1988, 150, 506-510. ; C. E. Brown, Y. Ishikawa, P. A. Hackett, and D. M. Rayner, *J. Am. Chem. Soc.*, 1990, 112, 2530-2536.
- [3] E. P. Wasserman, C. B. Moore, and R. G. Bergman, *Science*, 1992, 255, 315-318.
- [4] Y. Ishikawa and Ye Xie, *Chem. Lett.*, 2007, 36, 754-755. ; Y. Ishikawa and K. Kawakami, *J. Phys. Chem. A*, 2007, 111, 9940-9944.
- [5] P. E. M. Siegbahn, *J. Am. Chem. Soc.*, 1996, 118, 1487-1496.
- [6] M.-D. Su and S.-Y. Chu, *Chem. Eur. J.*, 1999, 5, 198-207.

OPTICAL AND CATALYTICAL PROPERTIES OF MICROWAVE PROCESSED ZnO POWDERS

S. Marković, A. Stanković, V. Rajić, and D. Uskoković

*Institute of Technical Sciences of the Serbian Academy of Sciences and Arts,
Knez Mihailova 35/IV, Belgrade 11001, Serbia
(smilja.markovic@itn.sanu.ac.rs).*

ABSTRACT

Microwave (MW) processing was used for synthesis of ZnO powders with nanospherical morphology. The phase purity and crystal structure of the powders were investigated by X-ray diffraction (XRD) and Raman spectroscopy. The particles morphology and size distributions were studied by FE-SEM and laser diffraction particle size analyzer, respectively. The optical properties were studied using UV-Vis diffuse reflectance and photoluminescence spectroscopy. It is found that the MW synthesized ZnO nanoparticles has increased visible light absorption, also decreased band gap energy (~0.15 eV) compared to bulk ZnO. The enhanced optical properties of ZnO powders are attributed to the existence of lattice defects introduced by fast microwave processing. The effects of lattice defects in ZnO crystal structure on its photocatalytic activity were examined *via* degradation of methylene blue (MB) under direct sunlight irradiation. A large efficiency of MB degradation was found after 6 h of irradiation.

INTRODUCTION

The removal of organic pollutants from wastewater is an important method in environmental protection. Methods such as biosorption, conventional activated sludge treatment process, electrochemical technologies and reverse osmosis have been applied on wastewater treatment. In recent 10 years a heterogeneous photocatalyst has received extensive attention for the degradation and mineralization of organic pollutants from water, where ZnO has established role [1]. However, an energy gap of 3.37 eV (368 nm) means that ZnO can only absorb UV light. Since sunlight is a source of clean and cheap energy, where UV light makes no more than 3–5% of the total sunlight, it is highly desirable to synthesize ZnO-based materials capable for visible light photocatalysts. Several approaches have been applied with the aim of changing the optical absorption properties and improving the visible light photocatalysis including the incorporation of transition metal ions into the crystal structure of a ZnO powder, surface

sensitization of ZnO particles to extend the spectral response into the visible region, etc. Here, we shows an enhanced optical and photocatalytical properties of nanostructured ZnO, based on lattice defects introduced by fast microwave processing.

EXPERIMENTAL

ZnO powders were prepared by microwave (MW) processing of a precipitate. The starting materials were $\text{Zn}(\text{CH}_3\text{COO})_2 \cdot 2\text{H}_2\text{O}$, NaOH, and PVP, as a surfactant. After the dissolution of zinc acetate dihydrate and PVP, an adequate amount of the aqueous solution of NaOH was added dropwise, resulting in a white precipitate. The as-prepared suspension was MW processed for 5 and 10 min, in a domestic oven (2.45 GHz, 800 W).

The phase purity and crystal structure ordering of the synthesized powders were analyzed by XRD and Raman spectroscopy. XRD patterns were recorded at Philips PW-1050 over a 2θ range $10\text{--}70^\circ$ with a step of 0.05° and a counting time of 5s. The μ -Raman spectra were recorded in the frequency interval of $50\text{--}3500\text{ cm}^{-1}$ (DXR Raman microscope, Thermo Scientific). The morphology of ZnO particles was observed by FE-SEM (SUPRA 35 VP Carl Zeiss) while the particle size distribution was determined using Mastersizer 2000 (Malvern Instruments Ltd., UK). Optical properties of the synthesized powders were studied by UV-Vis diffuse reflectance (Thermo Scientific, Evolution 600 UV-Vis spectrophotometer equipped with DRA-EV-600 diffuse reflectance accessory) and photoluminescence (PL) spectroscopy (Horiba Jobin Yvon Fluorolog FL3-22 spectrofluorometer with Xe lamp). The photocatalytic activity of ZnO nanoparticles was studied by the decomposition of a non-degradable dye methylene blue (MB) under direct sunlight irradiation at room temperature. In each of the experiments 100 mg of ZnO was mixed with 100 ml of MB (5, 10 and 15 ppm). Prior to sunlight irradiation, the suspension was magnetically stirred for 1 h in darkness to establish an adsorption-desorption equilibrium. During irradiation, stirring was maintained to keep the mixture in suspension. At specific time intervals 3 ml of aliquots was withdrawn and centrifuged at 8000 rpm during 10 min to remove nanoparticles from solution before the absorbance measurement. The concentration of MB after photocatalytic decomposition was calculated according to the absorbance value at 665 nm determined by UV measurements performed on a GBC Cintra UV-Vis spectrophotometer in the wavelength range of 300–800 nm.

RESULTS AND DISCUSSION

XRD patterns show that the synthesized ZnO powders are monophased, highly crystalline, a wurtzite-type hexagonal structure. Raman spectra revealed an

existence of lattice defects i.e. oxygen vacancies and zinc interstitials. FE-SEM discovered nanospherical morphology of the synthesized particles. Besides, it was found that the tendency of the particles agglomeration decrease with increases of MW processing time. Furthermore, particles size distribution is uniform with average diameter of ~ 70 nm. Figure 1 show results of XRD, Raman, FE-SEM and particle size distribution investigations of ZnO powder MW processed during 10 min.

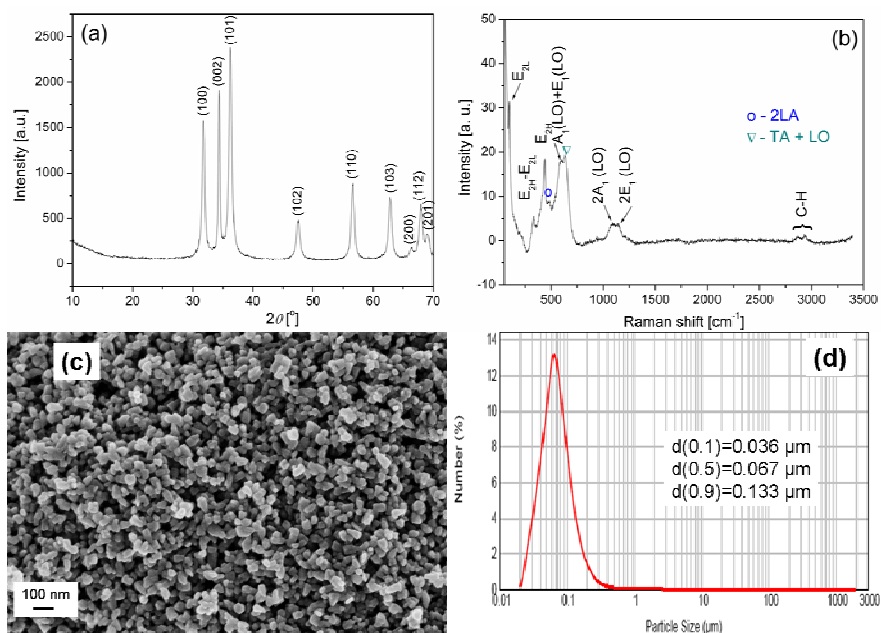


Figure 1. (a) XRD pattern; (b) Raman spectrum; (c) FE-SEM, and (d) particle size distribution of ZnO powder MW grown during 10 min.

The synthesized ZnO nanocrystals, compared to bulk ZnO, exhibit the red shift of the band gap energy (~ 0.15 eV), implying an absorption in the visible region (384 nm), Fig. 2(a). The enhanced visible light absorption of the synthesized ZnO nanocrystals is related to the introduction of lattice defects (oxygen vacancies and zinc interstitials). PL spectrum of synthesized ZnO nanoparticles shows two emission bands, Fig. 2(b). The violet emission at 415 and blue emission at 437 nm are attributed to the oxygen vacancies [2]. Results of the photocatalytic removal of MB are shown in Fig. 3, implying that the dye was being degraded.

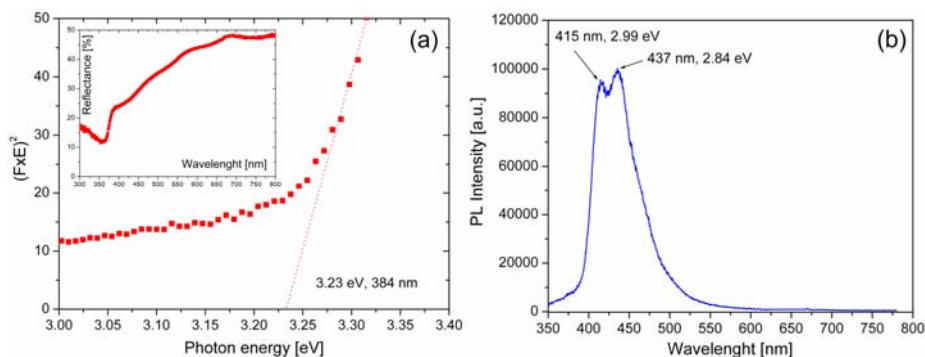


Figure 2. (a) Kubelka-Munk plot and band gap energy estimation with DRS (inset), and (b) PL spectrum of ZnO powder MW grown during 10 min.

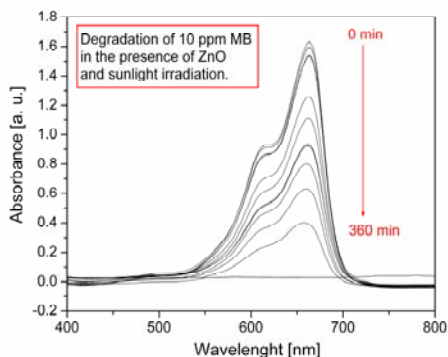


Figure 3. Absorption spectra of 10 ppm MB solution during sunlight irradiation in the presence of ZnO nanoparticles.

CONCLUSION

Microwave processed ZnO nanospheres have intrinsic crystalline defects, precisely, oxygen vacancies and zinc interstices, introduced by fast crystal growth. The crystalline defects enhance optical absorption in the visible spectrum, yielding possibilities for efficient heterogenic photocatalysis under sunlight irradiation.

ACKNOWLEDGEMENT: This study was supported by the Ministry of Education, Science and Technological Development of the Republic of Serbia under grant No. III45004.

REFERENCES

- [1] R. Qui, D. Zhang, Y. Mo, L. Song, E. Brewer, X. Huang, Y. Xiong, *Journal of Hazardous Materials*, 2008, 156, 80–85.
- [2] R. Wu, Y. Yang, S. Cong, Z. Wu, C. Xie, H. Usui, K. Kawaguchi, N. Koshizaki, *Chemical Physics Letters*, 2005, 406, 457–461.

ON THE MECHANISM OF ETHYLENE GLYCOL OXIDATION OVER AG-CONTAINING CATALYSTS: A THEORETICAL STUDY

M.A. Salaev¹, O.Kh. Poleshchuk², and O.V. Vodyankina¹

¹ *Department of Physical and Colloidal Chemistry, Tomsk State University,
634050, Tomsk, Russia*

² *National Research Tomsk Polytechnic University, 634050, Tomsk, Russia
(mik.salaev@gmail.com)*

ABSTRACT

A theoretical interpretation of the mechanism of ethylene glycol (EG) oxidation to glyoxal over Ag-containing catalysts is considered. A model system, representing the interaction of Ag cluster with process adsorbates and/or intermediates, is proposed. Both partial oxidation of EG to glyoxal and CO₂ formation routes are reconstructed, and reaction profiles are generated. The roles played by the most important reaction intermediates participating in the process under consideration (atomic oxygen, ethylenedioxy and 2-oxoethoxy species) are discussed.

INTRODUCTION

Partial oxidation of alcohols to produce valuable organic compounds has always been of interest to experimental and theoretical science. Recently, more attention has been given to the process of ethylene glycol oxidation into glyoxal over IB metal catalysts [1, 2]. Novel supported silver catalysts were developed [3] with the active component immobilized in silicate-phosphate matrix [1] and organized as various neutral and charged silver clusters (Ag₄, Ag₄²⁺, etc.) over the support surface. Despite wide experimental investigations there were no attempts to look at the process from the quantum-chemical point of view. Thus, the aim of the present work was to undertake systematic theoretical studies of the main structural parameters and interaction energies of the most important reaction intermediates and adsorbates in EG oxidation process as well as to construct energy profiles of the major reaction routes.

EXPERIMENTAL

In the present paper the systems containing neutral Ag₄ cluster and/or adsorbates/intermediates were calculated at B3LYP/DGDZVP level of

theory (Fig. 1). The calculations were carried out using the Gaussian'09 program package installed at SKIF "Cyberia" supercomputer of TSU.

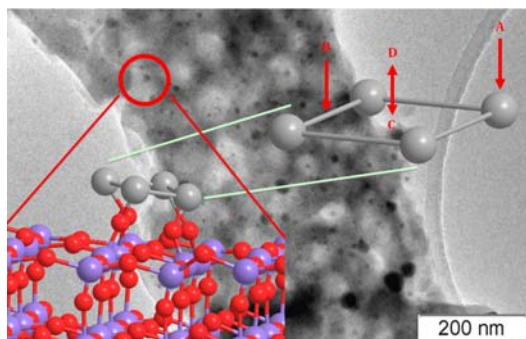


Figure 1. Schematic representation of the model taken for calculations (TEM picture adapted from [1])

Geometry of all obtained structures was fully optimized. In all cases the nature of stationary point was checked by vibrational frequency calculations. The majority of the optimized structures was in global energy minimum and had real frequencies only. When the structure had imaginary frequencies, IRC calculations were carried out to determine the transition

state. The thermodynamic parameters of the molecules calculated were corrected for zero-point vibrational energy (ZPVE) and reduced to normal conditions (298.15 K, 1 atm) using thermal corrections to enthalpy and free energy. The absence of imaginary vibrational frequencies confirmed the stationary character of structures.

RESULTS AND DISCUSSION

The process mechanism, taken for the calculations, was formulated on the basis of experimental results obtained in [1-5]. In Figure 2 one can see the resulting energy profile containing the key component interactions in the process of EG oxidation over Ag-containing catalysts. Here ZO and ZO₂ correspond to adsorbed atomic and molecular oxygen species, Z₂EG is adsorbed ethylene glycol, ZEDO is adsorbed ethylenedioxy species, ZOEO is adsorbed 2-oxoethoxy species, ZFA is adsorbed formate species, ZH and ZH₂ are adsorbed atomic and molecular hydrogen species, ZCO₃ is adsorbed carbonate species, ZH₂O is adsorbed water.

According to the results obtained, only slight activation of gas phase molecules and process intermediates is observed under oxygen-lean conditions. Oxygen atoms in atop/bridge sites participate in partial oxidation reactions, while hollow sites are active in total oxidation processes. Different energetics causes the opportunity for these species to display different activity in the subsequent activation and transformation of EG and other species. In the most energetically favorable system EG is coordinated via both oxygen atoms with respect to different atoms of the cluster, which does not agree with the proposition on bidentate or chelating correlation of

monolayered EG species made by [4]. A step-by-step activation of OH-groups takes place resulting in scission of OH bonds and formation of EDO oxametallacycle, which correlates with the propositions made in [4]. The results of the calculations demonstrate the following geometry parameters of the adsorbed EDO species: $r(\text{C-O})=1.419 \text{ \AA}$, $r(\text{C-C})=1.554 \text{ \AA}$, $r(\text{C-H})=1.105 \text{ \AA}$, angle $(\text{O-C-C})=115.5^\circ$, angle $(\text{O-C-H})=109.5^\circ$, angle $(\text{H-C-H})=106.4^\circ$. Under oxygen-lean conditions EDO species was shown to interact with silver cluster via both oxygen atoms located in two bridge positions.

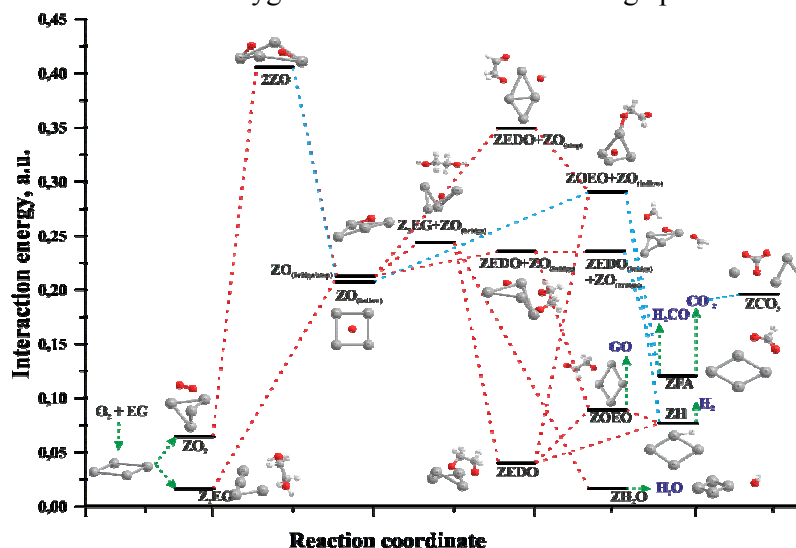


Figure 2. Energy profile for the main processes calculated at B3LYP/DGDZVP level of theory.

When cluster model contains two oxygen atoms in different site positions, a structure is formed where both oxygen atom and EDO species are located in bridge position. The resulting geometry reflects the process of C-C bond cleavage and formation of two adsorbed activated formaldehyde molecules. One of the activated molecules is adsorbed via C=O oxygen atom and one of hydrogen atoms interacting with silver and surface oxygen atom, respectively. Another possible geometry consisting of silver cluster and EDO and atomic oxygen species adsorbed in atop position, reflects C-H bond activation followed by transfer of H atom to atomic oxygen in atop position resulting in formation of surface adsorbed OH and OEO species. The OEO species reacts with surface oxygen to yield formate which is believed to be a source of carbon dioxide and formaldehyde. The geometrical parameters of the optimized adsorbed OEO structure are as

follows: $r(\text{C-O})=1.395 \text{ \AA}$, $r(\text{C=O})=1.213 \text{ \AA}$, $r(\text{C-C})=1.527 \text{ \AA}$, $r(\text{C-H})=1.105 \text{ \AA}$, $r(\text{C-H})_{\text{ald}}=1.123 \text{ \AA}$, angle (O-C-C)= 112.0° , angle (O-C-H)= 112.5° , angle (O-C-H)_{ald}= 121.0° , angle (H-C-H)= 106.0° . The formate species is characterized by the following parameters: C=O and C-H bond lengths are 1.266 and 1.107 \AA , respectively, while (O-C-H) angle is 115.3° . Probably, formate species participates in two processes: its direct decomposition results in formation of adsorbed CO_2 and H species, while its interaction with surface oxygen may lead to formation of adsorbed CO_2 and OH species. The formed adsorbed CO_2 species may also interact with surface oxygen to yield carbonate species over silver.

The thermochemical results obtained quantitatively reflect the transformations assumed to take place over the Ag-containing catalysts of EG oxidation to glyoxal. The calculated heat effects have adequate values and correlate with the known experimental results. However, in case of molecular hydrogen the values were lower, which was caused by the structure of the DGDZVP basis set.

CONCLUSION

A detailed investigation of the mechanism of EG oxidation over Ag_4 silver cluster has been carried out at B3LYP/DGDZVP level of theory. The results obtained for all the species involved within common approach and methods will be useful in further detailed elaboration of the process mechanism.

The ethylene glycol oxidation profile has been generated. The profile reflects the processes of partial oxidation of ethylene glycol to glyoxal and its deep oxidation to carbon dioxide. It was shown that bridge site is preferable for atomic oxygen adsorption, and participates in ethylene glycol activation, while hollow site is involved in deep oxidation processes. Most important reaction intermediates were also revealed. Thus, ethylenedioxy and 2-oxyethoxy species were found to be the basic reaction intermediates transforming into major reaction products.

ACKNOWLEDGEMENT

This work was partially supported by the Russian Fund for Basic Research (Grant no. 13-03-98052).

REFERENCES

- [1] G.V. Mamontov et al., *Catal. Today*, 2013, 203, 122-126.
- [2] O.V. Magaev et al., *Appl. Catal. A*, 2008, 344, 142-149.
- [3] TSU, RU2340395 (C1) (2008).
- [4] A.J. Capote, R.J. Madix, *J. Amer. Chem. Soc.*, 1989, 111, 3750.
- [5] A.J. Capote, R.J. Madix, *Surface Science*, 1989, 214, 276-288.

GENERAL FACTORIAL DESIGN IN CATALYTIC WET PEROXIDE OXIDATION OF TARTRAZINE

P. Banković, A. Ivanović-Šašić, N. Jović-Jovičić and T. Mudrinić

*University of Belgrade – Institute of Chemistry, Technology and Metallurgy,
Center for Catalysis and Chemical Engineering, Njegoševa 12, 11000
Belgrade, Republic of Serbia.*

ABSTRACT

Al,Fe-pillared clays (PILCs) have shown good performance in catalytic wet peroxide oxidation (CWPO) of organic pollutants in water. In this work, Al,Fe-PILC prepared with the pillaring solution containing pillaring cations in $\text{Fe}^{3+}/(\text{Al}^{3+}+\text{Fe}^{3+})$ molar ratio of 0.15 was used as a catalyst. The influence of the initial concentration of tartrazine azo-dye on its degradation rate using CWPO was investigated. The results were processed using the general factorial design in order to optimize the degradation of the tartrazine azo-dye by Al,Fe-PILC employing the CWPO. Two factors, namely time and tartrazine dye concentration at six and three levels, respectively were involved in the design, while the residual tartrazine dye concentration in the solution after CWPO was the dependent variable. The significance of individual factors and their interactions were estimated based on their *F*- and *p*-values using ANOVA. Different polynomial models were tested and the most adequate regression model was proposed.

INTRODUCTION

The discharge of colored wastewaters into natural waterbodies leads to the reduction of both sunlight penetration and dissolved oxygen concentration. Furthermore, some dyes pose serious health threats to humans because of their carcinogenicity and toxicity [1]. Catalytic wet peroxide oxidation (CWPO) is one of the advanced oxidation processes in which pillared clays (PILCs) are used as catalysts in the removal of organic water pollutants [2]. Permanent micro and/or mesoporosity, and thermal and chemical stability along with developed surface, surface acidity and the possibility of the incorporation of catalytically active species make PILCs interesting for the application as catalysts in CWPO of organic dyes in water.

In previous works of the authors of the present paper, iron and aluminium containing PILCs showed to be efficient in the CWPO removal of tartrazine azo-dye from water [3]. The investigated PILCs were synthesized and thoroughly characterized [4]. The catalytic role of Fe^{3+} and beneficial

influence of temperature on the dye degradation were proven [3]. In this work, the influence of the initial tartrazine concentration on its rate of removal by CWPO was investigated at equal temperature, pH as well as H_2O_2 and catalyst concentration conditions. The conventional optimization processes neglect the interaction effects of process variables. Therefore, in this study, general factorial design [5] was employed to define CWPO reaction. In this way it was possible to determine interaction between chosen variables i.e. time and initial dye concentration.

EXPERIMENTAL

Smectite rich bentonite clay from Bogovina was used in this work for pillaring. Pillared clay was synthesized using pillaring solution that contained pillaring cations in the $\text{Fe}^{3+}/(\text{Al}^{3+}+\text{Fe}^{3+})$ molar ratio of 0.15 (denoted as AlFe15 PILC). The metal cation/bentonite ratio of 10 mmol $(\text{Al}^{3+}+\text{Fe}^{3+})/\text{g}$. was used for the synthesis of the catalyst. Detailed synthesis procedure and experimental setup are described elsewhere [3, 4].

The catalytic tests were carried out in a Pyrex reactor, thermostated by a Julabo MC 4 circular heater, and equipped with a stirrer. Aqueous solutions of tartrazine (100 ml) were stirred with 0.5 g of the solid catalyst and 35% hydrogen peroxide was added in excess (1 ml). The CWPO tests were carried out at 60 °C. Aliquots were taken at predetermined periods of time. Supernatant solutions were separated from the solid phase by centrifugation at 17000 rpm for 5 min and analyzed by UV-Vis spectrophotometry. The spectra were obtained using a Thermo Electron Nicolet Evolution 500 UV-VIS spectrophotometer.

The influence of the initial tartrazine concentration on its rate of removal by CWPO was investigated at equal temperature, pH as well as H_2O_2 and catalyst concentration conditions (Figure 1). The initial tartrazine concentrations were $93.6 \times 10^{-6} \text{ mol dm}^{-3}$, $46.8 \times 10^{-6} \text{ mol dm}^{-3}$ and $18.7 \times 10^{-6} \text{ mol dm}^{-3}$.

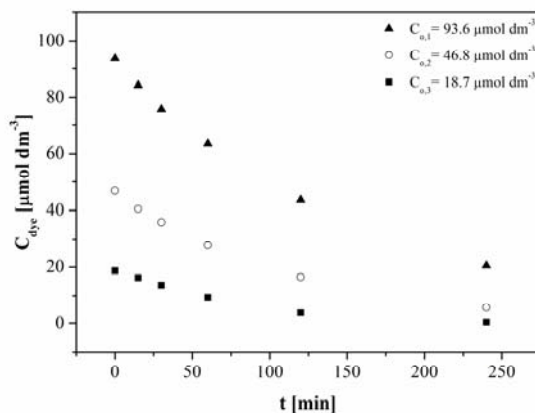


Figure 1. CWPO of tartrazine on AlFe15 PILC – the influence of initial dye concentration

STATISTICAL ANALYSIS

For the statistical analysis, time (A) and initial tartrazine dye concentration (B) were chosen to be independent factors, while tartrazine dye concentration in the solution after CWPO was chosen to be the dependent variable. Since A was changed on six levels and B on three levels the total of 18 experiments was tested using Design Expert 7.0.0 Trial program. Data obtained from the general factorial design were used to determine the regression coefficients for different regression models and the significance of the factors and their combinations was evaluated by the analysis of variance (ANOVA) [5].

RESULTS AND DISCUSSION

The ANOVA was performed in order to evaluate the significance of individual factors and their interaction effects based on their F - and p -values. The third order polynomial, second order polynomial and modified second order polynomial were tested. Generally, if $p < 0.05$, the analyzed factor and its interaction is significant, while higher F -values indicate greater significance [5]. Based on these factors, the most suitable regression equation among the investigated ones was found. Modified second order polynomial that considered only the significant terms and excluding the insignificant ones was adopted and presented in Table 1.

For selected model all obtained p -values were lower than 0.0001, indicating that both of the factors (time and initial tartrazine dye concentration) and their interactions had influence on the concentration of tartrazine after CWPO.

Table 1. ANOVA results.

Source	Sum of Squares	df	Mean Square	F -value	p -value prob > F
Model	13875.09	4	3468.77	1021.32	< 0.0001 significant
A-Time	4329.33	1	4329.33	1274.70	< 0.0001
B-Concentration	4689.48	1	4689.48	1380.74	< 0.0001
AB	1002.06	1	1002.06	295.04	< 0.0001
A ²	249.10	1	249.10	73.34	< 0.0001
Residual	44.15	13	3.40		
Corr. Total	13919.24	17			

The quality of fit of the polynomial model equation was also evaluated by the coefficient of determination (R^2 value). The obtained adjusted R^2 value

(AdjR² = 0.9959) is in reasonable agreement with R² = 0.9968 indicating a very good fit. The adopted model that included only significant terms is as follows:

$$C_t = 2.411 - 0.191A + 0.940B - 2.933 \cdot 10^{-3}AB + 6.944 \cdot 10^{-4}A^2$$

The positive coefficients of the terms indicate an increasing effect on C_t , while the negative ones indicated a decreasing effect on C_t .

CONCLUSION

Catalytic wet peroxide oxidation (CWPO) of azo dye tartrazine was performed. Synthesized and previously characterized Al,Fe-pillared clay was used as catalyst. The influence of the initial concentration of tartrazine azo-dye on its degradation was tested at equal temperature, pH as well as H₂O₂ and catalyst concentration conditions. General factorial design was employed to define CWPO reaction. The ANOVA was performed in order to evaluate the significance of individual factors and their interaction effects based on their F- and p-values. Different regression models were tested and modified second order polynomial that considered only the significant terms was found to be the most appropriate.

The obtained coefficient of determination value indicated that 99.68% of variation in the obtained tartrazine dye concentration after time can be explained by the fitted model.

ACKNOWLEDGEMENT

This work was supported by the Ministry of Education, Science and Technological Development of the Republic of Serbia (Grant No. III 45001 and 172015).

REFERENCES

- [1] D.C. Kalyani, P.S. Patil, J.P. Jadhav, S.P. Govindwar, *Bioresource Technology* 2007, 99, 4635-4641.
- [2] L. Chirchi, A. Ghorbel, *Applied Clay Science*, 2002, 21, 271–276.
- [3] P. Banković, A. Milutinović-Nikolić, Z. Mojović, N. Jović-Jovičić, M. Žunić, V. Dondur, D. Jovanović, *Applied Clay Science*, 2012, 58, 73-78.
- [4] P. Banković, A. Milutinović-Nikolić, Z. Mojović, N. Jović-Jovičić, M. Perović, V. Spasojević, D. Jovanović, *Microporous & Mesoporous Materials*, 2013, 165, 247-256.
- [5] Ž. R. Lazić, *Design of Experiments in Chemical Engineering*, Wiley-VCH Verlag, GmbH & Co. KGaA, Weinheim, 2004.

ETHYLBENZENE DEHYDROGENATION OVER UNSUPPORTED AND γ - Al_2O_3 -SUPPORTED NiO- V_2O_5 CATALYSTS

I.Y. Petrov and B.G. Tryasunov

Laboratory of Catalysis in Coal Chemistry, Institute of Coal Chemistry & Chemical Materials Science, SB RAS, 18 Sovetsky Ave., Kemerovo 650000, Russia (ipetrov@kemcity.ru)

ABSTRACT

The reduction behavior and catalytic activities of binary NiO- V_2O_5 systems (NiO/(NiO+ V_2O_5) = 0÷1) and Na₂O-NiO- V_2O_5 / γ - Al_2O_3 catalysts [2 wt.% Na₂O; (NiO+ V_2O_5) = 11 wt.%; NiO/(NiO+ V_2O_5) = 0÷1] for ethylbenzene dehydrogenation have been studied. Dehydrogenation activities of unsupported and γ - Al_2O_3 -supported NiO- V_2O_5 -based catalysts have been found to be associated with mainly vanadium oxide species contained in these samples. Both series of NiO- V_2O_5 -based catalysts exhibited maximal styrene yields at NiO/(NiO+ V_2O_5) molar ratio of ~ 0.15.

INTRODUCTION

NiO- V_2O_5 -based catalysts are rather active in partial oxidation of alcohols [1] and in oxidative dehydrogenation of hydrocarbons [2,3]. γ -Alumina-supported NiO- V_2O_5 catalytic systems promoted by Na₂O are also effective in non-oxidative dehydrogenation of ethyltoluenes [4], and they can be used for dehydrotreatment of mesitylene-containing fractions of C₉-aromatics to improve the separation of pure mesitylene from ethyltoluene impurities [5]. However, the contribution of nickel and vanadium components in the dehydrogenation activity of Na₂O-NiO- V_2O_5 / γ - Al_2O_3 catalysts and influence of NiO/(NiO+ V_2O_5) ratios on this catalytic reaction still remained unclear. In the present work the effects of NiO/(NiO+ V_2O_5) molar ratios and catalyst reduction degrees on the catalytic properties of unsupported and γ -alumina-supported NiO- V_2O_5 samples in ethylbenzene dehydrogenation have been investigated.

EXPERIMENTAL

NiO- V_2O_5 catalysts with various NiO/ V_2O_5 ratios (0-100 mol.% NiO) were prepared by mixing aqueous solutions of corresponding amounts of ammonium metavanadate (V) and nickel (II) nitrate hexahydrate, followed

by drying (120°C, 4 h) and calcining (600°C, 6 h) in air of evaporated precipitates. Na₂O-NiO-V₂O₅/γ-Al₂O₃ catalysts [2 wt.% Na₂O; (NiO+V₂O₅) = 11 wt.%; NiO/(NiO+V₂O₅) = 0÷1] were obtained by sequential impregnation of commercial γ-Al₂O₃ (200 m²/g) with aqueous solutions of corresponding amounts of NH₄VO₃, Ni(NO₃)₂·6 H₂O and Na₂CO₃, followed by drying (120°C, 4 h) and calcining (600°C, 6 h) in air of the impregnates after each component deposition. For comparison, 10%V₂O₅/γ-Al₂O₃, 2%Na₂O-10%V₂O₅/γ-Al₂O₃, 1%NiO/γ-Al₂O₃, 2%Na₂O-1.0%NiO/γ-Al₂O₃, and 2%Na₂O/γ-Al₂O₃ samples were also synthesized. BET specific surface areas of the catalysts were determined by N₂ adsorption at -196°C. Thermally treated samples were also characterized by X-ray diffraction (XRD) method (a HZG-4.0 instrument; Ni-filtered CuK_α-irradiation). Catalytic activities of the above catalytic materials in a model reaction of ethylbenzene dehydrogenation (T = 620°C, P = 0.1 MPa, τ_c = 1 s) were measured using conventional pulse chromatographic method. The reduction experiments with γ-Al₂O₃-supported materials were performed at 620°C in the same pulse catalytic reactor by injecting H₂ pulses into a flow of helium (25 ml He/min) fluxing through the catalyst bed; catalyst reduction degrees were estimated by the amount of H₂O formed. Temperature-programmed thermogravimetry in a flow of H₂ (100 ml/min) in combination with XRD analysis of the reduced samples was applied to study the reduction behavior of unsupported NiO-V₂O₅ systems.

RESULTS AND DISCUSSION

The results obtained are shown in Table 1 and in Figs 1-2. The phase composition of oxidized binary NiO-V₂O₅ samples consists of the following bulk phases: V₂O₅, NiO, nickel meta- and pyrovanadates (Table 1). Mostly roentgenamorphous vanadium and/or nickel species were present in the calcined γ-Al₂O₃-supported catalysts (in view of a fact that only γ-Al₂O₃ phase was observed in the XRD patterns). But at NiO/(NiO+V₂O₅) molar ratios ≥ 0.67, weak XRD lines from bulk NiO phase were also registered in the γ-Al₂O₃-based samples. Catalytic activity of binary NiO-V₂O₅ catalysts for ethylbenzene dehydrogenation (styrene yields) has been found to be due to mostly V₂O₅ phase; other phases present in the NiO-V₂O₅ samples (nickel vanadates, NiO) catalyzed mostly ethylbenzene cracking and dealkylation reactions. Dehydrogenating properties of Na₂O-NiO-V₂O₅/γ-Al₂O₃ catalysts can also be ascribed to mainly vanadia species since styrene yields decreased with NiO increasing, while γ-Al₂O₃ and Na₂O/γ-Al₂O₃ samples were practically inactive in this reaction. Maximal dehydrogenation

activities of both unsupported and γ -Al₂O₃-supported NiO-V₂O₅-based catalysts were observed at NiO/(NiO+V₂O₅) molar ratios of ~ 0.15 (Fig. 1).

Table 1. Characteristics of oxidized and reduced binary NiO-V₂O₅ catalysts

Content (mol.%)		S _{BET} (m ² /g)	Phase composition of the catalysts studied ^a	
NiO	V ₂ O ₅		Oxidized ^b	Reduced ^c
0	100	0.4	V ₂ O ₅	α -V ₂ O ₃
10	90	3.1	V ₂ O ₅	α -V ₂ O ₃
20	80	3.3	V ₂ O ₅	α -V ₂ O ₃
40	60	4.2	Ni(VO ₃) ₂ ; V ₂ O ₅ ; Ni ₂ V ₂ O ₇	α -V ₂ O ₃ ; Ni ^o
50	50	8.3	Ni ₂ V ₂ O ₇ ; V ₂ O ₅	Ni ^o ; α -V ₂ O ₃
75	25	14.2	NiO; Ni ₂ V ₂ O ₇	Ni ^o
100	0	7.1	NiO	Ni ^o

^a Phases are ranged according to the decrease in intensities of their strongest X-ray lines.

^b Calcined in air at 600°C for 6 h.

^c Reduced in a flow of hydrogen (100 ml H₂/min) with using a temperature-programmed heating (10°C/min) up to T \sim 700°C.

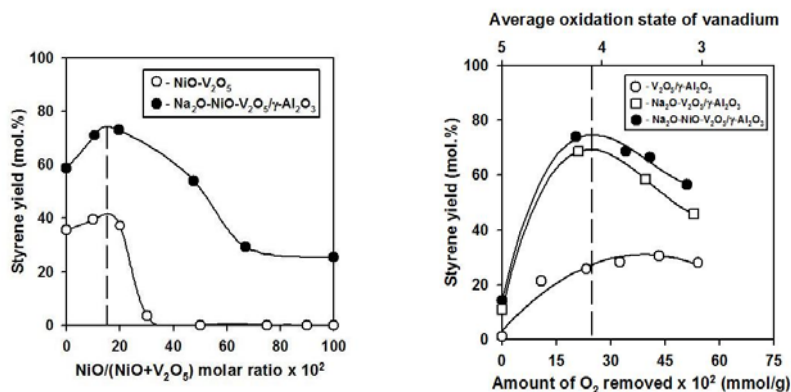


Figure 1. Effect of NiO/(NiO + V₂O₅) molar ratio on the dehydrogenation activities of NiO-V₂O₅-based systems.

Figure 2. Dehydrogenation activities of V₂O₅/γ-Al₂O₃-based catalysts as functions of their reduction degrees and vanadium oxidation states.

During the reaction or hydrogen treatment, Ni²⁺- and V⁵⁺-containing compounds present in the oxidized NiO-V₂O₅ materials are progressively

reduced up to Ni^0 particles and V^{3+} -containing species, respectively (Table 1). On the other hand, $\gamma\text{-Al}_2\text{O}_3$, $2\%\text{Na}_2\text{O}/\gamma\text{-Al}_2\text{O}_3$, $1\%\text{NiO}/\gamma\text{-Al}_2\text{O}_3$ and $2\%\text{Na}_2\text{O}-1\%\text{NiO}/\gamma\text{-Al}_2\text{O}_3$ samples were not reduced under the chosen reaction conditions. This means that mostly vanadia species could be subjected to the reduction in γ -alumina-supported V_2O_5 -based catalysts containing small amounts of Na_2O and/or NiO . Their reduction rates (estimated by 50% reduction degrees of the catalysts) changed according to the following sequence: $2\%\text{Na}_2\text{O}-1\%\text{NiO}-10\%\text{V}_2\text{O}_5/\gamma\text{-Al}_2\text{O}_3 > 2\%\text{Na}_2\text{O}-10\%\text{V}_2\text{O}_5/\gamma\text{-Al}_2\text{O}_3 > 10\%\text{V}_2\text{O}_5/\gamma\text{-Al}_2\text{O}_3$. But the reduction degrees (amounts of O_2 removed from the catalyst surface) for completely reduced V-containing $\gamma\text{-Al}_2\text{O}_3$ -supported samples decreased in the order of: $2\%\text{Na}_2\text{O}-10\%\text{V}_2\text{O}_5/\gamma\text{-Al}_2\text{O}_3 > 10\%\text{V}_2\text{O}_5/\gamma\text{-Al}_2\text{O}_3 > 2\%\text{Na}_2\text{O}-1\%\text{NiO}-10\%\text{V}_2\text{O}_5/\gamma\text{-Al}_2\text{O}_3$. Such behavior may imply that nickel species somewhat retard the reduction of vanadium species. Assuming that under reduction conditions chosen, only vanadium ions could be reduced in the supported V-containing catalysts studied, average oxidation states of vanadium for these preliminarily reduced γ -alumina-supported samples were calculated and correlated with the changes in their dehydrogenation activities. Maximal activities were observed at the catalyst reduction degrees corresponding to the formation of V^{4+} ions (Fig. 2). It is supposed that small addition of NiO and Na_2O to $\gamma\text{-Al}_2\text{O}_3$ -supported V_2O_5 -containing systems facilitates the formation and stabilization of V^{4+} ions providing the increased activity of $\text{NiO-V}_2\text{O}_5$ -based catalysts in ethylbenzene dehydrogenation.

CONCLUSION

Catalytic activity of unsupported and γ -alumina-supported $\text{NiO-V}_2\text{O}_5$ -based catalytic systems for ethylbenzene dehydrogenation is due to predominantly vanadium oxide species. Promoting effect of small additives of NiO and Na_2O on the performance of $\text{Na}_2\text{O-NiO-V}_2\text{O}_5/\gamma\text{-Al}_2\text{O}_3$ catalysts may be related to the stabilization of V^{4+} ions possessing the higher activities in ethylbenzene dehydrogenation.

REFERENCES

- [1] R. Maliński, J. Gallus-Olender, *React. Kinet. Catal. Lett.*, 1979, 11, 377-381.
- [2] R. Juárez López, N.S. Godjayeva, V. Cortés Corberán, J.L.G. Fierro, E.A. Mamedov, *Appl. Catal. A.*, 1995, 124, 281-296.
- [3] B. Zhaorigetu, W. Li, H. Xu, R. Kieffer, *Catal. Lett.*, 2004, 94, 125-129.
- [4] USSR Pat. N 1398162 (1985).
- [5] USSR Pat. N 1338325 (1985).

POROUS CLAYS HETEROSTRUCTURES (PCH'S). SYNTHESIS, CHARACTERIZATION AND CATALYTIC APPLICATION

C. B. Delgado, C. P. González, F. G. Martínez, A. C. Perdigón Aller and B. O. Marina

Inorganic Chemistry Group; Department of Chemistry and Process & Resources Universidad de Cantabria. Av. Los Castros s/n 39005-Santander. Spain. (carmen.blanco@unican.es)

ABSTRACT

Porous Clays Heterostructures (PCH's), are synthesized from clays by exchange process using lower molar ratios of decylamine/ tetraethyl orthosilicate as it was described by the literature, being a more economic synthesis process. These materials have resulted adequate supports for the Rh catalysts (1%Rh) through an organometallic component. The particle size of the Rhodium is in the nanometres' scale (2,6-4,7 nm). The catalytic behaviour was studied by the hydrogenation or transformation of acetone in gas phase at atmospheric pressure (mild conditions) and a temperature range between 180-80°C.

INTRODUCTION

Porous Clays Heterostructures (PCH's) are a new class of acid solids with a porous structure first described by Pinnavaia et al [1-2]. These materials show an special pore size between the supermicropore and the small mesopore. These PCH's are synthesized from clays by exchange process. It has been described a narrow relation between the obtained pore size in these materials with the surfactant and the source of silica used in the synthesis [3].

The present work has a double objective, in the first part, it is synthesized and characterized PCH's with different molar ratios of co-surfactant/silica source and, secondly it is studied the capability of these materials as supports for Rhodium catalyst and their catalytic behavior in the hydrogenation of acetone in mild conditions of pressure and temperature.

EXPERIMENTAL

As raw material, a montmorillonite from Wyoming is used. It will be modified with an ionic surfactant and different molar ratios of decylamine/tetraethyl orthosilicate (TEOS) (20/150, 20/70 and 20/20) which are lower proportions than the ratios are used in the literature.

PCH materials were synthesized as follow: In the first step, the interlayer cations were exchanged for organic hexadecyltrimethylammonium cations (CTA). The amount of organic cations used for exchange was twice the cation exchange capacity of the raw materials. The samples were added to an aqueous solution of CTABr. After, it was stirred at room temperature for 24 hours. The excess of salt was removed by washing with desionized water and centrifugation. In the next step, neutral amine co-surfactant (decylamine) and TEOS were added in different molar ratios described above. The materials were recovered by filtration. In order to eliminate the organic material, they were calcined. By this way, the samples with a bidimensional pore structure were obtained.

The incorporation of the metallic phase (1% Rh) on the PCH's used as supports was made by impregnation in acetone medium and adsorption in organometallic solution of Rh [4-5] at room temperature. A catalyst with Wy as support has been prepared for comparative effects.

The supports and catalysts were characterized by various physical-chemical techniques: XRD, adsorption-desorption nitrogen, adsorption-desorption of ammonia and/or cyclohexylamine to determine the acidity, and chemisorption of O₂-H₂ in order to know the metallic dispersion and the particle size.

The catalytic behaviour was studied in the hydrogenation or transformation of acetone in gas phase at atmospheric pressure (mild conditions) and a temperature range between 180-80°C in interval of 20°C. All catalysts were calcined and reduced in situ at 200°C in air flow and at 500°C in hydrogen flow, respectively. The products were analyzed through Gas Chromatography.

RESULTS AND DISCUSSION

The XRD pattern obtained from the Wy sample exchanged with CTA⁺ show basal spacing increases from 12.9Å for the raw material to 21.0Å. This indicates that the exchange of sodium ions with the CTA in the sample has been successful.

The PCH's samples synthesized have a high specific surface area, being the highest in the Wy20/150 (577 m²/g) and Wy20/20 (599 m²/g) samples, compared with the raw material (32 m²/g). The Wy20/20 sample shows the highest pore volume (0.380 cc/g) and pore size (35.6Å). The acidity of these materials is stable up to a maximum temperature of the catalytic test of 500°C and higher than the raw material (12.88 cc/g for Wy20/20 sample against 0.44cc/g for the Wy sample).

Porous Clays Heterostructures (PCH's) synthesized have resulted adequate supports for the Rh catalysts (1%Rh) through an organometallic component

in mild conditions (room temperature and atmospheric pressure). The particle size of the Rhodium is in the nanometres' scale (2,6-4,7 nm) and the metallic dispersion between 41 and 25% (Table 1).

Table 1. Metallic Dispersion and particle diameter \varnothing (nm) of Catalysts.

Catalyst	Tred.(300°C) Dispersion (%)	\varnothing (nm)	Tred.(500°C) Dispersion (%)	\varnothing (nm)
Rh/Wy	41	2.7	-	-
Rh/Wy20/150	9.1	11.9	23.4	4.7
Rh /Wy20/70	12.4	8.7	32.3	3.4
Rh/Wy 20/20	12.0	9.0	25.5	4.3

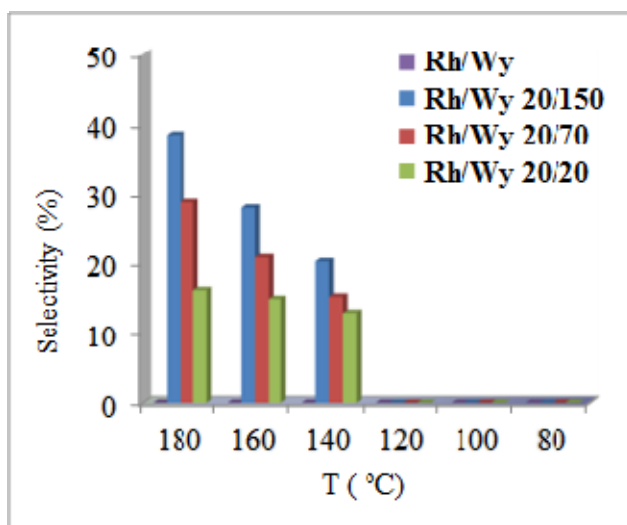


Figure 1. Selectivity to MIBK (T_{red}=500°C).

The synthesized catalysts possess acidity, but lower than the supports. This can be due to the possible anchored of Rhodium in the acid centres of them. The bifunctional synthesized catalysts have resulted more active in the temperature interval from 180 to 100°C. The conversion increases when the temperature of reaction increases and the selectivity, in the transformation of acetone towards methyl isobutyl ketone (MIBK), is higher for the catalysts that show more acidity (Rh/Wy20/150) (Figure 1). When the Wy

clay without modification is used as support for preparing the catalyst (Rh/Wy), it was not found any selectivity in the reaction.

CONCLUSION

Porous Clays Heterostructures (PCH's) from a montmorillonite (Wy) using lower molar ratios of decylamine/TEOS as it was described by the literature, being a more economic synthesis process, have been synthesized. These materials show better physicochemical properties than the raw clays.

Porous Clays Heterostructures (PCH's) synthesized have resulted adequate supports for the Rh catalysts (1%Rh) through an organometallic component in mild conditions. The particle size of the Rhodium is in the nanometres' scale and the acidity is stable up to a maximum temperature of 500°C. The conversion increases when the temperature of reaction increases and the selectivity in the transformation of acetone towards MIBK is higher for the catalysts that present more acidity (Rh/Wy20/150).

ACKNOWLEDGEMENT

The University of Cantabria of Spain (Project 51.VP10.64005) supported this work.

REFERENCES

- [1] Galarneau, A. Barodawalla, T.J. Pinnavaia, *Nature*, 1995, 374, 529-531.
- [2] M. Polverejan, Y. Liu, T.J. Pinnavaia, *Chem. Mater.*, 2002, 14 (5), 2283- 2288.
- [3] J. Pires, A.C. Araujo, A.P. Carvalho, M.L. Pinto, J.M. González-Calbet, J. Ramírez-Castellanos, *Micropor. Mesopor. Mater.*, 2004, 73, 175-180.
- [4] C. Blanco, R. Ruiz, C. Pesquera, F. González, *Appl. Catal. A: Gen.*, 2004, 257 (2), 165-175.
- [5] C. Blanco, V. Krstic, F. González, C. Pesquera, *Chem. Industry*, 2011, 65 (1), 37- 42.

SYNTHESIS AND TEXTURAL CHARACTERISTICS OF NICKEL BASED CATALYST SUPPORTED ON PERLITE

V. Radonjić^{1*}, J. Krstić¹, D. Lončarević¹, M. Stanković¹, D. Jovanović¹,
N. Vukelić², D. Nikolova³ and M. Gabrovska³

¹*IChTM, University of Belgrade, Department of Catalysis and Chemical Engineering, Njegoševa 12, 11000 Belgrade, Serbia*

**E-mail: vradonjic@nanosys.ihtm.bg.ac.rs*

²*Faculty of Physical Chemistry, University of Belgrade, 11000 Belgrade, Serbia*

³*Institute of Catalysis, Bulgarian Academy of Sciences, Acad. G. Bonchev str., bl. 11, Sofia 1113, Bulgaria*

ABSTRACT

Nickel supported on perlite was synthesized by precipitation-deposition method of $\text{Ni}(\text{NO}_3)_2 \cdot 6\text{H}_2\text{O}$ and $\text{Mg}(\text{NO}_3)_2 \cdot 6\text{H}_2\text{O}$ solution with Na_2CO_3 on three differently prepared expanded perlite with identical composition ($\text{Ni}/\text{SiO}_2=1.1$ and $\text{Ni}/\text{Mg}=10/1$). Investigation was conducted in order to elucidate the possibility of using perlite as a novel support type, for preparation of nickel based precursor catalyst, potentially applicable in vegetable oil hydrogenation process. Different characterization techniques, He-pycnometry, Hg-porosimetry and N_2 -physisorption were used. Determining the precursor texture shows a successfully deposited nickel phase on its perlite support with promising results.

INTRODUCTION

Perlite is an amorphous volcanic glass, light gray, with SiO_2 composition, higher than 70 wt.% and 2 to 5 wt.% of combined water. Commercially, the term perlite includes any volcanic glass that will expand dramatically when heated quickly, up to 20 times, forming a lightweight frothy material [1]. Perlite has a significant applicability in construction industry, agriculture, and as an industrial filter aid, but there are just a few examples as a catalyst support. Currently, metallic nickel supported on different natural sources of silica represents the commonly applied commercial catalyst for the process of oil hydrogenation, due to its high activity, availability and low cost [2-4]. The precipitation of nickel salt with sodium carbonate in the presence of a silica slurry leads to the formation of different nickel species: nickel basic carbonate, nickel phyllosilicate, etc. Obtained material can vary considerably with the changes in the precipitation conditions, synthesis temperature, Ni/SiO_2 ratio and textural characteristics of silica support [5]. The aim of this work is to examine the effect of nickel deposition, under the

same precipitation conditions on differently pretreated expanded perlite, in order to obtain a precursor for vegetable oil hydrogenation process.

EXPERIMENTAL

Materials and methods. All the chemicals used in precursor synthesis described in this paper are “pro analysis” purity grade. Expanded perlite was supplied with the courtesy of Termika, Zrenjanin, R. Serbia, Perlite PF-295. Three different pretreatment procedures were used: first washed with distilled H₂O on 90 °C for 30 min (PF-N), second, with 10% solution of Na₂CO₃ on 90 °C for 4h (PF-B) and third with 9M HCl in reflux on 100 °C for 4h (PF-A), all under vigorous stirring. Obtained supports were vacuum washed with hot distilled H₂O (≈80 °C) until neutral pH and dried in an oven at 110 °C for 24h. Precursors were synthesized with identical composition ($n_{\text{Ni}}/n_{\text{SiO}_2}=1.1$ and $n_{\text{Ni}}/n_{\text{Mg}}=10$) by precipitation-deposition method. Aqueous solutions of Ni(NO₃)₂·6H₂O and Mg(NO₃)₂·6H₂O, solid anhydrous Na₂CO₃ with molar ratio 1.5 towards Ni²⁺, an aqueous suspensions containing 2.0 wt.% of the supports PF-N, PF-B and PF-A were prepared. In externally heated PTFE reaction vessel equipped with a magnetic stirrer, Ni-Mg nitrate solution was added, heated up to 90 °C and co-precipitated with Na₂CO₃ under vigorous stirring. Hence, the hot aqueous suspension of the support (PF-N, PF-B or PF-A) was added at once into the reaction vessel. The obtained suspension was aged for 30 min at the same temperature and stirring rate, after which was filtered and thoroughly washed with hot (≈80 °C) distilled water until neutral pH. Finally, the precursors were dried at 110 °C for 24h, grounded to powder, dried again and stored. **Characterization.** The composition of the supports and precursors were determined by ICP-OES method (Thermo Scientific iCAP-6500 Duo) after acid microwave digestion was applied. Density measurements were performed by gas pycnometry (Pycnomatic ATC). Textural parameters of supports and precursors were obtained by N₂-physisorption (Sorptomatic 1990) and mercury porosimetry (P.A.S.C.A.L. 140 and 440) measurements.

RESULTS AND DISCUSSION

Chemical compositions of the prepared supports and precursors are presented in Table 1 and Table 2, respectively. Although the chemical composition of the starting material PF-295 is not shown because of confidential issues, it can be said that the H₂O pretreatment causes barely significant changes in PF-N support. For PF-B and PF-A most obvious changes, compared to PF-N, is SiO₂ content. Acid pretreatment (PF-A) removes some of cations causing the increase in SiO₂. In contrast, base

prepared (PF-B), due to the base formation, leads to the increase of sample mass and consequently, SiO₂ decrease.

Table 1. The chemical composition of the supports

Support	Chemical composition (wt. %)								
	SiO ₂	Al ₂ O ₃	Fe ₂ O ₃	CaO	MgO	K ₂ O	Na ₂ O	MnO	Loss on Ignition
PF-N	74.10	13.69	0.81	0.70	0.12	4.64	3.62	0.08	2.51
PF-B	72.73	12.87	0.83	0.74	0.14	4.01	4.26	0.09	1.38
PF-A	76.82	12.20	0.63	0.67	0.08	4.38	2.62	0.08	2.14

Chemical composition results of the precursors show that the Ni/Mg and Ni/SiO₂ molar ratio was achieved accordingly to the specified synthesis procedure, with slightly different amount of nickel in different precursors.

Table 2. Weight percentage and molar ratio of Ni, Mg and SiO₂ of the precursors

Precursor	(wt. %)			molar ratio	
	Ni	Mg	SiO ₂	Ni/Mg	Ni/SiO ₂
Ni/PF-N	28.41	1.22	26.73	9.6	1.09
Ni/PF-B	32.20	1.32	30.05	10.1	1.10
Ni/PF-A	31.94	1.30	30.43	10.2	1.07

Textural characteristics and skeleton densities of the prepared samples are presented in Table 3. Due to high value of intruded mercury volume during the first Hg porosimetry run for both supports and precursors, the second run was conducted in order to resolve the nature of this behaviour. Results show obvious differences between precursors and supports.

Table 3. Textural characteristics of supports and precursors

Sample	Hg-porosimetry		N ₂ -physisorption				He-pycnometry
	V _{tot-R1} , cm ³ ·g ⁻¹	V _{tot-R2} , cm ³ ·g ⁻¹	D _{med} , µm	V _{meso} , cm ³ ·g ⁻¹	V _{micro} , cm ³ ·g ⁻¹	S _{BET} , m ² ·g ⁻¹	ρ, g·cm ⁻³
PF-N	2.56	2.13	5.50	0.015	0.002	6.0	2.23
Ni/PF-N	1.86	0.06	4.11	0.130	0.053	140	2.45
PF-B	2.56	1.49	5.21	0.011	0.002	5.7	2.13
Ni/PF-B	1.17	0.18	2.64	0.115	0.048	140	2.26
PF-A	2.16	1.72	4.72	0.038	0.001	2.2	2.40
Ni/PF-A	1.71	0.11	3.98	0.113	0.047	129	2.70

For supports, a high value of total Hg intruded specific volume in first run (V_{tot-R1}) is not caused by support characteristics (pores system volume or interparticles voids), rather from the compressibility of the supports. That is obvious, because the V_{tot-R2} is also high. On the contrary, no evidence of precursor compressibility was observed. Precursors exhibit very small V_{tot-R2} values and are the same order of magnitude to V_{meso} results obtained by N₂ physisorption, indicating that beside high interparticle porosity, intraparticle porosity exists in some extend. Determined values of dominant void diameter D_{med} ≈ 5 µm, originate from interparticle species rather than

the pore system, for both supports and precursors. Nitrogen physisorption isotherms of all supports are the same, and according to the IUPAC classification [6] are Type III

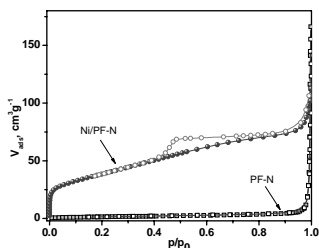


Figure 1. The N₂ isotherms at 77 K of the PF-N support and Ni/PF-N precursor

(Figure 1). This type of isotherm is characteristic for weak adsorbate-adsorbent interactions and can be associated with nonporous adsorbents. The obtained values of specific surface area, and small values of meso and micropore volume, confirms a nonporous nature of the supports. The

precursor isotherm type is dramatically different and can be classified as IIb with the type H3 hysteresis, characteristic for aggregates of plate-like particles with non-rigid slit-shapes. This is obviously contributed by formation of Ni-species, most probably in the form of nickel basic carbonate, on the surface of the support. Increases of skeleton density for precursors compared to the supports, confirm this assumption.

CONCLUSION

Nickel catalyst precursors supported on perlite were prepared by deposition-precipitation method on differently activated perlite support. Although, predetermined Ni/Mg and Ni/SiO₂ molar ratios in precursors were achieved, amount of nickel is slightly different. Used synthesis procedure enables deposition of nickel species on the support. Thus, obtained materials are promising for the preparation of nickel catalyst for vegetable oil hydrogenation.

ACKNOWLEDGEMENT

This work is supported by the Ministry of Education, Science and Technological development of the Republic of Serbia (Grants no. III 45001).

REFERENCES

- [1] M. Alkan, M. Doğan, J. Colloid Interface Sci., 1998, 207, 90-96.
- [2] M. Balakos, E. Hernandez, Catal. Today, 1997, 35, 415-425.
- [3] A. Wright, A. Wong, L. Diosady, Food Res. Int., 2003, **36**, 1069-1072.
- [4] M.Fernández, G. Tonetto, G. Crapiste, D.Damiani, J.Food Eng., 2007, 82, 199-208.
- [5] K. Ghuge, A. Bhat, G. Babu, Appl. Catal. A: Gen., 1993, 103, 183-204.
- [6] F. Rouquerol, J. Rouquerol, and K. Sing, in Adsorption by Powders and Porous Solids, Principle, Methodology and Applications, 1999, A. Press, NY.

EFFECT OF Mg ADDITIVE ON THE VEGETABLE OIL HYDROGENATION ACTIVITY OF Ni/SiO₂ CATALYSTS

J. Krstić^{1*}, V. Radonjić¹, M. Gabrovska², D. Nikolova²,
L. Bilyarska², K. Tenchev² and N. Vukelić³

¹University of Belgrade, Institute of Chemistry, Technology and Metallurgy,
Department of Catalysis and Chemical Engineering, Belgrade 11000,
Serbia

*E-mail: jkrstic@nanosys.ihtm.bg.ac.rs

²Institute of Catalysis, Bulgarian Academy of Sciences, Sofia 1113, Bulgaria

³Faculty of Physical Chemistry, University of Belgrade, 11000 Belgrade,
Serbia

ABSTRACT

The effect of magnesium addition on activity of Ni/SiO₂ catalysts for sunflower oil hydrogenation, synthesized using two types of different commercial silica gels was studied. It was shown that the presence of magnesium in MgNi/SIG-C catalyst contributes to the formation of appropriate pore system and easy reducible Ni²⁺ species at 430°C, which generate sufficient number of accessible Ni⁰ active sites. Contribution of different silica gel types on catalytic properties is also recognized.

INTRODUCTION

Hydrogenation of vegetable oils is a traditional oleochemical process aiming to change the physical properties of the oils as well as to enhance the oxidation and thermal stability of the hydrogenated products. In the view of high activity, inert nature of the metal relative to the oil, availability and economic consideration, metal nickel, supported on different sources of silica, is the most appropriate catalyst for this reaction. While numerous studies have been focused on improvement of the catalyst preparation, there are only scarce attempts to elucidate the role of additives or modifiers on the catalytic performance in vegetable oil hydrogenation [1,2]. The purpose of the present work was to investigate the effect of Mg addition on the hydrogenation activity of Ni/SiO₂ systems.

EXPERIMENTAL

Mg-modified samples were synthesized with identical composition (SiO₂/Ni=1.0 and Mg/Ni=0.1) by co-precipitation using aqueous solutions of Ni(NO₃)₂·6H₂O, Mg(NO₃)₂·6H₂O and Na₂CO₃ on SiO₂ supports that are

denoted MgNi/SIG-A and MgNi/SIG-C. By analogy with non-modified Ni/SiO₂ samples, two types of commercial silica gel (SIG-A and SIG-C), differing in textural parameters, were applied as sources of silica support [3]. Detailed description of the preparation procedure is reported in our recent paper [4].

Preliminary reduction of the precursors in an as-prepared state (without calcinations) was performed in a laboratory set-up using a quartz reactor by means of a “dry reduction” method at 430°C for 5 h with 1:1 = H₂:N₂ gas mixture, at a flow rate of 10 l/h and heating rate of 1.5°C/min. After cooling down to room temperature, the reduced precursors were impregnated with pure paraffin oil in order to avoid catalyst passivation, due to the exceptional pyrophority of the metallic nickel.

Partial hydrogenation of a sunflower oil was performed in a 1000 cm³ glass reactor Series 5100 (Parr, USA), computer coupled with Mass Controller F-201C and Pressure Meter F-502C (Bronkhorst, Nederland) under the following conditions: oil mass - 900 g; catalyst concentration - 0.06 wt. % Ni with respect to the amount of oil; stirring rate - 1200 rpm; hydrogenation temperature - 160°C and H₂ pressure - 0.2 MPa. The activity of the catalysts was evaluated by measuring the changes in the Refraction Index at 50°C (RX-5000α, Atago) of the starting oil and periodically collected partially hydrogenated oil. The quantity of the consumed hydrogen during the process was determined by post processing integration of the differential data from the Mass Flow Controller F-201C.

The temperature programmed reduction (TPR) experiments were accomplished by a 5% H₂/Ar gas mixture, at flow rate 20 cm³/min and heating rate 10°C/min in the temperature range 50–900°C, using Thermo Scientific TPRDO1100 system. Two TPR procedures were used: 1. Normal TPR and 2. TPR after reduction of the samples at 430°C for 2h, denoted as ReTPR.

RESULTS AND DISCUSSION

A diminution of the Refraction Index (RI) value of the crude oil (1.46368)

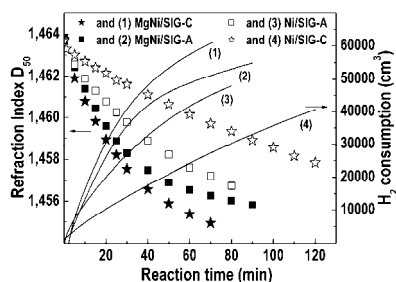


Figure 1. The changes in the RI and the volume of the consumed hydrogen vs. the reaction time

and the quantity of the consumed hydrogen as a function of hydrogenation time for the studied catalysts are represented in Figure 1. It can be seen that the value of RI at the end of the hydrogenation reaction downs to the level of 1.45495 (MgNi/SIG-C), 1.45582 (MgNi/SIG-A), 1.45674 (Ni/SIG-A) and 1.45783 (Ni/SIG-C). The obtained results are in accordance

with the quantity of the consumed hydrogen (cm^3) at the end of the reaction, namely: MgNi/SIG-C (61395) > MgNi/SIG-A (54868) > Ni/SIG-A (48013) > Ni/SIG-C (40632). The comparison of the hydrogen consumption at one and the same hydrogenation time (70 min) normalized for the amount of the consumed hydrogen by Ni/SIG-C (most inactive catalyst) reveals 1.65, 1.87 and 2.23 times greater values for Ni/SIG-A , MgNi/SIG-A and MgNi/SIG-C catalysts, respectively. The obtained data point out the dominant hydrogenation activity of the MgNi/SIG-C catalyst.

As we shown in previous paper [5], the higher activity of non-modified Ni/SIG-A catalyst was ascribed to the facilitated reduction of the Ni^{2+} species at 430°C and to the creation of adequate number of accessible Ni^0 active sites on the surface of catalyst. The lower catalytic activity of Ni/SIG-C catalyst was attributed to its pore system which doesn't provide the accessibility of the reactant molecules involved in the hydrogenation reaction (triacylglycerols and/or hydrogen) to the active Ni^0 sites [5].

A possible interpretation of the catalytic activity for Mg-containing catalysts may be found in TPR experiments accomplished by two consecutive procedures.

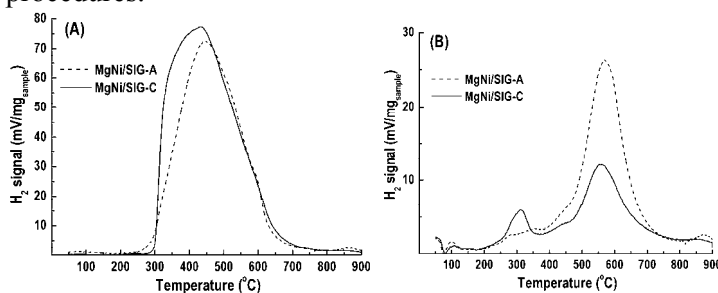


Figure 2.
The TPR
profiles (A)
and ReTPR
(B) of the
Mg-
modified
precursors

The normal TPR profile of MgNi/SIG-A sample is characterized by a symmetric profile, temperature maximum (T_{max}) at 446°C as well as a high-temperature shoulder at $\sim 600^\circ\text{C}$ (Fig. 2A). On the contrary, the TPR profile of MgNi/SIG-C is not symmetric, but displayed a well-resolved T_{max} at 431°C and a negligible high-temperature shoulder at $\sim 600^\circ\text{C}$. Calculation of total peak area for both samples show 17.1% higher reducibility of Ni^{2+} species in MgNi/SIG-C solid compared to MgNi/SIG-A . Due to the fact that chemical analyses of precursors confirm similar concentration of Ni^{2+} for both samples, a possible explanation can be found in the existence non-reducible Ni species in sample MgNi/SIG-A which cannot be reduced in the applied temperature range.

ReTPR profiles of pre-reduced at $430^\circ\text{C}/2\text{h}$ precursors (Fig. 2B) suggest a facilitated reduction of Ni^{2+} species up to 430°C in MgNi/SIG-C sample. The smaller the area under the ReTPR curve means smaller amounts of

reducible species. Consequently, that means higher reducible efficiency in first run (up to 430°C) and large amount of easily reducible species. Only 11.8% of MgNi/SIG-C precursor remains unreduced vs. 26.1% for MgNi/SIG-A. Due to the fact that preparation catalyst procedure was also conducted at $T_{\max}=430^{\circ}\text{C}$, it is correct to assume that the higher MgNi/SIG-C activity originated from higher amount of Ni^0 generated through applied reduction process.

It is worth noting that, the higher hydrogenation activity of MgNi/SIG-C can be related not only to the presence of larger number of Ni^0 active sites on the catalyst surface but also to larger average pore diameter of MgNi/SIG-C precursor (15.1 nm) compared to MgNi/SIG-A (9.2 nm) [6]. Larger pore diameter allows faster diffusion of the triacylglycerol molecules through the pore system of the catalyst, reflecting on the faster rate of the reaction and higher hydrogenation activity.

CONCLUSION

Magnesium presence in MgNi/SIG-C catalyst contributes to the formation of appropriate pore system and easy reducible Ni^{2+} species at temperature up to 430°C which generates sufficient number of accessible Ni^0 active sites on the surface of the most active catalyst for the sunflower oil hydrogenation.

ACKNOWLEDGEMENT

This work is supported by the Ministry of Education, Science and Technological development of the Republic of Serbia (Grants no. III 45001).

REFERENCES

- [1] E. Jang, M. Jung, D. Min, *Compr. Rev. Food Sci. F.*, 2005, 1, 22-30.
- [2] J. Veldsink, M. Bouma, N. Schöön, A. Beenackers, *Catal. Rev. - Sci. Eng.*, 1997, 39, 253-318.
- [3] D. Nikolova, J. Krstić, L. Spasov, D. Simeonov, D. Lončarević, Pl. Stefanov, D. Jovanović, *Russ. J. Phys. Chem. A*, 2011, 85, 2380-2385.
- [4] M. Gabrovska, J. Krstić, P. Tzvetkov, K. Tenchev, M. Shopska, N. Vukelić, D. Jovanović, *Russ. J. Phys. Chem. A*, 2011, 85, 2392-2398.
- [5] J. Krstić, M. Gabrovska, D. Lončarević, D. Nikolova, D. Simeonov, M. Stanković, N. Vukelić, *PHYSICAL CHEMISTRY 2012*, in: *Proc. 11th Int. Conf. Fundam. Appl. Aspects Phys. Chem.*, Belgrade, Serbia, 2012, 175-177.
- [6] M. Gabrovska, D. Nikolova, M. Shopska, P. Tzvetkov, L. Spasov, D. Simeonov and D. Jovanović (in press in current issue).

PHOTOCATALYTIC DECOLORISATION OF SELECTED ORGANIC DYES BY MESOPOROUS TiO₂ THIN FILMS

A. Zarubica¹, M. Vasic¹, M. Marinkovic¹, N. Stojkovic¹ and J. Nedeljkovic²

¹*Faculty of Science and Mathematics, University of Nis, Visegradska 33,
18000 Nis, Serbia*

²*Vinca Institute of Nuclear Sciences, University of Belgrade, P.O. Box 522,
11001 Belgrade, Serbia*

ABSTRACT

The mesoporous TiO₂ films were prepared by dip coating technique combined with the evaporation-induced self-assembly method using selected polymer templates. Influence of specific surface area, pore size, (nano)crystal structure and morphology of TiO₂ films on the photocatalytic behaviour was investigated. In addition, particular process parameters were considered in decolorisation of organic dyes, such as: thickness of TiO₂ films, initial concentration of selected pollutants and number of reaction cycles.

INTRODUCTION

One of the major global problems is water pollution. The large amount of organic dyes used in textile manufacturing processes and other industries represents an increasing environmental danger owing to their toxic, carcinogenic and mutagenic nature [1].

Due to their numerous favorable properties TiO₂ thin films have been commonly used photocatalysts for degrading a wide range of organic pollutants. Several techniques and preparation process parameters can be used in order to obtain photocatalyst with the desired properties.

The evaporation-induced self-assembly method [2-4] using various titania precursors and templating polymers has been used in order to prepare mesoporous TiO₂ films. It is proposed and shown that the type of polymer template has a substantial influence on the porosity of the final material [5].

The aim of this study was to investigate the photocatalytic activity of homogenous and crack-free TiO₂ films with templated mesoporosity, prepared by using two different polymers (Pluronic F127 and PSM02). In this paper photocatalytic decolorisation of methylene blue (MB) and crystal violet (CV) was used in order to test photocatalytic activity of the TiO₂ thin

films as a function of porosity, crystallinity, particle size, and thickness (catalyst dosage).

EXPERIMENTAL

Templated TiO₂ thin films were prepared by using silicon wafers as substrates. Precursor solutions for dip coating were prepared using TiCl₄ dissolved in dry ethanol under an inert atmosphere. An alcohol-water mixture containing either Pluronic F127 or PSM02 polymer was added and molar ratio between TiCl₄ and F127 was adjusted to 1 : 0.001, while the molar ratio between TiCl₄ and PSM02 was 1 : 0.01. These solutions were stirred at room temperature for 24 hours and the addition of deionized water led to a molar ratio between selected solution constituents TiCl₄ : EtOH : H₂O = 1 : 30 : 10. The TiO₂ films were deposited onto silicon substrates by dip coating combined with the evaporation-induced self-assembly method. Calcination of the TiO₂ films was carried out at 450 °C for 15 min. The physico-chemical characterization of the catalysts were conducted using textural (BET), structural (XRD) and morphological (SEM/TEM) analyses. Photocatalytic efficiency of mesoporous TiO₂ thin films was tested in the decolorisation reactions of MB and CV over a broad range of initial concentrations and reaction cycles. Changes in concentrations of organic dyes were monitored by using UV/VIS spectra. Catalyst dosage in each photocatalytic test was 28±2 mg. The organic dyes, like methylene blue and crystal violet, were selected as model pollutants in photocatalytic test reaction. In order to establish the equilibrium of potential sorption process, thin films were tested during 12 h. The UV lamp (ROTH Co.) characterized with following working features: 16W, 2.5 mW/cm² and λ_{max} = 366 nm was used.

RESULTS AND DISCUSSION

BET surface areas of TiO₂ films obtained by the dip coating technique in the presence of F127 and PSM02 templates after calcination at 450 °C are shown in Table 1. The characteristics of pore system in titania thin films can be related to the applied preparation method, used polymer template and titania precursor, calcination temperature and finally substrate surface properties. The specific surface area may have a significant effect on the photocatalytic efficiency of titania thin films [5]. The TiO₂ film templated with F127 exhibits BET surface area of 48 m²/m² and pore size up to 10 nm, while titania based thin film with PSM02 poses BET surface area of 20 m²/m² with pores of 22 nm in size (Table 1). In accordance with developed pore system and larger BET surface area, TiO₂ film templated with F127 has shown higher efficiency in photocatalytic decolorisation of selected organic dyes comparing with titania based film templated with PSM02 (Fig. 3). The XRD analysis (Fig. 1) indicated the presence of TiO₂ in anatase crystal

phase with a small amount of nonstoichiometric Ti_2O_3 . The crystallite size of anatase phase, calculated by Scherrer's equation, was found to be 12 nm (Table 1). The XRD pattern of TiO_2 film was recorded exclusively for the film of an adequate thickness to obtain reliable data (TiO_2 - F127, thickness of 270 nm). It is expected that the crystal phase composition of TiO_2 - PSM02 film, after the calcination at the same temperature (450 °C), is also crystalline and characterized with high amount of anatase crystal phase.

Table 1. Textural and structural properties of titania thin films

Photocatalyst – polymer	BET surface area (m^2/m^2)	Average pore size (nm)	Crystal phases	Crystallite size (nm)
TiO_2 - F127	48	10	TiO_2 anatase / Ti_2O_3	12
TiO_2 - PSM02	20	22	/	/

FE-SEM micrographs, the top view, show that TiO_2 film prepared by using PSM02 polymer as a template, leads to formation of crack-free mesoporous TiO_2 films with larger pores (20-22 nm) (Fig. 2b) compared to the films prepared by using Pluronic F127 polymer (8-10 nm) (Fig. 2a).

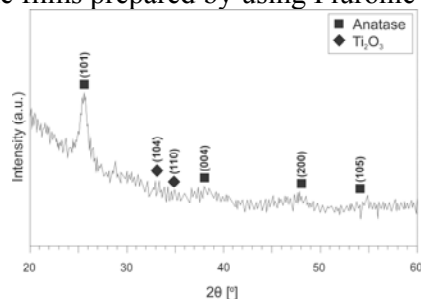


Figure 1.
The XRD pattern of TiO_2 -F127 thin film with thickness of 270 nm [5]

The images of cross-section of the TiO_2 films prepared by using PSM02 polymer indicated the elliptical shape of pores, and a lower level of their interconnectivity. On the other hand, the polymer Pluronic F127 used for film preparation resulted with a cubic-like porosity in the titania film surface with interconnected mesopores ordered in a short range.

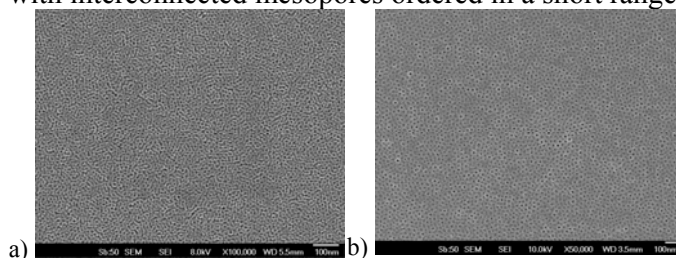


Figure 2.
FE-SEM images of ordered mesoporous titania thin films templated with different polymer matrices: a) F127,

BET specific surface area, pore size and level of pores connectivity all together affect photocatalytic activity of titania thin films. It can be observed that photocatalytic decolorisation process of selected dyes is the most effective when thicker mesoporous TiO₂ films (higher catalyst dosage) with larger specific surface area (TiO₂-F127, 48 m²/m²) was used. Also, under the same experimental conditions, the photocatalytic degradation of MB is faster compared to the degradation of CV (Fig. 3). Most likely, this effect is a consequence of different structures of the organic dyes.

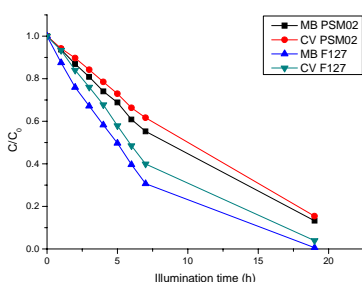


Figure 3.
Decolorisation kinetics of MB and CV using mesoporous titania thin films (TiO₂-F127 and TiO₂-PSM02)

CONCLUSION

The dip coating technique was proved to be effective and relatively simple technique to obtain desired morphology of ordered mesoporous TiO₂ thin films. Complete degradation/decolorisation of the selected organic dyes was achieved. The obtained kinetic data of photodegradation reactions were correlated with the properties of TiO₂ thin films (specific surface area, pore size and shape, and crystallite size).

ACKNOWLEDGEMENT

The authors wish to thank to the Ministry of Education and Science and Technological Development of the Republic of Serbia for a financial support (Projects: ON 172061 and III 45020).

REFERENCES

- [1] J.R. Dominguez, J. Beltran, O. Rodriguez, *Catal. Today*, 2005, 101, 389-395.
- [2] B. Smarsly, D. Grosso, T. Brezesinski, N. Pinna, C. Boissiere, M. Antonietti, C. Sanchez, *Chem. Mater.*, 2004, 16, 2948-2952.
- [3] J.M. Wu, M. Antonietti, S. Gross, M. Bauer, B.M. Smarsly, *Chem. Phys. Chem.*, 2008, 9, 748-757.
- [4] J. Tang, Y.Y. Wu, E.W. McFarland, G.D. Stucky, *Chem. Commun.*, 2004, 14, 1670-1671.
- [5] A. Zarubica, M. Vasic, M.D. Antonijevic, M. Randjelovic, M. Momcilovic, J. Krstic, J. Nedeljkovic, *Mater. Res. Bull.*, 2014, 57, 146-151.

PREPARATION OF Ni/DIATOMITE HYDROGENATION CATALYST PRECURSORS: EFFECT OF COUNTER IONS ON TEXTURAL CHARACTERISTICS

M. Stanković¹, V. Radonjić¹, J. Krstić¹ and D. Marinković²

¹*University of Belgrade, Institute of Chemistry, Technology and Metallurgy, Department of Catalysis and Chemical Engineering, Njegoševa 12, 11000 Belgrade, Serbia,*

²*University of Belgrade, Institute of Chemistry, Technology and Metallurgy, Department of Ecology and Technoeconomics, Njegoševa 12, 11000 Belgrade, Serbia.*

ABSTRACT

Diatomite supported nickel catalyst precursors (Ni/D) were prepared by the precipitation-deposition (PD) method using different nickel salts such as nitrate, chloride, acetate and formate. The effect of counter ions (NO_3^- , Cl^- , CH_3COO^- , and HCOO^-) on the texture of prepared samples was studied. For determination of the textural characteristics mercury intrusion porosimetry (MIP) and N_2 physisorption techniques were used. MIP and physisorption data (pore volume, pore size distribution, porosity as well as N_2 adsorption-desorption isotherms and BET surface area) showed that counter ions were found to have a profound effect on the microstructure and porosity characteristics of Ni/D precursors. An order of the counter ions effect on the textural characteristics of prepared precursors was determined.

INTRODUCTION

High loading silica supported nickel catalysts are used extensively in processes of edible oils hydrogenations. These catalysts are often prepared by Ni ion deposition from aqueous solutions onto proper support, followed by a suitable thermal activation procedure corresponding to reduction step. The nature of deposition method and the choice of precursor complex control the formation of isolated supported phases (nickel basic carbonate) or of supported intermediate phases (nickel hydrosilicates). The hydrogenation activity of the catalysts depends not only on the distribution of nickel as basic carbonate and silicate, but also on the accessibility of free metal surface area in suitable pore dimension [1]. The pore structure of supported catalyst controls transport phenomena and governs selectivity in edible oils hydrogenations.

The choice of nickel precursor salt, in other terms, the choice of the counter ions accompanying Ni cation, is crucial as it governs the solubility of salt and its ability to decompose during reduction. In the following activation step the precursor must be fully transformed into metal particles without leaving side species that may modify the properties of the support. For transition metals nitrate, chloride and sulfate anions are generally selected as counter ions, due to their commercial availability and low price.

The aim of this work was to prepare Ni/D catalyst precursors by DP method with well developed textural parameters. The effect of four Ni salts containing NO_3^- , Cl^- , CH_3COO^- , and HCOO^- anions on the textural characteristics of catalyst precursors was examined.

EXPERIMENTAL

Catalyst precursors were prepared using PD method. Precipitation of nickel was performed by addition of anhydrous sodium carbonate (Na_2CO_3) to a solution containing corresponding nickel salt and magnesium nitrate. The deposition of formed Ni-precipitates onto diatomite support (D) was carried out by addition of hot aqueous suspension of D to slurry containing Ni-precipitates. The same preparation procedure was employed for all the samples. Afterwards, the samples were aged, filtered, washed and finally dried at 110°C overnight. The resultant pale green materials were used as catalyst precursor samples. The sample code, Ni content and yield of the samples as well as preparation procedure are summarized in Table 1.

Table 1. Ni content, yield and PD procedure used to obtain Ni/D samples

Code ^a	Sample		PD procedure					
	Ni _{content} ^b /wt%	Yield /g	Ni salt ^c	Ni/SiO ₂ ^d /molmol ⁻¹	Ni/Mg /molmol ⁻¹	T _p ^e /°C	T _A ^f /°C	t _A ^g /h
Ni-N/D	36.3	7.89	¹ Ni(NO ₃) ₂	1.00	10	90	90	1
Ni-Cl/D	36.2	8.26	² NiCl ₂	1.00	10	90	90	1
Ni-Ac/D	36.6	7.99	³ Ni(CH ₃ COO) ₂	1.00	10	90	90	1
Ni-F/D	36.6	7.96	⁴ Ni(HCOO) ₂	1.00	10	90	90	1

^a N: nitrate, Cl: chloride, Ac: acetate, F: formate; ^b Ni content was determined gravimetrically with dimethylglyoxime; ^c ¹ Carlo Erba reagents min. assay: 99%, For analysis; ² Carlo Erba reagents min. assay: 98%, For analysis; ³ Alfa Aesar: 99+%; ⁴ Alfa Aesar: CAS 3349-06-2; ^d SiO₂ content in diatomite was: 97.9wt%; ^e Precipitation temperature; ^f Aging temperature; ^g Aging time.

Mercury porosimetry was performed on a Porosimeter Model 2000 equipped with the Macropore unit Model 120 manufactured by Carlo Erba. Nitrogen adsorption-desorption isotherms were measured at -196°C on a Sorptomatic 1990 (Thermo Finnigan) after the sample had been degassed at 110°C for 16 h.

RESULTS AND DISCUSSION

Porosimetry Results

Table 2 presents MIP data for prepared precursor samples and diatomite support. The intrusion curves of all precursors, which correspond to cumulative pore volume of the precursors and histograms of the chosen precursors Ni-N/D and Ni-F/D, are presented in Fig. 1. The histograms are used to elucidate distribution of pore sizes in a selected range.

Table 2. Summary of MIP data (macro- and mesoscale pore sizes)

Sample	V_{cum}^a /cm ³ g ⁻¹	D_{average}^b /nm	d_b^c /gcm ⁻³	P^d /%
Ni-N/D	0.391	220	1.19	47
Ni-Cl/D	0.246	220	1.39	34
Ni-Ac/D	0.228	272	1.48	33
Ni-F/D	0.118	74	1.72	20
D ^e	1.018	692	0.65	66

^aCumulative pore volume; ^bAverage pore diameter; ^cBulk density; ^dTotal porosity; ^eD support.

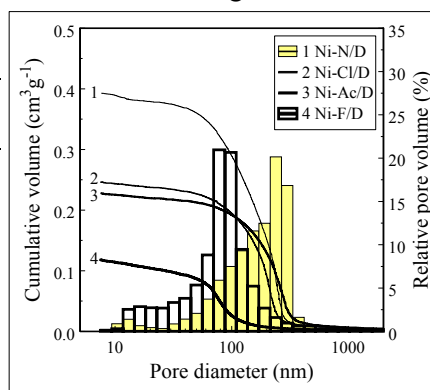


Figure 1. Pore size distribution (PSD) cumulative and histograms

Significant differences are observed.

Sample Ni-N/D shows a much larger cumulative intrusion volume with pores distributed in a pattern resembling a monomodal structure. This sample is very porous (total porosity: 47%, Table 2), with a large percentage (59 vol%) of pores in the 130-320 nm range. In the sample obtained from formate (Ni-F/D), it is obvious an overall decrease in cumulative intrusion volume and a significant reduction in percentage of large pores. In comparison with the support, precursors exhibit reduced porosity and cumulative intrusion volume (Table 2). This is consistent with predictions made for samples with high Ni content (Table 1) that are expected to contain filled pores and reduced pore volumes.

N₂ Physisorption Results In order to obtain porous parameters including specific surface area and pore volume in meso- and microscale pore sizes, N₂ adsorption-desorption isotherms were measured using liquid N₂ (-196°C). Fig. 2 compares the isotherm curves for the diatomite support and samples prepared with the highest (Ni-N/D) and the lowest (Ni-F/D) specific surface area. Values of the specific surface area (BET method), mesopore surface area (t-plot de Boer-Lippens method), micropore volume (Dubinin and Raduskevich method) and total pore volume at P/P₀ = 0.98 are listed in Table 3.

As can be seen from Fig. 2, the isotherms of the samples Ni-N/D and Ni-F/D cannot be classified as typical although they mostly resemble type II according to IUPAC classification. Isotherms for the precursors Ni-Cl/D and Ni-Ac/D (not shown) are very similar in shape to those that are shown in Fig. 2. A distinct increase in nitrogen volume in the low P/P_0 region indicates the presence of micropores associated with mesopores. The amount of nitrogen adsorbed increases gradually and hysteresis loops are observed when $P/P_0 > 0.42$, indicating the existence of many meso- and macropores in the precursor samples as determined also by the results of porosimetry studies. Specific surface area (S_{BET}) was greatly enhanced after

Table 3. Summary of N_2 physisorption data (meso- and microscale pore sizes)

Sample	$S_{\text{BET}}^{\text{a}}$ /m ² g ⁻¹	$S_{\text{meso}}^{\text{b}}$ /m ² g ⁻¹	$V_{\text{total}}^{\text{c}}$ /cm ³ g ⁻¹	$V_{\text{micro}}^{\text{d}}$ /cm ³ g ⁻¹
Ni-N/D	224	22.8	0.201	0.086
Ni-Cl/D	208	11.6	0.170	0.078
Ni-Ac/D	223	7.8	0.161	0.085
Ni-F/D	177	9.3	0.150	0.071
D ^e	26	—	0.073	0.010

^aBET surface area; ^bSurface area in mesoscale pore sizes; ^cTotal pore volume; ^dMicropore volume. The difference between values of V_{total} and V_{micro} corresponds to the meso-pore volume; ^eD support.

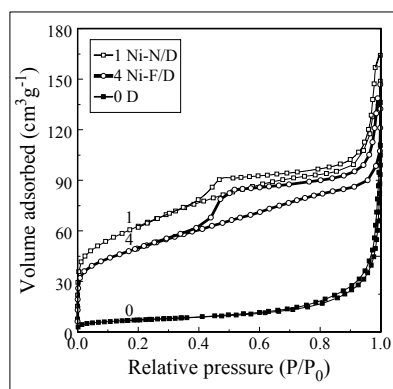


Fig. 2. Nitrogen adsorption-desorption isotherms

deposition Ni-precipitates onto diatomite support increasing in the following order $\text{Ni-N/D} \geq \text{Ni-Ac/D} > \text{Ni-Cl/D} > \text{Ni-F/D} \gg \text{D}$, as shown in (Table 3).

CONCLUSION

Nickel precursors supported on diatomite were prepared by PD method. The results showed that Ni-precipitates deposited from different nickel salts significantly affect the textural characteristics of the precursors. The sample from nitrate had the best textural properties among the studied precursors and therefore it can be expected that the catalyst prepared on its basis will show better characteristics in comparison to others.

ACKNOWLEDGEMENT

This work was supported by the Ministry of Education, Science and Technological Development of the Republic of Serbia (Project III 45001).

REFERENCES

- [1] G. P. Babu and R. S. Murthy in: Recent Developments in Catalysis: Theory and Practice, B. Viswanathan, C. N. Pillai (Eds.), Editions TECHNIP, 1992.

**PREPARATION OF CaO/ γ -Al₂O₃ CATALYST FOR BIODIESEL
FUELS. THE CATALYTIC ACTIVITY IN RELATION TO
THERMAL TREATMENT**

D. Marinković^{1*}, M. Stanković^{1**}, B. Nedić Vasiljević², A.V. Veličković³
and J. Avramović³

¹*University of Belgrade, Institute of Chemistry, Technology and Metallurgy,
*Department of Ecology and Technoeconomics, **Department of Catalysis
and Chemical Engineering, Njegoševa 12, 11000 Belgrade, Serbia,*

²*University of Belgrade, Faculty of Physical Chemistry, Studentski trg
12-16, 11000 Belgrade, Serbia,*

³*University of Niš, Faculty of Technology, Bulevar oslobođenja 124, 16000
Leskovac, Serbia.*

ABSTRACT

A heterogeneous base catalyst (CaO/ γ -Al₂O₃) for biodiesel production from sunflower oil was prepared by the impregnation method. The catalyst was characterized by means of MIP and XRD methods. The catalytic activity of the nitrate-derived CaO/ γ -Al₂O₃ was determined in relation to the calcination temperature ranging from 425 to 500°C. The reaction was carried out in a batch type of reactor equipped with a reflux condenser. The maximum yield of biodiesel of almost 95% was achieved with the catalyst calcined at 475 °C under the following reaction conditions: reaction temperature of 60 °C, methanol to oil molar ratio of 12/1, reaction time of 5 h.

INTRODUCTION

Biodiesel, fatty acid methyl esters (FAMES) derived from renewable resources such as vegetable oils or animal fats is expected to be one of the biomass-base alternative fuel for diesel fuel due to its numerous advantages such as: renewability, high biodegradability, low SO_x particulate matter content and lack of aromatic compounds. The classical method of biodiesel production is based on triacylglycerols transesterification to FAMES. Homogeneous base catalysts are the most conventional catalyst used in the biodiesel production. Transesterification with heterogeneous base catalysts is one of the very promising alternatives for producing biodiesel from vegetable oils. Kouzu et al. [1] used Ca-based catalysts such as CaO, Ca(OH)₂ and CaCO₃ as solid catalysts in the production of biodiesel from soybean oil with the biodiesel yield of 93, 12 and 0%, respectively.

Alumina supported CaO-based catalyst has also been used for production of biodiesel from vegetable oils [2]. It should be noted that catalytic activities most of them are not as high as those of the homogeneous catalysts. In addition, information regarding the influence of the thermal treatment of the catalyst in the final step of its preparation such as temperature and time duration of the calcination on their activity is quite scarce. Therefore, the aim of this study was to examine the effect of calcination temperature on the yield of biodiesel in the methanolysis of sunflower oil over the CaO/ γ -Al₂O₃ catalyst.

EXPERIMENTAL

Catalyst preparation

CaO/ γ -Al₂O₃ samples were prepared according to the wet impregnation (WI) method [3], using Ca(NO₃)₂·4H₂O as precursor salt, γ -Al₂O₃ (spherical shape, 1-3 mm in diameter) as support, and water as medium. The sample designation, CaO content and preparation procedure are shown in Table 1.

The calcination was performed in the nitrogen atmosphere (N₂ flow: 10 dm³/h) using a tube vertical furnace (Carbolite Furnaces CTF 12/75, Eurotherm 818P). The calcined samples were kept in a desiccator in the presence of silica and KOH pellets to avoid water and CO₂ contact with the

Table 1. CaO content and preparation procedure for CaO/ γ -Al₂O₃ samples

Sample		Preparation procedure					
Designation	CaO* /wt%	WI		Calcinations			
		C _{Ca(NO₃)₂} ^a /wt.%	t _{WI} ^b /h	T _{WI} ^c /°C	T _D ^d /°C	t _C ^e /h	T _C ^f /°C
Ca-425/ γ -Al ₂ O ₃	10.2	50	2	30	120	4	425
Ca-450/ γ -Al ₂ O ₃	10.9	50	2	30	120	4	450
Ca-475/ γ -Al ₂ O ₃	10.1	50	2	30	120	4	475
Ca-500/ γ -Al ₂ O ₃	9.6	50	2	30	120	4	500

^aImpregnation salt concentration; ^bWI time; ^cWI temperature; ^dDrying temperature ^eCalcination time; ^fCalcination temperature; *Gravimetric determination of calcium as CaC₂O₄·H₂O.

samples.

Catalyst characterization

Mercury intrusion porosimetry (MIP) was carried out on a Porosimeter 2000 series (Carlo Erba Strumentazione). Powder X-ray diffraction (XRD) patterns were collected by means of the Philips, PW 1710 diffractometer (Cu K α radiation).

Transesterification procedure

The activity of the prepared catalysts was examined in the methanolysis of sunflower oil. All transesterification runs were performed in a 250 ml three-neck glass flask equipped with a reflux condenser and a magnetic stirrer.

Experiments were conducted under the following conditions: catalyst loading of 0.5 wt.% CaO (relative to the amount of oil), methanol/oil molar ratio of 12/1, reaction temperature of 60 °C and reaction time of up to 5 h. After each interval, fractions of reaction mixture were captured for HPLC analysis. Reaction mixture was analyzed *off-line* by an Agilent 1100 Series HPLC (Zorbax® 5 µm Eclipse-XDB-C18 80 Å, LC Column 150 x 4.6 mm).

RESULTS AND DISCUSSION

Mercury porosimetry results are summarized in Table 2. The results indicated that the parameters of the porous structures such as pore volume, surface area and porosity of the samples were gradually increased with an

Table 2. Summary of MIP data

Sample	V_{cum}^a /cm ³ g ⁻¹	S_{Hg}^b /m ² g ⁻¹	$D_{av.}^c$ /nm	P^d /%
Ca-425/ γ -Al ₂ O ₃	0.322	59	20	50
Ca-450/ γ -Al ₂ O ₃	0.350	65	20	53
Ca-475/ γ -Al ₂ O ₃	0.455	89	20	59
Ca-500/ γ -Al ₂ O ₃	0.482	97	16	63
γ -Al ₂ O ₃ ^e	0.620	125	16	69

^aCumulative pore volume; ^bSurface area; ^cAverage pore diameter; ^dTotal porosity; ^eCommercial-Rhone Poulenc.

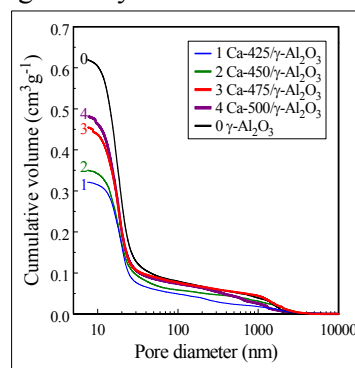


Figure 1. Pore size

increase in calcination temperature.

The XRD patterns of CaO/ γ -Al₂O₃ catalyst samples calcined at different temperatures and γ -Al₂O₃ support are shown in Fig. 2. Commercial support showed XRD reflections at 2-theta corresponding to the γ -Al₂O₃ in cubic phase (JCPDS 50-0741). XRD patterns of the calcined samples (Ca-500/ γ -Al₂O₃ not shown) were pronounced at similar 2-theta due to the γ -Al₂O₃ support. As indicated in Fig. 2, the typical XRD reflections indexed to Ca(NO₃)₂ for the samples which were calcined at lower temperatures (425 and 450 °C). This observation indicated that the impregnated precursor was not decomposed completely on the sample surface at temperatures below 450 °C. With increase in the calcination temperature from 450 to 475 °C, the characteristic reflections corresponding to Ca(NO₃)₂ disappeared and the well-defined diffraction reflections corresponding to CaO became more intensive in the XRD pattern.

Figure 3 shows the yield of FAME versus calcination temperatures after reaction time of 5 h. It was clearly seen that the activities of the samples were strongly influenced by the calcination temperatures. With respect to the yield to FAME, the calcination temperature of 475 °C appeared to be

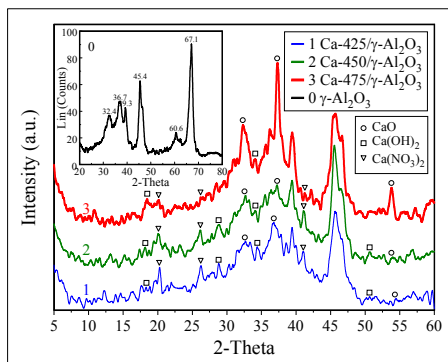


Fig. 2. XRD patterns of CaO/ γ -Al₂O₃ samples and γ -Al₂O₃ support

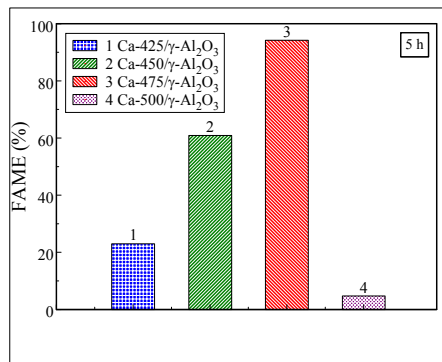
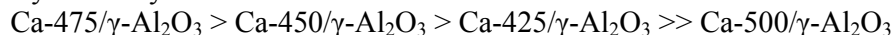


Fig. 3. Yields of FAME produced by the sunflower oil methanolysis

most beneficial. However, the very low FAME yield was observed with the sample calcined at temperatures above 475 °C (Ca-500/ γ -Al₂O₃). It might be because of the crystallite aggregation caused by the increased degree of sintering of the active metal particles and/or the lack of strong basic sites where the methanolysis occurs [2].

CONCLUSION

The effect of different calcination temperatures for the nitrate-based CaO/ γ -Al₂O₃ catalyst was discussed in terms of the characteristics and activity of the catalysts. The results indicated that the catalyst sample calcined at 475 °C (Ca-475/ γ -Al₂O₃) exhibited higher activity in the methanolysis of sunflower oil compared to the samples calcined at lower (425 °C and 450 °C) and higher (500 °C) temperatures. Consequently, the following order of catalyst activity was established:



ACKNOWLEDGEMENT

This work was supported by the Ministry of Education, Science and Technological Development of the Republic of Serbia (Project III 45001).

REFERENCES

- [1] M. Kouzu, T. Kasuno, M. Tajika, Y. Sugimoto, S. Yamanaka, J. Hidaka, *Fuel*, 2008, 87, 2798-2806.
- [2] N. Pasupulety, K. Gunda, Y. Liu, G.L. Rempel, F.T.T. Ng, *Applied Catalysis A: General*, 2013, 452, 189-202.
- [3] M. Stanković, N. Jovanović in: *Stud. Surf. Sci. Catal.*, Vol. 110, 1145-1154, R.K. Grasselli, S.T. Oyama, A.M. Gaffney, J.E. Lyons (Eds.), Elsevier, 1997.

KINETIC STUDY OF COMPETITIVE Co^{2+} AND Sr^{2+} SORPTION BY BAUXITE RESIDUE

A. Milenković¹, I. Smičiklas¹, M. Šljivić-Ivanović¹ and N. Vukelić²

¹ University of Belgrade, "Vinča" Institute of Nuclear Sciences, Radiation and Environmental Protection Department, P.O. Box 522, 11000 Belgrade, Serbia (aleksmileks@gmail.com)

² University of Belgrade, Faculty of Physical Chemistry, Studentskitrg 12-16, P. O. Box 137, 11001 Belgrade, Serbia

ABSTRACT

Multi-component sorption studies are essential to identify the applicability of red mud as a low-cost sorbent for the simultaneous removal of metal ions from wastewaters. Sorption kinetics of Co^{2+} and Sr^{2+} ions was studied, at their different molar ratios in the mixture. The pseudo-second-order rate model best described the kinetics of metal sorption from binary metal systems. The increase of initial concentration of each cation in the mixture provoked its increased sorption capacity, but decreased sorption rate. Co^{2+} sorption was superior in terms of both the rate and the capacity, therefore exerted strong inhibitory effect on Sr^{2+} sorption.

INTRODUCTION

Due to high efficacy and low-cost, sorption processes can be applied for the decontamination of liquid radioactive wastes [1]. Nowadays, wastes and by-products from various industries are studied as potential sorbents [2]. Red mud, an alkaline by-product of alumina industrial production from bauxite ore, is an example of heterogeneous mineral material interesting for environmental applications [3].

In the previous study, alkaline red mud from "Birač" Alumina Factory (Bosnia and Herzegovina) was found to be a promising sorbent for ^{60}Co and ^{90}Sr ions [4]. These two radioactive isotopes go hand in hand as products of nuclear reactor operations: ^{60}Co is a corrosion product, while ^{90}Sr occurs by fission of uranium and plutonium. Therefore, multi-component sorption studies are required to identify the capabilities and limitations of red mud as a low-cost sorbent for the simultaneous removal of these metal ions from wastewater.

In this paper, time dependant sorption of ^{60}Co and ^{90}Sr was examined using mixtures with different molar ratios of selected cations.

EXPERIMENTAL

After settling, the liquid phase above red mud particles was decanted, whereas the solid residue was dried at 105°C and homogenized in the mortar. Stock solutions of Co²⁺ and Sr²⁺ ions (2·10⁻³ mol/dm³) were prepared by dissolving Co(NO₃)₂·6H₂O and Sr(NO₃)₂ salts, in deionized water. Simulated liquid wastes with different molar ratios of two cations (Co²⁺: Sr²⁺ = 1:2, 1:1 and 2:1) were prepared from stock solutions, keeping the overall cation concentration constant (2·10⁻³ mol/dm³). The initial pH of each mixture was adjusted to 5, with a few drops of 0.01 mol/dm³ HNO₃. The effect of contact time on the amount of cations removed was determined by equilibrating 0.1000 g of red mud with 20.00 cm³ of mixture solutions, on the laboratory shaker. At different time intervals ranging from 15 min to 48 h, one of the batches was taken for solid/liquid separation. Sorbed cation concentrations were determined by Perkin Elmer 3100 Atomic Absorption Spectrometer, as differences between initial and final concentrations.

RESULTS AND DISCUSSION

The amounts of Co²⁺ and Sr²⁺ sorbed at various time intervals from the mixed solutions are presented in the Fig. 1. It can be observed that the sorption onto red mud was generally fast during first hours of contact, followed by a slower reaction step. With the increase of initial concentration of each cation, equilibration time increased as well. Equilibrium times for Co²⁺ sorption were 6 h for 1:2 molar ratio to Sr²⁺, and 24 h for the ratios 1:1 and 1:2. Sorption of Sr²⁺ reached equilibrium in 6 h and 30 h, for Co²⁺: Sr²⁺ molar ratios 2:1 and 1:1, respectively, whereas for the ratio 1:2 sorbed amounts of Sr²⁺ slightly increased during the second day of equilibration.

Applicability of several kinetic models for the interpretation of experimental results was tested. Highest correlation coefficients (R²) between the model and the experimental results were obtained using the pseudo-second-order kinetic equation [5]:

$$\frac{t}{q_t} = \frac{1}{k_2 q_e^2} + \frac{t}{q_e} \quad (1)$$

where k₂ (g/(mmol min)) is the pseudo-second-order rate constant, q_e (mmol/g) the amount of cations sorbed at equilibrium, and q_t is the amount of cations sorbed at any time t. Calculated kinetic parameters are presented in Table 1. Calculated sorption capacities increased along with the initial concentration of a particular cation, whereas the rate constants decreased.

From binary solutions, Co²⁺ was sorbed more selectively on red mud surface, showing higher q_e and k₂ values. Considering equimolar mixture, Co²⁺ sorption capacity was almost twice the amount of Sr²⁺ sorbed (0.203 mmol/g

and 0.117 mmol/g, respectively). The equilibrium sorbed amounts from single metal solutions (initial cation concentration 10^{-3} mol/dm^3) were found to be 0.206 mmol/g for Co^{2+} and 0.197 mmol/g Sr^{2+} [4].

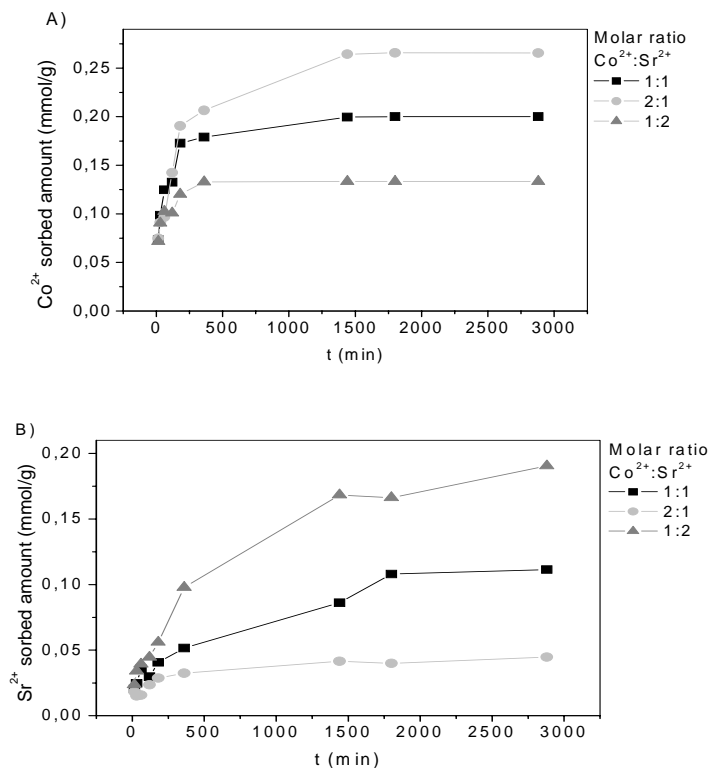


Figure 1. Effect of contact time on competitive Co^{2+} (A) and Sr^{2+} (B) sorption by red mud.

Table 1. The parameters of pseudo-second-order kinetic model for competitive Co^{2+} and Sr^{2+} sorption onto red mud

Molar ratio Co: Sr	Co^{2+}			Sr^{2+}		
	q_e mmol/g	k_2 g/(mmolmin)	R^2	q_e mmol/g	k_2 g/(mmolmin)	R^2
1:2	0.134	0.412	0.99	0.205	0.015	0.98
1:1	0.203	0.128	0.99	0.117	0.033	0.98
2:1	0.275	0.043	0.99	0.045	0.227	0.99

For each binary system, total sorption capacity remained relatively constant ($\Sigma q_e = 0.326 \pm 0.006 \text{ mmol/g}$). Individual and overall sorbed amounts are

presented in Fig. 2. The results demonstrate that the presence of Sr^{2+} ions in the mixture did not interfere with Co^{2+} sorption. Conversely, Co^{2+} inhibited removal of Sr^{2+} .

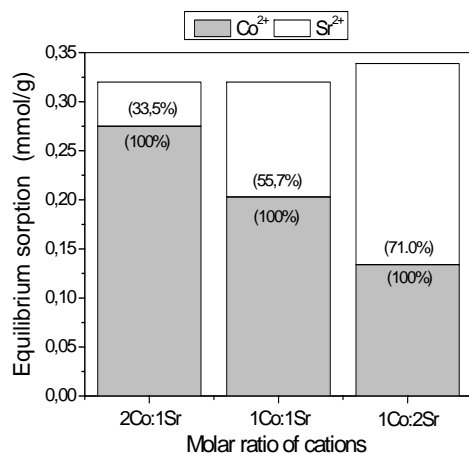


Figure 2. Individual and overall amounts of Co^{2+} and Sr^{2+} sorbed by red mud from binary mixtures.

CONCLUSION

With the increase of the initial concentration of a particular cation in the mixture, its sorption capacity increased, whereas the corresponding pseudo-second-order rate constant decreased. Considering experimental conditions applied in this study, red mud can be utilized for simultaneous removal of Co^{2+} and Sr^{2+} cations. However, coexisting Sr^{2+} ions did not affect Co^{2+} sorption capacity, while Co^{2+} exerted strong inhibitory effect on Sr^{2+} removal.

ACKNOWLEDGEMENT

This work was supported by the Ministry of Education, Science and Technological Development of the Republic of Serbia (Project III43009).

REFERENCES

- [1] IAEA-TECDOC-1336, Combined methods for liquid radioactive waste treatment, Final report of a coordinated research project, 1997–2001, Vienna 2003.
- [2] S. Bailey, T. R. Olin, M. A. Dean, A review of potentially low-cost sorbents for heavy metals, *Water Res.*, 1999, 33, 2469–2479.
- [3] S. Wang, H. M. Ang, M. O. Tadé, Novel applications of red mud as coagulant, adsorbent and catalyst for environmentally benign processes, *Chemosphere* 2008, 72, 1621–1635.
- [4] A. Milenković, I. Smičiklas, J. Marković, N. Vukelić, Immobilization of ^{60}Co and ^{90}Sr ions using red mud from aluminum industry, *Nuclear Technology & Radiation Protection*, 2014, 29, 79–87.
- [5] Y.S. Ho, G. McKay, Pseudo-second order model for sorption processes, *Process Biochem.*, 1999, 34, 451–465.

KINETIC STUDIES OF MICROWAVE EXTRACTION OF CAFFEINE FROM GUARANA SEED IN AQUEOUS SOLUTION

B.Koturević¹, J. Jovanović² and B. Adnađević²

¹*The Academy of Criminalistic and Police Studies, Cara Dusana 196, 11080
Belgrade, Zemun, Serbia*

²*Faculty of Physical Chemistry, Studentski trg 12-16, 11001 Belgrade,
Serbia (bora@ffh.bg.ac.rs)*

ABSTRACT

The kinetic of isothermal microwave extraction of caffeine from guarana seed in aqueous solution at 333, 338 and 343 K was investigated. The concentrations of the extracted caffeine in aqueous solution were determined by UV-VIS spectrophotometry. Model fitting method was used for determining kinetic model of caffeine extraction in conditions of microwave heating. It was found that the kinetic of caffeine extraction can be modeled by *first-order kinetics model*. The kinetic parameters, E_a (kJ/mol) and A (min⁻¹) of caffeine extraction were also determined. Applying isoconversional method it was established that kinetic of caffeine extraction from guarana seed is an elementary kinetic process. Furthermore, the mechanism model of caffeine extraction was suggested.

INTRODUCTION

Guarana (*Paullinia cupana*, Sapindaceae) is a shrubby, woody plant that grows in the areas with tropical heat and torrential rains [1]. Guarana seeds contain large amounts of methylxanthines (caffeine, theophylline and theobromine), tannins, saponins, polysaccharides, etc. [2]. Extract from guarana seed is widely used for its antibacterial, antifungal, antioxidant, anti-depressant and stimulant effects [3]. Nowadays caffeine extraction is carried out by conventional methods using different organic solvents (water, chloroform, methylene chloride), water organic solvent mixtures (water-ethanol) or by supercritical fluid extraction *with carbon dioxide*.

Since to our knowledge there are no data available on the kinetic of caffeine extraction from guarana seed using microwave heating, the aim of this paper is to examine the isothermal extraction of caffeine from guarana seed with water using microwave heating.

EXPERIMENTAL

For the purpose of studying the kinetics of caffeine extraction from guarana seed, powder form ($d_p \leq 500 \mu\text{m}$), (Grass Hut Treasures LLC, USA) is used. Distilled water was used as solvent. The extraction method is performed with batch method, as follows. In typical experiment, the 1 g of guarana seed powder was suspended in 80 mL of distilled water. The suspension was stirred continuously maintaining constant temperature (333, 338 and 343 K) in a microwave reactor (CEM, model Discovery, USA). At predetermined time intervals, *aliquots were taken* from the reaction mixture. Caffeine concentration in aliquot solution was determined by spectrophotometric method using caffeine calibration curve that was prepared using known caffeine standards. The *UV-VIS absorption spectrum* of caffeine water solution was recorded using spectrophotometer Agilent, model 8453, USA. The kinetic model of caffeine extraction was evaluated applying model-fitting method [4]. The kinetics complexity of extraction was established by the Friedman isoconversional method [5].

RESULTS AND DISCUSSION

The experimentally obtained isothermal kinetic curves of caffeine extraction in the aqueous solution (the dependence of concentration versus time) at different temperatures are shown in Figure 1.

Kinetic curves are identical in shape, so it is easy to recognize three characteristic shapes of the changes in concentration of caffeine on time. These shapes are a linear, convex and a saturation stage or plateau.

With increasing temperature of extraction, the slope of

the linear change is growing, length of the convex changes is reducing and the value of the reached caffeine concentration at plateau increases.

By applying the model fitting method it was determined that the kinetics of isothermal caffeine extraction under microwave heating can be kinetically modeled by *first-order kinetics model, and can be described by equation*:

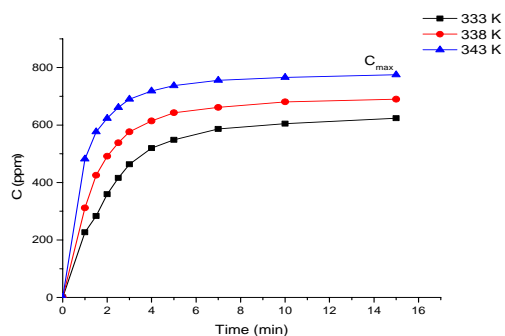


Figure 1. The dependence of caffeine concentration on time

$[-\ln(1-C/C_m)] = k_M \cdot t$, where k_M is the model rate constant.

If kinetics of extraction can be described by **first-order kinetics model**, then the dependence $[-\ln(1-C/C_m)]$ on time should give straight lines. The dependence of $[-\ln(1-C/C_m)]$ on time for the caffeine extraction under microwave heating at different temperatures is shown in Figure 2.

The dependence of $[-\ln(1-C/C_m)]$ on time at all investigated temperatures gives straight lines which allows calculation of the model rate constant (k_M) and kinetic parameters of extraction, namely, the activation energy (E_a) and preexponential factor (A). The model rate constants for all investigated

temperatures were calculated from the **slopes of these lines**. Since model rate constant is increasing with temperature, the kinetic parameters has been determined by applying the Arrhenius equation.

The effects of temperature of extraction on the k_M values and kinetic parameters E_a (kJ/mol) and A(min^{-1}), are given in Table I.

By applying Friedman's isoconversional method it was established that activation energy is independent on the degree of caffeine extraction (Figure 3) which indicates that the kinetic of caffeine extraction from guarana seed is an elementary

kinetic process. According to this, kinetic of caffeine extraction under

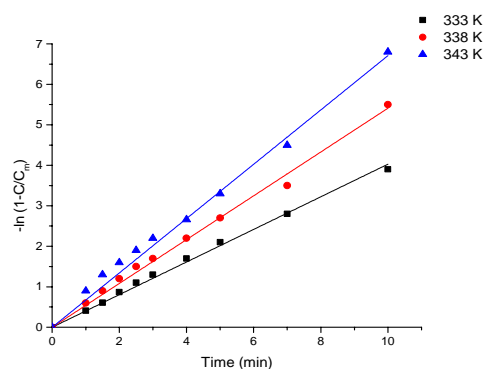


Figure 2. The plot of $[-\ln(1-C/C_m)]$ versus time for extraction of caffeine

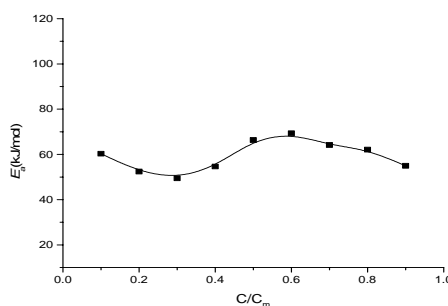


Figure 3. Dependence of E_a on degree of extraction

microwave heating is significantly faster than conventional extraction, and it is not limited by diffusion of water to caffeine molecule, but by the speed of caffeine dissolution in water.

Table 1. The effect of temperature on the k_M values and kinetic parameters of caffeine extraction

T (K)	k_M (min ⁻¹)	R ²	E_a (kJ/mol)	A (min ⁻¹)
333	0,408	0,9958		
338	0,541	0,9937	49,6	2,41 x 10 ⁷
343	0,671	0,9875		

CONCLUSION

Extraction of caffeine from guarana seed *under isothermal microwave reaction conditions* is significantly faster than conventional extraction. Caffeine extraction from guarana seed in aqueous solution is an elementary kinetic process. It was found that the kinetic of extraction can be modeled by *first-order kinetics model*. The values of the kinetic parameters are: $E_a=49,6$ kJ/mol and $A=2,41 \times 10^7$ min⁻¹.

ACKNOWLEDGEMENT

This investigation was supported by the Ministry of Science and Technical Development of the Republic of Serbia, through Project No.142025G.

REFERENCES

- [1] W.T. Baumann, H.B. Schulthess, K. Hanni, Journal of Phytochemistry, 1995, 39 (5), 1063-1070.
- [2] L. Hamerski, V.G. Somner, N. Tamaio, J. Med. Plants Res., 2013, 7 (30), 2221-2229.
- [3] L. Majhenič, M. Škerget, Ž. Knez, , Food Chem., 2007, 104, 1258-1268.
- [4] S. Vyazovkin, C.A Wight , Thermochim. Acta, 1999, 340/341, 53-68.
- [5] H. Friedman, J. Polym. Sci., 1964, C 6, 183–195.

KINETICS OF MINIEMULSION DITHIOBENZOATE-MEDIATED STYRENE POLYMERIZATION

N.S. Serkhacheva¹, N.I. Prokopov¹, A.V. Tolkachev¹, A.Yu. Gervald¹ and E.V. Chernikova²

¹*Lomonosov Moscow State University of Fine Chemical Technologies, pr. Vernadskogo 86, Moscow, Russia, natalia-serkhacheva@yandex.ru*

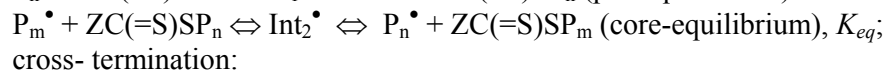
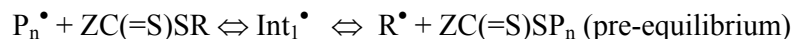
²*Lomonosov Moscow State University, Chemistry Department, Leninskie Gory, 1/3, Moscow, Russia*

ABSTRACT

Kinetics of miniemulsion RAFT polymerization of styrene in the presence of oil-soluble radical initiator AIBN mediated by benzyl dithiobenzoate (BDB) and polystyrene dithiobenzoate (PSB) was studied. The kinetic data were compared with results obtained for bulk styrene polymerization carried out in analogous conditions and miniemulsion BDB-mediated polymerization initiated by water-soluble initiator – potassium persulfate.

INTRODUCTION

Emulsion and miniemulsion free-radical polymerization are preferable techniques for synthesis of various commercial polymers. The developing of controlled radical polymerization has broadened capabilities of these processes allowing easy control of particle size distribution, molecular weight characteristics of the polymers formed and even the macromolecular architecture [1]. In particular, reversible addition-fragmentation chain transfer (RAFT) polymerization is a versatile approach resulting in realization of macromolecular design in conditions of both homogeneous and heterogeneous polymerization [2]. Its mechanism includes reactions of chain initiation, propagation and termination and the specific reactions of reversible chain transfer with formation of intermediate radicals:



and self-termination of these radicals [3]:



The most of publications devoted to miniemulsion RAFT polymerization are focused at the choice of appropriate agent for controlled synthesis

polymerization conditions [2]. Meanwhile, there is still lack of information about kinetic features of this process and its similarity and distinction from bulk polymerization except two publications devoted to styrene miniemulsion polymerization mediated by polystyrene dithiobenzoate [4, 5]. The main goal of this study was to compare kinetic regularities of styrene polymerization in the presence of low and high molecular weight RAFT agents for bulk and miniemulsion polymerization conditions.

EXPERIMENTAL

For bulk polymerization, a series of styrene solutions containing the same AIBN concentration 0.111 mol/L and various concentrations of RAFT agents (benzyl dithiobenzoate (BDB): 0.019, 0.039, 0.075, and 0.150 mol/L or polystyrene dithiobenzoate (PSB): 0.006, 0.009, 0.015, and 0.075 mol/L) were prepared. Solutions were poured in ampoules, degassed and sealed. Polymerization kinetics was studied by calorimetry under isothermal conditions at 70 °C. PSB was synthesized via bulk polymerization using 0.1 mol/L BDB and 0.01 mol/L AIBN; $M_n = 6100$, $PDI = 1.27$.

For miniemulsion polymerization, sodium dodecyl sulfate (SDS, 3 wt. %) was dissolved in water, mixed with monomer phase containing AIBN (0.111 mol/L with respect to styrene), hexadecane (4.6 wt. %) and BDB or PSB (0 – 0.15 mol/L with respect to styrene), and miniemulsified with ultrasonifier during 15 min. The obtained miniemulsion was charged into reactor HWS-Labortechnik, bubbled with nitrogen and heated at 70 °C; kinetics was studied by gravimetry.

Molar mass characteristics were determined by GPC in THF at 35°C using PS standards for calibration. Molar mass characteristics were determined by a Waters liquid chromatograph equipped with a RI410 refractive index detector and three columns packed with ultrastryragel with pore dimensions 10^4 , 10^5 Å and a Waters Styragel HR 5E linear column in THF at 35°C using PS standards for calibration.

RESULTS AND DISCUSSION

Kinetic features of styrene polymerization in bulk and miniemulsion initiated by AIBN (0.111 mol/L) in the presence of both BDB and PSB differ noticeably (as example, see Fig. 1).

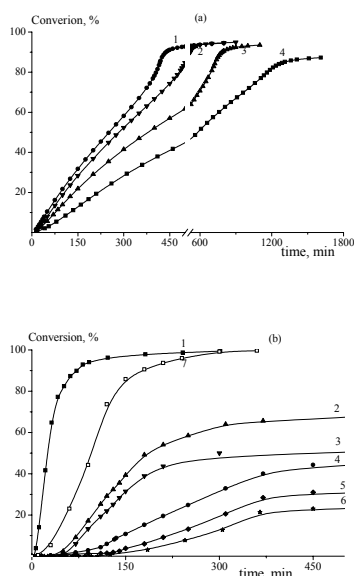


Figure 1. Kinetics of styrene RAFT polymerization in the presence of BDB (a) in bulk and (b) miniemulsion. a) $[BDB]_0 \times 10^2 = 2$ (1), 3.9 (2), 7.5 (3), 15 (4); b) $[BDB]_0 \times 10^2 = 0$ (1), 2 (1, 7), 3.9 (3), 7.5 (4), 15 (5), 22.5 mol/L (6); initiators: AIBN (1 – 6), KPS (7).

In the case of low molecular mass RAFT agent (BDB), in bulk polymerization (Fig. 1a): 1) no induction period is observed on kinetic curves; 2) the increase of BDB concentration causes rate retardation, which is due to both cross- and self-termination of intermediate radicals; 3) auto-acceleration is suppressed only when $[BDB]_0 \geq [AIBN]_0$; 4) the limited conversion are achieved slowly, while in miniemulsion polymerization (Fig. 1b): 1) the induction period is observed, its duration increase with rise of BDB concentration, i.e. steady-state is established at higher polymerization time comparing to bulk process; 2) the retardation is most pronounced at high BDB concentration comparing to bulk polymerization; 3) the values of limited conversion fall drastically with rise of BDB concentration; the limited conversions are achieved more rapidly comparing to bulk polymerization. In contrast to AIBN initiated miniemulsion polymerization, the use of potassium persulfate (KPS) even at lower concentration allow to increase noticeably polymerization rate and limited conversion (Fig. 1b, curve 7).

In the case of polymeric RAFT agent (PSB), polymerization in bulk is also retarded; however mainly due to cross-termination of intermediate radicals. In general, the polymerization rate at steady-state is higher comparing to BDB-mediated polymerization, and auto-acceleration is suppressed at lower concentrations of PSB. In miniemulsion polymerization the rate of the process is lower comparing to reaction in the absence of PSB. Retardation is also less pronounced in contrast to BDB-mediated process: induction period disappeared, while limited conversions are achieved already after 1 h from starting polymerization. According to Fukuda equation [6], polymerization rate R_p is described as: $(R_{p,0}/R_p)^2 = 1 + 2(k_t'/k_t)K_{eq}[RAFT]_0 + (k_t'/k_t)K_{eq}^2 \times [RAFT]_0^2$. The different shape of kinetic curves in bulk and miniemulsion under the similar experimental conditions allow to conclude that the

contribution of intermediate termination reactions in rate retardation in these systems is different. According to our previous results no Int_1 can be detected in styrene – BDB- AIBN system [7], while a low concentration of Int_2 slowly appears after some time from starting of heating. The estimation shows that at high RAFT agent concentration both termination reactions give contribution to rate retardation, while at low RAFT agent concentration cross-termination prevails. The slow establishing of steady state may be caused by increase of probability of termination reactions with participation of Int_1 in small droplets comparing to bulk polymerization. This conclusion is in agreement with kinetics of miniemulsion polymerization in the presence of PSB, in which steady-state is established more rapidly due to absence of Int_1 and with analysis of MWD of polymers formed: the presence of low molecular weight fraction in BDB-mediated and its absence in PSB-mediated miniemulsion polymerization. Essentially, that replacing of AIBN by KPS resulted in increase of polymerization rate; hence the contribution of intermediate termination reactions becomes lower.

CONCLUSION

The kinetic analysis revealed that kinetic features of miniemulsion styrene polymerization depends on the nature of RAFT agent (i.e. start of polymerization either from pre- or core-equilibrium) and of initiator (oil- or water-soluble). These results give a powerful tool to govern the kinetic regularities of miniemulsion RAFT polymerization.

REFERENCES

- [1] Miniemulsion polymerization technology. Ed. by V. Mittal. Wiley, Hoboken. 2010. 311 p.
- [2] A. Butte, G. Storti, M. Morbidelli, *Macromolecules*, 2001, 34 (17), 5885 – 5896.
- [3] K. Suzuki, Y. Kanematsu, T. Miura, M. Minami, S. Satoh, and H. Tobita, *Macromol. Theory Simul.*, 2014, 23, 136 – 146.
- [4] Handbook of RAFT Polymerization, Ed. by C. Barner-Kowollik. Wiley-VCH, Weinheim. 2008.
- [5] K. Suzuki, Y. Nishimura, Y. Kanematsu, Y. Masuda, S. Satoh, and H. Tobita, *Macromol. React. Eng.*, 2012, 6, 17 – 23.
- [6] Y. Kwak, A. Goto, T. Fukuda, *Macromolecules*, 2004, 37 (4), 1219 – 1225.
- [7] E. V. Chernikova, A. V. Tarasenko, E. S. Garina, V. B. Golubev, *Polymer Science, Ser. A*. 2006, 48 (10), 1046 – 1057.

METAMIZOLE AND TETRACYCLINE IN THE REACTION WITH Cu (II) AND HYDROGEN PEROXIDE

S. M. Sunarić¹ and S. S. Mitić²

¹*Faculty of Medicine, Department of Chemistry, Bulevar dr Zorana Djindjica 81, 18000 Niš, Republic Serbia, (ssunaric@medfak.ni.ac.rs)*
²*Faculty of Natural Sciences and Mathematics, Department of Chemistry, Višegradaska 33, 18 000 Niš, Republic Serbia*

ABSTRACT

In this paper the interfering effect of analgesic metamizole on the reaction of tetracycline with the Cu(II)/H₂O₂ reagent at pH 8.2 was described. It was observed that metamizole had an inhibitory effect on the tetracycline degradation with Fenton like reagent, which indicates its higher reactivity with Cu(II)/H₂O₂ system. The reactions occur at the drugs concentration levels which are expected after oral administration.

INTRODUCTION

Metamizole (sodium salt of the 1-phenyl-2,3-dimethyl-4-methylaminomethane sulphonate-5-pyrazolone; dipyrone, analgin, novalgin) is widely used as an analgesic drug and tetracycline is antibiotic which is used in patients allergic to penicillin. In many cases, patient is treated simultaneously with a few drugs representing different groups. Metamizole can produce allergy and chemical intolerance [1]. The system of hydrogen peroxide and Cu (II) ions is known as Fenton like reagent which generates highly reactive oxygen species. The production of reactive oxygen species is the process which is permanently occurred in human cells. Therefore, it is interesting to investigate simultaneous reaction of these two drugs with Fenton like reagent.

EXPERIMENTAL

The stock solution of tetracycline (1.00×10^{-4} mol/dm³) was freshly prepared by dissolving the required amount of tetracycline-hydrochloride, C₂₂H₂₄N₂O₈·HCl, (Sigma-Aldrich) in deionised water. The stock solution of metamizole (1.00×10^{-4} mol/dm³) was obtained by dissolving the required amount of metamizole-sodium C₁₃H₁₆N₃O₄SNa·H₂O in deionized water. The solution of Cu(II) (1.00×10^{-4} mol/dm³) was prepared by dissolving CuCl₂·2H₂O (Merck) in deionised water. Hydrogen peroxide solution (1.00 mol/dm³) was prepared just before use from a 35% commercial reagent (Merck). The tris-HCl buffer (pH 8.2) was obtained by mixing the solutions

of tris(hydroxymethyl)aminomethane (1.0 mol/dm^3) and HCl (1.0 mol/dm^3) in the appropriate ratio. The reaction rate was followed spectrophotometrically by Perkin-Elmer Lambda 15 UV/VIS spectrophotometer connected to a thermocirculating bath.

RESULTS AND DISCUSSION

In our previous paper [2] we have reported that degradation of tetracycline occurs when the solution of antibiotic is mixed with Cu(II), H_2O_2 and tris-buffer at pH 8.2. Investigating the selectivity of this reaction we have found that microgram quantities of metamizole have shown a strong interfering effect.

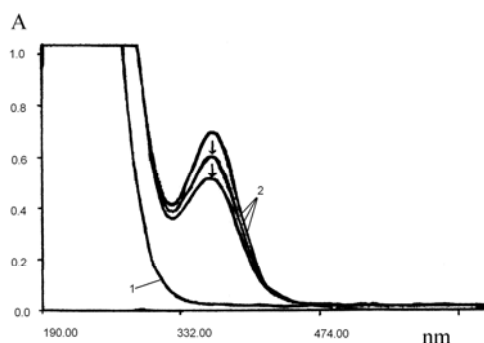


Figure 1. Absorption spectra of the mixtures: 1) metamizole- H_2O_2 -Cu(II)-tris buffer pH 8.2, 2) tetracycline- H_2O_2 -Cu(II)-tris buffer pH 8.2.

The absorption spectra of the reaction mixtures of tetracycline and metamizole with Fenton like reagent at pH 8.2 are presented on Figure 1. Reaction time is 1.5, 3.5 and 6 minutes from the start. The reactants concentrations are: tetracycline $4.67 \times 10^{-6} \text{ mol/dm}^3$, metamizole $4.00 \times 10^{-6} \text{ mol/dm}^3$; Cu(II) $0.67 \times 10^{-5} \text{ mol/dm}^3$; H_2O_2 $1.33 \times 10^{-2} \text{ mol/dm}^3$; tris-buffer 0.2 mol/dm^3 (pH 8.2) and $t=25^\circ\text{C}$. In the reaction of metamizole with Cu(II)/ H_2O_2 during first 10 minutes, absorption band below 300 nm was observed.

On the other hand, the reaction system consisted of tetracycline and Cu(II)/ H_2O_2 at the same pH has shown a strong absorption at 375 nm which decreases in the first 10 minutes. As shown in our previous work [2], this absorption band originated from tetracycline in weak alkaline solution. The decline in absorbance at 375 nm with time is a result of degradation of tetracycline which occurs in the presence of Cu(II)/ H_2O_2 reagent. On the Figure 2. absorption spectra of the mixture of tetracycline and metamizole with H_2O_2 /Cu(II) is presented. Reaction time is 1.5, 3.5 and 6 minutes from the start and reactant concentrations were: tetracycline $4.67 \times 10^{-6} \text{ mol/dm}^3$, metamizole $4.00 \times 10^{-6} \text{ mol/dm}^3$; Cu(II) $0.67 \times 10^{-5} \text{ mol/dm}^3$; H_2O_2 $1.33 \times 10^{-2} \text{ mol/dm}^3$; tris-buffer 0.2 mol/dm^3 (pH 8.2) and $t=25^\circ\text{C}$.

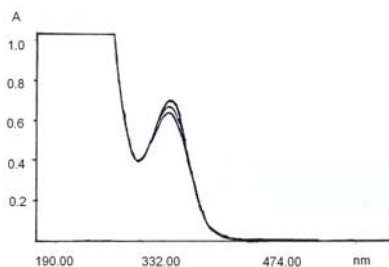


Figure 2. Absorption spectra of the mixture: tetracycline-metamizole- H_2O_2 - Cu(II)-tris buffer pH 8.2.

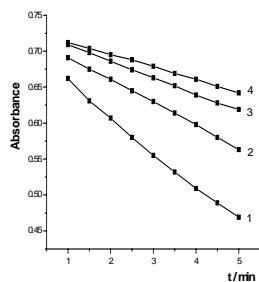


Figure 3. Kinetic curves for metamizole concentrations: 1) 0.00 mol/dm^3 , 2) $1.33 \times 10^{-6} \text{ mol/dm}^3$, 3) $3.33 \times 10^{-6} \text{ mol/dm}^3$, 4) $6.00 \times 10^{-6} \text{ mol/dm}^3$. The concentrations of the other reactants were: tetracycline, $4.67 \times 10^{-6} \text{ mol/dm}^3$, Cu(II), $0.67 \times 10^{-5} \text{ mol/dm}^3$; H_2O_2 $1.33 \times 10^{-2} \text{ mol/dm}^3$; tris-buffer 0.2 mol/dm^3 ; pH 8.2; $t = 25^\circ\text{C}$.

Comparing the rates of the absorbance decreasing at 375 nm for the reaction without and with metamizole (Figure 1. and Figure 2.) it can be concluded that $4.00 \times 10^{-6} \text{ mol/dm}^3$ of metamizole significantly inhibits the reaction of tetracycline with Cu(II)/ H_2O_2 reagent.

The changes in the reaction rates in the presence of metamizole can be explained by the fact that reactive oxygen species obtained by catalytic degradation of H_2O_2 with Cu(II) ions can react with metamizole too.

On the Figure 3. kinetic curves for the different metamizole concentrations are presented. The rates of the reaction were calculated as the slopes of the initial tangents to the absorbance-time curves, dA/dt [3]. At selected and constant concentrations of the other reactants, indicated in Figure 3. caption, reaction rate depended only on metamizole concentration. The slope of the curve $dA/dt = f(C_{\text{metamizole}})$ indicates a negative *pseudo*-first order with respect to metamizole in the range of metamizole concentrations of $0.47 \mu\text{g/cm}^3$ to $2.11 \mu\text{g/cm}^3$.

The equation (1) was used for the calculation of the relative rate constant at 298K, 303K and 308K (Table 1.):

$$dA/dt = k_r \cdot C^{-1}_{\text{Metamizole}} \quad (1)$$

By using Eyring equation,

$$\ln \frac{k_r}{T} = -\frac{\Delta H^\ddagger}{R} \cdot \frac{1}{T} + \ln \frac{k_B}{h} + \frac{\Delta S^\ddagger}{R} \quad (2)$$

and dependence $\ln(k_r/T)=f(1/T)$, activation enthalpy and activation entropy for the activated complex generated in the mixture of tetracycline and metamizole with Fenton like reagent were obtained. Free activation enthalpy and activation energy E_a at 298K were calculated from the equations:

$$E_a = \Delta H^\ddagger + R \cdot T \quad (3)$$

$$\Delta G^\ddagger = \Delta H^\ddagger - T \cdot \Delta S^\ddagger \quad (4)$$

and obtained values are given in (Table 2.).

The reaction is characterized with the value of the activation enthalpy which is expected for reactions in an aqueous solution. The large negative value of the activation entropy resulted in high positive value of the Gibbs energy of activation. All of this calculated thermodynamic parameters support the fact that the reaction of the tetracycline with Cu(II)/H₂O₂, monitored at 375 nm, is significantly slow in the presence of metamizole.

Table 1. The relative rate constant k_r

T/ K	$(k_r \pm SD^a) \times 10^7 / \text{mol dm}^{-3} \text{min}^{-1}$
298	0.91 ± 0.12
303	1.39 ± 0.10
308	1.82 ± 0.09

^a SD, standard deviation of the 3 different metamizole concentrations.

Table 2. Thermodynamic parameters of the activated complex for the metamizole-tetracycline reaction with Fenton-like reagent at pH 8.2.

T (K)	$E_a,$ kJ mol ⁻¹	$\Delta H^\ddagger,$ kJ mol ⁻¹	$\Delta S^\ddagger,$ J mol ⁻¹ K ⁻¹	$\Delta G^\ddagger,$ kJ mol ⁻¹
298	55.5	53.0	- 202.0	113.2

CONCLUSION

It was found metamizole had a strong inhibitory effect on the reaction of tetracycline with Fenton like reagent. Metamizole has excellent redox properties and can be easily oxidized. This characteristic could be important for its higher reactivity with Cu(II)/H₂O₂ reagent in weak alkaline solution.

REFERENCES

- [1] B. Anibarro, J. L. Fontela, *Ann. Allergy Asthma Immunol.*, 1997, 78, 345-346.
- [2] S.M.Sunarić, S.S.Mitić, Kinetic investigation of the tetracycline reaction with Fenton-like reagent at physiological pH, 9th International Conference on Fundamental and Applied Aspects of Physical Chemistry, Belgrade, 2008, 184-186,C-17-P.
- [3] *Chemical Kinetics and Mechanism*, M. Mortimer, P. Taylor ed., The Open University, Royal society of Chemistry, Cambridge, UK, 2002.

KINETICS OF CRYSTALLIZATION OF α -(Fe, Ni) PHASES IN AMORPHOUS $\text{Fe}_{37.5}\text{Ni}_{17.5}\text{Cr}_5\text{Co}_{15}\text{B}_{15}\text{Si}_{10}$ ALLOY

M. M. Vasić¹, V. A. Blagojević¹, D. M. Minić², B. David³, T. Žák³, D. M. Minić¹

¹*Faculty of Physical Chemistry, University of Belgrade, Serbia*

²*Military Technical Institute, Belgrade, Serbia*

³*Institute of Physics of Materials, Academy of Sciences of Czech Republic, Brno, Czech Republic*

ABSTRACT

Amorphous $\text{Fe}_{37.5}\text{Ni}_{17.5}\text{Cr}_5\text{Co}_{15}\text{B}_{15}\text{Si}_{10}$ alloy undergoes step-wise crystallization in temperature range 380-450 °C, corresponding to formation of different iron based phases. In order to determine kinetic triplet for crystallization of individual phases, the complex crystallization curve was deconvoluted into four steps. Overall values of kinetic parameters were determined using Kissinger's and Ozawa's methods, while effective values of activation energy at different values of α were determined using Ortega's isoconversional method. It was observed that kinetic model $\alpha^{0.53}(1-\alpha)^{1.11}$ best describes crystallization of α -(Fe, Ni) phase

INTRODUCTION

Iron based amorphous alloys have been a focus of extensive research in recent time due to their favorable properties including good soft magnetic properties, which are determined by magneto-elastic and annealing-induced anisotropies, good mechanical properties, high electrical resistivity, and high corrosion resistance [1, 2].

These materials are thermodynamically and kinetically metastable and tend to transform to more stable form under high pressure or high temperature, or as a result of prolonged activity at moderate temperature. Structural transformations could lead to loss of functional properties or to formation of nanocrystalline structure manifesting superior functional properties. Precise control of crystallization process could be used to create material with targeted properties. As part of our multidisciplinary study of the effect of chemical composition on crystallization mechanism of Fe-based amorphous alloys, kinetics and mechanism of crystallization of (Fe, Ni) phases was investigated by deconvolution of the complex process of crystallization of $\text{Fe}_{37.5}\text{Ni}_{17.5}\text{Cr}_5\text{Co}_{15}\text{B}_{15}\text{Si}_{10}$ amorphous alloy.

EXPERIMENTAL

Ribbon-shaped samples of amorphous $\text{Fe}_{37.5}\text{Ni}_{17.5}\text{Cr}_5\text{Co}_{15}\text{B}_{15}\text{Si}_{10}$ alloy were prepared using standard procedure of rapid quenching of a melt on a rotating disc (melt spinning method). Differential scanning calorimetry (DSC) measurements were conducted using DSC-50 analyzer (Shimadzu, Japan) at constant heating rates of 5, 8, 11 and 14 $^{\circ}\text{C}/\text{min}$ under nitrogen atmosphere, with a flow rate of 20 mLmin^{-1} . Calibration of the instrument was performed for each heating rate.

RESULTS AND DISCUSSION

DSC measurements revealed that the alloy was thermally stable up to temperatures of around 380 $^{\circ}\text{C}$ when step-wise crystallization occurred. Crystallization manifests as two overlapping peaks, the first around 393 $^{\circ}\text{C}$ and the second around 427 $^{\circ}\text{C}$. Based on peak shape, these processes involve several overlapping steps, which correspond to crystallization of different iron based phases, with α - and γ -(Fe, Ni) phases appearing first in the amorphous matrix, followed by iron-nickel silicate and Co_{23}B_6 . In order to determine kinetic parameters of their crystallization, complex crystallization peaks were deconvoluted, using Gaussian-Lorentzian cross-product function, into individual steps (Fig 1. a).

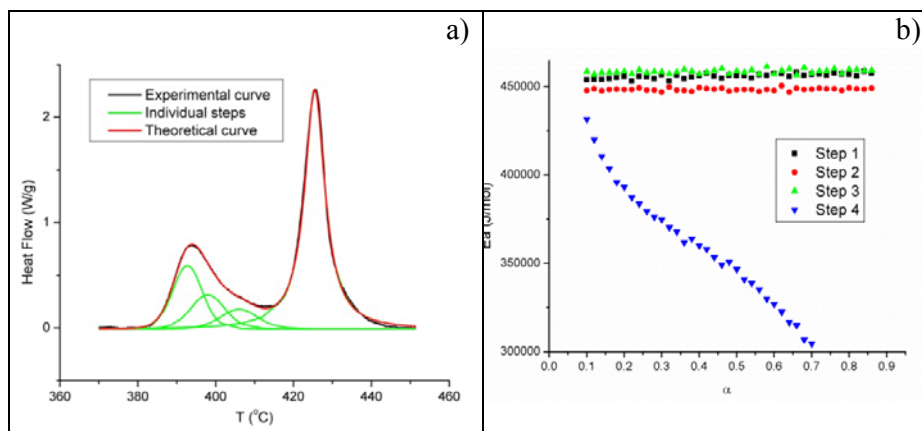


Figure 1. Deconvoluted DSC curve at heating rate $\beta = 8$ $^{\circ}\text{C}/\text{min}$ (a); Values of effective activation energy at different conversion degrees, α , for individual crystallization steps (b).

Application of Ortega's isoconversional method [4] showed, for the first three steps, constant values of effective activation energy over the whole course of process, indicating single-step processes (Fig 1. b). The fourth

step exhibited abrupt decrease of effective activation energy with conversion degree, which suggested that this step consists of more than one step.

Overall values of Arrhenius parameters for crystallization of α -(Fe,Ni) phase (Step 1) were determined using Kissinger's [5] and Ozawa's [6] methods (Table 1.). Obtained values are relatively high, which originates from simultaneous correlated movement of a large number of atoms.

Table 1. Kinetic parameters for crystallization of α -(Fe, Ni) phase, determined using Kissinger's and Ozawa's methods

	Kissinger	Ozawa
Ea (kJ/mol)	454 ± 14	443 ± 14
lnA	82 ± 3	81 ± 3

In addition to Arrhenius parameters, conversion function was determined to complete kinetic description of the process. Šesták-Berggren function in the form $\alpha^{0.53}(1-\alpha)^{1.11}$ was found to corresponds to crystallization of α -(Fe, Ni) phase, which was further validated using Master plot method, in which experimental and theoretical master curves are compared [7], and Perez-Maqueda's criterion, which is based on the independency of kinetic parameters on heating rate [8].

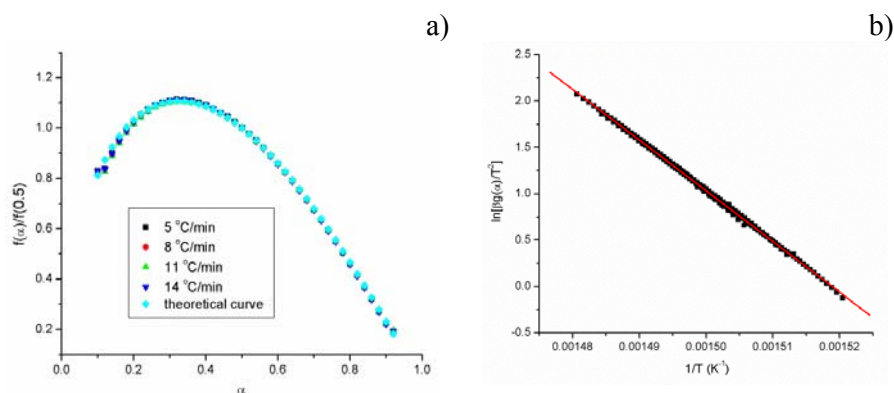


Figure 2. Validation of the determined kinetic triplet of the crystallization of α -(Fe,Ni): Master plot (a) and Perez-Maqueda's criterion (b).

Master plot showed full accordance between theoretical and experimental curves (Fig. 2 a), while application of Perez-Maqueda's criterion on data from all heating rates yielded plots corresponding to straight line,

confirming validity of the obtained kinetic triplet (Fig. 2 b). Kinetic model in this form could be associated with process controlled by nucleation, growth of nuclei and their branching and interaction [9].

CONCLUSION

Thermal analysis of amorphous $\text{Fe}_{37.5}\text{Ni}_{17.5}\text{Cr}_5\text{Co}_{15}\text{B}_{15}\text{Si}_{10}$ alloy showed step-wise crystallization process in the temperature range 380-450 °C. Complex crystallization curve was deconvoluted into individual steps, wherein the first step corresponds to formation of α -(Fe, Ni) phase. Kinetic parameters for that process were determined using isoconversional and non-isoconversional methods. It was found that conversion function in the form $\alpha^{0.53}(1-\alpha)^{1.11}$ best describes crystallization of α -(Fe, Ni) phase, corresponding to a process controlled by nucleation, growth of nuclei, and their branching and interaction.

REFERENCES

- [1] K. Biswas, S. Ram, L. Schultz, J. Eckert, *J. Alloy. Compd.*, 2005, 397, 104.
- [2] Y. Dong, A. Wang, Q. Man, B. Shen, *Intermetallics*, 2012, 23, 63.
- [3] R. Singhal, U.C. Johri, R.M. Singru, *J. Mater. Sci.*, 1993, 28, 975.
- [4] A. Ortega, *Thermochim. Acta*, 2008, 474, 81.
- [5] H.E. Kissinger, *Anal. Chem.*, 1957, 29, 1702.
- [6] T.J. Ozawa, *J. Therm. Anal.* 1970, 2, 301.
- [7] F.J. Gotor, J.M. Criado, J. Málek, N. Koga, *J. Phys. Chem. A*, 2000, 104, 10777.
- [8] L.A. Pérez-Maqueda, J.M. Criado, F.J. Gotor, J. Malék, *J. Phys. Chem. A*, 2002, 106, 2862.
- [9] J. Šesták, G. Berggren, *Thermochim. Acta*, 1971, 3, 1.

KINETICS OF TRANSESTERIFICATION OF SUNFLOWER OIL IN CONDITIONS OF HYDRODYNAMIC CAVITATION

B. Adnadjević and J. Jovanović²

*Faculty of Physical Chemistry, Studentski trg 12-16, 11001 Belgrade,
Serbia (bora@ffh.bg.ac.rs)*

ABSTRACT

A novel type of hydrodynamic cavitation device based on combination of Ventury tube and orifice was constructed. The effects of temperature (298-318K), molar ratio CH₃OH/triglyceride (M=3-12) and catalyst concentration (Cc=0.5-1.5) on the kinetics of transestrification of sunflower oil with methanol was investigated. It was found that the kinetics of transestrification of sunflower oil can be modelled by the kinetics of first order chemical reaction. The values of kinetic parameters were calculated: $E_a = 56 \text{ kJ mol}^{-1}$ and $\ln(A/\text{min}^{-1}) = 22$. It was shown that neither molar ratio $M > 3$ nor the catalyst concentration $Cc > 0.5\%$ have influence on the kinetics of transestrification of sunflower oil in conditions of hydrodynamic cavitation.

INTRODUCTION

Biodiesel can be produced by various different conventional method such as alkali catalysts, acid catalysis, lipase catalysis etc [1,2]. The oil (fat) and alcohols are immiscibly, so that their reaction takes place at the interface in a very slow process. Gogate et al [3] presented possibilities for significant acceleration of numerous chemical reactions in liquids phase by applying cavitations. With that in mind, in this paper kinetics of transestrification of sunflower oil with methanol in conditions of hydrodynamic cavitation was investigated.

EXPERIMENTAL

Materials: Sunflower oil produced from Dijamant-Zrenjanin, R.Serbia, Methanol, p.a, purchased from Carlo Erba, Italy and sodium methoxide, p.a., purchased from Acros, USA. Transestrification of Sunflower oil was carried out in newly constructed hydrodynamic device which was based on combination of Ventury tube and orifice.

The effect of temperature on the kinetics of transesterification was carried out maintaining the following reaction conditions: $M = 3.0$, $Cc = 1\%$, reaction

time $t=1\text{min}$ within temperature range $T = 298 - 328 \text{ K}$. The effect of molar ratio $\text{CH}_3\text{OH}/\text{triglyceride}$ on the kinetics of transesterification was investigated under the following reaction conditions: $T = 298\text{K}$, $C_c=1\%$, $t=1\text{min}$ by varying M within the range $M=3-12$. In order to determine the effect of catalyst concentration on kinetics of transesterification, C_c was varied within the range $0.5\%-1.5\%$, under the following reaction conditions: $T = 298\text{K}$, $M=3$, $t=1\text{min}$.

Degree of transesterification (DT) was determined by gas chromatography [4] and calculated as:

$$DT = \frac{\frac{\text{weightbiodiesel}}{MWb}}{\frac{\text{weightoil} \times 3}{MWO}} \text{biodieselconcentration}(\%) \quad (1)$$

where: $MW = \sum MW_i \times x_i$ is the mean molecular weight of the biodiesel/oil. The MWb is the mean molecular weight of the biodiesel which was calculated averaging the individual molecular weights (MW_i) of each methylester, according to biodiesel fatty acid alkyl ester analysis (x_i) and the MWO is the mean molecular weight of the oil, which was calculated averaging the individual molecular weights (MW_i) of each constituents triglyceride according to the fatty acid oil analysis (x_i).

RESULTS AND DISCUSSION

Figure 1 presents, as an example, conversion curves of sunflower oil transesterification in the conditions of hydrodynamic cavitation.

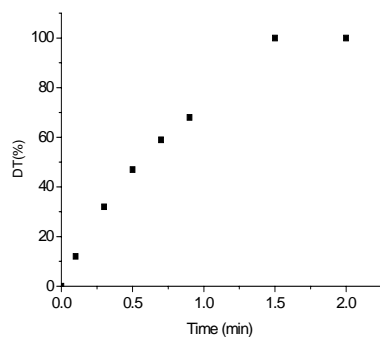


Figure 1. Conversion of sunflower oil curve transesterification

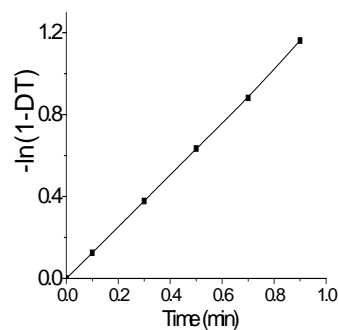


Figure 2. Plot of $[-\ln(1-DT)]$ on time

By applying the model fitting method we found that conversion curves of sunflower oil transesterification can be modelled by the kinetics of first order chemical reaction. The dependence $-\ln[1-DT]$ vs. time are presented in Figure 2.

The dependence $-\ln[1-DT]$ on time, at all investigated temperatures, gives straight line at whole range of DT, which enables to calculate the constant rate of transesterification (k) in the field of cavitation. Since the constant rates increase in accordance with the Arrhenius equation, the kinetic parameters were calculated: $E_a = 56 \text{ kJ mol}^{-1}$ and $\ln(A/\text{min}^{-1}) = 22$.

Table 1 presents the effect of molar ratio on the kinetics of transesterification.

Table 1. Effect of molar ratio on the degree of transesterification

M	DT, %
3	100
4	100
6	100
9	100
12	100

As can be seen from the results presented in Table 1, it is easy to see that the values of the degree of transesterification of sunflower oil are practically independent of the molar ratio of in the conditions of hydrodynamic cavitation.

The effect of catalyst concentration on the kinetics of transesterification is given in Table 4.

Table 2. Effect of catalyst concentration on the degree of transesterification

Cc, %	DT, %
0.5	100
0.7	100
1.0	100
1.2	100
1.5	100

As obviously, in the conditions of hydrodynamic cavitation the catalyst concentration does not have any influence on the degree of transesterification of sunflower oil.

Dramatic increase in the rate of transesterification of sunflower oil (more than 500 times) in the conditions of hydrodynamic cavitation in comparison with the conventional conditions can be explained with the ability of cavitation device to disperse reacting molecules to non-sized particles. As a consequence of that reacting species are almost ideally mixed and the interface significantly increases. Due to that, the rate of

transestrification becomes very high even at room temperature and is possible at stoichiometry ratio of methanol and triglyceride $M=3$ and minimal catalyst concentration.

CONCLUSION

Hydrodynamic cavitation significantly increases the rate of transestrification and presents a very efficient method for biodiesel production. The kinetics of transestrification of sunflower oil with methanol in conditions of hydrodynamic cavitation can be modelled by the kinetics of first order chemical reaction. The kinetics of transestrification of sunflower oil in conditions of hydrodynamic cavitation is independent on molar ratio for $M>3$ and catalyst concentration $C_c>0.5\%$.

ACKNOWLEDGEMENT

This investigation was supported by the Ministry of Science and Technical Development of the Republic of Serbia, through Project No.142025G.

REFERENCES

- [1] F.M.A. H.A.Hanna, *Biores. Techn.*, 1990, 70, 1-15
- [2] T.M.Meta, A.A.Martins, N.A.Caetano, *Energy Reviews*, 2010, 14, 217-232
- [3] P.R.Gogate, *Chem.Eng.Proc.*, 2008, 47, 515-527
- [4] C.Plank, E.Lorbeer, *J.Chromatography A*, 1995, 697, 461-470.

NONLINEAR DYNAMICS

Dedicated to our young recently died
colleague Otto Hadač
(1982 – 2014)

BISTABLE PH SWITCHES AND OSCILLATIONS IN COMPARTMENTALISED ENZYME REACTIONS

A. Taylor

School of Chemistry, University of Leeds

ABSTRACT

The rate-pH dependence of enzyme-catalysed reactions in membranes [1] was proposed as a possible source of dynamical behaviour including bistability, oscillations and waves in biology; however, a robust experimental example of such a system is still lacking. Recent investigations [2] with the urea-urease reaction suggest this reaction may provide such an example: propagating fronts were observed in thin layers of the reaction mixture and bistability has been observed in a flow reactor and in enzyme loaded gel beads. Here we consider a simple model of the reaction in which an enzyme-loaded spherical particle exchanging matter (except the enzyme) with a reservoir containing an aqueous solution of substrate, urea, and acid. The incoming substrate is transformed in the enzyme-catalyzed process into a product that reacts with the acid, which leads to higher pH. As a result of the bell-shaped rate pH curve of the enzyme, rate acceleration is observed. In simulations, we examine the behaviour of the enzyme loaded cell and determine the parameters for bistability. We investigate the effect of enzyme loading and size of the particle on bistability. We also demonstrate that the transport rate of acid (kH) must be greater than that of urea (ks) for oscillations in a urease-loaded membrane and discuss why oscillations have been difficult to achieve experimentally.

REFERENCES

- [1] Caplan, S. R.; Naparstek, A.; Zabusky, N. J., *Nature* 1973, 245, 364.
[2] Hu, G.; Pojman, J.; Wrobel, M. M.; Scott, S. K.; Taylor, A. F., *J. Phys. Chem. B* 2010, 114, 14059.; Bansagi, Jr., T.; Taylor, A. F., *J. Phys. Chem. B* 2014, 118, 6092; Muzika, F.; Bansagi, Jr., T.; Schreiber, I.; Schreiberova, L.; Taylor, A. F., *Chem. Comm.* 2014.

IODINE INORGANIC REACTIONS IN ACIDIC SOLUTIONS AND OSCILLATING REACTIONS

G.Schmitz¹ and S.D. Furrow²

¹*Université Libre de Bruxelles, Ecole Polytechnique, Av. Franklin Roosevelt, 50, 1050 Brussels, Belgium (gschmite@ulb.ac.be).*

²*Penn State Berks College, Pennsylvania State University, Reading, Pennsylvania 19610, United States.*

ABSTRACT

In order to propose mechanisms of complicated chemical systems, it is necessary to study simpler subsystems. The mechanism we have proposed for the Bray-Liebhafsky (BL) oscillating reaction is based on kinetic studies of several reactions of iodine compounds between them and with hydrogen peroxide. Because the reactants of the non-catalysed Briggs-Rauscher (BR) oscillating reaction are the same as those of the BL reaction plus malonic acid, we propose now to extend the mechanism of the BL reaction to the BR reaction. With this aim, we add radical reactions of iodine compounds and of malonic acid. The choice of these reactions is based on our recent study of the unusual kinetics of the iodate reduction by high concentrations of hydrogen peroxide.

FOREWORD

"... to conduct my thoughts in such order that, by commencing with objects the simplest and easiest to know, I might ascend by little and little to the knowledge of the more complex..." This sentence by René Descartes in "Discourse on Method" was already at the top of our communication to the conference PHYSICAL CHEMISTRY 2012 and we continue to apply it to ascend by little and little to the understanding of the Bray-Liebhafsky [1-3] and Briggs-Rauscher [4-9] oscillating reactions. This involves studies of simpler systems, namely the reaction of iodine and its oxidation levels I(+1), I(+3) and I(+5) between them and with hydrogen peroxide.

INTRODUCTION

The Briggs-Rauscher (BR) oscillations are usually observed in acid systems containing iodate, hydrogen peroxide, an organic reducing compound like malonic acid (MA) and a metal-ion catalyst (Mn^{++} in the original recipe). However, BR oscillations are also observed in systems without metal-ion

catalyst provided the hydrogen peroxide concentration is sufficiently high [10]. On the other hand, the Bray-Liebhafsky (BL) oscillations are observed in acid systems containing only iodate and hydrogen peroxide. Although these oscillations are different from the BR oscillations and are observed under different conditions, we believe that the components of the BL reaction mechanism form a subset of the BR reaction mechanism. In other words, we try to build a BR mechanism adding reactions to our BL mechanism [3].

BRAY-LIEBHAFSKY SIMULATIONS

Our BL mechanism is shown schematically in Figure 1 and includes reactions (1) - (12) in Table I. Most of the rate constants were obtained from independent studies of subsystems.

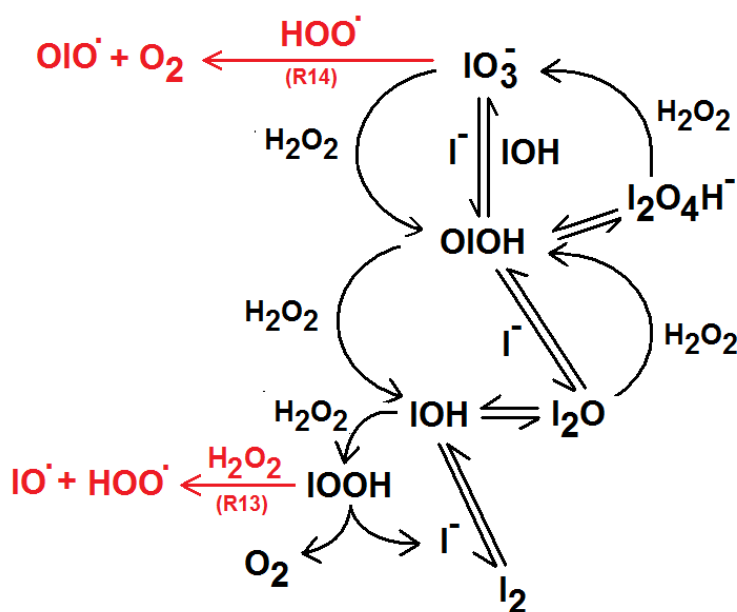


Figure 1. Black part: representation of the BL mechanism; down arrows correspond to reductions and up arrows to oxidations. Red part: initiation of the BR radical reactions.

The rate constant k_{+1} is known from studies of the Dushman reaction at low iodide concentrations [11, 12]. k_{-1} was measured by two different techniques [13, 14]. Recalculation of the raw results of these works and new measurements by one of us (S. Furrow) give $k_{-1} = 160 \pm 20$. The sum $R1 +$

R2 + R3 gives $\text{IO}_3^- + 2\text{I}^- + 3\text{H}^+ = 3\text{IOH}$. The thermodynamic equilibrium constant of this reaction, corrected for the effect of the ionic strength, is $k_{+1}k_{+2}k_{+3}/(k_{-1}k_{-2}k_{-3}) = 1.4 \times 10^9$ [3]. The rate of IOH disproportionation [14, 15] gives $k_{-2}k_{-3}/k_3 = 25$ and, with the known values of k_1 and k_{-1} , $k_2 = 4 \times 10^9$. I_2O is an intermediate compound with a quasi-stationary concentration. Thus, the results depend only on the ratio k_{-2}/k_3 . $k_3 = 10^7$ was used so that $[\text{I}_2\text{O}]$ remains very small but values ten times smaller or larger give the same results. k_3 is an essential parameter of the model. Its value is adjusted to obtain good simulations of the kinetics of the iodine oxidation by hydrogen peroxide [3] and must be revised if other parameters of the model are modified. The value of k_{-3} gives $k_{-2}/k_3 = 25/k_{-3}$. The rate law of reaction R4 is $k_4 [\text{IOH}][\text{I}^-] - k_{-4} [\text{I}_2]/[\text{H}^+]$ where k_{-4} was measured independently [3, 14] and k_4 is calculated from the equilibrium constant of R4 corrected for the effect of the ionic strength. Reaction R5 in the former version of the model is now split into two reactions, R5 and R6. The existence of the intermediate compound IOOH was proved formerly [16] and its importance in the modified model will appear hereafter. A recalculation of the results obtained by Liebhafsky [17] for the IOH reduction by hydrogen peroxide gives $k_5k_6/(k_{-5} + k_6) = 23$. The BL simulations depend only on this value but the BR simulations depend also on the ratios k_{-5}/k_6 and k_{13}/k_6 that are parameters of the model. The ratio k_7/k_3 is adjusted to the kinetics of the iodine oxidation by hydrogen peroxide [3]. Reaction R8 is the sum of two partial reactions, $\text{OIOH} + \text{OIO}^- \rightleftharpoons \text{I}_2\text{O}_4\text{H}^-$ (8a) and $\text{I}_2\text{O}_4\text{H}^- + \text{H}_2\text{O}_2 \rightarrow \text{IO}_3^- + \text{OIOH} + \text{H}_2\text{O}$ (8b) [18] giving $r_8 = k_8[\text{OIOH}]^2[\text{H}_2\text{O}_2]/([\text{H}^+](1 + \square_8[\text{H}_2\text{O}_2]))$ where $k_8 = k_{8a}k_{8b}K_a/k_{-8a}$, $\square_8 = k_{8b}/k_{-8a}$ and K_a is the acidity constant of OIOH. Reaction R9 of the 2011 model [3] has nearly no effect under the conditions of this study. The kinetics of reaction R10 was discussed formerly [19]. Reaction R11 is an empirical reaction added to the model to represent the perturbing effect of oxygen on the BL oscillations [3]. It has probably a radical mechanism that remains not elucidated. The simulations in Fig.2 were obtained using $r_{11} = 3500 [\text{O}_2][\text{I}^-][\text{H}^+]$ and a rate of oxygen escape from the solution equal to $5 \times 10^{-5}([\text{O}_2] - 2.5 \times 10^{-4})$. r_{11} was neglected for the BR simulations.

Numerical simulations of many subsystems and of experimental BL oscillations at 50° were presented before [3]. At 25° , the periods are long and the produced oxygen perturbs heavily making the observation of BL oscillations very difficult. However, one of us (S.F.) succeeded in obtaining the more or less reproducible oscillations shown in Fig.2a. The numerical

simulations using reactions R1 -R12 in table I shown in Fig.2b support further the proposed model.

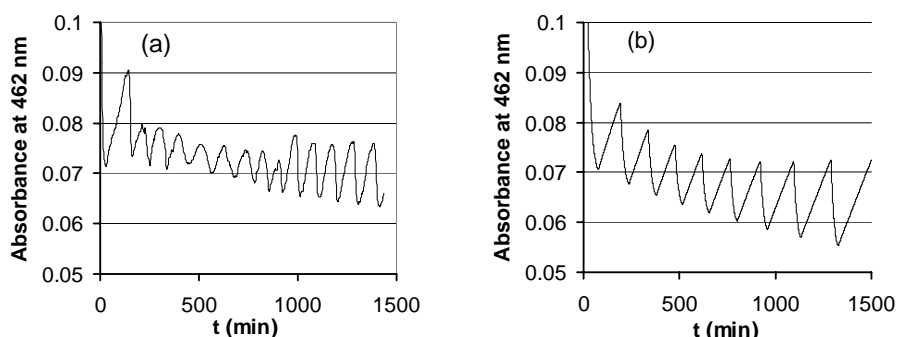


Figure 2. BL oscillations at 25°. Initial conditions $[\text{HClO}_4]_0 = 0.030\text{M}$, $[\text{KIO}_3]_0 = 0.035\text{M}$, $[\text{H}_2\text{O}_2]_0 = 0.16\text{M}$, $[\text{I}_2]_0 = 3\text{E-}4\text{M}$. Experimental results (a) and numerical simulation (b).

IODATE REDUCTION BY HYDROGEN PEROXIDE

The BL oscillations are explained by non radical reactions. On the other hand, the BR oscillations are suppressed by radical scavengers [8] and an extension of the BL mechanism to the BR reaction requires at least one reaction producing radicals. We have discussed this question formerly [10, 19] and proposed that it is reaction R13 followed by R14.

The radical reactions of iodine compounds are much less known than the non radical reactions so that reactions R15 to R17 are speculative. R14 + R15 is a chain reaction reducing iodate to OIOH and R16 + R17 is a chain reaction reducing OIOH to IOH so that iodate is finally reduced to I_2 . R18 to R21 are chain breaking reactions. Figure 3 gives examples showing that the model R1 - R21 is able to explain the main features of the iodate reduction by high concentrations of hydrogen peroxide, an order higher than two for hydrogen

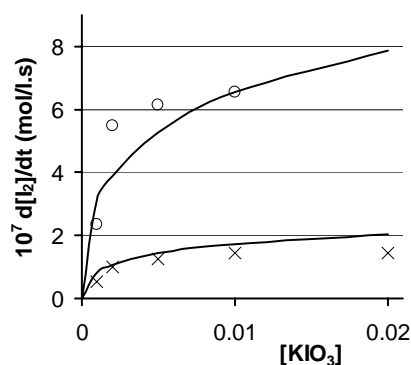


Figure 3. Initial rates of the iodate reduction. Experimental results for $[\text{HClO}_4]_0 = 0.1\text{M}$ and $[\text{H}_2\text{O}_2]_0 = 1\text{M}$ (o) or 2M (x) and simulated values (—).

peroxide and lower than one for iodate. Most of the rate constants are highly uncertain and they were not optimized for these simulations because we wanted to show that the proposed model can also give BR oscillations with the same set of rate constants.

SIMULATION OF NON-CATALYSED BR OSCILLATIONS

The third part of the model represents the organic part of the BR reaction with malonic acid (MAH). Iodomalonic acid (MAI) is an important intermediate in the BR reaction and the kinetics of reactions R22 and R23 is well known [6a]. Diiodomalonic acid [9b] should also be considered in a further version of the model. It is also accepted that the main products of the malonic acid oxidation, oxalic acid (OA), CO and CO₂, are produced by reactions of organic radicals [9b, c]. Reaction R27 is the simplest possible representation of these complicated reactions leading to the final products. We assume that the malonyl radical MA• is produced by reactions R24 and R25 but other reactions are possible. Reaction R26 producing the radical HOO• introduces a feedback that destabilized the stationary state (another feedback passes through IOH and IOOH producing radicals in reaction R13). At this state, the obtained simulations of the non-catalysed BR oscillations are only qualitative but the results in Figure 4 are stimulating.

CONCLUSION

The first part of the model in Table 1, reactions R1 to R12, explains the observed kinetics of many iodine inorganic reactions in acidic solutions and allows quantitative simulations of the BL oscillations. When the hydrogen peroxide concentration is high, the model must be completed with radical reactions explaining the kinetics of the iodate reduction by hydrogen peroxide. This second part of the model, reactions R13 to R21, is less well known because information about the reactions of iodine radicals is rare. The third part represents complicated organic reactions and we have adopted an oversimplification of them. Much work remains to be done according to the René Descartes method. We should have information about different subsystems involving reactions of radical iodine compound and of MA•. After that, we could introduce metal-ion catalyst reactions to extend the mechanism of the non-catalysed BR reaction to the classical BR reaction.

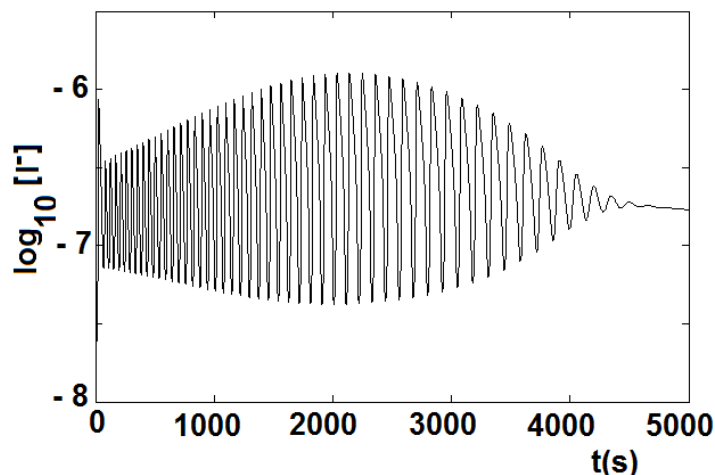


Figure 4. Simulated BR oscillations. $[\text{HClO}_4] = 0.10 \text{ M}$, $[\text{H}_2\text{O}_2]_0 = 2 \text{ M}$, $[\text{KIO}_3]_0 = 3 \times 10^{-3} \text{ M}$, $[\text{MAH}]_0 = 4 \times 10^{-3} \text{ M}$.

REFERENCES

- [1] Bray W. C., *J. Am. Chem. Soc.*, 1921, 43, 1262-1267; (b) Bray W. C., Liebhafsky H. A., *J. Am. Chem. Soc.*, 1931, 53, 38-44; (c) Matsuzaki I., Woodson, J., Liebhafsky, H. A., *Bull. Chem. Soc. Jap.*, 1970, 43, 3317-3317; (d) Liebhafsky H. A., Wu L. S., *J. Am. Chem. Soc.*, 1974, 96, 7180-7187.
- [2] (a) Kolar-Anić Lj., Čupić Ž., Anić S., Schmitz G., *J. Chem. Soc. Faraday Trans.* 1997, 93, 2147-2152; (b) Vukojević V., Anić S., Kolar-Anić Lj., *J. Phys. Chem. A* 2000, 104, 10731-10739; (c) Schmitz G., Kolar-Anić Lj., Anić S., Grozdic T., Vukojević V., *J. Phys. Chem. A* 2006, 110, 10361-10368; (d) Ivanović A., Čupić Ž., Janković M., Kolar-Anić Lj., Anić S., *Phys. Chem. Chem. Phys.* 2008, 10, 5848-5858.
- [3] (a) Schmitz G., *Phys. Chem. Chem. Phys.* 2010, 12, 6605-6615; (b) Schmitz G., *Phys. Chem. Chem. Phys.* 2011, 13, 7102-7111.
- [4] Briggs T. S., Rauscher W. C., *J. Chem. Educ.* 1973, 50, 496-496.
- [5] Epstein I. R., Pojman, J. A. *An Introduction to Nonlinear Chemical Dynamics*. Oxford University Press: New York, 1998.
- [6] (a) Furrow S. D., Noyes R. M., *J. Am. Chem. Soc.* 1982, 104, 38-42; (b) DeKepper, P., Epstein, I. R., *J. Am. Chem. Soc.* 1982, 104, 49-55.
- [7] Vukojevic V., Sørensen, P. G., Hynne, F. J., *J. Phys. Chem.* 1996, 100, 17175-17185.

- [8] (a) Furrow S. D., Cervellati, R., Amadori, G., *J. Phys. Chem. A* 2002, 106, 5841-5850; (b) Cervellati R., Höner, K., Furrow, S. D., Mazzanti, F., Costa, S., *Helv. Chim. Acta* 2004, 87, 133-155; (c) Furrow S. D., Aurentz, D. J., *J. Phys. Chem. A* 2010, 114, 2526-2533, (d) Cervellati R., Greco, E., Furrow S. D., *J. Phys. Chem. A* 2010, 114, 12888-12892.
- [9] (a) Szabó G., Csavdári A., Onel L., Bourceanu G., Noszticzius Z., Wittmann, M., *J. Phys. Chem. A* [2007](#), 111, 610; (b) Onel L., Bourceanu G., Wittmann M., Noszticzius Z., Szabó G., *J. Phys. Chem. A* [2008](#), 112, 11649; (c) Muntean N., Szabó G., Wittmann, M., Lawson T., Fülöp J., Noszticzius Z., Onel L., *J. Phys. Chem. A* 2009, 113, 9102; (d) Lawson T., Fülöp J., Wittmann M., Noszticzius Z., Muntean N., Szabó G., Onel L., *J. Phys. Chem. A* 2009, 113, 14095; (e) Muntean N., Lawson B. T., Kály-Kullai K., Wittmann M., Noszticzius Z., Onel L., Furrow S. D., *J. Phys. Chem. A* 2012, 116, 6630.
- [10] Schmitz G., Furrow S. D., *Physical Chemistry 2012*, Society of Physical Chemists of Serbia, Belgrade 2012, pp.227-232.
- [11] Furuichi R., Liebhafsky H.A., *Bull. Chem. Soc. Japan*, 1975, 48, 745.
- [12] Schmitz G., *Phys. Chem. Chem. Phys.*, 2000, 2, 4041.
- [13] Noszticzius Z., Noszticzius E., Schelly Z. A., *J. Phys. Chem.* 1983, 87, 510.
- [14] Furrow S.D., *J. Phys. Chem.* 1987, 91, 2129.
- [15] Schmitz G., *Int. J. Chem. Kinet.*, 2004, 36, 480.
- [16] (a) Ball J.M., Hnatiw J.B., *Can. J. Chem.*, 2001, 79, 304; (b) Schmitz G., *Russian J. Phys. Chem.*, 2009, 83(9), 1447.
- [17] Liebhafsky H. A., *J. Am. Chem. Soc.*, 1932, 54, 3504.
- [18] Schmitz G., and Furrow S.D., *Int. J. Chem. Kinet.*, 2013, 48, 525.
- [19] Schmitz G., Furrow S. D., *Phys. Chem. Chem. Phys.* 2012, 14, 5711-5717.

Table I. Model for the BL and non-catalyzed BR oscillating reactions. Mass action rate laws are used except when indicated in the text. The rate constants values (mol/l.s) are taken from the literature or estimated (values in italic) for the presented simulations.

Reactions	k_+	k_-
R1 $\text{IO}_3^- + \Gamma + 2 \text{H}^+ \rightleftharpoons \text{IOH} + \text{OIOH}$	1300	160
R2 $\text{OIOH} + \Gamma + \text{H}^+ \rightleftharpoons \text{I}_2\text{O} + \text{H}_2\text{O}$	3.0×10^9	2.53
R3 $\text{I}_2\text{O} + \text{H}_2\text{O} + \text{H}^+ \rightleftharpoons 2 \text{IOH} + \text{H}^+$	1×10^7	9.9×10^7
R4 $\text{IOH} + \Gamma + \text{H}^+ \rightleftharpoons \text{I}_2 + \text{H}_2\text{O}$	2.0×10^9	0.0017
R5 $\text{IOH} + \text{H}_2\text{O}_2 \rightleftharpoons \text{IOOH} + \text{H}_2\text{O}$	800	10
R6 $\text{IOOH} \rightarrow \Gamma + \text{H}^+ + \text{O}_2$	0.2	
R7 $\text{I}_2\text{O} + \text{H}_2\text{O}_2 \rightarrow \text{IOH} + \text{OIOH}$	1.52×10^7	
R8 $\text{OIOH} + \text{H}_2\text{O}_2 \rightarrow \text{IO}_3^- + \text{H}^+ + \text{H}_2\text{O}$	See text $k_8 = 2.2 \times 10^5$	$\alpha_8 = 20$
R9 $\text{OIOH} + \text{H}_2\text{O}_2 \rightarrow \text{IOH} + \text{O}_2 + \text{H}_2\text{O}$	0.2	
R10 $\text{IO}_3^- + \text{H}^+ + \text{H}_2\text{O}_2 \rightarrow \text{OIOH} + \text{O}_2 + \text{H}_2\text{O}$	1.3×10^{-7}	2.5×10^{-5}
R11 $\Gamma + \text{H}^+ + \frac{1}{2} \text{O}_2 \rightarrow \text{IOH}$	See text	
R12 $\text{IO}_3\text{H} \rightleftharpoons \text{IO}_3^- + \text{H}^+$	2.8×10^9	10^{10}
R13 $\text{H}_2\text{O}_2 + \text{IOOH} \rightarrow \text{IO}^\bullet + \text{HOO}^\bullet + \text{H}_2\text{O}$	0.1	
R14 $\text{IO}_3^- + \text{H}^+ + \text{HOO}^\bullet \rightarrow \text{OIO}^\bullet + \text{O}_2 + \text{H}_2\text{O}$	1×10^5	
R15 $\text{OIO}^\bullet + \text{H}_2\text{O}_2 \rightarrow \text{OIOH} + \text{HOO}^\bullet$	100	
R16 $\text{OIOH} + \text{HOO}^\bullet \rightarrow \text{IO}^\bullet + \text{O}_2 + \text{H}_2\text{O}$	5×10^9	
R17 $\text{IO}^\bullet + \text{H}_2\text{O}_2 \rightarrow \text{IOH} + \text{HOO}^\bullet$	9.8	
R18 $2 \text{HOO}^\bullet \rightarrow \text{H}_2\text{O}_2 + \text{O}_2$	9×10^5	
R19 $2 \text{OIO}^\bullet + \text{H}_2\text{O} \rightarrow \text{IO}_3^- + \text{H}^+ + \text{OIOH}$	5×10^9	
R20 $\text{OIO}^\bullet + \text{HOO}^\bullet \rightarrow \text{OIOH} + \text{O}_2$	$\sim (k_{18} \times k_{19})^{1/2}$	
R21 $2 \text{IO}^\bullet + \text{H}_2\text{O} \rightarrow \text{IO}_3^- + \Gamma + 2 \text{H}^+$	1×10^8	
R22 $\text{MAH} \rightleftharpoons \text{Enol}$	0.0039	91
R23 $\text{Enol} + \text{I}_2 \rightarrow \text{MAI} + \Gamma + \text{H}^+$	9.1×10^5	
R24 $\text{MAH} + \text{IO}^\bullet \rightarrow \text{MA}^\bullet + \text{IOH}$	2×10^6	
R25 $\text{MAI} + \text{IO}^\bullet \rightarrow \text{MA}^\bullet + \text{I}_2\text{O}$	1×10^5	
R26 $\text{MA}^\bullet + \text{H}_2\text{O}_2 \rightarrow \text{MAH} + \text{HOO}^\bullet$	1×10^3	
R27 $2 \text{MA}^\bullet \rightarrow \text{OA}, \text{CO}, \text{CO}_2 \dots$	1×10^8	

METHOD OF NONLINEAR DYNAMICS: PHENOMENOLOGICAL APPROXIMATE MAPPINGS

K.R. (Stevanović) Hedrih

*Mathematical Institute SANU, Belgrade, Serbia and
Faculty of Mechanical Engineering University of Niš, Serbia*

ABSTRACT

Phenomenological approximate mapping as an universal method of nonlinear dynamics is presented. The basic idea given by Mihailo Petrović and elaborated in his two books entitled: *Elements of mathematical phenomenology and Phenomenological mappings* is applied here on one physicochemical reaction system and a mechanical system. In particular, in both nonlinear systems the local dynamic nonlinear phenomena around stationary states are analyzed by the phenomenological approximate mappings. A general table with phenomenological linear and nonlinear approximate mappings around singular states is presented.

INTRODUCTION

Mihailo Petrović (*May 6, 1868, Belgrade - June 8, 1943, Belgrade*) is Serbian mathematician and scientist and one of three doctoral students of important French and World scientist Jules Henri Poincaré (29 April 1854, Nancy - 17 July 1912, Paris, France). He is author of two books: *Elements of Mathematical Phenomenology* [1], 1911, and *Phenomenological Mappings* [2], 1933. In these books it is shown that between numerous elements of mathematical phenomenology, mathematical and qualitative analogies are important for solution of scientific problems in different areas of sciences. Also, phenomenological mapping of nonlinear dynamical phenomena from one to the other system is useful method for transfer results and new knowledge about nonlinear dynamics from well known, already investigated system to the other not yet investigated system.

In this paper, a phenomenological approximate mapping as universal approximate method for investigation of phenomena that appear in vicinity of singular points or stationary states are presented and applied on several complex systems with nonlinear (one reaction system, one mechanical systems and an electrical system).

Combination of two methods: the phenomenological approximate mapping in local area around singular states and Lyapunov's theorems of system

stability give power analytical tool for investigation nonlinear dynamics of complex nonlinear system kinetic states.

In this paper phenomenological approximate mappings around singular points or stationary states are presented, as universal approximate method for investigation of nonlinear dynamics through separate investigation properties of each local nonlinear phenomenon in complex nonlinear dynamics with numerous nonlinear phenomena.

The physic-chemical system dynamic is nonlinear kinetics of two concentrations a and b of species A and B with a cubic autocatalytic reaction in an open reactor (Continuous Stirred Tank Reactor - CSTR).

The mechanical system dynamics is nonlinear dynamics of a heavy mass particle along rotate circle around vertical axis with eccentricity and with constant velocity.

METHOD OF PHENOMENOLOGICAL APPROXIMATE MAPINGS

EXAMPLE 1. Let us consider nonlinear dynamics of two concentrations a and b of species A and B with a cubic autocatalytic reaction in an open reactor (Continuous Stirred Tank Reactor - CSTR):



The time evolution of the concentrations of species A and B denoted by a and b , are described by the following first order nonlinear differential equations (for detail see References: [3]):

$$\frac{da}{dt} = k_f(a_o - a) - kab^2, \quad \frac{db}{dt} = k_f(b_o - b) + kab^2 \quad (2)-(3)$$

where a_o and b_o are constants as a consequence of permanent inflow of them and outflow of surplus of reaction mixture. Hence, the volume of reaction mixture in stationary state is also constant.

In the stationary states $\frac{da}{dt} = 0$ and $\frac{db}{dt} = 0$. From these conditions it is possible

to obtain one linear algebra equations and one nonlinear algebra cubic equation in the following form (see Refs. [3] and [4]):

$$(a_o - a_s) + (b_o - b_s) = 0, \quad a_s^3 - 2pa_s^2 + qa_s - \beta a_o = 0 \quad (4)-(5)$$

where the following denotations are introduced:

$$p = [a_o + b_o], \quad q = \left[\frac{k_f}{k} + (a_o + b_o)^2 \right], \quad \beta = \frac{k_f}{k} \quad (6)$$

Cubic equation (5), in general case, posses three roots, which can be denoted by a_s , $s=1,2,3$. Taking into account linear algebra equation (4)

there is corresponding pair of stationary state concentrations $a_s, b_s = (a_o - a_s) + b_o, s = 1, 2, 3$. These pairs of roots a_s , and $b_s = (a_o - a_s) + b_o, s = 1, 2, 3$ present three possible stationary states or singular points considered nonlinear reaction system described by the first order nonlinear differential equations (2)-(3). Obtained equation (4) valid for stationary state in the form: $(a_o + b_o) = (a_s + b_s)$.

From the first order nonlinear differential equations (2)-(3), is:

$$[(a_o + b_o) - (a + b)] = \frac{1}{k_f} \left[\frac{da}{dt} + \frac{db}{dt} \right] \quad (7)$$

and taking into account that a_o and b_o are constants, integration of (7) give:

$$[(a + b) - (a_o + b_o)] = [(a(t_o) + b(t_o)) - (a_o + b_o)] e^{-k_f [(a+b) - (a_o + b_o)] (t - t_o)} \quad (8)$$

where $a(t_o)$ and $b(t_o)$ are initial concentrations of species A and B. If we take at initial moments $t_o = 0$, that a_o and b_o are concentrations of species A and B, $a(t_o) = a(0) = a_o$ and $b(t_o) = b(0) = b_o$, then we obtain that $(a + b) = (a_o + b_o) = (a_s + b_s), s = 1, 2, 3$ if cubic algebra equation posses three real roots. This relation is valid at initial state, at stationary states and at arbitrary states for special case that initial values of concentrations $a = a(t)$ and $b = b(t)$ of species A and B are $a(t_o) = a(0) = a_o$ and $b(t_o) = b(0) = b_o$.

As all cubic equations, equation (5) has either one real and two conjugate complex solutions, or three real ones for $a_s, s = 1, 2, 3$. Consequently in the considered nonlinear reaction system there are two cases of solutions: *one case is nonlinear dynamics of two concentrations a and b of species A and B, with only one stationary state defined by a pair $a_s = a_1$ and $b_s = b_1, s = 1$; *other case is nonlinear dynamics of two concentrations a and b of species A and B, with three stationary states defined by three pairs $a_s, b_s = (a_o - a_s) + b_o, s = 1, 2, 3$. Roots of cubic algebra equation (5) is possible to obtain graphically by graph of function: $F(a) = a^3 - 2pa^2 + qa - \beta a_o$, for different values of parameters k_f, k, a_o and b_o or p, q, a_o and β . Special case is when two roots are equal (double root). In second case, when the stationary states are defined by three pairs $a_s, b_s = (a_o - a_s) + b_o, s = 1, 2, 3$, system posses trigger of coupled singularities. Depending of values of parameters k_f, k, a_o and b_o three stationary states will appear and coexist all together. They will appear or disappear in related

bifurcation points. From this point of view, k_f , k , a_o or b_o are bifurcation parameter.

For investigation nonlinear phenomena and nonlinear dynamics around stationary states is possible to applied phenomenological approximate mappings in local area around stationary each state using approximation of the system of nonlinear differential equations by linearization or by nonlinear approximations. After applications of the phenomenological approximate mapping by linearization from system (2)-(3) of nonlinear differential equations around stationary state defined by two stationary concentrations a_s , b_s , $s = 1,2,3$ of species A and B we obtain the following approximation:

$$\frac{da}{dt} \approx \langle -k_f - k[(a_o - a_s) + b_o]^2 \rangle (a - a_s) + \langle -2ka_s [(a_o - a_s) + b_o] \rangle (b - b_s), \quad s = 1,2,3 \quad (9)$$

$$\frac{db}{dt} \approx k[(a_o - a_s) + b_o]^2 (a - a_s) + \langle -k_f + 2ka_s [(a_o - a_s) + b_o] \rangle (b - b_s) \quad (10)$$

or after introducing denotation

$$\begin{aligned} p_{a,s} &= \left(\frac{\partial f(a,b)}{\partial a} \right) \Bigg|_{\substack{a=a_s \\ b=b_s=(a_o-a_s)+b_o}} = -k_f - kb_s^2 = -k_f - k[(a_o - a_s) + b_o]^2, \quad s = 1,2,3 \\ p_{b,s} &= \left(\frac{\partial f(a,b)}{\partial b} \right) \Bigg|_{\substack{a=a_s \\ b=b_s=(a_o-a_s)+b_o}} = -2ka_s b_s = -2ka_s [(a_o - a_s) + b_o], \quad s = 1,2,3 \\ q_{a,s} &= \left(\frac{\partial f_1(a,b)}{\partial a} \right) \Bigg|_{\substack{a=a_s \\ b=b_s=(a_o-a_s)+b_o}} = kb_s^2 = k[(a_o - a_s) + b_o]^2, \quad s = 1,2,3 \\ q_{b,s} &= \left(\frac{\partial f_1(a,b)}{\partial b} \right) \Bigg|_{\substack{a=a_s \\ b=b_s=(a_o-a_s)+b_o}} = -k_f + 2ka_s b_s = -k_f + 2ka_s [(a_o - a_s) + b_o], \quad s = 1,2,3 \end{aligned} \quad (11)$$

in the form:

$$\frac{d\tilde{a}}{dt} \approx p_{a,s} \tilde{a} + p_{b,s} \tilde{b}, \quad \frac{d\tilde{b}}{dt} \approx q_{a,s} \tilde{a} + q_{b,s} \tilde{b}, \quad s = 1,2,3 \quad (12)-(13)$$

Two roots of the characteristic equation of the system (12)-(13) are:

$$\lambda_{s,1/2} = \frac{1}{2}(p_{a,s} + q_{b,s}) \mp \frac{1}{2} \sqrt{(p_{a,s} + q_{b,s})^2 - 4(p_{a,s}q_{b,s} - p_{b,s}q_{a,s})}, \quad s = 1,2,3 \quad (14)$$

Results of the phenomenological approximate mapping of system nonlinear differential equations (2)-(3) by linearization around stationary state defined by two stationary concentrations a_s , b_s , $s = 1,2,3$ of species A and B in the form of the system (11)-(12) is possible present in the form of a linear differential equation second order in the form:

$$\frac{d^2\tilde{a}}{dt^2} + 2\delta_s \frac{d\tilde{a}}{dt} + \omega_s^2 \tilde{a} \approx 0, s = 1, 2, 3 \quad (15)$$

where $\tilde{a} = a - a_s$ and $\tilde{b} = b - b_s$ are concentrations of species A and B measured from corresponding stationary values, and

$$2\delta_s = (p_{a,s} + q_{b,s}), \omega_s^2 = (p_{a,s}q_{b,s} - p_{b,s}q_{a,s}), s = 1, 2, 3 \quad (16)$$

With aim to investigate nonlinear phenomena, we shall examine behaviour of the considered system in the vicinity of stationary states, that is, we shall examine the stability of the nonequilibrium stationary states. After phenomenological approximate mapping by linearization of the system of first order nonlinear differential equations (2)-(3) around stationary state defined by two stationary concentrations a_s and b_s , $s = 1, 2, 3$, obtained approximate first order linear differential equations are obtained in the form (12)-(13).

After introduce new coordinate of concentrations starting measurement from stationary state, $a_s + \tilde{a}$ and $b_s + \tilde{b}$ into the system of first order nonlinear differential equations (2)-(3), and taking into account, relations valid for stationary concentrations a_s , b_s , $s = 1, 2, 3$ of species A and B for arbitrary initial conditions:

$$k_f(a_o - a_s) + ka_s b_s^2 = 0 \text{ and } k_f(b_o - b_s) - ka_s b_s^2 = 0 \quad (17)$$

the system of first order nonlinear differential equations appear in the following form:

$$\frac{d\tilde{a}}{dt} = k(a_s - \tilde{a})[\tilde{b} - 2b_s]\tilde{b} - \tilde{a}(k_f + kb_s^2) \quad (18)$$

$$\frac{d\tilde{b}}{dt} = -k(a_s - \tilde{a})(\tilde{b} - 2b_s)\tilde{b} - (k_f\tilde{b} - k\tilde{a}b_s^2) \quad (19)$$

in which \tilde{a} and \tilde{b} are small and local coordinate around stationary state. Then is possible to produce better phenomenological approximate mapping around stationary state, using nonlinear approximation, taking account that these local coordinates \tilde{a} and \tilde{b} are small.

In Table 1., linear and non-linear phenomenological approximate mappings of nonlinear differential equations as well as approximations of solutions in vicinity of singular points are presented for general case. Details are visible from middle and right hand column.

Table 1. Linear and non-linear phenomenological approximate mappings by use approximation of nonlinear differential equations as well as approximations of solution in local area of system kinetic parameters

	Phenomenological approximate mappings by linearization - Linear phenomenological approximate mappings in local area around singular point $N_s(\varphi_s, v_s), s = 1, 2, 3, 4, \dots$	Phenomenological approximate mappings by nonlinear approximation - Non-linear phenomenological approximate mappings in local area around singular point $N_s(\varphi_s, v_s), s = 1, 2, 3, 4, \dots$
Differential equations	$\frac{d\varphi}{dt} = f(\varphi, v) ; \quad \frac{dv}{dt} = f_1(\varphi, v)$	$\frac{d\varphi}{dt} = f(\varphi, v) ; \quad \frac{dv}{dt} = f_1(\varphi, v)$
Phenomenological approximate mappings of system differential equations around in local area around singular point $N_s(\varphi_s, v_s), s = 1, 2, 3, 4, \dots$ by $\varphi(=)\varphi_s + \varphi$, $v(=)v_s + v$	$\frac{d\varphi}{dt} = \left(\frac{\partial f(\varphi, v)}{\partial \varphi} \right)_{\varphi=\varphi_s, v=v_s} \varphi + \left(\frac{\partial f(\varphi, v)}{\partial v} \right)_{\varphi=\varphi_s, v=v_s} v$ $\frac{dv}{dt} = \left(\frac{\partial f_1(\varphi, v)}{\partial \varphi} \right)_{\varphi=\varphi_s, v=v_s} \varphi + \left(\frac{\partial f_1(\varphi, v)}{\partial v} \right)_{\varphi=\varphi_s, v=v_s} v$	$\frac{d\varphi}{dt} = \left(\frac{\partial f(\varphi, v)}{\partial \varphi} \right)_{\varphi=\varphi_s, v=v_s} \varphi + \left(\frac{\partial f(\varphi, v)}{\partial v} \right)_{\varphi=\varphi_s, v=v_s} v + \frac{1}{2!} \left(\frac{\partial^2 f(\varphi, v)}{\partial \varphi^2} \right)_{\varphi=\varphi_s, v=v_s} \varphi^2 + \frac{1}{2!} \left(\frac{\partial^2 f(\varphi, v)}{\partial v^2} \right)_{\varphi=\varphi_s, v=v_s} v^2 + 2 \frac{1}{2!} \left(\frac{\partial^2 f(\varphi, v)}{\partial \varphi \partial v} \right)_{\varphi=\varphi_s, v=v_s} \varphi v + \frac{1}{3!} \left[\left(\frac{\partial^3 f(\varphi, v)}{\partial \varphi^3} \right)_{\varphi=\varphi_s, v=v_s} \varphi^3 + 3 \left(\frac{\partial^3 f(\varphi, v)}{\partial \varphi^2 \partial v} \right)_{\varphi=\varphi_s, v=v_s} \varphi^2 v + \left(\frac{\partial^3 f(\varphi, v)}{\partial \varphi \partial v^2} \right)_{\varphi=\varphi_s, v=v_s} \varphi v^2 + \left(\frac{\partial^3 f(\varphi, v)}{\partial v^3} \right)_{\varphi=\varphi_s, v=v_s} v^3 \right] + \dots$ $\frac{dv}{dt} = \left(\frac{\partial f_1(\varphi, v)}{\partial \varphi} \right)_{\varphi=\varphi_s, v=v_s} \varphi + \left(\frac{\partial f_1(\varphi, v)}{\partial v} \right)_{\varphi=\varphi_s, v=v_s} v + \left(\frac{\partial^2 f_1(\varphi, v)}{\partial \varphi^2} \right)_{\varphi=\varphi_s, v=v_s} \varphi^2 + \left(\frac{\partial^2 f_1(\varphi, v)}{\partial v^2} \right)_{\varphi=\varphi_s, v=v_s} v^2 + 2 \frac{1}{2!} \left(\frac{\partial^2 f_1(\varphi, v)}{\partial \varphi \partial v} \right)_{\varphi=\varphi_s, v=v_s} \varphi v + \frac{1}{3!} \left[\left(\frac{\partial^3 f_1(\varphi, v)}{\partial \varphi^3} \right)_{\varphi=\varphi_s, v=v_s} \varphi^3 + 3 \left(\frac{\partial^3 f_1(\varphi, v)}{\partial \varphi^2 \partial v} \right)_{\varphi=\varphi_s, v=v_s} \varphi^2 v + \left(\frac{\partial^3 f_1(\varphi, v)}{\partial \varphi \partial v^2} \right)_{\varphi=\varphi_s, v=v_s} \varphi v^2 + \left(\frac{\partial^3 f_1(\varphi, v)}{\partial v^3} \right)_{\varphi=\varphi_s, v=v_s} v^3 \right] + \dots$
Phenomenological approximate mappings of differential equations around in local area around singular point $N_s(\varphi_s, v_s), s = 1, 2, 3, 4, \dots$ by $\varphi(=)\varphi_s + \varphi$, $v(=)v_s + v$	$\frac{d^2\varphi}{dt^2} - \frac{d\varphi}{dt} \left(\frac{\partial f(\varphi, v)}{\partial \varphi} \right)_{\varphi=\varphi_s, v=v_s} + \left(\frac{\partial f(\varphi, v)}{\partial v} \right)_{\varphi=\varphi_s, v=v_s} \left(\frac{\partial f_1(\varphi, v)}{\partial \varphi} \right)_{\varphi=\varphi_s, v=v_s} - \left(\frac{\partial f(\varphi, v)}{\partial v} \right)_{\varphi=\varphi_s, v=v_s} \left(\frac{\partial f_1(\varphi, v)}{\partial \varphi} \right)_{\varphi=\varphi_s, v=v_s} \varphi =$	$\frac{d^2\varphi}{dt^2} - \frac{d\varphi}{dt} \left(\frac{\partial f(\varphi, v)}{\partial \varphi} \right)_{\varphi=\varphi_s, v=v_s} + \left(\frac{\partial f(\varphi, v)}{\partial v} \right)_{\varphi=\varphi_s, v=v_s} \left(\frac{\partial f_1(\varphi, v)}{\partial \varphi} \right)_{\varphi=\varphi_s, v=v_s} - \left(\frac{\partial f(\varphi, v)}{\partial v} \right)_{\varphi=\varphi_s, v=v_s} \left(\frac{\partial f_1(\varphi, v)}{\partial \varphi} \right)_{\varphi=\varphi_s, v=v_s} \varphi = F \left(\frac{\varphi, d\varphi}{dt} \right)$
Phenomenological approximate mappings of differential equation solution around in local area around singular point $N_s(\varphi_s, v_s), s = 1, 2, 3, 4, \dots$	<p>1* for</p> $\omega^2 = - \left(\frac{\partial f(\varphi, v)}{\partial v} \right)_{\varphi=\varphi_s, v=v_s} \left(\frac{\partial f_1(\varphi, v)}{\partial \varphi} \right)_{\varphi=\varphi_s, v=v_s} > 0$ $2\delta = - \left(\frac{\partial f(\varphi, v)}{\partial \varphi} \right)_{\varphi=\varphi_s, v=v_s} + \left(\frac{\partial f(\varphi, v)}{\partial v} \right)_{\varphi=\varphi_s, v=v_s} \left(\frac{\partial f_1(\varphi, v)}{\partial v} \right)_{\varphi=\varphi_s, v=v_s} > 0$ <p>approximate solution</p> <p>a* $\delta < \omega$</p> $\varphi(t) = e^{-\delta t} (A \cos t \sqrt{\omega^2 - \delta^2} + B \sin t \sqrt{\omega^2 - \delta^2})$ <p>Stable centre type singular point</p> <p>b* $\delta > \omega$</p> $\varphi(t) = e^{-\delta t} (A \operatorname{Ch} t \sqrt{\delta^2 - \omega^2} + B \operatorname{Sh} t \sqrt{\delta^2 - \omega^2})$ <p>No stable saddle type singular point</p> <p>2* for</p> $q^2 = \left(\frac{\partial f(\varphi, v)}{v} \right)_{\varphi=\varphi_s, v=v_s} \left(\frac{\partial f_1(\varphi, v)}{\partial \varphi} \right)_{\varphi=\varphi_s, v=v_s} > 0$ $\pm 2\delta = - \left(\frac{\partial f(\varphi, v)}{\partial \varphi} \right)_{\varphi=\varphi_s, v=v_s} + \left(\frac{\partial f(\varphi, v)}{\partial v} \right)_{\varphi=\varphi_s, v=v_s} \left(\frac{\partial f_1(\varphi, v)}{\partial v} \right)_{\varphi=\varphi_s, v=v_s} > 0$	<p>* for</p> $\omega^2 = - \left(\frac{\partial f(\varphi, v)}{\partial v} \right)_{\varphi=\varphi_s, v=v_s} \left(\frac{\partial f_1(\varphi, v)}{\partial \varphi} \right)_{\varphi=\varphi_s, v=v_s} > 0$ $2\delta = - \left(\frac{\partial f(\varphi, v)}{\partial \varphi} \right)_{\varphi=\varphi_s, v=v_s} + \left(\frac{\partial f(\varphi, v)}{\partial v} \right)_{\varphi=\varphi_s, v=v_s} \left(\frac{\partial f_1(\varphi, v)}{\partial v} \right)_{\varphi=\varphi_s, v=v_s} > 0$ <p>approximate solution</p> <p>a* $\delta < \omega$</p> $\varphi(t) = e^{-\delta t} (A \cos t \sqrt{\omega^2 - \delta^2} + B \sin t \sqrt{\omega^2 - \delta^2})$ <p>Stable centre type singular point</p> <p>Differential nonlinear approximate equation</p> $\frac{d^2\varphi}{dt^2} + 2\delta \frac{d\varphi}{dt} + \omega^2 \varphi = F \left(\frac{\varphi, d\varphi}{dt} \right)$ <p>By asymptotic method Krilov-Bogolybov-Mitropolski</p> <p>Phenomenological approximate solution is proposed in the form:</p> $\varphi e^{\delta t} = \bar{x} = a \cos \psi + \varepsilon U_1(a, \psi, \tau) + \varepsilon^2 U_2(a, \psi, \tau) + \dots$ $\frac{da}{dt} = \varepsilon A_1(a, \tau) + \varepsilon^2 A_2(a, \tau) + \dots$ $\frac{d\psi}{dt} = p + \varepsilon B_1(a, \tau) + \varepsilon^2 B_2(a, \tau) + \dots$ $\int_0^{2\pi} U_j(a, \psi, \tau) e^{i\psi} d\psi = 0 \quad j = 1, 2, \dots, m$

		$A_1(a,\tau) = -\frac{1}{2\pi a} \int_0^{2\pi} \tilde{F}(e^{-\delta\tau} \{a \cos \psi\}, e^{-\delta\tau} \{-a \sin \psi\}) e^{\delta\tau} \sin \psi d\psi$ $B_1(a,\tau) = -\frac{1}{2\pi a} \int_0^{2\pi} \tilde{F}(e^{-\delta\tau} \{a \cos \psi\}, e^{-\delta\tau} \{-a \sin \psi\}) e^{\delta\tau} \cos \psi d\psi$ $a\tilde{F}\left(\tilde{x}e^{-\delta\tau}, \frac{d\tilde{x}}{dt}e^{-\delta\tau}\right) = a\tilde{F}\left(\tilde{x}, \frac{d\tilde{x}}{dt}, \tau\right)$
--	--	---

Right column of Table 1 contain method of phenomenological approximate nonlinear mapping, and corresponding solution using asymptotic method Krilov-Bogolyubov-Mitropolski [5]. Also for linearized phenomenological mapping in left culms Lyapunov method for investigation stability of the stationary states.

EXAMPLE 2. Let us consider a mechanical system with nonlinear dynamics of a heavy mass particle along rotate circle around vertical axis with eccentricity and with constant velocity. Using analogous method as in example 1, and generalized method of phenomenological linear and nonlinear approximate mappings presented in Table 1, in Table 2 results for example 2 are presented [6].

CONCLUSION

Presented application of phenomenological approximate mappings in vicinity of stationary states of two nonlinear dynamics, in two disparate systems, first physic-chemical system and other pure classical mechanical system show that Petrović's theory is universal for investigation of nonlinear dynamic properties.

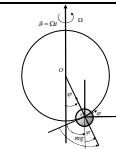
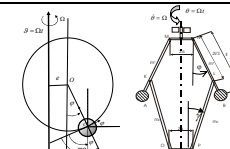
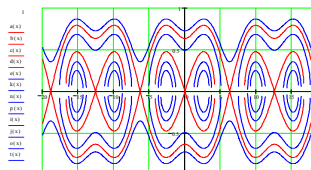
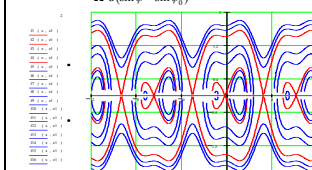
ACKNOWLEDGEMENT

This work was supported by the Ministry for Science of the Republic of Serbia (Grant no. ON174001) through Mathematical Institute SANU Belgrade and FME University of Niš.

REFERENCES

- [1] M. Petrović, *Elementi matematičke fenomenologije (Elements of mathematical phenomenology)*, Srpska kraljevska akademija, Beograd, 1911. str.789.
<http://elibrary.matf.bg.ac.rs/handle/123456789/476?locale-attribute=sr>
- [2] M. Petrović, *Fenomenološko preslikavanje (Phenomenological mapp)*, Srpska kraljevska akademija, Beograd, 1933. str. 33.
- [3] Lj. Kolar-Anić, Ž. Čupić, V. Vukojević, S. Anić, *Dinamika nelinearnih procesa*, Fakultet za fizičku hemiju, Univerzitet u Beogradu, Beograd 2011.
- [4] K. Hedrih (Stevanović), *Osnovi teorije melinearnih oscilacija (Theory of nonlinear oscillations)*, Niš, 1975. eLibrary,
<http://elibrary.matf.bg.ac.rs/handle/123456789/3768>
- [5] Yu. A. Mitropolyskiy, *Nestashionarnie proshesi v nelinyeynih sistemah*, AN USSR, Kiev. (in Russian), 1955.
- [6] K. Hedrih (Stevanović), (2005), *Nonlinear Dynamics of a Heavy Material Particle Along Circle which Rotates and Optimal Control*, Chaotic Dynamics and Control of Systems and Processes in Mechanics (Eds: G. Rega, and F. Vestroni), p. 37-45. IUTAM Book, in Series *Solid Mechanics and Its Applications*, Edited by G.M.L. Gladwell, Springer, 1995.

Table 2. Phenomenological approximate mappings around singular points-examples of linearization around singular points of a trigger of coupled three singular points

<p>Dynamical model Parameters</p> $\dot{\theta} = \Omega, \quad \lambda = \frac{g \sin \alpha}{\Omega^2}$ $\Omega_{rec}^2 = \frac{g \sin \alpha}{2l}$ $\varepsilon = \frac{e}{l}$		
<p>Differential equation</p>	$\ddot{\varphi} + \Omega^2(\lambda - \cos \varphi) \sin \varphi = 0$	$\ddot{\varphi} + \Omega^2(\lambda - \cos \varphi) \sin \varphi - \Omega^2 \varepsilon \cos \varphi = 0$
<p>Phase trajectory</p>	$\varphi^2 = \varphi_0^2 - 2\Omega^2 \left(-\lambda(\cos \varphi - \cos \varphi_0) + \frac{1}{4}(\cos 2\varphi - \cos 2\varphi_0) \right)$ 	$\varphi^2 = \varphi_0^2 - 2\Omega^2 \left(-\lambda(\cos \varphi - \cos \varphi_0) + \frac{1}{4}(\cos 2\varphi - \cos 2\varphi_0) - \Omega^2 \varepsilon (\sin \varphi - \sin \varphi_0) \right)$ 
<p>Singular points</p>	<p>$\varphi_s = s\pi, s = 0, \pm 1, \pm 2, \pm 3, \dots$</p> <p>1* $\lambda > 1$ Stable centre type points</p> <p>$\varphi_0 = 0, \varphi_{s=2k} = 2k\pi, s = 0, \pm 1, \pm 2, \pm 3, \dots$</p> <p>No stable saddle points</p> <p>$\varphi_1 = \pi, \varphi_{s=2k+1} = (2k+1)\pi, s = 0, \pm 1, \pm 2, \pm 3, \dots$</p> <p>2* $\lambda < 1$ No stable saddle points</p> <p>$\varphi_s = s\pi, s = 0, \pm 1, \pm 2, \pm 3, \dots$</p> <p>Stable centre type points</p> <p>$\varphi_s = \pm \arccos \lambda + 2s\pi, s = 0, \pm 1, \pm 2, \pm 3, \dots$</p> <p>Trigger of coupled three singular points</p> <p>$\varphi_0 = 0$ and $\varphi_{1,3} = \pm \arccos \lambda$</p>	<p>$f(\lambda_s) = 0$</p> $\lambda_s^4 - 2\lambda\lambda_s^3 + (\lambda^2 + \varepsilon - 1)\lambda_s^2 + 2\lambda\lambda_s - \lambda^2 = 0$ <p>$\varphi_s = \arccos \lambda_s$</p>
<p>Approximation of differential equation around singular point – a linearization as a phenomenological approximate mapping system dynamics in local area around singular point</p>	<p>Trigger of coupled three singular points</p> <p>$\varphi_0 = 0$ and $\varphi_{1,3} = \pm \arccos \lambda_m$ for $\lambda < 1$</p> <p>1* $\varphi_0 = 0$,</p> $\ddot{\varphi} + \Omega^2(\lambda - 1)\varphi = 0$ <p>2* $\varphi_{1,3} = \pm \arccos \lambda$</p> $\varphi \Rightarrow \varphi_{1,3} + \varphi$ $\ddot{\varphi} + \Omega^2(1 - \lambda)\varphi = 0$	<p>$f(\lambda_s) = 0$</p> $\lambda_s^4 - 2\lambda\lambda_s^3 + (\lambda^2 + \varepsilon - 1)\lambda_s^2 + 2\lambda\lambda_s - \lambda^2 = 0$ <p>$\varphi_s = \arccos \lambda_s$</p> <p>Trigger of coupled three singular points</p> <p>$\varphi_0 = \varphi_{00}$ and $\varphi_{1,3} = \pm \arccos \lambda_{1,3}$</p> <p>1* $\varphi_0 = \varphi_{00}$,</p> $\ddot{\varphi} + \Omega^2(\lambda - \cos(\varphi_{00} + \varphi))\sin(\varphi_{00} + \varphi) - \Omega^2 \varepsilon \cos(\varphi_{00} + \varphi) = 0$ <p>2* $\varphi_{1,3} = \pm \arccos \lambda_{1,3}, \varphi \Rightarrow \varphi_{1,3} + \varphi$</p> $\ddot{\varphi} + \Omega^2(\lambda - \cos(\varphi_{1,3} + \varphi))\sin(\varphi_{1,3} + \varphi) - \Omega^2 \varepsilon \cos(\varphi_{1,3} + \varphi) = 0$
<p>Approximation of differential equation solution around singular point – a linearization as a phenomenological approximate mapping system dynamics in local area around singular point</p>	<p>1* No stable saddle type singular point $\varphi_0 = 0$, for $\lambda < 1$</p> $\varphi(t) = ACh\Omega t \sqrt{\lambda - 1} + BSh\Omega t \sqrt{\lambda - 1}$ <p>2* Stable centre type singular point</p> <p>$\varphi_{1,3} = \pm \arccos \lambda$, for $\lambda < 1$</p> $\varphi \Rightarrow \varphi_{1,3} + \varphi$ $\varphi(t) = A \cos \Omega t \sqrt{\lambda - 1} + B \sin \Omega t \sqrt{\lambda - 1}$	<p>1* No stable saddle type singular point $\varphi_0 = \varphi_{00}$,</p> $\varphi(t) = AChqt + BShqt$ <p>2* Stable centre type singular point</p> <p>$\varphi_{1,3} = \pm \arccos \lambda_{1,3}, \varphi \Rightarrow \varphi_{1,3} + \varphi$</p> $\varphi(t) = A \cos pt + B \sin pt$

INTERMITTENT OSCILLATIONS IN BRAY-LIEBHAFSKY REACTION SYSTEM

I. Nuša Bubanja¹, S. Anić^{1,2} and Lj. Kolar-Anić^{1,2}

¹*Faculty of Physical Chemistry, University of Belgrade, Belgrade, Serbia*

²*Institute of Chemistry, Technology and Metallurgy, University of Belgrade,
Department of Catalysis and Chemical Engineering, Belgrade, Serbia*

ABSTRACT

Intermittent oscillations have been experimentally detected in the simplest homogeneous oscillatory chemical reaction, the Bray-Liebhafsky one, under open reactor (Continues well Stirred Tank Reactor, CSTR) condition without additional outflow of gaseous phase or any other additional perturbation of the reaction system. In experimental investigations, the temperature was control parameter, while the other parameters such as initial concentration of reactants in reactor, stirring rate and specific flow rate of the reactants into reaction mixture at CSTR were kept constant.

INTRODUCTION

The intermittent oscillations are phenomenon that can be found only in the nonlinear reaction systems.[1] In general, in such systems, can be observed that nearly periodic motion is interrupted by occasional irregular high-amplitude bursting oscillations or quiescent periods with none or very low-amplitude oscillations (gaps). The times between restored regular oscillations are statistically distributed, much like a random variable, even though the system is completely deterministic. The mentioned phenomenon was already obtained in the Bray-Liebhafsky (BL)¹ [2-4] reaction system under CSTR conditions when additional outflow of gaseous phase was present in experimental setup [5,6] as well as when U-tube for removing the surplus of reaction mixture was filled by the sintered glass [6]. In the current experiments intermittent oscillations were systematically investigated without additional outflow of gaseous phase and with simple U-tube for regulation of outflow of reaction mixture (Fig.1). Temperature was the control parameter.

¹ The BL reaction is the homogeneous oscillatory chemical reaction where hydrogen peroxide decomposes into the water and oxygen in the presence of iodate and hydrogen ions.

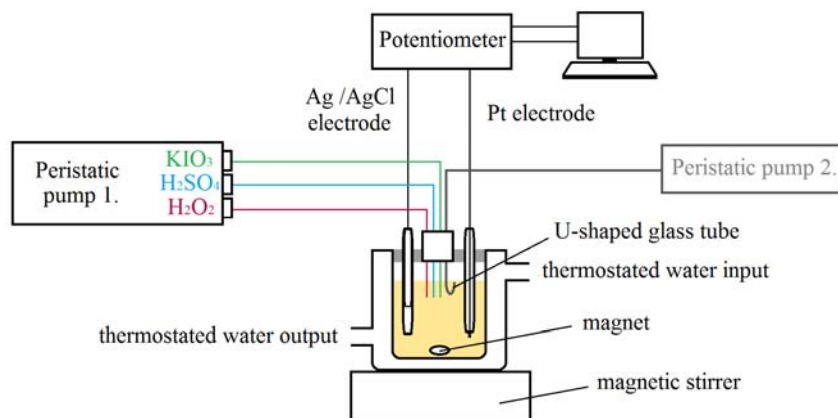


Figure 1. Schematic view of the entire experimental setup under CSTR conditions used in studies of the complex dynamical states of the BL reaction system.

EXPERIMENTAL

We have investigated a version of the BL reaction in which sulfuric acid was the source of H^+ and potassium iodate was the source of IO_3^- ions. Our attention was focused on the specific temperature-controlled evolution of the BL reaction carried out under CSTR or open reactor conditions (Fig. 1). Experiments were carried out at the temperature range from 61.0 °C to 64.7 °C with smallest step of 0.1 °C. For homogenization of the reaction mixture, a magnetic stirrer ($\sigma = 900$ rpm) was used. Amounts of species in the reactor were controlled by peristaltic pumps. Three of the channels were used to deliver the reactants (aqueous solutions of potassium iodate, sulfuric acid, and hydrogen peroxide) and one channel of the other pump was used to remove the surplus volume of the reaction mixture through a U-shaped glass tube. In this way, the volume of the reaction mixture was maintained constant at 22.2 mL. The working Pt electrode was connected to double-junction Ag/AgCl reference electrode. An electrochemical device (PC-Multilab EH4 16-bit ADC) coupled with a personal computer was used to record the potential-time evolution of the BL oscillator.

RESULTS AND DISCUSSION

It has been found that the smallest temperature change has a big influence on dynamic states of the BL reaction, particularly in the vicinity of the bifurcation where unstable nonequilibrium stationary state becomes the stable one (Fig. 2). There, the intermittent oscillations appear in narrow region of temperatures. At $T = 64.7$ °C (Fig 2.a) we can see the sustained

oscillations, whereas at $T = 61.0^\circ\text{C}$ (Fig. 2.e), the stable steady state is found. In between, different complex intermittent oscillatory states (Fig. 2. b, c, d), are obtained. As the temperature decreases total duration of gaps increases and total duration of bursts decreases, where bursts were defined as packages of large-amplitude oscillations and gaps were considered as periods between burst, or as packages of small-amplitude oscillations. Hence, the temperature dependence of the ratio between total duration of the bursts and the gaps, $Q_{B/G}$ is analyzed (Fig. 3).

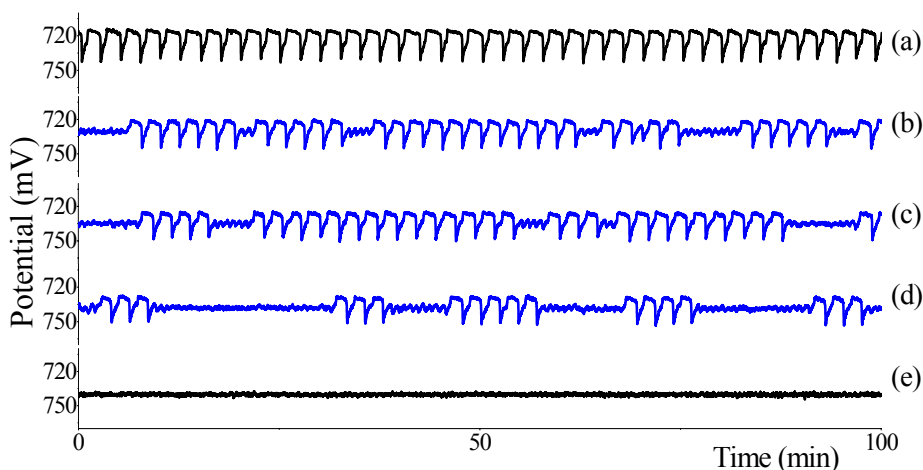


Figure 2. The oscillograms for BL reaction mixture in CSTR reactor with the following concentrations of reactants: $[\text{KIO}_3]_0 = 3.46 \cdot 10^{-2} \text{ M}$, $[\text{H}_2\text{SO}_4]_0 = 7.72 \cdot 10^{-2} \text{ M}$, $[\text{H}_2\text{O}_2]_0 = 2.40 \cdot 10^{-1} \text{ M}$ at temperature value: $T = 64.7^\circ\text{C}$ (a), $T = 63.7^\circ\text{C}$ (b), $T = 63.5^\circ\text{C}$ (c), $T = 63.3^\circ\text{C}$ (d) and $T = 61.0^\circ\text{C}$ (e). Only the segments of 100 minutes are given, although the experimental monitoring was longer.

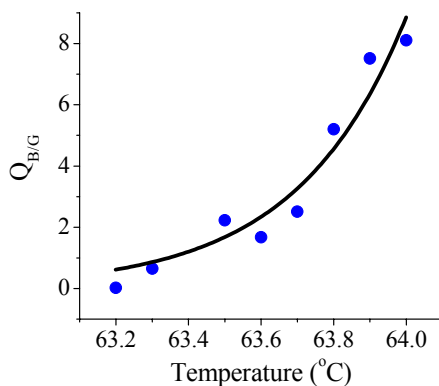


Figure 3. Temperature dependence of the ratio between total duration of the bursts and the gaps, $Q_{B/G}$.

CONCLUSION

In our presented investigation of the BL reaction under CSTR reactor conditions, where the temperature was control parameter, while the other parameters were taken as constant, intermittent chaos has been observed. For the first time, intermittent dynamic states were detected without any additional perturbation of the BL reaction system, so it could be concluded that this phenomenon is the specific property of the system.

ACKNOWLEDGEMENT

This work was supported by the Ministry for Science of the Republic of Serbia (Grant no. OI 172015).

REFERENCES

- [1] E. M. Izhikevich, *International Journal of Bifurcation and Chaos*, 2000, 10, 1171-1266.
- [2] W. C. Bray, *J. Am. Chem. Soc.*, 1921, 43, 1262-1267.
- [3] W. C. Bray, H. A. Liebafsky, *J Am. Chem. Soc.*, 1931, 53, 38-43.
- [4] H. A. Liebafsky, R. Furuichi, G. M. Roe, *J. Am. Chem. Soc.*, 1981, 103, 51-56 and other references therein.
- [5] V. Vukojević, S. Anić, Lj. Kolar-Anić, *J. Phys. Chem. A*, 2000, 104, 10731-10739.
- [6] Lj. Kolar-Anić, V. Vukojević, N. Pejić, T. Grozdić, S. Anić, *Deterministic Chaos in Open Well Stirred Bray-Liebafsky Reaction System*, in *Exsperimental Chaos*, S. Boccaletti, B. J. Gluckman, J. Kurths, L. M. Pecora, R. Meucci, O. Yordanov (Eds.), American Institute of Physics, AIP Conference Proceedings, Melville, New York, 2004, 742, 3-8.

EFFECTS OF GRADUAL CHOLESTEROL PULSES WITH NORMALLY DISTRIBUTED INTENSITY PROFILES ON THE HYPOTHALAMIC-PITUITARY-ADRENAL (HPA) AXIS DYNAMICS

A. Stanojević¹, Lj. Kolar-Anić^{1,2}, Ž. Čupić², V. M. Marković¹ and V. Vukojević³

¹ Faculty of Physical Chemistry, University of Belgrade, Studentski trg 12-16, 11000 Belgrade, Serbia. (anastann@yahoo.com)

² Institute of Chemistry, Technology and Metallurgy, University of Belgrade, Njegoševa 12, 11000 Belgrade, Serbia.

³ Karolinska Institutet, Department of Clinical Neuroscience, CMM L8:01, 17176 Stockholm, Sweden.

ABSTRACT

Transient perturbation of cholesterol levels, such as cholesterol elevation following food intake, affect the Hypothalamic-Pituitary-Adrenal (HPA) axis activity. However this effect is not easily studied experimentally and therefore remains poorly understood. We use mathematical modeling to investigate how gradual perturbations of cholesterol levels affect the dynamics of HPA axis hormones. For this purpose, externally induced cholesterol pulses of finite duration and with normally distributed intensity profile were used. Our study shows that pulse intensity, duration and the position of cholesterol discharge maximum with respect to the position of the maximum of cortisol daily rhythm of secretion are critical determinants of the perturbation effect on the HPA axis dynamics.

INTRODUCTION

The Hypothalamic-Pituitary-Adrenal (HPA) axis integrates the function of the hypothalamus, pituitary and adrenal glands through the action of steroid and peptide hormones, which are transported across the whole organism by the circulation system, on their corresponding receptors [1]. This complex nonlinear system functions under conditions far from thermodynamic equilibrium, and HPA axis hormones exhibit complex daily rhythms, with ultradian oscillations (period of 20 minutes to 2 hours), superimposed on circadian oscillations (period about 24 hours). The complex dynamics of the HPA system is an integral part and a necessary prerequisite for proper functioning of the entire organism. Qualitative changes in the HPA axis

dynamics and loss of dynamic regulation can lead to metabolic and neuropsychiatric diseases.

In this work, we study the effects of gradual, externally induced cholesterol surges on the HPA axis dynamics using mathematical modeling and numerical simulations. For this purpose, a low-dimensional model with five dynamic variables is used [2]. The dynamical variables are cholesterol, which is the only precursor of all steroid hormones, and HPA axis hormones: the corticotropin-releasing hormone (CRH), adrenocorticotrophic hormone (ACTH), cortisol (CORT) and aldosterone (ALDO).

NUMERICAL SIMULATIONS

Numerical simulations were performed in MATLAB, using the ode15s solver based on the Gear algorithm for integration of stiff differential equations. In all simulations absolute and relative tolerance errors were 3×10^{-20} and 1×10^{-14} , respectively. To emulate the dynamics of the unperturbed system, the following values of kinetic rate constants (k_i , $i = 1 - 13$) were used: $k_1 = 1.748 \times 10^{-4} \text{ M min}^{-1}$, $k_2 = 1.830 \times 10^{-8} \text{ M min}^{-1}$, $k_3 = 6.090 \times 10^{-11} \text{ M min}^{-1}$, $k_4 = 1.830 \times 10^4 \text{ min}^{-1}$, $k_5 = 7.442 \text{ M}^{-1} \text{ min}^{-1}$, $k_6 = 5.954 \times 10^{-2} \text{ M}^{-1} \text{ min}^{-1}$, $k_7 = 1.260 \times 10^{14} \text{ M}^{-2} \text{ min}^{-1}$, $k_8 = 7.050 \times 10^{12} \text{ M}^{-2} \text{ min}^{-1}$, $k_9 = 3.553 \times 10^{-2} \text{ min}^{-1}$, $k_{10} = 1.100 \times 10^{-1} \text{ min}^{-1}$, $k_{11} = 5.350 \times 10^{-2} \text{ min}^{-1}$, $k_{12} = 4.100 \times 10^{-1} \text{ min}^{-1}$, $k_{13} = 1.350 \times 10^{-1} \text{ min}^{-1}$. Initial concentrations were: $[\text{CHOL}]_0 = 3.4 \cdot 10^{-4} \text{ M}$, $[\text{CRH}]_0 = 1 \cdot 10^{-12} \text{ M}$, $[\text{ACTH}]_0 = 8 \cdot 10^{-8} \text{ M}$, $[\text{CORT}]_0 = 4 \cdot 10^{-8} \text{ M}$ and $[\text{ALDO}]_0 = 5 \cdot 10^{-9} \text{ M}$. Parameters of the circadian function D were: $d_1 = 0.88524$ и $d_2 = 0.957$. Time is given in hours (h) and molar concentration in $\text{M} = \text{mol dm}^{-3}$.

To simulate gradual and transient cholesterol surges, such as cholesterol entry into the blood circulation following food intake, which takes place through a series of biochemical processes in the digestive tract and the liver, and may last even several hours; cholesterol pulses of finite duration and normally distributed intensity profile were introduced by modifying the rate constant k_1 in the following way:

$$k_1 = 1.748 \times 10^{-4} \times (1 + A \times N(\tau, \sigma)) \quad (\text{Eq1})$$

$$N(\tau, \sigma) = \frac{1}{\sigma\sqrt{2\pi}} e^{-\frac{\tau^2}{2\sigma^2}}, \quad \tau = \frac{t - B}{C} \quad (\text{Eq2})$$

Here, A defines the intensity of the perturbation and is equal to 0 for the unperturbed system; B is a timing-related parameter that determines the position of the maximum of the normal distribution, *i.e.* the time (in hours) at which maximum discharge will take place; σ is the standard deviation of the underlying intensity distribution that defines the spreading of the pulsed

signal; C is a parameter through which the half-width and the intensity of the perturbation can be simultaneously changed; and t is the actual time during the day (in hours) in one circadian cycle.

In numerical simulations, the cholesterol pulse starts at the beginning of the numerical simulation, and its concentration gradually increases over time, reaching a maximum at the time specified by B . Thereafter, the concentration will gradually decrease, to the same value as before the rise of cholesterol level (Fig. 1 (CP)). The rate at which cholesterol is discharged is determined by the standard deviation σ – being fast when σ is small and, slow when σ is big.

RESULTS

The model shows that perturbation intensity (represented here by the parameter A), the pulse width (represented here by the standard deviation σ), and the time of discharge (represented here by the parameter B), are all relevant modulators of the HPA axis activity. While the effect of perturbation intensity is easy to understand intuitively (data not shown), the effect of pulse distribution and maximum discharge time is not easily predicted. We therefore show in Fig. 1 examples where these parameters were varied. When the position of the maximum of distribution is close to the maximum of the circadian oscillation, low values of σ increase the amplitude of ultradian oscillations (Fig. 1 (a1)). As the parameter σ increase, the effect of increasing the amplitude decreases (Fig. 1 (a2)) and for even higher values of σ the oscillations begin to be suppressed (Fig. 1 (a3)).

Results presented in Fig. 1 show that the effect of the perturbation on the HPA axis dynamics depends on the total intensity of the perturbation, the steepness of the pulse, but also of the relative position of the discharge maximum with respect to the phase of the circadian cortisol oscillation. The HPA axis dynamics is least perturbed when perturbation is applied during the active phase, *i.e.* during the downstream part of circadian oscillation (Figure 1(b1) and 1(b2)). In that case, only abrupt perturbations, with high σ values alter the amplitude of ultradian oscillations (Figure 1 (b3)).

CONCLUSION

A mathematical model was developed that can be used to study *in silico* the effect of gradual cholesterol discharge on the HPA axis dynamics. An important step forward was made by moving from modeling instantaneous perturbations, to modeling gradual perturbations whose intensity profile has the form of a normal distribution, which better reflects the situation *in vivo*.

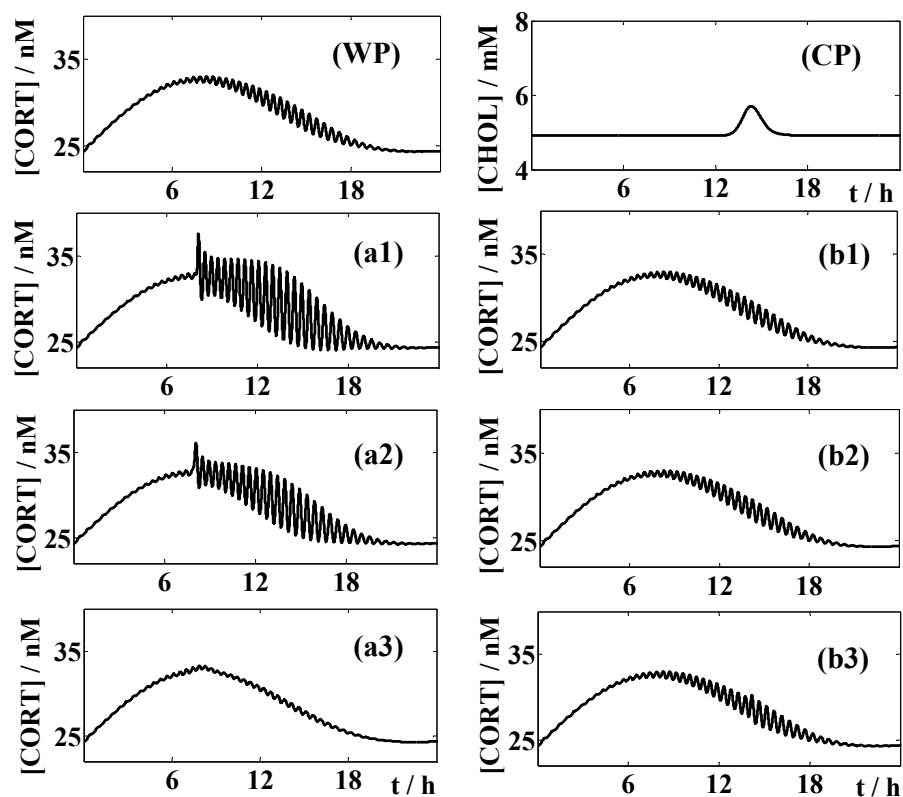


Figure 1. Temporal evolution of cortisol for gradual perturbations with cholesterol pulses of the same intensity, but different pulse width and maximum discharge time. Graph (WP) - the unperturbed HPA system. Graph (CP) - the cholesterol pulse applied in (b3). Graphs (a1-a3) and (b1-b3) show the effect of cholesterol pulses on the HPA axis dynamics when: $A = 1$, $C = 15$, $B = 8$ (a1-a3) and $B = 14$ (b1-b3). The pulse width was: (a1) and (b1) $\sigma = 0.1$; (a2) and (b2) $\sigma = 0.25$; (a3) and (b3) $\sigma = 2$.

ACKNOWLEDGEMENT -This work was supported by the Ministry of Education and Science of Republic of Serbia (Grants no. 172015, 45001).

REFERENCES

- [1] Felig P, Frohman L. A. *Endocrinology and Metabolism* (4th edn.). McGraw-Hill, New York, 2001.
- [2] Marković, V, Maćešić, S, Damjanović, S, Kolar-Anić, Lj. Inclusion of cholesterol in hypothalamic-pituitary-adrenal axis stoichiometric model, in *Physical Chemistry 2012*, Anić S, Čupić Ž. (eds), Society of Physical Chemists of Serbia, Belgrade, 2012, pp. 264-266 .

**PECULIARITIES OF THE OSCILLATORY BEHAVIOUR
IN THE CATALYTIC REACTION OF CO OXIDATION
OVER THE SUPPORTED PALLADIUM
NANOPARTICLES WITH THE DYNAMICALLY
CHANGING SURFACE MORPHOLOGY:
MONTE CARLO MODEL**

V.I. Elokhin^{1,2}, K.V. Kalgin^{2,3}, E.V. Kovalyov¹ and A.V. Matveev^{1,2}

¹ *Boriskov Institute of Catalysis, Siberian Branch of the Russian Academy of Sciences, prosp. Acad. Lavrentieva, 5, 630090, Novosibirsk-90, Russia (elokhin@catalysis.ru)*

² *Novosibirsk State University, 630090, Novosibirsk-90, Russia*

³ *Institute of Computational Mathematics and Mathematical Geophysics, Siberian Branch of the Russian Academy of Sciences, prosp. Acad. Lavrentieva, 6, 630090, Novosibirsk-90, Russia*

ABSTRACT

The stochastic model of the oscillatory dynamics in the CO oxidation reaction over the supported Pd nanoparticles (the driving force of oscillations is the formation and consumption of the subsurface oxygen on the metal nanoparticle) has been proposed. Furthermore it is necessary to take into account the contribution of CO_{ads} diffusion over the support onto the active metal particle surface (reverse spillover) giving the additional source of CO_{ads} flux to the particle through its perimeter. The dependence of the oscillatory dynamics on the size and surface roughening of the supported particle has been studied. The presence of CO_{ads} spillover determines the character of surface waves over the Pd nanoparticle – oxygen wave propagates from the central region of the particle to the perimeter, and the CO_{ads} reverse wave moves from the perimeter, always enriched by CO_{ads}, to the center of the particle. If the density of nanoparticles on the support is enough high, the synchronization of oscillations between neighboring Pd nanoparticles only due to diffusion of CO_{ads} over the support surface is possible.

INTRODUCTION

The catalytic properties of the supported metal nanoparticles differ drastically from those of the massive metals [1-3]. In particular, the shape and surface morphology of the metal nanoparticles are very sensitive to the changes in the composition of the reaction media (pressures of the reagents

and temperature). Furthermore, spillover (diffusion of the adsorbed species over the support surface) can substantially influence the catalytic activity and selectivity of the reactions under consideration. The theoretical study of supported catalysts is a rather complicated problem, and an analysis of reaction performance on the small particles almost inevitably requires use of atomic scale computer simulations taking into account the intrinsic heterogeneity of nanoparticles. The most effective tool for simulation of the spatiotemporal dynamics of adsorbed species on real catalytic surfaces, whose structure and properties can change under the influence of the reaction, are now the stochastic methods based on the Monte-Carlo technique permitting one to obtain the qualitatively new results [4].

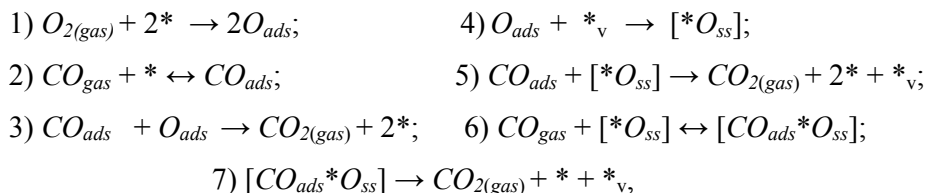
MODELS AND TECHNIQUES

The model of oscillatory dynamics of the $\text{CO} + \text{O}_2$ reaction over the supported Pd nanoparticle has been studied by means of Monte-Carlo technique. Thereto we combine the stochastic model for the imitating the supported nanoparticle with dynamically changing shape and surface morphology [5] and the usual kinetic Monte-Carlo approach to model the CO oxidation reaction over the Pd(110) single crystal [6]. Furthermore, according to [7] considering the kinetic features of CO oxidation reaction over Pd/ Al_2O_3 , it is necessary to take into account the contribution of CO_{ads} diffusion over the support onto the active metal particle surface (reverse spillover) giving the additional source of CO_{ads} flux to the particle through its perimeter. This can manifest as size-dependent reactivity of the supported catalysts, especially at the small sizes. The amount of CO_{ads} reaching the active nanoparticle is defined through the collection zone [7], which depends on the mean diffusion length of CO_{ads} on the support and on the density of nanoparticles.

As a model of the catalytic metal particle we shall consider the Kossel crystal located on a neutral support. The initial active particle consist of the finite number of elementary cells (metal atoms) situated in the columns of the cubic lattice. The surface morphology of the particle is defined by distribution of heights of the metal atom columns and can be changed due to the thermal diffusion of the surface atoms. The metal atoms attract the nearest neighboring ones and the atoms of the support. The attraction is characterized by energies: J_{mm} , the interaction energy between the nearest neighbor atoms situated at the same level and one on the lower, J_{ms} , the interaction energy between the metal atom and the rigid support underneath. To model the diffusion of the metal atoms over the metal and support surfaces the Metropolis algorithm [8] has been used. The diffusion proceeds via transfer of the randomly chosen surface metal atom from any column

onto one of the neighboring ones (for the boundary atoms it might be the cell of the support surface).

The following mechanism of the reaction was used for simulations [6]:



where * and $*_{\nu}$ – are the active centers of the surface and subsurface layers, respectively. CO can adsorb both over the surface of particle and the support (desorption coefficient of CO_{ads} from the support was assumed several times higher than that from the palladium particle) and then diffuse through the support (intensity of diffusion was assumed several times higher than that over the palladium particle). Oxygen can adsorb only on the available centers of the palladium particle, preferably on the terraces.

RESULTS AND DISCUSSION

The influence of both reaction parameters (rate coefficients and intensity of diffusion) as well as particles characteristics (size, degree of roughening, etc.) on the oscillatory behavior and chemical pattern formation over the particles surface has been studied. Before each simulation run the surface of nanoparticles was roughened at $T = 500K$. Decreasing of the particles linear size to less than ~ 7 nm, (depending on the chosen set of parameters) leads to the disappearing of oscillations. The main reasons for that phenomenon are the following: 1) decreasing of the particles size leads to the roughening (increasing of the defects concentration) of its surface and, hence, to the deficit of the available centers for oxygen adsorption; 2) the influence of the additional flux of CO_{ads} from the particles perimeter shifts the interval of oscillations to the higher values of the oxygen partial pressure. This influence is especially important for the small particles, at the increasing of the size (in our case > 40 nm) this influence is negligible, the period and the amplitude of oscillations coincide with that for the large rigid lattice without any roughening [6]. The presence of the CO_{ads} reverse spillover determines the character of concentration waves over the surface of Pd nanoparticle – oxygen wave propagates from the central region of the particle to its perimeter, and the CO_{ads} wave moves from the perimeter, always enriched by CO_{ads} to the centre of the particle. In the cases when the collection zones overlapped (e.g., the density of the particles on the support is high enough)

the synchronization of oscillations between neighboring local oscillators (nanoparticles) due to CO_{ads} diffusion over the support seems to be possible.

ACKNOWLEDGEMENT

This study was partially supported by the Russian Foundation of Basic Research (Grant no. 12-03-00766-a) and by Interdisciplinary Integration Project no. 47 of Siberian Branch of the Russian Academy of Sciences.

REFERENCES

- [1] V.P. Zhdanov, B. Kasemo. *Surf. Sci. Rep.*, 2000, V. 39, P. 25-104.
- [2] V.P. Zhdanov. *Surf. Sci.*, 2002, V. 500, P. 966-985.
- [3] V.I. Elokhin, A.V. Myshlyavtsev. In: *Dekker Encyclopedia of Nanoscience and Nanotechnology*, Vol. II. C.I. Contescu and K. Putyera, Eds.; Taylor & Francis: New York, 2009; pp. 782-793.
- [4] B. Temel, H. Meskine, K. Reuter, M. Scheffler, H. Metiu. *J. Chem. Phys.*, 2007, V. 126, P. 204711(1-12).
- [5] E.V. Kovalyov, V.I. Elokhin, A.V. Myshlyavtsev. *J. Comp. Chem.* 2008. V. 29. P. 79-86.
- [6] E.I. Latkin, V.I. Elokhin, A.V. Matveev, V.V. Gorodetskii. *J. Molec. Catal. A, Chemical*, 2000, V. 158, P. 161-166.
- [7] M. Boudart. *Topics in Catalysis*, 2000, V. 13, P. 147-149.
- [8] N. Metropolis, A.V. Rosenbluth, M.N. Rosenbluth, A.H. Teller, E. Teller. *J. Chem. Phys.*, 1953, V. 21, № 6, P. 1087-1092.

MEMORY STORAGE PHENOMENA AT DEVELOPED LIQUID-LIQUID INTERFACES: ELECTRODYNAMICS AND NANORHEOLOGY

A.M. Spasic¹, J.M. Jovanovic², R. Stevanovic³, M. Jovanovic⁴

¹*Institute for Technology of Nuclear and Other Mineral Raw Materials, Dept. of Chem. Engng., 86 F. d'Esperey St., 11000 Belgrade, Serbia, (a.spasic@itnms.ac.rs)*

²*Inovacioni Center, Dept. of Met. & Tech., University of Belgrade, 4 Karnegijeva St., 11000 Belgrade, Serbia.*

³*Institute for Chemistry, Technology, and Metallurgy, University of Belgrade, 4 Karnegijeva St., 11120 Belgrade, Serbia*

⁴*Dept. of Met. & Tech., University of Belgrade, 4 Karnegijeva St., 11000 Belgrade, Serbia.*

ABSTRACT

Over the last decade the biggest advances in physics, physical chemistry, and bio-chemistry have come from thinking smaller. This research takes an interdisciplinary approach to the elucidation of the momentum transfer phenomenon as well as the electron transfer phenomenon, at well-characterized developed, both, rigid and deformable liquid-liquid interfaces. The considered scales are micro, nano and atto, using various theoretical approaches. Micro scales may cover more or less classical chemical engineering insight, while nano and atto scales focus on modern molecular and atomic engineering.

INTRODUCTION

The objective of this research was a try to provide a new or different approach to elaborate the complex phenomena that occur at developed liquid-liquid interfaces. Since some phenomena that occur, for example, during the processes of breaking of emulsions or double emulsions, and coalescence are not well understood the introduction of theoretical models known in electrodynamics are needed. Such an approach can contribute to the deeper elucidation of the complex phenomena that occur at smaller separations, because the forces of electrical origin become dominant compared to the forces of mechanical origin, for example the terms electrical forces and electrical interfacial potential (EIP) could be more appropriate than the terms mechanical forces and interfacial tension.

Hence, for easier understanding of the physical events at developed liquid-liquid interfaces it was necessary to develop new concepts. The first is a concept of an *entity*, and the corresponding new classification of finely dispersed systems; this concept permit consideration of the electron transfer phenomenon beside the classical heat, mass, and momentum transfer phenomena commonly used in chemical engineering. The second concept is an introduction of almost forgotten basic electrodynamics element the *memristor* (M), and the corresponding memristive systems; this concept is needed because the fundamental electrodynamics elements, the *resistor* (R), the *inductor* (L), and the *capacitor* (C) are not sufficient for a satisfactory explanation of complex phenomena at developed liquid-liquid interfaces.

Using these two concepts, and taking into account electron and momentum transfer phenomena, as well as electro-mechanical analogies, a theory of electroviscoelasticity was proposed and applied to the selected emulsions and double emulsions. Now the electrodynamics elements are: the capacitor C and the memristor M as electroelastic elements, and the inductor L and the resistor R as electroviscous elements.

The theory of electroviscoelasticity was experimentally corroborated using the developed and constructed liquid-liquid contact cell for EIP measurements, and the nuclear magnetic resonance (NMR) spectrometer for energetic analysis [1-3].

The selected representative system, either electroviscoelastic droplet or droplet-film structure submerged into the other immiscible liquid phase, which is emulsion or double emulsion, could be considered as the particular example of memristive systems [2].

THEORETICAL CONCEPT OF AN *entity*

A new concept, based on entities, has been developed and applied for the elucidation of the electron and momentum transfer phenomena at, both, rigid and deformable interfaces in finely (micro, nano, and atto) dispersed systems. Hence, an entity can be defined as the smallest indivisible element of matter that is related to the particular transfer phenomena. Therefore, an entity can be a differential element of mass/demon, an ion, a phonon as quantum of acoustic energy, an infon as quantum of information, a photon, or an electron [1-3].

THEORETICAL CONCEPT OF *a memdiode* OR *a memristor*

Based on the definition of a “missing” basic element *memristor* for electrical circuit analysis, and taking into account four fundamental circuit variables, electric current i , electromotive force v , charge q , and magnetic flux φ the set of fundamental functional relations is given by:

$$dv = Rdi; dq = Cdv; d\phi = Ldi; d\phi = Mdq; d\phi = vdt; dq = idt; \quad (1)$$

Hence, the memristor as a current-controlled device is defined with the Eqs. (2) and (3), where w is the state variable of the device and R is a generalized resistance that depends upon the internal state of the device. In 1976 Chua and Kang generalized the memristor concept to a much broader class of nonlinear dynamical systems, named memristive systems, described by the Eqs. (4) and (5), where w is a set of state variables and R and f can, in general, be explicit functions of time .

$$v = R(w)i \quad (2) \quad \text{and} \quad \frac{dw}{dt} = i \quad (3); \quad v = R(w,i)i \quad (4) \quad \text{and} \quad \frac{dw}{dt} = f(w,i) \quad (5)$$

Further on, when an incidental uniform physical field, for example electromagnetic, is applied on the system emulsion/droplet or double emulsion/droplet-film-structure, causing the motions of both electrons and ions, than the memristance may be obtained as:

$$M(q) = R_{bul} \left[1 - \frac{\mu_i R_{int}}{D^2} q(t) \right] \quad (6)$$

where R_{int} is the low resistance at the interface and close to the interface layers, R_{bul} is the much higher resistance in the bulk layers, μ_i is the average ion mobility, D is the thickness of the considered fragment/"device" [2].

ELECTROMECHANICAL ANALOGY AND NANORHEOLOGY

Marangoni instabilities of the first and second order and possible electrical analogues were derived, and analyzed; also a number of various constitutive models of liquids were considered to help establishment of a new constitutive model of liquids, which is convenient to support developed electrified interfaces-small separations [1-3].

THEORY OF ELECTROVISCOELASTICITY-PREVIOUS WORK

The first model is the stretching tensor model, where the normal and tangential forces are considered, only in mathematical formalism, regardless to their origin, mechanical and/or electrical. The second model is classical integer order van der Pol derivative model:

$$C \frac{dv}{dt} + \left(\frac{1}{R} - \alpha \right) v + \gamma v^3 + \frac{1}{L} \int v dt = -2A_n \cos \omega t \quad (7)$$

where v is the overall potential difference at the junction point of the spherical capacitor C and the plate, L is the inductance caused by potential difference, and R is the ohm resistance (resistance of the energy transformation, electromagnetic into the mechanical or damping resistance), t is the time; α and γ are constants determining the linear and nonlinear parts

of the characteristic current and potential curves. A nonhomogeneous solution may be obtained only when Eq. (7) is linearized, where A is the amplitude, and ω is the frequency of the incident oscillation. Finally, the third model comprise an effort to generalize the previous van der Pol differential equations, both, linearized and nonlinear; where the ordinary time derivatives and integrals are replaced by the corresponding fractional-order time derivatives and integrals of order $p < 2$ ($p = n - \delta$, $n = 1, 2$, $\delta \ll 1$).

EXPERIMENTAL CORROBORATION

In order to justify and corroborate more general approach the obtained calculated results were compared to those experimentally measured using the representative liquid-liquid system [1-3].

RESULTS AND DISCUSSION

Now, according to the presented electrohydrodynamic approach, emulsions and double emulsions will be considered as the particular example of memristive systems! More details, foundations and development of this research can be found in CHISA (1987-2014), PHYSICAL CHEMISTRY (1992-2012), and references [1-3].

IMPLICATIONS AND CONCLUSIVE REMARKS

Adhesive processes, rupture processes, coalescence, colloid and interface science, chemical and biological sensors, electro-analytical methods, biomedicine (hematology, genetics, electroneurophysiology).

The basis for extension of transfer phenomena, including electron transfer, in Colloid and Interface Science & Chemical Engineering!

ACKNOWLEDGMENTS

Financial support by Ministry of Education and Science – Republic of Serbia, grants: former 142034 and present 34009 and 46010.

REFERENCES

- [1] J-P. Hsu, A.M. Spasic, Interfacial Electroviscoelasticity and Electrophoresis, CRC Press-Taylor & Francis, Boca Raton London New York, 2010.
- [2] A.M. Spasic, J.M. Jovanovic, M. Jovanovic, Adv. Colloid Interface Sci., 2012; 174, 31-49.
- [3] A.M. Spasic, M.P. Lazarevic, M.V. Mitrovic, D.N. Krstic in: Finely Dispersed Particles: Micro-, Nano-, and Atto-Engineering, A.M. Spasic, J.P. Hsu (Eds.), CRC Press-Taylor and Francis, Boca Raton London N.Y., 2006.

THE INFLUENCE OF CHEMICALLY INERT Li^+ AND Cs^+ IONS ON BRAY-LIEBHAFSKY (BL) DYNAMICS OR WHY LARGER CATION HAS MORE IMPACT ON BL REACTION

M. C. Milenković¹, I.Ž. Ljubić¹ and D. R. Stanisavljev¹

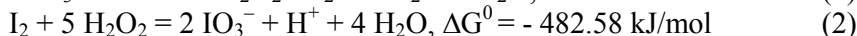
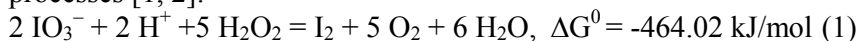
¹Faculty of Physical Chemistry, Belgrade University, Studentski Trg 12, Belgrade (maja.milenkovic@ymail.com)

ABSTRACT

The influence of the chemically inert alkali metal cations Li^+ and Cs^+ on the Bray–Liebhafsky (BL) oscillatory reaction dynamics is investigated by the addition of different concentrations of lithium and cesium sulfate in the reaction mixture. Beside the common sulfate ion and expected modification of the system acidity, one small effect is observed connected with the dimension of investigated cations. Larger cation has more impact on the BL reaction dynamics. Since it is known that cations are chemically inert and do not affect BL chemical reaction, the observed effect may be related with the changed extent of water hydrogen bonding and the specific role of bulk water in reaction mechanism.

INTRODUCTION

Bray-Liebafsky reaction is the periodic decomposition of hydrogen peroxide in acidic solution in the presence of potassium iodate [1]. The reaction may be described with the periodical domination of two complex processes [1, 2]:



Despite that both processes are thermodynamically favorable, process (2) (without present iodate) and at the acidity of the BL reaction, does not significantly occur for hours! It seems obvious that process (2) need large activation energy. Despite of this, process (2) in BL becomes periodically dominant one. It can indicate that during the BL reaction the specific energy barriers are efficiently overcome enabling formation of reactive components and facilitated iodine oxidation. In the process of molecular activation, water can play important role since it is present in high excess and due to large heat capacity may efficiently store energy released in chemical reactions. The role of water structuredness and the extent of hydrogen bonding on various processes are under examination [3,4]. The structure of

hydrogen bonds may be affected by presence of various ions due to their effective radius and electrostatic interaction with water dipoles. In this work we investigated the effects of different chemically inert Li^+ and Cs^+ cations by the addition of the corresponding sulfate salts to the BL reaction mixture.

EXPERIMENTAL

For the investigation of the influence of Li^+ and Cs^+ cations on Bray-Liebafsky reaction dynamics, alkali metal sulfates: Li_2SO_4 (from Merck) and Cs_2SO_4 (from Fluka) are used. The Bray-Liebafsky reaction is composed of KIO_3 , H_2SO_4 and H_2O_2 (all from Merck). The used chemicals were of PA grade. Deionized water (18 $\text{M}\Omega$ cm) was applied for preparing all solutions.

The Bray-Liebafsky reaction mixture is formed of 18.5 ml potassium iodate $[\text{KIO}_3] = 0.1012$ M, 6.5 ml sulfuric acid $[\text{H}_2\text{SO}_4] = 0.192$ M, and 0.5 ml hydrogen peroxide $[\text{H}_2\text{O}_2] = 10.45$ M. The temperature of all experiments was maintained constant at $T_{\text{exp}} = 63.0 \pm 0.5$ °C using circular thermostat (Julabo F12 circulator). The reaction mixture was stirred with the magnetic stirrer at 220 rpm. The temporal evolution of BL system was recorded by means of a Pt electrode and $\text{Hg}/\text{Hg}_2\text{SO}_4$ reference electrode (Schott Instruments).

For comparing the effects of different cations, lithium and cesium sulfate concentrations of $3.04 \cdot 10^{-3}$ M, $6.08 \cdot 10^{-3}$ M, $12 \cdot 10^{-3}$ M and $17 \cdot 10^{-3}$ M are prepared. The BL reaction is perturbed after five regular oscillations, by addition of 0.5 ml Li_2SO_4 or Cs_2SO_4 of mentioned concentration and the effects on reaction dynamics is investigated.

RESULTS AND DISCUSSION

The perturbation of BL system, after five oscillations, with lithium or cesium sulfates is represented in figure 1. In all experiments, before addition

of sulfates, mean period $\tau_{1-5} = t_{1-5}/5$ and average amplitude $A_{1-5} = \left(\sum_{i=1}^5 A_i \right) / 5$

for the first five oscillations are determined and compared with the corresponding values after perturbation. After the addition of alkali sulfates, the time of the prolonged monotonous evolution $\tau_{\text{ind}2}$, the mean period $\tau_{6-10} = t_{6-10}/5$,

and average amplitude $A_{6-10} = \left(\sum_{i=6}^{10} A_i \right) / 5$, for the next five

oscillations are determined. Results obtained for different concentration of Li^+ and Cs^+ ions are presented in Table 1.

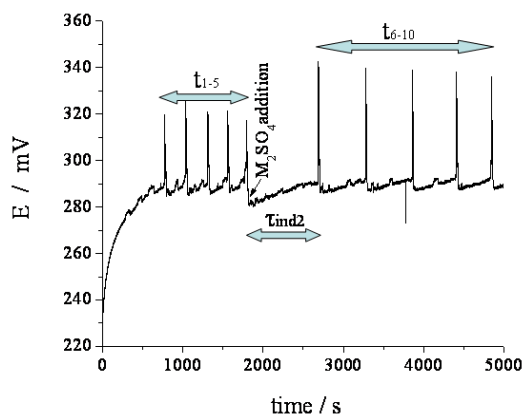


Figure 1. The characteristic oscillogram representing the effects of added sulfates, t_{1-5} – the duration of the first five unperturbed oscillations, $\tau_{\text{ind}2}$ – prolonged period of monotonous evolution and t_{6-10} – the duration of the five oscillations after addition of M_2SO_4 , (where M is Li or Cs).

As shown in Table 1., Cs^+ as the larger cation (ionic radius 0.167 nm), than Li^+ cation (ionic radius 0.076 nm) slightly favor monotonous evolution by: increasing second induction period, slight diminishing the amplitude of oscillations and extending the average oscillatory period.

Table 1. The effects of various Li^+ and Cs^+ concentrations on the BL reaction parameters: $\tau_{\text{ind}2}/\tau_{1-5}$, A_{6-10}/A_{1-5} and τ_{6-10}/τ_{1-5} .

Li^+ and Cs^+ ions concentration / 10^{-3} M	$\tau_{\text{ind}2}/\tau_{1-5}$		A_{6-10}/A_{1-5}		τ_{6-10}/τ_{1-5}	
	Li^+	Cs^+	Li^+	Cs^+	Li^+	Cs^+
6.08	1.54	1.56	1.31	1.21	1.30	1.28
12.16	1.80	1.98	1.27	1.23	1.40	1.45
24	2.60	2.80	1.50	1.44	1.70	1.80
34	3.21	3.51	1.67	1.58	1.96	2.18

One of the reasons for the influence of salts is related with the effect of common ion (SO_4^{2-}). Because the BL reaction is conducted in sulfuric acid, addition of sulphates reduces the system acidity. However, added $LiSO_4$ and $CeSO_4$ are strong electrolytes and because of the same stoichiometric concentrations, contribution of sulfate anion should be the same in corresponding experiments. The second possible reason is related with ion activity (effective concentration) and may be different due to the dependence of the activity coefficients of the ion size [5]. According to Debye-Hückel theory and its modifications [5], the largest activity coefficient belongs to Li^+ and decreases for larger cations. In other words, Li_2SO_4 should be more “active” in the BL system than the salts with larger

cations. In practice, the opposite trend is observed, suggesting that different salt activities are not the main explanation for the presented results. From obtained results it can be concluded that larger cations slightly enhance monotoneous evolution and thus decrease the contribution of oxidative process (2). One possible explanation is that larger cation, Cs^+ , has more impact on the BL reaction mechanism due to their breaking effects on the extent of hydrogen bonding. Whether ions are marked as structure makers or breakers depends of how the extent of hydrogen bonds differs from that in pure water. According to Marcus [4], structure making ion is Li^+ , structure breaking ions are K^+ , Rb^+ and Cs^+ whereas Na^+ is a border– line– ion separating two groups. Such interpretation of results support the idea that changed dynamics of hydrogen bonds may influence the specific reaction pathways. This aspect of chemical oscillators is not well understood and deserves further investigations.

CONCLUSION

Effects of chemically inert Li^+ and Cs^+ ions on the BL reaction dynamics are investigated by comparing the changes of the oscillograms provoked by the same amount of added lithium and cesium sulfates. Beside, common ion effect resulted in alternating system acidity, one newly effect is found. Observed effect is related with different size of investigated cations. Larger cation Cs^+ has more impact on BL dynamics, than two time smaller Li^+ ion. Since cations are not directly involved in chemical reactions, we proposed that investigated cations influence the reaction mechanism by differently changing the structure of surrounding water and hydrogen bond dynamics.

ACKNOWLEDGEMENT

This work was supported by the Ministry for Science of the Republic of Serbia (Grants no. 172015).

REFERENCES

- [1] W.C. Bray, J. Am. Chem. Soc. 1921, 43, 1262-1267.
- [2] S. Furrow, J. Phys. Chem. 1987, 91, 2129-2135.
- [3] D. Stanisavljev, N. Begović, Z. Žujović, D. Vučelić, G. Bačić, J. Phys. Chem. 1998, 102, 6883-6886.
- [4] Y. Marcus, Chem. Rev. 2009, 109, 1346-1370.
- [5] J. O. Bockris, et al. Modern Electrochemistry. Plenum Press, New Yourk, 1970.

MERGING AND ANNIHILATION OF SADDLE LOOP, SUPERCRITICAL AND SUBCRITICAL ANDRONOV- HOPF BIFURCATIONS

B. Stanković¹, Ž. Čupić², S. Mačešić¹, N. Pejić³ and Lj. Kolar-Anić^{1,2}

¹*Faculty of Physical Chemistry, University of Belgrade, Belgrade, Serbia*

²*Institute of Chemistry, Technology and Metallurgy, University of Belgrade,
Department of Catalysis and Chemical Engineering, Belgrade, Serbia*

³*Faculty of Pharmacy, University of Belgrade, Serbia*

ABSTRACT

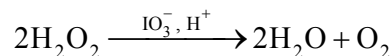
By numerical examinations of dynamic states that can be simulated by the model of the Bray-Liebhafsky (BL) oscillatory reaction and well-known bifurcations that appear at the borders between the stable and unstable steady states, we have found interesting merging of saddle loop, supercritical and subcritical Andronov-Hopf bifurcations resulting in their annihilation. As the BL reaction is described by the model having six variables, relatively simple bifurcations produce complex scenario of their merging and many problems related with their detection.

INTRODUCTION

Bifurcations between stable and unstable steady states, where oscillatory evolution emerges in function of a control parameter, were systematically analyzed by Andronov [1] in two variable systems. Nevertheless, in general, the nonlinear reaction systems in chemistry, physical chemistry and biochemistry are multi-variable ones and their dynamic states are functions of all of these variables. In such complex systems the determination of bifurcations is not easy.

In the case of simple reaction systems Maselko and other authors [2-5] explained how bifurcations can be distinguished experimentally and numerically. For this purpose, it is useful to observe both the amplitudes and the time period of the periodic orbits emerging in bifurcation points, as well as the presence or the absence of hysteresis.

The numerical analysis of bifurcations is performed here on the six-dimensional model of the Bray-Liebhafsky (BL) oscillatory reaction system in open reactor (continuously stirred tank reactor - CSTR) [6]. As the control parameters are taken specific flow rate, j_0 , and initial concentration of hydrogen peroxide, $[\text{H}_2\text{O}_2]_{\text{in}}$. The BL oscillatory reaction, that is, the hydrogen peroxide decomposition in the presence of iodate and hydrogen ions:



is a very complex process where the numerous intermediate species such as I_2 , I^- , HIO , HIO_2 and I_2O take place:

NUMERICAL INVESTIGATIONS

We were using MATLAB program package for numerical simulation of the time series obtained by the model of the BL oscillatory reaction (Table 1) under isothermal CSTR conditions ($T = 60.0\text{ }^\circ\text{C}$). System of the ordinary differential equations was integrated using the ode15s algorithm with variable step. In all simulations relative and absolute error tolerance values were 3×10^{-14} and 1×10^{-20} , respectively. Both, initial iodate and hydrogen ions concentrations were $4.74 \times 10^{-2}\text{ M}$ and $9.58 \times 10^{-2}\text{ M}$ respectively. Initial concentrations of intermediate species were $[\text{I}_2]_0 = 1 \times 10^{-5}\text{ M}$, $[\text{I}^-]_0 = 1.7 \times 10^{-8}\text{ M}$, $[\text{IOH}]_0 = 9.2 \times 10^{-8}\text{ M}$, $[\text{IO}_2\text{H}]_0 = 3.2 \times 10^{-7}\text{ M}$ and $[\text{I}_2\text{O}]_0 = 5.3 \times 10^{-10}\text{ M}$, whereas initial hydrogen peroxide concentrations, which are set to be equal to inflow hydrogen peroxide concentration, varied from 0.0300 M to 0.0370 M . An attempt to perform bifurcation analysis using MATCONT [7], program which utilize methods of numerical continuation, was inefficient in detection of the bifurcations due to system complexity.

RESULTS AND DISCUSSION

Specific flow rate for several inflow hydrogen peroxide concentrations in the range $0.0069\text{ M} \leq [\text{H}_2\text{O}_2]_{\text{in}} \leq 0.0175\text{ M}$ was varied systematically. As the result of that, Andronov-Hopf (both supercritical and subcritical) and saddle loop bifurcations were found (Figure 1). We have also found that, for low inflow hydrogen peroxide concentration (in the range $0.0069\text{ M} \leq [\text{H}_2\text{O}_2]_{\text{in}} \leq 0.0075\text{ M}$), three transformations of interest occur simultaneously. One is the transformation of supercritical to subcritical Andronov-Hopf bifurcation, during which several complex mixtures of these two bifurcations were obtained, second is the complex transformation of supercritical Andronov-Hopf bifurcation to saddle-loop one, while the third transformation is the merging of these two complex bifurcations obtained on different sides of oscillatory region into the one before their annihilation (Figure 2.).

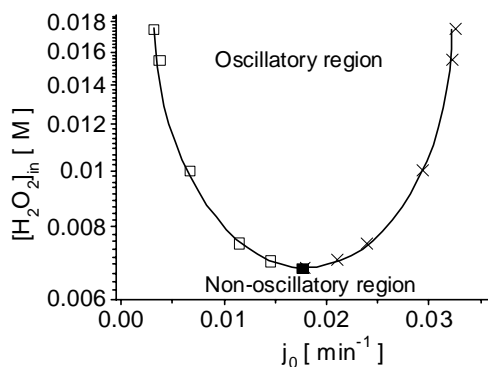


Figure 1. Dynamic states of the BL reaction as function of the control parameters j_0 and $[H_2O_2]_{in}$. The open (\square) and solid (\blacksquare) squares indicate supercritical and subcritical Andronov-Hopf bifurcation points, respectively. Crosses (\times) denote saddle loop bifurcation point.

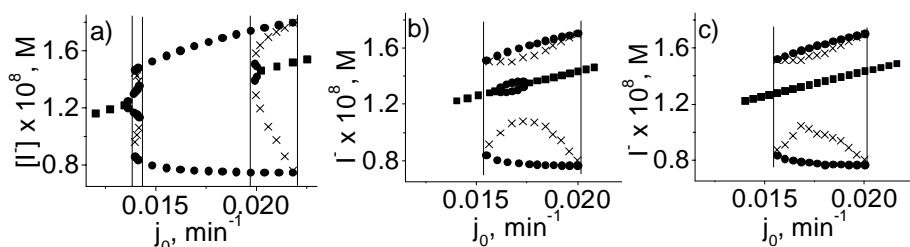


Figure 2. Evolution of the bifurcations with respect to initial concentration of hydrogen peroxide (a) 0.0071, b) 0.00691 and c) 0.0069M).

By full squares (\blacksquare) and full circles (\bullet), the stable steady states and the envelopes of oscillations obtained at given j_0 (the stable limit cycle) are denoted, respectively, whereas the crosses (\times) represent the position of unstable limit cycles.

To prove that the stable steady state transforms to unstable one through supercritical Andronov-Hopf bifurcation, we have analysed the dependence between the square of amplitudes and j_0 as the control parameter [1, 3]. We determined the subcritical Andronov-Hopf bifurcation as one in which large-amplitude oscillations do not change amplitude and period significantly in a vicinity of bifurcation point as one vary flow rate, whereas, saddle loop bifurcations is determined by the fact that the periods of oscillations is linearly proportional to the logarithm of bifurcation parameter displacement. [5] In all cases the hysteresis was examined by changing the initial iodine concentrations.

Here, it is found that with decreasing of hydrogen peroxide concentration in inflow, the bifurcation diagrams obtained in respect to flow rate at selected $[\text{H}_2\text{O}_2]_{\text{in}}$, have changed their shapes.

With decreasing of $[\text{H}_2\text{O}_2]_{\text{in}}$, (Figs. 2b)), the supercritical Andronov-Hopf bifurcation totally enter into the subcritical one, such that with decreasing control parameter j_0 , the large limit cycle suddenly changed to stable steady state as it is the case of the simple subcritical Andronov-Hopf. Inside the subcritical Andronov-Hopf, the supercritical Andronov-Hopf is present too and it can be found with increasing j_0 . However, the strong influence of right bifurcation where with decreasing of $[\text{H}_2\text{O}_2]_{\text{in}}$, the supercritical Andronov-Hopf bifurcation totally enter into the saddle-loop one, is obvious. Branches of two supercritical Andronov-Hopf bifurcations become connected and as a result an isola is formed.

In Fig 2c it can be seen that with further decreasing of $[\text{H}_2\text{O}_2]_{\text{in}}$ isola diminishes and finally vanish. The merged subcritical Andronov-Hopf and saddle-loop bifurcations gives the interesting dynamic outline where the unique hysteresis is found. The oscillatory region disappears when these deformed (untypical) subcritical Andronov-Hopf and saddle loop bifurcations collide and annihilate each other. This is the end of oscillatory domain in the considered parameter plane.

ACKNOWLEDGEMENT

This investigation was supported by the Ministry of Education and Science of Republic of Serbia, under the projects No. 172015 and 45001.

REFERENCES

- [1] Andronov A. A., Vitt A. A., Khaikin S.E., Theory of Oscillations. Pergamon, New York, 1966.
- [2] Maselko J. J., *Chem. Phys.*, 1982, 67, 17-26.
- [3] Hopf E, Ber. Math.-Phys. Klasse Sachs. Akad. Wiss. Leipzig 1942, 94, 1-22
- [4] Bar-Eli K., Brøns M., *J. Phys. Chem.* 1990, 94, 7170-7177.
- [5] Gaspard P., *J. Phys. Chem.* 1990, 94:1-3
- [6] Kolar-Anić Lj., Čupić Ž., Schmitz G., Anić S. *Chem. Eng. Sci.*, 2001, 65, 3718-3728.
- [7] Dhooge, A., Govaerts, W., Kuznetsov, Y. A., Mestrom, W., Riet, A. M., & Sautois, B. (2006). MATCONT and CL MATCONT: Continuation toolboxes in matlab. *Universiteit Gent, Belgium and Utrecht University, The Netherlands*

GHOST OF THE LOST FIXED POINT IN A MODEL OF THE BRAY-LIEBHAFSKY REACTION

Ž. Čupić¹, S. N. Blagojević², S. M. Blagojević³, S. Anić² and A. Ivanović-Šašić¹

¹*ICH_{TM}– Department of Catalysis and Chemical Engineering, University of Belgrade, Njegoševa 12,*

²*Institute of General and Physical Chemistry, Studentski trg 12–16,*

³*Faculty of Pharmacy, University of Belgrade, Vojvode Stepe 450,*

ABSTRACT

Dynamic states of numerically simulated Bray–Liebhafsky reaction in a continuously fed well stirred tank reactor were further investigated by the Poincaré 1D maps in the vicinity of the bifurcation where fixed point vanishes. Ghost of the lost fixed point was found and its influence on the long term dynamics is analyzed.

INTRODUCTION

The model of the Bray–Liebhafsky BL reaction [1] under isothermal continuously fed well stirred tank reactor (CSTR) conditions [2] was used to analyze variety of dynamic states. Numerical simulations have shown that various simple and complex periodic as well as various types of chaotic oscillatory states were obtained for different values of the flow rate j_0 as control parameter [3]. Poincaré or 1D maps were used to make a distinction between periodic and aperiodic (chaotic) motion in phase space [4], [5]. Maps with small number of discrete points correspond to periodic dynamic states, while complex patterns with infinite number of points in maps indicate chaotic states, which occur when previously stable periodic orbit loses its stability. The subject of present work is the behavior of the BL system in the vicinity of bifurcation, where periodic orbit loses its stability by the annihilation with unstable periodic orbit.

METHODS

All calculations were performed using MATLAB program package. The differential equations derived from the model were integrated using the ode15s solver. Relative and absolute error tolerance values of 3×10^{-14} and 1×10^{-20} were used in all simulations. Initial values of the concentrations were: $[\text{IO}_3^-]_0 = 0.0474 \text{ mol dm}^{-3}$, $[\text{H}^+]_0 = 0.0958 \text{ mol dm}^{-3}$, and $[\text{H}_2\text{O}_2]_0 = 0.155 \text{ mol dm}^{-3}$. We analyzed time series of iodide ion concentrations,

obtained for different values of the flow rate j_0 as control parameter in the interval of the dynamical states between 2^1 and 1^1 . For typical Poincaré map, time series with 2×10^6 data points at time interval of about 2000 min were appropriate in most cases.

The maps obtained in this way are generated by extensively long movement of the system over the attractor, achieved after long enough transient periods. Although the Poincaré maps of chaotic systems are very useful, Poincaré maps of periodic systems give limited amount of information about the phase space surrounding periodic orbit. Thus, additional insight in system dynamics is needed. For this purpose new form of 1D maps is invented, enabling one to record movement over the manifold and hence named “manifold 1D maps” to be distinct from classical Poincaré maps, which will be assigned here as “attractor 1D maps”.

RESULTS AND DISCUSSION

In Fig. 1, overlapping attractor 1D maps (circles) and manifold 1D maps (crosses) are given for flow rate values $j_0 = 4.861 \times 10^{-3} \text{ min}^{-1}$ (Figure 1a), $4.870 \times 10^{-3} \text{ min}^{-1}$ (Figure 1b), $4.8710 \times 10^{-3} \text{ min}^{-1}$ (Figure 1c) and $4.882310 \times 10^{-3} \text{ min}^{-1}$ (Figure 1d). In corresponding narrow flow rate interval, dynamics is changing between periodic states $2^1 1^1$ (Figure 1a) and 1^1 (Figure 1c) and (Figure 1d), passing through chaotic oscillations of the mixed mode form with long sequences of 1^1 and sporadically occurring 2^1 oscillations. Small number of points (circles in Figure 1 a, c and d) in the attractor 1D map confirms periodicity.

Existence and stability of the periodic orbits in phase space is directly given by the existence and stability of the fixed points in corresponding Poincaré 1D maps. Once we have 1D map, fixed points are easily identified as the cross-points (FPu - unstable and FPs - stable fixed point in Figure 1 c and d) between the map and the main diagonal. Moreover, the stability of the fixed point is uniquely determined by the slope of the tangent on the 1D map in the fixed point. If the slope magnitude is higher than one, fixed point is unstable. However, attractor 1D maps are not so easily constructed if the simple periodic states are obtained. Instead of the 1D maps, only several distinct points are obtained in these cases, without indication of the 1D object embedding the points (note attractor 1D maps - circles in Figures 1 a, c and d). To accomplish insight into the system dynamics, new form of 1D maps “manifold 1D maps” is introduced here.

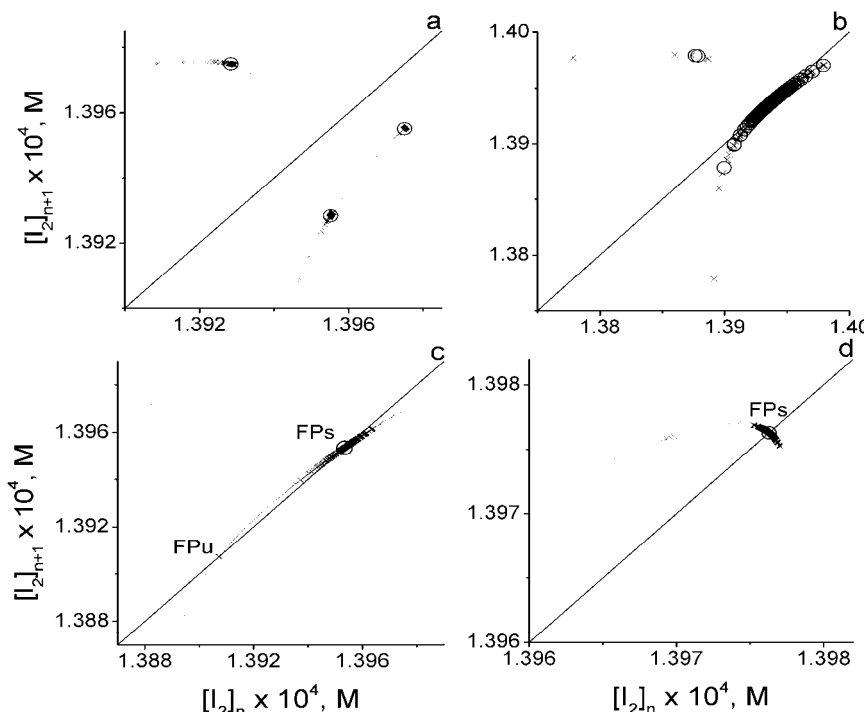


Figure 1. Overlapping attractor 1D maps (circles) and manifold 1D maps (crosses) for the flow rate: (a) $j_0 = 4.861 \times 10^{-3} \text{ min}^{-1}$, (b) $j_0 = 4.870 \times 10^{-3} \text{ min}^{-1}$, (c) $j_0 = 4.8710 \times 10^{-3} \text{ min}^{-1}$ and (d) $j_0 = 4.882310 \times 10^{-3} \text{ min}^{-1}$. Time interval of about 2000 min. FPU - unstable, FPs - stable fixed point.

The new manifold 1D maps are obtained from sequences of short simulations with initial conditions (concentrations) systematically varied in very small steps. In present study, small changes of hydrogen peroxide initial concentrations were used. The initial concentrations of all other species were generated by one, long enough, preliminary simulation, ensuring that attractor is reached by the end, in the same way as in classical attractor 1D maps. Thus, in generated sequences of short numerical simulations, movement over the manifold is recorded. The 1D maps are then generated in the same way as previously described elsewhere [5] for classical Poincaré maps.

From the plot of the manifold 1D map it is obvious that periodic dynamics obtained for the highest value of the flow rate is a consequence of the stability of the only fixed point (FPs in Figure 1d). With decreasing flow rate values, first, new unstable fixed point occurs and then, two fixed points, stable and unstable one, (FPs and FPU in Figure 1c) approach to each other

and finally merge (Figure 1b), before they annihilate (Figure 1a). Annihilation of the fixed points in the map, corresponds to the annihilation of the stable and unstable periodic orbits in the phase space.

Before the merging and annihilation, the time needed to achieve periodic state becomes longer and longer since more and more cycles is needed to reach fixed point. For the critical values of the control parameter 1D map exactly touches the main diagonal. Theoretically, this point could be achieved only in infinite time. However, immediately after the annihilation, system exist in the vicinity of the main diagonal for a very long time, taking very large number of cycles, eventually passing by and then, moving away from the fixed point.

The reason for so long cycling in small part of the phase space is the vicinity of the main diagonal. One say that ghost of the stable fixed point is still present after the annihilation and attracts dynamical system keeping it close to the main diagonal for a very long periods.

CONCLUSION

By means of “manifold 1D maps”, generated here, we found and explain unexpected long term behavior of the BL system in the vicinity of the bifurcation point where one of the fixed points vanishes. Ghost of the fixed point remained to attract trajectories and hold them in nearby phase space for a very long time.

ACKNOWLEDGMENT

The support of this research by the Ministry of Education, Science and Technological Development of Republic of Serbia through projects No.172015 and 45001 is gratefully acknowledges.

REFERENCES

- [1] W. C. Bray, H. A. Liebhafsky, *J. Am. Chem. Soc.*, 1931, 53, 38–44
- [2] Lj. Kolar-Anić, Ž. Čupić, G. Schmitz and S. Anić, *Chem. Eng. Sci.*, 2010, 65, 3718–3728 and references therein.
- [3] A. Ivanovic-Šašić, V. Marković, S. Anić, Lj. Kolar-Anić, Ž. Čupić, *Phys. Chem. Chem. Phys.*, 2011, 13, 20162–20171.
- [4] S. Blagojević, S. Blagojević, Ž. Čupić, 11th International Conference on Fundamental and Applied Aspects of Physical Chemistry PHYSICAL CHEMISTRY 2012, Belgrade, 2012, Proceedings, Vol. 1, 270-272.
- [5] R. C. Hilborn, *Chaos and Nonlinear Dynamics*, 2nd edition, Oxford University Press, 2000.

ELECTROCHEMISTRY

NOVEL ELECTROCATALYTIC MATERIALS FOR DIRECT BOROHYDRIDE FUEL CELLS

D.M.F. Santos, B. Šljukić, and C.A.C. Sequeira

*Institute of Materials and Surfaces Science and Engineering, Instituto Superior Técnico, Universidade de Lisboa, 1049-001 Lisboa, PORTUGAL.
(diogosantos@tecnico.ulisboa.pt)*

ABSTRACT

Direct borohydride fuel cells (DBFCs) are electrochemical devices that convert the chemical energy contained in sodium borohydride (NaBH_4) directly into electric energy. An alkaline solution of NaBH_4 is generally used as the fuel for the DBFC, whereas oxygen (O_2) or hydrogen peroxide (H_2O_2) are used as the oxidant. Most of the research on the DBFC is focused on the development of inexpensive electrocatalysts that are able to efficiently catalyse the fuel cell reactions. The present paper briefly reviews the main studies that the Lisbon electrochemistry group has carried out in the last few years in the development of new electrocatalytic materials for NaBH_4 oxidation and for $\text{O}_2/\text{H}_2\text{O}_2$ reduction. These contributions have substantially increased the interest of the fuel cells scientific community in the DBFC, pushing the DBFC to the initial steps of commercialisation stage.

MOTIVATION

Fuel cells (FCs) are electrochemical devices that convert chemical energy into electricity. The electron flow is generated from spontaneous redox reactions occurring at the electrodes. As long as fuel and oxidant are supplied to the FC compartments, the device can operate in continuous mode. Typical FCs use hydrogen (H_2) as the fuel and oxygen (O_2) as the oxidant. However, safety issues and the high costs involved in gas storage in pressurised containers have led some researchers to drive their focus to room-temperature liquid-feed FCs.

It was almost a decade ago when our Lisbon electrochemistry group started its pioneering work in the research and development of the direct borohydride fuel cell (DBFC). It uses a sodium borohydride (NaBH_4) aqueous solution as the fuel and oxygen (O_2) or hydrogen peroxide (H_2O_2) as the oxidant. When H_2O_2 is used as the oxidant, the reactants storage, thermal management and internal processing is simplified. Additionally, it makes the DBFC a promising solution for space, underwater, and specific terrestrial applications where O_2 is not available [1].

Our initial studies intended to learn about the fundamentals of the anodic oxidation of NaBH_4 [2-4]. Later, to decrease the current cost of the NaBH_4 fuel, our group investigated its electrosynthesis [5], which required the development

of analytical methods for the NaBH_4 determination [6,7]. Next step involved the optimisation of the DBFC operation, by tuning the fuel, oxidant, and membrane compositions [8-10]. For the last few years, our group has prepared, characterised, and studied new materials for the anode [11-16] and for the cathode [17-20], looking for high electrocatalytic activity at lower prices.

These contributions have increased the interest in the DBFC, as it is well expressed by the large increase in the number of publications observed in the last decade.

Figure 1 shows the number of papers concerning the DBFC until 2010. These advances are expected to push the DBFC to the initial steps of commercialisation stage. The advantages of high energy density and room temperature operation suggest future use of the DBFC for portable applications (e.g., cell phones, laptops).

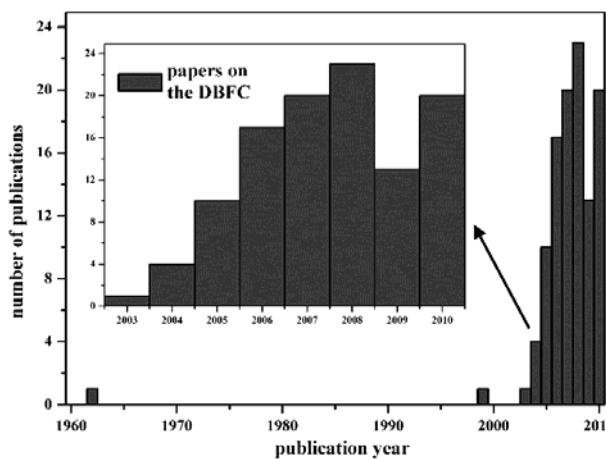


Figure 1. Evolution of the number of publications concerning the DBFC until 2010 [1].

ELECTROCATALYSTS FOR BH_4^- OXIDATION

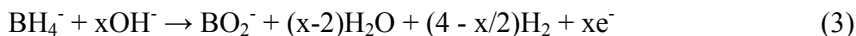
NaBH_4 is a solid white powder that was traditionally used as a specialty reducing agent in the manufacture of pharmaceuticals and as a bleaching agent in the manufacture of paper. But for the last decade it gained increasing importance as hydrogen/energy carrier. It is considered as hydrogen (H_2) carrier when it is used to generate H_2 by taking advantage of its hydrolysis reaction (Eq. 1).



NaBH_4 can also be used as an energy carrier, by directly powering a DBFC as a liquid fuel (dissolved in NaOH aqueous solution). In that case, the BH_4^- anodic oxidation is given by Eq. 2.



However, most electrode materials are simultaneously catalytic for the BH_4^- hydrolysis and for its oxidation reaction. That means that, in practice, the reaction defining BH_4^- oxidation will be that given by Eq. 3,

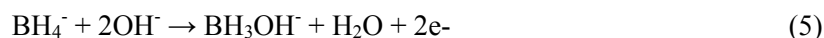
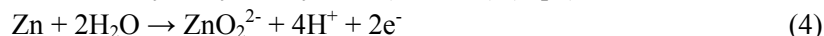


with x being the actual number of exchanged electrons, known as the coulombic number.

In order to better understand the mechanism and fundamentals of the BH_4^- oxidation reaction (BOR) in alkaline media, in our initial studies we used cyclic voltammetry (CV) [2], chronopotentiometry (CP) [3], chronoamperometry (CA) and chronocoulometry (CC) [4] using a solid gold (Au) disc electrode. Au was selected because it is considered to have a coulombic number close to 8, therefore allowing the calculation of kinetic and diffusional parameters without the influence of the parasitic BH_4^- hydrolysis reaction.

Although Au is of interest for fundamental studies, its price makes it prohibitive for practical applications. Moreover, BOR kinetics in Au are relatively slow when compared to that in platinum (Pt) electrodes, although the latter is also catalytic for BH_4^- hydrolysis. In that sense, our group has looked for low-cost materials that are simultaneously catalytic for BOR and inactive for the BH_4^- hydrolysis.

A zinc (Zn) anode was tested for BOR using CV, CA, and CP measurements [11]. CV results indicated a number of exchanged electrons of 4. A possible mechanism involves initial oxidation of Zn (Eq. 4) followed by partial oxidation of BH_4^- to hydroxyborohydride (BH_3OH^-) (Eq. 5).



To enhance the kinetics of BOR, our group engaged in studying several Pt alloys. Carbon-supported $\text{Pt}_{0.75}\text{M}_{0.25}$ (with $\text{M} = \text{Ni}$ or Co) electrocatalysts were studied for BOR using CV and linear scan voltammetry with rotating disc electrode (LSV RDE) [13]. Main kinetic parameters (charge transfer coefficients, number of electrons exchanged, standard heterogeneous rate constants and activation energies) for BH_4^- oxidation were determined. $\text{Pt}_{0.75}\text{Ni}_{0.25}/\text{C}$ electrocatalyst was found to be more active for BOR than $\text{Pt}_{0.75}\text{Co}_{0.25}/\text{C}$, with both of them showing superior activity than Pt/C.

On the basis of improved three-dimensional hydric factors of

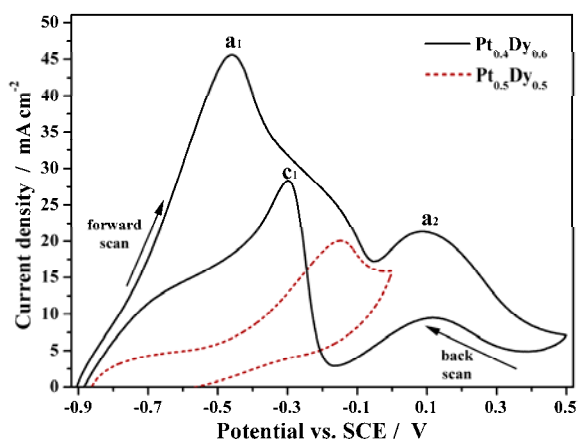


Figure 2. CVs of PtDy alloy electrodes in 0.03 M NaBH_4 + 2 M NaOH solution at a scan rate of 0.1 V s^{-1} and temperature of 25°C .

composite electrocatalysts, it is believed that Pt alloyed with rare earth (RE) materials can lead to increased catalytic activity. Therefore, several Pt-RE alloys, with RE being cerium (Ce), holmium (Ho), samarium (Sm) and dysprosium (Dy) were tested for BOR [12,15]. An average value of 2 exchanged electrons was found for these electrodes. Figure 2 shows CVs obtained for PtDy intermetallic alloys with different compositions, with Pt_{0.4}Dy_{0.6} showing superior activity.

Considering the beneficial addition of the RE elements, we have replaced Pt noble metal by inexpensive nickel (Ni) in the alloy electrodes. Ni-RE alloys, with RE being Ce, Sm, and Dy were then synthesised and successfully tested for the BOR [14,16]. The Ni-RE alloys showed good activity and low overpotentials for BOR, at relatively low electrode cost.

ELECTROCATALYSTS FOR O₂ / H₂O₂ REDUCTION

The oxygen reduction reaction (ORR) proceeds either by 4-electron or by 2-electron mechanism, with former being the desirable mechanism in fuel cells. 4-electron direct reduction of O₂ to hydroxyl ion (OH⁻) is represented by Eq. 6.



while 2-electron mechanism includes two successive 2-electron processes with hydroperoxide ion (HO₂⁻) as intermediate. This mechanism involves 2-electron reduction of O₂ to HO₂⁻ (Eq. 7), with HO₂⁻ intermediate species undergoing subsequent 2-electron reduction to OH⁻ (Eq. 8).



Pt represents the most commonly used electrocatalyst in fuel cells due to its high activity and stability, though having disadvantage of high cost and limited supplies. Manganese dioxide (MnO₂) has been pointed out as a potential alternative cathodic material due to its abundance, low cost and high electrocatalytic activity [18,21]. Namely, activity of MnO₂-based electrocatalysts for the ORR in alkaline medium was found to be lower than that of Pt, Au and Ag in pure NaOH solution, but activity of MnO₂-based electrocatalyst changed only slightly in the presence of traces of BH₄⁻ while that of Pt, Au and Ag decreased [21]. Electrocatalysts of MnO₂ supported on activated carbon (AC) were prepared by low-temperature (ltMnO₂/AC) and high-temperature (htMnO₂/AC) procedures [18]. Kinetic study of the ORR at two electrocatalysts revealed that 2 electrons were exchanged at the ltMnO₂/AC and 4 at the htMnO₂/AC, with significantly higher current densities observed for the htMnO₂/AC. Furthermore, Tafel slopes were found to be quite different for the two electrocatalysts, i.e., 140 and 64 mVdec⁻¹ for ltMnO₂/AC and htMnO₂/AC, respectively. The obtained values indicated small contribution of the activated carbon in electrocatalysis of the ORR as Tafel slope for the

ORR at pure carbon is close to 30 mV dec^{-1} [18]. Apparent activation energy was evaluated to be 44.2 kJmol^{-1} , which is in good agreement with that reported for the ORR on carbon-supported MnO_x electrocatalysts in strong alkaline media [18]. The observed differences in the ORR mechanism and current densities could be due to the presence of different manganese oxide phases in the two prepared electrocatalysts, i.e., due to the crystalline structure and surface concentration of Mn^{3+} ions.

The two electrocatalysts tolerance to presence of BH_4^- was also investigated. In the presence of NaBH_4 in the alkaline supporting electrolyte, the activity of ltMnO_2/AC for the ORR was significantly suppressed, while that of htMnO_2/AC remained high. Yet, evaluated number of transferred electrons for htMnO_2/AC was somewhat lower ranging from 2.6 to 3.8. The electrocatalyst high BH_4^- tolerance was further supported by only slight change in the ORR onset potential value upon addition of BH_4^- to the supporting electrolyte. The onset potential was found to shift for only 0.15 V, while onset potential at carbon-supported Pt electrode shifted for 1 V upon the addition of BH_4^- [17]. htMnO_2/AC high electrocatalytic activity for the ORR in alkaline media, as well as its good BH_4^- tolerance, strongly suggests potential application of this electrocatalyst as cathode material in DBFCs.

The H_2O_2 electroreduction in acidic media proceeds *via* two parallel pathways: direct (Eq. 9) and indirect one (Eq. 10 followed by Eq. 11) [17].



Furthermore, direct H_2O_2 reduction reaction is known to proceed *via* two parallel mechanisms in acidic media [17]. The first, “normal” mechanism, which commonly occurs at more negative potentials, consists of two consecutive steps, as described by Eq. 12 and Eq. 13.



For higher overpotentials (more negative) this reaction path proceeds at higher current densities. At lower overpotentials, the reaction mechanism involves adsorbed hydroxyl groups, OH_{ads} , as catalytic species (Eq. 14).



Additional production of OH_{ads} through this reaction (Eq. 14) makes the mechanism autocatalytic. Increase of current densities with decrease of overpotential is characteristic for this reaction path.

The direct pathway is preferable because of lower activation barrier and therefore faster kinetics of the H_2O_2 reduction as a 2-electron process than the 4-electron O_2 reduction. Also, the standard electrode potential for the direct reduction of H_2O_2 is higher than that for O_2 reduction (1.77 V against 1.23 V

vs. SHE), so the direct H_2O_2 reduction yields larger DBFC cell voltages. Conversely, the indirect pathway implicates gas management making cell system more complex. Therefore, cathode materials selectively catalysing H_2O_2 electroreduction *via* direct pathway are required.

The study of carbon-supported Pt-alloys ($\text{Pt}_{0.75}\text{M}_{0.25}/\text{C}$, with $\text{M} = \text{Ni}$ or Co) as electrocatalysts for H_2O_2 reduction in a 0.03 M H_2O_2 + 0.1 M HClO_4 solution revealed comparable activity with that of Pt/C electrocatalyst, with $\text{Pt}_{0.75}\text{Co}_{0.25}/\text{C}$ exhibiting the best performance [17]. The number of electrons transferred at the Pt/C electrode was found to be close to 1, whereas at the $\text{Pt}_{0.75}\text{Ni}_{0.25}/\text{C}$ and $\text{Pt}_{0.75}\text{Co}_{0.25}/\text{C}$ electrodes the number of transferred electrons was close to 2 and 1.7, respectively, in accordance with the proposed 2-electron mechanism for H_2O_2 reduction at metal surfaces in acidic media. H_2O_2 reduction reaction at the three investigated electrocatalysts proceeds by both “normal” as well as the autocatalytic mechanism. Namely, autocatalytic mechanism was observed to be the main one at $\text{Pt}_{0.75}\text{Ni}_{0.25}/\text{C}$, while “normal” H_2O_2 reduction was predominant process at $\text{Pt}_{0.75}\text{Co}_{0.25}/\text{C}$ and of Pt/C.

Our latest research focus the development of cathode materials for H_2O_2 reduction in alkaline media, which may be represented by Eq. 8 or Eq. 15.



The studied materials include pure ceramic specimens, i.e., perovskite oxides, as opposed to the usual carbon-supported electrocatalysts, thus avoiding cross-contributions of the support materials [19,20]. The first study performed on button type electrodes of LaCoO_3 (LC), $\text{La}_{0.84}\text{Sr}_{0.16}\text{CoO}_3$ (LSC), $\text{La}_{0.8}\text{Sr}_{0.2}\text{Fe}_{0.8}\text{Co}_{0.2}\text{O}_3$ (LSCF), and $\text{La}_{0.7}\text{Sr}_{0.3}\text{MnO}_3$ (LSM) revealed the highest activity for H_2O_2 reduction in alkaline solution of LSM, while other three materials showed minimal (LC) or none (LSC, LSCF) electroactivity [19]. Number of 0.8 electrons involved in H_2O_2 reduction at LSM at 25 °C was evaluated from chronopotentiometric measurements. Latest study involved La_2NiO_4 ceramic discs, but it indicated vague activity of the studied perovskite for H_2O_2 reduction in alkaline media, requiring further clarification prior to its potential use as cathode in DBFCs [20].

DIRECT BOROHYDRIDE FUEL CELLS

Membrane separator presents another key component of the DBFC, also affecting its efficiency. The membrane is particularly important when H_2O_2 solution is used as the oxidant, as the two liquid reactants need to be efficiently separated. These fuel cells are usually known as direct borohydride/peroxide fuel cells (DBPFCs) and are described by Eq. 16 (the sum of Eq. 2 and Eq. 9).



Within our work, several different commercially available membrane separators were tested in a laboratory DBPFC with Pt cathode and Pt anode,

and evaluated cell parameters are summarised in Table 1. The highest peak power density of 96 mW cm^{-2} was reached employing Nafion N117 membrane at a potential of 0.60 V and current density of 160 mA cm^{-2} [9]. However, these values were observed to decrease during long-term cell operation. Conversely, cation- and anion-exchange membrane, CMI-7000S and AEM-7001, showed higher stability and durability [10]. Furthermore, the highest energy density of 171 Whkg^{-1} and specific capacity of 448 Ahkg^{-1} were obtained for DBPFCs using CMI-7000S membrane, confirming better performance of this separator.

Table 1. Electrochemical parameters of the DBPFCs employing the studied membrane separators [9,10].

	Open-circuit voltage /V	Short circuit current density / (mAcm^{-2})	Peak power density / (mWcm^{-2})	Cell voltage at peak power density /V	Current density at peak power density / (mAcm^{-2})	Specific capacity / (Ahg^{-1})	Energy density / (Whkg^{-1})
AMI-7001S	1.79	188	49	0.60	82	423	129
CMI-7000S	1.75	230	56	0.55	101	448	171
Nafion N117	1.84	348	96	0.60	160	76	45
Nafion 115CS	1.86	321	87	0.60	145	69	41
Nafion NRE-212	1.81	259	79	0.60	132	66	39
IONAC MC-3470	1.77	291	86	0.60	144	37	22
IONAC MA-3475	1.76	251	67	0.60	112	31	19

Operational parameters influencing the DBFC performance include the anolyte and catholyte composition, as well as operating temperature. Experimental results showed that the best lab DBPFC performance, employing two Pt electrodes and a Nafion N117 membrane, was obtained with anolyte containing $1.0 \text{ M NaBH}_4 + 4.0 \text{ M NaOH}$ and a catholyte containing $5.0 \text{ M H}_2\text{O}_2 + 1.5 \text{ M HCl}$ [8]. Generally, increase of the cell peak power density was observed with increase of the temperature from 25 to 65°C [8,11,14,15,19]. Table 2 summarises cell parameters obtained employing different studied anode and cathode materials with the mentioned fuel and oxidant compositions at 25°C . It could be noticed that DBPFC employing materials studied in our group often outperform the cell employing benchmark Pt electrodes.

Table 2. Electrochemical parameters of the DBPFCs employing the studied cathode and anode materials [8,11,14,15,19].

Cathode	Anode	Open circuit voltage /V	Peak power density / (mWcm^{-2})	Cell voltage at peak power density /V	Current density at peak power density / (mAcm^{-2})	Short circuit current density / (mAcm^{-2})
Pt	Pt	1.74	98	0.50	196	394
Pt	$\text{Pt}_{0.5}\text{Dy}_{0.5}$	1.73	186	0.44	423	/
Pt	$\text{Pt}_{0.4}\text{Dy}_{0.6}$	1.73	298	0.50	595	/
Pt	Zn	2.14	470	1.10	426	1050
Pt	$\text{Ni}_{0.95}\text{Ce}_{0.05}$	1.95	58	0.45	129	/
Prussian Blue @ Pt	Pt	1.79	116	0.70	165	/
LSM	Pt	1.00	8.2	0.30	28	52

ACKNOWLEDGEMENT

Thanks to Foundation for Science and Technology(FCT,Portugal) for postdoctoral research grants SFRH/BPD/91853/2012 (D.M.F. Santos) and SFRH/BPD/77768/2011 (B. Šljukić).Part of the work was done in collaboration with the University of Belgrade-Faculty of Physical Chemistry (projects OI172043 and III45014, funded by the Ministry of Education, Science and Technological Development).

REFERENCES

- [1] D.M.F. Santos, C.A.C. Sequeira, *Renew. Sustain. Energy Rev.*, 2011,15, 3980-4001.
- [2] D.M.F. Santos, C.A.C. Sequeira, *Electrochim. Acta*, 2010, 55, 6775-6781.
- [3] D.M.F. Santos, C.A.C. Sequeira, *J. Electrochem. Soc.*, 2010,157, F16-F21.
- [4] D.M.F. Santos, C.A.C. Sequeira, *J. Electrochem. Soc.*,2009,156, F67-F74.
- [5] D.M.F. Santos,C.A.C. Sequeira, *Int. J. Hydrogen Energy*,2010, 35, 9851-9861.
- [6] D.M.F. Santos, C.A.C. Sequeira, *J. Electroanal. Chem.*,2009, 627, 1-8.
- [7] B. Šljukić, D.M.F. Santos, C.A.C. Sequeira, C.E. Banks, *Anal. Methods*,2013, 5, 829-839.
- [8] D.M.F. Santos, P.G. Saturnino, R.F.M. Lobo, C.A.C. Sequeira, *J. Power Sources*,2012, 208, 131-137.
- [9] D.M.F. Santos, C.A.C. Sequeira, *J. Electrochem. Soc.*,2012,159, B126-B132.
- [10]B. Šljukić, A.L. Morais, D.M.F. Santos, C.A.C. Sequeira, *Membranes*,2012, 2, 478-492.
- [11] D.M.F. Santos,C.A.C.Sequeira, *J. Electrochem. Soc.*,2010,157,B13-B19.
- [12] D.M.F. Santos, P.G. Saturnino, D. Macciò, A. Saccone, C.A.C. Sequeira, *Catal. Today*,2011, 170, 134-140.
- [13] B. Šljukić, J. Milikić, D.M.F. Santos, C.A.C. Sequeira, *Electrochim. Acta*,2013, 107, 577-583.
- [14] D.M.F. Santos, B. Šljukić, L. Amaral, D. Macciò, A. Saccone, C.A.C. Sequeira, *J. Electrochem. Soc.*,2014, 161, F594-F599.
- [15] B. Šljukić, J. Milikić, D.M.F. Santos, C.A.C. Sequeira, D. Macciò, A. Saccone, *J. Power Sources* (*submitted*).
- [16] D.M.F. Santos, B. Šljukić, L. Amaral, C.A.C. Sequeira, D. Macciò, and A. Saccone, *ECS Transactions* (*accepted*).
- [17] A.L. Morais, J.R.C. Salgado, B. Šljukić, D.M.F. Santos, C.A.C. Sequeira, *Int. J. Hydrogen Energy*,2012, 37, 14143-14151.
- [18] B. Šljukić, D.M.F. Santos, C.A.C. Sequeira, *J. Electroanal. Chem.*,2013, 694, 77-83.
- [19] D.M.F. Santos, T.F.B. Gomes, B. Šljukić, N. Sousa, C.A.C. Sequeira, F.M.L. Figueiredo, *J. Power Sources* (*submitted*).
- [20] D.M.F. Santos, N. Sousa, B. Šljukić, C.A.C. Sequeira, F.M.L. Figueiredo, *ECS Transactions* (*accepted*).
- [21] M. Chatenet, F. Micoud, I. Rouche, E. Chainet, J. Vondrak, *Electrochim. Acta* 2006, 51, 5452-5459.

ELECTROCHEMICAL OXIDATION OF FORMIC ACID ON Pt- AND Pd-BASED BIMETALLIC CATALYSTS

M. D. Obradović¹, S. Lj. Gojković²

¹ *Institute of Chemistry, Technology and Metallurgy, University of Belgrade, Njegoševa 12, Belgrade, Serbia. (obradovic@ihm.bg.ac.rs)*

² *Faculty of Technology and Metallurgy, University of Belgrade, Karnegijeva 4, Belgrade, Serbia.*

ABSTRACT

Electrochemical oxidation of HCOOH was studied on single metal Pt, Pt/C and Pd black catalysts, on bimetallic surfaces of Pt-Au and Pd-Au bulk electrodes as well as on Pt-Co/C, Pt-Au/C and Pt-Pd nanocatalysts. The electrocatalysts were characterized by cyclic voltammetry and CO_{ads} stripping, while the HCOOH oxidation was examined under the potentiodynamic and potentiostatic conditions. The results indicate that the ensemble effect is crucial for high selectivity of Pt-based surfaces toward dehydrogenation path. The enhancement of HCOOH oxidation rate on Pd-based surfaces was reached through electronic modification exhibited by the second metal. Our results also point out that the self-poisoning of the electrocatalyst by CO_{ads} produced by the incomplete CO₂ reduction is related to the strength of the Pt- and Pd-adsorbate bond, which has to be considered in designing of an electrocatalyst for HCOOH oxidation.

INTRODUCTION

Polymer electrolyte membrane fuel cell (PEMFC) using formic acid as a fuel, i.e. direct formic acid fuel cell (DFAFC) is a viable power generator for portable electronic devices [1]. Its advantages over direct methanol fuel cell (DMFC) are higher theoretical open circuit voltage, lower crossover of HCOOH through the polymer membrane compared to CH₃OH and non-toxicity of HCOOH. A problem that still needs to be resolved is the activity and stability of the anode electrocatalyst.

It is generally accepted that on Pt surface HCOOH oxidizes to CO₂ via a dual path mechanism [2,3,4]. Direct path is dehydrogenation of HCOOH molecule without forming of CO_{ads}. Indirect path comprises dehydration of HCOOH molecule with the formation of CO_{ads} and its further oxidation to CO₂. In order to prevent poisoning of the catalyst by CO_{ads}, the dehydrogenation path has to be predominant. This can be achieved by combining Pt with some other metal performing its role through (i) bifunctional mecha-

nism, (ii) electronic effect, or (iii) ensemble effect [5]. Bifunctional mechanism is operative when the second metal is capable to adsorb oxygen-containing species at lower potentials than Pt, thus facilitating the oxidation of CO_{ads} formed on Pt sites. Electronic effect refers to the modification of the electronic structure of Pt atoms, generally resulting in change of the adsorption ability of Pt. If this modification weakens the bond between Pt and CO_{ads} , the electronic effect reduces Pt poisoning. The ensemble effect is based on the fact that the dehydration path requires at least three contiguous Pt atoms, whereas the dehydrogenation path requires at most two Pt atoms [6]. Therefore, when large Pt surface is interrupted by foreign atoms, dehydrogenation path is favored and CO_{ads} formation is suppressed.

Contrary to Pt, investigation of HCOOH oxidation on Pd indicated that the reaction on this metal proceeds exclusively through the dehydrogenation reaction path, since no poisoning CO_{ads} could be detected under the potentiodynamic conditions [7]. Despite this, slow deterioration of the activity of Pd anode during the DFAFC operation was reported [8].

SINGLE METAL Pt AND Pd ELECTROCATALYSTS

Polarization curves of HCOOH oxidation on polycrystalline Pt [9] and Pt/C nanocatalyst [10,11] show well-established feature of this reaction. At low potentials HCOOH oxidizes through the direct path with the simultaneous formation of CO_{ads} in the indirect path [2]. Increasing coverage of CO_{ads} reduces the number of Pt sites available for the direct path, and the current density reaches a plateau. Subsequent formation of oxygen containing species on Pt enables the oxidative removal of CO_{ads} . As more Pt sites are being released, the HCOOH oxidation current increases until Pt-oxide, inactive for HCOOH oxidation, is formed. This results in the current peak. In the backward sweep the sharp raise of HCOOH oxidation current coincides with reduction of Pt oxide. The currents are much higher than in the forward sweep, because Pt surface is freed of CO_{ads} .

Potentiodynamic polarization curves of HCOOH oxidation on Pd black [12,13] showed no significant hysteresis between the anodic and the cathodic direction, thus indicating low poisoning by CO_{ads} . This is in accord with the literature data [7] about the predominance of the dehydrogenation path.

Based on the above mentioned bifunctional, electronic and ensemble effect, various types of bimetallic Pt-Au, Pt-Co, Pd-Au and Pt-Pd catalysts were prepared and investigated [9-13] in order to enhance the activity of Pt and Pd catalysts for HCOOH oxidation.

Pt-Au ELECTROCATALYST

Polycrystalline Pt and Au electrodes were electrochemically modified by sub-monolayers of Au and Pt, respectively [9]. These surfaces served as the model catalysts to establish the role of the ensemble and the electronic effect in the HCOOH oxidation, since Au cannot provide oxygen containing species necessary for the bifunctional effect. It was assumed that electronic modification of Pt by Au atoms will be favoured on Au electrode modified by Pt, because all the Pt atoms are in contact with Au substrate, while on Pt electrode modified by Au only the Pt atoms contacting the circumference of Au islands can be altered by the presence of Au. On both types of the Pt-Au surfaces the surface fraction of Pt was varied between 0.14 and 0.86.

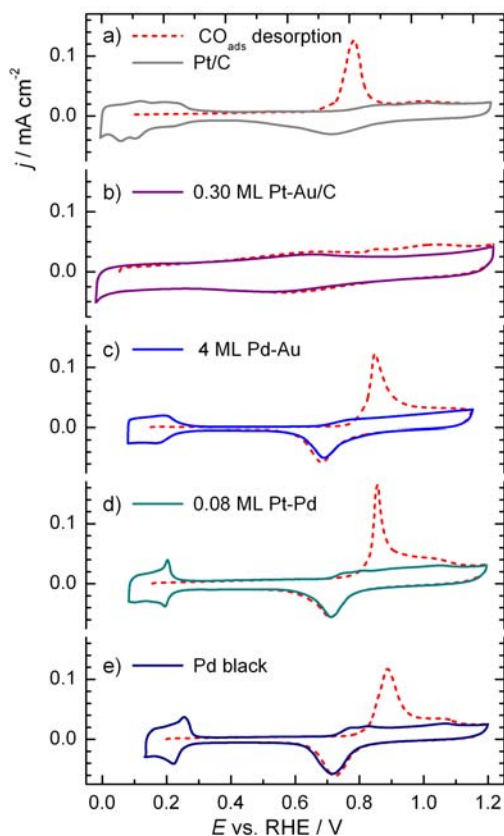


Fig 1. Stripping voltammograms of CO_{ads} and the first subsequent cyclic voltammograms recorded in 0.1 M H_2SO_4 ; $\nu = 20 \text{ mV s}^{-1}$.

on pure Pt was found, which imply that Au substrate exhibits an electronic influence on Pt atoms deposited on it. The same behaviour was also

In addition to the model catalysts, Pt-Au/C nanoparticles were prepared by simultaneous reduction of Au and Pt precursors in the presence of high area carbon and by reduction of Pt precursor on already prepared Au/C nanoparticles [10]. The Pt:Au surface ratio of on the prepared nanoparticles was 0.70:0.30, 0.55:0.45 and 0.30:0.70.

Since the cyclic voltammogram of Pt-Au electrodes show characteristics of both Pt and Au surfaces, the Pt:Au surface ratio was determined by using the charges for the oxide reduction of the pure Pt and Au surfaces. A negative shift in the peak potential for the Pt oxide reduction on Au surfaces modified by Pt with respect to the peak position

observed for the Pt-Au/C nanoparticles. The onset and the peak potentials for the CO_{ads} oxidation on bare Pt and on Au modified Pt electrode are similar. This result as well as the same peak potentials for the Pt oxide reduction on these two surfaces confirms the assumption that the electrochemical behavior of bare Pt and Pt partially covered by Au are similar due to lack of the electronic modification of Pt by Au. The CO_{ads} oxidation on Au modified by Pt and on Pt-Au nanoparticles is delayed with respect to Pt (Fig. 1a and 1b) and the peak potential is as more positive as the Pt surface fraction decreases. Stronger adsorption of CO and OH species on Pt in contact with Au has also been reported for the bulk and surface Pt-Au alloys [14] and ascribed to the electronic interactions.

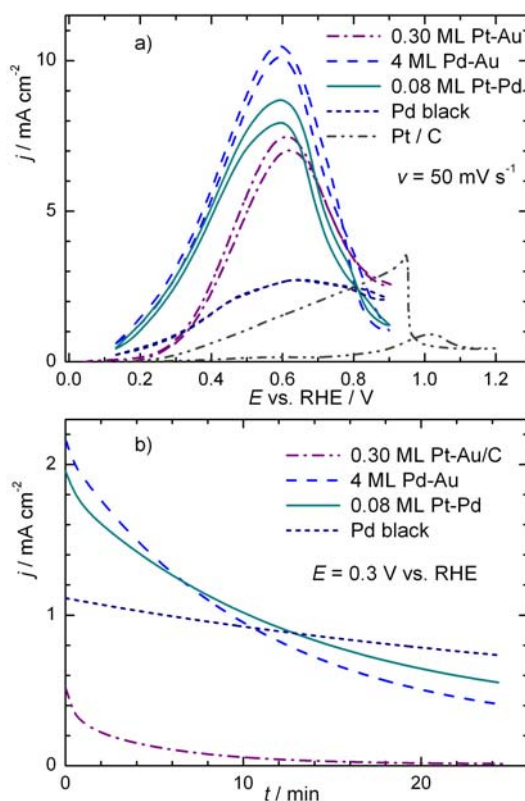


Fig.2 a) Potentiodynamic polarization curves in 0.1 M H_2SO_4 + 0.5 M HCOOH and b) Decay of the HCOOH oxidation.

dehydration path as the size of Pt domains on the Pt-Au surface decreases (ensemble effect). The HCOOH oxidation rate is similar on Au modified Pt and on Pt modified Au surfaces with a similar Pt fraction, although they

On bimetallic Pt-Au surfaces the HCOOH oxidation takes place exclusively at Pt sites, because Au is inactive for the oxidation of organic molecules before the oxide region. As Pt surface fraction decreases, the plateau corresponding to HCOOH dehydrogenation increases and transforms to peak (Fig.2a). Also, the peak corresponding to the reaction on the Pt sites released after CO_{ads} oxidation decreases and even vanishes on the curve for surfaces with the Pt fraction below 0.3. The backward scan for the same surfaces is almost retraced with the forward one, which shows that Pt is not poisoned by CO_{ads} . This indicates that dehydrogenation path overcomes the

differ in electronic modification of Pt atoms. This leads to a conclusion that the ensemble effect is crucial for high selectivity of Pt-Au surfaces toward dehydrogenation path.

When the activities of Pt-Au surfaces and bare Pt were compared at the potential of 0.4 V, all of them calculated per Pt surface area, it was found that the most active Au electrode modified by Pt sub-monolayer and the most active Pt-Au/C nanocatalyst exhibited about fifty and forty times higher current densities than bulk Pt and Pt/C nanocatalyst, respectively. It is interesting that the Pt-Au/C catalyst with Pt fraction of 0.30, which was found to be the most active under the potentiodynamic conditions, in a chronoamperometric test lost its activity rapidly (Fig.2b). The potentiodynamic curve recorded for this catalyst after the activity loss show a profile typical for dehydrogenation of HCOOH without poisoning by CO_{ads} . Thus, instability of Pt islands on the Au surface is not responsible for the activity loss. However, deactivation by CO_{ads} produced by the CO_2 reduction can not be excluded. The reason for so rapid poisoning of the catalyst with Pt fraction of 0.30 could be the strongest electronic modification of Pt by neighboring Au atoms because in this catalyst the Pt surface fraction is the lowest and consequently the number of Pt atoms in close contact with Au is the highest.

Pt-Co ELECTROCATALYST

Bulk Pt_3Co and $\text{Pt}_3\text{Co}/\text{C}$ and PtCo/C nanocatalysts were investigated for the CO_{ads} and HCOOH oxidation [11]. Pt_3Co alloy with Co electrochemically leached from the surface (“Pt skeleton”) was employed to separate electronic effect from the ensemble and bifunctional effects of Co.

The oxidation of CO_{ads} on Pt_3Co commenced earlier than on Pt. This can be attributed to the weakened bond between Pt and CO_{ads} , but also to the facilitated CO_{ads} oxidation by the oxygen-containing species adsorbed on Co atoms. The CO_{ads} oxidation on Pt_3Co with “Pt skeleton” structure was similar as on Pt surface indicating that bifunctional mechanism is stronger than the electronic modification of Pt by Co.

The onset potentials for the HCOOH oxidation on Pt_3Co alloy and on Pt were similar. CO_{ads} was present on both electrodes, but the coverage was lower on Pt_3Co than on Pt. As a consequence, the HCOOH oxidation current density at 0.4 V was about seven times higher on Pt_3Co . On “Pt skeleton” and bulk Pt the indirect path is predominant over the direct path and the coverage by CO_{ads} is substantial. This suggests that the enhanced activity of Pt_3Co alloy compared to Pt is caused by the ensemble effect. The comparison of CO_{ads} and HCOOH oxidation on $\text{Pt}_3\text{Co}/\text{C}$ and PtCo/C with the same reaction on Pt/C were qualitatively the same as on bulk materials.

Pd-Au ELECTROCATALYST

Polycrystalline Au electrode was modified by electrodeposition of thin Pd films ranging from 1 to 17 monolayer (ML) equivalents [12]. The CO_{ads} stripping charge was used for the determination of the Pd surface area. The cyclic voltammograms of Pd-Au films show that hydrogen adsorption/desorption charge increases with increasing Pd thickness. The potentials of Pd-oxide formation and Pd-oxide reduction on Pd modified Au films are slightly more positive comparing to Pd black (Fig.1c and 1e). Au substrate also influences oxidation of CO_{ads} on Pd. The onset potential of CO_{ads} oxidation on 1 ML Pd-Au is more positive than on Pd black, while with increasing Pd thickness it shifts negatively and approaches the onset potential on Pd black. Stronger bonding of the adsorbates on Pd in contact with Au than on pure Pd originates in the electronic modification of Pd by Au, as predicted by Norskov's group [15].

Potentiodynamic polarization curves of HCOOH oxidation on Pd black and Pd-Au show enlarged activity with increasing Pd thickness, reaching a maximum current density at 4 ML Pd-Au film (Fig.2a). At the thicker Pd layers the activity slowly decreases and the position of the maximum shifts positively reaching a potential of the plateau on Pd black. However, the current densities on the thickest Pd-Au film are still three times higher than on Pd black. The potential of maximum current is well below the potential for Pd-oxide formation, so the water-surface interactions could explain the deactivation of Pd for HCOOH adsorption and oxidation [14]. Bonding of HCOOH molecule with Pd on Pd-Au surfaces is also stronger than on pure Pd, which explains higher HCOOH oxidation rate on Pd-Au.

The results of the chronoamperometric stability test of Pd black and Pd-Au electrodes (Fig.2b) reveal that the least active surface of Pd black exhibits the lowest activity loss of 35 %. The highest activity loss of even 80 % was detected on 4 ML Pd-Au, which is the surface with the highest currents under the potentiodynamic conditions. After the stability test, 4 ML Pd-Au was subjected to the potential cycling. It was shown that the activity increased over cycling suggesting that deactivation at 0.3 V is caused by accumulation of a species that can be oxidatively removed from the surface. It was postulated that this species is CO_{ads} formed in the electrochemical reduction of CO_2 , which is the product of HCOOH oxidation [16]. The experiments with the electrochemical reduction of CO_2 dissolved in the electrolytes supported this assumption.

Pt-Pd ELECTROCATALYST

Pd black was modified by 0.02–0.12 ML of Pt by spontaneous displacement method [13]. The CO_{ads} stripping charge was used for the determination of the electrochemical active surface area. The activity of Pt-Pd catalysts for the CO_{ads} oxidation is similar to Pd black (Fig.1d and 1e). Although the CO_{ads} stripping peaks for pure Pt and Pd are separated by ca. 0.2 V, the CO_{ads} stripping for the Pt-Pd catalysts show a singular peak.

Modification of Pd black by sub-monolayer of Pt significantly enhances its activity for HCOOH oxidation (Fig. 2a). With increasing of Pt coverage from 0.02 to 0.08 ML the maximum current density raises, but further increase in Pt coverage leads to a gradual decrease in the activity. The hysteresis between the forward and backward scans on Pt-Pd catalyst is minor, indicating that direct path in HCOOH oxidation predominates.

The current-time transients presented in Fig.2b show that the initial activity of Pt-Pd is much higher compared with Pd black. However, the activity loss of even 75% was observed for Pt-Pd catalyst over 25 min.

The activity of the most active modified surfaces toward HCOOH oxidation in potentiodynamic and potentiostatic conditions is presented in Fig.2a and 2b. Pt-Au binds the HCOOH molecules too strongly and the poisoning by CO_{ads} formed as the product of CO_2 reduction is more intense than on Pt-Pd and Pd-Au catalysts. Rational synthesis and optimization of catalytic properties of nanoparticles consisting of an Au core, covered by a Pd shell, onto which Pt clusters are deposited is challenge for the future investigation.

CONCLUSION

A high selectivity of Pt-based surfaces toward dehydrogenation path is reached on Au and Pd surfaces modified by a low amount of Pt. Electronic modification of Pd and Pt by Au substrate causes their stronger interactions with HCOOH and CO, thus increasing HCOOH oxidation rate, but also accelerating the poisoning by CO_{ads} formed in the incomplete reduction of CO_2 as the reaction product. Therefore, the activity and the stability of the electrocatalyst have to be balanced.

ACKNOWLEDGEMENT

This work was financially supported by the Ministry of Education, Science and Technological Development of the Republic of Serbia (Grant No. 142054).

REFERENCES

- [1] X. Yu, P. G. Pickup, *J. Power Sources*, 2008, 182, 124-132.
- [2] A. Capon, R. Parsons, *J. Electroanal. Chem.*, 1973, 44, 205–231.
- [3] A. Miki, S. Ye, M. Osawa, *Chem. Commun.*, 2002, 1500-1501.
- [4] C. A. Rice, A. Bauskar, P. G. Pickup in: *Electrocatalysis in Fuel Cells: A Non- and Low- Platinum Approach*, Ch.4, M. Shao (Ed.), Springer-Verlag, London, 2013.
- [5] T. D. Jarvi, E. M. Stuve, in: J. Lipkovski, P. N. Ross (Eds.), *Electrocatalysis*, Wiley–VCH, 1998.
- [6] A. Cuesta, M. Escudero, B. Lanova, H. Baltruschat, *Langmuir*, 2009, 25, 6500–6507.
- [7] M. Baldauf, D. M. Kolb, *J. Phys. Chem.* 1996, 100, 11375–11381.
- [8] P. K. Babu, H. S. Kim, J. H. Chung, E. Oldfield, A. Wieckowski, *J. Phys. Chem. B*, 2004, 108, 20228–20232.
- [9] M. D. Obradović, A. V. Tripković, S. Lj. Gojković, *Electrochim. Acta*, 2009, 55, 204–209.
- [10] M. D. Obradović, J. R. Rogan, B. M. Babić, A. V. Tripković, A. R. Gautam, V. R. Radmilović, S. Lj. Gojković, *J. Power Sources.*, 2012, 197, 727–729.
- [11] M. D. Obradović, A. V. Tripković, S. Lj. Gojković, *J. Solid State Electrochem.*, 2012, 16, 587–595.
- [12] M. D. Obradović, S. Lj. Gojković, *Electrochim. Acta*, 88 (2013) 3843–389.
- [13] M. D. Obradović, S. Lj. Gojković, *J. Solid State Electrochem.*, DOI: 10.1007/s10008-014-2509-9.
- [14] E. Irissou, F. Laplante, S. Garbarino, M. Chaker, D. Guay, *J. Phys. Chem. C* 2010, 114, 2192–2199.
- [15] A. Ruban, B. Hammer, P. Stoltze, H. L. Skriver, J. K. Nørskov, *J. Mol. Catal. A-Chem.* 1997, 115, 421–429.
- [16] H.-X. Zhang, S.-H. Wang, K. Jiang, T. Andréb, W.-B. Cai, *J. Power Sources*, 2012, 199, 165–169.

CARBON-SUPPORTED Mo₂C ELECTROCATALYSTS FOR HYDROGEN EVOLUTION REACTION

L. Amaral¹, B. Šljukić¹, D. M. F. Santos¹, A. Stojanović², R. P. Rocha³,
C. A. C. Sequeira¹ and J. L. Figueiredo³

¹*Materials Electrochemistry Group, ICEMS, Instituto Superior Técnico, Universidade de Lisboa, 1049-001 Lisboa, Portugal*

²*Faculty of Physical Chemistry, University of Belgrade, Studentski trg 12-16, 11158 Belgrade, Serbia*

³*Laboratory of Catalysis and Materials - Associate Laboratory LSRE/LCM, Faculdade de Engenharia, Universidade do Porto, Porto, Portugal*

ABSTRACT

Mo₂C nanoparticles supported on two different carbon materials, carbon nanotubes and carbon xerogel, were prepared and characterized using XRD, SEM and TGA. These were subsequently tested as electrocatalysts for hydrogen evolution reaction in acid media. Using linear scan voltammetry main reaction parameters were determined including Tafel slope, charge transfer coefficient and exchange current density. Durability of the two materials was also investigated and proved to be satisfactory.

INTRODUCTION

Hydrogen (H₂) is seen as a clean fuel as no greenhouse gases are evolved during its use [1]. Still, main current methods for H₂ production employ fossil fuels. Water electrolysis represents a simple and clean method for H₂ production, but this process is too expensive at the moment. Its high price results from high overpotential needed to operate the electrolysis cell and consequently, high energy consumption during the process. Overpotential value is related to electrode materials properties. Two characteristics crucial for a material to be accepted as a suitable electrocatalyst for hydrogen evolution reaction (HER) are its electrocatalytic activity and its stability. Transition metal carbides (TMC) are known to have platinum (Pt)-like electronic and catalytic properties, but significantly lower cost [2]. Furthermore, grafting of these materials on to a high-surface area conductive support increases their activity.

EXPERIMENTAL

Molybdenum carbide (Mo₂C) nanoparticles were grafted on both carbon nanotubes (CNTs) and on carbon xerogel (CXG). First, aqueous solution of

ammonium molybdate (0.788 g in 6 ml) was added dropwise to the carbon support (1 g), following a modified incipient wetness impregnation method, and the mixture was homogenised in an ultrasonic bath for 30 min. The samples were next dried at 110 °C overnight. Carburisation was achieved in a tube furnace increasing the temperature from ambient to 800 °C at 13 °C min⁻¹ rate under nitrogen flow, and then holding it at 800 °C for 2 h. CNTs were purchased from NANOCYL™ (NC3100 series) and pre-treated with hydrochloric acid [3] prior to impregnation, while CXG was prepared by an adapted literature procedure [4].

Electrocatalysts structures were examined by XRD analysis with Philips 1050 Bruker D8 Advance with CuK $\alpha_{1,2}$ radiations in 10-80° 2 θ range. Content of Mo₂C in the electrocatalysts was determined performing TGA with TA SDT 2960 at a heating rate of 10 °C min⁻¹ under the air flow. The morphology was examined by SEM using JEOL JSM 7001F microscope.

The working electrodes were prepared by uniformly depositing the corresponding catalytic ink on conductive substrates and drying them under vacuum at 120 °C overnight. The catalytic inks were prepared by mixing Mo₂C/CNT or Mo₂C/CXG electrocatalyst powder (95%) with poly(vinylidene fluoride) binder (5%) in N-methyl 2-pyrrolidone solvent. The electrocatalyst loading on the electrode was 8.2 and 6.3 mg cm⁻² for Mo₂C/CNT and Mo₂C/CXG, respectively. Geometric area of the substrate was used to calculate the current densities.

Electrochemical measurements were done in a single-compartment glass cell with a Pt counter electrode and saturated calomel electrode (SCE) as reference. The electrocatalysts were tested for HER by recording linear sweep voltammograms (LSV) in 0.1 M HClO₄ aqueous solutions at a scan rate of 0.5 mV s⁻¹ and at temperature of 25 °C. Durability tests were done using chronopotentiometry (CP) by recording the overpotential needed to drive 10 mA cm⁻² current density for 2 h.

RESULTS AND DISCUSSION

Formation of α -Mo₂C on to CNTs and on to CXG was confirmed by XRD analysis. The amount of carbide formed was similar for both carbon supports (ca. 27%). However, SEM images showed quite different morphology of the two electrocatalysts, Fig. 1. Mo₂C nanoparticles are observed to be dispersed on CNTs, while particles were found to be agglomerated in the case of Mo₂C/CXG.

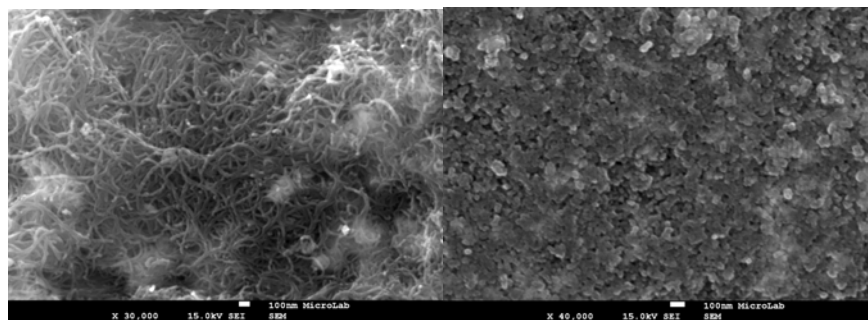


Figure 1. SEM images of Mo₂C/CNT (left) and Mo₂C/CXG (right).

Polarization curves presenting current density, j , as a function of potential, E , were recorded for the two studied electrocatalysts with similar current densities obtained, Fig. 2. These were further used for construction of Tafel plots presenting dependence of overpotential, η , on $\log j$ (Eq. 1),

$$\eta = a + b \log j = \frac{2.3RT}{\alpha nF} \log j_0 - \frac{2.3RT}{\alpha nF} \log j \quad (1)$$

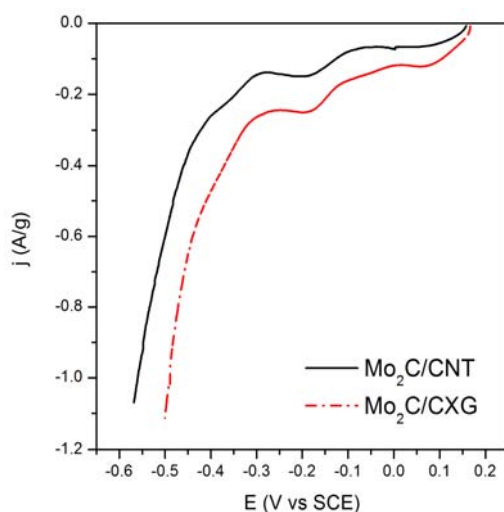


Figure 2. Polarization curves of two studied electrocatalysts in 0.1 M HClO₄

where b is the Tafel slope, R is the universal gas constant, T is temperature, α is charge transfer coefficient, F is the Faraday constant and j_0 is the exchange current density. Similar b values of 338 and 348 mV dec⁻¹ were obtained for Mo₂C/CNT and Mo₂C/CXG, respectively. These values were found to be significantly higher than expected values for HER in acid media and generally higher than values reported when using other non-Pt electrocatalysts [5]. Accordingly, low α values of 0.16 were obtained for the two Mo₂C/C electrocatalysts. j_0 values of 2.56 and 3.93 x 10⁻²

mA cm⁻² were obtained for HER at Mo₂C/CNT and Mo₂C/CXG, respectively. Value of j_0 mainly depends on the electrode material, on its composition, structure and some physical parameters such as surface roughness. j_0 value can also be influenced by adsorbed species, electrolyte composition and temperature. Table 1 summarizes the obtained parameters

for HER at the studied electrocatalysts. Values of overpotential necessary to drive current density of 300 mA g^{-1} (η_{300}) were also compared with lower value obtained for $\text{Mo}_2\text{C}/\text{CXG}$ indicating its higher activity for HER. This was further supported by higher specific current density value (j_{300}) obtained at $\text{Mo}_2\text{C}/\text{CXG}$ than at $\text{Mo}_2\text{C}/\text{CNT}$ at the same overpotential of 300 mV.

Table 1. Direct comparison of HER activity of two different carbon-supported Mo_2C electrocatalysts in acid media at 25 °C.

Catalyst	η_{300} (mV)	j_{300} (mA g^{-1})	b (mV dec^{-1})	α	$j_0 \times 10^{-2}$ (mA cm^{-2})	R^2
$\text{Mo}_2\text{C}/\text{CXG}$	238	450	348	0.16	3.93	0.99
$\text{Mo}_2\text{C}/\text{CNT}$	333	249	338	0.16	2.56	0.99

Durability tests showed good performance for the two electrocatalysts. The overpotential necessary to drive a current density of 10 mA cm^{-2} was found to be stable at 40 and 50 mV for $\text{Mo}_2\text{C}/\text{CNT}$ and $\text{Mo}_2\text{C}/\text{CXG}$, respectively.

CONCLUSIONS

Mo_2C electrocatalysts supported on CNTs and on CXG were prepared and found to have similar composition and structure, but distinctively different morphology. Evaluation of HER activity of the two electrocatalysts in acid media indicated higher activity of $\text{Mo}_2\text{C}/\text{CXG}$ compared to $\text{Mo}_2\text{C}/\text{CNT}$. Furthermore, durability tests showed a constant and stable overpotential necessary to drive 10 mA cm^{-2} over 2 h.

ACKNOWLEDGEMENTS

The authors thank FCT, Portugal, for postdoctoral research grants SFRH/BPD/91853/2012 (D.M.F. Santos), SFRH/BPD/77768/2011 (B. Šljukić), and SFRH/BPD/97453/2013 (L. Amaral), a PhD grant SFRH/BD/95411/2013 (R.P. Rocha), and for project PTDC/SEN-ENR/121265/2010, as well as to the Ministry of Education, Science and Technological Development of Republic of Serbia for support within the project No. III45014.

REFERENCES

- [1] D.M.F. Santos, B. Šljukić, C.A.C. Sequeira, D. Macciò, A. Saccone, J.L. Figueiredo, *Energy* 2013, 50, 486-492.
- [2] H.H. Hwu, J.G. Chen, *Chem. Rev.* 2005, 105, 185-212.
- [3] W.F. Chen, C.H. Wang, K. Sasaki, N. Marinkovic, W. Xu, J.T. Muckerman, Y. Zhu, R.R. Adzic, *Energy Environ. Sci.* 2013, 6, 943-951.
- [4] N. Job, R. Pirard, J. Marien, J.-P. Pirard, *Carbon* 2004, 42, 619-628.
- [5] E. Navarro-Flores, Z. Chong, S. Omanovic, *J. Mol. Catal. A: Chem.* 2005, 226, 179-197.

PHENOL ELECTROOXIDATION USING ELECTRODES BASED ON ACID-TREATED AND Ni-IMPREGNATED BENTONITE

T. Mudrinić, Z. Mojović, M. Žunić, A. Milutinović-Nikolić and
D. Jovanović

*University of Belgrade-IChTM, Center for Catalysis and Chemical
Engineering, Njegoševa 12, Belgrade (tihana@nanosys.ihtm.bg.ac.rs)*

ABSTRACT

Electrooxidation of phenol in acidic solution was investigated on modified bentonite-based glassy carbon electrode (GCE). The modification of bentonite was performed in two steps. First bentonite was acid treated and then nickel species were incorporated in acid-treated bentonite. Incorporation of nickel species was achieved by either impregnation with $\text{Ni}(\text{NO}_3)_2 \cdot 6\text{H}_2\text{O}$ or by impregnation-decomposition method using nickel acetylacetonate $[\text{Ni}(\text{acac})_2]$. The change in phase and chemical composition was monitored by XRD. The electrochemical behavior was tested by cyclic voltammetry. The higher current density and lower potentials of phenol oxidation wave were obtained for acid-treated bentonite based GCE, while presence of nickel led to better stability of modified GCE regarding electrode fouling.

INTRODUCTION

Electrochemical oxidation processes have been recognized as an alternative method for treating wastewaters containing organic molecules. The oxidation of various organic pollutants at different electrode materials has been extensively investigated [1]. Phenol is the most commonly investigated compound as model organic compound in electrooxidation processes [2, 3]. Many electrode materials suffer from electrode fouling by formation of insulating polymeric film during electrooxidation of phenol. Modification of the electrode surface is one of approaches to overcome the problem of electrode fouling. Clays modified using oxidation/reduction species have proven to be good electrode surface modifiers [4, 5].

The goal of this work was to incorporate nickel in acid treated bentonite and apply these materials as GCE modifiers in the electrochemical oxidation of phenol.

EXPERIMENTAL

Bentonite from seldom investigated deposit Mečji Do Serbia ($< 75 \mu\text{m}$) was used as raw material (MD). First bentonite was treated with 1 M HCl at 70 °C for 30 min and designed as MD_A. Incorporation of nickel species into the acid-treated bentonite was performed by either impregnation with Ni(NO₃)₂·6H₂O or by impregnation-decomposition method using nickel acetylacetonate [Ni(acac)₂] [4]. The sample was impregnated with 0.5 M Ni(NO₃)₂·6H₂O at 300 °C for 2h and designed as MD_A/Ni(NO₃)₂. The impregnation-decomposition procedure with Ni(acac)₂ was performed at 430 °C in order to transform Ni(acac)₂ into NiO. The procedure was repeated until mass ratio of Ni/MD_A of 0.1 was reached. This sample was designed as MD_A/Ni(acac)₂.

The XRD analyses were performed using Philips PW 1710 X-ray powder diffractometer with a Cu anode ($\lambda=0.154178 \text{ nm}$). The GCE surface was coated with 10 μl of homogeneous mixture of each modified bentonite and carbon black dispersed in Nafion® solution and applied as working electrode [4]. The reference electrode was Ag/AgCl, KCl (3M), while a platinum foil served as a counter electrode. The electrooxidation of phenol was investigated in 10 mM phenol + 0.1 M H₂SO₄. The device used for electrochemical measurements was 797 VA Computrace Metrohm.

RESULTS AND DISCUSSION

The main minerals identified in all samples were smectite (S), cristobalite (Cb), quartz (Q) and feldspar (F) (Fig. 1) [6]. In the Ni containing samples d_{001} value was 0.97 nm characteristic for dehydrated smectites caused by applied heat treatment. Among impregnated samples only MD_A/Ni(acac)₂ showed new reflections at around 43.1° and 37.1° 2θ characteristic for nickel oxide [6].

Cyclic voltammograms (CV) were obtained for GCE modified with each of modified bentonite in acidic phenol solution. The polarization rate was 10 mVs⁻¹ in the range of potential from hydrogen evolution at -0.3 V to oxygen evolution at 1.1 V. CVs were first obtained in 0.1 M H₂SO₄. The freshly prepared electrodes were then tested under the same conditions

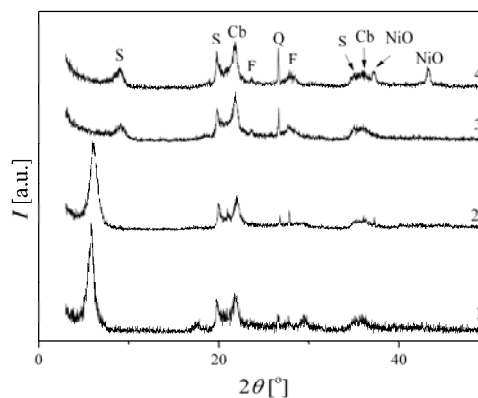


Figure 1. XRD patterns of: (1) MD; (2) MD_A; (3) MD_A/Ni(NO₃)₂ and (4) MD_A/Ni(acac)₂.

in 10 mM phenol + 0.1 M H₂SO₄. CVs were similar for all investigated electrodes and for clarity sake only CVs for MD_A/Ni(acac)₂ are presented in Figs. 2. The CV obtained in the supporting electrolyte (dashed line in Fig. 2a) is presented together with the first cycle recorded in phenol containing solution (solid line in Fig. 2a). In Fig. 2b ten successive cycles in phenol containing solution are presented.

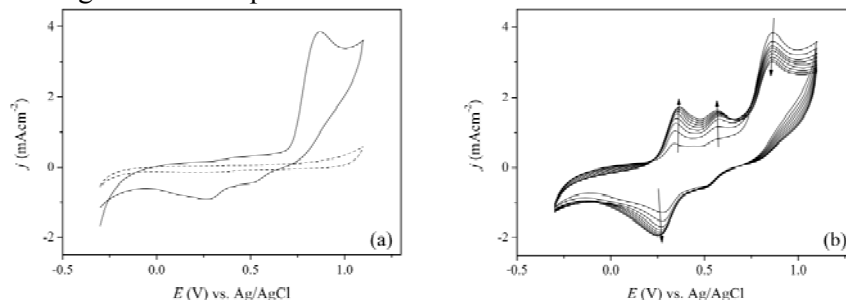


Figure 2. CVs of the MD_A/Ni(acac)₂: (a) 0.1 M H₂SO₄ (dashed line) and the first cycle in phenol containing solution (solid line); (b) Successive cycles in phenol containing solution. Arrows indicate changes during cycling.

During electrooxidation of phenol in the first cycle the phenol oxidation wave and pair of waves that correspond to the reduction of hydroquinone and catechol were obtained for all synthesized electrode materials. During successive cycling additional pair of waves that correspond to hydroquinone and catechol oxidation was registered [5]. Successive cycling increased the current density of waves associated with phenol oxidation products. On the other hand, successive cycling resulted in decreased intensity of the phenol oxidation wave for all investigated electrodes. Differences between electrochemical parameters obtained for GCE coated with different materials are summarized in Table 1.

Table 1. Electrochemical parameters of investigated modified electrodes.

Modifier	E [mV]	j_1 [mAcm ⁻²]	j_x [mAcm ⁻²]	$(j_1-j_x)/j_1$ [%]
MD	939	1.06	0.24	77.4
MD _A	863	3.40	2.18	35.9
MD _A /Ni(NO ₃) ₂	878	2.07	1.49	28.0
MD _A /Ni(acac) ₂	868	3.87	2.99	22.7

Where: E – potential of phenol oxidation peak, j_1 and j_x – current density at phenol oxidation peak, in the first and tenth cycle, respectively.

The current density for phenol oxidation wave increased in following order MD < MD_A/Ni(NO₃)₂ < MD_A < MD_A/Ni(acac)₂. The higher current densities for MD_A based electrodes might be induced by better accessibility to active sites for phenol oxidation. Also, potential at phenol oxidation wave shifts

toward lower potentials in MD_A based electrodes. Such finding indicates better electrode activity. Incorporation of nickel in modified bentonite based GCE resulted in improvement of the stability of these electrodes. The introduction of nickel by impregnation/decomposition method in MD_A was found to be the most promising modification regarding the use of investigated modified bentonites in surface coating of GCE.

CONCLUSION

Electrooxidation of phenol was investigated on glassy carbon electrode (GCE) coated with raw (MD), acid-treated bentonite (MD_A) and acid-treated bentonite impregnated with either Ni(NO₃)₂ (MD_A/Ni(NO₃)₂) or nickel acetylacetonate (MD_A/Ni(acac)₂). Phenol oxidation process on all synthesized electrode materials showed similar response with difference in electrochemical parameters. The higher current density and lower potentials of phenol oxidation wave were obtained for MD_A based GCE. The incorporation of nickel species into MD_A caused better stability of modified GCE regarding electrode fouling. The GCE modified with MD_A/Ni(acac)₂ was more stable than GCE modified MD_A/Ni(NO₃)₂. The presence of nickel has important role in the stability of the GCE in the phenol electrooxidation process and further investigation of this phenomenon is still in progress.

ACKNOWLEDGEMENT

This work was partially supported by the Ministry of Education, Science and Technology Development of the Republic of Serbia (Project Nos. III 45001 and ON 172026).

REFERENCES

- [1] C. A. Martínez-Huitle, S. Ferro, *Chemical Society Reviews*, 2006, 35, 1324-1340.
- [2] Environmental Protection Agency, Appendix A to Part 423—126 Priority Pollutants, (2014), <http://water.epa.gov/scitech/methods/cwa/pollutants.cfm>
- [3] X.Li, Y.Cui, Y. Feng, Z. Xie, J. Gu, *Water Resarch* 2005, 39, 1972-1981.
- [4] Z. Mojović, P. Banković, A. Milutinović – Nikolić, B. Nedić, D. Jovanović, *Applied Clay Science* 2010, 48, 179-184.
- [5] P. Banković, Z. Mojović, A. Milutinović-Nikolić, N. Jović-Jovičić, S. Marinović, D. Jovanović, *Applied Clay Science* 2010, 49, 84–89.
- [6] International Center for Diffraction Data—JCPDS, Swarthmore, PA, USA, 2003.

THE INFLUENCE OF NAFION ON OXIDATION OF GLUCOSE ON GOLD ELECTRODE FROM ALKALINE SOLUTIONS

T. Mudrinić, Z. Mojović and A. Ivanović-Šašić

*University of Belgrade, Institute of Chemistry, Technology and Metallurgy,
Department of Catalysis and Chemical Engineering, Njegoševa 12, 11000
Belgrade, Republic of Serbia*

ABSTRACT

The influence of Nafion on oxidation of glucose on gold electrode in 0.1 M NaOH solution was investigated. The presence of Nafion on the surface of gold electrode decreased the rate of glucose oxidation in alkaline solution. The mechanism of glucose oxidation is not changed by the presence of Nafion.

INTRODUCTION

The electrooxidation of sugars, particularly glucose, was investigated for applications in glucose sensors as well as fuel cells for cardiac pacemakers. The enzyme-based glucose sensors are developed and thoroughly investigated and so far showed good sensitivity and selectivity. However, major drawback of enzyme-based glucose sensors is their lack of stability of enzymes. For this reason the investigation on non-enzymatic glucose sensors raised a great interest. The practical application of non-enzymatic sensors is hindered by their lack of selectivity and fouling of the electrode [1]. The gold electrode showed good electrocatalytic activity for glucose oxidation in neutral and alkaline electrolytes. The gold electrode also shows high sensitivity toward chloride ions in neutral solutions [2], what makes this electrode inadequate for application under physiological conditions. The modification of gold electrode by different metal ad-layers showed some improvement [3]. Nafion (perfluorinated sulphonate ionomer) has negative charge, so foreign species such as ascorbic acid, paracetamol, uric acid, etc. are readily repelled [4]. The aim of this paper was to investigate influence of Nafion on glucose oxidation on gold electrode in alkaline solution.

EXPERIMENTAL

Glucose oxidation on gold electrode was investigated in a 0.1 M NaOH in a three-electrode glass cell with Ag/AgCl (sat'd) as a reference electrode,

while a platinum foil served as a counter electrode. The influence of Nafion was investigated on Nafion covered gold electrode. The droplet of solution of Nafion (5 wt. %) was placed on the gold electrode. After evaporation of solvent Nafion film was formed on the electrode surface. Device used for the electrochemical measurements was a 757 VA Computrace Metrohm.

RESULTS AND DISCUSSION

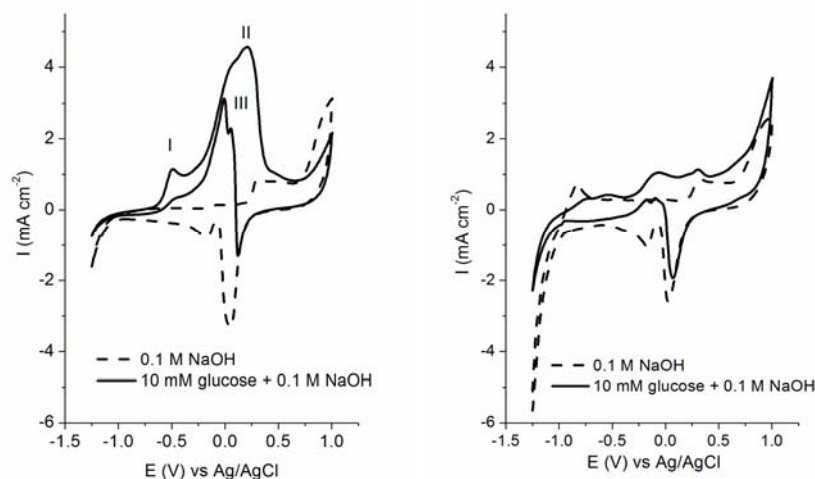


Figure 1. Voltammograms of bare gold electrode (left) and Nafion covered gold electrode (right) in 0.1 M NaOH without (dashed) and with 10 mM glucose (solid).

The cyclic voltammograms of Au electrode in 0.1M NaOH (Fig.1) show peaks of gold oxide formation and reduction at 0.30 and 0.05 V, respectively. The cyclic voltammogram recorded in the presence of glucose is presented at the same figure. The anodic peak at -0.6 V is followed by broad peak at approximately 0 V. The peak at -0.6 V is ascribed to the formation and adsorption of intermediate compounds, while the other peak represents the direct oxidation of glucose in the anodic direction (II). This peak has a large left shoulder indicating the occurrence of several reactions [5]. The cathodic peak on the negatively going sweep corresponds to direct oxidation of glucose in cathodic direction. The direct oxidation of glucose occurs after the oxides are removed from the surface of the electrode. The AuOH sites are considered to be the active species for glucose oxidation. Therefore, the rate of glucose oxidation depends on the number of AuOH sites. The oxidation of glucose starts with the formation of AuOH, and

proceeds until gold oxide is formed at sufficiently high positive potentials and the current of glucose oxidation decreases. In negative going sweep the catalytic oxidation of glucose starts again as soon as gold oxide is reduced and AuOH sites are formed again.

Cyclic voltammograms at different scan rates were recorded in order to investigate the kinetics of glucose oxidation. Plotting $\log i$ vs. $\log v$ shows that peak II is controlled by diffusion (slope close to 0.5). However, the same plot for peak I shows two slopes. At higher scan rates (150 - 500 mVs^{-1}) the slope is close to 0.5 indicating diffusion controlled process. However, at lower scan rates (10 - 100 mVs^{-1}) the obtained slope amounts 0.17 indicating a mechanism with numerous adsorbed species and products formed [6]. The current density of re-oxidation peak III decreases and the peak position shifts toward negative direction with increased scan rates, which indicates the poisoning of the electrode surface [7]. The potentials of peaks I and II are proportional to the logarithm of scan rate. From the slope of the E_p vs. $\log v$ curve, the Tafel slope can be obtained. The obtained Tafel slopes amount 50 and 56 V dec^{-1} for peaks I and II, respectively, what indicates that a two-electron transfer process is the rate limiting step for these reaction. The current function ($i_p/v^{1/2}$) of peak I decreases with v , which is characteristic of a coupled chemical reaction following the electron transfer (EC mechanism) [8]. This type of mechanism occurs quite frequently in organic compounds which undergo electrochemical oxidation or reduction and produce a reaction species (radical or radical ions) that tend to dimerize. The current function of peak II shows slower decline indicating that process is not free from kinetic complications.

The cyclic voltammogram of Nafion covered gold electrode (Au/Nafion) exhibited additional anodic peak in comparison to CV of bare gold electrode (Fig. 1). This peak appeared in the potential region of hydrogen desorption. Upon successive addition of increasing amounts of glucose this peak started to diminish followed by the appearance of new peak at somewhat higher potentials. This peak might be associated to the adsorption and partial oxidation of glucose. The oxidation of glucose and formed gluconolactone at higher potential are clearly separated, although the obtained currents are about five times lower than currents obtained on bare gold electrode. At the reverse sweep the peak of reduction of gold oxide gradually decrease and two separated peaks of oxidation of glucose/glucose products appeared.

Plotting $\log i$ vs. $\log v$ shows that peak II is controlled by diffusion (slope close to 0.5). As in the case of bare gold electrode, this plot for peak I showed two slopes. At higher scan rates (150 - 500 mVs^{-1}) the slope is close to 0.8 indicating mixed controlled process. At lower scan rates (10 - 100 mVs^{-1}) the obtained slope amounts 0.3 what suggests a mechanism with

numerous adsorbed species and products formed. The current function ($i_p/v^{1/2}$) of both peaks decreases with v which is characteristic of a coupled chemical reaction following the electron transfer (EC mechanism).

CONCLUSIONS

The influence of Nafion on oxidation of glucose on gold electrode in alkaline solution was investigated. The presence of Nafion on the surface of gold electrode lead to decrease of the rate of glucose oxidation in alkaline solution. The decrease of reaction rate is consequence of reduced concentration of glucose and OH ions at the electrode surface. It seems that the mechanism of glucose oxidation is not changed by the presence of Nafion.

ACKNOWLEDGMENT

This work was supported by the Ministry of Education, Science and Technological Development of Republic Serbia (contract No III 45001).

REFERENCES

- [1] K.E. Tonghill, R.G. Compton, *Int. J. Electrochem. Sci.*, 2010, 5, 1246-1301.
- [2] Z.B. Vassilyev, O.A. Khazova, N.N. Nikolaeva, *J. Electroanal. Chem.*, 1985, 196, 127-144.
- [3] S.B. Aoun, Y. Dursun, T. Koga, G.S. Bang, T. Sotomura, I. Taniguchi, *J. Electroanal. Chem.*, 2004, 567, 175–183.
- [4] H. Liu, J. Deng, *Electrochim. Acta*, 1995, 40, 1845–1849.
- [5] M. Tominaga, T. Shimazoe, M. Nagashima, I. Taniguchi, *Electrochem. Commun.*, 2005, 7, 189–193.
- [6] P. Parpot, P.R.B. Santos, A.P. Bettencourt, *J. Electroanal. Chem.*, 2007, 610, 154–162.
- [7] A. Liu, E. Liu, G. Yang, N. Win Khun, W. Ma, *Pure Appl. Chem.*, 2010, 82, 2217-2229
- [8] A. Bard, L. Faulkner, *Electrochemical Methods Fundamental and Applications*, Wiley, Chichester 1980.

DINUCLEAR COPPER (II) OCTAAZAMACROCYCLIC COMPLEX IN A PVC COATED GRAPHITE AS A VOLTAMMETRIC SENSOR FOR DETERMINATION OF GALLIC ACID

B. B. Petković¹, D. Stanković², M. Jović², A. T. Ivanović³ and J. Pavlović⁴

¹*Department of Chemistry, Faculty of Natural Sciences and Mathematics, University of Priština, Lole Ribara 29, 38220 Kosovska Mitrovica, Serbia (bedpet@orion.rs)*

²*Innovation center of the Faculty of Chemistry, University of Belgrade, P.O. Box 118, 11158 Belgrade, Serbia*

³*Mining and Metallurgy Institute, Zeleni bulevar 35, 19210 Bor, Serbia*

⁴*Department of Chemistry, Faculty of Natural Sciences and Mathematics, University of Niš, Višegradska 33, 18000 Niš Serbia*

ABSTRACT

A novel efficient differential pulse voltammetric (DPV) method for determination of the gallic acid (GA) was developed by using an electrochemical sensor based on $[\text{Cu}_2\text{tpmc}](\text{ClO}_4)_4$ immobilized in PVC matrix and coated on graphite (CGE). The proposed method is based on the gallic acid oxidation process at formed reversible $[\text{Cu}_2\text{tpmcGA}]^{3+}$ complex at the electrode surface. Voltammogram of sensor recorded in a HNO_3 as a supporting electrolyte at pH 2, resulted with two linear calibration curves (for higher and lower GA concentration range) measured in 2.5×10^{-7} to 1.0×10^{-4} M of GA. The detection limit at CGE was 1.48×10^{-7} M.

INTRODUCTION

Gallic acid (GA), a type of phenolic acid, is occurring in plants in the form of free acids, esters, catechin derivatives and hydrolysable tannins [1]. As one of the most biologically-active phenolic compounds of plant origin, gallic acid is commonly used in the pharmaceutical and food industry. GA serves as a standard for determining the phenol content of various analytes by the Folin-Ciocalteu spectrophotometric method and the results are reported in gallic acid equivalents. The measurement of “total phenols” is a good indication of the level of antioxidants present in the sample [2].

Besides other methods, electrochemical methods were also employed for phenolic compounds determination in various types of samples. Cyclic, differential pulse and adsorptive stripping voltammetric techniques on

glassy carbon electrode (GCE) were mostly used in reported works [3]. The main disadvantage of GCE used for this purpose was polymerization and adsorption of investigated and other species on the electrode itself.

We examined application possibility of simple and efficient sensor for rapid differential pulse voltammetric determination of GA at low concentrations, based on previously synthesized $[\text{Cu}_2\text{tpmc}](\text{ClO}_4)_4$ complex immobilized in a PVC matrix. Intention was to find an efficient voltammetric sensor resistant to polymerization on the electrode surface due to its modification.

EXPERIMENTAL

Electrode preparation: The initial macrocyclic ligand $\text{N},\text{N}',\text{N}'',\text{N}'''$ -tetrakis(2-pyridylmethyl)-1,4,8,11-tetraazacyclotetradecane (*tpmc*) and the next synthesized $[\text{Cu}_2\text{tpmc}](\text{ClO}_4)_4$ complex which was electroactive sensor material, were prepared by the procedure described in literature [4,5]. Electrode was prepared in the way reported before [6]. The membrane coated on graphite was allowed to dry in air over night and activated by 10^{-4} M GA solution for about 24 h in order to GA molecules to be captured and formed $[\text{Cu}_2\text{tpmcGA}]^{3+}$ complex ion.

Electrochemical measurements: Cyclic and differential pulse voltammetric measurements were carried out with a conventional three-electrode electrolytic cell on a Metrohm 797 VA Computance instrument (Herisau, Switzerland). The triple-electrode system consisted of a working electrode, graphite electrode modified with PVC membrane with activated dinuclear $\text{Cu}(\text{II})/\text{tpmc}$ complex as sensor component, a reference Ag/AgCl , KCl (3 M) (Model 6.0728.010) and an auxiliary separate platinum rod electrode (Model 6.0340.000). The cyclic and the differential pulse voltammograms of standard GA solutions were recorded in the potential range from 0.0 to 1.0 V, using a scan rate of 100 mV/s (for CV) and 10mV/s (for DPV), a modulation time of 40 ms, and a pulse amplitude of 50 ms.

RESULTS AND DISCUSSION

Cyclic voltammograms of 10^{-4} M GA in HNO_3 solution as supporting electrolyte (pH about 2) at graphite and graphite coated with activated $[\text{Cu}_2\text{tpmc}](\text{ClO}_4)_4$ complex immobilized in PVC matrix (CGE) are presented in Fig. 1, a and b. Voltammogram analysis revealed that the peak current decreases in every next cycle due to absorption and polymerization of GA on the bare electrode surface. On the other hand, coating of the membrane over the graphite prevents polymerization (b) graph, Fig.1. Cycling at coated electrode barely changed the shape of the cyclovoltammograms.

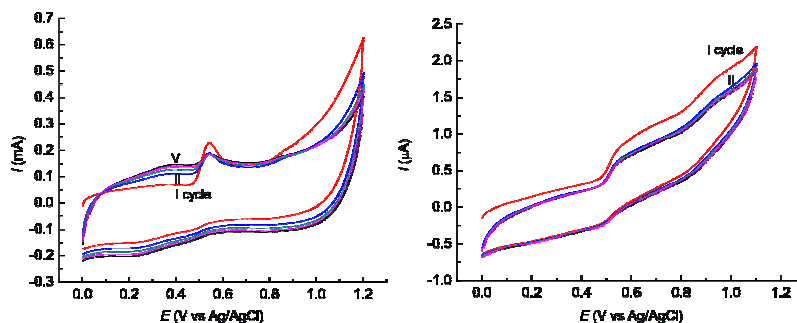


Figure 1. Cyclic voltammetric profiles resulting from the electrochemical oxidation of 10^{-4} M gallic acid in HNO_3 solution (pH about 2) at bare graphite (a) and coated graphite electrode (b); scan rate of 100 mV/s

Differential pulse voltammetry (DPV) was selected as a suitable electroanalytical technique for determination of GA because of its low background currents and low detection limits. DPV study at electrodes with and without complex in PVC matrix at the large GA concentration in 10^{-2} M HNO_3 showed that response of the CGE came only from the dinuclear copper/*tpmc* complex immobilized in a polymer matrix. The optimal modulation time of 40 ms and pulse amplitude of 50 ms were chosen taking into account the width and height of the peak of quantitation (0.5V).

Differential pulse voltammograms of various concentrations of GA from 1.0×10^{-4} to 2.5×10^{-7} M recorded on CGE were showed in Fig.2 (a).

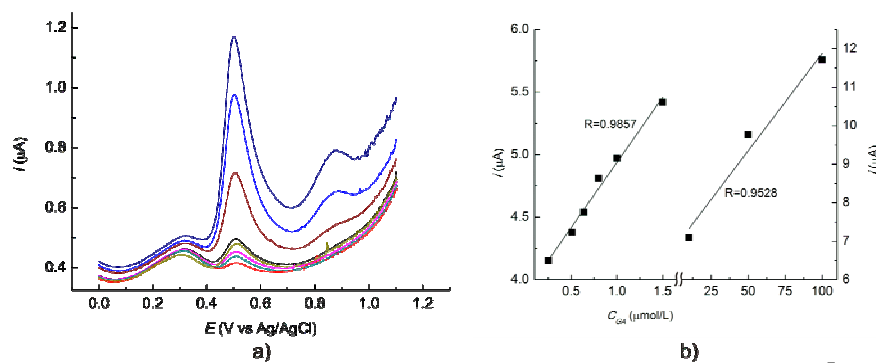


Figure 2. DPV of CGE with GA added in concentration of 2.5×10^{-7} – 1×10^{-4} M, pH = 2 (a); calibration curves for GA (b).

The calibration curve was constructed by plotting the current density of first anodic peak vs. the concentration of GA. There are two resulting calibration linear plots (Fig. 2 (b)). The higher concentration range is described by the regression equation: $I_p (10^{-7} \text{ A}) = 5.06 \times 10^4 \times C_{GA} + 6.8209$, where I_p is the current density of first anodic peak and C_{GA} is the concentration of gallic acid expressed in mol/L (correlation coefficient, $r = 0.9528$). The lower concentration range is expressed by the relationship: $I_p (10^{-7} \text{ A}) = 3.895 \times C_{GA} + 1.14 \times 10^6$ ($r = 0.9857$), and with detection limit (LOD) of GA determination of $1.48 \times 10^{-7} \text{ M}$. The limiting point, $2.63 \times 10^{-7} \text{ M}$ vs. 6.9310^{-7} A , is obtained by extrapolating of the linear plots. The relative standard deviation for a GA concentration of $5 \times 10^{-5} \text{ M}$ was 0.25% ($n = 3$).

CONCLUSION

The present study is related to the application of complex $[\text{Cu}_2\text{tpmc}](\text{ClO}_4)_4$ immobilized in PVC matrix as a modifier and coated on graphite electrode as a sensor material employed for determination of the gallic acid. Electroactive $[\text{Cu}_2\text{tpmcGA}]^{3+}$ is used as a sensor material for determination of low concentrations of GA at simple coated CGE by sensitive DPV technique. The proposed electrode exhibited the advantage of simple preparation, good reproducibility and electrochemical surface stability. Detection limit obtained by proposed electrode is comparable with those one previously reported in the literature for the determination of GA.

ACKNOWLEDGEMENT

Financial support for this study was granted by the Ministry of Science and Technological Development of the Republic of Serbia, Project Number 45022.

REFERENCES

- [1] M. Naczki, F. Shahidi, *J. Pharm. Biomed. Anal.*, 2006, 41, 1523.
- [2] P. A. Kilmartin, H. Zou, A. L. Waterhouse, *J. Agric. Food Chem.*, 2001, 49, 1957.
- [3] A. Sánchez Arribas, M. Martínez-Fernández, M. Chicharro, *Trends in Analytical Chemistry*, 2012, 34, 78.
- [4] S. Chandrasekhar, W. L. Wallz, L. Prasad, J. W. Quail, *Can. J. Chem.*, 1997, 75, 1363.
- [5] E. Asato, H. Toftlund, S. Kida, M. Mikuriya, K. Murray, *Inorg. Chim. Acta*, 1989, 165, 207.
- [6] B. B. Petković, S. P. Sovilj, M. V. Budimir, R. M. Simonović, V. M. Jovanović, *Electroanalysis* 2010, 22, 1894.

ELECTROCHEMICAL CORROSION STUDIES ON BIOFUNCTIONALIZED STAINLESS STEEL SURFACE

L. Floroian¹, M. Badea², D. Floroian¹, and C. Samoila³

¹*Automation and Information Technology Department, Transilvania University of Brasov, Romania,*

²*Fundamental, Prophylactic and Clinical Specialties Department, Transilvania University of Brasov, Romania,*

³*Materials Science Department, Transilvania University of Brasov, Romania.*

ABSTRACT

A solution is proposed to remove the major inconvenience caused by corrosion of stainless steel implants in human body fluids by coating with thin films of composite polymer-antibiotic-bioactive glass nanostructures. Electrochemical corrosion studies of the coatings under conditions which simulate their biological interaction with the human body were performed. The equivalent electrical circuits that fit the plots of the electrochemical impedance were found. The results support the unrestricted usage of coated stainless steel as a cheap and proper alternative for human implants manufacture.

INTRODUCTION

A significant progress has been observed in development of the materials for different specific applications in medicine and biology [1]. These materials have the ability to behave similar to specific biological tissue. Stainless steel is a very popular metallic material because of its relatively low cost, ease of fabrication and reasonable corrosion resistance [2]. However, stainless steel is susceptible to a number of localized corrosions, such as crevice and pitting, intergranular and stress corrosion cracking. Shortcomings of stainless steel materials during implantation have been reported [3] due to their high nickel content and to the aggressive biological effects. The corrosion products include iron, chromium, nickel and molybdenum and because of their effects [4], stainless steel is used just as temporary implants to help bone healing, as well as fixed implants like in artificial joints.

Here, a solution is proposed to remove the inconvenience caused by corrosion of stainless steel implants in human body by coating with thin

films of polymer-antibiotic-bioactive glasses nanostructures. The resistance to corrosion of the stainless steel implants coated using high sensitive electrochemical methods has been investigated. Electrochemical measurements involving corrosion and electrochemical impedance spectroscopy studies were carried out in physiological solutions in order to investigate the corrosion behavior of the medical grade stainless steels, bare or covered with different bioactive films, and to compare their performance with that of the titanium electrode. The corrosion resistance parameters were inferred and compared. The involved electrochemical parameters were estimated and the electrical parameters of the circuits were found out by fitting the experimental data via equivalent electric circuits.

EXPERIMENTAL

For the deposition of composite polymer-antibiotic-bioglass coatings onto 316 L stainless steel substrates, MAPLE technique was applied. MAPLE was developed after 1998 [5], compulsory for the transfer of delicate materials. A suspension of 0.5% bioglass and 2% doxycycline in a solution of 3% PMMA in chloroform was prepared and frozen. This composition kept at a constant temperature with a liquid nitrogen cooler served as a target for a thin layer deposition on 316L stainless steel substrates. The optimum MAPLE conditions were: 550 mJ/cm² laser fluence, 5000 subsequent laser pulses for the deposition of each structure, substrates placed at 0.03 m separation distance from target.

Electrochemical impedance spectroscopy (EIS) analysis was carried out three times for each sample in the same freshly filled electrochemical cell using PC-controlled system Autolab PGSTAT 100 Eco Chemie by means of FRA 4.9 software. An alternating voltage with 0.01V amplitude was applied, scanning from 10,000 Hz to 0.1 Hz with 10 points per frequency decade, and auto-integration time of 5 s. The software calculates and records the real and imaginary parts of electrochemical impedance (Z_{real} and Z_{imag}) together with the phase and represents them in Nyquist and Bode diagrams. Based upon the principles of electrochemical spectroscopy, the equivalent electric circuit that best fits the experimental data was found with the help of FRA 4.9 software and optimum electrical parameters were

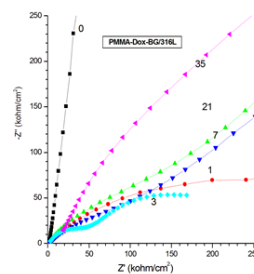


Figure 1. EIS plot of PMMA-Dox-BG61/316L thin films after 0, 1, 3, 7, 21 and 35 days of immersion in SBF.

obtained: electrical resistance of the solution, charge transfer resistance and constant phase element.

RESULTS AND DISCUSSION

The electrochemical evolution of the samples under conditions which simulate their biological interaction with the human body was analysed. To this purpose, samples of PMMA-Dox-BG61 thin films were introduced in SBF at 37° C and the electrochemical impedance spectra were recorded after different immersion times. All measurements were performed in triplicate, in the same single compartment electrochemical cell, freshly filled with appropriate solutions. The EIS plots (the Nyquist diagrams) for all electrodes were recorded in the open circuit potential (OCP) configuration presented in Figure 1. The equivalent electrical circuits that fit the plots of electrochemical impedance were found using FRA 4.9 software.

The Nyquist diagram for bare stainless steel electrode is a semicircle with a very large radius that means the sample behaves like pure capacitive impedance suggesting the presence on the surface of a highly stable film. The equivalent circuit is the Randles circuit from Figure 2. The charge transfer resistance reaches a high value of 9752.17 k Ω /cm², while the capacitance has a very small value of 23.59 μ F/cm².

After 3, 7 or 21 days of immersion in SBF, the Nyquist diagrams show two semicircles that suggest two simultaneous processes: the BG61

dissolution in SBF and the adsorption of some electrolyte ions on surface. The equivalent circuit is $R_s(Q_1[R_1(R_2Q_2)])$ from Figure 3. The BG61 dissolution process is characterized by decreasing of the charge transfer resistance and increasing of the capacitance; a large decrease in the roughness factor n value shows the flat surface degradation due to bioglass dissolution.

In the same time, the condensation and repolymerisation of a SiO₂-rich layer on surface, the migration of PO₄³⁻ and Ca⁺ ions through this layer followed by adsorption on surface forming a carbonated hydroxyapatite HCA film take place. The parallel group $[R_2Q_2]$ corresponds to this outer layer.

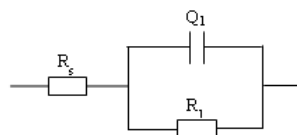


Figure 2. The equivalent circuit $R_s(Q_1R_1)$.

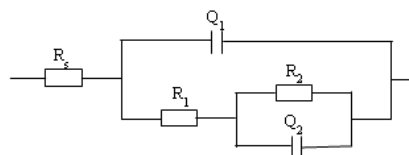


Figure 3. The equivalent circuit $R_s(Q_1[R_1(R_2Q_2)])$.

After 35 days of immersion in SBF, we get a single time constant Nyquist diagram, and the growing of HCA layer only takes place. The new apatite-like layer has an n factor of 0.86 and presents a high charge transfer resistance. This evidence points to the formation on surface of a highly stable compact film, with characteristics close to pure capacitive impedance that shields implant against environmental agents. The EIS fitting generated an equivalent circuit $R_s(Q_1R_1)$ (figure 2).

CONCLUSION

The formation of a hydroxyl carbonate apatite superficial layer was evidenced on PMMA-Dox-BG61/316L samples after immersion in SBF at 37° C as an effect of ions exchange with the fluid, concurrently with the bioglass decomposition. PMMA is not dissolved in SBF but remain on 316L surface. Electrochemical impedance spectroscopy measurements demonstrated that, as an effect of immersion in biological fluids, the stainless steel corrosion is slowed down and the metal ions release into the body is inhibited. More precisely, the nanostructured PMMA-Dox-BG61/316L coating ensures the preservation of the stainless steel surface bioactivity and serves as an efficient shield against corrosion.

ACKNOWLEDGEMENT

This paper is supported by the Sectorial Operational Programme Human Resources Development (SOP HRD), financed from the European Social Fund and by the Romanian Government under the project number POSDRU/159/1.5/S/134378.

REFERENCES

- [1] J. Marciniak, Eng. Biomater, 1997, 1, 12-20.
- [2] K. Yayaa, Y. Khelfaouia, B. Malkib, M. Kerkara, Corrosion Science, 2011, 53 (10) 3309–3314.
- [3] G. Rondelli, P. Torricelli, M. Fini, R. Giardino, Biomaterials, 2005, 26 (7) 739-744.
- [4] M. Cieřlika, W. Reczyńskib, A.M. Janusc, K. Engvalld, R. P. Sochae, A. Kotarbaa, Corrosion Science, 2009, 51 (5) 1157–1162.
- [5] D.B. Chrisey, A. Pique, R.A. McGill, J.S. Horwitz, B.R. Ringeisen, D.M. Bubb, P.K Wu, Chem. Rev., 2003, 103, 553-576.

NEW ELECTROANALYTICAL METHOD FOR SENSITIVE DETECTION OF OCHRATOXIN A

L. Floroian¹, M. Badea², M. Moga², D. Floroian¹,
A.S. Scollo³ and D.A. Perini³

¹*Automation and Information Technology Department, Transilvania
University of Brasov, Romania,*

²*Fundamental, Prophylactic and Clinical Specialties Department,
Transilvania University of Brasov, Romania.*

³*University of Milan, Italy*

ABSTRACT

A new electroanalytical method for sensitive detection of ochratoxin A (OTA), a common toxic contaminant in various kinds of plants products, was reported. A four-step reaction protocol was elaborated to modify the gold electrode and obtain the sensing substrate. All the steps of the immunosensor elaboration and the immunochemical reaction between ochratoxin A and the surface-bound antibody were interrogated using cyclic voltammetry (CV) and electrochemical impedance spectroscopy (EIS). The impedance change, due to the specific immuno-interaction at the immunosensor surface was utilized to detect ochratoxin A. The increase in electron-transfer resistance (Ret) values was proportional to the concentration of OTA in the range of 1–20 ngmL⁻¹, with a detection limit of 0.5 ngmL⁻¹.

INTRODUCTION

Ochratoxin A (OTA) is a mycotoxin produced by *Aspergillus ochraceus* and *Penicillium verrucosum*, known to contaminate a variety of food commodities, such as cereals, coffee beans, beans, grapes, dried fruit. OTA is one of the most toxic compound and widespread from the ochratoxins group. Studies have shown that this molecule can have several toxicological effects such as nephrotoxic, hepatotoxic, neurotoxic, teratogenic and immunotoxic and it is believed to cause increased oxidative stress at a cellular level [1-4]. The concerns about OTA contamination lead to the development of high-performance detection techniques for quality assessment.

In this work a new electroanalytical method were developed based on a four-step reaction protocol to modify the gold electrode for sensitive determination of OTA.

EXPERIMENTAL

Prior to modification, polycrystalline Au electrode was subjected to electrochemical pretreatment by applying 10 potential cycles between 0.0 and 1.5 V/pseudo Ag reference electrode, with 100mVs^{-1} scan rate, in 0.5M sulfuric acid, until the CV characteristic for a clean Au surface is obtained.

The gold electrode was first modified using bovine serum albumin, creating a layer that prevents non-specific binding of OTA on gold and then was activated with N-(3-dimethylaminopropyl)-N'-ethylcarbodiimide / N-Hydroxysuccinimide solution. The ochratoxin A antibody was immobilized and then OTA samples were added.

The electrochemical measurements were carried out with a computer-controlled Autolab PGSTAT100 potentiostat/galvanostat (Eco Chemie, The Netherlands). Screen-printed Au electrodes (SPCEs) were obtained DropSens (Spain). The electrodes incorporate a conventional three-electrode configuration, which comprises a disk-shaped Au working (1.6-mm diameter, ca. 0.02 cm^2 geometrical area, and roughness factors of 1.2–1.4), Au counter and silver pseudo-reference electrodes. The impedance spectra were recorded using a sinusoidal ac potential perturbation of 10 mV (rms), in the frequency range 10^4 to 0.1 Hz, superimposed on a dc potential of +0.128 V, the potential of the redox ferri/ferrocyanide couple $[\text{Fe}(\text{CN})_6]^{4-/3-}$, and readings were taken at 20 discrete frequencies per decade. The impedance spectra were plotted in the form of Nyquist plots. All measurements were performed in a solution of 1mM ferri/ferrocyanide couple (1 + 1 mixture) in KCl 0.1 M, as background electrolyte at room temperature.

RESULTS AND DISCUSSION

EIS can give detailed information on the dielectric constant and barrier properties of the layer changes in the modification process. Figure 1 shows the Nyquist impedance spectra observed upon the stepwise modification

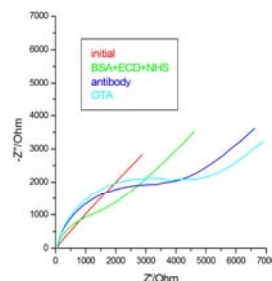


Figure 1. EIS Nyquist spectra of each modification electrode step.

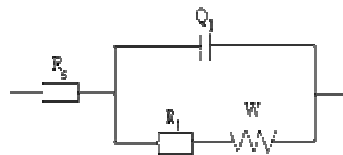


Figure 2. Equivalent circuit.

process. The bare Au electrode reveals an extremely small semicircle domain (red curve), implying a very low electron-transfer resistance R_1 of the redox probe. After the electrode was grafted with BSA-EDC-NHS film, the R_1 was significantly increased (green curve), due to the deposition of an organic layer on the electrode surface with negatively charged terminal carboxylic groups COO^- which acts as an electrostatic barrier that repels the $[\text{Fe}(\text{CN})_6]^{4-/3-}$ anions and hinders the ability of the redox probe to access the layer and regards the electron transfer kinetics between the redox probe and the electrode. Subsequently, antibodies were covalently combined onto the BSA-EDC-NHS modified electrode and a remarkable drop in the R_1 was observed (blue curve). It is likely that the covalent attachment of the antibody to the carboxyl terminus will neutralize the negative charge of BSA-EDC-NHS modified electrode. Afterwards, the R_1 increased when the immunosensor was used to detect the OTA (light blue curve), the OTA binding to surface-bound Ab could offer additional negative charges.

The impedance data were fitted to equivalent circuit shown in the Figure 2 that includes the solution resistance (R_s), the electron transfer resistance (R_1), the constant phase element (Q) and the Warburg impedance element (W).

Ideally, W and R_s represented the bulk properties of the electrolyte solution and diffusion features of the redox probe in solution and, thus, are not affected by modifications of the electrode surface. The changes in R_1 were much larger than those in other impedance components. Thus, R_1 was a suitable signal for sensing the interfacial properties of the prepared immunosensor during all these assembly procedures.

The equivalent circuit parameters of the fitting curves for the various steps of the immunosensor elaboration and the immunochemical reaction between antibody and ochratoxin A were determined.

To evaluate the immunochemical reaction between Ab and OTA, we exposed the Ab/BSA-EDC-NHS/Au electrode to various concentrations of OTA.

It was found that the diameter of the Nyquist circle increased with the adding of OTA. The difference between R_1 before and after incubation with OTA is considered the analytical signal. As it can be seen in Figure 3, there is a steady linear increase in ΔR_1 as OTA concentration increases. This is

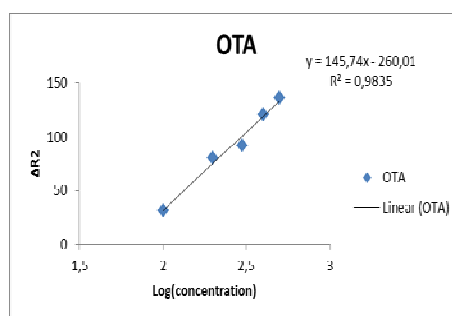


Figure 3. The calibration curve.

the calibration curve which allows to determine the OTA concentration of any solution if its ΔR_1 is known.

CONCLUSION

A new label-free, highly sensitive, cost-effective and fast EIS immunosensor for OTA detection was developed. The casting of the protective BSA layer on the gold electrode prevents any nonspecific binding between OTA and the gold surface, thus enhancing the specificity of the biosensor. The specific Ab-OTA interaction induces an increase in electron transfer resistance showing a greater impedance signal, without any amplification step. The detection of OTA was achieved in EIS on a linear range between 0.01 and 5 ng/mL.

ACKNOWLEDGEMENTS

The writing of this work has received partial funding from the European Community's Seventh Framework Programme (FP7/2007-2013) under grant agreement n° 245199. It has been carried out within the PlantLIBRA project (website: www.plantlibra.eu). This report does not necessarily reflect the Commission views or its future policy on these areas.

REFERENCES

- [1] A. Pfohl-Leskowicz, R.A. Manderville, *Molecular Nutrition & Food Research*, 2007, 51, 61–99.
- [2] N. Adányi, I.A. Levkovets, S. Rodriguez-Gil, A. Ronald, *Biosens. Bioelectron*, 2007, 22, 797–802.
- [3] E. Tully, S.P. Higson, R. O’Kennedy, *Biosens. Bioelectron*, 2008, 23, 906–912.
- [4] J. Wang, J.A. Carlisle, *Diamond Relat. Mater*, 2006, 15, 279–284.

ELECTROCHEMICAL RESPONSE OF *p*- NITROPHENOL AT ORGANOCCLAY MODIFIED GLASSY CARBON ELECTRODE

M. Žunić¹, A. Milutinović-Nikolić¹, D. Stanković², D. Manojlović²,
N. Jović-Jovičić¹, P. Banković¹ and Z. Mojović¹

¹*University of Belgrade- Institute of Chemistry, Technology and Metallurgy,
Center for Catalysis and Chemical Engineering, Njegoševa 12, 11000
Belgrade, Republic of Serbia*

²*University of Belgrade, Faculty of Chemistry, Studentski trg 12-16,
Belgrade, Republic of Serbia*

ABSTRACT

Bentonite clay from seldom investigated locality Mečji Do (MD) in Serbia was organomodified. The organomodification was performed with benzyltrimethylammonium (BTMA) bromide and obtained sample was denoted as BTMA-MD. The clay sample (either Na-enriched clay or BTMA-MD) was deposited as a thin film on glassy carbon electrode (GCE) and tested toward electrooxidation of *p*-NP. Modification of GCE with BTMA-MD significantly increased current density and enhanced the electrode stability at *p*-NP oxidation wave in comparison to bare GCE and GCE electrode modified with Na-enriched clay.

INTRODUCTION

Bentonite clay dominantly consists of smectite minerals. Smectite can be modified with quaternary alkylammonium cations leading to material (organoclay) with different surface properties in comparison with raw clay [1]. Recent papers reported the investigation of organoclays as electrode materials for the detection of ascorbic and uric acids [2], methylparathion pesticide [3], mesotrione herbicide [4], etc.

Phenol and its derivatives, have toxic effects on humans, animals and plants, even at very low concentrations. In particular, *p*-nitrophenol (*p*-NP) is included in the US Environmental Protection Agency List of Priority Pollutants. [5]. Based on these facts, wastewater treatment and detection of *p*-NP in effluents are two major research directions. Electrochemical methods have lately received considerable attention in the determination of phenolic compounds due to advantages like fast response, cheap instrumentation, simple operation, etc. Determination of pollutants using

clay-modified electrode has attracted the attention of electrochemists because of their common availability and their unique properties [6]. In this work bentonite clay from seldom investigated locality Mečji Do in Serbia was modified with benzyltrimethylammonium (BTMA) bromide and the obtained material was denoted as BTMA-MD. Electrochemical investigation toward the electro-oxidation of *p*-NP was performed on a glassy carbon electrode (GCE) support with thin film of homogeneously deposited clay (either Na-enriched or BTMA-MDs).

EXPERIMENTAL

The following chemicals were used as received: benzyltrimethylammonium (BTMA) bromide (Alfa-Aesar) with a purity of 98% and *p*-NP p.a. (CIBA). Bentonite clay was obtained from Mečji Do, Serbia. It was crushed, ground and sieved through a 74 μm sieve. The Na-enriched bentonite (Na-MD) and organoclay (BTMA) were prepared by previously described procedure [7]. The introduced amount of BTMA cations in reaction mixture was equal to CEC value of Na-MD.

X-ray diffraction (XRD) patterns of the powders of Na-MD and the BTMA-MD were obtained using a Philips PW 1710 X-ray powder diffractometer with a Cu anode ($\lambda=0.154178$ nm).

In order to prepare modified electrodes the mixture of clay sample (Na-MD or BTMA-MD) and 10 mass % of carbon black (Vulcan XC72, Cabot Corporation) was homogeneously dispersed in original Nafion® solution (Sigma-Aldrich) using an ultrasonic bath. The 5 μL of the obtained dispersion was dropped onto the GCE surface. The solvent was removed by evaporation at 90 °C. The obtained electrodes were used as working electrodes, the reference electrode was Ag/AgCl in 3 M KCl and Pt foil was the counter electrode. The device used for the electrochemical measurements was 797 VA Computrace, Metrohm (Herisau Switzerland). Cyclic voltammograms (CVs) were recorded at the potential scan rate of 10 mVs^{-1} in 0.1 M H_2SO_4 solution.

RESULTS AND DISCUSSION

The XRD patterns of investigated samples are presented in Figure. 1. The investigate samples dominantly consists of smectite with minor quantities of associated minerals like cristobalite, feldspar and quartz [8]. The larger smectite d_{001} - value of the BTMA-MD indicated that the interlamellar spacing of smectite was expanded by the intercalated BTMA cations.

The obtained d_{001} value of 1.47nm corresponded to monolayer arrangement of BTMA cations between smectite layers [9].

The electrochemical behavior of *p*-NP on the freshly prepared bare and clay modified GCE was studied using multisweep cyclic voltammetry and the obtained CVs are presented in Figure. 2.

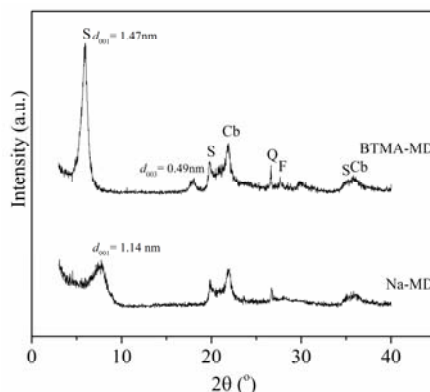


Figure. 1. XRD of investigated clays (S = Smectite, Cb = Cristobalite, F = Feldspar, Q = Quartz).

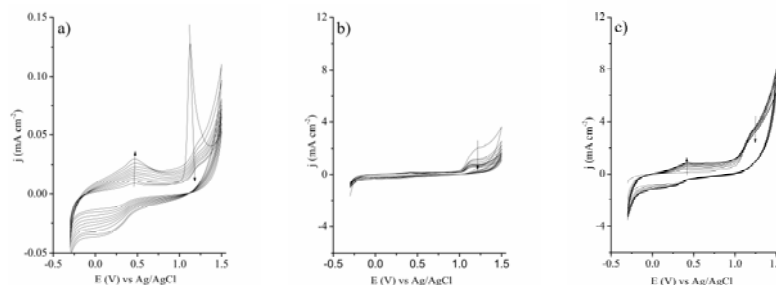


Figure. 2. CVs in 10 mM *p*-NP+0.1 M H₂SO₄ of (a) bare GCE electrode (80 times enlarged scale) and clay-based electrodes: (b) Na-MD; (c) BTMA-MD. The scan rate was 10 mV s⁻¹. Arrows indicate changes during cycling.

The obtained currents for bare GCE were 15-26 times lower than the currents obtained for clay-modified GCE. Also, bare GCE displayed a rapid loss of activity. The obtained current densities at *p*-NP oxidation wave in the first and tenth cycle are summarized in Table 1.

Table 1. Current densities at *p*-NP oxidation wave in the first (I) and tenth (X) cycle and relative decrease of current density after ten cycles.

Sample	j_I [mA cm ⁻²]	j_X [mA cm ⁻²]	$(j_I - j_X)/j_I$ [%]
Bare GCE	0.13	0.02	84.6
Na-MD	2.03	0.56	72.4
BTMA-MD	3.36	3.00	10.8

Modification of GCE with Na-MD or BTMA-MD significantly increased current densities at *p*-NP oxidation wave in comparison to bare GCE. Also, it can be observed (Table 1) that incorporation of BTMA cations in structure of smectite dramatically improved stability of clay modified electrode.

CONCLUSION

Bentonite clay from seldom investigated locality Mečji Do (MD) in Serbia was Na-enriched (Na-MD) and organomodified with benzyltrimethylammonium (BTMA-MD). The XRD data confirmed monolayer arrangement of BTMA intercalated in smectite. The glassy carbon electrode (GCE) containing either Na-MD or BMA-MD clay, was tested in the electrooxidation of *p*-NP in acidic media. The results indicated that the incorporation of BTMA into smectite enhanced the electrode stability toward the electrooxidation of *p*-NP in comparison with bare GCE and modified GCE containing Na-MD. The current density for the *p*-NP oxidation wave was highest for BTMA-MD.

ACKNOWLEDGEMENT

This work was supported by the Ministry of Education, Science and Technological Development of the Republic of Serbia (Project III 45001 and ON 172030).

REFERENCES

- [1] L. Zhu, X. Ren, S. Yu, *Environ. Sci. Technol.* 1998, 32, 3374-3378.
- [2] J. C. K. Mbougouen, I. T. Kenfack, A. Walcarius, E. Ngamenia, *Talanta* 2011, 85, 754-762.
- [3] H. L. Tcheumi, I. K. Tonle, E. Ngameni, A. Walcarius, *Talanta* 2010, 81, 972-979.
- [4] J. K. Wagheu, C. Forano, P. Besse-Hoggan, I. T. Kenfack, E. Ngameni, C. Mousty, *Talanta* 2013 (103) 337-343.
- [5] Toxic Substance Control Act, US Environmental Protection Agency, Washington, DC, 1979.
- [6] C. Mousty, *Appl. Clay Sci.* 2004, 27, 159-177.
- [7] N. Jović-Jovičić, A. Milutinović-Nikolić, P. Banković, Z. Mojović, M. Žunić, I. Gržetić, D. Jovanović, *Appl. Clay Sci.* 2010, 47, 452-456.
- [8] International Center for Diffraction Data - Joint Committee on Powder Diffraction Standards, Powder diffraction data, Swarthmore, PA, USA, 1990.
- [9] F. Bergaya, G. Lagaly, in: *Developments in Clay Science, Handbook of Clay Science*, second ed, Vol. 5A, F. Bergaya, G. Lagaly (Eds.), Elsevier Ltd, Amsterdam, 2013.

INFLUENCE OF PROPERTIES OF METAL CATIONS ON THEIR REMOVAL BY ELECTROPERMUTATION

A.Mehellou¹, R.Delimi¹, Z. Benredjem¹ and C. Innocent²

¹Laboratory of Water Treatment and Valorization of Industrial Wastes, Department of Chemistry, Faculty of Sciences, Badji-Mokhtar University, P.O. Box 12, 23000, Annaba, Algeria. Fax: +213 38 87 27 50.

E-mail: rachid.delimi@univ-annaba.dz

²Institut Européen des Membranes, Univ. Montpellier 2, CNRS, ENSCM CC 047 place Eugène Bataillon, 34095 Montpellier cedex 5, France.

Fax: +33 467 14 91 19. E-mail: christophe.innocent@univ-montp2.fr

INTRODUCTION

The pollution of surface waters by heavy metals is considered hazardous to human health and the environment [1]. The EP using ion-exchange resin was revived by Strathmann and Kock [2] for treating effluents containing lead ions. However, few works have been reported on the study of the phenomena governing the process of this method as well as the correlation between them. In this respect the present work was undertaken to investigate the correlation between the properties of the bivalent metallic cations and their transfer processes using electropermutation (EP) from diluted solutions. In this study, four metallic cations which exist frequently in wastewaters namely Cd(II), Zn(II), Pb(II) and Mg(II) were selected

EXPERIMENTAL

The EP process was realized using a laboratory Plexiglas cell with five compartments, all of which had the same dimensions. The width, the length and the thickness were 2.3, 3.3 and 1 cm respectively. These compartments were separated by cation exchange membranes (CEMs) and anion exchange membranes (AEMs) with an effective area of 7.59 cm², equal to the area of each platinized-titanium electrode. The central compartment was packed by wet cation exchange resin (CER) and fed with the same solution under opened circuit mode.

The initial concentration of the fed was 10⁻³ eq.L⁻¹ for each metallic cation. The applied current density and the flow rate of the fed solution were 10 mA.cm⁻² and 3 mL.min⁻¹ respectively. The nature of regenerating acid solutions was HNO₃, HCl and H₂SO₄.

RESULTS AND DISCUSSION

Influence of the cation-exchange membrane nature

The removal of the metal cations is followed by measuring their transfer flow. The significance of the transfer is different from one metallic cation to another, but for all the tested CEMs, the transfer flux follows the order: $J_{\text{Pb(II)}} > J_{\text{Cd(II)}} \geq J_{\text{Zn(II)}} > J_{\text{Mg(II)}}$. Based on what Kielland and Marcus [3] have reported, the classification of metallic cations in terms of decreasing hydration ionic radius follows the order: $r_{\text{Mg(II)}} > r_{\text{Zn(II)}} \geq r_{\text{Cd(II)}} > r_{\text{Pb(II)}}$. Thus, we conclude that the significance of the transfer of metal cations varies in the opposite direction of their hydration radii

Table 1: Average molar flux (J) and transport number ($t_{\text{M(II)}}$) of metallic cations through different CEM in EP process.

CEM	J(10^{-8} mol.s $^{-1}$) and $t_{\text{M(II)}}$							
	Cd(II)		Zn(II)		Pb(II)		Mg(II)	
CMX	2.742	0.069	2.424	0.061	3.422	0.087	1.815	0.046
CDS	2.618	0.066	2.358	0.059	3.170	0.080	1.588	0.040
N-117	2.548	0.064	2.367	0.060	2.998	0.076	2.180	0.055

The transfer flux results (Tab.1) show that, except for Mg(II) with N-117, the importance of transfer flux of metallic cations in terms of the nature of CEMs follows the order: $J_{\text{M(II)}}(\text{CMX}) > J_{\text{M(II)}}(\text{CDS}) > J_{\text{M(II)}}(\text{N-117})$. For the metallic cations transfer, the membrane CMX seems to be more efficient compared to the others.

Influence of the nature of electro-regeneration cation

The results presented in Table 2 show that, the EP process gives removal rates varying between 89 and 99 %. The order of removal rates variation in terms of the nature of cation of electro-regeneration is: $R_{\text{M(II)}}^{\text{R}}(\text{H}^+) > R_{\text{M(II)}}^{\text{R}}(\text{NH}_4^+) > R_{\text{M(II)}}^{\text{R}}(\text{Na}^+)$. It is important to note that this order is similar to the metallic cations order transfer.

Table 2: Removal rate (R^{R}) of metallic cations by EP process with different electro-regeneration cation. CEM: CMX; Co-ion: NO_3^- .

Electro-regeneration cation	$R^{\text{R}}(\%)$			
	Cd(II)	Zn(II)	Pb(II)	Mg(II)
H^+	99.6	99.5	99.8	99.2
Na^+	92.2	91.5	94.9	89.5
NH_4^+	95.7	92.1	97.4	90.1

Calculated values of $\frac{\bar{D}_{Pb}}{D_{Mg}}$ are lower than 0.4. That is opposed to the case of aqueous solution where it is greater than unity, as shown in the literature

$$[4]: \frac{D_{Pb}}{D_{Mg}} = 1.34$$

CONCLUSION

- The importance of the metallic cations transfer through the CEMs tested changes according to the same order of their affinities towards the IEMs: $J_{Pb(II)} > J_{Cd(II)} \geq J_{Zn(II)} > J_{Mg(II)}$.
- The transfer order of the metallic cations varies in reverse order of the hydration ionic radius of these cations: $r_{Mg(II)} > r_{Zn(II)} \geq r_{Cd(II)} > r_{Pb(II)}$.
- The transfer flux of the metallic cations based on the nature of CEMs follows the order: $J_{M(II)}(CMX) > J_{M(II)}(CDS) > J_{M(II)}(N-117)$.
- The nature of the electro-regeneration cations has a neat influence on their transferred quantities and removal rates which are in the order: $(H^+) > (NH_4^+) > (Na^+)$.
- The obtained removal rates were in the range 89 - 99%.

REFERENCES

- [1] K.A. Graeme and C.V. Pollack, J. Emerg. Med., 1998, 16, 45-56.
- [2] H. Strathmann and K. Kock, J. Am. Chem. Soc., 1980, 102, 139-Poly.
- [3] Y. Marcus, Ionic Radii in Aqueous Solutions, Chem Rev, 1988, 88, 1475-1498.
- [4] D.R. Lide, Handbook of Chem. and Phys., 83rd, CRC Press, LLC, 2002-2003.

ASSESSMENT OF ANTIOXIDANT ACTIVITY OF SOME PHENOLIC COMPOUNDS BY POLAROGRAPHY

J. Dimitrić Marković¹, B. Pejin², S. Gorjanović³, F. Pastor⁴, Z. S. Marković⁵ and D. Sužnjević³

¹*University of Belgrade, Faculty of Physical Chemistry, Belgrade, Serbia.
(markovich@ffh.bg.ac.rs)*

²*University of Belgrade, Institute for Multidisciplinary Research - IMSI,
Department of Life Sciences, Belgrade, Serbia.*

³*Institute of General and Physical Chemistry, Belgrade, Serbia.
(desanka.suznjevic@gmail.com)*

⁴*University of Belgrade, Faculty of Chemistry, Belgrade, Serbia.*

⁵*State University of Novi Pazar, Department of Biochemical and Medical
Sciences, Novi Pazar, Serbia.*

ABSTRACT

Antioxidant (AO) activity of three phenolic natural compounds, namely delphinidin, malvin and pelargonidin, was determined using direct current polarographic assay based on decrease of anodic current originating from hydroxoperxydroxomercury(II) complex formed in alkaline solutions of hydrogen peroxide at potential of mercury oxidation. The slope of the dependence between the percentage of the decrease and volume of gradually added samples (linear part) were used to express AO activity. Delphinidin showed the highest AO activity (33 ± 5 %/ μmol) followed by pelargonidin (28 ± 1 %/ μmol) and malvin (24 ± 1 %/ μmol). The experimental results obtained are in good agreement with the existing literature data.

INTRODUCTION

The pigments anthocyanins, one of the most widely distributed classes of flavonoids in plants, possess ability to scavenge free radicals; their most common aglycon forms are anthocyanidins delphinidin and pelargonidin (Fig. 1). Different substituents in ring B of these compounds are considered to be responsible for differences in their antioxidant (AO) activity.

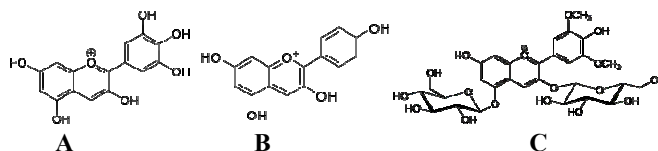


Figure 1. Anthocyanidins (a. delphinidin & b. pelargonidin) and anthocyanin (c. malvin)

Actually, many assays have been applied to determine AO activity of phenolics including anthocyanins and anthocyanidins. Direct current (DC) polarographic assay based on decrease of anodic current originating from hydroxoperhydroxomercury(II) complex (HPMC) formation in the alkaline solutions at potential of mercury oxidation has recently been developed and optimized [1]. Until now this assay has been applied on various samples, both phenolics and non-phenolics [1-3]. However, the AO activity of delphinidin, malvin and pelargonidin has not been evaluated before with DC polarographic assay. Hence, this study aims to give an insight into AO activity of selected natural products using the aforementioned assay, comparing the experimental data with the results for other classes of phenolic compounds (benzoic acids and their cinnamic analogues, flavonons and flavan-3-ols) previously obtained using the same assay.

EXPERIMENTAL

The current-potential (i-E) curves were recorded, as described previously [1], using the polarographic analyser PAR (Princeton Applied Research), model 174A, equipped with X-Y recorder (Houston Omnigraphic 2000). A dropping mercury electrode (DME) with a programmed dropping time of 1 s as working electrode, saturated calomel electrode (SCE) as a reference and a Pt-foil as auxiliary electrode were used. Polarograms were recorded from potential of 0.1 V towards negative direction with a scan rate of 10 mV/s. Samples (4 mM) were gradually added (5 aliquots of 50 μ L) into 20 mL of starting 5 mM hydrogen peroxide (Merck Darmstadt, Germany) in Clark & Lubs (CL) buffer (pH 9.8). The solutions of delphinidin chloride, malvin (malvidin-3,5-diglucoside) and pelargonidin chloride (Sigma-Aldrich, Munich, Germany) were prepared immediately before i-E curves recording.

RESULTS AND DISCUSSION

The AO activity of delphinidin, malvin and pelargonidin were assessed using DC polarography. As an example, polarograms of 5 mM solution of hydrogen peroxide in CL buffer (pH 9.8) recorded before and after the addition of 5 aliquots of malvin are showed herein (Fig. 2). Remaining anodic limiting current (i_{lr}) obtained upon addition of natural products tested

was compared with height of initial limiting current (i_{l0}), while percentage of i_l decrease was calculated upon each addition. A dose-dependent effect on HPMC anodic current was observed. Plot of percentage of i_l decrease calculated upon each addition vs malvin concentration is also shown (Fig. 2, insert).

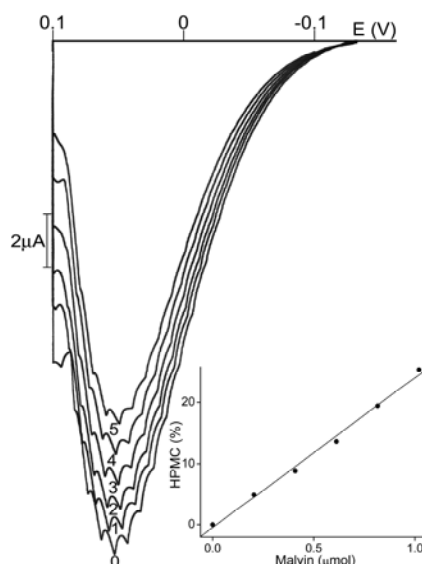


Figure 2. Polarographic curves obtained by gradual addition of malvin (4 mM) in 5 aliquots of 50 μ L in 20 mL of buffered (CL buffer, pH 9.8) solution of 5 mM hydrogen peroxide. Insert: percentage of decrease of anodic limiting current (i_l) vs malvin added (μ mol).

The slope of the linear part of dose-response curves has been used as criterion of AO activity. The highest activity has been ascribed to delphinidin with three OH groups in B ring (33 ± 5 %/ μ mol) followed by pelargonidin with only one OH group (28 ± 1 %/ μ mol). The degree of hydroxylation in the B ring is likely to affect AO activity as previously showed by other assays [4,5]. Lower activity of malvin (24 ± 1 %/ μ mol) is also in accordance with the existing literature data [4]. Indeed, sugar moiety is believed to decrease the AO ability of anthocyanins. It's worth noting that these experimental data are in good agreement with those one obtained using standard spectrophotometric DPPH [4] and EPR superoxide anion radical assays [5]. According to DC polarographic assay used, these anthocyanidins exhibited lower AO activity than flavan-3-ols, but significantly higher than cinnamic and benzoic acids (Fig. 3) [1-3].

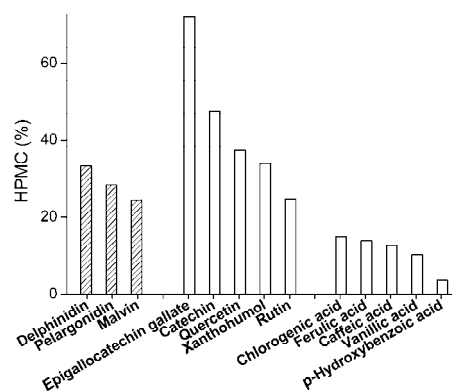


Figure 3. Antioxidant activity of various natural products assessed by DC polarographic anodic wave of hydroxoperxydroxomercury(II) complex (HPMC).

CONCLUSION

According to the best of our knowledge, this is the first report of AO activity of selected natural products assessed by polarography. Further studies will include computational approach aiming to give detailed insight into observed antioxidant potential of common anthocyanidins and anthocyanins using DC polarographic anodic wave of hydroxoperxydroxomercury(II) complex (HPMC).

ACKNOWLEDGEMENT

This work was supported by the Ministry of Education, Science and Technological Development of the Republic of Serbia (Research Grants Nos. 172015, 172053, 31093 and 43010).

REFERENCES

- [1] D. Sužnjević, F. Pastor, S. Gorjanović, *Talanta*, 2011, 85,1398-1403.
- [2] S. Gorjanović, D. Komes, F. T. Pastor, A. Belščak-Cvitanović, L. Pezo, J. Hečimović, D. Sužnjević. *Journal of Agricultural and Food Chemistry*, 2012, 60, 9573-9580.
- [3] S. Gorjanović, F. T. Pastor, R. Vasić, M. Novaković, M. Simonović, S. Milić, D. Sužnjević. *Journal of Agricultural and Food Chemistry*, 2013, 61, 9089-9096.
- [4] M. P. Kahkonen, M. Heinonen, *Journal of Agricultural and Food Chemistry*, 2003, 51, 628-633.
- [5] Y. Noda, T. Kaneyuki, A. Mori, L. Packer. *Journal of Agricultural and Food Chemistry*, 2002, 50, 166-171.

MICELLIZATION OF CETYLTRIMETHYLAMMONIUM BROMIDE IN ACETONITRILE–WATER MIXTURE: A CONDUCTIVITY STUDY

A. Janošević Ležaić, A. Malenović, J. Goronja, and N. Pejić

*University of Belgrade–Faculty of Pharmacy, Vojvode Stepe 450, 11000
Belgrade, Serbia, E-mail: ajanosevic@yahoo.com*

ABSTRACT

The effect of the dipolar aprotic solvent, acetonitrile (ACN), on the micellization of cationic surfactant, cetyltrimethylammonium bromide, CTAB, was studied by conductance method. Specific conductivity of CTAB in ACN–water (10/90 v/v) binary mixtures was measured in the temperature range of 20.0–35.0 °C. The critical micelle concentrations, CMC were estimated from the dependence of the specific conductivity on surfactant concentration. It was found that the CMC is temperature dependent. Moreover, the values of CMC decreased to a certain minimum and then increased with the temperature, displaying a U-shaped behavior.

INTRODUCTION

Cetyltrimethylammonium bromide, CTAB is cationic surfactant widely used as antiseptic, solubilizing agent for pharmaceuticals, in electrophoresis of proteins, in hair conditioning products, and so forth. Because of its amphiphilic nature, the CTAB molecules aggregate to form micelles in solution. The minimum concentration at which the phenomenon of micellization starts is the so-called critical micelle concentration, CMC. Micellization is highly dependent on different factors: solvent nature, additives such as cosolvent and cosurfactants, temperature, *etc.*

It is well known that the behavior of a surfactant solution is greatly influenced by the presence of even very small amounts of organic compounds. A particular organic additive may affect the process of micellization either by being incorporated into the micelles or by modifying the solvent-surfactant or solvent-micelle interaction. The investigation of cosolvent influence on micellar and physicochemical properties of surfactants has wide interests in both the fundamental and in the applied research, considering significant application of surfactants in water-free or water-poor media (as lubricants or cleaners).

In our earlier work [1] we reported the effects of cosolvent (propylen glycol, PG) on the micellization of CTAB in PG–water (30/70 v/v) binary mixture.

In the present paper our study is extended to the ACN since this additive is generally used in the mobile phase in micellar liquid chromatography and micellar electrokinetic chromatography. In these techniques, CMC is necessary to predict solute retention (and hence the separation selectivity). Also, ACN as cosolvent can be used in different industrial processes including surfactants. Thus, in this work, determination of the CMC of CTAB in ACN–water (10/90 v/v) binary mixture at different temperatures (20.0–35.0 °C) by conductometric measurements, was achieved.

EXPERIMENTAL

The conductivity measurements of the examined surfactant system were carried out with digital conductivity meter HI8820N (Hanna instruments, Portugal) with the accuracy $\pm 0.5\%$, and with the matching HI17684W probe that uses the 4-ring method. Specific conductivity values of each set containing 15 different CTAB concentrations at a fixed solvent composition were taken at different temperatures (20.0, 25.0, 30.0 and 35.0 °C). A circulating water bath was used for maintaining those temperatures within uncertainties of ± 0.2 °C.

RESULTS AND DISCUSSION

The CMC value of CTAB in ACN–water (10/90 v/v) binary mixture was determined from inflection in plot of specific conductivity, κ against concentration of CTAB, c_{CTAB} at a given temperature. The obtained plot, $\kappa = f(c_{\text{CTAB}})$ is a curve which consists of two segments (premicellar and postmicellar); each plot shows the single break point, at a certain temperature. The data points above and below the inflection were fit by the least square method ($R \geq 0.998$ in all cases) to two equations of the form: $\kappa = A + S \times c_{\text{CTAB}}$, and by two equation solving, the point of intersection, CMC was obtained.

Fig. 1. shows representative conductivity versus concentration for CTAB in ACN–water (10/90 v/v) mixture, at $T = 20.0$ °C. The obtained CMC were: 1.55 mmol L^{-1} (20.0 °C), 1.41 mmol L^{-1} (25.0 °C), 1.56 mmol L^{-1} (30.0 °C) and 1.76 mmol L^{-1} (35.0 °C).

The CMC decreased to a certain minimum point and then increased with temperature increase (Fig. 2.). Fig 2. is 3rd-order polynomial function fitted to the CMC ($R = 1$). Minimum of function correspond to $\text{CMC}^* = 1.403 \text{ mmol L}^{-1}$ and $T^* = 24.3$ °C. The reduced both CMC and temperature, $\text{CMC}_r = \text{CMC}/\text{CMC}^*$ and $T_r = T/T^*$, for examined surfactant system were determined from CMC^* and T^* . Moreover, the effect of temperatures on the CMC can be shown by the power law: $\ln|\text{CMC}_r - 1| = \ln A + n \ln|T_r - 1|$. The

obtained characteristic exponent, n is 1.5. This quantity is a bit higher than CTAB–water system value [3].

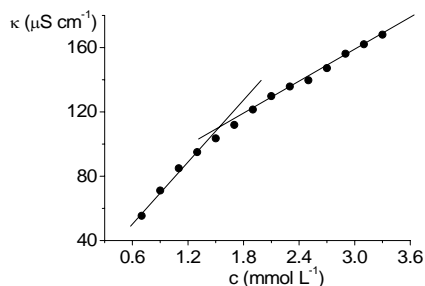


Figure 1. Plot of specific conductivity, κ versus total concentration of CTAB, c_{CTAB} in ACN–water mixture (10% (v/v)) at 20.0 °C

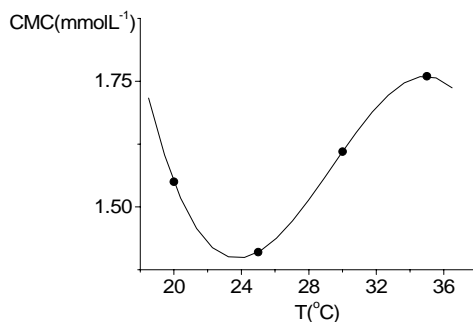


Figure 2. CMC of CTAB in ACN–water mixture (10% (v/v)) as a function of temperature

CONCLUSION

Micellization of CTAB in ACN–water (10/90 v/v) binary mixtures is affected by temperature. In the examined temperature range of 20.0 – 35.0 °C, the CMC decreases to a minimum value and then increases, displaying U-shaped behavior. The obtained both minimum CMC and temperature are $\text{CMC}^* = 1.403 \text{ mmol L}^{-1}$ and $T^* = 24.3 \text{ }^\circ\text{C}$. Furthermore, the temperature CMC dependences can be described by a power law between CMC_r and T_r from which the characteristic exponent $n = 1.5$ is obtained.

ACKNOWLEDGEMENT

This work was partially supported by the Ministry for Education, Science and Technological Development of the Republic of Serbia (Grants no. 172015 and 172052).

REFERENCES

- [1] N. Pejić, A. Janošević, J. Rogić, N. Paunović, *Arh. Farm.*, 2012, **62**, 429–442.
- [2] P. Carpena, J. Aguiar, P. Bernaola-Galván, C. Carnero Ruitz, *Langmuir*, 2002, **18**, 6054–6058.
- [3] G.D. Noudeh, M. Housaindokht, B.S.F. Bazzaz, *J. App. Sci.*, 2007, **7**, 47–52.

ELECTROCHEMICAL BEHAVIOR OF QUINOXALINE AT GLASSY CARBON AND BORON DOPED DIAMOND ELECTRODE

J.Pantić, M. M. Aleksić¹ and V.Kapetanović²

University of Belgrade, Faculty of Pharmacy, ¹Department of Physical Chemistry and Instrumental methods maras@pharmacy.bg.ac.rs ²Department of Analytical Chemistry, Vojvode Stepe 450, 11000 Belgrade, Serbia

ABSTRACT

The electrochemical behavior of Quinoxaline (QUI) was investigated by cyclic (CV), differential pulse (DPV) and square wave (SW) voltammetry using glassy carbon (GCE) and boron doped diamond electrode (BDDE). Chloride, acetate, phosphate and ammonia buffers (pH 2.0-10.0) were used as supporting electrolytes and pH influence on electrochemical behavior of QUI was analyzed. The reduction of QUI occurs as quasi-reversible reaction in acid medium, reaching the full reversibility in alkaline solutions. Reduction process involves the transfer of two electrons and two protons at the pyrazine ring of quinoxaline. In acid solutions QUI reduction product is further oxidized in one electron process irreversibly. The nature of electrode processes was found to be controlled by diffusion.

INTRODUCTION

Quinoxaline, also called as benzopyrazine (Fig. 1.) is heterocyclic compound containing benzene and pyrazine ring. Pyrazines are stable, colorless compounds soluble in water [1,2]. QUI exists in three different forms in solutions, depending on pH value. Theoretically [2], at pH<1.2 both nitrogen atoms are protonated, in pH range 1.2 – 4.0 one nitrogen atom is deprotonated, while at pH > 4 both of them are deprotonated. The electrochemical behavior of quinoxalines is significantly influenced by the pH due to the protonation of its electroactive groups.

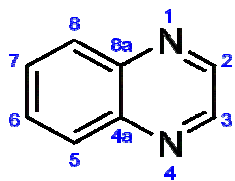


Figure 1. QUI structure

As a result of this the shift of the peak potential can be observed. QUI represents the basic part in the structure of some antibiotics [1], preparations for smoking cessation (Varenicline), antiglaucoma agents (Brimonidine) [3,4] and recently it has been used as an antineoplastic drug [1] in cancer treatment.

EXPERIMENTAL

The voltammetric measurements were performed with an μ Autolab analyzer (EcoChemie, Utrecht, The Netherlands). Three-electrode system was employed: Ag/AgCl as reference electrode, Pt-auxiliary electrode, and GCE and BDDE electrodes as working electrodes. Before each experiment the GCE and BDDE were manually polished using the aqueous slurry of Al_2O_3 powder (particle size $0.05\mu\text{m}$) on a smooth polishing pad, rinsed with bidistilled water and then sonicated in absolute ethanol. To improve the electroanalytical response, after polishing, BDDE was either cathodically or anodically pretreated to obtain hydrogen or oxygen-terminated electrode [3]. Cathodic and anodic pretreatment were done in 0.25 moldm^{-3} H_2SO_4 by applying the potential of -1.5 V and $+1.2\text{ V}$ for 60 s , respectively. Chloride, acetate, phosphate and ammonia buffers were used as supporting electrolytes. An appropriate volume of supporting electrolyte of different pHs were placed in electrochemical cell, de-aerated for 10 minutes with high purity nitrogen and QUI stock solution was added to make its final concentration of $1\times 10^{-4}\text{ moldm}^{-3}$, $2\times 10^{-5}\text{ moldm}^{-3}$ and $5\times 10^{-5}\text{ moldm}^{-3}$ for CV, DPV and SW, respectively. The cyclic voltammograms were recorded at scan rate ranged $10 - 100\text{ mVs}^{-1}$. The experimental parameters for DPV were: pulse width 50 ms , scan rate 5 mVs^{-1} and pulse amplitude 50 mV . For SWV the following conditions were selected: frequency 25 Hz and potential increment 2 mV , corresponding to an effective scan rate of 50 mVs^{-1} , and the pulse amplitude of 100 mV .

RESULTS AND DISCUSSION

The redox behavior of $1\times 10^{-4}\text{ moldm}^{-3}$ QUI was initially studied by CV in 0.1 moldm^{-3} acetate buffer pH 5.4. The cyclic voltammograms were recorded in three successive scans starting from 0.0 V , towards -1.35 V and reversing to the positive potential limit of $+1.45\text{ V}$, at a scan rate 100 mVs^{-1} . Both electrodes showed similar behavior. On the first negative-going scan, one cathodic peak (I_c) was obtained at $E_p \sim -0.6\text{ V}$. Changing the scan direction, one main anodic peak (I_a) appeared at $E_p \sim -0.5\text{ V}$ and one additional anodic peak (II_a) at potential $E_p = +0.15\text{ V}$ at GCE, and $E_p = +0.25\text{ V}$ at BDDE were noticed. Recording the cyclic voltammograms in the opposite direction starting from 0.0 V going to $+1.45\text{ V}$ and reversing to -1.35 V under the same conditions, the second anodic peak (II_a) was not present in the first scan, but it appeared in the second and third scan (Fig. 2.). All recorded CVs at different pH values indicate the same behavior at both electrodes: the irreversibility of process represented by second anodic peak (II_a), and the partial reversibility (increasing with pH) of the process

represented by cathodic and first anodic peaks (I_c and I_a). The reduction peak (I_c) exists at all investigated pH values, and the peak potential was shifted to more negative values with increasing pH.

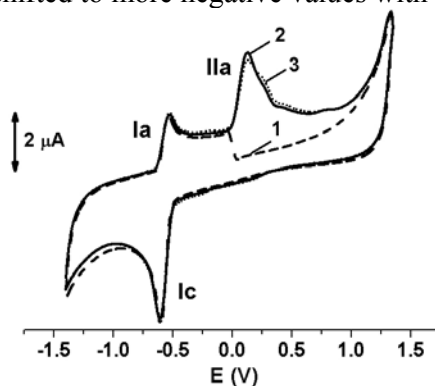


Figure 2. CV of $1 \times 10^{-4} \text{ mol dm}^{-3}$ QUI, pH 5.4; (---) first, (—) second and (···) third scan in the positive direction at scan rate of $v=100 \text{ mVs}^{-1}$

The linear dependence of E_p vs. pH was obtained following the equations: $E_{p,Ic} = -0.339 \text{ V} - 0.051 \text{ V} \times \text{pH}$ at GCE, and $E_{p,Ic} = -0.330 \text{ V} - 0.059 \text{ V} \times \text{pH}$ at BDDE. Both slopes of 51 mV and 59 mV suggested the same number of electrons and protons involved in the reduction process. Analyzing the difference between peak potential and half-height peak potential, the number of electrons transferred in the rate determining step is found to be $n = 2$, suggesting that the reduction occurs with the transfer of two electrons and two protons.

Cyclic voltammograms were recorded at different scan rates ranged from 10 to 100 mVs^{-1} . A linear dependence of $\log I_{p,Ic}$ vs. $\log v$ was obtained at all investigated pH using both electrodes. The corresponding slopes which were always less than 0.5 indicated the diffusion controlled process.

The oxidation peak (I_a) exists also at all investigated pH values, and the peak potential was shifted to more negative values with increasing pH. The linear dependence of E_p vs. pH with slopes of 57 mV (at GCE) and 53 mV (at BDDE), as well as the difference between peak potential and half-height peak potential, also suggested that two electrons and two protons are involved in this redox process. Second oxidation peak (IIa) is present at both electrodes at $\text{pH} < 7$. Its peak potential and intensity are pH dependent. Results indicate that the process is irreversible, diffusion controlled, and involves the transfer of one electron and one proton.

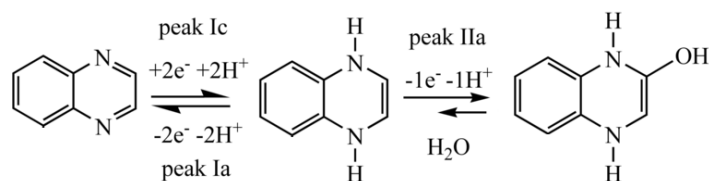
The width at the half height of the DPV peaks I_c and I_a representing redox process at the pyrazine ring recorded in 0.1 mol dm^{-3} acetate buffer pH 3.6, indicates the transfer of two electrons what is in accordance with the results obtained by CV. Second DPV anodic peak, IIa, showed the width at the half height of $W_{1/2} \sim 120 \text{ mV}$ indicating that the oxidation of the QUI reduction product occurs with the transfer of one electron.

Square wave voltammetry is a powerful technique with possibility to reveal if the electron transfer reaction is reversible or not, based on sampling the

current in positive and negative-going pulses at the same time, so peaks that correspond to the reduction and oxidation may be obtained at the same time in the same scan. SW voltammograms were recorded at pH 2.15, 3.6 and 8.0. One peak corresponding to peak Ic was obtained in total cathodic current. In acid medium peak current in backward component was lower than in forward one, while at pH 8.0 forward and backward current components were equal, confirming redox process to be quasi-reversible reaction in acid medium, reaching the full reversibility in alkaline solutions. To investigate the oxidation process, SW voltammograms were recorded in the opposite direction. In the backward component of the I_{IIa} peak current, a small peak appears with lower peak current in backward component than in forward one, indicating the process being not completely irreversible as suggested by CV, but more likely, quasi-reversible.

CONCLUSION

According to the results obtained, the redox mechanism of QUI at GCE and BDDE was postulated and presented in the Scheme 1. The mechanism established could be very useful and recognizable for further studies of structurally similar compounds containing this ring.



Scheme 1. Electrochemical redox mechanism of QUI

ACKNOWLEDGEMENT

This work was supported by the Ministry of Education, Science, and Technological Development of the Republic of Serbia, Grant no. 172033.

REFERENCES

- [1] K. Patidar, M. Jeyakandan, A. K. Mobiya, G. Selvam, *PharmTech*, 2011, 3, 386-396.
- [2] A. Albert, J. N. Phillips, *J. Chem. Soc.* 1956, 1294-1304.
- [3] V. Radulović, M. Aleksić, V. Kapetanović, D. Agbaba, *Electroanalysis*, 2013, 25, 230-236.
- [4] M. Aleksić, V. Radulović, V. Kapetanović, D. Agbaba, *Electrochim. Acta*, 2013, 106, 75-81.

VOLTAMMETRIC AND THEORETICAL STUDY OF CEPHALOSPORINS AT THE MERCURY ELECTRODE

K. Nikolić¹, M. M. Aleksić² and V. Kapetanović³

¹*Department of Pharmaceutical Chemistry, ²Department of Physical Chemistry and Instrumental Methods (maras@pharmacy.bg.ac.rs)*

³*Department of Analytical Chemistry, Faculty of Pharmacy, University of Belgrade, Vojvode Stepe 450, 11000 Belgrade, Serbia*

ABSTRACT

Study of the electroreduction behavior and adsorption of seven cephalosporins at the mercury electrode surface has been performed using Adsorptive Stripping Differential Pulse Voltammetry (AdSDPV). The Quantitative Structure Property Relationship (QSPR) study of the cephalosporins adsorption at the mercury electrode, based on the density functional theory B3LYP/6-31G(d,p) calculations of molecular parameters, explains well the process of adsorption of the examined cefpodoxime proxetil, cefotaxime, desacetylcefotaxime, cefetamet, ceftriaxone, ceftazidime, and cefuroxime axetile. QSPR study defined that cephalosporins with lower electron density on the nitrogen atom of the N-O bond, lower charge of sulphur in the thiazine moiety, higher principal moment of inertia and higher number of hydrogen bond accepting groups should express high adsorption on the mercury electrode.

INTRODUCTION

Methoxyimino cephalosporins are semi-synthetic β -lactam antibiotics bearing methoxyimino group in the side chain at C7 position, which is reducible at mercury electrode. The modern voltammetric techniques for electrochemical study and determination of low concentrations of cephalosporins *in vivo* are based on the adsorptive accumulation of cephalosporins at DME and solid electrodes as well. [1-6].

The reduction mechanism of the methoxyimino cephalosporins at DME was established and reported in our previous papers [7-11]. Now we extend our AdSDPV study on structurally related ceftriaxone, ceftazidime, and cefuroxime axetile and performed QSPR study on the whole cephalosporin's data set. To our knowledge, there is no experimental or theoretical study on the relationship between cephalosporine structure properties and electrochemical behavior.

EXPERIMENTAL

Cephalosporins (CEF) were from Sigma and all chemicals were of analytical grade quality. The Britton-Robinson (BR) universal buffer was prepared from stock solutions of 0.04M boric, orthophosphoric and acetic acids with the appropriate volumes of 0.2M NaOH.

Selection of dominant molecules/ions species at experimental pH 2.0-3.5 have been performed using the Marvin 5.5.1.0 program. The minimum energy conformations of the analyzed compounds were obtained by using the B3LYP hybrid functional included in the 3-21G basis set (B3LYP/3-21G). Molecular descriptors of the obtained molecular models were computed by MarvinSketch 5.1.5.0, Chem3D Ultra 7.0.0 and CS Gaussian 98 (B3LYP/6-31G (d, p) programs. The experimentally determined slope ($\Delta i_p/\Delta v$) and the computed molecular parameters of the examined cephalosporins were used to build the Partial Least Square regression (PLS) - QSPR model and to examine electrochemical adsorption and electro-reduction mechanism of the cephalosporins.

RESULTS AND DISCUSSION

The mechanism of the metoxyimino cephalosporins at DME confirmed that cephalosporins reduction was mostly complicated by the effects of adsorption at the electrode surface.

The symmetrical shape of voltammetric peaks of cefpodoxime, cefotaxime, desacetylcefotaxime and cefetamet, as well as the pronounced maxima of the curves presenting the current intensity vs. pH, indicated the strong adsorption of these compounds at mercury surface. The linear dependence of i_p vs. v is also characteristic for adsorption controlled processes, and the higher slope is obtained when the adsorption is more pronounced. The experimentally obtained slopes ($\Delta i_p/\Delta v$, Table 1) indicates the electrochemical adsorption at the mercury electrode for some cephalosporins investigated. It is obvious that the adsorption prevails in an acid medium. The differences observed between the investigated compounds are the consequence of specific adsorption and different orientation of these molecules at the mercury surface. It was established that more the bulky C7 substituent was, the adsorption was more pronounced. Since all these compounds possess the 2-aminothiazole ring at C7, which is planarly oriented to the mercury surface, it may be assumed that this ring has a great role in adsorption. The presence of NH_3^+ group of aminothiazole ring in acid medium, contributes to the adsorption, due to the electrostatic forces with mercury surface in the negative potential range. Also, the presence of electron donors, as nitrogen and oxygen atoms in the side chain,

increases the adsorption of metoxyimino cephalosporins, due to the electron density increase of thiazole ring.

Although the substituent in C2 and C3 position shows less contribution to the adsorption related to C7 substituent, the presence of these different structures causes the difference in adsorption characteristics. Therefore, more complex structure of cefpodoxime proxetile and ceftriaxone related to desacetilcefotaxime and cefetamet explains more strongly pronounced adsorption.

The QSPR study of ceftriaxone, cefpodoxime proxetile, ceftazidime, cefotaxime, desacetilcefotaxime, cefuroxime axetile, and cefetamet adsorption at the mercury electrode, was performed by use of the PLS regression. In the QSPR study, the experimentally determined slope ($\Delta i_p/\Delta v$), obtained with use of the AdSDPV technique on the mercury electrode, were used as dependent variables, while the computed molecular parameters of the examined compounds were considered as independent variables. Optimal combination of the most relevant descriptors (HBA, Electron Density of Nitrogen of the N-O bond (ED(N)), PMIY, HBA-HBD, PSA, MR, ClogP, Radius, and Mulliken Charge of Sulphur in the thiazine moiety (Chrg(S)) for QSPR models building were selected on basis of the R^2 , Q^2 , RMSEP values of the obtained PLS models. The PLS-QSPR-model with three significant components, $R^2=0.990$, $Q^2=0.907$, with the lowest RMSEP (4.074) and the highest r^2 (Obs vs. Pred; 0.995), was selected for further study (Table 1). The obtained statistical parameters of the PLS-QSPR model pointed on a good prognostic capacity of the developed QSPR model (Table 1). Prediction of the slope ($\Delta i_p/\Delta v$), with use of the developed PLS-QSRR-model, can be applied to the other related cephalosporins.

Table 1. Observed and QSPR-predicted electrochemical adsorption on the mercury electrode (slope ($\Delta i_p/\Delta v$)).

Compound	Slope ($\Delta i_p/\Delta v$) [$\mu\text{AV}^{-1}\text{S}$]	QSPR-Predicted slope ($\Delta i_p/\Delta v$) [$\mu\text{AV}^{-1}\text{S}$]
Ceftriaxone (+/-, +)	134.07	131.172
Cefpodoxime proxetile	65.80	70.531
Ceftazidime	35.56	33.735
Cefotaxime	17.40	22.870
Desacetilcefotaxime	16.30	19.774
Cefuroxime axetile	14.43	10.052
Cefetamet	13.70	9.126

Total Charge Density Maps on the molecular orbital surfaces have confirmed higher electron densities around the nitrogen of the cephalosporins with lower adsorption on the mercury electrode surface, such as cefotaxime, desacetilcefotaxime, cefuroxime-axetile, and cefetamet.

CONCLUSION

Our AdSDPV study of the electro-reduction behaviour and adsorption of metoxyimino cephalosporins on a mercury electrode surface has been extended on a different, but structurally closely related cephalosporins, ceftriaxone, ceftazidime, and cefuroxime axetile.

The QSPR study defined the influence of the most significant molecular parameters on adsorption at the mercury electrode surface.

Prediction of the electrochemical adsorption ($\Delta i_p/\Delta v$) with use of the PLS-QSPR model is a very helpful tool which could be applied to the other related cephalosporins.

ACKNOWLEDGEMENT

This work was partially supported by the Ministry for Science of the Republic of Serbia (Grants no. 172033).

REFERENCES

- [1] G. Bernacca, L. Nucci, F. Pergola, *Electroanalysis*, 1994, 6, 327-332.
- [2] S. Altinoz, A. Temizer, *J. Pharm. Sci.*, 1990, 79, 351-353.
- [3] M. Avramov-Ivić, V. Kapetanović, M.M. Aleksić, P. Zuman, *J. Serb. Chem. Soc.*, 2000, 65, 47-53.
- [4] B. Dogan, A. Golcu, M. Dolaz, S.A. Ozkan, *Curr. Pharm. Anal.*, 2009, 5, 197-207.
- [5] P. Nigam, S. Mohan, S. Kundu, R. Prakash, *Talanta*, 2009, 77, 1426-1431.
- [6] Q. Xu, A.J. Yuan, R. Zhang, X. Bian, D. Chen, X. Hu, *Curr. Pharm. Anal.*, 2009, 5, 144-155.
- [7] M.M. Aleksić, V. Kapetanović, J. Atanacković, B. Jocić, M. Zečević, *Talanta*, 2008, 77, 131-137.
- [8] M.M. Aleksić, Lj. Milovanović, V. Kapetanović, *J. Pharm. Biomed. Anal.*, 2003, 32, 957-966.
- [9] M.M. Aleksić, M. Ilić, V. Kapetanović, *J. Pharm. Biomed. Anal.*, 2004, 36, 899-903.
- [10] M.M. Aleksić, V. Kapetanović, *J. Electroanal. Chem.*, 2006, 593, 258-266.
- [11] P. Zuman, V. Kapetanović, M.M. Aleksić, *Anal. Lett.*, 2000, 33, 2821-2857.

***IN SITU* EVALUATION OF INTERACTION BETWEEN VARENICLINE AND DNA USING DNA-ELECTROCHEMICAL BIOSENSOR**

N.Lijeskić, M.M. Aleksić¹ and V. Kapetanović²

¹*Department of Physical Chemistry and Instrumental Methods
(mara@pharmacy.bg.ac.rs),*

²*Department of Analytical Chemistry, University of Belgrade, Faculty of
Pharmacy, Vojvode Stepe 450, 11000 Belgrade, Serbia*

ABSTRACT

The interaction between Varenicline (VAR) and DNA was investigated by square wave voltammetry (SWV) using DNA-modified glassy carbon electrode as biosensor in acetate buffer pH 4.6. A SW voltammogram of DNA layer at DNA-electrochemical biosensor showed two anodic peaks corresponding to the oxidation of deoxyguanosine ($E_p = +1.03V$), and deoxyadenosine ($E_p = +1.28V$). A SW voltammogram of VAR shows one peak ($E_p = +0.22V$) due to the oxidation of Varenicline reduction product. Binding interaction was investigated by incubating DNA-electrochemical biosensor for 10 min in the VAR solution. Recorded SW voltammogram showed change in intensity of the VAR, deoxyguanosine and deoxyadenosine peaks due to the interaction.

INTRODUCTION

The development of an electrochemical DNA-biosensor that can be used to sense *in vivo* oxidative damage of DNA is of crucial importance. In health preventing perspective, detection of *in vivo* oxidative damage to DNA can be very useful for screening the effect on DNA caused by different oxidizing substances, especially carcinogens. For this purpose voltammetric methods are very suitable since they are inexpensive and fast procedures. Electrochemical DNA-biosensors can be used to investigate the interaction of drug substances with double helix DNA in order to determine the type of the specific interaction between drugs and DNA base pairs, and to elucidate electrochemical mechanism of the interaction. This kind of research helps understanding the real action scenario that occurs in living cell [1].

There are two main binding modes between drugs and DNA: covalent and non-covalent. The most common mode of non-covalent binding is intercalation. Intercalation results from insertion of a planar aromatic system between dsDNA base pairs [2]. An electrochemical biosensor for detecting

DNA-drug interaction consists of an electrode with DNA layer on its surface. DNA-electrochemical biosensors enable the study of the interaction of DNA immobilized on the electrode surface with analytes in solution, with DNA acting as a promoter between the electrode and the substance under study. Interactions of the surface-confined DNA with a DNA damaging agent are converted, via changes in electrochemical properties of the DNA recognition layer, into measurable electrical signals [3].

VAR was used as model molecule for investigation of DNA-drug interaction. VAR is quinoxaline derivative. Quinoxaline is planar aromatic molecule and represents the basic part in the structure of some anticancer drugs [4]. According to the structure and activity of similar compounds the interaction of VAR and DNA may be predicted.

EXPERIMENTAL

In this study square wave (SW), and cyclic voltammetry (CV) were used. The measurements were performed with μ Autolab analyzer (EcoChemie, Utrecht, The Netherlands) in three-electrode system containing glassy carbon working electrode (GCE), Ag/AgCl reference and Pt-auxiliary electrode. Acetate buffer pH = 4.6 was used as supporting electrolyte. The DNA-electrochemical biosensor was prepared by successively covering the GCE surface with three drops of $100 \mu\text{g mL}^{-1}$ DNA solution in 0.1 mol dm^{-3} acetate buffer, pH 4.6. After placing each drop on the top of the electrode surface, the electrode was dried under a flux of N_2 , and the multilayer DNA biosensor was formed.

Varenicline modified GCE was prepared by immersing the electrode in $100 \mu\text{g mL}^{-1}$ VAR solution in 0.1 mol dm^{-3} acetate buffer, pH 4.6, for 10 min without potential applied. After washing in water in order to remove the unbound varenicline molecules, modified electrode was placed in pH 4.6, 0.1 mol dm^{-3} acetate buffer electrolyte and SW voltammogram was recorded. Before each experiment the GC electrode surface was polished manually with aqueous slurry of Al_2O_3 powder ($\varnothing 0.05 \mu\text{m}$) on a smooth polishing pad, then sonicated for 2 min in ethanol. All reagents were p.a. purity grade. Standard of VAR was kindly donated by ALIMS. Double-stranded calf thymus DNA was purchased from Sigma-Aldrich.

RESULTS AND DISCUSSION

Electrochemical behavior of VAR was studied by using CV. In the whole pH range one cathodic peak with E_p ranged from -0.4 V at pH 2.0 up to -0.90 V at pH 12.0, appears when the potential was scanned within the range of 0.00 V to -1.20 V . Changing the scan direction slightly pronounced anodic peak appeared at potentials similar to the cathodic peak, indicating

the quasi-reversibility of the process. With further increasing of positive potential, second anodic peak appeared at E_p ranged from 0.4 V at pH 2 to 0.03 V at pH 8. Recording the cyclic voltammograms in the opposite direction, starting from 0.0V, going to +1.6V and reversing to -1.2 V under the same conditions, the second anodic peak was not present in the first scan, but it appeared in the second scan. According to this result and having in mind that reduction process is not fully reversible, second anodic peak probably corresponds to the irreversible oxidation of VAR reduction product formed at GCE surface during the first scan.

The scan rate studies were carried out to assess whether the process at the electrode surface was under diffusion or adsorption control. Using the concentration of 2.5×10^{-4} mol dm⁻³ of VAR at different pH values, the voltammetric peak currents were followed as the scan rate was varied over the range of 5 - 100 mVs⁻¹. The linear response of I_p vs. scan rate was obtained (I_p (A) = $233 v$ (Vs⁻¹) + 6.905, $r=0.994$, pH=4), indicating the adsorption nature of the electrode process. This was confirmed by the slope of the plot of the logarithm of the peak current vs. logarithm of the scan rate which was between 0.5 and 1.0 what is characteristic for the adsorption controlled processes.

Varenicline strong and irreversible adsorption on the surface of electrode was used for making varenicline-modified electrode. Varenicline modified GCE was prepared by placing the 20 μ L drop of 100 μ g mL⁻¹ VAR solution

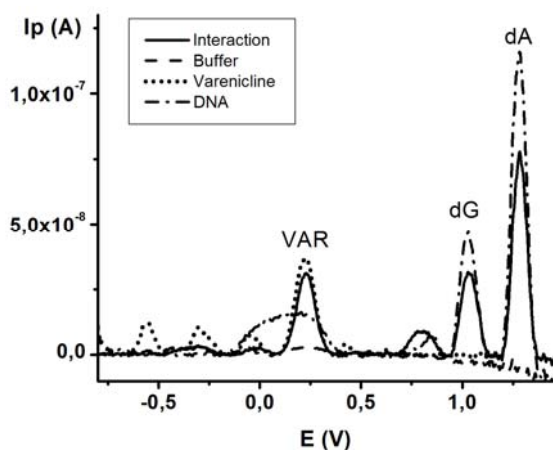


Figure 1. SW voltammograms in 0.1 mol dm⁻³ acetate buffer pH 4.6: VAR (···), DNA (---) and DNA-VAR interaction (—), buffer(---),

obtained. SW voltammogram of DNA layer at DNA-electrochemical

for a 10 min accumulation period without potential applied. Recorded SW voltammogram of VAR adsorbed on GCE showed one peak ($E_p = +0.22$ V) due to oxidation of VAR reduction product (Fig.1.).

SW voltammetry method was optimized for electrochemical oxidation of DNA layer at DNA-electrochemical biosensor using experimental design.

Optimal conditions: pH 4.6, frequency 25 Hz, potential increment 1 mV, and pulse amplitude 5 mV, were

biosensor showed two anodic peaks corresponding to the oxidation of deoxyguanosine, dG, ($E_p = +1.03$ V), and deoxyadenosine, dA, ($E_p = +1.28$ V) as presented in Fig.1.

Interaction was studied by comparing SW voltammograms obtained on Varenicline modified GCE, DNA modified GCE and incubating DNA-electrochemical biosensor for 10 min in the $100 \mu\text{g mL}^{-1}$ VAR solution (0.1 mol dm^{-3} acetate buffer, pH 4.6). Recorded SW voltammogram showed decreased peaks of the VAR ($\Delta I_p = 10$ nA), deoxyguanosine ($\Delta I_p = 17$ nA) and deoxyadenosine ($\Delta I_p = 42$ nA) due to the binding interaction. The effect of the incubation time on the DNA-VAR interaction was also investigated.

CONCLUSION

The decrease of VAR peak intensity indicates its consumption from the adsorbed layer. The decrease of DNA oxidation peaks may be attributed to the mechanism that involves condensation and formation of more rigid structures due to the intercalation of VAR into DNA strands [5] what leads to the conformational changes in the DNA structure.

All these results proved the interaction between DNA and VAR at modified glassy carbon electrode. This study used simple electroanalytical methodology and showed the potential use of DNA/GCE biosensor for investigation of DNA-drug interaction and potential genotoxic effects.

REFERENCES

- [1] M. Oliveira-Brett, V. C. Diculescu, A. M. Chiorcea-Paquim, S. H. P. Serrano, in *Comprehensive Analytical Chemistry*, Vol 49, S. Alegret, A. Merkoc (Eds.) *Electrochemical Sensor analysis (ECSA)*. Section F. *Biosensors*, 2007, vol 49, p. 413-437.
- [2] R. Palchaudhuri, P. J Hergenrother, *Current Opinion in Biotechnology*, 2007, 18, 497–503.
- [3] K Odenthal, J Gooding, *Analyst*, 2007, 132, 603–610.
- [4] M. N. Noolvi, H. M. Patel, V. Bhardwaj, A. Chauhan, *European Journal of Medicinal Chemistry*, 2011, 46, 2327–2346.
- [5] A. D. Rodrigues Pontinha, S. M. Alves Jorge, A.M. Chiorcea Paquim, V. C. Diculescu, A.M. Oliveira-Brett, *Physical Chemistry Chemical Physics*, 2011, 13, 5227–5234.

KINETICS OF HYDROGEN EVOLUTION REACTION ON COBALT ELECTRODE IN AQUEOUS CHLORIDE SOLUTIONS.

H. Tissaoui¹, J. Bouteillon² and M. Molteni².

¹*LTEVDI, Département de Chimie, Faculté des Sciences, Université de Annaba, BP 12, 23000 Algérie.*

²*LEPMI, ENSEEG, BP75 38402 St Martin D'Hères, France.*

ABSTRACT

The hydrogen evolution reaction on cobalt electrode in aqueous chloride solutions was studied by performing current-potential measurements. The experiments were made in the 17.5-46.5°C temperature range. The pH of the studied solutions varied in the range 1.90 to 6. The cathodic polarization curves were plotted at different angular speed rotating disc electrode varying from 500 to 5000 rev/min. From this study it was found that the reaction proceeds via the Butler-Volmer mechanism and the kinetic parameters of the process were determined.

INTRODUCTION

The relative position of cobalt and hydrogen in the scale of standard potentials leads to a continuous competition for the deposition of these two elements. Hydrogen evolution weakens the current efficiency of cobalt and creates polarization phenomena [1]. The preferred orientation and the mechanical behavior of deposits, their hydrogen content and internal stresses depend primarily on the deposition rates of cobalt and hydrogen [2]. Depending on the pH and on the applied potential or current, the hydrogen evolution reaction occurs simultaneously with cobalt electrodeposition [3].

EXPERIMENTAL

A temperature-controlled cell used. The working electrode was a cobalt ("J. M. products", 99.99% purity) rotating disk embedded in a Teflon tube. A platinum rod was used as the counter electrode; the reference electrode was a SCE. The supporting electrolyte was sodium chloride. The pH value was adjusted from 1 to 6, by using HCl and the experiments were carried out at temperatures ranging from 17.5 to 46.5 °C. The cobalt disk electrodes were polished with abrasive papers (grade 600 and 1200), then with 6 and 1 micrometer diamond pastes. Finally, the electrodes were washed for 10 minutes with acetone under an ultrasonic field, rinsed with deionised water,

just before the experiment. The electrolyte was flushed for 15 minutes by an argon flow before the electrochemical studies, which were carried out using a potentiostat-galvanostat EG&G PAR Model 273.

RESULTS AND DISCUSSION

A series of experimental stationary polarisation curves obtained at pH = 1.9 are reported on figure 1. The proton reduction wave starts from $E = -0.6$ V/SCE, whereas the Nernst H_2/H^+ equilibrium potential is equal to -0.36 V/SCE. The proton reduction is slow and limited by diffusion only at very negative potentials, and can be considered as a quasi-reversible reaction.

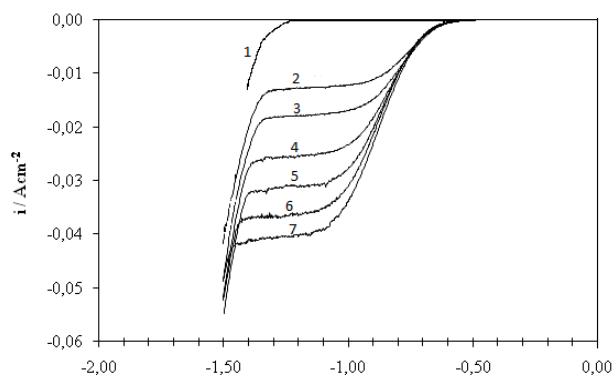


Figure 1 : The steady polarization curves related to the hydrogen evolution on a rotating cobalt disc electrode, for various electrode rotation speeds. Temperature : 17,5 °C, electrolyte : NaCl 1M, pH=1,90, 1: neutral NaCl solution (1M), 2 :500 rpm, 3 : 1000 rpm, 4 : 2000 rpm, 5 : 3000 rpm, 6 : 4000 rpm, 6 : 5000 rpm.

A well known procedure [4], involving the study of the dependence of i on ω , makes it possible to determine kinetics data from the mixed region of the $i(E)$ curve. Moreover, for cathodic overpotentials $\eta_c < -2.3RT/2(1-\alpha)nF$, it is not necessary to consider both the forward and backward reactions, and the equation $i(\omega)$ simplifies to: $1/i = 1/i_{act,H_2/H^+} + 1/i_{\infty,H^+}$ (1)

Thus, taking into account the expressions of $i_{act,H_2/H^+}$, the activation current density related to the H_2/H^+ couple, and i_{∞,H^+} , the convective diffusion current density limit of H^+ :

$$i_{act,H_2/H^+} = i_0 \exp(-(1-\alpha_{H^+})F\eta/RT) \quad (2)$$

$$i_{\infty,H^+} = 1.61v^{1/6}/nF(H^+)_0D_{H^+}^{2/3}\omega^{1/2}, \quad (3)$$

equation (1) becomes:

$$1/i = 1/i_0 \exp(-(1-\alpha_{H^+})F\eta/RT) + 1.61v^{1/6}/nF(H^+)_0D_{H^+}^{2/3}\omega^{1/2} \quad (4)$$

Plots of $1/i$ versus $f(1/\sqrt{\omega})$ reported on figure 2 were drawn for several

values of the potential selected in the range -0.85 to -1.01 V/ECS. The currents used to construct figure 2 were corrected for base line current.

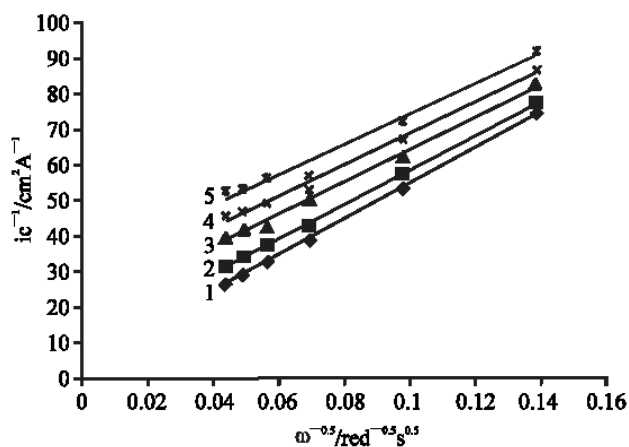


Figure 2: i_c^{-1} ($A^{-1} cm^2$) vs $\omega^{-0.5}$ ($rad^{-0.5} s^{0.5}$) curves related to hydrogen evolution on a rotating disc electrode, for various cobalt electrode potentials: 1: -1.01 V/SCE, 2: -0.948 V/SCE, 3: -0.90 V/SCE, 4: -0.875 V/SCE, 5: -0.85 V/SCE, 6: -0.80 V/SCE.

These plots are linear and reasonably parallel, in keeping with equation (4). They intercept the $1/i$ axis at negative values which correspond to the activation current density. The corresponding (i , η) couples of values reported on table 1 are used to obtain the Tafel plot related to the H_2/H^+ exchange.

Table 1: A series of (i , η) values related to the H_2/H^+ exchange.

η (V)	-0.650	-0.588	-0.540	-0.514	-0.494
$I / (A cm^{-2})$	0.256	0.098	0.054	0.041	0.032

The exchange current density obtained is $i_{0,H^+/H_2} = 4.2 \cdot 10^{-5} A \cdot cm^{-2}$, the cathodic transfer coefficient computed from the slope is 0.33. This value is comparable to that found by Peraldo Bicelli [5] The kinetics of the reduction of the proton on a cobalt electrode can be described by a classical Butler-Volmer equation [6]:

$$I_c (A/cm^2) = - i_{0,H^+/H_2} \exp [- \beta n F \eta / RT] = - 4.2 \cdot 10^{-5} \exp [-0.33 F \eta / RT]$$

The plot of the limiting current density of convective diffusion of proton in

function of the square root of the angular speed of rotating disc electrode shows that the Levitch's law is checked for each temperature and the diffusion limited current density of the reduction of the proton increases with temperature. The plot of the limiting current density of convective diffusion of proton in function of the square root of the angular speed of rotating disc electrode shows that the Levitch's law is checked for each temperature and the diffusion limited current density of the reduction of the proton increases with temperature. The values of the diffusion coefficient of the proton, at different temperatures, are reported in Table 2. Values are comparable to those in the literature [7].

Table 2: values of diffusion coefficients of proton at different temperatures

Température/°C	17,5	28,5	36	46,5
$D \cdot 10^5 / \text{cm}^2 \cdot \text{s}^{-1}$	4,70	5,5	6,2	7,05

The variation of the diffusion coefficient with temperature satisfies the Arrhenius law. The quantity $\ln(D/\text{cm}^2/\text{s})$ is a linear function $f(1/T)$:

$$\ln(D / \text{cm}^2 / \text{s}) = 1270.2 T^{-1} - 5.6369$$

The value of the activation energy of the proton diffusion calculated from the slope of the line is 10.56 kJ / mol.

CONCLUSION

The kinetics of the reduction of the proton on a cobalt electrode can be described by a classical Butler-Volmer equation. The exchange current density measured in NaCl 1M, at pH=1,90 and temperature = 17,5 °C was equal to $4.2 \cdot 10^{-5} \text{A} \cdot \text{cm}^{-2}$, the cathodic transfer coefficient computed from the slope is 0.33. The values of the diffusion coefficient of the proton, at different temperatures, were determined and the value of the activation energy of the proton diffusion calculated is 10.56 kJ / mol.

REFERENCES

- [1] C. Feneau, R. Breckpot, *Métallurgie IX*, 1969, 3, 115-125.
- [2] A.C. Fank, P.T.A Sumodjo, *Electrochimica Acta* 2014, 132, 75-82.
- [3] S. Floate, M. Hyde, *J. Electroanal. Chem.* 2002, 523, 49-63.
- [4] D. Pletcher, *Instr. Meth. in Electrochemistry*, Ellis Horwood, 1985.
- [5] L. Peraldo Bicelli, *J. Analytical Chemistry* 1975, 63, 238-244.
- [6] A. J. Bard, L. R. Faulkner, *Electrochimie*, Masson 1983
- [7] C. Robert, *Hand book of chemistry and physics* 66th ed. CRC Press 1986

PSEUDOCAPACITANCE BEHAVIOR OF POLYANILINE IN AERATED HCl AND H₂SO₄ SOLUTIONS

M. Vujković¹, M. Milenković¹, M. Jevremović², M. Gizdavić Nikolaidis³,
D. Stanisavljev¹ and S. Mentus¹,

¹*Faculty of Physical Chemistry, University of Belgrade, Studentski trg 12-16, P.O. Box 137, Belgrade, Serbia.*

²*Public Company Nuclear Facilities of Serbia, 12-14 Mike Petrovica Alasa, Vinca, 11351 Belgrade, Serbia*

³*School of Chemical Sciences, The University of Auckland, Private Bag 92019, Auckland 1142, New Zealand*

^{*}*The Serbian Academy of Science and Arts, Kenz Mihailova 35, 11158 Belgrade, Serbia*

ABSTRACT

High conducting polyaniline (PANI) nanofibres deposited onto glassy carbon support were studied in sulphuric (1 mol dm⁻³ H₂SO₄) and hydrochloric (1 mol dm⁻³ HCl) acid by both potentiodynamic and complex impedance methods. A large charge storage capacity was obtained in each of investigated acid solutions, particularly in HCl one. For instance, specific capacity amounting to 340 Fg⁻¹ was observed potentiodynamically in 1 mol dm⁻³ HCl at a scan rate of 10 mVs⁻¹.

INTRODUCTION

Over the past years, the use of polyaniline (PANI) in various fields of advanced technology including electronics, catalysis, energy storage, sensors, biochemistry and so on, was the focus of active research. Thanks to an electrochemical reversibility of redox reactions, stability in various environments and significantly lower cost compared to metal-based oxides, PANI has attracted enormous interests in the field of supercapacitor applications [1]. The aim of this study was to examine the capacity storage performance of polyaniline nanofibers prepared by oxidative polymerization of aniline using an oxidizing agent KJO₃ in a strong acidic solution.

EXPERIMENTAL

PANI nanofiber structures were synthesized by a facile method described in a previous report [2]. KJO₃ (0.432 g) was added to an aqueous solution of 1.25 mol dm⁻³ hydrochloric acid (12 ml) followed by addition of 0.48 ml of aniline under stirring for 10 minutes. The reaction mixture was filtered and

washed thoroughly with distilled water and acetone, and finally isolated PANI precipitate was dried in a vacuum oven at 40 °C overnight.

For electrochemical investigations, the working electrode was made from the synthesized material (85%), carbon black (10%) and poly(vinylidene fluoride) (PVDF) binder (5% PVDF solution) homogeneously mixed in N-methyl 2-pyrrolidone. The slurry was treated for about 40 min in an ultrasonic bath, deposited homogeneously on a conductive support, and dried under vacuum at 120 °C for 4h. The electrolytes were 1 mol dm⁻³ HCl and 1 mol dm⁻³ H₂SO₄.

Both cyclic voltammetric (CV) and impedance measurements were performed in a three-electrode type electrochemical cell, with the Pt as counter electrode, and saturated calomel electrode (SCE) as reference electrode, connected to Gamry PCI4/300 Potentiostat/Galvanostat. Impedance measurement was performed within the frequency range between 10⁻²-10⁵Hz by applying an AC signal of 5mV amplitude.

RESULTS AND DISCUSSION

As reported previously [2], the PANI has dominantly nanofibrillar morphology, and displays the high electronic conductivity of 2.69 S cm⁻¹. Figure 1 shows the cyclic voltammograms obtained by potentiodynamic cycling of PANI at 20mVs⁻¹ in the potential range between -0.2 and 0.8V vs. SCE in aqueous solutions of 1mol dm⁻³ HCl and 1mol dm⁻³ H₂SO₄.

The presence of the pseudocapacitive cathodic and anodic peaks is associated to the reversible redox processes of PANI in acidic aqueous medium [3]. The first couple of oxidation/reduction peaks positioned at ~0.27/0.06 V vs. SCE corresponds to transition between reduced leucoemeraldine and emeraldine salt. The broad peak positioned at 0.5 V vs. SCE is generally attributed to the formation of benzoquinone degradation products and formation of cross-linked polyaniline chains by direct reaction between parts of the polyaniline chain itself. Further oxidation of emeraldine salt is associated by further doping by ions so pernigraniline salt is obtained [3]. However, potential was swept up to 0.8V vs. SCE in order to avoid PANI

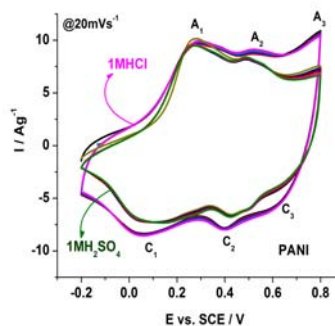


Figure 1. Potentiodynamic cycling of PANI in acidic electrolytes during first ten cycles

overoxidation and thus ensure excellent stability of capacity upon initial cycling as evidenced by overlapping of CV curves. Having in mind that electrochemical capacitance is proportional to the area under the CV curves, obviously, somewhat better charge storage of PANI was achieved in HCl than in sulfuric solution.

Figure 2 shows the CVs of PANI in 1 mol dm^{-3} HCl and 1 mol dm^{-3} H_2SO_4 recorded at different scan rates. The CVs kept its basic shape at all scan rates, indicating stable and reproducible capacitance behavior. The values of capacity obtained by integration of corresponding CV curves are presented in Table 1.

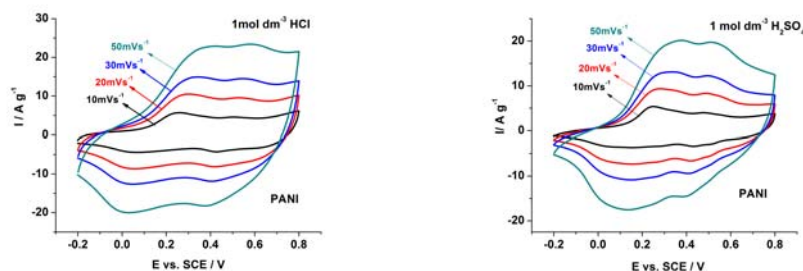


Figure 2. Cyclic voltammograms of PANI in 1 mol dm^{-3} HCl (left) and 1 mol dm^{-3} H_2SO_4 (right) recorded at different scan rates

Table 1. Specific gravimetric capacitance (Fg^{-1}) of PANI calculated from cyclic voltammetry measurements at different potential scan rates.

Scan rates/ mVs^{-1}	Anodic capacitance / Fg^{-1}		Cathodic capacitance Fg^{-1}	
	HCl	H_2SO_4	HCl	H_2SO_4
10	340.6	264	314.3	240.8
20	323.4	251	310.3	238.1
30	307.9	237	299.4	228.9
50	279.4	220	273.8	215.3
100	227.2	192	222.8	189.2

Specific capacitance decreases with the increase of the scan rate, which is a common behavior of all supercapacitor, attributed to limited ability of ions to penetrate into surface pores at higher current rates. At the scan rate of 10 mVs^{-1} , capacity in HCl solution amounted to 340 Fg^{-1} which is in the range of N-doped carbonized PANI-based materials [4]. Higher capacitance in HCl was evidenced at all scan rates and can be attributed to lower charge of Cl^- ions vs. SO_4^{2-} ions [3]. The lowest efficiency, expressed as the ratio of cathodic and anodic capacitance at 10 mVs^{-1} , can be attributed to the

formation of some higher amount of irreversible pernigraniline form upon cycling compared to the one formed at higher sweep rates.

The differences in the charge storage abilities in HCl and H₂SO₄ solutions was observed also by impedance measurements. Figure 3 shows the frequency dependence of capacity in both acidic aqueous electrolytes at a common applied voltage of 0.47 V vs SCE. As found by CV method, higher capacities in HCl solutions, may originate from easier accessibility of Cl⁻ ions to the pores of PANI surface. From Figure 3 it can be observed that the capacitance value still remains high up to 1 Hz which is very important from the practical point of view.

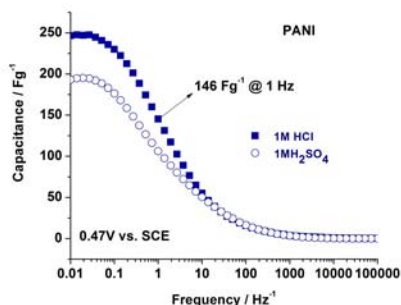


Figure 3. Capacitance vs. frequency

CONCLUSION

The nanofibrous PANI synthesized by a simple chemical oxidation route was shown as promising material for supercapacitor applications. Its high pseudocapacitance performance in acidic aqueous electrolytic solutions originate from a very high electronic conductivity and developed surface rich in active redox groups. Additionally, the choice of acid counterion is the factor of charge storage capability. Namely, specific capacities of PANI at 10mVs⁻¹ amounted to 340 Fg⁻¹ in HCl and 264 Fg⁻¹ in H₂SO₄.

ACKNOWLEDGEMENT:

This work was supported by the Ministry of Sciences and Environmental Protection of Serbia (Project III 45014 and 172015)

REFERENCES:

- [1] G.A. Snook, P. Kao, A. S. Best, *J. Power Sources*, 2011, 196, 1-12.
- [2] M. R. Gizdavić-Nikolaidis, M. Jevremović, D. R. Stanisavljev, Z. D. Zujović, *J. Phys. Chem. C*, 2012, 116, 3236-3241.
- [3] R. Pauliukaite, C. M. A. Brett, A. P. Monkman, *Electrochim. Acta*, 2004, 50, 159-167.
- [4] M. Vujković, N. Gavrilov, I. Pašti, J. Krstić, J. Travas-Sejdić, G. Cirić-Marjanović, S. Mentus, *Carbon*, 2013, 64, 472-486.



PHYSICAL CHEMISTRY 2014

12th International Conference
on Fundamental and Applied Aspects of
Physical Chemistry

Proceedings
Volume II

The Conference is dedicated to the
25. Anniversary of the Society of Physical Chemists of Serbia

September 22-26, 2014
Belgrade, Serbia

ISBN 978-86-82475-31-6

Title: PHYSICAL CHEMISTRY 2014 (Proceedings)

Editors: Ž. Čupić and S. Anić

Published by: Society of Physical Chemists of Serbia, Studenski trg 12-16,
11158, Belgrade, Serbia

Publisher: Society of Physical Chemists of Serbia

For Publisher: S. Anić, President of Society of Physical Chemists of Serbia

Printed by: “Jovan” Printing and Publishing Company; 200 Copies;

Number of pages: 3+385; **Format:** B5; Printing finished in September
2014.

Text and Layout: “Jovan”

Neither this book nor any part may be reproduced or transmitted in any form or by any means, including photocopying, or by any information storage and retrieval system, without permission in writing from the publisher.

200 - Copy printing

Contents

Volume II

Biophysical Chemistry, Photochemistry, Radiation Chemistry	443
Radiochemistry, Nuclear Chemistry	551
Material Science	589
Solid State Physical Chemistry	719
Macromolecular Physical Chemistry	757

BIOPHYSICAL CHEMISTRY,
PHOTOCHEMISTRY,
RADIATION CHEMISTRY

DELIVERY SYSTEMS FOR TRANSPORT OF DRUGS INTO THE SKIN AS STUDIED BY EPR

M. Šentjurc

Jožef Stefan Institute, Ljubljana, Slovenia

ABSTRACT

Kinetic EPR (electron paramagnetic resonance) imaging methods and EPR oximetry are applied to the investigation of different delivery systems for transport of drugs into the skin. As the delivery systems water solutions, hydrophilic gel and liposomes of different composition and size were used. The *in vitro* and *in vivo* results are compared.

INTRODUCTION

Skin is a barrier which protects the body from injuries due to chemicals, microorganisms, sunlight or bumps. Therefore the transport of chemicals, especially hydrophilic substances, into the skin is strongly hindered. To overcome the barrier function of skin it is necessary to find the appropriate delivery system to facilitate the transport of the drug or skin care substances, into or even through the skin. Different delivery systems have been developed such as liposomes, nanoparticles, microemulsions, hydrogels, ointments, etc and their efficacy have been investigated [1].

One of the methods by which the efficacy of the delivery system could be measured is EPR. Two methods have been used to follow the transport of drugs into the skin in different delivery systems. One, applicable *in vitro* on skin slices is one-dimensional EPR imaging (1D-EPRI) together with the reduction kinetic imaging [2,3,4] and the other is EPR oximetry which is applicable *in vivo* [5,6].

EXPERIMENTAL

Delivery systems Water solution, hydrophilic gel prepared from hydroxyethylcellulose, liposomes composed of dimyristoyl- or dipalmitoyl-phosphatidylcholine (DMPC or DPPC) and hydrogenated or non-hydrogenated soya lecithin (HSL and NSL) at different concentrations of cholesterol in multilamellar liposomes were prepared.

EPR imaging (1D-EPRI) and reduction kinetic imaging methods The water soluble nitroxide spin probe ASL (spin labeled tempocholine) was used as a model of a hydrophilic drug. The delivery system was put in the contact with the surface of the skin slice (stratum corneum, fresh pig ear skin) and placed into the spectrometer.

1D-EPRI[2]: Magnetic field gradient of 0.25 T/m was applied in the direction orthogonal to the skin surface. Due to the diffusion of the spin probe into the skin the line-shape of 1D-EPRI spectra became asymmetric. For a quick reference, asymmetry of the spectra ($l = l_1/l_2$, Fig. 1A) was measured and alteration of l with time after being in contact with the delivery system, the transport parameter $\Delta l = l_{30} - l_{5min}$, was determined. For more precise determination of the transport the experimental spectra has to be fitted with the spectra evaluated from the corresponding concentration profiles of the spin probe in the tissue sample.

Reduction kinetic imaging[3,4]: The method explores the ability of tissue to reduce nitroxides to non-paramagnetic hydroxylamines (EPR invisible). The kinetics of the spin probe reduction was determined by measuring the intensity decrease of the EPR spectra with time after application of the delivery system with the probe to the skin. The reduction kinetics and evolution of the concentration profiles were calculated separately for liposome entrapped spin probes and for the released one using a three compartment model: reservoir of the delivery system (thread with liposomes), epidermis and dermis, taking into account that in the compartments the transport of the entrapped and the released probes and the decay rates of liposomes are different.

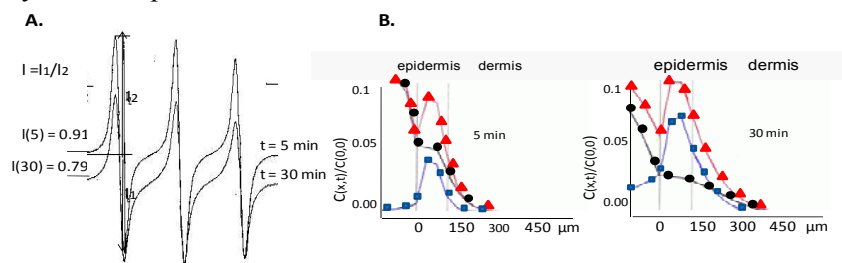


Figure 1. A.) EPR spectra in presence of 0.25 T/m magnetic field gradient 5 and 30 min after application of liposomes to the skin. B.) Reduction kinetic concentration profile in epidermis and dermis 5 and 30 min after application of liposomes to the skin separately for released ■, entrapped ● and total ▲ spin probe.

EPR oximetry As a model of a drug a blood flow modifying agent, benzyl nicotinate (BN) was introduced into the delivery system. The response of organism was followed by measuring the partial pressure of oxygen (pO_2) in the skin by EPR oximetry, using lithium phtalocyanineparamagnetic probe inserted into the skin. When BN penetrates into the skin it increases oxygen concentration at the site of the probe and the line width of the EPR

spectra broadened due to the interaction between oxygen and probe (the line-width is proportional to pO_2).

RESULTS

EPR imaging results on pig ear skin (in vitro measurements) From Table 1 one can see that cholesterol (Ch) strongly influences the transport of ASL into the skin. Diffusion into the dermis and changes in asymmetry parameter ΔI were observed only for liposomes composed of phospholipid:cholesterol ratio 7:3 or 1:1 (mol:mol) and were not observed for nonhydrogenated soya lecithin (NSL) liposomes. On the other side the size of liposomes does not influence the transport significantly as long the diameter of liposomes is more than 100 nm [3,4].

Table 1. Influence of liposome composition and size on the transport parameter (ΔI) and parameters used in the calculation of the EPR spectra amplitude decrease of the hydrophilic spin probe ASL, which was applied to the skin entrapped in liposomes. k_2 = rate of liposome disintegration, D = diffusion coefficient. In thread and dermis k_2 is below 0.1.

sample	ΔI	k_2 ($10^{-3}s^{-1}$)		D ($10^{-7}cm^2s^{-1}$)	
	($I_{30}-I_{5min}$)	epidermis	thread	epidermis	dermis
ASL in water	0.00	-	14±4	0.33±0.06	<1
DMPC:Ch (10:0)mol:mol	0.00	14.0 ± 4.0	1.5±0.2	0.7±0.2	<1
DPPC:Ch(10:0)mol:mol	0.00	3.0±1.5	0.6±0.2	0.8±0.2	<1
DMPC:Ch(7:3)	0.04±0.02	10.0±1.0	1.6±0.2	10.0±4.0	3.5±1.0
DPPC:Ch(7:3)	0.08±0.02	7.2±0.8	1.6±0.2	13.0±4.0	12.0±4.0
DMPC:Ch(5:5)	0.08±0.02	10.0±1.0	1.3±0.2	11.0±4.0	5.1±1.0
DPPC:Ch(5:5)	0.11±0.02	7.2±0.8	1.7±0.2	13.0±4.0	14.0±4.0
HSL:Ch(5:5)MLV	0.08±0.02	7.6 ±0.8	2.2±0.3	15.0±5.0	4.9±1.0
HSL:Ch(5:5)-200 nm	0.06±0.02	6.4±0.6	1.7±0.3	13.0±4.0	4.8±1.4
NSL:Ch(5:5)	0.00	3.5±1.5	1.1±0.3	1.6±0.4	<1

Rate constant of ASL reduction $k_1 = 1 \text{ l mol}^{-1}\text{s}^{-1}$ is taken to be the same in the epidermis and dermis, while the concentration of the reducing agent in the epidermis is $3 \times 10^{-2} \text{ mol/l}$ and in the dermis $9 \times 10^{-4} \text{ mol/l}$, as calculated from the best fit to the reduction kinetic curve for ASL in water (Data taken from ref. 3 and 4).

Results of EPR oximetry in mice (in vivo measurements) In Fig. 2 the changes in partial oxygen pressure (ΔpO_2) in mice after application of BN applied to the skin in hydrogel or in liposomes of different composition (HSL or NSL with 50 mol% cholesterol) is shown. The effect of BN was evaluated by lag-time (t_{lag}), time needed for maximum pO_2 increase (t_{max}), maximal increase of pO_2 and overall effectiveness expressed by the area under the response time curve (AUC)[5].

The composition of delivery system significantly affects the time when BN starts to act and to a lesser extent the maximum increase of pO_2 and effectiveness of BN action. BN in HSL:Ch (5:5) liposomes, which show maximal transport into the skin in *in vitro* experiments, starts to act immediately after application, while other delivery systems show a pronounced delay in BN action.

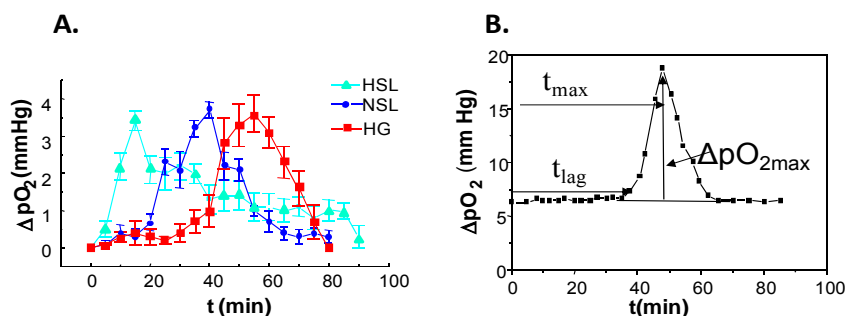


Figure 2. A. The time course of pO_2 in mouse skin after application of 0.83% wt/wt BN in HSL:CH (5:5 mol%) ▲, NSL:CH (5:5 mol%) ●, hydrophilic gel ■. B. Designation of parameters measured.

DISCUSSION

BN is well known vasodilator that can penetrate through the stratum corneum barrier. Therefore it is not surprising that its action is observed with all delivery systems used. According to our results the main influence of the systems is to accelerate BN action.

In vivo results confirm previous *in vitro* findings observed with HSL and NSL liposomes with 50 mol% cholesterol. For HSL liposomes it was typical that after the maximum was reached, the pO_2 decreased only to a certain level, which was maintained for a prolonged period, indicating sustained release of liposomes, while NSL liposomes achieved maximum only after 40 min and after 60 min there is no more effect. According to *in vitro* measurements HSL enables the transport of entrapped substance deeper into the skin, while NSL liposomes only into the stratum corneum. This could explain faster response of organism after application of HSL.

LITERATURE

- [1] Y.S.R. Elnaggar, W.M. El-Refaie, M.A. El-Massik, O.Y. Abdallah, J. Control Release, 2014, 180 10.
- [2] F. Demšar, P. Cevc, M. Schara, J. Magn. Res. 1986, 69, 258.
- [3] K. Vrhovnik, J. Kristl, M. Šentjerc, J. Šmid-Korbar, Pharm. Res. 1998, 15, 525.
- [4] M. Šentjerc, K. Vrhovnik, J. Kristl, J. Control Release 1999, 59, 87.
- [5] J. Kristl, Z. Abramović, M. Šentjerc, AAPS Pharm Sci, 2003, 5, Article 2 (<http://www.pharmsci.org>).

TETRAPLEX DNA STRUCTURES IN BIOMEDICAL AND BIOSENSING APPLICATIONS

B. Juskowiak,¹ A. Dembska,¹ A. Gluszynska,¹ J. Kosman,¹ E. Rajczak,¹ P. Rzepecka,¹ A. Swiatkowska,¹ and S. Takenaka²

¹Faculty of Chemistry, Adam Mickiewicz University, Umultowska 89b, 61-614 Poznan, Poland, E-mail: juskowia@amu.edu.pl

²Department of Applied Chemistry, Kyushu Institute of Technology, Kitakyushu, Japan

ABSTRACT

Certain DNA sequences that are guanine- or cytosine-rich can form four-stranded structures called G-quadruplexes and i-motifs, respectively. These tetraplex DNA forms have recently received great attention because such sequences are often found in a genome.

An anticancer therapy has been proposed that targeted telomerase with G-quadruplex binding ligands that stabilize G-quadruplex structures and inhibit telomerase activity. Moreover, the unique structure of tetraplexes has also stimulated development of new bioanalytical assays. Current activities of our research group related to above mentioned applications of DNA tetraplexes are reported in this contribution.

INTRODUCTION

Many important genomic regions, especially in gene promoters and telomeres, consist of repeating sequences potentially able to form tetraplexes on both DNA strands [1]. Namely, G-rich strands are able to form G-quadruplexes whereas complementary C-rich strands can adopt i-motif structure [2]. Intramolecular G-quadruplexes exhibit four-stranded structures containing folded DNA strand, with G-tracts in parallel or antiparallel orientations. This arrangement is stabilized by

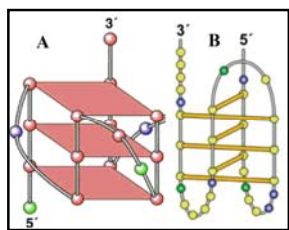


Figure 1.
Tetraplex DNA structures: (A) G-quadruplex, (B) i-motif.

metal cations (e.g. Na^+ , K^+) bound in a central channel of quadruplex and by $\pi-\pi$ nonbonded attractive interactions between neighboring G-tetrads. Four guanines that form the tetrad are held together on a plane, interacting via Hoogsteen bonding (Fig. 1A). Different G-quadruplex structures exist, depending on the orientation of the strands and the *syn/anti* conformations of guanines [3]. The C-rich strand forms the so-called i-motif with intercalated C-C⁺ base pairs (Fig. 1B). Folding into i-motif architecture is a more demanding process since it must be preceded by protonation of cytosines [2,4]. The stability of the i-motif depends on pH, and C-rich repeats may fold into

a stable i-motif at slightly acidic pH. There are different possible i-motif structures with different intercalation and looping topologies [4].

These tetraplex DNA forms have recently received great attention because G-rich (G - guanine) and C-rich (C-cytosine) sequences are often found in a genome e.g., in telomeric DNA or in oncogene promoter regions, and because of their potential links to mechanisms that relate to cancer and other diseases. An anticancer therapy has been proposed that targeted telomerase with G-quadruplex binding ligands. A number of small molecules have been reported in recent years that stabilize G-quadruplex structures and inhibit telomerase activity [5,6].

On the other hand, the unique structural features of tetraplexes have also stimulated development of new bioanalytical assays for several targets [6,7]. Analyte induced intramolecular folding of a flexible single-stranded specially designed DNA molecule properly labeled with reporter groups into a compact G-4 or i-motif DNA structure is a structural transition leading to the development of a molecular device that generates an analytical signal [7,8].

Here, we report current developments of our research group related to above mentioned applications of DNA tetraplexes.

SMALL LIGANDS CAPABLE OF TELOMERASE INHIBITION

Taking advantages of the ability of some ligands to bind G-rich sequences and to stabilize G-quadruplex structures, new strategies in the anticancer therapy have been developed [5]. One is based on the inhibition of telomerase, a reverse transcriptase that is active in most cancer cells. Ligand that induces folding of telomeric DNA (primer for telomerase) into G-quadruplex conformation may inhibit telomerase. As a consequence, telomerase cannot effectively elongate telomeric DNA that leads to telomere shortening and death of tumor cells [5]. In accordance with a second strategy, which concerns stabilization of G-quadruplexes in gene promoter regions, small ligand molecules may stop the growth of cancer cells by interacting with promoter G4 structures and blocking gene expression. Both strategies are driving forces in the anticancer drug discovery research and provide motivation for design of new selective G-quadruplex ligands [6].

We recently reported new DNA interacting papaverine derivatives (ligands **1** and **2**, Fig. 2), which bind to G-quadruplex with a much higher affinity than to single- and double-stranded DNAs [9-10]. The ligands exhibited remarkable cytotoxicity and ability to inhibit telomerase activity [11].

The common feature of G-quadruplex ligands is presence of planar aromatic system that enables G-4 binding mode consisting in stacking of ligand on the plane of exposed guanine tetrad (end-stacking). However, not only the presence of such

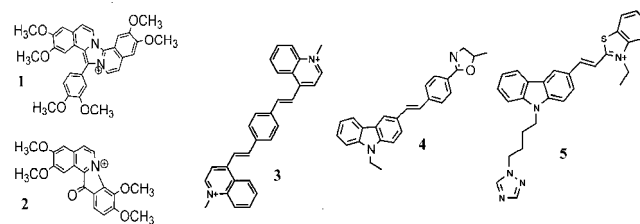


Figure 2. G-4 DNA ligands: **1** and **2** – papaverine oxidation products, **3** – photoisomerizable E,E-isomer, **4,5** – carbazole derivatives.

structural constituents determines the strength and the mode of interaction, but also the spatial arrangement of these groups may affect binding affinity and preferences of the ligand. For example, the *cis-trans* photoisomerization is a suitable tool that allows controlled manipulation of the ligand conformation [12,13]. We have shown that the quadruplex-binding affinity could be switched by light, e.g., the E,E and E,Z isomers of ligand **3** interacted with parallel and antiparallel tetraplexes exhibiting different binding selectivity. The E,Z-**3** showed higher binding preference for c-myc DNA (a propeller-type quadruplex), whereas the E,E-**3** favorably interacted with telomeric DNA (a basket-type quadruplex). The presence of quadruplex DNA hampered photoisomerization of quadruplex-bound ligand [15]. Another group of synthesized ligands contained carbazole scaffold that is recognized as bioactive component (ligands **4** and **5**, Fig. 2). They showed G-4 binding affinity, potential telomerase inhibition and fluorescence properties that depended on the interaction with DNA [14,15].

FLUORESCENT PROBES WITH TETRAPLEX DNA MOTIFS

Structural changes associated with the formation of tetraplex assemblies upon binding K^+ ions by oligonucleotides possessing sequences of human telomere DNA or thrombin binding aptamer (TBA), led to the development of potassium-sensing oligonucleotide (PSO) probes, in which two fluorescent dyes were attached to both termini of a particular oligonucleotide [16-23]. The combination of dyes included fluorescence resonance energy transfer (FRET) [17,18,22,23] and excimer emission approaches [16,19-21]. The structural changes upon binding K^+ ion could be monitored by a fluorescence technique. These systems showed a very high preference for K^+ over Na^+ ion, which was suitable for fluorescence imaging of the potassium concentration gradient in a living cell [23]. In the case of human telomere DNA, it was also possible to follow the polymorphism of its tetraplex structures. To mimic cellular conditions, the interactions between oligonucleotides or fluorescent probes bearing human telomere sequence and positively charged DODAB lipid monolayer at the air-aqueous interface were studied by surface film balance and fluorescence measurements [24,25].

A pH sensor was constructed with cytosine-rich c-myc sequence labeled with pyrene at both termini. The monomer fluorescence of pyrene labels underwent quenching upon i-motif formation at pH below ca. 7.0 [26]. Another sensor based on RET sequence showed in preliminary study a pH-dependent excimer emission. Another fascinating feature of G-4 DNAs is their ability to form DNazymes with peroxidase activity. After binding of hemin, the complex can catalyze oxidation of suitable substrates by H_2O_2 [8]. Attempts to exploit this system for telomerase detection were recently reported. Improvement of catalytic activity of the system based on human telomeric sequence was attained in the presence of Brij 58 surfactant and by applying a thermal treatment procedure (heating/rapid cooling) to prepare G-quadruplex/hemin complexes [27]. Further studies to improve sensitivity of the assay by application of fluorogenic substrates are in progress.

REFERENCES

- [1] T.A. Brooks, S. Kendrick, L. Hurley, *FEBS J.*, 2010, 17, 3459–3469.
- [2] A.T. Phan, J. L. Mergny, *Nucleic Acids Res.*, 2002, 30, 4618-4625.
- [3] S.M. Kerwin, *Curr. Pharm. Design*, 2000, 6, 441-471.
- [4] J.L. Mergny, L. Lacroix, X. Han, J.L. Leroy, C. Helene, *J. Am. Chem. Soc.*, 1995, 117, 8887-8898.
- [5] F. Lavelle, J.-F. Riou, A. Laoui, P. Mailliet, *Crit. Rev. Oncol. Hemat.*, 2000, 34, 111-126.
- [6] S. Balasubramanian, S. Neidle, *Curr. Opin. Chem. Biol.*, 2009, 13, 345-353.
- [7] B. Juskowiak, *Anal Bioanal Chem.*, 2011, 399, 3157–3176.
- [8] J. Kosman, B. Juskowiak, *Anal. Chim. Acta*, 2011, 707, 7-17.
- [9] B. Juskowiak, E. Galezowska, N. Kaczorowska, T. Hermann, *Bioorg. Med. Chem. Lett.*, 2004, 14, 3627-3630.
- [10] E. Galezowska, A. Masternak, B. Rubis, A. Czyrski, M. Rybczynska, T. Hermann, B. Juskowiak, *Int. J. Biol. Macromol.*, 2007, 41, 558-563.
- [11] B. Rubis, M. Kaczmarek, N. Szymanowska, E. Galezowska, A. Czyrski, B. Juskowiak, T. Hermann, M. Rybczynska, *Investig. New Drugs*, 2009, 27, 289-296.
- [12] I. Czerwiska, B. Juskowiak, *Chem. Pap.*, 2011, 65, 242–245.
- [13] I. Czerwiska, B. Juskowiak, *Int. J. Biol. Macromol.*, 2012, 51, 576– 582.
- [14] A. Gluszynska, K. Bajor, I. Czerwiska, D. Kalet, B. Juskowiak, *Tetrahed. Lett.*, 2010, 51, 5415-5418.
- [15] A. Gluszynski, E. Rajczak, B. Juskowiak, *Chem. Pap.*, 2013, 67, 1231-1239.
- [16] S. Nagatoishi, T. Nojima, B. Juskowiak, S. Takenaka, *Angew. Chem. Int. Ed. Engl.*, 2005, 44, 5067-5070.
- [17] S. Nagatoishi, T. Nojima, E. Galezowska, B. Juskowiak, S. Takenaka, *ChemBioChem*, 2006, 7, 730-1737.
- [18] S. Nagatoishi, E. Galezowska, A. Gluszynska, B. Juskowiak, S. Takenaka, *Anal. Chim. Acta*, 2007, 581, 125-131.
- [19] H. Hayashida, J. Paczesny, B. Juskowiak, S. Takenaka, *Bioorg. Med. Chem.*, 2008, 16, 9871-9881.
- [20] A. Dembska, B. Juskowiak, *J. Fluoresc.*, 2010, 20, 1029-1035.
- [21] A. Dembska, B. Juskowiak, *J. Photochem. Photobiol. A*, 2010, 212, 36-42.
- [22] S. Takenaka, B. Juskowiak, *Anal. Sci.*, 2011, 27, 1167-1172.
- [23] K. Ohtsuka, S. Sato, Y. Sato, K. Sota, S. Ohzawa, T. Matsuda, K. Takemoto, N. Takamune, B. Juskowiak, T. Nagaib and S. Takenaka, *Chem. Commun.*, 2012, 48, 4740–4742.
- [24] B. Juskowiak, J. Paczesny, *J. Colloid. Interface Sci.*, 2012, 365, 150-155.
- [25] B. Juskowiak, A. Swiatkowska, *Colloids and Surfaces A: Physicochem. Eng. Aspects*, 2013, 417, 250– 255.
- [26] A. Dembska, P. Rzepecka, B. Juskowiak, *J. Fluoresc.*, 2013, 23, 807-812.
- [27] J. Kosman, B. Juskowiak, *Cent. Eur. J. Chem.*, 2012, 10, 368-372.

THE POTENT ANTICANCER DRUG TRIAPINE DOES NOT BIND TO HUMAN SERUM ALBUMIN

M.Grozdanić and A.Popović-Bijelić*

*University of Belgrade, Faculty of Physical Chemistry, EPR laboratory,
Studentski trg 12-16, 11000 Belgrade, Serbia, *ana@ffh.bg.ac.rs*

ABSTRACT

The interactions of the anticancer drug Triapine®, and its Fe, Cu, and Ga complexes, with human serum albumin (HSA), were investigated. The drug-binding affinities for HSA were studied by electron paramagnetic resonance (EPR) spin labeling technique, using 5-, and 16-doxyl stearic acids. The results indicate that Triapine does not bind to HSA, which may account for its reported high cytotoxicity. The Ga(III) and Fe(III) complexes show the same behavior as Triapine, whereas the redox active Fe(II) complex appears to damage the protein via radical oxygen species. Moreover, competition between the Cu(II) complex and 16-doxyl stearic acid, for the HSA binding sites, is observed.

INTRODUCTION

Human serum albumin (HSA) is the major protein of blood plasma [1]. It is a monomeric protein composed of three structurally homologous domains. Apart from its main physiological role, the transport of non-esterified fatty acids, HSA also reversibly binds a wide range of drugs. Consequently, HSA plays a central role in drug pharmacokinetics and pharmacodynamics, since the drugs that bind to HSA have longer biological lifetimes, and are more homogeneously distributed in the body [2]. However, drugs that do not bind to HSA may be more potent, as the unbound fraction of the drug exhibits pharmacologic effects.

HSA contains two major drug-binding sites, I (the warfarin binding site), and II (the benzodiazepine binding site). These sites overlap with three of the seven high affinity long-chain fatty acid (FA) binding sites, site I with FA7, and site II with FA3 and FA4. Therefore, competition between the fatty acids and drugs for the same binding sites is possible, although cooperativity and no influence have been observed in some cases [2]. The binding of FAs to HSA can be studied by electron paramagnetic resonance (EPR) spectroscopy using spin labeled FAs [3,4]. This technique provides information about the free and the bound spin labels (SLs), and their specificity for the binding sites on the HSA protein. Consequently, the effect

of drug-binding to HSA may be assessed indirectly by measuring the extent of SL binding to HSA.

In this work, EPR spin labeling was used to investigate the interaction of a phase II trial anticancer drug 3-aminopyridine-2-carboxaldehyde thiosemicarbazone (Triapine®, TP), and its metal (Fe, Cu, Ga) complexes, with HSA. TP belongs to a class of α -N-heterocyclic thiosemicarbazones, which is currently among the most potent inhibitors of ribonucleotide reductase (RNR) activity [5]. The RNR enzyme is considered to be a target for anticancer drugs, since its inactivation stops DNA synthesis and repair. TP is an excellent metal chelator, and it is proposed that its Fe(II)-form is responsible for its high cytotoxicity [6].

EXPERIMENTAL

Chemicals. Human serum albumin and spin labeled fatty acids (5-, and 16-doxyl stearates) were obtained from Sigma-Aldrich. Triapine, diligand complexes Ga(III)TP₂ and Fe(III)TP₂, and the monoligand Cu(II)TP complex, were synthesized at the Institute of Inorganic Chemistry, University of Vienna.

Sample preparation. 0.4 μ l of 25 mM SL stock solution (in ethanol) was allowed to dry before the addition of HSA. Control samples contained 0.1 mM HSA in 0.9 % NaCl, pH 7.4 phosphate buffer, and the samples used to evaluate the effect of drugs on the binding of SLs contained 0.1 mM HSA and 0.1 mM drug, ([SL] / [HSA] = 3). All samples were incubated for 30 minutes at 22 °C prior to EPR measurements.

EPR spectroscopy. The X-band (9.8 GHz) EPR spectra were recorded on a Bruker Eleksys-II EPR spectrometer at room temperature under the following conditions: microwave power 10 mW, modulation amplitude 2 G, modulation frequency 100 kHz, conversion time 240 ms. Spectra were analyzed using Bruker Xepr software.

RESULTS AND DISCUSSION

The EPR spectra of 5-, and 16-doxyl stearic acids (5DS and 16DS, respectively) strongly bound to HSA are fully anisotropic since the SL's motion is severely restricted (Figure 1). The amount of the bound SL may be determined from the intensity of the low-field EPR peak (I_{LF}), and the amount of the unbound SL is estimated from the intensity of the high-field peak (I_{HF}).

The effect of TP and its metal complexes on the binding of SLs was measured in samples containing HSA and drugs in equimolar concentrations, while the concentration of the SL was three times higher. The determined ratio of the free/bound SL for the control sample (no drugs),

and the samples containing the drugs is shown in Figure 2. It is observed that TP, Ga(III)TP₂, and Fe(III)TP₂ complexes do not change the extent of 5DS and 16DS binding to HSA. It is expected that the influence of TP and the Ga complex should be quite similar, since Ga(III)TP₂ dissociates in solution to give the free ligand. The Fe(III)TP₂ complex is very stable and the fact that its presence does not affect the binding of SLs may suggest that it does not bind to HSA.

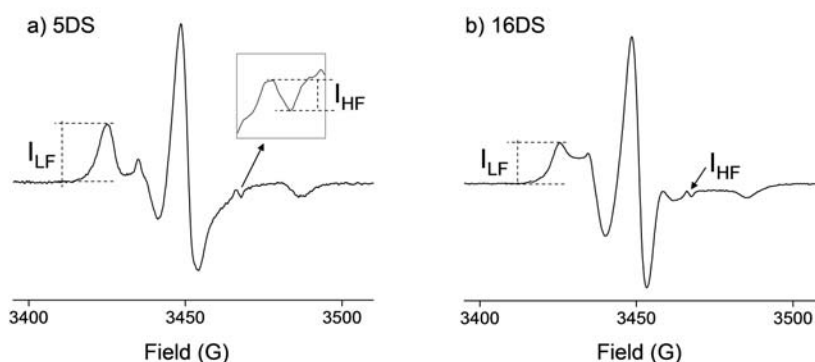


Figure 1. Characteristic EPR spectra of a) 5DS/HSA, and b) 16DS/HSA complexes. I_{LF} and I_{HF} correspond to the low-field and the high-field peak intensities, respectively. EPR conditions are given in the Experimental section.

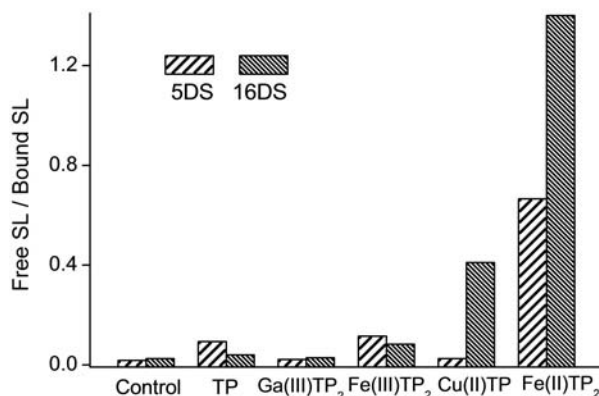


Figure 2. The ratio of the free and bound spin labels to HSA in presence of Triapine (TP), Ga(III)TP₂, Fe(III)TP₂, Cu(II)TP, and Fe(II)TP₂ complexes.

Cu(II)TP decreases the binding of 16DS, but not 5DS. This is in accord with previous reports that copper thiosemicarbazone radiopharmaceutical complexes bind strongly to HSA, either to drug site I, or non-specifically [7]. Since the binding of 5DS was not decreased by the presence of Cu(II)TP, it may indicate that this SL found an alternative binding site on

the protein. Fe(II)TP₂ greatly decreases the binding of 5DS and 16DS. The Fe(II) redox active complex produces reactive oxygen species (ROS) in solution [6], and it is likely that the ROS damage the protein [8], or at least cause its fragmentation into subunits. Given that the FA binding sites are located at the interfaces of the subunits, the SLs cannot bind to the protein.

CONCLUSION

HSA represents a nonspecific transporter of many drugs and therefore greatly influences their solubility, distribution and biological half-lives. Here we used EPR spin-labeling to evaluate the binding affinity of Triapine, and its metal complexes with Fe(II), Fe(III), Cu(II), and Ga(III), for HSA. It was determined that Triapine does not bind to HSA, which suggests that it is transported in blood plasma as a free ligand. Among the investigated metal complexes, only Cu(II)TP exhibits competitive binding for HSA with 16DS. Developing an easy-to-use and a high through output technique for the assessment of drug-binding affinity for HSA is still a challenge. Typical methods, like ultrafiltration, equilibrium dialysis, fluorescence titrations, or microcalorimetry, require large amounts of both, protein and drug. EPR spin labeling with the use of selected spin labels, could be an alternative, as it is highly sensitive and requires only microliter sample volumes.

ACKNOWLEDGEMENT

We thank Christian Kowol and Vladimir Arion (Institute of Inorganic Chemistry, University of Vienna) for preparing and providing thiosemicarbazones, and Goran Bačić and Miloš Mojović (Faculty of Physical Chemistry, University of Belgrade) for helpful comments. This work was supported by the Ministry for education, science and technological development of Serbia (grant no. III41005).

REFERENCES

- [1] T. Peters Jr., *All About Albumin*, Academic Press, 1995.
- [2] G. Colmenarejo, *Med. Res. Rev.* 2003, 23, 275-301.
- [3] J.D. Morriset, H.J. Pownall, A.M. Gotto, *J. Biol. Chem.* 1975, 250, 2487-2494.
- [4] T.G. Gantchev, M.B. Shopova, *Biochim. Biophys. Acta* 1990, 1037, 422-434.
- [5] T.B. Chaston, D.B. Lovejoy, R.N. Watts, D.R. Richardson, *Clin. Cancer Res.* 2003, 9, 402-414.
- [6] J. Shao, B. Zhou, A.J. Di Bilio, L. Zhu, T. Wang, C. Qi, J. Shih, Y. Yen, *Mol. Cancer Ther.* 2006, 5, 586-592.
- [7] N.E. Basken, C.J. Mathias, M.A. Green, *J. Pharm. Sci.* 2009, 98, 2170-2179.
- [8] A. Popović-Bijelić, C.R. Kowol, M.E. Lind, J. Luo, F. Himo, E.A. Enyedy, V.B. Arion, A. Gräslund, *J. Inorg. Biochem.* 2011, 105, 1422-1431.

**PRELIMINARY STUDIES OF THE PRODUCTION OF
SUPEROXIDE ANION RADICAL IN TARDIGRADES
(*Macrobiotus richtersi*)**

A. Savic¹, A. Pavicevic², R. Guidetti³, A. Turi⁴ and M. Mojovic²

¹*Institute for Multidisciplinary Research, University of Belgrade, Kneza
Viseslava I, Belgrade, Serbia (asavic@imsi.rs)*

²*Faculty of Physical Chemistry, University of Belgrade, Studentski Trg 12-
16, Belgrade, Serbia*

³*Department of Biology, University of Modena and Reggio Emilia, Via
Campi 213-D, Modena, Italy*

⁴*Student, Faculty of Sciences, University of Novi Sad, Trg Dositeja
Obradovica 3, Novi Sad, Serbia*

ABSTRACT

Tardigrades are phylum of small animals (<0.1 mm to 1 mm) widely distributed all over the world. Unique adaptabilities allow tardigrades to survive even in most extreme environments on Earth. However, the biochemistry behind the adaptation still remains unclear. Up to date, EPR studies of tardigrades were never performed. We demonstrate that spin-trap DEPMPO can be successfully applied for *in vivo* studies of the production of free radicals in tardigrades. The results show that tardigrades, without any external influences, produce superoxide anion radical ($\bullet\text{O}_2^-$). After the recording procedure, animals remained alive for several days, indicating that the presence of DEPMPO can be considered as not harmful.

INTRODUCTION

Tardigrades, also known as the “water bears” or “moss bears”, are cosmopolitan organisms which can be found in different habitats in terrestrial, freshwater and marine environments. Some species are able to survive both extreme cold (-273 °C [1]) and extreme hot conditions (+151 °C [1]). Tardigrades can even survive in space [2]. One of the unique adaptations involves the state of anhydrobiosis in which tardigrades can survive for decades [3].

However, it is a surprise that biochemistry of these remarkable processes remained unexplained. Electron paramagnetic resonance spectroscopy (EPR), certainly the method of choice for studies of free radicals, was never used for studying tardigrades.

For the first time, it has been shown that spin-trap DEPMPO (5-(Diethoxyphosphoryl)-5-methyl-1-pyrroline-N-oxide) can be used for *in vivo* studies in tardigrades. DEPMPO was the spin-trap of choice because of its ability to simultaneously trap several different free radical species, providing different signals for each spin adduct. This feature makes spin trapping technique much more desirable in comparison to specific fluorescence probes, which are often influenced by other types of free radicals, redox agents and microenvironments of fluorophores.

EXPERIMENTAL

Eutardigrada species *Macrobiotus richtersi* (Figure 1) were collected from leaf litter obtained from the garden in Modena, Italy. Leaf litter was gently hydrated for 45 minutes, and then sieved. Animals were manually collected (1000 animals) and stored in refrigerator at +4 °C in pots filled with mixture of distilled and mineral water Prolom (50/50 % v/v).

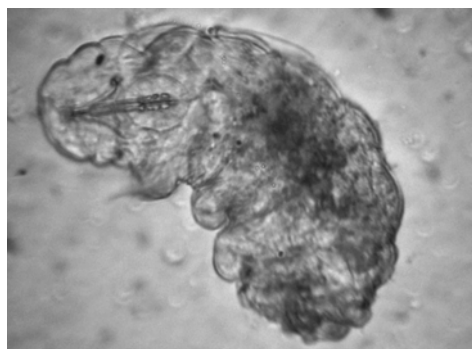


Figure 1.
Light microscopy image of *Macrobiotus richtersi*. Size of the animal is approximately 700 μm .

Spin-trap DEPMPO was purchased from Enzo Life Sciences and purified according to the protocol described by Jackson et al. [4].

EPR spectra were recorded using Bruker Elexsys II E540 X-band spectrometer. Applied parameters were: microwave frequency 9.85 GHz, microwave power 15.9 mW, magnetic field center 3425 G, sweep width 200 G, modulation amplitude 2 G, modulation frequency 100 kHz, conversion time 60 ms, number of accumulations 30.

Animals were cleaned several times in fresh water until the present stable free radicals originating from humic compounds, which remained from soil, were removed.

2 μl of DEPMPO was added to the sample (1000 animals in 28 μl of water). The sample was stored in gas permeable teflon tubes, and transferred to quartz cuvettes for the EPR measurement.

RESULTS AND DISCUSSION

Several well-discernable peaks were observed in the EPR spectrum, doubtlessly showing that tardigrades are producing superoxide anion radical (O_2^-) without the influence of any external factors (Figure 2).

The structure of DEPMPO/OOH spin adduct is shown in Figure 3.



Figure 2. EPR spectra of DEPMPO/OOH spin adduct recorded in tardigrade sample.

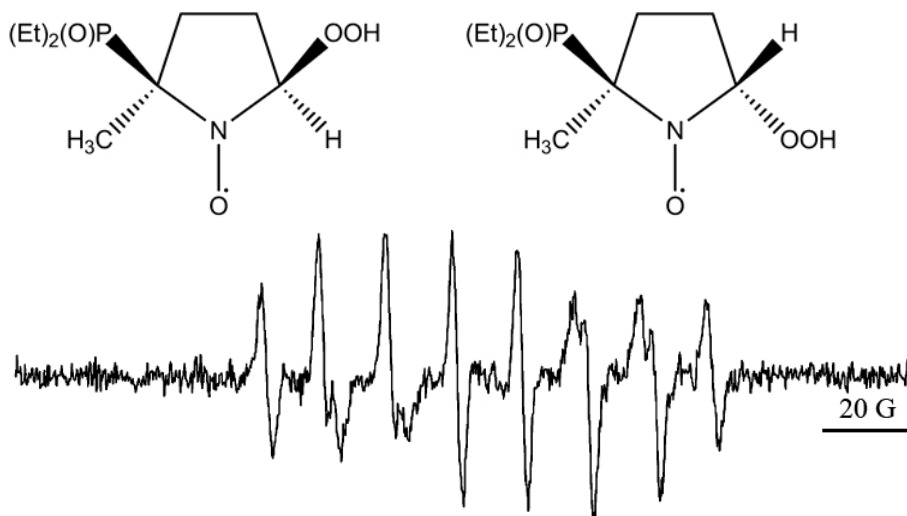


Figure 3. Structure of DEPMPO/OOH spin adduct that exists as diastereoisomer [5], and simulated DEPMPO/OOH spectrum with added white noise. Parameters: $aP=50.15$, $aN=13.00$, $aH \beta=11.30$, $aH=0.85$, 0.35 ; $aP=48.68$, $aN=13.80$, $aH \beta=0.88$, $aH=10.2$, 0.41 , 0.34 ; $aP=40.80$, $aN=13.30$, $aH \beta=1.50$, $aH=10.00$.

CONCLUSION

Results from this preliminary study are important because they open whole new approach for understanding the metabolism of tardigrades.

After the treatment, animals stayed alive for days, thus DEPMPO can be considered as the trap of choice for *in vivo* measurements of free radicals production in tardigrades.

Future studies will examine the effect of different stressful conditions on free radical production. According to previous results, stressful conditions could involve extreme temperatures, UV radiation and changes in partial pressure of gases in solution.

Synergistic approach could be done combining the fluorescence spectroscopy/microscopy with EPR spectroscopy.

ACKNOWLEDGEMENT

This work was supported by short-term fellowship program of Federation of European Biochemical Societies (FEBS) and the Ministry for Science of the Republic of Serbia (Grants no. OI173017, III43010, III41005).

REFERENCES

- [1] D. Horikawa, Biol. Sci. Space, 2008, **22**(3), 93 – 98.
- [2] K.I. Jonsson, E. Rabbow, R.O. Schill, M. Harms-Ringdahl, P. Rettberg, Curr. Biol., 2008, **18**(7), 729 – 731.
- [3] J.C. Wright, Comp. Zool., 2001, **240**(3), 563 – 582.
- [4] S.K. Jackson, K.J. Liu, M. Liu, G.S. Timmins, Free Radic. Biol. Med., 2002, **32**(3), 228 – 232.
- [5] A. Rockenbauer, J.L. Clement, M. Culcasi, A. Mercier, P. Tordo, S. Pietri, J. Phys. Chem. A, 2007, **111**, 4950 – 4957.

IN VITRO EVALUATION OF DIAZINON AND ITS DEGRADATION PRODUCTS NEUROTOXICITY POTENTIAL IN RAT BRAIN SYNAPTOSOMES

M. Čolović¹, V. Vasić¹, N. Avramović², D.Djurić³ and D.Krstić²

¹ *Department of Physical Chemistry, Vinča Institute of Nuclear Sciences, University of Belgrade, Serbia*

² *Institute of Medical Chemistry, School of Medicine, University of Belgrade, Serbia*

³ *Institute of Medical Physiology "Richard Burian", School of Medicine, University of Belgrade, Serbia*

ABSTRACT

Toxic effects of diazinon and its degradation products, diazoxon and 2-isopropyl-6-methyl-4-pyrimidinol (IMP), were investigated *in vitro* by determining the inhibition of acetylcholinesterase (AChE), Na⁺/K⁺-ATPase and ecto-ATPase activity in rat brain synaptosomes after 1 hour exposure toward varying concentrations. Dose-dependent AChE and Na⁺/K⁺-ATPase inhibition was obtained in the presence of diazinon, while diazinon concentrations below 0.1 mM did not noticeably affect ecto-ATPase activity. Diazinon oxidation product, diazoxon was found as the most toxic investigated compound. Diazoxon induced dose-dependent and almost complete inhibition of AChE, Na⁺/K⁺-ATPase and ecto-ATPase at the highest investigated concentration (0.1 mM), while hydrolysis product of diazinon, IMP did not remarkably influence their activities.

INTRODUCTION

Organophosphorus pesticides (OPs) are the most widely used pesticides worldwide and their metabolites are widespread across different populations. The primary mechanism of OP toxicity is the inhibition of AChE in the central and peripheral nervous system [1]. Diazinon (O,O-diethyl-O-(2-isopropyl-4-methyl-6-pyrimidinyl phosphorothionate) is a commonly used thionophosphorous OP to control a variety of insects in agriculture and household environment [2]. Diazinon can be transformed to the more toxic diazoxon due to the enzymatic reaction in birds, fish, insects and mammals [3], while IMP and its hydroxylated metabolites were reported to be much less toxic as compared to its parent compound diazinon [4]. Adenosine triphosphatases (ATPases) are a group of enzymes which play an important role in intracellular functions and critical for cellular

viability because they control many essential cellular functions, and are considered to be a sensitive indicator of toxicity [5, 6].

In the present study we investigated *in vitro* toxicity potential of various doses of diazinon and its degradation products (diazoxon and IMP) by determining the activity of AChE and ATPases (Na^+/K^+ -ATPase and ecto-ATPase) in rat brain synaptosomes which behave as minicells and represent a suitable model system for *in vitro* toxicity evaluation.

EXPERIMENTAL

Synaptosomes were isolated from the brain of *Wistar albino* rats and incubated at 37°C for 1 hour in the presence of desired concentrations of diazinon, diazoxon and IMP. Activities of AChE and ATPases (Na^+/K^+ -ATPase and ecto-ATPase) were measured by standard spectrophotometric methods [7, 8].

RESULTS AND DISCUSSION

The influence of 1 hour exposure to increasing concentrations (within the range 10^{-9} - 10^{-4} mol/l) of diazinon and its degradation products (diazoxon and IMP) on the activity of synaptosomal AChE, expressed as a percentage of the control value (obtained without inhibitor), is presented in Figure 1. It is clearly apparent that inhibitor efficiency of diazinon, diazoxon and IMP is quite different. At the concentration of 1×10^{-5} mol/l diazoxon almost completely inhibited AChE activity (85%), while the same concentration of diazinon inhibited only 24% activity. The half-maximum inhibition (IC_{50} , 1h) of the enzyme activity was achieved at $(6.7 \pm 0.2) \times 10^{-8}$ mol/l of diazoxon, while the effects of the same concentration of diazinon as well as IMP on the enzyme activity were negligible. Moreover, the presence of the highest investigated diazinon concentration (1×10^{-4} mol/l) was not able to reach half-maximum inhibition. The dependence of Na^+/K^+ -ATPase and ecto-ATPase activity on various concentrations (10^{-7} - 10^{-4} mol/l) of diazinon and its degradation products is presented in Figure 2 (a and b). The obtained results (Figure 2a) show that hydrolysis product of diazinon (IMP) did not remarkably alter Na^+/K^+ -ATPase activity. Unlike IMP, diazinon and its oxidation products (diazoxon) inhibited the enzyme in concentration-dependent manner, but with various potencies. The presence of the maximal investigated diazoxon concentration (1×10^{-4} mol/l) induced almost complete inhibition, while the same concentration of its parent compound (diazinon) decreased the enzyme activity approximately 50% related to control (Figure 2a). The obtained results for ecto-ATPase (Figure 2b) show similar sensitivity of the enzyme toward diazoxon and IMP as in the case of

Na^+/K^+ -ATPase, while diazinon did not cause ecto-ATPase activity inhibition more than 15 %.

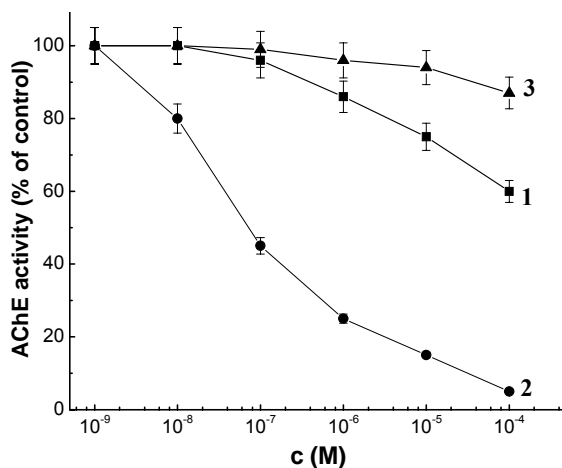


Figure 1. Inhibition of AChE activity in rat brain synaptosomes after 1 hour exposure to different concentrations of diazinon (1), diazoxon (2) and IMP (3).

CONCLUSION

In the present work the activities of AChE, Na^+/K^+ -ATPase and ecto-ATPase have been used to investigate neurotoxic effects of diazinon and its decomposition products. The results of our study show that diazinon and its oxidation product, diazoxon, inhibited synaptosomal AChE and ATPases activity in concentration-dependent manner but with varying potencies. Diazoxon demonstrated the strongest neurotoxic effect through the reduction of AChE activity, and the obtained inhibition of Na^+/K^+ -ATPase and ecto-ATPase suggests ion exchange as well as purinergic signaling disrupting effect of the oxo analog of diazinon. On the contrary, IMP was found as a non toxic diazinon metabolite.

Considering the obtained changes of the physiologically important parameters, synaptosomes, which functionally behave as minicells, could be recommended as a suitable model system for *in vitro* toxicity evaluation of OPs and their degradation products.

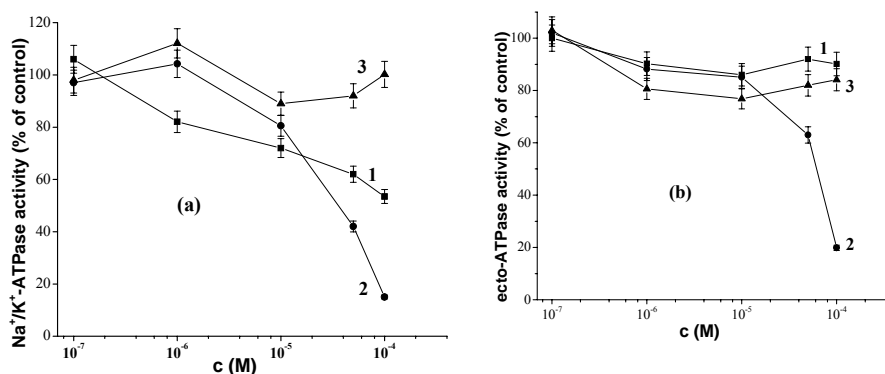


Figure 2. The dependence of rat brain synaptosomal Na⁺/K⁺-ATPase (a) and ecto-ATPase (b) activity on increasing concentrations of diazinon (1), diazoxon (2) and IMP (3).

ACKNOWLEDGEMENT

This work was financially supported by the Ministry of Education, Science and Technological Development of the Republic of Serbia (Project No. 172023).

REFERENCES

- [1] F. Nachon, X. Brazzolotto, M. Trovaslet, P. Masson, *Chem. Biol. Interact.*, 2013, 206, 536-544.
- [2] C. Cox, *J. Pestic. Reform*, 1992, **12**, 30-35.
- [3] Q. Zhang, S.O. Pehkonen, *J. Agric. Food Chem.*, 1999, 47, 1760-1766.
- [4] Y. Ku, J.L. Chang, S.C. Cheng, *Water, Air, Soil Pollut.*, 1998, 108, 445-456.
- [5] E.O. Oruc, D. Usta, *Environ. Toxicol. Phar.*, 2007, **23**, 48-55.
- [6] M. Čolović, D. Krstić, S. Petrović, A. Leskovic, G. Joksić, J. Savić, M. Franko, P. Trebše, V. Vasić, *Toxicol. Lett.*, 2010, 193, 9-18.
- [7] G.L. Ellman, K.D. Courtney, V. Andreas, R.M. Featherstone, *Biochem. Pharmacol.*, 1961, **7**, 88-90.
- [8] V. Vasić, D. Jovanović, D. Krstić, G. Nikezić, A. Horvat, L. Vujisić, N. Nedeljković, *Toxicol. Lett.*, 1999, 110, 95-104.

QSAR MODELLING OF ANTICANCER ACTIVITY OF 17-PICOLYL AND 17-PICOLINYLIDENE ANDROSTENE DERIVATIVES

S. Kovačević¹, S. Podunavac-Kuzmanović¹, S. Gadžurić², E. Djurendić², J. Ajduković² and L. Jevrić¹

¹University of Novi Sad, Faculty of Technology, Department of Applied and Engineering Chemistry, Bulevar cara Lazara 1, 21000 Novi Sad, Serbia

²University of Novi Sad, Faculty of Sciences, Department of Chemistry, Biochemistry and Environmental Protection, Trg Dositeja Obradovića 3, 21000 Novi Sad, Serbia (strahko@uns.ac.rs)

ABSTRACT

Cytotoxic activity (IC₅₀) of a series of eighteen 17-picolyl and 17-picolinylidene androstene derivatives towards human prostate cancer cell line (PC-3) was predicted using artificial neural network approach. Prediction was based on *in silico* molecular descriptors selected applying stepwise regression and partial least squares methods. Two excellent neural networks were established. They can be used for prediction of cytotoxic activity of structurally similar compounds and can give necessary guidelines for synthesis of new anticancer agents.

INTRODUCTION

The anticancer activity of 17-picolyl and 17-picolinylidene androstene derivatives has been proven in our previous studies [1-4]. The effect of these compounds on cell proliferation has been tested against a wide range of common cancer cell lines: human breast adenocarcinoma ER+ (MCF-7), human breast adenocarcinoma ER- (MDA-MB-231), colon cancer (HT-29), human cervix carcinoma (HeLa) and prostate cancer AR- (PC-3). In searching for new compounds with increased anticancer activity, chemometric quantitative structure-activity relationships (QSAR) approach is welcome because it eliminates trial-and-error element in drug design and gives us useful guidelines for selection of optimal molecular structure. The QSAR analysis includes the following steps: molecular structure optimization, molecular descriptors calculation, descriptors selection, model generation and model validation.

The study presented in this paper is based on construction of the reliable QSAR models which can be applied in prediction of cytotoxic activity (IC₅₀) of 17-picolyl and 17-picolinylidene androstene derivatives against

human prostate cancer cell line based on calculated molecular descriptors (topological, physicochemical, electrostatic, pharmacokinetic and lipophilicity descriptors). The QSAR models were obtained applying artificial neural networks (ANNs) technique. Prior to ANN analysis, the descriptors selection was carried out by stepwise regression (SR) combined with partial least squares (PLS) method.

EXPERIMENTAL

The synthesis and determination of cytotoxic activity of the analysed compounds towards PC-3 cells line (IC_{50} , μM) are presented in literature [1-3]. The basic structures of the studied compounds are shown in Figure 1.

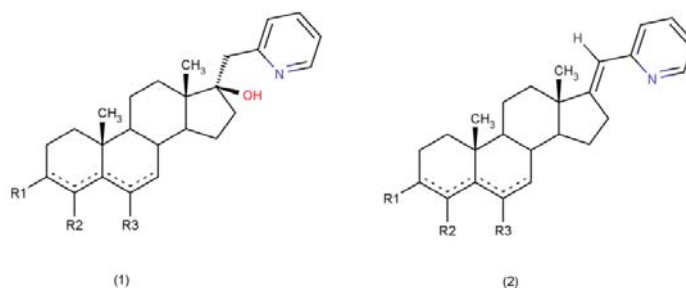


Figure 1. Basic structures of (1) 17-picolyl and (2) 17-picolinylidene androstene derivatives.

Calculations of 250 2D and 3D molecular descriptors were carried out applying ALOGPS 2.1, MarvinSketch, Molinspiration, PreADMET, ChemBio3D, Parameter Client Program and ADRIANA.Code software. Prior to ANN analysis, the output data (IC_{50}) were normalized by *min-max* normalization method and scaled in 0.01-0.99 range. Stepwise regression was carried out in NCSS&GESS software, while ANN and PLS methods were performed in Statistica 10 program. The descriptors selected by SR were subjected to PLS analysis. The most important descriptors in PLS were selected on the basis of variance importance in projection (VIP) values. The descriptors with VIP value higher than 0.3 were included in ANN analysis.

RESULTS AND DISCUSSION

The SR-PLS descriptors selection method presented the following descriptors as the most important: skin permeability (SP), Madin-Darby canine kidney cells permeability (MDCK) and salt solubility (S+SF). These descriptors served as the input data in ANN analysis. The training set contained 12 compounds, while test and validation set had 3 compounds each.

Self-training multilayer perceptron neural networks method with Broyden-Fletcher-Goldfarb-Shanno training algorithm was applied to train 1000 networks. The selection of the best predictive model was achieved based on correlation coefficients for training set (R_{train}), test set (R_{test}) and validation set (R_{val}), and root mean square errors for training set ($RMSE_{train}$), test set ($RMSE_{test}$) and validation set ($RMSE_{val}$). According to these parameters, two ANNs were selected as the best. Their statistical characteristics and architecture are presented in Table 1.

Table 1. Statistical parameters of the ANNs applied for prediction of IC_{50} .

The hidden activation in MLP 3-4-1 was logistic and in MLP 3-71-1 network was exponential, while output activations were identity (MLP 3-4-1) and sine (MLP 3-71-1).

Net. name	R_{train}	R_{test}	R_{val}	$RMSE_{train}$	$RMSE_{test}$	$RMSE_{val}$
MLP 3-4-1	0.9927	0.9937	0.9945	0.0007	0.0002	0.0012
MLP 3-71-1	0.9909	0.9920	0.9912	0.0008	0.0003	0.0010

The comparisons between experimental and predicted IC_{50} values are presented in Figure 2A and residuals distribution in Figure 2B.

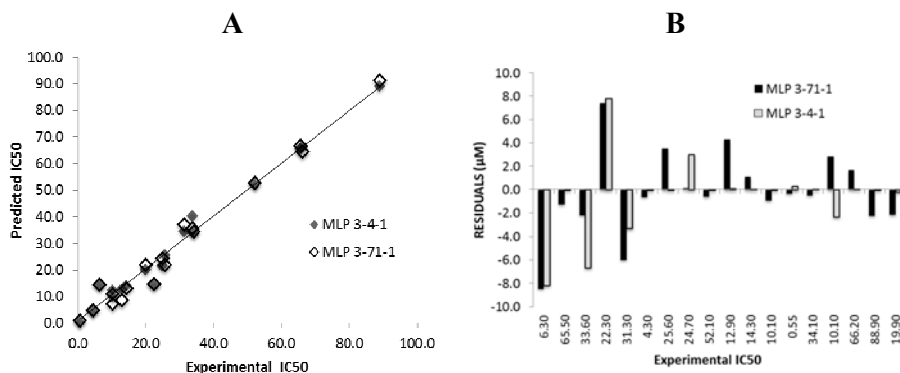


Figure 2. Experimental *versus* predicted IC_{50} values (A) and residuals distribution (B).

From the presented results it can be concluded that the established ANNs excellently predict the cytotoxic activity of the studied compounds. This was confirmed with correlation coefficients very close to 1, low RMSE values and with the low magnitude of the randomly distributed residuals (less than 9 μM).

Global sensitivity analysis showed the dominant influence of S+SF descriptor on variations in IC₅₀ for both of selected ANNs.

CONCLUSION

The ANNs with outstanding prediction performance of cytotoxic activity of 17-picolyl and 17-picolinylidene androstene derivatives were established. Their prediction ability was confirmed with the excellent statistical measures and with the comparison of the experimental and predicted data, hence they can successfully be used for prediction of IC₅₀ of structurally similar compounds.

ACKNOWLEDGEMENT

This paper was performed within the framework of the research projects No. 172021, No.172012 and No.172014, supported by the Ministry of Education, Science and Technological Development of the Republic of Serbia and the project No. 114-451-2373/2011, financially supported by the Provincial Secretariat for Science and Technological Development of Vojvodina.

REFERENCES

- [1] E. A. Djurendić, J. J. Ajduković, M. N. Sakač, J. J. Čanadi, V. V. Kojić, G. M. Bogdanović, K. M. Penov Gaši, *European Journal of Medicinal Chemistry*, 2012, 54, 784-792.
- [2] E. A. Djurendić, J. J. Ajduković, M. N. Sakač, J. J. Čanadi, V. V. Kojić, G. M. Bogdanović, K. M. Penov Gaši, *ARKIVOC*, 2009, 13, 311-323.
- [3] E. Djurendić, J. Daljev, M. Sakač, J. Čanadi, S. Jovanović Šanta, S. Andrić, O. Klisurić, V. Kojić, G. Bogdanović, M. Djurendić-Brenesel, S. Novaković and K. Penov Gaši, *Steroids*, 2008, 73, 129-138.
- [4] K. M. Penov Gaši, M. Dj. Djurendić Brenesel, E. A. Djurendić, M. N. Sakač, J. J. Čanadi, J. J. Daljev, T. Armbruster, S. Andrić, D. M. Sladić, T. Božić, I. Novaković, Z. Juranić, *Steroids*, 2007, 72, 31-40.

**COMPARATIVE ^{13}C MAS NMR ANALYSIS OF
BIOMOLECULES IN FUNGI *Grifola frondosa* AND
*Phycomyces blakesleeanus***

Z. Miladinović¹, A. Klaus², J. Vunduk², M. Žižić³ and J. Zakrzewska¹

¹*Institute of General and Physical Chemistry, Studentski trg 12-16, 11000
Belgrade, Serbia*

²*Faculty of Agriculture, University of Belgrade, Nemanjina 6, 11080
Belgrade, Serbia*

³*Institute for Multidisciplinary Research, Kneza Višeslava 1, 11030
Belgrade, Serbia*

ABSTRACT

^{13}C DP MAS NMR spectroscopy was used for characterization and quantification of biomolecules present in fruit body of *G. frondosa* and mycelium of *P. blakesleeanus*. Quantitative analysis show higher contents of polysaccharides in the biomass of *G. frondosa*.

INTRODUCTION

Polysaccharides, especially β -glucans are marked as main source of therapeutic significance of certain fungi such as *G. frondosa* [1]. On the other hand, in mycelium of *P. blakesleeanus* amino-sugars are anticipated as the main carbohydrate (45%); uronic acids about 25%, glucose and fucose 10% and galactose nearly 6%. [2].

Cross-polarization (CP) was established to enhance sensitivity of ^{13}C MAS NMR spectrum of solid samples. However, for molecular segments with long aliphatic chains (lipids) undergoing fast, isotropic reorientation, dipolar interactions are averaged to zero and CP MAS is incapable to observe such structures. Direct polarization (DP) ^{13}C MAS NMR spectroscopy provide opportunity to detect both mobile and rigid structures, and represents more reliable method for characterization of different biomolecules present in the fungal cells.

The aim of this study was characterization and quantification of biomolecules present in fruit body of edible fungus *G. frondosa* and mycelium of lower fungus *P. blakesleeanus*, as contrast, by using ^{13}C DP MAS NMR spectroscopy.

EXPERIMENTAL

For cultivation of *G. frondosa* substrate containing wheat straw, wheat and oak sawdust from the mountain Goč, Serbia and modified natural clinoptilolite, a suspension based on potassium, was used. The wild type strain of *P. blakesleeanus* (Burgeff) (NRRL 1555(-)) was used in this work. The mycelium was grown as explain in [3].

Solid-state ^{13}C DP MAS NMR spectra of dry fungi samples were acquired on Bruker MSL-400 spectrometer upgraded with Apollo console (Tecmag, USA) operating at 100.63 MHz for ^{13}C . Spectra were acquired using single-pulse excitation of 10 μs duration, with high power ^1H decoupling, recycle delay of 30 s, and under MAS rotation of 4 kHz. ^{13}C chemical shifts were externally referenced to glycine carbonyl signal (176.4 ppm).

RESULTS

Fig. 1 shows ^{13}C DP MAS NMR spectra of fruit body of *G. frondosa* and *P. blakesleeanus* mycelium. Signals in both spectra can be assigned to: 0 - 45 ppm, alkyl-C (mainly lipids and proteins from membranes); 45 - 110 ppm, O-alkyl-C (polysaccharide moiety); 110 - 160 ppm, aromatic-C (mainly aromatic amino acids and unsaturated fatty acids); 160 - 200 ppm, COOH-C/CONH-C (mainly fatty acids and peptide bonds) [4,5].

Polysaccharides peaks can be found in O-alkyl region (45- 92 ppm), with the main peak at 72 ppm assigned to C2, C3, and C5 of carbohydrates; and di-O-alkyl region (90-110 ppm), where region from 99 to 105 ppm is linked with anomeric C in either α or β configuration [6]. In *G. frondosa*, main polysaccharide, identified as grifolan, consisting of (1 \rightarrow 3)(1 \rightarrow 6)- β -d-glucan, shows characteristic resonance at: 103 ppm-C1, 72 ppm-C2, around 76 ppm-C3 and C5, 69 ppm-C4, and 62 ppm-C6 [7]. On the other hand, broad signal of anomeric C ranged from 90 - 104 ppm in *P. blakesleeanus* (Fig. 1b) indicates contribution of different kind of polysaccharides [2]. The signals at 175 ppm (C=O), 55 ppm (C2), and 23 ppm (CH₃) may indicate the presence of chitin. Moreover, the peak of C1 carbon of chitin is positioned near 104 ppm. The small signal near 83 ppm may arise from C3 carbons (1 \rightarrow 3)- α -glucan, although the C4 carbons of chitin has signal near that chemical shift. Peak at about 55 ppm could originate from N-substituted alkyl carbon in proteins and peptides [8] and aminosugars [2], but also from C2 of chitin [9]. In the case of *G. frondosa*, peak at 83 ppm of C4 originated from chitin shows negligible intensity indicating minor quantity of this polysaccharide.

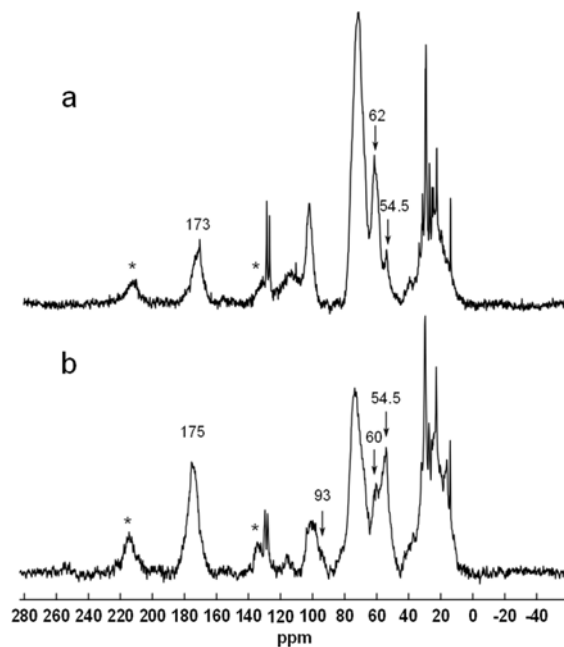


Figure 1. ^{13}C DP MAS NMR spectra of (a) *G. frondosa* fruit body; (b) *P. Blakesleeanus* mycelium. Spinning sidebands are labeled with asterisk.

In NMR spectrum of *P. blakesleeanus*, peak of anomeric carbon shows small shoulder around 93 ppm that could be attributed to aldoses or anomeric carbon of α -reducing end units from some oligosaccharides [10]. According to Pizzoferrato et al. [5], the bands around 90 ppm are due to the remaining carbons of the glucidic moiety.

Relative amount of protein/lipids and chitin to polysaccharide component in fungi samples were calculated as described by Pizzoferrato et al. [5], i.e., by the ratio of area of peak at 170 and 103 ppm; 20 and 103 ppm, for estimation protein/polysaccharide proportion, and the peaks at 55 and 103 ppm for comparison of chitin to total polysaccharide content. Results are given in Table 1, showing that mycelium of *P. blakesleeanus* has higher content of COOH/CONH - C and alkyl-C, both signals mainly assigned to lipids and proteins, than the fruit body of *G. frondosa*. On the other hand, the fruit body of *G. frondosa* shows a higher level of O-alkyl-C, assigned to polysaccharides.

Table 1. NMR peak intensity ratios for characteristic spectral regions.

Sample	173/103 ppm	54/103 ppm	20/103 ppm
<i>G. frondosa</i>	2.42	0.29	0.45
<i>P. blakesleanus</i>	3.86	1.16	0.71

CONCLUSION

Comparison of ^{13}C DP MAS NMR spectra of *G. frondosa* and *P. blakesleanus* indicate presence of different type and amount of polysaccharides. Quantitative analysis of deconvoluted NMR spectra reveals that β -d-glucans are main polysaccharide component in fruit body of *G. frondosa*, while *P. blakesleanus* contains more peptide and aminosugars components, as expected.

ACKNOWLEDGEMENTS

This work was supported by projects OI 173040, III46001, and III 46010 of Ministry of Education, Science and Technological Development, Republic of Serbia and EU Commission project AREA, No 316004.

REFERENCES

- [1] T. Mizuno, C. Zhuang, *Food Rev. Int.*, 1995, 11, 135–149.
- [2] A.J. Laere, A.R. Carlier, J.A. Assche, *Arch. Microbiol.*, 1977, 112, 303–306.
- [3] M. Žižić, M. Živić, I. Spasojević, J. Bogdanović Pristov, M. Stanić, T. Cvetić-Antić, J. Zakrzewska, *Res. Microbiol.*, 2013, 164, 61–69.
- [4] F. Peter-Valence, C. Llarena-Hernandez, M. Largeteau, J.M. Savoie, F. Ruaudel, F. Ziarelli, E. Ferré, A.M. Farnet, *J. Agric. Food Chem.*, 2011, 59, 8939–8943.
- [5] L. Pizzoferrato, P. Manzi, F. Bertocchi, C. Fanelli, G. Rotilio, M. Paci, *J. Agric. Food Chem.*, 2000, 48, 5484–5488.
- [6] N. Ohno, I. Suzuki, T. Yadomae, *Chem. Pharm. Bull.*, 1986, 34, 264–268.
- [7] A. Synytsya, M. Novák, *Carbohydr. Polym.*, 2013, 92, 792–809.
- [8] M.-F. Dignac, H. Knicker, I. Kögel-Knabner, *Org. Geochem.*, 2002, 33, 1715–1726.
- [9] G. Cárdenas, G. Cabrera, E. Taboada, S.P. Miranda, *J. Appl. Polym. Sci.*, 2004, 93, 1876–1885.
- [10] P. Dais, A.S. Perlin, *Carbohydr. Res.*, 1982, 100, 103–116.

HOW DIFFERENT WEED MANAGEMENT AFFECTS FREE ENERGY AND LIGHT CONSUMPTION BY MAIZE LEAVES

V. Dragičević¹, I. Spasojević¹, M. Simić¹, B. Nikolić², Z. Dumanović¹
and V. Jovanović³

¹Maize Research Institute "Zemun Polje", Slobodana Bajića 1, 11185
Zemun Polje, Serbia. (vdragicevic@mrizp.rs)

²Institute for Plant Protection and Environment, Teodora Drajzera 9,
11040 Beograd, Serbia

³Institute of Pesticides and Environmental Protection, Banatska 31b, 11080
Belgrade, Serbia

ABSTRACT

The aim of experiment was to investigate the influence of two cropping systems (monoculture and maize-wheat rotation) and three weed control systems (hoeing, herbicide application and control) on free energy, contents of chlorophyll and carotenoids, and their relationships with light intensity in crop. High carotenoids, ΔG of free water, low chlorophyll content and low potential of light transformation into biosynthetic processes could signify stress in monoculture. Weed control measures had tendency to decrease ΔG of bulk water and to increase and decrease ΔG of bound water in monoculture and rotation, indicating different structural changes.

INTRODUCTION

Interrelationships between factors that affect crop growth are complex. Stress in agro-ecological system can be quantified by thermodynamics [1]. Plants react to stress by varying in chlorophyll and carotenoid contents, while some herbicides have positive effects on chlorophyll synthesis [2]. Sun [3] also recognized free energy input by water as a presumable plant growth factor. Maize monoculture (continuous maize at the same field) shows negative impact on crop and environment, while rotation with other crops can decrease number of pathogens and weeds and increase soil fertility.

The objective of this study was to investigate the influence of two cropping systems (monoculture and maize-wheat rotation) and three weed control systems (control, hoeing and herbicide application) on free energy, contents of chlorophyll and carotenoids, and their relationships with light intensity in crop.

EXPERIMENTAL

Experiment with two maize hybrids (ZP 677-H1 and ZP 606-H2) grown in monoculture and maize-wheat rotation included sub-treatments: control, hoeing and herbicide application. Chlorophyll *a*, *b* and total carotenoids were determined colorimetrically [4]. Light intensity was measured with LICor-1000 quantum meter and presented as subtractions between plant top and middle part and middle part and plant bottom. The difference between fresh and dry biomass (after drying at 60 °C, 105 °C and 130 °C) referred to contents of free, bulk and bound water, calculated by sorption isotherm [3]:

$$\Delta G = -RT \ln(a_w)$$

where a_w is the relative water content achieved after drying at *T* (60, 105 and 130 °C), *R* is the gas constant (8.3145 J mol⁻¹ K⁻¹) and ΔG is differential free energy. The experimental data were statistically processed by regression analysis.

RESULTS AND DISCUSSION

The highest carotenoids and the lowest chlorophyll contents were recorded in monoculture (Tab. 1), what could with high ΔG of free water indicate stress presence [5], tied with endergonic processes and energy spending.

Table 1. Content of photosynthetic pigments and free energy in maize leaves

Treatment	Photosyn. pigments (mg g ⁻¹)				ΔG (J mol ⁻¹)		
	Carot.	Chl. <i>b</i>	Chl. <i>a</i>	Chl. <i>a/b</i>	Free w.	Bulk w.	Bound w.
Monoculture							
Control	0.42	0.53	0.94	1.78	1.08	10.51	13.65
H1 Herb.	0.74	0.43	0.55	1.27	1.07	9.07	14.34
Hoeing	0.64	0.36	1.03	2.87	0.97	9.03	15.16
Control	0.41	0.67	1.37	2.05	1.09	10.69	11.47
H2 Herb.	0.65	0.55	1.51	2.74	1.10	9.53	15.07
Hoeing	0.36	0.84	1.82	2.15	1.08	9.20	14.85
Rotation							
Control	0.42	0.71	1.75	2.47	0.99	9.66	18.57
H1 Herb.	0.38	0.87	1.80	2.06	1.01	10.17	12.58
Hoeing	0.50	0.98	1.85	1.89	1.03	9.67	17.74
Control	0.47	0.60	1.71	2.86	1.11	10.68	15.20
H2 Herb.	0.38	0.81	1.79	2.21	1.07	10.28	12.02
Hoeing	0.46	0.75	1.75	2.34	1.06	9.46	13.07

Meanwhile, increased contents of chlorophyll *a* and *b* were noticed in hoeing treatment. Together with decreased chlorophyll *a/b* ratio, it signifies shade presence [6]. Hoeing and herbicide treatment, compared with control had tendency to decrease ΔG of bulk water (exergonic reactions), as well as to increase ΔG of bonded water in monoculture and to decrease it in rotation, indicating different structural changes induced by treatments [7].

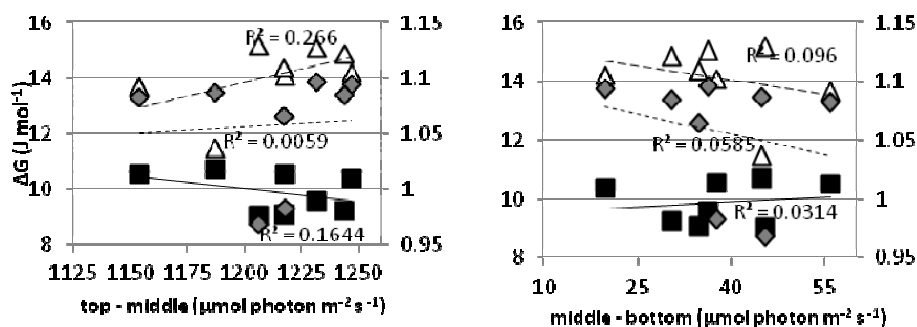


Figure 1. Interdependence between light intensity and ΔG at different maize parts grown in monoculture (\diamond - ΔG free water; \blacksquare - ΔG bulk water; \triangle - ΔG chemically bound water)

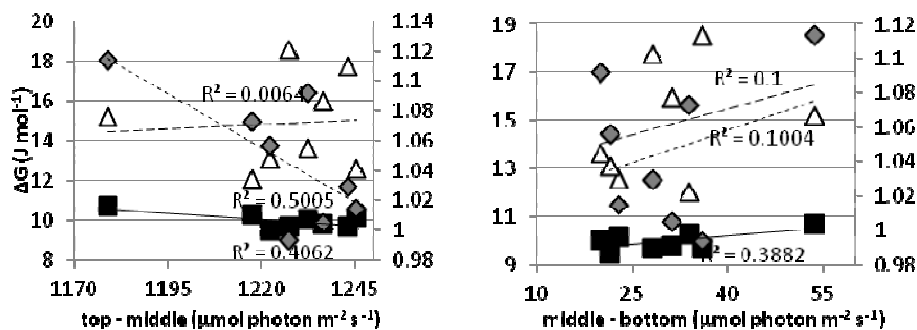


Figure 2. Interdependence between light intensity and ΔG at different maize parts grown in maize-wheat rotation (\diamond - ΔG free water; \blacksquare - ΔG bulk water; \triangle - ΔG chemically bound water)

According to regression analysis, correlation between ΔG of free water and light intensity (top-middle part) in monoculture was significant and positive (Fig. 1), but negative in rotation (Fig. 2). This could indicate connection between increased light harvest and higher energy expenditure in monoculture, as well as energy release in rotation field, which could be spent on some other processes, such as biosynthesis in coupled reactions [8,

9]. Only in rotation field, all three ΔG were positively correlated with light intensity (middle-bottom part), indicating that in shade conditions, much more of absorbed energy was spent on endergonic reactions.

CONCLUSION

High carotenoids and ΔG of free water, low chlorophyll content and possibly low potential of light transformation into biosynthetic processes could signify monoculture as undesirable practice, while increased chlorophyll content and potential of light transformation to other energy forms (present in lower ΔG of free water) could denote positive impact of rotation on maize crop. Moreover, weed control measures with decrease in ΔG of bulk water and fluctuations in ΔG of bound water in monoculture and rotation could indicate different structural changes.

ACKNOWLEDGEMENT

This work was supported by the Ministry of Education, Science and Technological Development of the Republic of Serbia (Grant no. TR-31037).

REFERENCES

- [1] M. Neményi, *Cereal Res. Comm.*, 2009, 37, Suppl. 1, 529-532.
- [2] P. Bónis, T. Árendás, C.L. Marton, Z. Berzsenyi, *Acta Agron. Hungar.*, 2006, 54, 517-520.
- [3] W.Q. Sun, in: *Desiccation and Survival in Plants: Drying Without Dying*, Black M. & Pritchard H. W. (Ed.), CABI Publishing, New York, USA, 2002, 47-91.
- [4] M.R. Sarić, R.R. Kastori, M. Petrović, Ž. Stanković, B.Đ. Krstić, N.M. Petrović, *Praktikum iz fiziologije biljaka*. Beograd: Naučna knjiga, 1990.
- [5] A. Mafakheri, A. Siosemardeh, B. Bahramnejad, P.C. Struik, Y. Sohrabi, *Austral. J. Crop Sci.*, 2010, 4, 580-585.
- [6] C.K. Beneragama, K. Goto, *Tropical Agric. Res.*, 2010, 22, 12 – 25.
- [7] R.L. Baldwin, *J. Mol. Biol.*, 2007, 371, 283–301.
- [8] O. Kedem, S.R. Caplan, *Trans. Faraday Soc.*, 1965, 61, 1897-1911.
- [9] V. Dragicevic, S. Sredojevic, in: *Thermodynamics - Systems in Equilibrium and Non-Equilibrium*. Ed. Juan Carlos Moreno Piraján, INTECH, Rijeka, Croatia, 2011, 1-20.

IMPACT OF ROOT MANIPULATION AND BRASSINOSTEROIDS ON GROWTH, PHOTOSYNTHESIS AND THERMODYNAMICS OF MAIZE AT LOWER TEMPERATURES

B. Nikolić¹, V. Dragičević², H. Waisi³, S. Đurović¹, Z. Milićević¹, I. Spasojević² and M. Brankov²

¹ *Institute for Plant Protection and Environment, Teodor Drajzer Str., No. 9, 11040 Belgrade, Serbia (correspondence: bogdannik@mail2world.com)*

² *Maize Research Institute "ZemunPolje", Slobodan Bajić Str., No. 1, 11185 Zemun Polje, Zemun-Belgrade, Serbia*

³ *Institute for the Development of Water Resources "Jaroslav Černi", Jaroslav Černi Str., No. 80, 11226 Belgrade, Serbia*

ABSTRACT

Analysis of growth and dry matter partitioning in plants grown in different volume pots indicates that has large differences between those plants. Manipulation of a level of plant brassinosteroids had slightly influence on these processes. Those differences are caused by different content of free energy in whole plants or in plant parts of plants grown in different volume pots. Also this indicates that the plants grown in small pots are more susceptible to the stress, and there action is modulated by the inhibition of the synthesis of brassinosteroids. Noticed differences between plants grown in different volume pots had parallel changes in photosynthesis parameters.

INTRODUCTION

Interrelationships between factors that affect crop growth are complex. The redistribution of assimilates from different plant parts a key factor in the crop yielding and it depends on the plant hormonal status (particularly brassinosteroids: BRs)[1] and the stress presence [2]. From that point, we investigated maize (ZP505) by methods of root manipulation [3] and treating with 24-epibrasinolide (24-EBL) and propiconazole (PZR -as inhibitor of the brassinosteroids synthesis) [4] during period of suboptimal temperature (14-19 °C) for the maize growth.

EXPERIMENTAL

Maize plants (ZP505) were grown in half-shade ($PAR_{max} \approx 500 \mu\text{mol photon cm}^{-2} \text{ s}^{-1}$) one month, in the pots of $V=5 \text{ l}$ (2/3 so called "5 plants") and $V=11 \text{ l}$ (1/3 so called "11 plants"), until the beginning of September 2013, when $\frac{1}{2}$ of 5 l plants grown were replanted in $V=11 \text{ l}$ pots (so called "5→11 plants").

Then samples for analysis of dry matter partitioning and plant growth [5] and thermodynamic calculations [6] were taken, while the remaining plants were transferred to full daylight (PARmax1500 mmol photon cm⁻² s⁻¹). After 7 days of light acclimation, 1/3 of plants were treated with 24-EBL ($\approx 10^{-6}$ mol) solution, other 1/3 with PZR ($\approx 10^{-6}$ mol) solution and 1/3 were control (K) plants. Treatment was repeated after 7 days. Then parameters of chlorophyll a (Chla) fluorescence [7, 8] were measured and calculated. After 2 weeks experiment was finished, with the final Chla fluorescence measurements, together with the final analysis of growth and thermodynamic parameters. During experiment, outside temperature was mainly suboptimal (T=14-19 °C) for maize growth.

RESULTS AND DISCUSSION

Growth analysis indicates that transplantation of maize plants from the small to larger pots (“5→11 plants”) has the greatest impact on the growth, while manipulation of the BRs content in plants has only marginal effect on growth (data not shown), what isn't obvious by monitoring total fresh (TFW) and dry weight (TDW) of plants (Table 1). It is notable that during the experiment the relative leaf mass (ratio of dry mass of leaves against total dry plant mass; LMR) was reduced and relative root mass (ratio of dry mass of roots against total dry plant mass; RMR) rose at “5 plants”, regardless the way of BRs content manipulation in plants (Table 1). In “11 plants” or “5→11 plants”, we noted a slight LMR and relative stem mass (ratio of dry mass of stem against total dry plant mass; SMR) increase and RMR decrease; where treatment with PZR slightly emphasizes this trend (Table 1). In control and plants treated with 24-EBL, ΔG_{105} values of leaves and stems at “5 plants” and “5→11 plants” are lower than in “11 plants”, but in the case of root ΔG_{105} situation is reversed. In the plants treated with the PZR situation is inverted, meaning that the inhibition of BRs synthesis affects the change of free energy in different organs of maize plants (Table 1). Indeed, PZR treatment affected the root volume of “5 plants” (Table 1). However, if the change in free energy was considered in whole maize plant (ΔG_{105tot}) we note that this parameter is higher in “5 plants”, whereas PZR treatment (Table 1) increases change of free energy in the “5→11 plants”. So the “5 plants” have higher free energy values, indicating their higher susceptibility to the stress, but the reaction is modulated by the inhibition of BRs synthesis. How applied treatments affect the photosynthesis of maize estimated by fluorescence of Chla? The “5 l plants” have high values of RC PS₂ activity indicators (Fv/Fm, Fv/F₀), except in PZR treated plants, while the values of the parameters are same in the “11 plants” (Table 2). It is similar in the case of parameters of photochemical efficiency (Φ_{PS_2} , qP).

Table 1. Parameters of maize (ZP 505) plant growth and matter partitioning and changes of thermodynamic parameters during manipulation of root status and plant content of BRs

Treatments during trial	FW (g) leaves	DW (g) leaves	ΔG_{105} leaves ($J mol^{-1} K^{-1}$)	LMR ($g g^{-1}$) leaves	FW (g) stem	DW (g) stem	ΔG_{105} stem ($J mol^{-1} K^{-1}$)	SMR ($g g^{-1}$) stem	FW (g) root	DW (g) root	ΔG_{105} root ($J mol^{-1} K^{-1}$)	RMR ($J g g^{-1}$)	V root (ml)	TFW (g)	TDW (g)	ΔG_{105} tot ($J mol^{-1} K^{-1}$)	a_w tot ($g g^{-1}$)
Start K 5	4,94	0,46	0,3526	0,561	3,24	0,23	0,1581	0,280	0,68	0,13	0,6135	0,159	-	8,86	0,82	0,3055	0,9074
Start K 11	9,13	0,81	0,5081	0,587	6,45	0,35	0,2713	0,254	2,28	0,22	0,3490	0,159	-	17,86	1,38	0,2530	0,9227
End K 5→11	29,28	2,83	0,3870	0,567	34,42	1,52	0,1684	0,305	4,50	0,64	0,5123	0,128	3,9	68,2	4,99	0,2390	0,9268
End K 5	14,06	1,96	0,3601	0,492	15,01	1,16	0,1574	0,291	8,09	0,86	0,5163	0,216	5,5	37,16	3,98	0,3562	0,8929
End K 11	36,18	3,19	0,5201	0,584	38,95	1,61	0,2518	0,295	5,09	0,66	0,3578	0,121	3,8	80,22	5,46	0,2218	0,9319
End 24-EBL5→11	28,74	3,11	0,2981	0,571	31,94	1,56	0,1383	0,286	5,15	0,78	0,5198	0,143	4,8	65,83	5,45	0,2039	0,9372
End 24-EBL5	13,38	2,04	0,3196	0,481	15,85	1,22	0,1420	0,288	9,11	0,98	0,4823	0,231	3,9	38,34	4,24	0,3685	0,8894
End 24-EBL11	38,58	3,49	0,4720	0,563	46,01	1,98	0,2529	0,319	4,79	0,73	0,3533	0,118	4,4	89,38	6,20	0,2261	0,9306
End PZR 5→11	29,41	3,12	0,2902	0,590	31,2	1,53	0,1327	0,289	3,61	0,64	0,4366	0,121	4,3	64,22	5,29	0,2704	0,9176
End PZR 5	12,80	1,91	0,3073	0,457	16,45	1,36	0,2315	0,325	8,66	0,91	0,6671	0,218	6,8	37,91	4,18	0,3675	0,8897
End PZR 11	30,65	3,55	0,2921	0,608	32,41	1,69	0,1754	0,289	3,99	0,60	0,3190	0,103	3,8	67,05	5,84	0,2184	0,9329

Table 2. Parameters of fluorescence of Chla measured at youngest full developed leaves of same maize plants as in Table 1

Treatments during trial	Fv/Fm (r.u.)	Fv/F ₀ (r.u.)	Φ PS ₂ (r.u.)	qP (r.u.)	NPQ (r.u.)	ETR (μmol quantum m ⁻² s ⁻¹)	RFD ₇₃₀ (r.u.)
Start K 5→11	0,813	4,361	0,091	0,278	3,077	28,90	3,690
Start K 5	0,812	4,361	0,206	0,389	3,217	49,06	4,739
Start K 11	0,794	4,078	0,156	0,383	2,989	42,43	4,335
End K 5→11	0,786	3,756	0,100	0,305	3,144	21,55	3,925
End K 5	0,839	5,250	0,104	0,389	3,376	28,75	4,300
End K 11	0,793	3,836	0,107	0,389	2,944	33,56	3,711
End 24-EBL 5→11	0,836	5,117	0,180	0,500	3,876	45,53	5,228
End 24-EBL 5	0,837	5,283	0,151	0,333	5,111	39,35	6,444
End 24-EBL 11	0,792	3,822	0,088	0,389	3,126	22,77	3,788
End PZR 5→11	0,805	4,137	0,091	0,444	3,182	27,17	4,067
End PZR 5	0,753	3,066	0,153	0,472	3,194	38,55	4,183
End PZR 11	0,785	3,667	0,081	0,389	2,799	18,47	3,485

All NPQ values (photoprotective processes indicator) were high, indicating that the plant fight stress (low temperature), regardless of treatment. Finally, two different indicators of overall photosynthesis (ETR, RFD₇₃₀) point that maize plant struggles with stress and the handling of brassinosteroids content had negative effect on “11 plants”. It is well known that BRs coordinate optimal plant growth and development (especially in the early stages) as well as to modulate plant responses to stressful environmental conditions [1]. Also it is well known that manipulation of plant roots (by volume change of the pots in which the plants grow) affect the overall phytohormone balance [3]. Bearing all this in mind, as a result of the suppression of the level of BRs in plants (treatment with PZR) modulates described changes of growth, photosynthesis and thermodynamic parameters, we assume that in the conditions of low environmental temperatures (with particularly inhibitory effect on photosynthesis of maize [2]) the interrelationship between BRs and cytokinins (synthesized in the plant roots) significantly affect the growth and development of maize plants.

ACKNOWLEDGEMENT

This work was supported by the Grants (No. TR31018 and 31037) of Serbian Ministry of Education, Science and Technological Development.

REFERENCES

- [1] S.D. Clouse, J.M. Sasse, *Ann. Rev. Plant Physiol. Plant Mol. Biol.*, 1998, 49, 427–51.
- [2] W. Larcher, *Physiological Plant Ecology. Ecophysiology and Stress Physiology of Functional Groups*. 4th Ed., Springer, Berlin, Heidelberg, Germany, 2003
- [3] H. Poorter, O. Nagel, *Austral. J. Plant Physiol.*, 2000, 27, 595-607.
- [4] T. Hartwig, C. Corvalan, N.B. Best, J.S. Budka, J.Y. Zhu, S. Choe, B. Schulz, *PloSOne*, 2012 7, 5, e36625.
- [5] C.C. De Groot, L.F.M. Marcelis, R. Van den Boogaard, H. Lambers, *Funct. Plant Biol.*, 2002, 11, 1319-1328.
- [6] W.Q. Sun in: *Desiccation and Survival in Plants: Drying Without Dying*, CABI Publishing, New York, USA, 2002, 47-91.
- [7] K. Maxwell, G. Johnson, *J. Exp. Bot.*, 2000, 51, 659-668.
- [8] H.K. Lichtenthaler, J.A. Miede, *Trends Plant Sci*, 1997, 2, 316-320.

ASSOCIATION OF FEMALE GONADAL HORMONES AND IMMUNITY IN DEPRESSION

M. Mitić, I. Lukić, J. Đorđević and M. Adžić

Department of Molecular Biology and Endocrinology, VINČA Institute of Nuclear Sciences, University of Belgrade, Serbia

ABSTRACT

In this study, we examined the influence of immunity on depressive-like behavior in females in the context of gonadal hormones. We used neuroinflammatory model of depression elicited by lipopolysaccharide (LPS) administration on naïve and ovariectomized (OVX) females and examined the effects of estradiol (E2) and/or progesterone (P4) replacement therapy on Wistar rat behavior. LPS induced depressive-like behavior in both naïve and OVX females. Our behavioral data indicated that E2 and P4 applied alone had opposite effects compared to the E2/P4 combination. The supplementation of both hormones attenuates detrimental effects of LPS-induced inflammation, particularly through stimulation of noradrenergic transmission. Overall immune challenge with LPS is able to induce depressive-like behavior either of naïve or ovariectomized females, particularly depending on ovarian hormones background.

INTRODUCTION

The vulnerability to depression in women is associated with the hormonal fluctuations during their life [1]. The negative symptomology associated with depression is greater in premenstrual and postpartum periods, as well as after menopause or oophorectomy, when women's 17β -estradiol (E2) levels are decreased [2]. Preclinical evidence also points out that E2 affects depressive-like behavior. Reduced depressive-like behavior has been found in females during proestrous, when E2 levels are high, compared to females in diestrous, when E2 levels are low [3]. Within multifactorial origins of depression, chronic inflammation has received increasing attention. Elevated biomarkers of inflammation, cytokines and acute-phase proteins, have been found in depressed patients [4]. Also, it has been shown that gender is the risk factor for depression upon administration of some inflammatory stimuli [5]. To explore the interplay of female gonadal hormones and inflammation in the etiology of depression, we utilize neuroinflammatory model of depression elicited by lipopolysaccharide (LPS) administration on naïve and

ovariectomized females and examine the effects of E2 and/or progesterone (P4) replacement therapy on animal behavior.

EXPERIMENTAL

Naïve and ovariectomized adult 3-month females were administered intraperitoneally with LPS (dose of 500 µg/kg of body mass) and with 17 β-estradiol (E2) (10 µg/kg) and with progesterone (P4) (4 mg/kg). Both steroids were administered subcutaneously dissolved in sesame oil vehicle. Modified forced swim test (FST) was used to test depressive-like behavior. Data are presented as a mean ± SD and analyzed by Two and Three-way ANOVA. The statistical significance was accepted at $p < 0.05$.

RESULTS AND DISCUSSION

The LPS treatment increased immobility in both naïve ($F=21.54$, $p < 0.05$) and ovariectomized females (LPS x OVX interaction, $F=149.08$, $p < 0.05$) (Figure 1), and decreased swimming in both naïve ($F=6.67$, $p < 0.05$) and ovariectomized females (LPSxOVX interaction, $F=107.46$, $p < 0.05$).

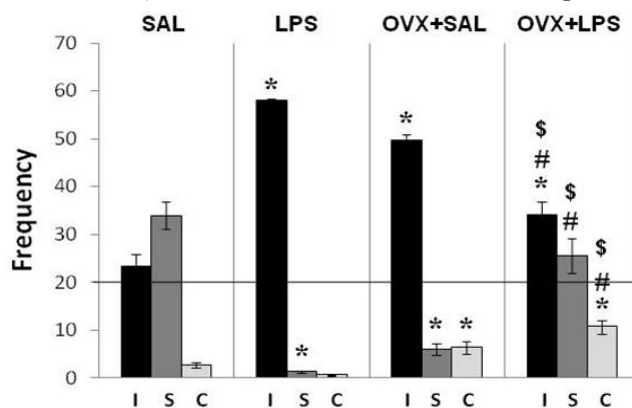


Figure 1. Changes in swimming (S), climbing (C) and immobility (I) (frequency) in the FST in naïve and ovariectomized (OVX) female upon immune challenge. Naïve and ovariectomized females were assigned to the following groups: control (SAL-saline solution, $n=14$), LPS-group ($n=14$), ovariectomized females treated i.p. with saline (OVX+SAL, $n=10$) and ovariectomized females treated i.p. with LPS (OVX+LPS, $n=10$). Data and presented as mean ± SD, $p < 0.05$ (* vs SAL, # vs LPS, \$ vs OVX+SAL).

The climbing behavior was significantly affected both by ovariectomy (OVX, $F=67.09$, $p < 0.05$) and upon LPS treatment of OVX females (LPSxOVX interaction, $F=14.67$, $p < 0.05$). OVX females treated with

vehicle or LPS exhibited significantly increase in climbing compared to controls ($p < 0.05$), to naïve females treated with SAL group ($p < 0.05$) or LPS ($p < 0.05$).

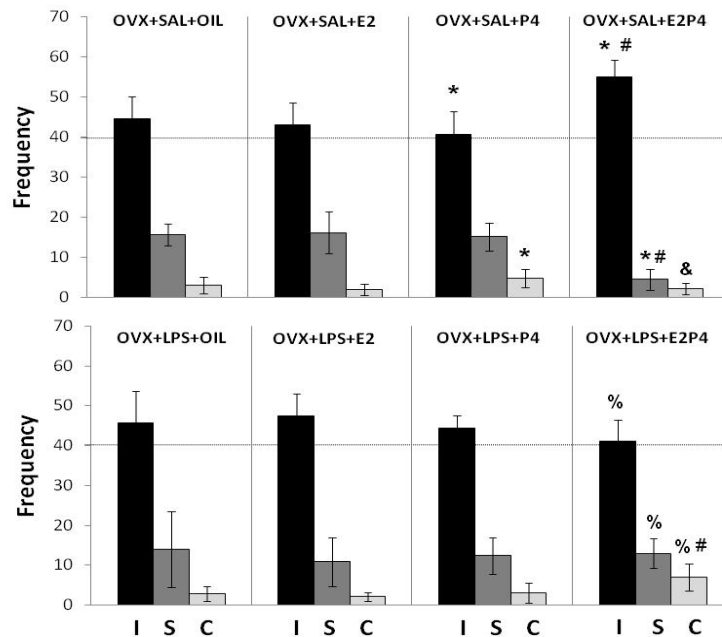


Figure 2: Changes in swimming (S), climbing (C) and immobility (I) (frequency) in FST in ovariectomized (OVX) female rats treated with saline (SAL), lipopolysaccharide (LPS), and hormones (solely E2 and P4 or in combination E2P4). Ovariectomized females were divided in eight experimental groups: ovariectomized-control-control group (OVX+SAL+OIL, $n=8$), ovariectomized-control-E2 group (OVX+SAL+E2, $n=8$), ovariectomized-control-P4 group (OVX+SAL+P4, $n=8$), ovariectomized-control-E2P4 group (OVX+SAL+E2P4, $n=8$), ovariectomized-LPS-control group (OVX+LPS+OIL, $n=8$), ovariectomized-LPS-E2 group (OVX+LPS+E2, $n=8$), ovariectomized-LPS-P4 group (OVX+LPS+P4, $n=8$) and ovariectomized-LPS-E2P4 group (OVX+LPS+E2P4, $n=8$). Data are presented as mean \pm SD, $p < 0.05$ (* vs SAL+OIL, #E2P4 vs other groups, & E2P4 vs P4, and % LPS+E2P4 vs SAL+E2P4).

In Figure 2, P4 administration significantly decreased immobility ($F=14.59$, $p < 0.05$) and in parallel increased climbing ($F=16.41$, $p < 0.05$) of OVX females. Concomitant treatment with both E2 and P4 significantly increased

immobility (E2xP4 interaction, $F=57.81$, $p<0.05$) while decreased swimming (E2xP4 interaction, $F=48.71$, $p<0.05$) and climbing (E2xP4 interaction, $F=4.53$, $p<0.05$). The increase in immobility upon parallel E2 and P4 treatment of OVX rats was significantly higher in comparison to the control group and to the group treated solely with either E2 or P4 ($p<0.05$). Administration of E2 and P4 to OVX females significantly increased climbing compared to all other LPS groups (E2 x P4 interaction, $F=16.36$, $p<0.05$). Significant decrease in immobility (LPSxE2xP4 interaction, $F=40.78$, $p<0.05$) with concomitant increase in swimming (LPSxE2xP4 interaction, $F=22.25$, $p<0.05$) and climbing (LPSxE2xP4 interaction, $F=19.08$, $p<0.05$) was detected upon E2P4 treatment in LPS injected animals.

CONCLUSION

The current study demonstrates that immune challenge with LPS is able to induce depressive-like behavior either of naïve or ovariectomized females. Individual treatment with E2 or P4 of LPS injected OVX rats did not affect behavior profile. However, when LPS-injected animals were treated with both hormones we found a significant increase in climbing compared to other OVX-LPS-groups. These results indicated that supplementation of both ovarian hormones could attenuate the detrimental effects of LPS induced inflammation, particularly through stimulation of noradrenergic transmission.

ACKNOWLEDGEMENT

This work was supported by the Ministry of Education and Science of the Republic of Serbia (Grants no. III41029).

REFERENCES

- [1] U. Halbreich, S. Endicott, S. Goldstein, J. Nee, *Acta. Psychiatr. Scand.* 1986, 74, 576–586.
- [2] K. Torizuka, M. Mizowaki, and T. Hanawa, *Nippon Yakurigaku Zasshi*, 2000, 115, 21–28.
- [3] F.K. Marcondes, K.J. Miguel, L.L. Melo, R.C. Spadari-Bratfisch, *Physiol. Behav.* 2001, 74, 435–440.
- [4] E. Haroon, C.L. Raison, A.H. Miller, *Neuropsychopharmacology* 2012, 37, 137-162.
- [5] Z. Pavlovic, D. Delic, N.P. Maric, O. Vukovic, M. Jašovic-Gasic, *Psychiatr. Danub.* 2011, 23, 370-377.

FLUOXETINE NORMALIZED NUCLEAR PHOSPHO-ERK1/2 SIGNALING IN STRESSED FEMALES

M. Mitić, I. Lukić, N. Božović, J. Đorđević and M. Adžić

*Department of Molecular Biology and Endocrinology,
VINCA Institute of Nuclear Sciences, Belgrade, Serbia,
University of Belgrade*

ABSTRACT

A growing body of evidence indicates extracellular signal-regulated kinase (ERK1/2) participates in various stress-induced responses which is considered to be involved in pathophysiology of depression. Surprisingly, the effect of antidepressants on ERKs is almost unexplored, particularly from the perspective of sexes. In the present study, we investigated the potential role of cytoplasm-nuclear distribution of phospho-ERK1/2 in the hippocampus of chronically stressed female and male Wistar rats and if those potential changes could be attenuated with chronic fluoxetine treatment. In females, stress induced cytosolic retention of phospho-ERKs, while in males it promoted the nuclear translocation of phospho-ERK 1/2. The effect of concomitant fluoxetine treatment was more pronounced in stressed females, with main focus on normalization of its nuclear phospho-ERK 1/2 levels.

INTRODUCTION

Fluoxetine is a widely used antidepressant, which acts via inhibiting 5-hydroxytryptamine (5-HT) reuptake in the central nervous system [1,2]. Novel theories propose that signal pathways related to synaptic plasticity may be the mechanism of antidepressant action in depression [3,4]. The extracellular signal-regulated kinase (ERK) signaling cascade is becoming the focus of much research in the regulation of emotional responses, since ERKs are predominantly found in hippocampus, a brain region which is implicated in stress response and depression [5,6]. Indeed, decreased ERK activity and expression found in post-mortem hippocampus of depressed suicide victims [6], as well as their altered levels in animal models of depression [6,7] support importance of ERK functioning in the aetiology of stress related disorders [5,8].

Upon stimulation, ERKs are activated by phosphorylation in the cytoplasm and then translocated to the nucleus where they can activate a number of transcription factors, such as Elk1 or CREB, resulting in altered gene

expression important for synaptic remodeling and long-term changes in synaptic efficacy. Surprisingly, the effect of antidepressants on ERKs is almost unexplored, particularly from the perspective of sexes.

The present study aims to investigate the potential role of cytoplasm-nuclear distribution of phospho-ERK1 and 2 (pERK1/2) in the hippocampus of chronically stressed female and male rats. We also analyzed if potential changes in their levels could be attenuated or reversed with chronic fluoxetine treatment.

EXPERIMENTAL

Adult female and males Wistar rats (3 months old) were divided into four groups (each consisted of $n=10$): (I) Control+Vehicle, (II) Control+Fluoxetine, (III) Stress+Vehicle (IV) Stress+Fluoxetine. The experiment consisted of two phases and lasted for 6 weeks (42 days). The first experimental phase (Stress) lasted 21 days, during which animals of Stress+Vehicle and the Stress+Fluoxetine were submitted to chronic psychosocial isolation (CPSI). The second experimental phase consisted of the vehicle or fluoxetine treatment for 21 days, while animals remained in the CPSI. Fluoxetine was dissolved in water and administered intraperitoneally (5mg/kg body mass) at daily base between 9:00 a.m. and 9:30 a.m. 24 hours after receiving the final dose animals were sacrificed, their hippocampi were removed and used for preparation the cytosolic and nuclear fractions. The levels of pERK1/2 were detected using Western blot with β -actin as a loading control. Data are presented as a mean \pm SEM and in each gender were analyzed by two-way ANOVA. To determine statistically significant gender differences we used three-way ANOVA employing stress, fluoxetine, and gender as the factors. All statistically significant differences are given as $p < 0.05$ in post-hoc Tukey test.

RESULTS AND DISCUSSION

In females, stress increased cytosolic levels of pERK 1/2 ($F=11.67$, $F=22.31$, $p<0.05$) (Fig. 1a), while it decreased their nuclear levels ($F=4.171$, $F=4.852$, $p<0.05$) (Fig. 1b), suggesting decreased nuclear translocation of pERK1/2, i.e. induced cytosolic retention of pERK 1/2. In males, stress decreased cytosolic levels of pERK1/2 ($F=13.720$, $F=14.130$, $p<0.05$) (Fig. 1 a), while it increased their nuclear levels ($F=53.911$, $F=36.122$, $p<0.05$) (Fig. 1b), suggesting elevated nuclear translocation of pERK 1/2 under stress. Three-way ANOVA revealed significant gender differences upon stress at the levels of pERK 1/2 in both cell compartments (gender \times stress interaction cytosol $F=3.621$, $F=3.542$, nucleus $F=2.121$, $F=3.923$, $p<0.05$) (Fig. 1 a and b).

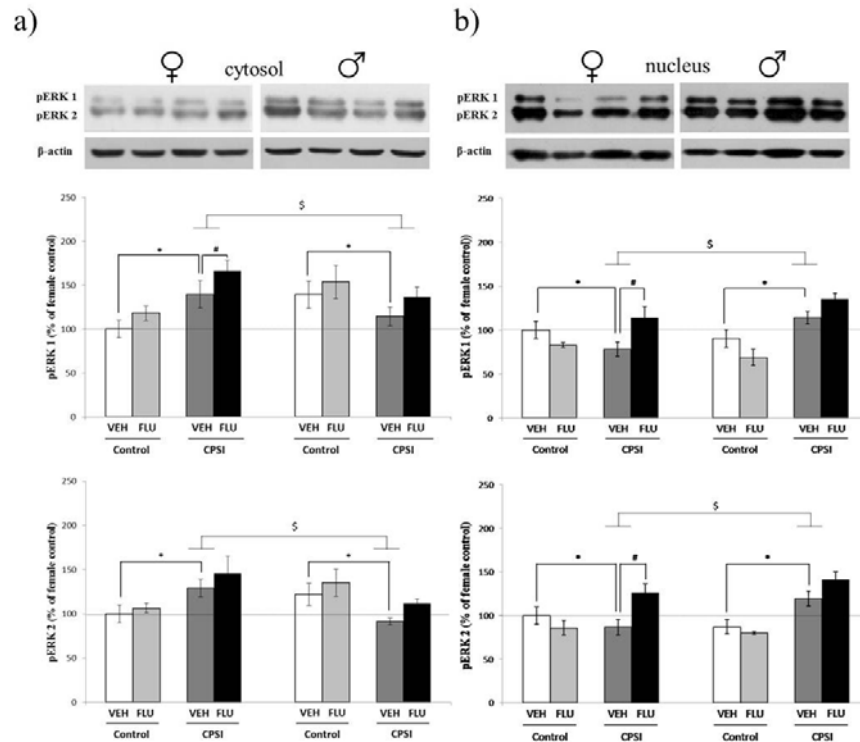


Figure 1. The levels of nuclear pERK 1/2 protein levels in the cytosol (a) and nucleus (b) in the hippocampus of control and stressed (CPSI) female (♀) and male (♂) Wistar rats treated with vehicle (VEH)/fluoxetine (FLU).

Data are presented as mean \pm SEM (*vs. CPSI, # vs. FLU treatment, \$ female vs. male).

Fluoxetine in stressed females increased cytosolic pERK 1 levels ($F=21.233$, $p<0.05$) (Fig. 1a) and both nuclear pERK 1 and 2 levels ($F=16.722$, $F=13.071$, $p<0.05$) (Fig. 1b). Overall these results of pERKs both cell compartments imply that fluoxetine treatment in stressed females predominantly up-regulated nuclear ERK signaling. In stressed males, fluoxetine treatment showed a trend of increase in the nuclear levels of pERK 1/2 (Fig. 1b), but without statistical significance. Three-way ANOVA showed no significant effects between genders on pERK1/2 upon fluoxetine treatment in stressed animals (Fig. 1 and b).

CONCLUSION

Our results provide evidence of gender-specific and compartment dependent regulation of pERK signaling in response to chronic fluoxetine treatment on stressed animals. In females, stress induced cytosolic retention of pERK1/2, while in males it induced opposite effect and promoted the nuclear translocation of pERK 1/2. The effect of concomitant fluoxetine treatment was more pronounced in stressed females, with main focus on normalization of nuclear pERK 1/2 levels.

ACKNOWLEDGEMENT

This work was supported by the Ministry of Science of the Republic of Serbia, grants no. III41029.

REFERENCES:

- [1] Cipriani, P. Brambilla, T. Furukawa, J. Geddes, M. Gregis, M. Hotopf, L. Malvini, C. Barbui, Cochrane. Database Syst. Rev., 2005, 4, CD004185.
- [2] H.J. Lee, J.W. Kim, S.V. Yim, M.J. Kim, S.A. Kim, Y.J. Kim, C.J. Kim, J.H. Chung, Mol. Psychiatry, 2001,6, 725-8.
- [3] H. Einat, P. Yuan, T.D. Gould, J. Li, J. Du, L. Zhang, H.K. Manji, G. Chen, J. Neurosci., 2003, 2, 7311-7316.
- [4] H.K. Manji, W.C. Drevets, D.S. Charney, Nat. Med., 2001,,7, 541-547.
- [5] C.H. Duman, L. Schlesinger, M. Kodama, D.S. Russell, R.S. Duman, Biol. Psychiatry, 2007, 61, 661-670.
- [6] V. Duric, M. Banasr, P. Licznerski, Nat. Med., 2010, 16, 1328-1332.
- [7] Č. Todorović, T. Sherrin, M.Pitts, C. Hippel, M. Rayner, J. Spiess, Neuropsychopharmacology, 2009, 34, 1416-1426.
- [8] F. Fumagalli, R. Molteni, F. Calabrese, A. Frasca, G. Racagni, M.A. Riva, J. Neurochem., 2005, 93, 1551-1560.

INVOLVEMENT OF PREFRONTAL CORTEX CDK5 PATHWAY IN LPS-INDUCED DEPRESSIVE-LIKE BEHAVIOR IN MALE AND FEMALE WISTAR RATS

Ž. Brkić, I. Lukić, M. Mitić, N. Božović, J. Brašanac, J. Đorđević and
M. Adžić

*VINCA Institute of Nuclear Sciences
P.O. Box 522, 11001 Belgrade, Serbia*

ABSTRACT

Systemic exposure to inflammatory challenges, such as lipopolysaccharide (LPS), can induce a central neuroinflammation, which has been associated with the development of major depressive disorder (MDD). Research data emphasize not only sex as an important factor in the pathogenesis of MDD but also point out a disturbance in cyclin-dependent kinase 5 (CDK5) pathway. Therefore, in this study, we investigated the effects of LPS treatment on depressive-like behavior as well as on the CDK5 and p35 levels in the cytosol and the nucleus of the prefrontal cortex of Wistar rats. Our results showed that LPS causes a depressive-like behavior in both sexes, as well as significant changes in the levels of CDK5 and p35, but only in the males. Such differences of CDK5 activity could contribute to the development of depressive-like behavior in males, while in females it seems that some other mechanisms could be involved in the induction of this behavior.

INTRODUCTION

Major depressive disorder is among the most prevalent and costly mental illnesses and many factors can lead to its development [1]. One of the factors that can be associated with the development of this disorder is inflammation. For example, systemic exposure to inflammatory challenges, such as LPS, can induce a central neuroinflammation, which could lead to the development of symptoms similar to MDD. [2] Furthermore, many stress-related mental disorders occur more often in females than in males; specifically, MDD is twice as common in women than in men. There are also sex-specific differences in response to the treatment of the disorder. [3] Thus, it is of major importance to consider the sex of the subject as one of the factors when studying and treating MDD. One of the proteins that has recently been associated with the development of MDD is cyclin-dependent kinase 5 (CDK5) [4]. CDK5 is a proline-directed serine/threonine kinase

that is active only in the central nervous system because of the neuron specific expression of its activating protein, p35. These two proteins have been implicated in synaptic plasticity, underlying learning and memory, and they have been connected to the development of a number of neuropsychiatric disorders.

Taking all this into consideration, we wanted to investigate whether there are sex-specific differences in changes of CDK5 and p35 levels in the cytosol and the nucleus of the prefrontal cortex (PFC) of Wistar rats upon LPS treatment which leads to the development of neuroinflammation.

EXPERIMENTAL

The experiments were performed on 3 months old Wistar rats, that were divided into four groups: two control groups consisted of female/male rats treated with saline solution for seven days and two groups of female/male rats treated with LPS for seven days. Depressive-like behavior was assessed by forced swim test (FST), in which immobility, swimming and climbing were measured during 5 minute sessions. Upon sacrifice, the prefrontal cortex was isolated from each animal. Cytoplasm and nucleus were prepared by differential centrifugation, and proteins were analyzed by Western blot technique. Data were analyzed by two-way ANOVA, followed by post-hoc Tukey test, and presented as a percentage of control values (female controls, set as 100%).

RESULTS AND DISCUSSION

Our results indicated a significant effect of LPS on the behavior of treated animals in both sexes (Table 1); specifically, in FST it increased immobility (LPS: $F=60.75$, $p<0.05$), and decreased swimming (LPS: $F=47.17$, $p<0.05$) compared to the controls. These changes indicate that the development of depressive-like behavior is induced by LPS.

Table 1. Results of forced swim test (FST). Data are presented as mean \pm SD; significant differences are the results of Tukey test, $*p<0.05$

FST	Female		Male	
	Control	LPS	Control	LPS
Immobility	23.21 \pm 13.01	58.05 \pm 1.69*	35.21 \pm 8.57	51.39 \pm 6.31*
Swimming	34.04 \pm 14.18	1.33 \pm 1.35*	21.38 \pm 9.54	6.22 \pm 4.79*
Climbing	2.69 \pm 2.29	0.62 \pm 0.59	3.42 \pm 2.53	2.39 \pm 2.06

As shown in Figure 1 (a and b), LPS affected CDK5 levels only in males, causing them to decrease in the cytosol (LPS: $F=5.96$, $p<0.05$; LPS*sex:

F=25.70, $p<0.05$) (Figure 1a) and increase in the nucleus (LPS: F=57.72, $p<0.05$; LPS*sex: F=67.04, $p<0.05$) (Figure 1b). There was also a significant sex effect on CDK5 levels in both the cytosol (F=10.71, $p<0.05$) and the nucleus (F=9.89, $p<0.05$), i.e. male controls had significantly higher levels of CDK5 in the cytosol and lower in the nucleus compared to the females. These data show an important sex difference in response of Wistar rats to LPS treatment in CDK5 distribution – in males the effect of the treatment is notable, while in females it does not affect CDK5 levels significantly.

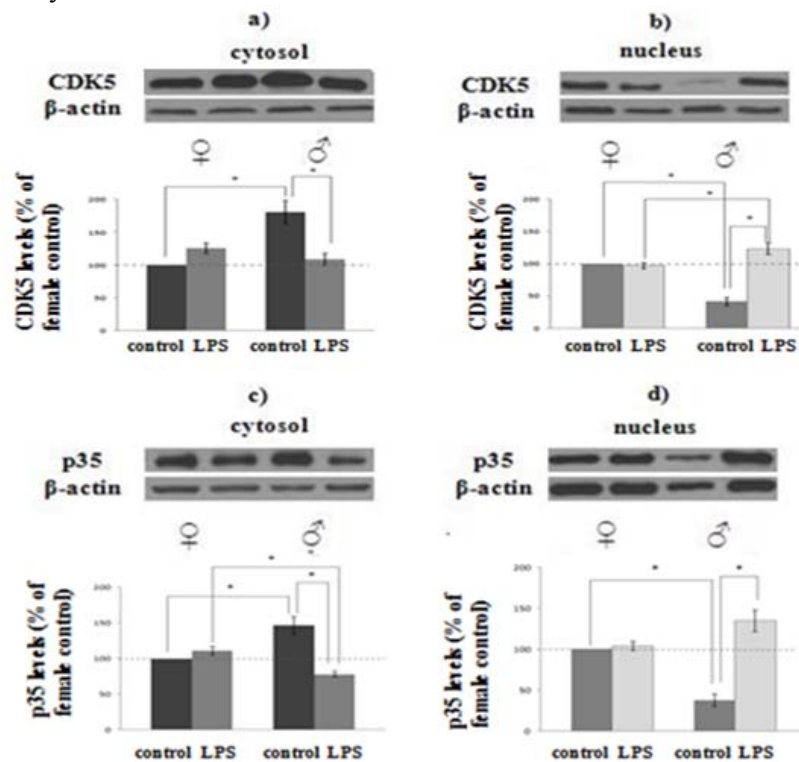


Figure 1. Western blot analysis of CDK5 (a,b) and p35 (c,d) protein levels in the cytosol (a,c) and the nucleus (b,d) of the prefrontal cortex of female and male Wistar rats treated with saline (control group) and LPS (500µg/kg). Results are presented as mean \pm S.E.M; significant differences are from Tukey test, * $p<0.05$ control vs. LPS treatment

As for the levels of p35, LPS affected its levels only in males, decreasing them in the cytosol (LPS: F=15.68, $p<0.05$; LPS*sex: 29.99, $p<0.05$) and increasing them in the nucleus (LPS: F=43.27, $p<0.05$; LPS*sex: F=35.95,

$p < 0.05$) (Figures 1c and 1d). There was a significant sex effect on p35 level in the nucleus as well ($F = 8.81$, $p < 0.05$), i.e. male controls had significantly lower nuclear levels of p35 compared to females (Figure 1d). Although Two-way Anova did not show any effect of sex on p35 distribution in the cytosol, Tukey test suggested otherwise – that male controls had significantly higher cytosolic levels of p35 than females (Figure 1c). These changes suggest that alterations in p35 distribution upon LPS treatment in males are affected in the same manner as changes in the distribution of CDK5, which indicates an increased nuclear CDK5 activity in the PFC of males upon an immune challenge that could be related to LPS-induced depressive-like behavior.

CONCLUSION

LPS treatment causes nuclear translocation of both CDK5 and p35 in males, which suggests increased nuclear CDK5 activity in the PFC of males upon an immune challenge, while it has no effect on the cellular localization of CDK5 and p35 in females. Such differences of CDK5 activity could contribute to the development of depressive-like behavior in males, while in females it seems that some other mechanisms are involved in the induction of this behavior.

ACKNOWLEDGMENT

This study was supported by III41029 project.

REFERENCES

- [1] E. J. Nestler, M. Barrot, R. J. DiLeone, A. J. Eisch, S. J. Gold, L. M. Monteggia, *Neuron*, 2002, 34, 13–25.
- [2] R. Dantzer, J. C. O'Connor, G. G. Freund, R. W. Johnson, K. W. Kelley, *Nat Rev Neurosci*, 2008, 9(1), 46–56.
- [3] C. Dalla, P. M. Pitychoutis, N. Kokras, Z. Papadopoulou-Daifoti, *Basic & Clinical Pharmacology & Toxicology*, 2009, 106, 226–233
- [4] W.-L. Zhu, H.-S. Shi, S.-J. Wang, C.-M. Xu, W.-G. Jiang, X. Wang, P. Wu, Q.-Q. Li, Z.-B. Ding, L. Lu, *International Journal of Neuropsychopharmacology*, 2011, 15, 795–809

**ANTIOXIDANT ACTIVITY OF LIGNICOLOUS FUNGI
SCHIZOPHYLLUM COMMUNE AND *FOMES
FOMENTARIUS*: ECO-FRIENDLY vs AIR POLLUTED
ENVIRONMENT**

M. Karaman¹, S. Gorjanović², M. Glumac¹ and Lj. Janjušević¹

¹University of Novi Sad, Faculty of Sciences, Department of Biology and Ecology, Novi Sad, Serbia. (maja.karaman@dbe.uns.ac.rs)

²Institute of General and Physical Chemistry, Belgrade, Serbia. (desanka.suznjevic@gmail.com)

³University of Belgrade, Faculty of Chemistry, Belgrade, Serbia.

ABSTRACT

The antioxidant (AO) activity of lignicolous fungi, namely *Schizophyllum commune* Fries and *Fomes fomentarius* (L.) J. Kickx f. 1867, was evaluated by polarographic assay based on the decrease of anodic current of hydroxoperhydroxomercury(II) complex (HPMC) formed in alkaline solutions of hydrogen peroxide at potential of mercury oxidation. The AO activity of *Sch. commune* and *F. fomentarius* collected from eco-friendly locations (423±26 and 808±56 %/mL, respectively) and exposed to air pollution (377±12 and 524±17 %/mL, respectively) were compared. Increase of AO activity induced by air pollution was not observed.

INTRODUCTION

Antioxidant (AO) activity of lignicolous fungi have been intensively studied for the last two decades. Phenolic compounds such as phenolic acids (e.g. fumaric, succinic, mallic, 4-hydroxybenzoic, etc.) and flavonoids (e.g. rutin, quercetin, etc.) [1,2], besides tocopherols, ascorbic acid and its analogues, carotenoids and terpenoids, have been found. The white-rot split-gill fungus *Schizophyllum commune* Fries is one of the world's most widely distributed lignicolous species. Although considered inedible in Europe, it is widely consumed in Mexico and elsewhere in the tropics [3]. *Fomes fomentarius* (L.) J. Kickx f. 1867, known as tinder fungus, is a species of plant pathogen broadly distributed on various tree species in Europe, Asia, Africa and North America. The species is not considered edible [4].

This work aimed to give an insight into AO activity of the aforementioned fungal species collected from eco-friendly and air polluted environments by recently developed polarographic assay HPMC based on the decrease of

anodic current of hydroxoperhydroxomercury(II) complex (HPMC) formed in alkaline solutions of hydrogen peroxide at potential of mercury oxidation [5].

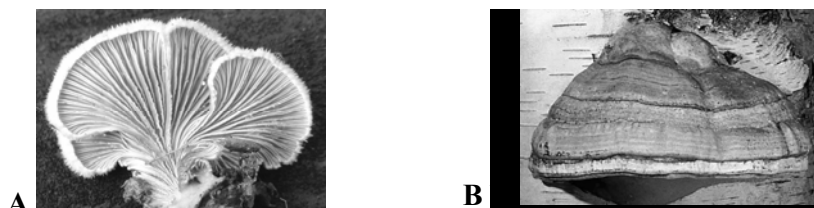


Figure 1. The lignicolous fungi *Schizophyllum commune* (A) and *Fomes fomentarius* (B).

EXPERIMENTAL

The composite samples of *Sch. commune* were collected from two different locations. The first sample of *Sch. commune* originated from eco-friendly locations in Fruška gora mountain (Serbia), while the second one originated from air polluted sites in the city area of Novi Sad (Serbia).

The individual samples of *F. fomentarius* were also collected from two different locations. The first sample originated from eco-friendly location in Ribnica (Slovenia), while the second one originated from air polluted site in Ribarsko ostrvo (Serbia).

All collected fungal samples were dried in oven (12 h, at 50 °C). The dried samples (200 g) were cutted in small pieces and hydrodistilled using the Clevenger apparatus modified by Montiz (4 h, at 100° C). The hydrodistillates were extracted with 96% ethanol for 96 h. The solvent was evaporated, while the dried residues were dissolved in pure dimethyl sulfoxide (DMSO) to a concentration of 20% (w/V).

The polarographic current-potential (i-E) curves were recorded, as described previously [5], using the polarographic analyser PAR (Princeton Applied Research), model 174A, equipped with X-Y recorder (Houston Omnigraphic 2000). A dropping mercury electrode (DME) with a programmed dropping time of 1 s as working electrode, saturated calomel electrode (SCE) as a reference and a Pt-foil as auxiliary electrode were used in the electrolytic cell. All i-E curves were recorded from 0.1 V vs SCE towards negative potentials with a scan rate of 10 mV/s. The current oscillations were damped with instrument filter. Diluted DMSO extracts (1:4) were gradually added in aliquots of 20 µL into 20 mL of starting 5 mM hydrogen peroxide (H₂O₂) (Merck Darmstadt, Germany) in Clark & Lubs (CL) buffer (pH 9.8).

RESULTS AND DISCUSSION

The AO activity of DMSO extracts of *Sch. commune* and *F. fomentarius* species was determined using the recently developed direct current polarographic assay based on decrease of anodic current of hydroxoperhydroxomercury(II) complex (HPMC). Decrease of anodic limiting current noticed upon gradual addition of the extracts was plotted against volume. Polarograms obtained by addition of the extracts of *Sch. commune* and *F. fomes* exposed to air pollution are shown on Fig. 2.

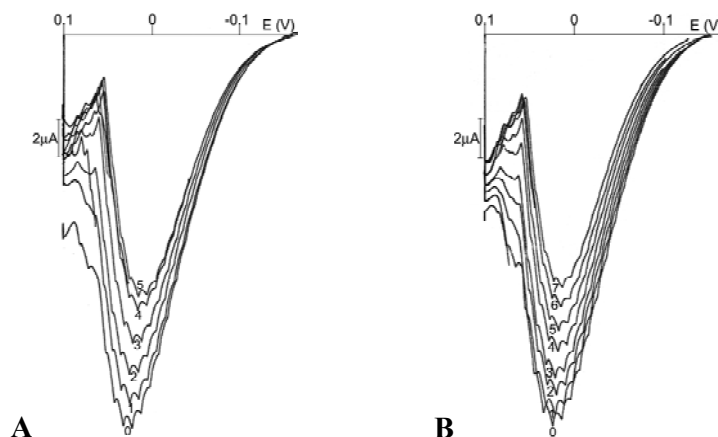


Figure 2. Anodic polarographic curves before (0) and after addition (1-5) of DMSO extracts of *Schizophyllum commune* (A) and after addition (1-7) of DMSO extracts of *Fomes fomentarius* (B) in aliquots of 20 and 10 μL respectively in 20 mL of 5 mM H_2O_2 in CL buffer (pH 9.8). The results presented refer to samples collected from air-polluted environment.

The slopes of the linear part of obtained plots, i.e. percentage of anodic currents height decrease per volume of the examined extracts added, were used as measure of AO activity. The AO activity of *Sch. commune* and *F. fomentarius* DMSO extracts collected from eco-friendly locations (423 ± 26 and 808 ± 56 %/mL, respectively) and exposed to air pollution (377 ± 12 and 524 ± 17 %/mL, respectively) were compared.

CONCLUSION

Increase of AO activity induced by air pollution was not observed. The further research is required to give more comprehensive insight into AO activity of these lignicolous fungi putting stress on a large number of factors including the genetic ones.

ACKNOWLEDGEMENT

This work was supported by the Ministry of Education, Science and Technological Development of the Republic of Serbia (Research Grants Nos. 172053, 172058, 31093 and 43010).

REFERENCES

- [1] M. Karaman, E. Jovin, R. Malbaša, Matavuly M., Popović M. *Phytotherapy Research*, 2010, 24, 1473-1481.
- [2] M. Karaman, M. Stahl, J. Vulić, M. Vesić, J. Čanadanović-Brunet. *International Journal of Food Sciences and Nutrition*, 2014, 65, 311-319.
- [3] F. Ruán-Soto, R. Garibay-Orijel, J. Cifuentes. *Ethnobiology and Ethnomedicine* 2006, 2, 3.
- [4] P. Sterry, B. Hughes, *Complete Guide to British Mushrooms & Toadstools*, HarperCollins, London, 2009.
- [5] D. Sužnjević, F. Pastor, S. Gorjanović, *Talanta*, 2011, 85, 1398-1403.
- [6] D. Sužnjević, F. T. Pastor, S. Gorjanović, S. Milić. 4th Regional South East Europe Symposium on Electrochemistry, Ljubljana, Slovenia, May 26-30, 2013, Programme and Book of Abstracts, p. 146.

EVALUATION OF THE ANTIOXIDANT ACTIVITY OF THE FRESHWATER SPONGE *Ochridaspongia rotunda* (Arndt, 1937) USING TWO POLAROGRAPHIC ASSAYS

B. Pejin¹, A. Talevska², S. Gorjanović³, F. Pastor⁴, T. Talevski⁵ and D. Sužnjević³

¹University of Belgrade, Institute for Multidisciplinary Research - IMSI, Department of Life Sciences, Belgrade, Serbia. (brspjn@gmail.com)

²University of Belgrade, Faculty of Biology, Belgrade, Serbia.

³Institute of General and Physical Chemistry, Belgrade, Serbia. (desanka.suznjevic@gmail.com)

⁴University of Belgrade, Faculty of Chemistry, Belgrade, Serbia.

⁵St. Clement of Ohrid University of Bitola, Hydrobiological Institute, Department of Cyprinid Fish, Ohrid, Macedonia.

ABSTRACT

The antioxidant (AO) activity of selected crude extracts of the freshwater sponge *Ochridaspongia rotunda* (Arndt, 1937) was evaluated *in vitro* by direct current polarography for the first time. The novel assay based on decrease of mercury reduction antioxidant power (MRAP) and the previously established one based on decrease of anodic current of hydroxoperhydroxomercury(II) complex (HPMC) in function of gradually added antioxidants were applied. According to the both assays the methanol extract exhibited higher AO activity than the acetone one (HPMC: 79±3 %/mL vs 47±2 %/mL; MRAP: 49±3 %/mL vs 28±1 %/mL). The results obtained indicate that *O. rotunda* methanol extract may be considered as a promising resource of novel natural products with potent AO activity.

INTRODUCTION

The freshwater sponge *Ochridaspongia rotunda* (Arndt, 1937), endemic to the oldest European Lake Ohrid (30–70 m depth), is considered to be without relatives in the current living world (Fig. 1) [1]. Most bioactive compounds from the sponges can be classified as antitumour, anti-inflammatory and antioxidant [2]. Since some of synthetic antioxidants have been found to be harmful for health, the search for effective antioxidants of natural origin is of great interest.

In the course of ongoing experiments of Pejin and co-workers [3], the antioxidant (AO) activity of the sponge *O. rotunda* was investigated. Herein we report *in vitro* AO activity of its selected crude extracts (methanol and

acetone) determined by polarographic assays based on anodic current of hydroxoperhydroxomercury(II) complex (HPMC) [4] and cathodic current of Hg(II) reducton, i.e. mercury reduction antioxidant power (MRAP) [5].



Figure 1. The freshwater sponge *Ochridaspongia rotunda* (Arndt, 1937).

EXPERIMENTAL

Biological material

The sample of *Ochridaspongia rotunda* (Arndt, 1937) was collected in Lake Ohrid in June 2013. Voucher specimen has been deposited in Hydrobiological Institute, Ohrid, Macedonia.

Extraction

The dried parts of *O. rotunda* were ground (4 g) and extracted thrice with methanol and acetone for 1 h at room temperature, respectively. Then the extracts were evaporated to dryness and stored at $-20\text{ }^{\circ}\text{C}$ until further use.

FTIR analysis

Fourier-transform infrared (FTIR) spectra of the extracts tested were recorded in the attenuated total reflection mode (ATR) using a Nicolet 6700 FTIR Spectrometer (Thermo Scientific).

Polarographic assays (HPMC and MRAP)

Polarographic i-E curves were recorded on Houston Instrument Omnigraphic 2000 X-Y recorder supplied with the Princeton Applied Research 174 Polarographic analyser. Dropping mercury electrode (DME) with programmed time of 1 s was used as a working one. Saturated calomel electrode (SCE) was used as reference and Pt-foil as auxiliary electrode. The initial potentials for i-E curve recording in both assays were 0.1 V and 0.2 V vs SCE, respectively. Initial solution for HPMC assay was prepared by addition of 0.1 mL of 1.00 M H_2O_2 in 19.9 mL of Clark&Lubs (CL) buffer of pH 9.8. Aliquots of 50 μL were added to obtain linear decrease of the anodic limiting current (i_l). Initial solution for MRAP assay was prepared by addition of 1 mL of 0.01 M HgCl_2 in 19 mL of CL buffer. Aliquots of 100 μL and 200 μL of the methanol and acetone extracts respectively were added to obtain linear decrease of cathodic i_l .

RESULTS AND DISCUSSION

The well-developed polarographic assay (HPMC) [4] and newly one (MRAP) [5] were applied to determine AO activity of the sponge *O. rotunda* methanol and acetone extracts. Selected polarograms illustrate the effects of the methanol extract on anodic current of HPMC (A) and cathodic current of Hg(II) reduction (B), respectively. Decrease of anodic limiting current (HPMC) and cathodic limiting current (MRAP) vs the extracts volumes was plotted (Fig. 2). The slopes of the linear part of obtained plots, i.e. percentage of either anodic or cathodic limiting current height decrease per volume of the extracts added, were used as a measure of AO activity.

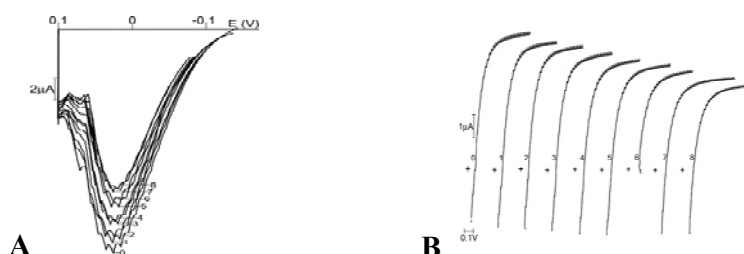


Figure 2. Influence of the sponge methanol extract gradual addition in 8 aliquots: **(A)** of 50 μL on anodic polarographic current of 5 mM H_2O_2 ; **(B)** of 100 μL on cathodic polarographic current of 0.5 mM HgCl_2 ; in CL buffer (pH 9.8), respectively. Plus sign denotes starting conditions, i.e. $i = 0$ and $E = 0.1 \text{ V vs SCE}$.

The extracts were proven to be active, but to a varying degree (Fig. 3). *O. rotunda* methanol extract exhibited higher AO activity according to both HPMC and MRAP assays ($79 \pm 3 \text{ \%/mL}$ and $49 \pm 3 \text{ \%/mL}$) than its acetone extract ($47 \pm 2 \text{ \%/mL}$ and $28 \pm 1 \text{ \%/mL}$).

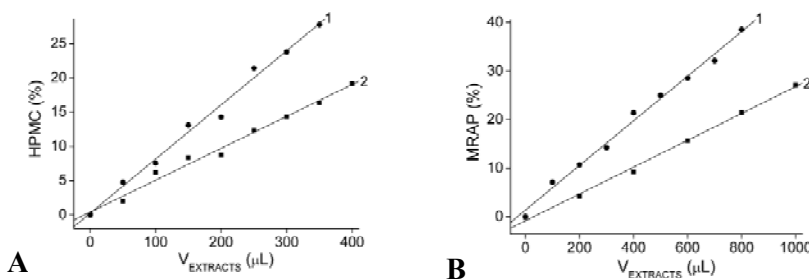


Figure 3. Percentage of decrease of anodic **(A)** and cathodic **(B)** limiting current (i_l) vs volume of the sponge extracts: methanol (●) and acetone (■).

The FTIR spectra of the extracts tested indicate carbonyl compounds, alcohols, fatty acids, sterols and no presence of aromatic natural products. It's worth noting that *O. rotunda* methanol extract *in vitro* displayed potent antibacterial activity (minimum inhibitory concentration /MIC/ 7.5-15.0 µg/mL and minimum bactericidal concentration /MBC/ 15-30 µg/mL), being more effective than the acetone extract [6]. In addition, the both extracts *in vitro* exhibited anti-quorum sensing activity and anti-biofilm activity (under review).

CONCLUSION

This preliminary screening of the sponge *O. rotunda* AO activity indicates for the first time its potential to offer novel antioxidant substances of natural origin. Further research will be focused towards isolation and identification of the sponge antioxidants and their possibly use in medicine.

ACKNOWLEDGEMENT

This work was supported by the Ministry of Education, Science and Technological Development of the Republic of Serbia (Research Grants Nos. 172053, 31093 and 43010).

REFERENCES

- [1] N. J. A. Hooper, R. W. M. van Soest. *Systema Porifera: A Guide to the Classification of Sponges*, Kluwer Academic/Plenum Publishers New York, 2002.
- [2] D. Sipkema, M. C. R. Franssen, R. Osinga, J. Tramper, R. H. Wijffels, *Marine Biotechnology*, 2005, 7, 142-162.
- [3] B. Pejin, C. Iodice, G. Tommonaro, S. De Rosa. *Journal of Natural Products*, 2008, 71, 1850-1853.
- [4] D. Sužnjević, F. Pastor, S. Gorjanović. *Talanta*, 2011, 85, 1398-1403.
- [5] D. Sužnjević, F. T. Pastor, S. Gorjanović, S. Milić. 4th Regional South East Europe Symposium on Electrochemistry, Ljubljana, Slovenia, May 26-30, 2013, Programme and Book of Abstracts, p. 146.
- [6] B. Pejin, A. Talevski, A. Ciric, J. Glamoclija, M. Nikolic, T. Talevski, M. Sokovic. *Natural Product Research*, In Press, doi:10.1080/14786419.2014.911297.

IN VITRO ANTIOXIDANT ACTIVITY OF SELECTED AUTOCHTHONOUS MACROFUNGI

Lj. Janjušević¹, M. Karaman¹, B. Pejin², F. Pastor⁴, M. Glumac¹,
M. Rašeta⁵ and D. Sužnjević³

¹University of Novi Sad, Faculty of Sciences, Department of Biology and Ecology, Novi Sad, Serbia. (ljiljana.janjusevic@dbe.uns.ac.rs)

²University of Belgrade, Institute for Multidisciplinary Research - IMSI, Department of Life Sciences, Belgrade, Serbia.

³Institute of General and Physical Chemistry, Belgrade, Serbia. (desanka.suznjevic@gmail.com)

⁴University of Belgrade, Faculty of Chemistry, Belgrade, Serbia.

⁵University of Novi Sad, Faculty of Sciences, Department of Chemistry, Biochemistry and Environmental Protection, Novi Sad, Serbia.

ABSTRACT

In this work the antioxidant (AO) activity of the methanol extracts of two autochthonous macrofungi *Bjerkandera adusta* (Willd.) P. Karst. and *Trametes versicolor* (L.) Lloyd (1920) was assessed using direct current polarographic HPMC assay and spectrophotometric ABTS assay. According to the both assays used, higher AO activity was ascribed to *B. adusta*: 480±14 vs 108±7 %/mL and 642±56 vs 162±14 mg Trolox equivalents/g extract, respectively. These results have indicated for the first time potential importance of *B. adusta* in searching for novel antioxidant agents.

INTRODUCTION

Autochthonous macrofungi are considered as a good source of natural antioxidants [1]. The aim of this work was to analyse *in vitro* the antioxidant (AO) activity of selected inedible fungal species, namely *Bjerkandera adusta* (Willd.) P. Karst. ([Meruliaceae](#)) and *Trametes versicolor* (L.) Lloyd (1920) (Polyporaceae) (Fig. 1), from habitats in Vojvodina (Serbia) close to each other. In order to evaluate AO activity, a polarographic hydroxoperhydroxomercury (II) complex (HPMC) assay and a spectrophotometric ABTS assay were applied for the first time, regarding the aforementioned biological material.

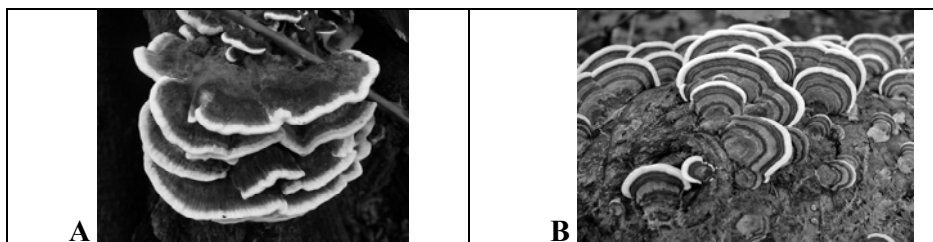


Figure 1. The autochthonous macrofungi *Bjerkanthera adusta* (A) and *Trametes versicolor* (B).

EXPERIMENTAL

Biological material and extraction procedure

B. adusta was collected in Novi Sad in April 2014, while *T. versicolor* originated from Iriški Venac (Fruška gora) in January 2014. After drying in an oven for 24 h at 50 °C, the biological material was ground to get the final powder (20 g). The powder was extracted with 200 mL methanol for 72 h, using shaker. Finally, the filtrate was evaporated to dryness and dissolved in methanol to reach the concentration of 20 % (w/V).

Polarographic HPMC assay

The polarographic current-potential (i-E) curves were recorded, as described previously [2], using the polarographic analyser PAR (Princeton Applied Research), model 174A, equipped with X-Y recorder (Houston Omnigraphic 2000). A dropping mercury electrode (DME) with a programmed dropping time of 1 s as working electrode, saturated calomel electrode (SCE) as a reference and a Pt-foil as auxiliary electrode were used in the electrolytic cell. All i-E curves were recorded from 0.1 V towards negative potentials with a scan rate of 10 mV/s. Diluted methanol extracts (1:4) were gradually added in aliquots of 20 μ L into 20 mL of starting 5 mM H₂O₂ (Merck Darmstadt, Germany) in Clark & Lubs (CL) buffer (pH 9.8).

Spectrophotometric ABTS radical scavenging assay

The assay was performed according to Arnao et al. [3] expressing the results obtained as the mean values of three separate measurements.

RESULTS AND DISCUSSION

The AO activity of the methanol extracts of the macrofungi *B. adusta* and *T. versicolor* was determined using the recently developed direct current polarographic assay based on decrease of anodic current of hydroxoperhydroxomercury (II) complex (HPMC) (Fig. 2) and common spectrophotometric ABTS radical scavenging assay.

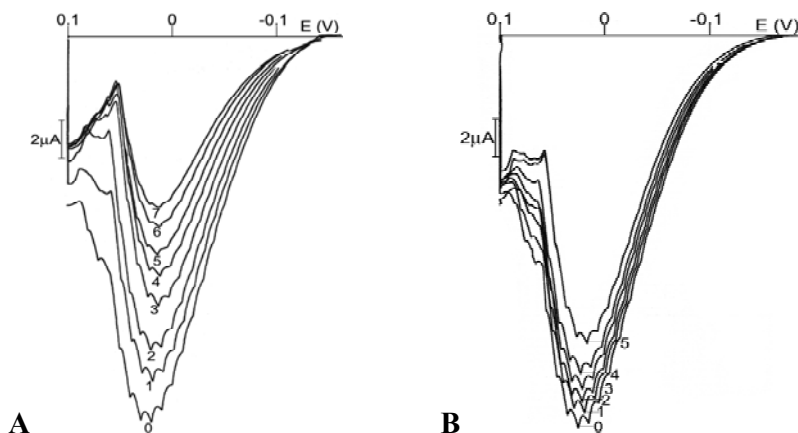


Figure 2. Anodic polarographic curves obtained by none (0) and gradual addition of the methanol extracts of *Bjerkandera adusta* (1-7) (A) and *Trametes versicolor* (1-5) (B) in aliquots of 20 μL in 20 mL of 5 mM H_2O_2 in CL buffer (pH 9.8).

Decrease of anodic limiting current noticed upon gradual addition of the extracts examined was plotted against the volume (Fig. 3). The slopes of the linear part of obtained plots i.e. percentage of anodic currents height decrease per volume of the methanol extracts added were used as a measure of AO activity. AO activity of 480 ± 14 and 108 ± 7 %/mL was ascribed to *B. adusta* and *T. versicolor*, respectively. The experimental data obtained by ABTS assay were in accordance with HPMC assay, 642 ± 56 vs 162 ± 14 mg Trolox equivalents/g extract, respectively. Till date, only AO activity of *T. versicolor* originating from Japan was assessed [4]. Indeed, the study of Kamiyama and co-workers (2013) showed that its different extracts, including the methanol one, possessed DPPH radical scavenging activity in the range of 15 to 51%.

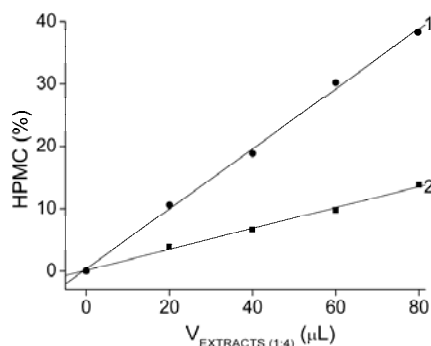


Figure 3. Percentage of decrease of anodic limiting current (i_l) vs volume of the methanol extracts of *Bjerkandera adusta* (●) and *Trametes versicolor* (■).

CONCLUSION

These results have indicated for the first time potential importance of the macrofungal species *B. adusta* in searching for novel antioxidant agents. The further research will be focused on the isolation and identification of its antioxidants including the monitoring of seasonal variation of *B. adusta* AO activity.

ACKNOWLEDGEMENT

This work was supported by the Ministry of Education, Science and Technological Development of the Republic of Serbia (Research Grants Nos. 172053, 172058, 31093 and 43010).

REFERENCES

- [1] M. Karaman, Lekovitost autohtonih makrogljiva, Zadužbina Andrejević, Beograd, 2012.
- [2] D. Sužnjević, F. Pastor, S. Gorjanović, Talanta, 2011, 85, 1398-1403.
- [3] M. B. Arnao, A. Cano, M. Acosta, Food Chemistry, 2001, 73, 239-244.
- [4] M. Kamiyama, M. Horiuchi, K. Umano, K. Kondo, Y. Otsuka, T. Shibamoto, International Journal of Nutrition and Food Sciences, 2013, 2, 85-91.

ANTIOXIDANT POTENTIAL OF THE RESURRECTION PLANT RAMONDA SERBICA

N. Mandić-Kovačević^{1*}, S. Živković², T. Rakić³ and
A. Popović-Bijelić¹

¹*Faculty of Physical Chemistry, University of Belgrade, Studentski trg 12-16, 11000 Belgrade, Serbia, *nebojsa_m@msn.com*

²*Institute for Biological Research "Siniša Stanković", University of Belgrade, Bulevar despota Stefana 142, 11060 Belgrade, Serbia*

³*Faculty of Biology, University of Belgrade, Studentski trg 16, 11000 Beograd, Serbia*

ABSTRACT

The resurrection plant *Ramonda serbica* was completely dehydrated for 14 days, reaching 4.2 % of the relative water content, and then fully rehydrated for 24 h. During dehydration, the total phenolic and flavonoid contents of leaf extracts significantly increased, and then gradually decreased upon rehydration. These changes directly correspond to the observed antioxidant activity of extracts towards the hydrophobic free radical DPPH. The scavenging potential towards the hydrophilic radical Tempone was maximal after 3 h of rehydration, indicating a strong oxidative burst upon water uptake.

INTRODUCTION

An exceptionally small number of higher vascular plant species have the ability to dehydrate their vegetative tissues and overcome drought conditions in the state of physiological inactivity or anabiosis. With an increase in ambient humidity, they readily absorb water, and recover all their physiological activities within several hours or days. These plant species are able to survive repetitive cycles of dehydration and rehydration, without losing their viability, and therefore they are called desiccation-tolerant, poikilohydric or resurrection plants.

The poikilohydric, vascular flowering plant *Ramonda serbica* Panč. & Petrov. (Gesneriaceae) is an endemic and relict plant of the Balkan Peninsula [1,2]. Its highly effective antioxidant system protects cells from reactive oxygen species (ROS), which are one of the most harmful consequences of water deficit and/or metabolic perturbations in cells [3]. Previous studies have shown that during dehydration and rewatering, *R. serbica* plants undergo changes in antioxidant enzyme activities of ascorbate peroxidase, glutathione reductase, superoxide dismutase, and polyphenol oxidase [4-6]. In addition, changes of the total content of various compounds that participate in its antioxidative protection, such as ascorbate, dehydroascorbate, reduced glutathione, and phenolic acids, have been observed.

In this work, we investigated the antioxidant potential of *R. serbica* extracts during the dehydration-rehydration cycle using electron paramagnetic resonance (EPR) spectroscopy. Namely, the capacity of the extracts for the removal of two nitrogen-centered radicals, 2,2-diphenyl-1-picrylhydrazyl (DPPH) and 4-oxo-2,2,6,6-tetramethylpiperidine-N-oxyl (Tempone) were determined.

EXPERIMENTAL

Plants were collected from their natural habitat in the vicinity of the city of Niš (SE Serbia). They were allowed to acclimatize for two weeks during which they were regularly sprayed with water in order to maintain their optimal water status. After acclimatization, the plants were not irrigated for 14 days, and they consequently dehydrated. Desiccated plants were then rewatered for the next 24 hours. Mature leaves from the middle of rosettes were used for analyses. They were harvested from the well watered control plants (C), moderately and completely desiccated plants (D1 and D2, respectively), and after 1, 3, 6, and 24 hours after the beginning of rehydration (R1, R2, R3, R4, respectively). The relative water content (RWC) of all leaves was determined according to Barr and Weatherley [7].

Preparation of plant methanol extracts. Leaves were crushed into powder using liq.N₂ and extracted with 80 % methanol (1:10, w/v). After 20 min centrifugation at 10,000×g, the supernatants were filtered through 0.2 μm cellulose filters (Agilent Technologies, Santa Clara, USA) and stored at 4 °C until use.

Determination of total phenolic content. Total phenolic (TP) content was quantified using the modified Folin–Ciocalteu assay [8]. 50 μl of plant extract was mixed with 475 μl of the 5 % sodium carbonate solution. The mixture was left for 3–5 min and then 475 μl of the 50 % Folin–Ciocalteu reagent was added. The solution was mixed and allowed to stand at room temperature in dark for 1 h. Absorbance was measured at 724 nm using UV–visible spectrophotometer (Agilent 8453, Agilent Technologies, Germany). The TP content was calculated from a standard calibration curve based on gallic acid and the results were expressed as mg of gallic acid equivalents (GAE) per gram of leaf dry weight (mg GAE g⁻¹ DW).

Determination of total flavonoid content. Total flavonoid (TF) content of the samples was determined according to [9], with some modifications. Briefly, 50 μl of plant methanolic extract was mixed with 600 μl ddH₂O, well shaken and mixed with 40 μl of 5 % KNO₂. The mixture was allowed to stand at room temperature for 6 min and subsequently 70 μl of 4.26 % AlCl₃ solution was added. After 5 min at room temperature, 240 μl of 1 M NaOH was added to the mixture and the solution was well mixed. The absorbance was measured at 510 nm. TF content in each extract was calculated from the standard curve based on rutin. The results are expressed as mg of rutin equivalents (RE) per gram of leaf dry weight (mg RE g⁻¹ DW).

EPR spectroscopy. The samples used for EPR measurements contained 30 μl of 200× diluted leaf methanolic extracts and 0.02 mM DPPH or 0.1 mM Tempone. The X-band (9.8 GHz) EPR spectra were recorded on a Bruker Elexsys-II EPR

spectrometer at room temperature under the following conditions: microwave power 10 mW, modulation amplitude 2 G, modulation frequency 100 kHz, conversion time 120 ms, acquisition time 2 min. Spectra were analyzed using Bruker Xepr software. Antioxidant activities of methanolic leaf extracts were determined from the relative heights of the middle EPR peak (DPPH), and the low-field EPR peak (Tempone), as described in [10] using the following formula: $AA(\%) = (1 - I_{extract} / I_{cont}) \cdot 100$, where I_{cont} and $I_{extract}$ are the relative heights of the EPR peaks in the spectrum of the control, and the sample containing the leaf extract, respectively.

RESULTS AND DISCUSSION

The relative water content (RWC) of the well watered control plants (C) decreased from 78.7 % to 61.4 %, in moderately dehydrated plants (D1), and finally to 4.2 % in the completely dried ones (D2). Upon rehydration, the RWC restored rapidly to 19.71 % (R1), 25.08 % (R2), 40.95 % (R3), and 65.1 % (R4) after 24 hours.

The total content of phenolic and flavonoid compounds during the dehydration-rehydration cycle is shown in Figure 1a. It is observed that the dehydrated leaves have the highest content of phenolic compounds, and that this amount is significantly decreased during the first six hours of rehydration. This reduction may be correlated with their role in the antioxidant protection during the strong oxidative burst that occurs at the beginning of rehydration. As previously suggested, the phenolic compounds act against ROS in the initial phase of plant rewatering, being substrates for peroxidases [5,6].

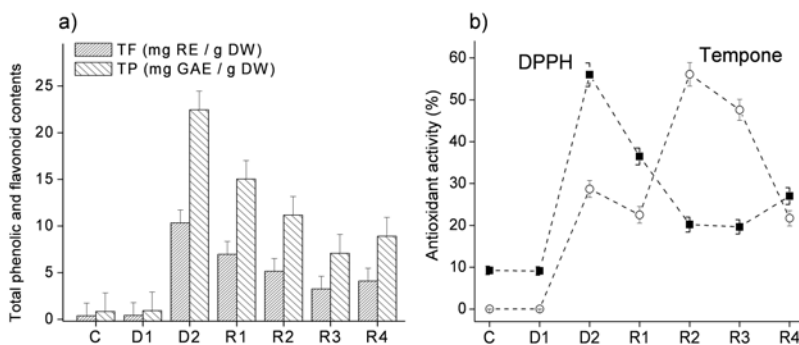


Figure 1. a) Total phenolic (TP) and flavonoid (TF) contents, and b) antioxidant activity towards free radicals, DPPH and Tempone, of *R. serbica* plants subjected to dehydration and rehydration. Error bars are standard deviation from two independent experiments.

The highest antioxidant activity of methanolic leaf extracts towards the free radical DPPH was detected in completely dehydrated and physiologically inactive leaves (D2), Figure 1b. The changes in the antioxidant potential towards DPPH correspond well to the changes in the concentrations of total phenolic and

flavonoid compounds, indicating their important role in protection against ROS, especially during dehydration.

The antioxidant activity of leaf extracts towards Tempone is also increased during dehydration (D2), however it reached its maximum after 3 h of rehydration (R2). This indicates that during the first few hours of rehydration, when the plants experience severe oxidative stress [6], they contain water-soluble compounds that can reduce the hydrophilic free radical Tempone. These compounds are likely to be part of the rehydration-induced antioxidant defense mechanism, and may protect the cells from elevated ROS production during the oxidative burst.

Taken together, the results show that the antioxidant defense system of *R. serbica* is well-coordinated during the dehydration and rehydration processes.

CONCLUSION

Ramonda serbica is a desiccation-tolerant plant that efficiently removes reactive oxygen species that form in water stressed plants, especially at the beginning of plant rewatering. The high capacity for the removal of the Tempone free radical in the initial phases of plant rehydration confirms the existence of the highly efficient ROS-detoxifying mechanisms during the strong oxidative burst. Our results also show that EPR spectroscopy is a valuable tool in the evaluation of the overall antioxidant capacity of plant extracts.

ACKNOWLEDGEMENT

This work was supported by the Ministry of education, science and technological development of Serbia (grants III41005, 173024, 173030).

REFERENCES

- [1] P. Černjavsky, Journal de la Soc. Bot. de Russie 1928, T.13, IV, 1-2.
- [2] S. Petrović, Glasnik Srpskog Učenog Društva 1885, Nova serija 62, 101-123.
- [3] T. Rakić, M. Lazarević, Ž. Jovanović, S. Radović, S. Siljak-Yakovlev, B. Stevanović, V. Stevanović, Front. Plant. Sci. 2014, 4, 550, 1-9.
- [4] A. Augusti, A. Scartazza, F. Navari-Izzo, C.L.M. Sgherri, B. Stevanović, E. Brugnoli Photosynth. Res. 2001, 67, 79-88.
- [5] C. Sgherri, B. Stevanović, F. Navari-Izzo, Physiol. Plant. 2004, 122, 478-485.
- [6] S. Veljović-Jovanović, B. Kukavica, F. Navari-Izzo, Physiol. Plant. 2008, 132, 407-416.
- [7] H.D. Barr, P.E. Weatherley, Austral. J. Biol. Sci. 1962, 15, 413-428.
- [8] V.L. Singleton, J.A.Jr. Rossi, Amer. J. Enol. Viticult. 1965, 16, 144-158.
- [9] F. Karadeniz, H.S. Burdulu, N. Koca, Y. Soyer, Turk. J. Agr. Forest. 2005, 29, 297-303.
- [10] J.M. Dimitrić Marković, Z.S. Marković, I.A. Pašti, T.P. Brdarić, A. Popović-Bijelić, M. Mojović, Dalton Trans. 2012, 41, 7295-7303.

G-QUADRUPLEX FRET PROBES AT THE LIPID MONOLAYER INTERFACE

B. Juskowiak and A. Swiatkowska

Faculty of Chemistry, Adam Mickiewicz University, Umultowska 89b, 61-614 Poznan, Poland, E-mail: juskowia@amu.edu.pl

ABSTRACT

Spectral properties and G-quadruplex folding ability of fluorescent oligonucleotide probes at the cationic dioctadecyldimethylammonium bromide (DODAB) monolayer interface are reported. Thrombin binding aptamer sequence and 21-mer with human telomeric sequence, were end-labeled with fluorescent groups (FAM and TAMRA) to give FRET probes, F19T and F21T, respectively. Fluorescence energy transfer efficiency of monolayer adsorbed probes increased in the presence of sodium or potassium ion in the subphase, which indicated that the probes retained their cation binding properties when adsorbed on the monolayer interface.

INTRODUCTION

Recently, several very sensitive potassium ion sensors have been reported, which are based on K^+ -dependent formation of G-quadruplex structures (G4 DNA) by guanine-rich oligonucleotides [1]. The common idea behind these sensors was to exploit metal cation binding properties of quadruplex-forming DNA sequences that were labeled with reporter fluorescent groups (Fig. 1). The fluorescence energy transfer (FRET) approach was utilized in most cases as a signal transduction strategy with the use of oligonucleotide being modified at both termini with suitable fluorophores (commonly FAM and TAMRA as a FRET pair) [1]. Potassium, which has ionic radius of approximately 1.3 Å, fits exceptionally well in the cavities between guanine tetrads and stabilizes resulting quadruplex structure. In an unbound state, both termini of oligonucleotide probe are separated and the probe exhibits unperturbed fluorescence spectrum dominated by FAM emission. In the presence of K^+ , the quadruplex structure is developed that enables fluorophores to be arranged in a close proximity causing generation of different fluorescence spectrum (quenched FAM band and enhanced TAMRA emission). The preferential ability of potassium to stabilize guanine tetraplexes is well known.

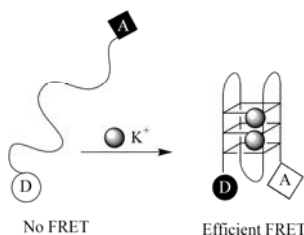


Figure 1. Principle of FRET signal generation by oligonucleotide probe as result of K^+ induced G-quadruplex formation.

To understand performance of these probes and their interactions with cell components, for example cell membrane, we studied interaction of G4 DNA probes with cationic lipid monolayer. DODAB amphiphile was used for monolayer formation at the air/aqueous subphase interface. Fluorescence spectra of probes at different experimental conditions (surface pressure, salt concentration) were recorded using Langmuir trough and spectrofluorimeter equipped with a fiber optic accessory.

EXPERIMENTAL

Diocetadecyldimethylammonium bromide (DODAB) was purchased from Sigma-Aldrich, and was used as received. F19T FRET probe was synthesized and HPLC-purified by Eurogentec, Belgium. FAM and TAMRA labels were attached to termini of an extended TBA aptamer [$G_2T_2G_2TGTG_2T_2G_2AT_3$] using six-carbon linkers. A computer-controlled film balance system (Langmuir trough small, KSV NIMA, Finland) equipped with a platinum Wilhelmy plate pressure sensor was used to carry out monolayer related study. Fluorescence measurements were carried out using Cary Eclipse spectrofluorimeter (Agilent Technologies, Australia). For the fluorescence measurements of monolayer adsorbed probe, a system consisting of Langmuir trough and spectrofluorimeter equipped with an Eclipse fiber optic accessory (Agilent Technologies, Australia) was adapted. The DODAB monolayer was formed on a subphase containing probe at a strand concentration of 8.3 nM (charge ratio of DODAB: probe was 1:1). Fluorescence emission spectra were recorded in the 480 – 800 nm range with the excitation wavelength of 470 nm for FRET measurements.

RESULTS AND DISCUSSION

Spectral properties of the fluorescent probe F19T were first investigated in buffer solution in order to verify its ability to generate FRET signal upon G-quadruplex formation. Metal cation, Na^+ and K^+ , and temperature effect on FRET process were examined. Figure 2A shows fluorescence spectra for F19T recorded in buffer solution containing varying concentrations of K^+ ion.

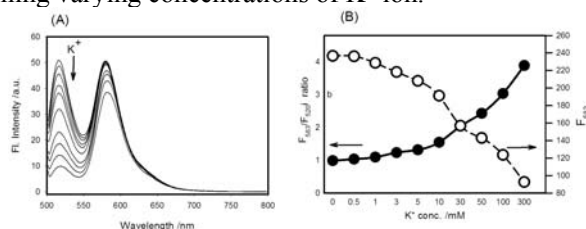


Figure 2. (A) Potassium ion effect on the fluorescence spectra of 0.2 μ M F19T probe at $\lambda_{exc} = 470$ nm. Conditions: 5 mM Tris-acetate buffer (pH 7.5), CH_3COOK conc.: 0 - 300 mM. (B) Effect of K^+ on FRET efficiency expressed as F_{583}/F_{520} ratio (solid line) and on directly excited TAMRA emission (dashed line).

As evident from Fig. 1 A, increase in metal ion concentration causes dramatic quenching of the FAM emission band at 520 nm, whereas the intensity of the TAMRA band at 583 nm slightly decreases. We have previously shown that TAMRA fluorescence is not significantly affected by K^+ concentration [2]. The observed lack of strong sensitized emission from TAMRA can be explained in terms of quenching effect of oligonucleotide bases on TAMRA emission, which is supported by emission profiles of TAMRA excited directly at 560 nm (dashed line in Fig. 2B). The efficient TAMRA quenching ($\sim 70\%$) is not compensated by FRET, and a decrease in TAMRA sensitized emission is therefore observed. Solid line profile (Fig. 2B) represents effect of potassium ion concentration on FRET efficiency expressed as a fluorescence ratio F_{583}/F_{520} . Significant increase in FRET response is observed for K^+ concentration range of 10 – 300 mM.

Our earlier results showed that interactions with G4 DNA shifted the π -A isotherm of the cationic Langmuir film to lower molecular areas when compared with the reference isotherm recorded in the absence of DNA [3,4]. The π -A isotherm recorded on F19T containing subphase was also shifted into lower surface area per molecule, especially at higher surface pressure region ($\pi > 5$ mN/m). The compaction of DODAB monolayer observed in the presence of G4 DNA probe is in good agreement with results reported for unmodified oligonucleotides and indicates that DNA molecules can replace weakly bound acetate ions, causing more efficient neutralization of DODAB monolayer charges [3,4].

The efficiency of FRET process of adsorbed probe was investigated at the interface of a DODAB monolayer spread on TEAA subphase. Since adsorption and spectral characteristics of fluorescent labels may be affected by charge density of monolayer, the effect of surface pressure of monolayer on probe performance was first examined and results are shown in Fig. 3A.

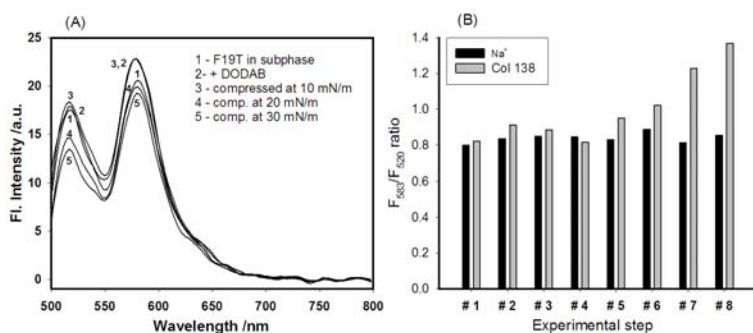


Figure 3. (A) Effect of surface pressure of DODAB monolayer on the fluorescence spectra of F19T probe. (B) Dependence of FRET efficiency for F19T at DODAB monolayer interface before (#1 - #3) and after addition of 50 mM Na^+ (black bars) or 5 mM K^+ (gray bars) (#4 - #8). Consecutive experimental steps: #1 - F19T in subphase, #2- DODAB added, #3 – comp. 30 mN/m, #4 – cation added, #5 – decompressed, #6 - #9 comp. 30 mN/m and spectra recorded at 15 min intervals.

Positions of the fluorescence bands agree with solution spectra of the probe but fluorescence intensity varies with experimental conditions. Spreading of DODAB monolayer on the probe solution ($\pi = 0$ mN/m) caused enhancement of both FAM and TAMRA fluorescence (spectrum 1 versus spectrum 2 in Fig 3A). In contrast, compression of monolayer (spectra 3, 4, 5 in Fig. 3A) exerted rather quenching effect than expected further fluorescence enhancement. Low sensitivity of F19T fluorescence to monolayer compression can be explained by weak interactions between probes and monolayer that results in loosely adsorbed oligonucleotide probes on monolayer interface. Binding selectivity of adsorbed F19T probe was next examined. Variations of FRET efficiency of F19T probe for particular steps of the experiment are compared for sodium and potassium in Fig. 3B. Addition of 50 mM sodium ion (black bars) into subphase behind the barrier imposed negligible effect on the FRET efficiency of F19T probe (#4 - #8) comparing with that for F19T probe before Na^+ addition (#1 - #3). The lack of probe sensitivity to sodium ion is in good agreement with measurements carried out in bulk solution and supports literature reports on low binding affinity of TBA aptamer to sodium cation [1,5]. Taking into account concentration of sodium and potassium at these experiments, one can conclude that the F19T probe has a potential to be used for potassium gradient monitoring close to the external surface of cell membrane.

CONCLUSIONS

Spectral properties and G-quadruplex folding ability of F19T probe were characterized in bulk solution and at the cationic DODAB monolayer interface. Fluorescence spectra and FRET efficiency of probe exhibited modest dependency of the presence of DODAB monolayer and its compression state (surface pressure) showing gradual increase with compression of monolayer (higher surface pressure). FRET enhancement observed also in the absence of metal cations suggested formation of intermolecular aggregates induced by cationic character of DODAB monolayer interface. The probe adsorbed on monolayer interface exhibited K^+/Na^+ binding selectivity, similarly as it was observed for probes in bulk solution.

ACKNOWLEDGEMENTS

This work was supported by the National Science Center (NCN) of Poland (Grant NCN No. 2011/01/B/ST4/01188)

REFERENCES

- [1] S. Takenaka, B. Juskowiak, *Anal. Sci.*, 2011, 27, 1167-1172.
- [2] S. Nagatoishi, T. Nojima, E. Galezowska, B. Juskowiak, S. Takenaka, *ChemBioChem*, 2006, 7, 730-1737.
- [3] B. Juskowiak, J. Paczesny, *J. Colloid. Interface Sci.*, 2012, 365, 150-155.
- [4] B. Juskowiak, A. Swiatkowska, *Colloids and Surfaces A: Physicochem. Eng. Aspects*, 2013, 417, 250– 255.
- [5] N. Kumar, S. Maiti, *Biochem Biophys. Res. Commun.*, 2004, 319, 759-7

SYNTHESIS OF CHROMOGENIC SUBSTRATE FOR SCREENING OF PULLULAN-DEGRADING MICROORGANISMS

D. M. Jakovljević¹, J. Nikolić², A. Djurić², G. Đ. Gojgić-Cvijović¹,
V.P. Beškoski^{1,2} and M. M. Vrvic^{1,2}

¹*ICH_{TM} – Department of Chemistry, University of Belgrade, Njegoševa 12,
P.O. Box 473, 11000 Belgrade, Serbia (djakovlj@chem.bg.ac.rs)*

²*Faculty of Chemistry, University of Belgrade, Studentski trg 12-16,
P.O. Box 51, 11158 Belgrade, Serbia.*

ABSTRACT

A chromogenic substrate was obtained by coupling azo dye Congo red to microbial polysaccharide pullulan. The synthesized product was characterized by spectral techniques and elemental analysis. Results showed that dye-labelled glycan can be successfully used for the screening of microorganisms possessing enzymes that selectively catalyze the cleavage of glycosidic linkages characteristic for this polysaccharide.

INTRODUCTION

Methods based on stained polysaccharide as chromogenic substrates have been reported for the routine assay of different enzymes that specifically hydrolyses chemical linkages significant for certain polysaccharides [1,2]. These substrates are sensitive and highly specific for the target enzymes. Pullulan, one of the extracellular polysaccharides produced by yeast like fungus *Aureobasidium pullulans* is biodegradable, nontoxic and soluble in water, why has great applications in various field, from food industry to medicine and pharmacy [3].

It is a linear α -D-glucan having D-glucopyranose units connected by α -(1,4)- and α -(1,6)-glucosidic bonds. Its main structural characteristic are maltotriose repeating units mutually connected by (1,6)- α -D-glucosidic linkages (Fig.1). Congo red, the sodium salt of 3,3'-([1,1'-biphenyl]-4,4'-diyl)bis(4-aminonaphthalene-1-sulfonic acid) is a benzidine-based anionic diazo dye (Fig. 2) that is widely used for staining different substrates, some of which have commercial application in medicine and microbiology [4].

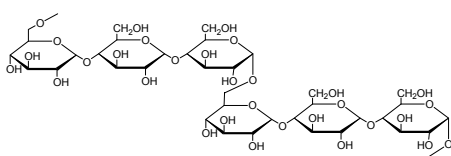


Figure 1. Pullulan

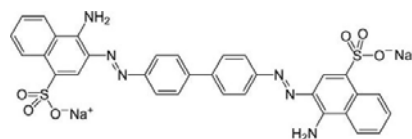


Figure 2. Congo red

In this work a synthesis of stained pullulan with dye Congo red has been reported. The resulting product was characterized by HNMR, UV-Vis and elemental analysis. The aim of this work was the obtaining a new dye labeled glucan as a potential chromogenic material for sensitive screening test of microorganisms that selectively hydrolyzes characteristic linkages of this polymer. Also, this material could potentially be used for the determination of activity of crude enzyme preparations.

EXPERIMENTAL

Pullulan used in this work is produced by *A. pullulans*, strain CH-1 (ICHTM, Collection of Microorganisms) [5,6]. Other reagents and solvents were purchased from commercial sources and used without further application. Pullulan and Congo red were prepared separately, by dissolution in distilled water and then mixed together. The reaction was performed with stirring (50°C, 1 h) and, at different times, equal portions of Na₂SO₄ were added. Then aqueous solution of a Na₃PO₄ was added and reaction maintained at 50°C with extensive stirring for 1 h. Reaction mixture was centrifuged (4000 rpm, 15 min) and the precipitate was resuspended in distilled water and purified of unreacted dye by dialysis. Resulting solution was lyophilized. The ¹H-NMR spectra (Fig. 3) were done on a **Varian Gemini (200 MHz) NMR** spectrometer. UV-VIS spectral characteristics of free dye and product (Fig. 4 and Fig. 5) were recorded using a GBC Cintra 40 spectrophotometer. Elemental analysis (C,H,N,S) was performed using a Vario EL III, CHNS/O Elemental Analyzer, Elementar Analysen systeme GmbH.

RESULTS AND DISCUSSION

The coupling pullulan with Congo red was confirmed by ¹H-NMR data (Fig. 3). The ¹H-NMR spectrum of stained pullulan showed a characteristic signals relating to the polysaccharide and Congo red. In ¹H-NMR spectrum among signals at 5.0 ppm, and 5.4 ppm corresponding to the anomeric protons of α -(1,6)- and α -(1,4)-glucopyranoses, respectively, characteristic for pullulan, can be seen peaks in aromatic part of the spectrum, in the region of 7.0 ppm - 9.0 ppm, related to the signals of aromatic rings of the Congo red dye.

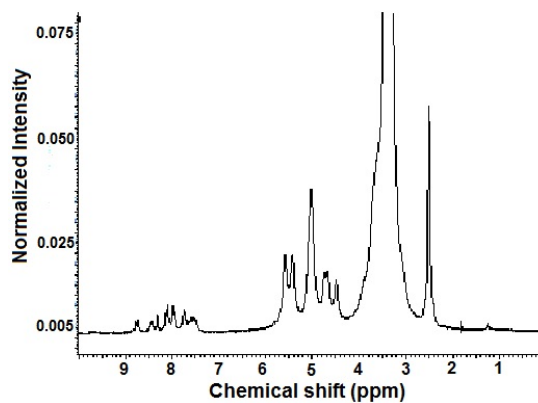


Figure 3. ^1H -NMR spectrum of stained pullulan with Congo red

Additional evidence that pullulan was coupled with Congo red was found in the results of elemental analysis (Table 1.). The content of dye in coupled polysaccharide is reflected by the increase of nitrogen and sulphur content.

Table 1. Elemental analysis of starting substances and reaction product

	% N	% C	% H	% S
Pullulan	/	44.4	6.2	/
Congo red	12.1	55.1	3.1	9.2
Pullulan-Congo red	1.4	35.4	5.2	0.9

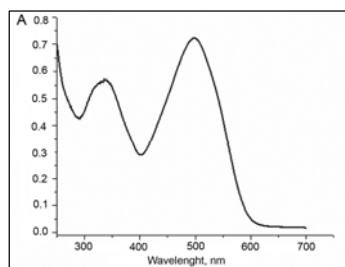


Figure 4. UV-VIS spectrum of pullulan-Congo red

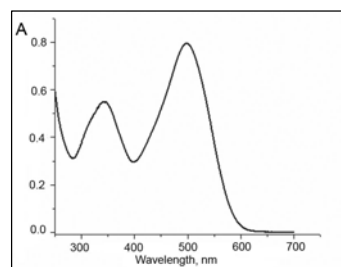


Figure 5. UV-VIS spectrum of Congo red dye

UV-VIS spectral properties of pullulan coupled with Congo red (Fig. 4) did not differ from those of free dye (Fig. 5). Free dye in distilled water (0.8

mg/ml) show two maximum absorption peaks of different intensity, the first peak at 340 nm and the second peak at 498 nm. The spectrum of pullulan-coupled Congo red (2,0 mg/ml) showed a identical shape of the curve with the maximums at the same wavelengths of the spectrum.

CONCLUSION

The dye labeled pullulan was obtained through coupling of this polysaccharide and azo dye Congo red. This novel stained material can be used as potential chromogenic substrate for rapid and sensitive screening test for microorganisms possessing enzymes that selectively hydrolyze α -(1,6)-glycosidic bonds characteristic for pullulan.

ACKNOWLEDGEMENT

This work was supported by the Ministry of Education and Science, Republic of Serbia, Project No. III 43004.

REFERENCES

- [1] L.N. Ten, W.T. Im, M.K. Kim, M.S. Kang, S.T. Lee, *J. Microbiol. Methods*, 2004, 56, 375-82.
- [2] N. X.Y. Ling, F. Pettolino, M.L. Liao, A. Bacic, *Carbohydr. Res.*, 2009, 344, 1941–1946.
- [3] K.C Cheng, A Demirci, J.M. Catchmark, 2011, *Appl. Microbiol. Biotechnol.* 92, 29-44.
- [4] D. P. Steensma, *Arch Pathol Lab Med.*, 2001, 125, 250-252.
- [5] D. M. Jakovljević, M. M. Vrvić, M. Dj. Radulović, M.S. Hranisavljević-Jakovljević, *J. Serb. Chem. Soc.*, 2001, 66, 377.
- [6] M. Đ. Radulović, O. G. Cvetković, S. D. Nikolić, D. S. Đorđević, D. M. Jakovljević, M. M. Vrvić, *Biores. Technol.*, 2008, 99, 6673-6677.

**FTIR AND SEM-EDX SPECTROSCOPIC
CHARACTERIZATION OF BIOMATERIAL CALCIUM
PHOSPHATE/POLY-(DL-LACTIDE-CO-GLYCOLIDE)
UNDER *IN VITRO* SIMULATED PHYSIOLOGICAL
CONDITIONS**

Ž.Mitić¹, S. Stojanović¹, S. Najman¹, M. Cakić², N. Ignjatović³, D.
Uskoković³, A. Stolić¹ and M. Trajanović⁴

¹*Faculty of Medicine, University of Niš, RS-18000 Niš, Serbia*
(zak_chem2001@yahoo.com)

²*Faculty of Technology, University of Niš, RS-16000 Leskovac, Serbia*

³*Institute of Technical Sciences of the Serbian Academy of Sciences and
Arts, RS-11000 Belgrade, Serbia*

⁴*Faculty of Mechanical Engineering, University of Niš, RS-18000 Niš,
Serbia*

ABSTRACT

Changes in calcium phosphate/poly-(DL-lactide-co-glycolide) (CP/PLGA) nanoparticles and ions content after incubation in Dulbecco's Modified Eagle Medium (DMEM) at 37°C were examined in this study. Fourier transform infrared (FTIR) spectroscopy provided molecular structure information related to CP/PLGA nanoparticles and the semi-quantitative analysis of calcium and phosphorous content in CP/PLGA nanoparticles before and after incubation in DMEM was determined by SEM-EDX spectroscopy. SEM analysis revealed changes in morphology while EDX results show that concentration of calcium and phosphorous ions increases after incubation in DMEM and FTIR results show degradation of CP/PLGA polymer component and precipitation of the material similar to hydroxyapatite (HAp) on its surface.

INTRODUCTION

Composite material calcium phosphate/poly-DL-lactide-co-glycolide (CP/PLGA) is used in the engineering of bone tissue. PLGA provides highly porous architecture, similar to trabecular bone, and CP gives strength. [1,2]. Biomimetic properties of CP/PLGA reduce the formation of the fibrous capsule on the interface material/tissue and improve adhesion of osteoprogenitor cells, which ultimately enhances and accelerates the osteogenic process. Dulbecco's Modified Eagle Medium (DMEM) is suitable for the cultivation and maintenance of most types of mammalian

cells, due to its characteristic composition, since provides physiologically necessary ingredients in physiological amounts to the cells, and so presents an environment that mimics the physiological. During the examination of biomaterials *in vitro* on cell cultures, the biomaterials interacts with DMEM so the aim of our study was to investigate any changes of CP/PLGA that occurs due to the interaction of the material with medium.

EXPERIMENTAL

Appropriate amount of CP/PLGA nanomaterial was incubated in Dulbecco's Modified Eagle Medium for 3 days at 37°C.

The FTIR spectra as an average of 200 scans were recorded at room temperature on a BOMEM MB-100 spectrometer equipped with a standard DTGS/KBr detector in the range of 4000–400 cm^{-1} with a resolution of 2 cm^{-1} . In the region all spectra were baseline-corrected and area-normalized. A Fourier self-deconvolution method was applied to enhance the resolution in a spectral region of 4000–400 cm^{-1} .

The morphology of nanoparticles, previously gold-coated, was analyzed on scanning electron microscope (SEM, JEOL JSM 5300), equipped with energy dispersive X-ray spectrometer (EDX, QX-2000) operating at 20 kV. The semi-quantitative analysis of calcium and phosphorus content in biomaterials was determined by EDX spectroscopy.

RESULTS AND DISCUSSION

The IR spectrum of CP/PLGA nanomaterial before incubation in DMEM is shown in Fig. 1a. The IR spectrum is characterized by absorption bands arising from CP and PLGA, determined by analogy with the IR spectra of pure CP and the same PLGA standard samples. Absorption bands with maxima at 1094, 1034, 603 and 564 cm^{-1} arise from the phosphate groups of CP [3]. The wide absorption band with centroid on the approx. 3420 cm^{-1} is the result of stretching vibrations of all types of the hydrogen bound OH groups and H₂O molecules [4]. Sharp band at 3567 cm^{-1} needs attribute to $\nu(\text{OH})$ vibration of the free OH groups, which has not been included in the formation of hydrogen bonds. Absorption bands at 1420 cm^{-1} and 631 cm^{-1} are attributed to the bending vibrations of OH group. The band on the approx. 1600 cm^{-1} is the result of $\delta(\text{HOH})$. Characteristic absorption bands at 1750 cm^{-1} and at about 2926 cm^{-1} are attributed to the stretching vibrations of the C=O and C–H group of PLGA, respectively [5]. Absorption band at 1457 cm^{-1} originates from the bending vibrations of CH₂ group. In area of approx. 860–875 cm^{-1} carbonate band appears from carbonate substitution for hydroxyl and phosphate groups in CP [6].

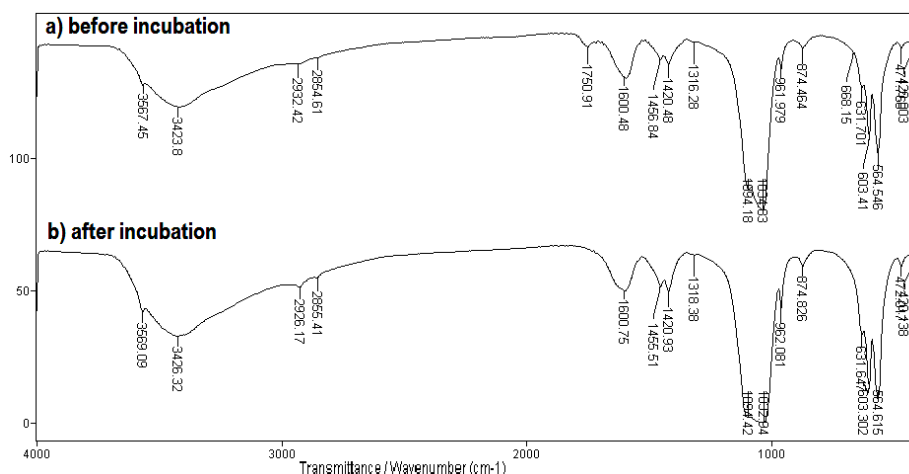


Figure 1. FTIR spectra of CP/PLGA nanomaterial before (a) and after incubation (b) in DMEM

The IR spectrum of CP/PLGA nanomaterial after incubation in DMEM is presented in Fig. 1b. The IR spectrum contains already mentioned absorption bands arising from CP/PLGA nanocomposites (as illustrated in Fig. 1a), except characteristic absorption band at 1750 cm^{-1} which was attributed to the stretching vibrations of the C=O group of PLGA. Absence of the absorption band in the region of 1750 cm^{-1} after incubation in DMEM indicates that the complete polymer PLGA degradation process took place. The IR band changes intensity in the region of OH^- and PO_4^{3-} group vibrations, which were registered on the nanocomposites after incubation in DMEM, may indicate to the formation of hydroxyapatite (HAP) similar nanomaterial on the surface. The analysis of IR spectra of the CP/PLGA nanocomposites, registered after incubation, enables these interactions to be identified. Broadening and intensity increasing of the strong IR bands approx. 3420 cm^{-1} and 1034 cm^{-1} , corresponding to the OH^- and PO_4^{3-} (Fig. 1b), shows the presence of HAP and its interaction with phosphate groups [7]. It implies that the hydrogen bonding may be formed between the CP/PLGA phosphate groups and O–H groups of the HAP [8]. The formation of hydroxyapatite on the surface of the nanocomposites after incubation in DMEM was attributed probably to the ionic exchange between CP/PLGA particles and DMEM.

Changes in chemical composition during incubation in DMEM can be monitored using EDX spectroscopy. For CP/PLGA sample is characteristic that after incubation in DMEM, changes in chemical composition of single components are observed. In the primary stadium of the experiment calcium

and phosphorus ions concentration simultaneously increases after incubation of CP/PLGA in DMEM, and new layer consisting mainly of hydroxyapatite is formed. Additionally, Ca/P ratio approx. 1.65 can indicate the presence of HAp [4]. Furthermore, SEM analysis shows changes in morphology of the samples' surface during the incubation in DMEM, and CP/PLGA powders show structures consisted of non-uniform agglomerates with various average particle sizes.

CONCLUSION

FTIR analysis of CP/PLGA nanomaterial shows that absence of the absorption band in the region of 1750 cm^{-1} after incubation in DMEM indicates that the polymer PLGA degradation process took place. EDX results show changes in chemical composition of single components after incubation in DMEM and SEM investigations revealed changes in morphology.

ACKNOWLEDGEMENT

This work was supported by the Ministry of Education, Science and Technological development of the Republic of Serbia (Grant III 41017).

REFERENCES

- [1] N. Ignjatović, D. Uskoković, *Advances in Applied Ceramics*, 2008, 107, 142–147.
- [2] N. L. Ignjatovic, Z. R. Ajdukovic, V. P. Savic, D. P. Uskokovic, *Journal of Biomedical Materials Research - Part B Applied Biomaterials*, 2010, 94, 108–117.
- [3] B.O. Fowler, M. Marković, W.E. Brown, *Chemistry of Materials*, 1993, 5, 1417–1423.
- [4] T. Ishikawa, M. Wakamura, S. Kondo, *Langmuir*, 1989, 5, 140–144.
- [5] N. Ignjatović, V. Savić, S. Najman, M., Plavšić, D. Uskoković, *Biomaterials*, 2001, 22, 571–575.
- [6] J. Barralet, S. Best, W. Bonfield, *Journal of Biomedical Materials Research*, 1998, 41, 79–86.
- [7] M. Vukelić, Ž. Mitić, M. Miljković, J. Živković, N. Ignjatović, D. Uskoković, J. Živanov-Čurlis, P. Vasiljević, S. Najman, *Journal of Applied Biomaterials and Functional Materials*, 2012, 10, 43–48.
- [8] S. Zhou, X. Zheng, X. Yu, J. Wang, J. Weng, X. Li, B. Feng, M. Yin, *Chemistry of Materials*, 2007, 19, 247–253.

THE ANTIMICROBIAL ACTIVITY OF TRIANGULAR SILVER NANOPATES ON COTTON FABRIC PRETREATED WITH CHITOZAN

I. Vukoje¹, V. Lazić², V. Vodnik^{1*}, B. Jokić³,
S. P. Ahrenkiel⁴, J. M. Nedeljković¹ and M. Radetić³

¹*Institute of Nuclear Sciences Vinča, University of Belgrade, P.O. Box 522,
11001 Belgrade, Serbia, *(vodves@vinca.rs)*

²*Inovation Center, Faculty of Tecnology and Metallurgy, University of
Belgrade, Karnegijeva 4, 11120 Belgrade, Serbia*

³*Faculty of Tecnology and Metallurgy, University of Belgrade,
Karnegijeva 4, 11120 Belgrade, Serbia*

⁴*South Dakota School of Mines and Tecnology, 501 E. Saint Joseph St.,
Rapid City, SD 57701, USA*

ABSTRACT

Triangular silver nanoplates are a type of most-studied noble-metal nanostructures over the past decade, owing to their special structural architecture, outstanding plasmonic features across both visible and IR regions, and catalytic properties for a wide range of applications. Herein, we used these nanoparticles to deposit on cotton (Co) fabric pretreated with biopolymer chitosan (CHT) and investigated their antimicrobial activity. The antimicrobial efficiency of the coated fabrics was evaluated toward Gram-negative bacteria *E. coli*, Gram-positive bacteria *S. aureus* and fungus *C. albicans*. It was found that deposited silver nanoparticles imparted excellent antimicrobial properties to Co fabric.

INTRODUCTION

Silver nanoparticles (AgNPs) are one of the well-known antibacterial substances with multimode level of antimicrobial action, which could be used industrially for several purposes, including amendments to textiles and cosmetics, food processing, water treatment, etc.[1,2]. Their antimicrobial activity depends on size, shape, functional surface coverage and stability in the growth medium. On the other hand, textile materials, in particular cotton under certain conditions, can support the growth of different microbes [1]. One promising innovation is to impart these textiles with antimicrobial properties. Since the chitosan has been exploited in textile finishing, with great metal-complexing capacity due to a free amino and hidroxy groups, we explored its characteristic to enhance deposition of triangular Ag

nanoplates on the Co fabric. Besides, we used low concentration of CHT to avoid its antimicrobial activity, providing possibility to solely investigate antimicrobial effect of triangular Ag nanoplates.

EXPERIMENTAL

Triangular Ag nanoplates were obtained by one step seedless route [3,4]. Aqueous solutions of AgNO_3 (0.1 mM, 25 mL), $\text{Na}_3\text{C}_6\text{H}_5\text{O}_7$ (30 mM, 1.5 mL), H_2O_2 (30 wt%, 60 μL) and PVP (0.7 mM, 1.5 mL) were mixed with 150 μL (0.1 M) of NaBH_4 under vigorous stirring. The solution immediately turned pale yellow, then orange and pink, and finally blue and at the end of the reaction, indicating a finished growth process of nanoplates. The final content of the AgNPs in the colloid solution determined by atomic absorption spectrometer was 11 mg/l.

The optical properties of the AgNPs were studied by Thermo Evolution 600 UV-Vis spectrophotometer, while the morphology and their size were analyzed with a JEM-2100 LaB6 transmission electron microscope (TEM) operated at 200 kV.

Co fabric was first treated with 0.3% CHT solution (solution-to-fabric ratio 30:1), then washed with distilled water, squeezed at pressure of 2 kg/cm^2 and dried at room temperature. Then, 1g of Co fabric or CHT-treated Co fabric was immersed in 25 mL of colloid of triangular AgNPs for 30 min and dried at room temperature.

The antimicrobial activity of Co fabrics loaded with AgNPs was tested against *E. coli* (ATCC 25922), *S. aureus* (ATCC 25923), and *C. albicans* (ATCC 10259) using the standard test method ASTM E 2149-01 [5]. Microbial inoculums was prepared in tryptone soy broth, supplemented with 0.6% yeast extract, and left overnight in thermostat at 37°C. One gram of sterile fabric cut into small pieces was placed in flask with 50 mL of sterile sodium hydrogen phosphate buffer solution (pH = 7.2), which was then inoculated with 500 μL of microbial inoculums and shaken for 2 h at 37°C. A 100 μL volume of aliquots from the inoculums previously subjected to decimal dilution with sterile physiological saline solution were placed in sterile Petri dishes, covered with tryptone soy agar, and incubated for 24h at 37°C. After incubation period, the colony forming units (CFU) of each plate were determined. The percentage of microbe growth reduction (R, %) was calculated using the equation $R = \frac{C_0 - C}{C_0} 100$, where C_0 is the number of

CFU on the control fabric (untreated Co fabric without AgNPs) and C is the number of CFU after deposition of AgNPs on either untreated or CHT-treated Co fabrics.

RESULTS AND DISCUSSION

The morphology study of the initial solution of AgNPs by TEM measurements clearly reveals the presence of triangular and truncated-triangular NPs with edge length between 40-60 nm and thickness of about 5 nm (Figure 1a). Absorption spectrum of AgNPs dispersion contains three distinctive peaks, which indicates the presence of fine triangular AgNPs, Figure 1b. The observed peaks at 332, 466 and 754 nm are assigned to the out-of-plane quadrupole resonance, in-plane quadrupole resonance and in-plane dipole plasmon resonance, respectively [6].

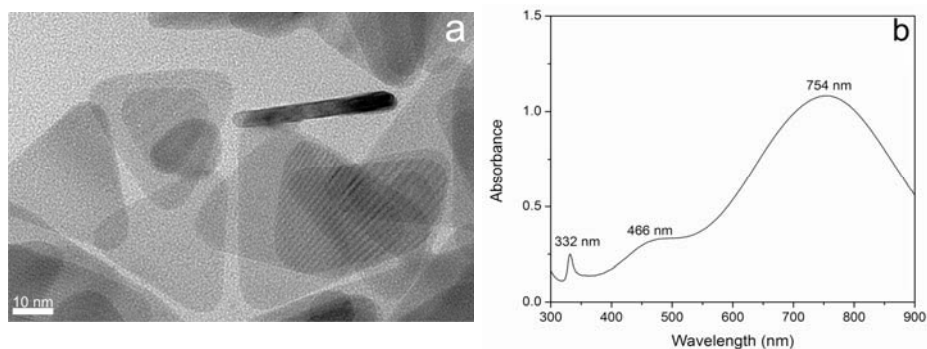


Figure 1. a) TEM image of triangular Ag nanoplates, and b) Absorption spectrum of their colloid dispersion.

Besides, the third peak is very sensitive to the sharpness of the tips on the triangles and for truncated triangles it could be blue-shifted in comparison to the position of resonance band for the perfect prism ($\lambda = 770$ nm), without influence on other resonances. For this reason, the observed blue-shift of third peak ($\lambda = 754$ nm) can be explained by higher yield of truncated prisms with blunt edges in comparison to the perfect prisms.

Antimicrobial activity of untreated and CHT-treated Co fabric impregnated with Ag nanoplates was tested after applied sterilization procedure and compared with CHT-treated Co fabric. It was found that CHT-treated Co fabric impregnated with AgNPs reached maximum microbial reduction in the case of *E. coli* and *C. albicans* ($R = 99.9\%$) and this reduction was $R = 99.6\%$ in the case of *S. aureus*. On the other hand, the values of microbial reduction of untreated Co fabric impregnated with AgNPs were $R = 99.9\%$, 56.9% and 28.4% against *E. coli*, *S. aureus* and *C. albicans*, respectively. Besides, control CHT-treated Co fabric without AgNPs did not show any antimicrobial activity due to low content of CHT on the surface of Co fabric. The results of these antimicrobial tests, clearly indicated that binding

of AgNPs to free amino and hydroxy groups of CHT impregnated Co fabric, induced larger content of deposited AgNPs on the Co fabric compared to untreated fabric, and therefore, higher levels of antimicrobial activity. Furthermore, the encouraging results obtained can be related to the shape of NPs, namely truncated triangular Ag nanoplates, which provide crystalline facets of higher reactivity (high atom densities) and, presumably, a higher rate of ions release from their tips and edges compared to other shapes of NPs.

CONCLUSION

The presented results demonstrated advantage of using CHT-treated Co fabric impregnated with AgNPs instead of untreated Co fabric in order to enhance the antimicrobial activity of coated textiles. Furthermore, this study showed that triangular Ag nanoplates have excellent antimicrobial activity against *E. coli*, *S. aureus* and *C. albicans* strains and could be used to prepare antimicrobial fabrics.

ACKNOWLEDGEMENT

This work was financially supported by the Ministry of Education and Science of Republic of Serbia (research project numbers: 172056 and 45020).

REFERENCES

- [1] V. Ilić, Z. Šaponjić, V. Vodnik, B. Potkonjak, P. Jovančić, J. Nedeljković, M. Radetić, *Carbohydr Polym*, 2009, 78, 564–569.
- [2] E. Guibal, S. Cambe, S. Bavle, J. M. Taulemesse, T. Vincent, *J Colloid Interfaces Sci*, 2013, 393, 411-420.
- [3] A. P. Kulkarni, K. Munechika, K. M. Noone, J. M. Smith, D. S. Ginger, *Langmuir*, 2009, 25, 7932-7939.
- [4] I. Vukoje, V. Lazić, V. Vodnik, M. Mitrić, B. Jokić, S. P. Ahrenkiel, J. M. Nedeljković, M. Radetić, *J Mater Sci*, 2014, 49, 4453-4460.
- [5] ASTM Designation E 2149-01, 2001.
- [6] R. Jin, Y. W. Cao, C. A. Mirkin, K. L. Kelly, G. C. Schatz, J. G. Zheng, *Science*, 2001, 294, 1901-1903.

ANTIBACTERIAL ACTIVITY OF COPPER NANOPARTICLES

U. Bogdanović¹, V. Lazić², V. Vodnik^{1*}, M. Budimir¹, Z. Marković¹, S. Dimitrijević³, and J. V. Džunuzović⁴

¹*Vinča Institute of Nuclear Sciences, University of Belgrade, P. O. Box 522, 11001 Belgrade, Serbia, *(vodves@vinca.rs)*

²*Innovation Center Faculty of Technology and Metallurgy, University of Belgrade, Karnegijeva 4, 11000 Belgrade, Serbia,*

³*Department of Bioengineering and Biotechnology, Faculty of Technology and Metallurgy, University of Belgrade Karnegijeva 4, 11000 Belgrade, Serbia*

⁴*Institute of Chemistry, Technology and Metallurgy-Center of Chemistry, University of Belgrade, Studentski trg 12-16, 11000 Belgrade, Serbia*

ABSTRACT

Copper nanoparticles (CuNPs), with an average particle size of about 5 nm, was prepared by the simple chemical reduction procedure. TEM and UV–Vis spectroscopy contributed to the analysis of size and optical properties of CuNPs, and their antibacterial activity was evaluated toward human pathogenic bacteria *Escherichia coli* and *Staphylococcus aureus*, in a concentration dependent manner. The changes in the cell membrane morphology of tested strains were investigated by atomic force microscope (AFM), after 2 h of their contact with CuNPs. It was found that CuNPs cause different types of cell membrane disruptions, as well as that *S. aureus* bacteria were slightly resistant to the cell membrane damage than *E. coli*.

INTRODUCTION

As a result of growing microbial resistances to multiple antimicrobial agents and development of resistant strains, there is increasing demand for novel antibacterial materials, such as metal NPs. Their main advantage is high surface area to volume ratio compared to bulk material, which provide a large active surface in the contact with microorganisms. Because of high cost of metals like silver and gold, material chemist have focused their attention on exploring possibilities of using CuNPs as ultimate antimicrobial agent [1,2]. Copper toxicity originates not only from the generation of oxidative stress but also from its tendency to alternate between its cuprous, Cu(I), and cupric, Cu(II), oxidation states, differentiating CuNPs from other metal NPs. The both ions-mediated bactericidal mechanisms involve the

inhibition of cellular energy-transducing capabilities and accumulated damage at multiple cellular sites. In this study, the rapid inactivation of the two prokaryote cells by small and bare CuNPs is presented.

EXPERIMENTAL

Synthesis of CuNPs. The Cu hydrosol was prepared under inert atmosphere and vigorous stirring, by the chemical reduction of the weakly acidic (pH = 3 – 4) copper (II) chloride hydrate (0.5 mM) solution, using NaBH₄ (13.2mM) as a reducing agent and ascorbic acid (1.25mM) as a protective agent.

Antimicrobial assays. The antimicrobial activity of the CuNPs was quantitatively assessed in a physiological saline solution (8.5 g NaCl in 1 L of distilled water). *E. coli* (ATCC 25922) and *S. aureus* (ATCC 25923) bacteria were used like a test species. Microbial inoculum was prepared in tryptone soy broth (TSB, Torlak, Serbia), supplemented with 0.6% Yeast Extract (Torlak, Serbia), and left overnight at 37 °C. 3 mL of test solutions with different concentrations of the Cu hydrosol were inoculated with 1% inoculum (30 µL) as well as control sample without CuNPs. The Cu hydrosol was used in the form in which it had been prepared. All tubes were first incubated at 37 °C for 2 h, and after that, 100 µL aliquots was removed and subjected to decimal dilution with sterile physiological saline. From all dilutions 100 µL aliquots were placed in sterile Petri dishes, covered with trypton soy agar (Torlak, Serbia) and incubated 24 h at 37 °C. After incubation period the colony forming units (CFU) of each plate was determined. The percentage of microbial growth reduction (R, %) was calculated using the equation $R = [(C_0 - C)/C_0] \cdot 100$, where C₀ is the number of CFU from control sample and C is the number of CFU from the treated samples.

Characterization. Particles characterizations were performed with Termoscientific Evolution 600 spectrophotometer and transmission electron microscopy (TEM) JEOL–1200EX. Morphological changes of bacterial cell were recorded by AFM (Quesant-Scope Universal Scanning, USA).

RESULTS AND DISCUSSION

Initially, the formation of CuNPs was visually indicated by the color change of the reaction mixture from light blue to reddish-brown. The observed color originates from the strong absorption of the CuNPs when the frequency of the electromagnetic field becomes resonant with the coherent electron motion. As a results, the surface plasmon resonance (SPR) peak at 562 nm is appeared in the absorption spectrum of the CuNPs (Fig. 1). During the NPs grow, metal-catalyzed hydrolysis of borohydride ions and association

of negative charges (BH_4^- and BO_3^{3-}) with the CuNPs, took place [3]. These ions can temporarily stabilize the CuNPs by adsorption onto their surface, providing Coulomb repulsions between them and preventing their aggregation, which was also corroborated by TEM measurement (Fig. 1, inset). The dark spots on the TEM image present almost spherical CuNPs, with an average diameter of 5.3 ± 0.1 nm.

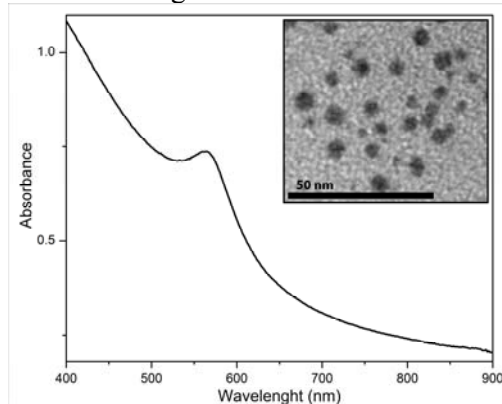


Figure 1. UV – Vis spectrum of CuNPs;
Inset: TEM image of CuNPs

Results of the biological activity trials on the tested strains showed that microbial sensitivity toward different CuNPs concentration (8, 16 and 32 ppm), vary depending on the microbial species. After 2 h of their contact, CuNPs were able to reduce 99.9 % of *E. coli* and 98.0 % *S. aureus* strains, at high CuNPs concentrations of 32 ppm. It was found that microbial reduction reached maximum

against *E. coli* at all CuNPs concentration, but only with concentration of 32 ppm there was no microbial growth (<10). Besides, Cu NPs were shown good antibacterial activity against *S. aureus*, but only one or two logarithm units reduction of initial number of colonies in the presence of 8 and 16 ppm or 32 ppm of the CuNPs concentration, respectively. The results indicate that all tested concentration of CuNPs are more effective against *E. coli* than *S. aureus*.

Antibacterial activity of CuNPs was visually confirmed by AFM measurements, before and after 2h of their contact with CuNPs (Fig. 2). It can clearly be seen that surface of untreated rod-shaped *E. coli* and *S. aureus* spheres is smooth and compact, (Fig. 2a, 2b insets). Electrostatic interaction between Cu ions and membrane phospholipids causes disruption of the *E. coli* cell wall in the form of grooves and pores, and splitting strains' apical ends (Fig. 2a). The shape of treated cocci cell appeared to be damaged with greatly roughened surface texture as a consequence of reaction amine and carboxyl groups in peptidoglycan layer with Cu ions, (Fig. 2b). Comparing the data of these two strains, the effect of the CuNPs on the cell morphology was much less intense in the case of *S. aureus* than for *E. coli*, probably because of the thicker peptidoglycan layer and intrinsic difference in the cell wall structure. To conclude, the changes in cells morphology, as well as the possible damage caused by there cycling redox

reactions between Cu^{2+} and Cu^+ at the surface of the cells and their electrostatic interactions with peptidoglycans and lipids will affect the bacteria in processes such as the respiratory chain, and cell division, finally causing the death of the cell.

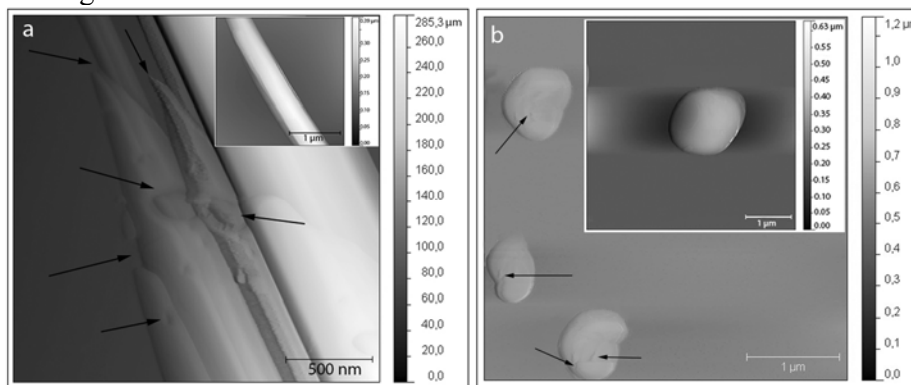


Figure 2. AFM images of (a) treated and untreated *E. coli* (inset); (b) treated and untreated *S. aureus* (inset).

CONCLUSIONS

The above set of results have shown evidence that prepared CuNPs with large and free surface to liberate ions, have a high and rapid antibacterial activity, visible after 2 h of their contact. These NPs have the advantage to closely interact with cell membrane, causing its damages and disturb its permeability and respiration function. Fast control of pathogenic microbes by these NPs, offering an inexpensive disinfectant for the rapid treatment of wastewater generated from hospitals.

ACKNOWLEDGEMENTS

This work was supported by the Ministry of Education, Science and Technological Development of the Republic of Serbia (Grants 172056 and TR 31035).

REFERENCE

- [1] M. Raffi, S. Mehrwan, T.M. Bhatti, J.I. Akhter, A. Hameed, W. Yawar, M.M. Hasan, *Annals of Microbiology*, 2010, 60, 75-80.
- [2] U. Bogdanović, V. Lazić, V. Vodnik, M. Budimir, Z. Marković, S. Dimitrijević, *Materials Letters*, 2014, 128, 75–78.
- [3] V.V. Vodnik, J.M. Nedeljković, *Journal of Serbian Chemical Society*, 2000, 65, 195-200.

INFRARED SPECTROSCOPY ANALYSIS OF THE MAIZE GRAIN CHEMICAL CONTENT

Č. N. Radenović^{1,2}, G. V. Maksimov³, N. S. Delić¹, G. J. Stanković¹,
M. D. Sečanski¹, M. D. Pavlović⁴ and N. Mitić⁵

¹*Maize Research Institute, Zemun Polje Belgrade, Serbia ,
(radenovic@sbb.rs)*

²*Faculty of Physical Chemistry, University of Belgrade, Belgrade, Serbia,*

³*Faculty of Biology, M. V. Lomonosov State University, Moscow, Russia,*

⁴*Institute of general and Physical Chemistry, Bio-lab, Belgrade, Serbia.*

⁵*Faculty of Mathematics, University of Belgrade, Belgrade.*

ABSTRACT

Fourier Transformed Infrared spectroscopy (FTIR) of maize inbred lines (ZPPL 186, ZPPL225 and M1-3-3 Sdms.) grains, with high-quality traits, were performed in order to determine their possible conformational and functional properties. The existence of spectral bands varying in number, intensity, shape, frequency and kinetics has been determined. These bands are determined by valence oscillations and deformation oscillations of the following functional groups: alkanes, alkenes, alkynes, amides, alcohols, ethers, carboxylic acids, esters, aldehydes and ketones that are characteristic for biogenic compounds of carbohydrates, vitamins, pigments and dietary fibres. On the basis of results obtained, it may be concluded that conformational and functional properties of the three studied inbred lines were mainly similar.

INTRODUCTION

The Fourier Transformed Infrared spectroscopy (FTIR) method was applied to diagnose, at the molecular level, the state of biogenic compounds and life functions of three (ZPPL 186, ZPPL225 and M1-3-3 Sdms) maize inbred lines grains. Previously, we [1] described changes in the molecular structure of carotenoids in grain of various maize hybrids and inbred lines and showed that the structure of these molecules can be used as a molecular marker in evaluation of agronomic values of maize inbred lines and hybrids. The aim of this study was to develop methods of the registration of the IR spectrum of grain of observed maize inbred lines, and to identify conformational and functional changes in molecular bonds in grain biogenic compounds by the analysis of these changes.

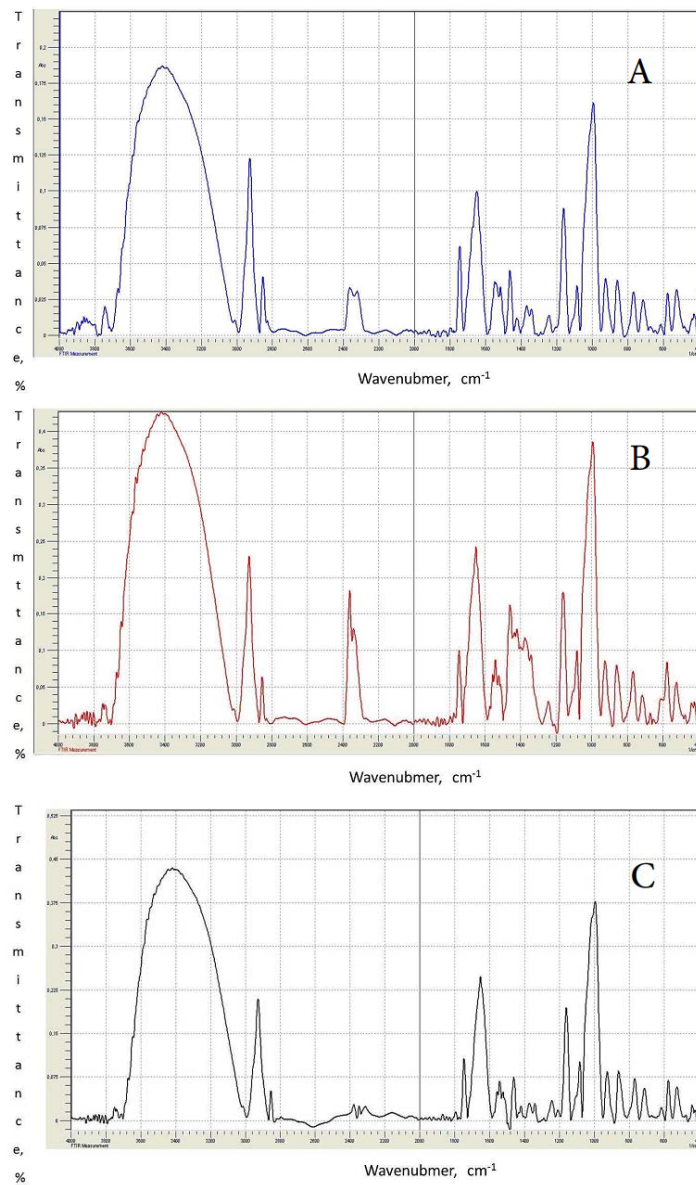


Figure 1. FTIR spectra of the maize inbred lines grains: (A) ZPPL 186, (B) ZPPL 225 and (C) M1-3-3 Sdms.

Table 1. Conformational and functional FTIR spectra properties of inbred lines maize grain organic molecules caused by valence vibrations.

*Characteristic IR regions of valence vibrations of organic molecules according to which our obtained results were compared in relation to the compound class and the functional group. [Source: Vollhardt & Schore, 1996, ref.: 3]

Maize inbred lines	Intensity of the most pronounced spectral bands, %	Wavenumber, cm ⁻¹	Biogenic organic molecule*	
ZPPL 186	81.5	3400 3200-3650* 3250-3500*	alcohols amines alkynes	
	73.0	1000 1000-1260*	alcohols ethers	
	58.0	2900 2840-3000* 2500-3300*	alkenes carboxylic acids	
	50.0	1700 1690-1750*	aldehydes ketones	
	38.0	1175 1000-1260	alcohols ethers	
	36.0	1350 1000-1260*	alcohols ethers	
	100	3410 3200-3650 3250-3500*	alcohols amines alkynes	
	ZPPL 225	94.5	3260-3330* 1000 1000-1260*	alcohols ethers
		53.0	1675 1620-1680* 1690-1750*	alkenes aldehydes, ketones
		51.0	2925 2500-3300* 2840-3000*	carboxylic acids, alkenes
48.0		2375 2100-2260* 2220-2260*	alkynes nitriles	
39.5		1175 1000-1260*	alcohols, ethers	
M1-3-3 Sdms		76.5	3400 3200-3650* 3250-3500*	alcohols amines
	66.5	1000 1000-1260*	alcohols, ethers	
	48.5	1650 1620-1680*	alkenes	
	36.5	2950 2500-3300* 2840-3000*	carboxylic acids, alkenes	
	34.5	1175 1000-1260	alcohols, ethers	

EXPERIMENTAL

Plant material. The following three maize inbred lines with high-quality traits were studied: ZPPL 186, ZPPL225 and M1-3-3 Sdms. Inbreeds were grown at The Maize Research Institute, Zemun Polje, Belgrade, Serbia.

Methods. FTIR spectroscopy of homogenised (with KBr addition), maize inbred lines grains was done by the IR spectroscope (Shimadzu IRPrestige-21), in the range of 4000 - 400 cm^{-1} . Grains chemical composition of was done by the methods described previously [2].

RESULTS AND DISCUSSION

Grain maize inbred lines FTIR spectrum is characterized by 22-24 spectral bands in the range of 4000-400 cm^{-1} . Spectral bands can be differently pronounced, can be of uneven intensity (transmittance, %), particular kinetics and of various widths at the base. Five or six spectral bands for each studied maize inbred line were analysed and the following data were gathered and compared with the literature data [3]: intensity (%), value of the experimentally established wavenumber, wavenumber range, and at the end, the classes of organic molecules with their functional groups. (Table 1). When the same parameters for the studied maize inbred lines were compared, (Table 1), it appeared that there is no differences for spectral bands at 3400, 2950, 2925, 2900, 1175 and 1000 cm^{-1} . However, maize inbred lines differed at 2375, 1700, 1675, 1650 and 1350 cm^{-1} . It turns out that we dealt with: (1) aldehydes and ketones (ZPPL 186 at 1700 cm^{-1}), and then alcohols and esters (ZPPL 186 at 1350 cm^{-1}); (2) alkenes and nitriles (ZPPL 225 at 2375 cm^{-1}), and then alkanes, aldehydes and ketones (ZPPL 255 at 1675 cm^{-1}) and (3) alkenes (M1-3-3 Sdms at 1650 cm^{-1}). On the basis of results obtained, it can be concluded that the conformational and functional properties of the three studied inbred lines have similar properties.

ACKNOWLEDGEMENT

This work was partially supported by the Ministry for Science of the Republic of Serbia (Grants no. 172015 and TR 31055).

REFERENCES

- [1] Č. Radenović, M. Jeremić, G. V. Maximov, M. M. Mišović, B. V. Trifunović, Journal of Scientific Agricultural Research 1994, 55, 33-47.
- [2] Č. Radenović, D. M. Grodzinskij, M. Filipović, Physiology and Biochemistry of Cultivated Plants 2010, 42, 187-201.
- [3] P. C. Vollhardt, N. E. Schore, Organic Chemistry. W.H. Freeman and Company, United States, pp. 387-412, 472-473, 828, 1996.

ASSESSMENT OF LEAD ACCUMULATION BY LEAVES OF *CYNADON DACTIYON* AND NEEDLES OF *PINUS PINEA*

M. Alushllari^{1*} and N. Civici¹

*Institute of Applied Nuclear Physics, University of Tirana, Albania,
(m.alushllari@gmail.com)*

ABSTRACT

Lead is easily accumulated in the edible parts of leafy vegetables, grain and fruit crops. The accumulation of lead in agricultural soils is potentially hazardous to ecosystems and human health. The aim of this study is the determination of lead in leaves of *Cynadon dactiyon* and needles of *Pinus pinea* grown around the former Battery Production Factory Berat, Albania, as well as calculated bioaccumulation factor, soil to plant. Samples are analyzed for their content of lead by using Atomic Absorption Spectrometry in the Institute of Applied Nuclear Physics, University of Tirana, Albania. From the results obtained, concentrations of biological samples were found to be very high (1.5-4 mg/kg). The concentration ranges of lead in biological samples collected are compared with the Maximum Contaminant Levels specified by the Directive No. 1881/2006 Brussels. Concentrations of lead were measured also in surface soil, near the root of plant species. The concentrations in representative surface soil samples is about 4-19 times higher than lead levels recommended by European Union according the Directive 86/278/EEC. In addition we have calculated bio accumulation factor soil to plant.

INTRODUCTION

There are many metals that support life, as well as the normal functioning of the human body, animals and plants species [1]. The presence of heavy metals is dangerous because they have tendency to bio accumulate [2]. Lead is known as one of the most toxic heavy metals in the environment. Lead is inclined and tends to be accumulated in the environment. Lead and its compounds are toxic which can enter the human body through food, water, and air [3]. The high level of lead has a negative impact on the natural environment and the health of livestock and human. The sources of emissions of lead in the environment are natural and anthropogenic. The exposure to lead in the environment results in a wide range of negative effects, depending from the level of lead and time of extended. As a result, the contamination of soils has influence on the increasing the lead levels in vegetation [4]. Mining, refining, utilization and disposal of heavy metals have increased occupational as well as non-occupational exposure to numerous elements. The environmental protection is and remains the main goal of the society. Subject area is the former Battery Production Factory in the city of Berat, Albania. It was designed to produce batteries for passengers' cars and trucks, other military and

technical equipment. During its activity (20 years) except primary production, this factory has produced solid, liquid and gaseous waste in the environment. The purpose of this study is the determination of lead in leaves of *Cynadon dactiyon* and needles of *Pinus pinea* grown around the former Battery Production Factory as well as calculation of determinate BAF soil to plant. One of the used methods for determination of heavy metals in the environmental components is AAS. The level of Pb in soil samples was compared to the values recommended by the European Community according to Directive 86/278 EEC, while for biological samples level of lead was compared by Directive No. 1881/2006, Brussels [5] [6].

MATERIALS AND METHODS

Both representative soil and vegetation were collected around the former Battery Production Factory, Berat, at a distance about 5-50 m from factory building. This Factory is located in the northeastern city of Berat, with respective coordinate: 40° 42' 24.82" N and 19° 58' 59.42" E. During the sampling we have chosen 4 stations and we have collected a total 11 soil and vegetation samples in this area. 4 samples were surface soils samples and 7 were vegetation samples (four were *Cynadon dactiyon* and three *Pinus pinea* samples). Soil samples are collected at the surface soil 0-5cm, while vegetation samples were random vegetation in this area. Represented soil samples analyzed using Atomic Absorption Spectrometer Aanalyst 800 Perkin Elmer with Atomic Absorption Spectrometry Flame method, Perkin-Elmer. Hollow cathode lamp used as radiation source. Acids used for the digestion of samples were Merck and Perkin Elmer. Digestion soil samples are prepared using a procedure recommended by Environmental Protection Agency was used as the conventional acid extraction method [7]. Biological samples are digestion according method AOAC 1990 [8] [9]. Instrumental conditions for lead are based on Analytical Methods of AAS from Perkin Elmer. Three applications were carried out for the measurement of calibration standards and measurement of samples. A quality control material IAEA-Soil7 was analyzed in parallel with the soil samples and IAEA_336 Lichen was analyzed for biological samples. To check the instrumental drift, an aqueous standard solution was analyzed after every three samples.

RESULTS AND DISCUSSIONS

In the Tables 1 and 2 are presented the mean concentrations of lead and Relative Standard Deviation percentage (% RSD), Standard Deviation (SD) and calculated Hazardous Quoted [10] respectively in representative soil and vegetation samples, collected inside of the territory of the Battery Production Factory.

Table 1. Concentration of lead in soil and vegetation; calculated HQ and BAF.

Nr	Sampling	Code in AAS	Pb(mg/kg)	SD	%RSD	HQ	BAF
Results for soil samples							
1	S_1	P1 T1-surface soil	3008	33.09	1.1	10	
3	S_2	P2 T1- surface soil	5663	7.36	0.13	18.9	
6	S_3	P3 T1- surface soil	1135	41.98	3.7	3.8	
7	S_4	P4 T1- surface soil	5511	22.04	0.4	18.4	
Results for vegetation samples							
1	S_1	P1_BS- <i>Cynadon dactiyon</i>	3.226	0.05	1.7	0.0034	
2	S_2	P2_BS- <i>Cynadon dactiyon</i>	3.501	0.03	0.8	0.003	
3	S_2	P2_PN- <i>Pinus pinea</i>	2.227	0.05	2.4	0.0004	
4	S_3	P3_BS- <i>Cynadon dactiyon</i>	1.519	0.12	8	0.0002	
5	S_3	P3_PN- <i>Pinus pinea</i>	3.437	0.48	14	0.0006	
6	S_3	P3_PT- <i>Pinus pinea</i>	3.829	0.34	9	0.0013	
7	S_4	P4_PT <i>Pinus pinea</i>	4.034	0.2	16.2	0.0007	

We have calculated HQ in representative soil samples and it was found to be 3.8-18.9 times higher than normal. In biological samples lead was found in the order 1.5mg/kg-4mg/kg. The lead levels in vegetation samples are compared with the MCL specified by the Directive 1881/2006 (0.1 mg/kg dw). In the Figure 1 is presented the summary of dependence of the lead concentrations in soil and vegetation samples respectively, calculated HQ (for surface soil samples) and calculated BAF soil to plant. In the Figure 2 & 3 are presented contour plot of lead concentration against N&E coordinates respectively in soil and vegetation samples. In the Figure 4 is shown correlation factor between concentration of lead in soil and vegetation. This correlation was very weak, with factor 0.0274.

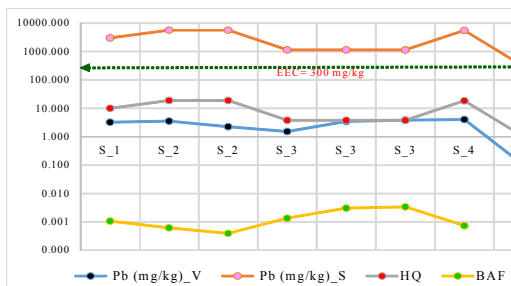


Figure 1. Pb in soil and vegetation, HQ, BAF

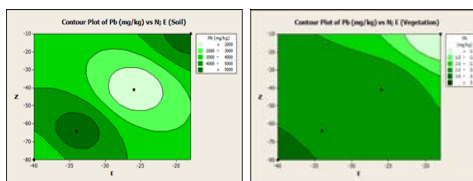


Figure 2&3. Contour plot of Pb spatial distribution in soil and vegetation.

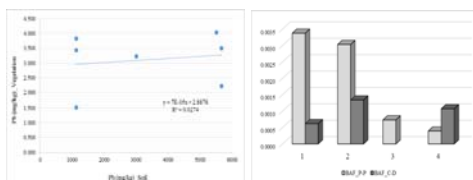


Figure 4. Correlation between all samples. Fig 6: Compare of BAF soil to P-d; P-n

Graphs in figure 5 present variation of calculated BAF soil to vegetation, for *Cynodon dactylon* (P-d) and *Pinus pinea* (P-n), respectively.

CONCLUSION

During this investigation fraction of lead was found to be present in all representative soil and vegetation analyzed samples. Lead concentrations in samples was found above the MCL concentrations recommended by Directive 86/278/EEC and Directive No. 1881/2006, Brussels for fraction of lead respectively in soil and in vegetation. Calculated HQ for soil samples was above 1, so the area around of the former Battery Production Factory in the city of Berat, Albania where samples are collected was contaminated with lead. Calculated BAF for soil to vegetation samples was low, because the mean concentrations of lead in soil and in vegetation were not in the same order. Environment pollution and BAF depends on the concentration of lead in soil and vegetation as well as its duration of exposure. The high concentrations of lead affect environment ecosystems and human health. Lead contamination of this territory was caused by the activity of the factory. Often industrial pollution produced by the manufacturing process, have been uncontrolled.

REFERENCES

- [1] Alushllari M., Civici N. and Deda A., (2014),. *Scientia Agriculturae*. Page 76-79. DOI: 10.15192/PSCP.SA.2014.1.2.7679.
- [2] Censi P, Spoto SE, Saiano F, Sprovieri M, Mazzola S, Nardone G, Di Geronimo SI, Punturo R, Ottonello D, (2006) *Chemosphere* 64: page1167-1176.
- [3] Alushllari M., Civici N, (2014). *Applied Science Reports*. 122-124. DOI: 10.15192/PSCP.ASR.2014.1.3.122125.
- [4] ZakrzeWski SF (2002). *Environmental Toxicology* 3Rd Edition. Oxford University Press. USA, pp.5-45.
- [5] EEC, Economic European Communities. (2006). The Council Directive 86/278/EEC on protection of the environment.
- [6] EEC, Economic European Communities. (2006). Setting maximum levels for certain contaminants in foodstuffs. *Official Journal European Communities*, L 364/5-L 364/24, Directive No. 1881/2006, Brussels.
- [7] Anonymous,-EPA,-Method-3050B.
www.epa.gov/osw/hazard/testmethods/sw846/pdfs/3050b.pdf.
- [8] AOAC, 1990. *AOAC official methods of analysis*. 15th ed. Association of Official Analytical Chemists, Arlington, Virginia. Page 84–85.
- [9] AOAC (1990). *Official Method of Analysis*. Association of Official Analytical Chemists, Arlington, USA.
- [10] U.S. EPA (Environmental Protection Agency). 2006. *Provisional Peer Reviewed Toxicity Values for Aluminum (CASRN 7429-90-5)*. U.S. Environmental Protection Agency, National Center for Environmental Assessment, Superfund Technical Support Center, Cincinnati, OH. October23.

THE EFFECTS OF DIAZINON AND ITS DEGRADATION PRODUCTS ON OXIDATIVE STRESS PARAMETERS IN RAT BRAIN SYNAPTOSOMES

M. Čolović¹, V. Vasić¹, N. Avramović², D. Djurić³ and D. Krstić²

¹ *Department of Physical Chemistry, Vinča Institute of Nuclear Sciences, University of Belgrade, Serbia*

² *Institute of Medical Chemistry, School of Medicine, University of Belgrade, Serbia*

³ *Institute of Medical Physiology "Richard Burian", School of Medicine, University of Belgrade, Serbia*

ABSTRACT

In *vitro* evaluation of oxidative stress responses to various concentrations of diazinon and its degradation products, diazoxon and 2-isopropyl-6-methyl-4-pyrimidinol (IMP) was investigated by determining antioxidant enzymes activity (catalase (CAT), superoxide dismutase (SOD) and glutathione peroxidase (GPx)) and lipid peroxidation level in rat brain synaptosomes. Diazinon showed negligible prooxidative properties causing increase in antioxidant enzymes activity and lipid peroxidation level up to 10%. Increasing concentrations of diazinon oxidation product, diazoxon activated CAT (up to 20%), SOD (up to 50%), GPx (up to 25%), and significantly increased the content of lipid peroxidation indicator (up to 50%). The investigated hydrolysis product of diazinon, IMP did not remarkably influence the activity of CAT, GPx and lipid peroxidation level (up to 10%), while it induced SOD stimulation up to 30%.

INTRODUCTION

Oxidative stress has been reported as one of the adverse effects in poisoning by organophosphorus pesticides (OPs) in both humans and animals [1, 2]. Investigations have shown that pesticides can damage the balance between prooxidants and antioxidants, resulting in both the increased production of reactive oxygen species (ROS) and attenuation of the antioxidant barrier of the organism [3, 4]. The key enzymes for the detoxification of ROS in all organisms are superoxide dismutase (SOD; EC 1.15.1.1), catalase (CAT; EC 1.11.1.6) and glutathione peroxidase (GPx; EC 1.11.1.9).

The aim of this study was to investigate *in vitro* effect of various doses of organophosphorous insecticide diazinon and its degradation products

(diazoxon and IMP) by determining antioxidant enzymes activity (CAT, SOD, GPx) and lipid peroxidation level in rat brain synaptosomes.

EXPERIMENTAL

Synaptosomes were isolated from the brain of *Wistar albino* rats and incubated at 37°C for 1 hour in the presence of desired concentrations of diazinon, diazoxon and IMP (within the range 1×10^{-7} - 1×10^{-4} mol/L). Antioxidant enzymes activities and malondialdehyde (MDA) content as a lipid peroxidation indicator were determined using standard methods [5].

RESULTS AND DISCUSSION

The influence of exposure for 1 hour toward increasing concentrations of diazinon, diazoxon and IMP on the activity of CAT, SOD and GPx is presented in Figure 1 (a-c). Obtained results show that the activity of synaptosomal CAT (Figure 1a) was not affected by diazinon as well as by its hydrolysis product IMP, at all investigated concentrations. Unlike these two compounds, diazoxon significantly increased synaptosomal CAT in a dose-dependent way. The presence of maximal investigated diazoxon concentration (1×10^{-4} mol/l) increased CAT activity up to 23% in comparison with the control.

Specific SOD activity in the absence (control) and presence of various concentrations of diazinon and its degradation products, diazoxon and IMP is presented in Figure 1b. The obtained results show that diazinon does not result in significant changes in the enzyme activity. Actually, the highest investigated concentration (1×10^{-4} mol/l) increases SOD activity approximately 10%. The products of diazinon hydrolysis and oxidation, IMP and diazoxon cause concentration-dependent activation of the antioxidant enzyme. At the highest investigated concentration (0.1 mM), diazoxon stimulates SOD activity about 50% related to control, while IMP causes 30% alteration (Figure 1b).

Similar to the results obtained for CAT, diazoxon induces the increase in GPx activity, while diazinon and IMP do not result in statistically significant change of the enzyme activity (Figure 1c). Increasing diazoxon concentrations induce the gradual activation of GPx up to 25%, obtained at the maximal investigated concentration (0.1 mM).

The effect of diazinon, diazoxon and IMP on the level of MDA is shown in Figure 2. In the case of IMP and diazinon, MDA content was changed up to about 10% compared to untreated synaptosomes, at the highest concentration (0.1 mM). On the contrary, the MDA level is gradually increased with increasing concentrations of diazoxon, reaching the highest increase of about 50% at a concentration of 0.1 mM (Figure 2).

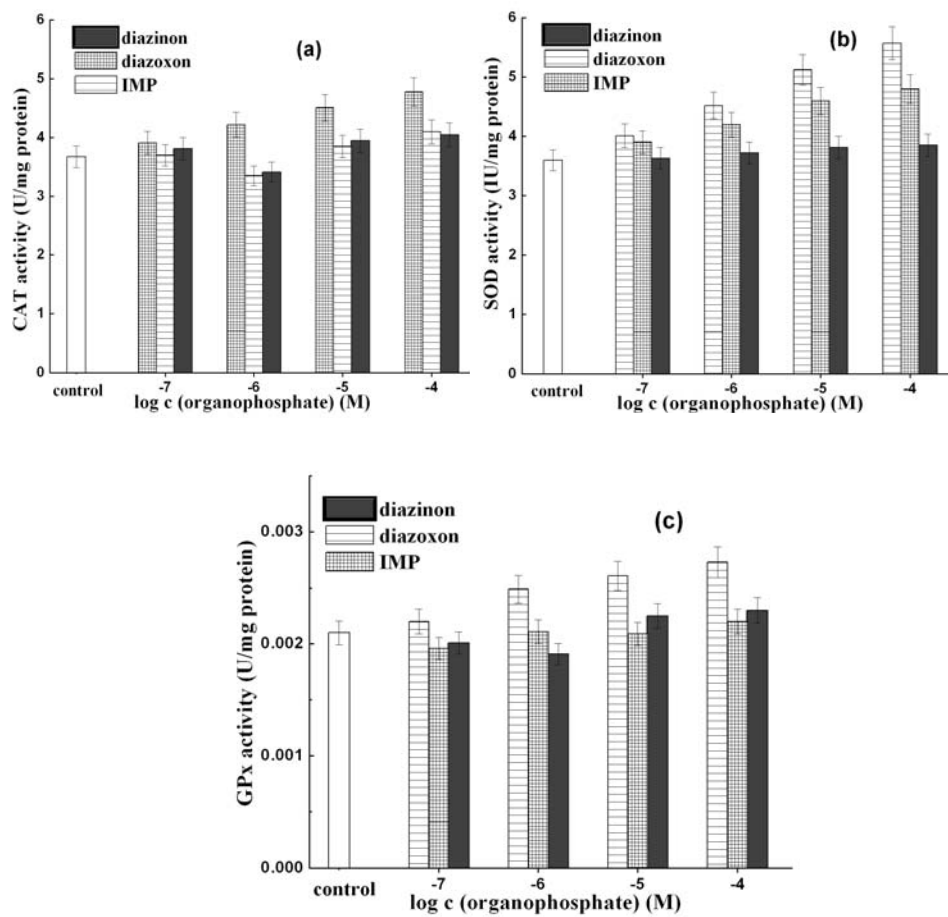


Figure 1. CAT (a), SOD (b) and GPx (c) activities in rat brain synaptosomes in the absence (control) and presence of different diazinon, diazoxon and IMP concentrations.

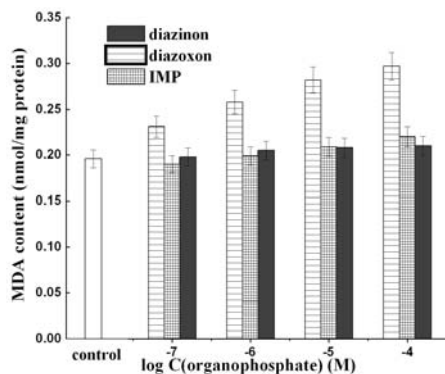


Figure 2. MDA contents in rat brain synaptosomes in the absence (control) and presence of different diazinon, diazoxon and IMP concentrations.

CONCLUSION

The present study demonstrated that diazinon and its decomposition products differ in the induced changes of antioxidant enzymes activity as well as lipid peroxidation. Actually, synaptosomal CAT and GPx activities and MDA level were not significantly affected by diazinon and its hydrolysis product IMP at all investigated concentrations, while the highest investigated IMP concentration stimulated SOD activity about 30%. However, diazoxon, in comparison with its parent compound (diazinon), possesses much stronger prooxidative potential causing the significant activation of antioxidative enzymes as well as the increase in lipid peroxidation, as oxidative stress responses. It suggests that nonspecific toxic effects of diazinon appear as a consequence of its transformation that occurs in the environment and metabolic pathways.

ACKNOWLEDGEMENT

This work was financially supported by the Ministry of Education, Science and Technological Development of the Republic of Serbia (project 172023).

REFERENCES

- [1] Altuntas, N. Delibas, *Biomed. Res.*, 2002, 13, 43–47.
- [2] M. Akhgari, M. Abdollahi, A. Kebryaezadeh, R. Hosseini, O. Sabzevari, *Hum. Exp. Toxicol.*, 2003, 22, 205–211.
- [3] B. Karademir Catalgol, S. Ozden, B. Alpertunga, *Toxicol. in Vitro*, 2007, 21, 1538–1544.
- [4] A. Mohammad, R. Arkam, S. Shahin, N. Shekoufeh, R. Ali, *Med. Sci. Monit.*, 2004, 10, 141–147.
- [5] E.O. Oruc, D. Usta, *Environ.Toxicol. Phar.*, 2007, 23, 48–55

CHARACTERIZATION OF ADVANCED MAIZE INBRED LINES AND HYBRIDS BY THE METHODS OF PHYSICAL - CHEMISTRY

Č. N. Radenović^{1,2}, G. V. Maksimov³, R. J. Petrović¹, N. S. Delić¹,
G. J. Stanković¹, M. D. Pavlović⁴ and M. V. Beljanski⁴

¹Maize Research Institute, Zemun Polje Belgrade, Serbia

²Faculty of Physical Chemistry, University of Belgrade, Belgrade, Serbia
(radenovic@sbb.rs)

³Faculty of Biology, M. V. Lomonosov State University, Moscow, Russia,

⁴Institute of general and Physical Chemistry, Bio-lab, Belgrade Serbia

ABSTRACT

Using different Chemical and Physicochemical methods, characteristics of two inbred lines (ZPPL 146 and ZPPL 159) and three high quality derived hybrids (ZP 633, ZP 735 and ZP 737) are analysed and described.

INTRODUCTION

Maize, or corn, is one of most important cereal crop in human and domestic animals nutrition, which is grown widely throughout the world in a range of agro-ecological environments. In order to increase the yield and nutritive value of maize numerous hybrid and inbred lines are produced. Here, we report on characteristics of two inbred lines (ZPPL 146 and ZPPL 159) and three high quality derived hybrids (ZP 633, ZP 735 and ZP 737), [1].

EXPERIMENTAL

Plant material. Two of maize inbred lines: (ZPPL 146 and ZPPL 159) and three high quality derived maize hybrids (ZP 633, ZP 735 and ZP 737), produced by Maize Research Institute Zemun Polje, Belgrade, were analysed.

Methods. Grains chemical composition of was done by standard methods described in [2]. Leaf carotenoid content of maize inbred and hybrid lines was done by the Raman Resonant Spectroscopy (RRS) in the range of 1800 - 900 cm^{-1} , as described previously [3, 4].

RESULTS AND DISCUSSION

Table 1. presents results of chemical content of maize inbred lines and hybrids, which are higher, or in the range of average, in comparison to the literature data [5, 6].

Table 1. Chemical content of maize inbred lines and hybrids grains

Chemical content of maize inbred and hybrid lines grain	Range of chemical content. Literature data*	Average of chemical content. Literature data*	Average of chemical content of maize inbred and hybrid lines grain				
			Lines		Hybrids		
			ZPP L	ZPP L	ZP 633	ZP 735	ZP 737
Humidity (%)	7-23	16	10,24	10,12	9,90	9,84	10,15
Starch (%)	61-78	71,7	67,80	66,26	68,23	64,39	67,86
Proteins (%)	6-12	9,5	10,22	12,57	11,11	12,27	11,57
Fats (oleum) (%)	1-5,7	4,3	7,53	5,38	6,11	5,82	7,16
Ashes (%)	1,1-3,9	1,4	1,48	1,45	1,51	1,54	1,47
Cellulose (%)		3,0	2,26	2,33	2,37	2,43	2,00
Pentoses (Ribose and deoxyribose)	5,8-6,6	6,2					
Fibers	8,3-11,9	9,5					
Celulose + lignin	3,3-4,3	3,3					
Total sugar (Glucose)	1,0-3,03	2,6					
Yellow pigment ($\mu\beta\text{CE/g d.m.}$)**			19,0	18,10	27,30	21,90	21,60
Total carotenoids (mg/kg)	12-36	26	33,2	31,8	32,4	28,3	27,8

* Source: WHITE and JONSON, 2003, [ref.: 2]

** Done by the method: AACC, 1995, [ref.: 3]

RRS of maize inbred line ZPPL 146 leaf, in interval of 1800 - 900 cm^{-1} , reveals six characteristic bands at 962, 1026, 1160, 1187, 1206 and 1520 cm^{-1} . Two of them, (I_{1160} , I_{1520}), possess significant intensity, while four of them, (I_{926} , I_{1026} , I_{1160} , I_{1206}), are with lower intensity, and may be associated with the presence of glutens and phosphate and amide functional groups (Fig. 1.). Dominant spectral bands (I_{1160} , I_{1520}), that belong to carotenoids from thylacoid membrane, are connected to conformational transitions and are usually analyzed and presented as difference ($I_{1160}-I_{1520}$), or, more frequently quotient (I_{1160}/I_{1520}) of their intensities. Changes at 1520 cm^{-1} reflects conformational changes at $-\text{C}=\text{C}-$ bond, while changes at 1160 cm^{-1} reflects changes at $=\text{C}=\text{C}=\text{C}$ bond. Carotenoids such as β -carotene and xanthophylls (cryptoxanthin and zeaxanthin) are important constituents of photosynthetic membrane. Changes in their structure may be reflected in complex biochemical processes, such as photosynthesis. Since conformational transitions of carotenoids molecules reflects influence of the environmental factors (i.e., critical temperature), RRS could be useful tool for diagnostic of the overall phenotypic characteristics of analyzed inbred and hybrid maize lines.

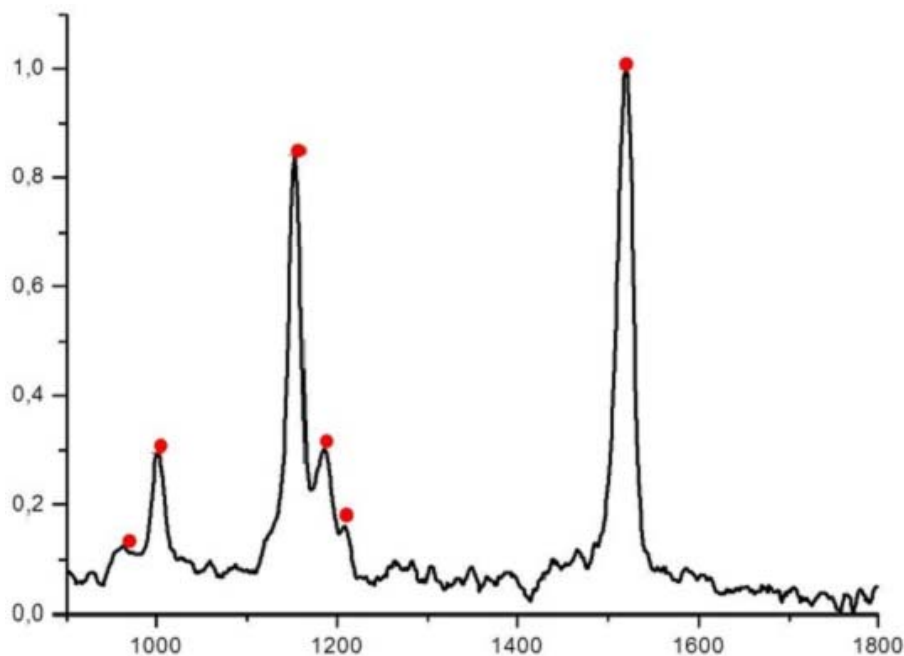


Figure 1. Maize inbred line ZPPL146 leaf RRS reveals six characteristic bands at 962, 1026, 1160, 1187, 1206 and 1520 cm^{-1} , marked with dots. Abscissa: Raman frequency [cm^{-1}]. Ordinate: Raman Intensity (I), [a. u.].

CONCLUSION

Relevant chemical and physicochemical characteristics of maize inbred lines and hybrids are presented. They are important in estimation of nutritive values of maize inbred and hybrid lines. RRS of maize leaf could be useful tool for determination of substantial phenotypic traits of maize inbred lines and hybrids.

ACKNOWLEDGEMENT

This work was partially supported by the Ministry for Science of the Republic of Serbia (Grants no. 172015 and TR 31055).

REFERENCES

- [1] Č. Radenović, M. Filipović, M. Babić, G. Stanković A. Radojčić, M. Sečanski, J. Pavlov, D. Branković, D. Selaković, *Genetica*, 2008, 40, 121-133.
- [2] P. J. White, L. A. Johnson, (eds), *Corn: Chemistry and Technology*, AACC, Minesota, 1990, 71-101.
- [3] AACC methods. Edit American Association of Cereal Chemistry, USA 1995, 14-50.
- [4] Č. Radenović, M. Jeremić, G. V. Maksimov, M. M. Mišović, B.V. Trifunović, *J. Sci. Agric. Res.*, 1994, 55, 33-47.

**DISCRIMINANT ANALYSIS IN DIAGNOSIS OF
LOCALLY ADVANCED BREAST CANCER (LABC).
AN EPR SPIN LABELING STUDY**

A. Pavićević¹, S. Šušnjar², and G. Bačić¹

¹*Faculty of Physical Chemistry, University of Belgrade, Studentski trg 12-16, 11000 Belgrade, Serbia. (aleks.pavicevic@ffh.bg.ac.rs)*

²*Institute for Oncology and Radiology of Serbia, Pasterova 14, 11000 Belgrade, Serbia*

ABSTRACT

Conformational changes in human serum albumin (HSA), induced by binding of certain metabolites, released by cancer cells may be studied by a sensitive spin labeling technique which involves the use of nitroxide labeled stearic fatty acids and EPR spectroscopy. The typically used spin label for these kinds of measurements is 16-DS. However, we showed that 5-DS must be used in parallel with 16-DS since they have different abilities to fit into hydrophobic pockets of the HSA. Therefore, in this study, we used both 5- and 16-DS for labeling sera from LABC patients and healthy volunteers. The acquired EPR spectra were decomposed into the two main spectral components. We show, using discriminant analysis, that the contributions from these components could be used to distinguish between sera of LABC patients and healthy volunteers. Thus, we propose the spin labeling EPR spectroscopy, combined with discriminant analysis, to be a reliable biomarker for diagnosis of LABC.

INTRODUCTION

Human serum albumin (HSA) is a major blood plasma protein, synthesized in the liver. HSA is capable of binding wide range of endogenous and exogenous compounds, such as metal ions, heme, bilirubin, drugs, polypeptides and up to 11 equivalents of fatty acids, depending on the chain length [1,2]. Certain diseases as cancer, myocardial ischemia, diabetes, liver and kidney failure are followed by excretion of different metabolites to blood, where they bind to HSA and may cause changes in its conformation and binding affinity. These changes can be detected by electron paramagnetic resonance (EPR) using nitroxide labelled fatty acids. So far, 16-doxyl stearic acid (16-DS) has been commonly used for this purpose, due to its structural congruence with HSA and the position of doxyl group at the end of the hydrocarbon chain [3]. However, results of our recent study

suggest that 5-doxy stearic acid (5-DS), or at least the joint use of 5-DS and 16-DS, is better approach for the detection of conformational changes in HSA. The aim of this study was to compare the 5-DS and 16-DS binding to HSA as a biomarker in diagnosis of LABC. For this purpose, EPR spectra of 5-DS and 16-DS complexes with human sera were decomposed into the five spectral components using EPRSIM-C software [4]. The two components designated as MES (anisotropic tumbling with full averaging of all rotations) and MEM (anisotropic tumbling with partial averaging of all rotations), are the main constituents of the EPR spectra, and correspond to the strongly and weakly bound components, respectively. Contributions of these components were processed by discriminant analysis algorithm.

EXPERIMENTAL

Blood sera samples were obtained from 10 LABC patients and 20 healthy volunteers. The concentration of HSA in blood sera was determined and sera were stored at -80°C . Ethanol solution of 5-DS and 16-DS was added to the sample tube and left to dry for 15 minutes. In final solution, the [HSA]:[spin label] molar ratio was 1:2. Plasma (30 μl) was added to the dried 5-DS or 16-DS and incubated at room temperature for 30 minutes. EPR measurements were performed on ELEXSYS II E540 X-band (9.85 GHz) EPR spectrometer using following parameters: field center 3510 G, sweep width 200 G, microwave power 10 mW, modulation amplitude 2 G, modulation frequency 100 kHz, acquisition time 120 s, 4 scans. Spectral decomposition was performed using EPRSIM-C software [4]. The obtained contributions of two main components, designated as MES and MEM, were further processed by discriminant analysis algorithm.

RESULTS AND DISCUSSION

In the recent study it was concluded that MES corresponds to the strongly, and MEM to the weakly bound spin label. Average values of the contributions of these components, together with their standard deviations, are given in Table 1. The difference in contributions of both components between LABC patients and healthy volunteers showed to be more significant for the 5-DS than for the 16-DS. Also, it is clear from standard deviations, that the dispersion of these values is less for the 5-DS than for the 16-DS. These results can indicate, prior to discriminant analysis, that 5-DS bound to HSA is the better candidate for distinguishing between LABC patients and healthy volunteers. Discriminant analysis algorithm, obtained by training of separately and jointly used MES and MEM contributions of 5- and 16-DS, showed diverse results. The classification performed by training and cross-validation is shown in Figure 1. It could be observed that,

when the algorithm is trained only by the values of 5-DS, and jointly by the values of 5- and 16-DS, 100% of the samples are correctly classified. However, the classification accuracy when using only 16-DS is 73.3%. Current literature data indicate that the accuracy of using HSA/EPR/16-DS technique is between 87% [5] and 92% [6], which differs significantly from the results presented in this work. The possible cause for this disagreement may be the fact that these authors, during sample preparation, have not evaporated ethanol solution which was in the contact with the HSA [6,7], which consequently caused HSA denaturation. Furthermore, discriminant analysis has been performed using nine parameters [6], which have also made this approach unreliable.

Table 1. MES and MEM contributions to the spectra of 5-DS and 16-DS bound to the HSA of LABC patients and healthy volunteers, and their corresponding standard deviations.

		MES	σ (MES)	MEM	σ (MEM)
LABC patients	5-DS	0.745	0.013	0.183	0.013
	16-DS	0.756	0.027	0.147	0.022
Healthy volunteers	5-DS	0.689	0.011	0.229	0.018
	16-DS	0.756	0.026	0.174	0.013

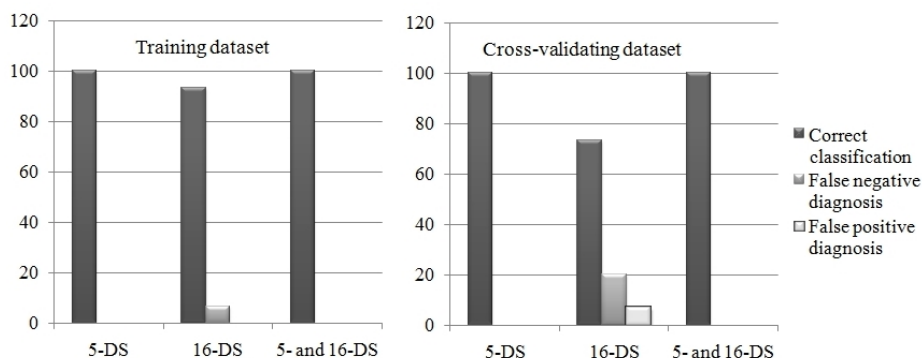


Figure 1. Results of discriminant analysis performed on training and cross-validating datasets when MES and MEM contributions of 5-DS and 16-DS are analyzed separately and together.

Distinguishing between LABC patients and healthy individuals showed to be more accurate using 5- than 16-DS. Therefore we propose 5-DS, or at

least combination of 5- and 16-DS, to be utilized for diagnosis of LABC by HSA/EPR/spin labeling technique.

CONCLUSION

This study shows that the EPR spin-labeling technique which is used for the detection of conformational changes in HSA, combined with spectral decomposition and discriminant analysis, may be used as an accurate diagnostic tool for LABC. This method is probably more sensitive than classic biomarkers and could be used in the follow-up studies.

ACKNOWLEDGEMENT

The realization of this study was supported by the Ministry of Education and Science of the Republic of Serbia (project #41005).

The present work benefited from the input of Professors Miloš Mojović and Ana Popović-Bjelić, who provided valuable comments, and ideas for the undertaking of the research summarized here.

REFERENCES

- [1] G. Fanali, A. di Massi, V. Trezza, M. Marino, M. Fasano, P. Ascenzi, *Mol. Aspects Med*, 2012, 22, 209-290
- [2] A. A. Bhattacharya, T. Grüne, S. Curry, *J. Mol. Biol*, 2000, 303(5), 721-732.
- [3] A. Gurachevsky, E. Shimanovitch, T. Gurachevskaya, V. Muravsky, *Biochem. Biophys. Res. Comm*, 2007, 360(4), 582-856.
- [4] J. Strancar, T. Koklic, Z Arsov, B. Filipic, D. Stopar, M. A. Hemminga, *J. Chem. Inf. Model*, 2005, 45(2), 394-406.
- [5] S. C. Kazmierczak, A. Gurachevsky, G. Mathes, V. Muravsky, *Clin. Chem*, 2006, 52(11), 2129-2134.
- [6] A. Gurachevsky, S. C. Kazmierczak, A. Jörres, V. Muravsky, *Clin. Chem. Lab. Med*, 2008, 46(9), 1203-1210.
- [7] A. Gurachevsky, E. Muravskaya, T. Gurachevskaya, L. Smirnova, V. Muravsky, *Canc Invest*, 25(6), 378-383.

PROBING SPIN-PROBES. THE EPR IN VIVO STUDY OF PHARMACOKINETICS OF TWO SPIN-PROBES

M. Mojović^{*1}, A. Pavićević¹, S. Stamenković², M. Jovanović², P. R. Andjus² and G. Bačić¹

¹*Faculty of Physical Chemistry, University of Belgrade, Studentskitrg 12-16, 11000 Belgrade*

²*Faculty of Biology, University of Belgrade, Studentskitrg 12, 11000 Belgrade*

**Corresponding author: milos@ffh.bg.ac.rs*

ABSTRACT

The aim of the study was to investigate the pharmacokinetics of the two nitroxide spin-probes: TEMPOL and 3CP. Electron paramagnetic resonance (EPR) L-band *in vivo* study of the reduction rate for injected nitroxides in rats was performed. Spin-probe 3CP showed to be 4 times more resistant to the endogenous reducing agents in physiological environment than TEMPOL indicating its high applicability for *in vivo* EPR studies. The influence of nitroxide flushing effect by bloodstream on the EPR signal reduction was also studied and overall kinetics is analyzed. Taken together, these results provide a firm base for future studies where the influence of some pathological states (such as cancer) or therapeutic irradiation on redox status of tissues will be examined.

INTRODUCTION

Free radicals are involved in virtually every biological process. The EPR spectroscopy is a resonant technique widely used for the *in vivo* detection of EPR active species in various types of biological samples. Standard EPR machine is an X-band EPR operating at around 9.5 GHz where the volume of investigated biological samples is limited to some 100 μl due to the high dielectric losses in water. The L-band EPR allows *in vivo* investigation of small animals (mouse or rat). From the beginning of *in vivo* EPR, the main topic of studies was pharmacokinetics of nitroxides by which one can reveal pathological changes in tissues [1-4]. Additional research also has been devoted to the development of probes tailored for different pathological conditions. Nevertheless, the choice of proper nitroxide and their pharmacokinetics are still to be investigated. Here we investigated the reduction of the two selected spin-probes which are representative of two classes of spin probes to establish the ground for further investigation.

MATERIALS AND METHODS

Healthy 2-2.5 month's old rats were used. All animals were grown under normal living conditions. Spin probes TEMPOL and 3CP were purchased from Sigma. Animals were anesthetized by intramuscular injection of Ketamine (0,1ml/100g b.w.) and Xylazine (0,06ml/100g b.w.). Rats were placed into the rat-bed equipped with the rat-blanket which is connected to the thermostat unit for keeping rat temperature at around 33°C during the anesthesia which was controlled using thermocouple inserted into the anus. The bed was loaded into the Bruker Elexsys II EPR spectrometer with rats in supine position with L-band surface coil placed above the rat liver area. Experimental settings were: sweep width = 100G, modulation amplitude = 2G; microwave power = 10mW, scan time = 20s, number of scans = 4. After experimental settings were established and control baseline spectrum was recorded, the spin probe (1ml, 2 μ mol/g b.w.) was slowly injected either into the tail vein or intramuscularly and the EPR spectra were immediately acquired. Some animals were killed by injection of KCl which induces almost immediate cardiac arrest.

RESULTS AND DISCUSSION

The intensity of EPR signal of spin-probes TEMPOL and 3CP was measured as the average value of the low-field and the middle EPR peaks triplet (see inserts in Fig 1). The reduction rates of two nitroxides are obviously different. This is in agreement with the well known fact that five-member ring nitroxides (3CP) are more resistant to reduction than six-member ring nitroxides (Tempol). Also, note that reduction kinetic is not single exponential indicating that more than one process is involved [1, 5]. Experiments with animals killed with KCl showed faster clearance from the liver, contrary to the expectation that cutting off the blood flow will prolong the signal from the organ since there is no wash-out by circulating blood.

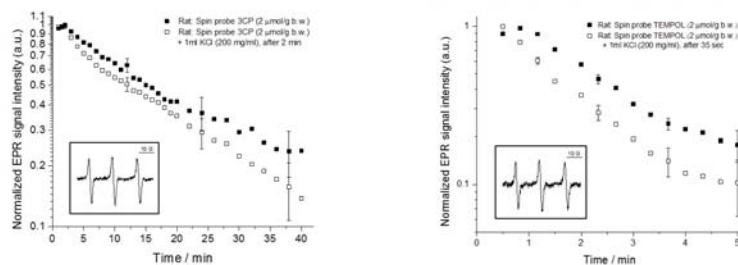


Figure 1. Normalized EPR signal (arbitrary units) intensity reduction rate in upper abdomen region for spin-probes injected in rat's tail vein.

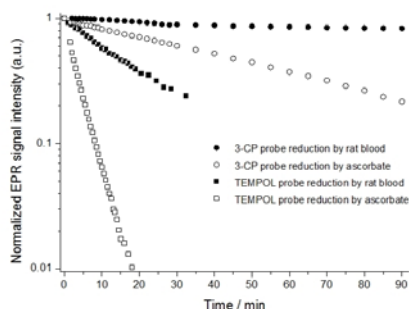


Figure 2. *In vitro* reduction of spin probes by blood or ascorbate. Measurements were performed in the gas permeable Teflon tubes. Concentration of spin-labels 0.2 mM, concentration of ascorbate 2 mM. Concentration of nitroxides in blood was 0.05 μ M in 1 ml of fresh blood.

By comparing data in Figs. 1 and 2 it is obvious that reduction *in vitro* by blood and even with potent reducing agent, ascorbate, is slower than reduction *in vivo*. Consequently, signal decay in Fig. 1 can only be reduction of spin-probes by endogenous intracellular reducing agent. Faster reduction in rats killed by KCl can be explained by the deprivation of oxygen, since it is well known that reduction under hypoxic condition is faster than under normal tissue oxygenation [6].

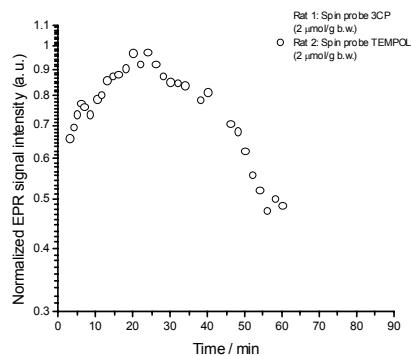


Figure 3. *Intramuscular injection of nitroxides*

Reduction of nitroxides when intramuscular injection is applied shows completely different situation (Fig. 3). Now the dominant feature is the time for nitroxides to reach the liver and not to be reduced along the way. Again the reduction of Tempol signal is much faster than for 3CP, but it should be noted, that unlike for the i.v. injection, signal persisted for almost an hour, which is consistent with similar previous studies [7].

CONCLUSION

Behavior of both nitroxides is as expected based on their chemical formulas. The reduction of both nitroxides reflects redox status of the tissue and is sensitive to tissue oxygenation. This is a solid base for further investigation of pathological processes. The choice of nitroxide and the route of administration will have to be tested in each particular process under investigation.

ACKNOWLEDGEMENT

This study was supported by the Ministry of Education and Science of the Republic of Serbia (Grant #41005).

REFERENCES

- [1] G.Bačić, M.J.Nilges, R.L.Magin, et al., *Magn Reson Med*, 1989, 10, 266.
- [2] L.J.Berliner, X.Wan, *Magn Reson Med*, 1989, 9, 430.
- [3] H.Utsumi, E.Muto, S.Masuda, A.Hamada. *BBRC*, 1990, 172, 1342.
- [4] V.V.Khramtsov, *InTech*, 2012, 11, 317.
- [5] N.Nishino, H.Yasui, H.Sakurai, *Free Rad Res*, 1999, 31, 35.
- [6] H.M.Swartz, M.Sentjurc, P.D.Morse II. *BBA*, 1986, 888, 82.
- [7] B.Gallez, G.Bačić, F.Goda, et al., *Magn Reson Med* ., 1996, 35, 97.

PARAMAGNETIC METALS IN NERVOUS TISSUE OF SOD1-G93A MOUSE MODEL OF AMYOTROPHIC LATERAL SCLEROSIS

A. Popović-Bijelić^{1*}, M. Mojović¹, S. Stamenković², P. Anđus² and G. Bačić¹

¹University of Belgrade, Faculty of Physical Chemistry, EPR laboratory, Studentski trg 12-16, 11000 Belgrade, Serbia. *ana@ffh.bg.ac.rs

²University of Belgrade, Faculty of Biology, Studentski trg 16, 11000 Belgrade, Serbia.

ABSTRACT

Metal content of the spinal cord and brain tissues from wild type (WT) and age-matched G93A-SOD1 transgenic amyotrophic lateral sclerosis (ALS) model rats was studied using low temperature X-band electron paramagnetic resonance (EPR) spectroscopy. The 20 K EPR spectra of the cortex and hippocampus do not exhibit differences between the WT and G93A-SOD1 rats. The brainstem and spinal cord from the G93A-SOD1 rats contain more oxidized Fe-S clusters, and 1.5 – 2 times more MnSOD than those from the WT rats. There is an additional signal observed only in the spinal cord from G93A-SOD1 rat in the terminal phase of the disease. The origin of this signal is discussed.

INTRODUCTION

Amyotrophic lateral sclerosis (ALS) is a progressive and fatal neurodegenerative disorder characterized by the dysfunction and death of neurons in the motor pathways of the cerebral cortex, brain stem and spinal cord. One tenth of ALS cases occurs in familial forms (fALS), among which 20-25% are caused by mutations in the *SOD1* gene, which encodes a protein, Cu,Zn-superoxide dismutase (SOD1) [1]. There is accumulating evidence from both *in vitro* and *in vivo* studies pointing to increased recruitment of mutated forms of SOD1 to the mitochondrial inter-membrane space, leading to mitochondrial dysfunction and increased production of reactive oxygen species [2]. Furthermore, numerous studies have linked neurological diseases to elevated amounts of iron. Magnetic resonance imaging studies have shown that the progressive accumulation of iron in specific brain regions of ALS patients is proportional to the severity of the disease [3]. Consequently, it has been proposed that the released iron generates hydroxyl radicals via the Fenton reaction, which in turn releases

new iron from ferritin. Studies of the cerebrospinal fluid (CSF) of ALS patients showed an increased amount of free radicals compared to the CSF of healthy individuals, but did not show any changes in CSF total iron content [4]. These results indicated that it is not the amount of iron, but rather its form, that is responsible for the increased free radical formation in CSF of ALS patients.

In light of these observations, and the fact that only free or loosely bound iron is redox active, the objective of this study was to investigate the form of endogenous iron in ALS model rats. More specifically, the aim of this work was to evaluate the metal content of the spinal cord and brain of G93A-SOD1 transgenic ALS model rats, and compare it with age-matched wild type rats using low temperature X-band electron paramagnetic resonance (EPR) spectroscopy.

EXPERIMENTAL

Sprague-Dawley wild type (WT) and transgenic G93A-SOD1 rats with ALS Functional Rating Scale (ALSFRS) scores 2 (terminal stage of the disease) and 4 (less advanced stage of the disease) were anesthetized, and transcardial perfusion was performed using physiological solution. The spinal cord (SC) and brain were removed, and brainstem (BS), hippocampus (HC), and cortex (CTX) were isolated. Intact tissues, frozen in liquid N₂, were directly inserted into EPR quartz cuvettes.

The X-band (9.5 GHz) EPR spectra were recorded at 4, 10, 20, 40 and 77 K on a Bruker Elexsys-II EPR spectrometer with an Oxford Instruments ESR900 helium cryostat under the following conditions: microwave power 5 mW, modulation amplitude 10 G, modulation frequency 100 kHz, conversion time 240 ms.

RESULTS AND DISCUSSION

Low temperature EPR spectra of all investigated rat spinal cord and brain tissue samples exhibit peaks that arise from membrane-bound ($g = 6$) and free ($g = 3$) cytochrome *c*, mononuclear unspecifically bound “dirty” iron ($g = 4.3$), and at least two types of Fe-S clusters from the electron transport chain complexes I and II (anisotropic signals around $g \sim 2$), Fig 1. In addition, the six-line signal centered at $g = 2$, and the axial signal at $g = 2.1$, are attributed to MnSOD, and Cu,ZnSOD, respectively. The 20 K EPR spectra of CTX and HC samples do not exhibit differences between the WT and G93A-SOD1 rats. For BS and SC samples, there is a difference in the types of Fe-S clusters and in the amount of MnSOD observed in WT and G93A-SOD1 rats. Namely, the G93A-SOD1 samples contain more oxidized Fe-S clusters, and 1.5 – 2 times more MnSOD than the WT samples.

Moreover, the G93A-SOD1 SC sample obtained from the rat in the terminal phase of the disease (ALSFRS score 2) showed an additional signal centered around $g = 2.4$ which is not present in the EPR spectrum of the WT SC sample, or the G93A-SOD1 SC sample with the ALSFRS score 4.

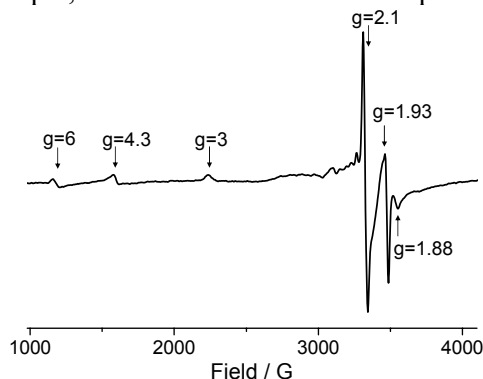


Figure 1. EPR spectrum of the WT rat cortex at 20 K. Arrows denote characteristic EPR peaks which were used for signal assignment

In order to gain more information about the origin of this signal, EPR spectra were recorded at 4, 10, 20, 40 and 77 K, Fig 2. It should be noted here, that this sample also contained 2.5 times more MnSOD than the WT samples.

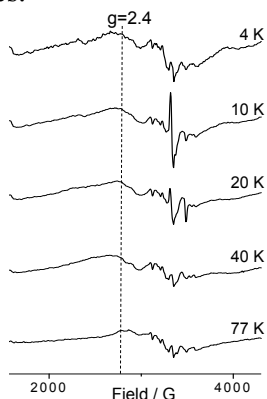


Figure 2. Variable temperature EPR spectra of the G93A-SOD1 rat spinal cord (ALSFRS score 2). Dashed line denotes the place in the spectra where the additional signal centered around $g = 2.4$ was detected

Figure 2 shows that the broad signal at $g = 2.4$ observed at 20 K is shifted towards a limiting g value of ~ 2.5 at 4 K and that it essentially disappears at 77 K. This type of spectral temperature dependence may suggest that this signal arises from polynuclear ferric aggregates, as proposed previously [5]. Room temperature EPR spectra of the same sample did not give any further information about the origin of the signal at 2.4, as the spectra of the WT and G93A-SOD1 SC samples did not exhibit marked differences, most probably due to the low concentration of metals. Even though it may seem

plausible to assign the $g = 2.4$ signal to ferric aggregates, it cannot be ruled out that this signal arises from copper in the Cu,ZnSOD protein. Namely, the g - and the hyperfine coupling constant anisotropies depend on the metal-ligand bond geometries and in this case may suggest that the $g = 2.4$ signal comes from a Cu, ZnSOD protein which has lost Zn, or even has another Cu atom bound in this position. Further metal reconstitution studies of the purified G93A-SOD1 mutated protein are needed to confirm this possibility.

CONCLUSION

EPR spectroscopy of intact spinal cord and brain tissues of wild type and G93A-SOD1 transgenic ALS model rats was performed at low temperatures. All investigated samples exhibit signals that may be assigned to membrane-bound and free cytochrome *c*, mononuclear Fe(III), at least two types of Fe-S clusters, MnSOD and Cu,ZnSOD. The results showed no significant variations between the amounts of mononuclear, unspecifically bound “dirty” iron. Furthermore, EPR spectra of CTX and HC samples did not exhibit differences between the WT and G93A-SOD1 rats. The BS and SC G93A-SOD1 samples showed increased amounts of oxidized Fe-S clusters, and MnSOD, compared to the corresponding WT samples. The G93A-SOD1 SC sample, obtained from the rat in the terminal phase of the disease, showed an additional signal at $g = 2.4$. Although its origin is still not confirmed to be Fe ions organized in superparamagnetic or antiferromagnetic domains, or Cu ions in the mutated Cu,ZnSOD protein, it may serve as a biomarker for the ALS terminal phase.

ACKNOWLEDGEMENT

This work was supported by the Ministry for education, science and technological development of Serbia (grant no. III41005).

REFERENCES

- [1] Y. Furukawa, *Neurology Research International*, 2012, Article 32326.
- [2] P. Vehvilainen, J. Koistinaho, G. Goldsteins, *Frontiers in Cellular Neuroscience*, 2014, 8, Article 126.
- [3] A. Ignjatović, Z. Stević, S. Lavrnić, M. Daković, G. Bačić, *Journal of Magnetic Resonance Imaging*, 2013, 38, 1472–1479.
- [4] A. Ignjatović, Z. Stević, D. Lavrnić, A. Nikolić-Kokić, D. Blagojević, M. Spasić, I. Spasojević, *Amyotrophic Lateral Sclerosis* 2012, 13, 357–362.
- [5] S. Aime, B. Bergamasco, D. Biglino, G. Digilio, M. Fasano, E. Giamello, L. Lopiano, *Biochimica et Biophysica Acta* 1997, 1361, 49–58.

PHOTOINDUCED 6 π -ELECTROCYCLIZATION OF STYRYL-SUBSTITUTED AZINES

T. M. Aliyev, D. V. Berdnikova, E. N. Gulakova, Y. V. Fedorov and O. A. Fedorova

A.N. Nesmeyanov Institute of Organoelement Compounds of Russian Academy of Sciences, 28 Vavilova str., 119991 Moscow, Russia

ABSTRACT

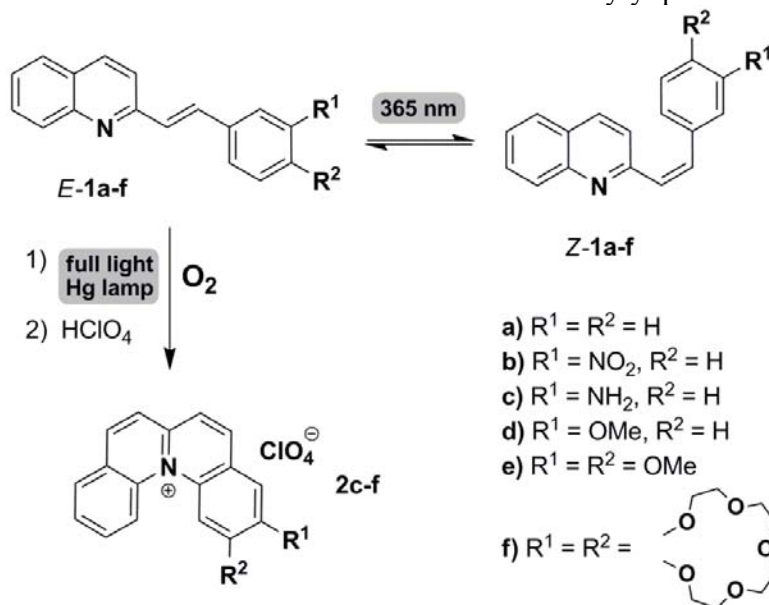
Photoinduced electrocyclic reaction involving C-N bond formation of 2-styrylazines resulting in formation of potentially biologically active derivatives was investigated. The dependence of substituents in phenyl ring and the structures of heteroaromatic moiety on the cyclization were also studied.

INTRODUCTION

Biological activity of polycondensed heteroaromatic compounds is of significant interest due to its high potential in producing of new antitumor, antibacterial and fungicidal drugs [1]. The chemotherapeutic effect of such molecules is reached by strong interaction of extended heteroaromatic π -systems with DNA [2]. Such DNA-ligand complexes prevent normal passing of the physiological processes involving nucleic acid and thus lead to the cell death. Significant synthetic difficulties of obtaining polycyclic aromatics by means of classical organic synthesis induce chemists to search for alternative approaches. One of the most powerful, however not extensively studied methods is the photocyclization of stilbenes and their heterocyclic analogs [3]. Depending on the structure of starting hetarylphenylethenes, the photocyclization may result in the formation of either neutral or positively charged products, which possess different biological activity. In particular, positively charged fused heteroaromatics are typical DNA-intercalators and therefore are of interest as potential DNA-targeting drugs [2]. From this point of view, the investigation of phototransformation mechanism plays an important role in the development of practical applications of hetarylphenylethenes in biology and medicine.

RESULTS AND DISCUSSION

To study the influence of substituents in phenyl ring on photocyclization, styrylquinolines **1a-f** were prepared according to published protocols [4,5].

Scheme 1. Photochemical transformations of 2-styrylquinolines

To develop the possible phototransformation pathways of 2-styrylquinolines, first we examined the photoreaction of **1a-f** in acetonitrile upon irradiation with filtered light at 365 nm (Figure 1a) in air saturated solutions. In these experiments photostationary equilibria of *E* and *Z* isomers were reached.

Irradiation of **1a-f** in the presence of air oxygen with unfiltered output of a Hg lamp resulted in more complicated behavior. Under these conditions unsubstituted 2-styrylquinoline **1a** and its nitro derivative **1b** underwent photodestruction of the molecular skeleton. The photochemical transformation of amino-, methoxy- and crown-substituted styrylquinolines **1c-f** upon irradiation with unstrained light resulted in the appearance of new absorption bands in the spectral region of 400-500 nm, which were assigned to heteroaromatic species **2c-f** (Figure 1b). The exclusive formation of C-N photocyclization products has been unambiguously proven by NMR data. Heteroaromatic compounds **2d-f** were successfully isolated as perchlorate salts by recrystallization from MeOH with small addition of HClO_4 with moderate-to-good yields **2d**: 52%, **2e**: 70%, **2f**: 45%.

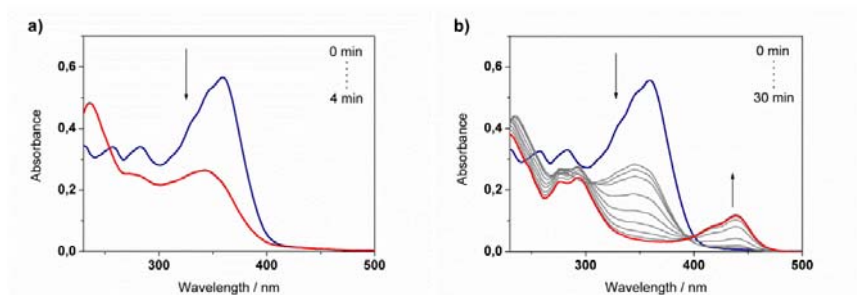
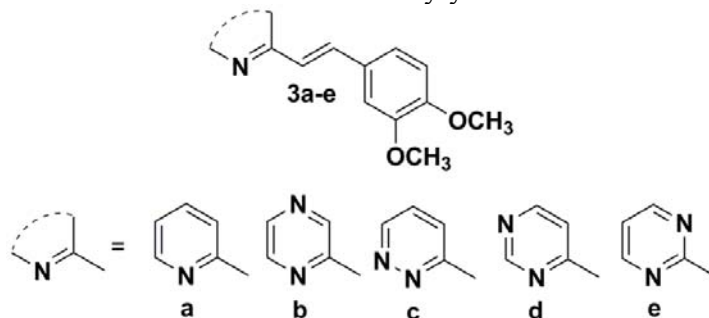


Figure 1. Spectral changes during the photolysis of the **1f** acetonitrile solution: (a) filtered light, $\lambda = 365$ nm; (b) full light; in both cases $c = 2 \cdot 10^{-5}$ M, Hg lamp, 20 °C.

To define the role of heteroaromatic moiety on the photocyclization dimethoxystyryl-substituted azines **2a-e** where obtained by condensation of veratric aldehyde with corresponding 2-methylheterocycle according to published protocols [4,5].

Scheme 2. Structure of styrylazines **3a-e**



Irradiation of air saturated acetonitrile solutions of **3a-e** with unfiltered light of high pressure Hg lamp resulted in the formation of a new long-wavelength absorption band. In case of pyridine, pyrazine and pyridazine derivatives the photocyclization products were isolated as perchlorates with yields 85%, 50%, 45% respectively. By means of NMR spectroscopy, the structures of the obtained products were undoubtedly proven. Using water as a solvent allowed us to reduce the reaction time and to increase the yields of photoproducts.

Unfortunately, photolysis of both acetonitrile and aqueous solutions of pyrimidine derivatives **3d-e** did not give any of desired compounds, resulting mostly in products of photodestruction. In order to prevent the degradation of starting molecules, the filtered output of Hg lamp with $\lambda > 290$ nm, was used. According to the NMR and absorption spectroscopy data, irradiation of acetonitrile solutions of **3d-e** with filtered light resulted in a

complex mixture of photocyclization and photodegradation products, and it was impossible to isolate pure heteroaromatic cations.

CONCLUSION

We have demonstrated that the photocyclization effectiveness is strongly dependent on the electronic factors of the substituents in the styryl moiety. Thus, the process is favored only in the presence of donor groups, whereas acceptor groups or the absence of any substituents do not support the photocyclization. Moreover, the increasing number of N-atoms in heterocyclic moiety reduces photostability of photocyclic products, especially for pyrimidine derivatives. We suppose that styrylazines **3d-e** as well as their photocyclization products can undergo competitive photoreactions resulting in formation of pyrimidine dimers [6].

REFERENCES

- [1] Hendry, L. B.; Mahesh, V. B.; Bransome Jr., E. D.; Ewing, D. E. *Mutat. Res.* 2007, *623*, 53; (b) Wheate, N. J.; Brodie, C. R.; Collins, J. G.; Kemp, S.; Aldrich-Wright, J. R. *Mini-Rev. Med. Chem.* 2007, *7*, 627; (c) Neidle, S.; Thurston, D. E. *Nat. Rev. Cancer* 2005, *5*, 285; (d) Baraldi, P. G.; Bovero, A.; Fruttarolo, F.; Preti, D.; Tabrizi, M. A.; Pavani, M. G.; Romagnoli, R. *Med. Res. Rev.* 2004, *24*, 475.
- [2] (a) Xie, Y.; Tam, V. K.; Tor, Y. in *The chemical biology of nucleic acids*, ed. G. Mayer, John Wiley & Sons, Chichester, 2010; (b) Haq, I. in *Nucleic acids in chemistry and biology*, ed. G. M. Blackburn, M. J. Gait, D. Loakes, D. M. Williams, Royal Society of Chemistry, Cambridge, 2006; (c) Ihmels, H.; Otto, D. *Top. Curr. Chem.* 2005, *258*, 161.
- [3] (a) Jørgensen, K. B. *Molecules* 2010, *15*, 4334; (b) Hagen, S; Hopf, H. *Top. Curr. Chem.* 1998, *196*, 45; (c) Blackburn, E. V.; Timmons, C. J. *Q. Rev. Chem. Soc.* 1969, *23*, 482; (d) Gulakova, E. N.; Berdnikova, D. V.; Aliyev, T. M.; Fedorov, Y. V.; Godovikov, I. A.; Fedorova, O. A. *J. Org. Chem.* 2014, *79*, 5533.
- [4] Fedorova, O. A.; Andryukhina, E. N.; Mashura, M. M.; Gromov, S. P. *ARKIVOC* 2005, *xv*, 12.
- [5] Gulakova, E. N.; Sitin, A. G.; Kuzmina, L. G.; Fedorova, O. A. *Russ. J. Org. Chem.* 2011, *47*, 245.
- [6] Setlow, R. B. *Science* 1966, *153*, 379.

RADIATION STABILITY OF HYBRID COMPOSITES BASED UREA-FORMALDEHYDE RESIN MODIFIED WITH MICRO- AND NANO-TiO₂

S. Samaržija-Jovanović¹, V. Jovanović¹, B. Petković¹,
G. Marković² and M. Marinović-Cincović³

¹*Faculty of Natural Science and Mathematics, University of Priština Lole
Ribara 29, 38220 Kosovska Mitrovica, Serbia (vojani@sbb.rs)*

²*Tigar, Nikole Pašića 213, 18300 Pirot, Serbia,*

³*University of Belgrade, Institute of Nuclear Science Vinča, Mike
Petrovića Alasa 12-14, 11000 Belgrade, Serbia*

ABSTRACT

The thermal stability of organic-inorganic composites prepared by a two-stage polymerization of urea-formaldehyde resin (UF) with micro- and nano-TiO₂ before and after irradiation has been investigated. Composites of urea-formaldehyde and particles of TiO₂ of different size were synthesized, namely: *Composite 1* (UF+ micro-TiO₂) and *Composite 2* (UF + nano-TiO₂). The thermal stability of obtained materials was studied by non-isothermal thermo-gravimetric analysis (TG), differential thermal gravimetry (DTG) and differential thermal analysis (DTA). Hybrid composites based on UF resin have been irradiated (50 kGy) and after that their radiation stability was evaluated on the basis of thermal behavior. DTG peaks of both composites are shifted to a higher temperature after irradiation, but *Composite 1* after irradiation shows less change in thermal behavior than *Composite 2*.

INTRODUCTION

As a typical amino resin, UF resin adhesive possesses some advantages, such as fast curing, good performance in the panel, water solubility, the non toxicity of resin and resin products, the environmental compatibility of resin bonded products and lower price [1]. High-energy radiation is a well-known technique for modification of polymers. Radiation stability-resistance is the ability of the polymer to retain irradiation despite initial chemical and physical properties, macrostructure and microstructure, i.e. to avoid crosslinking and/or degradation. However, little work concerning the effects of γ -irradiation on the thermal properties of modified UF resins has been done. The goal of this work was to determine the radiation stability of the synthesized micro- and nano-TiO₂-based urea-formaldehyde composites

based on their thermal behavior. The thermal behavior of two types TiO₂-based UF hybrid composites (unirradiated and irradiated) was investigated using non-isothermal TGA, DTG and DTA.

EXPERIMENTAL

The following materials were used in the study reported here: Urea (Alkaloid-Skopje, FYR of Macedonia); 35% formaldehyde (Unis-Goražde, Bosnia and Herzegovina); micro- and nano-TiO₂ (Sigma-Aldrich, Germany). Two types of TiO₂-based UF hybrid composites with formaldehyde-to-urea (F/U) ratio of 0.8 were synthesized using the same procedure [1]. Irradiations were performed in air in the Co-60 radiation sterilization unit with the dose rate of 10 kGy⁻¹ and the total absorbed dose of 50 kGy. The thermal stability was investigated by non-isothermal thermogravimetry (TG, DTA) using a Setaram Setsys Evolution 1750 instrument (France). Samples (6±0.2 mg) were placed in alumina crucibles. An empty alumina crucible was used as a reference. The samples were heated from 30 to 600°C in a 20 cm³/min flow of argon atmosphere with a heating rate of 10°C/min. The temperatures at maximum decomposition rate were determined from the peak maxima of the DTG curves.

RESULTS AND DISCUSSION

The thermal behavior of unirradiated and irradiated hybrid composites based on UF resins occurs in three and four main stages (Figure 1 and 2). The mass loss at different temperatures is summarized in Table 1. The rate of the thermal decomposition reaction before and after irradiation, shows more than one maximum rate with temperature is increasing. This behavior indicated that thermal decomposition of these resin passed through multiple stages, depending on the state of decomposition and not on the components [2, 3].

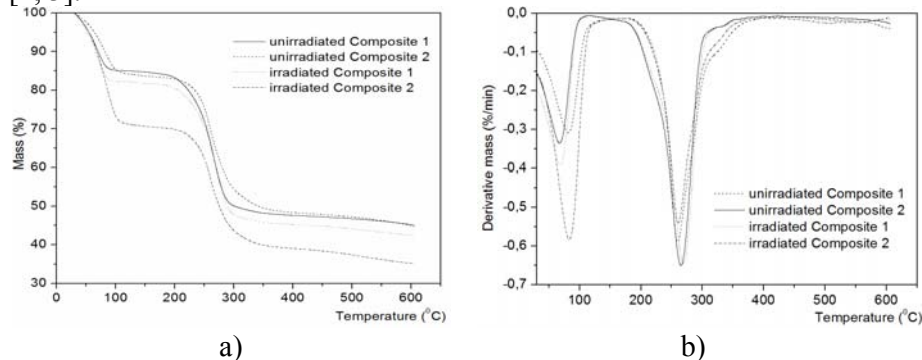


Figure 1. TGA (a) and DTG (b) curves of unirradiated and irradiated hybrid composites based on UF resin.

The first-step degradation occurs in the temperature region around 30–140°C for all samples; and with a DTG peaks observed around 68–81°C and 81–84°C for unirradiated and irradiated modified UF composites, respectively, indicating water and formaldehyde evaporation.

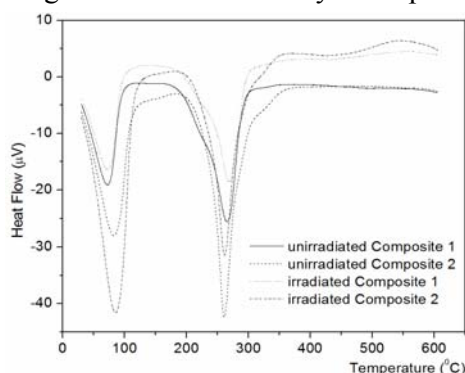


Figure 2. DTA curves of unirradiated and irradiated hybrid composites based on UF resin

Table 1. DTG, DTA data of peak values, and total mass loss for unirradiated and irradiated hybrid composites based on UF resin.

Samples	Dose of γ -irradiation (kGy)	DTG peak values (°C)	DTA Endothermic peak values (°C)	Total mass loss (%)
Composite 1	0	67.9	71.9	54.8
		218.9*	219.7*	
		265.0*	264.9*	
	50	335.8	327.7	57.6
		68.5	72.8	
		217.3*	222.4*	
Composite 2	0	269.1*	269.3*	55.2
		339.8	324.2	
		441.1	441.1	
	50	81.4	82.5	64.5
		259.5*	260.4*	
		334.4*	330.4*	
		83.8	85.2	
		260.4*	261.4*	
		331.9*	323.3*	
		507.0	456.1	

*overlapping peaks

The minimum of the endothermic peak attributed to water evaporation which comes to lower temperatures for *Composite 1* than *Composite 2*. Main mass loss happened in the second stage. In this stage degradation occurs in the temperature region around 164–395°C for all samples. In Figure 1 can be notes that the second and third degradation regions are overlapped for all hybrid composites based on UF resins. In the DTA measurements (Figure 2) the endothermic peak with minimum at 264.9, 260.5 for unirradiated UF resin composites and at 269.3, 261.4°C for irradiated UF resin composites, respectively, is attributed to the degradation of methylene ether bridges into methylene bridges and cross linking reactions in the resins network [3]. Degradation of cured resin composite begins the liberation of formaldehyde from dimethylene ether groups. This kind of destruction can be regarded as post curing of resin composite, as released formaldehyde participates in further reaction, finally giving more stable methylene group.

The *Composite 1* showed lower values for total mass loss (54.8 and 57.6%) than *Composite 2* (55.2 and 64.5%) before and after irradiation, respectively.

CONCLUSION

1. DTG peaks of both composites are shifted to a higher temperature after γ -irradiation.
2. After irradiation, *Composite 1* shows minor changes in the thermal properties compared with *Composite 2*, which indicates that the *Composite 1* has more resistant to the effect of γ irradiation than *Composite 2*.
3. The total mass loss for *Composite 1* is less than that of *Composite 2*.

ACKNOWLEDGEMENT

Financial support for this study was granted by the Ministry of Science and Technological Development of the Republic of Serbia (Projects Numbers 45022 and 45020).

REFERENCES

- [1] S. Samaržija-Jovanović, V. Jovanović, S. Konstantinović, G. Marković, M. Marinović-Cincović, *J Therm Anal Calorim.*, 2011, 104, 1159–1166.
- [2] B. D. Park, SM. Lee, JK. Roh, *Eur. J. Wood Prod.*, 2009, 67, 121-123.
- [3] K. Siimer, T. Kaljuvee, T. Pehk, I. Lasn, *J Therm Anal Calorim.*, 2010, 99, 755–762.

Ag-PVA/CMC BLEND HYDROGEL NANOCOMPOSITE SYNTHESIZED BY γ -IRRADIATION FOLLOWED BY FREEZE/THAWING METHOD

J. Krstić*, J. Spasojević, A. Radosavljević,
N. Abazović, U. Jovanović and Z. Kačarević-Popović

*Vinča Institute of Nuclear Sciences, University of Belgrade, P.O. Box
522, 11001 Belgrade, Serbia (*jelenak@vinca.rs)*

ABSTRACT

Poly(vinyl alcohol)/carboxymethyl-chitosan (PVA/CMC) blend hydrogels were synthesized by γ -radiolysis followed by freeze/thawing (FT). Previous, the water-solubility of chitosan (CS) was obtained by γ -radiolytic acidic degradation. CMC molecular weight characterization was performed by a Zetasizer. The fluorescence measurements confirmed the presence of CMC in the PVA/CMC blend hydrogels. *In situ* preparation of Ag nanoparticles (AgNPs) in PVA/CMC blend hydrogel matrices has been performed exposing hydrogels, swollen in AgNO₃ solution, to γ -irradiation. The mathematical models applied for determination swelling kinetics showed that the initial concentrations of CMC and AgNPs directly have influence on the swelling parameters of Ag-PVA/CMC nanocomposites. Diffusion characteristics, determined by different diffusion models (Early Time (ET), Late Time (LT) and Eters (E)) are less due to the presence of AgNPs.

INTRODUCTION

Derivation of CS followed by graft modification (by alkyl or carboxymethyl groups), improve water solubility, antibacterial and antioxidant properties, without affecting its cationic character [1]. On the other hand, blending the CS with PVA improves tensile strength, flexibility, bulk and surface hydrophilicity. Therefore, combination of CMC with PVA as hydrogel blend stabilizer of AgNPs creates materials which will be useful in the range of applications [2].

In this investigation, AgNPs were synthesized *in situ* by γ -irradiation in previously obtained radiolytically crosslinked PVA/CMC blend hydrogel matrices followed by FT. The water-solubility of CS was obtained prior to crosslinking by radiolytic acidic degradation. The post irradiation FT procedure for the matrix preparation is performed in order to prevent dissolution of ungrafted CMC during *in situ* synthesis of AgNPs. Namely, at the lower concentrations, such as in the tested system, the grafting of CMC

chains is likely process. The aim of this investigation was to examine the influence of AgNPs and the concentration of CMC on the optical properties, morphology, structure and the swelling behavior of thus obtained nanocomposite blend hydrogels.

EXPERIMENTAL

1M acetic CS ($M_w=94.8\pm 8.74$ kDa) solution (5% w/w) was γ -irradiated up to 100 kGy, to reduce molecular weight down to $M_w=31.3\pm 4.73$ kDa. After neutralization with 1M NaOH, CMC molecular weight characterization was performed using a Zetasizer Nano ZS. The initial processing step in synthesis of Ag-PVA/CMC blend hydrogels was irradiation-induced crosslinking of PVA/CMC blend matrices (8%/2% w/w and 8%/4% w/w, samples S1 and S2 respectively) at a dose rate of 0.33 kGy/h up to an absorbed dose of 75 kGy, followed by FT up to 4 cycles. *In situ* synthesis of AgNPs in PVA/CMC was performed exposing samples (S1, S2) swollen in solution containing 8 mM AgNO₃ and 0.2 M 2-propanol (saturated with Ar) to γ -irradiation. The obtained nanocomposites were labeled as S3 and S4, respectively. Characterization of these systems was carried out by FTIR, fluorescence and UV-Vis spectroscopy, SEM and swelling measurements in water at 25 °C. Swelling process was monitored gravimetrically by measuring weights of swollen hydrogel at predetermined time intervals (t), until the initial weights were equilibrated. The swelling degree is $SD=(W_t-W_0)\times 100/W_0$, where W_t is weight of swollen hydrogel, and W_0 is the initial weight of the xerogel. Equilibrium swelling degree (SD_{eq}) was determined by getting the weight of hydrogel in equilibrium state (W_{eq}) instead the weight of swollen hydrogel in predetermined time intervals (W_t). The mathematical models (Power Law (PL), First-Order (FO) and Second-Order (SO)) were applied for determination of kinetics parameters of hydrogel swelling. For the initial stage ($SD/SD_{eq}\leq 0.6$), PL approach, $SD/SD_{eq}=kt^n$ (k is the kinetic constant, n is diffusion exponent) and FO equation, $SD/SD_{eq}=1-\exp(-kt)$, were used. SO kinetics was used for extensive stage of swelling, $t/SD=A+Bt$, ($B=1/SD_{eq}$, $A=1/v_0$ is the reciprocal of the initial swelling rate). Diffusion coefficients (D) were determined by the models based on solutions of Fick's law, using three approximations: ET (valid for the first 60% of sorption), LT (valid for the latter 40%), and E (valid for the whole range of swelling).

RESULTS AND DISCUSSION

Figure 1(a) shows the FTIR spectra of CMC and the initial CS. The two peaks at 1593 cm⁻¹ and 1418 cm⁻¹ of CMC are the characteristic absorption bands of the carboxyl group (ν_{as} -COO⁻ and ν_s -COO⁻), which indicate that

the carboxymethyl group is grafted onto the molecular chain of CS [3]. Figure 1(b) shows that PVA/CMC blend xerogel served as stabilizing agent for AgNPs. Decreasing in intensity and blue-shift of observed bands indicates possible formation of a coordination bond between AgNPs and COO^- , -NH_2 and -OH groups in PVA/CMC matrix.

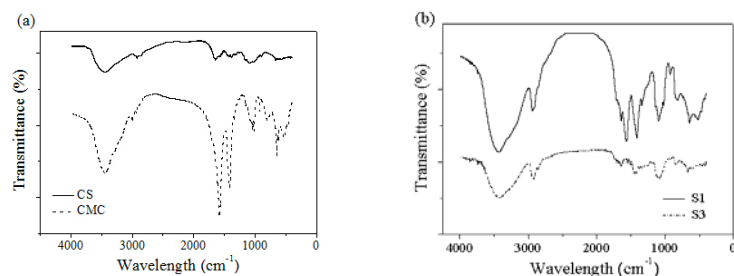


Figure 1. FTIR spectra of (a) pure CS and CMC, and (b) nanocomposite xerogel, S3, in comparing with pure S1 xerogel.

Fluorescence spectroscopy was employed to investigate the emission of crosslinked PVA/CMC blend after extraction in water (Figure 2(a)). Figure 2(b) shows UV-Vis spectra of Ag-PVA/CMC, experimentally obtained (solid line) and obtained by applying Mie theory (dashed line) [4]. AgNPs radii were determined by applying the computational analysis using the “MiePlot v.3.4” (<http://www.philiplaven.com/mieplot.htm>). In Figure 2(c) the micrographs of network (sample S4) and spherical particles (sample S3), obtained by scanning electron microscopy (SEM), are shown.

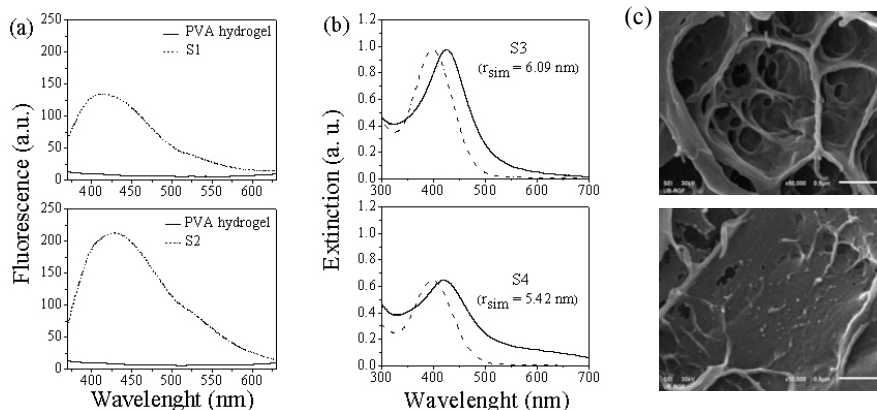


Figure 2. (a) Fluorescent spectra of PVA/CMC blend hydrogels; (b) UV-Vis spectra (solid line) and spectra obtained by applying Mie theory (dashed line); (c) SEM micrographs of S4 (up) and S3 (down).

The absorption of surrounding fluid by Ag-PVA/CMC blend hydrogel is affected by a simultaneous influence of the matrix and the presence of AgNPs. Doubly increasing of CMC concentration reduces swelling capacity. The water uptake in Ag-blend hydrogel increases comparing with pure PVA/CMC. At the initial stage of swelling, systems show Fickian diffusion ($n < 0.5$) for all samples (S1-S4) [5], meaning that media transport is driven by a concentration gradient rather than by convective flux (not limited by polymer relaxation). The diffusion constants are less due to the presence of AgNPs. The kinetic parameters and diffusion constants are presented in Table 1.

Table 1. Kinetic parameters and diffusion constants.

Sample	SD_{eq}^{exp} (%)	Power law kinetics		First-order kinetics		Second-order kinetics		Early time	Late time	Etters model
		k (1/h ⁿ)	n	SD_{eq} (%)	$k_{FO} \times 10^4$ (1/s)	SD_{eq} (%)	v_0 (%/min)	$D \times 10^7$ (cm ² /s)	$D \times 10^7$ (cm ² /s)	$D \times 10^7$ (cm ² /s)
S1	402±2	0.47	0.46	335	0.70	417	4.89	0.84	0.97	5.80
S2	351±1	0.43	0.40	300	0.77	361	4.99	0.93	1.05	6.38
S3	566±5	0.36	0.43	454	0.60	592	5.35	0.64	0.88	5.31
S4	497±4	0.42	0.37	406	0.66	515	5.91	0.75	0.95	5.77

CONCLUSION

Investigations show formation of a coordination bond between AgNPs and –COO⁻, –NH₂ and –OH groups of PVA/CMC matrix. Optical properties simultaneously depend on the concentration of CMC and on the presence of AgNPs. Swelling capacity decreases with increasing of CMC concentration, while the water uptake increases due to the presence of AgNPs. The media transport is driven by a concentration gradient (Fickian diffusion) while the diffusion constants are less due to the presence of AgNPs.

ACKNOWLEDGEMENT

This work is financed by the Ministry of Education, Science and Technological Development of the Republic of Serbia (project III 45005) and International Atomic Energy Agency (IAEA), CRP: F22051/Contract No. 16733.

REFERENCES

- [1] W. S. Choi, et al., Polym. Degrad. Stabil., 2002, 78, 533–538.
- [2] J. Krstić, et al., Rad. Phys. Chem., 2014, 96, 158-166.
- [3] P. Liang, et al., J. Cryst. Growth., 2004, 261, 571-576.
- [4] G.Mie, Ann. Phys., 1908, 25, 377–445.
- [5] J. Krstić, et al., J. App. Polym. Sci., 2014, 131, 40321

RADIOCHEMISTRY,
NUCLEAR CHEMISTRY

ABSORBED DOSE DISTRIBUTION AT VINČA RADIATION PLANT

B. Šećerov and D. Stančov

*Vinča Institute of Nuclear Sciences, University of Belgrade, 11001
Belgrade, P.O.Box 522, Serbia*

ABSTRACT

The aim of work is to correlate the absorbed dose distribution and gamma source activity in Vinča Radiation Plant. The measurements of absorbed doses obtained during the sterilization process of plastic medical products are compared with similar measurements made during the commissioning of this plant, but this time by using alanine dosimetry system. The influence of source activity to depth dose distribution is as expected, but there is no effect to the height dose distribution. The inhomogeneity of 13% of the dose across the box was determined is also done by alanine dosimetry system.

INTRODUCTION

Vinča Radiation Plant is mainly intended for the commercial radiation sterilization of medical devices. It consists of a plaque source, associated storage pool and shielding, product handling areas, and a shuffle-dwell conveyor system designed for either continuous or batch operation [1]. The facility parameters for sterilization are determined in accordance to international standards through process qualification by dose mapping in an irradiation container [2]. However, the complete set of relevant parameters for a suitable running of the plant can be obtained from the commissioning measurements [3]. Some of these measurements gave depth and height dose distribution when the source activity was 3.7×10^{15} Bq. The source rods had the same activity and occupied only the central part of the source frame (1m x 1m). The depth dose distribution was 50%, 30%, 20% among rows looking from the first one, and the height dose distribution was 13%, 30%, 32% and 25% from bottom to top. Dosimetry system was the radiochromic dye solution sealed in 5 ml glass ampoules. The source activity now is almost two times higher and several generations of source rods are mixed in this source frame (1m x 3m). It seems interesting to examine what is the influence of source activity and geometry to dose distribution. For this purpose, alanine pellet dosimeters were used due to their small size that enabled to put dosimeters in more positions in one box than in commissioning measurements.

EXPERIMENTAL

Fig.1 shows a schematic diagram of the arrangement of product boxes around the plaque source. The source frame (1 m x 3 m) is loaded with 6.88×10^{15} Bq of ^{60}Co placed into source rods (diameter 11.1 mm, length 451 mm). An automatic conveyor carries boxes through the source. One irradiation run consists of four sequential irradiation cycles, and in each cycle a given box passes through the irradiation room at one of four vertical levels, i.e. every box is irradiated in the same way.

L-alanine pellet dosimeters (diameter 3 mm, thickness 1.5 mm and mass between 37.5 – 37.6 mg) purchased from Aérial (Illkirch, France) were placed in the central part of standard box (46 cm x 46 cm x 43 cm) with product in three positions: 1) plane facing the source, 2) center, 3) back plane from the source. The boxes with dosimeters were loaded into three carriers. The carriers were positioned at the beginning of each subsequent row and then irradiated for 12 consecutive dwell times (509 s). After these 12 steps, each carrier reached the opposite end of its row.

This experiment enables the calculation of the absorbed dose for one irradiation run. The absorbed dose in central position in box should be obtained by summing up all absorbed dose values in central position (for all four boxes in all three rows). This corresponds to one half of a complete irradiation run for one box. The absorbed dose for the edge of box for a complete irradiation run one can obtain summing up the total sum of front and back plane of box, because passing from one row to next the box changes its position for 180° facing source rods.

The absorbed doses were measured by MiniScope MS300 ESR spectrometer using Aer'EDE Version 2.0.4. software for dose calculation.

RESULTS AND DISCUSSION

Fig. 2 presents the results of both the depth and the height absorbed dose distribution. Table 1. gives these results as a sum of all measured absorbed

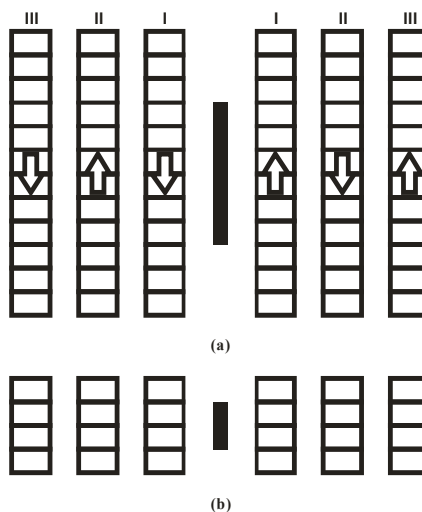


Figure 1. Horizontal (a) and vertical (b) arrangements and movements of box carriers within the irradiation room

doses in the same row and in the same position in the box. The total sum of the absorbed doses in central position is equal to one half of the absorbed dose for a complete irradiation run in this position, i.e. 26.84 kGy is the absorbed dose for central plane of box for complete irradiation run. The total sum of front and back plane of box gives the absorbed dose for the edge of box for a complete irradiation run, and it is 30.25 kGy. This is 13 % higher than the dose in central position and relate to dose uniformity in box with plastic products.

The dose distribution among rows is 65% first row, 23% second and 12% third row. Comparing dose distribution now with the previous [3], the absorbed dose in first row now is 16% higher and 7% and 9% lower for second and third row. Looking into the height dose distribution in one carrier, there is no changes in dose distribution without regard to changes in source activity.

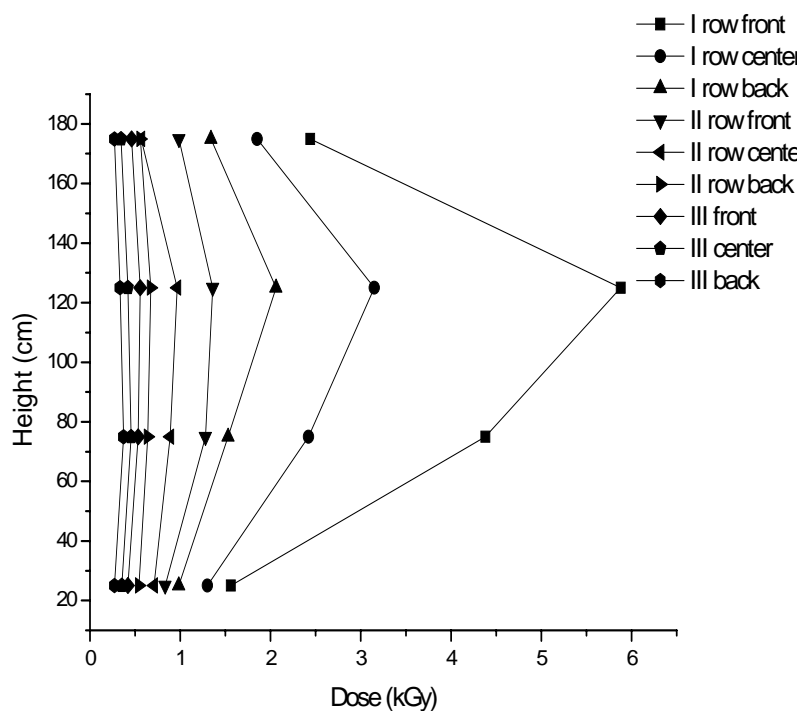


Figure 2. Height and depth dose distribution in the three rows of carriers

Table 1. The sum of absorbed doses in one row in the same position after 12 steps

Row	Sum of doses center (kGy)	Total center (kGy)	Sum of doses front (kGy)	Total front (kGy)	Sum of doses back (kGy)	Total back (kGy)
I	8.72		14.26		5.91	
II	3.13	13.42	4.46	20.69	2.41	9.56
III	1.57		1.97		1.24	

CONCLUSION

The absorbed dose distribution of complete irradiation run depends on source activity looking on depth distribution. The lower source activity gives better dose uniformity among rows which is expected. Meanwhile the height dose distribution remains the same. The nonuniformity of the dose within the box was 13%.

ACKNOWLEDGEMENT

The Ministry of Education and Science of the Republic of Serbia under Projects ON 172056 and III 45020 supported this work.

REFERENCES

- [1] V. M. Marković, R. Eymery and H. C. Yuan, *Radiat. Phys. Chem.*, 1977, 9, 625-631
- [2] ISO 11137 – 2006(E), *Sterilization of health care products – Radiation*, 2006
- [3] B. B. Radak, V. M. Marković and W. L. McLaughlin, *Radiat. Phys. Chem.*, 1979, 14

RESEARCH ON TREATMENT OF LIQUID RADIOACTIVE WASTE CONTAINING COBALT BY ADSORPTION ON POLY(ACRILIC ACID) HYDROGEL

N. Lazarević¹, J. Jovanović² and B. Adnadjević²

¹*Nuclear Facilities of Serbia, Mike Petrovica Alasa 12–14, 11351 Belgrade,
Vinca, Serbia*

²*Faculty of Physical Chemistry, Studentski trg 12-16, 11001 Belgrade,
Serbia (bora@ffh.bg.ac.rs)*

ABSTRACT

The poly(acrylic acid) hydrogel (PAA) has been suggested as adsorbent material to treat cobalt-60 in radioactive liquid waste. The kinetics of isothermal adsorption of cobalt ions from an aqueous solution onto PAA hydrogel was investigated in the temperature range from 298K to 315 K. The kinetic model of Co²⁺ adsorption $[1-(1-\alpha)^{1/3}]^2=kt$, was established by using the model-fitting method. The kinetic parameters of Co²⁺ adsorption ($E_a = 41 \text{ kJ mol}^{-1}$, $\ln [A/\text{min}^{-1}]=12$) were determined. It was found that cobalt adsorption was kinetically controlled process which is determined by the rate of three-dimensional diffusion Co²⁺ ions (D3).

INTRODUCTION

Increased operation of nuclear power plants and nuclear laboratory are the source of radioactive wastes released into environment. Enormous amounts of low-level liquid radioactive wastes (LLRW) are being produced as a results of operation, repair and disposal at those facilities. All of these LLRW were composed of different chemical and radiochemical composition [1]. The adsorption technologies using different adsorbents may be used for removal radioactive ions very successfully. The radioactive cobalt-60 with half-life ($t_{1/2} = 5.27 \text{ y}$) in the liquid waste came from neutron activation for corrosion products. Adsorption cobalt ions by different types of adsorbents have been the subject of several studies [2-4]. As an adsorbent, hydrogels are successfully applied for the removal of pollutants from aqueous solution as they are easily applicable, have high removal capacity and can be regenerated [5]. The cobalt ion (Co²⁺) removal capacities by hydrogel N,N-dimethylaminopropyl methacrylamide (DMAPMam) homopolymer and DMAPMam/itaconic acid (DMAPMam/IA) copolymers were investigated by taking into account of the initial metal ion concentration and pH of aqueous medium [6].

The aim of this research is to investigate the performance of PAA hydrogel in the treatment of radioactive liquid waste contained cobalt-60. Because of that, the kinetics of isothermal adsorption of cobalt ions from an aqueous solution onto PAA was investigated.

EXPERIMENTAL

In this research, the PAA hydrogel was synthesized by the procedure described in our previous work [7]. Adsorption of Co^{2+} on PAA hydrogel was carried by the batch method. Hydrogel powder ($m \sim 0.1$ g) was added to 200g aqueous solution of CoSO_4 (with Co^{2+} concentration 100 mg/L) and the adsorption vessel was placed in the thermostat at pre-determined temperature (298 K, 300 K, 308 K and 315 K). During the adsorption process, the adsorption system was homogenized by stirring at 600 rpm. Samples were taken from this adsorption system at regular time intervals. After centrifugation, concentration of Co^{2+} remaining in supernatant was determined by measuring the absorbance at 625 nm. The determination of Co^{2+} ions as Co-(thiocyanate) was carried out according to the published procedure in literature [8]. For that measurement a UV-Visible spectrometer (Cintra 10e, GBC Scientific equipment) was used.

The specific adsorption capacity of PAA hydrogel for Co^{2+} at a given temperature after certain adsorption period can be calculated from the equation: $x_s = (c_0 - c_i)m_s/m$, where: c_0 is the initial concentration of the Co^{2+} solution before adsorption (mg/L), c_i is the concentration of the Co^{2+} solution after a certain adsorption time (mg/L) and m_s is the mass of aqueous solution of CoSO_4 (g). The adsorption degree of Co^{2+} ions, α , is calculated from the equation $\alpha = x_s/x_{\max}$, where: x_{\max} is the maximum specific adsorption capacity of PAA hydrogel for Co^{2+} at a given temperature and is determined from experimental kinetic curves.

Kinetic model of Co^{2+} adsorption onto PAA hydrogel was examined by the so-called "model-fitting procedure"[9].

RESULTS AND DISCUSSION

The isothermal dependence of specific adsorption capacity of the PAA hydrogel for Co^{2+} vs. adsorption time (kinetic curves) is shown in Figure 1.

Applying the model fitting method we obtain that kinetics of Co^{2+} adsorption on PAA hydrogel can be described by theoretical kinetic model: $[1 - (1 - \alpha)^{1/3}]^2 = kt$, where k is the rate constant of adsorption of Co^{2+} on PAA hydrogel. This model is characteristic for the physicochemical processes whose kinetic is determined by the rate of three-dimensional diffusion (D3).

If model D3 describes the kinetics of the isothermal adsorption of Co^{2+} on PAA, then the dependence $[1 - (1 - \alpha)^{1/3}]^2$ on the adsorption time should be a straight line and from slopes of these straight lines the values of model constants has been determined. Since the increase of the model constant with temperature is obtained, the kinetic parameters were determined by applying the Arrhenius equation (Table I). The change of the model constant with temperatures and kinetics parameters, activation energy (E_a) and pre-exponent factor ($\ln A$) for the Co^{2+} adsorption is given in Table I.

With aim to investigate kinetic complexity, Friedman iso-conversional method [10] was applied to determine the dependence of the activation energy of the Co^{2+} adsorption on the PAA hydrogel on the degree of adsorbed Co^{2+} ions.

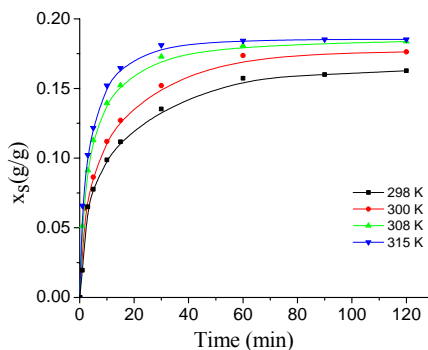


Figure 1. The isothermal kinetic curves of adsorption Co^{2+} ions on PAA hydrogel

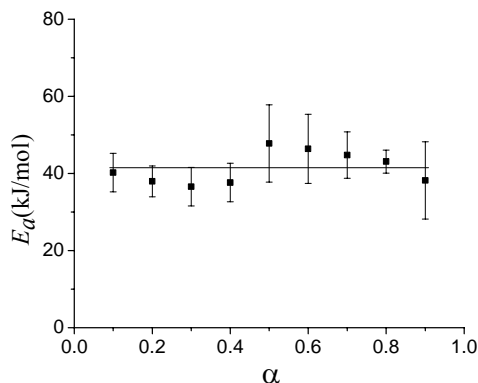


Figure 2. The dependence of E_a vs. adsorption degree

Table 1. The model constant of Co^{2+} adsorption and kinetic parameters

T (K)	$k \cdot 10^{-3}$ (min^{-1})	R	Kinetic parameters
298	7.4 ± 0.2	0.996	
300	8.31 ± 0.04	0.9999	E_a (kJ mol^{-1}) = 41 ± 4
308	14.1 ± 0.5	0.991	$\ln [A/\text{min}^{-1}] = 12 \pm 2$
315	17.5 ± 0.2	0.999	$R = 0.968$

As can be seen from the results presented in Figure 2, the values of the activation energy are practically independent of the adsorption degree, and in accordance with the model value $E_a = 41 \text{ kJ mol}^{-1}$. This implies that Co^{2+} adsorption on the PAA hydrogel is probably elementary process.

CONCLUSION

The PAA hydrogel is very efficient adsorbent for removal cobalt-60 from radioactive liquid waste. The adsorption of Co^{2+} ions onto the PAA hydrogel is a probably kinetically elementary process, which can be modeled with the theoretical kinetic model D3 described by the equation: $[1-(1-\alpha)^{1/3}]^2 = kt$.

ACKNOWLEDGEMENT

This investigation was supported by the Ministry of Science and Technical Development of the Republic of Serbia, through Project No.142025G.

REFERENCES

- [1] Y. Park, Y.C. Lee, W. S. Shin, S.J. Choi, Chem. Eng. J., 2010, 162, 685–695.
- [2] Y. A. Mustafa, M. J. Zaiter, J. Hazard. Mater., 2011, 196, 228–233.
- [3] S. Triantafyllou, E. Christodoulou, P. Neou-Syngourna, Clays Clay Miner., 1999, 47, No. 5, 567–572.
- [4] S. Rengaraj, Seung-Hyeon Moon, Water Res., 2002, 36, 1783–1793.
- [5] V. Behiari., M. Sotiropoulou, G. Bokias, P. Lianos, Colloids Surf. A, 2008, 312, 214–218.
- [6] N. Bas, A. Yakar, N. P. Bayramgil, J. Appl. Polym. Sci., 2014, 131, DOI: 10.1002/app.39569.
- [7] B. Adnadjevic, J. Jovanovic, N. Lazarevic, J. Appl. Polym. Sci., 2011 119, (3), 1805–1812.
- [8] A. F. Hussain, Nat. J. Chem., 2008, 30, 229–250.
- [9] S. Vyazovkin, C.A. Wight, Thermochim. Acta., 1999, 340/341, 53–68.
- [10] H. Friedman, J. Polym. Sci., 1964, C 6, 183–195.

PREPARATION AND CHARACTERIZATION OF ^{90}Y -LABELLED MAGNETIC NANOPARTICLES

M. Radović¹, P. Calatayud², D. Janković¹, B. Antić¹, V. Spasojević¹, G. F. Goya² and S. Vranješ-Džurić¹

¹“Vinča” Institute of Nuclear Sciences, University of Belgrade, P.O. Box 522, 11001 Belgrade, Serbia

²Instituto de Nanociencia de Aragón (INA), University of Zaragoza, Mariano Esquillor s/n, 50018- Zaragoza, Spain

ABSTRACT

The aim of this study is investigation of the potential of two novel types of multifunctional ^{90}Y -labelled magnetic nanoparticles (MNPs): Fe_3O_4 -Naked and polyethylene glycol 600 diacid functionalized Fe_3O_4 (Fe_3O_4 -PEGdiacid) MNPs as targeting vehicles to localize both radioactivity and magnetic energy at the tumor site.

The conditions for their synthesis and radiolabelling were optimized. MNPs were characterized based on the external morphology, size distribution and magnetic properties. These results were compared to assess the effect of the coating on the physicochemical characteristics of the particles. ^{90}Y -labelling of both Fe_3O_4 -Naked and Fe_3O_4 -PEGdiacid MNPs enabled the studies of biodistribution and biodegradation of magnetite particles *in vivo*.

INTRODUCTION

Magnetic nanoparticles have been intensively used for a wide variety of biomedical applications, such as contrast agents for magnetic resonance imaging (MRI), drug delivery and hyperthermia [1,2]. Since localized hyperthermia treatments lead to increased perfusion in the tumor region, MNPs are good choice as vehicles for a radionuclide delivery. The synergistic interaction between hyperthermia and radiation therapy is based on the heat effect that may make some cancer cells more sensitive to radiation or harm other cancer cells that radiation cannot damage [3,4].

In this work yttrium-90 (^{90}Y) was selected for the radiolabelling of MNPs as a clinically acceptable, long-range, β -emitting radionuclide with optimal nuclear-physical characteristics (decay half-life of 64.1h, $E_{\text{max}\beta}$ of 2.27 MeV) for use in radionuclide tumor therapy. ^{90}Y -labelling of MNPs open up the possibility for tracking of extremely small amounts of nanoparticles in the complex biological systems. Basic requirements of the radiolabelling

method are that structure or properties of nanoparticles remained unchanged after the radiolabelling and that the stability of radiolabelled product is sufficient to allow further *in vitro* and *in vivo* studies. Once the radiolabelling method is optimized, radioactive part of the radiolabelled compound could be used not only for studies of biological distribution but also in radiodiagnostic or radiotherapy [5].

MATERIALS AND METHODS

Iron oxide nanoparticles were prepared by two different methods. Fe₃O₄-Naked MNPs were produced by an oxidative hydrolysis of ferrous sulfate with NaOH [6]. Co-precipitation from ferrous/ferric chloride solutions in alkaline medium with the addition of PEG 600 diacid during the nanoparticles synthesis is used as a valid method for magnetite functionalization and preparation of Fe₃O₄-PEGdiacid MNPs [7,8]. Radiolabelling of MNPs was performed by mixing 0.5 mL aqueous suspension of Fe₃O₄-Naked MNPs and Fe₃O₄-PEGdiacid MNPs with 37 MBq ⁹⁰YCl₃ followed by incubation of reaction mixture at room temperature on a shaker for one hour.

RESULTS AND DISCUSSION

With the applied method very unstable Fe₃O₄-Naked MNPs of average size 80±5nm were obtained. DLS measurements of Fe₃O₄-PEGdiacid MNPs showed hydrodynamic diameter of 46±0.6nm, reflecting the effect of the coating polymer layer on the 10 nm magnetic cores (measured by TEM). Binding of PEG 600 diacid generate highly negative surface charge of Fe₃O₄-PEGdiacid MNPs (-28 mV at pH 7) providing electrostatic repulsion between MNPs, therefore stable suspension was achieved. Fe₃O₄-PEGdiacid MNPs displayed superparamagnetic behaviour at room temperature with saturated magnetization, Ms of 70 emu/g. The obtained specific power absorption value for Fe₃O₄-PEGdiacid MNPs was 200 W/g, indicated their potential in hyperthermia based cancer treatments. The zeta potential, FTIR and TGA results confirmed that Fe₃O₄ nanoparticles have been functionalized probably by coordinating via one of carboxylate groups from PEGdiacid, while negatively charged terminal carboxylate group provides an avenue to extended bond formation with positively charged ⁹⁰Y. Radiolabelling yield of both types of ⁹⁰Y-labelled MNPs, determined by measurement of radioactivity in MNPs precipitate after magnetic separation as well as by radiochromatography analysis, exceeded 97%.

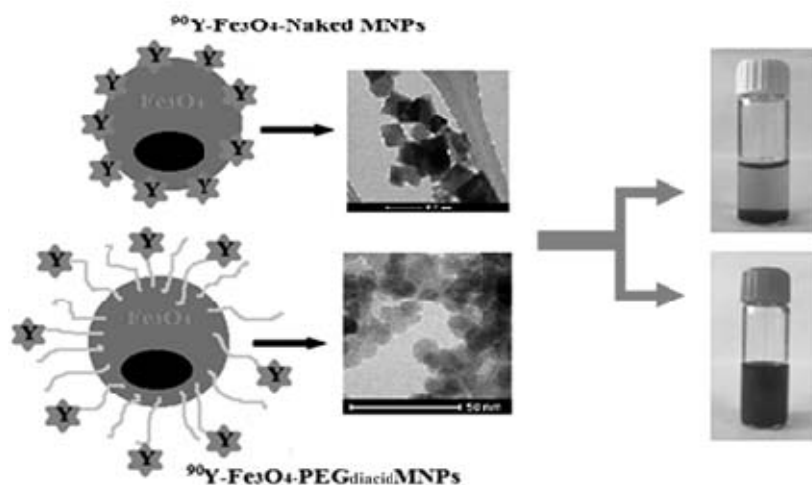


Figure 1. Colloidal stabilization of ^{90}Y -labelled Fe_3O_4 -Naked and Fe_3O_4 -PEGdiacid MNPs

CONCLUSION

We report here design and preparation of multifunctional ^{90}Y -labelled-MNPs with potential ability to perform concurrent tracking, imaging and therapeutic application *in vivo*. The Fe_3O_4 -PEGdiacid MNPs showed high phase purity and favorable physicochemical and magnetic characteristics for *in vivo* use. The obtained SPA value for Fe_3O_4 -PEGdiacid MNPs (200 W/g) indicates that these MNPs could be used as heating agents for *in situ* magnetic fluid hyperthermia protocols. Besides, high labeling yield and *in vitro* and *in vivo* stability of ^{90}Y -labelled-PEGylated magnetite nanoparticles create opportunities for their use as a multifunctional diagnostic and therapy agents.

REFERENCES

- [1] Mitra, A. Nan, B. R. Line, H. Ghandehari, *Curr Pharm Res.*, 2006, 12, 4729-4749.
- [2] G. F. Goya, V. Grazu, M. R. Ibarra, *Current Nanoscience*, 2008, 4, 1-16.
- [3] H. Maeda, J. Wu, T. Sawa, Y. Matsumura, K. Hori, *J Control Release*, 2000, 65, 271-284.
- [3] T. Tanaka, S. Shiramoto, M. Miyashita, Y. Fujishima, Y. Kaneo, *Int J Pharm.*, 2004, 277, 39-61.
- [4] U. Hafeli, *Physics and Chemistry Basis of Biotechnology*, 2002, 7, 213.
- [6] C. Riggio, M. P. Calatayud, C. Hoskins, J. Pinkernelle, B. Sanz, T. E. Torres, M. R. Ibarra, L. Wang, G. Keilhoff, G.F. Goya, V. Raffa, A. Cuschieri, *Int J Nanomedicine*, 2012, 7, 3155-3166.
- [7] R. Massart, V. Cabuil, *J Chim Phys.*, 1987, 84, 967-973.
- [8] J. Lee, T. Isobe, M. Senna, *J Colloid Interface Sci.*, 1996, 177, 490-494.

EFFICIENT SEPARATION OF Tc-99 FROM AQUEOUS SOLUTION USING PINECONE ACTIVATED CARBON

Z. Sandić^{1,2}, M. Momčilović², M. Mirković², M. Radović²,
D. Stanković², Lj. Suručić³, and D. Maksin²

¹University of Banja Luka, Faculty of Science, 78000 Banja Luka, Mladena Stojanovića 2, Bosnia and Herzegovina (Republic of Srpska).

²University of Belgrade, Vinča Institute of Nuclear Sciences, P.O.Box 522, Belgrade, Serbia. (dmaksin@vinca.rs)

³University of Belgrade, Faculty of Forestry, Kneza Višeslava 1, Belgrade, Serbia.

ABSTRACT

Sorption of radioactive ⁹⁹Tc-pertechnetate onto activated carbon prepared from pinecones was investigated. The parameters of contact time and Tc-99 concentration were varied. It was established that the sorption half-life, $t^{1/2}$, was very short ~ 2.2 min, thus making this sorbent an excellent candidate for immediate pollution remediation, which is very important in the case of nuclear accidents. The kinetic data were found to follow closely the pseudo-second-order (PSO) kinetic model. Boyd model established the sorption dependence only on film diffusion. The partitioning/distribution coefficient, K_d , attained was $2729 \text{ cm}^3 \text{ g}^{-1}$. The equilibration time was 3 h at room temperature ($T=298 \text{ K}$).

INTRODUCTION

High surface area, remarkable sorption capacity and efficient regeneration are among the most important characteristics of the non-hazardous porous activated carbon sorbent [1]. Diverse surface organic functional groups (ionized in solution depending on pH) are responsible for surface reactivity of activated carbon.

Tc-99 is among many hazardous radioisotopes often detected in the environment, being a long life (2.13×10^5 years) pure β -emitter and has a specific activity of 629.0 MBq g^{-1} . It is produced in large amounts by nuclear fission of ²³⁵U or ²³⁹Pu in nuclear reactors. The predominant form of Tc-99 under oxic conditions in surface and ground waters is pertechnetate oxyanion (⁹⁹TcO₄⁻), which is poorly sorbed by natural materials, highly soluble in water, and thus readily mobile in the environment [2]. Activated carbon has been demonstrated to retain ⁹⁹TcO₄⁻ efficiently in deionized water and the solutions of various electrolytes [3,4]. The high cost of

commercially produced activated carbon prompted research on novel, more efficient, low-cost, locally available and renewable activated carbonaceous materials. In this paper, pinecone-activated carbon was tested as sorbent for $^{99m}\text{TcO}_4^-$, using an easily measurable metastable nuclear isomer Tc-99m, rapidly decaying to Tc-99. Kinetic data for Tc(VII) removal was collected and fitted to kinetic models, and K_d was evaluated.

EXPERIMENTAL

Powdered activated carbon was derived by thermal–chemical process from the ground pinecones collected from Čair Park in Niš, Serbia; the BET surface area (S_{BET}) measurement of the sample was made by nitrogen adsorption at 77 K using Sorptomatic 1990 (Thermo Fisher Scientific, USA), the surface functional groups and pH_{PZC} were determined using the procedures described previously [1]. $^{99m}\text{TcO}_4^-$ sodium solution was eluted from $^{99}\text{Mo}/^{99m}\text{Tc}$ generator (Vinča Institute of Nuclear Sciences). $^{99m}\text{TcO}_4^-$ uptake from aqueous solutions was monitored at room temperature ($T=298$ K) in static experiments. 10 mg of sorbent was contacted with 4 cm^3 of ^{99m}Tc -pertechnetate aqueous solution at unadjusted pH. A blank experiment (no sorbent) was prepared in the same manner. At predetermined time intervals, solid phase was separated from the solutions by centrifugation: 5 min 3000 rpm (Heraeus-Christ Labofuge III Centrifuge, 6000 Max RPM, American Laboratory Trading, Inc.). From each vial (blank and sorbent containing), 100 mm^3 aliquots were taken and residual radioactivity was measured in supernatant solution. The specific activity of pertechnetate eluate was determined by a Capintec CRC-15 β dose calibrator and adjusted by adding saline solution to 4.35 GBq dm^{-3} . All ^{99m}Tc supernatant analyses were carried out using a $2\pi\gamma$ -solid-state scintillation detector (LKB Wallac 1282 Compugamma, Finland) with autosampler. Relative measurements of sorbed radioactivity were obtained using the following equation (R -sorbed pertechnetate activity (%), R_b -measured activity of reference or blank aliquot (cpm), R_s -activity of the supernatant aliquot (cpm)):

$$R = \frac{R_b - R_s}{R_b} \cdot 100\%$$

The sorption isotherms were measured by mixing 10 mg of activated carbon with 4 cm^3 sodium pertechnetate solution with the specific activity ranging from 11.9 to 95.6 GBq dm^{-3} . The equilibration time was 3 h.

RESULTS AND DISCUSSION

The characteristics of pinecone-activated carbon are given in Table 1. As known, predicting the rate at which sorption takes place in a given system is one of the critical factors in sorption system design. To the best of our knowledge, there is an obvious lack of literature regarding modeling the

kinetics of ⁹⁹Tc removal. Here, the kinetics of ^{99m}TcO₄⁻ sorption on pinecone activated carbon was examined using two kinetic models: PSO [5] and Boyd model with Reichenberg approximation [6] (Table 2), where Q_{eq} and Q_t denote the amounts of sorbed pertechnetate anions at equilibrium and at time t , respectively, k_2 - the rate constant of PSO sorption, $h=k_2Q_{eq}^2$ - the initial rate constant, F - the fractional attainment of equilibrium at time t , n - an integer defining infinite series solution and Bt - a mathematical function of F .

The correlation coefficient (R^2) for PSO model was equal to 0.999 suggesting that the ^{99m}TcO₄⁻ sorption on activated carbon obeyed PSO model (Table 3), indicating chemisorption involving valence forces through sharing or exchange of electrons between activated carbon functional groups and ^{99m}TcO₄⁻ [5].

Table 1. Relevant characteristics of pinecone activated carbon [1].

pH _{PZC}	3.06
S_{BET} , m ² g ⁻¹	1094
Surface functional groups, mmol g ⁻¹	
Carboxylic	1.742
Lactonic	0.723
Phenolic	0.493

Table 2 Kinetic models.

Kinetic model	Equation	Ref.	Q_e and Q_e^{calc} values obtained for PSO model fit showed excellent agreement confirming this assumption. The very short $t_{1/2}$ as well as very high h and Q_e values suggest that this activated carbon can be regarded as
PSO	$\frac{t}{Q} = \frac{1}{k_2 Q_e^2} + \frac{1}{Q_e} t$ $h = k_2 Q_e^2$	[5]	
Boyd equation	$F = 1 - \frac{6}{\pi^2} \sum_{n=1}^{\infty} \frac{1}{n^2} \exp(-n^2 Bt)$	[6]	

a highly efficient sorbent for ⁹⁹Tc. The Boyd plot does not pass through the origin in the shape of a straight line, thus implying that the process is film-diffusion controlled [6].

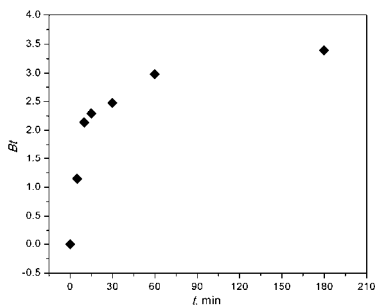


Figure 1. Boyd model.

In an attempt to avoid toxic radiation doses, the equilibrium investigation was limited to the linear isotherm part [4]. K_d (cm³ per g) was calculated according to the equation $S = K_d C$, where S represents the sorbed Tc activity on sorbent surface (GBq per g of activated carbon) and C is the equilibrium specific Tc activity (GBq per dm³ of solution). The Oak Ridge National Laboratory investigated several synthetic resins for ⁹⁹TcO₄⁻ removal from contaminated wastewater and also found linear adsorption isotherms, with

K_d values ranging from $902 \text{ cm}^3 \text{ g}^{-1}$ to $2370 \text{ cm}^3 \text{ g}^{-1}$ [7]. Holm et al. found the maximum K_d in the order of $10^6 \text{ cm}^3 \text{ g}^{-1}$ at pH 2 ± 4 for activated carbon; the equilibrium time was ca. 5 h, at room temperature, from deionized water [3]. Gu and associates found that K_d of $^{99}\text{TcO}_4^-$ exceeded $27000 \text{ cm}^3 \text{ g}^{-1}$ when actual groundwater was used, as well as $12000 \text{ cm}^3 \text{ g}^{-1}$ when background solutions of 0.01 M CaCl_2 and Na_2SO_4 were treated, after overnight equilibration [4].

Table 3. PSO kinetic model parameters.

Q_e , GB g^{-1}	1.71
$t_{1/2}$, min	2.2
Q_e^{calc} , GB g^{-1}	1.71
k_2 , g GB $^{-1}$ min $^{-1}$	0.351
h , GB g^{-1} min $^{-1}$	1.024
R^2	0.999

CONCLUSION

Activated carbon prepared from pinecones was investigated as a sorbent of radioactive $^{99}\text{TcO}_4^-$. Very short $t^{1/2}$ (~ 2.2 min) indicated that this sorbent can be an excellent candidate for immediate pollution remediation. The kinetic data adhered closely to PSO kinetic model, suggesting chemisorption. Boyd model verified

the sorption dependence only on film diffusion. The partitioning/distribution coefficient K_d , found was $2729 \text{ cm}^3 \text{ g}^{-1}$, after 3 h equilibration time at room temperature ($T=298 \text{ K}$).

ACKNOWLEDGEMENT

This work was supported by the Ministry of Education, Science and Technological Development Republic of Serbia (Grants no. TR 37021 and III 43009).

REFERENCES

- [1] M. Momčilović, M. Purenović, A. Bojić, A. Zarubica, M. Randelović, *Desalination* 2011, 276, 53–59.
- [2] K. Wildung, M. McFadden, T. R. Garland, *J. Environ. Qual.*, 1979, 8, 156-161.
- [3] E. Holm, T. Gäfvert, P. Lindhal, P. Roos, *Appl. Radiat. Isot.* 2000, 53, 153-157.
- [4] B. Gu, K.E. Dowlen, L. Liang, J.L. Clausen, *Sep. Technol.*, 1996, 6, 123-132.
- [5] Y.S. Ho, *J. Hazard. Mater.*, 2006, B136, 681-689.
- [6] X. Hu, J. Wang, Y. Liu, X. Li, G. Zeng, Z. Bao, X. Zeng, A. Chen, F. Long, *J. Hazard. Mater.*, 2011, 185, 306–314.
- [7] W.D. Bostik, P.E. Osborne, D.E. Beck, D.H. Bunch, R.L. Fellows, G.F. Sellers, J.L. Shoemaker, K.T. Bowser, D.T. Bostick, Oak Ridge K-25 Site, Martin Marietta Energy Systems, Inc. for the U. S. Department of Energy, 1995, <http://www.osti.gov/scitech/servlets/purl/95161>.

MATERIAL SCIENCE

RARE-EARTH MAGNETIC MATERIALS FOR VARIOUS USES

A. Grujić and J. Stajić-Trošić

*Institute of Chemistry, Technology and Metallurgy, University of Belgrade,
Njegoševa 12,
11000 Belgrade, Serbia*

ABSTRACT

Nanocrystalline rare-earth Nd-Fe-B magnetic materials with various Nd content were characterized and compared in order to verify most suitable alloy for bonded magnet application. Polymer bonded magnets (PBM) based on Nd-Fe-B alloy with stoichiometric Nd content are prepared by compression moulding method using different magnetic filler concentrations in range 5 to 95 wt%. In order to obtain hybrid magnetic composite materials, part of Nd-Fe-B particles is substituted with barium ferrite agglomerates. The structure, phase analysis, magnetic properties and dynamic mechanical behaviour are examined by varieties of techniques including Scanning Electron Microscopy (SEM), X-ray diffraction analysis (XRD) and ^{57}Fe Mössbauer spectroscopy (MS), Superconducting Quantum Interference Device (SQUID) magnetic measurements and Dynamic Mechanical Analysis (DMA), respectively.

The storage modulus (E') of Nd-Fe-B PBMs is considerably improved with the higher amount of magnetic particles. Magnetic measurements depict changes in the properties of the investigated composites with respect to amount of the added filler. Results show that the magnetic properties of hybrid magnets are within the range of magnetic properties of the pure components, whilst dynamic mechanical properties are improved compared to 'pure' PBMs - consist "only" Nd-Fe-B particles or barium ferrite agglomerates in polymer matrix.

INTRODUCTION

The studies of rare-earth Nd-Fe-B nanocrystalline materials have become very significant due to the fact that slight transformations in microstructures allow a tailoring of magnets with defined magnetic properties [1]. The compositions and processing conditions of alloys have a strong influence on microstructure in optimal magnetic state and consequently on magnetic properties [2]. The Nd-Fe-B alloys could be analyzed according to Nd content [3]. The alloys with reduced neodymium content (nanocomposite

alloys) have multiphase composition and in the optimal magnetic state they are composed of the nano-sized exchange coupled grains of soft and hard magnetic phases. Depending on the alloy composition two types of nanocomposites α -Fe/Nd₂Fe₁₄B and/or Fe₃B/Nd₂Fe₁₄B can be obtained [4]. The stoichiometric and Nd-rich Nd-Fe-B alloys have an almost monophase composition with dominant amount of Nd₂Fe₁₄B phase. While the stoichiometric alloys are characterized by some intergranular exchange coupling between the grains of the same hard magnetic phase [5,6] the Nd-rich alloys are composed of grains of hard magnetic Nd₂Fe₁₄B phase that are magnetically isolated (decoupled) by the intergranular layer of Nd-rich phases [7,8].

Besides high values of the remanence and coercivity, as well as their relatively high Curie temperatures (app 312 °C) [9] Nd-Fe-B magnetic alloys are identified suitable for research and further development of magnetic composite materials with polymer matrix, so called bonded magnets [10,11].

Development of bonded technology, exploring the possibility of applications of various types of magnetic powder and polymeric matrices, testing of their influence, as well as the influence of process parameters, to achieve optimal mechanical and magnetic capacities are in research focus during the last few years [12,13]. Research trend is reflected in development of bonded hybrid magnetic composite materials with improved dynamic mechanical capacities and noticeably lower cost due to the replacement of the expensive Nd-Fe-B magnetic powder with low cost ferrite magnetic materials, achieving satisfying values of the maximal magnetic energy.

In this study, the influence of Nd content on microstructure and magnetic properties of three types of Nd-Fe-B alloys was analyzed by comparing phase compositions and magnetic properties in optimized magnetic state. Selected alloy is used for polymer bonded magnet (PBM) production. One of the objectives is to give more insight on the role of Nd-Fe-B particles on dynamic mechanical and magnetic properties of Nd-Fe-B/epoxy composite materials. Replacing one fraction of Nd-Fe-B with barium ferrite the hybrid composite materials with upgraded dynamic mechanical properties is produced. Interactions between employed magnetic powders and interactions between magnetic powders and polymer binder are considered.

EXPERIMENTAL PROCEDURE

Three types of rapid quenched Nd-Fe-B alloys are produced by melt spinning method. Magnetic properties of particles are presented in Table 1. Magnetic properties of barium ferrite used for hybrid PBMs production is also presented in Table 1.

The applied thermosetting epoxy system is a combination of liquid mixture of Bisphenol A and Bisphenol F resins and cross linking agent (hardener) which cures fully at room temperature. The properties of cured epoxy resin are: density of resin 1.2 g/cm³, tensile strength 58 MPa and elongation 2.8%.

Table 1. Magnetic properties of starting alloys in optimal magnetic state

Alloy	Mark	B_r [kG]	H_{cb} [kOe]	H_{cj} [kOe]	$(BH)_{max}$ [MGOe]
Nd _{4.5} Fe ₇₇ B _{18.5}	NM-L	9.78	2.53	3.16	7.53
Nd _{11.7} (Fe,Co) ₈₀ B _{8.3}	NM-B	8.18	6.03	8.72	13.07
Nd ₁₄ Fe ₇₉ B ₇	NM-A	7.46	6.25	13.42	11.55
BaFe ₁₂ O ₁₉	Ba-Fe	2.3	1.9	3.6	1.3

The PBMs are produced by compression molding under a pressure of 4MPa at room temperature using a lab scale compression molding press.

Observations of starting particles were made on the JEOL JSM-5800 Scanning Electron Microscope, with the accelerating voltage of 20 kV. The phase compositions of the investigated alloys in optimized magnetic state were determined by X-ray diffraction analysis (XRD) and ⁵⁷Fe Mössbauer spectroscopy (MS) at room temperature. X-ray diffraction measurements were performed on an X'Pert PRO MPD multi-purpose X-ray diffraction system from PANanalytical using Co K α radiation. Mössbauer spectra were taken in the standard transmission geometry using a ⁵⁷Co(Rh) source. The calibration was done against α -iron foil data. For the MS fitting and decomposition, the CONFIT software package was used [14]. Magnetic properties of the starting alloys and PBMs were measured at ambient temperature using the Quantum Design MPMS 5XL Superconducting Quantum Interference Device (SQUID) magnetometer with magnetic field strength in the range -5 up to 5T. TA Instruments, DMA Q800 is used to obtain dynamic mechanical data for investigated PBMs and pure epoxy samples. These samples are tested using a three-point bend clamp with a 20mm span width and rectangular-edge probe, at a frequency of 1 Hz. Testing is done over a temperature range from 25 to 100°C with a temperature ramp of 3°C/min.

RESULTS AND DISCUSSION

The Nd-Fe-B alloys are brittle, angular plate-like shape particles. The micrographs of three type of Nd-Fe-B alloy are presented in Fig. 1. Process parameters of melt spinning process such as diameter of nozzle, displacement between wheel and nozzle, velocity of wheel, etc. are variable, and have direct impact on particle size and their microstructure [15].

Beside the chemical composition, three used particles have different size and particle distribution. Applying Image Pro Software on micro photos presented in Fig. 1, mean values of characteristic measures of particles are calculated and presented in Table 2.

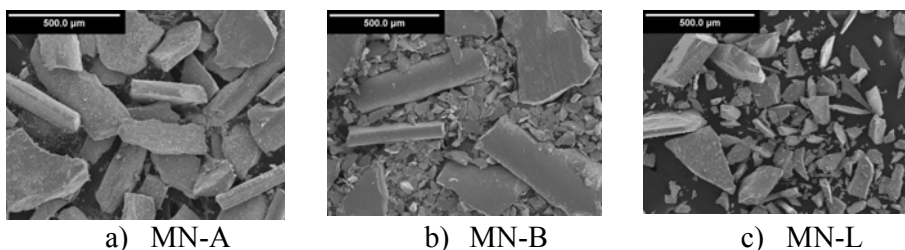


Figure 1. Micrographs of Nd-Fe-B particles with a) low, b) stoichiometric and c) rich Nd content

The results show that Nd-Fe-B alloy with increasing content of Nd is composed by bigger particles which are consequence of selected parameters of production process. Also, Nd content in starting alloy and particle size have direct impact on magnetic properties of magnets.

Table 2. Characteristic dimensions of used particles

Alloy	Area	Diameter (mean)	Roundness	Feret (min)	Feret (max)
MN-A	9316.558	100.6619	1.576581	82.58898983	155.8115
MN-B	2332.202	52.08814	1.517463	43.812839	74.37316
MN-L	1455.101	39.9037	1.573556	32.74556	60.37995

Phase analysis of alloys show mostly expected phases and much lower portion of unexpected phases. The results of XRD and Mossbauer spectroscopy analyses are presented in Table 3.

Table 3. Phase composition (XRD and MS) and relative fractions as taken from MS spectra

	MS				XRD	
	MN-L	MN-B	MN-A	MN-L	MN-B	MN-A
Nd ₂ Fe ₁₄ B	0.38	0.92	0.87	Nd ₂ Fe ₁₄ B	Nd ₂ Fe ₁₄ B	Nd ₂ Fe ₁₄ B
Nd _{1.1} Fe ₄ B ₄	0.04	0.05	0.05	Nd _{1.1} Fe ₄ B ₄	Nd _{1.1} Fe ₄ B ₄	Nd _{1.1} Fe ₄ B ₄
Fe ₃ B	0.58			Fe ₃ B		
Fe(Nd,B)			0.08			
Fe-para		0.03	(<<0.01)		Zr ₃ Fe	Fe ₁₇ Nd ₂

* For simplicity, proportionality between intensity of the Mössbauer lines (spectra) and amount of relevant Fe atoms is supposed.

The results of XRD and MS analysis show that the magnetically hard Nd₂Fe₁₄B phase and small amounts of non-ferromagnetic boride phase Nd_{1.1}Fe₄B₄ are present in all three alloys. The boron content of above 4.2 at% [16] is the main reason for appearance and identification of small amounts of Nd_{1.1}Fe₄B₄ phase. The Nd-Fe-B alloy with low Nd content has multiphase structure with the main hard magnetic phase Nd₂Fe₁₄B and the soft magnetic phases with high magnetization such as Fe₃B. These two phases have main role to forms the exchange coupled nanocomposite structure Fe₃B/Nd₂Fe₁₄B, directly responsible for the remanence enhancement. The alloy with the stoichiometric Nd₂Fe₁₄B content, besides the main hard magnetic phase, contain minor content of other phases like Nd_{1.1}Fe₄B₄, and limited content of paramagnetic iron, probably in a phase with Zr (X-Ray analysis). These phases are probably nanocrystalline and their influence on the magnetic properties is negligible. The small amount of Zr contributes to the further refinement of the hard magnetic grain structure [17] thus promoting the remanence enhancement via the interaction of exchange coupling between the grains. In addition to the dominant amount of hard magnetic Nd₂Fe₁₄B phase determined in the Nd-rich alloy, the Fe₁₇Nd₂ phase is identified. This phase can be understood as a representative of some minor amount of a Fe(Nd) solid solution. In the corresponding Fe (Nd) B Mössbauer component, non-magnetic Nd and B atoms are almost undistinguishable. Surprisingly, no traces of any thermal or other decomposition e.g. presence of α -Fe, Fe₂B phases were found.

The SQUID hysteresis loops of alloys are presented in Fig. 2. For various magnetic alloys corresponds the characteristic shape and area of the loop; for example, for Nd-Fe-B alloy with low Nd content high remanence and low coercivity, and vice versa, for alloy enriched with Nd low remanence and high coercivity. The alloy with stoichiometric Nd content has most

superior maximal magnetic energy $(BH)_{max}$ is often called high remanence and high coercivity magnetic materials. Due to experience, literature data and presented experimental work, this magnetic alloy has proven to be used for further production of polymer bonded magnets (PBM).

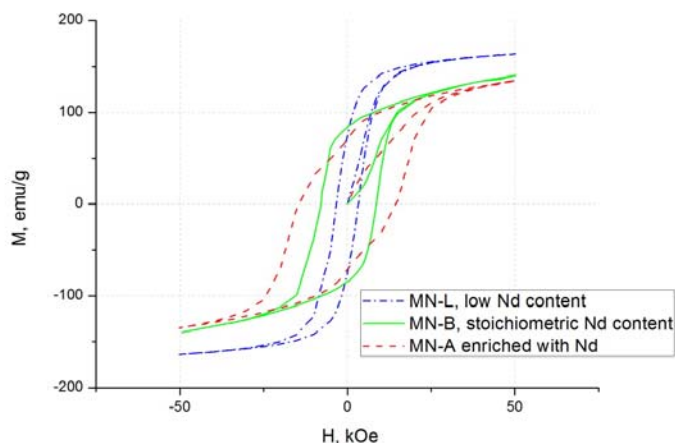


Figure 2. SQUID hysteresis loops of starting Nd-Fe-B alloys

Magnetic properties of PBMs are affected by magnetic properties of used particles and their weight (volume) ratio. It is known that PBMs have inferior magnetic characteristics compared to magnetic material obtained by convectional method (sintering for example), because in bonded technology maximal density of magnetic powder can not be achieved [18]. Magnetic properties of Nd-Fe-B/epoxy resin magnets with various particles content are presented in Fig. 3a.

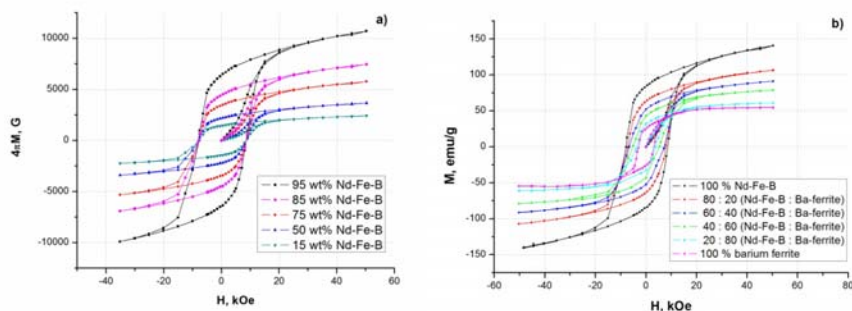


Figure 3. Hysteresis loops of a) PBMs with varous Nd-Fe-B content, and b) hybrid particles

Substituting a part of Nd-Fe-B particles with barium ferrite agglomerates hybrid PBMs are obtained. Hysteresis loops of hybrid magnetic particles are presented in Fig. 3b. The area of presented loops decreases with smaller content of Nd-Fe-B particles. Very important parameter for PBMs application is dynamic mechanical properties. Due to presence of polymer component, thermal stability of composites occurs only at the temperatures below the glass transition temperature T_g (around 50 °C for applied epoxy system).

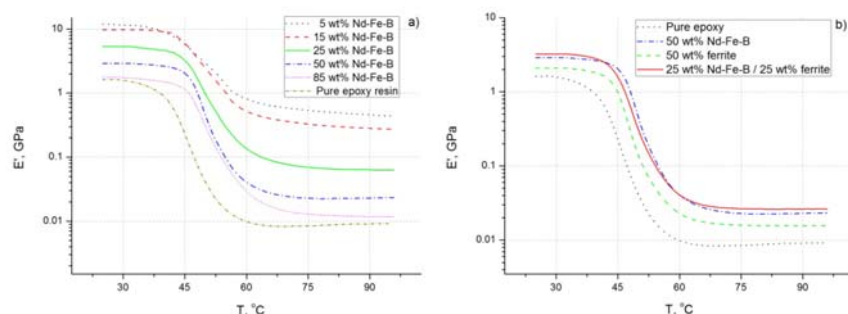


Figure 4. DMA curves for a) Nd-Fe-B/epoxy PBMs with various filler content, and b) Nd-Fe-B/ferrite/epoxy hybrid PBMs

This temperature could be upgraded using different polymer matrices, coupling agents and additives, or using metal matrices. Dynamic mechanical properties of Nd-Fe-B composites in polymer matrix could be improved by using smaller particles or by substitution a part of Nd-Fe-B particles with ferrite particles. Dynamic mechanical properties of Nd-Fe-B/epoxy and Nd-Fe-B/ferrite/epoxy PBMs are presented in Fig. 4. a and b, respectively. DMA curves show expected improving for increasing portion of magnetic particles. Also, for hybrid PBMs, higher value of storage modulus compared with “single” Nd-Fe-B/epoxy and/or barium ferrite/epoxy systems is obvious.

CONCLUSION

Characterization of high energy magnetic materials Nd-Fe-B-type clearly shows differences between three main types of particles with various neodymium contents. Parameters of melt spinning process have strong influence on alloys microstructure. For selected inputs three microstructures are obtained: nanocomposite between soft and hard magnetic phases for alloy with low Nd content; nanocrystalline with high impact of hard magnetic $\text{Nd}_{14}\text{Fe}_{1.1}\text{B}$ phase for alloy with stoichiometric Nd content, and

nanocrystalline structure with isolated $\text{Nd}_2\text{Fe}_{14}\text{B}$ grains with nonmagnetic phases, for alloy enriched with neodymium. According to results of phase composition, microstructure and magnetic properties, alloy with stoichiometric Nd content was selected for polymer bonded magnet production. Different polymer matrices and particles have lead to the projected magnetic and dynamic mechanical properties of PBMs. Composites with higher content of magnetic filler have upgraded magnetic and dynamic mechanical properties. Substituting a part of Nd-Fe-B particles with ferrite agglomerates, hybrid PBMs are obtained and analyzed. In this case, magnetic properties have inferior characteristics, but dynamic mechanical properties are improved. The balance between the magnetic properties and corresponding dynamic mechanical behaviour is an important issue for PBMs applications.

ACKNOWLEDGMENTS

This work has been supported by the Ministry of Science and Technological Development, Republic of Serbia /Projects 34011 & 45019/.

REFERENCES

- [1] H. Kronmüller, R. Fischer, M. Seeger, A. Zern, *J. Phys. D: App. Phys.*, 1996, 29, 2274-2283.
- [2] J.J. Croat, J.F. Herbst, R.W. Lee, F.E. Pinkerton, *J. Appl. Phys.*, 1984, 55, 2078.
- [3] E. Burzo, *Reports on Progress in Physics*, 1998, 61, 1099–1266.
- [4] E.F. Kneller, R. Hawig, *IEEE Trans. Magn.*, 1991, 27 3589.
- [5] T. Schreß, J. Fidler, H. Kronmüller, *J. Magn. Magn. Mater.*, 1994, 138, 291.
- [6] F. Matsumoto, H. Sakamoto, M. Komiya, M. Fujikura, *J. Appl. Phys.*, 1998, 63, 3507
- [7] I. Ahmad, H.A. Davies, R.A. Buckley, *J. Magn. Magn. Mater.*, 1996, 157-158, 31.
- [8] S.C. Wang, Y. Li, *J. Magn. Magn. Mater.*, 2005, 285, 177–182.
- [9] M. Sagawa, S. Fujimura, N. Togawa, H. Yamamoto, Y. Matsuura, *J. Appl. Phys.*, 1984, 55, 2083-2087,
- [10] D.N. Brown, Z. Chen, P. Guschl P, P. Campbell P, *J. Magn. Magn. Mater.*, 2006, 303 (2), e371–e374,
- [11] B.M. Ma, J.W. Herchenroeder, B. Smith, M. Suda, D. Brown, Z. Chen, *J. Magn. Magn. Mater.*, 2002, 239 (1-3), 418-423,
- [12] M.G. Garrell, A.J. Shih, B.M. Ma, E. Lara-Curzio, R.O. Scattergood, *J. Magn. Magn. Mater.*, 2003, 257 (1), 32–43,

- [13] M. Lahelin, I. Aaltio, O. Heczko, O. Söderberg, Y. Ge, B. Löfgren, S.P. Hannula, J. Seppälä, *Compos. Part A-Appl. S.*, 2004, 40 (2), 125–129,
- [14] T. Žák, CONFIT for Windows®95, in *Mössbauer Spectroscopy in Material Science*, M. Miglierini and D. Petridis (eds.), Bratislava, 385, 1999.
- [15] I.B. Kekalo, V.P. Menushenkov, *Rapid Quenched Hard Magnetic Materials Based on Nd-Fe-B*, MISiS, Moscow, 2000.
- [16] R. Coehoorn, D. B. de Mooij, C. de Waard, *J. Magn. Magn. Mater.*, 1989, 80, 101,
- [17] D. Goll, H. Kronmüller, in L. Schultz, K.H. Müller (eds) *Proc. of the 15th International Workshop on REM and Their Applications*, Dresden Werkstoff-Informationsgesellschaft, Frankfurt, 189, 1998.
- [18] X.H. Zhang, W.H. Xiong, Y.F. Li, N. Song, *Mater. Design*, 2009, 30 (4), 1386-1390.

A WAY FOR OPTIMIZATION OF THE NANOSIZE MATERIAL PRODUCTION

M. P. Anisimov

Nanoaerosol Research Laboratory, FSBSI Technological Design Institute of Scientific Instrument Engineering SB RAS (TDISIE SB RAS, anisimovmp@mail.ru), 41 Russkaya Street, 630058, Novosibirsk, Russia

ABSTRACT

The idea of semiempirical design of the nucleation rate surfaces over diagram of phase equilibria is discussed on the example of a simplified system. It is clear that one should develop the idea of semiempirical design considerably to get ability for the broad scientific and practical applications. The well developed data base on the semiempirical design of the nucleation rate surfaces needs to be established. A soft to optimise a technological cycle or scientific research will be developed with time.

INTRODUCTION

The essence of nanotechnology is the ability to work at the atomic, molecular and supramolecular levels, in the length scale of about 1–100 nanometers [1]. Various technologies for nanoclusters production are based on nucleation phenomena. Nanoclusters have vast field of applications like catalysts, coatings, sensors, miniaturizing of electronic components, design of effective medication, detection of gas phase compounds etc. For a reason it can be said that nanoclusters can more and more be considered as the building blocks for future technologies [2]. In material science, physical properties of metals depend on the conditions of crystal growth [3]. Recent findings suggest that homogeneous nucleation is common in the different technologies. Nucleation phenomenon is most commonly described by classical nucleation theory (CNT). While CNT theory predicts reasonable results qualitatively only, it can not be used as a quantitative tool in science and technology. The modern state of theory and experiments on homogeneous nucleation have been reviewed by several researchers, for example, [3-7]. A number of different theoretical alternatives have been proposed. On the other hand, experimental techniques for measuring nucleation rates of simple molecules are very few, but there is no data consistence of a different origin. Promising way to get the common view of nucleation is associated with the idea of semiempirical design of nucleation rate surfaces over the phase equilibria diagrams, which is developed, for example, in article [8].

SEMI-EXPERIMENTAL

The nucleation rate surfaces are arising from lines of phase equilibria [7]. Lines of interface equilibria can be continued through triple point to area of unstable equilibria. One get the multifold nucleation rate surface in that case. Multi-surface nucleation rates can be met more often than we usually think. It should be avoided the interpretation of multi-surface nucleation rate data in the one-surface approximation. That will give more adequate platform for inter-comparison of the experimental results and nucleation theory.

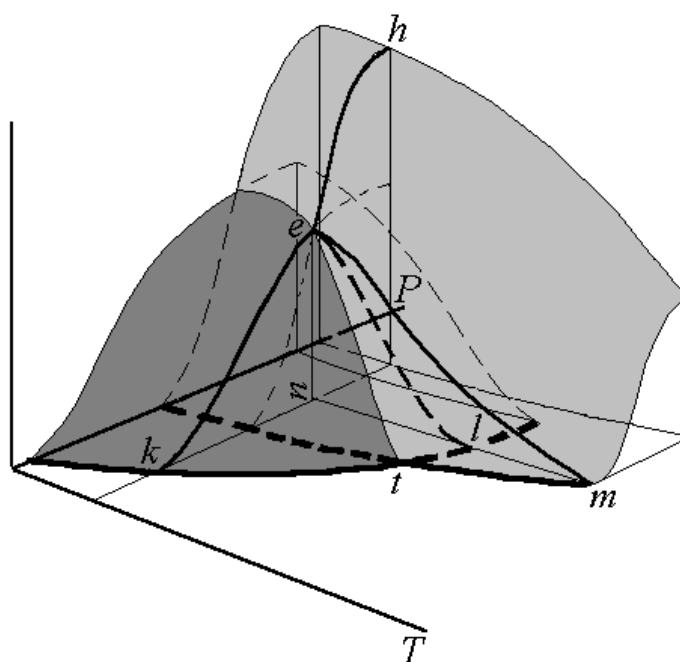


Figure 1. Nucleation rate surfaces over P - T diagram with triple point. Light grey color surface is for droplet nucleation and dark grey one for solid clusters (and their dashed continuations).

The nucleation rate surface can be designed over diagram of phase equilibria [8]. Figure 1 is representing a simplified nucleation rate (J) surface over pressure (P) – temperature (T) diagram with a triple point (t). The main assumptions which are used for design of the surfaces are formulated in article [8]. Let repeat the revised version of these assumptions briefly:

- (1) A single phase can exist beyond its interface equilibrium lines. The line of phase equilibria can exist at the conditions of other phase equilibria as an equilibria line of metastable phases.
- (2) The lines of phase equilibria are representing the zero nucleation rate lines for both phases.
- (3) A spinodal condition nucleation rate is highest one for the given constant pressure or temperature.
- (4) Nucleation rate at spinodal condition is larger for a less ordered phase.
- (5) Nucleation rate is equal to zero at the critical conditions.
- (6) Vapor-gas metastable equilibria have a metastable critical point.

Points (1)-(5) are revised versions of assumptions from [8]. Statement (6) is new. Schreinemakers [9] concluded that a line of phase equilibria pass across nonvariant point at a diagram of phase equilibrium. That phase equilibrium line is divided by that point on the stable and metastable phase equilibria segments. Triple point is nonvariant one. It is well known that vapor-liquid as well as solid-liquid equilibria lines are passing triple point (water, for example). It means that there are no reasons for vapor-solid equilibrium to end at the triple point. From other hand metastable segment of the solid-vapor equilibria temperature rise should be limited somewhere by temperature fluctuations. It looks plausible because even the small superheated states of solid or solid-vapor equilibrium is heavy detectable. That statement needs to be validated by the direct measurements now. We are using a guess that vapor-solid line of phase equilibria passes a triple point and its metastable segment has a metastable critical point.

Let make an imaginable experiment. One can take the saturated vapor at point *m* in Figure 1. The vapor sample can be chilled under the isobaric conditions. A droplet nucleation should be detected along the line *me*, which is resided to the nucleation rate surface (light grey color in Figure 1) for droplet generation. The solid particles appearance can be detected when vapor is reached a supersaturation at point *l*. A solid phase clusters should be generated according line *le*, which belongs to continuation of the dark grey surface in Figure 1. That surface is representing the nucleation rate surface for the solid clusters.

One can see the nucleation rate line, *ke*, (and its dashed continuation) for droplets at constant temperature and line, *eh*, (and its dashed continuation) for solid particles. The topology of the nucleation rate surface and a validity of these lines was proved in a direct experiment [10].

CONCLUSION

Idea of semiempirical design of the nucleation rate surfaces over diagram of phase equilibria was suggested in 1990-th [8]. That idea can be used as supporting technique for the nucleation theory development and for practical using to solve the nucleation problems in the various technologies. Semiempirically designed nucleation rate surfaces are helpful to optimise the broad spectrum of nucleation technologies and nanotechnologies in particular. One can easily find the optimal condition for nanosize material production simply using the view of the nucleation rate surface, which is helpful to find the highest nucleation rate for the given phase state. A simplified phase diagram and the nucleation rate surface was designed over that diagram. One should develop that idea considerably to get ability for the broad practical applications. The well developed data base on the semiempirical design of the nucleation rate surfaces needs to be established.

ACKNOWLEDGEMENT

The research is supported by the Russian Ministry for Science and Education through the grant of RSCF No 14-13-00836.

REFERENCES

- [1] M.C. Roco, *Journal of Nanoparticle Research*, 1999, 1, 435–438.
- [2] G. M. Schmid, M. Bäuml, I. Geerkens, et al., *Chem. Soc. Rev.*, 1999, 28, 179-185.
- [3] D.W. Oxtoby, *J. Phys Condens. Matter*, 1992, 4, 7627-7650.
- [4] R. Jaenicke, *Science*, 2005, 308 (5718), 73.
- [5] A. Laaksonen, V. Talanger, and D.W. Oxtoby, *Ann. Rev. Phys. Chem.*, 1995, 46, 489-524.
- [6] B. Senger, P. Schaaf, D. S. Corti, H. Reiss, et al., *J. Chem. Phys.* 1999, 110, 6421-6437.
- [7] M. P. Anisimov, *Russian Chemical Reviews* 2003, 72(7), 591-628.
- [8] M. P. Anisimov, P. K. Hopke, D.H. Rasmussen et al., *J. Chem. Phys.*, 1998, 109(4), 1435.
- [9] F.A.H. Schreinemakers: *Equilibria in ternary systems*. Carnegie Institution of Washington, 1965
- [10] L. Anisimova, P. K. Hopke, and J. Terry, *J. Chem. Phys.* 2001, 114(22), 9852-9855.

THE $\text{Li}_2\text{FeSiO}_4$ / C COMPOSITES OBTAINED FROM CELLULOSE GEL

M. Milović¹, D. Jugović¹, M. Mitrić², B. Jokić³, R. Dominko⁴ and D. Uskoković¹

¹*Institute of Technical Sciences of SASA, Belgrade, Serbia,*

²*Vinča Institute of Nuclear Sciences, University of Belgrade, Belgrade, Serbia,*

³*Faculty of Technology and Metallurgy, University of Belgrade, Belgrade, Serbia*

⁴*Laboratory for Materials Electrochemistry, National Institute of Chemistry, Ljubljana, Slovenia*

ABSTRACT

In this study, monoclinic polymorph of $\text{Li}_2\text{FeSiO}_4$ (space group $P2_1/n$) in composite with carbon has been synthesized by sol-gel method followed by rapid heating, short high-temperature delay, and subsequent quenching. Three composites were made with 3, 9 and 14 weight percent of the carbon. The effect of the carbon on structure, morphology and electrochemical performance of the prepared composites has been examined by X-ray diffractometry, scanning electron microscopy and galvanostatic cycling.

INTRODUCTION

Recently, an entirely new class of polyoxyanion cathodes based on the lithium transition-metal orthosilicates (Li_2MSiO_4 , $M = \text{Fe}$, Mn , and Co), has been attracting growing interest due to their potentially high theoretical capacities arising from the possibility of the extraction of two Li-ions per formula unit [1]. $\text{Li}_2\text{FeSiO}_4$ takes prominent position among this family of compounds due to its structural stability and natural abundance of iron. Here we report a simple method for the synthesis of $\text{Li}_2\text{FeSiO}_4/\text{C}$ composite based on a sol-gel precursor preparation, followed by short-time, high-temperature treatment. *In situ* created carbon restricts growth of $\text{Li}_2\text{FeSiO}_4$ particles and increases overall conductivity of the composite. In this work we examined how carbon content affects morphology and structure of the obtained powder and how it modifies electrochemical behavior of the $\text{Li}_2\text{FeSiO}_4$ cathode.

EXPERIMENTAL

The synthetic procedure was conducted via two steps. The first is sol-gel precursor preparation starting from Li_2CO_3 , $\text{Fe}(\text{NO}_3)_3 \cdot 9\text{H}_2\text{O}$, $\text{Si}(\text{OC}_2\text{H}_5)_4$ (TEOS) mixed in the molar ratio of 1:1:1:1. Water-soluble methylcellulose was used as a source of carbon. Three samples were synthesized with three different concentration of methylcellulose. The motivation for the sol-gel processing lies in the fact that it provides homogenous mixing of reactants at the molecular level [2]. The second step is calcination of the dried gel precursor. The calcinations were performed at 750°C in slightly reductive atmosphere ($\text{Ar} + 5\%\text{H}_2$). During pyrolytic degradation, methylcellulose decomposes to carbon, creating at the same time more reductive environment that prevents iron oxidation and formation of Fe^{3+} sites. According to mass percentage of carbon, the samples will be noted as LFS_3%C, LFS_9%C and LFS_14%C. X-ray diffraction data were collected on a Philips PW 1050 diffractometer with $\text{Cu-K}\alpha_{1,2}$ radiation (Ni filter) at the room temperature. Measurements were done in 2θ range of 10 - 70° with step size of 0.02° and counting time of 3s per step. The carbon content in the three samples was determined thermogravimetrically to be 3, 9 and 14 mass percent of the carbon. The morphology of the synthesized powders was analyzed by FESEM (TESCAN, MIRA3 XMU) at 20 kV. The particle size analyzer (PSA) Mastersizer 2000 (Malvern Instruments Ltd., UK) was used for the determination of the particle size distribution. Electrochemical measurements were performed at VMP3 potentiostat/galvanostat at 55°C . The cell consisted of two electrodes vacuum-sealed in triplex foil (coffee bag foil). Working electrode was made from synthesized material, carbon black and polyvinylidene fluoride (PVdF, Aldrich) mixed in 75:15:10 weight percent ratio and deposited on Al foil from slurry prepared in N-methyl-2-pyrrolidone. The working electrode and the counter electrode consisting of metallic lithium were separated with a Celgard separator. 1M solution of LiPF_6 (Chemmetall) in EC/DMC (Aldrich) was used as electrolyte. Galvanostatic charge/discharge tests were performed between 2 and 4 V at different current rates.

RESULTS AND DISCUSSION

The XRD patterns of the as-prepared samples are shown in Fig. 1. The crystal system was confirmed to be monoclinic, space group $P2_1/n$. There is no evidence of a crystalline carbon, so internal carbon could be treated as a contribution to the background. The mean crystallite size was calculated using X-ray Line Profile Fitting program (XFIT) based on a fundamental parameters convolution approach to generate line profiles [3]. The mean

crystallite sizes for the three samples are displayed in Table 1. There is noticeable crystallite size decrease when the carbon content increases.

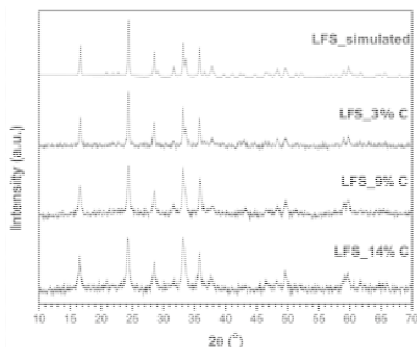


Figure 1. XRD patterns for the obtained samples and pattern simulated in $P2_1/n$.

powders with 14%C and 9%C. The particles are irregular in shape and highly agglomerated. However, the agglomeration is more pronounced in the sample with 9% of carbon. The particle size distribution curves of the powders (Fig. 2 insets) has a lognormal shape with mean particle size of 340 nm for the 14%C sample and 360 nm for the LFS_9%C sample. By comparing mean particle size with the mean crystallite size, it can be concluded that particles are polycrystalline, composed of number of crystallites.

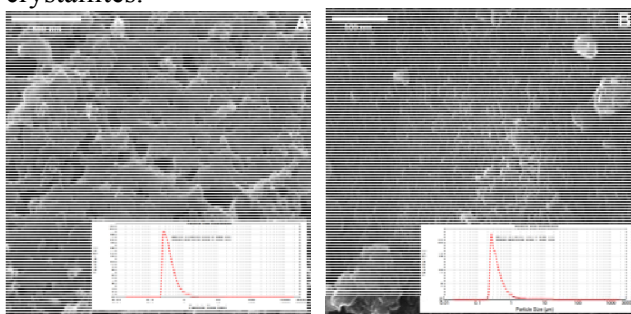


Figure 2. FESEM micrographs of the prepared powders: LFS_9%C (A) and LFS_14%C (B).

Fig. 3 shows the discharge curves and the cycling performance of the $\text{Li}_2\text{FeSiO}_4/\text{C}$ cathodes in the potential range of 2-4 V (vs. Li^+/Li) at current densities of C/10 and 1C. All samples exhibit excellent cycle stability at given voltage range. However, there exists apparent difference in specific capacity achieved between low and high carbon content samples. For the current density of C/10 the samples with 9% and 14% of carbon gave

Table 1. Calculated crystallite size.

Weight percent of carbon (%)	Crystallite size (nm)
3	30
9	18
14	15

The shape and morphology of the particles in $\text{Li}_2\text{FeSiO}_4/\text{C}$ composite samples were followed by electron microscopy measurements. Fig. 2. presents FESEM images for the

similar values of near 100 mAh/g discharge capacity. At the current density of 1C these two samples achieved two times lower but still significant value of ~ 50 mAh/g. This value is comparable with the value given by LFS_3%C sample at ten times lower current density.

As mentioned earlier, *in situ* made carbon prevents agglomeration and restricts $\text{Li}_2\text{FeSiO}_4$ particle growth. Access of lithium into depth of the particle is facilitated for the smaller particles (the diffusion path is shorter) leading to higher specific capacity. On the other hand, high amounts of carbon that surround the particle can block lithium diffusion, which leads to the decrease in the specific capacity. Finally, higher ratio of the carbon vs. active material leads to the decrease in energy density of the composite. Therefore, the optimal concentration of the carbon exists, above which there is no improvement in the electrochemical performance but setbacks can occur.

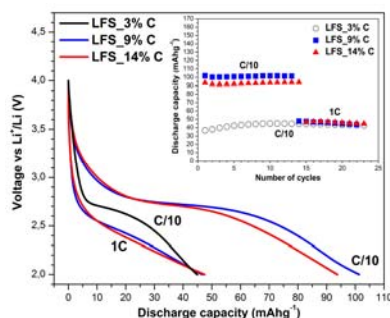


Figure 3. Discharge curves and cycling performance (inset) at C/10 and 1C

CONCLUSION

Monoclinic $\text{Li}_2\text{FeSiO}_4$ that crystallizes in $P2_1/n$ space group was synthesized by means of the sol-gel processing followed by quick solid-state reaction step at 750°C . The content of the *in situ* created carbon was effectively controlled throughout the synthesis procedure. The carbon in $\text{Li}_2\text{FeSiO}_4/\text{C}$ composite has multiple roles of which not all are positive. The effect of carbon on structure, morphology and electrochemistry of the $\text{Li}_2\text{FeSiO}_4$ was examined. The optimal concentration of carbon was found to be near 10% of composite weight.

ACKNOWLEDGEMENT

This work was supported by Grants no. III 45004 and III 45015 of the Ministry of Education, Science and Technological development of the Republic of Serbia and bilateral project no. 651-03-1251/2012-09/05 between the Republic of Slovenia and the Republic of Serbia.

REFERENCES

- [1] M. S. Islam *et al.* J. Mater. Chem. 2011, 21, 9811-9818.
- [2] L. L. Hench, J. K. West, Chem. Rev. 1990, 90, 33-72.
- [3] R. W. Cheary, A. Coelho, J. Appl. Cryst., 1992, 25, 109-121.

THE INFLUENCE OF DIFFERENT OXIDE NANOPARTICLES ON THERMAL CONDUCTIVITY OF NOVEL POLYURETHANE HYBRID MATERIALS

J. Pavličević¹, O. Bera¹, M. Jovičić¹, V. Teofilović¹, B. Pilić¹, M. Špírková²
and J. Budinski-Simendić¹

¹*University of Novi Sad, Faculty of Technology, Serbia*

²*Institute of Macromolecular Chemistry, Academy of Sciences of the Czech Republic, Czech Republic*

ABSTRACT

In this work, a series of polycarbonate-based polyurethane (PC-PU) nanocomposites containing different fillers (Al_2O_3 , TiO_2 or ZnO) were prepared using one-step procedure. The study of the filler influence on thermal conductivity of obtained novel polyurethane hybrids was performed, using proposed approach based on DSC measurements of latent heat of melting. A good accordance between experimental data and calibration curve was distinguished, enabling studying of thermally conductive properties of elastomers. Among of all prepared samples, polycarbonate-based polyurethane nanocomposite with 1 wt. % of TiO_2 filler showed the highest thermal conductivity (λ).

INTRODUCTION

The polyurethane nanocomposites are widely used elastomeric materials for various industrial applications (due to their good dynamic-mechanical, thermally conductive and barrier properties) [1]. Thermally conductive thermoplastics can be used in the electronics, aerospace and energy storage industries [2]. The novel PC-PU nanocomposites are engineering thermoplastics consisting of two phases (hard and soft) on the nanometer scale [3]. The heat transfer phenomenon in polymeric composite materials depends on the filler type and used matrix [4]. Uniform distribution of nanoparticles, their size, shape and surface characteristics are important for improving thermal conductivity of matrix that is accomplished via the flow of lattice vibration energy or phonons in its conductive pathways [5]. This work is focused on determination of thermal conductivity (λ) of prepared PC-PU hybrid materials and studying the influence of different nanoparticles (type and content) on λ value.

EXPERIMENTAL

The novel polyurethane nanocomposites in the form of films were prepared using one-step method in the bulk. During the synthesis, the number of OH groups belonging to polycarbonate diol and butanediol as chain extender was equal and the isocyanate index was kept constant (1.05). The description of the starting

components and detailed procedure are given in our previous paper [6]. Different hydrophilic nanoparticles (Al_2O_3 , TiO_2 and ZnO) were received from Evonik (Germany) and their specification is given in Table 1. The series of PC-PUs with Al_2O_3 or ZnO (0.5, 1, 2 and 3 wt. %) and with TiO_2 (0.5 and 1 wt. %), were obtained. Thermal conductivity of unfilled and filled samples (thickness from 200 to 300 μm) was studied using differential scanning calorimetry (DSC, Q20 TA Instruments), from 30 to 70 $^\circ\text{C}$ at the heating rate of 10 $^\circ\text{C}/\text{min}$. The samples (masses of about 3 mg) were placed directly on thermocouple. According to previous study of thermal properties of PC-PUs, where was no registered phase transition in temperature region below 55 $^\circ\text{C}$ [3], lauric acid was chosen for the calibration procedure due to its melting temperature of 45 $^\circ\text{C}$.

Table 1. The specification (type, commercial name and size) of nanoparticles.

Type of particles	Commercial name by Evonik	Size, nm
Al_2O_3	Aeroxide Alu C	13
TiO_2	Aeroxide PF2	20
ZnO	VP ZnO 20	20

RESULTS AND DISCUSSION

As DSC instrument detects the heat flow change, it is possible to be also used indirectly for obtaining the materials resistance to heat flow conduction. In order to determine the conduction resistance, it is necessary to keep all values in eq. 1 constant except K value (Q , A , ΔT):

$$Q = KA\Delta T \quad (1)$$

where Q is the amount of heat (flux), K is the heat transfer coefficient consisting of all the resistances that occur during heat transfer from the device to the lauric acid, A is the surface of exchange (constant - the bottom surface of DSC pans) and ΔT is the temperature difference.

Keeping the constant mass of lauric acid in DSC pans during the process of calibration, the heat flux was not changed. The surface exchange and dynamic temperature difference were always constant during the same measurements. In this way, it can be concluded that detected latent heat of melting will be only a function of thermal resistance of the material placed between the pan with lauric acid and heating surface of DSC instrument (eq. 2 and eq. 3):

$$Q_d = f(R) \quad (2)$$

$$R = \frac{d}{\lambda} \quad (3)$$

where Q_d is determined latent heat of melting, R is thermal conduction resistance, d is thickness and λ is the coefficient of thermal conductivity of obtained hybrid materials.

By measuring the apparent heat of materials with known thermal conductivity and thickness, (indirectly measuring R value from eq. 3), it is possible to obtain the calibration curve by the method of least squares. The equation 4 (Fig. 1), which parameters are fitted, is obtained from the eq.1:

$$R = \frac{a}{Q_d} - R_t \quad (4)$$

where a is new parameter ($a=A\Delta T$) and R_t is constant heat transfer parameter presenting the sum of the transfer heat resistance from DSC instrument on the material and from material to the DSC pan. The parameters a and R_t are fitted satisfying the limits.

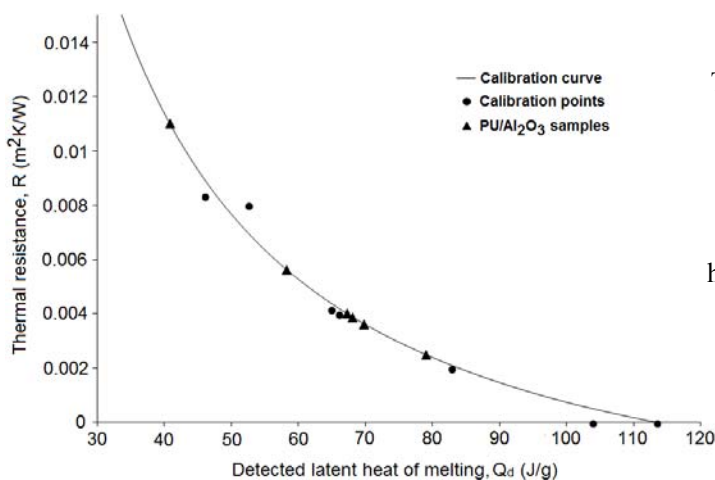


Figure 1.
The dependence of thermal resistance on detected latent heat of melting for PU/Al₂O₃ hybrid materials.

From Fig. 1 it can be noticed that eq. 4 is in a good accordance with the experimental data, with high value of determination coefficient ($R^2= 0.989$), which confirms the validity of the proposed approach. After estimating the thickness, parameters a and R_t , and measuring Q_d , it is possible to determine the thermal conductivity of obtained hybrid materials (eq. 5):

$$\lambda = d / \left(\frac{a}{Q_d} - R_t \right) \quad (5)$$

Thermal conductivity values of hybrids plotted against nanoparticles content are given in Fig. 2, where it can be noticed that 0.5 wt. % of ZnO and TiO₂ significantly increased thermal conductivity of PC-PU hybrids in regard to pure one (0.07 W/mK), while the presence of 0.5 wt. % of Al₂O₃ particles caused the lower λ value. Comparing thermal conductivity of all samples filled with 0.5 wt. % of different particles, the highest one was detected for PC-PU with TiO₂ (0.19 W/mK). PU/ZnO nanocomposite with filler content of 3 wt. % showed the

higher λ value (0.20 W/mK) compared to PU/Al₂O₃ with the same particle content (0.10 W/mK).

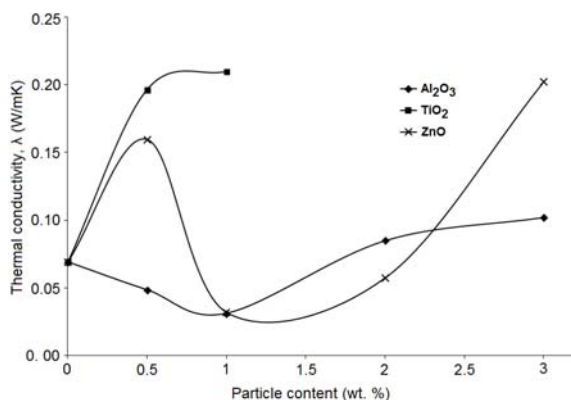


Figure 2.
The dependence of thermal conductivity of PC-PU on different particles.

CONCLUSIONS

PC-PU nanocomposites containing different fillers (Al₂O₃, TiO₂ or ZnO) were obtained by one-step method in bulk. The proposed approach based on DSC data was used to determine the dependence of thermal conductivity of elastomers on the type and content of particles. The highest λ values of all samples filled with 0.5 wt. % of different particles was determined for PC-PU/TiO₂ composite. PC-PU/ZnO hybrid with 3 wt. % of fillers showed the higher λ compared to PC-PU/Al₂O₃ with the same loading (0.20 W/mK).

ACKNOWLEDGEMENT

The work is financially supported by Ministry of Education and Science of the Republic of Serbia (Project No. III45022), Provincial Secretariat of Vojvodina for Science and Technological Development (114-451-2396/2011-01) and Czech Science Foundation (project No. 13-06700S).

REFERENCES

- [1] R. Poreba, M Špírková, L. Brožová, N. Lazić, J. Pavličević, A. Strachota, J. Appl. Polym. Sci., 2013, 127, 329–341.
- [2] S. Agarwal, M. Khan, R. Gupta, Polym. Eng. Sci., 2008, 48, 2474-2481.
- [3] M. Špírková, J. Pavličević, A. Strachota, R. Poreba, O. Bera, L. Kaprálková, J. Baldrian, M. Šlouf, N. Lazić, J. Budinski-Simendić, Eur. Polym. J., 2011, 47, 959-972.
- [4] X. Huang, P. Jiang, and T. Tanaka, IEEE Electr. Insul. M., 2011, 27, 8-16.
- [5] S. Kemaloglu, G. Ozkoc, A. Aytac, Polym. Compos., 2010, 31, 1398-1408.
- [6] J. Pavličević, M. Špírková, O. Bera, M. Jovičić, B. Pilić, S. Baloš, J. Budinski-Simendić, Compos. Part B-Eng., 2014, 60, 673-679.

CRYSTALLIZATION OF THE SILICA FIBERS DURING ITS DRAWING

A.Y. Kulesh¹, M.A. Eronyan², I.K. Meshkovskiy¹,
V. M. Zolotarev¹ and M.V. Tomkovich³

1. *University of Information Technologies, Mechanics, & Optics, Russia,
197101, St. Petersburg, Kronverkskiy av., 49.*

E -mail: parkur89@yandex.ru

2. *Research and Technology Institute of Optical Materials Science, Federal
State Unitary Enterprise, All-Russian Scientific Center "Vavilov State
Optical Institute", Babushkina street, 36/1, St. Petersburg, 192131 Russia.*

E -mail: eronyan@mail.ru.

3. *Ioffe Physical-Technical Institute of the Russian Science Academy,
Russia, 194021,*

St. Petersburg, Politekhnicheskaya street, 26

ABSTRACT

Technological outputs of the fiber silica glass crystallization in course of its drawing-out process have been presented. A calculation method and experimental researches upon the reflection spectra of the fiber and its representation with use of an electronic microscopy reveal presence of *crystalite* phase on the sample surface.

INTRODUCTION

Silica optical fibers have a specific statistical regularity distribution strength magnitude due to the presence of defects on the glass surface. The nature of that regularity is currently not definitively established. Strength of the meter long segments silica 125 microns fibers covered with polymeric cladding is about 6 GPa. At a considerable quantity of tests on the short fiber segments by two-point bending, individual samples showed a high level of strength (about 9 GPa) [1], what is probably due to the absence of defects. Later, when measuring the strength of fine short fibers obtained by this method, excluding crystallization of glass [2], the strength values reached being up to 10 - 26 GPa.

The present work objective is to investigate the silica glass crystallization process during the fiber drawing-out process.

EXPERIMENTAL

Investigations were carried out by means of the numerical and experimental methods.

Crystal layer thickness was evaluated by the calculation methods based on the published data on fiber cooling from 1750 to 1500 °C and a parabolic dependence of the crystal layer growth rate upon the time [3]. Such regularity is caused by the diffusion of oxygen into surface layer of glass.

Experimental study consisted in manufacturing the preform by modified chemical vapor deposition method, and drawing the 125 microns fibers at a speed of 60 and 10 m/min. Heating the preform up to a temperature of 2100 °C has been achieved in the furnace with cylindrical graphite heater where the high temperature zone was purged with high purity argon. The fiber segments of 25 - 30 mm in length did not carry protective polymer cladding and during investigations were not in contact with other objects. Its surface was scanned with use of the electron microscope "Quanta 200" equipped with X-ray microanalyzer. The IR reflection spectra of the densely packed fibers were recorded with use of the Bruker Tensor 27 Instrument. Some of these fibers were etched in a hydrofluoric acid solution during 5 minutes in order to remove the surface layer.

RESULTS AND DISCUSSION

Duration of the fiber stay in the temperature range of cristobalite formation (1750 - 1500 °C) during drawing-out process was calculated by experimental cooling rates [4]. Calculation results on crystallization of the fiber surface indicate the crystalline layer having a thickness about 6 nm. At the same time, studies on the fibers by the electron microscopy, have revealed presence of the irregular particles of 1-15 microns in size. Their size increases with decreasing the drawing-out rate. The X-ray microanalysis results of the particles indicate absence of any impurities.

Comparison of IR reflection spectra of the micron film cristobalite and the surface of the fibers confirms the crystallization of its surface (Fig. 1). Characteristic cristobalite reflection peak at 620 cm^{-1} appears in the not etched fiber IR spectrum, that confirms the anticipated nature of the formation of surface defects in the silica glass crystallization.

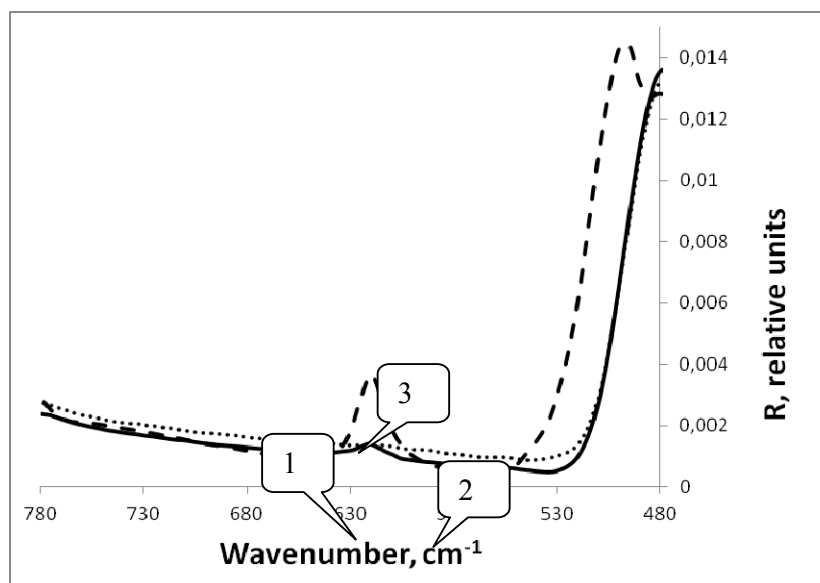


Figure 1. IR reflection spectra of the fiber samples before (1) and after (2) etching and micron α -cristobalite film formation on the surface of pure quartz (3). R – reflectance.

CONCLUSION

So, the investigation results indicate presence of cristobalite particles on the surface of the silica fiber. Statistical distribution of these defects may be an underlying cause, that determines the strength of the fiber.

ACKNOWLEDGEMENT

This work had been done in NRU ITMO and was supported by the Ministry of Education and Science of the Russian Federation under the Project 02.G25.31.0044.

REFERENCES

- [1] M.K. Tsibinogina, A.G. Andreev, V.S. Ermakov, et. al., Proc. VII International Conference "Applied Optics", St. Petersburg, 2006, 56.
- [2] G. Brambilla, D. N. Payne, Nano Lett., 2009. 9, 2, 831-835.
- [3] N.G. Ainslie, C.R. Morelock, D. Turnbull, Symposium on Nucleation and Crystallization in Glasses and Melts. Columbus, 1962, 97-107.
- [4] U. C. Paek, C. R. Kurkjian, J. Amer. Ceram. Soc., 1975, 58, 7-8, 330-335.

STRUCTURAL AND HYPERFINE STUDY OF THE Fe₂O₃/Mg NANOCOMPOSITE

B. Bouzabata, N. Boutabia, A. Djekoun and S. Alleg

Laboratoire de Magnétisme et de Spectroscopie des Solides, Département de Physique, Faculté des Sciences, Université de Annaba. B.P. 12, Annaba 23000, (Algeria), E-mail adress:hbouzabata@yahoo.com

ABSTRACT

In this study, the structural and local Fe environment changes during mechanochemical alloyed Fe₂O₃/Mg powders have been investigated. Milling process was carried during varying times up to 30h with a velocity of 250 rpm. The milled powders were characterized by X-rays diffraction (XRD) and Mössbauer spectrometry (MS). The solid state reaction between α -Fe₂O₃ and Mg starts rapidly. Milling for 1 hour leads to the formation of two bcc-Fe structures (substituted bcc-Fe₁ and pure bcc-Fe₂), magnesium oxide MgO, and a very weak concentration of the spinel MgFe₂O₄ phase in a superparamagnetic state. For higher milling times, it is seen an increase of the concentration of the MgFe₂O₄ and magnetite nanophases .

INTRODUCTION

Recently, there is a significant development in the studies of the nanocomposite alloys. Mechanical alloying can be used to produce this kind of composites [1,2,3]. The reduction of hematite (α -Fe₂O₃) powders by ball-milling has been reported when a mixture of α -Fe₂O₃ and magnesium (hcp-Mg) powders has been milled under argon atmosphere in a planetary ball mill [4] at a very low mill rotation speed of about 160 rpm . This nanocomposite can also be produced directly from milling Fe and MgO [5] or by precipitation method [6] or calcination [7] where it is revealed the formation of the magnesioferrite spinel MgFe₂O₄. The present work examines the process by which the structural changes occur in the mechanically alloyed α -Fe₂O₃/Mg powders mixture with a higher mill rotation speed.

EXPERIMENTS

Mechanical alloying was performed in a planetary ball mill. The starting materials were elemental powders of hematite (α -Fe₂O₃) and magnesium (Mg) enclosed in the vial under argon atmosphere. The ball to powder weight ratio was set to 16:1 and the milling was performed at 250 rpm. The mixture compositions corresponded to the expected stoichiometric chemical reaction that can be induced by the milling processes: α -Fe₂O₃ + 3Mg \rightarrow

$2\text{Fe} + 3\text{MgO}$. Structural changes were studied by X-ray diffraction (XRD) using $\text{K}\alpha(\text{Cu})$ radiation ($\lambda_{\text{Cu}}=1.5406 \text{ \AA}$). The structural and microstructural characteristics were derived from the refinement of X-ray patterns using Maud program [8] based on the Rietveld method [9] and Mössbauer spectra fitted with the least squares MOSFIT program[10].

RESULTS AND DISCUSSION

Structural study

Figure 1. shows the XRD patterns of the powders unmilled and milled from 1h to 30 h. As it is observed, the expected reaction between $\alpha\text{-Fe}_2\text{O}_3$ and Mg starts rapidly.

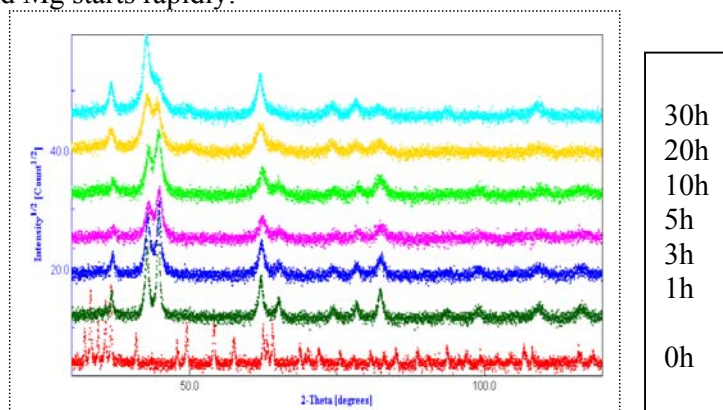


Figure 1: X ray patterns of the $\text{Fe}_2\text{O}_3/\text{Mg}$ powders unmilled (0h) and milled from 1 to 30 hours.

The Rietveld refinement of the XRD pattern milled for 1 hour, given in figure 2, results in the formation of four phases: two bcc-Fe structures (Fe_1 (pure iron) and Fe_2 (a substituted solid solution bcc-Fe(Mg))), magnesium oxide MgO and only about 1%(wt.) of the spinel MgFe_2O_4 ferrite phase. This rapid reaction might be due to the increase of the rotational speed. For high milling times, the formation of magnetite is observed and its increase is due to the expected oxidation of iron. The variations of the relative concentrations of Fe_1 , Fe_2 , MgO, Fe_2O_3 , Fe_3O_4 and MgFe_2O_4 phases as a function of milling times are shown in figure 3. Since the relative concentrations of Fe_2 remains almost constant (around 10%), the formation of the magnesioferrite is produced from the reaction of the Fe_1 with MgO phase. The presence of a small concentration of hematite (about 1.6% at 30 hours) is due to the partial transformation of magnetite under mechanical activation [11].

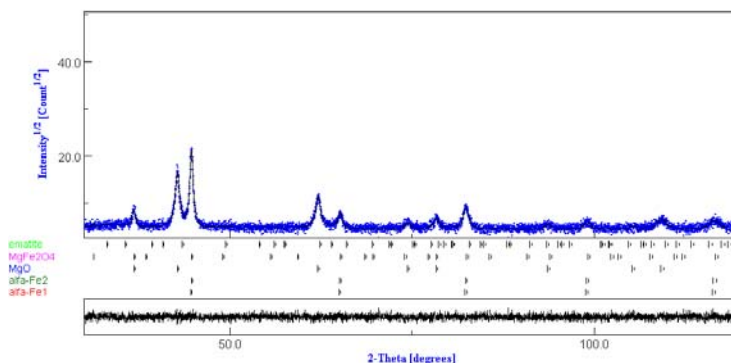


Figure 2 : Rietveld refinement of the XRD pattern of the $\text{Fe}_2\text{O}_3/\text{Mg}$ powder milled for 1h.

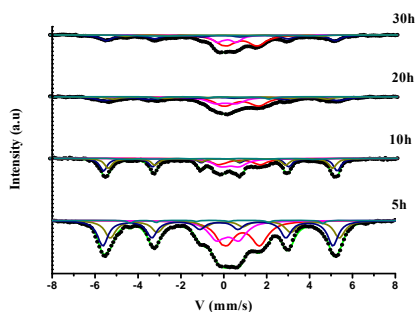


Figure 3. Relative concentrations of phases as a function of milling times

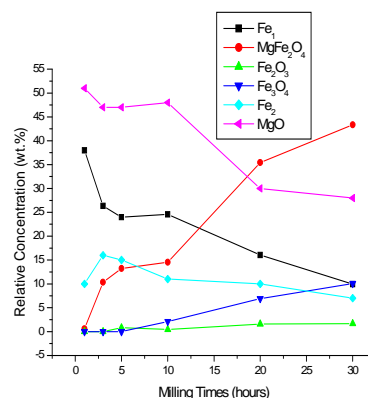


Figure 4. Mössbauer spectra of $\alpha\text{-Fe}_2\text{O}_3/\text{Mg}$ powders milled for 5h, 10h, 20h and 30h.

After 30 h of milling, the final average crystallite size of the two bcc-Fe structure attains 15 and 37 nm respectively for Fe_1 and Fe_2 , while it is about 16 nm and 20 nm for the MgO phase and MgFe_2O_4 respectively.

Hyperfine behavior

Figure 4 displays the room temperature Mössbauer spectra of the $\alpha\text{-Fe}_2\text{O}_3/\text{Mg}$ powders milled for 5, 10, 20 and 30 h that can be computer fitted with 4 components: 2 magnetic sextets (Fe_1 and Fe_2) and two doublets (superparamagnetic spinel ferrite and magnetite phases). The non observation of the hematite might be due to its very weak concentration. As the milling process progresses, one observes that the relative area of the doublets increases at the expense of the magnetic sextets and principally to

the growth of MgFe_2O_4 and magnetite phases. Both have hyperfine parameters with values of $QS1= 1.4 \text{ mm/s}$, $IS1= 0.7 \text{ mm/s}$ and $QS2= 0.8 \text{ mm/s}$, $IS2= 0.14 \text{ mm/s}$ close to the superparamagnetic MgFe_2O_4 [12] and magnetite [13] respectively. Evaluation of relative concentration of all phases from both XRD and Mössbauer spectra show that at 30 h of milling, the final ratio is about 17% for the substituted and pure Fe phase, 28% for the MgO phase, 43% for the superparamagnetic spinel magnesioferrite and probably less than 10% of magnetite.

CONCLUSIONS

Mechanical milling induces a rapid chemical reaction between $\alpha\text{-Fe}_2\text{O}_3$ and Mg. And the high intensity of the deformation processes favors, at low milling times, the formation of a superparamagnetic spinel MgFe_2O_4 with the presence of the substituted Fe (Mg) and magnesium oxide MgO phases. For higher milling times (higher than 10 h), the formation of nano magnetite is obtained from the oxidation of iron phases.

REFERENCES

- [1] Gaffet, E., Abdellaoui, M. and Malhouroux-Gagget, N., *Materials Transactions, JIM*, 1995, 36, (2), 198.
- [2] Schaffer, G. B. and Mc Cormick, P. G., *Materials Science Forum*, 1992, 88–90, 779.
- [3] Gaffet, E., Bernard, F., Niepce, J. C., Charlot, F., Gras, C., Le Caër, G., Guichard, J. L., Delcroix, P., Mocellin, A. and Tillement, O., *Journal of Material Chemistry*, 1999, 9, 305.
- [4] M. Sherif El-Eskandarany, H.N. El-Barhnasawy, H.A. Ahmed, N.A. Eissa, *J. Alloys Comp.*, 2001, 314, 286-295
- [5] S.Mukherjee, S.Kumar and D.Das, *J.Phys.D:Appl.Phys.* 2007, 40, 4425-4430
- [6] A.Azhari, M.Sharif Sh, F.Golestanifard, A.Saberi, *Materials Chemistry and Physics*, 2010, 124, 658-663
- [7] Bahgat M., *Journal of Mineral Processing and Extractive Metallurgy*, Volume 115, Number, 2006, 4, 195-200
- [8] Lutterotti, L. MAUD C.P.D., *News letter (IUCr)*, 2000, 24
- [9] Rietveld, H.M. *J.Appl.Crystallogr.*, 1996, 2, 65.
- [10] Varret, F. Teillet, J. Mosfit program, unpublished, 1976.
- [11] S.J.Steward, R.A.Borzi, E.D.Cabanillas, G.Punte, R.C.Mercader, *J. Magn.Magn.Mater.*, 2003, 260, 447-454
- [12] Mohamed I.M.Omer, A.A.Elbadawi, O.A.Yassin, *Journal of Applied and Industrial Sciences* (2013) 1(4)/20-23,
- [13] D. C. Culita, G. Marinescu, L.Patron, O. Carp, C.B. Cizmas, L. Diamandescu, *Materials Chemistry and Physics*, 2008, Volume 111, 2–3, 381-385.

THERMODYNAMICS AND X-RAY INVESTIGATION OF SOME THORIUM PHOSPHATES AND SILICATES

M.E. Manyakina and A.V. Knyazev

*Chemistry Department, Lobachevsky State University of Nizhni Novgorod
Gagarin Av. 23/2, 603950, Nizhni Novgorod, Russia
(mmanyakina@yandex.ru)*

ABSTRACT

The temperature dependence of heat capacity of $\text{KTh}_2(\text{PO}_4)_3$ has been measured for the first time in the range from 5.5 to 350 K by precision adiabatic vacuum calorimetry. The experimental data were used to calculate standard thermodynamic functions, namely the heat capacity, enthalpy, entropy and Gibbs function for the range from $T \rightarrow 0$ to 350 K. The value of the fractal dimension D in the function of multifractal generalization of Debye's theory of the heat capacity of solids was estimated and the character of heterodynamics of structure was detected. The decomposition and high-temperature phase transitions of some thorium-containing phosphates and silicates studied by differential scanning calorimetry and high-temperature X-ray diffraction.

INTRODUCTION

At the present time, decision radiochemical problems are impossible without fundamental information about the oxygen-containing compounds of thorium. The knowing of dependences "composition-structure-properties" is of great importance. The widespread minerals of thorium are oxide, silicates and phosphates [1-3]. The monoclinic $\text{KTh}_2(\text{PO}_4)_3$ (space group $C2/c$) structure, and the monazite structure, but these two are amongst the most important as they show the widest range of chemical composition. Several stoichiometric composition are known today for thorium-containing silicates: ThSiO_4 (Th : Si = 1 : 1), $\text{MM}'\text{CaTh}(\text{Si}_8\text{O}_{20})$ (Th : Si = 1 : 8), $\text{Ca}_6\text{Th}_4(\text{SiO}_4)_6\text{O}_2$ (Th : Si = 2 : 3), $\text{Na}_{12}\text{Th}_3(\text{Si}_8\text{O}_{19})_4 \cdot 18\text{H}_2\text{O}$ (Th : Si = 3 : 32). Among the mineral containing Th and Si, the most diverse are minerals with the general formula $\text{MM}'\text{CaTh}(\text{Si}_8\text{O}_{20})$ (M - □, Li, Na, K, Rb, Cs; M' - Na, Ca). In ekanite (space group $I422$), the M' positions are occupied by Ca ions. In turkestanite minerals (space group $P4/mcc$), the M positions are occupied by Na and K atoms. The goals of this work include calorimetric determination of the temperature dependences of the heat capacity of $\text{KTh}_2(\text{PO}_4)_3$ from 6 to 330 K, detection of the possible phase

transitions. We also present results of differential scanning calorimetry and high-temperature X-ray diffraction studies in order to obtain information about properties.

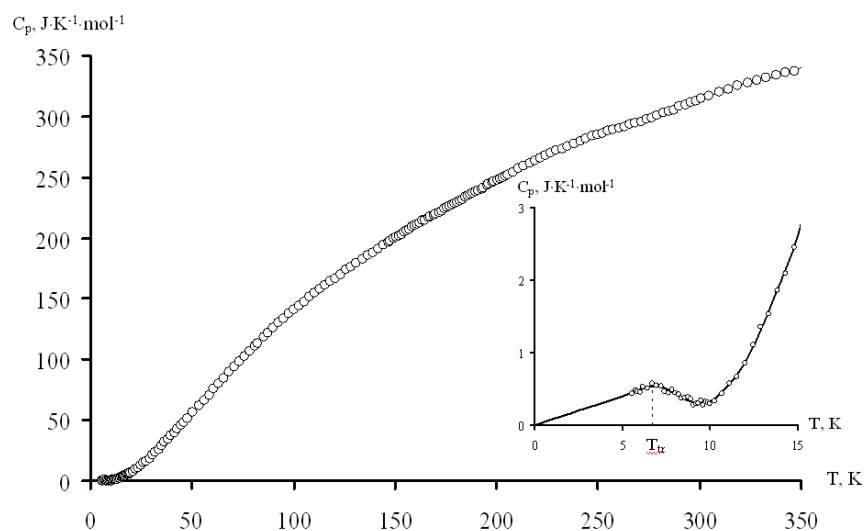
EXPERIMENTAL

The compounds were prepared by the solid-state reactions. For structural investigations, an X-ray diffraction pattern of samples were recorded on a Shimadzu X-ray diffractometer XRD-6000 in the 2θ range from 10° to 120° with scan increment of 0.02° . The high-temperature X-ray diffraction was carried out on a Shimadzu X-ray diffractometer XRD-6000 using Sample Heating Attachment HA-1001. To measure the heat capacity of the tested substances in the range from 5 to 340 K a BKT-3.0 automatic precision adiabatic vacuum calorimeter with discrete heating was used. The calorimeter was tested by measuring the heat capacity of high-purity copper and reference samples of synthetic corundum and K-2 benzoic acid. The analysis of the results showed that measurement error of the heat capacity of the substance at helium temperatures was within $\pm 2\%$, then it decreased to $\pm 0.5\%$ as the temperature was rising to 40 K, and was equal to $\pm 0.2\%$ at $T > 40$ K.

RESULTS AND DISCUSSION

The experimental values of the molar heat capacity of $\text{KTh}_2(\text{PO}_4)_3$ over the range from 5.5 to 350 K and the averaging $C_p = f(T)$ plot are presented in Figure 1. The heat capacity of this substance in interval from 10 to 350 K gradually increases with rising temperature and does not show any peculiarities, but over the range from 5.5 to 10 K there is seen an anomalous heat capacity [4]. The transition temperature of the sample under study $T_{tr} = 6.7 \pm 0.2$ K was estimated as the temperature of maximal C_p value within the temperature interval of the transition. In the literature, there are practically no results of a study of the temperature dependences of the heat capacity of thorium compounds at liquid-helium temperatures. However, it is known that thorium metal is diamagnetic. It becomes superconductor at temperatures below 1.4 K. Perhaps the presence of thorium in a compound contributed to this transition. To calculate the standard thermodynamic functions of the potassium dithorium trisphosphate, its values were extrapolated from the temperature of the measurement beginning at approximately 5.5 K to 0 K by graphic method. The absolute entropies of potassium dithorium trisphosphate and the corresponding simple substances were used to calculate the standard entropy of formation of the compound under study at 298.15 K, $\Delta_f S^\circ(298.15, \text{KTh}_2(\text{PO}_4)_3, \text{cr}) = -1186.3 \pm 1.4 \text{ J}\cdot\text{K}^{-1}$

mol^{-1} . Thermal analysis of the compounds $M_k\text{Th}_{3-k}(\text{PO}_4)_{4-k}$ showed that they are stable up to 1723 K, except for $\text{CsTh}_2(\text{PO}_4)_3$ whose thermogram exhibits an endothermic effect at 1588 K. This compound irreversibly



decomposes without melting.

Figure 1. Temperature dependence of heat capacity of $\text{KTh}_2(\text{PO}_4)_3$.

Table 1. Phase transition and melting temperatures of some thorium phosphates and silicates.

Compound	T_{tr} , K	T_{m} , K
$\text{KTh}_2(\text{PO}_4)_3$	6.7	
$\text{CsTh}_2(\text{PO}_4)_3$		1588
ThSiO_4	1498	
$\text{LiNaCaTh}(\text{Si}_8\text{O}_{20})$		1437*
$\text{Na}_2\text{CaTh}(\text{Si}_8\text{O}_{20})$		1498*
$\text{KNaCaTh}(\text{Si}_8\text{O}_{20})$		1494*
$\text{RbNaCaTh}(\text{Si}_8\text{O}_{20})$		1471*
$\text{CsNaCaTh}(\text{Si}_8\text{O}_{20})$		1537*

* new data

A study of the thermal stability of $MM'\text{CaTh}(\text{Si}_8\text{O}_{20})$ showed that $\text{Ca}_2\text{Th}(\text{Si}_8\text{O}_{20})$ is stable up to 1723 K, whereas turkestanite group compound incongruently melts at 1494 K. The reaction scheme can be presented as follows: $M\text{NaCaTh}(\text{Si}_8\text{O}_{20}) (\text{cr}) \rightarrow \text{ThSiO}_4 (\text{cr}, \text{huttonite}) + \text{SiO}_2(\text{cr}) + 0.5M_2\text{O} \cdot 0.5\text{Na}_2\text{O} \cdot \text{CaO} \cdot 6\text{SiO}_2 (\text{melt})$.

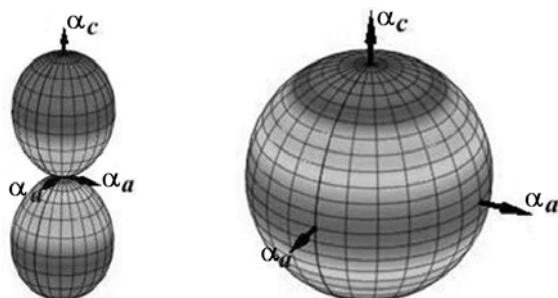


Figure 2.
3D thermal expansion
figures for
 $\text{RbNaCaTh}(\text{Si}_8\text{O}_{20})$ at 298
and 1173 K.

For a more illustrative representation of the information on thermal deformations in the compound, we have developed a visualizer for constructing three-dimensional thermal expansion figures on the basis of the Maple 16 software (Fig.2). A 3D figure is constructed in a spherical coordinate system, whose center is brought in coincidence with a lattice node to demonstrate the possible anisotropy of thermal deformations in different crystallographic directions.

CONCLUSION

Thermodynamic and high-temperature X-ray diffraction studies were performed some thorium-containing phosphates and silicates in a wide temperature range. We have created a visualizer thermal deformation of substances.

ACKNOWLEDGEMENT

The work was performed with the financial support of the Russian Foundation of Basic Research (Project Number 13-03-00152).

REFERENCES

- [1] V. Knyazev, N. G. Chernorukov, A. A. Sazonov, M. E. Komshina, Russian Radiochemistry, 2011, 53, 6, 587–592.
- [2] A.V. Knyazev, N.G. Chernorukov, M.E. Komshina, Russian Radiochemistry, 2012, 54, 5, 431-434.
- [3] A.V. Knyazev, M.E. Komshina, A.V. Zhidkov, A.S. Plesovskikh, Russian Journal of Inorganic Chemistry, 2013, 58, 10, 1172–1176.
- [4] A.V. Knyazev, N.N. Smirnova, M.E. Manyakina, A.N. Shushunov, Thermochemica Acta, 2014, 584, 67-71.

SURFACE MODIFICATION OF ANATASE NANOPARTICLES WITH SUBSTITUTED CATECHOLATE TYPE LIGANDS

T. D. Savić¹, M. I. Čomor¹, V. V. Tešević² and I. A. Janković¹

¹ *University of Belgrade, Vinča Institute of Nuclear Sciences, P.O. Box 522, 11001 Belgrade, Serbia*

² *Faculty of Chemistry, University of Belgrade, Studentski trg 12-16, 11058 Belgrade, Serbia*

ABSTRACT

The surface modification of nanocrystalline TiO₂ particles (45 Å) with catecholate-type ligands having electron donating (4-methylcatechol, 4MetCat) and electron withdrawing (4-nitrocatechol, 4NitCat) substituent groups, was found to alter the optical properties of nanoparticles in a similar way to catechol (Cat). The formation of the inner-sphere charge-transfer (CT) complexes results in a red shift of the semiconductor absorption onset compared to unmodified nanocrystallites, being slightly less pronounced in the case of electron withdrawing substituent. The investigated ligands have the optimal geometry for binding to surface Ti atoms, resulting in ring coordination complexes of catecholate type (binuclear bidentate binding - bridging) thus restoring six-coordinated octahedral geometry of surface Ti atoms. The binding structures were investigated by using FTIR spectroscopy.

INTRODUCTION

Widespread interest in the modification of TiO₂ surfaces with organic and organometallic molecules is largely motivated by the application of these materials in photocatalysis and photovoltaics [1]. Due to its large band gap ($E_g = 3.2$ eV), TiO₂ absorbs less than 5% of the available solar light photons. Sensitization of TiO₂ crystals and nanoparticles with appropriately chosen molecules can indeed lead to a significant red shift of their absorption threshold from the UV to the visible, thus improving the absorption of the solar spectrum as well as the efficiency of photocatalytic and photovoltaic devices. Owing to the large curvature of TiO₂ particles on the nanosize scale, the surface reconstructs in such a manner that distorts the crystalline environment of surface Ti atoms forming coordinatively unsaturated Ti atoms which are very reactive. Absorption of light by the CT complexes formed upon adsorption of modifier ligands onto TiO₂ yields to

the excitation of electrons from the chelating ligand directly into the conduction band of TiO₂ nanocrystallites (DSSC Type II). This results in a red shift of the semiconductor absorption compared to that of unmodified nanocrystallites and enables efficient harvesting of solar photons.

EXPERIMENTAL

The colloidal TiO₂ dispersions were prepared by the dropwise addition of TiCl₄ to cooled water [2]. Surface modification of TiO₂, in methanol/water=90/10 solutions at pH 2, resulting in the formation of CT complexes was achieved by the addition of surface-active ligands up to concentrations required to cover all surface sites. For the determination of CT complex binding constants the absorption spectra were recorded at room temperature using a Thermo Scientific Evolution 600 UV/Vis spectrophotometer. The stoichiometric ratio between Ti_{surf} atoms and modifiers in the CT complexes was checked by Job's method of continuous variation. Infrared spectra were recorded in attenuated total reflection (ATR) mode using a Nicolet 380 FTIR spectrometer equipped with a Smart Orbit™ ATR attachment containing a single reflection diamond crystal.

RESULTS AND DISCUSSION

When TiO₂ particles are on the nanosize scale, a large fraction of the atoms that constitute the nanoparticle is located on the surface, with significantly altered electrochemical properties. Among them, the existing undercoordinated (pentacoordinated, square pyramidal) defect sites are the source of novel, enhanced and selective reactivity of nanoparticles toward bidentate ligand binding. Upon binding, the new hybrid properties arise from the ligand-to-metal CT interaction due to orbital mixing between the molecular orbitals of the ligands and the conduction band orbitals of the nanoparticles. The CT complex formed leads to a shift in the effective band gap of the material to a lower energy i.e. the onset of the absorption of these CT nanocrystallites is red shifted when compared to unmodified TiO₂.

By extracting the corresponding onset energies from the absorption spectra of surface modified TiO₂ nanoparticles (Fig 1), the effective band gap energies ($E = hc/\lambda$) of Cat, 4MetCat and 4NitCat modified TiO₂ nanoparticles were calculated to be 2.1, 2.1 and 2.3 eV, respectively. From the absorption measurements (Benesi-Hildebrand plot), the stability constants were determined to be: 3200 M⁻¹ for Cat, 3200 M⁻¹ for 4MetCat and 2400 M⁻¹ for 4NitCat. Job's plots confirmed that the molar ratio between Ti_{surf} atoms and ligands in the complex is 2:1.

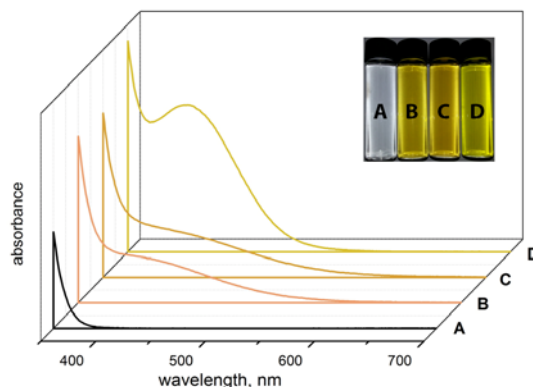


Figure 1. Absorption spectra of surface modified TiO₂: A) bare TiO₂; B) Cat; C) 4MetCat; D) 4NitCat

The ATR-FTIR spectra of Cat, 4MetCat and 4NitCat, free and adsorbed on TiO₂ nanoparticles are presented in Fig. 2. The main bands and their assignments [2, 3] in free modifiers (Fig. 2, upper curves) are as follows: first two bands from the left are bending $\delta(\text{CH})$ vibrations, followed by bending vibrations of the phenolic group $\delta(\text{OH})$ in the 1150 - 1450 cm^{-1} region coupled with the stretching vibrations of the phenolic group $\nu(\text{CO})$ in the 1200 - 1300 cm^{-1} region. The stretching vibrations of the aromatic ring $\nu(\text{C}=\text{C})$ are in the 1450 - 1650 cm^{-1} region. Substituent groups also contribute to the above presented vibration bands: $\delta(\text{CH})$ vibrations in the methyl group of 4MetCat are coupled to all bands in the 1000 - 1450 cm^{-1} region, while in the case of 4NitCat additional vibrations are coupled: $\nu(\text{CN})$ at 1079, 1120 and 1327 cm^{-1} , $\nu(\text{NO}_2)^{\text{sym}}$ at 1327 cm^{-1} and $\nu(\text{NO}_2)^{\text{asym}}$ at 1592 and 1628 cm^{-1} . Upon adsorption of catechol-type ligands onto TiO₂ (Fig. 2, lower curves) the difference between FTIR spectra of free and adsorbed modifiers appears, being most pronounced in the 1000 - 1450 cm^{-1} region, indicating surface complexation with phenolic groups bound to the oxide surface in bidentate form [2]. Bands around 1100 cm^{-1} and in the 1240-1300 cm^{-1} region, could be assigned quite confidently to aryl-oxygen-Ti stretching vibrations $\nu(\text{C}-\text{O}-\text{Ti})$ [4]. The binding of modifiers to TiO₂ via two adjacent phenolic groups even affects the stretching of the aromatic ring $\nu(\text{C}=\text{C})$ and the nitro group $\nu(\text{NO}_2)$ moving them to the lower wavenumbers.

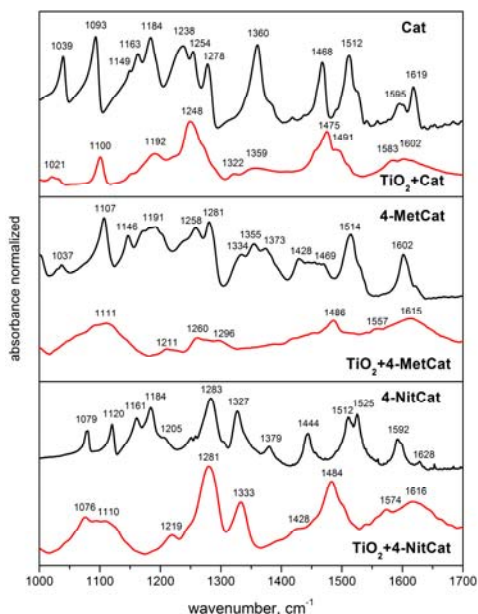


Figure 2. FTIR spectra of free ligands (upper curves) and adsorbed on TiO_2 (lower curves)

CONCLUSION

All investigated ligands (Cat, 4MetCat and 4NitCat) form inner-sphere charge-transfer complexes with TiO_2 nanoparticles ($d = 45 \text{ \AA}$). The binding of the modifier molecules to undercoordinated surface Ti atoms (defect sites) results in a significant shift in the onset of absorption to the visible spectral range. Both substituted modifiers decrease the effective band gap energy of surface modified TiO_2 i.e. less energy is

needed to inject an electron into the conduction band of TiO_2 nanoparticles, the effect being less pronounced in the case of electron-withdrawing group. From the Benesi-Hildebrand plot, the stability constants at pH 2 of the order 10^3 M^{-1} have been determined. The binding structures were investigated by FTIR spectroscopy. According to Job's method of continuous variation binding was found to be through bidentate binuclear (bridging) complexes.

ACKNOWLEDGEMENT

Financial support for this study was granted by the Ministry of Education, Science and Technological Development of the Republic of Serbia (Project 172056 and 45020).

REFERENCES

- [1] W. Macyk, K. Szaciłowski, G. Stochel, M. Buchalska, J. Kunczewicz, P. Łabuz, *Coord. Chem. Rev.*, 2010, 254, 2687-2701.
- [2] T. D. Savić, I. A. Janković, Z. V. Šaponjić, M. I. Čomor, D. Ž. Veljković, S. D. Zarić, J. M. Nedeljković, *Nanoscale*, 2012, 4, 1612–1619.
- [3] G. Socrates, *Infrared and Raman Characteristic Group Frequencies*, 3rd ed., John Wiley & Sons Ltd., England, 2001.
- [4] H. Gulley - Stahl, P. A. Hogan II, W. L. Schmidt, S. J. Wall, A. Buhrlage, H. A. Bullen, *Environ. Sci. Technol.*, 2010, 44, 4116-4121.

MORPHOLOGY TRANSFORMATION INDUCED BY CALCINATION: FROM TITANIA NANOTUBES TO NANOPARTICLES

M. Vranješ¹, Z. V. Šaponjić¹, M. Mitrić¹, B. Jokić² and
M. I. Čomor¹

¹*Vinča Institute of Nuclear Sciences, University of Belgrade, P. O. Box 522,
11001 Belgrade, Serbia*

²*Faculty of Technology and Metallurgy, University of Belgrade,
Karnegijeva 4, 11000 Belgrade, Serbia*

ABSTRACT

Titanium dioxide nanotubes (TNT) synthesized via hydrothermal method and calcined at various temperatures, from 200-800 °C are characterized using X-ray diffraction (XRD), UV/Vis spectroscopy and scanning electron microscopy (FESEM). Tubular structure of as prepared TNT was most probably lost after calcination at 200 °C. Elongated forms of titania with different aspect ratios were observed after calcination at all temperatures lower than 800 °C. Calcination at 800 °C induced complete transformation of TNT to nanoparticles. Shape transformation was accompanied with changes in degree of crystallinity and different anatase to rutile crystal phase ratio.

INTRODUCTION

Nanocrystalline TiO₂ has attracted great interest in last few decades due to their unique properties, crystal structures, morphologies and promising applications in various fields, such as dye sensitized solar cells, photocatalysis, sensing and optoelectronic devices [1]. The TiO₂ is mainly used as photocatalytic material in the processes of water and air purification due to excellent photo and chemical stability, nontoxicity, superior redox ability and low cost [2]. The performances of TiO₂ nanomaterial are highly dependent on its crystal structure, size and shape [3]. Convenient hydrothermal synthetic route applied for synthesis of titania nanotubes (TNT), using highly basic dispersion of TiO₂ nanoparticles as a precursor, was the most commonly applied method in the last decade [4]. These nanotubes were further used as a precursor for synthesis of anisotropic (1D) TiO₂ nanocrystals of different crystalline structures capable of vectorial electron transport necessary for creating efficient photoconversion systems [5]. This paper is mainly devoted to characterization of elongated titania

nanoparticles obtained by calcination of hydrothermally synthesized TNTs, in the range of temperatures from 200 to 800 °C.

EXPERIMENTAL

Chemicals: TiO₂ powder (p.a., Fluka), NaOH (ZorkaPharm), HCl (conc. Aldrich) were used without further purification. Milli-Q deionized water was used as a solvent. Titania nanotubes were synthesized by a hydrothermal treatment (48 h/120 °C) of TiO₂ powder (Fluka) in proton deficient aqueous solution (10 mol/dm³ NaOH) without shaking [3]. After autoclaving in Teflon vessel, the ensuing powder was separated from the solution using centrifuge. The powder was washed once using 1mol/dm³ HCl aqueous solution for 2 h and then several times using pure water until the water reached pH = 7. Synthesized nanotubes were dried at 70 °C. Portions of TNT powder were calcined in an oven, at 200 - 800 °C. The sizes and shapes of the used titania nanoparticles were determined using FESEM TESCAN Mira3 XMU at 20kV instrument. XRD patterns of the TNT were obtained using standard powder diffraction methods with a Philips PW1830 X-ray powder diffractometer using Cu K_α line. UV/Vis spectroscopy was performed using Thermo Scientific Evolution 600 UV-Vis spectrophotometer.

RESULTS AND DISCUSSION

In Figure 1 XRD patterns of as prepared TNT and calcined TNT at different temperatures (TNT – 200 to 800) is presented. Peaks appearing in XRD patterns of as prepared TNT at $2\theta = 25.4, 38, 48.3, 54, 55.2$ and 62.9 deg., can be assigned as anatase TiO₂ crystal planes: 101, 004, 200, 105, 211 and 204, respectively (JCPDS No. 21-1272). The appearance of reflection at $2\theta =$

24.5 deg. suggests existence of monoclinic TiO₂ (B) structure (PDF 74-1940) usually described as built-up from corner- and edge-sharing octahedra, similarly to the anatase titanium dioxide. Also, this peak could be assigned to hydrogen titanate. Both compounds follow anatase structure of nanotubes synthesized using hydrothermal method. The development of the clear anatase crystalline phase with characteristic peaks

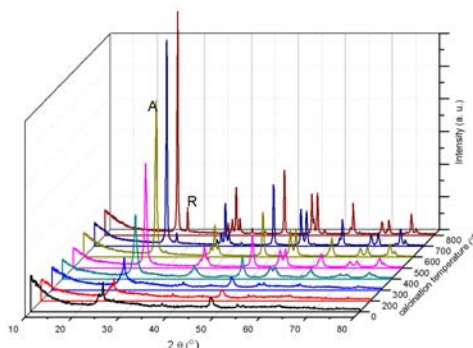


Figure 1 XRD patterns of as prepared and calcined TNT; calcination temperature presented as a z axis.

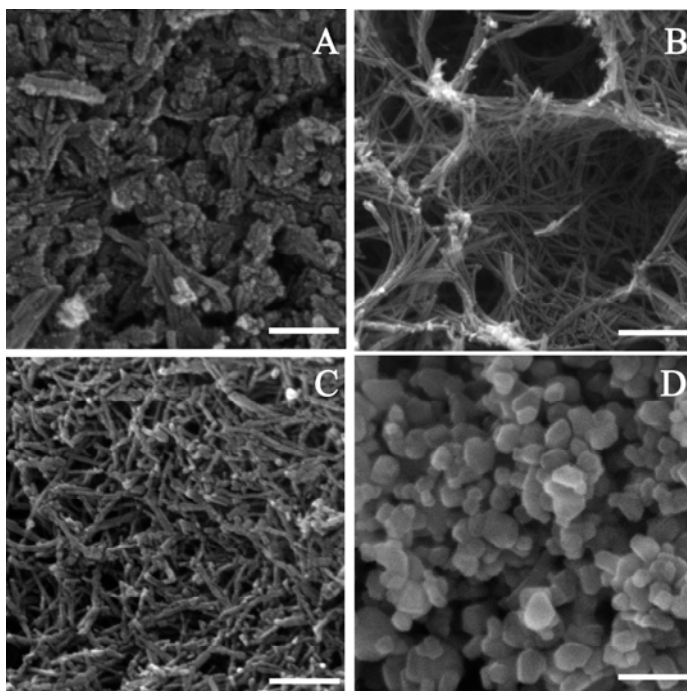


Figure 2 A typical FESEM images of as prepared (A) and calcined TNT samples at different temperatures: (B) 400 °C, (C) 600 °C, (D) 800 °C. Bar is 200 nm.

in XRD patterns at $2\theta = 25.5, 37, 38, 39, 48, 54, 55, 62, 63, 69, 70, 74-76$ deg. (JCPDS No. 21-1272) was observed for all calcined TNT samples. In the XRD pattern of the sample TNT-600, the appearance of the low intensity reflection at $2\theta = 28$ deg. suggested the initiation of the rutile phase formation.

Calcination temperature increase to 700 °C induced

further development of rutile crystalline phase which was confirmed by the increased intensity of the peak at $2\theta = 28$ deg. in the XRD pattern of the sample TNT - 700. In the sample calcined at 800 °C, the crystal phase composition consists of anatase and approximately 10 % of rutile. TEM measurements (not shown) confirmed expected morphology of as prepared TNT according to literature [5]. Reasonably uniform size distribution of tubes with outer diameter of about 10 nm and length that varies was observed. The changes in morphology of as prepared and calcined TNT were analyzed by FESEM, Fig. 2. Typical images of as prepared TNT, TNT- 400, TNT -600 and TNT -800 samples show that their morphology is significantly affected by the calcinations temperature. Until 400°C no significant changes between as prepared (Fig. 2A) and calcined TNT can be seen except loss of tubular structure and formation of wire like structures. The FESEM image of TNT-400, Fig. 2B, reveals pretty much uniform cylindrical morphology of nanocrystals whose diameter is around 13 nm while the length varies until few hundred nanometers. In the morphology of

the sample TNT-600, Fig.2C, cylindrical shape predominate but the average outer diameter is slightly higher, 15 nm, while the length is little bit shorter in comparison to nanocrystals calcined at 400 °C. The morphology of the sample TNT-800 was completely changed in comparison to previously mentioned. Nanoparticles with almost bimodal size distribution of 71 and 91 nm were obtained, Figure 2D. Cylindrical morphology in this sample completely disappeared and also the particles agglomeration increased, according to FESEM image. Despite significant changes in morphology between as prepared and calcined TNT, almost no changes in UV/Vis reflection spectra can be observed. All samples had absorption threshold at about 3.2 eV.

CONCLUSION

Titania nanotubes were successfully synthesized using hydrothermal method. They were used for preparation of different elongated titania nanocrystals by calcination in air. Obtained samples had different shapes, sizes and degree of crystallinity as well as different ratio between anatase/rutile crystalline phases. Anatase phase is dominant in all samples, even ones calcined at higher temperatures (700 – 800 °C), while the rutile phase formation was substantially postponed. Results showed that by increasing calcination temperature the degree of crystallinity also increases while the aspect ratio of titania nanoparticles decreases until almost spherical particles are obtained after calcination at 800°C.

ACKNOWLEDGEMENT

This work was partially supported by the Ministry for Science of the Republic of Serbia (Grants no. 172056 and 45020).

REFERENCES

- [1] X. Chen, S.S. Mao, *Chem. Rev.*, 2007, 107, 2891-2899.
- [2] M.A. Henderson, *Surf. Sci. Rep.*, 2011, 66, 185-297
- [3] CZ. Ding, G.Q. Lu, P.F. Greenfield, *J. Phys. Chem. B*, 2000, 104, 4815-4820.
- [4] T. Kasuga, M. Hiramatsu, A. Hoson, T. Sekino, K. Niihara, *Adv. Mater.*, 1999, 11, 1307-1312.
- [5] K. Kiatkittipong, A. Iwase, J. Scott, R. Amal, *Chem. Eng. Sci.*, 2013, 93, 341–349.
- [6] Z.V. Šaponjić, N.M. Dimitrijević, D.M. Tiede, A.J. Goshe, X. Zuo, L.X. Chen, A.S. Barnard, P. Zapol, L. Curtiss, T. Rajh, *Adv. Mater.*, 2005, 17, 965- 971.

BIOACTIVE PMMA-DOX-GLASS NANOCOMPOSITE FILMS FOR BIOMEDICAL APPLICATIONS

L. Floroian¹, M. Badea², D. Floroian¹ and C. Samoila³

¹*Automation and Information Technology Department, Transilvania University of Brasov, Romania,*

²*Fundamental, Prophylactic and Clinical Specialties Department, Transilvania University of Brasov, Romania,*

³*Materials Science Department, Transilvania University of Brasov, Romania.*

ABSTRACT

We report on the transfer of novel polymer-antibiotic-bioglass composites by matrix assisted pulsed laser evaporation to uniform thin layers onto stainless steel substrate. These coatings for implants merge mechanical advantages of the metallic substrate with the excellent bioactivity of the bioactive glass, corrosion protection of the polymer and antimicrobial effect of the antibiotics. For validate their bioactivity the structures were tested in simulated body fluid solution by Fourier transform infrared spectrometry. When they are in contact with body fluids, the films present the ability to stimulate the growth on their surface of hydroxylapatite, which is predominant mineral component of vertebrate bones. It can be concluded that this composition is suitable to be used as coatings on biological implants.

INTRODUCTION

Due to the fact that many diseases/malfunctions of tissues and organs and other medical conditions cannot be healed or even treated successfully by conventional medical procedures, the field of biomaterials has developed tremendously over the last years. Healthcare consumers nowadays need increasingly more advanced devices for diagnosis and treatment. New materials and innovative procedures and protocols to speed up osseointegration and subsequent bone repair and healing are needed to be developed.

In this study we investigate the possibility of using bioresorbable and bioactive composite made from polymethyl methacrylate (PMMA), doxycycline and bioactive glass BG for implants or prosthesis for bone restoration and dental surgery. These proposed coatings for implants merge mechanical advantages of the metallic substrate with the excellent

bioactivity of the bioactive glass, corrosion protection of the polymer and antimicrobial effect of the antibiotics.

EXPERIMENTAL

In experiments were used bioglasses further denoted BG that contained 56.5% SiO₂, 11% Na₂O, 3% K₂O, 15% CaO, 8.5% MgO, 6% P₂O₅. PMMA was dissolved in chloroform and into this solution was introduced the bioglass and doxycycline. This mixture was frozen and maintained to a constant temperature and it served as targets in thin layer deposition which was made using the matrix assisted pulsed laser evaporation technique (MAPLE).

An excimer laser was used (KrF* at 248 nm) with 25 ns pulse width, at 10 Hz repetition rates, focused to a 16 mm² spot size on the target. The best regime of deposition was identified for the next conditions: 0.55 J/cm² laser fluence, 0.02 torr pressure, 30 °C substrate temperature, 3 cm target-substrate distance and for the deposition of each film we applied 12500 subsequent laser pulses. Once frozen, the MAPLE target is mounted on a cryogenically cooled rotating target holder with the open die end facing the laser. Once the chamber is evacuated, the target is cooled to 100 K temperature.

The obtained films were characterized by Fourier transform infrared spectrometry (FTIR) using a Nicolet 380 apparatus equipped with an orbit ATR (diamond crystal), wavenumber range 7800 – 350 cm⁻¹, spectral resolution 0.4 cm⁻¹, S/N ratio 20000:1. The spectra were taken in the absorbance mode. The bioactivity of the films was assessed in vitro by soaking the composite material films into simulated body fluid (SBF) followed by FTIR spectroscopic analysis to determine the extent of hydroxyapatite formation on the bioactive surface. The SBF was prepared in according to Kokubo prescription [1] and the obtained solution had ionic concentration equal to human plasma.

The disks coated with sintered bioactive films were tested by immersion into 25.0 mL SBF preheated and maintained to 37°C. Tests are conducted after immersion from about 1 day to 2 weeks' immersion.

RESULTS AND DISCUSSION

In the PMMA+Dox+BG initial spectrum the peaks of BG prevail, such as the peaks at 753, 982 and 1008 cm⁻¹, belonging to Si-O bending vibration modes (Figure 1).

After one day's immersion into SBF solution, we can notice the growth of amplitude for all FTIR peaks that indicates the forming of a rich superficial layer, where all elements have a greater concentration. This is consistent

with other experimental observations made for bio glasses [2, 3] and it is accompanied by the loss of soluble silica into the solution, fact emphasized by the depreciation of the surface's quality observed by surface morphology analysis.

After two weeks of immersion, we could notice (Figure 2) the corresponding peaks for hydroxyapatite are well emphasized at 630, 865, 961, 1031 and 1090 cm^{-1} . They correspond to asymmetric stretching of P-O bond in $(\text{PO}_4)^{3-}$ (the peaks from 1031 and 1090 cm^{-1}) and respective symmetric stretching of P-O bond in $(\text{PO}_4)^{3-}$ (the peak from 961 cm^{-1}), to $(\text{HPO}_4)^{2-}$ replacing the $(\text{PO}_4)^{3-}$ - the peak from 865 cm^{-1} and also to the librational mode of OH (the peak from 630 cm^{-1}). At the same time the peaks' proper bioglass disappear.

These certify two things: the dissolution of the bioglass and the existence on the surface of a freshly growing carbonated hydroxyapatite

$\text{Ca}_{8.3}(\text{PO}_4)_{4.3}(\text{HPO}_4, \text{CO}_3)_{1.7}(\text{OH}, \text{CO}_3)_{0.3}$ which is the predominant mineral component of vertebrate bones. The growth of this layer demonstrates the ability of the material to achieve firmly bind to tissues a bioactive fixation through a chemical bond at the bone/implant interface.

This behavior is similar to that reported for bulk glasses in the $\text{SiO}_2\text{-Na}_2\text{O-K}_2\text{O-CaO-MgO-P}_2\text{O}_5$ system, immersed into SBF [4, 5], and it is in accordance with the mechanism of apatite formation described by Hench for bioglasses [3]. However the bioactivity of material is lower than that of pure bioglass BG films [6] where the growing

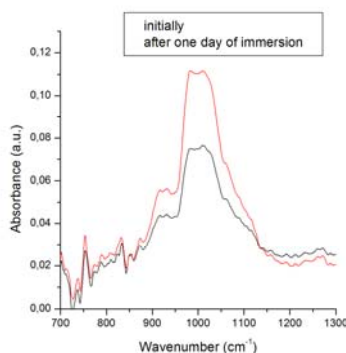


Figure 1. FTIR spectra of PMMA+Dox+BG film after one day of immersion into SBF.

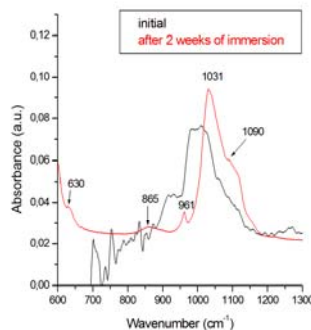


Figure 2. FTIR spectra of PMMA+Dox+BG film after two weeks of immersion into SBF

carbonated hydroxyapatite begins earlier, after few days of immersion. PMMA addition reduces the bone bonding ability of bioactive glasses.

CONCLUSION

We have reported the performance of PMMA-Dox-BG thin films by the matrix assisted pulsed laser evaporation technique, deposition made with preservation of the basic materials stoichiometry.

We have tested the obtained films in simulated body fluid solution and we have validated their bioactivity. When they are in contact with body fluids, the films present the ability to stimulate the growth of hydroxylapatite on their surface.

We can conclude that PMMA-Dox-BG composition is suitable for being used as coatings on biological implants and it allows the stable fixation to bone.

ACKNOWLEDGEMENT

This paper is supported by the Sectoral Operational Programme Human Resources Development (SOP HRD), financed from the European Social Fund and by the Romanian Government under the project number POSDRU/159/1.5/S/134378."

REFERENCES

- [1] T. Kokubo, H. Kushitani, S. Sakka, T. Kitsugi, T. and Yamamuro, J. Biomed. Mater. Res., 1990, 24, 721-734.
- [2] E. Saiz, A.P. Tomsia, A. Pazo, Acta Mater, 1998, 46, 2551-2556.
- [3] L .L. Hench, Bioceramics: from concept to clinic, J. Am. Ceram.Soc., 1991, 74, 1487-1492.
- [4] M. Ogino, F. Ohuchi, L.L. Hench, J Biomed Mater Res, 1980, 15, 55-62.
- [5] R. Hill, J Mater Sci Lett, 1996, 15, 1122-1130.
- [6] L. Floroian, B. Savu, G. Stanciu, A. C. Popescu, F. Sima, I.N. Mihailescu, R. Mustata, L.E.Sima, S.M. Petrescu, D. Tanaskovic, Dj. Janackovic, Applied Surface Science, 2008, 255, 3056-3062.

COMPUTER STUDY OF GRAIN COARSENING DUE TO DIFFUSION WITHIN CAPILLARY LIQUID BRIDGE

Z. S. Nikolic¹ and K. Shinagawa²

¹*University of Niš, Faculty of Electronic Engineering, Serbia*

²*Kagawa University, Faculty of Engineering, Japan*

ABSTRACT

This paper outlines finite element method for simulation of grain coarsening during liquid phase sintering. For the first time coarsening process will be treated within capillary liquid bridge.

INTRODUCTION

When a liquid phase is dispersed between solid grains, the liquid bridges with a curved meniscus shape will form. There are three possible states of liquid bridges between contacting grains: pendular, funicular, and capillary states, which, in order, can be observed for increasing degrees of saturation in a system of three or more solid grains with interstitial liquid phase. For low saturation of the void space (< 25%), small quantity of liquid is distributed as individual liquid bridges between grains forming the cluster of connected grains. This state is called a *pendular* state in which the liquid phase is present under the form of a catenoid meniscus. By increasing the amount of the liquid, the *funicular* state is obtained where both liquid bridges as well as some of the pores filled with liquid are present. The *capillary* state is reached when all voids are completely filled. As a matter of fact, the funicular state characterized by the co-existence of liquid bridges and liquid-filled pores can be treated as the transition state to the capillary state. Note that at least three grains are necessary for the presence of funicular or capillary liquid bridges.

Numerous researchers have studied liquid phase sintering (LPS) during the past few decades. Voorhees *et al.* [1] employed a boundary integral technique to determine the morphological evolution of a small number of particles during Ostwald ripening in two dimensions (2-D). The approach allows the bodies to change shape consistent with interparticle diffusional interactions and the interfacial concentrations as given by the Gibbs-Thomson equation. Recent advances in modeling grain coarsening within pendular liquid bridge using finite element (FE) mesh approach was reported [2, 3].

This paper describes 2-D method for simulation of a moving solid-liquid interface during LPS due to solution, diffusion and precipitation within capillary liquid bridge between three grains of different size. Simulation of the grain coarsening of W-Ni alloy will be demonstrated as a first step.

RESULTS AND DISCUSSION

The main characteristic of the solution-precipitation process is that the smaller solid grains dissolve at solid-liquid interface (thermodynamically unstable), diffuse through the liquid, and precipitate on the larger grains, where the concentration on solid-liquid interface, c , around a grain of radius R is given by the modified Gibbs-Thomson equation

$$\Delta c (\equiv c - c_0) = c_0 \cdot \frac{2\gamma_{SL}\Omega}{kT} \cdot \frac{1}{R}, \quad (1)$$

where c_0 is the equilibrium concentration of liquid in contact with the flat solid, γ_{SL} is the solid-liquid interfacial energy, Ω is the molecular volume of the solid, and kT has its usual meaning.

In FE analysis the 2-D concentration of liquid phase inside an element within liquid bridge can be interpolated from data c_i at three nodal points that define this element, i.e.

$$c(x, y) = [A]\{c_i\} = A_1c_1 + A_2c_2 + A_3c_3, \quad (2)$$

where $[A] = \{A_1 \ A_2 \ A_3\}$ is the shape function.

It can be seen from equation (1) that the concentration at liquid-solid interface with high curvature will be above that at liquid-solid interface with low curvature, thus a higher concentration around a smaller grain gives rise to a net flux of matter from smaller one to larger one. If D_L is the diffusivity of the solid in the liquid, then the flux vector is $\mathbf{q} = -D_L \nabla c$. In 2-D computer simulation the flux components q_x and q_y inside the triangular element can be computed by equation

$$\left. \begin{aligned} [q] &= -D_L [B]\{c\} \\ [q] &= \{q_x \ q_y\}^T, [B] = \{\partial[A]/\partial x \ \partial[A]/\partial y\}^T, \{c\} = \{c_1 \ c_2 \ c_3\}^T \end{aligned} \right\} \quad (3)$$

Applying three-grain model (Fig. 1a) we will simulate grain coarsening during LPS of W-Ni system with liquid nickel as a liquid bridge for data: the composition of the precipitated alloy, 99.55 at.% W, $c_0 = 35$ at.% W,

$\Omega = 9.53 \times 10^{-5} \text{ m}^3/\text{mol}$, $\gamma_{SL} = 0.35 \text{ J/m}^2$, $D_L = 10^{-9} \text{ m}^2/\text{s}$, $T = 1750 \text{ K}$.

For simulation of tungsten grain coarsening we will assume that morphological development on FE mesh (Fig. 1b) is governed by diffusion

through the liquid between grains, so that solid-liquid system is held isothermally and under interfacial equilibrium condition. The coarsening, which occurs by the exchange of solute between solid grains will be simulated so that we will compute first the concentration of liquid phase within liquid bridge and at liquid-solid interface points applying equation (2), then the time-dependent flux applying equation (3) (Fig. 1c) and then the time-dependent mass flow dM/dt at all liquid-solid interface points taking into account dissolution process ($dM(x, y, t)/dt < 0$) or precipitation process ($dM(x, y, t)/dt > 0$).

The time-dependent concentration of liquid phase in contact with the smaller grain is greater than in contact with the larger one. Therefore the smaller one dissolves in the liquid matrix and dissolved atoms flow from the matrix to the larger grain. Pure tungsten dissolved into the liquid, transports through the liquid and precipitates as W(Ni) solid solution (black area in Fig. 1d). It can be also seen that the largest grain undergoing precipitation only, medium grain undergoing dissolution and precipitation and smallest grain undergoing dissolution only.

CONCLUSION

The simulation result of grain coarsening is very similar to the results of Voorhees *et al.* [1], but our approach treats more realistic LPS case with limited amount of liquid in which liquid phase is located within liquid bridges only. Simpler case, grain coarsening within pendular liquid bridge, already reported in [4]. However, grain coarsening within capillary liquid bridge is more complex due to different diffusion field, as well as more complex dissolution and reprecipitation processes. To the best of our knowledge, there is no computer study of grain coarsening within capillary liquid bridge yet.

ACKNOWLEDGEMENT

The first author was performed present study under the project (Grant No. OI172057) supported by the Ministry of Education, Science and Technological Development of the Republic of Serbia.

REFERENCES

- [1] P.W. Voorhees, G.B. McFadden, R.F. Boisvert, D.I. Meiron, *Acta Metall.*, 1988, 36, 1, 207-222.
- [2] Z.S. Nikolic and K. Shinagawa, *Proc. of the 11th International Conference on Fundamental and Applied Aspects of Physical Chemistry - PHYSICAL CHEMISTRY 2012*, 2012, 1, 483-485.

- [3] K. Shinagawa and Z.S. Nikolic, Abstract Book, 25th Fall Meeting, The Ceramic Society of Japan, 2012, Nagoya University, Japan.
[4] B. Randjelovic, K. Shinagawa, Z.S. Nikolic, Science of Sintering, 2013, 45, 261-271.

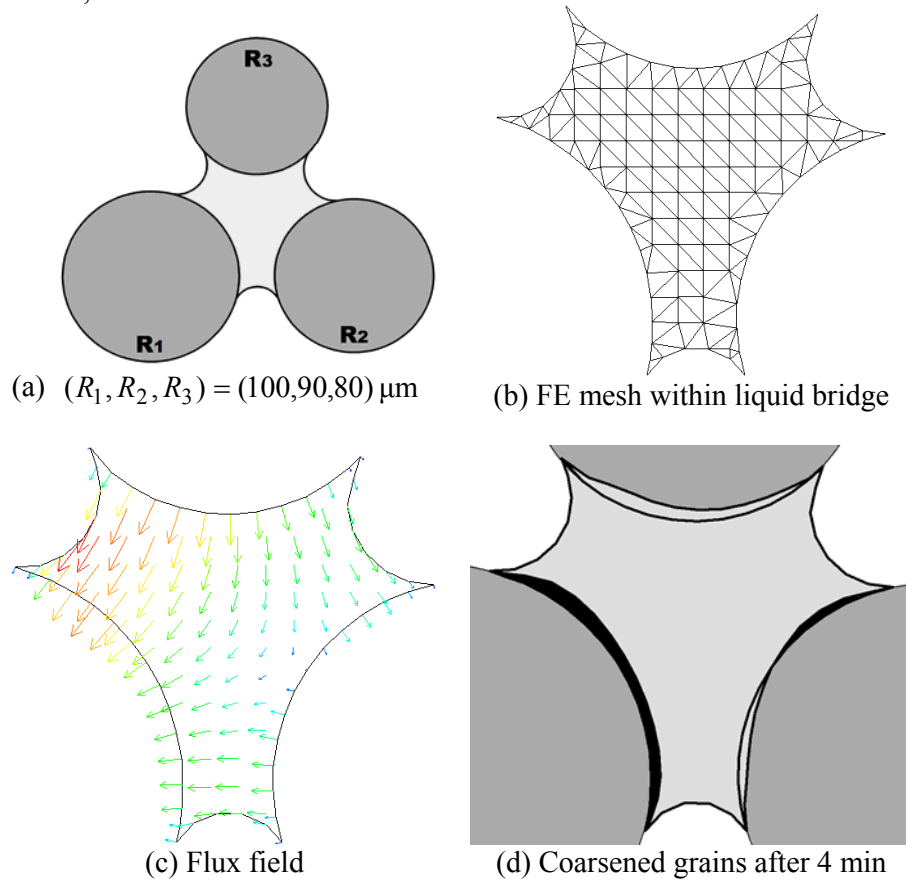


Fig. 1. Simulation of grain coarsening for three grain model.

ALLOY FORMATION BY UNDERPOTENTIAL DEPOSITION OF Mg ON Al FROM NITRATE MELTS

V. S. Cvetković¹, L. J. Bjelica², N. M. Vukićević³ and
J. N. Jovićević¹

¹University of Priština, Faculty of Sciences and Mathematics, K. Mitrovica, Serbia, (chupka976@hotmail.com),

²University of N. Sad, Faculty of Sciences and Mathematics, N. Sad, Serbia,

³University of Beograd, Institute of Chemistry, Technology and Metallurgy, Beograd, Serbia

ABSTRACT

Magnesium has been underpotentially deposited on aluminium electrodes from magnesium nitrate and magnesium nitrate-ammonium nitrate melts at temperatures ranging from 85°C to 200°C. Electrochemical techniques used were cyclic voltammetry and potential step. Deposits were studied by electron microscopy, EDS and XRD. In the magnesium UPD region on Al the processes of nitrate, nitrite and water (when present) reductions take part simultaneously with magnesium UPD. The underpotential deposition of magnesium leads to Al₃Mg₂, Mg₂Al₃ i Al₁₂Mg₁₇ alloys formation.

INTRODUCTION

One of the ways to obtain a metal, and/or an alloy, under very controlled conditions is a direct isothermal electrochemical deposition (electrodeposition). Detailed investigations of the processes involved in electrodeposition of metals and alloys lead to recognition of electrodeposition of metals on foreign substrates at potentials more positive than the equilibrium potential of the depositing metal (the underpotential deposition – UPD) [2]. Most of the initial experimental work was done in aqueous electrolytes until 1980-ties when the same phenomena was observed with aluminium on gold, silver and copper from chloride melts at temperatures bellow 573K [1].

It was soon found that a metal electrodeposited at UPD from aqueous solution, nonaqueous solutions and melts at room temperature onto cathode of a different metal can diffuse into the substrate and make alloys.

However, literature is rather poor in articles describing electrodeposition of magnesium from nitrate melts or magnesium underpotential deposition and alloy formation from nitrate melts is practically nonexistent [3]. One of the main reasons must be the fact that it is impossible to remove water from

magnesium nitrate hexahydrate by heating, because it decomposes before it loses water and transforms into magnesium (II) oxide.

The aim of this work was to establish whether there was an underpotential deposition of magnesium onto aluminium from magnesium nitrate melts, and if there was one does it lead to magnesium/aluminium alloys formation.

EXPERIMENTAL

Experiments were done under 99,99% Ar atmosphere in a electrochemical cell made of Pyrex glass placed in a heating mantle with temperature controlled (electronic thermostat) between 363 and 463K ± 2 K. Working electrode was 3mm thick 99,999% pure Al cylinder; reference electrode was 3mm diameter 99,999% Mg wire in a glass Luggin capillary; and anode was 99,999% magnesium in the shape of a curved rectangular shovel (7,5 cm² active surface area). Temperature in the cell was controlled with a thermocouple (± 3 K). Whole cell set up was placed into transparent plastic "glove box" in order to sustain a moisture free atmosphere around the cell.

The melts used for electrolytes were: Mg(NO₃)₂ x 6H₂O (at 340-400K), eutectic mixture Mg(NO₃)₂ x 6H₂O : NH₄NO₃ x XH₂O = 25 mas.% : 75 mas.% (at 380-450K), nonaqueous Mg(NO₃)₂ (at 440-500K), and nonaqueous eutectic mixture Mg(NO₃)₂ : NH₄NO₃ = 25 mas.% : 75 mas.% (at 390-500K). The procedure for water removal from magnesium nitrate hexahydrate consisted of two steps. First step: the mixture of 5g of magnesium nitrate hexahydrate and 15 cm³ of threemethylorthoformate was brought to boiling and kept for 90 minutes under reflux at 343K. Second step: after 90 minutes of previous treatment the mixture now consisting of an ethyl ester of formic acid, methanol and crystals of nonaqueous magnesium nitrate was submitted to vacuum distillation at 343K. Upon removal of the visible liquid the remaining crystals were vacuum dried for additional 60 minutes. Nonaqueous magnesium nitrate was kept in a closed glass container in a desiccator furnished with plenty of silicagel. Ammonium nitrate hexahydrate was dried for ten hours at 378K. Wanted amounts of magnesium nitrate alone, or mixtures with ammonium nitrate, were placed into the cell supplied with electrodes. Closed cell was then put into the heating mantel, argon supply was turned on and the system was heated gradually to the wanted temperature [4].

Electrochemical techniques used were: cyclic voltammetry and potential step. The potentials of working electrodes were measured in relation to the equilibrium potential of magnesium reference electrode in the melt used under given conditions.

The potential step method included change of the working electrode potential from an initial potential E_f to a potential, E_x (50 to 100 mV more

positive to aluminum equilibrium potential in the given melt). E_x potential was held constant for 120 minutes, whereupon the cathode was retrieved from the cell under the reigning potential in order to preserve deposited material or possible alloys formed during UPD or OPD of aluminum. The electrodes were successively washed with deionized water or absolute ethyl alcohol until visible remains of melt were removed. The surfaces of such electrodes were analyzed by scanning electron microscopy (SEM), energy dispersive spectrometry (EDS) and X-ray diffraction (XRD).

RESULTS AND DISCUSSION

SEM, EDS and XRD analysis of the Al working electrode surface exposed to linear sweep voltammetry as well as potential step regimes in the Mg UPD region (cathodically up to 50 mV vs. Mg) always showed presence of Mg, Al, oxygen and Al/Mg alloys irrespective of the moisture being present in the melt. Comparison of the EDS and XRD results obtained from

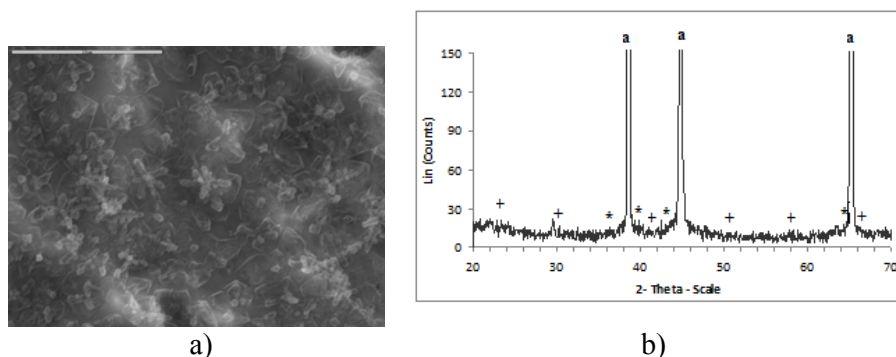


Figure 1. SEM and XRD data for the surface of the Al electrode after 120 minutes holding at the potential of $E_x = 0,050$ V vs. Mg in: a) $\text{Mg}(\text{NO}_3)_2 \times 6\text{H}_2\text{O}$ melt, $T = 370\text{K}$, mag. 5000x; b) in $\text{Mg}(\text{NO}_3)_2 \times 6 \text{H}_2\text{O}$ melt, $T = 380\text{K}$; (a) - (p c k) aluminium; (*) - Centered cubic $\text{Al}_{12}\text{Mg}_{17}$; (+) monoclinic $\text{Mg}(\text{NO}_3)_2 \times (\text{H}_2\text{O})_2$ [4].

Al electrodes exposed to the potentials between Al reversible potential and 50 mV vs. Mg at temperatures below 500 K strongly suggest magnesium UPD accompanied by substrate alloying with deposited magnesium, Fig. 1. The alloys identified by XRD analysis formed at the Mg UPD on Al characteristic for each of the melts used are shown in Table 1.

Table 1. The alloys formed at the Mg UPD on Al from nitrate melts

Melt	Substrate	Alloy 1	Alloy 2
1. $\text{Mg}(\text{NO}_3)_2 \times 6\text{H}_2\text{O}$	Al	$\text{Al}_{12}\text{Mg}_{17}$	
2. $\text{Mg}(\text{NO}_3)_2$	Al	$\text{Al}_{12}\text{Mg}_{17}$	Al_3Mg_2
3. $\text{Mg}(\text{NO}_3)_2 \times 6\text{H}_2\text{O} + \text{NH}_4\text{NO}_3 \times \text{XH}_2\text{O}$	Al	Al_2Mg	Mg_2Al_3
4. $\text{Mg}(\text{NO}_3)_2 + \text{NH}_4\text{NO}_3$	Al	$\text{Al}_{12}\text{Mg}_{17}$	Mg_2Al_3

CONCLUSION

Kolb-Przasnyski-Gerischer [2] propose an magnesium underpotential deposition on aluminum at potentials close to 0,1 V vs.Mg, because the half work functions difference in the case of Al and Mg is 0,20 to 0,30 eV.

However, this rule does not predict whether there are going to be alloys formed between the substrate metal and underpotentially deposited metal. And yet, the most pronounced effects of the magnesium underpotential deposition from magnesium nitrate melts onto aluminium substrate found were three alloys formed with the substrate Al. All the alloys obtained were formed at the potentials 50 to 100 mV positive to Mg reversible potential and at the temperatures several hundred Kelvin degrees lower than the temperatures which are, according to the phase diagrams, needed for their formation thermally. The alloys formed were $\text{Al}_{12}\text{Mg}_{17}$, Al_2Mg and Mg_2Al_3 .

ACKNOWLEDGEMENT

This work was partially supported by the Ministry of Education, Science and Technology of the Republic of Serbia (Grant OI 176018).

REFERENCES

- [1] G.L. Stafford, C.L. Hussey, Advances in electrochemical science and engineering, Vol. 7, Eds., Alkire, R.C., Kolb, D.M., Wiley-VCH, Verlag GmbH, Weinheim 2002, 275.
- [2] D.M. Kolb, M. Przasnyski, H.Gerischer, J. Electroanal. Chem., 1974, 54, 25-38.
- [3] D.A.Tkalenko, Makrokinetika katodnykh protsessov v gidroksi dnykh i nitratnykh rasplavakh, Naukova Dumka, Kiev 1993.
- [4] V. S. Cvetković, „Elektrohemijsko taloženje magnezijuma pri podpotencijalima iz rastopa nitrata“, Zadužbina Andrejević – PMF K. Mitrovica, Beograd, 2012.

FERROMAGNETIC RESPONSE OF NANOCOMPOSITES BASED ON POLYANILINE AND TiO₂ NANOCRYSTALS OF DIFFERENT SHAPE

M. Radoičić¹, Z. Šaponjić¹, Z. Konstantinović² and G. Ćirić-Marjanović³

¹*Vinča Institute of Nuclear Sciences, University of Belgrade,
Belgrade 11001, Serbia*

²*Institut de Ciencia de Materials de Barcelona, CSIC, Bellaterra,
08193 Barcelona, Spain*

³*Faculty of Physical Chemistry, University of Belgrade, Belgrade 11158,
Serbia*

ABSTRACT

Ferromagnetic polyaniline (PANI)/TiO₂ nanocomposites were synthesized by the oxidative polymerization of aniline with ammonium peroxydisulfate (APS), in the presence of colloidal TiO₂ nanoparticles and TiO₂ nanotubes, without added acid. The morphological, magnetic and structural properties of the PANI/TiO₂ nanocomposites were studied by SEM microscopy, SQUID magnetometer and FTIR spectroscopy. The electrical conductivity of synthesized nanocomposites was $\sim 10^{-3} \text{ Scm}^{-1}$. The room temperature ferromagnetic response significantly depends on shape of TiO₂ nanoparticles.

INTRODUCTION

Polyaniline (PANI) is one of the most important conducting polymers, due to its simple synthesis, unique doping/dedoping chemistry, low cost, high conductivity, and excellent environmental stability [1]. The crystallinity, solubility, thermal stability, electrical, magnetic and optical properties of PANI mainly depend on its oxidation state and protonation degree [2]. Depending on synthetic and isolation procedure, polyaniline contains various proportions of diamagnetic $[(-\text{B}-\text{NH}^+-\text{Q}-\text{NH}^+)_n(-\text{B}-\text{NH}-)_{2n}](\text{A}^-)_{2n}$ and paramagnetic units $[(-\text{B}-\text{NH}^+-\text{B}-\text{NH}-)_n](\text{A}^-)_n$, where B, Q and A⁻ denote a benzenoid ring, quinonoid ring and dopant anion, respectively. Magnetic properties of PANI and its derivatives have been extensively studied because they can provide important data on charge-carrying species and unpaired spins. It has been found that the magnetic susceptibility of doped PANI is strongly influenced by the manner of polymer preparation (e.g., doping level, dopant type), and measuring conditions (temperature, applied magnetic field) [3]. Although a numerous

studies on magnetic properties of PANI are published just a few of them reported on ferromagnetic behavior [4]. In this work, conducting PANI/TiO₂ nanocomposites have been prepared by the chemical oxidative polymerization of aniline in aqueous dispersions of TiO₂ nanoparticles and nanotubes, without added acid. Synthesized PANI/TiO₂ nanocomposites were studied by SEM analysis, FTIR spectroscopy and electrical conductivity measurements. In order to investigate the influence of the shape of TiO₂ nanoparticles on ferromagnetic response of PANI, magnetic susceptibility measurements were performed at room temperature.

EXPERIMENTAL

The colloidal dispersion of TiO₂ nanoparticles ($d \approx 4.5$ nm) was prepared by acid hydrolysis of TiCl₄ [5]. Titania nanotubes (outer and inner diameters 10 and 7 nm and length of few 100 nm) were synthesized by a hydrothermal process in alkaline medium [6]. PANI/TiO₂ nanocomposites were prepared by following procedures: the aqueous solution of APS (0.4 M, 25 ml) was poured into the aqueous solution of aniline (0.32 M, 25 ml). Thereupon dispersion of TiO₂ colloidal nanoparticles/nanotubes in water (50 ml) was added into the aniline/APS solutions. The reaction mixture was stirred for 3 h at room temperature. The precipitated PANI/TiO₂ nanocomposite was collected on a filter, rinsed with ethanol acidified with sulfuric acid (5×10^{-3} M), and dried in vacuum at 60 °C for 3 h. The mole ratios of aniline to TiO₂ nanoparticles and nanotubes were 80, (PT-80 and PT-NT-80). As a reference, the pure PANI sample was prepared by the same procedure.

RESULTS AND DISCUSSION

The changes in the morphology of the synthesized nanocomposites by varying a shape of TiO₂ nanoparticles are studied by SEM microscopy (Figure 1). The morphology of the nanocomposite samples (PT-80 and PT-NT-80) is significantly different compared to the morphology of pure PANI sample. Nanoribbons, as well as nanorods/tubes predominate in the non-uniform morphology of pure PANI sample. Incorporation of colloidal TiO₂ nanoparticles, as well as TiO₂ nanotubes caused predomination of nanotubular morphology in PANI/TiO₂ nanocomposite samples, while nanoribbons are not observed (Figure 1). PANI nanotubes have an outer diameter of 60–150 nm and a length up to few micrometers.

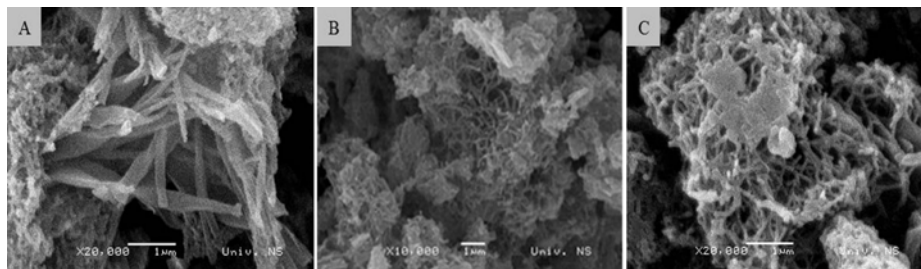


Figure 1. SEM images of the pure PANI (A) and PANI-TiO₂ nanocomposites PT-80 (B) and PT-NT-80 (C).

In the FTIR spectrum of PANI/TiO₂ nanocomposite, characteristic bands of PANI were observed at wavenumbers 1569, 1497, 1305, 1246, 1146 and 825 cm⁻¹ indicating the presence of emeraldine salt form of PANI chains in PANI and PANI/TiO₂ nanocomposites. Weak bands at 1635 and 1400 cm⁻¹ observed in the FTIR spectra of pure PANI and all nanocomposites can be attributed to the substituted phenazine-like units which are responsible for formation of polyaniline nanostructures.

The conductivity of both PANI-TiO₂ nanocomposites was $\sim 2.0 \times 10^{-3}$ S cm⁻¹, which is twice the conductivity of a pure PANI (9.1×10^{-4} S cm⁻¹) synthesized under the same conditions, without added TiO₂.

The field dependence magnetization after diamagnetic correction is shown in Figure 2. At room temperature, the weak ferromagnetic behavior can be observed in all samples. Pure PANI and PT-80 samples showed hysteresis loop with the coercive field of $H_c = 300$ Oe, remanent magnetization of $M_r = 4.35 \times 10^{-4}$ emu g⁻¹ and the saturation magnetization of

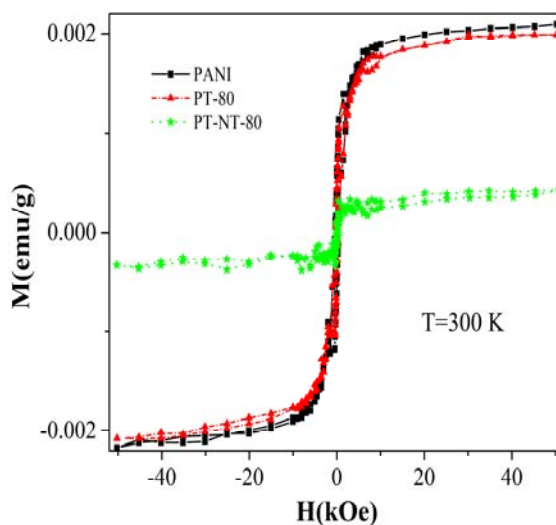


Figure 2. The magnetic field dependence of magnetization after diamagnetic correction at 300 K for the pure PANI and PANI/TiO₂ nanocomposite samples (PT-80 and PT-NT-80).

about $M_s=2 \times 10^{-3}$ emu g^{-1} . In comparison to pure PANI and PT-80 samples, PT-NT-80 nanocomposite sample exhibit much weaker ferromagnetic ordering. Saturation magnetization was approximately $M_s=2.5 \times 10^{-4}$ emu g^{-1} . The presence of TiO_2 nanotubes in PANI-based nanocomposite reduced several times the saturation magnetization value. Such behavior could be the consequence of the increased spin disordering as well as the reduction of the total number of magnetic moments. The reason for decrease of ferromagnetism in PT-NT-80 nanocomposite sample is conversion of single-charged polarons into double-charged bipolarons ($S=0$) induced by the presence of TiO_2 nanotubes.

CONCLUSION

PANI/ TiO_2 nanocomposites were successfully synthesized through the oxidative polymerization of aniline with ammonium peroxydisulfate in aqueous dispersions of TiO_2 nanoparticles and TiO_2 nanotubes, without added acid. FTIR measurements confirmed presence of conductive emeraldine salt form of PANI in all synthesized samples. Incorporation of TiO_2 nanoparticles and nanotubes caused significant changes in morphology and conductivity of nanocomposites compared to pure PANI. Much weaker ferromagnetic ordering in PANI/ TiO_2 nanocomposites which contains TiO_2 nanotubes is due to the presence of higher amount of double-charged bipolarons ($S=0$).

ACKNOWLEDGEMENT

This work was supported by the Ministry of Education, Science and Technological Development of the Republic of Serbia (Grants no. 172056 and 45020).

REFERENCES

- [1] K. Lee, S. Cho, S.H. Park, A.J. Heeger, C.-W. Lee, S.-H. Lee, *Nature*, 2006, 44, 65.
- [2] J. Stejskal, P. Kratochvíl, A.D. Jenkins, *Polymer*, 1996, 37, 367
- [3] Y. Long, Z. Chen, J. Shen, Z. Zhang, L. Zhang, H. Xiao, M. Wan, and J.L. Duvail, *J. Phys. Chem. B*, 2006, 110, 23228.
- [4] Y. Zhang, C. Zhu, and J. Kan, *J. Appl. Polym. Sci.*, 2008, 109, 3024.
- [5] T. Rajh, D. Tiede, M. Thurnauer, *J. Non-Cryst. Solids*, 1996, 207, 815.
- [6] Z.Šaponjić, N. Dimitrijević, D. Tiede, A. Goshe, X. Zuo, L.X. Chen, A.S. Barnard, P. Zapol, L. Curtiss L, T. Rajh, *Adv. Mater.*, 2005, 17, 965.

ROOM TEMPERATURE FERROMAGNETISM IN Cu^{2+} DOPED TiO_2 NANOCRYSTALS

M. Vranješ¹, J. K. Jakovljević¹, Z. Konstantinović², T. Radetić³, M. Stoiljković¹ and Z. Šaponjić¹

¹*Vinča Institute of Nuclear Sciences, University of Belgrade, P. O. Box 522, 11001 Belgrade, Serbia*

²*Institut de Ciència de Materials de Barcelona, CSIC, Campus UAB, 08193 Bellaterra, Spain*

³*Faculty of Technology and Metallurgy, University of Belgrade, Karnegijeva 4, 11120 Belgrade, Serbia*

ABSTRACT

Hydrothermal synthesis of Cu^{2+} doped TiO_2 nanocrystals, using dispersion of titania nanotubes in the presence of Cu^{2+} ions as precursor, which showed room temperature ferromagnetism, is reported. Morphology of Cu^{2+} doped TiO_2 nanocrystals was characterized by transmission electron microscopy (TEM). An average size of polygonal nanocrystals mainly of square/rectangular shape was around 13 nm. The x-ray powder diffraction (XRPD) analysis of resultant powder confirmed the anatase crystal phase of Cu^{2+} doped TiO_2 nanocrystals. Room temperature ferromagnetic ordering with saturation magnetic moment of the order of $2 \times 10^{-2} \mu_B$ per Cu atom was observed.

INTRODUCTION

Great practical motivation for exploring doped semiconductors lies in the possibility of combining their semiconductor characteristics with magnetic properties. Diluted magnetic impurities in semiconductors produces materials that show ferromagnetic ordering at room temperature and therefore are appealing for spintronics in which simultaneous control of charge currents and spin polarized currents will be possible. Progress in the field of diluted magnetic semiconductors (DMS) has revealed a numerous new physical phenomena, including spin coherence, a new ferromagnetism and spin-polarized photoluminescence [1,2]. Wide band metal oxide semiconductors (TiO_2 , ZnO) doped with Co, Cu and Ni [3-6] presents the class of diluted magnetic semiconductors that has been identified by theoretical considerations and proved as a good candidate for achieving room temperature ferromagnetism. In this paper we report on new synthetic procedure, structural and magnetic properties of Cu^{2+} doped TiO_2

nanocrystals. Using as a precursor titania nanotubes instead of molecular precursors we eliminated driving force problem that arises from the increase in the activation energy for nanocrystal nucleation in the presence of the dopant ions and consequent exclusion of the Cu^{2+} ions during nanocrystal growth.

EXPERIMENTAL

All chemicals were reagent-grade from Aldrich and used as received. Titania nanotubes were synthesized according to Kasuga et al. [7], using TiO_2 powder as a precursor. Cu^{2+} doped TiO_2 nanocrystals were synthesized using hydrothermal treatment (250 °C / 90 min) of a dispersion containing titania nanotubes (125 mg/50 ml) at pH=3 in the presence of $3,11 \times 10^{-4}$ M $\text{Cu}(\text{NO}_3)_2$. In order to remove the excess of Cu^{2+} ions the dispersion of Cu^{2+} doped TiO_2 nanocrystals was dialyzed against acidified water (pH=3) at 4 °C for 3 days. Water was changed daily. Films for magnetic characterization were prepared by drop casting of dialyzed dispersions of Cu^{2+} doped TiO_2 nanocrystals onto pre-cleaned glass substrate. The films were annealed in air for 2 min at 150 °C after each drop. The shape and size of Cu^{2+} doped TiO_2 nanocrystals were characterized using JEOL 100 CX transmission electron microscope operating at 100 kV. The XRPD pattern was obtained on a Philips PW-1050 automated diffractometer. The percent of Cu^{2+} ions in TiO_2 nanocrystals was determined using *inductively coupled plasma* (ICP) emission spectrometry. The field dependence of the magnetic moment was measured using a superconducting quantum interference device magnetometer (SQUID). Hysteresis loop measurement has been performed up to 60 kOe.

RESULTS AND DISCUSSION

The XRPD analysis of Cu^{2+} doped TiO_2 nanocrystals revealed the existence of a homogeneous anatase crystal phase, Figure 1. Conventional TEM image of Cu^{2+} doped TiO_2 nanocrystals, Figure 1, inset, confirmed relatively uniform size distribution of faceted nanocrystals with average size of 13 nm.

The magnetic response for film made of 0.34 at% Cu^{2+} doped TiO_2 nanocrystals as a function of magnetic field strength (H) was followed at room temperature. The

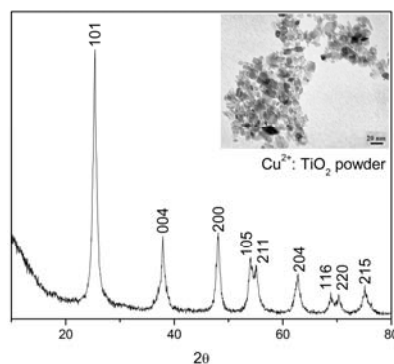


Figure 1. XRPD pattern of Cu^{2+} doped TiO_2 nanocrystals; Inset: TEM image of Cu^{2+} doped TiO_2 nanocrystals

magnetic field was applied parallel to the film surface. The diamagnetic contribution determined from the magnetic field dependence of magnetization at high field (for $H > 10$ kOe) was subtracted. The field dependent magnetization after diamagnetic correction is shown in Figure 2.

As can be seen from Figure 2, a weak room temperature ferromagnetic behaviour of Cu^{2+} doped TiO_2 nanocrystals was observed, with coercive field of $H_c \sim 200$ Oe and saturation magnetization (M_s) of the order of $2 \times 10^{-2} \mu_B/\text{Cu}$. Previous study indicated that the unexpected magnetism in such system could be the result of the interaction between the intrinsic defects and the doped ion [8]. There is couple of different carrier- mediated

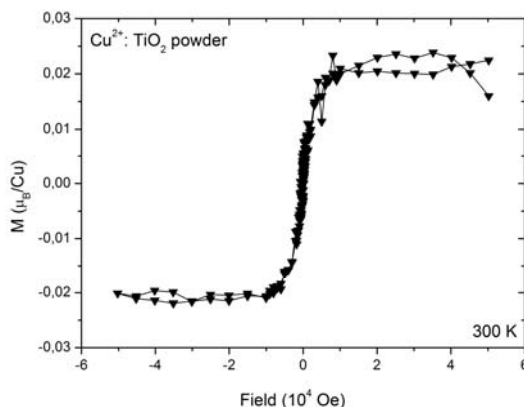


Figure 2. Magnetization curve for Cu^{2+} doped TiO_2 nanocrystals

mechanisms that could provide an explanation for the influence of oxygen vacancies and structural defects on the ferromagnetic ordering in DMSs: carrier mediated interaction such as Ruderman–Kittel–Kasuya–Yosida (RKKY) exchange, Zener double exchange or super exchange [5,8]. But, ferromagnetism in oxides with high electric resistance and low carrier densities such as the Cu^{2+} doped TiO_2 nanocrystals can be explained in terms of the noncarrier-mediated bound magnetic polaron (BMP) model [9]. When defects (oxygen vacancies) concentration increases they overlap many dopant ions to yield BMPs. This result in ferromagnetic coupling between Cu^{2+} ions mediated through oxygen vacancies. Li et al. proposed that substitutional Cu impurity binds easily with an oxygen vacancy (V_O) in TiO_2 to form the complex defect $\text{Cu}_{\text{Ti}}\text{-}V_O$, which relaxes to form the non-regular magnetic CuO_4 complex, in which the Cu ion is strongly magnetic [8]. This complex is similar to the magnetic one in other 3d transition metal-doped TiO_2 rutile films [10].

CONCLUSION

The polygonal Cu^{2+} doped TiO_2 nanocrystals ($d \sim 13$ nm) were synthesized applying hydrothermal treatment on dispersion of titania nanotubes in the presence of Cu^{2+} ions at pH=3. XRPD study confirmed the anatase crystal structure of Cu^{2+} doped TiO_2 nanocrystals and absence of any impurity phases (CuO , Cu_2O) in the sample. The weak ferromagnetic ordering at

room temperature with almost closed loop ($H_c \sim 200$ Oe) and saturation magnetic moment of the order of $2 \times 10^{-2} \mu_B/\text{Cu}$ atom were observed in film made of Cu^{2+} doped TiO_2 nanocrystals. The reason for observed weak ferromagnetism could be found in the interaction between the oxygen vacancy and the substitutional Cu impurity.

ACKNOWLEDGEMENT

This work was supported by the Ministry of Education, Science and Technological Development of the Republic of Serbia (project: 172056)

REFERENCES

- [1] R. Janisch, P. Gopal, N. A. Spaldin, *J. Phys. Condens. Matter*, 2005, 17, 657-689.
- [2] N. A. Spaldin, *Magnetic Materials*, Cambridge University Press, 2003.
- [3] N. Hong, W. Prellier, J. Sakai, A. Ruyter, *J. Appl. Phys.*, 2004, 95, 7378-7380.
- [4] J. Tian, H. Gao, H. Deng, L. Sun, H. Kong, P. Yang, J. Chu, *J. Alloy. Comp.* 2013, 581, 318-323.
- [5] S. K. S. Patel, N. S. Gajbhiye, *Mat. Chem. Phys.*, 2012, 132, 175-179.
- [6] M. Vranješ, Z. Konstantinović, A. Pomar, J. K. Jakovljević, M. Stoiljković, J. M. Nedeljković, Z. Šaponjić, *J. Alloy. Comp.* 2014, 589, 42-47.
- [7] T. Kasuga, M. Hiramatsu, A. Hoson, T. Sekino, K. Niihara, *Adv. Mater.*, 1999, 11, 1307-1311.
- [8] Q. K. Li, B. Wang, C. H. Woo, H. Wang, Z. Y. Zhu, R. Wang, *EPL*, 2008, 81, 17004.
- [9] J. M. D. Coey, M. Venkatesan, C. B. Fitzgerald, *Nat. Mater.* 2005, 4, 173-179.
- [10] S. Duhalde, M. F. Vignolo, F. Golmar, C. Chilotte, C. E. R. Torres, L. A. Errico, A. F. Cabrera, M. Renteria, F. H. Sanchez and M. Weismann, *Phys. Rev. B*, 2005, 72, 161313.

ENHANCED MICROWAVE SYNTHESIS OF POLYANILINE NANOMATERIALS

M. R. Gizdavic-Nikolaidis^{1,2}, M. Jevremovic³, D. R. Stanisavljev²,
G. A. Bowmaker¹ and Z. D. Zujovic^{1,4,5}

¹ *School of Chemical Sciences, The University of Auckland, Private Bag
92019, Auckland 1142, New Zealand (m.gizdavic@auckland.ac.nz).*

² *Faculty of Physical Chemistry, Studentski Trg 12-16, P.O. Box 137,
11001 Belgrade, Serbia.*

³ *Public Company Nuclear Facilities of Serbia, 12-14 Mike Petrovica Alasa,
Vinca, 11351 Belgrade, Serbia.*

⁴ *Institute of General and Physical Chemistry, Studentski Trg 12-16, 11001
Belgrade, Serbia.*

⁵ *MacDiarmid Institute for Advanced Materials and Nanotechnology,
Victoria University of Wellington, Wellington 6140, New Zealand*

ABSTRACT

Energy- and time-efficient enhanced microwave syntheses (EMS) of polyaniline (PANI) have been carried out. The GPC results showed that the molecular weight of the microwave-generated materials depends on the applied microwave power. FTIR spectroscopies confirmed the formation of PANI. The presence of a mixed morphology with the prevalence of nanofibers with different aspect ratios is confirmed through SEM. The conductivity of the samples (ca. 3-3.5 S cm⁻¹) is found to be relatively independent on the microwave power levels. The fact that the molecular weight depends on the power means that this approach can be fine-tuned to optimize conditions for a specific material using different power levels.

INTRODUCTION

Polyaniline (PANI) is one of the most extensively studied electrically conducting polymers. The specific characteristics make PANI applicable in various fields such as gas sensors, biosensors, actuators, anticorrosive coatings, electronic devices etc. A novel method of synthesis of PANI using a microwave assisted approach under controlled temperature (EMS) has been recently introduced [1,2].

EXPERIMENTAL

PANI was prepared by aniline oxidation with potassium iodate (KIO₃) or ammonium persulphate (APS). To an aqueous solution of 1.25 M

hydrochloric acid (12 mL) was added KIO₃ (0.432 g) or APS (0.4606 g). 0.480 mL of aniline was added to this solution. For conventional synthesis (CS) the solution was stirred for 10 min. We used for comparison purposes the previously obtained results for CS PANI sample synthesized after 5 h of stirring (giving the same yield as 10 min MW synthesized PANI) [1]. The reaction mixture was filtered and washed thoroughly with distilled water and acetone to eliminate low molecular weight oligomers and other impurities. The retentates were dried in a vacuum oven at 40 °C overnight. MW irradiation was performed in a single mode focused CEM reactor (Model Discover, CEM Co., Matthew, NC) operating at 2.45 GHz with ability to control output power. Each microwave (MW) synthesis was carried out for 10 minutes. The PANI MW synthesis using different oxidizing agent was performed in the power range from 3 to 70 W. Three samples for each microwave power (3, 10, 40, and 70 W) were prepared. All experiments were done under the same conditions by keeping constant irradiation power, temperature and initial reaction mixture volume. The temperature of (24±1) °C and mixing rate of 400 RPM are maintained in all experiments. Molecular weights were determined with Gel Permeation Chromatography (GPC) using a 300 × 7.5 mm Polypore column (Polymer Laboratories, UK). The PANI samples were dissolved in 5 mL of NMP to a 3 mg mL⁻¹ concentration. The eluent was NMP, and the flow rate was 0.3 mL min⁻¹. The molecular structure of PANI samples was investigated by FTIR. Scanning electron microscopy (SEM) carried out using a Philips XL30S Field Emission Gun with a SiLi (Lithium drifted) EDS detector with Super Ultra Thin Window. Electrical conductivity of compressed pellets of the PANI samples was measured using a Jandal Multi Height Four-Point Probe with DC current source, at ambient temperature.

RESULTS AND DISCUSSION

The yields of enhanced microwave and chemically synthesized PANI using KIO₃ and APS as oxidants, as a function of applied power, are all in the range 65-70% while the classical synthesis (CS) method took 5 h to achieve the same yield [1,2]. It is interesting that the percent yield differs only slightly for various microwave power levels. This may imply that the reaction was finished before the samples were taken out (10 min after the beginning of the reaction). At the same time, the yields of the samples obtained without the microwave power (CS synthesis) are only around 25% with stirring after 10 min, in agreement with previously published yields for PANI [1,2]. The final polymer molecular weights (M_w) depend significantly on the microwave irradiation power. The molecular weight using KIO₃ as the oxidizing agent increased from ca. 3900 g mol⁻¹ (3 W) up to 18 300 g

mol^{-1} (70 W). If micro heating was a major effect, molecular weight would decrease with the increasing power level (higher temperature) in analogy with the CS syntheses [3]. On the other hand, the M_w values for the samples obtained using APS were consistently higher, with a range from ca. 7400 g mol^{-1} (3 W) to 22 700 g mol^{-1} (70 W). The molecular weight for CS PANI was ca. 26 200 g mol^{-1} using KIO_3 and slightly higher (30 400 g mol^{-1}) using APS, in agreement with previously published results [4].

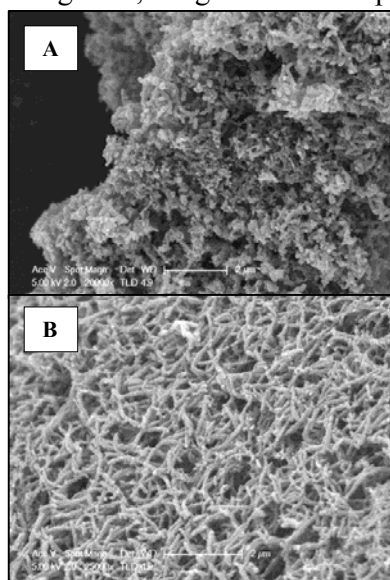


Figure 1. SEM micrographs of the EMS synthesized PANI using APS (A) and KIO_3 (B) at 70 W.

SEM micrographs of PANI samples synthesized in MW using APS and KIO_3 as an oxidizing agents are shown in Figure 1. All micrographs reveal a mixed nanofibrillar structures with different aspect-ratios. This means that the morphology depends to some extent on the microwave power. Despite their similarities, the morphologies of the samples prepared using APS and KIO_3 differ upon closer inspection [2]. Overall, the PANI samples synthesized using KIO_3 at higher power levels (Figure 1B) compared with the ones obtained with APS (Figure 1A) exhibit a compact and better defined, fiber-like morphology characterized with a higher aspect ratio. It has been shown that morphology depends on the nucleation and growth process and that nucleation and growth mechanisms of PANI depend on the anion type [1]. The

EMS samples exhibit mainly fibrillar or rod-like morphologies, regardless of MW power applied during the synthesis, although the quality (aspect-ratio) and the morphological homogeneity of materials do depend on the applied power and the anion type.

FTIR spectroscopies confirmed the formation of PANI structure in both CS and MW synthesized samples. The intense bands and shoulders around 1560 cm^{-1} and 1450-1470 cm^{-1} originate from C-C stretching in the quinonoid and benzenoid rings, around 1290 cm^{-1} from C-N stretching of the secondary aromatic amine, around 1240 cm^{-1} is related to the protonated C-N group. The intense and very broad band which appears at around 1080-1100 cm^{-1} is assigned to electronic bands that are usually considered to be a measure of the delocalization of electrons in the PANI structure. The bands at around 800 cm^{-1} originate from C-H out-of-plane bending in 1,4-disubstituted ring

structures (*para*-coupling), indicating the presence of the head-to-tail coupling during the polymerization. The electrical conductivity (EC) values for MW PANIs do not change significantly with the microwave power. At the same time MW PANI samples showed a higher conductivity (ca. 3-3.5 Scm^{-1}) compared with CS PANI samples ($\sim 0.5 \text{Scm}^{-1}$) after the reaction was completed. Comparison of these data with the molecular weight data implies that the molecular weight has no significant influence on the macroscopic electrical conductivity in the series produced at different microwave power levels, although there is a small increasing trend in conductivity values with increasing molecular weight. This is in agreement with the theoretically predicted weak dependence of electronic properties on chain length.

CONCLUSION

EMS of PANI was investigated, with microwave power levels varied, while the reaction system was kept at constant temperature of $24 \pm 1^\circ\text{C}$. GPC results showed that molecular weight depended on applied power. On the basis of SEM images, the presence of a mixed morphology with the predominance of nanofibrillar morphology was confirmed, while FTIR techniques confirmed that the microwave-generated materials structurally consist of PANI. At the same time these samples revealed a higher conductivity compared with conventionally obtained material. According to these results, it can be concluded that the microwave-enhanced approach can be used to optimize reaction conditions for obtaining PANI nanofibers with different molecular weight by varying microwave power.

ACKNOWLEDGEMENT

The authors acknowledge financial support from the Foundation for Research, Science and Technology, New Zealand (Contract No. UOAX0812) and Ministry for Science of the Republic of Serbia (Contract No.172015).

REFERENCES

- [1] M. Gizdavic-Nikolaidis, D. R. Stanisavljev, A. J. Easteal, *Macromol. Rapid Commun.* 2010, *31*, 657-661.
- [2] M. R. Gizdavic-Nikolaidis, M. Jevremovic, D. R. Stanisavljev, Z. D. Zujovic, *J. Phys. Chem. C* 2012, *116*, 3235-3241.
- [3] J. Stejskal, J., A. Riede, D. Hlavataa, J. Prokes, M. Helmstedt, P. Holler, *Synth. Met.* 1998, *96*, 55-61.
- [4] P. N. Adams, P. J. Laughlin, A. P. Monkman, A. P. *Synth. Met.* 1996, *76*, 157-160.

MEASUREMENT OF HARDNESS OF $\text{Cu}_x(\text{AsSe}_{1,4}\text{I}_{0,2})_{100-x}$ THIN AMORPHOUS FILMS BY MICROINDENTATION

D. Štrbac^{1,2*}, L. Šiđanin² and S. Lukić-Petrović¹

¹ *University of Novi Sad, Faculty of Sciences, Serbia*

² *University of Novi Sad, Faculty of Technical Sciences, Serbia*

ABSTRACT

The paper reports on hardness, fracture toughness and brittleness of the $\text{Cu}_x(\text{AsSe}_{1,4}\text{I}_{0,2})_{100-x}$ amorphous thin films obtained by microindentation, for $x=0$ at.%, 10 at.%, 15 at.%, 20 at.% and 25 at.%. Values of determined microhardness are in the interval of 748 MPa - 1137 MPa, and can be regarded as moderate in the category of chalcogenide glasses. Isotropic mechanical behaviour of the thin films surfaces was confirmed.

INTRODUCTION

Halo - chalcogenide glasses are known as attractive materials for fundamental research and practical applications due to their interesting structural, optical and electrical properties, high transparency at the telecommunication wavelengths and high non-linear refractive index [1, 2]. The halo-chalcogenides containing Ag and Cu are proven to have some additional attractive features, such as photo - induced structural changes [3], making these materials, especially in thin film form, attractive for applications in non - linear optical elements, optical recording media, antireflection coatings, component for memory switching, etc. [4]. Determination of mechanical properties of a material is of great interest for practical applications, especially of thin films, considering the existing knowledge of their general brittleness [5].

EXPERIMENTAL

Amorphous chalcogenide thin films of the $\text{Cu}_x(\text{AsSe}_{1,4}\text{I}_{0,2})_{100-x}$ type for $x=0$ at.%, 10 at.%, 15 at.%, 20 at.% and 25 at.% were deposited under a vacuum of 10^{-5} Torr on glass substrates by a vacuum thermal evaporation technique, from previously synthesized bulk samples. Bulk samples were synthesized in the cascade regime from high purity elemental components (99.998%), air quenched [14] and powdered for vacuum deposition. Standard glass microscope slides were used as substrates. The film thickness is controlled during vapour-deposition process by interference optical method. The microindentation measurements using Vicker's diamond pyramid indenters

were applied for determining the microhardness of thin films serial. The value of so called Vicker's microhardness was determined on the basis of the dimensions of the plastic micro-imprint of the indenter into the sample. For this purpose use was made of a Reichert Me F2 type microscope, supplied with the appropriate accessories. Measurements were carried at constant load, using minimal available indenter load mass of 1 g. The value of the microhardness is calculated as a mean value out of multiple points measuring at thin film surface. Fracture toughness [6] and brittleness values [7] were also determined.

RESULTS AND DISCUSSION

The thicknesses of the films were determined by the envelope method [8-10].

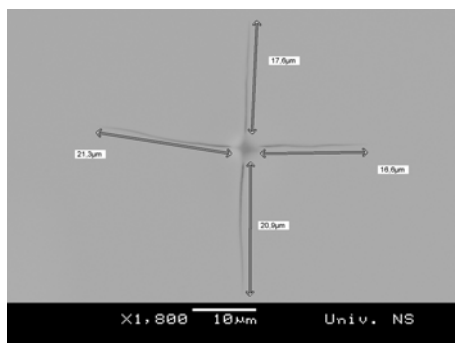


Figure 1. SEM image of the imprint in $\text{AsSe}_{1,4}\text{I}_{0,2}$ thin film

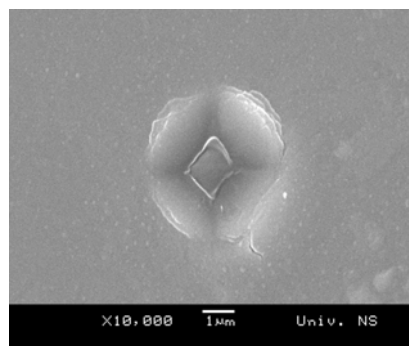


Figure 2. SEM image of the imprint in $\text{Cu}_{15}(\text{AsSe}_{1,4}\text{I}_{0,2})_{85}$ thin film

As it can be seen in Table 1, thicknesses of the thin films with 10 at.% and 15 at.% of Cu were estimated to be under 200 nm. It must be emphasized here that this thickness is too low for obtaining the representative imprints. Bearing in mind that the measurements of mechanical properties of thin films are generally influenced by substrates [11, 12], the obtained values of mechanical parameters for the thin films with 10 at.% and 15 at.% of Cu must be regarded as estimated values.

Based on empirical criterion introduced in Ref. [13], in the samples with 0 at.% and 25 at.% of Cu, radial-medial cracks were formed, while in the samples with 10 at.% and 20 at.% Palmquist cracks were formed [14]. Indentations in the film with 15 at.% did not induce crack formation and therefore fracture toughness and brittleness was not determined for that sample. Vicker's hardness, fracture toughness and brittleness values are presented in Tables 1 and 2. Figure 1. presents the SEM image of the

imprint in $\text{AsSe}_{1,4}\text{I}_{0,2}$ thin film. Figure 2. presents the SEM image of the imprint in thin film with 15 at.% of Cu. Images are obtained by computerized JEOL scanning electron microscope (type JSM - 6460 LV).

Table 1. Vicker's hardness of the $\text{Cu}_x(\text{AsSe}_{1,4}\text{I}_{0,2})_{100-x}$ amorphous thin films obtained by microindentation

x[at%]	0	10	15	20	25
d [nm]	314 ± 28	< 200	< 200	203 ± 15	928 ± 46
$\overline{2a}$ [μm]	4,53(7)		4,17(7)	4,31(7)	4,87(7)
	4,53(7)	4,39(7)	4,02(7)	4,39(7)	5,00(7)
	5,01(7)		3,83(7)	4,35(7)	
H_V [MPa]	888(27)		1050(40)	980(30)	767(22)
	888(27)	940(30)	1120(40)	940(30)	728(20)
	725(20)		1240(50)	960(30)	
$\overline{H_V}$ [MPa]	834(14)	940(30)	1137(25)	960(17)	748(15)

Table 2. Fracture toughness and brittleness of the $\text{Cu}_x(\text{AsSe}_{1,4}\text{I}_{0,2})_{100-x}$ amorphous thin films obtained by microindentation

x[at%]	\overline{c} [μm]	\overline{a} [μm]	K_{IC} [MPam ^{1/2}]	B [m ^{-1/2}]
0	18,70(5)	-	0,00996(4)	83340(1400)
10	5,55(5)	2,20(4)	0,0527(26)	18300(1000)
20	5,65(5)	2,26(4)	0,0559(23)	17500(800)
25	15,55(5)	-	0,01318(6)	63100(1200)

Compared to the values obtained for the bulk counterparts [15] obtained values of Vicker's hardness are less, fracture toughness is an order of magnitude less and brittleness is an order of magnitude higher.

CONCLUSION

During microhardness measurements using Vickers direct method, radial-median or Palmqvist cracks have occurred in the $\text{Cu}_x(\text{AsSe}_{1,4}\text{I}_{0,2})_{100-x}$ amorphous thin film samples, depending on the copper content. Values of determined microhardness of the $\text{Cu}_x(\text{AsSe}_{1,4}\text{I}_{0,2})_{100-x}$ amorphous thin films are moderate in the category of chalcogenide glasses. Vicker's hardness are less, fracture toughness is an order of magnitude less and brittleness is an order of magnitude higher, compared to the values obtained for the bulk counterparts. Isotropic mechanical behaviour of the thin films surfaces is determined.

ACKNOWLEDGEMENT

This work is supported by Provincial Secretariat of Science and Technological Development, APV and by the projects OI171022 and III45020 of the Ministry of Education, Science and Technological Development, RS.

REFERENCES

- [1] K. Ogusu, S. Maeda, M. Kitao, H. Li, M. Minakata, *J. Non-Cryst. Solids*, 2004, 347, 159-65
- [2] E. Marquez, J. M. Gonzalez-Leal, A. M. Bernal-Oliva, T. Wagner, R. Jimenez – Garay, *J. Phys. D. Appl. Phys.*, 2007, 40, 5351-5357
- [3] N. Bollee, P. Hertogen, G.J. Adriaenssens, C. Senemaud, A. Gheorghiu-de La Rocque, *Semiconductors*, 1998, 32, 873 – 878
- [4] M. Popescu, *J. Optoe. Adv. Mat.*, 2005, 4, 2189 – 2210
- [5] J. P. Guin, T. Rouxel, J. C. Sangleboeuf, I. Melscoët, J. Lucas, *J. Am. Ceram. Soc.*, 2002, 85, 1545 – 1552
- [6] B. R. Lawn, D. B. Marshall, *J. Am. Cer. Soc.*, 1979, 62, 347-
- [7] D. B. Marshall, B. R. Lawn, *Microindentation Techniques in Materials Science and Engineering*, ASTM, Philadelphia, PA (1986)
- [8] R. Swanepoel, *J. Phys. E: Sci. Instrum.*, 1983, 16, 1214 – 1222
- [9] R. Swanepoel, *J. Phys. E: Sci. Instrum.*, 1984, 17, 896–903
- [10] R. Swanepoel, *S. Afr. J. Phys.*, 1989, 12, 148 – 156
- [11] Y.C. Huang, S.Y. Chang, *Surface and Coatings Technology.*, 2010, 20, 3147 – 3153
- [12] S. Chen, L. Liu, T. Wang, *Surface and Coatings Technology.*, 2005, 1, 25 – 32
- [13] J. Gong, Z. Guan, *Mater. Lett.*, 2001, 49, 180-184
- [14] S. Palmqvist, *Jernkontorets Ann.*, 1957, 141, 300-307
- [15] S.R. Lukić, F. Skuban, D.M. Petrović, L. Šiđanin, *J. Mater. Sci. Lett.*, 2000, 19, 139 - 141

MICROSTRUCTURE CHANGES CAUSED BY THERMAL ETCHING OF SINTERED $ZnTiO_3$

N. Labus¹, J. Vujančević¹ and M.V. Nikolić²

¹ *Institute of Technical Sciences of SASA, Knez Mihailova 35, 11000 Beograd, Serbia*

² *Institute for Multidisciplinary Research, Kneza Viseslava 1, 11000 Beograd, Serbia*

ABSTRACT

Polishing and thermal etching was performed on $ZnTiO_3$ sintered ceramic. Two sets of specimens were recorded, on higher 1200°C/1100°C sintered/etched, and lower 900°C/800°C sintered/etched temperatures. Phase composition, crystallite sizes and grain size distributions before and after etching were compared. Grain size enlargement was noted.

INTRODUCTION

Thermal etching should represent grain sizes not changed by the etching procedure. Polishing preceding thermal etching is used to obtain a flat surface convenient for grain size measurements[1]. During etching the grain boundary ought to be emphasized since a grain boundary consists of an amorphous phase more prone to melting compared to crystalline grains[2]. Crystallite size determined with the Scherrer equation from x ray diffractograms represents a calculation of single crystalline domain i.e. a coherently scattering domain. The crystallite size can be observed as a rude measure of the homogeneity of the crystal structure inside the grain [3]. In the polycrystalline ceramics grain size is commonly monitored through a grain size distribution function[4]. Also, the geometry of grains after reheating indicates the mechanism of grain growth. By comparing changes of these values before and after thermal etching treatment, we determine exactness of such thermal treatment.

RESULTS AND DISCUSSION

After sintering of the compacted nanopowder performed at 900°C and 1200°C with isothermal holding of 1 hour microstructure was obtained using AFM. Same specimens were polished and then reheated. The sample sintered at 900°C was heated 10°C/min up to 800°C and held isothermally 20 minutes. Cooling was performed in a furnace with a cooling rate - 10°C/min. The second sample sintered at 1200°C, showed a phase transition

at 956°C to Zn_2TiO_4 spinel [5]. The obtained sintered specimen was reheated 10°C/min to 1100°C and held for 20 minutes, cooling within the furnace.

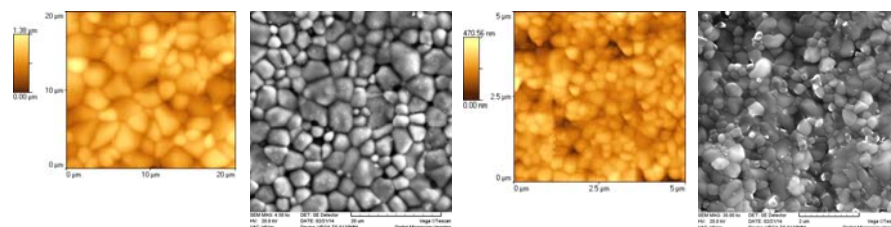


Figure 1. Microstructures for the higher temperature a) 1200°C/1100°C sintering/reheating, left AFM 1200°C, right SEM 1100°C and lower b) 900°C/800°C sintering/reheating, left AFM 900°C, right SEM 800°C.

After thermal etching i.e. second heating cycle SEM microstructures were recorded for 1200°C/1100°C and 900°C/800°C specimens. XRD diffractograms were used for crystallite size determination. Crystallite sizes, phase composition, and grain size distribution parameters are shown in tab.1 and 2. For the lower temperature 900°C/800°C the phase composition lost all $\text{Zn}_2\text{Ti}_3\text{O}_8$ while ZnTiO_3 transformed into Zn_2TiO_4 reducing its content. Even at temperatures that should preserve ZnTiO_3 phase, its metastability leads to formation of stable Zn_2TiO_4 . At the higher temperature 1200°C/1100°C Zn_2TiO_4 and TiO_2 rutile are interchanging their ratio in the favor of TiO_2 . Phase content changes are indicating intensive and unavoidable diffusion processes.

The grain size was determined by measurement of internal boundaries in three dimensional structures obtained by random sectioning. Although, expectations were that prolonged heating will enlarge crystallites, the crystallite size showed lowering of their domains when reheated. Due to phase metastability ZnTiO_3 , coherent domains are maximal when crystallization is achieved by sintering from nanopowder [6]. Grain size distributions are presented in fig.3, and tab.1. At lower temperature 900°C/800°C the grain size distribution shows a bimodal distribution originating from grain size coalescence. At higher temperature 1200°C/1100°C grain growth widened the distribution, now monomodal in shape. Comparing longer **a** to shorter **b** distance inside the grain calculated as mean average (m.av), ratio a/b size for 1200°C was $m_{.av}a/m_{.av}b$ 2.781/1.964 equals a/b ratio 1.415 and for 1100°C $m_{.av}a/m_{.av}b$ ratio is 3.898/2.814 which equals a/b 1.385 ratio. Longer grains in both temperatures lower and higher are thus getting bigger, but abnormal grain growth cannot be noted.

CONCLUSION

At lower temperature 900°C/800°C the crystallite size reduced almost three times, while the overall grain size increased by 34%. At higher temperature 1200°C/1100°C grain growth with pronounced bimodal distribution shape occurred, increased by 30% in size, where the composition did not substantially changed after etching. Crystallite sizes also reduced in this case.

Table 1. Phase composition, crystallite sizes and grain sizes, for the lower temperature 900°C/800°C sintering/reheating, and higher one 1200°C/1100°C sintering/reheating.

900°C/800°C sintering / reheating.				
Heating sintering 10°C/min 900°C 1h				
phase	Zn ₂ Ti ₃ O ₈	ZnTiO ₃	Zn ₂ TiO ₄	TiO ₂
Composition wt%	1.756	81.096	14.343	2.805
Crystallite size nm			142.7	
Grain size - GS	No.	Mean	St.dev.	St.err.
	168	0.3451	0.11374	0.00877
Gaussian fit GS	R ²	Center	Width	Height
1	0.9741	0.2963	0.13189	19.210
2		0.5272	0.24454	17.322
Reheating 800°C 10°C/min 800°C 20 min				
phase	Zn ₂ Ti ₃ O ₈	ZnTiO ₃	Zn ₂ TiO ₄	TiO ₂
Composition wt%	/	70.56	27.15	2.49
Crystallite size nm			37.28	
Grain size - GS	No.	Mean	St.dev.	St.err.
	173	0.45394	0.17416	0.01324
Gauss fit GS	R ²	Center	Width	Height
1	0.98617	0.27569	0.13470	25.588
2		0.40151	0.20789	
1200°C/1100°C sintering / reheating.				
Heating sintering 10°C/min 1200°C 1h				
phase	Zn ₂ TiO ₄			TiO ₂
Composition wt%	75.93%			24.7%
Crystallite size nm	68.4			
Grain size	No.	Mean	St.dev.d	St.err.
	62	2.785	0.777	0.0986
Gauss fit Grain size	R ²	Center	Width	Height
	0.97682	2.7768	1.7439	13.939
Reheating 1100°C 10°C/min 1100°C 20 min				
phase	Zn ₂ TiO ₄			TiO ₂
Composition wt%	71.51%			28.49%
Crystallite size nm	54.28			
Grain size	No.	Mean	St.dev.	St.err.
	108	3.898	1.3177	0.1268
Gauss fit Grain size	R ²	Center	Width	Height
	0.93128	3.5858	2.1549	16.853

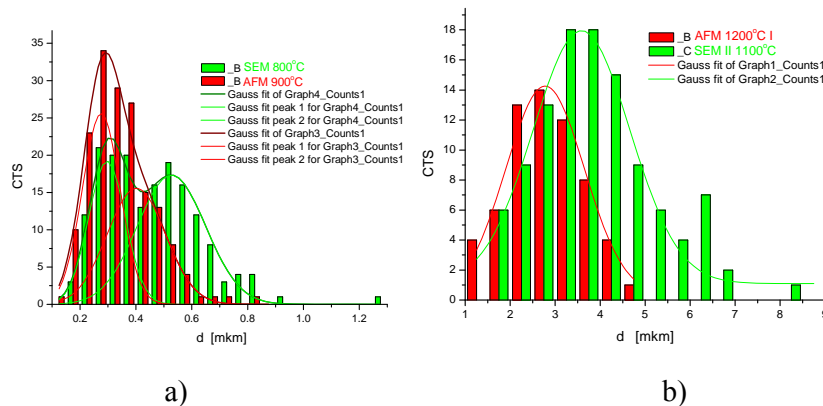


Figure 3. Grain size distributions for the sintering / reheating of the a) lower 900°C/800°C and b) higher 1200°C/1100°C temperature.

REFERENCE

- [1] Jeanne Ayache, Luc Beaunier, Jacqueline Boumendil, Gabrielle Ehret, Danièle Laub, *Sample Preparation Handbook for Transmission Electron Microscopy*, Techniques, Springer, 2010
- [2] Shen J. Dillon, Martin P. Harmer, Demystifying the role of sintering additives with “complexion”, *Journal of the European Ceramic Society*, 2008, 28 1485–1493.
- [3] Claudia Weidenthaler, Pitfalls in the characterization of nanoporous and nanosized materials, *Nanoscale*, 2011, 3, 792.
- [4] Mel.I.Mendelson, Average Grain Size in Polycrystalline Ceramics, *Journal of the American Ceramic Society*, 1969, Vol. 52, No.8, August, 443-446.
- [5] M.V. Nikolic, N. Labus, M.M. Ristic, Densification rate and phase structure changes during sintering of zinc titanate ceramics, *Ceramics International*, 2009, 35, 3217–3220.
- [6] ZnTiO₃ Pearson's Crystal Data, Database for Inorganic Compounds, Release 2013/14, Pierre Villars and Karin Cenzual (ed.), Dossier of: 1629506., Publ. ASM International.

APPLICATION OF PLACKETT-BURMAN STATISTICAL DESIGN FOR PREPARING MAGNESIUM DOPED ALUMINA

T. B. Novaković, Lj. S. Rožić, S. P. Petrović and Z. M. Vuković

University of Belgrade, IChTM-Department of Catalysis and Chemical Engineering, Njegoševa 12, Belgrade, Republic of Serbia

ABSTRACT

A sol-gel process was used to produce magnesium doped alumina. Many parameters of synthesis and calcination conditions affect the pore structure formation. In order to determine the most influential factors among concentration of magnesium nitrate, time and temperature of alcohol evaporation, annealing temperature, heating rate and time of annealing, a Plackett-Burman's design of experiments has been used. With a very limited number of experiments, this method allowed to obtain the first encouraging results. Results of analysis showed that two process variables, annealing temperature and time of annealing, play fundamental roles on textural properties of magnesium doped alumina.

INTRODUCTION

Mesoporous alumina is a very interesting material with broad applicability as adsorbents, coatings, porous ceramics, catalysts, and catalyst supports [1-4]. Active aluminas do not occur naturally and they are prepared mainly by hydrothermal or thermal transformations of aluminium hydroxides or alumogel. During annealing, organic groups are removed, and gel transforms to a more stable solid phase. This evolution involves a chemical modification, a crystallographic transformation of the solid matter and reorganization of the solid network and of the pore geometry [5].

Despite the large number of factors that can be modified in the whole process of obtaining alumina, the most studies on the synthesis used conventional methods. Conventional multifactor experimental design requires that only one variable be changed at a time to determine its effect. But when there are many parameters, this way is very laborious and it does not allow clear identification of the real influences of linked parameters. These limitations of conventional method can be overcome by optimizing all the affecting parameters collectively by statistical experimental design. Some of the popular choices in applying statistical designs as a screening test are Plackett-Burman (PB) design that involves a large number of factors

and relatively few runs. They are typically used to identify a few significant factors out of a large set.

In this work, magnesium doped alumina were prepared by varying simultaneously parameters of sol-gel synthesis and annealing conditions. A Plackett-Burman design was employed to determine the significant factors affecting the pore structure formation.

EXPERIMENTAL

Preparation of magnesium doped alumina

Magnesium doped alumina was prepared by the sol-gel method using aluminium alcoxide as a precursor. To prepare boehmite sols, aluminium isopropoxide was hydrolyzed in excess amount of water (100:1 H₂O-Al³⁺, mol) at 80°C, followed by the peptization with appropriate amount of HNO₃ (0.07:1 H⁺/Al³⁺, mol) to form stable colloidal sol [6]. The sol was kept at a constant temperature for the desired time under reflux conditions, during which most of the alcohol was evaporated. The freshly prepared boehmite sol and polyethylene glycol (PEG) or variable concentration of magnesium nitrate solution combined with PEG, were mixed together and then vigorous stirred in order to obtain a homogeneous Mg²⁺doped boehmite sol. The doped boehmite sols were then gelled at 40°C. The gels were heated from room temperature to the final temperature, which ranged between 500 and 1100 °C. The heating rate ranged between 2 and 10 °C/min. The samples were kept at final temperatures for a fixed period, which ranged from 1 to 10 h.

Experimental design

A set of experiments with Plackett-Burman (PB) design was adopted to develop magnesium doped alumina by sol-gel method. A total of 12 experimental trials involving 6 independent variables were generated by Minitab 16 (Pennsylvania State University). The independent variables screened were annealing temperature (X₁), heating rate (X₂), time of annealing (X₃), concentration of magnesium nitrate (X₅), time of alcohol evaporation (X₇) and temperature of alcohol evaporation (X₉). Three variables (X₄, X₆, X₈) are dummy variables employed to evaluate the standard errors of the experiment. Specific surface area (Y₁) was selected as the response variables.

Characterization of Mg(II) doped alumina

The nitrogen adsorption was performed at -196 °C and relative pressure interval between 0.05 and 0.98 in automatic adsorption apparatus (Sorpomatic 1990 Thermo Finningen). Before each measurement, the sample was degassed at 250 °C under vacuum for time enough (4 h < t < 10 h) to observe the absence of significant changes in vacuum stability. The

adsorbed amount of nitrogen was measured by volume at standard temperature and pressure. The specific surface areas (S_{BET}) and C were calculated by the BET method [7] from nitrogen adsorption isotherms, using data up to $p/p_0 = 0.35$.

RESULTS AND DISCUSSION

PB design for six variables at two levels was employed for screening sol-gel synthesis parameters and annealing conditions that significantly influenced on pore structure of magnesium doped alumina. The six assigned variables were screened in twelve experimental designs. Each independent variable was tested at two levels, high and low levels, which were denoted by (+1) and (-1), respectively (Table 1).

Table 1. Levels of the chosen variables tested in PB design

Variables	Symbol	Units	Low(-1)	High(+1)
Annealing temperature	X_1	$^{\circ}\text{C}$	500	1100
Heating rate	X_2	$^{\circ}\text{C min}^{-1}$	2	10
Time of annealing	X_3	h	1	10
Concentration of Mg(II)	X_5	mol Mg/mol Al_2O_3	0.03	0.06
Time of evaporation	X_7	h	60	72
Temperature of evaporation	X_9	$^{\circ}\text{C}$	85	95

The experiments were carried out according to the design matrix (Table 2), with each row representing one trial while each column represents a single variable. As shown in Table 2 the selected response variable exhibited a wide variation suggesting that the independent variables had a significant effect on the response parameter chosen.

Table 2. PB design variables with S_{BET} as response

Run	X_1	X_2	X_3	X_4	X_5	X_6	X_7	X_8	X_9	S_{BET}
1	1	-1	1	-1	-1	-1	1	1	1	16
2	1	1	-1	1	-1	-1	-1	1	1	73
3	-1	1	1	-1	1	-1	-1	-1	1	226
4	1	-1	1	1	-1	1	-1	-1	-1	31
5	1	1	-1	1	1	-1	1	-1	-1	78
6	1	1	1	-1	1	1	-1	1	-1	13
7	-1	1	1	1	-1	1	1	-1	1	296
8	-1	-1	1	1	1	-1	1	1	-1	282
9	-1	-1	-1	1	1	1	-1	1	1	312
10	1	-1	-1	-1	1	1	1	-1	1	76
11	-1	1	-1	-1	-1	1	1	1	-1	303
12	-1	-1	-1	-1	-1	-1	-1	-1	-1	314

In order to determine the influence of the most important parameters, a standardized Pareto chart (Fig. 1) was employed. It consists of bars with a length proportional to the absolute value of the estimated effects, divided by

the standard error. The bars are displayed in order of the size of the effects, with the largest effect on top. The Pareto chart revealed that annealing temperature had maximum standardized effect at 95 % confidence interval, while the concentration of magnesium nitrate, time of alcohol evaporation and temperature of alcohol evaporation did not have a significant effect on specific surface area.

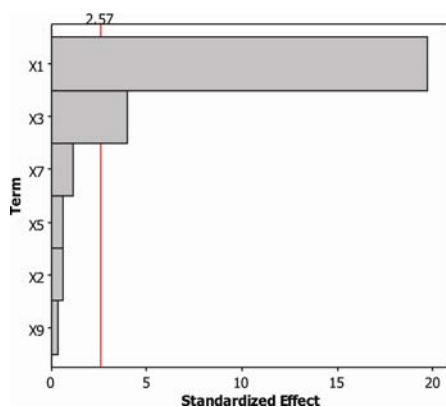


Figure 1. Pareto chart of standardized effects of independent variables

CONCLUSION

Magnesium doped alumina were prepared by sol-gel method, PB screening design helped in identifying the significant parameters that affected the response variables. Only two predetermined independent variables were found to affect

specific surface area as dependent variables. The next step is to examine the impact of existing independent variables on several response variables. Response variable affected by three or more independent variables will be used for process optimization using DOE strategy.

ACKNOWLEDGMENTS

This work was supported by the Ministry of Education and Science of the Republic of Serbia under projects numbers 172015, 172001 and III 45001.

REFERENCES

- [1] T. Novakovic, N. Radic, B. Grbic, V. Dondur, M. Mitric, D. Randjelovic, D. Stoychev, P. Stefanov, *Appl Surf Sci.*, 2003, 255, 3049-3055.
- [2] A.L. Ahmad, N.N.N. Mustafa, *Int J Hydrogen Energ.*, 2007, 32, 2010-2021
- [3] J. Čejka, *Appl Catal A-Gen.*, 2003, 254, 327-337
- [4] H. Arai, M. Machida, *Appl Catal A-Gen.*, 1996, 138, 161-176
- [5] A.C. Pierre, *Ceram Int.*, 1996, 23, 229-238.
- [6] B.E. Yoldas, *Am Ceram Soc Bull.*, 1975, 54 (3), 289-290.
- [7] S.H. Gregg, K.S. Sing, *Adsorption, Surface Area and Porosity*, Academic Press, New York (1967)

EFFECT OF $\text{La}_2\text{O}_3/\text{SrO}$ RATIO ON PROPERTIES OF $\text{La}_2\text{O}_3\text{-SrO-B}_2\text{O}_3$ GLASSES

S. V. Smiljanić¹, S. R. Grujić¹, M. B. Tošić², V. D. Živanović², S. D. Matijašević², J. D. Nikolić² and V. Topalović²

¹*Faculty of Technology and Metallurgy, Karnegijeva 4, University of Belgrade, 11000 Belgrade, Serbia. (grujic@tmf.bg.ac.rs)*

²*Institute for the Technology of Nuclear and Other Raw Mineral Materials, 86 Franchet d'Esperey St, 11000 Belgrade, Serbia*

ABSTRACT

Selected lanthanum-strontium-borate glasses were prepared by conventional melt-quenching technique. Density, molar volume, oxygen molar volume, oxygen packing density and structural transformations in the glass network were investigated according to substitution of SrO by La_2O_3 at constant B_2O_3 content. The density and the molar volume were increasing with increasing La_2O_3 content. In the same time, oxygen molar volume values were increasing opposite to oxygen packing density values. Three infrared spectral regions were observed in the vibrations modes in the lanthanum-strontium-borate glasses.

INTRODUCTION

Growing interest recently has been focused on alkaline earth-borate glasses due to their applications as laser hosts, nonlinear optical and other photonic devices [1].

The structure of vitreous B_2O_3 consists of a random network of $[\text{BO}_3]$ triangles connected by bridging oxygen at all three corners to form completely linked network. The addition of a network modifier in B_2O_3 glass could induce the conversion of $[\text{BO}_3]$ triangle to $[\text{BO}_4]$ tetrahedral. This conversion of boron from 3- to 4-fold coordination only occurs until the network reaches some critical concentration of tetrahedrally coordinated boron, after which additional network modifier causes the formation of non-bridging oxygen [2]. Therefore in borate glasses, the main structural units are both; $[\text{BO}_3]$ triangle and $[\text{BO}_4]$ tetrahedra forming different intermediate units like: boroxol rings, metaborate rings and chains, pentaborate, diborate, triborate and pyroborate.

The present study aims to characterize physical and structural features of selected lanthanum-strontium-borate glasses. For the synthesis were selected glass composition within the glass forming range of the constant

B₂O₃ content ($x = 71.4$ mol %). Physical properties of glasses were investigated by measuring the densities of glass samples and by calculating the molar volume, oxygen molar volume and oxygen packing density values. Structural features of the glasses were investigated by the Fourier transform infrared spectroscopy (FTIR).

EXPERIMENTAL

The glasses were obtained by conventional melt-quenching method, the reagent grade of H₃BO₃, SrCO₃ and La₂(CO₃)₃ were prepared for melting in electrical furnace by mixing and homogenizing in agate mortar. Mixture was placed in a covered platinum crucible in the electric furnace and melted at 1200 °C for 30 min. These melting conditions, covered crucible, relatively short melting time at relatively low temperature were optimized to minimize boron evaporation. The melt was cast and cooled on a stainless steel plate in air at room temperature. Measurements of the weight loss due to melting indicate that the glasses are within 1–2 wt% of desired compositions, consequently, the “as-batched” compositions are used in this study (Table 1). The obtained glasses were transparent, without visible bubbles in glasses [3].

Table 1. Compositions of studied glasses

Glass samples	Glass composition, x_i , mol %		
	La ₂ O ₃	SrO	B ₂ O ₃
1	5.7	22.9	71.4
2	9.5	19.1	71.4
3	14.3	14.3	71.4
4	19.1	9.5	71.4

The density of the glasses was determined using the pycnometer method. Glass samples were previously crushed, grinded and dried. Distilled water. The Fourier transform infrared spectroscopy (FTIR) was performed using MB Bomen Hartmann FTIR spectrometer in the wave number range 2000–400 cm⁻¹. The pellets for analysis were obtained by hand pressing the mixture of powdered glass and KBr.

RESULTS AND DISCUSSION

The density (ρ) of the glass samples determined in the present study are given in Table 2. The molar volume (V_m) of the glass samples, was calculated using the relative molecular mass (M) and density (ρ) by the following relation [4]:

$$V_m = \frac{\rho}{M}, \quad (1)$$

These values are included in Table 2 together with oxygen molar volume (V_o) and oxygen packing density (OPD) calculated using the following relations:

$$V_o = V_m \cdot \frac{1}{n}, \quad (2)$$

$$OPD = 1000 \cdot \frac{\rho}{M} \cdot n, \quad (3)$$

where n is the number of oxygen atoms per formula unit.

Table 2. Density (ρ) of the glass samples

Glass samples	ρ (g/cm ³)	V_m (cm ³ /mol)	V_o (cm ³ /mol)	OPD (mol/dm ³)
1	3.21	28.65	11.28	88.68
2	3.25	30.90	11.81	84.70
3	3.56	31.21	11.50	86.95
4	3.66	33.26	11.84	84.45

The density and molar volume of the glasses increase with increasing La₂O₃ content in glasses. The increase of the density could be explained by considering the higher relative molecular mass of lanthanum oxide as compared to relative molecular mass of strontium oxide. With increasing La₂O₃ content in glasses increase oxygen content that leads to formation of excess free volume and increasing molar volume of glass that opens up the glass structure. Oxygen molar volume increases opposite to oxygen packing density with increasing La₂O₃ content in glasses, indicating less tightly packing of glass network.

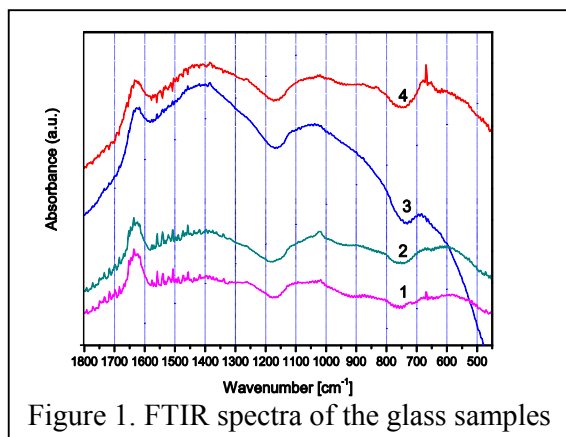


Figure 1. FTIR spectra of the glass samples

The IR absorption spectra of the glasses in the wave number region 2000-400cm⁻¹ are shown in Fig 1.

There are three main absorption bands at 1150-1600 cm⁻¹, 750-1150 cm⁻¹ and 400-750 cm⁻¹ that are independent of La₂O₃ content.

In addition, there is a peak at about 1640 cm⁻¹. The

absorption band in the region $1150\text{-}1600\text{ cm}^{-1}$ can be attributed to stretching vibration of $[\text{BO}_3]$ units with or without non-bridging oxygen [5]. Stretching of B-O bond in $[\text{BO}_4]$ tetrahedral units in various structural groups are found in the range $750\text{-}1150\text{ cm}^{-1}$ [5]. The third region $400\text{-}750\text{ cm}^{-1}$ appears due to the bending of B-O-B bonds in $[\text{BO}_3]$ and $[\text{BO}_4]$ units [6]. The band observed at $\sim 1640\text{ cm}^{-1}$ can be attributed to OH bending [7].

CONCLUSION

Investigation of the physical features of glasses showed that substitution of SrO by La_2O_3 increased the density, molar volume, oxygen molar volume and decreased oxygen packing density. The density increase is attributed to higher relative molecular mass of the glass containing more of La_2O_3 . The increasing of the molar volume can be explained by the increase of oxygen content that leads to formation of excess free volume. The decrease of the oxygen packing density indicates less tightly packing of glass network. Structural investigations show that glass structure consists of $[\text{BO}_3]$ and $[\text{BO}_4]$ units.

ACKNOWLEDGEMENT

The authors are grateful to the Ministry of Education, Science and Technological Development of the Republic of for financial support (Projects 172004 and 34001).

REFERENCES

- [1] M. Kaur, O. P. Pandey, S. P. Singh, *J Non Cryst Solids*, 2012, 358, 2589-2596.
- [2] J. E. Shelby, *Introduction to Glass Science and Technology*, The Royal Society of Chemistry, Cambridge, 2005.
- [3] S. Smiljanić, S. Grujić, M. Tošić, V. Živanović, J. Stojanović, S. Matijašević, J. Nikolić, *Ceram Int*, 2014, 40, 297-305.
- [4] S. Bale, S. Rahman, A.M. Awasthi, V. Sathe, *J Alloy Compd*, 2008, 460, 699-703.
- [5] Y. D. Yiannopoulos, G. D. Chyssikos, E. I. Kamitsos, *Phys Chem Glasses-B*, 2012, 42, 164-172.
- [6] E. Mansour, *J Mol Struct*, 2012, 1014, 1-6.
- [7] B. V. R. Chowdari, Z. Rong, *Solid State Ionics*, 1996, 90, 151-160.

INTERCALATION OF CATIONIC SURFACTANTS IN HIGH CHARGE MICAS

C. Blanco Delgado, C. Pesquera González, A. C. Perdigón Aller, B. Ortiz Marina, F. González Martínez, F. Aguado

Department of Chemistry and Process & Resources. 1 Department of Earth Science and Condensed Matter Physics. University of Cantabria. Av. Los Castros s/n 39005-Santander. Spain. (blancoc@unican.es)

ABSTRACT

We present in this work a insight into the intercalation properties of swellable high charge micas, with long primary, tertiary and quaternary amines. The organo-clay structure of the product has been analyzed using X-ray diffraction techniques. Thermogravimetric analysis and Fourier transform infrared spectroscopy have provided valuable information about the distribution and packing properties of the organo-clays, helping in the identification of the exchanged products. Special attention has been paid to the surfactant head group effect in the intercalation properties of high charge micas, mainly governed by the high layer charge of the silicate and by steric effects.

INTRODUCTION

Synthetic aluminosilicates with high negative charge, mica-type, have a great scientific interest due to their high cationic exchange capacity, compared with natural clays [1]. These synthetic mica-type silicates can have up to 468 meq/100g, while other swelling clays have a moderate layer charge with typical values as 80 meq/100g (Wyoming montmorillonite) to 170 meq/100g (saponite). Hence, they can be used as potential efficient adsorbents in the elimination of water contaminants and in the capture and immobilization of waste with high radioactivity [2-3]. On the other hand, high charge micas have showed recently a good capacity as novel precursors of mesoporous materials [4] with enhanced acidity for using in catalysts. Finally, it is necessary to improve the accessibility conditions in the interlayer space of the clay through the diffusion of surfactants and then, to overcome the electrostatic attraction in the clay.

In this work the intercalation properties of swellable high charge micas, with long primary, tertiary and quaternary amines are studied. The organo-clay structure of the product has been analyzed by using X-ray diffraction and Thermogravimetric analysis and Fourier transform infrared spectroscopy. It is important to study the effect of the surfactant head group

in the intercalation properties of high charge micas, mainly governed by the high layer charge of the clay and by steric effects.

EXPERIMENTAL

The synthesis of high charge micas with 4 negative charges per unit cell is made following the “NaCl melt” method described by Park et al. [5]. In order to get the ideal chemical composition $Na_nMg_6Si_{8-n}Al_nO_{20}F_4 \cdot xH_2O$ ($n = 4$) it was necessary to use near stoichiometric powder mixtures of SiO_2 , $Al(OH)_3$, MgF_2 , and an excess of NaCl. Reactants were well mixed by grinding and allowed to react in a Pt crucible at 900 °C for 15 h. After cooling, it was necessary to eliminate any soluble impurities present in the samples, for that, the samples were washed with deionized water. Finally, the samples were dried at room temperature. Its cation exchange capacity (CEC) is 468 mequiv/100g. The samples were characterized by powder X-ray diffraction for phase purity.

In order to open the clay layers, sodium saturated clays were left to react in a water solution of different ionic alkylammonium surfactants with the same alkyl chain length but different polar head group. With the following neutral amines: hexadecylamine [R-NH₂] and N,N dimethylhexadecylamine [R-N(CH₃)₂], the cations were obtained by protonation reaction with chlorhidric acid. In the other case, a quaternary ammonium salt of hexadecyltrimethylammonium [R-N(CH₃)₃⁺] was used. The organic-clays were prepared by cationic exchange reaction with the different surfactants. The concentration of ammonium components were 2.0 CEC of the clay, changing the temperature and time of contact in function of the size of the surfactants polar head until equilibrium. The organo-clay was recovered by centrifugation. The products were washed with deionised water to remove the excess of surfactants, and dried at room temperature

X-ray powder diffraction were obtained with a Bruker D8 Advance instrument from 1.5° to 10° 2θ.

Thermal analyses were performed in air atmosphere in TG-DSC Setaram equipment. In order to study the thermal decomposition of the organo-clay samples two regions were analyzed. The first one was between 25-160°C, which corresponds to the loss of the hydration water of the product. The second one, up to 850°C, due to the organic combustion of the surfactant intercalated between the layers in the mica.

Infrared spectra were obtained on Jasco 4200LE Fourier Transform Infrared spectrometer with a nominal resolution of 4 cm⁻¹. To obtain IR spectra KBr pressed disk technique was used.

RESULTS AND DISCUSSION

From the XR diffraction analysis (Table 1) is observed that the intercalation of the cationic surfactants between the layers in the raw mica has been successfully performed, because there is an increase of the basal spacing from 1.21 nm for the raw mica to 4.42 nm for the intercalated sample with the primary amine (R-NH₃⁺-Mica). In Table 1 is only collected the data of the first line reflection, but it is possible to observe up to five 00l reflections. This suggests a homogeneous distribution of the alkylammonium cations in the interlayer space of the mica.

Table 1. Molecules of water and ionic surfactants per unit cell and basal spacings of Na-4-Mica and intercalate samples.

Sample	Molecule H ₂ O/u.c.	Cation surfact./u.c.	d ₀₀₁ (nm)
Na-4-Mica	3.19	-	1.21
R-NH ₃ ⁺ -Mica	0.09	3.40	4.42
R-NH(CH ₃) ₂ ⁺ -Mica	1.62	1.79	3.27
R-N(CH ₃) ₃ ⁺ -Mica	1.84	1.11	3.84

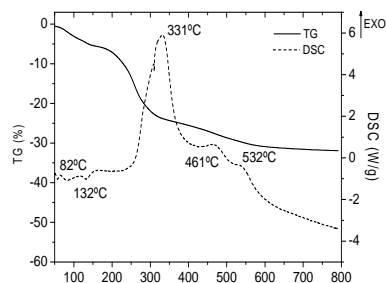


Figure 1. TG-DSC of R-N(CH₃)₃⁺-Mica sample.

It is remarkable that all the organo-clay samples reached a much greater interlayer spacing than in smectite or vermiculite clays for a similar process. This agrees with the much higher layer charge of the mica. Different arrangements of the alkylammonium cations in the interlayer space of the clays can be possible. When the arrangements were a paraffin-type structure, the distance reached for those clays was greater than 2.20 nm [6]. In our samples the smaller interlayer distance reached is 2.31 nm (taking into account that the height of the layer is 0.96 nm) for the R-N(CH₃)₃⁺-Mica, this indicate that their arrangements will be as a bilayer paraffin-type structure with an angle on the solid surface.

The thermal analysis results, Table 1, indicated that the cationic surfactants incorporated in the interlayer space of the mica were increased when the polar head size was decreased, reaching 3.40 cation surfactants per unit cell for the primary amine. Moreover, it was found that while the Na-4-Mica had 3.19 water molecules per unit cell, the water content in the organo-clay samples decreased to 0.09 molecules for the R-NH₃⁺-Mica sample. (In

Figure 1 TG-DSC of one of the samples has been added as an example). These results indicated that the synthesized samples showed a high hydrophobic character and they could be as potential efficient adsorbents in the elimination of water contaminants. The IR spectra (not show) of the organo-clay samples display new bands with respect to the raw mica due to the intercalated surfactants. The following bands are found in all the synthesized samples: Two bands at 2919 and 2848 cm^{-1} assigned to the asymmetric and symmetric methylene stretching [$\nu(\text{CH}_2)$]. The band at 2954 cm^{-1} ascribed to asymmetric stretching band of [$\nu(\text{CH}_3)$], and the band at around 1469 cm^{-1} is due to a bending vibration of the methylene groups [$\delta(\text{CH}_2)$]. The band at around 1021 cm^{-1} is assigned to bending vibration of C-N bond. For the R-NH₃⁺-Mica sample is also observed two new bands due to the primary amine, at around 1633 and 723 cm^{-1} assigned to the symmetric stretching and bending vibration of N-H bond respectively. These indicate the interaction between the cationic surfactants with the surface of the mica.

CONCLUSION

The synthesis of organo-micas from swellable high charge micas, with long primary, tertiary and quaternary amines has been successfully. The properties of these synthesized samples are function of the surfactant head group. It is found, from the XR diffraction analysis, that there is a homogeneous distribution of the alkylammonium cations in the interlayer space of the mica. Moreover, the synthesized samples show a high hydrophobic character and they could be as potential efficient adsorbents in the elimination of water contaminants.

ACKNOWLEDGEMENT

This work was supported by the Universidad of Cantabria (Project 51.VP10.64005).

REFERENCES

- [1] M. Gregorkiewitz, J. A Rausell-Colom, *Am. Mineral.*, 1987, 72, 515-527.
- [2] R. Ravella, S.Komarneni, C. E. Martínez, *Environ. Sci. Technol.*, 2008, 42, 113-118.
- [3] M.D. Alba, M.A. Castro, M. Naranjo, E. Pavón, *Chem. Mater.*, 2006, 18, 2867-2872.
- [4] A.C. Perdigón, D. Li, C. Pesquera, F. González, B. Ortiz, F. Aguado, C. Blanco, *J. Mater. Chem. A*, 2013, 1, 1213-1219.
- [5] M. Park, D. H. Lee, C.L.Choi, S.S. Kim, K.S. Kim, J. Choi, *J. Mater. Chem.*, 2002, 14, 2582-2589.
- [6] W.D. Johns, P.K. Sen Gupta, *Am. Mineral.*, 1967, 52, 1706-1724.

THE EFFECT OF BORON DOPING ON THE STRUCTURE AND PROPERTIES OF CARBONIZED HYDROTHERMAL CARBON

A. Kalijadis, J. Đorđević, T. Trtić-Petrović and Z. Laušević

Laboratory of Physics, Vinča Institute of Nuclear Sciences, University of Belgrade, P. O. Box 522, 11001 Belgrade, Serbia (anaudovicic@vinca.rs)

ABSTRACT

Structural and surface characterization of pristine and boron doped carbonized hydrothermal carbons (CHTC) is reported. Boron was introduced into glucose precursor solution with concentration of 0.2% and 1%. Following hydrothermal treatment, samples were carbonized to 1000°C and examined by Raman spectroscopy and temperature programmed desorption. Characterization of obtained samples as material for carbon paste electrode was performed by cyclic voltammetry measurements of the Fe (CN)₆^{3-/4-} redox couple. Structural analysis showed that lower boron content in precursor solution induced structure ordering, while higher amount of boron caused structural disorder of CHTC sample. Boron presence in CHTC samples reduced number of surface active sites for oxygen adsorption and consequently improved their electrochemical response as electrode material for carbon paste electrode.

INTRODUCTION

In recent years hydrothermal carbonization has demonstrated its capability of converting carbohydrate into highly functionalized carbon materials under mild processing conditions [1]. After additional carbonization, hydrothermal carbons (HTC) with various shape size, chemical compositions, and surface functional groups have shown novel and interesting intrinsic properties which allow widespread use of these materials [2].

Incorporation of heteroatoms into carbon materials affects their surface properties and oxidation resistance. Boron is by far the most widely used doping element in carbon. It enters the graphite lattice by substituting for carbon at the trigonal sites and consequently alters the electronic properties of the material [3].

The aim of this study was to investigate the effect of boron incorporation on the structural and surface characteristics of carbonized HTC. Additionally,

electrochemical characterization of carbonized boron doped HTC as material for carbon paste electrode was examined.

EXPERIMENTAL

To produce HTC, 2M water solution of D(+)-Glucose was prepared. Boric acid was used as source of boron and it was added in the starting solution to obtained boron concentration of 0.2% and 1%. After sealing, the autoclave was heated in programmable oven for 24 h at 180°C. All HTC samples were additionally carbonized in nitrogen to 1000°C. Obtained samples were marked as CHTC (undoped carbonized hydrothermal carbon) and boron doped samples as CHTCB_{0.2} and CHTCB₁.

Raman spectra were taken with an Advantage 532 Raman spectrometer (DeltaNu Inc.).

Temperature programmed desorption (TPD) in combination with mass spectrometry was used to investigate the quantity of surface oxygen groups. Evolution of CO and CO₂ to 1000°C was monitored with a quadrupole mass spectrometer (Extorr).

Carbon paste was made by intimate hand-mixing of carbonized HTC powders with the paraffin oil as a liquid binder. All pastes, homogenized at the same ratio of 1.2 g of material and 0.4 cm³ paraffin oil, were packed into a piston-driven Teflon holder.

A 797 VA Computrace analyzer (Metrohm) controlled by 797 VA Computrace software ver. 1.2 was applied for all voltammetric measurements.

RESULTS AND DISCUSSION

Table 1. Raman spectra parameters for CHTC, CHTCB_{0.2} and CHTCB₁

Sample	Peak	Peak position (cm ⁻¹)	Bandwidth (cm ⁻¹)	I _D /I _G
CHTC	D	1347	205	2.22
	G	1579	106	
CHTCB _{0.2}	D	1345	200	1.95
	G	1575	90	
CHTCB ₁	D	1345	215	2.6
	G	1580	103	

Table 1 shows Raman spectra parameters. The main features of these spectra are two broad peaks at 1350 cm⁻¹ (D band) and at 1590 cm⁻¹ (G band), commonly observed in mixture of graphitic and disordered sp²-bonded carbon. There are no significant changes in G and D peak positions

for CHTCH and CHTCB₁. However, the D peak bandwidth increased because of higher amount of B atoms, which occupy the lattice points to a greater extent and behave as defects for Raman scattering (higher values for I_D/I_G). For CHTCB_{0.2} sample all Raman parameters indicate increasing of structure ordering.

Table 2. Amounts of evolved CO, CO₂ and CO+CO₂ for CHTC, CHTCB_{0.2} and CHTCB₁

Sample	Q _{CO} (μmol/g)	Q _{CO₂} (μmol/g)	Q _{CO₂+CO} (μmol/g)
CHTC	195.9	115.9	311.8
CHTCB _{0.2}	24.6	15.9	40.5
CHTCB ₁	73.6	21.5	95.1

Amounts of evolved CO₂, CO obtained by TPD are summarized in Table 2. It can be noted that amounts of released CO₂ and CO for B doped samples are several times less compared to CHTC. This indicates that boron incorporation induced changes in electronic structure by reducing number of surface active sites for oxygen adsorption.

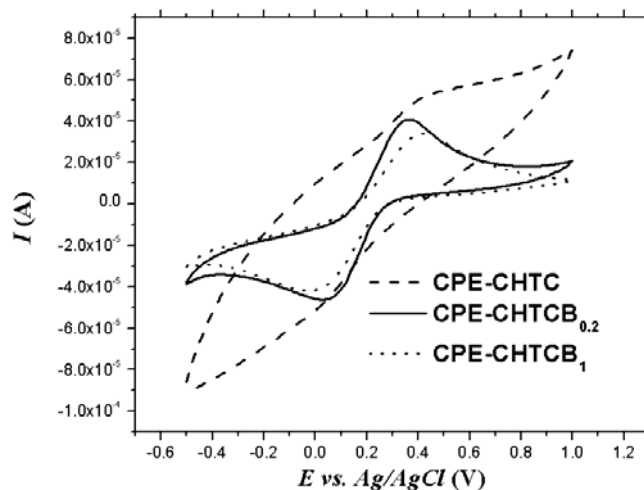


Figure 1. Cyclic voltammograms (50 mVs^{-1}) for $1 \text{ mmol K}_3\text{Fe}(\text{CN})_6 / \text{K}_4\text{Fe}(\text{CN})_6$ for electrode made from CHTC, CHTCB_{0.2} and CHTCB₁

Figure 1. shows cyclic voltammograms of $\text{Fe}(\text{CN})_6^{3-/4-}$ for carbon paste electrodes made from carbonized HTC samples (CPE-CHTC, CPE-

CHTCB_{0.2}, and CPE-CHTCB₁). It can be noted that on CPE-CHTC Fe (CN)₆^{3-/4-} exhibited a poor electrochemical behavior with broadened wave shape and high capacitive background current. Granger et al. [4] previously reported that several factors are known to influence redox-reaction kinetics at sp² carbon electrode: surface cleanliness, presence of adsorbed layers and fraction of edge plane exposed. According TPD results, the highest amount of surface oxygen groups was obtained for CHTC sample (Table 2), which caused the poor electrochemical behavior. Contrary to this, for boron doped samples drastically improved electrochemical responses were obtained and results are in compliance with TPD results. However, boron fraction of 1% worsens peaks intensity as well as the peak to peak potential separation compare to fraction of 0.2%.

CONCLUSION

Results showed that the different amount of boron allows obtaining carbonized hydrothermal carbons with modified structural, chemical and electrochemical characteristics compared to the pristine sample. It was shown that boron concentration of 0.2% in precursor solution generates structure ordering of carbonized sample, which induced a greater extent of surface active sites reduction for oxygen adsorption compared with sample with higher boron concentration. Modification of hydrothermal carbon with boron and its additional carbonization facilitate preparation of the material with good surface properties, which are important for the development and application of this material as a carbon paste electrode.

ACKNOWLEDGEMENT

We acknowledge the support to this work provided by the Ministry of Education and Science of Serbia through project *Physics and Chemistry with Ion Beams*, No. III 45006.

REFERENCES

- [1] B. Hu, K. Wang, L. Wu, S.-H. Yu, M. Antonietti, and M.-M. Titirici, *Advanced Materials*, 2010, 22, 813–828.
- [2] J. Hu, H. Li, X. J. Huang, *Solid State Ionics*, 2007, 178, 265-271.
- [3] X. Wu, L.R. Radovic, *Carbon*, 2005, 431, 1768–1777.
- [4] M. C. Granger, M. Witek, J. Xu, J. Wang, M. Hupert, A. Hanks, M. D. Koppang, J. E. Butler, G. Lucazeau, M. Mermoux, J. W. Strojek, and G. M. Swain, *Analytical Chemistry*, 2000, 72, 3793-3804.

THERMAL TREATMENT INFLUENCE ON THE SURFACE CHARACTERISTICS OF THE BORON-DOPED HYDROTHERMAL CARBON

A. Kalijadis¹, M. Vukčević², M. Maletić³, M. Laušević² and Z. Laušević¹

¹Laboratory of Physics, Vinča Institute of Nuclear Sciences, University of Belgrade, P.O.Box 522, 11001 Belgrade, Serbia (anaudovicic@vinca.rs)

²Faculty of Technology and Metallurgy, University of Belgrade, Kernegijeva 4, 11001 Belgrade, Serbia

³Innovation center Faculty of Technology and Metallurgy, University of Belgrade, Karnegijeva 4, 11000 Belgrade, Serbia

ABSTRACT

Boron-doped carbons were produced using hydrothermal carbonization of glucose carbohydrates under mild temperature (180°C). Boric acid was introduced into glucose precursor solution in order to obtain boron concentration of 0.2% and 1%. Two types of samples were prepared: hydrothermal carbons (HTC) and hydrothermal carbons thermally treated to 1000°C (HTCc). Characterization of the samples obtained was performed by scanning electron microscopy (SEM) and Fourier Transform Infrared Spectroscopy (FTIR). SEM analysis showed that higher boron concentration in the precursor solution caused enlargement of particle size for both types of samples, while the thermal treatment induced decrease of particle size. FTIR spectra showed that the different amount of boron in the precursor solution induced quite diverse effects on the surface chemistry of hydrothermal carbons before and after the thermal treatment.

INTRODUCTION

In the past decade, the hydrothermal treatment of carbohydrate gained an increasing interest in the field of material science. Many studies already focus on both applications and fundamental aspects motivated by the interest in producing carbonaceous powders with tunable sizes and surface properties [1]. The important advantage of hydrothermal carbon (HTC) is undoubtedly the possibility of modifying the surface or the bulk of the carbonaceous network by introducing heteroatoms.

Boron is by far the most widely used doping element in carbon. It has been suggested that boron-doping can introduce boron atoms into the substitutional positions in the carbon lattice. Also, boron can be distributed in the bulk of the carbon materials and can act as an intrinsic inhibitor which

reduces both the number of active sites and the reactivity of these sites [2]. Our previously obtained results showed that the number and nature of active sites, and consequently, the formation of surface oxides, depend on the distribution of boron in the polymer precursors [3].

After additional carbonization, hydrothermal carbons with various shape, size and surface functional groups have shown novel and interesting intrinsic properties which allow widespread use of these materials [4]. The aim of this study was to investigate effect of the thermal treatment on the morphology and the surface properties of boron doped HTC.

EXPERIMENTAL

To produce HTC, 2M water solution of D(+)-Glucose was prepared. Boric acid was used as source of boron and it was mixed with starting solution to obtained boron concentration of 0.2% and 1%. After sealing, the autoclave was heated in programmable oven for 24 h at 180°C. Obtained samples were marked as HTC, HTC/B_{0.2} and HTC/B_{1.0}. Each type of HTC samples were additionally carbonized in nitrogen to 1000°C and these samples were marked as HTCc, HTCc/B_{0.2} and HTCc/B_{1.0} (thermally treated samples).

Surface structure and morphology were studied by scanning electron microscopy (Mira Tescan X3). The functional groups of examined samples were identified with Fourier transform infrared (FTIR) spectroscopy (Bomem MB-Series, Hartmann & Braun). The FTIR measurements were performed at wavelengths in the range 4000–400 cm⁻¹.

RESULTS AND DISCUSSION

The SEM photographs of the hydrothermally carbonized samples and thermally treated samples are shown in Figure 1. In general, the morphologies of all samples consisting of carbon spheres with smooth surface. For both type of samples presence of 1% of boron in precursor solution induced a significant increase in particle size. For thermally treated samples general trend is the decrease of average particle size compared to hydrothermally carbonized samples, caused by the mass loss and shrinkage which occurred during thermal treatment.

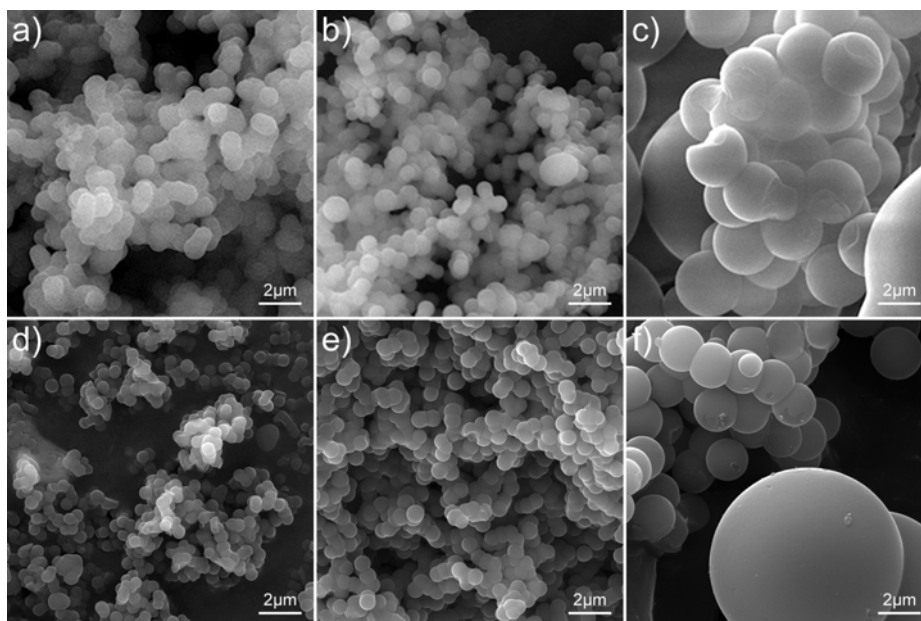


Figure 1. SEM photographs of all tested samples: a) HTC, b) HTC/B_{0.2}, c) HTC/B₁, d) HTCc, e) HTCc/B_{0.2} and f) HTCc/B₁

Figure 2 shows FTIR spectra of examined samples. The wide band between 3000 and 3700 cm^{-1} is assigned to the stretching vibrations of O-H (hydroxyl or carboxyl), and the bands around 2815–3000 cm^{-1} are the characteristic stretching vibrations of aliphatic C-H. The absorption bands near 1710 cm^{-1} is attribute to stretching vibration of -C=O from carbonyl and carboxyl groups. The out-of-plane bending vibration of aromatic C-H bands was observed in the region of 875–750 cm^{-1} , and the band at 1620 cm^{-1} are attributed to the C=C vibrations [5], suggesting the aromatization of the samples during the hydrothermal treatment. For hydrothermally carbonized samples boron addition of 0.2% in the precursor solution induced the formation of the highest number of the surface actives sites, while further increase of boron content reduced the number of surface actives sites. However, after thermal treatment FTIR spectra for sample HTCc/B_{0.2} shows the lowest intensity of the bands, indicating that incorporated boron acts as an inhibitor for formation of active sites. On the other hand, for the sample HTCc/B_{1.0} boron presence had catalytic effect on the formation of surface active sites.

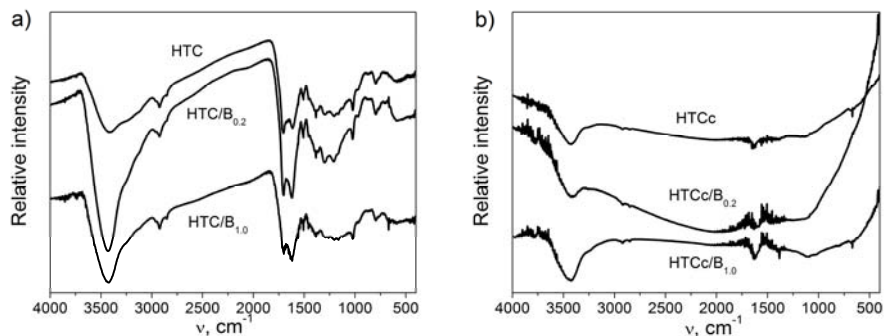


Figure 2. FTIR spectra of examined samples: a) before and b) after thermal treatment to 1000°C

CONCLUSION

It was established that boron addition of 1% into the precursor solution induces significant enhancement of the particles size for both hydrothermal carbon and thermally treated hydrothermal carbon. As it was expected, thermal treatment leads to decrease of particle size as a consequence of the mass loss and shrinkage processes. FTIR results show that thermal treatment induced reduction of the amount of surface oxygen groups. Nevertheless, for carbonized samples different amount of boron has quite a distinctive effect on the surface chemistry compared to untreated samples. Obtained results suggest that by applying boron addition and thermal treatment it is possible to create desired structural and surface properties of hydrothermal carbon.

ACKNOWLEDGEMENT

The authors wish to thank the Ministry of Education, Science and Technological Development of the Republic of Serbia for financial support through the projects No 45006 and No. 172007.

REFERENCES

- [1] C. Falco, N. Baccile, M.-M. Titirici, *Green Chemistry*, 2011, 13, 3273-3281.
- [2] X. Wu, L.R. Radovic, *Carbon*, 2005, 43, 1768–1777.
- [3] A. Kalijadis, Z. Jovanović, M. Laušević, Z. Laušević, *Carbon*, 2011, 49, 2671–2678.
- [4] J. Hu, H. Li, X. J. Huang, *Solid State Ionics*, 2007, 178, 265-271.
- [5] C.-M. Chen, Q. Zhang, M.-G. Yang, C.-H. Huang, Y.-G. Yang, M.-Z. Wang, *Carbon*, 2012, 50, 3572-3584

SURFACE MODIFICATION OF ZIRCONIA NANOPARTICLES WITH SELECTED ENEDIOL LIGANDS

M. Carević, T. D. Savić, N. D. Abazović,
I. A. Janković and M. I. Čomor

*University of Belgrade, Vinča Institute of Nuclear Sciences, P.O. Box 522,
11001 Belgrade, Serbia*

ABSTRACT

The colloidal ZrO₂ nanoparticles were hydrolytically synthesized and characterized using x-ray diffraction and UV/Vis spectroscopy. The surface modification of nanocrystalline particles with selected enediol ligands: catechol (CAT), 2,3-dihydroxynaphthalene (2,3-DHN), anthrarobin (ANT) and quercetin, was found to alter the optical properties of nanoparticles. The formation of the inner-sphere charge-transfer (CT) complexes results in a red shift of the semiconductor absorption onset compared to unmodified nanocrystallites, and a decrease of effective band gap upon increase of the electron delocalization after the inclusion of additional rings.

INTRODUCTION

Widespread interest in the modification of TiO₂ surfaces with organic and organometallic molecules is largely motivated by the application of these materials in photocatalysis and photovoltaics [1]. Similar behavior can be expected from the other non-toxic metal oxides like ZrO₂ which is the subject of this paper. In recent years, much attention has been paid to the preparation of high surface nano-zirconia, not only due to its wide application as a catalyst and catalyst support, but also for its use as an advanced material for structural engineering ceramics, oxygen sensors, fuel cells, and other interesting applications [2]. Zirconia has a large band gap, $E_g = 5$ eV, even larger than TiO₂ ($E_g = 3.2$ eV) and absorbs in far UV region [3]. We hope that sensitization of ZrO₂ crystals and nanoparticles with appropriately chosen molecules, enediol ligands, can lead to a significant red shift of their absorption threshold from the far UV to the visible, thus enabling and improving the absorption of the solar spectrum as well as its possible application as photocatalyst and photovoltaic material.

EXPERIMENTAL

All chemicals used were of highest possible quality (p.a.), Milli-Q deionized water was used as a solvent. The colloidal ZrO₂ dispersions were prepared by forced hydrolysis of ZrOCl₂ at 75°C for 24 hours with constant stirring. After hydrolysis clear dispersion was dialyzed against water until pH=5 was reached. Stoichiometric concentration of ZrO₂ was $\leq 0.06 \text{ M dm}^{-3}$. Crystal structure of the obtained zirconia was checked by using X-ray diffraction.

For XRD analysis, obtained colloidal ZrO₂ dispersions were dried on Si-carrier and XRD data were collected in 2θ range of 10°-60°, with scanning steps of 0.05°. As can be seen (Figure 1), crystal structure of obtained material is not quite developed yet.

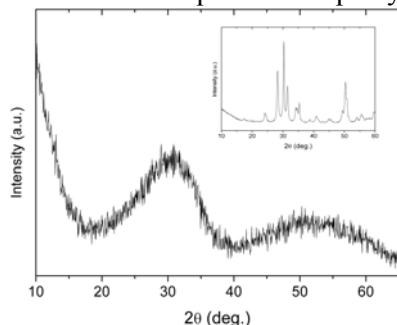


Figure 1. X-ray diffractogram of colloidal ZrO₂ dispersion. Inset: X-ray diffractogram of the same sample sintered at 600°C for 3h

Wide peaks and shoulders in diffractogram imply on presence of both amorphous and crystallized material. In order to confirm a formation of ZrO₂ nanocrystals, obtained material was dried at 70°C, and then sintered at 600°C for 3h. XRD data of acquired powder (Inset in Fig 1.) confirmed exclusive presence of ZrO₂ (mixed monoclinic and tetragonal phase).

The surface modification of ZrO₂ resulting in the formation of a CT complex was achieved by the

addition of surface-active ligands (catechol, 2,3-dihydroxynaphthalene, anthrabin and quercetin; structural formulas in Table 1) up to the concentrations required to cover all the surface sites.

The modifications were performed in methanol and allowed to react for 24 h to ensure complete complexation. Absorption spectra of surface modified ZrO₂ nanoparticles were recorded at room temperature in cells with 1 cm optical path lengths using a Thermo Scientific Evolution 600 UV/Vis spectrophotometer.

RESULTS AND DISCUSSION

When ZrO₂ particles are on the nanosize scale, a large fraction of the atoms that constitute the nanoparticle is located on the surface with significantly altered electrochemical properties. Among them, the existing undercoordinated defect sites are the source of novel, enhanced and selective reactivity of nanoparticles toward ligand binding. Upon binding, the new hybrid properties arise from the ligand-to-metal CT interaction due to

orbital mixing between the molecular orbitals of the ligands and the conduction band orbitals of the nanoparticles.

Table 1. Ligands used for modification of ZrO₂ nanoparticles, structural formulas and the effective band gaps (E_g) upon binding

ligand	Structural formula	E _g (eV)
1.	ZrO ₂	5
2. CAT		3.35
3. 2,3-DHN		3.44
4. ANT		1.78
5. Quercetin		2.03

All of the ligands investigated in this work, listed in Table 1, were found to undergo binding at the surface (Fig. 2), inducing new hybrid properties of the surface modified nanoparticle colloids. These hybrid properties arise from the ligand-to-metal charge-transfer (CT) interaction. By extracting the corresponding onset energies from the absorption spectra of surface modified ZrO₂ nanoparticles, the effective band gap energies (E_g = hc/λ) of CAT, 2,3-DHN, ANT and quercetin modified ZrO₂ nanoparticles in methanol were calculated to be: 3.35 eV, 3.44 eV, 1.78 and 2.03 eV, respectively.

CONCLUSION

All investigated ligands (CAT, 2, 3-DHN, ANT and quercetin) form inner-sphere charge-transfer complexes with ZrO₂ nanoparticles (d ~4 nm). The binding of the modifier molecules to undercoordinated surface Zr atoms (defect sites) results in a significant shift in the onset of absorption to the lower energy spectral range. The lowest shift was, as expected, achieved by modification with catechol (enediol with one aromatic ring) and the highest

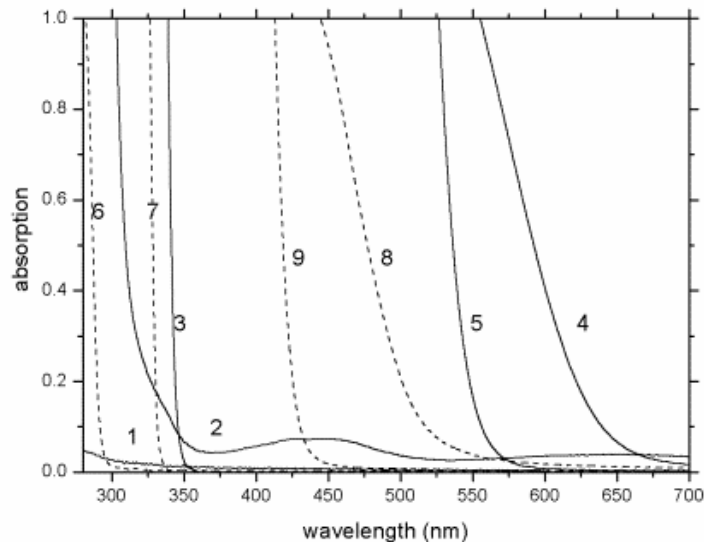


Figure 2. Absorption spectra of bare (1) and surface modified ZrO_2 nanoparticles with different ligands (0.45 mM): (2) CAT; (3) 2,3-DHN; (4) ANT, (5) quercetin. Spectra of pure modifiers are: (6)-(9), respectively.

with anthrabin (three fused aromatic rings) and quercetin (two fused rings with one as substituent), which proves positive effect of extended electron delocalization in modification.

ACKNOWLEDGEMENT

Financial support for this study was granted by the Ministry of Education, Science and Technological Development of the Republic of Serbia (Project 172056 and 45020).

REFERENCES

- [1] W. Macyk, K. Szaciłowski, G. Stochel, M. Buchalska, J. Kuncewicz, P. Łabuz, *Coord. Chem. Rev.*, 2010, 254, 2687-2701.
- [2] S.-F. Yin, B.-Q. Xu, *Chemphyschem.* 2003, 3, 277-281.
- [3] T. Rajh, L. X. Chen, K. Lukas, T. Liu, M. C. Thurnauer, D. M. Tiede, *J. Phys. Chem. B*, 2002, 106, 10543-10552.

SYNTHESIS OF GOLD NANOPARTICLES USING ALDEHYDE FUNCTIONALIZED LEVAN AS REDUCING AGENT

B. Kekez¹, G. Dj. Gojgić-Cvijović², D. M. Jakovljević²,
Lj. S. Živković³, V. P. Beškoski^{1,2} and M. M. Vrvic^{1,2}

¹Faculty of Chemistry, University of Belgrade, 11158 Belgrade, Studentski trg 16, P.O. Box 51, Serbia; ²Institute of Chemistry, Technology and Metallurgy, University of Belgrade, 11158 Belgrade, P.O. Box 473, Njegoševa 12, Serbia (djakovlj@chem.bg.ac.rs); ³Vinča Institute of Nuclear Science, University of Belgrade, 11001 Belgrade, P.O. Box 522, Serbia.

ABSTRACT

In this work, gold nanoparticles (AuNPs) were synthesized in aqueous solution by aldehyde functionalized microbial polysaccharide levan as a reducing agent. Resulting nanoparticles were characterized by UV-Vis spectroscopy and by particle size analysis.

INTRODUCTION

The field of nanotechnology is in significant development as a result of wide application in different areas. The unique properties of nanoparticles are directly related to their wide use. In the last years, the application of polysaccharides in preparing nanoparticles greatly increased due to high content of hydroxyl groups in the glycan molecule that represents excellent matrix for providing the stability of formed nanoparticles in solution [1,2]. In this context, levan has an interesting potential, because it represents the relatively unexplored member in this area. This microbial polysaccharide (Fig.1) generally consists of β -(2,6)-fructose residues and a one D-glucose residue at the nonreducing end of the chain. Branching that occurs through β -(2,1)-linkages is often short and sometimes consisting of a single fructose residue. Levans have the great potential for application in food, pharmaceutical, medical, cosmetic and chemical industries, due to high solubility in water, non-toxicity and biocompatibility [3]. Gold nanoparticles (size range 1-100 nm) have physical and chemical properties different from the same material in bulk form, preferably because of large surface/volume ratio. They exhibit, in comparison with other metals, unique optical, electronic and bioactivity properties [4].

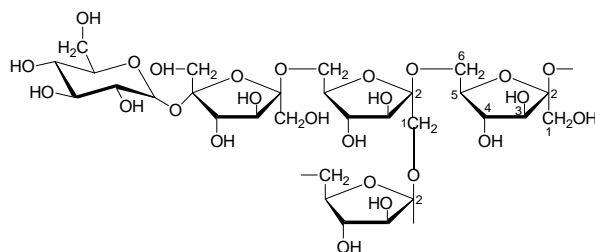


Figure 1. Structure of levan

This paper reports the formation of gold nanoparticles (AuNPs) in aqueous solution of partially oxidized levan with aim of obtaining potentially applicable nanoparticles in various fields.

EXPERIMENTAL

Aldehyde-functionalized levan was obtained in reaction with periodate salts in aqueous solution at room temperature for 24 h. The aqueous solution of 10 mM HAuCl_4 was mixed with aqueous solution of 0.062 mM partially oxidized levan, that has been previously purified by dialysis and lyophilization. This resulted in the almost immediate appearance of pale purple color which has become dark purple by heating at 100 °C for one minute. The obtained products were characterized by UV-Vis spectroscopy (GBC Cintra 40 spectrophotometer) and by photon correlation spectroscopy (PCS), instrument Zetasizer NS with 633 nm He-Ne laser (Malvern).

RESULTS AND DISCUSSION

The aqueous gold ions Au^{3+} were reduced to metallic gold Au^0 using aldehyde functionalized polysaccharide levan. Due to the high surface energy and extreme reactivity of AuNPs, the polysaccharide matrix of partially oxidized levan was stabilizing agent that prevented aggregation of obtained particles [5-7]. Levan contains different types of vicinal diol groups that can be subjected to periodate oxidation resulting in different types of dialdehyde structures.

The obtained particles were firstly characterized by UV-Vis data. UV-Vis spectrum of formed solution showed a strong absorption maximum at 520 nm (Fig. 2.) characteristic for AuNPs, due to its surface plasmon resonance. Their formation was confirmed visually too, based on the change in color of the solution, from pale yellow at the start of the reaction to dark purple.

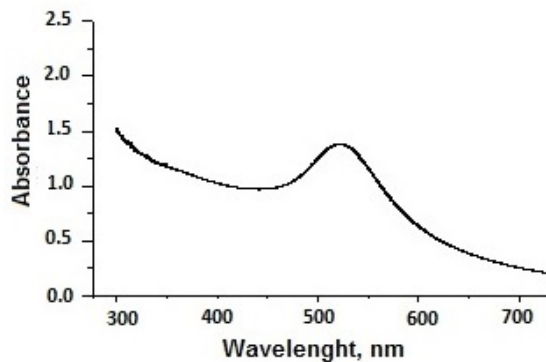


Figure 2. UV-Vis spectrum of gold particles synthesized by aldehyde functionalized levan

The size distribution of synthesized gold particles, based on backscattered light intensity, evidenced their nanometric size, Fig. 3. The strong Gaussian peak in the range 10-100 nm indicated that the particles exhibited mainly monomodal distribution (mean diameter of 95.5% particles 34.28 nm). A small amount (4.5%) of larger sized population (3010 nm) also present, pointed to some particles aggregation.

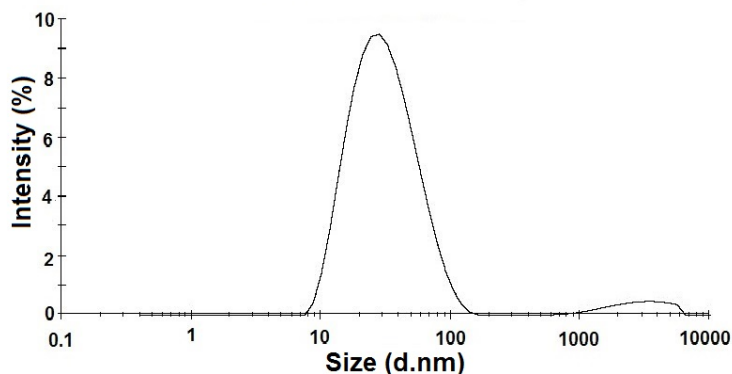


Figure 3. Size distribution of gold particles measured by PCS

CONCLUSION

In this work, a new route for the synthesis of gold nanoparticles in the aqueous medium using the aldehyde functionalized polysaccharide levan as a reducing agent was shown. The synthesis of AuNPs was confirmed by UV-Vis spectroscopy and by particle size analysis. Formation of thus obtained nanoparticles suggests that polyaldehyde levan is reducing agent as

well as stabilizing agent considering the stability of nanoparticles in this solution.

ACKNOWLEDGEMENT

This work was supported by the Ministry of Education and Science of the Republic of Serbia through Projects III 43004 and 45012.

REFERENCES

- [1] F. Freitas, V. D. Alves, M. A. M. Reis, *Trends Biotechnol.*, 2011, 29, 388-398.
- [2] A. M. G. C. Dias, A. Hussain, A. S. Marcos, A. C. A. Roque, *Biotechnol. Adv.*, 2011, 29, 142–155.
- [3] S. Pandey, G. K. Goswami, K. K. Nanda, *Carbohydr. Polym.*, 2013, 94 229–234.
- [4] L. Dykman, N. Khlebtsov, *Chem. Soc. Rev.*, 2012, 41, 2256-2282.
- [5] E. Callone, G. Carturan, M. Ischia, A. Sicurelli, *J. Mater. Res.*, 2007, 22, 3344-3354.
- [6] S. Hamed, S. M. Ghaseminezhad, S. A. Shojaosadati, S. Shokrollahzadeh, *Iran. J. Biotech.*, 2012, 10, 191-197.
- [7] C. K. Tagad, K. S. Rajdeo, A. Kulkarni, P. More, R. C. Aiyer, S. Sabharwal, *RSC Adv.*, 2014,4, 24014-24019.

REMARKABLE SORPTION PROPERTIES OF MgH₂-VO₂ NANOCOMPOSITES

S. Milošević¹, R. Vujasin¹, Lj. Matović¹, Ž. Rašković-Lovre¹, L. Pasquini²
and J. Grbović Novaković¹

¹*Vinča Institute of Nuclear Sciences, POB 522, 11000 Belgrade, Serbia
(radojka.vujasin@vinca.rs)*

²*Department of Physics and Astronomy, University of Bologna, v.le Berti
Pichat 6/2, I-40127 Bologna, Italy*

ABSTRACT

Composite of MgH₂□VO₂ has been synthesized by high-energy mechanical milling. The sorption properties of composites were examined by differential scanning calorimetry and sorption analysis. It has been shown that at relatively low temperature sorption reaction is notably enhanced. Complete desorption of pure MgH₂ at 380°C finishes after 30 minutes while composite material fully desorbs in less than 2 minutes even at lower temperatures.

INTRODUCTION

Much effort has been devoted on studies of metal hydrides for hydrogen storage. Metallic magnesium and magnesium based compounds are considered as promising candidates, since magnesium is an abundant, cheap and light metal with a high hydrogen sorption capacity (7.6 wt.%). Anyhow the problem of sluggish kinetics is main drawbacks of this material. It has been shown that high energy ball milling of magnesium hydride with various additives (oxide, non-oxide ceramics, amines etc.) improves the hydrogen sorption properties [1–3]. In contrast to bulk hydride, the form of fine powder has many advantages such large surface-to volume ratio which enhances hydrogen diffusion and nucleation of MgH₂. Regarding additives, metal oxide are both catalysts and very efficient milling agents that can create defects in magnesium hydride [4]. A wide range of different metal oxide was used to improve the properties of MgH₂ [5–7]. *Bobet et al.* reported the beneficial effect CeO₂ on MgH₂ sorption kinetics. *Bormann et al.* proposed that oxide interfaces attached to the oxide catalysts might locally destabilize the magnesium hydride phase [6]. *Oelerich et al.* investigated the influence of metal oxides on the sorption behaviour of nanocrystalline Mg-based systems [5]. The highest desorption rates are achieved with V₂O₅ and Fe₃O₄. Metal oxides, compared to the

MgH₂/transition metals composites, are dispersed homogeneously due to the brittleness. Oxides improves desorption kinetics even in very small doses. The fast sorption kinetics of composite may originate from a very high defect density, introduced at the surface of the metal oxide particles during high-energy ball milling [8].

On the other hand the catalytic nature of oxides originate from their vacant structure, therefore in this paper we have used VO₂(B) to enhance sorption properties of MgH₂

EXPERIMENTAL

Composite material was synthesized by high-energy ball milling using Spex 8000M mixer mill. 85 mass% of commercial of MgH₂ (Alpha Aesar 98%) and 15 mass % of hydrothermally synthesized VO₂(B) (from V₂O₅, Merck) was used as a precursors. Composite was milled for 2h using ball to powder ratio (BPR) 10:1. All samples were kept and handled in Ar atmosphere in a glove box. DSC measurements were performed in temperature range from 80 to 500°C, using 10K/min step. Desorption/absorption cycles were performed at different temperatures and corresponding pressures to determine the dependence of H₂ sorption concentration and temperature of activation using Hydrogen Sorption Analyser (HSA)

RESULTS AND DISCUSSION

HSA was used to examine the volume of hydrogen released from samples in a pre-set time period and temperature. In commercial MgH₂, at desorption temperature of 380°C, HSA curve reaches a plateau (maximum capacity of 5.7wt.%) after 30 min (see Fig. 1). At lower temperature (350°C) desorption begins only after 30 minutes, and after 100 minutes does not reach maximum desorption (reached ~4.5wt.%) even in a repeated cycle.

Also, capacity in absorption mode was significantly lower (~4.7wt.%) compared to absorption capacity at 380°C.

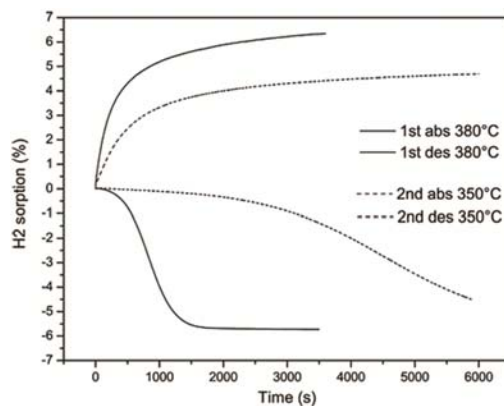


Figure 1. Sorption curves of commercial MgH₂

Milled composite material, with the addition of 15 mass% $\text{VO}_2(\text{B})$, shows significant acceleration of hydrogen desorption: at temperature of 360°C maximum capacity of 3.6 wt.% is reached after ~ 80 seconds. At 350°C , maximum desorption capacity of 3.6 wt.% is reached after ~ 95 seconds, and at temperature of 340°C capacity increases to 3.8wt.% and this value is reached after ~ 125 seconds (see Fig. 2).

DSC curves of commercial MgH_2 and composite material are shown in Figure 3. It can be see that temperature decreased from 454°C to 401°C with temperature onset at 385°C . Since the area under the peak is directly proportional to the change in enthalpy, by integration of DSC peaks it is obtained 1382J/g for commercial MgH_2 , and 1025J/g for synthesized composite. Decrease in enthalpy corresponds to decrease in hydrogen capacity which is in accordance with the results of hydrogen sorption measurements.

CONCLUSION

$\text{MgH}_2\text{-VO}_2$ composites were synthesized by mechanical milling. The sorption reaction was followed by differential scanning calorimetry and sorption analysis. Results indicate excellent catalytic activity of $\text{VO}_2(\text{B})$ in both adsorption and desorption process. The temperature onset for desorption is significantly decreased. The main fact is that composite demonstrate excellent reversibility in sorption reaction. The maximum capacity of hydrogen is released in less than 2 minutes from synthesized composites, representing a dramatic speed-up of kinetics performances comparing to the unprocessed MgH_2 .

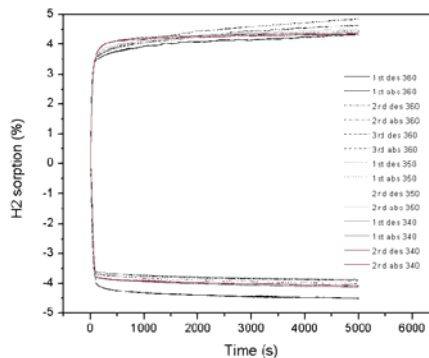


Figure 2. Cycling curves of composite material at 360°C

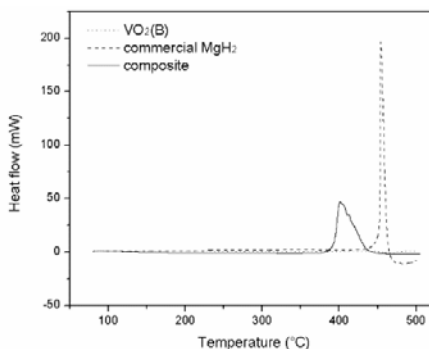


Figure 3. DSC curves of commercial MgH_2 and composite material

ACKNOWLEDGEMENT

This research was financially supported by Ministry of Education, Science and Technological Development of the Republic of Serbia under grant III 45012. The authors express their gratitude to COST Action MP1103 “Nanostructured Materials for Solid-State Hydrogen Storage”.

REFERENCES

- [1] L. Schlapbach, A. Zuttel, *Nature* 2001, 414, 353 – 358.
- [2] A. Zuttel, *Mater. Today*, 2003, 6, 24 – 33.
- [3] A. Bassetti, E. Bonetti, L. Pasquini, A. Montone, J. Grbovic, Vittori Antisari *Eur Phys J B* 2005, 43, 19 – 27.
- [4] *Hydrogen Fuel-production, transport and storage*, Taylor and Francis, 2008.
- [5] W. Oelerich, T. Klassen, R. Bormann, *J. Alloys Compd.* 2001, 315, 237 – 242.
- [6] J. L. Bobet, S. Desmoulins-Krawiec, E. Grigorova, F. Cansell, B. Chevalier, *J. Alloys Compd.* 2003, 351, 217 – 221.
- [7] A. Borgschulte, U. Bosenberg, G. Barkhordarian, M. Dornheim, R. Bormann. *Catal Today* 2007, 120, 262 – 269.
- [8] A. Borgschulte, M. Biemann, A. Zuttel, G. Barkhordarian, M. Dornheim, R. Bormann. *Appl. Surf Sci* 2008, 254, 2377 – 2384.

HYDROGEN DESORPTION FROM VACANT MgH₂

S. Kurko, R. Vujasin, A. Đukić, B. Paskaš Mamula, J. Grbović Novaković
and N. Novaković

*Vinča Institute for Nuclear Sciences, University of Belgrade, P.O. Box 522,
11000 Belgrade, Serbia (radojka.vujasin@vinca.rs)*

ABSTRACT

The hydrogen desorption properties of vacant MgH₂ structure were investigated both experimentally and theoretically. Ion irradiation by Ar⁸⁺ and Xe⁸⁺ ions were used to induce structural changes in MgH₂. Hydrogen desorption properties were investigated by temperature programmed desorption (TPD). To obtain deeper insight in structural changes during desorption theoretical calculations were performed using DFT approach within Abinit code. Results showed that there are several mechanisms involved in desorption process, which depend on defect concentration, their position and their interaction and ordering. It has been demonstrated that the changes in near-surface area play the crucial role in desorption kinetics.

INTRODUCTION

Magnesium and magnesium based alloys have a great potential as rechargeable hydrogen storage materials since its high hydrogen storage capacity (7.6 wt %) and reversible, relatively simple, endothermic hydrogen desorption reaction. However, slow kinetics and relatively high dehydrogenation temperature still limit its practical application [1]. Severe attempts have been made to overcome these drawbacks. The most used method is nanostructuring of material by mechanical milling with different types of dopants like transition metals, intermetallics, oxides, carbides [2-5], etc. Metal oxides such as VO₂ and CeO₂ that have vacant structure were proved as very effective catalysts [4, 5].

The other way to destabilize the MgH₂ structure and improve its hydrogen desorption kinetics is ion irradiation. By inert, heavy ion irradiation it is possible to create a considerable amount of defects, particularly vacancies and to control their quantity and depth distribution through sample [6]. It is especially important for the surface layer modification which condition is crucial for the hydrogen desorption properties of material. On the other hand, DFT calculations can give an insight in the stability of the system and consequently, the possible mechanism of desorption process. From these calculations one can also

determine the influence of vacancy position and concentration on the hydrogen desorption energy [7].

In this paper, mechanism of hydrogen desorption from MgH₂ irradiated with Ar⁸⁺ and Xe⁸⁺ ions is investigated and correlated with DFT calculation findings.

EXPERIMENTAL

Commercial (Alfa Aesar, (AA), of purity 98%, with initial mean particle diameter of 38 μm) MgH₂ powder was prepared as explained in our previous work and homogeneously irradiated using 120 keV and Ar⁸⁺ (sample A16) and Xe⁸⁺ (sample S16) ions with fluence of 10¹⁶ ions/cm² [6]. Interaction of incident ions with material was calculated using Monte Carlo method as implemented in SRIM package. X-ray analysis was by Siemens KRISTALLOFLEX D-500 device, with Cu-Kα Ni filtrated radiation (λ=1.5406 Å). Malvern 2000SM Mastersizer laser scattering particle size analysis system was used to obtain the quantitative MgH₂ particle size distributions. Homemade apparatus with a quadruple mass spectrometer EXTORR XT300 were used for TPD measurements. The kinetic parameters were deduced using non-isothermal approach.

For DFT calculations Abinit code and Troulliere Martins pseudopotentials were used. (110) plane was exposed and the supercell consists of 12 parallel atomic planes with total of 96 atoms, with H two-fold bonded surface atoms. The surface of the supercell was separated from its periodic image by 1,5 nm of vacuum.

RESULTS AND DISCUSSION

In the table 1 are given number of produced vacancies per incident ion and range of maximum ions in the sample. It can be seen that the Xe⁸⁺ ions produce about 50 % more vacancies than Ar⁸⁺ which are deposited nearer to

Table 1. SRIM, XRD, laser scattering and kinetic data for commercial (AA) and samples irradiated with Xe⁸⁺ (S16) and Ar⁸⁺ (A16) ions with fluence of 10¹⁶ ions/cm²

Sample	Produced vacancies per ion	Range maximum position (nm)	Crystallite size (nm)	Mean particle size (μm)	Avrami-parameter	E _a ^{des} (kJ/mol)
AA	-	-	83	38	3	372
S16	1818	85	45	21.7	4	97
A16	1244	175	76	22.6	2	215

the surface. XRD data showed small decrease in crystallite size for irradiated samples and shift of peaks towards higher angles as a consequence of material disordering. Besides, there are visible peaks of $\text{Mg}(\text{OH})_2$ and MgO phases in samples S16 and A16 as a consequence of high reactivity of MgH_2 towards oxygen and moisture from air. Mean particle size of irradiated samples is also reduced, but with no significant difference between samples A16 and S16. Hydrogen desorption temperatures are 720, 643 and 665 K for samples AA, S16 and A16 consequently. The best fitting of thermal data was achieved by using Avrami-Erofeev nucleation models and results given in table 1 show significant decrease in apparent activation energy for hydrogen desorption for both irradiated samples, but more pronounced for the sample S16. There can also be seen change in the dimensionality of nucleus growth from 3D in sample AA to 2D for A16 and random in S16. It can be assumed that the reduction of temperature and activation energies are caused

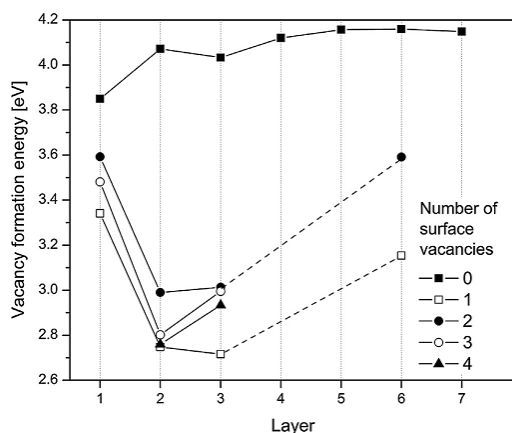


Figure 1. The H-vacancy formation energies in the (110) MgH_2 sub-surface layers as a function of surface coverage with H atoms. Configurations with 1 and 3H vacancies in 3rd and 6th layer are connected with dashed line.

by the increase of diffusion coefficient of hydrogen in subsurface layers of destabilized MgH_2 and increase in the number of active sites for hydrogen molecule recombination, both results of the vacant surface structure. This explanation is supported by Park et al. on type and behavior of defects in the magnesium hydride in conditions of extremely poor hydrogen, existing during dehydrogenation process [8]. These effects are dominant for the sample S16 that has more

vacancies closer to the sample surface. So, the concentration of defects has effect on desorption temperature and activation energy, while their position influences the reaction mechanism.

Results of DFT calculation (Fig. 1) showed that H-desorption energy strongly depends on number of surface H atoms and their configuration. Surface vacancies considerably lower the H-vacancy formation energies as well in the sub-surface layers. These results suggest that the role of surface

hydrogen concentration and distribution is decisive for the H-desorption kinetics, not only because of lowering the potential barrier for further H-desorption, but an increased number of surface hydrogen vacancies supports creation of the sub-surface vacancies network and make diffusion of bulk hydrogen atoms toward the surface easier.

CONCLUSION

The influence of structural changes induced by heavy ion irradiation using Ar and Xe ions on desorption properties of MgH₂. To obtain deeper insight in structural changes DFT calculations using Abinit code has been performed. It has been shown that the large concentration of the surface and near-surface vacancies promotes diffusion of H atoms toward the surfaces of grains, which lowers temperature and activation energy of H₂ desorption. Not only that concentration, but also the depth distribution of vacancies have strong influence on the desorption process.

ACKNOWLEDGEMENT

This research was financially supported by Ministry of Education, Science and Technological Development of the Republic of Serbia under grant III 45012.

REFERENCES

- [1] L. Schlapbach, A. Züttel, *Nature*, 2001, 414, 353-358.
- [2] J. Huot, G. Liang, S. Boily, A. Van Neste, R. Schulz, *J. Alloys Compd.*, 1999, 293, 495-500.
- [3] C. Suryanarayana, *Prog. Mater. Sci.*, 2001, 46, 1-184.
- [4] S. Milošević, Ž. Rašković-Lovre, S. Kurko, R. Vujasin, N. Cvjetičanin, Lj. Matović, J. Grbović Novaković, *Ceram. Int.*, 2013, 39, 51-56.
- [5] J. Gulicovski, Ž. Rašković-Lovre, S. Kurko, R. Vujasin, Z. Jovanović, Lj. Matović, J. Grbović Novaković, *Ceram. Int.*, 2012, 38, 1181-1186.
- [6] J. Grbović Novaković, Lj. Matović, S. Milovanović, M. Drvendžija, N. Novaković, D. Rajnović, M. Šiljegović, Z. Kačarević Popović, N. Ivanović, *Int. J. Hydrogen Energ.*, 2008, 33, 1876-1879.
- [7] A. J. Du, S. C. Smith, G. Q. Lu, *J. Phys. Chem. C*, 2007, 111, 8360-8365. 2008, 42, 337-351.
- [8] M. S. Park, A. Janotti, C. G. Van de Walle, *Phys Rev B*, 2009, 80, 064102.

GAMMA IRRADIATION INDUCED SYNTHESIS OF PbS/PVA HYDROGEL NANOCOMPOSITE

J. Kuljanin-Jakovljević, A. Radosavljević*,
J. Spasojević and Z. Kačarević-Popović

*Vinča Institute of Nuclear Sciences, University of Belgrade, P.O. Box 522,
11001 Belgrade, Serbia (*krkljes@vinca.rs)*

ABSTRACT

This work describes radiolytic *in situ* incorporation of lead sulfide nanoparticles (PbS NPs) in poly(vinyl alcohol) (PVA) hydrogel. Optical, structural, swelling and diffusion properties of prepared PbS/PVA hydrogel nanocomposite were investigated. Obtained results indicate formation of PbS NPs with a cubic crystal structure and diameter around 3 nm. Incorporation of PbS NPs in PVA hydrogel causes a change in the swelling and diffusion properties.

INTRODUCTION

In the last decade, the preparation of nanoparticles and nanomaterials has been very interesting subject in nanotechnology science. Organic polymers, especially hydrogels, are an attractive class of materials due to unique properties, and represent a good platform for nucleation and growth of NPs due to free space between the polymer chains that serve like nanoreactors in hydrogel swollen state (template synthesis). The mesoporous network of hydrogels as a matrix is a suitable template for the *in situ* synthesis, stabilization and distribution of metal NPs (Ag, Au) as well as semiconductor NPs (CdS, PbS). These nanocomposite materials have potential biomedical application, but also can be used for the fabrication of novel photonic materials and “solid state” solar devices where the spacing between NPs can be tuned for optimum photovoltaic efficiency.

The properties of nanocomposites are strongly dependent on the method of preparation and experimental conditions. Among a number of techniques reported for the synthesis of nanocomposite systems, the radiolytic method is one of the most promising strategies due to several advantages compared to conventional methods. The aim of this work was to investigate the possibility of the radiolytic *in situ* incorporation of PbS NPs within the PVA hydrogel, previously crosslinked also by gamma irradiation, as well as to explore the influence of PbS NPs on swelling and diffusion properties of polymer network.

EXPERIMENTAL

PVA solution (5 wt.%) was exposed to gamma irradiation (^{60}Co source, dose rate 0.5 kGy/h, absorbed dose 25 kGy) to induce crosslinking of polymer chains, and PVA hydrogel with 86% weight fraction of gel was obtained. Then, PVA xerogel was immersed in water solution of lead nitrate ($\text{Pb}(\text{CH}_3\text{CO}_2)_2$, $5 \cdot 10^{-4}$ M) and 1-dodecanethiol ($\text{CH}_3(\text{CH}_2)_{11}\text{SH}$, $1 \cdot 10^{-2}$ M), previously saturated with Ar in order to remove oxygen. The swelling of polymer network was carried out at room temperature for 24 h, and then the sample was gamma irradiated (dose rate 12.3 kGy/h, absorbed dose 3.2 kGy). The obtained PbS/PVA nanocomposite was characterized by UV-Vis, XRD, SEM and swelling measurement in water at 25°C. The crystalline domain size was determined from XRD by Sherrer formula ($D = k\lambda/\beta \cos\theta$, where $k=0.9$ is a constant for cubic structure, $\lambda=0.1541$ nm is the X-ray wavelength, β is the full width at half maximum, and θ is the diffraction angle), while the lattice constant was calculated as $a = d_{hkl}(h^2 + k^2 + l^2)^{1/2}$ (d_{hkl} is space between the planes in the atomic lattice, while h , k , and l are Miller indices). Swelling process was monitored gravimetrically by measuring mass of swollen hydrogel at predetermined time intervals (m_t), until the initial mass of xerogel (m_0) was equilibrated (m_{eq}). The swelling degree was calculated as $SD = (m_t - m_0)/m_0$, and the equilibrium swelling degree (SD_{eq}) was determined by replacing m_t with m_{eq} . Power law approach ($SD/SD_{eq} = kt^n$, where k is the kinetic constant related to the structure of the network, t is the time and n is the diffusion exponent) was used to determine the diffusion model and to calculate the kinetic parameters of diffusion. The values of the kinetic parameters k and n were determined from the intercept and slope, respectively, of the curves of $\ln(SD/SD_{eq})$ versus $\ln t$ by linear fitting at the initial stage of swelling ($SD/SD_{eq} \leq 0.6$). Diffusion coefficient was calculated as $D = k^{1/n} \pi \delta^2 / 16$, where δ is the sample thickness.

RESULTS AND DISCUSSION

The mechanisms of the formation of nanocrystalline sulfides under the gamma irradiation are not very clear up to now. However, when the solution containing Pb^{2+} ions and appropriate sulfur source is irradiated, a series of reaction will happen. It is well known that some radiolytic species, including e_{aq}^- , H_3O^+ , OH^\bullet , H^\bullet , H_2 and H_2O_2 are generated when water is γ -irradiated. The solvated electrons (e_{aq}^-) has so strong reducing capability that $\text{CH}_3(\text{CH}_2)_{11}\text{SH}$ can be reduced to S^- and further to S^{2-} . Then, the S^{2-} anion combines with Pb^{2+} cation to generate PbS NPs [1]. Thus formed PbS NPs are entrapped in the PVA network, and prepared PbS/PVA hydrogel nanocomposite is insoluble in water.

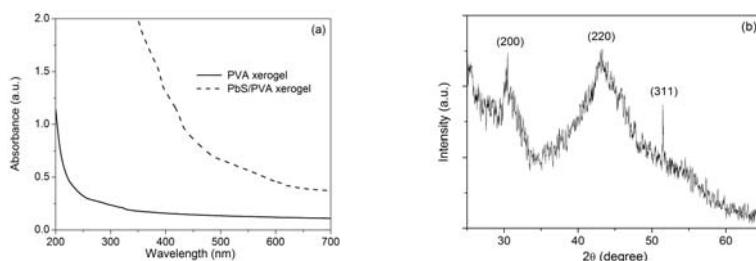


Figure 1. (a) UV-Vis absorption spectra of crosslinked systems and (b) XRD pattern of PbS/PVA xerogel nanocomposite.

Optical absorption spectra of PVA and PbS/PVA nanocomposite are presented in Fig. 1(a). The lack of excitonic peaks in the absorption spectra of nanocomposite is mainly explained by inhomogeneous broadening due to the size distribution of NPs, as well as by nature of polymer matrix. Moreover, the disappearance of the excitonic peak can be attributed to surface-related charge separation and polarization effects in PbS NPs, which were sensitive to the charges on the surfactant molecules [2]. In the case of investigated nanocomposite, the crosslinking of polymer chains induce the changes in the structure of polymer matrix, and probably thus leads to a change in the charge on the NPs surface.

The X-ray diffraction pattern of PbS-PVA nanocomposite is shown in Fig. 1(b). The XRD peaks correspond to Bragg's reflections from the crystalline planes (200), (220) and (311) of PbS NPs with the face centered cubic crystal structure (JCPDS Card File No. 5-592). The crystalline domain size (D) was found to be around 3 nm. Additionally, the lattice constant (a) was calculated and obtained value of 0.5917 nm for spacing $d_{220}=0.2092$ nm is close to the value from the JCPDS ($a_0=0.5937$ nm).

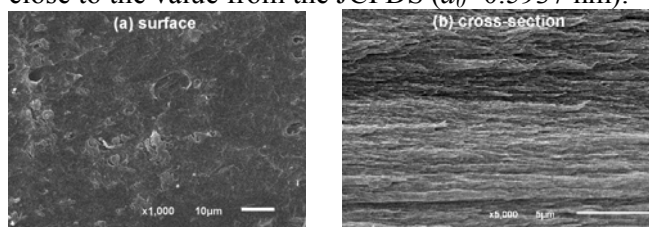


Figure 2. SEM micrographs of PbS/PVA xerogel nanocomposite

The SEM analysis shows that PbS/PVA nanocomposite has an uneven, partly open surface (Fig. 2(a)) with visible pores of different sizes, resulting from the evaporation of water from the sample during the lyophilization (process of sample preparation by freeze-drying). Fig. 2(b) indicates that the porous structure is a characteristic of the whole sample volume. Such a porous three-dimensional network structure is essential for the absorption and storage of large amounts of water within the hydrogel.

Swelling capacity is one of the most important parameters for evaluation the properties of hydrogels. Fig. 3 depicts the swelling curves of the PVA and PbS/PVA nanocomposite. It's clearly seen that isothermal kinetics swelling curves are similar in shape, but incorporation of PbS NPs in the PVA hydrogel induced the slightly decreased of swelling capacity and diffusion coefficient of PbS-PVA nanocomposite compared to pure PVA. Characteristic parameters of swelling process (SD_{eq} , k , n , D) for investigated systems are presented in Table 1. The obtained results indicate that hydrogel systems show non-Fickian or anomalous diffusion ($0.5 < n < 1$) when the rates of diffusion and polymer chain relaxation are comparable [3].

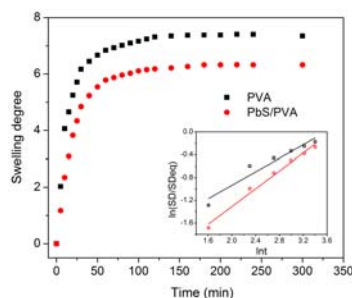


Table 1. Characteristic parameters obtained from swelling measurements.

Sample	SD_{eq}	k (1/min)	n	$D \times 10^7$ (cm^2/min)
PVA	7.35 ± 0.09	0.12	0.59	1.37
PbS/PV A	6.32 ± 0.06	0.06	0.78	1.25

Figure 3. Swelling curves of PVA and PbS/PVA nanocomposite in water at 25°C, and best linear fits of swelling curves (insert).

CONCLUSION

The PbS NPs, with diameter around 3 nm, have been successfully synthesized within the pores of PVA hydrogel using the gamma irradiation technique. Optical properties of PbS/PVA xerogel nanocomposite strongly depend on the structure of polymer matrix (crosslinked or uncrosslinked). Incorporation of PbS NPs into PVA hydrogel causes a slightly decrease in swelling capacity and diffusion coefficient compared to pure PVA, while non-Fickian diffusion transport mechanism remains unchanged.

ACKNOWLEDGEMENTS: This work is financed by the Ministry of Education, Science and Technological Development of the Republic of Serbia, projects III 45005 and 172056.

REFERENCES

- [1] M. Wu, et al., Colloids Surf., 2008, A 313-314, 35-39.
- [2] A. Martucci, et al., J. Non-Cryst. Solids, 2004, 345, 639-642.
- [3] J. Krstić, et al., Physical Chemistry 2010, Proceedings, 2010, Vol. I, 110-112.

STRUCTURAL CHARACTERISTICS OF Ag NANOPARTICLES SYNTHESIZED *in situ* WITHIN PNiPAAm HYDROGEL BY γ -IRRADIATION

J. Spasojević^{1,*}, A. Radosavljević¹, J. Krstić¹,
M. Mitrić¹, M. Kalagasidis Krušić² and Z. Kačarević-Popović¹

¹*Vinča Institute of Nuclear Sciences, University of Belgrade, P.O. Box 522, 11001 Belgrade, Serbia (*jelenas@vinca.rs),* ²*Faculty of Technology and Metallurgy, University of Belgrade, P.O. Box 3503, 11120 Belgrade, Serbia*

ABSTRACT

In this work, silver nanoparticles (AgNPs) are synthesized within thermo-responsive poly(N-isopropylacrylamide) (PNiPAAm) hydrogels of different concentrations, by γ -irradiation. The UV-Vis plasmon absorption characterization of AgNPs and its modeling using Mie theory showed that their diameters are less than 20 nm. The X-ray diffraction (XRD) data are consistent with the face centered cubic (FCC) crystal structure of bulk metallic Ag. The negative lattice strain (lattice contraction) was observed for the samples where the AgNPs are incorporated in the xerogel solid matrix of highest polymer concentration (15 wt.% PNiPAAm). The lattice parameter values are found to be higher than the bulk lattice parameter of Ag for larger nanoparticles formed in 5 wt.% PNiPAAm, whereas the crystallites were under tensile stress. On the other hand, for smaller nanoparticles formed in 15 wt.% PNiPAAm, crystallites were under compression stress (negative stress) whereby the lattice is contracted.

INTRODUCTION

The realization of potential application of metal nanoparticles in the fields such as optic, photonic, catalysis or in biomedicine, has led to the need to produce samples of well defined metal clusters stabilized in protective matrices. It is important because trends in the crystallite size/strain are related to the properties of the nanoparticles and consequently to the properties of the resulting nanocomposites [1].

The aim of this research was to investigate the influence of the concentration of the crosslinked polymer matrix of PNiPAAm in the form of hydrogel/xerogel as nanoreactor template on the structural characteristics of AgNPs synthesized *in situ* by γ -irradiation. Therefore, using the XRD structural analysis the various crystalline properties of these nanoparticles such as lattice parameter, size, strain and stress have been calculated.

Moreover, the UV-Vis plasmon absorption characterization of AgNPs and its modeling using Mie theory is performed [2]. The SEM analysis is used to investigate the morphology of PNiPAAm networks.

EXPERIMENTAL

Aqueous solutions of NiPAAm (5, 10 and 15 wt.%) (bubbled with Ar) were exposed to γ -irradiation, at room temperature, and at a dose rate of 0.5 kGy/h (total absorbed dose of 25 kGy) to induce crosslinking. The weight fraction of gel (ratio of the water-insoluble fraction to the feed monomer) was 95.5 (for 5 wt.% PNiPAAm), 97.3 (for 10 wt.% PNiPAAm) and 96.8 (for 15 wt.% PNiPAAm). The hydrogel samples were equilibrated in the solutions containing 1×10^{-2} M AgNO₃ and 0.2 M 2-propanol, and exposed to γ -irradiation (dose rate 12.3 kGy/h, total absorbed dose 18 kGy). Characterization of the as prepared AgNPs was carried out using Thermo Fisher Scientific Evolution 600 UV-Vis spectrophotometer. The surface morphology of the samples was observed using JEOL JSM-6610LV SEM. The XRD measurements were performed on Bruker D8 Advance Diffractometer (Cu K α_1 radiation, $\lambda = 0.1541$ nm).

RESULTS AND DISCUSSION

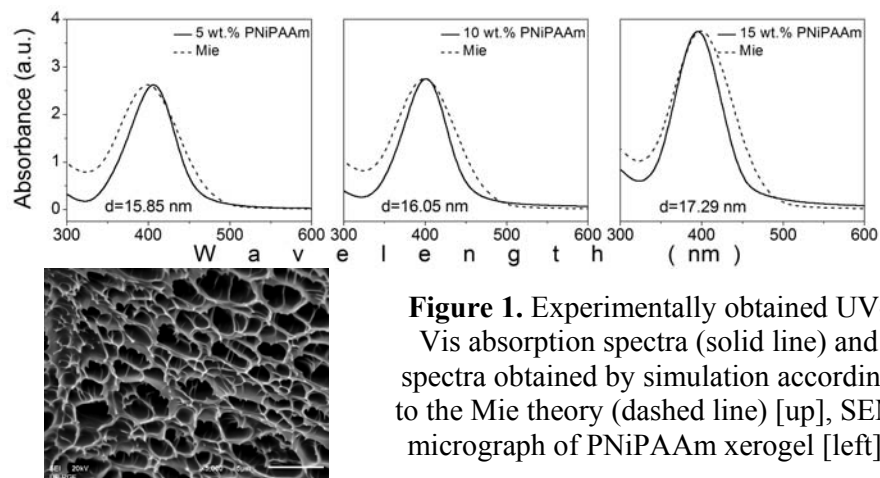


Figure 1. Experimentally obtained UV-Vis absorption spectra (solid line) and spectra obtained by simulation according to the Mie theory (dashed line) [up], SEM micrograph of PNiPAAm xerogel [left].

Figure 1(up) shows the UV-Vis spectra of the Ag-PNiPAAm hydrogel nanocomposites, experimentally obtained (solid line), and obtained by simulation according to the Mie theory (dashed line). The diameter of AgNPs was determined by applying the program, “MiePlot v.3.4”. The SEM micrograph of polymer network is shown in Figure 1(left).

The obtained XRD data (Figure 2) are consistent with the face centered cubic (FCC) crystal structure of bulk silver (JCPDS FileNo. 04-0783). The diffraction maxima at 2θ angle values correspond to the Bragg's reflections

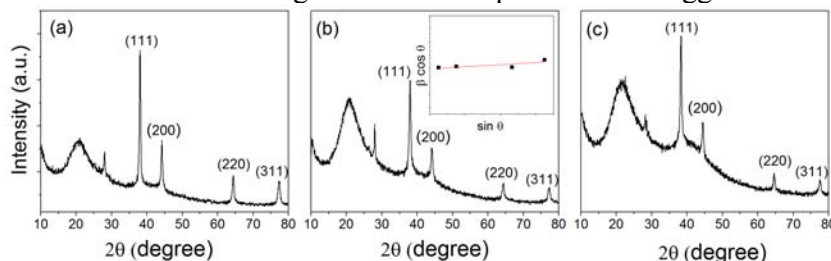


Figure 2. XRD patterns of AgNPs in PNIPAAm xerogel matrix (a) 5 wt.%, (b) 10 wt.% and (c) 15 wt.%.

from the crystal planes (111), (200), (220) and (311), ($d_0=0.236$ nm, $a_0=0.4086$ for the crystal plain (111)). To distinguish the effect of crystallite size induced broadening and lattice distortion induced broadening at full width at half maximum (FWHM) of XRD profile, Williamson-Hall plots [3] have been drawn for all the reflections of each sample (insert of Figure 2). Using the Eq. (1), the grain size and the lattice strain are determined from the intercept and the slope of line, respectively:

$$\beta \cos \theta = (k\lambda/D) + 4\varepsilon \sin \theta \quad (1)$$

where β is the FWHM in radian, θ is the diffraction angle, $k=0.9$ is a constant for cubic structure, $\lambda=0.1541$ nm is the X-ray wavelength, D is the grain size in nm, ε is the strain. Strain is defined by the relation $\varepsilon=\Delta d/d_0$ where d is the interplanar spacing [4]. The lattice strain thus obtained is from -0.001 to 0.002 (Figure 3(a)). Theoretical study predicts significant negative lattice strain (lattice contraction) for NPs smaller than 5 nm, but even for NPs of 30 nm the small lattice contraction is suggested [5]. The lattice contraction is caused by the bond-order loss and effective coordination number (CN) imperfection induced bond contraction at the surface shell. Here, lattice contraction was observed for the samples where the AgNPs are incorporated in the xerogel solid matrix of highest polymer concentration (15 wt.% PNIPAAm). The intrinsic stress (σ) is calculated on diffraction maxima (111), the most intense and well defined peak for FCC materials, using Eq. (2):

$$\sigma = (Y(a - a_0))/2\gamma a_0 \quad (2)$$

where a and a_0 are the lattice parameters of the prepared samples and bulk samples, respectively, while Y and γ are the Young's modulus and Poisson's

ratio of the bulk sample. The lattice parameter was calculated as $a = d_{hkl} (h^2 + k^2 + l^2)^{1/2}$ ($d = \lambda / 2 \sin \theta$ and h , k , and l are Miller indices) (Table 1).

Table 1. Summarized XRD data obtained for crystal plane (111).

PNiPAAm (wt.%)	2θ (degree)	β (degree)	a (nm)
5	38.1	0.38	0.4089
10	38.0	0.49	0.4099
15	38.3	0.53	0.4068

The lattice parameter values are found to be higher than the bulk lattice parameter of AgNPs for larger nanoparticles formed in 5 wt.% PNiPAAm, whereas the crystallites were under tensile stress (positive stress, as shown in Figure 3(b)). On the other hand, for smaller nanoparticles formed in 15 wt.% PNiPAAm crystallites were under compression stress (negative stress) whereby the lattice is contracted.

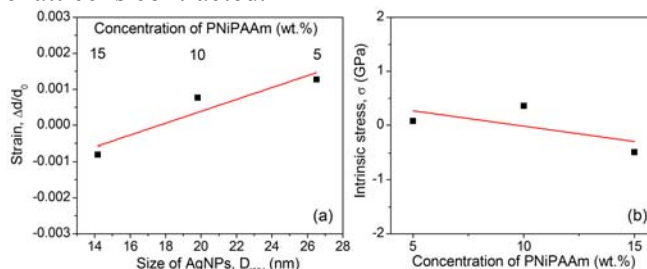


Figure 3. Lattice strain as a function of size of AgNPs (a) and lattice stress as a function concentration of PNiPAAm xerogel.

CONCLUSION

The changes of interplanar spacing and lattice parameter of crystalline AgNPs sensitively reflect their state of strain and stress depending on the formation conditions (the concentration of PNiPAAm hydrogel/xerogel matrix) and consequently on the diameter of AgNPs.

ACKNOWLEDGEMENTS

The Ministry of Education, Science and Technological Development of the Republic of Serbia (project III 45005).

REFERENCES

- [1] M. Dubiel, et al, Eur. Phys. J. D, 2001, 16, 229-232.
- [2] G.Mie, Ann. Phys., 1908, 25, 377-445.
- [3] M. Mazdi, et al, Int. J. Nano Dim., 2012, 2(4), 233-240.
- [4] G. Ouyang, et al, Phys. Chem. Chem. Phys., 2010, 12, 1543-1549
- [5] W.H. Qi, et al, J. Nanopart. Res., 2005, 7: 51-57.

MICROWAVE COLLOIDAL SYNTHESIS OF C/RuO₂ SUPERCAPACITIVE COMPOSITE

G. Šekularac¹, A. Dekanski¹, S. Drmanić²
and V. Panić¹

¹*Institute of Chemistry, Tehnology and Metallurgy - Department of Electrochemistry, University of Belgrade, Njegoševa 12, 11001 Belgrade, Serbia (gavrilo@ihm.bg.ac.rs)*

²*Faculty of Tehnology and Metallurgy, University of Belgrade, Karnagijeve 4, 11020 Belgrade, Srebia*

ABSTRACT

Preparation of RuO_xH_y/carbon black nanocomposite material was performed by the microwave (MW) impregnation. Vulcan XC-72 R (XC) were used as the carbon black substrate. Microwave-assisted synthesis was used to prepare RuO_xH_y sol, whereas nanocomposite material was obtained by microwave or ultrasonic (US) impregnation. A sample of the composite were calcined in nitrogen atmosphere at the temperature 300 °C for 1 h. The capacitive behavior of the composite was checked by cyclic voltammetry (CV) in 1 mol dm⁻³ H₂SO₄. The MW impregnation resulted in valuable increase in composite capacitance, while US impregnation by previously MW-synthesized RuO_xH_y sol showed poor capacitance improvement.

INTRODUCTION

Ruthenium oxide, RuO₂, is a well-known electrode material with excellent electrocatalytic features for many electrochemical processes. While the anhydrous, crystalline rutile RuO₂ is a metallic conductor [1], hydrous ruthenium oxide exhibits mixed electron/proton conductivity, which makes it a promising candidate for the use in energy-storage devices such as electrochemical supercapacitors [2–4]. The specific capacitance was reported to be as high as 720 F g⁻¹ and it is strongly dependent on the degree of structure ordering and crystalline water content [3–6]. The capacitive performances of hydrous ruthenium oxide can be improved if its pseudocapacitance is combined with double layer capacitance of carbon blacks [5,6]. This can be done by preparing the carbon-supported RuO_xH_y. The preparation procedure includes the precipitation of hydrous oxide from RuCl₃ in water [5,6] or Ru(OC₂H₅)₃ in ethanol solution [7] containing carbon black. In this work, the carbon-supported RuO_xH_y composite was prepared by an impregnation method, starting from hydrous ruthenium

oxide sol obtained by the microwave (MW) heating-assisted forced hydrolysis of RuCl_3 . The oxide particle size and distribution can be controlled during the sol preparation procedure [8], which is reflected in better properties of the composite. This MW-assisted method is expected to be advantageous if compared to precipitation procedure and classical forced hydrolysis method since MW synthesis is much faster and simpler. The aim of this work is to check if better supercapacitive properties could be gained by using MW heating. The investigation was focused on the synthesis process steps mainly, with routine checking of capacitive properties by cyclic voltammetry (CV).

EXPERIMENTAL

The ruthenium oxide sol was prepared by forced hydrolysis of RuCl_3 in acidic medium induced by MW heating [8,9]. 0.5 g of RuCl_3 was added into the 5 ml HCl aqueous solution having the concentration of 0.27 mol dm^{-3} . The 1 ml of this solution was added to 40 ml 0.27 mol dm^{-3} HCl aqueous solution to form the 11.1 g dm^{-3} RuCl_3 solution. This solution was heated in microwave at 350 W for 0–5 min with 1-min steps, 2 ml of sample was taken after each step. Sol samples were marked MW0–MW5, respectively. 180 mg of Vulcan XC-72 R (XC) was suspended in 60 ml of 0.27 mol dm^{-3} HCl in an ultrasonic (US) bath (40 kHz) at $25 \text{ }^\circ\text{C}$ for 1 h. Then 7 ml of this suspension was mixed with 1 ml of each MW0–MW5 sample and treated in US bath at $25 \text{ }^\circ\text{C}$ for additional 1 h (US impregnation). One of the samples was prepared in by MW impregnation method as follows and denoted as XMW. 60 mg of XC was mixed with 2 ml of MW5 and then it was heated in microwave at $100 \text{ }^\circ\text{C}$ for 7 min. After separation from the impregnating medium, the composites were dried in air at room temperature for 24 h. In order to check the influence of calcination temperature the samples were thermally treated under nitrogen atmosphere at $300 \text{ }^\circ\text{C}$ for 1 h. The prepared composite was US-dispersed in water and certain amount of the suspension was pipetted onto glassy carbon disk assembly substrate, which served as current connector, to make the amount of composite layer of 0.31 mg/cm^2 . The applied suspension was left to dry in air at room temperature and then covered by 10:1 (V/V) mixture of distilled water and commercial Nafion alcoholic solution (5 mass %, 1100 E.W., Aldrich). The covered layer was then dried in air at room temperature for about 24 h. The capacitive properties of the composites were investigated by CV in 1.0 mol dm^{-3} H_2SO_4 saturated with nitrogen. CV measurements were done at room temperature in a three-compartment cell equipped with Pt mesh as the

counter electrode and Ag/AgCl as the reference electrode. All potentials in the paper are referred to Ag/AgCl.

RESULTS AND DISCUSSION

The cyclic voltammograms of MW0–MW5, XMW and XC are shown in Figure 1A. The capacitive currents of the samples MW0–MW5 do not differ and are quite the same as those registered for XC. This shows that the applied US-assisted preparation did not result in impregnation. Apparently the surface acid–base properties of XC and RuO_xH_y particles are not suitable for composite formation. On the other hand, XMW showed valuable increase in capacitive performances, although the CV currents tend to decrease. The highest currents in cyclic voltammograms (I_{max}) are observed in anodic branch of CVs around 500 mV. I_{max} drops from 0.265 (XMW curve in Figure 1A) to 0.150 mA (XMWc20 curve in Figure 1A), while CV response enters the steady state. In the case of XC and MW0–MW5 samples, I_{max} is around 0.70 mA and poorly sensitive to cyclization. Figure 1B shows CVs of composite materials calcined at temperature of 300 °C. No temperature effects were registered in the case of MW0–MW5 samples. This confirms the absence of impregnation by US method. Calcinations of XMW sample (XMW300 curve in Figure 1B) caused the decrease of CV currents in comparison to XMW sample. However, the stability appears improved since I_{max} drops from 0.191 (XMW300 curve in Figure 1B) to 0.125 mA (XMW300c20 curve in Figure 1B) after 20 cycles, which were also required for the sample to enter the steady state CV response.

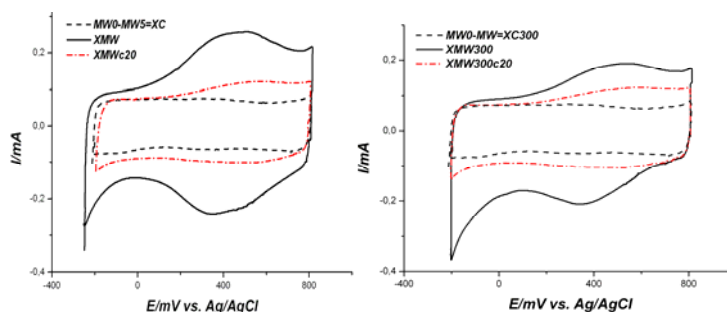


Figure 1. First and steady-state cyclic voltammograms of C/RuO₂ composites synthesized by US (MW0–MW5) and MW impregnation method (XMW); A) as-obtained and B) calcined at 300 °C in N₂ atmosphere. Electrolyte: 1 M H₂SO₄; room temperature; scan rate: 50 mV s⁻¹. The steady-state CVs have “c20” notation.

This is relatively smaller decrease in comparison to thermally non-treated XMW sample. It follows that calcinations cause the more defined structure

of the oxide, but also less hydrated, with the later known to be beneficial for the enhancement of pseudocapacitive performances.

CONCLUSION

Composite materials synthesized by microwave (MW) impregnation method showed valuable increase in capacitance in comparison to commercial carbon black (XC). The capacitance is unstable and drops to around 50 % from starting value, which is still much higher in comparison to XC. RuO_xH_y sol synthesized by forced hydrolysis with MW heating showed poor ultrasonic-assisted impregnation ability. MW impregnation method is very promising method for synthesis of supercapacitor composite materials and future work should focus to improve stability of composite materials synthesized by MW heating.

ACKNOWLEDGEMENT

This work is supported by the Ministry of Education, Science and Technological Development of the Republic of Serbia (Grants no. 172060 and 172013).

REFERENCES

- [1] S. Trasatti, in: *Interfacial Electrochemistry/Theory, Experiment and Applications*, A. Wieckowski (Ed.), Marcel Dekker, New York, 1999, p. 769.
- [2] S. Trasatti, W. O'Grady, in: *Advances in Electrochemistry and Electrochemical Engineering*, Vol. 12, H. Gerisher, C.W. Tobias (Eds.), Wiley, New York, 1981.
- [3] D. McKeown, P. Hagans, L. Carette, A. Russell, K. Swider, D. Rolison, *J. Phys. Chem., B*, 1999, 103 (23), p.4825-4832.
- [4] J.P. Zheng, T.R. Jow, *J. Electrochem. Soc.*, 1995, 142(8), p.2699-2703.
- [5] M. Ramani, B. Haran, R. White, B. Popov, *J. Electrochem. Soc.*, 2001, 148 (4), A374-A380.
- [6] J. Zhang, D. Jiang, B. Chen, J. Zhu, L. Jiang, H. Fang, *J. Electrochem. Soc.*, 2001, 148 (12), A1362-A1367.
- [7] D. Evans, J. Zheng, S. Roberson, in: *Proceedings of the Ninth International Seminar on Double Layer Capacitors and Similar Energy Storage Devices*, Deerfield Beach, USA, 2000.
- [8] V. Panić, A. Dekanski, S. Milonjić, R. Atanasoski, B. Nikolić, *Electrochim. Acta* 2000, 46 (2-3), p. 415-421.
- [9] V. Panić, A. Dekanski, S. Milonjić, R. Atanasoski, B. Nikolić, *Colloid. Surf.*, 1999, 157 (1-3), p.269-274.

FAST FABRICATION OF LARGE AREA CONCAVE MICROLENS ARRAYS

B. Murić¹, D. Grujić¹, D. Milovanović², D. Pantelić¹, D. Vasiljević¹ and B. Jelenković¹

¹*Institute of Physics, University of Belgrade, Pregrevica 118, Zemun 11080, Belgrade, Serbia (muric@ipb.ac.rs)*

²*VINČA Institute of Nuclear Sciences, University of Belgrade, Belgrade 11001, Serbia*

ABSTRACT

A single-step process for rapid fabrication of large-area concave microlens arrays using a diode-pumped solid state (DPSS) laser operating at 473 nm is developed. Using tartrazine sensitized gelatin layer treated with tot'hema - mixture of iron (II)-, manganese (II)- and copper(II)gluconate- (denoted short as tSTG) and a direct laser writing device developed in our laboratory, we could produce 10 000 uniform microlens arrays within 30 min. Uniform microlenses with different diameters and depth can be produced by varying the laser power, exposure time and dye concentration.

INTRODUCTION

Two dimensional (2D) microlens arrays, consisting of small lenses ranging in diameter from several micrometers to nearly 1 mm, find their applications in micro-optical devices, displays, biochemical systems, and artificial compound eyes [1-3]. Various methods are used for the microlens arrays fabrication: hot embossing, thermal reflow, droplet process and gray scale photolithography [4-6].

In this paper, we present a fast, single-step process for fabrication of large-area concave microlens arrays using a direct laser writing method. Within 30 min, 10 000 microlenses with a diameter of 50 μm and depth of 3 μm , were produced on a thin tSTG layer using blue laser light (473 nm). The layer is easy to prepare, cost-effective, elastic, biocompatible, thermally stable and nontoxic [7-9]. The produced microlens array can be used as a concave large-area microlens array, or as a mold for replication onto polydimethylsiloxane (PDMS) that is suitable for different applications [10].

RESULTS AND DISCUSSION

Thin tSTG layer was prepared on a glass microscope slide following the procedure described in our previous papers [7-9], using tartrazine, a lemon-

yellow, water soluble food dye (E 102) with maximum absorbance at (427 ± 2) nm, instead of eosin to modify the spectral properties of the material. The absorption spectrum of the tSTG layer was analyzed using a fiber-type spectrometer (Ocean Optics) equipped with a tungsten-halogen lamp. The absorption spectrum of the tSTG layer is shown in Figure 1.

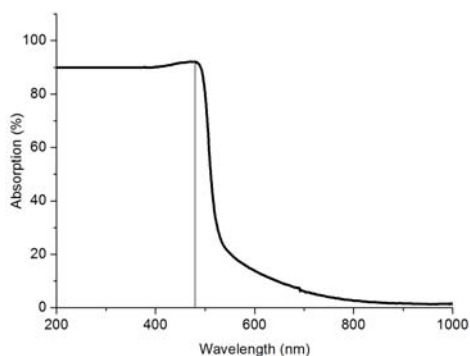


Figure 1. Absorption spectrum of tSTG layer

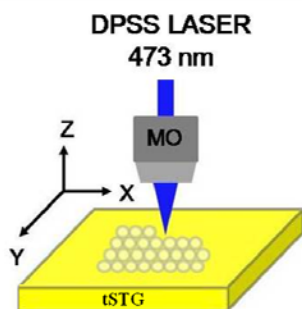


Figure 2. Scheme of the microlens array fabrication on the tSTG layer

The large-area microlens array was produced using the diode pumped solid state (DPSS) laser operating at 473 nm wavelength and output power of 50 mW to illuminate the tSTG layer, as shown in Figure 2.

The laser beam was focused with a microscope objective ($50\times$, 0,55NA) on the sample mounted on a precise xy - linear translation stage used for positioning the tSTG layer with step resolution of up to 25 nm and position repeatability of 2 μm . Software (developed in Microsoft Visual Studio) reads an image file and sends control data to the programmable controllers which coordinate the translation stage and the shutter. The microlens array is recorded lens by lens using the program which determines the microlens array parameters from the image file.

By controlling the laser power, exposure time and distance among neighbour microlenses we were able to create closely packed microlens arrays.

Also, we can change the microlens parameters such as: depth, diameter, focal length. Influence of exposure time on the lens depth, for the laser power of 20 mW, is shown in Fig. 3. As can be seen the lens depth rapidly grows, and increases with exposure time. After a few seconds, depending on the laser power the depth stops growing, reaching its final value (the lens is completely formed).

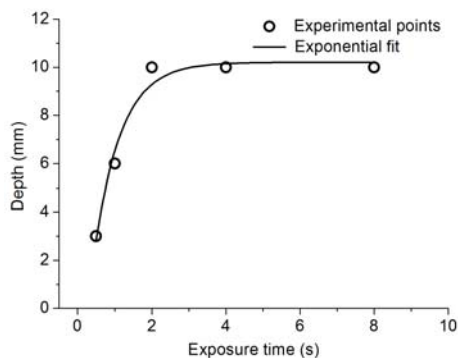


Figure 3. Variation of depth tSTG microlens with exposure

Array of 100 x100 microlenses was produced on the 100 μm thick tSTG layer irradiated by a DPSS laser operating at a 473 nm wavelength. The exposure time was 200 ms and laser power of 20 mW. The microlens array is produced on 1cm \times 1cm of tSTG layer. Profilometry was used to obtain three- and two-dimensional profiles of tSTG microlenses, shown in Figure 4.

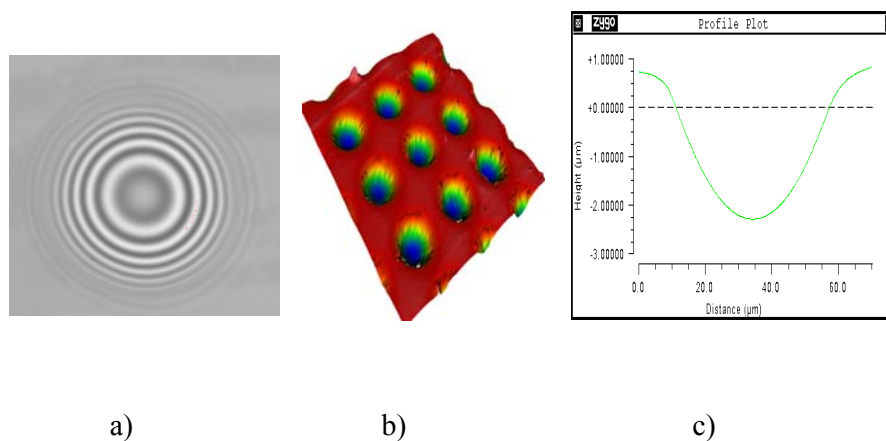


Figure 4. Surface profile of tSTG microlens array: a) Interference fringe pattern of a single microlens; b) 3D profile of the array; c) 2D surface profile of a single microlens; Morphology of the microlenses array was analyzed using non-contact profilometry (3D optical surface profiler - Zygo New View 7100).

The microlenses with diameter of 50 μm and depth of 3 μm are obtained with good repeatability. An image of the number “5” taken by a digital camera through the optical microscope and tSTG microlens array is shown in Fig. 5, and representing the image quality. Also, hexagonal closely packed microlens arrays were made, and can be used to imitate biological compound eyes structure.

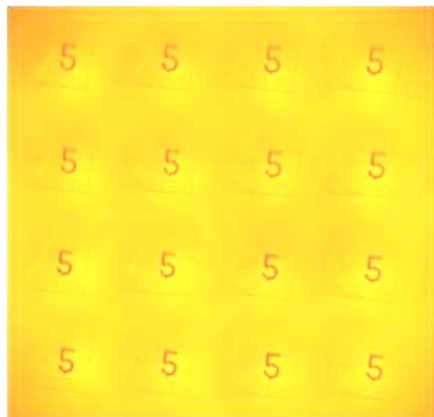


Figure 5. Image of number “5” taken through the microscope and tSTG microlenses array

CONCLUSION

In summary, a fast, single step fabrication process of 2D concave microlens arrays is described. 10 000 (array of 100x100) microlenses are produced on tartrazine sensitized tot’hema gelatin layer (short tSTG) by DPSS laser operating at 473 nm. Convex microlenses can be also mass replicated using the concave as molding templates.

The closely packed tSTG microlenses show good optical and imaging properties, and can be used for various applications such as: medical laser, optical sensors, light-field cameras, biological structure...

ACKNOWLEDGEMENT

This paper was written as a part of research on the projects ON 171038 and III 45016 supported by the Ministry of education, science and technological development of the Republic of Serbia.

REFERENCES

- [1] A Tripathi, N. Chronis, *J Micromech Microeng.* 2011, 21, 105024.
- [2] V. Lin, H. C. Wei, H. T. Hsieh, G. D. J. Su, *Sensors* 2011, 11, 10293–10307.
- [3] H. Zhang, L. Li, D. L. McCray, S. Scheiding, N. J. Naples, A. Gebhardt, S. Risse, R. Eberhardt, A. Y. Yi, *Opt. Expr.*, 2013, 21, 22232-22245.
- [4] F. Xiqiu, Z. Honghai, *Sensor Letters* 2008, 6, 266-271.
- [5] J. M. Pavia, M. Wolf, E. Charbon *Opt. Express* 2014, 22, 4202-4213.
- [6] S. J. Hwang, Y.X. Liu, G.A. Porter, *Opt. Express* 2013, 21, 30731-30738.
- [7] B. Murić, D. Pantelić, D. Vasiljević, B. Panić, *Opt. Mater.* 2008, 30, 1217-1220.
- [8] B. D. Murić, D. V. Pantelić, D. M. Vasiljević, B. M. Panić, *Appl. Opt.* 2007, 46 8527-8532.
- [9] A. J. Krmpot, G. J. Tserevelakis, B. D. Murić, G. Filippidis, D. V. Pantelić, *J. Phys. D: Appl. Phys.* 2013, 46, 195101.
- [10] Yi-S. Cherng, Guo-D. J. Su, *J. Micromech. Microeng.* 2014, 24, 015016.

ATOMIC SCALE ASPECTS OF PHASE TRANSITIONS IN SHAPE MEMORY ALLOYS

O. Adiguzel

*Physics Department, Firat University, 23169 Elazig, Turkey,
oadiguzel@firat.edu.tr*

ABSTRACT

Shape memory effect is characterized by the recoverability of desired shape of the material at different conditions. Shape memory effect is based on a solid state phase transition, martensitic transformation. Martensitic transformation is a first order thermal-induced transition and occurs in the materials on cooling from high temperature parent phase region called austenite phase. Martensitic transformation occurs as lattice twins in self-accommodating manner with the cooperative movements of atoms. The movement of atoms is confined into inter-atomic distances called lattice parameters on {110}-type planes of austenite matrix. Copper based alloys exhibit this property in metastable β -phase field, which have bcc- based structures at high temperature. These structures martensitically undergo the non-conventional structures on cooling from high temperature parent phase region.

INTRODUCTION

Shape memory alloys take place in a class of functional materials by exhibiting a peculiar property called shape memory effect. This property is characterized by the recoverability of a certain shape of material at different conditions. Shape memory effect is based on martensitic transformation which is a solid state phase transformation occurring with the cooperative movements of atoms in the alloy on cooling from high temperature austenite phase region. Shape memory effect refers to the shape recovery of materials resulting from martensite to austenite transformation when heated above reverse transformation temperature after deforming in the martensitic phase. These alloys also cycle between two certain shapes with changing temperature.

Copper based shape memory alloys exhibit this property in β -phase field. These alloys are metastable and undergo two ordered transitions on cooling, and bcc structures turn into B2(CsCl) or DO₃(Fe₃Al) -type ordered structures. These ordered structures martensitically undergo the non-conventional structures on further cooling, and structural changes in

All of these martensite phases are long-period stacking ordered structures, more specifically, microstructural evaluation provides a mechanism by which the transformation from the high temperature austenite phase to the low temperature martensite phase takes place [2, 3].

The lattice of high temperature austenite phase has high symmetry, while the product martensite has low symmetry, and martensitic transition requires special changes in symmetry and relations between the lattice parameters. The fundamental structures of the beta-type martensites are orthorhombic close-packed structures, and monoclinic distortion takes place in some cases by means of microstructural evaluation depending on the atomic distribution in nanoscale or angstrom scale and 18R structure is modified as M18R.

EXPERIMENTAL

In the present contribution, a CuZnAl alloy, Cu-26.1%Zn-4%Al(in weight) was investigated. Powder specimens for X-ray examination were prepared by filling the alloys. Specimens for TEM examination were also prepared from 3mm diameter discs and thinned down mechanically to 0.3mm thickness. An x-ray powder diffractogram taken from the quenched CuZnAl alloy sample is shown in Figure 2. An electron micrograph showing fine martensite structure and electron diffraction pattern take from taken from the quenched CuZnAl alloy samples are shown in Figure 3a and b, respectively. X-ray powder diffractograms and electron diffraction patterns reveal that this alloys exhibit superlattice reflections.

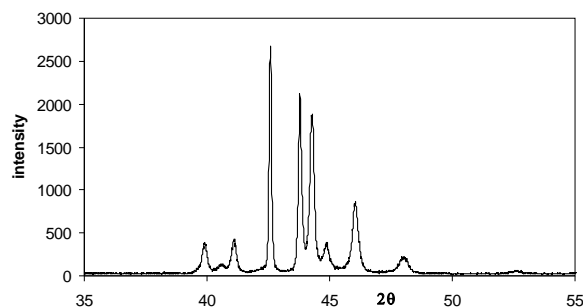


Figure 2. An x-ray diffractogram taken from the CuZnAl alloy sample.

A series of x-ray diffractograms taken in a large time interval show that peak locations and peak intensities change with ageing duration. In particular, some successive peak pairs whose Miller indices provide a special relation come close each other. These changes lead to the martensite stabilization and diffusion-controlled process [3]. Martensite stabilization

is a diffusion controlled phenomena, and this result leads to redistribution of atoms on the lattices sites.

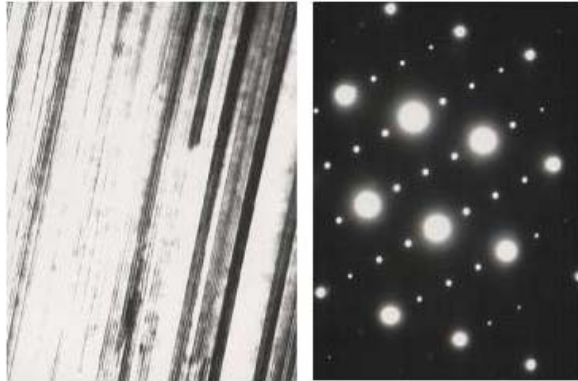


Figure 3. a) An electron micrograph of fine martensite structure ($\times 90k$), and (b) electron diffraction patterns taken from CuZnAl alloy sample.

Metastable phases of copper-based shape memory alloys are very sensitive to the ageing effects, and heat treatments can change the relative stability and the configurational order of crystal planes. Atom locations in the lattice sites in the crystal unit cell are also very important for the analysis and process of transformation.

CONCLUSIONS

It can be concluded from the above results that the copper-based shape memory alloys are very sensitive to the ageing treatments. The diffracted angles and intensities of x-ray diffraction peaks change with ageing duration in martensitic condition. In particular, some successive peak pairs come close each other. These changes lead to the martensite stabilization in the redistribution or disordering manner, and stabilization proceeds by a diffusion-controlled process.

Key Words: Shape memory effect, martensitic transition, lattice invariant shear, layered structures, stacking sequence.

REFERENCES

- [1] J. Ma, I. Karaman and R.D. Noebe, *International Materials Reviews*, 2010, 55 257-315.
- [2] Zhu, J.J, Liew, K.M, *Acta Materialia*, 2003, 51 2443-2456
- [3] O. Adiguzel, *Journal of Materials Processing Technology*, 2007, 185, 120-124.

SOLID STATE
PHYSICAL CHEMISTRY

VALENCE BAND GAPS AND PLASMA ENERGIES OF SOME NATURALLY OCCURRING SULPHUROUS MINERALS

R. Todoran, D. Todoran and Z. Szakacs

Department of Economics And Physics, Technical University of Cluj Napoca, North University Centre of Baia Mare, 62/A, Dr. V. Babes Street, Baia Mare, ROMANIA (szakacs@yaho.com)

ABSTRACT

The paper presents the determinations of the valence band gaps and plasma energies of the galena, sphalerite and chalcopyrite natural minerals. The work was carried out using differential optical reflectance spectroscopy of the clean mineral surfaces. The determination of the optical properties such as refractive index, real part of the complex dielectric constant and the location of certain van Hove singularities, was carried out using the framework of the Kramers-Kronig formalism.

INTRODUCTION

Studying optical and electrical properties of thin films formed in adsorption processes during froth flotation can be done via optical methods, permitting a good evaluation of the surface mechanisms, explaining the details of the adsorption processes of the collector reagents on the surface of the natural semiconductor minerals. A precursor to such studies must be the determination of optical and electrical functions of the natural mineral itself. Using the UV-VIS reflection spectra, and with the aid of Kramers-Kronig formalism, the following optical functions can be evaluated in the case of each natural mineral: the optical absorption coefficient, the refraction index, the absorption and extinction coefficient, the effective valence number, the dielectric permittivity and loss, the characteristic electrons loss functions, etc. One also can determine the width of the valence (pseudo)band gap and the electron plasma energy of the semiconductor.

EXPERIMENTAL SETUP AND THEORY

Optical methods allow “in situ” determinations of the evolution of the collector reagent adsorption thin layer formed on the surface of galena, sphalerite or chalcopyrite minerals without disturbing the internal development of the processes. Differential reflectance spectroscopy relies on monitoring the change of the relative reflectance of the adsorption

interface, permitting continuous evaluations. For such studies the reflectance of the clean mineral surface is needed. Studying this problem one can deduce the valence (pseudo)band gap and electron plasma energies of these minerals.

Considering a complex form of the refraction and absorption index $n^* = n + ik$, where n is the refractive index and k is the extinction coefficient, the dielectric coefficient $\varepsilon = \varepsilon_1 + i\varepsilon_2$ will take also a complex form, where ε_1 is the dielectric constant and ε_2 is the dielectric loss function. In a semiconductor, near the van Hove singularities, both $-Im \varepsilon^{-1}$ and $-Im (1 + \varepsilon)^{-1}$ will have extrema, as the electron energy losses are maximal. The dependence of these functions on incident photon energy determines the type of the special points, the form of the energy band in that particular energy region and the dispersion of the electron and hole effective masses.

The use of adequate software to cover by extrapolation a broader frequency domain is needed, knowing that the Kramers-Kronig formalism is exact only if all frequencies are taken into account and the experimental data is taken from a broad spectral domain. Processing the experimental optical reflectance spectra the mentioned quantities can be computed applying the three-parameter Kramers-Kronig formalism [1].

To compute the electron plasma energy E_{pv} , and the valence (pseudo)band gap E_g the following theoretical background was used.

The determination of the dielectric constant ε_1 leads to the use of [1]:

$$\varepsilon_1 - 1 = \left(\frac{E_{pv}}{E_g} \right)^2. \quad (1)$$

Knowing the refractive index n for semiconductors, one has:

$$\frac{n^2(h\nu) - 1}{n^2(h\nu) + 2} = \frac{1}{3} \frac{E_{pv}^2}{\left(\eta \frac{E_{pv} + E_g}{2} \right)^2 - (h\nu)^2}, \quad (2)$$

where and η is a non-dimensional parameter. The values of $n(h\nu)$ taken into account lay between $E_g/3\eta$ and E_g/η . The determination of the coefficient η must be done using a multi-electronic model. We used the Slater determinant, where the exchange energy is proportional with a correction factor determined by means of Hartree-Fock approximation [2]. Mathematical extrapolation gave the value of η equal with 1.366 for sphalerite, 1.369 for galena, and 1.412 for chalcopyrite.

The galena, sphalerite and chalcopyrite natural minerals were obtained from the Maramures county mining deposits.

The optical measurements were made using a SPECORD M-40 spectrophotometer in the domain of 200-900nm (1.37-6.25eV).

The resolution of the spectrophotometer is 10cm^{-1} in the $2000\text{-}4000\text{cm}^{-1}$ domain and of 5cm^{-1} below 2000cm^{-1} . The slit of the spectrophotometer had a width of 3mm, leading to mediated reflectance values over a small area on the surface of mineral samples. The reflectance of the mineral was taken relative to the normalized reflectance of an aluminium mirror.

The surface of the minerals was cleaned using chemical and physical methods. Polishing was obtained by polishing glass for roughness of $250\mu\text{m}$, polishing powder for roughness of $10\mu\text{m}$, then through mechanical abrasion using TiO_2 powder with granules of $0.02\mu\text{m}$ diameter. The removal of the oxide layer was made through chemical methods:

- galena samples were washed 5 times for 5 minutes in a solution of 30 parts HCl, 10 parts HNO_3 and one part CH_3COOH at 50°C [3];

- chalcopyrite samples were washed 3 times for 5 minutes in a solution of 2 parts CrO_3 , one part concentrated HNO_3 , 3 parts double distilled water at 80°C [4];

- sphalerite samples were washed 3 times for 3 minutes in concentrated boiling HNO_3 [5].

After the chemical ablation process, the sample surfaces were neutralized using double distilled water, and any foreign molecule was removed with a spray of argon gas, while the mineral was placed in a low pressure chamber (10^{-9} torr). After this procedure the time to surface oxidation takes several hours so it does not influence the results of our optical determinations.

RESULTS AND DISCUSSIONS

The position of the van Hove singularities can be determined, with good accuracy, from any of the variations of $-Im(1+\epsilon)^{-1}$ and $-Im\epsilon^{-1}$ vs. wavelength, that's why we only present the graphs for the first one in Figure 1. These values give the energies where ϵ_l and n should be determined to

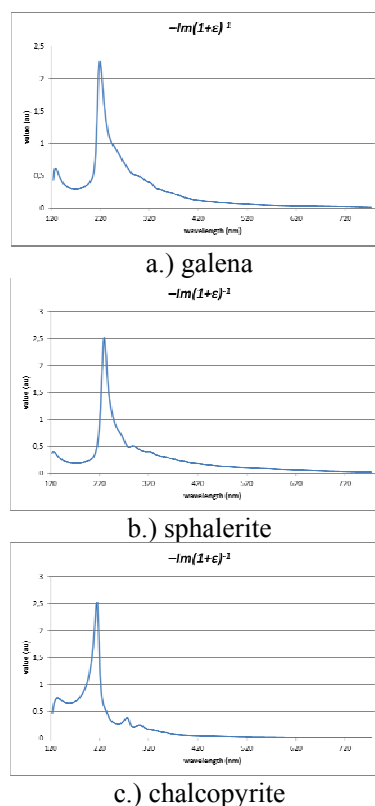


Figure 1. The variation of $-Im(1+\epsilon)^{-1}$ for the specified natural minerals

compute E_{pv} and E_g . The van Hove singularities are located at 220nm (5.62eV) in the case of galena, at 210nm (5.90eV) in the case of sphalerite, at 190nm (6.52eV) for chalcopyrite. For chalcopyrite one can observe multiple lower amplitude van Hove singularities, explained by the existence of multiple forbidden bands or by pseudo-energy band gap like behaviour. Using the equations (1) and (2) one computed the following values for the valence (pseudo)band gap and the valence plasma energy:

- for galena: $E_{pv}= 16.2eV$ and $E_g=0.43eV$
- for sphalerite: $E_{pv}= 13.1eV$ and $E_g=1.50eV$
- for chalcopyrite: $E_{pv}= 15.7eV$ and $E_g=1.42eV$

The values of E_{pv} and E_g determined by us can be compared with those present in the literature, determined using electrical measurements for grown, pure PbS and ZnS crystals [6]. These results are $E_{pv}= 15.1eV$ and $E_g=0.31eV$ for PbS, and $E_{pv}= 12.4eV$ and $E_g=1.44eV$ for ZnS. The differences between our results and the cited ones arise from the fact that we worked with natural minerals containing structural and compositional defects, and that our results represent mean values over a small surface area.

CONCLUSION

In the present work we determined the values of the electron plasma energy and the valence (pseudo)band gap for galena, chalcopyrite and sphalerite natural minerals by means of differential optical reflection spectroscopy. These results allow us to know the energetic and structural properties of the surfaces of the mentioned sulphurous minerals, and are important in understanding the mechanisms of the formation of the adsorption bonds on the surfaces, the energies that are needed in the modification or the movement of electrical charge on the surfaces, making easier to find the optimal mineral processing procedure to obtain the maximal adsorption.

REFERENCES

- [1] B. Jensen, A. Torabi, IEEE J. Quant. Electron., 1983, QE-19, 448-457
- [2] A. Davydov, Theorie du solide, Mir, Moscou, 1980
- [3] R. F. Brebrick and W. W. Scanlon, J. Chem. Phys. 1957, 27, 607-608
- [4] R.St.C. Smart, J. Amarantidis, W. Skinner, C.A. Prestidge, L. LaVanier and S. Grano, Scann. Microscopy, 1998, 12, 553-583
- [5] S. J. Czyzak, J. C. Manthuruthil and D. C. Reynolds, J. Appl. Phys. 1962, 33, 180-184
- [6] J.N. Zemel, J.D. Jensen, and R.B. Schoolar, Phys. Rev., 1965, 140, A330-A343

IMPACT OF OXYGEN DISORDER ON T_c SUPPRESSION IN Zn DOPEdREBa₂Cu₃O_{6+x} SUPERCONDUCTORS

M. M. Milić

*Laboratory of Theoretical Physics,
Institute of Nuclear Sciences "Vinca", University of Belgrade, P.O.Box 522,
11001 Belgrade, Serbia*

ABSTRACT

Conducting properties of REBa₂Cu₃O_{6+x}(RE123) type high T_c superconductors (RE=Y, 4f elements) are highly sensitive to the oxygen order in the oxygen deficient CuO_x planes which can be disrupted by doping with different metals, thus leading to a change of the superconducting transition temperature T_c . In this article we shall employ a simple theoretical model of charge transfer to study how $T_c(x)$ dependence is affected by the increase of oxygen disorder in the CuO_x planes, which is displayed in reduced average CuO chain length, l_{av} . The results indicate that though the increased oxygen disorder can produce significant decrease in T_c , it cannot be the only factor responsible for T_c reduction in Zn doped RE123 superconductors.

INTRODUCTION

Copper substitution by metal ions in REBa₂Cu₃O_{6+x} high- T_c superconductors was widely used to study superconductivity in these materials, no matter which copper site is substituted Cu1 in CuO_x planes or Cu2 in the superconducting CuO₂ planes [1,2]. It is of special interest to study influence of nonmagnetic Zn ions substitution for copper ions at Cu2 site. Though the mechanism of superconductivity suppression due to Zn doping is not fully understood yet, it is believed that the main cause is the pair breaking which occurs due to dipoles formation which act as strong scattering centers for charge carriers [1,3]. It was also observed that Zn doping produces oxygen depletion of the CuO_x planes followed by increased oxygen disorder in these planes, though the sample generally remains orthorhombic [3]. Increased oxygen disorder implies that length of CuO chains (sequences of Cu and O ions aligned along one of the crystallographic axes) formed in the CuO_x planes is decreased. Since charge carriers can be transferred only out of those CuO chains whose length, l , is equal to or greater than some critical length, l_{cr} , (usually assumed to be 3 or 4 oxygen ions) this chain length reduction is followed by a decrease in

charge carriers concentration in the superconducting CuO_2 planes, which consequently leads to a T_c suppression.

Therefore we find it interesting to investigate how reduction of the average CuO chain length, l_{av} , is reflected upon the superconducting transition temperature dependence on oxygen concentration, $T_c(x)$.

THEORETICAL MODEL

In order to study thermodynamics of oxygen ordering in the CuO_x planes of RE123 superconductor we have used the well-known ASYNNNI model (Asymmetric Next Nearest Neighbor Ising model) [4] defined by the Ising Hamiltonian, which includes repulsive nearest neighbor interaction $V_1 > 0$ between oxygen ions, and two types of next-to-nearest neighbor interactions: attractive interaction, $V_2 < 0$, which is mediated by copper atoms and direct repulsive interaction, $V_3 > 0$. Since the attractive V_2 interaction is the main factor governing formation of CuO chains, in what follows we will assume that oxygen disordering in the CuO_x planes caused by the Zn doping is due to reduced strength of this interaction. Weaker V_2 interaction will lead to the formation of shorter CuO chains and the overall average chain length will be reduced. Concentration of positive holes transferred out to the CuO_2 planes can be calculated by the use of the simple charge transfer model [5] where the number of holes in one CuO_2 plane per one Cu ion (doping), p , is given by the following expression:

$$p = \frac{\mu}{2} \left[x_1 \left(1 - \frac{1}{l_{av,1}} \right)^{l_{cr}-1} + x_2 \left(1 - \frac{1}{l_{av,2}} \right)^{l_{cr}-1} \right] \quad (1)$$

where $l_{av,1}$ and $l_{av,2}$ (x_1 and x_2) are average chain lengths (oxygen concentrations) on two non-equivalent sublattices of the CuO_x plain lattice, which are distinguishable in the Ortho II structural phase, and μ is the proportionality coefficient, $\mu \approx 0.19$ [5].

RESULTS AND DISCUSSION

In order to calculate quantities necessary to evaluate doping p , we have employed Cluster Variation Method (CVM) simulations of the ASYNNNI model in a 4,5-point clusters approximation. For values of the interaction parameters we chose those obtained from the first principle calculations (LMTO values): $V_1 = 6.9 \text{ mRy}$, $V_2 = -2.4 \text{ mRy}$, $V_3 = 1.1 \text{ mRy}$ [6]. The CVM simulations were performed at constant oxygen equilibrium temperature $T_{eq} = 450 \text{ K} = \text{const.}$, which is the best representative of the room temperature in experiments at which most of the samples are equilibrated.

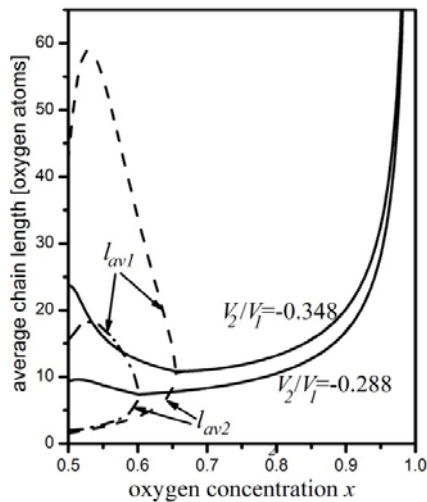


Figure 1. l_{av} as a function of x for two values of V_2 interaction.

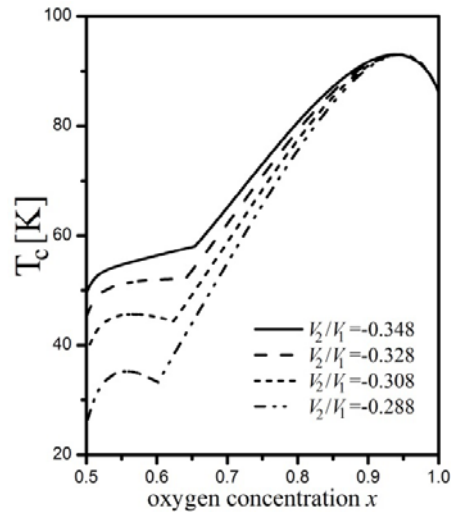


Figure 2. T_c as a function of x for different values of V_2 interaction.

The quantities of interest have been calculated for LMTO values of V_1 and V_3 interactions, and for four different values of V_2 interaction, one of them being the LMTO value and the other three values were chosen to have somewhat lower intensities so that oxygen disorder was increased. In the figure 1 we presented $l_{av}(x)$ dependences, calculated for two different V_2 values. One can observe that reduced intensity of V_2 interaction produces shorter CuO chains, which is particularly emphasized in the region of ortho II phase, where two different chain lattices can be distinguished. With further x increase, V_2 interaction has less and less influence on the length of CuO chains, since fulfilling of lattice with oxygen atoms necessarily leads to formation of longer CuO chains.

Employing expression (1) and the well-known empirical relation between T_c and doping p [7]:

$$T_c(p) = T_{c,max} [1 - 82.6(p - 0.16)^2] \tag{2}$$

we were able to calculate T_c as a function of x , and this dependence obtained for four different V_2 values and for $l_{cr}=4$ is shown in the figure 2. One can observe that T_c significantly decreases with V_2 interaction intensity reduction, this decrease being the most pronounced in the OII phase. However T_c is not so drastically reduced in the OI structural phase where the main T_c reduction due to Zn doping occurs. One can also observe that two lower $T_c(x)$ curves display a minimum at $x=x_{OII/OI}$, where transition from orthoII to orthoI structural phase occurs. Appearance of this minimum can be understood if one observe (figure 1) that in the region $x \in (0.5, x_{OII/OI})$ l_{av1} decreases,

implicating that the number of CuO chain with $l \geq l_{cr}$ which can transfer holes to the CuO₂ planes is decreased. This decrease cannot be compensated by the increase of average chain length on α_2 lattice where initially many CuO chains with $l \leq l_{cr}$ existed. Therefore T_c is reduced and minimum in $T_c(x)$ dependence is formed at $x_{OII/OI}$ when two sublattices become equivalent and l_{av} , as well as T_c , starts to increase. Though for $V_2/V_1 = -0.348 l_{av1}(x)$ and $l_{av2}(x)$ behave in the same way as in the $V_2/V_1 = -0.288$ case, decrease of l_{av1} does not produce chains with $l \leq l_{cr}$, since l_{av1} was initially much larger than l_{av1} for $V_2/V_1 = -0.288$. On the other hand chains with $l \geq l_{cr}$ are formed on the α_2 sublattice as x increases, and therefore T_c is enhanced in the region $x \in (0.5, x_{OII/OI})$ and no minimum exists.

CONCLUSION

CVM simulations of the ASYNNNI model were performed to investigate how the $T_c(x)$ dependence behaves with the increase of oxygen disorder in the chain planes of the RE123 superconductor, which is manifested in the reduction of the average chain length. Since T_c suppression observed in our simulations was not as drastic as the experimentally observed one in Zn doped RE123 samples [3] we conclude that oxygen disorder due to Zn doping can be only partially responsible for the experimentally observed T_c suppression. In order to make more precise estimation on the contribution of Zn doping induced oxygen disorder to the T_c reduction, experimental results on the average chain length in Zn doped RE123 samples are desirable.

ACKNOWLEDGEMENT

This work was supported by the Ministry of Education, Science and Technological Development of the Republic of Serbia (Prj. No.171027)

REFERENCES

- [1] R. Xue, H. Dai, Z. Chen, T. Li, Y. Xue, *Matt.Sci. and Tech.*, 2013, 178, 363–367.
- [2] M.Scavini, M. Coduri, M. Allieta, L. Mollica, M. Brunelli, L. Malavasi, A. Lascialfari, C. Ferrero, *J. Phys. Chem. C*, 2010, 114, 19509–19520.
- [3] R. K. Singhal, *J. Alloys and Comp.*, 2010, 495, 1–6.
- [4] L. T. Wille, D. de Fontaine, *Phys. Rev. B* 37, 1988, 37, 2227–2231.
- [5] V. M. Matic, N. Dj. Lazarov, M. Milic, *J. Alloys Compd.*, 2013, 551, 189–194.
- [6] P. A. Sterne, L. T. Wille, *Physica C*, 1989, 162-164, 223–224.
- [7] J. L. Tallon, C. Bernhard, H. Shaked, R. L. Hitterman, J. D. Jorgensen, *Phys. Rev. B*, 1995, 61, 12911–12914.

HIGH-TEMPERATURE INVESTIGATION OF THE SOME AURIVILLIUS PHASES

O.V.Krashenninnikova and A.V. Knyazev

*Chemistry Department, Lobachevsky State University of Nizhni Novgorod
Gagarin Av. 23/2, 603950, Nizhni Novgorod, Russia (okkraska@gmail.com)*

ABSTRACT

The compounds Bi_2MoO_6 , $\text{Bi}_4\text{V}_2\text{O}_{11}$ ($m = 1$), $\text{Bi}_3\text{NbTiO}_9$ ($m = 2$), $\text{Bi}_4\text{Ti}_3\text{O}_{12}$ ($m = 3$), $\text{BaBi}_4\text{Ti}_4\text{O}_{15}$ ($m = 4$), and $\text{Ca}_2\text{Bi}_4\text{Ti}_5\text{O}_{18}$ ($m = 5$) (Aurivillius phases with the general formula $\text{A}_{m-1}\text{Bi}_2\text{B}_m\text{O}_{3m+3}$) have been synthesized by solid state reactions. And also compounds $\text{Bi}_5\text{Nb}_3\text{O}_{15}$ ($m = 1,5$), $\text{Bi}_7\text{Ti}_4\text{NbO}_{21}$ ($m = 2,5$), $\text{CaBi}_8\text{Ti}_7\text{O}_{27}$ ($m = 3,5$) have been prepared ($\text{Bi}_4\text{A}_{2m-1}\text{B}_{2m+1}\text{O}_{6m+9}$). Using differential scanning calorimetry and high-temperature X-ray diffraction, we have studied their phase transitions.

INTRODUCTION

Bismuth-containing layered ferroelectrics are known as the Aurivillius phases have been the subject of researchers' ever increasing attention. The general formula of such compounds can be represented as $\text{A}_{m-1}\text{Bi}_2\text{B}_m\text{O}_{3m+3}$, where m is typically from 1 to 5 and can take fractional values. The so-called mixed Aurivillius phases form a peculiar family among the layer type bismuth compounds whose structure would be built up by a regular intergrowth of one half the unit cell of an m member superstructure and one half the unit cell of an $(m + 1)$ member superstructure along the stacking direction (fig.1). This intergrowth would lead to the general formula $\text{Bi}_4\text{A}_{2m-1}\text{B}_{2m+1}\text{O}_{6m+9}$. The A atoms most frequently have a valence of I, II, or III (or a combination of these) and a coordination number $\text{CN}_A > 6$. The B site is usually occupied by transition metals in octahedral coordination ($\text{CN}_B = 6$). The structure of these stoichiometric compounds is made up of slabs and blocks. Each slab consists of n layers of anion octahedra. For $n \rightarrow \infty$, its structure approaches the cubic perovskite structure. The blocks can be thought of as structural units of cubic BiF_3 [1].

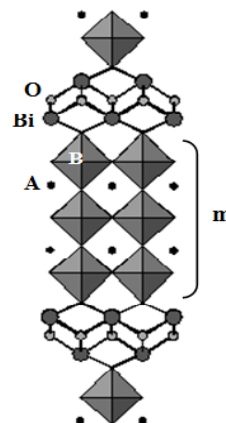


Figure 1.
The crystal structure of Aurivillius phases $\text{A}_{m-1}\text{Bi}_2\text{B}_m\text{O}_{3m+3}$ with $m = 3$

In this paper, we report high-temperature X-ray diffraction and thermal characterization of Aurivillius phases.

EXPERIMENTAL

The compounds were prepared by the solid-state reactions. The synthesized compounds were identified by X-ray diffraction. Diffraction patterns were collected at room temperature on a Shimadzu XRD-6000 X-ray diffractometer (CuK α radiation, reflection geometry) in the angular range $2\theta = 10^\circ$ – 80° with a scan step of 0.02° . High-temperature X-ray diffraction measurements (298–1173 K) were made on the Shimadzu XRD-6000 in the range $2\theta = 10^\circ$ – 60° with a scan step of 0.02° using a Shimadzu HA-1001 attachment. Thermal analysis was carried out with a SETARAM LABSYS differential scanning calorimeter in an argon atmosphere at a heating rate of 10 K/min and the NETZSCH DSC 204 F1 Phoenix at a heating rate of 5 K/min.

RESULTS AND DISCUSSION

Because of its layered nature, the ideal structure of Aurivillius phases has tetragonal symmetry (sp.gr. $I4/mmm$). At the same time, many compounds of this family have lower unit-cell symmetry due to octahedron-rotation-induced structural distortions. Nevertheless, most of the distorted structures undergo phase transitions on heating, which result, as a rule, in higher unit-cell symmetry and demonstrate that the Aurivillius phases tend to reach their “ideal” structure.

The compounds with $m \leq 3$ were synthesized as their low-temperature (LT), orthorhombic phases, whereas the compounds with $m > 3$ were obtained as their high-temperature (HT), tetragonal phases. Despite the differences in composition between the compounds, their in-plane unit-cell parameters a and b vary only slightly ($a = 5.43$ – 5.51 Å, $b = 5.39$ – 5.50 Å) and differ little. The difference between them does not exceed 0.7%. It is worth noting that the unit cell of the HT phases is half that of the LT phases and can be obtained by rotating the latter through 45° about the crystallographic axis c . According to our results, the out-of-plane unit-cell parameter c is a linear function of m (the number of layers per slab). Using differential scanning calorimetry, we determined the phase transition temperatures and melting points of the synthesized compounds. The phase transitions of Aurivillius phases can be divided into three groups: (1) reversible second-order transitions associated with sharp changes in the symmetry of the material, which can be characterized by a Curie temperature (T_C) (“normal” ferroelectric behavior); (2) slowly reversible second-order transitions, which also have a Curie temperature (relaxor-like

ferroelectric behavior); and (3) irreversible first-order transitions, associated with changes in structure type. The Aurivillius phases that undergo the first or second type of phase transition, and are stable up to their melting point, are of practical interest.

The compound Bi_2MoO_6 , which has only one octahedral layer per slab, undergoes the third type of phase transition (Table 1). Lower structure stiffness may lead to transformations resulting in the formation of framework structures from layered Aurivillius phases. At a temperature of 931 K, the compound in question undergoes an irreversible structural transformation into a zeolite-like monoclinic structure (sp. gr. $P2_1/c$) [2].

$\text{Bi}_4\text{V}_2\text{O}_{11}$ is the corresponding intrinsic oxygen deficient compound $(\text{Bi}_2\text{O}_2)_2(\text{VO}_{3.5}\square_{0.5})_2$ and exhibits, versus temperature, three main polymorphs α monoclinic, β orthorhombic and γ tetragonal [3]. The α -polymorph is stable from room temperature up to 723 K, β between 790 K and 850 K and γ , the most conductive polymorph, above 850 K up to the melting point around 1140 K (fig.2).

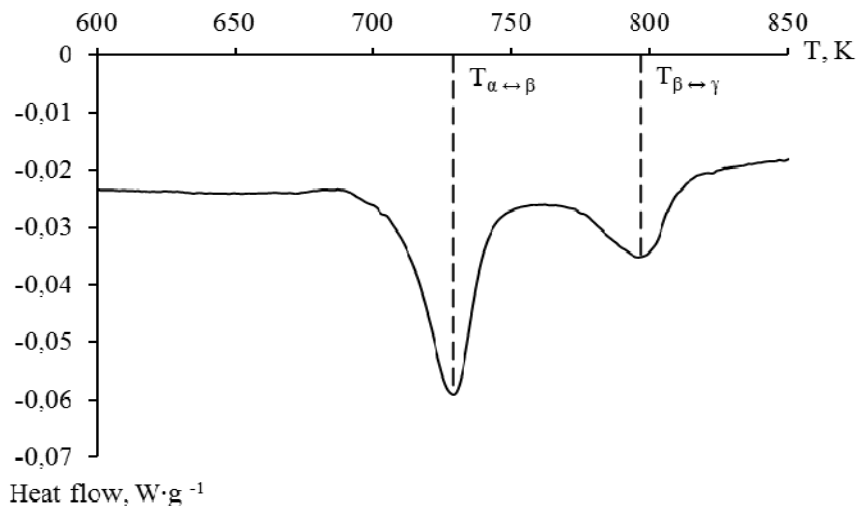


Figure 2. DSC curve for $\text{Bi}_4\text{V}_2\text{O}_{11}$.

The compounds $\text{Bi}_3\text{NbTiO}_9$ and $\text{Bi}_4\text{Ti}_3\text{O}_{12}$ undergo a first-order phase transition at temperatures of 1173 and 934 K, respectively. The lower Curie temperature of the $\text{Bi}_4\text{Ti}_3\text{O}_{12}$ compound is due to the large number of small bismuth atoms on the cuboctahedral site of the perovskite-like slab, which leads to considerable mobility of the octahedra with respect to each other. The presence of large barium atoms on the cuboctahedral site in the structure of the $\text{BaBi}_4\text{Ti}_4\text{O}_{15}$ compound reduces the mobility of the

octahedra to the extent that we observe the second type of phase transition. According to our and previous results [4], the $\text{Ba}_2\text{Bi}_4\text{Ti}_5\text{O}_{18}$ compound, which contains the largest number of barium atoms, has no HT phase. Using high-temperature and differential scanning calorimetry, we determined the two phase transitions for compound $\text{Bi}_7\text{Ti}_4\text{NbO}_{21}$ at about 943 K and 1103 K respectively. This sequence of phase transitions follows to change structure. The melting point of the synthesized Aurivillius phases has a tendency to decrease as the number of octahedra per slab increases (Table 1). This trend does not include the Bi_2MoO_6 compound, because its HT form is not an Aurivillius phase.

Table 1. The phase transition temperatures in some Aurivillius phases.

Compound	m	T_c , K	T_m , K
Bi_2MoO_6	1	931	1209
$\text{Bi}_4\text{V}_2\text{O}_{11}$	1	850	1140
$\text{Bi}_5\text{Nb}_3\text{O}_{15}$	1.5	773	1443
$\text{Bi}_3\text{NbTiO}_9$	2	1173	1482
$\text{Bi}_7\text{Ti}_4\text{NbO}_{21}$	2.5	1103	1457
$\text{Bi}_4\text{Ti}_3\text{O}_{12}$	3	934	1476
$\text{CaBi}_8\text{Ti}_7\text{O}_{27}$	3.5	940	1465
$\text{BaBi}_4\text{Ti}_4\text{O}_{15}$	4	663	1412
$\text{Ba}_2\text{Bi}_4\text{Ti}_5\text{O}_{18}$	5	-	1322

CONCLUSION

We have studied various Aurivillius phases, identified the mechanisms of their phase transitions, and determined their Curie temperatures.

ACKNOWLEDGEMENT

The work was performed with the financial support of the Russian Foundation of Basic Research (Project Number 13-03-00152).

REFERENCES

- [1] Aleksandrov, K.S. and Beznosikov, B.V., *Perovskity. Nastoyashchee i budushchee*. Novosibirsk, 2004, 231.
- [2] A. V. Knyazev, O. V. Krashenninnikova, V. Zh. Korokin. *Inorganic Materials*. 2014, 50, 2, 170–178.
- [3] R.N. Vannier, E. Pernot, M. Anne, O. Isnard, G. Nowogrocki, G. Mairesse, *Solid State Ionics*, 2003, 157, 147–153.
- [4] Aurivillius, B. and Fang, P.H, *Phys. Rev.*, 1962, 126, 893.

POWDER DIFFRACTION DATA FOR 4-DODECYLOXYPHENYL 4'-DECYLOXYBENZOATE

D. Obadović¹, M. Cvetinov², M. Stojanović², S. Rakić²,
A. Vajda³, K. Fodor-Csorba³ and N. Éber³

¹Faculty of Education, University of Novi Sad, Sombor, Serbia

²Department of Physics, University of Novi Sad, Novi Sad, Serbia

³Institute for Solid State Physics and Optics, Budapest, Hungary

ABSTRACT

Determination of crystallographic data are of interest for the industry of liquid crystalline displays. Here we present X-ray study on smectic liquid crystal 4-dodecyloxyphenyl 4'-decyloxybenzoate. It has been shown that at the room temperature, compound is in crystalline smectic phase whose unit cell parameters could be determined: lattice constants $a = 1.523(3)\text{nm}$, $b = 1.132(2)\text{nm}$, $c = 0.916(1)\text{nm}$, inclination angles $\alpha = 96.287(113)^\circ$, $\beta = 92.587(161)^\circ$, $\gamma = 102.222(184)^\circ$ and volume of unit cell $V = 1.530\text{nm}^3$. Space group determined is $P-1$.

INTRODUCTION

Modern materials for liquid crystalline display industry are multicomponent mixtures comprised of individual liquid crystalline substances. Resulting physicochemical characteristics of mixtures are highly dependant on polymorphism and molecular structure and properties of starting compounds. Thus, full characterisation of liquid crystalline substances including crystallographic data are of interest for the industry [1].

4,4'-alkyl/alkoxyphenylbenzoates represent a long known, huge family of prototypal calamitic liquid crystals [2]. Even though, crystallographic data on these compounds are scarce. In this paper we present X-ray study on 4-dodecyloxyphenyl 4'-decyloxybenzoate (Figure 1.), which is smectic member of homologous series, exhibiting smectic SmA and SmC phases.

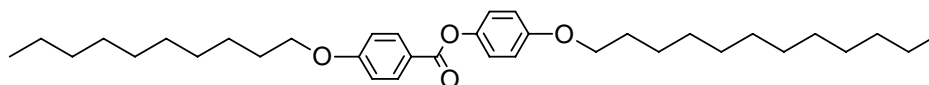


Figure 1. Structural formula of 4-dodecyloxyphenyl 4'-decyloxybenzoate

EXPERIMENTAL

The mesomorphic properties of unoriented samples of compounds under investigation were observed by polarizing microscopy (POM) equipped with a hot stage.

The diffraction pattern for the investigated compound was recorded at room temperature with a Seifert V-14 powder diffractometer equipped with a goniometer in the Bragg–Brentano ($\theta:2\theta$) geometry, using CuK radiation ($\lambda\text{CuK}\alpha_1 = 1.5406\text{\AA}$, generator setting: 30kV, 30mA). Silver behenate was used as an external standard. XRD data were collected over the angular range from 4° to $50^\circ 2\theta$ with a step size of 0.02° and a counting time of 4s per step.

Software EXPO2013 was employed for profile fitting procedure and determination of unit cell in reciprocal space [3].

RESULTS AND DISCUSSION

Temperatures of mesophase transitions under investigation are shown in Table 1.

Table 1. Temperatures of mesophase transitions [$^\circ\text{C}$] for compound under the study obtained by POM in cooling (Cr – crystalline, SmC – smectic C, SmA – smectic A, I – isotropic phase).

Cr	T [$^\circ\text{C}$]	SmC	T [$^\circ\text{C}$]	SmA	T [$^\circ\text{C}$]	I
•	66.5	•	78.0	•	80.0	•

The experimental powder diffraction pattern is depicted in Figure 2.

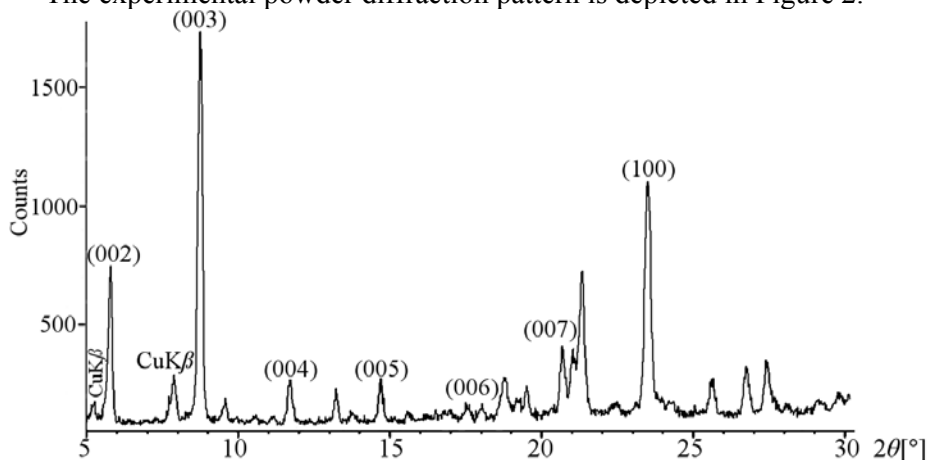


Figure 2. Experimental powder diffraction pattern of 4-dodecyloxyphenyl 4'-decyloxybenzoate

Observed Bragg angles as well as indexed lines are presented in Table 2. The X-ray diffraction study confirmed the existence of a more ordered smectic phase, which is primarily characterized by a number of sharp equidistant reflections at low Bragg angles indicating preserved long range lamellar ordering. Moreover, existence of numerous sharp peaks in proximity of $2\theta = 20^\circ$ are indicative of preserved long range in-plane order, strongly suggesting that this more ordered phase is crystalline smectic phase (CrX). The use of aligned (monodomain) sample would be necessary to fully clarify the content of unit cell and thus to resolve clearly the nature of the CrX phase. Satellite reflections from unfiltered $\text{CuK}\beta$ radiation could be observed in vicinity of very intense $\text{CuK}\alpha$ peaks. These peaks were recognized and excluded from the peak set selected for automatic indexing procedure.

Table 2. Observed Bragg angles [$2\theta_{\text{obs}}$], interplanar distances [d_{obs}], relative intensities [I_{rel}] and Miller indices of indexed reflections [hkl] of title compound

$2\theta_{\text{obs}}[^\circ]$	$d_{\text{obs}}[\text{nm}]$	$I_{\text{rel}}[\%]$	hkl
5.383		7.15	
5.959	1.48194	37.08	002
8.040		17.11	
8.901	0.99271	100.00	003
9.738	0.90750	12.29	
11.860	0.74558	17.42	004
13.380	0.66120	10.76	
14.859	0.59570	13.59	005
17.860	0.49620	8.34	006
18.920	0.46866	22.14	
19.680	0.45074	16.02	
20.837	0.42597	24.73	007
21.203	0.41870	65.78	
23.659	0.37575	99.48	100
25.780	0.34531	15.72	
26.919	0.33094	20.08	
27.580	0.32316	20.54	

Unit cell parameters were found to be: lattice constants $a = 1.523(3)\text{nm}$, $b = 1.132(2)\text{nm}$, $c = 0.916(1)\text{nm}$, inclination angles $\alpha = 96.287(113)^\circ$, $\beta = 92.587(161)^\circ$, $\gamma = 102.222(184)^\circ$ and volume of unit cell $V = 1.530\text{nm}^3$.

Space group determined is $P-1$. The figures of merit achieved are $F_{17} = 25$ and $M_{17} = 17$ [4].

CONCLUSION

Structural characteristics of the liquid crystal 4-dodecyloxyphenyl 4'-decyloxybenzoate was studied by powder X-ray diffraction. At room temperature the compound is in crystalline smectic phase whose unit cell parameters could be determined.

ACKNOWLEDGEMENT

This work was partly supported by the research Grant No. OI171015 from the Ministry of Education and Science of the Republic of Serbia and the Hungarian Research Fund OTKA K81250.

REFERENCES

- [1] K. Takada, T. Noma, T. Togano, T. Mukaide, and A. Iida, Powder Diffraction, 2004, 19, 01, 53-55.
- [2] T. T. Blair, M. E. Neubert, M. Tsai, and C.-c. Tsai, Journal of Physical and Chemical Reference Data, 1991, 20, 1, 189-204.
- [3] A. Altomare, C. Cuocci, C. Giacovazzo, A. Moliterni, R. Rizzi, N. Corriero, and A. Falcicchio, Journal of Applied Crystallography, 2013, 46, 4, 0-0.
- [4] P. d. Wolff, Journal of Applied Crystallography, 1972, 5, 3, 243.

INFLUENCE OF π - π AROMATIC INTERACTION ON FORMATION OF SMECTIC MESOPHASES

M. Cvetinov¹, D. Obadović², M. Stojanović¹, S. Rakić¹,
A. Vajda³, K. Fodor-Csorba³ and N. Éber³

¹*Department of Physics, University of Novi Sad, Novi Sad, Serbia*

²*Faculty of Education, University of Novi Sad, Sombor, Serbia*

³*Institute for Solid State Physics and Optics, Budapest, Hungary*

ABSTRACT

Smectic mesophases are common phases among liquid crystalline compounds. Together with nematic phase, they form cornerstone of contemporary industry of liquid crystalline displays. Using UV/VIS spectrometry, it is possible to demonstrate that formation of highly-ordered, hard smectic phases is dependent on the existence of aromatic π - π interaction.

INTRODUCTION

In order to achieve usable mesophase range and properties, contemporary materials for liquid crystalline display industry are based on multicomponent mixtures comprised of individual liquid crystalline substances. Among the mesophases most commonly used in the industry are nematic and smectic phases. Although the principal forces that stand behind the formation of specific mesophases are steric effect, dipole interaction and aromatic interaction, their exact contribution to mesophase formation is not yet fully elucidated [1].

In this work we show influence of aromatic interaction on resulting polymorphism of three selected compound. Shown on Figure 1. and 2. are 4-dodecyloxyphenyl 4'-decyloxybenzoate (compound **I**) and 4-decyloxyphenyl 4'-butyloxybenzoate (compound **II**), which belong to the homologue group of 4,4'-alkyl/alkoxyphenylbenzoates, long known, huge family of prototypal calamitic liquid crystals [2-4]. These components are selected on the basis of their uniform rigid core that possess ester group. Yet, in addition to molecular assymetry around their rigid core, their total length is also different.

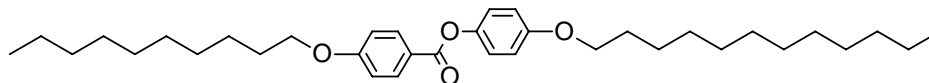


Figure 1. Structural formula of compound **I**

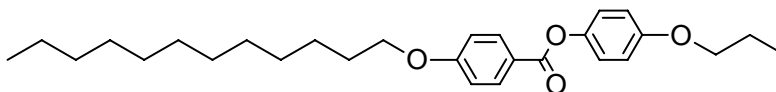


Figure 2. Structural formula of compound **II**

Third compound is ethyl 4'-(9-decen-1-iloxy)-1,1'-biphenyl-4-carboxylate (compound **III**, Figure 3.) [5]. Its rigid core is characterized by absence of ester linkage.

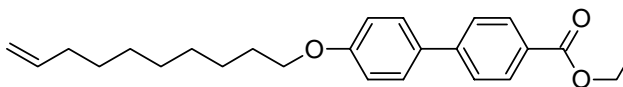


Figure 3. Structural formula of compound **III**

EXPERIMENTAL

The mesomorphic properties of unoriented samples of compounds under investigation were observed by polarizing microscopy (POM) equipped with a hot stage. The absorbance curves at wavelength range of 190-600nm were determined by a SPECORD 205 spectrophotometer (Analytik Jena, Germany).

RESULTS AND DISCUSSION

Temperatures of mesophase transitions for compounds under the study are given in Table 1. The widest temperature range of smectic phases is found in compound **III**, which exhibit 10.5°C wide smectic SmE mesophase and 12.3°C wide smectic SmA mesophase. Both compound **I** and compound **II**, which belong to the same homologue series, exhibit soft smectic phases (SmA and/or SmC) in the temperature range of about 14°C.

Table 1. Temperatures of mesophase transitions [°C] for compounds under the study obtained by POM in cooling (Cr – crystalline, SmE – smectic E, SmC – smectic C, SmA – smectic A, N – nematic, I – isotropic phase).

Compound	Cr	T[°C]	SmE	T[°C]	SmC	T[°C]	SmA	T[°C]	N	T[°C]	I
I	•	66,5			•	78,0	•	80,0			•
II	•	65,0					•	79,5	•	81,0	•
III	•	73,6	•	84,1			•	96,4			•

The experimental UV/VIS spectrograms of compounds **I**, **II** and **III** are depicted in Figure 4., 5. and 6. respectively.

Diffuse *K* band [6] spanning range of 240-320nm is found only in compound **III**. Such a wide *K* band shows extended conjugation that is uninterrupted neither by linking groups such as ester bond in compounds **I**

and **II**, nor by extreme torsion that can happen between biphenyl rings in rigid core. In this way essential prerequisites for existence of π - π aromatic interaction are met, which further encouraged appearance of highly ordered smectic phase.

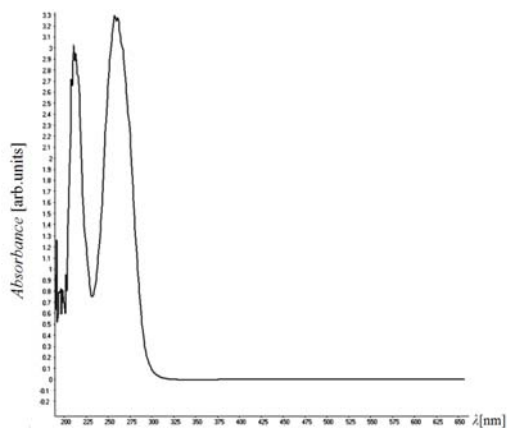


Figure 4. Experimental UV/VIS spectrogram of compound **I**

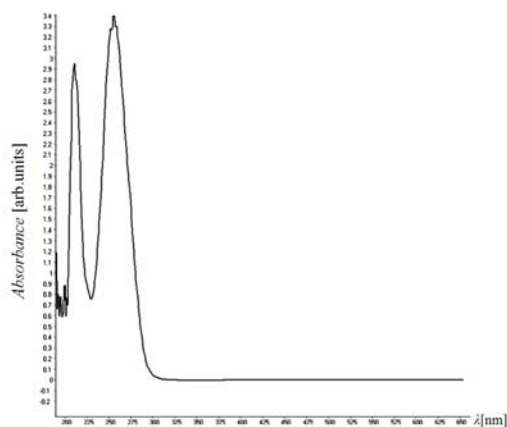


Figure 5. Experimental UV/VIS spectrogram of compound **II**

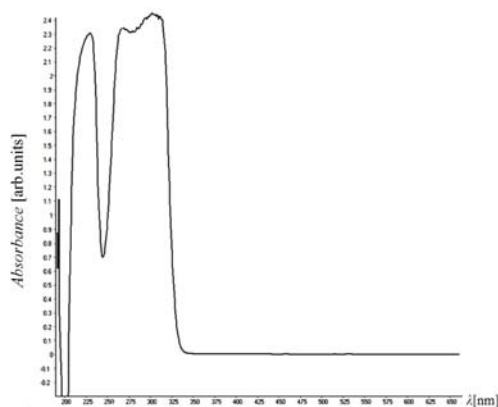


Figure 6. Experimental UV/VIS spectrogram of compound **III**

CONCLUSION

Formation of highly-ordered smectic phases, such as hard smectic SmE phase, is found to be reliant on the existence of π - π aromatic interaction. By carefully formulating structure of liquid crystalline compound, it is possible to tune degree of conjugation of the compound and intensity of the π - π aromatic interaction.

ACKNOWLEDGEMENT

This work was partly supported by the research Grant No. OI171015 from the Ministry of Education and Science of the Republic of Serbia and the Hungarian Research Fund OTKA K81250.

REFERENCES

- [1] D. Demus, J. W. Goodby, G. W. Gray, H. W. Spiess, and V. Vill, Handbook of Liquid Crystals, Handbook of Liquid Crystals: Four Volume Set, John Wiley & Sons, 1998.
- [2] T. T. Blair, M. E. Neubert, M. Tsai, and C.-c. Tsai, Journal of Physical and Chemical Reference Data, 1991, 20, 1, 189-204
- [3] M. E. Neubert and A. D. Vries, Molecular Crystals and Liquid Crystals, 1987, 145, 1, 1-15
- [4] S. Kumar, Liquid Crystals: Experimental Study of Physical Properties and Phase Transitions, Cambridge University Press, 2001.
- [5] Z.-S. Xu, R. P. Lemieux, A. Natansohn, P. Rochon, and R. Shashidhar, Liquid Crystals, 1999, 26, 3, 351-359
- [6] P. S. Kalsi, Spectroscopy of Organic Compounds, New Age International (P) Limited, 2004.

CRITICAL LINEAR LATTICE DIMENSION OF THE FOUR –DIMENSIONAL ISING MODEL ON THE CREUTZ CELLULAR AUTOMATON

Ganimet Mülazımoğlu KIZILIRMAK

Physics Department, Ahi Evran University, 40100, Kırşehir-TURKEY.

ABSTRACT

The four-dimensional Ising model is simulated on the Creutz cellular automaton (CCA) near the infinite-lattice critical temperature with the linear dimensions $4 \leq L \leq 22$. The critical exponents for the order parameter, the magnetic susceptibility and the specific heat are obtained from the results of simulations by using finite-size scaling relations. In this study conducted highly detailed, two different types of behavior were determined as a result of varying linear lattice dimension. Critical linear lattice dimension have been identified as $L = 14$.

INTRODUCTION

While the four-dimensional Ising model is not directly applicable to real magnetic systems, it is useful to investigate the influence of dimensionality on phase transitions [1]. The Creutz cellular automaton [2] has proven to be a fast alternative research tool in Ising model investigations near the critical regions of the lattices [3, 6]. As the dimension or the lattice size increases, the simulation of the Ising model by the conventional Monte Carlo method becomes impractical and faster algorithms are need. The Creutz cellular automaton does not require high-quality random numbers, it is an order of magnitude faster than the conventional Monte Carlo method, and compared to Q2R cellular automaton [4], it has the advantage of fluctuating internal energy from which the specific heat can be computed.

The purpose of this study is determined to critical linear lattice dimension.

EXPERIMENTAL

The four-dimensional Ising model with nearest-neighbor pair interactions is simulated on the Creutz cellular automaton near the infinite-lattice critical temperature with the linear dimensions $4 \leq L \leq 22$. Three variables are associated with each site of the lattice. The value of each site is determined from its value and those of its nearest-neighbors at the previous time step. The updating rule, which defines a deterministic cellular automaton, is as follows: of the three variables on each site, the first one is the Ising spin B_i .

Its value may be 0 or 1 or 2. The Ising spin energy of the lattice for the model is given with $H_I = -J \sum_{\langle i,j \rangle} S_i S_j$, where $S_i = 2B_i - 1$, $\langle i,j \rangle$ denotes the sum over all nearest neighbor pairs of sites. The second variable is for the momentum variable conjugate to the spin (the demon). The kinetic energy associated with the demon, H_K , is an integer, which is equal to the change in the Ising spin energy for any spin flip. The total energy $E = H_I + H_K$, is conserved. The third variable provides a checkerboard style updating, and so it allows the simulation of the Ising model on a cellular automaton.

The simulations are carried out on simple hypercubic lattices L^4 of linear lattice dimensions $4 \leq L \leq 22$ with periodic boundary conditions. The cellular automaton develops 10^6 sweeps for each run with 1 run for each total energy. The simulations were studied for kT/J and E/J values in the interval $2 \leq kT/J \leq 8$ and $-2 \leq E/J \leq 6$, respectively.

RESULTS AND DISCUSSION

The temperature dependence of the functions for the magnetic susceptibility (χ), the specific heat (C), order parameter (M) and Binder parameter (g_L) are analyzed for the lattice with $4 \leq L \leq 22$. The temperature variation of the Binder parameter has been shown in Fig. 1.

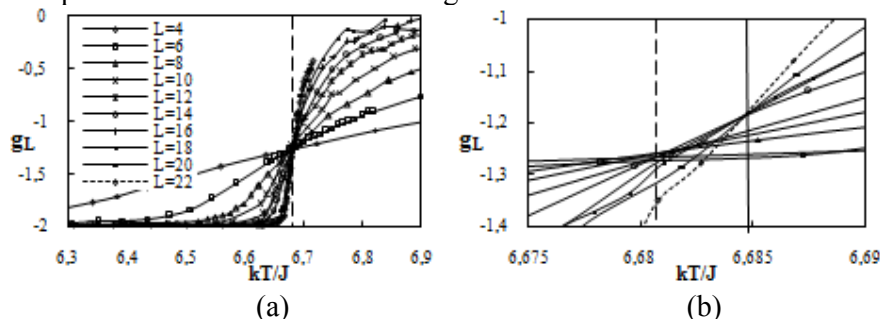


Figure 1. (a) The Binder cumulant as a function of kT/J (b) The figure on the right side is enlargement around the critical point

The intersection point of the g_L curves gives the infinite lattices critical temperature T_c as $L \rightarrow \infty$ [5]. As shown in Fig. 1, in contrast to other studies the g_L curves indicate two different behaviors in interval $4 \leq L \leq 22$. For $L = 4, 6, 8, 10, 12$ the intersection point of curves gives $T_c = 6.6845 \pm 0.0005$ and for $L = 14, 16, 18, 20, 22$ the intersection point of curves gives $T_c = 6.6807 \pm 0.0024$ approximately.

The finite-size lattice critical temperatures obtained from the susceptibility maxima $T_c^x(L)$ and the specific heat maxima $T_c^C(L)$ are determined. The dependences of the critical temperatures $T_c^x(L)$ and $T_c^C(L)$ obtained from the magnetic susceptibility or the specific heat maxima are given with $T_c(\infty) - T_c(L) \propto L^{-1/\nu} \log^{-1/6}(L)$. The finite-size scaling relation for $T_c^x(L)$ is used to get the critical temperatures of the infinite lattice (Fig. 2). As can be seen from the Fig. 2, by varying lattice linear dimension in range $4 \leq L \leq 22$ two different types of $T_c^x(L)$ behavior have been detected.

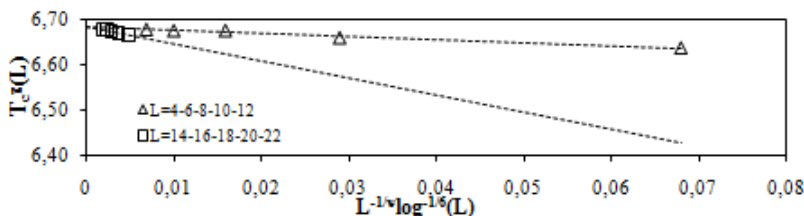


Figure 2. The plots of $T_c^x(L)$ against $L^{-1/\nu} \log^{-1/6}(L)$ with $\nu = 1/2$.

The computed values of the critical temperatures ($T_c(\infty)$) for the infinite lattice are $T_c(\infty) = 6.6807 \pm 0.0134$ ($4 \leq L \leq 12$), $T_c(\infty) = 6.6844 \pm 0.0339$ ($14 \leq L \leq 22$), for T_c^x and $T_c(\infty) = 6.6810 \pm 0.0134$ ($4 \leq L \leq 12$), $T_c(\infty) = 6.6871 \pm 0.0339$ ($14 \leq L \leq 22$) for T_c^C .

Table 1. The critical exponent values of the order parameter and the magnetic susceptibility for $T_c(L)$ and $T_c(\infty)$.

L	$\beta(T_c^x(L))$	$\beta(T_c^x(\infty))$	$\bar{\beta}(T_c^x(L))$	$\bar{\beta}(T_c^x(\infty))$
$4 \leq L \leq 12$	0.4745 ± 0.0007	0.4908 ± 0.0009	0.3594 ± 0.0025	0.3840 ± 0.0035
$14 \leq L \leq 22$	0.4839 ± 0.0001	0.4954 ± 0.0001	0.3723 ± 0.0012	0.3941 ± 0.0020
L	$\gamma(T_c^x(L))$	$\gamma(T_c^x(\infty))$	$\bar{\gamma}(T_c^x(L))$	$\bar{\gamma}(T_c^x(\infty))$
$4 \leq L \leq 12$	1.0610 ± 0.0238	1.1047 ± 0.0254	1.4163 ± 0.0095	1.4743 ± 0.0096
$14 \leq L \leq 22$	1.0446 ± 0.0004	1.0777 ± 0.0001	1.3403 ± 0.0046	1.4106 ± 0.0089

The critical exponents for the order parameter, the magnetic susceptibility and the specific heat are obtained from the results of simulations by using finite-size scaling relations [6].

Table 2. The values of critical exponents according to finite-size scaling functions for the four-dimensional Ising model.

L	β/ν	γ/ν	α/ν
$4 \leq L \leq 12$	1.0025 ± 0.0001	$1,9935 \pm 0,0001$	0.0577 ± 0.0011
$14 \leq L \leq 22$	1.0459 ± 0.0033	$1,8751 \pm 0,0003$	0.0326 ± 0.0176

As seen from Table 1 and Table 2 the critical exponents and finite-size scaling functions show two different behaviors to be in interval $4 \leq L \leq 12$ and in interval $14 \leq L \leq 22$.

CONCLUSION

The Ising model in $d = 4$ dimension is simulated on the Creutz cellular automaton for finite-size lattices with the linear dimensions $4 \leq L \leq 22$. In this study conducted with great precision, two different types of behavior were determined as a result of varying linear lattice dimension. Critical size dimension have been identified as $L = 14$. The average value of these two different behaviors is in agreement with the results of other studies [7].

ACKNOWLEDGEMENT

This study was supported by the Ahi Evran University under Scientific Support Project No: PYO-Fen.4010.14.009.

REFERENCES

- [1] H. W. J. Blöte and R. H. Swendsen, Phys. Rev. B, 1980, 22, 4481.
- [2] M. Creutz, Ann. Phys., 1986, 167, 62.
- [3] B. Kutlu and N. Aktekin, Phys. A, 1994, 208, 423; N. Aktekin, Physica A, 1995, 219, 436; N. Aktekin, Int. J. Mod. Phys. C, 1997, 8, 287; N. Aktekin, Phys. A 1996, 232, 397; N. Aktekin, J. Stat. Phys., 1996, 232, 397; N. Aktekin, A. Günen, Z. Sağlam, Int. J. Mod. Phys. C, 1999, 10, 875; N. Aktekin, Ş. Erkoç, Physica A, 2001, 290, 123.
- [4] W.M. Lang and D. Stauffer J. Phys. A, 1987, 20, 5413.
- [5] K. Binder, M. Nauenberg, V. Pivovarov and A. P. Young, Phys. Rev. B, 1985, 31, 1498.
- [6] N. Aktekin, J. Stat. Phys., 2001, 104, 1397.
- [7] Z. Merdan, R. Erdem, Phys. Lett. A, 2004, 330, 403; Z. Merdan, A. Duran, D. Atille, G. Mülazımoğlu and A. Günen, Physica A, 2006, 366, 265; Z. Merdan, A. Günen and G. Mülazımoğlu, Int. J. Mod. Phys. C, 2005, 16, 269; Z. Merdan, A. Günen and Ş. Çavdar, Physica A, 2005, 359, 415; Z. Merdan and D. Atille, Physica A, 2007, 376, 327.

NEAR-SURFACE HYDROGEN DYNAMICS IN TITANIA

R. Vujasin, B.P. Mamula, I. Milanović, J. Grbović Novaković
and N. Novaković

*Vinča Institute of Nuclear Sciences, University of Belgrade, POB 522,
11001 Belgrade, Serbia (radojka.vujasin@vinca.rs)*

ABSTRACT

The hydrogen interaction with the TiO₂ (110) surface has been investigated using pseudopotential and PAW methods with addition of U Hubbard term. The hydrogen diffusion behavior and thermodynamic properties were calculated by means of full relaxation of structure in every step of bulk diffusion. The results show the existence of potential barriers close to every atomic layer, the trends of barriers and overall system energy lowering away from surface and the occurrence of preferential H sites within each interlayer basin. These findings go in favor of previously experimental findings of TiO₂ low surface H coverage and observed easy diffusion of hydrogen from reduced surface into the TiO₂ bulk or at least in near surface region.

INTRODUCTION

Titania (rutile-structure TiO₂) attracts a lot of interest because of its many achieved and possible future applications, non-toxicity and safe usage. This material is used as a white pigment and for optical coating [1], as a photocatalyst for air and water purification and as a self-cleaning surface [2] and for hydrogen production using photochemical splitting of water [3]. Modified TiO₂ films could be promising alternative for spin-based electronic devices [4]. TiO₂ is also known as a good catalyst [5,6].

Another possible application of TiO₂ is in improvement of (de)sorption properties of hydrides. A large number of experimental studies confirm that the addition of metal oxides, such as TiO₂, has beneficial effect on destabilization of MgH₂ matrix and can cause improvement of this material's kinetic properties [6-10]. Further, several numerical studies on hydrogen motion through oxide surface has been done to understand the mechanism of the reaction [11,12].

Yin *et al.* [13] have investigated hydrogen coverage on TiO₂ (110) surface under different experimental conditions of exposure to atomic hydrogen. They obtained that maximum H monolayer coverage on TiO₂ (110) surface is only 70% at room temperature, regardless of applied partial pressure of

hydrogen. This result was confirmed using scanning tunneling microscopy and high-resolution electron energy loss spectroscopy. The same authors confirmed that during the heating of the hydrogenated sample, H atoms have migrated *into* the TiO₂ bulk. This is unusual since desorption of H₂ (or H₂O) molecules into the gas phase is common behavior of reduced oxides surface. Filippone *et al.* carried out research which showed that hydrogen behaves as a deep donor in rutile phase and forms an OH⁺ complex, where H forms bond with a prevailing ionic character [15]. With addition of Hubbard term U, they showed that electronic localization effects have major influence on nature of bonding and charge distribution as a consequence of hydrogen interstitial. Also, Ti⁺³ species are formed as a result of localization of H and OH⁺ electronic levels on some Ti neighbors [15]. The reduction of Ti⁺⁴ atoms to Ti⁺³ raises the possibility that all hydrogen atoms are adsorbed as protons onto outer oxygen atoms [11].

In this paper we have investigated the interaction of H atom with TiO₂ (110) surface and its behavior in the near-surface region of rutile TiO₂.

DETAILS OF CALCULATIONS

Investigation of atomic hydrogen behavior on rutile TiO₂ (110) surface and in the near-surface region were done using two methods available in Abinit code [16-18]. Plane waves based calculations with Troullier - Martins norm-conserving pseudopotentials (PP) and projected augmented waves (PAW with GGA+U) methods were used. The value of U_{eff} was 2.0 eV. The energy cut-off of the plane wave basis set was 816 eV.

In case of PP calculations (1x1)(110) supercell with 12 atomic layers and 25 atoms was constructed. Slab supercell (2x1)(110) with 21 atomic layers and 85 atoms was constructed in the case of PAW calculation. The surface of the supercells was

separated from its periodic image by 15 Å of vacuum. Three bottom layers were fixed to simulate the bulk. The rest of supercell atoms were subject to

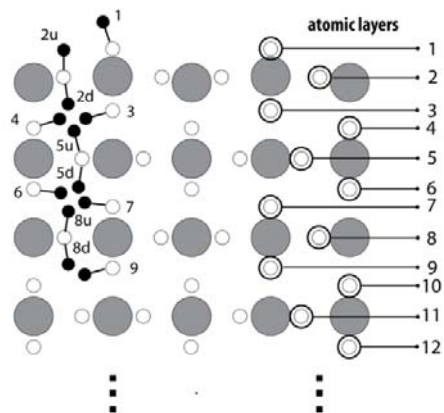


Figure 1. Side view of slab supercell - atomic layers and initial positions of H atoms.

the relaxation of atomic positions. It is assumed that hydrogen atom forms short OH bonds and that diffusion consists of “jumps” between neighboring O sites. Further, calculations were performed to obtain relaxed structures with different arrangements, where H atom was bounded to O atoms in different atomic layers.

RESULTS AND DISCUSSION

In Fig. 2, the energy differences as function of H distance from surface are given for both PP and PAW (GGA+U) calculations. Energy differences were shown on x axis, with energy of configuration **1** used as reference, marked with horizontal line. As distance reference from surface, z-coordinate of O_{2s} atom in slab supercell without H was used, marked as vertical short-dashed line. The characteristic “periodic” dependence of energy on hydrogen position depth is visible. In case of PP calculations “degeneration” of opposite configurations (i.e. 2d and 5u, 3 and 4) was not observed. According to [13,15] the barriers for jump from one oxygen atom to another range from 0.5 to 1.1 eV, depending on the position of bonding oxygen atoms and distance from surface. These barriers could be overcome at modest temperatures (in accordance with [13]). The details of energy profile, like barriers, are not visible in approach presented here. However, initial and final states, corresponding to jump from one O atom to the next can provide details and possible pathways of hydrogen drift from and to the surface.

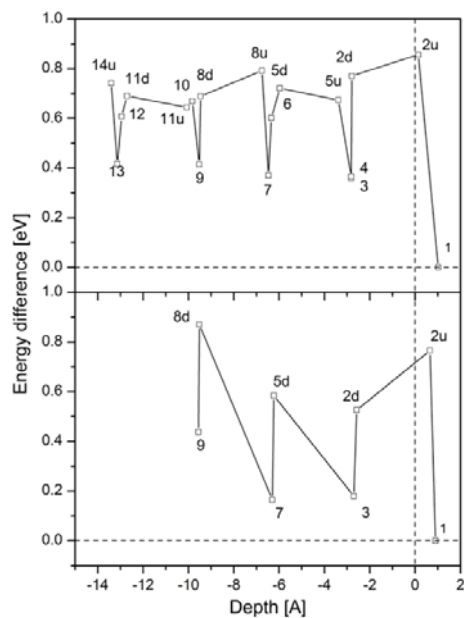


Figure 2. Slab system energy change as a function of hydrogen atom distance from the surface. Top) PAW, bottom) PP.

CONCLUSION

In this paper we have presented the results of electronic structure calculations of (1x1) and (2x1) (110) slabs of TiO₂ – H system. The degree

of H influence on host lattice clearly depends on H concentration and charge redistribution mechanism (GGA or GGA+U). In case of PP calculations, there is a preferred direction perpendicular to surface in a sense of preference of closer-to-surface configurations, at least in the few atomic layers close to the surface. This preference was not observed in PAW calculations. The characteristic energy profile of close-to surface area show that atomic layers parallel to surface act like barriers for hydrogen drift into the bulk. At the same time, hydrogen should “jump” within the same interlayer basin fairly easy. The rise of energy of configurations close to bottom surface of slab supercell can be attributed to non relaxed and stressed structure due to fixed positions of the lowest atomic layers. From the same reason it is hard to estimate how deep influence of surface goes. Larger supercell calculations showed that the influence of surface is constrained to only few atomic layers closest to vacuum.

ACKNOWLEDGEMENT

This work was supported by Serbian Ministry of Education, Science and Technological Development under the Grant III 45012. Calculations have been partially performed using ENEA-GRID facility, Italy.

REFERENCES

- [1] U. Diebold, Surf Sci Rep 2003, 48, 53-229.
- [2] A. Fujishima, T.N. Rao, D.A. Tryk, J Photochem Photobiol C: Photochem Rev 2000, 1, 1-21.
- [3] A. Fujishima, K. Honda, Nature, 1972, 238, 37-38.
- [4] Y. Matsumoto et al, Science, 2001, 291, 854-856.
- [5] M.A. Henderson, Surf Sci Rep, 2011, 66, 185-297.
- [6] D.L. Croston, D.M. Grant, G.S. Walker, J Alloys Compd, 2010, 492, 251-258. W. Oelerich, T. Klassen, R. Bormann, J Alloys Compd, 2001, 315, 237-242.
- [7] M. Polanski, J. Bystrzycki, J Alloys Compd, 2009, 486, 697-701.
- [8] H. Hirate et al, J Alloys Compd, 2011, 509S, S612-615.
- [9] K.S. Jung, D.H. Kim, E.Y. Lee, K.S. Lee, Catal Today, 2007, 120, 270-275.
- [10] J. Leconte et al, Surf Sci, 2002, 497, 194-204.
- [11] H.-T. Chen et al, ChemPhysChem, 2007, 8, 849-55.
- [12] X.-L. Yin et al, ChemPhysChem, 2008, 9, 253-6.
- [13] F. Filippone et al, Phys Rev B, 2009, 80, 245203.

A NEW HIGH PRESSURE PHASE AND STRUCTURAL PHASE TRANSITIONS OF MAGNESIUM FLUORIDE

H. Ozturk, C. Kurkcu and C. Kurkcu

Physics Department, Ahi Evran University, Kirsehir, 40100, TURKEY

ABSTRACT

The pressure-induced phase transition in magnesium fluoride (MgF_2) is studied using an *ab-initio* constant-pressure technique up to 800 GPa. Three high-pressure phases of MgF_2 are successfully observed through constant pressure simulations. MgF_2 undergoes a phase transformation from the tetragonal structure to the cubic structure with space group $Fm\bar{3}m$ at 280 GPa. This transformation proceeds via three intermediate phases with space groups $Pnmm$, $Immm$ and $R\bar{3}m$. Upon further increase of pressure a gradual phase change to the orthorhombic structure with space group $Pnma$ occurs at 500 GPa. Another phase transformation from the orthorhombic structure to tetragonal structure with space group $I4/mmm$ is seen at 720 GPa. The transition pressures are also calculated from the Gibbs free energy, and it is found that the structural phase transformations occur at 20 GPa for $Fm\bar{3}m$, at 45 GPa for $Pnma$ and at 260 GPa for $I4/mmm$. As far as we know, the last phase has not been obtained in any previous studies.

INTRODUCTION

The investigation of materials under high pressure has become a very important topic in recent years. The high-pressure behavior of MgF_2 is reasonably inquisitive. Inquisitive structural features of phase transformation mechanism are still mysterious because of difficulties in monitoring movements of atoms in the experiments. Reliable dynamical simulations are needed because of the difficulties in understanding the atomistic motions while performing the experiments.

Whereas some studies [1-3] give prominence to that the tetragonal rutile-type MgF_2 should be transformed into an orthorhombic CaCl_2 -type structure with space group $Pnmm$, some other studies [4-6] underline that this material should be transformed into a cubic fluorite-type structure with space group $Fm\bar{3}m$ at high pressures. The results of this study applying conjugate-gradient method support the later transformation.

MgF_2 crystallizes in a tetragonal rutile-type structure with space group $P4_2/mnm$ at ambient conditions. Although this crystal also has the same rutile-type structure as the transition metal compounds of AF_2 -type, Mg is

not a transition metal; namely, Mg has no d-electrons. Lack of these electrons and the highly ionic character of MgF_2 simplify theoretical studies. The phase transitions of MgF_2 are found at lower pressures than in many dioxides thanks to the higher compressibility of this material and relative sizes of its ions.

COMPUTATIONAL

The computations were achieved using the *ab-initio* program SIESTA based on pseudopotentials and a localized basis set [7]. Calculations were performed in the density functional theory (DFT). For the exchange correlation energy the generalized gradient approximation (GGA) was performed [8]. Double zeta plus polarized basis sets were applied. A uniform mesh with a plane wave cut-off of 150 Rydberg was used with the purpose of representation of the electron density, the local part of the pseudopotentials, the Hartree and the exchange-correlation potential. A simulation cell of 96 atoms was selected and the periodic boundary conditions were used. Gamma point sampling was employed for the Brillouin zone integration.

To apply pressure to the system, conjugate-gradient method was used. Firstly the system was relaxed at zero pressure, after that pressure was increased step by step. For each value of the applied pressure, the structures were allowed to relax and to catch their equilibrium volumes and lowest energies by optimizing their lattice vectors and atomic positions together until the maximum atomic forces were getting smaller than 0.01 eV \AA^{-1} and the stress tolerances were getting less than 0.5 GPa.

RESULTS AND DISCUSSION

We calculate the equilibrium phase transition pressure from the Gibbs free energy, $G = E_{\text{tot}} + PV - TS$. Since calculations are made at zero temperature the TS term is neglected. Therefore, the static enthalpy can be expressed as $H = E_{\text{tot}} + PV$, where pressure is obtained by direct differentiation of the calculated energy-volume curves *i.e.*, $P = -dE_{\text{tot}}/dV$. We take the energy-volume calculations into account and the thermodynamic criterion of equal free energies to study the stability of different phases of MgF_2 . The calculated energy-volume relations are fitted to the third-order Birch-Murnaghan equation of states given by

$$P = 1.5 B_0 \left[\left(\frac{V}{V_0} \right)^{-\frac{7}{3}} - \left(\frac{V}{V_0} \right)^{-\frac{5}{3}} \right] \times \left\{ 1 + 0.75 (B_0' - 4) \left[\left(\frac{V}{V_0} \right)^{-\frac{2}{3}} - 1 \right] \right\}$$

where P is the applied pressure, V is the volume at pressure, V_0 , B_0 and B'_0 are the volume, bulk modulus and its pressure derivative at ambient pressure [9,10]. Fig. 1 shows the computed total energies of the orthorhombic structure with space group $Pnma$ and tetragonal structure with space group $I4/mmm$ as a function of volume.

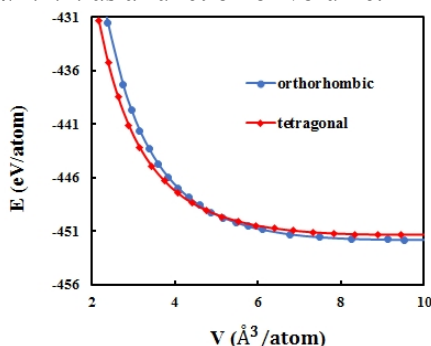


Figure 1. The energy curves of MgF_2 structures as a function of volume.

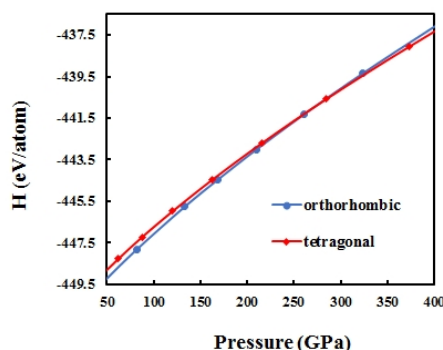


Figure 2. The enthalpy curves of MgF_2 structures as a function of pressure.

For the reason that structural phase transitions in simulations occur through the entire simulation cells, systems need cross a notable energy barrier for transition one phase to another phase. Enthalpy calculations give commonly realistic transition pressures relative to experimental transition pressures. The phase transitions emerge when the enthalpies of the two phases equal to each other. Thus, we compute the enthalpies of the two phases and plot them as a function of pressure in Fig. 2. We can conclude from the enthalpy curves that the phase transformation from the orthorhombic structure to the tetragonal structure with space group $I4/mmm$ occurs at about 260 GPa. This structure is depicted in Fig. 3.

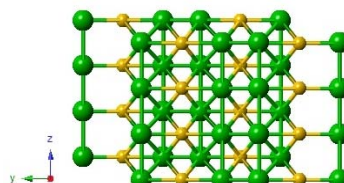


Figure 3. Tetragonal structure of MgF_2 with space group $I4/mmm$ at 720 GPa.

CONCLUSION

We have used a constant pressure *ab-initio* technique to study the behavior of MgF_2 under the hydrostatic pressure and estimated three structural phase transformations. The tetragonal rutile-type structure of MgF_2 undergoes a phase transformation to the cubic structure with space group $Fm\bar{3}m$ at 20 GPa. This transformation proceeds through three intermediate phases with

space groups $Pn\bar{m}$, $Im\bar{m}m$ and $R\bar{3}m$. The cubic structure of MgF_2 transforms to the orthorhombic structure with space group $Pnma$ at 45 GPa and this orthorhombic structure transforms to tetragonal structure with space group $I4/m\bar{m}m$ at 260 GPa. The Mg–F bond lengths range from 1.839 to 1.999 Å and Mg is ten-fold coordinated by F and the F–F bond lengths range from 1.828 to 2.274 Å and F is five-fold coordinated by Mg for this tetragonal structure. As far as we know, although the first two high-pressure phases are comparable to the findings of previous studies, the last phase obtained in this study have not been observed in any other earlier studies.

ACKNOWLEDGEMENT: This study was supported by the Ahi Evran University under Scientific Support Project No: PYO-Fen.4010.14.008.

REFERENCES

- [1] J. Haines, J.M. Leger, F. Gorelli, D.D. Klug, J.S. Tse, Z.Q. Li, Phys. Rev. B, 2001, 64, 134110-1-10.
- [2] V. Kanchana, G. Vaitheeswaran, . Rajagopalan, J. Alloy and Comp., 2003, 352, 60-65.
- [3] H. Öztürk, C. Kürkçü, C. Kürkçü, J. Alloy and Comp., 2014, 597, 155-160.
- [4] N.L. Allan, R.I. Hines, M.D. Towler, W.C. Mackrodt, J. Chem. Phys. 1994, 100, 4710-4711.
- [5] K. Nishidate, M. Baba, T. Sato, K. Nishikawa, Phys. Rev. B, 1995, 52, 3170-3176.
- [6] H. Öztürk, C. Kürkçü, C. Kürkçü, J. Alloy and Comp., 2014, 609, 185.
- [7] P. Ordejon, E. Artacho, J.M. Soler, Phys. Rev. B, 1996, 53, R10 441.
- [8] J.P. Perdew, K. Burke, M. Ernzerhof, Phys. Rev. Lett., 1996, 77, 3865.
- [9] F. Birch, Phys. Rev., 1947, 71, 809–824.
- [10] F.D. Murnaghan, Proc. Natl. Acad. Sci. USA, 1944, 30, 244–247.

AB INITIO CALCULATIONS OF HIGH-PRESSURE STRUCTURAL PHASE TRANSITION IN CHROMIUM DIOXIDE

C. Kurkcu^{1,2} and H. Ozturk¹

¹ *Physics Department, Faculty of Arts and Sciences, Ahi Evran University, Kirsehir, 40100, Turkey*

² *Physics Department, Institute of Science, Gazi University, Ankara, Turkey*

ABSTRACT

The structural phase transition of chromium dioxide (CrO_2) are investigated using density functional theory (DFT) within the Ceperley-Alder (CA) form of local density approximation (LDA). We investigate the structural behavior of CrO_2 under the hydrostatic pressure up to 500 GPa. At 220 GPa, tetragonal rutile-type structure with space group $P4_2/mnm$ of CrO_2 transforms to orthorhombic CrO_2 -type structure with space group $Pnmm$. At 440 GPa, CaCl_2 -type structure of CrO_2 transforms to another orthorhombic structure with space group $Cmc2_1$. We also study the stability of these phases from the total energy and enthalpy computations. According to these investigations, the phase transformations should occur from the tetragonal rutile-type structure to the CaCl_2 -type structure around 15 GPa and from the CaCl_2 -type structure to the another orthorhombic structure with space group $Cmc2_1$ around 85 GPa.

INTRODUCTION

As a half-metal and ferromagnet, chromium dioxide has attracted remarkable interest owing to its importance. This substance is considered as an ideal material for developing spintronic devices, tunneling magnetoresistance devices, magnetic heads, magnetic random access memories and magnetic field sensor [1-11].

Chromium dioxide crystallizes in the tetragonal rutile-type structure at ambient conditions like TiO_2 , MnO_2 , RuO_2 , SnO_2 and GeO_2 , etc. Among these rutile-type dioxides, CrO_2 has special importance because CrO_2 is the only half-metallic ferromagnet. Maddox et al. [3] experimentally observed a phase transformation from the rutile to the CaCl_2 -type structure at pressure of 12 ± 3 GPa. We have also obtained by ab initio calculations this phase transformation at about 15 GPa in good agreement with their study.

COMPUTATIONAL

The calculations were performed with the ab initio program SIESTA [12]. The method is based on the density functional theory (DFT) within the Ceperley-Alder (CA) form of local density approximation (LDA). A uniform mesh with a plane wave cut-off of 200 Ry was used with the aim of representing the electron density, the local part of the pseudopotentials, and the Hartree and the exchange–correlation potential. A simulation cell of 96 atoms with periodic boundary conditions has been chosen. In order to apply pressure to the system, we used conjugate-gradient method. The system was first equilibrated at zero pressure, and then the pressure was gradually increased by a rise of 20.0 GPa. For each value of the applied pressure, the structure was permitted to relax and find its equilibrium volume and lowest-energy by optimizing its lattice vectors and atomic positions together until the maximum atomic forces were smaller than $0.01 \text{ eV } \text{Å}^{-1}$ and the stress tolerances were less than 0.5 GPa.

RESULTS AND DISCUSSION

The pressure was gradually increased beginning from the zero-pressure structure and the structure of CrO_2 at each applied pressure was analyzed using the KPLOT program [13]. At 0 GPa, we have found rutile-type structure of CrO_2 with space group $P4_2/mnm$ and depicted it in Fig. 1.

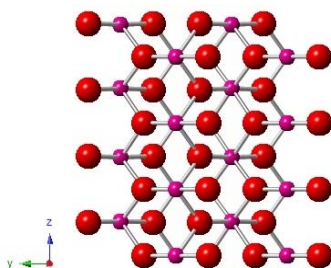


Figure 1. (Color online) Rutile-type structure of CrO_2 at zero pressure.

This structure of CrO_2 has 6 atoms per unit cell. Cr is six-fold coordinated by O and the Cr-O bond lengths range from 1.773Å to 1.863Å for this structure. Cell parameters of this structure are obtained as $a=b=4.3754 \text{Å}$ and $c=2.5932 \text{Å}$. These results are in good agreement with literature [11]. A phase transformation from rutile-type structure with space group $P4_2/mnm$ to the orthorhombic structure with space group $Pnmm$ has been found at 220 GPa. This orthorhombic structure is depicted in Fig. 2.

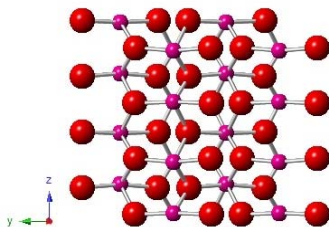


Figure 2. (Color online) Crystal structures of CrO₂ at 220 GPa.

This structure of CrO₂ has also 6 atoms per unit cell. Cr is six-fold coordinated by O and the Cr-O bond lengths range from 1.641 Å to 1.743 Å for this structure. Cell parameters of this structure are obtained as $a=3.7145\text{Å}$, $b=4.2312\text{Å}$ and $c=2.1888\text{Å}$.

At 440 GPa we have found another phase transformation from orthorhombic structure with space group *Pnmm* into another orthorhombic structure with space group *Cmc2₁*. As far as we know, this phase has not been obtained in any previous studies. This structure is depicted in Fig. 3.

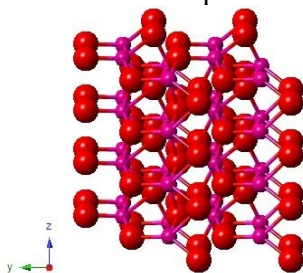


Figure 3. (Color online) Crystal structures of CrO₂ at 440 GPa.

This structure has 12 atoms per unit cell and is denser than the first two phases of CrO₂ obtained in this study. In this structure of CrO₂, Cr is seven-fold coordinated by O and the Cr-O bond lengths range from 1.615 Å to 1.725 Å. Cell parameters of this phase are obtained as $a=2.0887\text{Å}$, $b=7.4108\text{Å}$ and $c=3.6589\text{Å}$.

The polyhedral views of CrO₂ phases obtained in this study are illustrated in Fig. 4.

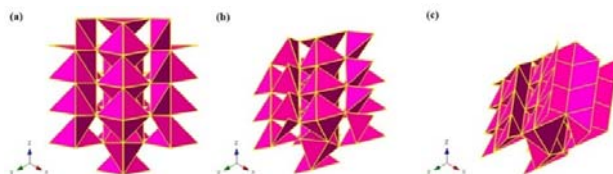


Figure 4. Polyhedral views of CrO₂ phases: a) $P4_2/mnm$ phase at zero pressure, b) $Pnnm$ phase at 220 GPa and c) $Cmc2_1$ phase at 440 GPa.

CONCLUSION

We have predicted three pressure-induced structural phase transitions in CrO₂. Rutile-type structure of chromium dioxide undergoes a phase transition to orthorhombic CaCl₂-type structure with space group $Pnnm$. This result is important both as a model for TiO₂ at high pressure and owing to the fact that the rutile → CaCl₂-type transition is a first step in the phase transition sequence.

REFERENCES

- [1] K. Schwarz, J. Phys. F: Met. Phys. 1986, 16 L211–L215.
- [2] K.P. Kamper, W. Schmitt, G. Guntherodt, R.J. Gambino, R. Ruf, Phys. Rev. Lett., 1987, 59, 2788–2791.
- [3] B.R. Maddox, C.S. Yoo, D. Kasinathan, W.E. Pickett, R.T. Scalettar, Phys. Rev. B, 2006, 73, 144111.
- [4] R.M. Hazen, L.W. Finger, J. Phys. Chem. Solids, 1981, 42, 143–151.
- [5] J. Haines, J.M. Leger, S. Hoyau, J. Phys. Chem. Solids, 1995, 56, 965–973.
- [6] V. Kanchana, G. Vaitheeswaran, M. Alouani, J. Phys. Condens. Matter, 2006, 18, 5155–5162.
- [7] A.Y. Kuznetsov, J.S. De Almeida, L. Dubrovinsky, R. Ahuja, S.K. Kwon, I. Kantor, A. Kantor, N. Guignot, J. Appl. Phys., 2006, 99, 053909-1-7.
- [8] V. Srivastava, M. Rajagopalan, S.P. Sanyal, Eur. Phys. J. B., 2008, 61, 131–139.
- [9] S.F. Matar, G. Demazeau, Chem. Phys. Lett., 2005, 407, 516–521.
- [10] V.A. Sidorov, A.V. Rakhmanina, O.A. Morya, Solid State Com., 2006, 139, 360–362.
- [11] Y. Li, J. Hao, Solid State Com. 2012, 152, 1216–1220.
- [12] P. Ordejon, E. Artacho, J.M. Soler, Phys. Rev. B, 1996, 53, R10 441-444.
- [13] R. Hundt, J.C. Schön, A. Hannemann, M. Jansen, J. Appl. Crystallogr., 1999, 32, 413–416.

MACROMOLECULAR
PHYSICAL CHEMISTRY

SURFACE ENERGY IN FORECAST OF POLYMER APPLICATION IN MEMBRANE MATERIAL SCIENCE

Yu. G. Bogdanova and V. D. Dolzhikova

*Chemistry Department, Lomonosov Moscow State University,
Leninskie Gory, 1/3, Moscow, Russia. (yulibogd@yandex.ru)*

ABSTRACT

The surface energy of amorphous polymer films (γ_{SV}), its dispersive (γ_{SV}^d) and polar (γ_{SV}^p) components were determined using contact angle measurements. The interrelation between the dispersive component of surface energy, polymer fractional free volume and gas permeability of polymer membranes were found.

INTRODUCTION

Surface (γ_{SV}) and interfacial «polymer-liquid» (γ_{SL}) energy of solid materials and its alteration during the contact of material with different media determine the different processes proceeding at the interface (adsorption, adhesion, change of mechanical strength, etc.) [1]. That is why this values may be a parameter of forecast of polymer efficiency for practical tasks decision.

Contact angle measurements are widely used for the γ_{SV} determination [2]. In present work new perspectives of this method for membrane materials efficiency prediction are shown.

EXPERIMENTAL

Films of amorphous polymers, which are perspective for membrane materials creation, were studied (Fig.1); films thickness was 300÷500 nm. Polynorbornenes, poly(4-methyl-2-pentine) (PMP) and poly[1-(trimethylsilyl)-1-propine (PTMSP) were synthesized and characterized in Topchiev Institute of Petrochemical Synthesis, RAS. Also commercial statistic copolymers tetraflyuroethylene with 2,2,4-thrifluoro-5-thrifluorometoxy-1,3-dioxolane (Hyflons®ADX, Solvay-Solexis) and 2,2-bis(thrifluoromethyl)-4,5-difluoro-1,3-dioxolane (Teflons®AF, Du Pont) were studied. Literature data about physical-chemical characteristics (glass transition temperature T_g , gas (O_2) permeability P , fractional free volume FFV) of polymers investigated were used. Polymer films were prepared by coating from solutions at the surface of solid carriers (Alumina plates) with size 10x15x1 mm. 1 wt% of metathesis polynorbornenes solution in

toluene, 1 wt % of additive polynorbornenes solution in cyclohexane and 1 wt % of AD and AF in octafluorotoluene were used; then films were dried during 48 h at 20 °C. PTMSP and PMP films were prepared in accordance to technique described in [3] without solid carrier.

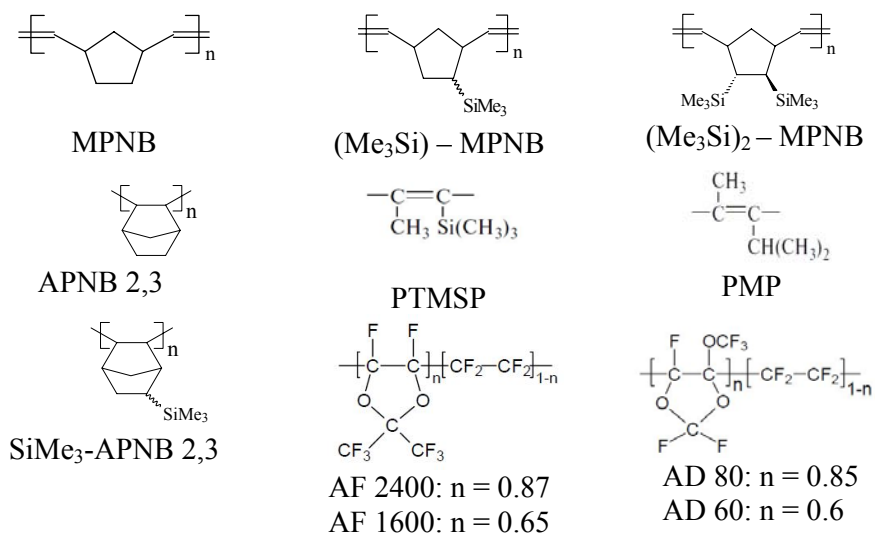


Figure 1. Structural formulae of monomer links of polymers investigated.

Owens-Wendt-Kaelble approach for the determination of surface energy of polymer films γ_{SV} , its dispersive γ_{SV}^d and polar γ_{SV}^p components was used [2]. Contact angles of test liquids (water and ethylene glycol) were measured by sessile drop technique with accuracy 1 degree. The accuracy of γ_{SV} , γ_{SV}^d , γ_{SV}^p values determination was 1 mJ·m⁻². All measurements were performed at 20 °C. It is essential, that the determination of γ_{SV} and measurements of gas permeability ($P(O_2)$) were performed for the same synthetic samples of polymers and very close conditions of films preparation.

RESULTS AND DISCUSSION

Since the structure of surface layers of polymer membranes influence strongly in processes of transport and separation of gases and liquids, surface energy characteristics may be used as parameters permitting to predict permeability of polymer films. Neglecting the small-scale mobility of macromolecules, interactions of polymer coils in the film in the first approximation can be considered from the point of contact interactions between particles phase.

The energy of average contact between the polymer coil-particles $u(av)$ may be a measure of this interaction. The principal possibility of such approach is illustrated by the similarity of dependencies of surface tension of low molecular weight liquids and surface energy of polymers from its evaporation energy and energy of cohesion, respectively (Fig.2).

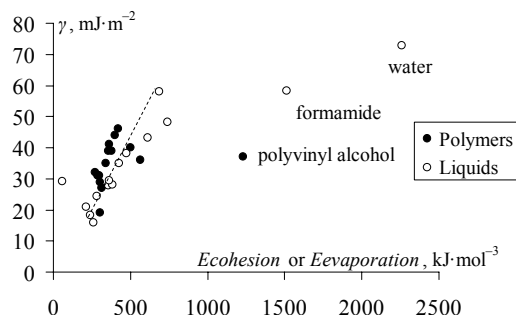


Figure 2. The dependence of polymer surface energy and surface tension of low molecular liquids (20 ÷ 25 °C) from energy of cohesion of polymer and evaporation heat, respectively (handbook data).

The general character of dependencies of surface energy from energy of cohesion for polymers in the different phase states should be mentioned. The deviation from linear dependence between the bulk and surface characteristics is observed for substances, which are able to the formation of hydrogen bonds. The $u(av)$ depends on the distance between the particles, which, in turn, is determined by its packing density. In the short-range order within the dispersion interaction, characterized by the lowest energy among other types of intermolecular forces [4], may be more sensitive to changes in the distance. On the other hand, the polymer density is related with its free volume, which has a decisive influence on the mass transfer in films of glassy polymers. Polymer free volume is determined by the low-range order, which, in turn, depends from interaction of polymer links [5]. Lateral interactions of unrelated links influence on the magnitude of the surface energy. Thus, the same factor affects on a free volume and surface energy.

We obtained good correlation between the experimentally determined γ_{SV}^d values and literature data of FFV is observed for all investigated polymers, exclude AD (Fig.3). In many cases gas permeability P is related with polymer fractional free volume FFV :

$$P = A \cdot \exp(-B / FFV),$$

where A and B are the constants, individual for each gas [6]. So, the correlation of experimentally determined γ_{SV}^d values with literature data about gas permeability of polymer films (Fig. 4) is the direct consequence of the dependence presented at Fig. 3.

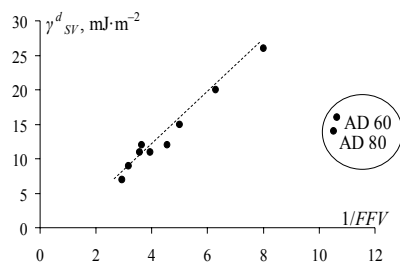


Figure 3. The dependence of dispersive component of surface energy of amorphous polymer films from polymer fractional free volume.

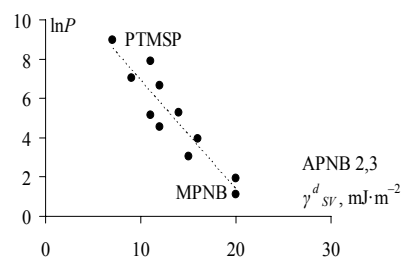


Figure 4. The dependence of gas (O_2) permeability (P , Barrer) from dispersive component of surface energy of amorphous polymer films.

Of course, the correlations experimentally obtained seem to be semi empirical and require further theoretical analysis. Nevertheless, ones illustrate the sensitivity of polymer surface energy characteristics to the packing density of macromolecules in surface layers [7].

CONCLUSION

So, generalization and analysis of results obtained makes it possible to determine new perspectives for the use of contact angle measurements for comparison of the transport properties of polymer films and optimizing of polymer choice for the creation of polymer membranes.

ACKNOWLEDGEMENT

This work was supported by the Russian Foundation of Basic Research (Grants № 14-03-00142a, № 14-08-00893a).

REFERENCES

- [1] A.W. Adamson, Physical Chemistry of Surfaces, John Wiley and Sons, New York, 1976.
- [2] J. Kloubek, Adv. in Colloid and Int. Sci., 1992, 38, 99–142.
- [3] A. V. Volkov, V. V. Volkov, V. S. Khotimskii, Vysokomol. Soed., Ser.A., 2009, 51(11), 2113–2128, *in russian*.
- [4] J. W. Steed, J. L. Atwood, Supramolecular chemistry, John Wiley and Sons, Ltd., Chichester, 2000.
- [5] V. G. Rostiashvili, V. I. Irzhak, B. A. Rosenberg, Glass transition of polymers, Khimiya, Leningrad, 1987, *in russian*.
- [6] J.Y. Park, D.R. Paul, J. Membr. Sci., 1997, 125, 23–39.
- [7] L. M. Bogdanova, V. I. Irzhak, B. A. Rosenberg, N. S. Enikolopyan, Dokl. AN USSR, 1983, 268(5), 1139–1141, *in russian*.

THE EFFECT OF THE SAMPLE PREHISTORY ON THE SURFACE PROPERTIES OF BINARY COPOLYMERS: CONCORDANCE OF FTIR-ATR SPECTROSCOPY AND WETTING

J.V. Kostina¹, E.V. Chernikova², A.V. Plutalova² and V.V. Yulusov²

¹*Topchiev Institute of Petrochemical Synthesis,
29, Leninsky Prospect, Moscow, Russia (julia@ips.ac.ru)*
²*Lomonosov Moscow State University, Chemistry Department,
1/3, Leninskie Gory, Moscow, Russia,*

ABSTRACT

On a series of copolymers based on styrene and *n*-butyl acrylate of various composition and monomer unit distribution in the chain we demonstrate the influence of solvent thermodynamic quality on the chain conformation in the surface layer of the films by means of two different methods, namely wetting and ATR-FTIR spectroscopy. Correctness of comparing the results obtained by these techniques is discussed. Also the experimental data were confirmed by quantum chemistry modeling.

INTRODUCTION

The combination of IR spectroscopy with quantum chemistry modeling make possible to explain numerous fine points of the influence of (co)polymer structure and conformation set of elementary unit on the physical-chemical properties of polymer films [1–3]. ATR-FTIR technique, in particular, allows getting information about change of conformation set of macromolecules on the surface of polymer films. The values of contact angles by-turn give access to the energetic characteristics of the surface, such as dispersive (γ_{sv}^d) and polar (γ_{sv}^p) components of polymer surface energy (γ_{sv}). Below we present the systematic study of films of the series of copolymers with continuously changing composition and monomer unit distribution by above mentioned methods and compare the data extracted from these different approaches.

EXPERIMENTAL

The binary copolymers of styrene and *n*-butyl acrylate (BA) of various composition and monomer unit distribution obtained via a controlled radical polymerization (compositionally homogeneous, gradient **GC** or block-copolymer **BC**) and conventional radical polymerization (compositionally

heterogeneous, random **RC**) have been studied (Table 1). Their synthesis and characterization is fully described in [4].

Polymer films were prepared by dropping of 1 wt.% solutions in toluene or acetone on KBr pellets with subsequent drying during 2 h in air at room temperature. The choice of the solvent was based on different thermodynamic quality with respect to styrene (good and bad respectively). The FTIR-spectra were recorded using a Bruker IFS 66v/s IR spectrometer in two modes: transmission (FTIR, 4000–400 cm^{-1} , resolution 1 cm^{-1}) and attenuated total reflection (ATR, 4000–600 cm^{-1} , resolution 2 cm^{-1}) using IR-microscope Hyperion2000, conjugated with IFS 66v/s. For surface energy characteristics measurement, Owens-Wendt-Kaelble approach was used (test liquids were water and diiodomethane) [5]. Contact angles of test liquids were measured by sessile drop technique with accuracy of 1 degree. The accuracy of γ_{SV} value determination was 1 $\text{mJ}\cdot\text{m}^{-2}$.

Table 1. Characteristics of (co)polymers (F_S – styrene mole fraction in copolymer)

Sample	F_S , %	$M_n \times 10^{-3}$	PDI
PS	100	25.8	1.20
GC-10	10	25.8	1.21
RC-10	10	19.6	1.18
RC'-25	25	353.9	1.93
GC-25	25	16.6	1.25
PBA	0	36.8	1.53

RESULTS AND DISCUSSION

Solvent influence on chain conformation in films of homopolymers PS and PBA was studied first by FTIR and ATR-FTIR spectroscopy on samples casted from toluene and acetone. Influence of solvent on conformational ordering of functional groups in the polymer chain was shown for the block (FTIR, transmission) and surface (ATR-FTIR) films for homopolymers. The most significant conformational differences were found in the range of absorption of CH deformation vibrations in mono-substituted aromatic ring (δ_{CH} at 750–698 cm^{-1}), the fact which confirms the different arrangement of aromatic rings along the main backbone (Fig.1). A ratio of absorbance band intensity δ_{CH} in aromatic ring with respect to ν_{CHal} in aliphatic group of backbone (A_{757}/A_{2924}) was chosen as criterion, which characterizes the arrangement of benzene rings along the main backbone. Results are presented in Table 2 (spectra normalized with respect to the absorption band $\nu_{\text{CH}}=3025 \text{ cm}^{-1}$ intensity). The differences in chain conformation set may be related to the extent of sample thermodynamic non-equilibrium: film formed from toluene is more close to the equilibrium state (PS after annealing) as compared with film casted from acetone.

The analysis of ATR-FTIR data also indicates that the surface layer contains more aromatic groups in the film casted from acetone with respect to the one prepared from toluene solution. It correlates fairly well with the values of dispersive component of specific surface energy γ_{SV}^d ; the latter indicates the higher packing density for PS film made from toluene solution (Table 2). Our selection of structural criteria set was approved by quantum chemistry calculations, where differences in geometry (dihedral angles for instance) were obtained for polymeric chain fragment associated with acetone or toluene molecule via non-covalent interaction).

Similarly, we found and approved the structural criterion for the orientation characteristics of functional groups in PBA film casted from solutions in the same solvents. In this case, the measure was the ratio of $\nu_{C=O}$ band intensity with respect to ν_{CHal} band intensity. Again this criterion well correlates with γ_{SV}^p value (Table 2) and is quite sensitive to the conformational changes.

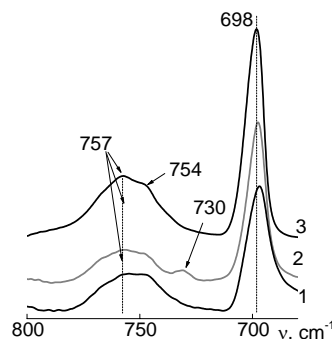


Figure 1. The fragments of FTIR-spectra of PS films formed from acetone (1) and toluene (2) solutions. FTIR-spectrum of PS (Aldrich, 9×10^4 , $T_g = 100$ °C) film after annealing (3) is given for comparison

Table 2. Comparison of data obtained from IR-spectroscopy and interfacial angle measurements for homopolymers

Sample / Solvent, method	A_{757}/A_{2924}	A_{1730}/A_{2924}	γ_{SV}^d	γ_{SV}^p	γ_{SV}
PS (annealing), FTIR	1.87				
PS, toluene, FTIR	1.12				
PS, acetone, FTIR	0.81				
PS, acetone, FTIR-ATR	0.46		42	9	51
PS, toluene, FTIR-ATR	0.68		45	1	46
PBA, acetone		4.81	41	5	46
PBA, toluene		4.92	40	9	49

We applied our treatment for copolymers (Table 1), and compared obtained results with the values of γ_{SV}^p and γ_{SV}^d . An excellent agreement between results obtained by ATR-FTIR and by surface wetting was observed; as example see data given in Table 3. Similar results were obtained for all

studied gradient copolymers. On the contrary, the random copolymers do not exhibit the dependence from solvent thermodynamic quality irrespectively on the comonomer amount in the copolymer.

Table 3. Comparison of data obtained from IR-spectroscopy and interfacial angle measurements for copolymers

Sample / Solvent	A_{757}/A_{2924}	A_{1730}/A_{2924}	γ_{SV}^d	γ_{SV}^p	γ_{SV}
GC-10 toluene	0.21	3.00	39	7	46
GC-10 acetone	0.15	2.17	47	0	47
RC-10 toluene	0.20	4.77	46	0	46
RC-10 acetone	0.20	4.97	46	0	46

The quantum chemistry calculations for gradient copolymer confirmed that the non-covalent interaction with the solvent may orient the functional groups of monomer units depending on the quality of the solvent.

CONCLUSION

We would like to stress the fact that results obtained by two different methods of surface studies are in good agreement. Hence a valuable information about influence of both factors – chain structure and solvent nature on the macromolecule conformation in bulk and on surface of the film can be revealed using the proposed structural criteria.

ACKNOWLEDGEMENT

This work was supported by the Russian Foundation for Basic research (№ 14-03-00142a, №14-03-00155a).

REFERENCES

- [1] Yu.V. Kostina, G.N. Bondarenko, A.Yu. Alent'ev and Yu.P. Yampol'skii, *Polymer Science, A*, 2007, 49, 1, 74 - 85
- [2] O.Yu. Rusakova, Yu.V. Kostina, A.S. Rodionov, G.N. Bondarenko, A.Yu. Alent'ev, T. K. Meleshko, N.V. Kukarkina and A.V. Yakimanskii, *Polymer Science, A*, 2011, 53, 9, 791–799.
- [3] J. Kostina, G. Bondarenko, M. Gringolts, A. Rodionov, O. Rusakova, A. Alentiev, A. Yakimanskii, Yu. Bogdanova, V. Gerasimov, *Polym. Int.*, 2013, 62, 1566-1574.
- [4] E. V. Chernikova, V. V. Yulusov, E. S. Garina, Yu. V. Kostina, G. N. Bondarenko, and A. Yu. Nikolaev, *Polym. Sci., Ser. B*, 2013, 55, (3 – 4), 176 – 186.
- [5] J. Vojtechovska, L. Kvitek, *Acta Univ. Palacki. Olomouc. Facultas Rerum Naturalium, Chemica*, 2005, 44, 25-48.

REVERSIBLE 3D TO 2D FRAMEWORK TRANSFORMATION OF NI-BASED COORDINATION POLYMER

N. Begović^{1,2}, V. A. Blagojević¹, N. N. Stojanović¹, A. A. Radulović², D. Poleti³ and D. M. Minić¹

¹*Faculty of Physical Chemistry, University of Belgrade, Serbia
(dminic@ffh.bg.ac.rs)*

²*Institute of General and Physical Chemistry, Belgrade, Serbia*

³*Faculty of Technology and Metallurgy, University of Belgrade, Serbia*

ABSTRACT

Binuclear Ni-based coordination polymer was found to undergo reversible 3D to 2D framework transformation during dehydration around 365K with further thermal degradation around 570K. Correlation between experimental measurements and DFT calculations suggest formation of a layered 2D framework, which remains stable even after thermal degradation around 570K. XRD measurements show loss of long-range structure corresponding to each degradation process. Rehydration of the dehydration product is possible in saturated water vapor to regain the structure of the initial coordination polymer.

INTRODUCTION

Coordination polymers, or metal organic frameworks have been a focus of particular interest in recent times due to their low cost, flexibility and versatile chemistry [1, 2]. Their frameworks are composed of a wide variety of structures: one-dimensional (1D), 2D and 3D, depending on their coordination bonds. Materials that exhibit guest-responsive reversible transformations from 2D framework to 3D framework represent a very interesting class of materials because they can exhibit not only properties characteristic of a 3D framework, but also stimulus-responsive properties based on 2D-3D transformation [3, 4].

As a part of our multidisciplinary study of transition metal based coordination polymers, this paper investigates thermally activated reactions of binuclear hexaaqua- μ -[1,2,4,5-benzenetetracarboxylato(4-)]-bis(ethylenediamine) dinickel (II) tetrahydrate [5], with a particular focus on polymeric products and their structure and properties. Combination of different experimental techniques and DFT calculations was used to investigate and explain, in as much detail as possible, the structure of the polymer products formed by dehydration and degradation reactions of this compound and reversible nature of some of its transformations.

EXPERIMENTAL

The initial hexaaqua- μ -[1,2,4,5-benzenetetracarboxylato(4-)]-bis(ethylenediamine) dinickel (II) tetrahydrate was synthesized as described in Ref. [5] from commercially available chemicals of analytical grade. The X-ray powder diffraction (XRD) spectra were obtained using Philips PW-1710 automated diffractometer, using Cu K α line, operated at 40 kV and 30 mA, in Bragg-Bentano geometry. Thermogravimetric analyses were conducted using a Q500 TGA (TA Instruments) with sample weight of 10.0 ± 0.5 mg, and a heating rate of 5 K min^{-1} , in nitrogen atmosphere with gas flow rate of 50 mL min^{-1} . DSC measurements were carried out at the same heating rate, using DSC Q1000 (TA Instruments) with sample weights of 2.0 ± 0.2 mg, in nitrogen atmosphere with gas flow rate of 50 mL min^{-1} . All DFT calculations were performed simulating aqueous solution with continuous dielectric model using Gaussian 09 [6] program package. All structures were fully optimized using C-PCM solvation method with Klamt [7] radii, using the hybrid HF/DFT method with a combination of the three-parameter Becke [8] exchange and the Lee-Yang-Parr (B3LYP) [9] non-local correlation functional.

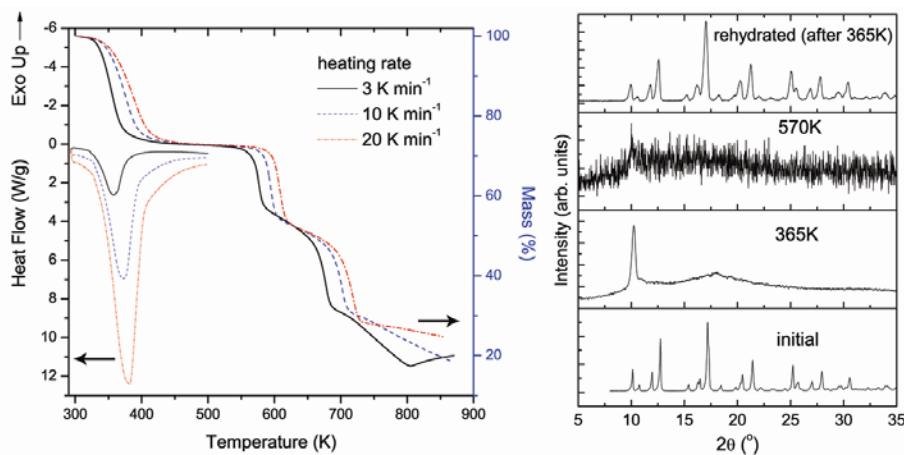


Figure 1. DSC/TG curves (left) and XRD patterns (right) showing thermal degradation of $[\text{Ni}_2(\text{en})_2(\text{H}_2\text{O})_6(\text{pyr})]\cdot 4\text{H}_2\text{O}$ complex.

RESULTS AND DISCUSSION

DSC scan shows that $[\text{Ni}_2(\text{en})_2(\text{H}_2\text{O})_6(\text{pyr})]\cdot 4\text{H}_2\text{O}$ coordination polymer is stable up to about 330 K and undergoes endothermic degradation in 330 – 400 K region (Figure 1). TGA scan shows three distinct losses of mass: one in the temperature region investigated by DSC measurements, and two outside of it. The loss of mass of around 27%, corresponding to the first

process observed in both TGA and DSC, was correlated with the loss of 10 water molecules. The second peak in TG, around 570K, can be correlated with release of ethylene diamine. XRD pattern of the initial coordination polymer shows a crystalline structure, with numerous well defined sharp peaks in 10-35° region, which provide a good description of the structure. This crystal lattice exhibits P21/c group and having ten water molecules and BTCA ligand, suggests substantial potential for polymerization.

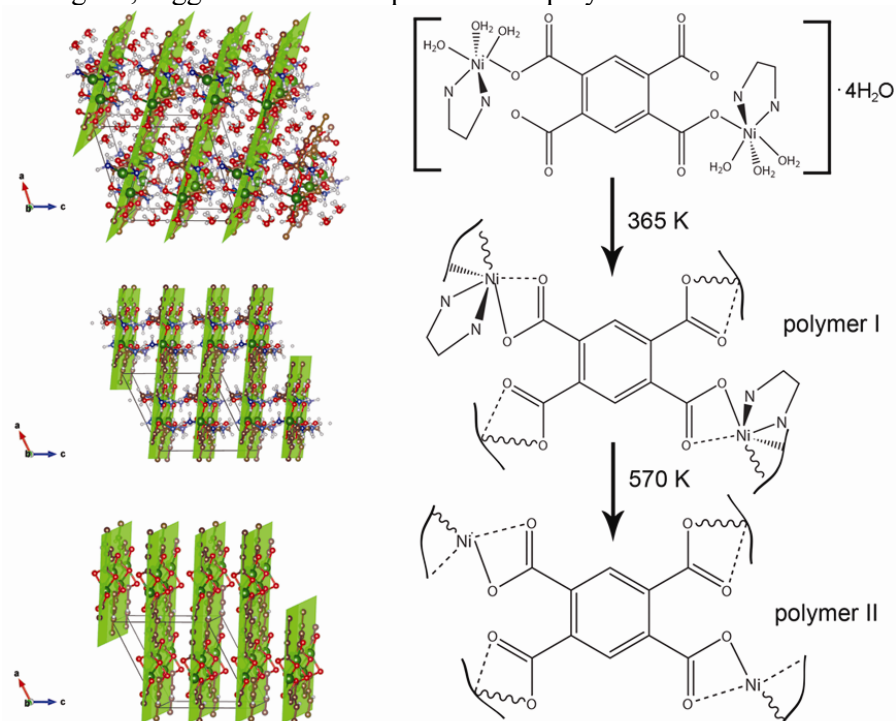


Figure 2. Calculated structures of individual products (left) and reaction scheme (right) of thermal degradation of $[\text{Ni}_2(\text{en})_2(\text{H}_2\text{O})_6(\text{pyr})]\cdot 4\text{H}_2\text{O}$.

DFT calculations were correlated with experimental results to determine detailed structures of thermal degradation products (Figure 2). These show that the initial complex undergoes polymerization during dehydration, around 365K, resulting in 2-dimensional layered structure with weak interconnectivity between the layers (polymer I). Further thermal degradation around 570K results in loss of this interconnectivity, due to the release of ethylene diamine, although 2-dimensional layers should remain unaffected (polymer II). These structural changes are visible in XRD patterns, manifesting as increasing loss of long-range structure after each

degradation process, because the 3D bond network of the initial coordination polymer depends on hydrogen bonding of water. In polymer I this is replaced with fewer hydrogen bonds from ethylene diamine, while interlayer connectivity is absent in polymer II. When the dehydration product (polymer I) is exposed to saturated water vapor, it reabsorbs water and reverts back to the structure of the initial coordination polymer, exhibiting a reversible 3D to 2D framework transformation.

CONCLUSION

It was established that binuclear $[\text{Ni}_2(\text{en})_2(\text{H}_2\text{O})_6(\text{pyr})]\cdot 4\text{H}_2\text{O}$ complex undergoes reversible 3D to 2D framework transformation around 365K, with further degradation around 570K. These both result in layered 2D polymer structures, with loss of long-range structure after each successive degradation process.

ACKNOWLEDGEMENT

This research was supported by the Ministry of Education, Science and Technology of Republic of Serbia under the projects 172015, 172020, TR-31055, TR-31093 and III 45007.

REFERENCES

- [1] C. Janiak, Dalton Trans., 2003, 2781.
- [2] H. Li, M. Eddaoudi, M. O'Keeffe and O. M. Yaghi, Nature, 1999, 402 276
- [3] W. Kaneko, M. Ohba, S. Kitagawa, J. Am. Chem. Soc., 2007, 129, 13706.
- [4] Y. Luo, K. Bernot, G. Calvez, S. Freslon, C. Daiguebonne, O. Guillou, N. Kerbellec, T. Roisnel, CrystEngComm, 2013, 15 1882.
- [5] D. Poleti, D. R. Stojakovic, B. V. Preselnic, R. M. Herak, Acta Cryst. C44, 1988, 242.
- [6] M. J. Frisch, G. W. Trucks and J. A. Pople, *Gaussian 09, revision B.2*; Gaussian, Inc., Pittsburgh, PA, 2009.
- [7] S. Sinnecker, A. Rajendran, A. Klamt, M. Diedenhofen, F. Neese, J. Phys. Chem. A, 2006, 110, 2235.
- [8] A. D. Becke, Phys. Rev. A, 1998, 38, 3098.
- [9] C. Lee, W. Yang, and R. G. Parr, Phys. Rev. B, 1988, 37, 785.

NEW METHOD TO CALCULATE HANSEN SOLUBILITY PARAMETER FOR EPDM

I. Stanciu¹

¹*University of Bucharest, Faculty of Chemistry, Department of Physical Chemistry, Bvd. Regina Elisabeta, no. 4-12, 030018 Bucharest, Romania.
(istanciu75@yahoo.com)*

ABSTRACT

The global and partial solubility parameters and radii of interaction spheres poly(ethylene-co-propylene) rubber (EPDM) were determined from solubility data and intrinsic viscosities using 9 solvents by the classical Hansen's method and an improved one. The poly(ethylene-co-propylene) rubber (EPDM) is recommended as viscosity improvers for multi-grade mineral oils, to estimate their efficiency of lubricating additive components for the mineral oil SAE 10W-40.

INTRODUCTION

Solubility parameters are the most used quantities for the selection of solvents for polymers and to predict their compatibility with some other compounds or materials. That is why the solubility parameters of a polymer must be accurately known.

The total solubility parameters, δ , defined by Hildebrand [1] as the square root of the cohesive energy density, CED:

$$\delta = (CED)^{1/2} = (\Delta E^V/V)^{1/2} \quad (1)$$

where ΔE^V is the energy of vaporization and V – the molar volume, is a measure of all the intermolecular forces responsible for the compound cohesion.

The first step in differentiation of interactions types was made by Praunsnitz et al. [2, 3], who divided the cohesive energy in two components: one due to the dispersion (d) and the one due to all the other types of forces (a). Thus, the total solubility parameter can be written as [4, 5]:

$$\delta = (\delta_d^2 + \delta_p^2 + \delta_h^2)^{1/2} \quad (2)$$

The determination of the solubility parameters of many substances being a difficult and laborious undertaking, some correlation between solubility parameters and other physical properties were established [6 – 9].

A more accurate method to predict the solubility of a polymer in a solvent was developed using an elaborated equation taking account of entropy effects, polymer-polymer, polymer-solvent and solvent-solvent interactions [10]. The equation was also used for oligomers [10].

The object of this paper was to determine the partial and total solubility parameters for poly(ethylene-co-propylene) rubber (EPDM) is recommended as viscosity improvers for multi-grade mineral oils, to estimate their efficiency of lubricating additive components for the mineral oil SAE 10W-40.

EXPERIMENTAL

The polymer poly(ethylene-co-propylene) (DSM Elastomers Europe B.V.) was used EPDM . The poly(ethylene-co-propylene) rubber (EPDM) of weight average molecular weight $\overline{M}_w = 1.12 \times 10^5 \text{ g mol}^{-1}$, a number average molecular weight $\overline{M}_n = 4.73 \times 10^4 \text{ g mol}^{-1}$. Their ratio, which can be taken as a measure of copolymer polydispersity, is 2.37.

The poly(ethylene-co-propylene) rubber (EPDM) was dissolved in solvent: n-heptane, cyclohexane, benzene, toluene, o-xylene, chloroform, trichloroethylene, carbon tetrachloride and benzene chloride. The solutions were prepared by dissolving each polymer in the solvent at room temperature and concentrations of between 0.025 and 1%.

The viscosities of the solvents and solution were determined using two Schott Ubbelohde- type viscometers (0a and Ia), selected according to the values of their constant, so that the margins of the uncertainty, inherent in the Hagenbach-Couette correction, does not exceed the error allowed for the measurements. Intrinsic viscosities were determined from the dependence of reduced viscosity on polymer concentration and their extrapolation to zero polymer concentration.

RESULTS AND DISCUSSION

Determination of the partial and global solubility parameters of a polymer by the classical (Hansen's) method [4, 5] consists in testing polymer solubility in different solvents with known global and partial solubility parameters. The solubility parameters, the intrinsic viscosities obtained and the normed ones for used solvents are given in Table 1.

The method considers that good solvents of a polymer can be represented into the three-dimensional space of coordinate's δ_d , δ_p , δ_h as a system of material points with different weights.

The equations of the coordinates of the mass centre are [12]:

$$\delta_d = \frac{\sum (\delta_{di} \times [\eta]'_i)}{\sum [\eta]'_i} \quad (3)$$

$$\delta_p = \frac{\sum (\delta_{pi} \times [\eta]'_i)}{\sum [\eta]'_i} \quad (4)$$

$$\delta_h = \frac{\sum (\delta_{hi} \times [\eta]'_i)}{\sum [\eta]'_i} \quad (5)$$

where $[\eta]'_i$ is the intrinsic viscosity of the polymer in solvent i normalized to unity. Normalization to unity was made by dividing the intrinsic viscosities in the solvents given in table 1 by the maximum value obtained. The highest value of R_i is considered the radius of interaction sphere. The equation used to compute R_i is the well-known Hansen's relation:

$$R_i = [4(\delta_{di} - \delta_d)^2 + (\delta_{pi} - \delta_p)^2 + (\delta_{hi} - \delta_h)^2] \quad (6)$$

Table 1. The solvents used, their global and partial solubility parameters, intrinsic and normed viscosities at 25°C

Solvents	δ , (MPa) ^{1/2}	δ_d , (MPa) ^{1/2}	δ_p , (MPa) ^{1/2}	δ_h , (MPa) ^{1/2}	$[\eta]$, dl/g	$[\eta]'_i$
n-Heptane	15.3	15.3	0	0	1.5739	0.6062
Cyclohexane	16.8	16.8	0	0.2	2.2385	0.8622
Benzene	18.6	18.4	0	2.0	0.6872	0.2646
Toluene	18.2	18.0	1.4	2.0	0.7289	0.2807
o-Xylene	18.0	17.8	1.0	3.1	1.2697	0.4890
Chloroform	19.0	17.8	3.1	5.7	0.4726	0.1820
Triclorethylen e	19.0	18.0	3.1	5.3	1.6174	0.6229
Carbon tetrachloride	17.8	17.8	0	0.6	2.5962*	1.0000
Benzene chloride	19.6	19.0	4.3	2.0	0.6370	0.2453

*The maximum value of intrinsic viscosity at which normation was made.

The Hansen solubility parameters obtained using the two methods are given in Table 2.

Table 2. The Hansen solubility parameters obtained by the classical and the new method

Method	δ , (MPa) ^{1/2}	δ_d , (MPa) ^{1/2}	δ_p , (MPa) ^{1/2}	δ_h , (MPa) ^{1/2}	R , (MPa) ^{1/2}
Classical	17.6	17.5	0.8	1.0	4.8
new	17.5	17.4	1.0	1.8	4.5

CONCLUSION

The poly(ethylene-co-propylene) rubber (EPDM) is recommended as viscosity improvers for multi-grade mineral oils, to estimate their efficiency of lubricating additive components for the mineral oil SAE 10W-40.

The method presented determines more accurately the Hansen solubility parameters and the radius of interaction sphere of a polymer, due to the combination of intrinsic viscosity data (used to determine the Hildebrand solubility parameters) with Hansen solubility parameters and an improved mathematical method.

REFERENCES

- [1] S. Husain, W. J. Koros, *Journal of Membrane Science*, 2007, 288(1), 195-207.
- [2] C. A. Irani, C. Cozewith, *Journal of applied polymer science*, 1986, 31(6), 1879-1899.
- [3] C. M. Hansen, *Journal of paint technology*, 1967, 39.511, 505-510.
- [4] E. A. Grulke, *Solubility parameter values. Polymer handbook 3*, 519-559, 1999.
- [5] A. Forster, J. Hempenstall, I. Tucker, T. Rades, *International journal of pharmaceutics*, 2001, 226(1), 147-161.
- [6] R. S. Ruoff, D. S. Tse, R. Malhotra, D. C. Lorents, *The Journal of Physical Chemistry*, 1993, 97(13), 3379-3383.
- [7] H. Lian, J. R. Lin, T. F. Yen, *Fuel*, 1994, 73(3), 423-428.
- [8] I. A. Wiehe, *Fuel science & technology international*, 1996, 14(1-2), 289-312.
- [9] F. Gharagheizi, *QSAR & Combinatorial Science*, 2008, 27(2), 165-170.
- [10] U. Siemann, *European polymer journal*, 1992, 28(3), 293-297.

Co(II) SELF-ASSEMBLED MONOLAYERS ON GOLD: CONTACT ANGLES AND QUARTZ CRYSTAL MICROBALANCE DATA

V. D. Dolzhikova, Yu. G. Bogdanova, A. G. Majouga and E.K.
Beloglazkina

*Chemistry Department, Lomonosov Moscow State University,
Leninskie Gory, 1/3, Moscow, Russia. (yulibogd@yandex.ru)*

ABSTRACT

The formation of self-assembled monolayers (SAMs) of disulfide based on 2-(2-pyridyl)benzimidazole and its complex with Co(II) at the gold surface were investigated using contact angle measurements and quartz crystal microbalance (QCM) method. The optimal conditions for formation of metallocomplex surfaces were determined. The Co(II) monolayer formation time was 1h and concentration of CoCl_2 in ethanol solution was 10^{-3}M .

INTRODUCTION

The formation of self-assembled monolayers (SAMs) of thiols, disulfides and sulfides on gold has been studied during the last 30 years [1, 2]. The strong chemical adsorption of sulfur-containing molecules on gold, stability, a high level of order and the different terminal group of organosulfur molecules provide an unique properties of SAMs connected with the transport charge, biological and photochemical activity. The employment of complexes of transition metals with terminal groups of SAMs allows obtaining the compact catalysts and metallocomplex surfaces.

EXPERIMENTAL

SAMs of disulfide based on 2-(2-pyridyl)benzimidazole (Fig. 1) and its complex with Co(II) were investigated using contact angle measurements and quartz crystal microbalance method (QCM).

The samples of Silicon ($0,5 \times 0,5$ cm) with vacuum gold evaporated were used. The thickness of gold film was 50 ± 10 nm. The gold plates were

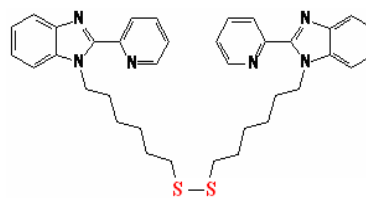


Figure 1. Structure of disulfide based on 2-(2-pyridyl)benzimidazole.

immersed into 10^{-3}M solution of ligand (L) in methanol for different time (from 1s to 24h , Table 1). After drying (2 h at room temperature) the advancing (θ_a) and receding (θ_r) contact angles were measured.

The fraction (X) of modified gold surface was calculated using molecular theory of heterogeneous surfaces wetting and Cassie-Baxter equation [3]. The free surface energy (γ_s) of SAMs including dispersive (γ_s^d) and polar (γ_s^p) components were calculated using the two-liquid method and Owens-Wendt-Kaelble approach [4, 5]. The method enables to determine the γ_s as the sum of polar γ_s^p and dispersive γ_s^d contributions using two different liquids. The probe liquids (water, W and ethylene glycol, EG) were used. We used these liquids because the values of surface tension γ_L and its dispersive γ_L^d and polar γ_L^p components are well known [4]. The relationship between the equilibrium contact angle of liquid phase deposited onto a solid surface is derived from the general Fowkes expression [4]

$$\gamma_L(1+\cos\theta) = 2(\gamma_L^d\gamma_s^d)^{1/2} + 2(\gamma_L^p\gamma_s^p)^{1/2} : (1),$$

$$\gamma_s = \gamma_s^d + \gamma_s^p.$$

The adsorption (Γ) of L was measured by QCM (*in situ*) using AT-cut quartz sensor with gold electrodes (200 nm thickness). The adsorption of L was calculated using Sauerbrey equation [6]:

$$\Delta f = -C_f \Delta m, \quad (2)$$

where Δf – the observed frequency change in Hz, Δm – the change in mass per unit area in $\text{g}\cdot\text{cm}^{-2}$, C_f – the sensitivity factor for crystal ($56,6 \text{ Hz}\cdot\mu\text{g}^{-1}\cdot\text{cm}^2$ for a 5 MHz AT-cut quartz crystal at room temperature). The sensor was immersed into L solution. After SAM formation ($\Delta f = \text{const}$) (Fig.1) the sensor was put out from solution and after solvent evaporation the contact angles of water and ethylene glycol were measured. Then the modified sensor was immersed into 10^{-3}M solution of CoCl_2 in ethanol (Fig. 2). When the process of complexation was finished the amount of bound cobalt with SAM was found.

RESULTS AND DISCUSSION

The results obtained (Table 1) show that when the time of gold surface modification increases the contact angles hysteresis $\Delta\theta = (\theta_a - \theta_r)$ decreases. This is the evidence of SAM homogeneous on gold. The γ_s^p values increase and γ_s^d values decrease. The complete modification of gold surface occurs in 1 hour. The γ_s of SAM surface is close to one's of polyimides surfaces [7, 8]. The adsorption of L was calculated from (2) and its value was $\Gamma = 7.4 \cdot 10^{-6} \text{ mol}\cdot\text{m}^{-2}$ ($\Delta f = 52.0 \text{ Hz}$, $M_L = 620 \text{ g}\cdot\text{mol}^{-1}$) (Fig.

2). The contact angles of water and ethylene glycol were measured on modified gold surface. Its values were 55 and 42 degree respectively. The total surface energy $\gamma_s = \gamma_s^d + \gamma_s^p = 7.8 + 38.3 = 46.1 \text{ (mJ}\cdot\text{m}^{-2}\text{)}$ is close to value presented in Table (1) and close to free surface energy of polyimides. The adsorption of L on gold electrode $\Gamma(\text{L}) = 7.0 \cdot 10^{-6} \text{ mol}\cdot\text{m}^{-2}$.

Table 1. Wetting properties (θ_a , θ_r , $\Delta\theta$, degree), surface energy of monolayers (γ , $\text{mJ}\cdot\text{m}^{-2}$) and fraction of coverage of gold surface (X , %).

time , s	Water			EG	γ_s^d	γ_s^p	γ_s	X , %
	θ_a	θ_r	$\Delta\theta$					
0	80	76	4	–				
1	76	45	31	55	16.6	13.3	29.9	17
5	74	52	22	54	15.3	16.2	31.5	26
10	73	54	19	52	16.3	15.5	31.8	30
30	69	61	8	53	11.1	22.4	33.5	46
180	66	57	9	48	12.6	23.4	36.0	58
300	65	57	8	48	11.6	25.1	36.7	62
600	63	60	3	45	12.2	26.1	38.3	70
1800	58	55	3	43	9.4	33.4	42.8	90
3600	55	53	2	40	9.1	36.4	45.5	100
86400	55	54	1	40	9.1	36.4	45.5	100

It is known, that formation of metallocomplex surfaces occurs due to coordination of metal ions through the lone electron pairs of the nitrogen atom of terminal hydantoin groups [9].

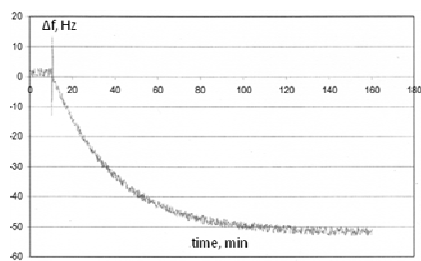


Figure 2. SAM formation on gold.

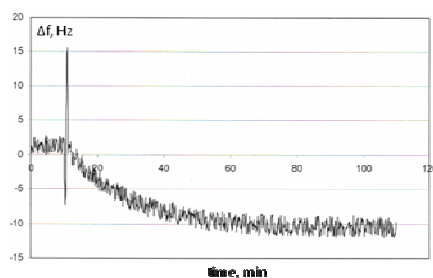


Figure 3. Co^{II} complexation with SAM.

The complex formation $\text{Co}(\text{II})$ with SAM is finished in 1 hour, $\Delta f = 10.9 \text{ Hz}$ (Fig. 3) $\Gamma(\text{Co}^{\text{II}}) = 7.0 \cdot 10^{-6} \text{ mol}\cdot\text{m}^{-2}$. So, $\Gamma(\text{L}) : \Gamma(\text{Co}^{\text{II}}) \approx 1:1$. According to literature data, during the disulfides molayer formation $-\text{S}-\text{S}-$ bond breaks and two equivalent fragments are obtained. After addition of Co^{II} ions using QCM method we observed that in metallocomplex layer two benzimidazole

fragments bound one Co^{II} ion, that is well-known from the coordinational chemistry of cobalt.

The complexation of transition ions with terminal groups of thiols and disulfides was used to reversible 2D and 3D architectures based on gold nanoparticles and sulfur containing benzimidazole ligands [10].

CONCLUSION

The results obtained show a good agreement between the contact angle measurements and QCM method data in study of kinetic of formation of organosulfur SAMs at the gold surface and in determination of the optimal time of complexation of metal ions with ligand, grafted at the gold surface. The combination of contact angle measurements and QCM method permits to control promptly the homogeneity and fraction of coverage of gold surface with organosulfur ligand, efficiency of its complexation with metal ions during the formation of metallocomplex surface and composition of this surface.

ACKNOWLEDGEMENT

This work was partially supported by the Ministry for Science of the Republic of Serbia (Grant №14-03-00142a).

REFERENCES

- [1] A. Ulman, *Chem. Rev.*, 1996, 96, 1533 – 1554.
- [2] J. C. Love, L. A. Estroff, J. K. Knebel, R. G. Nuzzo, G. M. Whitesides, *Chem. Rev.*, 2005, 105, 1103 – 1169.
- [3] J. Genzer, K. Efimenko, *Biofouling*, 2006, 22, 339 – 360.
- [4] J. Kloubek, *Adv. in Colloid and Interface Sci.*, 1992, 38, 99 – 142.
- [5] P. F. Rios, H. Dodiuk, S. Kenig, S. McCarthy, A. Dotan, *J. Adhesion Sci. Technol.*, 2007, 21, 227 – 241.
- [6] G. Sauerbrey, *Z. Physik*, 1959, 155, 206 – 222.
- [7] N. B. Melnikova, V. I. Ignatov, V. D. Dolzhikova, B. D. Summ, *Moscow Univ. Chem Bull.*, 1998, 39(6), 413 – 417.
- [8] K. H. Kim, Y. G. Kim, Y. Kwon, *Macromolecular Research*, 2009, 17, 388 – 396.
- [9] E. K. Beloglazkina, A. G. Majouga, I.Y. Yudin et al., *Rus. Chem. Bull.*, 2006, 55(6), 1 – 13.
- [10] R. B. Romashkina, E. K. Beloglazkina, A. G. Majouga et al., *Mend. Comm.*, 2011, 21, 129 – 131.

INFLUENCE OF RESIDUAL SOLVENT ON SURFACE ENERGY OF POLY(STYRENE/*n*- BUTYLACRYLATE) BINARY COPOLYMERS OF DIFFERENT MICROSTRUCTURE

Yu. G. Bogdanova¹, J. V. Kostina², V. D. Dolzhikova¹,
A. V. Plutalova¹, E. V. Chernikova¹ and V. V. Yulusov¹

¹*Lomonosov Moscow State University, Chemistry Department,
1/3, Leninskie Gory, Moscow, Russia, (yulibogd@yandex.ru)*

²*Topchiev Institute of Petrochemical Synthesis,
29, Leninsky Prospect, Moscow, Russia.*

ABSTRACT

Polymer films based on styrene/*n*-butyl acrylate copolymers of various chain microstructure have been formed from different solvents. Their surfaces have been investigated by contact angles measurements and FTIR-ATR spectroscopy. It was found that the solvent nature and chain structure affect macromolecule conformation in thin films.

INTRODUCTION

The macroscopic properties of polymer films may vary depending on their prehistory, in particular, on chemical structure of residual solvent, which is often kept in polymer films. Recently the efficiency of combination of contact angle measurements with FTIR-ATR spectroscopy for investigation of residual solvent influence on surface properties of amorphous polymer films have been demonstrated [1].

The main idea of this study was to establish the regularities in changes of surface energy values of polymer films (γ_{SV}), its dispersive (γ_{SV}^d) and polar (γ_{SV}^p) components and to compare the results obtained with change in polymer FTIR data.

EXPERIMENTAL

The binary copolymers of styrene and *n*-butyl acrylate of various composition and chain microstructure obtained via a controlled and conventional radical polymerization have been studied (Table 1). In particular, gradient copolymer, GC-10, and compositionally homogeneous random copolymers, RC-60a and RC-10, were synthesized via a RAFT polymerization using dibenzyl trithiocarbonate [2], while compositionally

heterogeneous random copolymer, RC-60b, was synthesized via bulk conventional radical polymerization.

Table 1. Characteristics of (co)polymers: F_S – styrene mole fraction in copolymer, M_n – number average molecular mass, PDI – polydispersity index.

Polymer sample	PS*	RC-60a	RC-60b	GC-10	RC-10	PNBA**
F_S , %	100	60	60	10	10	0
$M_n \times 10^{-3}$	25.8	14.5	230.9	25.8	52.0	36.8
PDI	1.20	1.24	1.32	1.12	1.41	1.53

*PS – polystyrene; ** PNBA – poly(*n*-butyl acrylate).

Polymer films were prepared by coating of 1 wt. % solutions in toluene and acetone on the surfaces of solid carriers (glass and alumina plates, size 10×15×1 mm) with subsequent drying at 2 h in air at room temperature. The choice of the solvent was based on its different thermodynamic quality with respect to styrene (toluene is a good solvent, while acetone is a bad one). The surface tensions of toluene and acetone equal to 23.8 and 28.4 mJ·m⁻² respectively were measured by Wilhelmy plate method.

Values of $\gamma_{SV} = \gamma_{SV}^d + \gamma_{SV}^p$ were determined using Owens-Wendt-Kaelble approach. The test liquids used were water and diiodomethane [3]. Contact angles of liquids were measured by sessile drop technique with accuracy of 1 degree. The accuracy of γ_{SV} value determination was 1 mJ·m⁻².

For FTIR spectroscopy investigations polymer films were formed on KBr plates. The IR spectra were recorded using a Bruker IFS 66v/s IR spectrometer in two modes: transmission (4000–400 cm⁻¹, resolution 1 cm⁻¹) and attenuated total reflection (ATR, 4000–600 cm⁻¹, resolution 2 cm⁻¹) using IR-microscope Hyperion2000, conjugated with IFS 66v/s (Ge crystal). Spectra were processed using OPUS software (Bruker).

It was shown that the nature of carrier does not have the influence on contact angles of test liquids on polymer surface. Hence, the comparison of the results of investigation using contact angles measurements and FTIR-ATR data is quite reasonable. All measurements were performed at 20 °C.

RESULTS AND DISCUSSION

Experiments have shown that in fact two factors are responsible for macromolecules chain conformation in thin polymer films, which can be estimated from surface energy values, namely composition homogeneity of copolymers and monomer distribution in polymeric chain. The values of dispersive and polar components of surface energy of polymer films depend

on the nature (thermodynamic quality) of residual solvent in the case of composition of heterogeneous random copolymer RC-60b (Table 2). It may be due to the presence of the chains enriched with styrene that were formed at low and middle monomer conversions and the chains enriched with n-butyl acrylate formed at high monomer conversions in polymer synthesis. In contrast, in the case when copolymer consists of the macromolecules of close composition with random distribution of monomer units no influence of the residual solvent on surface energy can be found.

The influence of chain microstructure can be revealed from the samples GC-10 and RC-10. Again, no influence of the residual solvent on surface energy can be found for random compositionally homogeneous copolymer, while gradient structure affects it strongly.

Table 2. Surface energy (γ_{SV} , $\text{mJ}\cdot\text{m}^{-2}$) of polymer films formed from different solvents, its dispersive (γ_{SV}^d) and polar (γ_{SV}^p) components.

Sample	toluene			acetone		
	γ_{SV}^d	γ_{SV}^p	γ_{SV}	γ_{SV}^d	γ_{SV}^p	γ_{SV}
PS	45	1	46	42	9	51
RC-60a	43	3	46	45	2	47
RC-60b	41	3	44	36	<i>close to 0</i>	36
GC-10	39	7	46	47	<i>close to 0</i>	47
RC-10	46	<i>close to 0</i>	46	46	<i>close to 0</i>	46
PNBA	40	9	49	41	5	46

Regularities of alteration of γ_{SV}^d and γ_{SV}^p modes are in a good agreement with FTIR data. The differences in the conformational composition of the polymer chains, which correlate with γ_{SV}^d , were estimated by a qualitative difference in the IR spectra (for example, wavenumbers and quantity of absorption bands maximums). The relative content of polar and non-polar groups at the films surfaces was analyzed using the ratio of absorption bands intensities (A) of valence vibrations ν_{CH} and ν_{CO} (A_{2924}/A_{1730}) in ATR-spectra. Spectra were normalized by $\nu_{\text{CH}} 2960\text{cm}^{-1}$.

As an example, the FTIR spectra of GC-10 film formed from acetone (1, 3) and toluene (2, 4) from bulk (transmission, 1, 2) and surface (ATR, 3, 4) are presented on Fig. 1. The variations in spectra can be observed between bulk and surface (1 and 3, 2 and 4) as well between two solvents (3 and 4). The uniform conformational composition in case of the film, formed from acetone, leads to more dense of polymer chains packing and, in consequence, to higher γ_{SV}^d value (Table 2). For film, formed from toluene and acetone, ratios A_{2958}/A_{1730} are 0.28 and 0.23 respectively. Thus, the

film, formed from toluene, contains more polar groups at the surface layer. This result correlates with higher γ_{SV}^p value (Table 2).

The absence of qualitative differences in FTIR spectra of RC-10 films, formed from toluene and acetone, indicates the identical conformational composition of its surface layers; γ_{SV}^d are the same for these films (Table 2). Close A_{2924}/A_{1730} values (0.28 and 0.27 for films, formed from toluene and acetone respectively) correspond to the same (close to zero) γ_{SV}^p values.

CONCLUSION

The analysis of reflection and absorption polymer FTIR spectra combining with the determination of γ_{SV}^d and γ_{SV}^p values of polymer films may be informative technique for study of polymer films in non-equilibrium state and interpretation of its surface properties. So, investigations in this field will be continued.

ACKNOWLEDGEMENT

This work was supported by the Russian Foundation for Basic research (№ 14-03-00142a, №14-03-00155a).

REFERENCES

- [1] J. Kostina, G. Bondarenko, M. Gringolts, A. Rodionov, O. Rusakova, A. Alentiev, A. Yakimanskii, Yu. Bogdanova, V. Gerasimov, Polym. Int., 2013, 62, 1566 – 1574.
- [2] E. V. Chernikova, V. V. Yulusov, E. S. Garina, Yu. V. Kostina, G. N. Bondarenko, A. Yu. Nikolaev, Polym. Sci., Ser. B, 2013, 55 (3 – 4), 176 – 186.
- [3] J. Vojtechovska, L. Kvitek, Acta Univ. Palacki. Olomouc. Facultas Rerum Naturalium, Chemica 2005, 44, 25 – 48.

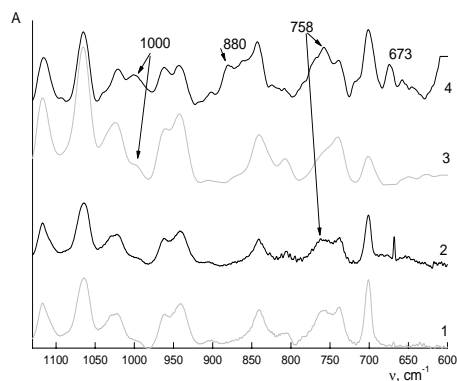


Figure 1. Fragment of FTIR spectrum of GC-10 films, formed from acetone (1,3) and toluene (2,4); transmission (1,2) and ATR (3,4) modes.

KINETICS STUDY OF MOLYBDENUM SORPTION ON AMINO-FUNCTIONALIZED COPOLYMER

B. Ekmešćić¹, T. Tomković¹, S. Vidojković¹, D. Maksin²,
J. Marković² and A. Nastasović¹

¹University of Belgrade, Institute of Chemistry, Technology and Metallurgy,
Njegoševa 12, Belgrade, Republic of Serbia. (bojanae@chem.bg.ac.rs)

²University of Belgrade, Vinča Institute of Nuclear Sciences, P.O. Box 522,
Belgrade, Republic of Serbia.

ABSTRACT

Macroporous crosslinked poly(glycidyl methacrylate-co-ethylene glycol dimethacrylate) [PGME-deta] functionalized with diethylene triamine was used for removal of Mo(VI) oxyanions from aqueous solutions. Kinetics of Mo(VI) sorption was investigated in batch experiments by varying initial Mo(VI) concentration. Sorption kinetics data was fitted to chemical-reaction and particle-diffusion models. It was shown that Mo(VI) sorption adhered to the pseudo-second-order kinetic model, with a definite influence of pore diffusion. The maximum Mo(VI) sorption capacity at pH 2.0 and 298K was 391 mg g⁻¹.

INTRODUCTION

Molybdenum (Mo) is a relatively rare chemical element that became of great importance in alloys production and as an inhibitor for steel corrosion due to its low toxicity [1]. In aqueous environment, Mo exists mainly in the form of molybdate and/or other Mo polyanions, depending on the solution pH. At low concentrations, Mo is essential for normal growth of animals and plants, but it can be also considered as a pollutant when its concentration exceeds 5 mg dm⁻³ in the environment (surface and ground water). The degree of toxicity of Mo and its compounds ranks between Zn(II) and Cr(III) compounds [2]. Therefore, the removal of those species from the environment is a matter of vital importance. Polymeric resins have been increasingly investigated as sorbents for the sorption of toxic pollutants because of their controllable pore structure, stable physical and chemical properties and their ability of regeneration and reuse. The presented work was directed at the removal of Mo(VI) oxyanions from aqueous solution using macroporous PGME-deta. Kinetic data were collected at four different initial concentrations and analyzed using four kinetic models including the evaluation of the kinetic parameters.

EXPERIMENTAL

Macroporous crosslinked copolymer of glycidyl methacrylate (GMA) and ethylene glycol dimethacrylate (EGDMA) were prepared through suspension copolymerization (EGDMA content was 20 mass %) and functionalized with diethylene triamine, as described elsewhere [3]. The sorption kinetics of Mo(VI) oxyanions from aqueous solutions with different initial concentrations ($C_i = 0.01, 0.02, 0.05$ and 0.1M ; $\text{pH}=2.0$) was studied in batch experiments at room temperature ($T=298\text{K}$). For determination of Mo(VI) sorption rates, 0.50 g of copolymer PGMA-deta was contacted with 50 cm^3 of metal salt solution. In each experiment, 0.5 cm^3 were withdrawn from the system at predetermined time intervals, diluted to 50 cm^3 and Mo(VI) residual concentration was determined by ICP-OES (Thermo Scientific iCAP6000).

RESULTS AND DISCUSSIONS

The speciation of Mo(VI) oxyanions and the surface charge of sorbent are dependent on pH value and initial concentration [4]. In this study, the maximum experimental sorption capacity for PGME-deta was found to be 391 mg g^{-1} at 298K . Namely, at pH 2.0 a large number of PGME-deta amino groups are in their protonated cationic form and electrostatic interaction occurs between the sorbent and negatively charged oxyanions in solution leading to Mo(VI) uptake. For example, Elwakeel et al. reported Mo(VI) sorption capacity of $336\text{-}380\text{ mg g}^{-1}$ for chemically modified magnetic chitosan resins [2]. Magnetic resins grafted with tetraethylenepentamine displayed Mo(VI) sorption capacity of $407\text{-}593\text{ mg g}^{-1}$ [1].

Table 1. Kinetic models.

Kinetic model	Equation	Ref.
PFO	$\log(Q_e - Q_t) = \log Q_e - \frac{k_1 t}{2.303}$	[5]
PSO	$\frac{t}{Q} = \frac{1}{k_2 Q_e^2} + \frac{1}{Q_e} t$	[5]
IPD	$Q_t = k_{id} t^{1/2} + c_{id}$	[5]
Mckay	$\log(1 - F) = -\left(\frac{S}{2.303}\right)t$	[6]

Table 1. where: Q_t -amount of sorbed metal ions at time t , Q_e -amount of sorbed metal ions at equilibrium, k_1 -PFO rate constant, k_2 -PSO rate constant, k_{id} -IPD coefficient, C_{id} -intercept of IPD plot, S -rate parameter. Kinetic parameters calculated from these four kinetic models are presented in Table 2.

In order to investigate the controlling mechanism of Mo(VI) sorption by PGME-deta, the sorption data were treated with four kinetic models i.e. the pseudo-first-order (PFO), the pseudo-second-order (PSO), the intraparticle diffusion (IPD) and the Mckay's model. The applied equations are listed in

Table 2. Kinetic parameters for Mo(VI) using PGME-deta as sorbent (pH=2.0, T=298K)

C_i , M	0.01	0.02	0.05	0.1
Q_e , mg g ⁻¹	91	155	210	391
PFO				
$k_1 \cdot 10^3$, min ⁻¹	2.76	2.53	2.76	4.14
Q_e^{calc} , mg g ⁻¹	69	108	164	277
R^2	0.906	0.953	0.980	0.906
PSO				
$k_2 \cdot 10^3$, g mg ⁻¹ min ⁻¹	0.105	0.0530	0.0358	0.0367
Q_e^{calc} , mg g ⁻¹	97	161	222	400
R^2	0.983	0.978	0.980	0.997
IPD				
k_{1id} , mg g ⁻¹ min ^{-0.5}	3.05	5.33	6.84	20.5
C_{1id} , mg g ⁻¹	13.7	17.4	21.5	22.8
R^2	0.987	0.997	0.961	0.981
k_{2id} , mg g ⁻¹ min ^{-0.5}	1.47	2.72	3.80	3.96
C_{2id} , mg g ⁻¹	35.1	51.2	66.6	239.3
R^2	0.999	0.998	0.983	0.993
McKay				
$S \cdot 10^3$, min ⁻¹	3.71	3.59	3.27	7.05
R^2	0.955	0.987	0.955	0.993

As shown in Table 2, the PSO equation fitted well the experimental data, indicating that the Mo(VI) oxyanions sorption onto PGME-deta is surface-reaction controlled.

Most sorption processes take place through multistep mechanism, especially when porous sorbents are used [7]. Due to the fact that PFO and PSO kinetic models cannot show influence of diffusion on the process, IPD and McKay's models were applied. IPD plots showed two different slopes of the linear plots in two different time intervals, with a non-zero values of C_{id} (Figure 1), suggesting that IPD was rate-controlling, but not exclusively. The sorption of Mo(VI) ions onto PGME-deta is controlled by IPD along with boundary layer diffusion [2].

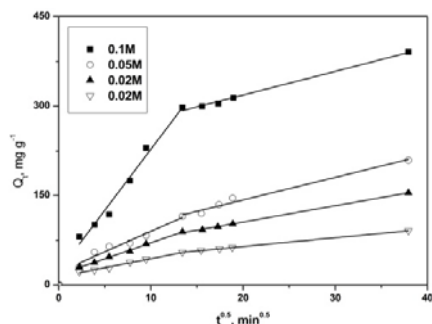


Figure 1. IPD plots for Mo(VI) by PGME-deta at 298K and pH 2.0

At different Mo(VI) concentration Mckay's plots were linear in the initial 180-min period with $R^2 \geq 0.955$ and passed quite near the origin, as an indication that IPD was a major rate determining mechanism particularly in the initial sorption period (Figure not shown).

CONCLUSIONS

The removal of Mo(VI) oxyanions from aqueous solutions was studied using macroporous amino-functionalized crosslinked copolymer, PGME-deta. Kinetics of Mo(VI) sorption was investigated in the initial metal concentration range 0.01-0.1M and analyzed using four kinetic models. Mo(VI) sorption by PGME-deta obeys the PSO kinetic model. The results show that the sorption reaction is controlled by IPD with some degree of boundary layer control. Mckay's model confirms that Mo(VI) sorption is pore diffusion controlled especially in initial period of the reaction.

ACKNOWLEDGEMENTS

The work was supported by the Ministry of Education, Science and Technological Development of the Republic of Serbia (Projects No. III 43009 and III 45001).

REFERENCES

- [1] Atia, A. Donia, H. Awed, J. Hazard. Mater., 2008, 155, 100-108.
- [2] K. Elwakeel, A. Atia, A. Donia, Hydrometallurgy, 2009, 97, 21-28.
- [3] R. Hercigonja, D. Maksin, A. Nastasović, S. Trifunović, P. Glodić, A. Onjia, J. Appl. Polym. Sci., 2012, 123, 1273-1282.
- [4] R. Navarro, J. Guymán, I. Saucedo, J. Revilla, E. Guibal, Macrom. Biosci., 2003, 3, 552-561.
- [5] O. Abdelwahab, Egypt. J. Aquat. Res., 2007, 33, 125-143.
- [6] Y. S. Ho, Bioresource Technol., 2005, 96, 1292-1296.
- [7] A. Ip, J. Barford, G. Mckay, Chem. Eng. J., 2010, 157, 434-442.

POLYETHERSULFONE MEMBRANES WITH INTEGRATED ADSORBENT PARTICLES FOR HEAVY METALS CAPTURE

T. Tomković¹, F. Radovanović¹, A. Nastasović¹, J. Marković², B. Ekmešćić¹, S. Vidojković¹ and A. Onjia²

¹ *University of Belgrade, Institute for Chemistry, Technology and Metallurgy, Njegoševa 12, Belgrade, Republic of Serbia.*
(ttomkovic@chem.bg.ac.rs)

² *University of Belgrade, Vinča Institute of Nuclear Sciences, P.O. Box 522, Belgrade, Republic of Serbia*

ABSTRACT

Novel polyethersulfone membranes with integrated submicron adsorbent particles were prepared by combining photoirradiation with liquid phase inversion. These particles consist of cross-linked poly(glycidyl methacrylate-co-acrylamido-2-methylpropane sulfonic acid), pGMA-AMPS. After membrane preparation, the epoxide groups were reacted with diethylene triamine to incorporate amine functionalities. Membranes were characterized using FTIR-ATR, SEM and dynamic adsorption of copper from a dilute solution. Effects of monomer concentrations on the properties and separation performance of membrane adsorbers are presented.

INTRODUCTION

Polyethersulfone (PES) is frequently used for making high performance ultrafiltration membranes [1]. Various functionalization methods, such as surface or bulk modification of PES material, are often used to incorporate desired functionalities or improve wettability [2]. Macroporous beads obtained by radical suspension polymerization of glycidyl methacrylate (GMA) are very attractive as adsorbents in biochemical and chemical separations [3], due to its ability to integrate separation and purification steps for processing large amounts of product in relatively short times [4]. In this paper, novel PES membranes with submicron crosslinked adsorbent particles of GMA-AMPS copolymer were prepared by combining liquid phase inversion with photopolymerization followed by amination of the epoxide groups under alkaline conditions.

EXPERIMENTAL

Materials

Glycidyl methacrylate (GMA, reagent grade), trimethylolpropane triacrylate (TMPTMA), N-methyl-2-pyrrolidone (NMP, 99% purity), diethylene triamine (DETA, reagent grade), sodium hydroxide (NaOH), hydroquinone, 2-acrylamido-2-methylpropane sulfonic acid (AMPS) and copper (II) chloride dihydrate ($\text{CuCl}_2 \cdot 2\text{H}_2\text{O}$, reagent grade) were purchased from Sigma Aldrich. Polyethersulfone (PES, Ultrason E 7020P) was provided by BASF. The photoinitiator (bis(2,4,6-trimethylbenzoyl)-phenyl-phosphine oxide (Irgacure 819) was obtained from Ciba SC as a gift. All chemicals were used without purification.

Membrane preparation

Sodium salt of AMPS was prepared by dissolving equivalent quantities of NaOH and AMPS, 0.1% hydroquinone in water followed by its crystallization upon acetone addition, filtration and drying under vacuum.

Solutions of GMA, sodium salt of AMPS, cross-linker TMPTMA and solvent NMP were mixed in vials cooled with ice and protected from ambient light, then combined with PES solution and photoinitiator, cast on a glass plate, and exposed to UV irradiation under nitrogen blanketing. Irradiated films were immersed into water bath to prepare final membranes. Obtained membranes were functionalized with DETA by heating them in a solution containing 5g DETA and 100g distilled water for 8 hours at 80°C under reflux conditions.

Membrane characterization

FTIR-ATR analysis was conducted with Thermo Scientific Nicolet 6700 instrument equipped with Smart ATR Diamond accessory.

SEM analysis was performed with JEOL JSM-6610 L instrument using W filament as an electron source. Air-dried membrane samples were fractured after cooling in liquid nitrogen and sputtered with gold.

Feed solution containing 2 ppm Cu^{2+} in deionized water was permeated through membranes at 0.5 bar transmembrane pressure using a Millipore stirred cell, Model 8050. The concentration of Cu^{2+} in permeate was determined using Atomic Absorption Spectrophotometry.

RESULTS AND DISCUSSION

FTIR-ATR spectra of a typical PES membrane with adsorbent particles taken before and after functionalization are presented in Fig. 1. Strong carbonyl peaks at 1726 cm^{-1} and epoxide peaks at 907 cm^{-1} originate from GMA, while the peak at 1042 cm^{-1} corresponds to the sulfonic acid group present in AMPS. It can be seen that the epoxide peak at 907 cm^{-1} after functionalization was significantly reduced.

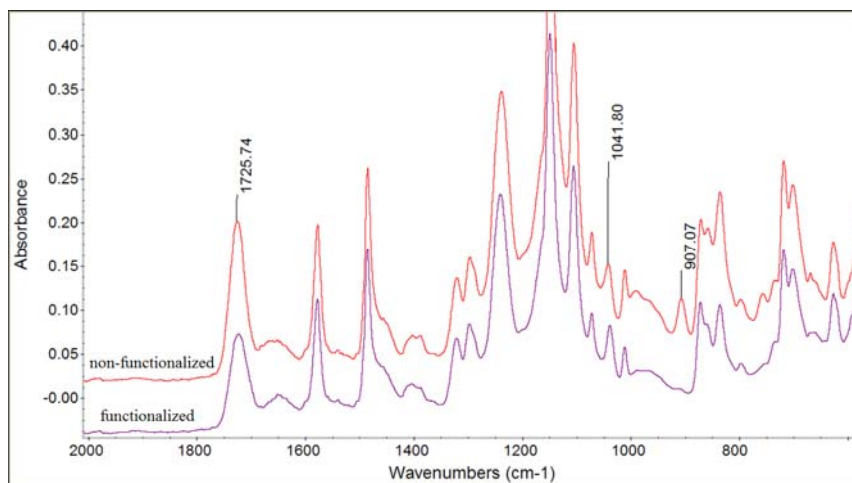


Figure 1. FTIR-ATR spectra of a membrane (11% PES, 2 mmol/g GMA, 1 mmol/g AMPS and 15 mol % TMPTMA), before and after functionalization

Fig. 2 presents SEM images of a membrane with initial concentrations of 2.0 mmol/g GMA and 1.0 mmol/g AMPS. The interconnected structure of crosslinked pGMA-AMPS submicron particles embedded within porous PES membrane is clearly visible.

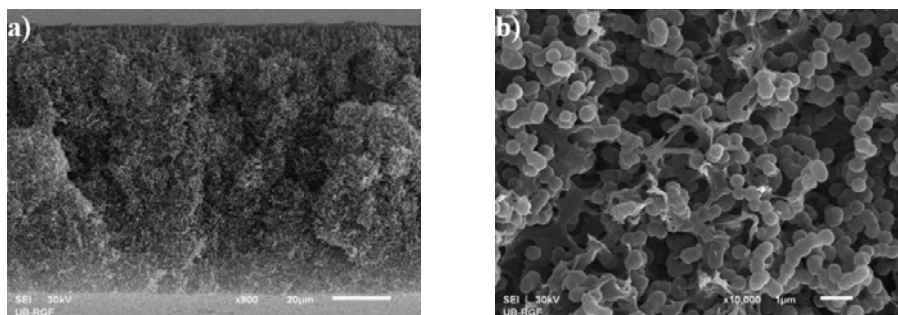


Figure 2. SEM images of a PES membrane with 2.0 mmol/g GMA and 1.0 mmol/g AMPS: a) cross-section, b) middle part at 10k magnification.

The separation performances of functionalized and non-functionalized membranes are shown in Fig. 3. Heavy metal capture occurs by electrostatic binding between sulfonic group present in AMPS and Cu^{2+} , while, in the case of functionalized membranes, by additional chelating action of the amino groups. Best separation performance was achieved with the functionalized membrane with 1 mmol/g AMPS and 2 mmol/g GMA.

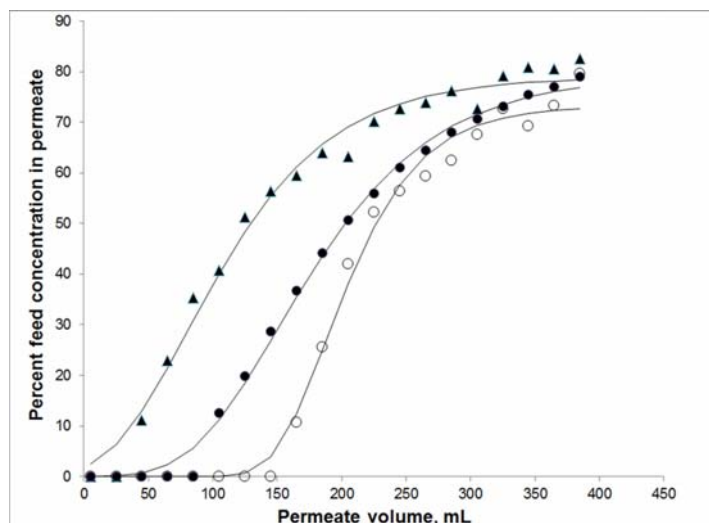


Figure 3. Filtration of Cu solution through functionalized PES membranes made with 0.75 mmol/g sodium salt of AMPS (▲) and 1.0 mmol/g sodium salt of AMPS (○) and non-functionalized membrane with 1.0 mmol/g sodium salt of AMPS (●)

CONCLUSION

Novel PES membrane adsorbers were prepared by combining liquid phase inversion with photopolymerization followed by post-amination. SEM images show interconnected network of submicron particles. Dynamic adsorption performance of these membranes using a dilute Cu^{2+} solution indicated that they could be useful for capture of heavy metals.

ACKNOWLEDGEMENT

This work has been funded by Serbian Ministry of Education, Science and Technological Development through the projects TR 32008, III 43009.

REFERENCES

- [1] M. Ulbricht, M. Riedel, U. Marx, *J. Membrane Sci.*, 1996, 120, 239-259.
- [2] F. Radovanović, A. Nastasović, T. Tomković, D. Vasiljević-Radović, A. Nešić, S. Veličković, A. Onjia, *React. Funct. Polym.*, 2014, 77, 1-10.
- [3] N. Miletić, R. Rohandi, Z. Vuković, A. Nastasović, K. Loos, *React. Funct. Polym.*, 2009, 69, 68-75.
- [4] J. Thömmes, M. R. Kula, *Biotechnol. Prog.*, 1995, 11, 357-367.

FEATURES OF POLYCONJUGATED SYSTEM FORMATION UNDER LOW-TEMPERATURE IR-PYROLYSIS: INFLUENCE OF COMONOMER NATURE AND REACTION MEDIA DURING SYNTHESIS

J. V. Kostina¹, E. V. Chernikova², N. I. Prokopov³, A. Yu. Gervald³,
A. Yu. Nikolaev³, A. A. Baskakov^{1,2} and S. M. Kishilov²

¹*Topchiev Institute of Petrochemical Synthesis,
Leninsky Prospekt, 29, Moscow, Russia julia@ips.ac.ru.*
²*Lomonosov Moscow State University, Chemistry Department,
Leninskie Gory, 1/3, Moscow, Russia,*
³*Lomonosov Moscow University of Fine Chemical Technologis,
pr. Vernadskogo 86, Moscow, Russia*

ABSTRACT

The differences in mechanism of polyconjugated system formation and its structure under low-temperature IR-pyrolysis depending on copolymer synthesis conditions were determined by ATR IR-spectroscopy. Systematic studies were carried out using acrylonitrile / methyl acrylate and acrylonitrile / methyl acrylate / itaconic acid copolymers with low content of comonomers synthesized via radical polymerization in DMSO, DMF, aqueous solution of NaNCS, and in water.

INTRODUCTION

Pyrolysis of polyacrylonitrile (PAN) and its copolymers leads to polyconjugated system formation (PCS), which structure at earlier low-temperature stages is pre-determined by such factors as copolymer chemical composition and sample prehistory, in particular, the possible non-covalent interactions between functional side groups and residual solvent that may influence the orientation of the former along the main polymeric chain [1]. Recently, it have been found that the relative amount of N atoms in PCS surface layer affects H and O atoms adsorption and it leads to different type of conductivity (protonic or electronic) [2]. PAN pyrolysis under the action of incoherent IR-radiation leads to formation of PCS at lower temperature and time comparing to thermal annealing [3].

The aim of the present research was to establish 1) the systematic differences in PCS structure under low-temperature IR-pyrolysis of AN copolymers comparing to PAN homopolymer depending from reaction medium used in polymer synthesis and copolymer composition; 2) the

possibility of governing of PCS structure at the initial stage of its formation for directed changes of physical-chemical properties of materials on its basis.

EXPERIMENTAL

Binary and ternary copolymers have been synthesized via radical polymerization using AIBN as an initiator at 70 °C. Table 1 summarizes molar mass characteristics of resulting copolymers formed in various reaction media.

Table. Characteristics of AN binary copolymers and terpolymers

Sample No	Sample	Solvent	Monomer feed %, AN/MA/IA	$M_w \times 10^{-3}$	M_w/M_n
1	PAN-MA	H ₂ O	95/5/0	214	4.72
2		NaNCS (aq.)	95/5/0	168	1.85
3		DMSO	95/5/0	110	1.97
4		DMF	95/5/0	40	1.89
1'	PAN-MA-IA	H ₂ O	94/5/1	255	2.84
2'		NaNCS (aq.)	94/5/1	88	2.43
3'		DMSO	94/5/1	58	1.84
4'		DMF	94/5/1	41	1.81

IR-pyrolysis of dry powder samples was performed in a special lab pulsed photon annealing device in Ar-atmosphere conducted at 25, 100, 140, 150, 160, 170, 180 and 200 °C in the IR-chamber [3]. The structure of forming PCS structure of these samples was investigated by ATR spectroscopy at each temperature of IR-pyrolysis. The ATR spectra were recorded using IR-microscope Hyperion 2000 (Ge crystal, 4000–600 cm⁻¹, resolution 2 cm⁻¹), conjugated with vacuum spectrometer IFS 66v/s (Bruker).

RESULTS AND DISCUSSION

The influence of reaction media on the PCS formation and its structure was studied for AN binary copolymers (Samples 1–4, Table) and terpolymers (Samples 1'–4', Table) and compared with commercial PAN. Analysis of ATR-IR-spectra of binary copolymers revealed the conformational differences of the main chain comparing to PAN (deformation vibrations in the region of 1500–800 cm⁻¹) and the shift of absorption bands maximum of stretching vibrations –C≡N and –C=O groups in copolymers comparing to corresponding homopolymers. Analogous, but less pronounced, effects were observed in ATR-IR-spectra of terpolymers. Hence, the reaction media can

affect the conformational composition of copolymer via change of CN and CO-groups polarization and orientation along main polymeric chain due to non-covalent polymer – solvent interactions. Previously, this effect for homopolymers was described in [1].

PCS formation was studied for both AN binary and ternary copolymers; however more interesting features in PCS mechanism formation distinct from PAN were found for terpolymers (Fig. 1).

ATR-IR-spectra given on Fig. 1 were normalized to absorption band of ν_{CN} for the each temperature. By to 160 °C PCS was the most developed for Sample 4' and less developed for Sample 1'. Moreover, ATR-IR-spectra of the Samples 1'–4' recorded at 160 °C, and hence their structure varies drastically. It means that kinetics of PCS formation is different. This result allows easy control of definite type of conjugation in copolymers samples by simple

change of reaction media during polymer synthesis. Towards the completion of pyrolysis two types of PCS can be observed. Type I is characterized by extensive length of conjugation or similar length of with minor defects (absorption bands referred to δ_{CHH} at 1450 cm^{-1} are absent). In contrast Type II is characterized by short conjugation segments separated by defects (e.g., individual residual CH_2 -groups). Type I was observed in ATR-spectra of PCS as intensive region of absorption with feebly pronounced maxima below 1300 cm^{-1} and as similar intensive maxima of absorption bands at 1585 and 1367 cm^{-1} (Sample 1' and PAN). The PCS of Type II can be distinguished in ATR-spectra as intensive maxima of absorption bands at 1585, 1367 and 1252 cm^{-1} (Samples 2' and 4'). Thus depending from conformational composition of initial copolymer, which is due to the influence of non-covalent interactions, two different types of PCS may be obtained. Details the impact of non-covalent interactions on the orientation of functional groups along the polymer chain with quantum-chemical modeling results in other papers by the authors represented. ATR-spectra of

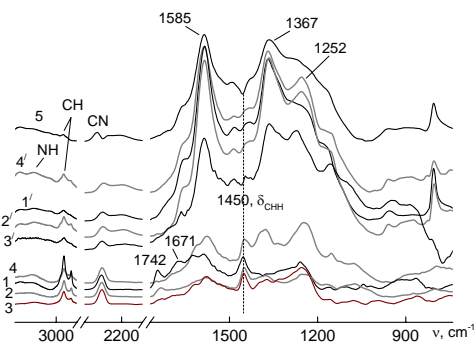


Figure 1. ATR-IR-spectra of polymers 1' – 4' (Table) at 160°C (curves 1–4) and 200°C (curves 1'–4'). PCS structure of PAN at 200°C of IR-pyrolysis (curve 5).

copolymers at 100 °C of IR-pyrolysis are of particular interest. For Samples 1', 3' and 4' the absorption bands at 1850 and 1780 cm^{-1} are observed in the spectra, which may be referred to formation of either cyclic or cross-linked carbonyl containing structures (lacton, lactam, anhydride, imide, etc.) as intermediate structure in PCS. One embodiment of the reaction mechanism of PCS formation provides for primary generation of C=N bonds and further developing of conjugation due to formation of C=C bonds at more intense pyrolysis. The appearance of C=C bonds results to noticeable bathochromic shift in UV-spectra [4]. Our quantum-chemical calculations of theoretical vibration spectrum with various content of C=N and C=C bonds in model show the analogous shift for the theoretical C=N frequency value to the long-wave region upon C=C formation. Under definite conditions and copolymer composition the ability to govern the content of C=N and C=C bonds in the macromolecule appears, which allow control of conductivity type in PCS under conditions of selective adsorption of atomic H and O.

CONCLUSION

The influence of reaction media of polymer synthesis on AN conformational chain composition and as a consequence on mechanism, kinetics and structure of PCS was shown. The ability to govern the relative content of conjugated C=N и C=C bonds was assumed. The obtained results may cause interest for developing of materials with proton or electron conductivity through specific atomic hydrogen or oxygen adsorption on partly formed PCS.

ACKNOWLEDGEMENT

This work was supported by the Russian Foundation for Basic research № 14-03-00155a.

REFERENCES

- [4] E.V. Chernikova, Z.A. Poteryaeva, A.V. Shlyakhtin, N.I. Prokopov, A.Yu. Gervald, A.Yu. Nikolaev, V.R. Durflot, E.A. Dubova, Yu.V. Kostina, A.S. Rodionov, M.N. Efimov, A.S. Cherevan', G.N. Bondarenko, *Polymer Science*, 2013, B55, Vol.1–2, 1–13
- [5] N. Anikeev, I. Zaporotskova, D. Polikarpov, *Book of Abstract, EPF 2013, Italy*, P7-5
- [6] L.M. Zemtsov, G.P. Karpacheva, M.N. Efimov, D.G. Muratov, and K.A. Bagdasarova, *Pol. Sci.*, 2006, A48, 633.
- [7] N.S. Batty *Macromolec.Chem.*, 1981, B. 182, 1, 71

INVESTIGATION OF THERMAL DEGRADATION OF RUBBER BASED ON DIFFERENT NETWORK PRECURSORS

I. S. Ristić¹, B. Ikonić¹, R. Radičević¹, B. Pilić¹, T. Radusin²,
V. Aleksić³ and N. Vukić¹

¹*University of Novi Sad, Faculty of Technology, Bul cara Lazara 1, Novi Sad, Serbia (ivancekaris@yahoo.com)*

²*University of Novi Sad, Institute of Food Technology, Bul cara Lazara 1, Novi Sad, Serbia*

³*University of East Sarajevo, Faculty of Technology, Karakaj bb, Republic of Srpska, BiH*

ABSTRACT

Kinetic parameters of thermal degradation of rubber materials were investigated by thermogravimetric analysis (TGA). Rubber samples, based on butadiene-nitril and polyurethane elastomers, were prepared with different types of oil (referent oil, mineral and processing oil). The influence of network precursors and oil types on the kinetic of rubber decomposition was investigated by Šatava-Šesták and Flynn-Wall-Ozawa methods. Kinetic analysis showed that activation energy (E_a) values are all positive, indicating that the thermooxidative degradation process of rubbers is non-spontaneous. Also, substitution of referent oil with mineral or processing oil enhanced thermal stability of rubber, increasing the degradation time.

INTRODUCTION

Rubber is a multi-component material with elastic properties which is its main features, and due to its characteristics has a specific role and application in various fields. When designing the composition of raw material for the preparation of rubbers, it is very important to make such a choice of initial components which could produce the material for specific applications by crosslinking reaction. During the crosslinking of macromolecules, by selecting the types and quantities of the initial components, elastic material with the desired mechanical, chemical and thermal properties could be obtained. Knowing kinetic of rubber thermal degradation is very important from the point of applications, because during degradation many properties of rubber decreased and offer clues to understand degradation mechanism. Therefore, contemporary research and industrial practice in rubber industry focused on the investigation of thermal properties of rubbers in order to obtain new types of elastomeric materials

for specific high-temperature applications. The aim of this study is the investigation of the influence of oil types on the degradation kinetic of rubbers based on different network precursors (butadiene-nitril and polyurethane). Also, was evaluated kinetic models which consider a three-dimensional diffusion process for the investigation of degradation kinetics of rubber materials based on different network precursors.

EXPERIMENTAL

The samples were prepared by mixing the components, Table 1, on the laboratory rollers ("Veb Getriebe Ohorn 8506"-Germany), 20 minutes at 50 °C. Curing was performed in the press at 120 °C. Thermal stability of prepared samples was investigated by thermogravimetric analyser (TGA 701 LECO (Leco Corp.,USA)) with three different heating rates (3, 5 and 20 °C), in air atmosphere from 25 to 700°C.

Table 1. Composition of investigated rubbers (phr)

	PUR-R	PUR-M	PUR-P	NBR-R	NBR-M	NBR-P
Rubber	100.00	100.00	100.00	100.00	100.00	100.00
Sulphur	8.60	8.60	8.60	0.97	0.97	0.97
Curing activator	0.76	0.76	0.76	6.10	6.10	6.10
Curing accelerator	1.99	1.99	1.99	3.05	3.05	3.05
Dioctylphthalate oil	5.43	0	0	24.39	0	0
Mineral oil	0	5.43	0	0	24.39	0
Process oil	0	0	5.43	0	0	24.39
Carbon black	91.77	91.77	91.77	91.46	91.46	91.46
Other ingredients	1.90	1.90	1.90	11.58	11.58	11.58

*R-referent (Dioctylphthalate oil) oil, M-mineral oil, P-processing oil

RESULTS AND DISCUSSION

Activation energies of degradation process for different rubbers were summarised in Tables 2 and 3. Different types of mathematical integral function of conversion, $g(\alpha)$, were applied, where the function $g(\alpha)=[1-(1-\alpha)^{1/3}]^2$ was denoted as a D3 model and function $g(\alpha)=(1-2/3\alpha)^{1/3}-(1-\alpha)^{2/3}$ as a D4 model. These two models were used because considered three-dimensional diffusion process [1]. For fixed heating rates, β , (3, 5, 20 K/min), the values of activation energy (E_a) and pre-exponential factor (A) can be obtained using Šatava-Šesták method (Eq. (1)) at any selected $g(\alpha)$ [2].

$$\ln g(\alpha) = \ln \frac{A_s E_s}{R\beta} - 5.330 - 1.0516 \frac{E_s}{RT} \quad (1)$$

Table 2. Values of activation energy and pre-exponential factor obtained for the thermal decomposition of polyurethane base rubber from Šatava-Šesták method

Sample	$\beta=3\text{K/min}$			$\beta=5\text{K/min}$			$\beta=20\text{K/min}$			
	E_s (kJ/mol ⁻¹)	$\ln A_s$	R^2	E_s (kJ/mol ⁻¹)	$\ln A_s$	R^2	E_s (kJ/mol ⁻¹)	$\ln A_s$	R^2	
PUR-R	D3	82.06	8.371	0.967	96.29	10.56	0.974	115.2	12.88	0.951
	D4	81.41	8.183	0.969	95.74	10.41	0.975	114.0	12.60	0.953
PUR-M	D3	86.71	8.610	0.973	98.15	10.88	0.980	121.0	13.84	0.957
	D4	86.10	8.440	0.963	97.54	10.71	0.977	119.8	13.54	0.973
PUR-P	D3	77.78	7.703	0.965	95.63	10.81	0.979	120.8	14.61	0.964
	D4	77.18	7.529	0.967	94.67	10.56	0.981	119.3	14.23	0.964

Table 3. Values of activation energy and pre-exponential factor obtained for the thermal decomposition of NBR based rubber from Šatava-Šesták method

Sample	$\beta=3\text{K/min}$			$\beta=5\text{K/min}$			$\beta=20\text{K/min}$			
	E_s (kJ/mol ⁻¹)	$\ln A_s$	R^2	E_s (kJ/mol ⁻¹)	$\ln A_s$	R^2	E_s (kJ/mol ⁻¹)	$\ln A_s$	R^2	
NBR-R	D3	87.98	7.858	0.949	92.33	8.335	0.966	125.6	13.54	0.945
	D4	87.46	7.720	0.951	91.64	8.146	0.968	124.3	13.22	0.945
NBR-M	D3	90.63	8.010	0.958	107.1	11.09	0.978	131.3	14.37	0.957
	D4	89.97	7.834	0.959	106.3	10.86	0.979	129.9	14.04	0.957
NBR-P	D3	92.09	9.765	0.991	98.35	10.34	0.991	115.4	12.33	0.963
	D4	91.35	9.565	0.991	97.45	10.10	0.992	113.8	11.96	0.963

From Tables 2 and 3 can be concluded that E_a values increasing with substitution of referent oil with processing and mineral oil, which imply higher thermal stability of these samples. As it was expected, with a higher heating rate higher values of E_a were obtained for all samples.

For transformation of non-isothermal data to isothermal in this work Flynn-Wall-Ozawa model (Eq. (2)) was used [2].

$$\ln \beta = \ln\left(\frac{AE}{Rg(\alpha)}\right) - 5.330 - 1.0516 \frac{E}{RT} \quad (2)$$

The values of the time required to achieve apparent degradation degree of different rubber samples are summarized in the Table 4. Degradation of samples deviated from the predictable data at degradation degree higher than 50%, which is expected due to higher contents of carbon black in the samples and its hindering effect.

Table 4. Dependence of degradation time on rubber composition for apparent degradation degrees

α	Time (min)					
	PUR-R	PUR-1	PUR-2	NBR-R	NBR-1	NBR-2
0.05	0.092	0.166	0.166	0.199	0.205	0.357
0.1	0.133	0.357	0.364	0.579	0.677	1.051
0.15	0.186	0.686	0.707	1.326	2.780	3.040
0.2	0.272	1.281	1.327	2.745	19.396	9.868
0.25	0.446	2.415	2.498	5.394	276.605	39.473
0.3	0.904	4.692	4.833	10.356	1123.776	213.087
0.35	2.571	9.573	9.794	19.724	/	1648.105
0.4	9.269	20.867	21.194	37.729	/	15953.430
0.45	15.782	49.465	50.059	73.245	/	83734.900
0.5	/	129.741	132.419	145.796	/	/

Substitution of referent (dioctylphthalate) oil with chipper mineral and processing oils increases the thermal stability for both investigated rubbers, and increases the time to reach apparent degree of degradation, Table 4. Results obtained by D3 and D4 models were similar, which confirmed presumption about diffusion controlled degradation of rubber, due to steric effect of carbon black.

CONCLUSIONS

The kinetic of thermal degradation process of the investigated rubber materials was successfully investigated by applied models, D3 and D4. In comparison to the samples with referent oil, the thermal stability of the rubbers prepared with mineral and processing oil are improved. At a given degradation temperature, the degradation rate of the samples with mineral and processing oil are lower than those of the rubber with referent oil, which indicated a higher durability and potential usage in high temperature applications.

ACKNOWLEDGEMENTS

This work was supported by the Ministry of Education, Science and Technological Development of the Republic of Serbia (Grant no. III45022).

REFERENCES

- [1] L. Nunez, F. Fraga, M. R. Nunez, M. Villanueva, *Polymer*, 2000, 41, 4635–4641.
- [2] M. Huang, S. Lv, C. Zhou, *Thermochimica Acta*, 2013, 552, 60-64.

EFFECT OF PVC PLASTISOL COMPOSITION AND PROCESSING CONDITION ON TENSILE RESISTANCE

R. Radovanović¹, M. Jovičić² and B. Pilic²

¹ *OOO JUTEKS RU, Dorozhnaya street 10, 601301 Kameshkovo, Russia*

² *University of Novi Sad, Faculty of Technology, Bulevar cara Lazara 1, 21000 Novi Sad, Serbia*

ABSTRACT

In this paper the influence of concentration of blowing agent and calcium carbonate filler as well as temperature and time of the blowing process on the tensile resistance of the PVC foam were studied. Moreover, regression analysis was performed in order to determine the significance of studied parameters influence tensile resistance. Tensile resistance is defined by four values: Maximum Power (F_{\max}), Maximum Power Extension (dL_{\max}), Tensile Strength (F_{break}) and Tensile Strength Extension (dL_{break}). The influence of all parameters (concentration of blowing agent and calcium carbonate filler as well as temperature and time of the blowing process) on the four mentioned values is practically the same. For that reason we have chosen only Maximum Power F_{\max} as the representative for the model analysis.

INTRODUCTION

In the last decade of the previous century demand for polymeric foams has risen dramatically [1]. Trend of growth has continued at a rapid pace in the whole world. The cause of this are the numerous excellent properties that encompass light weight, excellent strength/weight ratio, superior insulating abilities, and energy absorbing performance and comfort features of polymeric foams [2]. Precise timing of foam expansion and careful choice of temperature are critical for the foam properties. At high temperatures, the melt viscosity is low so rapid gas expansion can cause cell rupture and collapse [3]. Different studies have dealt with the influence of processing conditions on foam density and thus on the foam properties [3]. Study of CaCO_3 particle size effect in foam formulations [4] proved that smaller particle size enables efficient fusion of the compound.

In this study it was investigated the effect of four parameters on tensile resistance of PVC foam. The parameters that were studied are temperature (in the stable range of 180 - 196 °C), expansion time (in the range 90-150s), calcium carbonate filler concentration (40-100 phr) and azodicarbonamide

blowing agent concentration (0.8 - 1.2 wt. %). Multiple regression analysis was employed in order to determine the significance of the influence of the different parameters on the tensile resistance.

EXPERIMENTAL

The plastisol consists of PVC powder (Solvic 367SF, Solvin, France), PVC extender (Solvic 266SF, Solvin, Belgium), dioctyl phthalate plasticizer (Roshalskiy Zavod Plastifikatorov, Roshaly, Russian Federation), azodicarbonamide blowing agent (MC-2, OOO Norteks, Moscow, Russian Federation), ZnO kicker (BC OM, Bellit, Saransk, Russian Federation), TiO₂ (R103, DuPont, Germany), calcium carbonate filler (Omycarb 40 UR, Omya Ural, Russian Federation, with particle size $26 \pm 5 \mu\text{m}$), viscosity regulator (Viskobyk 4041, BYK Chemie, Germany) and dispersing agent (Dispersplast 1138, BYK Chemie Germany). Nine different formulations were prepared with three different calcium carbonate concentrations (40, 70 and 100 phr) and three different blowing agent concentrations (0.8; 1.0; and 1.2 wt. %). The ratio of blowing agent to kicker percent was 3:1 in all nine prepared formulations.

Poly (vinyl chloride) plastisols were prepared by mixing the appropriate components in a laboratory vacuum mixer (LPE, Werner Mathis AG, Switzerland). The prepared plastisols were coated on a silicon paper and were left to gel for 30 s at 150 °C in an oven (LTF, Werner Mathis AG, Switzerland). The samples were expanded into foam at five different temperatures (180, 184, 188, 192 and 196 °C) and in three different time periods (90, 120 and 150 s). The tensile resistance was measured by mechanical test machine (Zwick/ Roell Z005) on samples 50 mm wide and 200 mm long with linear elongation speed of the material at 100 mm/min.

RESULTS AND DISCUSSION

The main goal of this study was to determine which of the four studied parameters (concentration of calcium carbonate – X_1 , concentration of blowing agent – X_2 , foam expansion time – X_3 and temperature – X_4) has the significant influence on the tensile resistance of the foam. Efforts were made to find the appropriate linear correlation with the least number of independent variables that would predict mentioned characteristic with an acceptable level of accuracy. In the first step, linear correlation between tensile resistance and each parameter was separately determined. The highest value of correlation coefficient (R) and the lowest root mean square error (RMSE) among four correlations indicate that calcium carbonate concentration (CaCO₃) is the best predictor on the tensile resistance of PVC foam. At the same time azodicarbonamide blowing agent with the highest

regression coefficient (-37.4) indicates biggest negative impact on tensile resistance. Further on, forward stepwise analysis was performed, including new parameters in the model in the order of their significance. Steps of models are given below:

$$E1 = b_0 + b_1X_1 \quad (E1)$$

$$E2 = b_0 + b_1X_1 + b_2X_2 \quad (E2)$$

$$E3 = b_0 + b_1X_1 + b_2X_2 + b_4X_4 \quad (E3)$$

$$E4 = b_0 + b_1X_1 + b_2X_2 + b_3X_3 + b_4X_4 \quad (E4)$$

In table 1 all parameter models are shown. First, we have tried to improve model E1 by including one more parameter. The effect of including each of the three remaining parameters was explored. F ratio shows how individual parameters affect the model if we include them. The higher F ratio means the higher significance.

Table 1. Regression coefficients (b_i), correlation coefficient (R), root mean square error (RMSE), sum of square (SS) and F ratio for different correlation models for tensile resistance dependence on studied parameters

Model	R	RMSE	SS	F
$E1 = 99.1 - 1.25X_1$	0.6661	10.3	11170	106
$E2 = 139.27 - 1,28X_1 - 39,23X_2$	0.8119	8.1	16597	128
$E3 = 344,1 - 1,28X_1 - 39,23X_2 - 1,09X_4$	0.9290	5.1	21726	275
$E4 = 355,56 - 1,28X_1 - 39,23X_2 - 0,1X_3 - 1,09X_4$	0.9446	4.6	22464	269

In the model E3 and E4, F ratio value is higher more than twice compared with model E2, meaning higher significance, and correlation coefficient (R) for E3 and E4 model are almost the same. Therefore, since the model E3, with three parameters, is simpler, it was our model of choice. Comparison of the values of the tensile resistance predicted by the model and the experimental values were compared and the points that differ more than 2σ were disbanded (4 points from the total of 135 points).

Table 2. Intercept, regression coefficient b_i , correlation coefficient (R), root mean square error (RMSE) of correlations between tensile resistance and each single studied variables (Model E1)

Parametar name	Variable designation	Intercept b_0	Coefficient b_i	R	RMSE
CaCO ₃ (%)	X1	99,1	-1,25	0,6661	10,2618
ADCA (%)	X2	100,57	-37,4	0,4428	12,3357
Time (s)	X3	74,49	-0,1	0,1712	13,5551
Temperature (°C)	X4	267,88	-1,09	0,4513	12,2772

Although analysis (model E1 – table 2; individual impact of independent variables) has indicated that concentration of the calcium carbonate (CaCO_3) is the most important predictor that determines the tensile resistance trend. At the same time the linear regression analysis shows that blowing agent has the highest regression coefficient and influence on tensile resistance as well. Tensile can be performed in a very narrow range of temperature and time. Optimal processing conditions are in temperature range of 188-192 °C with a foaming time of 120 seconds. Adding calcium carbonate filler has negative effect on the tensile resistance but significance of its effect (expressed as F ratio) is relatively low (Table 1). This information is very important as it shows that with the addition of the filler, the price of the product can be lowered with an insignificant change of the tensile resistance.

CONCLUSIONS

In this study effect of temperature, foaming time, calcium carbonate and blowing agent concentration on tensile resistance was investigated. Correlation models that describe these relations were developed. It was found out that all studied parameters have negative influence on tensile resistance. The most negative effect on tensile resistance shows the blowing agent concentration while the calcium carbonate concentration is the best predictor of the model. Increase of the calcium carbonate concentration in the foam lowers the tensile resistance but it was found out that its influence is not significant. These findings confirm usefulness of calcium carbonate in order to lower the cost of the PVC foam products. This means that the mixture formulation and the process conditions must be optimized in order to obtain the desired characteristics and sustainable cost.

ACKNOWLEDGMENTS

This study was supported by the Ministry of Education, science and technological development of the Republic of Serbia, Project No. III 45022. We specially thank associates working in Juteks DD development sector laboratories in Russia and Slovenia for their technical assistance.

REFERENCES

- [1] J. Patterson, *Addit. Technol.*, 1998, 4, 26–29.
- [2] H. Demir, M. Sipahioğlu, D. Balköse, S. Ülkü, *J. Mater. Process. Technol.*, 2008, 195, 144-153.
- [3] E. Rabinovitch, J. Isner, J. Sidor, D. Wiedl, *Spe/Antec Proceedings* 1997, 3, 3554-3559.
- [4] B. Azimipour, F. Marchand, *J. Vinyl. Addit. Technol.*, 2006, 12, 55-57.

INFLUENCE OF ALKYL GALLATE SURFACE MODIFIED TiO₂ NANOPARTICLES ON THE RHEOLOGICAL PROPERTIES OF ALKYD RESIN

T. S. Radoman¹, V. V. Vodnik², J. V. Džunuzović³, K. B. Jeremić⁴, A. D. Marinković⁴ and E. S. Džunuzović⁴

¹*Innovation center, Faculty of Technology and Metallurgy, University of Belgrade, Karnegijeva 4, Belgrade 11120, Serbia.*

²*Laboratory for Radiation Chemistry and Physics "Gamma", Institute of Nuclear Science Vinca, University of Belgrade, Mike Petrovica Alasa 12-14, 11001 Belgrade, Serbia. (vodves@vinca.rs)*

³*Institute of Chemistry, Technology and Metallurgy (ICTM)-Center of Chemistry, University of Belgrade, Studentski trg 12-16, 11000 Belgrade, Serbia.*

⁴*Faculty of Technology and Metallurgy, University of Belgrade, Karnegijeva 4, 11120 Belgrade, Serbia.*

ABSTRACT

The influence of alkyl gallate surface modified TiO₂ nanoparticles on the rheological properties of long oil alkyd resin, based on soybean oil, was investigated. Surface modification of TiO₂ nanoparticles, obtained by acid catalyzed hydrolysis of titanium tetraisopropoxide, was performed with propyl, lauryl or cetyl gallate. The average particle size and the crystal structure of synthesized nanoparticles were estimated by transmission electron microscopy and X-ray diffraction. The gallate chemisorption onto surface of TiO₂ nanoparticles was confirmed by FTIR and UV spectroscopy. The examined dispersions were prepared by the addition of modified TiO₂ nanoparticles to the commercial alkyd resin. The viscosity of the prepared dispersions was higher than viscosity of the pure resin and it increased with increasing length of hydrophobic part of the gallate used for surface modification of TiO₂ nanoparticles. This occurred because the increase of their hydrodynamic volume led to the increase of the effective volume fraction of particles in dispersion.

INTRODUCTION

Alkyds are the most common synthetic resins used in the paint industry due to their unique properties, such as good wetting, good mechanical properties, durability, good anticorrosive properties, high gloss, etc. Besides, one of their advantages is that they are available from renewable

resources. Keeping in mind that the properties of alkyd resins (ARs) depend in great extent on the type of the used vegetable oil, distinguished features of the alkyd resins give the possibility of using the same procedure to develop a number of products with different properties [1]. In order to improve the quality of coatings, a great number of inorganic pigments were incorporated in coating formulation. Pigments have influence on optical properties, corrosion resistance, hardness, flexibility, adhesion and durability of coatings. When the paint (coating) is wet, pigments affect the rheology and influence the ease of application (spray, brush,...), film formation (flow and leveling) and sag resistance. That influence depends on the pigment size, its concentration, type of the applied surface modification, etc. However, the commercially available pigments are micro-sized. Therefore, in recent years, attempts have been made to use nano-sized pigments. It has been found that incorporation of nanoparticles in polymer resin-based coatings improves barrier properties, reduces the formation of blistering or delamination and enhances the integrity and durability of coatings. In particular, depending on the type, concentration, size, shape and dispersion quality of the nanoparticles in the polymer matrix, a superior barrier properties, UV and mechanical resistance, as well as improved thermal stability and optical properties can be achieved [2]. The aim of this work was to investigate the influence of incorporation of TiO₂ nanoparticles surface modified with different alkyl gallates on the rheological properties of alkyd resin.

EXPERIMENTAL

The commercially available alkyd resin, CHS-ALKYD S 653 W 70 (70 wt.% solution of AR in white spirit), was purchased from Spolchemie. The colloidal TiO₂ dispersion was synthesized by hydrolysis of titanium tetraisopropoxide (TCI Europe) at 80 °C under a stream of dry nitrogen, for 8 hours. Modification of colloidal particles with three gallates (propyl (PG), lauryl (LG) and cetyl gallate (CG); Sigma-Aldrich) was performed in the same manner. The dispersions (1 wt.% of TiO₂, calculated with respect to the mass of alkyd resin) were prepared by adding appropriate amount of modified nanoparticles to the AR. X-Ray diffraction (XRD) measurements were performed on a Phillips PW1710 powder diffractometer. The average particle size of the TiO₂ nanoparticles was determined by a transmission electron microscopy (JEOL-1200EX). FTIR spectra of dry, unmodified and modified, TiO₂ nanoparticles were recorded on a Bomem MB 100 FTIR spectrophotometer. The absorption spectra of the TiO₂ colloid in water and TiO₂ surface modified nanoparticles in chloroform were recorded using a Perkin-Elmer Lambda 35 UV/Vis spectrometer. The complex dynamic

viscosity (η^*) of the prepared dispersions was determined with a Rheometrics mechanical spectrometer RMS-605, operating in frequency sweep mode, using a cone and plate geometry at 25 °C and at a strain of 5% (the linear viscoelastic region).

RESULTS AND DISCUSSION

The average particle size of 3.9 ± 0.9 nm of the synthesized TiO_2 nanoparticles was estimated by TEM. The anatase crystal structure of the obtained TiO_2 nanoparticles was confirmed by X-ray diffraction. The formation of a charge transfer complex between the TiO_2 nanoparticles and gallates was confirmed by FTIR (Fig. 1). PG was bonded to the surface Ti atoms through the adjacent $-\text{OH}$ groups, forming binuclear (bridging) complex. The absorption spectrum of the surface modified TiO_2 nanoparticles is red-shifted compared to the unmodified TiO_2 nanoparticles, indicating charge transfer complex formation (Fig. 2) [3,4].

Frequency dependences of the complex viscosity of dispersions are shown in Fig. 3. The viscosity of all dispersions is higher than viscosity of unfilled resin. Gallates adsorbed on the surface of TiO_2 nanoparticles are used to prevent agglomeration of TiO_2 nanoparticles and to improve their interaction with alkyd resin. The dispersions are sterically stabilized and particle repulsion originates from the interactions between chemisorbed gallate layers.

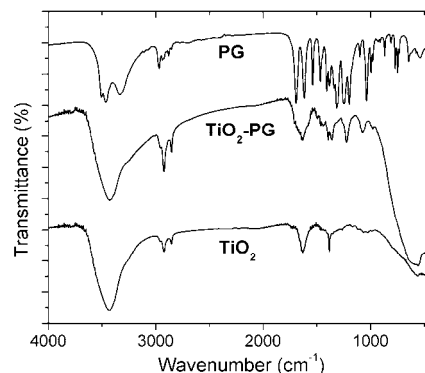


Figure 1. FTIR spectra of the TiO_2 nanoparticles, PG and TiO_2 nanoparticles modified with propyl gallate (TiO_2 -PG).

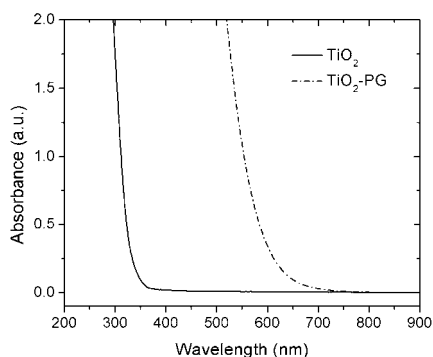


Figure 2. UV spectra of TiO_2 and TiO_2 -PG nanoparticles.

Gallate adsorbed layer enhances effective radius of individual TiO_2 particles, thus leading to an effective increase of volume fraction of TiO_2 , causing an increase of the viscosity of dispersion due to the good particle-resin interaction. The TiO_2 -CG dispersion has the highest viscosity, indicating the presence of the thickest adsorbed layer and the biggest effective radius of TiO_2 particles due to the longest alkyl chain length of gallate used for surface modification of TiO_2 .

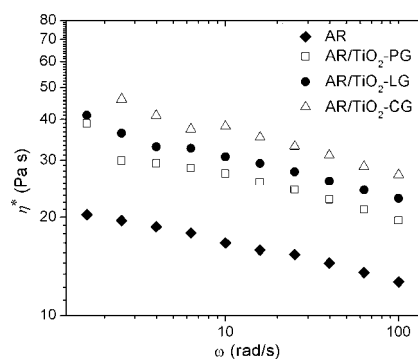


Figure 3. Frequency dependence of the η^* of dispersions of TiO_2 -PG, TiO_2 -HG and TiO_2 -LG nanoparticles in AR at 25 °C.

CONCLUSION

The formation of a charge transfer complex between the TiO_2 nanoparticles and the alkyl gallates was confirmed by FTIR and UV spectroscopy. The viscosity of the prepared dispersions was higher than viscosity of the pure resin and it increased with increasing length of hydrophobic part of the gallate used for the surface modification of TiO_2 nanoparticles. This occurred because of the increase of the effective radius of TiO_2 particles due to the increased thickness of the gallate adsorbed layer.

ACKNOWLEDGEMENT

This work was partially supported by the Ministry of Education, Science and Technological Development of the Republic of Serbia (Grants no. 45020 and 172062).

REFERENCES

- [1] Hofland, *Prog. Org. Coat.*, 2012, 73, 274-282.
- [2] H. Shi, F. Liu, E. Han, Y. Wei, *J. Mater. Sci. Technol.*, 2007, 23, 551-558.
- [3] T.S. Radoman, J.V. Džunuzović, K.B. Jeremić, A.D. Marinković, P.M. Spasojević, I.G. Popović, E. S. Džunuzović, *Hem. Ind.*, 2013, 67, 923-932.
- [4] T.S. Radoman, J.V. Džunuzović, K.B. Jeremić, B.N. Grgur, D.S. Miličević, I.G. Popović, E.S. Džunuzović, *Mater. Design*, 2014, doi: 10.1016/j.matdes.2014.05.015.

NOVEL SILOXANE BASED POLYURETHANE NANOCOMPOSITES

I. S. Stefanović¹, M. Špírková², R. Poręba², M. Steinhart², D. Micić³, V. Tešević⁴ and M. V. Pergal¹

¹University of Belgrade, ICTM, Njegoševa 12, Belgrade, Serbia (marijav@chem.bg.ac.rs); ²Institute of Macromolecular Chemistry AS CR, v.v.i. (IMC), Heyrovského 2, Prague, Czech Republic; ³Institute of General and Physical Chemistry, Studentski trg 12-16, Belgrade, Serbia; ⁴Faculty of Chemistry, Studentski trg 12-16, Belgrade, Serbia.

ABSTRACT

A series of novel thermoplastic polyurethanes (TPUs) nanocomposites based on α,ω -dihydroxy ethoxy propyl poly(dimethylsiloxane) (EO-PDMS), 1,4-butanediol (BD) and 4,4'-diphenylmethane diisocyanate (MDI) was synthesized by *in situ* two-step polyaddition reaction in solution using modified clay (Cloisite 30B). The clay percentage in the nanocomposites was 1, 3, 5, 8 and 10 wt% in relation to the polymers. The aim of this study was to improve some properties of TPUs by the addition of clay nanoparticles. The prepared nanocomposites were characterized using FTIR, AFM and DSC analyses. The influence of nanoparticles dispersion on the morphology and thermal properties of TPUs was investigated.

INTRODUCTION

Segmented polyurethanes (TPUs) are an important class of thermoplastic elastomers, which have potential use as a biomaterial [1]. TPUs are linear block copolymers typically constructed with hard and soft segments (HS and SS), which cause the formation of microphase separated morphology [2]. They have very desirable properties, such as high abrasion resistance, flexibility and elasticity [3]. However, polyurethanes have some disadvantages, such as poor thermal stability and poor gas-barrier properties. These disadvantages are overcome by introducing inorganic fillers, especially nanoclay particles based on Montmorillonite [4]. Also, the incorporation of poly(dimethylsiloxane) into the polymer chain can enhance some properties of TPUs such as: low surface energy, thermal stability and flexibility. The objective of this work was to synthesize nanocomposites based on organoclay (Cloisite 30B) and polyurethane as matrix. The way, in which the dispersion of the clay nanoparticles may affect the structure,

thermal and morphological properties of TPUs was analyzed by different experimental techniques.

EXPERIMENTAL

α,ω -Dihydroxy ethoxy propyl poly(dimethylsiloxane) (EO-PDMS) (from ABCR, $M_n = 1000$ g/mol) was dried over molecular sieves before use. 4,4'-Diphenylmethane diisocyanate (MDI) (Aldrich, purity > 98 %), was used as received. 1,4-Butanediol (BD) (Aldrich) was purified by vacuum distillation. Cloisite 30B (Rockwood) was dried in vacuum oven at 30 °C for 24h. Tetrahydrofuran (THF) (Moss Hemoss) and *N,N*-dimethylacetamide (DMAc) (Merck) were distilled and purified before use. The catalyst in this reaction was stannous octanoate ($\text{Sn}(\text{Oct})_2$) (Aldrich).

TPU nanocomposites (PUNC) with 20 wt% of HS were prepared with addition of organically modified montmorillonite clay (Cloisite 30B) by *in situ* two-step polyaddition reaction in solution of THF/DMAc (1:1 v/v). Hard segment of TPUs, which were prepared in the form of films, consist of MDI and BD, while EO-PDMS was used as the SS. Different content of organoclay (1, 3, 5, 8 and 10 wt%) was incorporated into TPU matrix.

FTIR spectra were recorded using attenuated total reflection (ATR) mode on Nicolet 6700 FTIR spectrometer. AFM analysis was carried out on atomic force microscope (DimensionIcon, Bruker), equipped with the SSS-NLC probe, Super Sharp SiliconTM-SPM-Sensor (NanoSensorsTM Switzerland; spring constant 35 N/m, resonant frequency ≈ 170 kHz). Measurements were performed under ambient conditions using the tapping mode AFM technique. Differential scanning calorimetry (DSC) was carried out on a DSC Q1000V9.0 Build 275 thermal analyzer. The DSC scans were recorded under nitrogen atmosphere, in the temperature range from -90 to 230 °C, at a heating and cooling rate of 10 and 5 °C/min, respectively.

RESULTS AND DISCUSSION

The molecular structures of the TPU and polyurethane nanocomposites were confirmed by FTIR spectroscopy (Figure 1). Characteristic bands of samples appeared at 3310 cm^{-1} ($\nu_{\text{N-H}}$), 2960 and 2880 cm^{-1} (ν_{sym} and ν_{asym} of C-H), 1710 cm^{-1} ($\nu_{\text{C=O}}$), 1545 and 1260 cm^{-1} ($\nu_{\text{C-N}} + \delta_{\text{N-H}}$ i.e., amide II and amide III), 1030 and 1080 cm^{-1} ($\nu_{\text{Si-O-Si}}$ and $\nu_{\text{C-O-C}}$), 1600 cm^{-1} ($\nu_{\text{C=C}}^{\text{arom}}$) and 800 cm^{-1} ($\rho_{\text{C-H}}$ in SiCH_3). However, the bands of the organoclay at 520 cm^{-1} ($\nu_{\text{Si-O-Al}}$) and 460 cm^{-1} ($\delta_{\text{Si-O-Si}}$) are also observed in the spectra of the nanocomposites. These bands indicate that the polyurethane chains are incorporated into the galleries of layered silicates from organoclay.

AFM analysis was used to investigate topography of the samples (Figure 2). The addition of clays significantly affected the topography of TPU nanocomposites in comparison with neat TPU. Based on AFM results it can be assumed that organoclay particles are homogeneously dispersed in the TPU matrix with 3 wt% of organoclay. Similar situation was observed for other TPU nanocomposites with 1, 5, 8 and 10 wt% of clay. RMS surface roughness, R_q values, ranged from 30.5 to 93.6 nm for TPU nanocomposites, while for the neat TPU sample, R_q value was 9.23 nm (Table 1). The samples with higher R_q values have rougher surface.

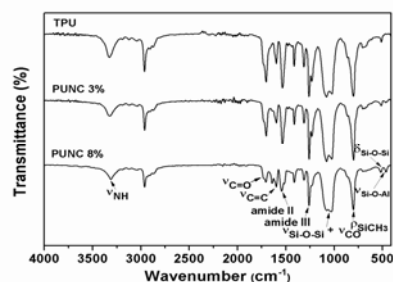


Figure 1. ATR-FTIR spectra of neat TPU and TPU nanocomposites with 3 and 8 wt% of organoclay

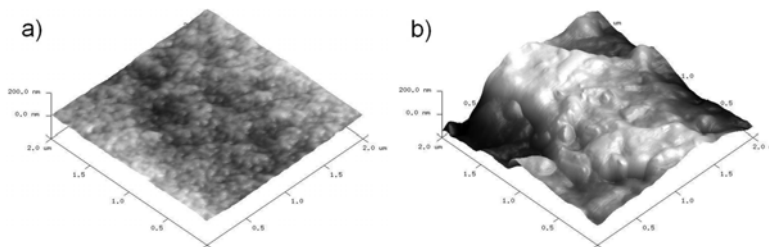


Figure 2. 3D AFM images of the cross-section of films of the neat TPU **a)** and TPU nanocomposites with 3 wt% of organoclay **b)** (scan area $2 \times 2 \mu\text{m}$)

Table 1. R_q values and DSC results of the neat TPU and TPU nanocomposites

DSC results showed that melting (T_m) and glass transition temperatures (T_g) of HS shift toward higher temperatures upon increasing	Sample	R_q (nm)	$T_{g\text{HS}}$ ($^{\circ}\text{C}$)	$T_{m\text{HS}}$ ($^{\circ}\text{C}$)	ΔH_m (J/g)	X_c %	$X_{c\text{HS}}$ %
		TPU	9.23	32	157	3.9	4.3
	PUNC 1%	92.1	15	169	3.6	3.9	17.9
	PUNC 3%	62.0	21	166	3.4	3.7	17.0
	PUNC 5%	53.9	29	185	2.8	3.1	14.2
	PUNC 8%	93.6	29	182	3.0	3.3	15.1
	PUNC 10%	30.5	28	186	3.3	3.6	16.5

the organoclay content to 5 wt%, but then there are no significant changes when the organoclay content increased up to 10 wt%. The total degree of

crystallinity (X_c) and degree of crystallinity of HS ($X_{c\text{ HS}}$) as well as enthalpy of melting (ΔH_m) of nanocomposites is lower in comparison with the neat TPU. The presence of layered silicates from organoclay in the TPUs can result in the more ordered HS, having higher T_m values, but on the other hand show losses in the degree of crystallinity of HS.

CONCLUSION

In this study, the TPU nanocomposites were successfully prepared by *in situ* two-step polyaddition reaction in solution. FTIR spectra of TPU nanocomposites showed characteristic peaks of urethane carbonyl group, stretching band of urethane –NH group, amide II and III stretching vibrations and characteristic bands of clay particles associated with the stretching Si-O-Al and bending of Si-O-Si. The band positions of distinctive functional groups of the TPUs are identical to those of the TPU nanocomposites, confirming that the chemical structure of TPUs is not significantly altered in the presence of silicate layers. AFM analysis confirmed well dispersion of organoclay nanoparticles in the TPU matrix. DSC results showed that T_m and T_g values of HS shift toward higher temperatures from 166 to 185 and from 15 to 29 °C, respectively upon increasing the organoclay content to 5 wt%, after which measured values do not change significantly. The degree of crystallinity of nanocomposites is lower in comparison with the neat TPU. The obtained results showed that low clay loading (≤ 5 wt%) have affected thermal properties of TPUs, which is significant for preparation of this kind of polyurethane materials.

ACKNOWLEDGEMENTS

This work was financially supported by the Ministry of Education, Science and Technological Development of the Republic of Serbia (Project No. 172062) and Czech Science Foundation (GACR, Project No. 13-06700S).

REFERENCES

- [1] D.J. Martin, L.A.P. Warren, P.A. Gunatillake, S.J. McCarthy, G.F. Meijs, K. Schindhelm, *Biomaterials*, 2000, 21, 1021 – 1029.
- [2] T. Choi, J. Weksler, A. Padsalgikar, J. Runt, *Polymer*, 2009, 50, 2320 – 2327.
- [3] R. Vermette, H.J. Griesser, G. Laroche, R. Guidoin, *Biomedical Applications of Polyurethanes*. Texas: Landes Bioscience; 2001.
- [4] O.I.H. Dimitry, Z.I. Abdeen, E.A Ismail, A.L.G. Saad, *J. Polym. Res.*, 2010, 17, 801 – 813.

SYNTHESIS AND CHARACTERIZATION OF POLYURETHANES CROSS-LINKED WITH ALIPHATIC HYPERBRANCHED POLYESTER

J. V. Džunuzović and M. V. Pergal

*Institute of Chemistry, Technology and Metallurgy (ICTM)-Center of
Chemistry, University of Belgrade, Studentski trg 12-16, 11000 Belgrade,
Serbia. (marijav@chem.bg.ac.rs)*

ABSTRACT

Two series of cross-linked polyurethanes (PUs) based on hydroxyethoxy propyl terminated poly(dimethylsiloxane) (EO-PDMS) or hydroxyl propyl terminated poly(dimethylsiloxane) (HP-PDMS) macrodiols, Boltorn[®] aliphatic hyperbranched polyester of the second pseudo generation (BH-20) and 4,4'-methylenediphenyl diisocyanate (MDI) were synthesized using two-step polymerization in solution. The influence of the type and content of soft PDMS segment on swelling behavior and thermal properties of PUs was investigated. The obtained results revealed that cross-linking density decreases, while thermal stability increases with increasing soft segment content. Furthermore, PUs based on EO-PDMS have higher cross-linking density and better thermal stability than samples synthesized using HP-PDMS.

INTRODUCTION

Hyperbranched polymers (HBPs) attract large scientific attention because of their specific chemical and physical properties, which are quite different from those of their linear counterparts. The reasons for such high interest in this well-known class of dendritic polymers are complex, three-dimensional, globular structure, presence of a great number of end functional groups and low entanglement degree of HBPs [1]. Beside other various application possibilities, HBPs have also found their potential practical use as cross-linking agents for different polymers, such as polyurethanes [2,3]. The presence of numerous adequate functional groups in HBP provides fast curing of PUs and formation of highly cross-linked material with good chemical resistance and mechanical properties. On the other hand, thermal stability, surface properties, water and fire resistance of conventional PUs can be considerably improved by incorporation of poly(dimethylsiloxane) (PDMS) macrodiols into PUs, since PDMSs have low glass transition

temperature, good thermal and oxidative stability, high flexibility, low surface tension, low moisture permeability, etc. [4].

EXPERIMENTAL

Boltorn[®] aliphatic hyperbranched polyester of the second pseudo generation (BH-20) ($M_n=1340$ g/mol; functionality=12), prepared from 2,2-bis(hydroxymethyl)propionic acid and ethoxylated pentaerythritol, was supplied by Perstorp Specialty Chemicals AB (Sweden) and dried at 50 °C under vacuum for 48 h before use. EO-PDMS ($M_{n(1H\ NMR)}=1200$ g/mol) and HP-PDMS ($M_{n(1H\ NMR)}=960$ g/mol) were purchased from ABCR and dried over molecular sieves. MDI was supplied by Aldrich. Two samples with 15 and 30 wt.% of soft PDMS segment (numbers written in the name of PU samples) were synthesized in each series. Simplified synthesis reaction of PUs based on the HP-PDMS is shown in Fig. 1, while details of the synthesis are given elsewhere [2]. FTIR spectra were recorded using attenuated total reflection mode on NICOLET 380 FTIR spectrometer. Equilibrium swelling measurements were done at room temperature by immersion of the samples in tetrahydrofuran (THF; J. T. Baker) for 24 h. The equilibrium swelling degree, q_e , was calculated with conventional gravimetric method. Density of the prepared materials was determined at 20.1 °C, using pycnometer and distilled water as medium. Thermal stability of PUs was determined using TGA Q500 V6.3 Build 189 instrument under nitrogen, at a heating rate of 10 °C/min, from 25 to 700 °C. Cross-linking density, ν , was calculated using Flory-Rehner equation [5]:

$$\nu = -\frac{\ln(1 - V_{PU}) + V_{PU} + \chi V_{PU}^2}{V_s \left(V_{PU}^{1/3} - \frac{V_{PU}}{2} \right)} \quad (1)$$

where, χ represents polymer-solvent interaction parameter equal to 0.34, V_s is molar volume of the THF (81.7 cm³/mol) and V_{PU} is the volume fraction of the crosslinked polymer in the swollen specimen.

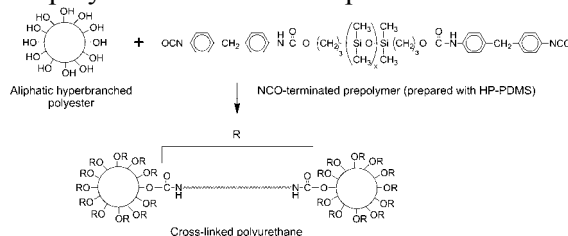


Figure 1. The simplified reaction pathway of the preparation of cross-linked PU based on the HP-PDMS macrodiol (PU_{HP}).

RESULTS AND DISCUSSION

The chemical structure of the synthesized PUs was confirmed by FTIR spectroscopy (Fig. 2). In the FTIR spectrum of BH-20 absorption bands characteristic for the hydroxyl groups (3300 cm^{-1}), carbonyl ester groups (1723 cm^{-1}), C-O linkage of ester groups ($1040\text{-}1210\text{ cm}^{-1}$), ether groups ($1010\text{-}1120\text{ cm}^{-1}$), $-\text{CH}_2-$ and $-\text{CH}_3$ groups ($2900\text{-}3000\text{ cm}^{-1}$) are observed. In the FTIR spectra of PUs, absorption bands characteristic for the amide II and amide III vibrations (1258 cm^{-1} and 1537 cm^{-1}), Si-O-Si and C-O-C groups (1015 and 1080 cm^{-1}), Si- CH_3 linkage (790 cm^{-1}), symmetric and asymmetric $-\text{CH}_2-$ and $-\text{CH}_3$ (2961 , 2903 and 2875 cm^{-1}), aromatic C=C (1596 and 1412 cm^{-1}) and hydrogen-bonded $-\text{NH}$ stretching vibration (3306 cm^{-1}) are visible. The formation of urethane bonds is confirmed by the absence of isocyanate ($-\text{NCO}$) peak at 2260 cm^{-1} .

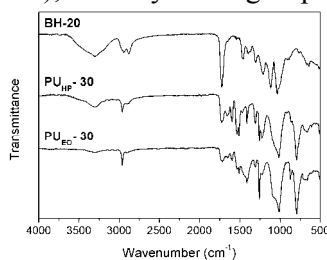


Figure 2. FTIR spectra of BH-20 and selected PUs.

According to the values listed in Table 1, q_e and molecular weight of polymer chain between cross-links, M_c , of PUs increase, while ν decreases with increasing PDMS content, due to the lower HBP content. PUs synthesized using EO-PDMS are less swellable in THF, and consequently have higher ν and lower M_c than PU_{HP} samples.

Table 1. Density, ρ , equilibrium swelling degree, q_e , cross-linking density, ν , and molecular weight of polymer chain between cross-links, M_c , calculated as ρ/ν , of the synthesized PUs.

Sample	ρ (g/cm ³)	q_e	$\nu \times 10^4$ (mol/cm ³)	M_c (g/mol)
$\text{PU}_{\text{HP}}\text{-15}$	1.11	1.56	6.88	1610
$\text{PU}_{\text{HP}}\text{-30}$	1.12	1.96	3.50	3200
$\text{PU}_{\text{EO}}\text{-15}$	1.09	0.81	21.32	510
$\text{PU}_{\text{EO}}\text{-30}$	1.05	1.85	5.22	2010

Thermal stability of the synthesized cross-linked PUs was examined by thermogravimetric (TG) analysis and in Fig. 3 are given selected TG (Fig. 3a) and thermogram derivative (DTG) curves (Fig. 3b) of PUs. Thermal decomposition of all synthesized cross-linked PUs in nitrogen occurs via a four-step process between 250 and 650 °C. The first DTG peak (around 300 °C) corresponds to the temperature at maximum rate of weight loss during the first step of the thermal degradation, which occurs due to the

decomposition of the urethane groups. During the second step of thermal degradation (around 330 °C) ester components decomposed, while in the third step (around 400 °C) degradation of PDMS macrodiols occurred. During the fourth step (between 500 and 650 °C) aromatic compounds decomposed. The obtained results show that samples with lower PDMS content have lower thermal stability. Also, PUs prepared using EO-PDMS are more stable than PUs based on HP-PDMS, indicating that hydroxyethoxy propyl terminated PDMS is more efficient in improving thermal stability of cross-linked PUs based on BH-20 than HP-PDMS macrodiol.

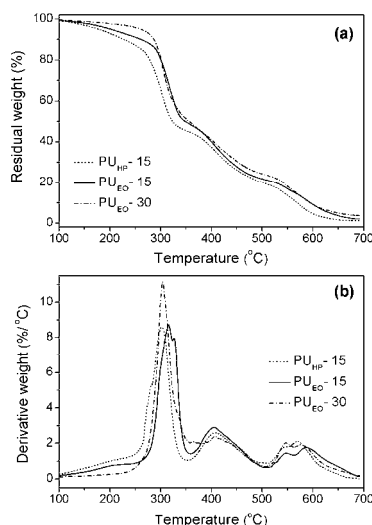


Figure 3. a) TG and b) DTG curves of PUs with different PDMS content.

CONCLUSION

Two series of cross-linked PUs based on BH-20, MDI and EO-PDMS or HP-PDMS have been synthesized. The cross-linking density increased, while thermal stability decreased as the soft segment content decreased. PU samples based on EO-PDMS have higher cross-linking density and better thermal stability than materials based on HP-PDMS. The obtained results indicate that combination of BH-20 crosslinker and PDMS based macrodiols yields cross-linked PUs with good thermal properties.

ACKNOWLEDGEMENT

This work was financially supported by the Ministry of Education, Science and Technological Development of the Republic of Serbia (research project number: 172062).

REFERENCES

- [1] B.I. Voit, A. Lederer, *Chem. Rev.*, 2009, 109, 5924-5973.
- [2] J.V. Džunuzović, M.V. Pergal, R. Poręba, S. Ostojić, N. Lazić, M. Špírková, S. Jovanović, *Ind. Eng. Chem. Res.*, 2012, 51, 10824-10832.
- [3] M.V. Pergal, J.V. Džunuzović, R. Poręba, D. Micić, P. Stefanov, L. Pezo, M. Špírková, *Express Polym. Lett.*, 2013, 7, 806-820.
- [4] P. Majumdar, D. C. Webster, *Macromolecules*, 2005, 38, 5857-5859.
- [5] P.J. Flory, J.H. Rehner, *J. Chem. Phys.*, 1943, 11, 521-526.

THERMOPLASTIC POLYURETHANES BASED ON POLY(DIMETHYLSILOXANE): STRUCTURE AND THERMAL BEHAVIOR

I. S. Stefanović¹, D. Godevac¹, V. Tešević² and M. V. Pergal¹

¹ *University of Belgrade, ICTM, Njegoševa 12, Belgrade, Serbia (marijav@chem.bg.ac.rs);* ² *Faculty of Chemistry, University of Belgrade, Studentski trg 12-16, Belgrade, Serbia.*

ABSTRACT

Segmented polyurethanes are an important class of thermoplastic elastomers which have potential use as a biomaterial. Biostability, biocompatibility and some other features of polyurethanes can be improved by the introduction of poly(dimethylsiloxane) in the polymer chain. A series of novel thermoplastic polyurethanes was synthesized by two-step polyaddition reaction in solution from 4,4'-diphenylmethane diisocyanate (MDI), 1,4-butanediol (BD) and poly(propylene oxide)-*b*-poly(dimethylsiloxane)-*b*-poly(propylene oxide) (PPO-PDMS). The content of PPO-PDMS (i.e. soft segment) was varied between 40 and 90 wt%. The influence of PPO-PDMS content on the structure and thermal properties of copolymers was investigated by FTIR, ¹H and 2D NMR spectroscopy, as well as by DSC analysis.

INTRODUCTION

Thermoplastic polyurethanes (TPUs) are linear segmented copolymers consisting of a high molecular weight macrodiol, called the soft segment (SS), and a diisocyanate and low molecular weight diol, which form the hard segment (HS). Thermodynamic incompatibility between SS and HS results in a phase separated structure [1]. The introduction of poly(dimethylsiloxane) (PDMS) macrodiol, into the polyurethane structure provides some good properties of prepared materials, such as: low surface energy, excellent thermal, oxidative and hydrolytic stability, flexibility and biocompatibility [2]. The aim of this work was to investigate the effect of soft segment content on the structure and thermal properties of the synthesized TPUs.

EXPERIMENTAL

Poly(propylene oxide)-*b*-poly(dimethylsiloxane)-*b*-poly(propylene oxide) (PPO-PDMS) (from ABCR, $M_n = 2900$ g/mol) was dried over molecular

sieves before use. 4,4'-Diphenylmethane diisocyanate (MDI) (Aldrich, purity > 98 %) was used as received. 1,4-Butanediol (BD) (Aldrich) was purified by vacuum distillation. Tetrahydrofuran (THF) (Moss Hemoss) and *N,N*-dimethylacetamide (DMAc) (Merck) were distilled before use. The catalyst was stannous octanoate (Sn(Oct)₂) (Aldrich).

A two-step polymerization was employed to synthesize novel TPUs. Firstly, the isocyanate terminated prepolymer was prepared by the reaction between the PPO-PDMS and MDI in solution of DMAc/THF, at 80 °C for 40 min in nitrogen atmosphere, and in presence of catalyst. Then, solution of BD in DMAc/THF was added to the –NCO terminated prepolymer, at the same temperature and the reaction was proceeded for 10 hours. The last two numbers in the name of the sample represent the weight percent of the HS.

FTIR spectra were recorded using Nicolet 6700 FTIR spectrometer.

NMR experiments were collected on Bruker Avance 500 spectrometer. The ¹H NMR (at 500 MHz) and 2D NMR spectra (HSQC, HMBC and ROESY) of copolymers were measured using DMSO-*d*₆ as the solvent.

Differential scanning calorimetry (DSC) was conducted using a DSC Q1000V9.0 Build 275 thermal analyzer. The copolymers were analyzed under a nitrogen atmosphere in the temperature range from -90 to 230 °C at a heating and cooling rate of 10 and 5 °C/min, respectively.

RESULTS AND DISCUSSION

The molecular structure of the copolymers was confirmed by FTIR spectroscopy. Characteristic absorption bands appeared at 3330 cm⁻¹ ($\nu_{\text{N-H}}$), 2970 and 2895 cm⁻¹ (ν_{sym} and ν_{asym} of C-H), 1705 cm⁻¹ ($\nu_{\text{C=O}}$), 1600 and 1415 cm⁻¹ ($\nu_{\text{C=C}}^{\text{arom}}$), 1540 cm⁻¹ (amide II) and 1230 cm⁻¹ (amide III), 1020 and 1080 cm⁻¹ ($\nu_{\text{Si-O-Si}} + \nu_{\text{C-O-C}}$) and 810 cm⁻¹ ($\rho_{\text{C-H}}$ in SiCH₃).

The molecular structure of the TPUs was also investigated by ¹H NMR spectroscopy. In ¹H NMR spectra (Figure 1), the signals of the –SiCH₃ protons appeared at 0.03 ppm. All methylene protons, derived from propylene groups connected to PDMS, can be observed at 0.47, 1.48 and 3.26 ppm. The protons at 1.69 and 4.09 ppm originated from the central and terminal methylene groups from the BD. The signal of methylene protons from the MDI residue appeared at 3.77 ppm. The protons at 7.08 and 7.34 ppm were from the aromatic ring and at 8.53 and 9.50 ppm were from the urethane –NH group present in the HS and SS. Also, the signals of the methyl, methylene and methine protons from the poly(propylene oxide) residue appeared at 1.00, 3.38 and 3.40 ppm, respectively.

The composition of the TPUs was determined from the ¹H NMR spectra. The values for the weight fraction of the SS ranged from 38.5 to 88.6%,

which are in relatively good agreement with the values predetermined from the composition of the feed (Table 1).

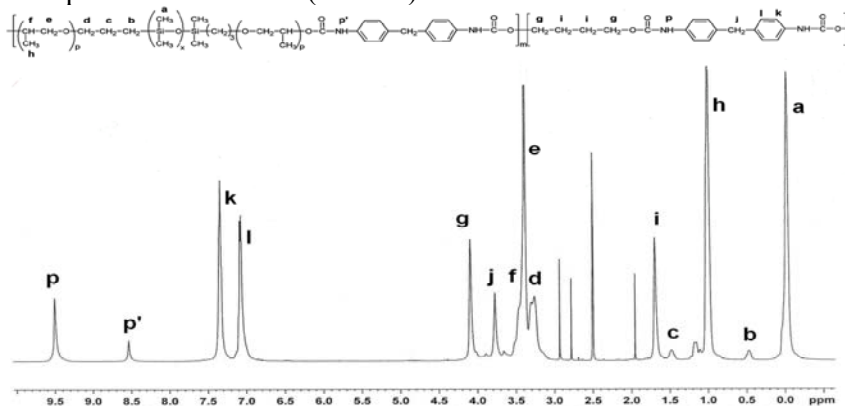


Figure 1. ^1H NMR spectra of the PU-PPO40 copolymer

The assignments of the carbon and proton resonances in the structures were also confirmed by two-dimensional NMR spectroscopy. The chemical shifts of some overlapped and/or barely visible signals in ^1H NMR spectra can be solved with COSY, HSQC and ROESY spectra. The overlapped signals *f*, *e* and *d* in the ^1H NMR spectrum were determined and separated using HSQC correlations. Also, from HMBC spectra it can be concluded that MDI is incorporated into SS and HS.

Table 1. Composition and some DSC data of the TPU

Sample	wt% SS (in feed)	wt% SS NMR	T_{gHS} ($^{\circ}\text{C}$)	T_{mHS} ($^{\circ}\text{C}$)	T_{gSS} ($^{\circ}\text{C}$)
PU-PPO10	90.3	88.6	14.7	-	-73.2
PU-PPO20	82.0	77.8	14.9	-	-69.1
PU-PPO30	69.8	65.9	14.9	-	-64.6
PU-PPO40	60.1	60.4	14.8	118.4	-66.0
PU-PPO50	47.8	47.9	14.8	130.5	-64.5
PU-PPO60	39.9	38.5	14.8	131.7	-64.4

The obtained DSC thermograms are shown in Figure 2 and results are summarized in Table 1. The DSC curves show transitions which correspond to the melting temperatures of HS (T_{mHS}), glass transition temperatures of the HS (T_{gHS}) and SS (T_{gSS}). The T_{mHS} of TPUs ranged from 118 to 132 $^{\circ}\text{C}$, and increased with decreasing content of PPO-PDMS segment. The T_{mHS}

was observed only in sample with lower SS content. The T_{gHS} were similar for TPUs and their values were approximately 15 °C. The T_{gSS} that correspond to the PPO units in SS, were between -73 and -65 °C, and increased with decreasing content of SS.

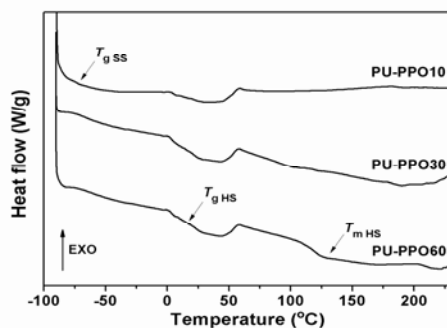


Figure 2. DSC thermograms (second heating run) of TPUs with different content of PPO-PDMS

CONCLUSION

In this work, novel TPU copolymers based on PPO-PDMS were prepared by two-step polyaddition reaction in solution. The multiblock structure and composition of the obtained copolymers were confirmed by FTIR, ^1H and 2D NMR spectroscopy. DSC analysis showed that TPUs exhibit two glass transition temperatures, one corresponding to the hard segment and the second to the PPO units in soft segment, and a melting temperature of hard segment.

ACKNOWLEDGEMENT

This work was financially supported by the Ministry of Education, Science and Technological Development of the Republic of Serbia (Project No. 172062).

REFERENCES

- [1] L.Rueda-Larraz, B.F. d’Arlas, A. Tercjak, A. Ribes, I. Mondragon, A. Eceiza, *Eur. Polym. J.*, 2009, 45, 2096 – 2109.
- [2] L.F. Wang, Q. Ji, T.E. Glass, T.C. Ward, J.E. McGrath, M. Muggli, G. Burns, U. Sorathia, *Polymer*, 2000, 41, 5083 – 5093.

PERRHENATE SORPTION BY AMINO-FUNCTIONALIZED GLYCIDYL METHACRYLATE COPOLYMER: INVESTIGATION OF RHENIUM AS AN ANALOGUE OF RADIOACTIVE TECHNETIUM

Z. Sandić^{1,2}, D. Maksin², A. Nastasović³, J. Marković², R. Hercigonja⁴, S. Milutinović² and A. Onjia²

¹*University of Banja Luka, Faculty of Science, 78000 Banja Luka, Mladena Stojanovića 2, B&H (Republic of Srpska). (zvjezdana.sandic@gmail.com)*

²*University of Belgrade, Vinča Institute of Nuclear Sciences, P.O. Box 522, 11001 Belgrade, Serbia.*

³*University of Belgrade, Institute of Chemistry, Technology and Metallurgy, Njegoševa 12, 11000 Belgrade, Serbia.*

⁴*Faculty of Physical Chemistry, University of Belgrade, Studentski trg 12-16, 11001 Belgrade, Serbia.*

ABSTRACT

In order to define the favorable conditions for radioactive technetium (⁹⁹Tc) uptake, the sorption behavior of its non-active chemical analogue rhenium (⁷⁵Re) on amino-functionalized macroporous hydrophilic copolymer was studied. The pseudo-second-order (PSO) model provided the best fit for the kinetic data, while the intraparticle diffusion (IPD) model indicated a pronounced influence of the porous structure on the sorption rates. The maximum sorption capacity was found to be 84 mg g⁻¹ and 74 % removal efficiency was reached after 180 min in citrate buffer at pH 5.0.

INTRODUCTION

Tc-99 is a key constituent of nuclear waste produced in large quantities by nuclear fission of ²³⁵U or ²³⁹Pu in nuclear reactors. Its behavior can be predicted by investigating ⁷⁵Re, its excellent chemical analogue, owing to their similar electronic configuration, stereochemistry and thermodynamic properties, thus evading the use of a radioactive element at high concentrations i.e. doses [1]. Solvent extraction and ion exchange appear to be the most effective methods for the separation and removal of pertechnetate (⁹⁹TcO₄⁻) and perrhenate (ReO₄⁻) from aqueous media [2]. Formerly successfully tested poly(glycidyl methacrylate-co-ethylene glycol dimethacrylate) grafted with diethylene triamine [PGME-deta] for ⁹⁹TcO₄⁻ sorption at low concentrations [3], was the subject of this study as ReO₄⁻ sorbent at high concentrations.

EXPERIMENTAL

A macroporous PGME sample (with 40 mass% of crosslinker) was prepared by radical suspension copolymerization in the shape of spherical beads with the average particle diameter of 150-300 μm and modified with diethylene triamine [PGME-deta] [3]. The copolymer sample was analyzed for its C, H, N content using the Vario EL III device (GmbH Hanau Instruments, Germany), and the amino group concentration was calculated (Table 1). The porosity parameters (for relevant abbreviations and definitions please consult Ref. [3,4]) were determined by high pressure mercury intrusion (Carlo Erba Porosimeter 2000, operating interval 0.1-200 MPa). pH_{PZC} was ascertained as published elsewhere [4].

Table 1. Relevant characteristics of PGME-deta [3,4].		pH dependence for ReO_4^- sorption by PGME-deta was determined by monitoring Re(VII) uptake in the pH range of 1-13 in batch experiments, using appropriate buffer solutions [3]. The same mass of each sample (50 mg) was contacted with 1 cm^3 of NaReO_4 solution with the initial concentration of 5000 mg dm^{-3} and 4 cm^3 of the buffer solution, at $T=298$ K. The sorption dynamics data was subsequently collected from deionized (DI) water adjusted to pH 5.0 with 0.1M HCl and from citrate buffer at pH 5.0. Re(VII) in supernatant was measured by ICP-OES Thermo Scientific CAP6000.
$S_{s,Hg}$, $\text{m}^2 \text{ g}^{-1}$	55	
V_s , $\text{cm}^3 \text{ g}^{-1}$	0.91	
$D_{V/2}$, nm	107	
D_{av} , nm	96	
Amino group concentration, mmol g^{-1}	5.01	
pH_{PZC}	7.8	

RESULTS AND DISCUSSION

The ReO_4^- sorption dependence on pH (Figure 1a) was in concurrence with the previously established thesis that non-specific sorption of ReO_4^- happens via electrostatic interaction at the amine groups [1,3].

Table 2. Kinetic models.		Determining the dynamics, specifically the rate of Re(VII) removal in the particular solid/solution system is one of the critical factors for the effective design of the sorption system [6]. With the aim to investigate the controlling mechanism of this sorption process, three kinetic models were applied to the experimental data, i.e. the
Kinetic model	Equation	Ref.
PFO	$\log(Q_e - Q_t) = \log Q_e - \frac{k_1 t}{\ln 10}$	[5]
PSO	$\frac{t}{Q} = \frac{1}{k_2 Q_e^2} + \frac{1}{Q_e} t \quad h = k_2 Q_e^2$	[6]
IPD	$Q_t = k_{id} t^{1/2} + C_{id}$	[7]

pseudo-first (PFO), the pseudo-second order (PSO) and the intraparticle diffusion (IPD) model (Table 2) [5, 6, 7]. For relevant abbreviations and definitions in Table 2 please consult Ref. [5-7].

Table 3. Kinetic parameters for ReO_4^- sorption by PGME-deta ($T=298$ K).

C_i , mg L^{-1}	Unadjusted pH	Citrate buffer
Q_e , mg g^{-1}	61	84
PFO		
k_1 , min^{-1}	0.00622	0.0355
Q_e^{calc} , mg g^{-1}	38	33
R^2	0.901	0.845
PSO		
$k_2 \cdot 10^3$, $\text{g mg}^{-1} \text{min}^{-1}$	0.488	3.349
h , $\text{mg g}^{-1} \text{min}^{-1}$	1.91	23.3
$t_{1/2}$, min	32.8	3.6
Q_e^{calc} , mg g^{-1}	63	83
R^2	0.999	0.999
IPD		
k_{1id} , $\text{mg g}^{-1} \text{min}^{-0.5}$	3.37	14.1
C_{1id} , mg g^{-1}	11.8	0.886
R^2	0.976	0.999
k_{2id} , $\text{mg g}^{-1} \text{min}^{-0.5}$	0.634	N/A
C_{2id} , mg g^{-1}	37.4	N/A
R^2	0.980	N/A

PFO kinetic model was not appropriate for this system since R^2 values were rather low. The theoretical Q_e^{calc} values calculated from PSO model are very close to the experimental Q_e values, with $R^2=0.999$. The best fit of PSO model implies that the sorption process is surface-reaction controlled, with chemisorption involving valence forces through sharing or exchange of electrons between PGME-deta and ReO_4^- [6].

To identify the influence of pore diffusion on sorption, the IPD equation was used (Figure 1b) [7]. The plots Q_t vs. $t^{1/2}$ did not pass through the origin indicating that even though the sorption process involved IPD, it was not the only rate-controlling step [7]. The positive value of C_{id} is indicative of some degree of boundary layer control [7].

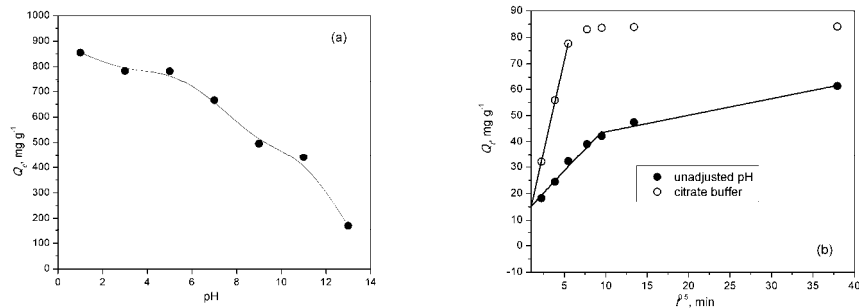


Figure 1. ReO_4^- Sorption as function of pH (a) & intraparticle diffusion (b).

The removal efficiency in citrate buffer reached 74% in 180 min, while in DI water only 42% as the consequence of pH_{PZC} value shifting the pH of the

working solution towards neutral. Thus, in near neutral conditions, super capacity can be achieved at high Re(VII) concentrations: 84 mg g⁻¹ in citrate buffer and 61 mg g⁻¹ in DI water adjusted to pH 5.0 after 24 h.

Very few papers deal with ReO₄⁻ sorption and its kinetics. The maximum capacity of 60 mg g⁻¹ for quaternized 4-vinylpyridine and divinylbenzene resin [8], and 0.46 mmol g⁻¹ for chitosan modified carbon materials [9] were reported, which are comparable to the values presented in Table 3.

CONCLUSION

The sorption behavior of one of the principal constituents of nuclear waste radioactive ⁹⁹Tc can be predicted by studying its non-active chemical analogue ⁷⁵Re. Thus, ReO₄⁻ removal from aqueous solutions by amino-functionalized macroporous hydrophilic resin was studied in order to define the favorable conditions for ⁹⁹Tc uptake. Non-specific sorption of ReO₄⁻ via electrostatic interaction at the protonated amine groups was demonstrated to occur most likely. PSO kinetic model fitted the kinetic data best, while IPD model revealed a pronounced influence of the porous sorbent structure on the sorption rates. Good removal efficiency of 74 % and maximum sorption capacity of 84 mg g⁻¹ were accomplished.

ACKNOWLEDGEMENT

This work was supported by the Ministry of Education, Science and Technological Development of the Republic of Serbia (Grants no. TR 37021 and III 43009).

REFERENCES

- [1] E.Kim, M.F. Benedetti, J. Boulègue, *Water Res.*, 2004, 38, 448-454.
- [2] H. Michel, G. Barci-funel, J. Dalmasso, G. Ardisson, *Radiochim. Acta*, 1997,78,153-158.
- [3] R. Hercigonja, D. Maksin, A. Nastasović, S. Trifunović, P. Glodić, A. Onjia, *J. Appl. Polym. Sci.*, 2012, 123, 1273-1282.
- [4] S. Marinović, A. Milutinović-Nikolić, M. Žunić, Z. Vuković, D. Maksin, A. Nastasović, D. Jovanović, *Russ. J. Phys. Chem. A*, 2011, 85, 2386-2391.
- [5] S. Lagergren K. Sven. Vetenskapsakad. Handl, 1898, 24, 1-39.
- [6] Y.S. Ho, *J. Hazard. Mater.*, 2006, B136, 681-689.
- [7] F. Wua, R. Tseng, R. Juang, *Chem. Eng. J.*, 2009, 153, 1-8.
- [8] D. Jermakowicz-Bartkowiak, B.N. Kolarz, *React. Funct. Polym.*, 2011, 71, 95-103.
- [9] L.A. Zemskova, A.V. Voit, Y.M.Nikolenko, V.I. sergienko, I.D. Troshkina, A.V. Plevaka, S.B. Maiborod, A.M. Chekmarev, *J. Nucl. Radiochem. Sci.*, 2005, 6, 221-222.

PALLADIUM SORPTION BY AMINO-FUNCTIONALIZED MACROPOROUS COPOLYMER FROM CHLORIDE–NITRATE SOLUTIONS

Z. Sandić^{1,2}, D. Marković², T. Novaković³, Z. Miladinović⁴ and R. Hercigonja⁵

¹University of Banja Luka, Faculty of Science, 78000 Banja Luka, Mladena Stojanovića 2, B&H (Republic of Srpska). (zvjezdana.sandic@gmail.com)

²University of Belgrade, Vinča Institute of Nuclear Sciences, P.O. Box 522, 11001 Belgrade, Serbia.

³University of Belgrade, Institute of Chemistry, Technology and Metallurgy, Njegoševa 12, 11000 Belgrade, Serbia.

⁴University of Belgrade, Institute for General and Physical Chemistry, Studentski trg 12-16, 11000 Belgrade, Serbia.

⁵Faculty of Physical Chemistry, University of Belgrade, Studentski trg 12-16, 11001 Belgrade, Serbia.

ABSTRACT

Macroporous poly(glycidyl methacrylate-co-ethylene glycol dimethacrylate) with attached diethylene triamine [PGME-deta] with high amino-group content was used for the investigation of the Pd(II) sorption kinetics from mixed chloride/nitrate aqueous solutions in acidic medium (pH 2.0) at $T=298$ K. Four kinetic models were employed in order to comprehend the mechanism of Pd(II) sorption. The maximum experimental Pd(II) sorption capacity at initial pH 2.0 and 298 K was 20 mg g^{-1} .

INTRODUCTION

Due to their high cost and low availability, precious metals separation and recovery from wastes such as spent catalysts or scraps, and extraction from ores has become vital [1]. Precious metal palladium (Pd) applications include medical, catalytic and electrical/electronic uses, due its corrosion/oxidation resistance, electrical conductivity and catalytic activity. Amongst various processes for Pd recovery, sorption is the method with great potential due to high efficiency and selectivity [2]. The prospect of the application of inexpensive and easily synthesized macroporous glycidyl methacrylate-based copolymer with amino ligand (PGME-deta) as a sorbent for the removal of Pd(II) complexes from chloride–nitrate solutions was tested in static conditions. Four kinetic models [pseudo-first order (PFO),

pseudo-second order (PSO), Boyd and Mckay] were fitted to elucidate the mechanism of Pd(II) sorption from aqueous solutions (pH 2.0) at 298 K.

EXPERIMENTAL

PGME with 20 mass% crosslinker was synthesized by suspension copolymerization in the shape of spherical beads with the average particle diameter of 150-300 μm and functionalized with diethylene triamine; PGME-deta was subsequently characterized [3]. In static conditions, 0.50 g of the copolymer was contacted with 50 cm^3 of 500 mg dm^{-3} Pd(II) solution prepared by mixing the appropriate amounts of the standard solution (1000 mg dm^{-3} $\text{Pd}(\text{NO}_3)_2$ in 0.5M HNO_3 ; pH = 0.3; Merck, Germany) and $2.1 \cdot 10^{-3}$ M $\text{NaCl}_{(\text{aq})}$ to achieve equal quantities of chloride and nitrate in the working solution. The initial pH of this solution was adjusted with 5M $\text{NaOH}_{(\text{aq})}$ to pH=2.0. After predetermined time intervals 0.50 cm^3 solution aliquots were withdrawn and, with adequate dilutions, Pd(II) in supernatant was determined by ICP-OES (Perkin Elmer, Model ICP 400).

RESULTS AND DISCUSSION

The investigations of Pd(II) sorption by porous vinylpyridine anion exchangers from chloride solutions [4], as well as on carbon adsorbents from nitric acid solutions [2] have been published.

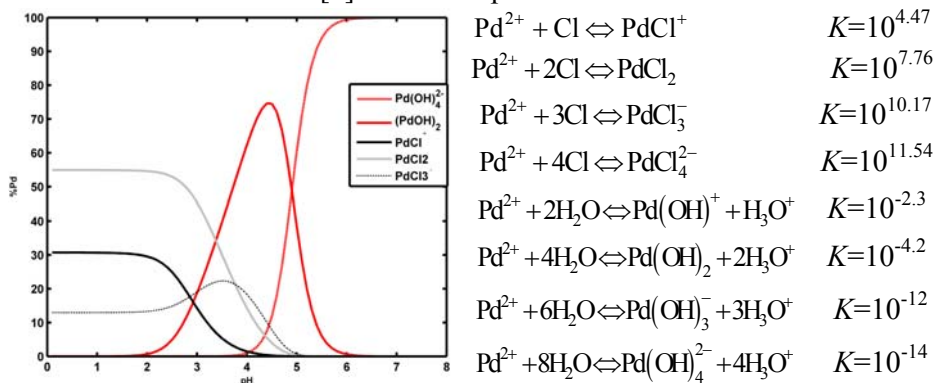


Figure 1. Speciation of palladium (500 mg dm^{-3}) as the function of pH calculated using ChemEQL 3.1 and the stability constants applied for graph construction [6]. The species comprising $\leq 5\%$ total are not shown ($\text{Pd}(\text{OH})_3^-$, $\text{Pd}(\text{OH})^+$, Pd^{2+} , PdCl_4^{2-}).

Crosslinked chitosan containing approximately the same amount of nitrogen as PGME-deta (Table 1) [5] also binds chloropalladate species efficiently [6]. In the case of this study (mixed chloride-nitrate solutions), it should be mentioned that the hydrated Pd(II) ions and their mononitrate complexes are

almost absent when $\text{HNO}_{3(\text{aq})} \leq 0.01 \text{ M}$ [2]. Therefore, only graphs representing the speciation of chloropalladate complexes and Pd(II) hydrolysis products are shown in Figure 1. As for the mixed Pd-Cl⁻-OH⁻ species, it appears that these can be disregarded, too [1]. Ruiz et al. already demonstrated that the optimum pH for Pd sorption on modified chitosan was 2.0 in the presence of chloride ions, involving protonated amino groups [6]. Therefore, pH 2.0 was chosen as optimal given that the PGME-deta amino group content is high (Table 1).

Table 1. Relevant characteristics of PGME-deta [3].

$S_{Hg}, \text{m}^2 \text{g}^{-1}$	$V_S, \text{cm}^3 \text{g}^{-1}$	$d_{V/2}, \text{nm}$	C_{AG}, mmol^{-1}	%C	%H	%N
29	0.89	212	6.51	52.4	8.1	9.1

Table 2. Kinetic parameters for Pd(II) using PGME-deta (pH=2.0, $T=298\text{K}$)

PFO				PSO			
$Q_e,$ mg g^{-1}	$k_1,$ min^{-1}	$Q_e^{calc},$ mg g^{-1}	R^2	$k_2,$ min^{-1}	$h,$ $\text{mg g}^{-1} \text{min}^{-1}$	$Q_e^{calc},$ mg g^{-1}	R^2
20	0.093	6	0.879	0.053	17.6	18	0.999

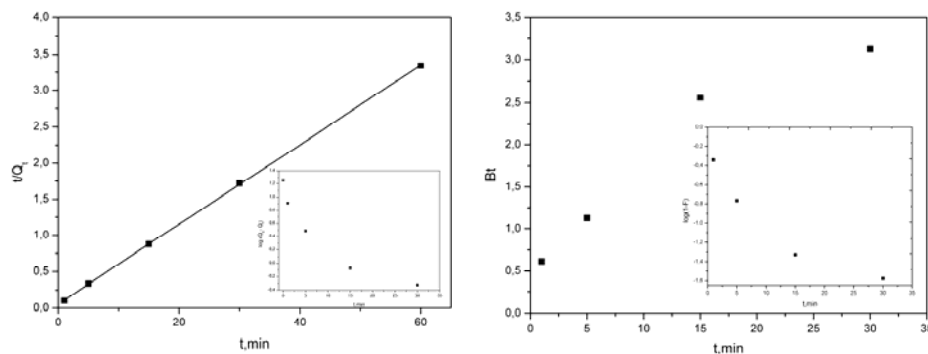


Figure 2. PFO [7] (a), PSO [8] (b), Boyd plot [9] (c) and McKay plot [10] (d) for Pd(II) sorption onto PGME-deta.

Please refer to the cited papers for abbreviations and definitions given in Tables 1 and 2 and Figure 2.

The theoretical Q_e^{calc} values calculated from the PSO model are very near to the experimental Q_e values, with $R^2=0.999$ (Table 2), indicating chemisorption of Pd(II) species on the protonated amino groups involving

valence forces through sharing or exchange of electrons as the surface-reaction mechanism [6,8] (Figure 2). Boyd and Mckay plots suggest particle and film diffusion control of Pd(II) sorption on PGME-deta [9,10].

CONCLUSION

The high amino-group content of macroporous glycidyl methacrylate based copolymer with attached diethylene triamine [PGME-deta] is the key characteristic for its capability to sorb metal ions through several mechanisms dependent on the solution pH including ion-exchange or chelation. The PSO kinetic model accurately describes the sorption behavior over the whole time period and provides a good calculated capacity compared to the experimental value of 20 mg g^{-1} , indicating chemisorption of Pd(II) species on the protonated amino groups which involves valence forces through sharing or exchange of electrons. Boyd and Mckay models confirm both particle and film diffusion as rate-controlling.

ACKNOWLEDGEMENT

This work was supported by the Ministry of Education, Science and Technological Development of the Republic of Serbia (Grants no. TR 37021 and III 43009).

REFERENCES

- [1] Y.H. Kim, Y. Nakano, *Water Res.*, 2005, 39, 1324–1330.
- [2] O.N. Kononova, A.N. Lukianov, M.V. Derevyashkin, A.G. Kholmogorov, S.V. Kachin, N.G. Goryaeva, *J. Porous Mater.*, 2008, 15, 61–66.
- [3] D.D. Maksin, A.B. Nastasović, A.D. Milutinović-Nikolić, Lj.T. Suručić, Z.P. Sandić, R.V. Hercigonja, A.E. Onjia, *J. Hazard. Mater.*, 2012, 209-210, 99-110.
- [4] O.N. Kononova, A.G. Kholmogorov, E.V. Mikhlina, *Hydrometallurgy*, 1998, 48, 67-72.
- [5] M.T. Yen, J.H. Yang, J.L. Mau, *Carbohydr. Polym.*, 2009, 75, 15–21.
- [6] M. Ruiz, A.M. Sastre, E. Guibal, *React. Funct. Polym.*, 2000, 45, 155 – 173.
- [7] S. Lagergren K. *Sven. Vetenskapsakad. Handl*, 1898, 24, 1-39
- [8] Y.S. Ho, *J. Hazard. Mater.*, 2006, B136, 681-689.
- [9] X. Hu, J. Wang, Y. Liu, X. Li, G. Zeng, Z. Bao, X. Zeng, A. Chen, F. Long, *J. Hazard. Mater.*, 2011, 185, 306–314.
- [10] Y. S. Ho, *Bioresource Technol.*, 2005, 96, 1292-1296.

MONOLITHIC POROUS POLYMER COMPOSITE

T. Novaković¹, A. Nastasović¹, Z. Vuković¹ and Lj. Suručić²

¹University of Belgrade, Institute of Chemistry, Technology and Metallurgy, Njegoševa 12, 11000 Belgrade, Serbia. (tnovak@nanosys.ihtm.bg.ac.rs)

²University of Belgrade, Faculty of Forestry, Kneza Višeslava 1, 11001 Belgrade, Serbia

ABSTRACT

Porous monolithic glycidyl methacrylate (GMA) and ethylene glycol dimethacrylate (EGDMA) copolymer [PGME] and composite with alumina (PGME/alumina) were synthesized by radical copolymerization in a cast and functionalized by reaction of diethylene triamine (deta) with epoxy groups. Additionally, amino functionalized PGME and PGME/alumina were loaded with chromium [Cr(VI)] ions. All the samples were characterized using FTIR-ATR spectroscopy, SEM and mercury porosimetry.

INTRODUCTION

Porous polymeric monoliths are a new generation of separation medium for chromatographic application, high-throughput bioreactors enzyme immobilization, molecular recognition, in advanced detection systems and microfluidic chip applications [1,2]. Monoliths are prepared by polymerization in a cast (cylinders, disks, plates, etc.) of a mixture consisting of monomers (hydrophobic, hydrophilic, ionizable, and zwitterionic), initiator and porogen. In general, chelating GMA based copolymers with amino groups are selective towards multivalent metal ions [like Cr(VI), Pt(IV), Rh(III), Au(III), etc.] over the alkali and alkali earth metals and applicable for industrial separation and concentration of these metals [3]. In this study, macroporous PGME monoliths were modified in two ways: by addition of alumina in the reaction mixture (PGME/alumina) and by additional amino-functionalization (PGME-deta and PGME/alumina-deta). The influence of amino-functionalization and Cr(VI) ions immobilization on physico-chemical properties of synthesized monoliths was investigated.

EXPERIMENTAL

For PGME synthesis, the reaction mixture consisted of 1.74 g of GMA, 1.16 g of EGDMA, 0.29 g of azobisisobutyronitrile (AIBN), 3.04 g of

cyclohexanol and 0.76 g of tetradecanol. For PGME/alumina synthesis, 1.45 g of boehmite sol was added in above mentioned reaction mixture. The copolymerization was carried out in a glass tube (i.d. of 15 mm) at 343 K for 2 h and at 353 K for 4 h. Monoliths were then purified by extraction in a Soxhlet apparatus with ethanol for 16 h and dried in vacuum at 313 K. To prepare boehmite sols, aluminium isopropoxide was hydrolyzed in excess amount of water (100:1 $\text{H}_2\text{O}-\text{Al}_3^+$, mol) at 358 K, followed by the peptization with appropriate amount of HNO_3 (0.07:1 H^+/Al_3^+ , mol) to form stable colloidal sol. The sol was kept at a constant temperature (368 K) for 72 h under reflux conditions, during which most of the alcohol was evaporated [3]. For amino-functionalization, a mixture of 3.0 g of PGME or PGME/alumina, 13.1 g of DETA and 125 cm^3 of toluene was left at room temperature for 24 h, then heated at 353 K for 6 h. Modified samples were filtered, washed with ethanol, dried and labeled as PGME-deta and PGME/alumina-deta. Cr(VI) ions were sorbed from acidic aqueous solutions ($C_0 = 0.1 \text{ M}$; $\text{pH} = 1.8$) at room temperature ($T = 298 \text{ K}$). In batch experiment under static conditions (without stirring) 0.50 g of copolymer was suspended in 50 cm^3 of metal salt solution. The concentration of Cr(VI) in the aqueous phase was measured by flame atomic absorption spectroscopy (FAAS) (PerkinElmer 3100).

Pore size distributions were determined by a high pressure mercury intrusion porosimeter Carlo Erba Porosimeter 2000, operating in the interval from 0.1 to 200 MPa. Infrared spectra were taken in attenuated total reflection (ATR) mode using a Nicolet 380 FTIR spectrometer equipped with a Smart Orbit™ ATR attachment containing a single-reflection diamond crystal. SEM analysis was performed with JEOL JSM-6610 L instrument using W filament as an electron source. Air-dried membrane samples were fractured after cooling in liquid nitrogen and sputtered with gold.

RESULTS AND DISCUSSION

Doping polymers with metal oxides enhances hardness, thermal conductivity, resistance to abrasion, thermal shock and chemical attack, etc.; which substantially broadens the potential applications in various fields, especially in adsorption purposes [4,5]. In this study, the role of alumina, amino-functionalization and immobilization of Cr(VI) ions on physico-chemical properties of PGME based composites was investigated. The results from FTIR spectroscopy indicate the presence of -NH and -NH₂ groups in amino-functionalized samples (bands at 3300 cm^{-1} [$\nu(\text{NH}_2)$], 1660 cm^{-1} [$\delta(\text{NH}_2)$, $\delta(\text{NH})$] and 1560 cm^{-1} [$\delta(\text{NH})$]). A strong OH bending at

1080 cm^{-1} indicates alumina incorporation in polymer/ alumina composites [6]. Two new peaks at ca. 790 cm^{-1} and ca. 900 cm^{-1} indicate the presence of Cr–O and Cr=O in PGME-deta/Cr and PGME/alumina-deta/Cr [7]. The incorporation of alumina in PGME had the significant influence on the composite morphology. As seen in Figure 2, alumina promotes the formation of smaller primary globules and their agglomerates, which results in more compact spatial arrangement in PGME/alumina compared to PGME. Amino-functionalization and chromium sorption have caused considerable alteration of porosity parameters (Table 1). The most prominent changes of S_{Hg} and $d_{V/2}$ were observed between PGME-deta and PGME (3.7 times lower S_{Hg} and 12 times higher $d_{V/2}$ for PGME-deta) and between PGME /alumina and PGME/alumina-deta/Cr (4.4 times lower S_{Hg} and 20 times higher $d_{V/2}$ for PGME/alumina-deta/Cr). Therefore,

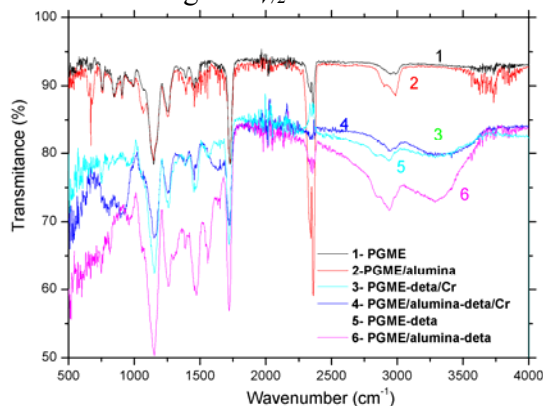


Figure 1. FTIR spectra of indicated samples

considerable enhancement of the pore size can be achieved by introduction of alumina in the reaction mixture, amino functionalization and/or immobilization of Cr(VI) ions. Large pores/channels (> 1 μm) obtained within the scope of this investigation are desirable for applications requiring a high liquid or gas flow through the medium at a reasonably low pressure, like HPLC [8].

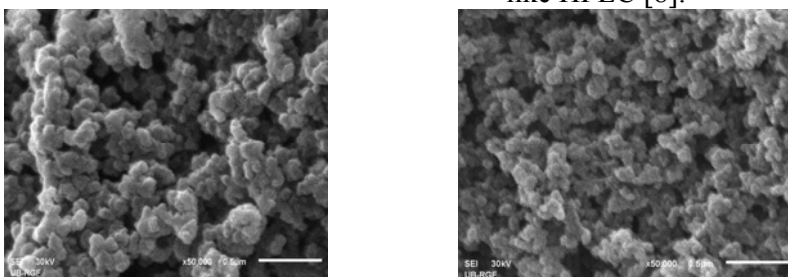


Figure 2. SEM micrographs (cross-section): PGME (left), PGME/alumina (right).

Table 1. Textural properties of the composite samples.

Sample	S_{Hg} (m ² g ⁻¹)	V_s (cm ³ g ⁻¹)	$d_{V/2}$ (nm)	P (%)
PGME	63	1.09	92	58
PGME/alumina	83	1.16	87	60
PGME-deta	17	1.01	1126	79
PGME/alumina-deta	50	1.26	163	81
PGME-deta/Cr	13	1.18	1427	83
PGME/alumina-deta/Cr	19	0.92	1722	84

^a S_{Hg} , specific surface area, V_s , specific pore volume and $d_{V/2}$, pore diameter corresponding to the half of the pore volume.

CONCLUSION

The results in this investigation show that properties of porous monolithic glycidyl methacrylate (GMA) and ethylene glycol dimethacrylate (EGDMA) copolymer [PGME] and composite with alumina (PGME/alumina) could be altered within a very broad range, by introduction of alumina in the reaction mixture, amino-functionalization and/or immobilization of Cr(VI) ions.

ACKNOWLEDGEMENT

This work has been funded by Serbian Ministry of Education, Science and Technological Development through the projects (III 43009, 172015 and III 45001).

REFERENCES

- [1] R.D. Arrua, M.C. Strumia, C.I.A. Igarzabal, *Materials*, 2009, 2, 2429-2466.
- [2] S. Xie, R. W. Allington, J. M. J. Fréchet, F. Švec, *Modern Advances in Chromatography Advances in Biochemical Engineering/Biotechnology*, 2002, 76, 87-125.
- [3] A. Nastasović, D. Jakovljević, Z. Sandić, D. Đorđević, Lj. Malović, S. Kljajević, J. Marković, A. Onjia, in: *Reactive and Functional Polymers Research Advances*, Ch. 2, M. I. Barroso ed. Nova Science Publishers, Inc., Hauppauge, New York. 2007.
- [4] R. Gangopadhyay, A. De, *Chem. Mater.*, 2000, 12, 608–22.
- [5] C. P. Wong, S.B. Raja, *J. Appl. Polym. Sci.* 1999, 74, 3396–403.
- [6] B.E. Yoldas, *Am. Ceram. Soc. Bull.*, 1975, 54, 289-290.
- [7] S. Deng, R. Bai, *Water Res.*, 2004, 38, 2423-2431.
- [8] C. Viklund, F. Švec, J.M.J. Fréchet, K. Irgum, *Chem. Mater.* 1996, 8, 744-750.



PHYSICAL CHEMISTRY 2014

12th International Conference
on Fundamental and Applied Aspects of
Physical Chemistry

Proceedings
Volume III

The Conference is dedicated to the
25. Anniversary of the Society of Physical Chemists of Serbia

September 22-26, 2014
Belgrade, Serbia

ISBN 978-86-82475-32-3

Title: PHYSICAL CHEMISTRY 2014 (Proceedings)

Editors: Ž. Čupić and S. Anić

Published by: Society of Physical Chemists of Serbia, Studenski trg 12-16,
11158, Belgrade, Serbia

Publisher: Society of Physical Chemists of Serbia

For Publisher: S. Anić, President of Society of Physical Chemists of Serbia

Printed by: “Jovan” Printing and Publishing Company; 200 Copies;

Number of pages: 3+342; **Format:** B5; Printing finished in September
2014.

Text and Layout: “Jovan”

Neither this book nor any part may be reproduced or transmitted in any form or by any means, including photocopying, or by any information storage and retrieval system, without permission in writing from the publisher.

200 - Copy printing

Contents

Volume III

Environmental Protection, Forensic Sciences, Food Physical Chemistry	831
Phase Boundaries	989
Complex Compounds	1023
General Physical Chemistry	1057
Geophysical Chemistry	1075
Education, History	1085
Pharmaceutical Physical Chemistry	1099
Author Index	1161

ENVIRONMENTAL PROTECTION,
FORENSIC SCIENCES,
FOOD PHYSICAL
CHEMISTRY

METHODS FOR QUANTITATIVE ANALYSIS WITH SINGLE-MOLECULE SENSITIVITY IN FORENSIC APPLICATIONS

V. Vukojević¹

¹*Department of Clinical Neuroscience, Center for Molecular Medicine, Karolinska Institute, 17176 Stockholm, Sweden*

ABSTRACT

Detection of minute quantities of substance in microliter volumes of sample is a daily challenge in forensic analysis. Experimental techniques that can fulfill these requirements are not numerous. The aim of this paper is to introduce Fluorescence Correlation Spectroscopy (FCS) and Fluorescence Cross-Correlation Spectroscopy, methods for quantitative analysis with single-molecule sensitivity and discuss their potential for forensic analysis.

INTRODUCTION

FCS is a quantitative method with single molecule-sensitivity that uses statistical analysis of fluorescence intensity fluctuations recorded over time to obtain information about molecular numbers and their transporting and/or kinetic properties [1 - 4]. Principles of FCS were formulated about thirty years ago, when the method was successfully applied in the founding laboratories to measure in solution the concentration, diffusion coefficient and kinetic rate constants of fluorescent molecules and their interactions [5 - 9]. In spite of this significant breakthrough, which confirmed that quantitative analysis with single-molecule sensitivity is possible, early FCS measurements were complex, requiring long signal acquisition and tedious data analysis. More widespread application of FCS became possible only after confocal optical arrangement and ultra-sensitive and ultra-fast photon detectors, such as avalanche photodiode (APD) detectors were implemented in FCS [10, 11]. Application of these innovations significantly improved the signal-to-noise ratio (SNR), enabling single-molecule detection sensitivity, low excitation intensities and short measurement times.

FCS MEASUREMENTS AND DATA ANALYSIS

A schematic presentation of a typical experimental setup for FCS is given in Fig. 1. To induce fluorescence, the sample is illuminated by incident light delivered by a continuous wave laser. The laser beam is reflected by a

dichroic mirror and sharply focused by the objective to form a miniature volume element, whose size is determined by the diffraction of light. The volume from which fluorescence is detected is further reduced by a pinhole (confocal aperture) in the image plane, rejecting stray and out of focus light and keeping the Raman scattered light to a minimum. In this way, fluorescence is detected from a minute observation volume element (OVE) that is about $2 \times 10^{-19} \text{ m}^3$. This enables a sub-micrometer resolution and specific detection at defined loci, as well as quantitative and background-free analysis. The light emitted by fluorescing molecules passing through the confocal volume element is separated from the exciting radiation and the scattered light by a dichroic mirror and barrier filter, and transmitted to the single-photon avalanche photodiode (APD) detector, which responds with an electrical pulse to each detected photon. The number of pulses originating from the detected photons, recorded during a specific time interval, corresponds to the measured light intensity. Thus, in one FCS experiment we register changes in fluorescence intensity in time.

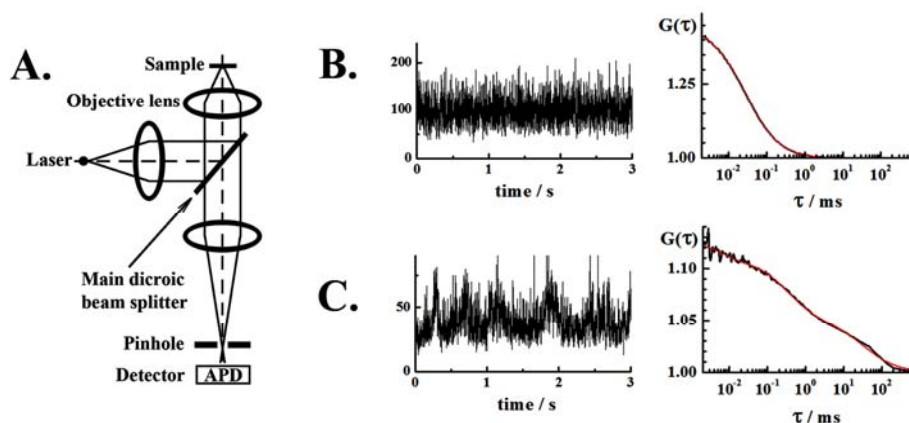


Figure 1. FCS measurements and data analysis. **A.** Schematic drawing of an inverted confocal microscope. **B.** and **C.**

Fluorescence intensity fluctuations (left) and corresponding autocorrelation curves (right) recorded in a standard solution of Rhodamine 6G (Rh6G) in water (**B.**) and on the cellular plasma membrane (**C.**). Autocorrelation analysis (**B.**, right) shows that the average number of Rh6G molecules in the OVE is 2.3, which corresponds to a 23 nM solution. Autocorrelation analysis (**C.**, right) shows that the average number of molecules recorded at the plasma membrane is 9.2. The biphasic curve shows two inflection points, reflecting the presence of two fractions that can be distinguished by

lateral diffusion. The molar fraction of the faster component, with respect to the slower one is 0.6:0.4.

To evaluate the gathered data, *i.e.* to analyze time series sampled during one run, statistical methods are applied to detect non-randomness in the data. Typically, this is done by temporal autocorrelation analysis, but other methods such as higher order autocorrelation functions[12, 13], fluorescence intensity distribution analysis (FIDA) [14, 15], photon-counting histograms (PCH) [16, 17], and the recently developed fluorescence cumulant analysis (FCA) [18] and time-integrated fluorescence cumulant analysis (TIFCA) [19, 20] can be also applied. However, the temporal autocorrelation analysis of fluorescence intensity fluctuations is still the most frequently used method in FCS applications.

In temporal autocorrelation analysis, the normalized autocorrelation function $G(\tau)$ is first derived:

$$G(\tau) = 1 + \frac{\langle \delta I(t) \cdot \delta I(t + \tau) \rangle}{\langle I(t) \rangle^2} \quad (1)$$

relating the fluctuation in fluorescence intensity measured at a certain time point t , $\delta I(t) = I(t) - \langle I(t) \rangle$, which is given as the difference in fluorescence intensity $I(t)$ and the mean fluorescence intensity over the recorded time-series ($\langle I(t) \rangle$), and its intensity measured at a later time, $\delta I(t + \tau) = I(t + \tau) - \langle I(t) \rangle$. For further analysis, $G(\tau)$ is plotted as a function of different lag times τ , also called autocorrelation times, to construct the corresponding autocorrelation curve (Fig. 1B and C, right). In molecular systems undergoing stochastic fluctuations, random variations of $G(\tau)$ around the value $G(\tau) = 1$ would be observed. For processes that are not random, an autocorrelation curve builds up with a maximal limiting value of $G(\tau)$ as $\tau \rightarrow 0$, decreasing to the value of $G(\tau) = 1$ at long times, indicating that correlation between the initial and the current property value has been lost. For simple systems, with only one chemical species and one process that underlies the fluorescence intensity fluctuations, autocorrelation curves with only one characteristic time are being observed (Fig. 1B, right). In complex systems, where more than one process underlies the fluorescence intensity fluctuations, or chemical species with different diffusion times exist, more than one characteristic time can be observed if the processes are sufficiently well separated in time (Fig. 1C, right).

To obtain information about the average number of molecules observed, the so-called non-uniform part of the normalized autocorrelation function is

used, $g(\tau) = G(\tau) - 1$. In this case one observes a maximal limiting value of $g(\tau)$ as $\tau \rightarrow 0$ that decreases to the value of $g(\tau) = 0$ at long times. The limiting value of $g(\tau)$, as $\tau \rightarrow 0$, is then inversely proportional to the absolute concentration of the fluorescing molecules. Both the normalized autocorrelation function $G(\tau)$ and its non-uniform part $g(\tau)$ are independent of the properties of the experimental setup, such as the laser intensity, fluorescence quantum yield and detection efficiency [1]. A comprehensive description of autocorrelation analysis and the derivation of autocorrelation function for the simplest case, free three-dimensional (3D) diffusion in an isotropic medium, can be found at <http://www.biotec.tu-dresden.de/cms/index.php?id=151> [21]. We present here the most relevant results.

To extract the information about molecular numbers (N) and lateral diffusion times (τ_D), the experimental autocorrelation curves is fitted using autocorrelation functions derived for the appropriate model system [1]. For measurements performed in solution, a model for free 3D diffusion with triplet contribution is typically used:

$$G(\tau) = 1 + \frac{1}{N} \cdot \left(\sum_i \frac{y_i}{\left(1 + \frac{\tau}{\tau_{Di}}\right) \sqrt{1 + \frac{w_{xy}^2}{w_z^2} \frac{\tau}{\tau_D}}} \right) \cdot \left[1 + \frac{T}{1-T} \exp\left(-\frac{\tau}{\tau_T}\right) \right] \quad (2)$$

In equation (2), N is the average number of molecules in the OVE, i is the number of components that can be distinguished by difference in diffusion, τ_{Di} is the diffusion time of the i -th component and x_i is its relative amplitude ($\sum x_i = 1$), T is the average equilibrium fraction of molecules in the triplet state, τ_T is the triplet state relaxation time. The diffusion times, τ_{Di} , of the investigated components is determined from the autocorrelation function (2) that best matches the actual, experimentally determined autocorrelation curve. For the autocorrelation curve shown in Fig. 1 B, only one characteristic decay time is observed, indicating that there is only one component whose diffusion time can be estimated from the inflection point of the autocorrelation curve and the average number of molecules from the amplitude of the autocorrelation curve. For the example shown in Fig. 1 C, the autocorrelation curve is biphasic, showing two characteristic decay times, which indicates that two components with different diffusion times are detected. Again, the amplitude reflects the total number of fluorescence molecules, and the contribution of one component with respect to the other

is determined by their relative amplitudes. For the example shown in Fig. 1 C, the total number of molecules is 9.2, 60 % of molecules (about 5.5 molecules on the average) show shorter diffusion times ($\tau_{D1} \approx 3$ ms), whereas about 3.7 molecules (on the average) show a longer diffusion time ($\tau_{D2} \approx 70$ ms).

The diffusion time τ_D is related to the translation diffusion coefficient D through the relationship:

$$\tau_D = \frac{w_{xy}^2}{4D} \quad (3)$$

where w_{xy} is the so-called lateral radius, *i.e.* the radial distance of the focused laser beam at which the collected fluorescence intensity has dropped by a factor of e^2 compared to its peak value in the center. This parameter is derived in calibration measurements, using standard aqueous solutions of fluorescent molecules whose diffusion coefficients are known. For this purpose, fluorescent properties of the standard dye need to match the properties of the fluorescent protein, and identical optical settings have to be applied for FCS measurements (Figs 1B and C). Diffusion coefficients of organic fluorophores typically used as reference in FCS can be found at http://www.picoquant.com/technotes/appnote_diffusion_coefficients.pdf [22]. The lateral radius w_{xy} depends on the instrumental setting, but the theoretical limit for a diffraction-limited spot gives size-range from 200-270 nm for the typically used excitation wavelengths 488-633 nm.

FLUORESCENCE CROSS-CORRELATION SPECTROSCOPY (FCCS) MEASUREMENTS AND DATA ANALYSIS

Fluorescence cross-correlation spectroscopy (FCCS) takes advantage of two fluorophores, which can be spectrally distinguished, and analyses the covariance between them to unambiguously establish whether interactions between distinctly labeled molecules occur. Typically, the following fluorophore pairs are being used, rhodamine 6G (Rh6G) and cyanine 5 (Cy5), or Alexa488 and Alexa633. Rh6G and Alexa488 can be excited at 488 nm and Cy5 and Alexa633 at 633 nm, and emit in the green and red part of the visible spectrum, respectively. The fluorescent signal is further spectrally selected by a band pass filter (BP 505-540 nm) for Rh6G or Alexa 488, and a long pass filter (LP655) for Cy5 or Alexa633. The signal from each fluorophore is recorded in a separate detector channel, and temporal correlation analysis is performed between them, to identify instances when the signal is observed in both detectors simultaneously. If this occurs

randomly, such as when the fluorescently labeled molecules are not interacting, random variations of $G(\tau)$ around the value $G(\tau) = 1$ would be observed in the cross-correlation curve, *i.e.* a cross-correlation curve would not build up. If, on the other hand, the molecules interact, an autocorrelation curve builds up with a maximal limiting value of $G(\tau)$ as $\tau_D \rightarrow 0$. Again, the amplitude of $G(\tau)$ decreases to 1 at long times, indicating that correlation between the initial and the current property value has been lost. A screen print from a real FCCS measurement is shown in Fig. 2.

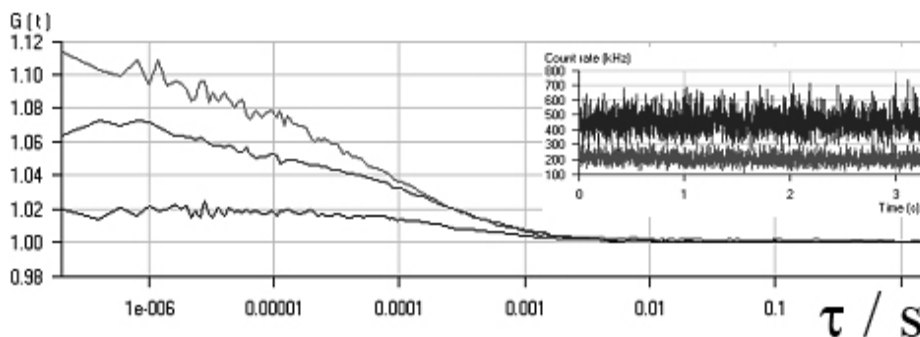


Figure 2. FCCS measurements and data analysis. Autocorrelation curves reflecting properties of the Cy5 labeled molecule (top), Rh6G labeled molecule (middle) and the cross-correlation curve (bottom) showing that the Rh6G and Cy labeled molecules interact forming stable complexes. Corresponding fluorescence intensity fluctuations are shown in the insert.

As in FCS, the average number of singly-labeled molecules is determined from the amplitude of the autocorrelation curves (light and dark gray curves in Fig. 2), and the number of dually-labeled molecules (N_{gr}) is determined from the ratio of cross-correlation amplitude (A_{cc} , black curve in Fig. 2) and the autocorrelation amplitudes (A_{Rh6G} and A_{Cy5}):

$$\frac{1}{N_{cc}} = \frac{N_{gr}}{(N_g + N_{gr})(N_r + N_{gr})} \quad \text{or} \quad N_{gr} = \frac{A_{CC}}{A_{Rh6G} \cdot A_{Cy5}} \quad (4)$$

FCS AND FCCS IN FORENSIC SCIENCE

Thus far, FCS and FCCS based analytical protocols are not standardly used in forensic science, even though it was realized early on that these methods may be invaluable for forensic analysis [10, 23].

An FCCS protocol was recently described for the detection of adrenocorticotrophic hormone (ACTH) [24]. This protocol relies on the

usage of two distinctly labelled antibodies which recognize the N- or the C-terminal of ACTH. In this way the possibility of obtaining false-positive or negative results was significantly reduced and single-molecule sensitivity was obtained. The two-antibodies approach described in [24] may be regarded as a prototype approach for peptide and protein detection in biological samples.

A novel fluorescence-based method for detection of blood was recently developed and applied to detect blood cells and DNA molecules *in situ* [25]. This method relies on the usage of fluorescently labelled antibodies for protein detection and on fluorescent probes for DNA staining, and fluorescence microscopy imaging for their visualization. In its present form, the method aims at detecting low levels of material. The protocols described in this study can be readily transferred and applied for quantitative analysis with single-molecule/single-particle sensitivity using FCS and FCCS.

The speed of FCS and FCCS analyses can be efficiently improved by using microfluidic devices to flow the analytes [26] or by quickly scanning the laser beam through a static solution [27]. In either case, photophysical processes that compete with fluorescence can be significantly reduced by limiting the fluorophores exposure to the illuminating light. The signal-to-noise ratio (SNR) is additionally improved because the frequency of encountering fluorescent molecules is increased by the flow/scanning. This reduces the time required for an analysis, enabling high-throughput.

CONCLUSION

FCS and FCCS, quantitative methods with single-molecule sensitivity which also require small sample volumes – an analysis can be performed in a volume of about 50 μL , are indispensable for biomedical research, clinical analysis and forensic science. Application of these methods in routine laboratories is not yet widespread. The aim of this work is to introduce these methods and highlight their potential for forensic applications.

ACKNOWLEDGEMENT

This work was partially supported by the Karolinska Institute Research Funds and the Ministry for Science of the Republic of Serbia (Grant no. 172015).

REFERENCES

- [1] V. Vukojević, A. Pramanik, T. Yakovleva, R. Rigler, L. Terenius, G. Bakalkin. *Cell. Mol. Life Sci.* 2005, 62, 535-550.
- [2] T. Jovanović-Talisman, V. Vukojević. *J. Serb. Chem. Soc.* 2013, 78, 1671-1688.

- [3] E. L. Elson. *Methods Enzymol.* 2013, 518, 11-41.
- [4] J. Ries J, P. Schwillle. *Bioessays* 2012, 34, 361-368.
- [5] D. Magde, W. W. Webb, E. Elson. *Phys. Rev. Lett.* 1972, 29, 705-708.
- [6] M. Ehrenberg, R. Rigler. *Chem. Phys. Lett.* 1972, 14, 539-544.
- [7] E. L. Elson, D. Magde, D. Biopolymers 1974, 13, 1-27.
- [8] M. Ehrenberg, R. Rigler. *Chem. Phys.* 1974, 4, 390-401
- [9] D. E. Koppel. *Phys. Rev. A* 1974, 10, 1938-1945.
- [10] R. Rigler, Ü. Mets, J. Widengren, P. Kask. *Eur. Biophys. J.* 22, 1993, 169-175.
- [11] M. Eigen, R. Rigler. *Proc. Natl. Acad. Sci. USA* 1994, 91, 5740-5747.
- [12] N. L. Thompson. *Topics in fluorescence Spectroscopy, Volume 1: Techniques*, J. R. Lakowicz (ed.), Plenum Press, New York, USA 1991 337.
- [13] H. Qian, E. Elson, *Biophys. J.* 1990, 57, 375-380.
- [14] P. Kask, K. Palo, D. Ullmann, K. Gall, *Proc. Natl. Acad. Sci. USA* 1999, 96, 13756-13761.
- [15] P. Kask, K. Palo, N. Fay, I. Brand, U. Mets, D. Ullmann, J. Jungmann, J. Pschorr, K. Gall, *Biophys. J.* 2000, 78, 1703-1713.
- [16] Y. Chen, J. D. Müller, P. T. C. So, E. Gratton, *Biophys. J.* 1999, 77, 553-567.
- [17] L. N. Hillesheim, J. D. Müller, *Biophys. J.* 2003, 85, 1948-1958.
- [18] J. D. Müller, *Biophys. J.* 2004, 86, 3981-3992.
- [19] B. Wu, J. D. Müller, *Biophys. J.* 2005, 89, 2721-2735.
- [20] B. Wu, Y. Chen, J. D. Müller, *Biophys. J.* 2006, 91, 2687-2698.
- [21] E. Petrov, Derivation of expressions for the FCS correlation function. 2005 <http://www.biotec.tu-dresden.de/cms/index.php?id=151>
- [22] P. Kapusta, PicoQuant Application Note 2010.
- [23] Z. Földes-Papp. *Exp. Mol. Pathol.* 2007, 82, 147-155.
- [24] M. G. Puchinger, C. A. Zarzer, P. Kügler, E. Gaubitzer, G. Köhler. *EURASIP J. Bioinform. Syst. Bio.* 2012, 17, 1-10.
- [25] R. Thorogate, J. C.S. Moreira, S. Jickells, M. M.P. Miele, B. Daniel. *Forensic Science International: Genetics* 2008, 2, 363-371.
- [26] M.H. Horrocks, H.T. Li, J.U. Shim, R. T. Ransinghe, R. W. Clarke, W.T.S. Huck, C. Abell, D. Klenerman, *Anal. Chem.* 2012, 84, 179-185.
- [27] V. Vukojević, M. Heidkamp, Y. Ming, B. Johansson, L. Terenius, R. Rigler, *Proc Natl Acad Sci USA*, 2008, 105, 18176-18181.

REMOVAL OF NICKEL PHTHALOCYANINE DYE FROM WASTEWATER USING PHOTOVOLTAIC ELECTROCOAGULATION

K. Dermentzis, D. Marmanis, A. Christoforidis, N. Kokkinos and E. Apostolidou

Department of Petroleum & Natural Gas Technology, Kavala Institute of Technology, 65404 Agios Loucas, Kavala, Greece (demerz@otenet.gr)

ABSTRACT

In the present work the decolorization treatment of colored nickel phthalocyanine wastewater was studied using the electrocoagulation process with sacrificial aluminum electrodes powered by a photovoltaic collector without batteries. The photovoltaic electrocoagulation system is made versatile according to the instantaneous solar irradiation by adjusting the wastewater flow rate to the current intensity supplied by the photovoltaic panel. All parameters affecting the efficiency of the process were considered, such as initial pH, conductivity, flow rate and operating time. The proposed process is appropriate for decolorizing colored textile dye wastewaters and especially for small applications in remote and isolated locations without connection to public electric grid.

INTRODUCTION

Electrocoagulation (EC) is an emerging technique for wastewater remediation closely related to chemical coagulation. This process consists of providing electrical current to a sacrificial anode and creating metallic hydroxide flocs inside the wastewater by electrodisolution of soluble anodes made of aluminum or iron. The electrochemically generated Al^{3+} or Fe^{3+} at the anode and the OH^- ions at the cathode combine to form in situ the coagulants $\text{Al}(\text{OH})_3$ or $\text{Fe}(\text{OH})_3$ respectively, effecting the coagulation and co-precipitation of particulates from the solution by adsorption.

The present paper discusses an electrochemical decolorization treatment of nickel phthalocyanine (Ni-pc) dye wastewater using the EC process with aluminum electrodes, directly powered by a PV array. The photovoltaic electrocoagulation (PV-EC) system is made versatile according to the instantaneous solar irradiation by adjusting the wastewater flow rate to the current density supplied by the PV panel. Operating parameters that affect the PV-EC process, such as pH, current density, conductivity, flow rate and operating time are determined.

EXPERIMENTAL

The photovoltaic module used was SUNPOWER (Maxeon Cell Technology) SPR-327NE-WHT-D made from monocrystalline silicon with a surface area of 1.63 m² and a peak power of 327 W. The experiments were conducted in Kavala Institute of Technology (latitude 40° 55', longitude 24° 22' and altitude 138 m above the sea level).

Voltage and current were measured by a multimeter (PHYWE). Conductivity was measured by means of a conductometer (WTW). The pH and the temperature were measured by a temperature sensitive pH-meter (WTW). The wastewater was circulated by a peristaltic pump.

All EC experiments were conducted at room temperature in a 500 mL electrochemical reactor in which the nickel phthalocyanine (Ni-pc) dye solutions of 200 mL were placed and slowly stirred with a magnetic bar at 500 rpm. Three aluminum plates (10cm x 2.5cm x 0.5cm) immersed to a 6cm depth with an effective area of 15cm² each were used as electrodes in the experiments. The electrodes were situated 0.5cm apart from each other. KCl, as supporting electrolyte, was added to every treated solution. Samples were extracted every 2.5 minutes, filtered with Whatman filter paper (Grade 40) and analyzed by UV-Vis spectrophotometry ($\lambda_{\text{max}}=620\text{nm}$).

Figure 1 shows the experimental set up.

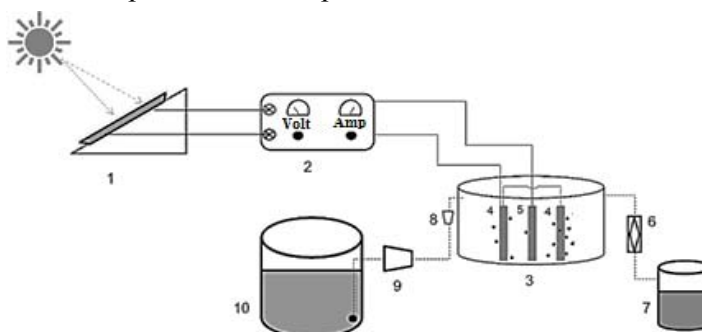


Figure 1. Experimental setup: 1. PV Solar module, 2. Regulator, 3. EC reactor, 4. Anode, 5. Cathode, 6. Filter, 7. Treated solution, 8. Flow meter, 9. Peristaltic pump, 10. Wastewater deposit.

RESULTS AND DISCUSSION

Effect of initial pH

In our previous work [1] the treatment of Ni-pc solutions was optimized by means of conventional EC. It was found that maximum removal efficiencies were achieved in near neutral pH values. The optimum near neutral pH value for EC was suggested also by other researchers [2,3].

Effect of applied current density

Measurements were carried out at various current densities, constant dye concentration of 100 mg/L and pH 6.5. According to Table 1 the removal rate of Ni-pc increased, as expected, with increasing current density. In 10, 5 and less than 5 minutes of electrolysis time at the corresponding current densities of 5, 10 and 20 mA/cm², the dye has been quantitatively eliminated (>99.9%) and its concentration fell under the apparatus detection limit (0.08 mg/L).

Table 1. Concentration variation of Ni-pc with time and current density

Time (min)	[Ni-pc]* (mg/L)	[Ni-pc]** (mg/L)	[Ni-pc]*** (mg/L)
0	100	100	100
2.5	26.3	5.6	0.3
5	2.7	8.4	<0.08
7.5	0.1	<0.08	
10	<0.08		

*5mA/cm², **10 mA/cm², ***20 mA/cm²

Effect of conductivity

The wastewater conductivity affects immediately the applied voltage and therefore the electrical energy consumption. The removal percentage of the Ni-pc dye is hardly affected and remains constant over 99.9 % for the three tested wastewater conductivities of 1500, 3000 and 4500 µS/cm (Table 2).

Table 2. Electrocoagulation results for various wastewater conductivities

Conductivity (µS/cm)	Voltage (V)	Energy consumption (kWh/m ³)	Dye removal percentage (%)
1500	18.4	0.42	>99.9
3000	9.5	0.23	>99.9
4500	5.2	0.12	>99.9

Effect of flow rate

The current density supplied by the PV array depends on the solar irradiation and the temperature of the PV modules. These parameters cannot be controlled and will change continuously through the hours in a day or suddenly through clouds crossing or changes in wind speed. Valero *et al.* [3] proposed a clever mode of operation in order to make the PV-EC system versatile to instantaneous solar irradiation by keeping constant the ratio current density/flow rate. Thus, when the current density supplied by the PV

array changes, also the working flow rate must proportionally change to maintain this ratio constant. This operation way implies that the volume of treated wastewater is directly related to the solar energy incident on the panels.

The experiments with constant current density and flow rate were conducted at a sunny midday and in short periods to keep approximately constant values of solar irradiation. As can be obtained from Table 3, by increasing the current density the cell voltage and flow rate increase proportionally, while the residence time decreases. The dye removal percentage is not affected and remains over 99.9%.

Table 3. EC results for different wastewater flow rates.

Flow rate (L/h)	Current density (mA/cm ²)	Voltage (V)	Residence time (min)	Removal percentage (%)
0.5	5	7.1	24	>99.9
1.0	10	14.5	12	>99.9
2.0	00	29.8	6	>99.9

CONCLUSION

This paper shows the feasibility of performing remediation of dye house effluents by directly connecting the electrocoagulation reactor to the photovoltaic generator. The PV-EC system is made versatile to instantaneous solar irradiation by adjusting the wastewater flow rate and keeping constant the ratio current density/flow rate. The dye removal percentage remains high for the three tested wastewater flow rates of 0.5, 1.0 and 2.0 L/h and the three wastewater conductivities of 1500, 3000 and 4500 $\mu\text{S}/\text{cm}$. The proposed PV-EC process could present some advantages for treatment of dye house effluents in isolated places without electric grid.

REFERENCES

- [1] K. Dermentzis, D. Marmanis, E. Valsamidou, A. Christoforidis, K. Ouzounis, , *Environ. Engin. Manage. J.*, 2011, 10, 1703-1709.
- [2] M.S. Secula, I. Cretescu, S. Petrescu, *Desalination*, 2011, 277, 227-235.
- [3] Valero D., Ortiz J.M., Exposito E., Montiel V., Aldaz A., *Solar Energy Mater. Solar Cells*, 2008, 92, 291-297.

IMMOBILIZATION OF LACCASE ON MAGNETIC CHITOSAN-CLAY BEADS: APPLICATION FOR PHENOL REMOVAL

T. Aydemir¹ and S. Güler¹

1 Celal Bayar University, Science and Arts Faculty, Chemistry Department, Manisa, TURKEY

ABSTRACT

Laccase, the blue oxidase enzyme with high potency in green synthesis and biodegradation of phenolic compounds, was immobilized on magnetic-chitosan-clay beads using glutaraldehyde cross-linking agent. The structure and morphology of composite beads were characterized by SEM, TGA and FTIR analysis. The maximum activity and Michaelis constant (V_{\max} and K_m) of laccase immobilized on chitosan composite beads, were found to be 12.05 U/mg and 0.410 mM, respectively. The immobilized laccase exhibited improved thermal stability, a wide range of pH stability and high tolerance against inactivating agents such as NaN_3 and cysteine. Finally, the immobilized laccase was operated in a batch system, and phenol was successfully removal in the enzyme reactor.

INTRODUCTION

Removal of phenols from industrial water effluents is an important practical problem, since many of these compounds are toxic and their presence in drinking and irrigation water is a health hazard. Conventional purification methods such as solvent extraction, adsorption on activated carbon and chemical oxidation suffer from serious drawbacks such as high cost and formation of hazardous by-products. The use of free laccase (benzenediol: oxygen oxidoreductase, E.C.1. 10.3.2) which catalyse the oxidative coupling of phenol compounds resulting in the formation. However, enzymes have some limitations for nonbiological applications. Thus, for many industrial applications, enzymes have to be immobilized, via very simple and cost-effective protocols, in order to improve the properties of enzymes, such as activity, stability, and selectivity [1,2]. Many different carriers have been used for enzymes immobilization. Among them, chitosan as a macromolecular material exhibits many interesting properties, namely biocompatibility, availability of reactive functional groups for chemical modifications, hydrophilicity, mechanical stability, regenerability, and ease of preparation in different geometrical configurations suitable for a chosen biotransformation. Recently, there has been a growing interest in chemical or physical modification of chitosan to improve its solubility and widen its environmental and biomedical applications [1-6]. In this study, laccase was immobilized on chitosan-clay-magnetic beads, and the conditions for immobilization and characterization of the immobilized enzyme

were studied systematically. Application of the immobilized system in phenol removal was investigated in a batch system.

EXPERIMENTAL

Materials

Laccase (EC 1.10.3.2: p-diphenol:dioxygen oxidoreductase) from *Trametes versicolor*, chitosan and 2,2-azinobis(3-ethylbenzthiazolin-6-sulfonate) (ABTS), sodium triphosphate pentabasic (TPP), nanoclay (hydrophilic bentonite, average particle size: $\leq 25 \mu\text{m}$, $\text{H}_2\text{Al}_2\text{O}_6\text{Si}$, 180.1 g/mol) were purchased from Sigma–Aldrich (USA).

Preparation of chitosan beads

Fe_3O_4 nanoparticles were prepared by the co-precipitating method [7]. 2 g chitosan were dissolved in 100 ml of 2% acetic acid with constant stirring on mechanical stirrer for 1 h. 1 g magnetic nanoparticles Fe_3O_4 and 1 g clay were added to the chitosan gel with stirring for 3 h. The resulting chitosan-clay- Fe_3O_4 slurry was added drop wise into TPP (pH 8.2) solution under vigorous stirring using a syringe. Then, the beads were washed with deionized water. The structure and morphology of prepared supports were characterized by scanning electron microscope (SEM), thermal gravimetric analysis (TGA) and FTIR analysis. ***Immobilization of laccase*** Chitosan- clay-magnetic beads were treated with 4% glutaraldehyde solution in 0.05M acetate buffer (pH 5.0) for 2 h at 25°C, and washed with deionized water [2,5]. An amount of cross-linked composite beads (0.5 g) was mixed laccase solution (1mg/ml) and the immobilization reaction was carried out at 4°C. The immobilized laccase beads were stored in 0.05 M acetate buffer (pH 5.0) at 4°C until use. The immobilization conditions including enzyme loading, immobilization time and the amount of glutaraldehyde were optimized.

Characterization of immobilized enzymes

The activity of free and immobilized laccase was determined spectrophotometrically at with a UV–vis spectrophotometer at $\lambda_{\text{max}} = 420 \text{ nm}$ with 1 mM ABTS as substrate in 0.1 M acetate buffer (pH 5.0) [3]. One unit (U) of laccase activity was defined as the amount of enzyme needed to oxidize 1 μmol of ABTS ($\epsilon = 36000 \text{ M}^{-1} \text{ cm}^{-1}$ per minute. The thermal and pH stabilities of free and immobilized enzymes were examined by measuring the activity of enzyme after the enzyme had been in the solutions for 1 h respectively, at different temperatures (20–70 °C) and different pH (3.0–8.0). The storage stability was evaluated by storing the free and immobilized enzyme at 4 °C for 2 month and the enzyme activity was measured every week. The kinetic parameters were estimated from the Lineweaver–Burk plot by varying the substrate ABTS at the temperature of the maximum activity.

Removal of phenol

Application of the immobilized system in phenol removal was investigated in a batch system. The residual phenolic compounds were measured on the basis of colorimetric method with potassium ferricyanide and 4-aminoantipyrine (4-AAP) with a UV–vis spectrophotometer at $\lambda_{\text{max}} = 510 \text{ nm}$.

RESULTS AND DISCUSSION

The morphological structure of magnetic chitosan-clay beads presented in Fig. 1 revealed by SEM analysis showed that magnetic chitosan-clay beads were well dispersed on the chitosan surfaces, indicating a homogeneous combination of the constituents. The average diameter of the dry and wet beads is 0.35 mm and 1.5 mm respectively. Used as the support material, magnetic carriers can be easily separated from the reaction medium and effectively controlled by applying a magnetic field, thus the use of magnetic particles can reduce the capital and operational costs (Fig. 2). The yield of the immobilization

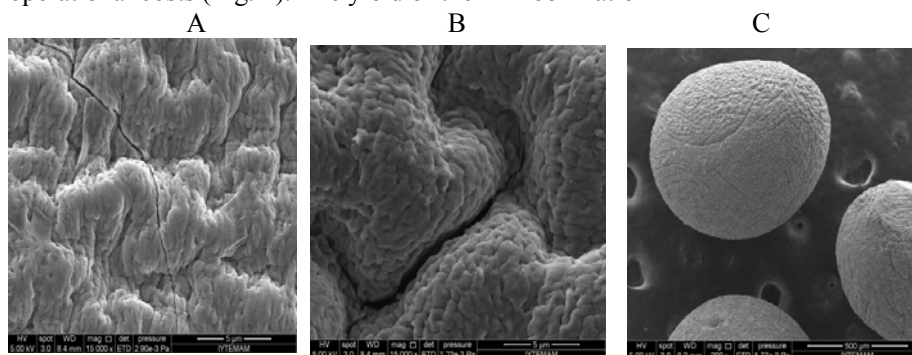


Figure1. SEM micrograph of (A) natural chitosan (15,000 \times) and (B-C) magnetic-chitosan-clay-beads (B:15,000 \times , C: 200 \times).

and enzyme activity were recorded % 75 and 2.90 U/g carrier. The K_m values were found to be for the free and immobilized laccase 0.297 mM and 0.410 mM, respectively. The increase in K_m value indicated the reduction in the affinity of laccase for binding substrate after laccase immobilization. These results were similar with other investigations reporting significant affinity decreases for the immobilized biocatalyst [4-6]. The apparent V_{max} value of the immobilized was 12.05 U/g, while V_{max} value of free laccase was 26.96 U/g. Nevertheless, the immobilized laccase exhibited remarkably improved stability properties to various parameters, such as temperature, reuse, and storage time. In addition, immobilization improved the stability of laccase in the acidic region. A similar change was observed in several cases of enzymes immobilized on different carriers [5]. During the study of reusability, laccase immobilized on chitosan-composite bead retained 76% of initial activity after 10 cycles (Fig. 3). The immobilized enzyme was tested for its ability to removal of phenol in a batch system. Phenol removal value of immobilized enzyme were obtained about 80% at the end of 4 h (Fig. 4).



Figure 2.

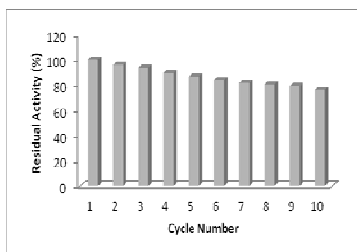


Figure 3.

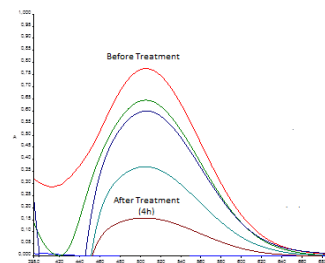


Figure 4.

Figure 2. Demonstration of magnetic separation of magnetic-chitosan-clay beads.

Figure 3. Reusability potential of immobilized enzyme on composite beads.

Figure 4. UV-Vis spectrum of phenol solution (10 ppm) before and after treatment by immobilize laccase.

CONCLUSION

Laccase was immobilized on the surface of magnetic chitosan beads by formation of the Schiff's base. The immobilized laccase exhibited the maximal enzyme activity at pH 5.0. The K_m of immobilized and free laccase for ABTS were 0.410 mM and 0.297 mM in acetate buffer (50 mM, pH 5.0) respectively. The thermal, operational, and storage stabilities of the enzyme were improved greatly after they were immobilized on the surface of the magnetic-chitosan-clay beads. The immobilized laccase was operated in a batch reactor for the removal of phenol from aqueous solution. These results demonstrate that the immobilized enzymes are used in wastewater treatment.

REFERENCES

- [1] T. Xie, A.M. Wang, L.F. Huang, H.F. Li, Z.M. Chen, Q.Y. Wang et al. *African Journal of Biotechnology*, 2009,8, 4724–4733.
- [2] M. Y. Abdelaala, T. R. Sobahia, H.F. Al-Shareef, *International Journal of Biological Macromolecules*, 2013, 55, 231–239.
- [3] M. F. Fernández, M. A. Sanromán, D. Moldes, *Biotechnology Advances*, 2013, 31, 1808–1825.
- [4] J. T. Chacko¹, K. Subramaniam, *International Journal Of Environmental Sciences* 2011, 6, 1-8,
- [5] E. Başak , T. Aydemir , A. Dinçer, S.Ç. Becerik, *Artificial Cells Nanomedicine And Biotechnology*, 2013, 41, 408–413.
- [6] E. Başak, T. Aydemir, *Artificial Cells Nanomedicine And Biotechnology*, 2013, 41, 408–413.
- [7] C. Pan, B.Hu, W. Li, Y.Sun, H.Ye, X. Zeng, *Journal of Molecular Catalysis B:Enzymatic*, 2009, 61, 208–215.

MATHEMATICAL MODELING OF PESTICIDE ADSORPTION ON ACTIVATED HEMP FIBERS

M. Vukčević¹, I. Pajić-Lijaković¹, A. Kalijadis², Z. Laušević² and M. Laušević¹

¹*Faculty of Technology and Metallurgy, University of Belgrade, Karnegijeva 4, 11001 Belgrade, Serbia (marijab@tmf.bg.ac.rs)*

²*Laboratory of Physics, Vinča Institute of Nuclear Sciences, University of Belgrade, P.O.Box 522, 11001 Belgrade, Serbia*

ABSTRACT

Activated carbon obtained by carbonization and activation of waste hemp fibers was used as an efficient, low-cost sorbent for pesticide removal. Data obtained from batch and continuous process of pesticide adsorption was used for development of the mathematical model that describes the phenomenon of pesticide transport through the porous sorbent matrices. Effective diffusion coefficient and the pesticide concentration profile within the activated hemp fibers, obtained as results of proposed model, give the insight in the mechanism and the rate of adsorption process and pesticide transport through the sorbent. A good agreement between model prediction and the experimental data indicates that the proposed mathematical model can be successfully used for optimization and selection of appropriate adsorption process for pesticide removal.

INTRODUCTION

One of the methods used to deal with purification of water contaminated by pesticides is adsorption on activated carbon. In the recent years there is a growing interest in utilizing the use of low-cost and abundantly available lignocellulosic materials as precursors for the preparation of activated carbons. In our previous work [1], short hemp fibers obtained as a waste from textile industry were used as a carbon precursor. Activated hemp fibers, obtained by carbonization and activation of waste hemp fibers, were successfully applied as a sorbent in solid-phase extraction procedure for the pesticides analysis in water samples. In this work, effectiveness of activated hemp fibers (ACh) as a sorbent for pesticide removal from polluted water was tested through the sorption of dimethoate, nicosulfurone and carbofuran, in batch and continuous flow process. In order to describe the process of pesticide adsorption on activated hemp fibers, we have extended and upgrade our previously developed mathematical model [2].

EXPERIMENTAL

Activated hemp fibers (sample ACh129) were obtained by carbonization at 1000 °C and activation at 900 °C, using KOH as an activating agent [1]. Adsorption of pesticides on the ACh129 was performed from the aqueous solution of pesticide mixture in batch system, with constant shaking, and in continuous flow system, with flow rate of 1 ml/min. Initial concentration of each pesticide in the mixture was 25 mg/dm³. The pesticides concentration after adsorption was determined by liquid chromatography-tandem mass spectrometry (LC-MS/MS).

RESULTS AND DISCUSSION

Mathematical model is based on pesticides mass balance equations for two phases: the liquid solution and the fixed bed under batch and continual flow conditions. Model is based on Fick's second law, and considers the adsorption of pesticides, from the pesticide mixture solution, on the activated hemp fibers. Based on morphological analysis, made by scanning electron microscopy, and activated hemp fiber textural characteristics [1], for the model consideration fibers were presented as a cylinder, consisting of the non-porous core region (radius R_{core}) and porous annular region ($\Delta R = R_f - R_{core}$, ΔR is annular region width and R_f is fiber radius) where pesticide adsorption occurs.

Model prediction for the decrease of pesticide concentration in the solution, during adsorption in the batch process, is well fitted with the experimental data (Figure 1). Pesticides balance equation is formulated, as shown in the literature [2], and it was solved analytically by Fourier's dividing of the variables and using Baseless functions. The general solution of the model balance equation determines the pesticide concentration profiles within the annular porous region of the activated fibers (Figure 2). Profile of pesticides reaches its equilibrium relatively fast and after 5 minutes the pesticide concentration through the porous annular region of fiber is constant.

The model parameter which represents the specific rate of pesticide concentration change, λ_i^2 , effective diffusion coefficient, D_{ei} , and equilibrium concentration of pesticide within the ACh129, along with experimentally obtained equilibrium pesticide concentrations are presented

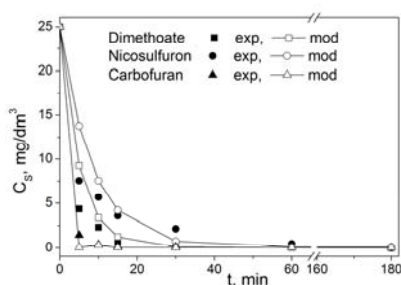


Figure 1. Pesticide concentration in the solution as a function of the adsorption time

in Table 1. For purpose of comparison, equilibrium concentration of pesticide within the commercial activated carbon C_{AC} , is also presented in Table 1.

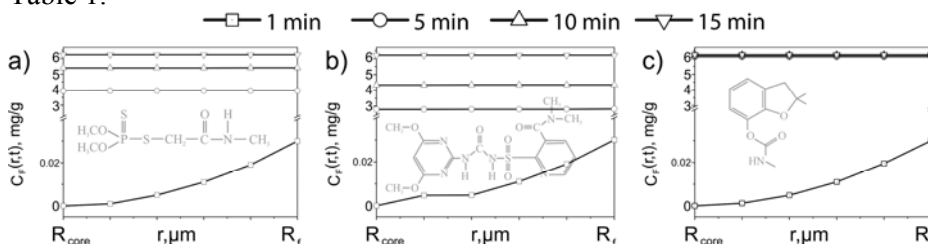


Figure 2. Concentration profile of dimethoate (a), nicosulfuron (b) and carbofuran (c) within the annular region of the ACh129

Pesticide concentration within the ACh129 obtained as a model prediction are well correlated with the ones obtained experimentally. Higher extent of resistance to the nicosulfuron and dimethoate transport is shown through the lower values for both specific rate of concentration change and effective diffusion coefficient. Due to the fact that the structure of pesticides plays an important role in adsorption, the steric hindrance caused by nicosulfuron high molecular weight and chemical structure may be the reason of its slower adsorption on the ACh129 surface. Due to the aromatic structure of carbofuran, dispersion forces between the π electron density of the graphene layers on the ACh and the aromatic ring of the adsorbate should be expected, and therefore the faster adsorption. On the other hand, adsorption of dimethoate is not forced by mentioned π - π interactions, due to the absence of aromatic ring, which induce slower adsorption.

Table 1. Model parameters that describes the pesticide transport through the porous matrices of ACh129 during batch adsorption

Pesticid e	M (g/mol)	λ^2 (min ⁻¹)	D_e / D_0	$C_{Feq,mod}$ (mg g ⁻¹)	$C_{Feq,exp}$ (mg g ⁻¹)	C_{AC} (mg g ⁻¹)
D	229	0.20	0.065	6.234	6.232	6.001
N	410	0.12	0.045	6.210	6.215	5.407
C	221	0.80	0.265	6.222	6.228	5.746

* D-dimethoate, N-nicosulfuron, C-carbofuran

For continual flow system, balance equation of the pesticide concentrations in the hemp fibers is similar as for the batch process, while the balance equation for solution is considered within two regimes. In the Regime I, the pesticide inflows $Q C_{S0i}$ are totally adsorbed by the fibers and the outer flows are $Q C_{Si}(t) \approx 0$, while in the Regime II, only partial adsorption of the pesticide inflows are achieved.

The pesticide concentrations in out flow solution, for continual flow process, in the Regime II were calculated using developed mathematical model, while in the Regime I these concentrations were $C_{S0i}(t) \approx 0$. The relative error of 5% was obtained between the model prediction and experimental data (Figure 3). Using this mathematical model, the breakthrough time (t_B) and the pesticides concentration on the ACh129 at the breakthrough point ($C_F(t_B)$) (Table 2), can be determined.

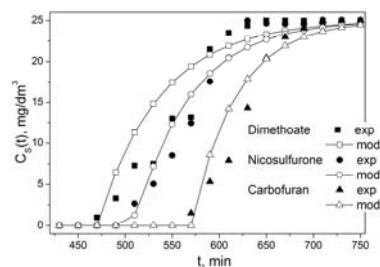


Figure 3. Continual process of pesticide adsorption on ACh129

Table 2. The ACh129 adsorption capacity at breakthrough time

Pesticide	t_{Bi} , min		$C_{Fi}(t_B)$, mg/g	
	experiment	model	experiment	model
Dimethoate	472	473	24.69	23.64
Nicosulfuron	499	512	25.74	25.59
Carbofuran	567	575	28.95	28.74

CONCLUSION

Activated hemp fibers have proven to be an efficient low-cost sorbent for pesticides removal. Effective diffusion coefficient and the pesticides concentration profile through the ACh129, obtained by developed mathematical model, show that mechanism of pesticide transport was influenced by the pesticide structure. Proposed mathematical model enables the deeper insight into the multi-scale phenomena of the pesticides transport through the porous matrices, which is essential for designing the filters for pesticide removal.

ACKNOWLEDGMENT

The authors wish to thank the Ministry of Education, Science and Technological Development of the Republic of Serbia for financial support through the projects No 172007 and No 45006.

REFERENCES

- [1] M. Vukcevic, A. Kalijadis, M. Radisic, B. Pejic, M. Kostic, Z. Lausevic, M. Lausevic, Chem Eng J 2012, 211-212, 224-232.
- [2] M. Vukčević, B. Pejić, A. Kalijadis, I. Pajić-Lijaković, M. Kostić, Z. Laušević, M. Laušević, Chem Eng J 2014, 235, 284-292.

HOMOGENEOUS AND HETEROGENEOUS PROCESSES INDUCED BY IRON(III) IN ENVIRONMENTAL PHOTOCHEMISTRY

E.M. Glebov^{1,2}, I.P. Pozdnyakov^{1,2}, V.P. Grivin¹, V.F. Plyusnin^{1,2}, X.
Zhang³, F. Wu³ and M.N. Timofeeva⁴

¹ *Voevodsky Institute of Chemical Kinetics and Combustion,
3, Institutskaya Str., Novosibirsk 630090, Russia (glebov@kinetics.nsc.ru)*

² *Novosibirsk State University,*

2, Pirogova Str., Novosibirsk 630090, Russia

³ *Department of Environmental Science, Hubei Key Lab of Biomass
Resource Chemistry and Environmental Biotechnology, School of Resources
and Environmental Science, Wuhan University*

Wuhan 430079, P. R. China

⁴ *Boreskov Institute of Catalysis,*

5 Lavrentyev Pr., 630090 Novosibirsk, Russia

ABSTRACT

Two aspects of environmental photochemistry are discussed. The first is the primary mechanism of the photolysis of Fe(III) complexes with carboxylic acids. Absorption of a light quantum results in an inner-sphere electron transfer resulted in the formation of a long-living (up to several milliseconds) complex between Fe(II) and organic radical. The second aspect is the impact of clays and clay materials on the photochemistry in water solutions. Both homogeneous and heterogeneous processes were examined. In all the cases, the spectral and kinetic properties of short-lived intermediates were characterized by means of laser flash photolysis.

INTRODUCTION

Light-initiated photochemical reactions of Fe(III) complexes effect on a number of iron-dependent processes leading to photochemical production of CO and CO₂, absorption of oxygen, and formation of active oxygen-containing compounds (AOC), such as $\cdot\text{OH}$, $\text{HO}_2\cdot$, H_2O_2 in aqueous solutions. Both homogeneous and heterogeneous processes can be responsible for the AOC formation. For mimicking the processes in natural waters, one should know the details of the reaction mechanisms. This knowledge could be obtained from time-resolved experiments allowing to detect short-lived intermediates of photochemical reactions.

In this work, a mechanistic study of the photolysis of Fe (III) complexes with carboxylic acids (tartaric, pyruvic, glyoxalic and lactic) in solutions was performed by means of nanosecond laser flash photolysis. Mimicking the heterogeneous processes in natural waters, photodegradation of organic compounds initiated by the photolysis of iron-rich clays was investigated.

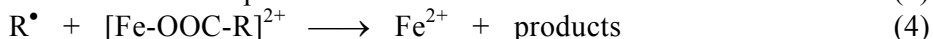
EXPERIMENTAL

A laser flash photolysis setup [1] based on a YAG laser with excitation at 266 and 355 nm and pulse duration of 5–6 ns was used.

Synthetic clay montmorillonite KSF was purchased from Sigma-Aldrich. The natural aluminosilicate containing more than 95% of a calcium-rich montmorillonite (LAS) and natural aluminosilicate (AS) were obtained from beds located in Mukhortala (Buryatia) and Khumuluut (Mongolia), respectively. The sodium containing layered aluminosilicate (Na-LAS) and aluminosilicate (Na-AS) and pillared interlayered clays (PILC) Al,Fe-AS and Al,Fe-LAS were prepared using the procedure described in [2].

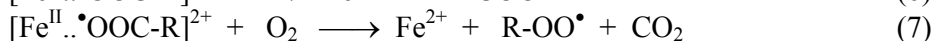
RESULTS AND DISCUSSION

Photochemistry of Fe(III) carboxylates It was proposed in the literature [3] that the primary photochemical processes for Fe(III)-carboxylate complexes was an inner-sphere electron transfer from the ligand to the central ion followed by an escape of an organic radical to the solution bulk (reactions 1, 2). This mechanism was put forward based on the analysis of the final reaction products, which needed confirmation by means of direct methods.



Laser flash photolysis of Fe(III)-carboxylate complexes with methyl viologen dication (MV^{2+}) as a scavenger of organic radicals was performed. For all the studied complexes the immediate formation of Fe(II) accompanied by an escape of an organic radical to the solution bulk was shown to be a side reaction. The main primary intermediate was characterized as a long-living (up to several milliseconds) complex of Fe(II) with an organic radical stabilized in the first coordination sphere (further – radical complex, RC). The reactions of RCs are responsible for the final reaction products. The literature mechanism of photolysis was modified (reactions 5-7) [4]. The information concerning quantum yields for different $[\text{Fe-OOC-R}]^{2+}$ complexes is collected in Table 1.





When photolysis is performed in the presence of different substrates (like in natural aquatic systems), the formation of the “secondary” radicals via the

Table 1. Quantum yields of photolysis (355 nm) of $[\text{Fe-OOC-R}]^{2+}$ complexes in aqueous solutions (pH 3.0) (quantum yields of Fe(III) disappearance $\phi(\text{Fe}^{\text{III}})$, Fe(II) formation in deaerated $\phi(\text{Fe}^{\text{II}})_{\text{Ar}}$ and aerated $\phi(\text{Fe}^{\text{II}})_{\text{Air}}$ solutions, and free radicals formation ϕ_{R})

Complex	$\phi(\text{Fe}^{\text{III}})$	$\phi(\text{Fe}^{\text{II}})_{\text{Ar}}$	$\phi(\text{Fe}^{\text{II}})_{\text{Air}}$	ϕ_{R}
$[\text{Fe}^{\text{III}}\text{Gly}]^{2+}$	0.70	1.05	0.80	≤ 0.01
$[\text{Fe}^{\text{III}}\text{Pyr}]^{2+}$	0.53	1.0	0.46	≤ 0.01
$[\text{Fe}^{\text{III}}\text{Tart}]^{2+}$	0.47	0.44	0.40	0.07
$[\text{Fe}^{\text{III}}\text{Lact}]^{2+}$	0.22	0.40	0.22	≤ 0.002

decay of RCs (Reaction 6) and the oxidation of RCs by oxygen (Reaction 7) could affect the content of the final reaction products.

Clay-assisted photochemical processes

Photochemistry of montmorillonite KSF gives as example of clay-assisted homogeneous light-induced process [5]. The formation of the hydroxyl radical upon the photolysis of KSF was observed in the laser flash photolysis experiments. MV^{2+} , which was known as an acceptor of $\bullet\text{OH}$ radicals, was used to capture the organic radicals. The formation and decay of $\text{MV}^{\bullet}(\text{OH})^{2+}$ radical cation was observed. The removal of the particulate matter did not affect the initial concentration of $\text{MV}^{\bullet}(\text{OH})^{2+}$. Therefore, the leached Fe(III) is responsible for the formation of $\bullet\text{OH}$ radicals upon the photolysis of aqueous KSF samples.

For Na-clays and PILC materials, neither $\bullet\text{OH}$ formation nor Fe(III) leaching was not detected. Nevertheless, these catalysts exhibit a sufficient effect on phenol photoionization [6]. Both aquated electrons and phenoxy radicals were monitored in laser flash photolysis experiments. The increase in quantum yields of PhO^{\bullet} radicals formation (20-90%, Table 2) was explained by the heterogeneous processes. Two reaction pathways are possible: (i) electron transfer from a phenol molecule situated in the solution bulk to a Fe(III) cation located on the clay surface, and (ii) electron transfer from a phenol molecule adsorbed to the catalyst surface.

Table 2. Relative quantum yields of PhO[•] radicals formation (φ/φ_0) upon the photolysis of phenol in the presence of Na-clays and PILC.

Sample	[Fe] (mg/g)	pH (1g/L)	φ/φ_0
Na-AS	50 ± 1	8.0	1.2 ± 0.2
Al,Fe-AS	50 ± 1	6.1	1.2 ± 0.2
Na-LAS	50 ± 1	6.3	1.9 ± 0.3
Al,Fe-LAS	50 ± 1	5.5	1.5 ± 0.2

CONCLUSIONS

Photolysis of Fe(III) carboxylates plays an important role in the photochemical processes occurring in natural aqueous systems with pH value close to neutral. The formation of long-lived radical complexes could affect the content of final reaction products.

Effect of montmorillonite KSF clay suspension on photodegradation of organic compounds is explained by reactions of the leached Fe(III) cations. For Na-clays and PILC materials the photocatalytic effect is caused by heterogeneous reactions.

ACKNOWLEDGEMENT

The work was supported by the Russian Foundation of Basic Research (grant № 12-03-00482-a).

REFERENCES

- [1] I.P. Pozdnyakov, V.F. Plyusnin, V.P. Grivin, D.Yu. Vorobyev, N.M. Bazhin, S. Pages, E. Vauthey, *J. Photochem. Photobiol. A: Chem.*, 2006, 181, 37-43.
- [2] M.N. Timofeeva, S.Ts. Khankhasaeva, Yu.A. Chesalov, S.V. Tsybulya, V.N. Panchenko, E.Ts. Dashinamzhinova, *Appl. Catal. B: Environ.*, 2009, 88, 127-134.
- [3] B.S.Faust, R.G. Zepp, *Env. Sci. Technol.*, 1993, 27, 2517-2522.
- [4] E.M. Glebov, I.P. Pozdnyakov, V.P. Grivin, V.F. Plyusnin, X. Zhang, F. Wu, N. Deng, *Photochem. Photobiol. Sci.*, 2011, 10, 425-430.
- [5] X. Zhang, F. Wu, N. Deng, I.P. Pozdnyakov, E.M. Glebov, V.P. Grivin, V.F. Plyusnin, N.M. Bazhin, *React. Kinet. Catal. Lett.*, 2008, 94, 207-218.
- [6] E.M. Glebov, I.P. Pozdnyakov, V.P. Grivin, V.F. Plyusnin, N.M. Bazhin, X. Zhang, F. Wu, M.N. Timofeeva, *Photochem. Photobiol. Sci.*, 2013, 12, 1939-1947.

DESORPTION OF ^{137}Cs FROM *BRACHYTHECIUM MILDEANUM* (SCHIMP.) SCHIMP MOSS USING ACID SOLUTIONS

A. Čučulović¹ and D. Veselinović²

¹*INEP-Institute for the Application of Nuclear Energy, University of Belgrade, Banatska 31b, 11080 Zemun, Serbia, anas@inep.co.rs*

²*Faculty of Physical Chemistry, University of Belgrade, P.O. Box 137, 11000 Belgrade, Serbia*

ABSTRACT

Desorption of ^{137}Cs from *Brachythecium mildeanum* (Schimp.) Schimp moss was performed. The following solutions were used for desorption: H_2SO_4 (**I**), HNO_3 (**II**) and their mixture $\text{H}_2\text{SO}_4\text{-HNO}_3$ (**III**), with pH values of 4.61; 5.15 and 5.75; and also distilled water (**D**) pH 6.50. After five successive desorptions, each lasting 24h, 20.5-37.6% ^{137}Cs was desorbed from the moss using the solutions, while 30.7% of the starting content was desorbed using distilled water. The first desorption desorbed the highest amount of ^{137}Cs (11.3%-18.4%) compared to the starting content in moss. It was determined by measuring activity.

INTRODUCTION

The leading radionuclide, from the viewpoint of the formation of tissue doses and radio-biological consequences is ^{137}Cs (chemical and biochemical homologue of potassium). The physical half-life of ^{137}Cs in moss is long (30.2 years). The retention time of ^{137}Cs in an organism also depends on damages in the organism it is polluting. The accident in Chernobyl (26.4.1986, Ukraine) released a large amount of polluting radionuclides into the environment – 10^{18} Bq, of which 3.7×10^{16} Bq of ^{137}Cs [1].

Moss is an ancient, primitive group of organisms with a specific structure and specific ecology compared to higher flora.

They are good bioindicators and biomonitors of pollution of the environment as they cannot excrete absorbed materials, but accumulate them in tissue or on the surface in amounts depending on their adaptability to chemical changes in the environment [2-4].

Air pollutants are deposited on mosses in three ways: as an aqueous solution (rain, fog), in gaseous form or as disperse particles. The accumulation of pollutants in mosses occurs through a number of different mechanisms.

Atmospheric fallout reaches moss by moist fallout (rain, snow, dew) or dry fallout (sedimentation, aerosols soot). Salts and other solid substances and different gases dissolve in atmospheric water. Acid rain is fallout polluted by acids formed from SO_2 , NO_x and dissolving other acidic compounds. In a polluted atmosphere pH values of the fallout can be significantly changed. In our previous work we followed desorption of ^{137}Cs from *Homalothecium sericeum* (Hedw.) Schimp moss using acid solutions (pH from 4.60 to 5.75) [5], while in this work we analyzed *Brachythecium mildeanum* (Schimp.) Schimp moss. In this work we attempted to investigate whether ^{137}Cs could be isolated with acid solutions as simulated acid rain without destruction of the moss cellular structure, which would imply that the whole amount of ^{137}Cs in the plant is ion-exchangeable.

EXPERIMENTAL

Brachythecium mildeanum (Schimp.) Schimp moss, originating from the National park Djerdap, Serbia, was collected in 2006, (10 g dry mass) and covered with 200 mL of distilled water (D) and acid solutions: (I) H_2SO_4 , (II) HNO_3 and (III) $\text{H}_2\text{SO}_4\text{-HNO}_3$. Solutions (I) and (II) were made by adding concentrated H_2SO_4 , HNO_3 , respectively to 200 mL of distilled water (pH 6.50) to the required pH value: 4.60; 5.15 and 5.75. Solution (III) was obtained by mixing 100 mL of solution (I) and 100 mL of solution (II) with identical pH values. Samples were consecutively desorbed with a solution five times and desorption series were repeated twice. Desorptions were performed at room temperature and lasted 24 hours. After each desorption, after filtration, moss samples were dried at room temperature to a constant mass. In this work we have used the described method for ^{137}Cs desorption from moss, the same as in our previous papers [5,6], as there is no standard method for ^{137}Cs desorption. Activity levels of ^{137}Cs were measured in samples before and after each desorption on an ORTEC-AMETEK gamma spectrometer with 8192 channels, resolution of 1.65 keV and efficiency of 34% at 1.33 MeV ^{60}Co , with a measurement error below 5%. Specific activities were calculated based on measurements (Bq/kg). The pH value of a solution was measured on a pH meter (MA 5730 Iskra).

RESULTS AND DISCUSSION

Table 1 shows the activity of ^{137}Cs (Bq/kg) in *B. mildeanum* (Schimp.) Schimp moss before desorption and the percentage of non-desorbed ^{137}Cs in moss after each of the five consecutive desorptions using solutions (I), (II) and (III), and also distilled water (D), and also the total amount (%) of desorbed ^{137}Cs . Activity levels of ^{137}Cs in samples of moss before desorption were from 3417 Bq/kg to 3463 Bq/kg. Five successive steps with

distilled water desorbed 30.7% of the initial $^{137}\text{Cs}^+$ in *B. mildeanum*. With acid solutions (I), (II) and (III) the amount of total desorbed $^{137}\text{Cs}^+$ ranged from 20.5% (III, pH 5.75) of the initial radiocesium in moss to 37.6% (I, pH 4.60). Comparing obtained results with the previous ones obtained for desorption from *H. sericeum* moss (from 22.8% (III, pH 5.75) to 33.2% (III; pH 4.60), distilled water 31.8%), leads to the conclusion that the moss type does not influence on ^{137}Cs desorption. The first desorption, in accordance with previous research, desorbed the most ^{137}Cs in relation to the starting activity in moss (11.3%-18.4%).

Changes in the desorbed amount of ^{137}Cs depending on the number of consecutive desorptions give exponential curves.

Table 1. Activity of ^{137}Cs in moss before desorption (Bq/kg), percentage of remaining ^{137}Cs in moss after each desorption, total desorbed ^{137}Cs from moss (%) and values of the starting activity of ^{137}Cs (C_{0e}), determined by extrapolation of the curves, given as a percentage in relation to the values of $C_0(100\%)$ in starting solution*

pH	4.60			5.15			5.75			6.50
Solution	I	II	III	I	II	III	I	II	III	D
Activity of ^{137}Cs in moss before desorption (Bq/kg)										
	3417	3422	3463	3433	3435	3459	3421	3439	3445	3438
Percentage of remaining ^{137}Cs in moss after each desorption (%)										
I	82.9	84.2	87.2	81.6	81.6	86.8	88.7	83.1	87.2	83.7
II	70.1	76.1	80.1	75.3	75.3	81.2	82.1	77.8	84.1	75.2
III	66.0	72.7	76.9	72.1	72.1	77.1	75.8	75.7	82.9	72.1
IV	63.7	70.0	75.9	70.1	70.1	76.6	75.2	73.5	80.7	70.1
V	62.4	68.8	75.0	69.0	69.0	76.2	74.7	73.1	79.5	69.3
Total desorbed ^{137}Cs from moss (%)										
	37.6	31.2	25.0	31.0	31.0	23.8	25.3	26.9	20.5	30.7
C_{0e} (%)	83.5	86.1	88.2	83.1	83.1	88.2	90.0	90.5	88.2	87.4
ΔC_0^{**}	16.5	13.9	11.8	16.9	16.9	11.8	10.0	9.50	11.8	12.6

* solution compositions are given in the Material and Methods

** $\Delta C_0 = 100 - C_{0e}$ (%)

Using equation (1) from our previous paper [5]

$$\ln C_x = \ln C_0 - an_x \quad (1)$$

i.e. the change of the sorbed amount of substance, C_x , in the sorbent with the desorption number, n_x , for successive desorptions with the same volume of desorption solution the value C_0 has been determined by extrapolation on

$n_x=0$, C_0 is the content of the sorbed substance (^{137}Cs) before desorption and a is a constant.

From Eq. (1), it follows that the dependence of the logarithm of the amount of sorbed substance in the solid state is a linear function of the number of successive volumes employed during desorption. For real systems, this is valid when only one type of sorption exists, or if one type is dominant, so that the others can be disregarded

CONCLUSION

The results indicate that NO_3^- and SO_4^{2-} anions do not have a significant influence on desorption of ^{137}Cs . Reduction of the percentage of desorbed ^{137}Cs with the increase of the pH value, i.e. reduction of the concentration of H^+ ions, indicates that they have a significant, but not dominant influence on the desorption of ^{137}Cs from moss. The results of this and previous research [5] indicate that the moss type does not have an influence on ^{137}Cs desorption.

ACKNOWLEDGEMENT

This work was partially supported by the Ministry of Education, Science and Technological development of the Republic of Serbia (Grants no. III43009).

REFERENCES

- [1] Savezni komitet za rad, zdravstvo i socijalnu zaštitu, Nivo radioaktivne kontaminacije čovekove sredine i ozračenost stanovništva Jugoslavije 1986. godine usled havarije nuklearne elektrane u Černobilju, Beograd, 1987.
- [2] A. Čučulović, R. Čučulović, T. Cvetić Antić, D. Veselinović, Arch. Biol. Sci., Belgrade, 2011, 63(4), 1117-1125.
- [3] A. Čučulović, D. Popović, R. Čučulović, J. Ajtić, Nucl. Technol. Radiat., 2012 27(1), 44-51.
- [4] A. Čučulović, R. Čučulović, M. Sabovljević, D. Veselinović, Arch. Biol. Sci., Belgrade, 2012, 64(3), 917-925.
- [5] A. Čučulović, D. Veselinović, Hem. Ind., 2013, 67(6), 975-980.
- [6] A. Čučulović, D. Veselinović, Š.S. Miljanić, J. Serb. Chem. Soc., 2007, 72(7), 673-678.

NONLINEAR MODELLING OF HPLC RETENTION OF A SERIES OF PESTICIDES USING NEURAL NETWORKS WITH BROYDEN-FLETCHER-GOLDFARB-SHANNO ALGORITHM

S. Kovačević¹, S. Gadžurić², L. Jevrić¹, S. Podunavac-Kuzmanović¹,
and M. Vraneš²

¹University of Novi Sad, Faculty of Technology, Department of Applied and Engineering Chemistry, Bulevar cara Lazara 1, 21000 Novi Sad, Serbia

²University of Novi Sad, Faculty of Sciences, Department of Chemistry, Biochemistry and Environmental Protection, Trg Dositeja Obradovića 3, 21000 Novi Sad, Serbia (slobodan.gadzuric@dh.uns.ac.rs)

ABSTRACT

The main aim of this study was to establish the artificial neural networks (ANNs) with the ability to precisely predict the reversed-phase HPLC retention time of a set of 77 pesticides extracted from groundwater based on *in silico* molecular descriptors. After training of 1000 ANNs applying Broyden-Fletcher-Goldfarb-Shanno training algorithm, three of them were selected as the best. The statistical and validation parameters of these networks indicate their outstanding prediction ability.

INTRODUCTION

Artificial neural networks (ANNs) are a nonlinear tool that is usually trained using iterative techniques. The most recommended techniques for training of ANNs are the Broyden-Fletcher-Goldfarb-Shanno (BFGS) and scaled conjugate gradient algorithms [1]. These algorithms perform significantly better than the more traditional algorithms, for example gradient descent. Generally speaking, they are more computationally demanding and memory intensive [1]. However, these algorithms may require a smaller number of iterations for ANN training given their fast convergence rate and more intelligent search criterion.

ANNs can be very useful method in searching for complex relationships between variables. Therefore, they have been applied in many quantitative structure-retention relationship (QSRR) studies, where their main aim is prediction of retention behaviour of analysed compounds [2-5]. In this paper QSRR analysis with ANN method was applied in order to establish suitable model for prediction of retention behaviour of diverse pesticides in reversed-phase (RP) HPLC. Structure-retention relationships can facilitate

insight into the mechanisms governing chromatographic separation. Based on the established QSRRs it is possible to improve separations of compounds by changing chromatographic conditions.

EXPERIMENTAL

The results of chromatographic separation of pesticides, extracted from groundwater samples, are presented in literature [6]. The identified compounds can be classified as fungicides, herbicides, metabolites, insecticides and plant growth regulators. They have neutral, acidic and basic characteristics.

Calculation of 125 2D molecular descriptors (lipophilicity, physicochemical, topological and biological descriptors) was achieved by using SimulationPlus ADMET predictor™, MarvinSketch and Molinspiration software. Stepwise regression procedure was carried out in NCSS & GESS software to obtain most suitable descriptors as input data for the ANNs. ANN analysis was carried out by Statistica 10 program.

RESULTS AND DISCUSSION

Stepwise regression routine presented five molecular descriptors which are the most suitable for prediction of retention time ($\log t_r$). These descriptors are the following: lipophilicity descriptor (KOWWIN), specific inhibition constant for the CYP 3A4-mediated metabolism of testosterone (MET_3A4_Ki_tes), molecular weight (MWt), second order simple connectivity index (χ^2) and maximum sigma Fukui index on carbon (EEM_XFc). These descriptors served as the input and $\log t_r$ was the output data in ANN analysis.

The whole set of compounds was divided into three subsets: training set (53 compounds), test set (12 compounds) and validation set (12 compounds).

The input and output data were processed by multilayer perceptron (MLP) feedforward ANN model with BFGS training algorithm in self-training mode. The values of weights of neurons were predetermined by the applied software. The selection of the most appropriate ANNs was achieved on the basis of correlation coefficients for training set (R_{train}), test set (R_{test}) and validation set (R_{val}), and root mean square errors for training set ($RMSE_{train}$), test set ($RMSE_{test}$) and validation set ($RMSE_{val}$). Analysis resulted in the best three out of thousand trained ANNs, which can be applied for precise prediction of $\log t_r$. The architectures of selected networks are presented in Table 1.

Table 1. The architectures of the established networks.

Net. name	Hidden activation	Output activation
MLP 5-10-1	Tanh	Identity
MLP 5-8-1	Exponential	Tanh
MLP 5-17-1	Tanh	Tanh

Statistical characteristics of selected networks are presented in Table 2. As it can be seen from the data in Table 2, the networks have quite similar statistical characteristics.

Table 2. Characteristics of the established neural networks.

Net. name	R_{train}	R_{test}	R_{val}	RMSE _{train}	RMSE _{test}	RMSE _{val}
MLP 5-10-1	0.9614	0.9256	0.9772	0.0028	0.0035	0.0035
MLP 5-8-1	0.9830	0.8996	0.9747	0.0012	0.0044	0.0038
MLP 5-17-1	0.9827	0.9031	0.9747	0.0012	0.0039	0.0043

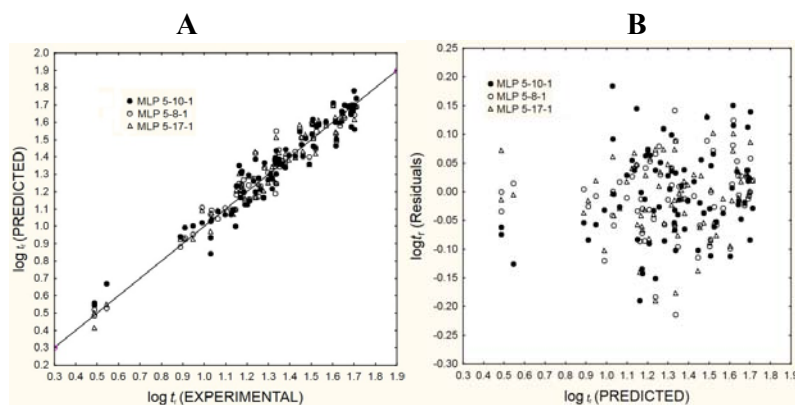
**Figure 1.** Comparison of the experimental and predicted $\log t_r$ values (A) and distribution of residuals (B).

Figure 1A indicates an excellent concurrence between the experimental and predicted $\log t_r$ data. This is confirmed with the random distribution of the residuals around $y = 0$ axis and their low values (Figure 1B). The low RMSE values, high correlation coefficients ($R > 0.90$) and the magnitude of the residuals indicate an outstanding fitting of the experimental and predicted $\log t_r$ data with the established neural networks. Therefore, they can be used for precise prediction of the retention behaviour of structurally similar pesticides under the applied chromatographic conditions.

The influence of every molecular descriptor in input layer on variations of $\log t_r$ is estimated by global sensitivity analysis. The sensitivity coefficients describe the change in the network's outputs due to variations in the

parameters that affect the network [7]. The sensitivity index values for input variables for all three ANNs are presented in Table 3. Global sensitivity analysis showed that lipophilicity parameter KOWWIN has the highest influence on variations in $\log t_r$ values.

Table 3. The results of global sensitivity analysis.

Descriptor	MLP	MLP	MLP
	5-10-1	5-8-1	5-17-1
KOWWIN	8.4	32.3	14.3
MWt	3.1	9.9	2.5
MET_3A4_Ki_tes	4.4	5.5	4.9
χ^2	3.2	5.1	3.8
EEM_XFc	1.3	1.4	1.1

CONCLUSION

Applied descriptors selection method and artificial neural networks methodology with BFGS algorithm resulted in three outstanding networks which can successfully be used for prediction of the retention behaviour of structurally similar pesticides in RP-HPLC.

Sensitivity analysis revealed that the lipophilicity parameter KOWWIN has the highest influence on $\log t_r$ values in all three selected networks.

ACKNOWLEDGEMENT

This paper was performed within the framework of the research projects No. 172012 and No. 172014 supported by the Ministry of Education, Science and Technological Development of the Republic of Serbia and the project No. 114-451-2373/2011, financially supported by the Provincial Secretariat for Science and Technological Development of Vojvodina.

REFERENCES

- [1] C. M. Bishop, *Neural networks for pattern recognition*, Clarendon Press, Oxford, 1995.
- [2] Z. Garkani-Nejad, *Chromatographia*, 2009, 70, 869-874.
- [3] E. Konož, A. H. M. Sarrafi, A. Feizbakhsh, *Z. Dashtbozorgi, Journal of Chemistry*, 2013, 2013, 1-13.
- [4] H. Karimi, H. Noorizadeh, A. Farmany, *ISRN Chromatography*, 2012, 2012, 1-9.
- [5] A. G. Fraggaki, E. Farmaki, N. Thomaidis, A. Tsantili-Kakoulidou, Y. S. Angelis, M. Koupparis, C. Georgakopoulos, *Journal of Chromatography A*, 2012, 1256, 232-239.
- [6] K. Vandecasteele, I. Gaus, W. Debreuck, K. Walraevens, *Analytical Chemistry*, 2000, 72, 3093-3101.
- [7] M. H. Shojaeefard, M. Akbari, M. Tahani, F. Farhani, *Advances in Materials Science and Engineering*, 2013, doi:10.1155/2013/574914

HEAVY METALS AND POLYCYCLIC AROMATIC HYDROCARBONS ASSOCIATED TO AIRBORNE PM10 IN GYŐR, HUNGARY

Zs. Csanádi, A. Szabó Nagy and J. Szabó

Department of Physics and Chemistry, Széchenyi István University, Egyetem square 1, H-9026 Győr, Hungary. (csanadi.zsofia@sze.hu)

ABSTRACT

Atmospheric concentrations of some heavy metal compounds (Pb, Cd, As, Ni) and polycyclic aromatic hydrocarbons (PAHs) were identified and determined in airborne PM10 particles in an urban area of Győr, northwest area of Hungary in 2011. The PM10 concentrations ranged from 11 to 119.14 $\mu\text{g}/\text{m}^3$ with the mean value of 47.43 $\mu\text{g}/\text{m}^3$. The annual average concentration of PM10 indicates a polluted area however the PM10 levels in the sampling periods without heating show excellent or good air quality. The levels of heavy metals indicate an excellent air quality. The total PAH concentrations (sum of the concentrations of 19 individual PAH compounds) varied between 0.88 and 95.80 ng/m^3 with the mean value of 20.06 ng/m^3 . The annual average concentration of benzo[*a*]pyrene was two times higher than the EU air quality target value.

INTRODUCTION

Atmospheric aerosols play an important role in air quality. Monitoring the particulate matter with an aerodynamic diameter smaller than 10 μm (PM10) and PM10-bound heavy metals and polycyclic aromatic hydrocarbons (PAHs) could have important environmental significance and health protection aspects [1].

The aim of this work was to give an overview about the levels of some selected heavy metals (Pb, Cd, As and Ni) and PAHs in the PM10 aerosol fraction in an urban area of Győr, Hungary with high traffic density during the year 2011. Győr is a dynamically developing city due to its good geographic situation and as an emphasized centre in automotive industry. The Industrial Park of Győr provides place for significant and varied industrial activity. The levels of pollutants determined in our study were compared with the EU and the Hungarian air quality standards [1-3]. The Hungarian air quality index (AQI) was also used for the assessment [2].

EXPERIMENTAL

Győr (47°41'02"N, 17°38'06"E) is the most important city in the northwest area of Hungary halfway between Wien, Bratislava and Budapest situated on one of the important roads of Central Europe. The city is the sixth largest in Hungary, and one of the seven main regional centres of the country. The number of inhabitants is about 128,500. The sampling site is located at the junction of Tihanyi Árpád street and Ifjúság boulevard, where the main pollution source is the traffic.

PM10 aerosol samples were collected in four sampling periods at 14 day intervals, continuously for 24 hours in 2011 at the monitoring site of Győr. A Digital High Volume DHA80 (Digital Elektronik AG, Switzerland) sampler was used for collection ambient aerosol particles, which were chemically analysed later. Samples are taken onto high purity Advantec QR-100 quartz fibre filters (size: 150 mm diameter) for a period of 24 h at a flow rate of 30 m³/h into a container with about 700 m³ volume capacity. The particle total mass was determined by weighing of the sampling filters before and after sampling and the PM10 concentration calculated from the weighed mass on the filter and the sampling volume.

The concentrations of heavy metals (Pb, Cd, As and Ni) in the PM10 aerosol fraction were measured by graphite furnace atomic absorption spectroscopy (SOLAAR MQZ, Unicam Ltd., Cambridge, UK) equipped with Zeeman and deuterium background correctors, a graphite furnace GF9 and an autosampler according to the Hungarian standard method procedure [4]. The liquid-solid extraction of other half of the filter and PAH analysis were conducted in accordance with the Hungarian standard method procedure [5]. A gas chromatography-mass spectrometry (GC/MS) system consisting of an Agilent 6890 gas chromatograph with an Rtx-5MS Integra GC column and an Agilent 5973 mass spectrometer was used in the study.

RESULTS AND DISCUSSION

Table 1 shows the data measured for PM10 aerosol fraction with heavy metal and PAH compounds. The PM10 concentrations varied between 11 and 119.14 µg/m³ with the mean value of 47.43 µg/m³. The highest concentration was detected in winter. The annual average mass concentration of PM10 slightly exceeded the EU and the equivalent Hungarian limit value (40 µg/m³). The reason is probably the effect of public heating. The annual AQI for PM10 indicate a polluted area. The comparison of the 24-hour PM10 concentrations with the 24-hour AQI values show acceptable, polluted or heavily polluted results in heating season, while indicate excellent or good air quality in the samplings of spring and summer.

The annual average concentrations of each heavy metal (Pb, Cd, As and Ni) observed for Győr were below the permitted levels. The AQI results show that the study area has excellent air quality with respect to heavy metals.

The total PAH concentrations ranged from 0.88–95.80 ng/m³ with the mean value of 20.06 ng/m³. Four and five-ring PAHs including fluoranthene, pyrene and benzo[*b+k+j*]fluoranthene were the dominant species in the samples. The best known PAH compound is the highly carcinogenic benzo[*a*]pyrene (BaP) [6]. The concentration of BaP ranged from 0.41 to 6.92 ng/m³ with the mean of 2.97 ng/m³ in winter, and ranged from 0.02 to 0.43 ng/m³ with the mean of 0.09 ng/m³ in the sampling periods without public heating. The annual average concentration of BaP was two times higher than the EU and the equivalent Hungarian air quality target value (1 ng/m³). According to the Hungarian annual average limit value for BaP (0.12 ng/m³) the AQI indicate a heavily polluted area.

Table 1. Concentrations of PM10, heavy metals and PAHs in an urban site of Győr in 2011

Compound	Sampling period			
	16 February– 1 March	4–17 May	1–14 August	1–15 November
PM10 µg/m ³	46.59–110.68	15.39–29.44	11.00–29.10	42.60–119.14
Heavy metals ng/m ³				
Pb	11.11–40.75	2.95–17.00	1.34–7.08	7.53–24.81
Cd	0.20–0.73	0.28–1.34	0.05–0.53	0.19–0.57
As	0.25–1.21	0.28–1.04	0.26–6.64	0.24–1.32
Ni	1.03–19.53	2.22–5.86	3.13–8.64	1.23–5.91
PAHs ng/m ³				
Naphthalene	0.58–0.90	0.11–0.64	0.29–0.38	0.18–0.31
2-Methylnaphthalene	0.35–0.83	0.12–0.32	0.10–0.19	0.04–0.09
Acenaphthylene	0.03–0.99	ND	ND	ND–0.02
Acenaphthene	0.02–0.13	ND–0.03	ND	ND
Fluorene	0.07–0.91	0.03–0.09	0.03–0.04	ND–0.02
Phenanthrene	1.12–7.58	0.10–0.28	0.09–0.14	0.02–0.37
Anthracene	0.08–0.80	ND–0.03	ND–0.02	ND–0.06
Fluoranthene	2.04–17.70	0.11–0.53	0.03–0.09	0.28–5.43
Pyrene	1.59–12.12	0.09–0.50	0.04–0.09	0.40–6.54
Benz[<i>a</i>]anthracene	0.79–6.19	0.03–0.14	0.01–0.07	0.19–6.99
Chrysene	1.17–4.62	0.08–0.26	0.02–0.09	0.27–6.72
Benzo[<i>b+k+j</i>]fluoranthene	3.52–16.39	0.25–1.51	0.06–0.26	0.96–10.41
Benzo[<i>e</i>]pyrene	2.32–9.15	0.11–0.53	0.03–0.12	0.25–3.06
Benzo[<i>a</i>]pyrene	0.87–6.86	0.03–0.43	0.02–0.09	0.41–6.92
Indeno[123- <i>cd</i>]pyrene	0.81–7.88	0.06–0.45	0.03–0.11	0.43–5.36
Dibenz[<i>ah</i>]anthracene	0.09–0.96	ND–0.05	ND–0.07	0.04–0.76
Benzo[<i>ghi</i>]perylene	0.89–6.43	0.07–0.52	0.03–0.12	0.32–3.61
Total PAHs	16.95–95.80	1.33–5.09	0.88–1.68	4.20–56.56

ND: Not detected

CONCLUSION

PM10 aerosol samples were collected in the urban site of Győr, Hungary during four sampling periods in 2011. Concentrations of heavy metals (Pb, Cd, As and Ni) and 19 individual PAH compounds were analysed from the samples.

The annual average concentration of PM10 indicates a slightly polluted area. However, the concentrations of PM10 exhibit large variability during the sampling periods. Levels of airborne heavy metal compounds were relatively low, below the permitted concentrations. The annual average concentration of BaP was two times higher than the EU air quality target value. However, the concentrations of BaP show large variability during the sampling periods with and without public heating.

ACKNOWLEDGEMENT

We are indebted to József Erdős, István Vass, Bálint Kauker, Zsuzsanna Károly Némethné, Tünde Takács Kovácsné, Lajosné Bakódy and Péter Lautner (North Transdanubian Regional Environmental Protection and Nature Conservation Inspectorate Laboratory, Hungary) for chemical analyses and site information.

REFERENCES

- [1] EEA, Air quality in Europe - 2013 report, European Environment Agency, Luxembourg, 2013.
- [2] OMSZ ÉLFO, Summary of the OLM PM10 sampling program in 2011, Reference Centre for Air Quality Protection, 2012. (in Hungarian)
- [3] 4/2011 (I.14.), Guidelines for the air load levels and the stationary point source emissions. (in Hungarian)
- [4] MSZ EN 14902:2006, Ambient air quality. Standard method for the measurement of Pb, Cd, As and Ni in the PM10 fraction of suspended particulate matter.
- [5] MSZ ISO 12884:2003, Ambient air. Determination of total (gas and particle-phase) polycyclic aromatic hydrocarbons. Collection on sorbent-baked filters with gas chromatographic/mass spectrometric analyses.
- [6] F. Wania, D. Mackay, Environ. Sci. Technol., 1996, 30, 390-395.

WATER QUALITY OF LAKE PALIĆ IN THE PERIOD 2011-2013

T. D. Grozdić, A. Hegediš, M. Nikčević and G. Mesaroš

*Institute for multidisciplinary research, Kneza Višeslava 1a, 11000 Belgrade,
Serbia(gtomisi@imsi.bg.ac.rs)*

ABSTRACT

Determination of water quality is based on the results of the physico-chemical parameters of Lake Palić. Water sampling was carried out on the first and third embankments and in the fourth sector of Lake Palić, in the period from 2011 to 2013. Apart from examining the physico-chemical parameters of the quality of water of Lake Palić, the Serbian Water Quality Index (SWQI) was determined, as well as the concentration of chlorophyll "a", saprobity index (Pantle-Buck) and lake trophicity. The aim of the research is to determine water quality of the lake, and the impact of the treatment plants for municipal water and wastewater from the towns of Subotica and Palić on the water quality of the lake.

INTRODUCTION

Lake Palić is divided into four sectors [1 and 2]. Treated wastewater (municipal and industrial) from the town of Subotica is discharged into the first sector of the lake (from the central treatment plant), while lake water drains from the fourth sector into the Palić-Ludaš canal, and from there into Lake Ludaš and the river Tisa.

Since over time it was determined that treated wastewater from Subotica is still burdened with organic matter, nitrogen and phosphorus compounds, reconstruction and expansion of the existing facilities for wastewater treatment began in 2006. The plant capacity was increased from 26000 m³ to 32000 m³ on a non-rainy day or 72000 m³ on a rainy day. The reconstruction and expansion were completed in 2009 [2].

In order to test water quality in Lake Palić the following is tested: physico-chemical, microbiological and biological parameters, and water quality index (SWQI) is determined [3, 4 and 5]. The paper discusses the above parameters, obtained by analysing the quality of the lake water in the period 2011-2013. The aim of this paper is to demonstrate the impact of the city wastewater treatment plant operations on the quality of the water of Lake Palić.

EXPERIMENTAL

Physicochemical analysis of water quality of the lake includes the following parameters: water temperature, pH, percentage of oxygen saturation, chemical oxygen demand (COD from KMnO_4), a five-day biological oxygen demand (BOD_5), content of suspended solids, total nitrogen, total phosphorus, and chlorophyll "a" [3]. Determination of these and all other parameters was performed by the authorized laboratory – the Institute of Public Health of Subotica. Sampling was done at the lake entrance (I embankment), in the lake (III embankment) and at the lake outlet (IV sector). Determination of chlorophyll "a" was performed in the years from 2011 to 2013. Heavy metals, pesticides and other industrial pollution are on the borderline of sensitivity and, therefore, were not considered in the paper. Samples for quantitative analysis were collected with a 2L hydrobiological bottle from different depths of the lake. The samples were immediately stabilized in 4% formaldehyde in plastic bottles, with the volume of 1 litre. The content of chlorophyll "a" was determined by spectrophotometry. Saprobiological analysis was performed using the index by Felfoldy or Carlson and based on the use of phytoplankton as an indicator of the degree of saprobity. The obtained average monthly results' values will be analysed in this paper.

RESULTS AND DISCUSSION

Based on the water quality testing of Lake Palić in 2011, 2012, and 2013, high levels of suspended solids were noted. Their data are similar to those in 2005 [6], i.e. in the period before the reconstruction of the central treatment plant for wastewater of Subotica. These values were increasing from year to year, as can be seen from the Table 1. Unequal values of suspended matter can be observed depending on the location of water sampling – at the lake entrance (1st embankment), in the lake (3rd embankment) and at the lake outlet (4th sector). The minimum value of 9 mg/L was recorded in December 2013 (4th sector), and the maximum of 100 mg/L in April 2012 (4th sector). According to a certain amount of suspended solids in the 4th sector, whence from the water drains to the final recipient – the river Tisa, water quality is at the upper limit for Class III, which it often exceeds, and so it is sometimes in Class IV of water quality. Saprobic index by Felfoldy or Carlson is determined by the bioindicator value representative of plankton community and is in the range of 2.00 to 2.39.

Serbian Water Quality Index (SWQI) characterized the water in Lake Palić as poor, throughout 2012 and 2013, see Table 1.

Based on the results of water quality testing it was concluded that the degree of saprobity in all cases is defined as β -mesoeutrophic [6].

Table 1. Indicators of water quality (SWQI) in 2012 and 2013. Samples of water from the 3rd embankment and 4th sector of Lake Palić.

	Jan. 2012	Feb. 2012	Mar. 2012	Apr. 2012	May 2012	Jun. 2012
3 rd emb.	64	63	60	60	59	53
4 th sec.	64	58	59	52	60	60
	Jul. 2012	Aug. 2012	Sep. 2012	Oct. 2012	Nov. 2012	Dec. 2012
3 rd emb.	53	50	50	43	60	56
4 th sec.	41	42	50	41	59	53
	Jan. 2013	Feb. 2013	Mar. 2013	Apr. 2013	May 2013	Jun. 2013
3 rd emb.	55	61	61	55	49	53
4 th sec.	67	62	59	63	56	41
	Jul. 2013	Aug. 2013	Sep. 2013	Oct. 2013	Nov. 2013	Dec. 2013
3 rd emb.	51	51	44	52	50	75
4 th sec.	44	44	57	48	48	73

By analysing the results of physico-chemical analysis of the parameters, which are indicators of the organic load in the water, it can be established that the waters of Lake Palić are still very burdened with organic pollution. Concentrations of nutrients, as indicators of water quality, are also on the rise. Concentration of total nitrogen increased in all localities of the lake, and concentration of total phosphorus is high and uniform throughout the year. High concentrations of nitrogen, ammonia nitrogen and phosphorus have as a result an intensive organic production, with negative

consequences on the eutrophication of the lake.

The regime of oxygen throughout the year is in negative state for the 1st and 3rd embankments and 4th sector of the lake. Due to a constant load of organic substances perennial hyperproduction of phytoplankton is present. As a consequence of this state, we note uniformly high concentrations of oxygen, extremely high pH values, as well as significant amounts of suspended solids.

Based on the saprobity index, water quality of the 1st sector corresponds to Classes III-IV of water quality. Water quality of the 4th sector belongs to Class IV, and sometimes it is beyond the prescribed classes of water quality. Based on these facts, it can be concluded that the water quality at the outlet of the lake is worse than at the lake entrance. Based on the results of several years of water quality testing, a trend of increasing saprobity of the lake is found. High density and biomass of phytoplankton was also detected, as well as concentration of chlorophyll "a", all of which points to an intense eutrophication of the lake, which is mesoeutrophic by nature.

CONCLUSION

Serbian Water Quality Index (SWQI) characterized the water in Lake Palić as poor, throughout 2012 and 2013.

Since the lake is the recipient of treated wastewater from Subotica, the quality of treated wastewater (effluent) is of great importance for water quality of the lake. It is very important that the newly built treatment plants for wastewater (municipal and primarily treated industrial wastewater) from Subotica and Palić resorts, through efficient operation, not provide lower content of organic matter and nutrients in the water after waste treatment [6].

Water pollution is affected to a great extent by the fact that Lake Palić is an unstable ecosystem, with a large amount of sludge and increased eutrophication process.

ACKNOWLEDGEMENTS

This research has been carried out thanks to the resources of the project TR 39007 Ministry of Education and Science of the Republic of Serbia.

REFERENCES:

- [1] Dj.Seleši, Voda Palićkog jezera od 1781. do 1999. godine., JVP Palić-Ludaš, Subotica, 2000.
- [2] Dj.Seleši, Voda Ludaškog jezera., JVP Palić-Ludaš, Subotica, 2006.
- [3] ISO 10260 Water quality: Measurement of biochemical parameters- Spectrometric determination of the chlorophyll-a concentration, 1992.
- [4] Uredba o klasifikaciji voda i kategorizaciji vodotokova , Sl. list SFRJ, br. 6/78; Zakon o vodama, Sl.glasnik RS, 30/2010 and 93/2012.
- [5] Pravilnik o nacionalnoj listi indikatora zaštite životne sredine, Sl.glasnik RS, 37/2011.
- [6] T.Grozdić,A.Hegediš,M.Nikčević and G.Mesaroš, Kvalitet vode jezera Palić, *Ecologica*, 2011, 64, 657-663.

WATER QUALITY OF PROTECTED NATURE RESERVE “UVAC”

T. D. Grozdić, A. Hegediš, M. Mićković and Z. Gačić,

*Institute for multidisciplinary research, Kneza Višeslava 1a, 11000 Belgrade,
Serbia, (gtomisi@imsi.bg.ac.rs)*

ABSTRACT

The research plan anticipates the determination of water quality by determining physico-chemical parameters, and ichthyological researches of water accumulations Uvac, Zlatar and Radoinja. The aim of the research is to define the quality of water and other impacts on the ecological status.

Water samples were taken in the same location, before and after the hydroelectric power plant in August and November 2011. Ichthyological researches in the accumulations were done in the course of several years, in April 2007, April, July and August 2008.

INTRODUCTION

"Decree on the Amendments of the Decree on the Protection of Special Nature Reserve "Uvac" (Official Gazette of the Republic of Serbia, no. 25/06) [1], determined the protection zone of the Special Nature Reserve "Uvac", thus including in the protected area all the waters of the Uvac basin upstream from the dam profile on the accumulation "Radoinja". The main reasons for amending the Decree on the Protection of Special Nature Reserve "Uvac" are the provision of the integral protection of the area that represents a unique natural and functional unit, and raising the management organization of the protected nature reserve to a higher level. The protected area is characterized by high levels of biodiversity, with a prominent presence of rare and endangered species of national and international importance. In addition to being an important component of the overall diversity, ichthyofauna of this area is also an important natural resource whose sustainable use can greatly improve the management and protection of the natural reserve.

Previous researches concerning the area under consideration were inadequate and incomplete. In the past thirty years, they mainly took place in the form of making medium-term plans for the improvement of fishery within the fishing areas to which these waters belonged before the separation. Current state of the research and status of the discussed aquatic habitats within the reserve require systematic environmental and fishery

wise research, in order to acquire the basis for the sustainable use of fish resources, with the simultaneous application of modern conservation measures.

EXPERIMENTAL

Samples for quantitative analysis were collected with a 2L hydrobiological bottle from the surface. The samples were immediately stabilized in 4% formaldehyde in plastic bottles, with the volume of 1 litre. Physicochemical tests included the following parameters: pH, oxygen saturation percentage, COD, BOD₅, consumption of KMnO₄, content of suspended solids, nitrate, nitrite and total phosphorus [2 and 3]. Determination of the above parameters was performed by the Institute for Occupational Safety, Novi Sad, for the year 2011. Sampling and analysis were carried out twice a year, before and after the hydroelectric power plant (HPP). Sampling and testing was done for the waters of Lakes Uvac, Zlatar and Radoinja. The analysed results are for August and November 2011. Samples of the fish fauna were taken from representative profiles. Identification of the species was carried out in accordance with Simonović (2001) [4].

RESULTS AND DISCUSSION

Based on the physicochemical parameters of the lake water, Uvac belongs to Class II, see Table 1. Some parameters are above the maximum permissible concentration (MPC), and these are ammonia, nitrite, dissolved oxygen and BOD₅. The increased concentration of ammonia was detected in August 2011, when an increased consumption of KMnO₄ and increased concentration of suspended solids were noticed. After three months the sample was taken again, and then some variation of the above parameters was observed. The concentration of suspended solids is reduced almost by half but there is an increase in the concentration of BOD₅, nitrate and ammonia. All this indicates that after the induced increase of the above mentioned MPC parameters, the disintegration of the organic material occurs. The ecosystem is trying to establish balance i.e. self-purification occurs.

Table 1. Physico-chemical parameters of water quality of Lake Uvac measured August and November 2011th year.

Parameter	Lake Uvac			
	August		November	
	upstream of HPP	downsrem to HPP	upstream of HPP	downsrem to HPP
Height above sea level (m)	962-978			
Water tempe- rature (°C)	22.7	23.5	11.1	11
Dissolved oxygen (mg/l)	4.96	5.11	4.96	5.01
Conductivity (µS/cm)	214	232	264	260
pH value	8.20	8.19	8.09	8.13
Turbidity	24.8	23.9	8.5	7.6
Amonijak	0.63	0.54	0.85	0.42
Nitrites	0.07	0.05	0.15	0.11
Nitrates	0.61	0.44	3.58	2.55
Chloride	4.05	5.32	10.02	6.01
COD	48	32	40	18
BOD ₅	6	4	8	4
consumption KMnO ₄	32	24.2	4	0.8
Suspended solids	57	52	19.5	6.5
Total P	<0.2	<0.2	0.22	< 0.2
Fats and oils	3.5	6	29	12
Zn	0.045	0.031	0.014	0.011
Mn	0.002	<0.002	0.029	0.022
Fe	0.059	0.054	<0.06	<0.06
Pb	0.033	0.029	0.053	0.035
As	<0.001	<0.001	<0.001	< 0.001
Hg	<0.001	<0.001	<0.0005	<0.0005
Total coliform bacteria cfu/ml	nd.	nd.	5	1

Hydrological (physico-chemical) parameters of water quality point to a well-preserved environment and favourable conditions for the life of hydrobionics in the waters of the Special Nature Reserve "Uvac". During the research 19 species of fish were documented, representatives of six families (Cyprinidae, Salmonidae, Cobitidae, Gobiidae, Centrarchidae and Gadidae). The most abundant species were of the family Cyprinidae (61.3 %), along with the Salmonidae (11.1 %) and Cobitidae (11.1 %), while the presence of the Gobiidae, Gadidae and Centrarchidae families is 5.5 % (or one species) each [5]. The listed species are mostly autochthonous in the accumulations but partly they are present due to wrong planning of water stocking. Research results for the ichthyological fauna of the accumulations will be presented in another paper.

CONCLUSION

The analysis of the physico-chemical parameters showed that water quality of accumulation Uvac, Zlatar and Radoinja is of Class II. Concentrations of nutrients, as indicators of water quality, are small but increasing, particularly in Lake Radoinja. Concentration of total nitrogen is increased in all locations, while concentrations of total phosphorus are low and consistent throughout the year. The solubility of oxygen is 10-20 % above the maximum allowed concentration in lakes Uvac, Zlatar and Radoinja, and somewhat increased amounts of suspended solids were observed.

ACKNOWLEDGEMENTS

This research has been carried out thanks to the resources of the project TR 39007 Ministry of Education and Science of the Republic of Serbia.

REFERENCES:

- [1] Decree on Amending the Decree on the Protection of Special Nature Reserve "Uvac", Official Gazette of RS, No. 25/06; Uredba o klasifikaciji voda i kategorizaciji vodotokova Sl. list SFRJ, br. 6/78; Zakon o vodama, Sl.glasnik RS,30/2010 and 93/2012.
- [2] ISO 10260 Water quality (1992): Measurement of biochemical parameters-Spectrometric determination of the chlorophyll-a concentration
- [3] R.PANTLE, H.BUCK, Die Biologische Überwachung der Gewässer und die Darstellung der und die Darstellung der 96(18),1955,604.
- [4] P.Simonović, Ribe Srbije. Biološki fakultet, Zavod za zaštitu prirode Srbije i NNK, Beograd, 2001.
- [5] B.Mićković and A.Hegediš, Srednjoročni program unapređenja ribarstva na području Specijalnog rezervata prirode „Uvac“ za period 2006 – 2010 godina, 2006.

VERTICAL DISTRIBUTION OF ^{137}Cs IN THE UNDISTURBED SOIL PROFILES IN THE BASIN OF PČINJA RIVER, SOUTHEASTERN SERBIA

J. Petrović¹, M. Đorđević², M. Đokić², R. Dragović², M. Nikolić², M. Čujić¹ and S. Dragović³

¹University of Belgrade, Institute for the Application of Nuclear Energy, Belgrade, Serbia. (jelenap@inep.co.rs)

²University of Niš, Faculty of Science and Mathematics, Department of Geography, Niš, Serbia.

³University of Belgrade, Vinča Institute of Nuclear Sciences, Belgrade, Serbia.

ABSTRACT

The ^{137}Cs activity concentrations in six undisturbed soil profiles collected during 2013 in the basin of Pčinja River, southeastern Serbia, were determined gamma-ray spectrometrically. Average value of six undisturbed soil profiles by layers was calculated and vertical distribution of ^{137}Cs activity concentration at 5 cm interval samples was shown by average profile. The ^{137}Cs activity concentrations varied between 0.29 and 70.9 Bq kg⁻¹ with a mean of 10.7 Bq kg⁻¹. Even 27 years after Chernobyl accident 74% of deposited ^{137}Cs was found in the first 20 cm of the soil.

INTRODUCTION

Knowledge of ^{137}Cs vertical distribution in soil, which is the ^{137}Cs main reservoir, is very important for an assessment of external dose. The ^{137}Cs vertical migration in soil is influenced by the physico-chemical properties of soils, quantity and intensity of precipitation fallen since ^{137}Cs deposition, absorption and re-deposition by plants and biological characteristics of soils [1]. In the undisturbed soil the ^{137}Cs shows very slow vertical migration. Different characteristics (physical, chemical and biological) of individual soil horizons influence the migration and retention of ^{137}Cs through the profile.

Until 1986 the ^{137}Cs activity concentrations in soil of Serbia was < 5 Bq kg⁻¹, and in most plants, except mosses and lichens, have been below detection limits [2]. Immediately after the Chernobyl accident ^{137}Cs activity concentrations were up to 50 kBq kg⁻¹ in soil [3], with very inhomogeneous spatial distribution, and in some plant species reached 3 kBq kg⁻¹ [2].

Due to strong denudation and fluvial erosion in the basin of Pčinja River southeastern Serbia, soils are washed out from certain locations, especially

from those at higher slopes. The aim of this study was to present the vertical distribution and behavior of ^{137}Cs activity concentration in these soils, based on collected undisturbed profiles.

EXPERIMENTAL

A total of six undisturbed soil profiles were collected during 2013 in the basin of Pčinja River, southeastern Serbia. Soil samples were collected at 5 cm intervals from the uppermost layer down to 50 cm. All samples were dried to constant weight at room temperature. Dried samples were mechanically homogenized, sifted through a 2 mm mesh sieve, packed into 0.5 L Marinelli beakers and weighed.

The ^{137}Cs activity concentration were measured using HPGe gamma-ray spectrometer ORTEC-AMETEK (34% relative efficiency and 1.65 keV FWHM for ^{60}Co at 1.33 MeV). The ^{137}Cs activity concentration of each sample was measured for 3.6 ks. The energy calibration and relative efficiency calibration of the gamma-ray spectrometer were carried out using 0.5 L Marinelli calibration source MBSS2 supplied by Czech Metrological Institute. Gamma Vision 32 MCA emulation software was used to analyzed the gamma-ray spectra [4]. The ^{137}Cs activity concentration was determined from its gamma-ray line at 661.6 keV. The software package SPSS 16.0 (Statistical Package for the Social Sciences) for Windows was employed for descriptive statistics of the results [5].

RESULTS AND DISCUSSION

In order to reveal general behavior of ^{137}Cs in soil in the basin of Pčinja River vertical distribution of ^{137}Cs activity concentration at 5 cm interval samples was shown by average profile (Fig. 1.) which represents calculated average value based on the measured values of ^{137}Cs activity concentration for six undisturbed soil profiles by layers.

It was noted that ^{137}Cs activity concentration decreased with soil depth up to 40 cm and then slightly increased down the profile. The re-distribution of ^{137}Cs in deeper soil layers could be consequence of number of factors. For that reason, further investigation, which would include the influence of e.g. type of soil, chemical properties, organic matter content, biological activity of microorganisms in soil, and climatic conditions (such as rainfall, temperature, or humidity) on the ^{137}Cs distribution in soils are required.

Basic descriptive statistics of ^{137}Cs activity concentration across all six undisturbed soil profiles (all soil layers are consider as equal) is presented in Table 1. The mean value of ^{137}Cs activity concentration was 10.7 Bq kg^{-1} , with a range of 0.29 to 70.9 Bq kg^{-1} .

Petrović et al. (2013) and Dragović et al. (2012) reported mean ¹³⁷Cs activity concentration of 15.3 and 18.5 Bq kg⁻¹, respectively, for Belgrade area [6-7], and Dugalic et al. (2010) reported average ¹³⁷Cs activity

Table 1. Basic descriptive statistics of ¹³⁷Cs activity concentration in soil in the basin of Pčinja River.

Parameter	¹³⁷ Cs (Bq kg ⁻¹)
Mean	10.7
Mode	0.80
Standard deviation	14.5
Range	70.6
Minimum	0.29
Maximum	70.9

concentration of 36.4 Bq kg⁻¹ for the territory of western Serbia [8], which is higher than the mean value of ¹³⁷Cs in soil obtained in this study.

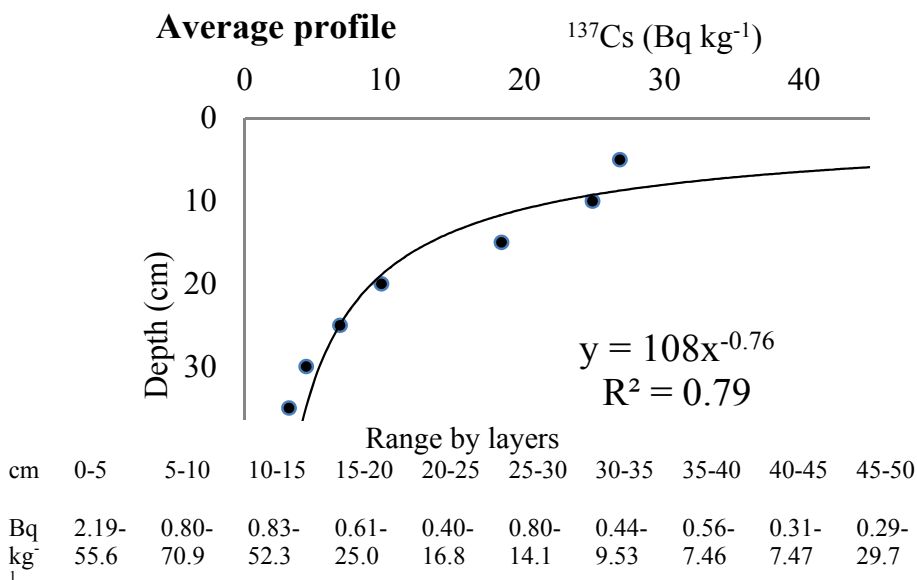


Figure 1. Vertical distribution of ¹³⁷Cs activity concentration in soil in the basin of Pčinja River.

Based on the results for the average profile the highest amount of total ¹³⁷Cs in the soil (25%) was in the first soil layer (0-5 cm), while the lowest one (2.46%) was in the eighth soil layer (35-40 cm). The 74% of the total ¹³⁷Cs in the soil in the basin of Pčinja River was found in the first four soil layers

(0-20 cm) and only 26% was found in the last six soil layers (20-50 cm), which indicates the slow migration of ^{137}Cs in the deeper soil layers. Clouvas et al. (2007) indicated that the vertical migration of ^{137}Cs in soil is a very slow process [9]. Karadeniz and Yaprak (2008) found 42-97% of the ^{137}Cs deposition in the first 10 cm of soil in Izmir, Turkey 18 years after Chernobyl accident [10].

CONCLUSION

From average profile, it is clear that ^{137}Cs activity concentration decreases with the soil depth. Mean value of ^{137}Cs activity concentration in soil was 10.7 Bq kg^{-1} . About 74% of the ^{137}Cs deposition was determined in the first 20 cm of soil profile in the basin of Pčinja River, southeastern Serbia.

ACKNOWLEDGEMENT

This work was supported by the Ministry of Education, Science and Technological Development of the Republic of Serbia (Project no. III43009).

REFERENCES

- [1] P. L. Nimis, *Studia Geobot.*, 1996, 15, 3-49.
- [2] D. Popović, V. Spasić-Jokić, *Military Medical and Pharmaceutical Journal of Serbia*, 2006, 63, 481-487.
- [3] Levels of radioactive contamination of the environment and the exposure of the population of Yugoslavia in 1986 due to Chernobyl nuclear power plant accident, Federal Committee for Labour, Health and Social Welfare, Belgrade, 1987.
- [4] ORTEC, Gamma Vision 32, Gamma-Ray Spectrum Analysis and MCA Emulation, Version 5.3, ORTEC, Oak Ridge, 2001.
- [5] SPSS (Statistical Package for the Social Sciences) Version 16.0, Chicago, Illinois, 2007.
- [6] J. Petrović, M. Čujić, M. Đorđević, R. Dragović, B. Gajić, Š. Miljanić, S. Dragović, *Environ. Sci.: Processes Impacts*, 2013, 15, 1279-1289.
- [7] S. Dragović, B. Gajić, R. Dragović, L. Janković-Mandić, L. Slavković-Beškoski, N. Mihailović, M. Momčilović, M. Čujić, *J. Environ. Monit.*, 2012, 14, 127-137.
- [8] G. Dugalic, D. Krstic, M. Jelic, D. Nikezic, B. Milenkovic, M. Pucarevic, T. Zeremski-Skoric, *J. Hazard. Mater.*, 2010, 177, 697-702.
- [9] A. Clouvas, S. Xanthos, G. Takoudis, M. Antonopoulos-Domis, G. Zinoviadis, T. Vidmar, A. Likar, *Radiat. Prot. Dosim.*, 2007, 124, 372-377.
- [10] Ö. Karadeniz, G. Yaprak, *Radiat. Prot. Dosim.*, 2008, 131, 346-355.

CHANGES IN TREE-RING CHEMISTRY IN PLANE (*Platanus acerifolia* Ait.) AND SOURCE APPORTIONMENT

D. M. Marković¹, I. R. Milošević², G. Roglić³, D. Manojlović³

¹The Faculty of Applied Ecology, Singidunum University, Lazarevački drum 13, Belgrade, Serbia; ²Institute of Physics, University of Belgrade, Pregrevica 118, Belgrade, Serbia; ³Faculty of Chemistry, University of Belgrade, Studentski trg 13-15, Belgrade, Serbia. (*novovic@ipb.ac.rs)

ABSTRACT

Changes in xylem chemistry in plane (*Platanus acerifolia* Ait.) tree-rings, sampled from the King Aleksandar Boulevard, Belgrade, were examined. In plane tree-rings at chosen location Fe was most abundant, while Ni was least present. The concentration increase can be seen from 1989 to 2009 for Ba, Cu, Fe, Mn, Ni and Sr, while decrease can only be seen for Pb in that period. In the case of Zn and Al concentration increase can be noticed from 1998 to 2009. Unmix receptor model was run for the obtained element concentrations and three sources were obtained.

INTRODUCTION

The plane is a large deciduous tree growing to 20–35 m tall, with a trunk up to 3 m or more in circumference and it is a popular urban roadside tree. The bark is usually pale grey-green and smooth. A large number of various bioindicators are used to assess the quality of the environment, and mosses are the most common. Choosing tree-rings as potential bioindicators was due to trees large geographic distribution, long living and the fact that each year tree forms a new tree-ring that can be easily dated. Dendroanalysis is based on the assumption that the chemical content of an annual growth ring at least partially reflects the chemistry of the environment in which the tree-ring was formed [1, 2].

EXPERIMENTAL

Tree-rings of plane (*Platanus acerifolia* Ait.) were collected from the King Aleksandar Boulevard, Belgrade in 2010, when the reconstruction of the boulevard had begun and the plane trees were cut. Two trees of similar size were selected, at breast height (1.3 m), for our purposes together with corresponding soil samples at 0-20 cm depth. For further analysis the disks were cut into segments with a stainless steel knife. Each plane core was divided into 3 year segments starting from 1935 to 2009. The content of

elements in solution samples was determined by inductively coupled plasma atomic emission spectrometry (ICP-OES). ICP-OES measurement was performed using Thermo Scientific iCAP 6500 Duo ICP (Cambridge, United Kingdom) spectrometer. The digestion was performed on an Advanced Microwave Digestion System (ETHOS 1, Milestone, Italy). In the digestion, about 0.5 g of powdered tree-ring sample precisely weighed was mixed in each clean vessel with a mixture of 3 ml H₂SO₄ and 5 ml HNO₃ and then heated with microwave energy for 30 min. The temperature was controlled with a predetermined power program. After cooling and without filtration, the solution was diluted to a fixed volume of 25 ml.

RESULTS AND DISCUSSION

On Figures 1, 2 and 3 mean three-year concentrations of the investigated elements (Pb, Ni, Cu, Zn, Sr, Mn, Fe, Al i Ba) in plane tree-rings were shown, as well as width of vessel lumen (L), width of tree-rings (R) and rainfall (RR [3]) in the period from 1935 to 2009. The rank of the investigated elements in plane tree-rings was as follow

Fe>Mn>Al>Sr>Ba>

Pb>Zn>Cu>Ni.

From figures 1, 2 and 3 increasing concentrations of Ba, Cu, Fe, Mn, Ni and Sr in the period from 1989 to 2009 can be seen, while for Zn and Al from 1998 to 2009. At the investigated location

during the last 20 years (1989-2009) the percentage increase of Ba (13%), Cu (24%), Fe (27%), Mn (16%), Ni (43%), Sr (31%), and Zn (67%) concentrations over that compared to the entire period (1935-2009) can be seen, while the percentage increase for Al and rainfall was less than 1%. The vehicles number increased by 631 in the busiest hour in the period from 1999 to 2006 at the study site [4]. In the case of Pb, width of tree-rings and vessel lumen (Figure 1 and 3) it can be noticed a decrease in the period from 1989 to

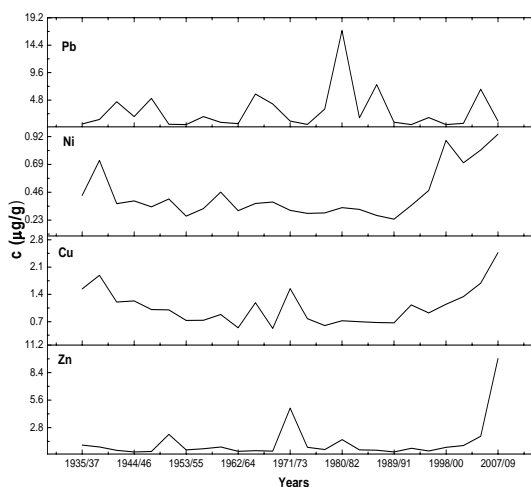


Figure 1. Mean Pb, Ni, Cu and Zn concentrations ($\mu\text{g/g}$) in plane (*Platanus acerifolia* Ait.) tree-rings at King Aleksandar Boulevard from 1935 to 2009.

2009 which amounts to 39%, 61% i 4%, respectively. Traffic activity appears to be the main source of trace metals at this site. From Figure 1 we can observe the highest Pb concentration in the plane tree-rings in the period 1980/82 and one characteristic period with low Pb concentration (1989-2009). The characteristic Pb minimum

concentration obtained in that period can be connected with the crisis of the nineties in our region as well as with the higher use of cars on unleaded petrol. Absence of correlations between element concentration in tree-rings and rainfall were observed. Weak Pearson's correlation was noticed only for Pb (0.38). Plane trees try to simultaneously decrease their growths as they are stressed by the pollution [5]. Large decrease of the R can be seen in the period when element concentrations have increase.

Unmix receptor model was run for the obtained element concentrations. Three factors were chosen as the optimum number for this model. The element profiles of the sources

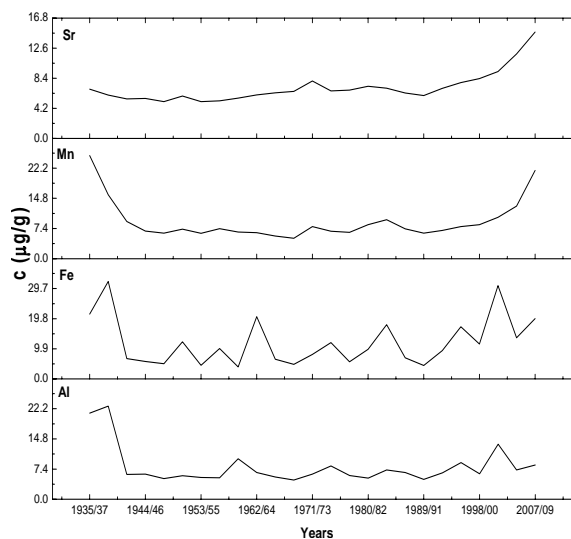


Figure 2. Mean Sr, Mn, Fe and Al concentrations ($\mu\text{g/g}$) in plane (*Platanus acerifolia* Ait.) tree-rings at King Aleksandar Boulevard from 1935 to 2009.

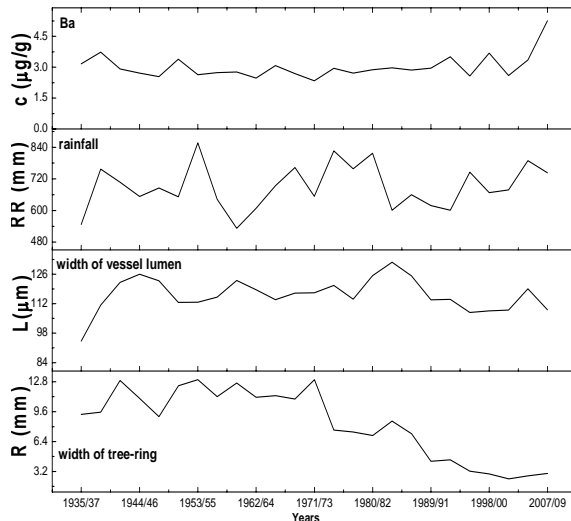


Figure 3. Mean Ba concentrations ($\mu\text{g/g}$), width of vessel lumen-L (μm) and tree-ring-R (mm) in plane tree-rings and rainfall-RR (mm).

Table 1. The element profile of the sources for plane tree-rings resolved by Unmix.

	Traffic exhaust	Mixed road dust	Soil
Al	9.5	11.5	78.9
Ba	15.5	22.0	62.5
Cu	11.7	25.3	63.0
Fe	7.3	14.4	78.4
Pb	91.5	3.1	5.4
Mn	12.1	25.1	62.9
Ni	13.7	21.2	65.1
Zn	3.0	85.4	11.6
Sr	16.9	25.6	57.5
%	20	26	54

Mn, Ni, Ba, Cu and Sr was resolved as **soil** and it has average contribution of 54%. Al and Fe are typical soil constituents. Metals may enter trees through roots, leaves, or bark to become incorporated in tree rings. Uptake by roots is still considered the major pathway by which metals enter trees.

CONCLUSION

At the investigated location during the last 20 years (1989-2009) the increase of Ba, Cu, Fe, Mn, Ni, Sr, and Zn concentrations can be seen, and decrease of Pb and width of tree-rings. Traffic activity at this site appears to be the main reason. Three factors were chosen as the optimum number and interpreted as traffic exhaust, mixed road dust and soil.

ACKNOWLEDGEMENT

This work was supported by the Ministry of Education and Science of the Republic of Serbia (Grants no. III 43007 and OI 171005).

REFERENCES

- [1] I. Amato, Anal Chem, 1988, 60, 1103A-1107A.
- [2] S.A. Watmough, T.C. Hutchinson, Environ Pollut, 1996, 93, 93-102.
- [3] RHMZS, Meteorološka stanica-Observatorija Beograd, 1935-2009.
- [4] Saobraćajni fakultet, Institut Saobraćajnog fakulteta, Istraživanje karakteristika saobraćaja na području grada Beograda, 1999-2006.
- [5] S.A.A. Korori, H.K. Valipour et al., World Academy of Science, Engineering and Technology, 2010, 69, 186-189.
- [6] Z. Mijić, A. Stojić et al., Atmos Environ, 2010, 44, 3630-3637.

LARCH Ca/Al RATIO IN TREE-RINGS AS AN INDICATOR OF SOIL ACIDIFICATION

I. R. Milošević¹, D. M. Marković², G. Roglić³ and D. Manojlović³

¹*Institute of Physics, University of Belgrade, Pregrevica 118, Serbia.
(novovic@ipb.ac.rs)*

²*The Faculty of Applied Ecology, Singidunum University, Lazarevački drum 13, Serbia.*

³*Faculty of Chemistry, University of Belgrade, Studentski trg 12-16, Serbia.*

ABSTRACT

Soil acidification is a globally important issue which causes base cation loss and phytotoxic element increase, especially Al, in the soil. Ca and Al concentrations were measured in larch tree-rings (*Larix europaea* Lam.) and corresponding soil samples from four forestry locations. Ca/Al ratio rather than Ca or Al alone could be a better indicator of soil acidification. Observed positive correlation ($PK=0.75$, $p<0.01$) between pH and Ca/Al ratio in soil can be regarded as an evidence of changes in Ca/Al ratio in soil solution by soil acidification. Ca/Al ratio in tree-rings showed a decreasing pattern for all sites except for the AK location. This decreasing pattern of Ca/Al ratio in tree-rings is believed to reflect historical changes of the soils by soil acidification.

INTRODUCTION

Forestry areas are more efficient at intercepting airborne particulate material than other types of vegetation, so the environment within wooded urban enclaves can be modified. One of the reasons of forest decline could be the soil acidification. Soil acidification is associated with decreases in exchangeable Ca and increases in Al concentrations in soil, leading to low Ca/Al ratio in soil solutions. The disturbed soil solution chemistry can thus result in characteristic Ca/Al ratios in tree-rings. As tree-rings can serve as a datable archives of environmental change, Ca/Al ratio of their tree-rings may show decreasing pattern in accordance with the progress of soil acidification [1-3].

EXPERIMENTAL

Tree-rings of larch (*Larix europaea* Lam.) from three woodland locations in Serbia and one from Montenegro were collected together with soil (0-20 cm in depth). The first one is Avala (AA), a mountain located 16 km south-east of Belgrade. The Belgrade-Niš highway, Kružni put and regional road to

Mladenovac runs east, north and west from the mountain. The second location is REIK Kolubara (AK). Larch at the Kolubara location has been applied for the rehabilitation by afforestation of the mechanically damaged land. The third location was Kučevo (AKU). Samples were taken from the management unit Donji Pek. The fourth location was village Trepča in Andrijevića municipality in the north-east part of Montenegro (ACG). At Kučevo and Andrijevića locations anthropogenic impact is low because there are no major industrial facilities and roads.

Three larch and Douglas-fir trees of similar size were selected at each location. Stem disks were taken from felled trees at breast height (1.3 m). For further analysis the disks were cut into segments with a stainless steel knife. Each core was divided into 3 year segments starting from 1980 to 2009. The content of elements in solution samples was determined by inductively coupled plasma atomic emission spectrometry (ICP-OES). ICP-OES measurement was performed using Thermo Scientific iCAP 6500 Duo ICP spectrometer equipped with CID86 detector, standard glass concentric type nebulizer, quartz torch, and alumina injector and purged with argon. The digestion of tree-rings was performed on an Advanced Microwave Digestion System ETHOS 1, using HPR-1000/10S high pressure segmented rotor. In the digestion, about 0.5 g of powdered tree-ring sample precisely weighed was mixed in each clean vessel with a mixture of 3 ml H₂SO₄ and 5 ml HNO₃ for tree-ring sample and then heated with microwave energy for 30 min. After cooling and without filtration, the solution was diluted to a fixed volume of 25 ml. Samples of soil were examined by sequential extraction using the Tessier procedure [4].

The method involves five fractions (exchange-able, carbonate, Fe/Mn oxides, organic and residual), in which the mobility and bioavailability of elements decrease with increasing extraction phase. The extraction was carried out progressively based on an initial amount of about 1.0 g of soil, accurately weighed. The first three fractions form “mobile content”, i.e. the part of the total

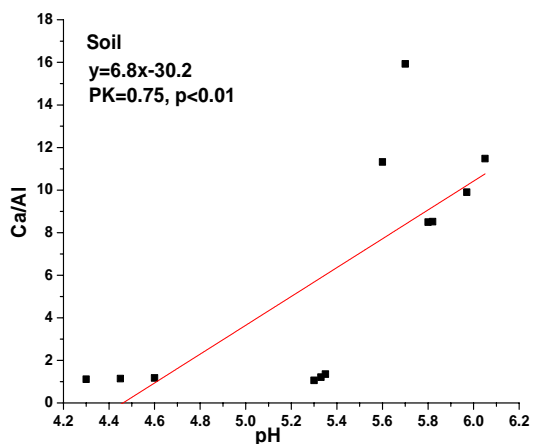


Figure 1. Relationship between Ca/Al ratio of “mobile content” in soils and soil pH

concentration which under certain conditions can be mobilized and thus enter biogeochemical cycles. Soil pH was measured as follows: 5.0 g of soil was precisely weighed and 5ml of 1M KCl added. The suspension was then subjected to continuous agitation for 10 min and left to stand before pH was determined.

RESULTS AND DISCUSSION

Figure 1 shows relationship between soil pH and Ca/Al ratio of “mobile content” in soil. Across the four sites pH ranged from 4.30 to 6.05. Relationship between soil pH and Ca/Al ratio was assessed by simple regression analysis using all the soil data regardless of sites. As soil pH decreases from 5.5 to 4.0, Al ions take the exchange sites in soil colloids, resulting in a low Ca/Al ratio [3]. Observed positive correlation ($R^2=0.75$, $p<0.01$) can be regarded as an evidence of changes in Ca/Al ratio in soil solution by soil acidification suggesting that progress of soil acidification increased exchangeable Al, while inducing leaching of Ca. Decomposition of coniferous tree litter have also contributed to the soil acidification [3].

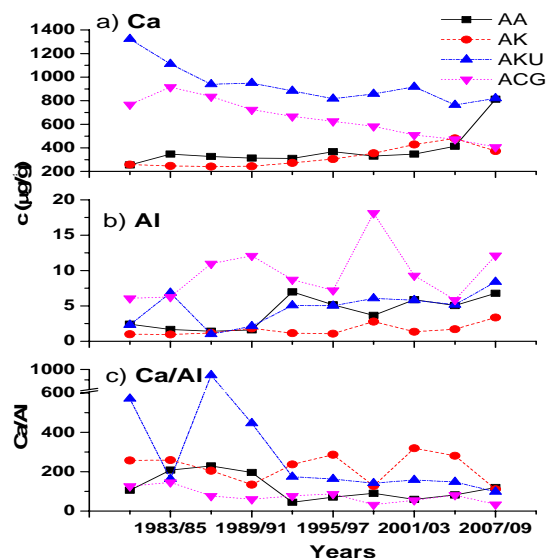


Figure 2. Mean trends in Ca and Al concentrations, as well as Ca/Al ratio in larch tree-rings at four examined locations.

Mean Ca concentrations in larch tree-rings from the AKU and ACG locations have decreasing trend, while at locations AA and AK slightly increasing trend (Figure 2a). Mean Al concentrations in larch tree-rings were increasing at all locations (Figure 2b). The decline of the Ca tree-ring concentration may indicate soil acidification history but such pattern can be a natural process due to reduced cation binding capacity of trees towards the

cambium in larch tree-rings [3, 5]. Therefore, Ca/Al ratio rather than Ca or Al alone could be a better indicator of soil acidification as their ratio can overcome the physiological pattern of single cation in tree-rings [6]. Based on the mean Ca and Al concentrations in tree-rings their ratio was calculated and the obtained values are shown in Figure 2c. Ca/Al ratio showed a decreasing pattern for all sites except for the AK location. This decreasing pattern of Ca/Al ratio in tree-rings is believed to reflect historical changes of the soils by soil acidification.

CONCLUSION

The decrease of the Ca/Al ratio in larch tree-rings in the period from 1992 to 2009, relative to the entire period of study, was the biggest at AKU location and amounts to 53%. At this location the lowest soil pH at the time of sampling was measured. At AA and ACG locations decreasing percentage were smaller and amounts 30% and 25% respectively, while at the AK location small increase of 1% was detected. Ca/Al ratio in tree-rings could serve as an indicator of historical soil acidification.

ACKNOWLEDGEMENT

This work is a part of projects III 43007 and OI 171005 financed by the Ministry of Education and Science of the Republic of Serbia.

REFERENCES

- [1] J.-H. Kwak, S.-S. Lim, H.-J. Park, S.-I. Lee, K.-H. Lee, H.-Y. Kim, S.X. Chang, S.-M. Lee, H.-M. Ro, W.-J. Choi, *Water Air Soil Pollut*, 2009, 199, 95-106.
- [2] J.-H. Kwak, S.-S. Lim, S.X. Chang, K.-H. Lee, W.-J. Choi, *J Soils Sediments*, 2011, 11, 709–721.
- [3] K.-S. Lee, D.V. Hung, J.-H. Kwak, S.-S. Lim, K.-H. Lee, W.-J. Choi, *Korean J Environ Agric*, 2011, 30, 229-233.
- [4] A. Tessier, P.G.C. Campbell, M. Bisson, *Anal Chem*, 1979, 51, 844-851.
- [5] E.A. Voganov, A.M. Grachev et al., *Doklady Biol Sci*, 2013, 453, 375-379.
- [6] D.R. DeWall, J.S. Tepp, B.R. Swistock, W.E. Sharpe, P.J. Edwards, *J Environ Qual*, 1999, 28, 299-309.

**THE EFFICIENCY OF CLAYEY
PELLETS FOR Zn(II) IONS REMOVAL
FROM A WASTE PRINTING
DEVELOPER**

J. Kiurski¹, J. Ranogajec², M. Vučinić Vasić¹, V. Kecić¹ and I. Oros¹

¹*University of Novi Sad, Faculty of Technical Sciences, Trg Dositeja
Obradovica 6, 21000 Novi Sad, Serbia (kiurski@uns.ac.rs)*

²*University of Novi Sad, Faculty of Technology, Bulevar cara Lazara 1,
21000 Novi Sad, Serbia*

ABSTRACT

The effect of clay dosage and contact time on adsorption efficiency of fired and unfired clay pellets for Zn(II) ions removal was studied in a laboratory batch mode. The adsorption efficiency of Zn(II) ions removal from the waste printing developer was the function of clay dosage and its composition. The maximum adsorption efficiency of 94.1% was achieved with unfired clay pellets. Therefore, clayey pellets could be a good economical alternative for the purification of waste printing developers.

INTRODUCTION

Zinc, as one of the most toxic heavy metal, is becoming a serious threat to environment [1, 2]. Evidently, waste printing developers should be treated before discharging into recipient. Among various purification methods, adsorption is one of the effective and widely used method for-removal of heavy metals. A great number of low-cost adsorbents have been studied for the removal of metal ions, such as clay [1], bentonite [2] and zeolite [3].

The objective of this study was to investigate the efficiency of fired and unfired clay pellets as adsorbents for Zn(II) ions removal from a waste printing developer. The study included the evaluation of two experimental factors: clay dosage and contact time.

EXPERIMENTAL

The sample of waste printing developer was taken from an offset printing facility, Novi Sad (Serbia).

The raw material mixture that contains natural pozzolanic material (PM), waste glass (WG), surface active material (SAM) and wooden dust (WD) was shaped by extrusion, dried (105 °C, 24h) and fired at 1020 °C ($\tau=2h$) in laboratory conditions. The fired and unfired clayey pellets with different

initial size ($d_1 \approx 8$ mm, $d_2 \approx 15$ mm, noted as FCP8 and UFCP15, respectively) were chosen for the adsorption process.

The PSD (Particle Size Distribution) analysis of both clayey samples was performed using a Malvern Mastersizer 2000 Particle Size Analyzer equipped with a Scirocco 2000 dry dispersion unit.

The adsorption experiment of Zn(II) ions onto fired and unfired clay pellets, FCP8 and UFCP15, was studied in laboratory batch mode under the following conditions: 0.04 - 0.24 g clayey pellets, 25 mL waste printing developer, shaking speed 160 rpm, and shaking time 30/60 min. At the end of the predetermined time intervals, the solutions are centrifuged for 10 minutes at 3000 rpm and then filtered through a quantitative filter paper (Advantec, grade 5°C). The equilibrated Zn(II) ion concentrations were determined in the acidified filtrate (conc. HNO_3) by Inductively Coupled Plasma Mass Spectrometry (ICP-MS) method using a PerkinElmer Elan 5000 mass spectrometer.

RESULTS AND DISCUSSION

The results of PSD analysis, Figure 1, represent the particle size distribution obtained for the fired FCP8 and unfired sample UFCP15. For FCP8, the maximum of particle size was found at 126.1 μm (4.7%), whereas the sample UFCP15 had the maximum at particle size of 501.8 μm (5.5%). This broader distribution of the particle size for UFCP15 has influenced a better adsorption process.

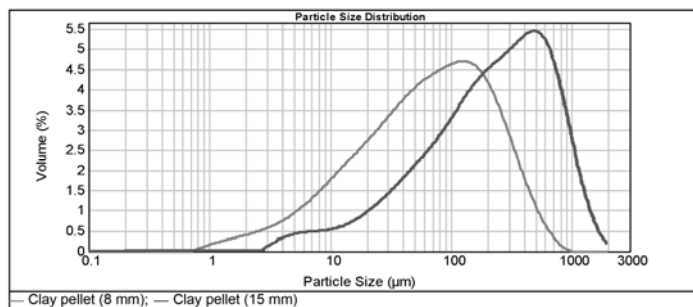


Figure 1. PSD analysis of the fired and unfired clayey pellets.

The influence of contact time on Zn(II) ions adsorption, Figure 2, shows a sharp increase in capacity uptake within 30 minute for UFCP15, after which the equilibrium has been established. Whereas the sample FCP8, shows a slightly different shape of the curve with the equilibrium established at 60 minute.

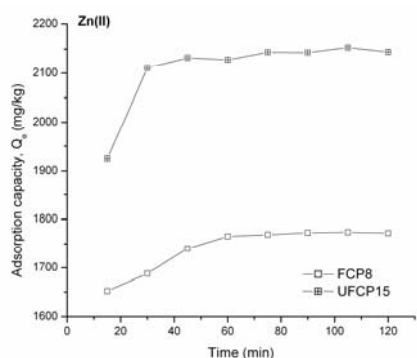


Figure 2. Influence of the contact time on the adsorption of Zn(II) ions.

The observed fast adsorption rate can be explained by the availability of active sites on the clay surface that gradually became time occupied with maximum capacities (about 1750 and 2100 mg/kg for FCP8 and UFCP15, respectively) achieved in 30/60 min of the experiment.

Beside the availability of more active sites on the clay surface, the clay dosage also influenced the increase of the adsorption efficiency, Figure 3. The maximum adsorption efficiency of 94.1% was achieved with the sample UFCP15 due to the pellet composition.

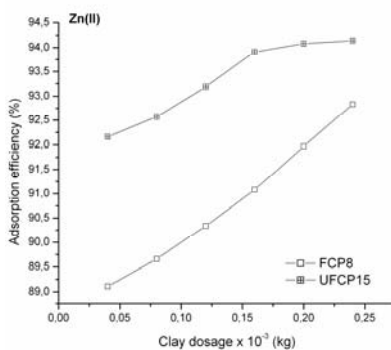


Figure 3. Influence of the clay dosage on the adsorption efficiency.

The values of distribution coefficient (K_d) increase with the decrease of the clay dosage, Figure 4, indicating the opposite trend in relation to Figure 3. Considering the effect of the pellets size, the following decrease order was obtained according to the values of distribution coefficients: UFCP15 > FCP8.

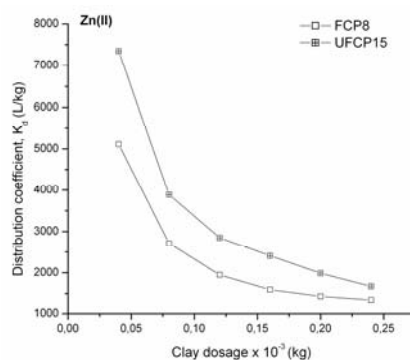


Figure 4. Influence of the clay dosage on the distribution coefficient.

CONCLUSION

The elimination of undesired and potentially harmful Zn(II) ions from the waste printing developer was successful by using the fired and unfired clay pellets. The results showed that the adsorption efficiency of Zn(II) ions removal increased with the increasing of clay dosage. The unfired clay pellets achieved the highest removal efficiency (94.1%) with particle size of 501.8 μm and pellet size of 15 mm in relation to fired clay pellets (92.8%). Evidently, the designed clayey pellets could be the promising adsorbents in the future treatment of waste printing developers.

ACKNOWLEDGEMENT

This work was partially supported by the Ministry for Science of the Republic of Serbia (Grant No. TR 34014).

REFERENCES

- [1] J. Kiurski, J. Ranogajec, S. Vučetić, D. Zorić, S. Adamović, I. Oros, J. Krstić, *Appl. Clay Sci.*, 2012, 65(65-66), 48 - 52.
- [2] S. Kubilay, R. Gurkan, A. Savran, T. Sahan, *Adsorption*, 2007, 13, 41 - 51.
- [3] E. Erdem, N. Karapinar, R. Donat, *J. Colloid. Interface. Sci.*, 2004, 280, 309 - 314.

MUTUAL INFLUENCE OF THE INDOOR POLLUTANTS DURING PHOTOCOPYING PROCESS

J. Kiurski¹, S. Aksentijević², I. Oros¹ and V. Kecić¹

¹*University of Novi Sad, Faculty of Technical Sciences, Trg Dositeja Obradovića 6, 21000 Novi Sad, Serbia (kiurski@uns.ac.rs)*

²*Business Technical College, Užice, Trg Svetog Save 34, Serbia*

ABSTRACT

The paper investigates the mutual correlation between ozone, non-methane hydrocarbons and nitrogen dioxide in working premises of one photocopying facility in Novi Sad, Serbia. Using multiple linear regression model and software package STATISTICA 10, the concentrations of occupational hazards were mutually correlated. Based on the obtained multiple coefficients of determination, a medium positive and a weak correlation between the observed variables were determined. Ternary graphs were constructed in order for better presentation of the mutual influence of the measured organic pollutants concentrations. The results showed that variable could be presented by the general regression model: $y = b_0 + b_1x_{i1} + b_2x_{i2}$.

INTRODUCTION

Non-methane hydrocarbons (NMHCs) are known to have an important role on air quality due to their high reactivity. Short chain alkanes (C₂ - C₅) are predominantly emitted because of extensive usage of toner during photocopying process. They can generate tropospheric ozone (O₃) through atmospheric chemical reactions with nitrogen oxides (NO_x) and radicals with relatively high NO_x concentrations [1]. In this way, they present a potential public health concern. Therefore, printing industry has been making efforts to reduce emissions of reactive NMHCs and NO_x in the atmosphere in order to improve the indoor environment [2].

Considering that our previous work included examination of various gases released during photocopying process [3, 4], the main objective of this study was to investigate a quantitative correlation as well as the strength of the correlation between ozone, non-methane hydrocarbons and nitrogen dioxide.

EXPERIMENTAL

Multiple regression analysis was used to determine the nature of relationship and a form of dependence between ozone, non-methane hydrocarbons and nitrogen dioxide concentrations. Data analysis was performed using software STATISTICA version 10. As an dependent variable O_3 concentration was selected, while NMHC and NO_2 concentrations present independent variables. The processed data were obtained from five days measurements at three sampling points during three time intervals.

RESULTS AND DISCUSSION

Correlation analysis determined whether there is quantitatively agreement between the observed phenomena as well as the strength of the agreement [5]. The results of regression analysis are presented in Table 1.

Table 1. The results of regression analysis.

Sampling point	Multiple coefficient of determination	SD	t
A	0.4313	0.0023	2.5961
B	0.4882	0.0018	0.6310
C	0.1909	0.0028	4.0379

Multiple coefficients of determination with values of 0.4313 and 0.4882 at sampling points A and B indicate a medium positive correlation between the observed variables. In contrast, a weak positive correlation is observed at sampling point C, with multiple coefficients of determination of 0.1909.

Standard error of regression (SD) shows the average deviation of the regression line from the empirical relationships between the observed phenomena. The bigger error, the less reliable is prediction based on the used regression models.

Value of $t_{critical}$ for n-k degrees of freedom and a significance level of 0.05 is 1.7823. The obtained values of parameter t are higher than $t_{critical}$ at sampling points A and C, which certainly (> 95 %) confirms a presence of positive correlation between the observed phenomena. At sampling point B parameter t is less than $t_{critical}$ so there is not enough evidence to confirm the correlation between the parameters.

Ternary graphs of sampling points with the highest correlation coefficient were constructing by using software package STATISTICA 10. Figures 1-3 represent the spatial dependence of O_3 concentration on NMHC and NO_2 concentrations at sampling points A, B and C, respectively.

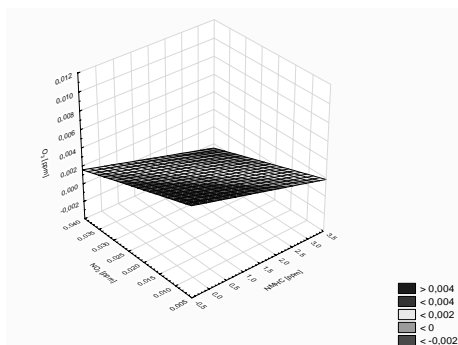


Figure 1. Ternary graph of regressive surface at sampling point A.

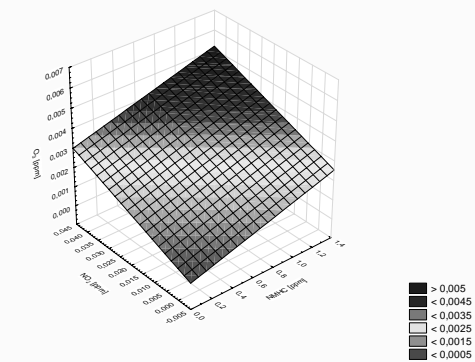


Figure 2. Ternary graph of regressive surface at sampling point B.

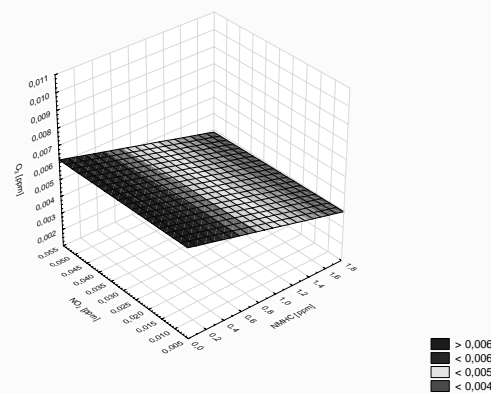


Figure 3. Ternary graph of regressive surface at sampling point C.

In the three-dimensional graphs, x-axis represents the concentration of non-methane hydrocarbons, y-axis the concentration of nitrogen dioxide, and z-axis the concentration of ozone. The resulting surface shows an average stacking variation of investigated variables, which can be presented by the

general regression model: $y = b_0 + b_{1x_1} + b_{2x_2}$. Independent variables x_1 and x_2 present the concentration of non-methane hydrocarbons and nitrogen dioxide respectively, while dependent variable y presents the ozone concentration. Therefore, the following individual regression models presented by equations are obtained:

Sampling point A: $\hat{y} = 0.0061 - 0.0010x_1 - 0.1247x_2$

Sampling point B: $\hat{y} = 0.00061 + 0.00156x_1 + 0.5272x_2$

Sampling point C: $\hat{y} = 0.00626 - 0.00128x_1 - 0.00184x_2$

Obtained regression equations allow measuring the quantitative agreement between the variation of variables and more accurate knowledge of their mutual relations.

CONCLUSION

A multiple linear regression analysis was performed to predict and determine the mutual correlation between dependent variable (ozone concentration) and independent variables (non-methane hydrocarbons and nitrogen dioxide concentrations). The software package STATISTICA 10 was used for this evaluation. The obtained multiple coefficients of determination indicated a medium positive correlation (sampling point A and C) and a weak correlation (sampling point B) between the observed variables. Ternary graphs were constructed in order to better represent the mutual influence of the pollutants.

ACKNOWLEDGEMENT

This work was partially supported by the Ministry for Science of the Republic of Serbia (Grant no. TR 34014).

REFERENCES

- [1] D.R. Worton, W.T. Sturges, C. E. Reeves, M.J. Newland, S.A. Penkett, E. Atlas, V. Stroud, K. Johnson, N. Schmidbauer, S. Solberg, J. Schwander, J.M. Barnola, *Atmos. Environ.*, 2012, 54, 592 – 602.
- [2] M. Noguchi, M. Bae, K. Yamashita, Y. Yanagisawa, *Build. Environ.*, 2009, 44, 1489 – 1492.
- [3] J. Kiurski, V. Kecić, I. Oros, S. Aksentijević, N. Ralević, Paper presented at the 19th International Symposium on Analytical and Environmental Problems, Szeged, Hungary, 2013, 161 - 164.
- [4] V. Kecić, S. Aksentijević, I. Oros, J. Kiurski, 15. Danube-Kris-Mures-Tisa (DKMT) Euroregion Conference on Environment and Health, Novi Sad, Serbia, 2013, 181 - 186.
- [5] M. Žižić, M. Lovrić, D. Pavličić, *The methods of statistical analysis*, Faculty of Economics, Belgrade, 2006. (in Serbian)

COMPARISON OF VARIOUS BOVINE BONE TREATMENTS FOR THE PREPARATION OF EFFECTIVE Ni(II) SORBENT MATERIAL

M. Šljivić-Ivanović, A. Milenković, M. Jović and I. Smičiklas

University of Belgrade, "Vinča" Institute of Nuclear Sciences, Radiation and Environmental Protection Department, P.O. Box 522, 11000 Belgrade, Serbia. (marijasljivic@vin.bg.ac.rs)

ABSTRACT

Animal bones are reach source of calcium hydroxyapatite which was approved as a good sorbent material for heavy metals and radionuclides. Various treatments can reduce the content of bone organic phase and improve sorption properties. In this study sorption capacities of raw bovine bones (B) and samples obtained by chemical treatment using NaOH (B_{NaOH}), by heating at 400 °C (B_{400}) or by combined chemical and thermal treatment ($B_{NaOH+400}$), were compared. It was shown that sorbents exhibited different sorption mechanisms towards Ni(II) ions, and that maximum sorption capacities increased in the order $B < B_{NaOH} < B_{400} < B_{NaOH+400}$. Synergetic effect of chemical and thermal treatment produced the material with highest sorption efficiency.

INTRODUCTION

Nickel is a heavy metal which ions affect human health [1]. This metal is frequently found in industrial products and articles of common use, mostly stainless steel and variety of alloys, catalysts, rechargeable batteries, etc. [2]. Furthermore, liquid radioactive waste often contains long half-lives radioactive isotopes ^{59}Ni and ^{63}Ni [3]. The purification of wastewaters containing Ni(II) ions can be conducted using different sorbent materials.

Previously, it was reported that thermal treatment of bones, especially at 400°C, can improve their sorption capacity toward Co(II) ions [4]. Comparison of various chemical reagents for the treatment of fish bones has revealed that treatment with NaOH produced sorbent with highest efficiency for Cu(II) removal [5].

In this study, sorption of Ni(II) ions was tested and compared using four different materials obtained from animal bones. The performance of untreated bones, was compared with the samples obtained under previously determined optimum conditions for chemical [5] and thermal [4] treatments, as well with the sample exposed to combined chemical/thermal treatment.

Sorption experiments were conducted at room temperature, in the wide range of initial Ni(II) concentrations.

EXPERIMENTAL

Sorbents were prepared from bovine femur bone, boiled three times in water for the removal of fat tissue. After drying at 80°C, bones were crushed and milled (sample B). Thermally treated sample B₄₀₀ was obtained by heating of B at 400°C, for 4h, in the preheated electrical oven. Chemically treated sample B_{NaOH} was prepared by mixing 50 g of B with 1 dm³ of 2 mol/dm³ NaOH, for 3 h, at 60°C. The sample was washed on the Buhner funnel with the excessive amounts of distilled water, and then dried at 80°C. Finally, B_{NaOH+400} was produced by applying previously described thermal treatment on sample B_{NaOH}.

Sorption experiments were conducted in batch conditions. Separate batches were prepared in 0.05 dm³ polypropylene centrifuge tubes. Each one contained 0.1 g of sorbent and 20 mL of solution prepared from NiCl₂ salt and distilled water. The initial Ni(II) concentrations varied between 10⁻⁴ and 6x10⁻³ mol/dm³, whereas the initial pH values were 6±0.1. In order to achieve equilibrium, suspensions were mixed on the overhead shaker at 10 rpm, for 24 h. Subsequently, liquid phases were separated from spent sorbents by centrifugation at 7000 rpm for 10 min. Equilibrium pH values were measured in clear supernatants. Determinations of residual Ni(II) concentrations, as well as the concentrations of Ca(II) ions released from bio-apatite phase, were performed on Perkin Elmer 3100 Atomic Absorption Spectrometer. The amounts of Ni(II) removed from the solution were calculated as the differences between the initial and the equilibrium concentrations.

RESULTS AND DISCUSSION

The sorption isotherms of Ni(II) onto raw and differently treated bovine bones are presented in Figure 1,a. It is evident that each treatment influenced the increase of sorption capacity in respect to raw sample. Thus, sorbed amounts of Ni(II) generally increased in the order B<B_{NaOH}<B₄₀₀<B_{NaOH+400}. Considering the most concentrated solution applied in this study, sorbed amounts were 0.35 mmol/g, 0.30 mmol/g, 0.28 mmol/g and 0.22 mmol/g, for B_{NaOH+400}, B₄₀₀, B_{NaOH} and B, respectively.

Equilibrium pH values (Fig. 1,b) decreased along with the increase of initial metal concentration, in the order B≈B₄₀₀<B_{NaOH}<B_{NaOH+400}. This phenomenon can be related to the specific cation sorption followed by the release of surface H⁺ ions, or to the hydrolysis and precipitation of Ni(II). Ni(II) removal from aqueous media using samples B_{NaOH} and B_{NaOH+400} was

especially enhanced in the low concentration range (10^{-4} - 5×10^{-4} mol/dm³), where equilibrium solution pH were ~ 8 , which is Ni(OH)₂ precipitation threshold.

The sorption of Ni(II) from the solutions of different initial concentrations, was followed by almost linear increase of aqueous Ca(II) concentration (Fig. 1,c). This sorbate concentration dependent relationship between sorbed metal quantity, equilibrium pH and the quantity of released Ca(II), indicates that several sorption mechanisms were operating: specific cation sorption, ion-exchange with Ca(II) from HAP-phase crystal lattice, Ni(II) hydrolysis and precipitation. Furthermore, the complexation of Ni(II) with the organic phase of bone is likely to occur.

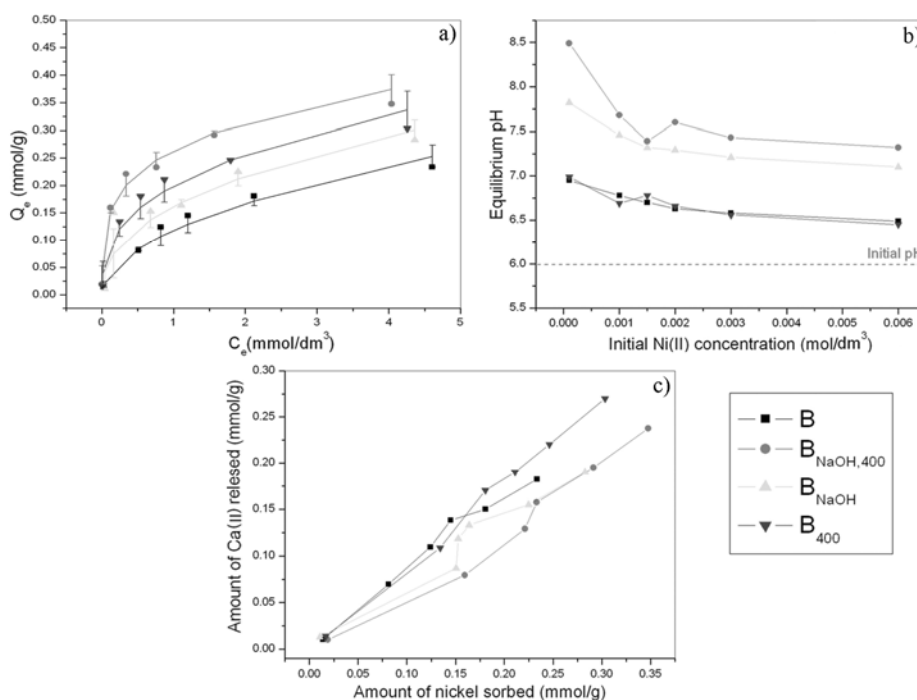


Figure 1. **a)** Ni(II) sorption isotherms (symbols - experimental points, lines – fitting by Freundlich equation, error bars - deviations between experimental and predicted values), **b)** Relationship between equilibrium pH values and initial Ni (II) concentration, and **c)** Relationship between amounts of released Ca(II) ions and sorbed Ni(II) amounts.

Sorption isotherms were well described using Freundlich theoretical model, in the following linear form:

$$\ln Q_e = \ln K + 1/n \cdot \ln C_e$$

where K ($\text{mmol}^{1-(1/n)} \cdot \text{dm}^{3/n} \cdot \text{g}^{-1}$) and n are the Freundlich constants related to the capacity and intensity of the sorption process. Model parameters are summarized in Table 1. Based on the correlation coefficients (R), a good agreement exists between the model and experimental data. The calculated K values increased in the order $B < B_{\text{NaOH}} < B_{400} < B_{\text{NaOH}+400}$.

Table 1. Parameters of Freundlich isotherm model.

Parameter	K ($\text{mmol}^{1-(1/n)} \cdot \text{dm}^{3/n} \cdot \text{g}^{-1}$)	n	R
B	0.118	1.78	0.993
$B_{\text{NaOH}+400}$	0.264	3.14	0.991
B_{NaOH}	0.162	1.65	0.865
B_{400}	0.200	2.02	0.974

CONCLUSION

All investigated treatments improved sorption capacity of bovine bone toward Ni(II) ions, when compared to the raw sample. For initial metal concentrations higher than 10^{-4} mol/ dm^3 sorption capacities increased in the order $B < B_{\text{NaOH}} < B_{400} < B_{\text{NaOH}+400}$. The results indicate that the material with the highest sorption efficiency towards Ni(II) was produced by the combination of chemical and thermal treatment.

ACKNOWLEDGEMENT

This work was supported by the Ministry of Education, Science and Technological Development of the Republic of Serbia (Project III43009).

REFERENCES

- [1] S. Kasprzak, Jr. F. W. Sunderman, K. Salnikow, *Mutat. Res. – Fund. Mol. M.*, 2003, 533, 67-97.
- [2] J. R. Davis, *Uses of Nickel*, ASM Specialty Handbook: Nickel, Cobalt, and Their Alloys, ASM International, 2000.
- [3] O. Fisera, F. Sebesta, *J. Radioanal. Nucl. Chem.*, 2010, 286, 713-717.
- [4] S. Dimović, I. Smičiklas, I. Plečaš, D. Antonović, M. Mitrić, *J. Hazard. Mater.*, 2009, 164, 279-287.
- [5] B. Kizilkaya, A. A. Tekinay, Y. Dilgin, *Desalination*, 2010, 264, 37-47.

MOBILITY OF Co^{2+} AND Sr^{2+} IONS IN THE CONTAMINATED SOIL: COLUMN STUDY

S. Dimović¹, I. Smičiklas¹ and M. Šljivić-Ivanović¹

¹University of Belgrade, “Vinča” Institute of Nuclear Sciences, Radiation and Environmental Protection Department, P.O. Box 522, 11000 Belgrade, Serbia (ivanat@vinca.rs)

ABSTRACT

The mobility of pollutants in the soil is closely related to their toxicity, and thus very important information for the selection of remediation strategies. In this study, leaching of Sr^{2+} and Co^{2+} ions from contaminated soil was investigated and compared under dynamic conditions. As a model soil, a sample from the “Vinča” Institute was tested. The soil artificially contaminated with inactive Sr^{2+} and Co^{2+} ions was packed in the columns, while acidic rain water was used as a leaching solution. Desorption of both cations was the most pronounced at the beginning, reaching the peak after the second day for Co^{2+} and after the seventh day for Sr^{2+} . During the course of experiment (37 days), cumulative percentages of desorbed Co^{2+} and Sr^{2+} were 0.7% and 19.8 %, respectively. The results indicated significantly higher soil affinity towards Co^{2+} ions. In spite of its higher total concentration in the soil, Co^{2+} mobility was much lower compared to Sr^{2+} .

INTRODUCTION

Radioactive isotopes of ^{90}Sr and ^{60}Co are important environmental pollutants which arise during regular operation of nuclear power plants and research reactors. They can end up in soil as a result of accidental spills of liquid radioactive waste. ^{90}Sr is also widespread due to above-ground nuclear testing. The remediation of contaminated soil includes various *in-situ* and *ex-situ* methods [1]. Mobility of the particular pollutant in the soil is the major factor influencing the selection of appropriate clean-up technology.

In this study, the mobility of ^{90}Sr and ^{60}Co was studied and compared using the soil sample from the “Vinča” Institute. This location serves as a nuclear waste repository, therefore, soil contamination with various radionuclides is possible.

EXPERIMENTAL

Surface sample of soil was taken to a depth of approximately 20 cm. The soil was dried in air atmosphere, crushed and sifted in order to separate a fraction of particle size < 2 mm for further experiments. Two portions of sifted soil were placed into plastic containers and mixed with the $5 \cdot 10^{-2}$ mol/dm³ of cobalt or strontium containing solution, at 1:2 solid/solution ratio. Inactive Co²⁺ and Sr²⁺ ions in the form of nitrate salts were used. The suspensions were allowed to equilibrate for one month. The soil was separated from the residual metal solution by filtering, and finally dried in air at room temperature. The total concentrations of Sr²⁺ and Co²⁺ ions in the contaminated samples were determined by ICP-OES method, using iCAP-6500 Duo (Thermo scientific, United Kingdom). Prior to measurements, each contaminated sample (0.5 g) was mixed with 7 cm³ of concentrated HNO₃ and 2 cm³ of 30% H₂O₂ and subjected to acid digestion in a microwave oven (CEM MDS 2100).

Two polypropylene bottles (0.5 dm³) were used to make appropriate columns. They were attached to the laboratory stands upside down, and the soil samples were placed between two PVC dredgers. The lower ends were covered with filter paper and layer of plastic pellets to retain the soil. At column top, Raschig rings were added to allow uniform elution and to minimize loss of evaporation. Contaminated soils (200 g) were packed in the columns. Rain water collected at the same site, was used as a leaching solution. Its initial pH was adjusted to 5 by a few drops of 0.1 mol/dm³ HNO₃, to mimic more aggressive - acid rain scenario. 100 cm³ of such solution were added daily to the top of each column, for a total time period of 37 days. The concentrations of metal cations in the leached fractions were determined.

RESULTS AND DISCUSSION

Chemical analysis showed that, under the same experimental conditions, total concentration of Co²⁺ in the contaminated soil was 8260 mg/kg, whereas 4450 mg/kg of Sr²⁺ was detected. The results indicated significantly higher capacity of soil towards Co²⁺ ions.

Desorption of studied cations from the contaminated soil varied as a function of time (Fig.1). Rapid grow of desorbed amounts was detected at the beginning of the process. The maximum was reached after 2 days for Co²⁺, whereas after 7 days for Sr²⁺. The longer time required to reach the maximum desorption, as well as the higher concentrations of leached Sr²⁺ ions confirm that a large quantity of Sr²⁺ was weakly associated with the soil. From the day 5, only small oscillations in Co²⁺ desorption were noted until the end of experiment. On the other hand, Sr²⁺ leached amounts

fluctuated, and reached another peak between 24. and 26. day. This illustrates the process complexity. Namely, various phenomena such as diffusion, convection, ion-exchange, specific cation sorption as well as formation and dissolutions of secondary phases, may occur simultaneously with different rates [2].

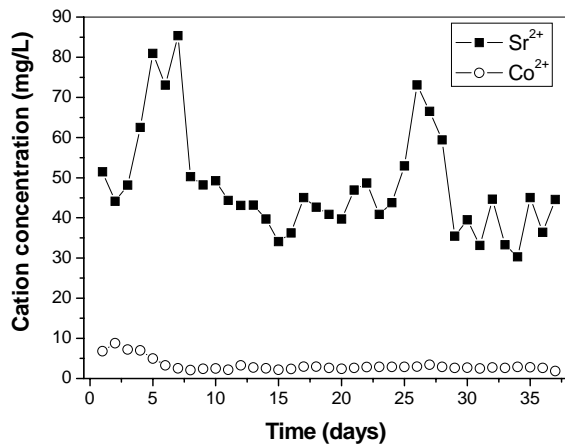


Figure 1. Time dependant concentrations of cations leached from contaminated soil.

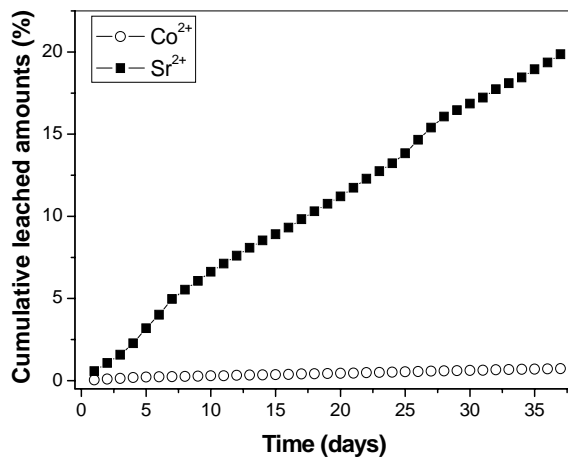


Figure 2. Cumulative percentages of leached metal cations

At the end of the experiment, cumulative percentages of desorbed Co^{2+} and Sr^{2+} (Fig. 2) were 0.7% and 19.8 %, respectively.

The inorganic contaminants can be bound to components of soil by several mechanisms [3]. Preferred sorption and considerably lower desorption of Co^{2+} in respect to Sr^{2+} , indicate different binding mechanisms of these ions to soil components. Due to high electronegativity, Co^{2+} ions are significantly subjected to ion-change reactions, and formation of complex compounds with organic phase of soil [4]. The weak alkaline reaction of the studied soil with water [5] enhances the sorption on oxides and aluminosilicates, and favors the hydrolysis and precipitation of Co^{2+} ions.

CONCLUSION

Although total concentration of Co^{2+} in the contaminated soil was initially higher in respect to Sr^{2+} , leached amounts were less significant. Higher electronegativity of Co^{2+} , together with weak alkaline soil/water reaction, influenced its significantly lower mobility. Due to the different mobility of Co^{2+} and Sr^{2+} cations in the contaminated soil, different remediation strategies should be considered.

ACKNOWLEDGEMENT

This work was supported by the Ministry of Education, Science and Technological Development of the Republic of Serbia (Project III43009).

REFERENCES

- [1] IAEA-TECDOC-1086, Technologies for remediation of radioactively contaminated sites, International Atomic Energy Agency, Vienna, Austria, 1999.
- [2] D. Kossoff, K. A. Hudson-Edwards, W. E. Dubbin, M. A. Alfredsson, *Chem. Geol.*, 2011, 281, 52–71.
- [3] H. B. Bradl, *J. Colloid Interface Sci.*, 2004, 277, 1-18.
- [4] R. G. McLaren, C. A. Backes, *Soil Sci. Soc. Am. J.*, 1998, 62, 332-337.
- [5] S. Dimović, I. Smičiklas, M. Šljivić-Ivanović, B. Dojčinović, *J. Soil Sediment.*, 2013, 13, 383–393.

**CORRELATIONS BETWEEN METEOROLOGICAL
PARAMETERS AND ^7Be SPECIFIC ACTIVITY
MEASURED AT GROUND LEVEL AIR IN BELGRADE,
SERBIA**

A. Samolov^{a,*}, S. Dragović^b and M. Daković^c

^a*Military Technical Institute, Belgrade, Serbia*

^b*Vinča Institute of Nuclear Sciences, Belgrade, Serbia*

^c*Faculty of Physical Chemistry, University of Belgrade, Serbia*

ABSTRACT

Standard gamma-ray spectrometric analysis of air samples was performed in Belgrade (Serbia) during 2009-2011 and values of ^7Be specific activities were obtained. Meteorological data from the same period were collected, as well, and correlations between them were calculated. Values of correlation coefficient are low, but in accordance with the literature.

INTRODUCTION

The radionuclide ^7Be ($t_{1/2}=53.3$ d) forms in the stratosphere and upper atmosphere in reactions of spallation on nuclei of oxygen and nitrogen by beams of protons and neutrons from cosmic radiation. Almost immediately after creation, atoms of ^7Be are captured by aerosol particles and follow their paths through the air masses. Aerosol particles contain most of the air pollutant particles, so they can be used as a tracer for circulation pathways in the atmosphere, as well as for deposition kinetics of atmospheric macro and micro particles.

It is well known that the production of ^7Be depends on the intensity of cosmic radiation reaching the upper atmosphere. Seasonal variation of ^7Be in the lower layers of the atmosphere depends on the vertical and horizontal flow of air masses [1]. Continuous daily monitoring of ^7Be concentration in surface air can provide information on solar activity by using a simple gamma-spectrometric method [2], since the ^7Be concentration in the air is independent of human activities, i.e. nuclear tests and technological development. In this study, we present results of ^7Be specific activities measurements in near-ground air by using standard gamma-spectrometric procedure, and correlations between ^7Be specific activity and meteorological parameters.

EXPERIMENTAL

Air sampling was conducted in the period from March 2009 to December 2011 at Kumodraz, on the outskirts of Belgrade, Serbia. Standard sampling procedure was performed. Samples were collected weekly, with a total of 101 samples. Digital samplers were capable of measuring temperature, pressure and relative humidity. Values for wind speed, insolation (sunny hours per day), global Sun warming and precipitation were provided by the Republic Hydrometeorological Service of Serbia.

The measurements were performed on a gamma-ray spectrometric system AMETEK-AMT (ORTEC, USA) with a coaxial high-purity germanium (HPGe) detector with relative efficiency of 59.2% measured on the line 1.33 MeV ^{60}Co . Resolution of the device was 1.78 keV on the line 1.33 MeV ^{60}Co . Gamma-ray spectrometric analyses were conducted on the device calibrated to the filter geometry. ^7Be specific activity of air samples was evaluated from its line at 477.6 keV, for 250 000 s by using the Gamma Vision 32 software package [3].

RESULTS

The ^7Be average monthly activities for the period from March 2009 to December 2011 are presented in Figure 1. Table 1 presents descriptive statistics on experimental data, while Table 2 presents correlation coefficients of meteorological parameters of air and ^7Be specific activities.

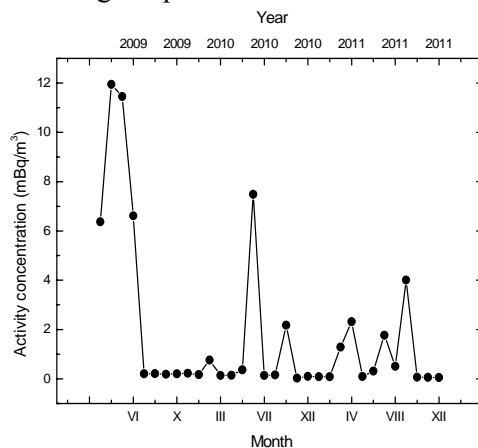


Figure 1. The ^7Be average monthly activity for the period from March 2009 to December 2011 measured at Kumodraz, Belgrade

Table 1. Descriptive statistics of experimental data for the period from March 2009 to December 2011

Experimental data	mean	standard deviation	median	mode	min	max	skewness	kurtosis
specific activity (mBq/m ³)	1.8	3.4	0.2	/	0.02	14.8	2.4	4.7
maximum temperature (°C)	21.9	9.2	23.1	28.3	-0.6	36.1	-0.7	-0.1
precipitation (mm)	11.1	12.9	6.9	0.0	0.0	58.2	1.5	2.1
insolation (h)	38.5	21.4	38.4	63.2	0.0	88.3	0.1	-1.0
global Sun warming (W/cm ²)	1268.3	697.4	1288.3	1667.3	1	2615.8	0.05	-1.0
wind speed (m/s)	2.5	0.7	2.3	2.2	1.3	4.9	0.9	1.3
maximum pressure (mm Hg)	711.4	18.1	707.9	707.9	683.8	765.1	1.1	0.7
relative humidity (%)	83.9	15.0	89.0	89.0	25.0	100.0	-2.0	3.9

Table 2. Correlation coefficients of meteorological parameters of air and ⁷Be specific activities

Meteorological parameter	Correlation coefficient
wind speed (m/s)	-0.24
insolation (h)	0.20
precipitation (mm)	-0.17
maximum pressure (mm Hg)	-0.15
maximum temperature (°C)	0.16
relative humidity (%)	-0.04
global Sun warming (W/cm ²)	0.23

DISCUSSION

The ⁷Be specific activity was in the range from 0.03 mBq/m³ to 11.95 mBq/m³ (see Fig. 1). This is in agreement with the results for the Belgrade area obtained by other authors, whose values ranged from 0.6 mBq/m³ to 7 mBq/m³ [4] and from 1.9 mBq/m³ to 10.2 mBq/m³ [5]. It is characteristic that the maximum values are observed in summer and minimum in winter, which was observed in all studies. Todorovic et. al. (2010) reported that the average ⁷Be activities for five years, observed in the Vinca Institute (outskirts) and in downtown Belgrade, were 2.54 mBq/m³ and 2.73 mBq/m³ respectively. Activity values found in our study, obtained for the period of less than three years, and at one location (outskirts) were 1.8 mBq/m³.

Positive correlation was observed between air temperature and specific activity which was consistent with the results of other authors [4, 6, 7]. Considering the fact that insolation, global Sun warming and air temperature are correlated, a positive sign of the correlation coefficient between these parameters and specific activity seems quite logical. The correlation coefficient between precipitation and specific activities was negative, which can be due to the removal of ^7Be by wet deposition [8]. Negative sign in cases of wind speed and pressure show possible inverse correlation, while relative humidity doesn't seem to have any influence on ^7Be specific activity [6, 7]. Some authors have stated that this might be due to the type of climate or to the height of the sampling location [6]. However, values of all correlation coefficients are rather low. It has been suggested [7] that correlation can be improved if sampling is performed on a daily basis instead of on a weekly basis as done here.

CONCLUSION

The results presented here are in accordance with the literature. Maximum specific activity values in the summer could be explained with vertical air mixing and a transport of cosmogenic radionuclides towards low atmospheric level. Moreover, seasonal variations seem to be more related to temperature and parameters correlated with it, and precipitation, than to other meteorological parameters.

REFERENCE

- [1] D. Todorović, D. Popović, G. Djurić, *Environment International*, 1999, 25(1), 59.
- [2] S. Kikuchi, H. Sakurai, S. Gunji, F. Tokanai, *Journal of Environmental Radioactivity*, 2009, 100, 515.
- [3] *Gamma Vision 32*, Gamma-Ray Spectrum Analysis and MCA Emulation, Version 5.3., ORTEC, Oak Ridge, USA, 2001.
- [4] D. Todorović, D. Popović, J. Nikolić, J. Ajtić, *Radiation Protection Dosimetry*, 2010, 142, 308.
- [5] N. Lazarević, D. Rajić, M. Jevremović, A. Nouri, A. Jamhour, *Scientific Technical Review*, 2009, 3-4, 65.
- [6] M. Raneli, S. Rizzo, E. Tomarchio, IAEA-CN-145/174P (2007).
- [7] E. Krajny, L. Osrodka, M. Wojtylak, B. Michalik, J. Skowronek, *Nukleonika*, 2001, 46, 189.
- [8] S. Kikuchi, H. Sakurai, S. Gunji, F. Tokanai, *J. Environ. Radioact.*, 2009, 100, 515.

STUDY OF THE DEGRADATION PARAMETERS OF CONGO RED USING FENTON PROCESS

A. Smara¹ and H. Necib¹

¹LTEVDI, Chemistry Department, Faculty of Sciences, University Badji Mokhtar of Annaba, BP 12 RP Annaba ; Algeria

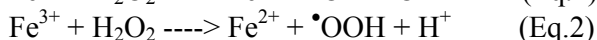
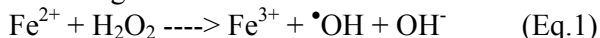
ABSTRACT

Among the industries using large quantities of water, we find the textile and tannery industries. These industries generate an important pollution which is often difficult to eliminate. The effects of these industries, particularly on the fauna and flora are serious [1], [2]. In this study, the efficiency of the Advanced Oxidation Process (AOP) has been investigated to degrade a model molecule as an industrial dye, namely Congo red, CR.

Among the processes used for the treatment of industrial effluents, the AOPs are attracting much interest. These processes can lead, under optimal conditions, to a complete mineralization yielding CO₂, H₂O and the corresponding mineral acids.

INTRODUCTION

The AOPs are based on the in situ generation of the hydroxyl radicals ($\bullet\text{OH}$) known as powerful oxidizing species which can oxidize recalcitrant organic molecules [3], [4]. Among the AOPs the Fenton process is based on the following reactions:



In this paper the results of the study on the discoloration parameters of Congo red are presented. The parameters under investigation were solution pH, concentration of Fe²⁺ catalyst and concentration of H₂O₂. Furthermore, under optimum conditions the discoloration of CR was found to reach 90% after 3 hours.

EXPERIMENTAL

The degradation of CR was studied using a batch reactor consisting of a beaker under constant stirring in the absence of light. The normalized concentration of the residual concentration of CR was measured using a UV-Vis spectrophotometer (Equinox) at $\lambda = 504 \text{ nm}$. All the reagents used (H₂O₂, 33%; FeSO₄.7H₂O; HNO₃; Methanol) were of analytical grade. The pH of solutions were monitored using a pH-meter « HANNA »

RESULTS AND DISCUSSION

Figure 1 shows that at pH = 3 the degradation rate of CR reaches a maximum of 90%. This is in agreement with previous studies which indicate that the optimum pH value yielding the highest rate of degradation for Fenton process is the range 2 - 4 [5]. In this pH interval the Fe^{2+} ions are very reactive leading to a maximum production of hydroxyl radicals $\bullet\text{OH}$.

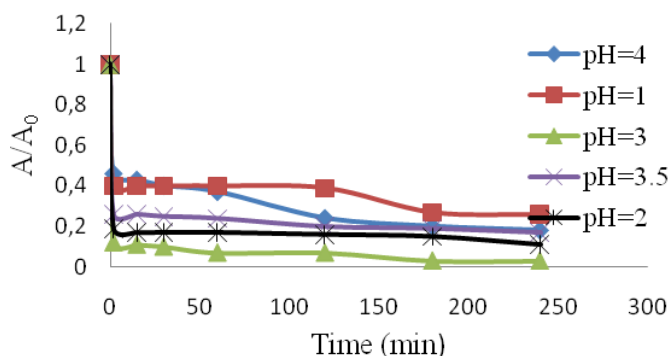


Figure 1: Effect of pH on the degradation of Congo red
 Conditions: CR concentration $C_0 = 50$ mg/l, $[\text{H}_2\text{O}_2] = 5 \cdot 10^{-2}$ M ;
 $[\text{Fe}^{++}] = 5 \cdot 10^{-5}$ M; $\lambda = 504$ nm

From figure 2 it is clear that the dye degradation increases with the increase of the Fe^{2+} ions concentration within a given interval which is due to the production of Fe^{2+} ions by Fenton process. However, the excessive addition of Fe^{2+} ions has a negative effect on the discoloration rate of dye. Indeed, for a Fe^{2+} concentration exceeding (0.0001 M), the degradation rate is significantly reduced. This is probably due to the side reaction between $\bullet\text{OH}$ and Fe^{2+} .

Figure 3 shows that the increase of H_2O_2 concentration yields an increase in the degradation efficiency of CR in the concentration range [0.00001 – 0.05M]. Consequently it can be assumed that a concentration of 0.05 M of H_2O_2 is an optimum concentration. Beyond this value, the degradation efficiency decreases. This is due to the trapping of $\bullet\text{OH}$ radicals by excess H_2O_2 .

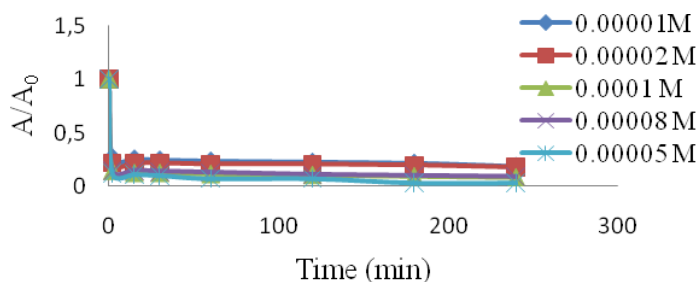


Figure 2: Effect of Fe^{2+} concentration on the degradation of Congo red
 Conditions : CR concentration $C_0 = 50 \text{ mg/l}$, $[\text{H}_2\text{O}_2] = 5 \cdot 10^{-2} \text{ M}$; $\text{pH} = 3$;
 $\lambda = 504 \text{ nm}$.

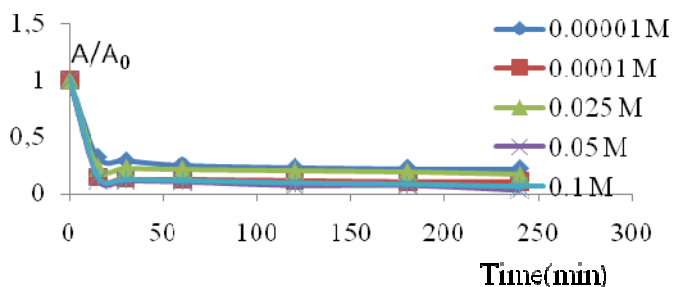


Figure 3: Effect of H_2O_2 concentration on the degradation of Congo red
 Conditions : $C_0 = 50 \text{ mg/l}$, $[\text{Fe}^{++}] = 5 \cdot 10^{-5} \text{ M}$; $\text{pH} = 3$; $\lambda = 504 \text{ nm}$

Figure 4 represents the evolution of the degradation rate of CR under the optimum conditions. It can be noticed that the initial degradation rate is relatively small followed by a faster process leading to an almost complete degradation (90%) after 180 minutes.

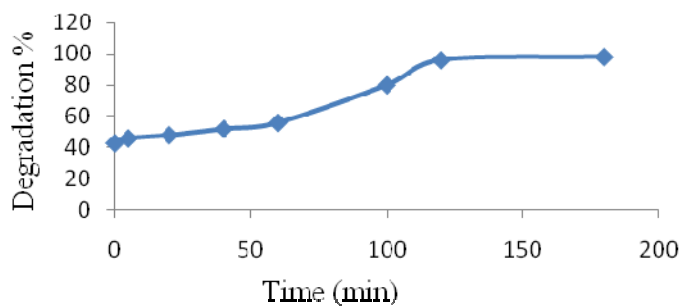


Figure 4: Degradation rate of CR using $\text{H}_2\text{O}_2/\text{Fe}^{++}$ system.
 Conditions: $C_0 = 50 \text{ mg/l}$; $[\text{H}_2\text{O}_2] = 5 \cdot 10^{-2} \text{ M}$; $\text{pH} = 3$; $[\text{Fe}^{++}] = 5 \cdot 10^{-5} \text{ M}$;

$$\lambda = 504 \text{ nm}$$

CONCLUSION

The present study demonstrated the efficiency of the AOP in degrading Congo red. The results obtained in the present study showed that at pH = 3 the discoloration of CR is more significant. Furthermore, the increase of H₂O₂ and Fe²⁺ ions favors the dye degradation. However, an excess of these substances had a negative effect. Optimal concentrations of 0.05 M and 5.10⁻⁵M were retained for H₂O₂ and Fe²⁺ respectively. Under the optimal conditions obtained the degradation of CR was 90% after 3 hours.

ACKNOWLEDGEMENT

The authors acknowledge the financial support of the Ministry of Higher Education (Algeria) through the research project grant (E01120/11/0065).

REFERENCES

- [1] K.T. Chung, G.E. Fluk, A.E. Andrews, Mutagenicity testing of some commonly used dyes, *Applied Environmental Microbiology*, 1981, 42 641-648.
- [2] M.A. Brown, S.C. DeVito, Predicting azo dye toxicity, *Critical Reviews in Environmental Science and Technology*, 1993, 23 249-324.
- [3] I. Gulkaya, and al, Importance of H₂O₂/Fe⁺⁺ ratio in Fenton's treatment of a carpet dyeing wastewater. *Journal of Hazardous Materials*, 2006, 136, 763-769.
- [4] J. De Laat, G. Truong Le, B. Legube, A comparative study of the effects of chloride, sulphate and nitrate ions on the rates of decomposition of H₂O₂ and organic compounds by Fe⁺⁺/H₂O₂ and Fe⁺⁺⁺/H₂O₂, *Chemosphere*, 2004, 55, 715-723.
- [5] H. Gallard, J de Laat, B. Legube, Influence du pH sur la vitesse d'oxydation des composés organiques par Fe(II)/H₂O₂, *New Journal of Chemistry*, 1998, 22,263-268.

OCCURRENCE AND CONCENTRATIONS OF PHARMACEUTICALS AND PESTICIDES IN GROUNDWATER IN SERBIA

M. Radišić¹, N. Dujaković¹, S. Kovačević², N. Šenk², M. Dimkić³, M. Laušević¹

¹*Faculty of Technology and Metallurgy, University of Belgrade Karnegijeva
4, 11000 Belgrade, Serbia*

²*Faculty of Technical Sciences, University of Novi Sad, Trg Dositeja
Obradovića 6, 21000 Novi Sad, Serbia*

³*Jaroslav Černi Institute for the Development of Water Resources,
Jaroslava Černog 80 11226 Pinosava-Belgrade, Serbia*

ABSTRACT

Occurrence of 17 pharmaceuticals, 2 metabolites and 15 pesticides were investigated in groundwater in Serbia. Groundwater samples were collected from drainage system near Danube River and groundwater source on the bank of Morava River. Sampling was conducted in the period from 2010 to 2013, mostly in spring or early summer and fall. Occurrence of pharmaceuticals and pesticides was also monitored in corresponding surface water. The total number of analysed samples was 65. Concentrations of investigated analytes in surface water were higher for Morava than for Danube River. However, the occurrence of investigated analytes was less frequent, in lower concentrations in Morava than in Danube groundwater. Pharmaceuticals and pesticides were detected in low concentrations ($>100 \text{ ng l}^{-1}$) in 72 % of investigated Danube River groundwater and in 42% of investigated Morava River groundwater samples.

INTRODUCTION

The aim of this work was to monitor occurrence of pharmaceuticals and pesticides in groundwater (GW) in several drainage systems near Danube River and groundwater source on Morava River bank. Surface waters may be an important source of groundwater pollution. Therefore corresponding surface waters (SW) were also monitored. The following pharmaceuticals and metabolites were chosen for this study: sulfamethoxazole, trimethoprim, erythromycin, azitromycin, doxycycline (antibiotic); diazepam, bromazepam, lorazepam, carbamazepine (sedatives); bisoprolol, metoprolol, enalapril, clopidogrel, atorvastatin, amlodipine, simvastatin (cardio vascular); diclofenac (analgoantipyretic); 4-formylaminoantipyrine, AAA, 4-

acetylaminoantipyrine, FAA (metamizole metabolites). The investigated pesticides include: atrazine, simazine, propazine, linuron, monuron, diuron (herbicides); monocrotophos, dimethoate, malathion, imidacloprid, acetamiprid, tebufenozide, carbofuran, carbaryl (insecticides); carbendazim (fungicide).

EXPERIMENTAL

Groundwater samples were collected from drainage system near Danube River and groundwater source on the bank of Morava River in the period from the year 2010 to 2013, mostly in spring or early summer and fall. Samples were analyzed using previously developed methods for pharmaceutical and pesticide analysis [1, 2]. Sample preparation consisted of solid-phase extraction using Oasis HLB cartridges, 100 mL of the water sample (pH = 6), and methanol-dichloromethane (1:1) as extraction solvent. As for the LC-MS² method, the chromatographic separation of compounds was performed on a reverse-phase Zorbax Eclipse[®] XDB-C18 column, 75 mm × 4.6 mm ID and 3.5 μm particle size. The mobile phase consisted of water, methanol and 10% acetic acid. The mass spectrometric measurements were obtained using the quadrupole ion trap mass spectrometer with positive electrospray ionization. The most abundant MS² fragment was used for quantification, while other MS² and/or MS³ fragments were used for conformation of investigated analytes. Calibration was conducted using the standard addition method.

RESULTS AND DISCUSSION

Concentrations of pharmaceutical and pesticide residues detected in investigated samples are presented in Table 1. Additionally, maximum concentrations and number of positive observations are listed. In all the samples of surface water and groundwater the most frequently found were pharmaceuticals: carbamazepine, metamizole metabolites AAA and FAA and pesticide carbendazim.

In all tested surface water samples of Morava River at least one of the investigated analytes was found. Out of all monitored compounds, ten were found to be present in Morava River surface water, seven pharmaceuticals, including metamizole metabolites, and three pesticides. In Morava River groundwater only three of all investigated analytes were found (carbamazepine, AAA and FAA), in 42 % of samples. Average concentrations found for AAA and FAA were ten and two times, respectively, lower in groundwater than in surface water. In comparison to surface water, concentration of carbamazepine was not significantly lower

in groundwater. Among pesticides, carbendazim was found in 33 % of surface water samples but it was never detected in groundwater. In the most of the positive samples more than one analyte was found, ranging from maximum 7 in surface water to maximum 3 in groundwater.

Table 1. Occurrence and average concentrations observed for pharmaceuticals and pesticides in surface waters (SW) and groundwater (GW) (maximum concentrations and number of positive samples per compound are given between brackets)

Compound	Morava River		Danube River	
	SW (n=12)	GW (n=12)	SW (n=12)	GW (n=29)
<i>Pharmaceuticals</i>				
Carbamazepine	39 (65, 7)	29 (75, 4)	22 (30, 8)	12 (41, 15)
AAA (N-acetil-4- aminoantipirin)	302(520, 10)	30 (53, 5)	125 (260, 8)	34 (105, 9)
FAA (4-formilamino- antipirine)	138 (248, 6)	61 (70, 2)	65 (144, 8)	38 (67, 15)
Ttimethoprim	223 (-, 1)	-	110 (-, 1)	-
Lorazepam	20 (-, 1)	-	-	-
Bisoprolol	4 (6, 2)	-	-	5 (-, 1)
Sulfamethoxazole	11 (-, 1)	-	-	-
Azithromycin	-	-	56 (-, 1)	44 (68, 2)
Metoprolol	-	-	35 (-, 1)	-
Clopidogrel	-	-	-	5 (-, 1)
<i>Pesticides</i>				
Carbendazim	82 (296, 4)	-	13 (23, 5)	29 (88, 13)
Atrazine	165 (-, 1)	-	12 (21, 2)	23 (64, 9)
Dimethoate	5 (7, 2)	-	-	1 (-, 1)
Carbofuran	-	-	-	5 (6, 3)
Propazine	-	-	8 (-, 1)	< LOQ (-, 3)
Simazine	-	-	8 (-, 1)	< LOQ (-, 3)

In Danube River groundwater, more compounds were detected than in surface water. The most frequently detected analytes were carbamazepine, AAA and FAA. In 84 % of surface water samples 2–6 analytes were detected. In groundwater 72 % of analysed samples contained 1–7 of investigated analytes, pointing out to the accumulation problem. Generally, concentrations found for pharmaceuticals in groundwater were lower than in

surface water. Pesticides, carbendazime and atrazine were more frequently and with higher concentrations detected in groundwater than in surface water. Atrazine (banned in Serbia in 2008) and carbendazim are relatively stable in the environment and their presences in groundwater most likely due to the accumulation.

CONCLUSION

In this work occurrence of pharmaceuticals and pesticides in groundwater (GW) in several drainage systems near Danube River and groundwater source on Morava River bank were monitored. Analytes and their concentrations were compared with those obtained in related surface water. In Morava river groundwater less analytes were found and in lower concentrations than in surface water. Only carbamazepine was not significantly reduced. In Danube River groundwater more analytes were found than in related surface water. Concentrations found in groundwater were generally lower than in surface water. Pesticides, atrazine and carbendazim were detected more frequently and in higher concentrations in Danube River groundwater, pointing out the accumulation problem.

ACKNOWLEDGEMENT

The authors thank the Ministry of Education and Science of the Republic of Serbia (projects No. 172007, TR 37014) for providing financial support.

REFERENCES

- [1] S.Grujić, T.Vasiljević, M.Laušević, *J of Chromatogr A*, 2009, 1216 4989–5000.
- [2] N. Dujaković, S. Grujić, M. Radišić, T. Vasiljević, M. Laušević, *Anal Chim Acta*, 2010, 678, 63–72.

APPLICATION OF RAW AND MODIFIED CLAY FOR THE REMOVAL OF HEAVY METALS FROM AQUEOUS SOLUTIONS

K. Kumrić¹, A. Đukić² and Lj. Matović²

¹Laboratory of Physics, ²Laboratory of Materials Sciences, Vinča Institute of Nuclear Sciences, University of Belgrade, P.O. Box 522, Belgrade, Serbia. (kkumric@vinca.rs)

ABSTRACT

This work represents a fundamental study of the simultaneous sorption of heavy metals from aqueous solutions by locally available raw and mechanochemically activated natural clay. The obtained results show that the investigated clay, as an economical and efficient sorbent, has potential for application in the treatment of heavy-metal-contaminated wastewaters.

INTRODUCTION

Wastewaters containing heavy metals as contaminants originate from a large number of metal-related industries and mines. Heavy metals are toxic and nonbiodegradable, and their presence in streams and lakes causes serious environmental problems. To avoid water pollution, treatment, that is, the removal of heavy-metal ions from industrial wastewaters, is needed before disposal. Among other conventional techniques, adsorption appears to be an attractive process in view of its efficiency and simplicity of operation, as well as the availability of a wide range of adsorbents [1 - 3].

Clay minerals are good adsorbents for metal ions from aqueous solutions owing to their high cation-exchange capacities, high abundance and local availability, nontoxicity, chemical and mechanical stability, low costs, and ability to be recycled [4]. To improve the adsorption characteristics of the clays, different techniques of modification (acid activation, intercalation and pillaring, mechanochemical activation, etc.) can be applied. In comparison with other methods, mechanochemical activation represents an environmentally friendly and inexpensive method of materials modification. The aim of this study was to investigate the simultaneous removal of Pb(II), Cu(II), Cd(II) and Zn(II) ions using locally available raw and mechanochemically activated clay as adsorbents. The effect of the time of adsorption and the adsorbent concentration on the process efficiency was observed.

EXPERIMENTAL

The raw natural clay used as an adsorbent was obtained from the mine Bogovina (Serbia). Mechanochemical activation (milling) was performed in air in a Turbula type 2TC mixer at ball-to-powder ratio (BPR) fixed at 4:1. The milling times tested were 2 and 19 h.

Batch experiments were carried out at room temperature by mixing an adequate amount of the clay and 25 cm³ of working multimetal ion solution in closed polyethylene bottles. Multimetal ion solution was prepared in milli-Q water using the analytical reagent grade chemicals Pb(NO₃)₂, Cd(NO₃)₂, Cu(NO₃)₂ and ZnCl₂. The total metal ion concentration in the working solution was 50 mg dm⁻³ at pH 5.5. The samples were shaken at stirring speed of 200 rpm for different periods of time (ranging from 30 s to 24 h). After that, the liquid phases were separated from the solid phases by filtration. The residual concentration of heavy-metal ions in each sample was determined with a 797 VA Computrace polarography system (Metrohm, Switzerland) using the Metrohm's procedure No. 231/2 e.

The efficiency of the adsorption process was evaluated by the two parameters: (1) the removal efficiency of particular metal ion, E , that represents the percentage of the metal ion removed from the initial solution and (2) the adsorption capacity of the clay, q_e , that represents the amount of metal ion adsorbed per unit mass of the adsorbent.

RESULTS AND DISCUSSION

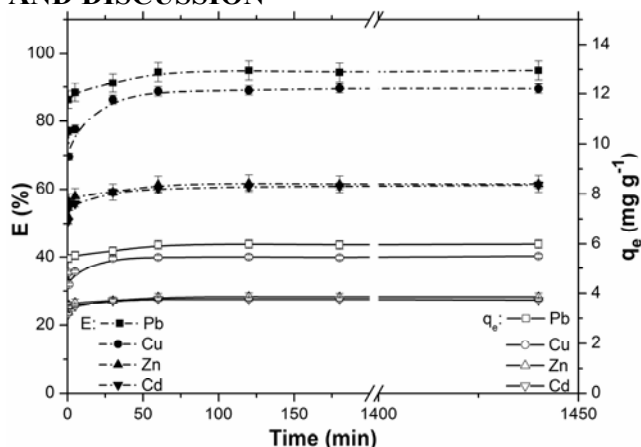


Figure 1. Effect of contact time on the adsorption of Pb(II), Cu(II), Cd(II) and Zn(II) by the raw clay at the fixed adsorbent concentration of 2 g dm⁻³. Fig. 1 shows the effect of contact time on the adsorption of Pb(II), Cu(II), Cd(II) and Zn(II) onto the raw clay. As can be seen, the equilibrium

adsorption was established after 60 min of contact, and the maximum uptake on the raw clay for all investigated metals was reached: 94.7% (6.0 mg g^{-1}) for Pb(II), 89.2% (5.4 mg g^{-1}) for Cu(II), 61.6% (3.8 mg g^{-1}) for Zn(II) and 60.8% (3.7 mg g^{-1}) for Cd(II). After equilibrium was reached, the contact time had no longer influence on the metal-ion adsorption.

In addition, it is evident that, after only 5 min of adsorption, the E values of Pb(II), Cu(II), Cd(II) and Zn(II) exceeded 85% of their values at equilibrium. This implies that the sorption mainly took place at the surface of the sorbent during the initial stage. The adsorption time of 60 min was used for the rest of the study.

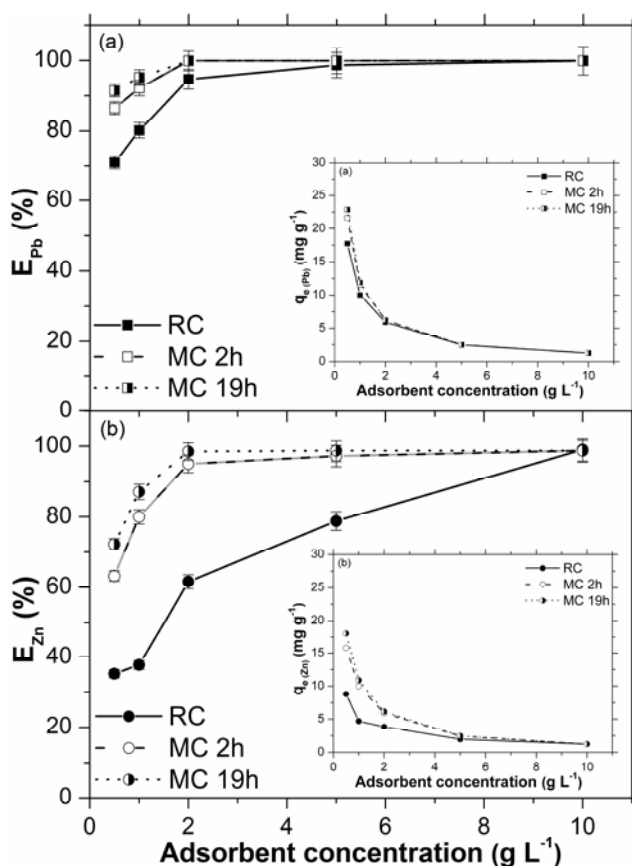


Figure 2. Effect of adsorbent concentration on the adsorption of (a) Pb(II) and (b) Zn(II) onto raw clay (RC) and 2- (MC 2h) and 19-h milled clay (MC 19h)

The effect of the adsorbent concentration was studied using raw and 2- and 19-h milled clays as adsorbents. The results obtained for Pb(II) and Zn(II)

ions are shown in panels a and b, respectively, of Fig. 2, and for the other two ions, Cu(II) and Cd(II), the obtained dependencies were similar. Obviously, upon increasing the adsorbent concentration, the amounts of adsorbed metal ions (i.e., their E values) increased. It can be explained by the fact that the number of available adsorption sites increased with increasing amount of clay and, hence, the E values of metal ions increased. The maximum removal efficiency for the raw clay was attained at the adsorbent concentration of 10 g dm^{-3} , whereas the same removal effect, using the 2- and 19-h milled clays, was achieved at an adsorbent concentration of 2 g dm^{-3} . Thus, the modification of the used raw clay by mechanical milling not only improved the adsorption characteristics of the adsorbent, in terms of the E values of the investigated heavy metal ions, but also reduced, by a factor of 5, the amount of adsorbent necessary to achieve the highly efficient removal of metal ions from aqueous solutions.

CONCLUSION

Raw natural clay from the Serbian mine Bogovina is an effective adsorbent for the simultaneous removal of heavy metals from aqueous solutions. The results showed that equilibrium was established after 60 min of contact. Mechanochemical activation of the raw clay significantly improved the adsorption behavior of the adsorbent and reduced the amount of adsorbent necessary to achieve the highly efficient removal of Pb(II), Cu(II), Cd(II) and Zn(II) ions by a factor of 5.

ACKNOWLEDGEMENT

We acknowledge the support to this work provided by the Ministry of Education, Science and Technology Development of Serbia through the projects No. III 45006, No. III 45012 and No. III 45001.

REFERENCES

- [1] Y.-J. An, Y.-M. Kim, T.-I. Kwon, S.-W. Jeong, *Science of the Total Environment*, 2004, 326, 85-93.
- [2] C. A. Oliveira Ribeiro, Y. Vollaire, A. Sanchez-Chardi, H. Roche, *Aquatic Toxicology*, 2005, 74, 53-69.
- [3] S. Babel, T. A. Kurniawan, *Journal of Hazardous Materials*, 2003, 97, 219-243.
- [4] M. Malandrino, O. Abollino, A. Giacomino, M. Aceto, E. Mentasti, *Journal of Colloid and Interface Science*, 2006, 299, 537-546.

HORIZONTAL DISTRIBUTION OF HEAVY METAL CONCENTRATIONS IN URBAN PARK SOIL

M. Todorović¹, M. Kuzmanoski¹ and T. Ljubenović²

¹ *Institute of Physics, University of Belgrade, Pregrevica 118, 11080 Belgrade, Serbia*

² *The Faculty of Chemistry, University of Belgrade, Studentski Trg 12/16, 11000 Belgrade, Serbia*

ABSTRACT

Soil samples, collected in an recreational park area in Belgrade, at different distances from the street, were analyzed for concentrations of Cr, Cu, Mn, Ni and Zn. All elements except for Zn showed larger concentrations at distances from the street up to 50 m. While Zn concentration did not show systematic variability with distance from the street, it varied along the street, with the largest value near the junction. Manganese showed gradual decrease with increasing distance from the street, while other metals did not show consistent decreasing trend.

INTRODUCTION

While heavy metals are naturally present in soil, studies show that their concentrations are higher in soils in urban areas [1]. Their elevated concentrations, particularly in urban parks and recreational areas where people easily come in contact with soil, can have harmful effects on human health. Heavy metal pollution of urban soil may have a variety of sources, mainly traffic emissions, but also weathering of building and pavement surface, industrial emissions, and waste incinerators [2]. Traffic emission comes from engine fuel combustion and wearing of vehicle parts such as brakes and tires, thus contributing to the environmental concentration of metals, such as Cr, Cu, Mn, Ni and Zn [3]. Here, we examine the influence of traffic on soil heavy metal pollution in a Belgrade urban park.

EXPERIMENTAL

The soil samples were collected in May 2013, in a park in a Belgrade residential area, located between Nikola Tesla Boulevard, characterized with high traffic density, and Sava river. Three transects perpendicular to the boulevard were chosen for sample collection (Figure 1). Topsoil samples (0-10 cm depth) were taken using a stainless steel shovel, at 8 to 12 locations along each transect, with distances of 10 m to 20 m between them. At each

sampling location four sub-samples were taken from a rectangular of approximately $2\text{ m} \times 2\text{ m}$ and mixed to obtain a composite sample. A total of 36 composite samples were made by mixing and homogenizing the collected sub-samples, and placed into polyethylene bags. The measurements of Cr, Cu, Mn, Ni and Zn concentrations in the soil samples, pressed into pellets, were performed using a PANalytical's MiniPal 4 X-ray fluorescence (XRF) spectrometer and the analysis of the spectral data was performed using MiniPal/MiniMate software. Detailed description of the measurements is given elsewhere [4].

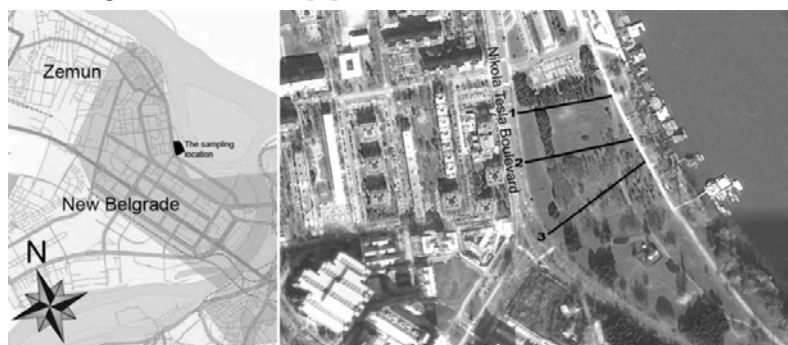


Figure 1. The three transects at the sampling location.

RESULTS AND DISCUSSION

A total of 36 samples collected along the three transects perpendicular to the street were analyzed for heavy metal content. The average abundance order of heavy metals in the samples was: $\text{Mn} > \text{Cr} > \text{Zn} > \text{Ni} > \text{Cu}$. Large differences were obtained between minimum and maximum concentrations for all metals of interest, showing their high variability in the study area. Concentrations of elements are within the ranges of values reported for Belgrade urban soil in other studies [5, 6]. The exception is Cr, which showed higher concentration values than those reported in these studies. Heavy metal concentrations did not show large variability along the street. The exception is Zn, with the largest concentration near the junction. Since Zn is mainly originating from tire abrasion, this can be associated with car deceleration due to traffic lights at the junction [7].

Variability of the elements of interest along each transect generally had similar pattern, with larger concentrations at distances from the street up to 50 m. Figure 2. shows the average element concentrations at three distance intervals: less than 30 m, 30 - 50 m, and more than 50 m.

Element concentrations were not consistently decreasing with distance. Copper, Ni and Cr showed maximal concentrations at distances of about 30 - 50 m from the street. This was particularly notable for Cu concentration.

Major traffic-related sources of Cu, Ni and Cr are brake linings and combustion of unleaded petrol and diesel fuels [3]. Their increase could be attributed to the accumulation caused by the tree tops preventing further intrusion of the emitted pollutants. In addition to the described concentration variability with distance from the street, Cu concentration also showed decrease with distance from nearby car parks (Figure 1). Copper and Ni concentrations at distances from the street above 50 m showed little variability and similar values along the three transects. The concentration of

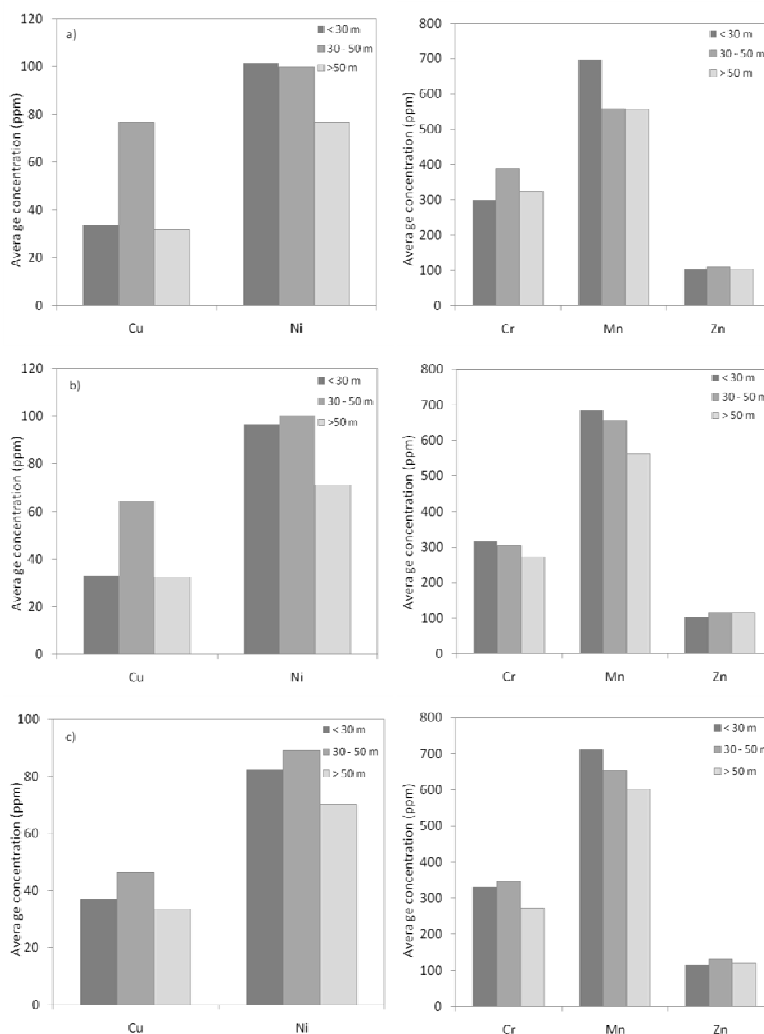


Figure 2. Average element concentrations at the three distance intervals along (a) transect 1; (b) transect 2; and (c) transect 3.

Zn exhibited variability in the examined area, however without systematic trend, or correlation with distance from the street and from the car parks, suggesting prominent influence of an alternative source which is not related to traffic. It should also be noted that the fast fallout of Zn-containing particles emitted from tire abrasion could be responsible for the absence of decreasing trend with distance from the street [7]. Conversely, concentration of Mn showed gradual decrease with increasing distance from the street, suggesting that traffic emissions may be an important source.

CONCLUSION

This paper presents preliminary results of analysis of horizontal distribution of heavy metal concentrations in a recreational park area in Belgrade. Soil samples, collected at different distances from the street, were analyzed for concentrations of Cr, Cu, Mn, Ni and Zn. The largest concentrations of Cu, Cr and Ni were obtained at distances of 30 - 50 m, while concentration of Mn showed clear decrease with increasing distance from the street. Zinc concentration did not show systematic variability, however it varied along the street and showed the maximal value near the junction. Absence of the decreasing trend with increasing distance from the street might be attributed to some additional sources, not related to traffic. In order to provide more insight into the effect of traffic on the park soil pollution, further analysis at higher depths, along with pollution mapping are required.

ACKNOWLEDGEMENT

This paper was realized as a part of the project No III43007 financed by the Ministry of Education and Science of the Republic of Serbia within the framework of integrated interdisciplinary research for the period 2011-2014.

REFERENCES

- [1] M. Biasioli, R. Barberis, F. Ajmone-Marsan, *Sci. Total Environ.*, 2006, 356, 154–164.
- [2] B. Wei and L. Yang, *Microchem. Jour.*, 2010, 94, 99–107.
- [3] EEA emission inventory guidebook 2009, <http://www.eea.europa.eu/>.
- [4] M. Kuzmanoski, M. Todorović, M. Aničić Urošević, S. Rajšić, *Hem. Ind.*, 2014, doi:10.2298/HEMIND131105001K.
- [5] I. Gržetić and R. H. A. Ghariani, *J. Serb. Chem. Soc.*, 2008, 73, 923-934.
- [6] M. Marjanović, M. Vukčević, D. Antonović, S. Dimitrijević, Đ. Jovanović, M. Matavulj and M. Ristić, *J. Serb. Chem. Soc.*, 2009, 74, 697-706.
- [7] G. Weckwerth, *Atmos. Environ.*, 2001, 35, 5525-5536.

GAS-CHROMATOGRAPHY MASS SPECTROMETRY DETERMINATION OF PHTHALATE ESTERS CONCENTRATION IN WATER SAMPLES

D. Milojković¹, T. Anđelković¹ and G. Kocić²

¹*Faculty of Science and Mathematics, University of Niš, Višegradska 33,
Niš, Serbia. (dannica.milojkovic@gmail.com)*

²*Faculty of Medicine, University of Niš, Bulevar dr Zorana Đinđića 81, Niš,
Serbia.*

ABSTRACT

Dimethyl phthalate (DMP), benzylbutyl phthalate (BBP) and diethylhexyl phthalate (DEHP) are substances that are mainly used as additives in plastics in aim to increase their flexibility. The goal of this investigation was determination of DMP, BBP and DEHP concentration in six water samples by GC-MS in single ion monitoring (SIM) and full scan (FS), for comparing the mode sensitivity. The results indicate the presence of DEHP and absence of BBP and DMP in all water samples. Average values for DEHP in water samples were 0.236-1.634 µg/L. Since the maximum allowed concentration for DEHP is 6 µg/L, the examined water samples don't influence to human health. A care should be taken in usage of distilled water in laboratory, since the level of DEHP could be significantly high.

INTRODUCTION

Phthalates, dialkyl or alkyl aryl esters of 1,2-benzenedicarboxylic acid, are well-known polymer additives that are used in formulations of plastics to make it soft and pliable. According to the literature, each phthalate shows different positive or negative impacts and toxicological properties, so each of them should be considered separately. Phthalates are commonly found in many consumer products, like beverage and drinking water containers. Products that contain phthalates can result in human exposures through direct contact and use, indirectly through leaching into other products (water, milk, food, etc.), because phthalates are not covalently bound to the plastics. Phthalate migration from plastic packaging specially can be enhanced in critical conditions of usage, such as long storage times, high storage temperature, etc. [1-2].

EXPERIMENTAL

All reagents used were *pro analysis* or HPLC grade purity. All used laboratory dishes were made of glass.

Fresh distilled water was collected from *water distillation apparatus directly into glass container*. Distilled water stored in plastic container was the distilled water from the *same water distillation apparatus*, stored in plastic container for 20 days before the analysis. Tap water sample was collected from local distribution network. Samples, that were commercially available, were purchased from market in Serbia and used as received, after water storage for one month in plastic bottles with plastic screw caps.

Water samples (150 ml of each) were mixed with 20 mL of hexane by using ultrasonic bath for 30 minutes per sample. Hexane extracts were evaporated to dryness under a nitrogen flow. The residue was redissolved in 1.0 mL hexane and analysed by GC-MS.

Gas chromatographic analyses were performed on a Hewlett Packard 6890 Gas Chromatograph equipped with an Agilent 5973 Mass Selective Detector and a DB-5 MS capillary column (30 m × 250 mm × 0.25 mm) for chromatographic separation. The MSD was used in SIM mode at m/z 149 and m/z 163. The identification of target compounds was based on the relative retention time, the presence of target ions and their relative abundance. The quantification ion was m/z 149 for BBP and DEHP and m/z 163 for DMP. Target ions and retention times for the investigated phthalates by GC-MS are given in the Table 1.

Table 1. Target ions and retention times for the investigated phthalates by GC-MS

Phthalate	m/z	Retention time (min)
DMP	163, 194	8.03
BBP	149, 91, 206, 238	16.02
DEHP	149, 167, 279, 150	18.39

RESULTS AND DISCUSSION

In both acquisition modes three analyzed phthalates were separated. Calibration curves were constructed. Linearity was good in the range from 0.25 to 50 mg/L with determination coefficients higher than 0.988.

Chromatograms and mass spectra showed that operation of a GC-MS in SIM mode provides detection of phthalates with increased sensitivity compared to FS mode. SIM acquisition mode ensures the elimination of difficult matrix interferences and the selectivity is greatly enhanced. In the Figure 1 and Figure 2 are shown MS spectra for DEHP recorded under FS and SIM mode, respectively.

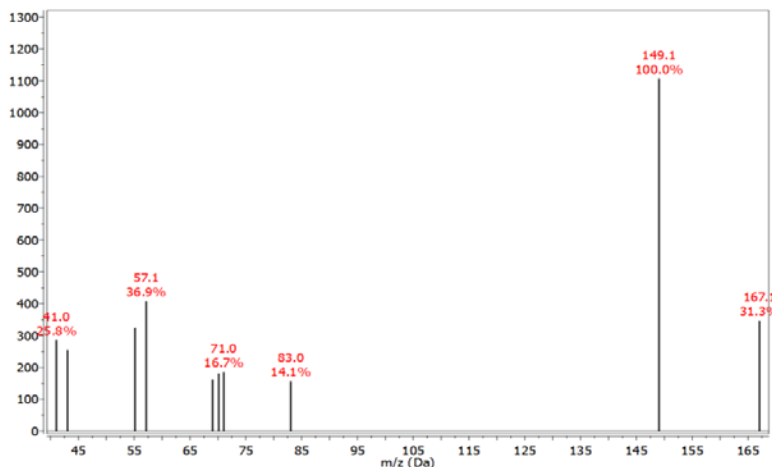


Figure 1. MS spectrum recorded under FS acquisition mode

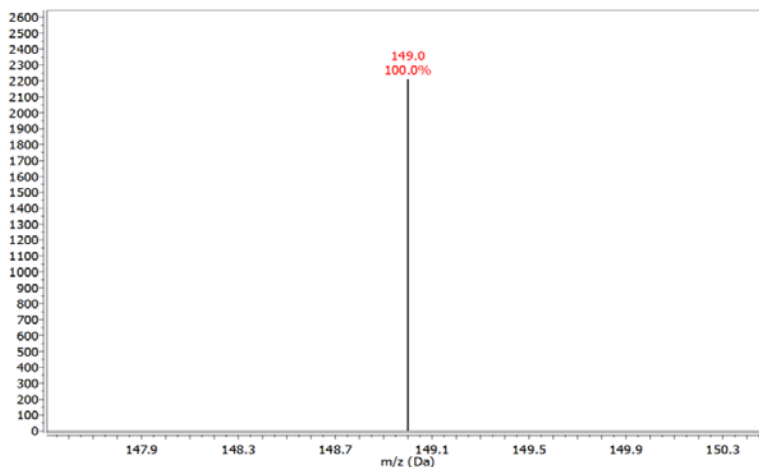


Figure 2. MS spectrum recorded under SIM acquisition mode

GC-MS analysis showed that only one of these phthalates, DEHP, was detected in the samples of water. The reason for that could be enormous use of DEHP as a plasticizer in manufacturing of the packaging material. Determined DEHP might be leached from package, for example, plastic bits for automatic pipettes contains DEHP. Laboratory air also contains DEHP. According to the Table 2, the highest concentration of DEHP in natural bottled mineral water. Also, distilled water contains some amount of DEHP. This is a problem for laboratory analysis and contamination of

samples. The amount of DEHP in distilled water from plastic container is greater than the amount in fresh distilled water, due to DEHP leaching from plastic container. Amounts of DEHP in carbonated bottled mineral water are similar. DEHP is the only compound regulated in United States of America by US EPA (2009) at a maximum level of 6.0 $\mu\text{g/L}$ and in World Health Organization (WHO) at level which is 8.0 $\mu\text{g/L}$. All analyzed six water samples are below that limits.

Table 2. Phthalates concentration in the investigated water samples

	Phthalate concentration ($\mu\text{g/L}$)					
	Tap water	Fresh distilled water	Distilled water from plastic container	Carbonated bottled mineral water		Natural bottled mineral water
				1	2	
DMP	n.d.	n.d.	n.d.	n.d.	n.d.	n.d.
BBP	n.d.	n.d.	n.d.	n.d.	n.d.	n.d.
DEHP	n.d.	0.224	0.935	0.318	0.236	1.634

CONCLUSION

This study shows that single ion monitoring is more sensitive in quantification of phthalate. Also, determined concentration of phthalates in water samples do not represent any risk for human health as can be seen by comparing the concentrations found to the existing US EPA regulation or WHO regulations. No significant correlation was found between concentrations of DEHP and the physical and chemical properties of the different water samples.

ACKNOWLEDGEMENT

This work was supported by the Ministry of Education, Science and Technological Development of the Republic Serbia and was performed as a part of Project TR 31060.

REFERENCES

- [1] L. Castle, A. Mayo, J. Gilbert, Food Additives and Contaminants, 1989, **6**, 437–443.
- [2] M.P. Sauvant, D. Pepin, J. Bohatier, Food Additives Contaminants, 1995, **12**, 567–584.

SOURCE APPORTIONMENT STUDY IN BELGRADE URBAN AREA

M. Todorović¹, M. Perišić¹, A. Stojić¹ and S. Rajšić¹

¹*Institute of Physics Belgrade, University of Belgrade, Pregrevica 118, 11080 Belgrade, Serbia (marija.todorovic@ipb.ac.rs)*

ABSTRACT

Unmix receptor model was applied on pollutants concentration data set obtained from two monitoring stations in Belgrade (Serbia) urban area. The aim of this work was to resolve potential emission sources and assess average source contributions. Three main source profiles were resolved for each sampling site. Two of them, traffic and mixed combustion processes, were common for both locations, while the third ones, heavy oil burning and secondary aerosol accumulation, reflect the difference in sampling site environments.

INTRODUCTION

Estimation of the quantitative relationship between ambient air quality and pollutant sources is a significant topic of air pollution research known as source apportionment. Receptor modeling, based on pollutant concentrations measured at the receptor site, is a widely used method of providing information about potential emission sources. Several source apportionment studies of air pollutants (particulate matter, its chemical components and gaseous pollutants) have successfully applied Unmix receptor model for this purpose [1]. Belgrade district is the commercial center of the Republic of Serbia and, as important intersection of roads and industry, requires special attention. Recently developed air quality monitoring network in Belgrade allows determination and control of pollution levels, which are needed for concrete actions in order to identify sources and reduce pollutant emission. In this study Unmix model was applied on data sets obtained from two monitoring stations for identifying main emission sources and their average contributions.

METHODOLOGY

Data sets of measured pollutant concentrations at two monitoring sites in Belgrade urban area were obtained from the Institute of Public Health of Belgrade [2]. Sampling site “Bulevar Despota Stefana” (BDS) is located in

the city center, with heavy and slow traffic in busy canyon street, while “Belgrade Bus Station” (BBS) is in the vicinity of the train and two main city bus stations. US EPA Unmix receptor model [3] was applied on data sets containing SO₂, NO₂, CO, PM₁₀, As, Cd, Mn, Ni, Pb, Cl⁻, NO₃⁻, SO₄²⁻, NH₄⁺, K⁺, BaP daily concentrations in the case of BDS, and soot, SO₂, NO₂, PM₁₀, As, Cd, Mn, Ni, Pb and BaP daily concentrations in the case of BBS.

RESULTS AND DISCUSSION

Concentrations of PM₁₀ were significantly higher than prescribed annual limit value (40 μg m⁻³) at both sites for each year during the analyzed period. According to previous studies in Belgrade [4], PM₁₀ emission reduction is required to comply with the Air Quality Standard. Unmix receptor model was applied in order to recognize the main types of sources whose emission reduction would improve the air quality. Three main source types were reconstructed for each sampling site. At BDS sampling site, source profiles were identified as mixed combustion processes (fossil fuel and biomass burning), secondary aerosols and traffic (include both, emissions and resuspension of particles on the roads). Profile of the first type is characterized by the dominance of As, Cd and 3,4 benzo(a)pyrene, and, along with medium loadings of Pb, and K⁺ and NO₃⁻ ions, it can be interpreted as mixed combustion processes [5]. The second profile is dominated by NH₄⁺ and SO₄²⁻ ions, with the loading of NO₃⁻ ions that is not negligible and can be related to secondary aerosols formation enhanced by the effect of canyon street that prevents ventilation. A third profile is predominantly composed of the gases (NO₂, SO₂ and CO), Mn, Ni, and Cl⁻, wherein the chlorine presence is a consequence of salt resuspension from the roads during winter [6]. Estimated mean contributions of reconstructed source profiles are shown in Figure 1(left). In addition to the pronounced influence of emissions from traffic and other combustion processes, Unmix resolved third profile at the BBS with high loadings of SO₂, Cd and Pb, attributed to heavy oil burning, which is most probably the consequence of proximity of two bus stations and a river marine to the sampling site. Estimated mean contributions of reconstructed source profiles at this location are shown in Figure 2 (right).

Table 1. The chemical source profiles (%) resolved by Unmix model at the BDS sampling location

Species	Source I	Source II	Source III
SO ₂	27.8	0	72.2
NO ₂	34.7	3.5	61.8
CO	33.9	10.2	55.8
PM ₁₀	40	17.4	42.6
As	67	9.3	23.7
Cd	74.5	0.5	25
Mn	13.7	1.4	84.9
Ni	18.6	10.7	70.7
Pb	50.4	11.7	37.9
Cl	26.9	7.6	65.4
NO ₃ ⁻	44.3	37.3	18.4
SO ₄ ²⁻	17.4	66	16.6
NH ₄ ⁺	22.4	77.6	0
K ⁺	48.5	28.2	23.3
BaP	89.1	10.9	0

Table 2. The chemical source profiles (%) resolved by Unmix model at the BBS sampling location

Species	Source I	Source II	Source III
Soot	0	37.1	62.9
SO ₂	40.2	19.8	40
NO ₂	10.5	0	89.5
PM ₁₀	2.2	33.6	64.2
As	23.9	74	2.1
Cd	80.9	0	19.1
Cr	27.7	8.7	63.6
Mn	4.8	0	95.2
Ni	0	5.3	94.7
Pb	100	0	0
BaP	0	100	0

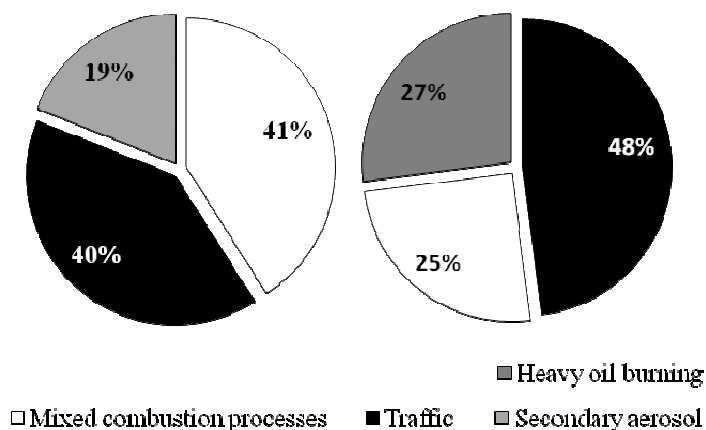


Figure 1. Average source contributions at BDS (left) and BBS (right)

CONCLUSION

Both sampling sites represent urban locations under the high influence of traffic emission, heating plants and residential heating units. Higher traffic contribution at BBS and existence of heavy oil use, makes the main distinction, while the additional difference is reflected in presence of secondary aerosols source profile in canyon street environment.

ACKNOWLEDGEMENT

This paper was realized as part of projects No III43007 and No III41011 financed by the Ministry of Education, Science and Technological Development of the Republic of Serbia within the framework of integrated and interdisciplinary research for the period 2011-2014.

REFERENCES

- [1] Y. Songa, S. Xiea, Y. Zhanga, L. Zengb, L.G. Salmonc, M. Zhengd, *Sci. Total Environ.*, 2006, 372, 278–286.
- [2] Institute of Public Health Belgrade, Serbia, available from <http://www.beoeko.com/> (in Serbian)
- [3] U.S. Environmental Protection Agency, 2007. EPA Unmix Version 6.0, available from <http://www.epa.gov/heasd/research/unmix.html>.
- [4] M. Perisic, Z. Mijic, A. Stojic, S. Rajsic, 4th Webiopat workshop and conference, 2013, 64-68.
- [5] L. Morawskaa, J. Zhang, *Chemosphere*, 2002, 9, 1045–1058.
- [6] C.A. Belis, F. Karagulian, B.R. Larsen, P.K. Hopke, *Atmos. Environ.*, 2013, 69, 94–108.

ASSESSING PM₁₀ REQUIRED SOURCE EMISSION REDUCTION IN OBRENOVAC

M. Perišić¹, M. Todorović¹ and S. Rajšić¹

¹*Institute of Physics Belgrade, University of Belgrade, Pregrevica 118, 11080 Belgrade, Serbia (marija.todorovic@ipb.ac.rs)*

ABSTRACT

Mass concentrations of PM₁₀ (particle matter with aerodynamic diameter less than 10 μm) were measured from 2011 to 2013 in Obrenovac (Serbia) seriously affected by industrial pollution. The main purpose of this study was to assess the frequency of daily PM₁₀ limit values exceedances, as well as the emission source reduction required to comply with air quality standard. Since annual and daily mean values were exceeded for each year, the required source emission reduction was estimated to be within the range 46-108%. In recent years, the decreasing trend of PM₁₀ concentrations was observed.

INTRODUCTION

European Union Air Quality Standard (AQS) [1] established the PM₁₀ annual limit values of 40 μg m⁻³ and daily concentration of 50 μg m⁻³ not to be exceeded more than 35 days per year. In places that have surrounding industrial facilities, it is very difficult to achieve the required environmental standards. Thermal Power Plants "Nikola Tesla" A and B are the dominant sources of air pollution in Obrenovac (Serbia) and exceedances of the limit values occur during the whole year, which could greatly affect the human health and life quality [2]. By using statistical methods of fitting the measured concentrations to known distribution functions it is possible to predict the number of exceedances, as well as to evaluate the required reduction of the sources emission to achieve AQS. Information about dynamics of pollutants and necessary reduction at the sampling site contributes to the implementation of emission abatement technologies in large combustion plants.

METODOLOGY

Hourly PM₁₀ mass concentration data for the period 2011-13 were obtained from the “Obrenovac” automatic monitoring station of the Institute of Public Health of Belgrade [3].

For statistical analysis three theoretical frequency distributions lognormal, Pearson type 5 and Weibull were used to fit complete data set. Kolmogorov-Smirnoff (K-S) and Anderson-Darling (A-D) statistical tests were used for evaluating the goodness of fit. Required source emission reduction for each year was calculated on the basis of distribution that best fit measured concentrations and rollback equation [4]. For each year estimated reductions are shown in a minimum - maximum range, where background concentrations used in rollback equation were set to zero and the measured value in suburban environment, respectively [5]. In addition, concentration trends were analyzed with the Openair software [6].

RESULTS AND DISCUSSION

During the analyzed period, PM₁₀ annual mean values were in the range from about 50 to 96 µg m⁻³ (Table 1), which exceeds the EU air quality guideline. During the same period, daily mean PM₁₀ concentrations exceeded the value of 50 µg m⁻³ for 450 days. PM₁₀ pollution in Obrenovac is mainly associated with coal combustion in thermal power plants and individual heating units.

Table 1. Mean, maximum and minimum values of PM₁₀ [µg m⁻³]

	Mean	Max	Min	Mean			
				Winter	Spring	Summer	Autumn
2011	62.43	347.37	7.04	61.56	25.96	65.61	95.33
2012	96.07	392.03	13.14	70.00	77.13	105.53	128.38
2013	49.69	286.61	6.71	101.6	24.81	26.46	40.37

For each year, increase in concentrations during the heating seasons (October - March) was noticeable. In addition, PM₁₀ concentration trend is presented in Figure 1. Increasing of concentrations and positive trend can be seen, with the highest PM₁₀ values obtained during 2012. The occasional scattering of particles from the surrounding ash dumps could have contributed significantly to measured concentrations in this period.

Decreasing concentrations during 2013 and reduction of the number of exceedances were most probably consequence of industrial plants renewal.

However, this PM₁₀ emission decline still is not enough to match the AQS.

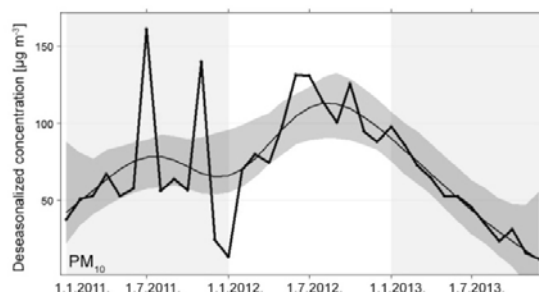


Figure 1. Trend of PM₁₀ mass concentrations during the period 2011-2013.

Statistical tests indicate the best fit of lognormal distribution for PM₁₀ concentrations measured during 2011 and 2012, and Pearson type 5 for 2013. Evaluated maximum emission reductions were in interval from 70 to 108% (Figure 2), indicating that reducing just the local source emissions might not be sufficient to comply with AQS.

Table 2. Estimated distribution parameters, goodness of fit tests and comparison between predicted and observed number of exceedances

Year	Probability Density Function (PDF)	Parameters		Goodness of fit		Number of exceedances of daily limit value	
		Shape	Scale	K-S	A-D	Predicted	Observed
2011	Lognormal	0.74	3.85	0.026	0.229	153	
	Pearsons type 5	2.01	72.65	0.056	1.801	137	147
	Weibull	1.34	68.69	0.074	3.992	169	
2012	Lognormal	0.62	4.38	0.056	0.716	216	
	Pearsons type 5	2.59	168.84	0.102	3.36	208	214
	Weibull	1.72	108.39	0.057	1.623	215	
2013	Lognormal	0.79	3.55	0.095	3.135	107	
	Pearsons type 5	1.98	52.59	0.047	0.605	95	89
	Weibull	1.16	52.91	0.148	11.345	129	

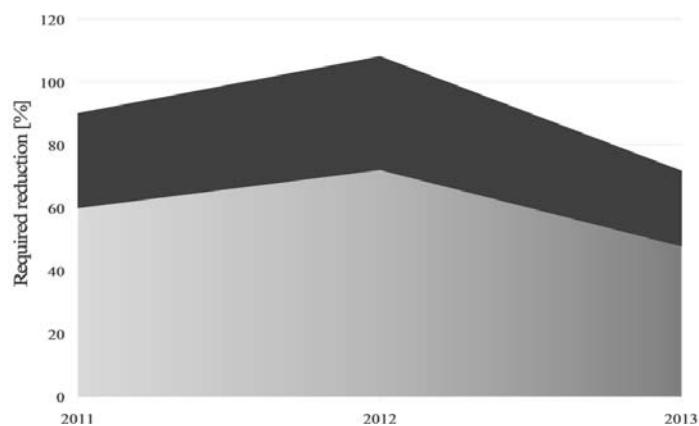


Figure 2. Estimated range of required source emission reduction based on three years monitoring period

CONCLUSION

Based on the three-year period of measured concentrations, analysis shows significant PM₁₀ pollution impact in Obrenovac. According to estimated source emission reduction, more strict mitigation measures are necessary for this area to comply with the AQS. Announced general reconstruction of power plants may contribute to this cause in the near future.

ACKNOWLEDGEMENT

This paper was realized as part of projects No III43007 and No III41011 financed by the Ministry of Education, Science and Technological Development of the Republic of Serbia within the framework of integrated and interdisciplinary research for the period 2011-2014.

REFERENCES

- [1] Directive 2008/50/EC.
- [2] C.A. Pope, D.W. Dockery, J. Schwartz, *J. Inhal. Toxic.*, 1995, 1-18.
- [3] Institute of Public Health Belgrade, Serbia, available from <http://www.beoeko.com/> (in Serbian)
- [4] P.G. Georgopoulos, J.H. Seinfeld, *Environ. Sci. Tech.*, 1982, 401-416.
- [5] V. Aleksandropoulou, K. Eleftheriadis, E. Diapouli, K. Torseth, M. Lazaridis, *Jour. Environ. Monitor.*, 2012, 266-278.
- [6] D.C. Carslaw, K. Ropkins, *Environ. Mod. Soft.*, 2012, 27-28, 52-61.

PREPARATION OF CELLULOSE ACETATE-MONTMORILLONITE COMPOSITES FOR WASTE WATER TREATMENT

M. Stanković¹, A. Mitić¹, N. Krstić¹, D. Djordjević¹, R. Nikolić¹ and A. Bojić¹

¹*Department of Chemistry, Faculty of Natural Sciences and Mathematics, University of Niš, Višegradska 33, 18000 Niš, Serbia (majstan@gmail.com)*

ABSTRACT

In this paper, cellulose acetate/Na-activated montmorillonite composite materials were synthesized and used as adsorbent for removing Cu(II) ions and methylene blue from aqueous solutions. Method for making composites consisted of mechanically mixing the Na-activated montmorillonite clay with cellulose acetate. The objective was to investigate the effect of clay percentage on the sorption behavior of composite samples.

INTRODUCTION

Natural materials such as clay minerals can be used for the removal of a wide spectrum of pollutants (inorganic - heavy metal ions, as well as organic - pesticides, organic dye, etc.) from waste waters because of their high specific surface area, chemical and mechanical stability, availability and low cost. The disadvantage of application of clay minerals in this purpose is difficulties to separate the clays from the solution after the adsorption because of the small particle size and the powder materials are not suitable for recycling. Therefore clay minerals were dispersed in the polymer matrix and provided adsorption sites [1]. A lot of different clay minerals have been used in the manufacture of polymer/clay composites, such as kaolinite, illite, but montmorillonite is favored for two reasons. First, it allows chemical modification that makes compatible the organic matrix. Second, it can be found in the nature in the mineralogical pure state, which reduces costs [2].

Cellulose acetate was used as polymer matrix because it could be easily produced into different forms.

The experimental part of the paper was focused on getting the sorbents based on cellulose acetate (CA) and Na-activated montmorillonite (Na-MMT), and examination the influence of clay percentage on the sorption behavior. The composite materials were tested for removal the Cu(II) ions

and methylene blue (MB) from the model wastewater in the stationary conditions. MB was chosen in this study because of its known strong adsorption onto solids and its recognized usefulness in characterizing adsorptive material [3].

EXPERIMENTAL

Preparation of CA is carried out as follows: 2.0 g of the cellulose, 80 mL of glacial acetic acid, 20 mL of acetic anhydride and 12 drops of concentrated sulfuric acid were stirred in the Erlenmeyer flask during 8 hours until the cellulose dissolves. Thereafter the solutions were poured out within the beaker containing 400 mL of cold deionized water and CA was separated as a precipitate. The precipitate is squeezed on a Buchner funnel and washed with deionized water. CA was dissolved in acetone and Na-MMT was added in different range to get material comprising: 75% CA and 25% clay (hereinafter CG25), 50% CA and 50% clay (CG50), and 25% CA and 75% clay (CG75). The resulting materials were dried in an oven at 105 °C during 24 hours.

The adsorption equilibrium experiments were conducted in 250 mL Erlenmeyer flasks, containing 125 mL of the Cu(II) ion solution (the concentration of 50.0 mg L⁻¹) and 0.5 g of sorbent material. The initial pH value was adjusted to 5.0, using HNO₃ or NaOH solutions, the concentration of 0.1/0.01 M. Aliquots of solutions (4.0 mL) were withdrawn at preset time intervals, the sorbent material was removed by centrifugation and the supernates were analyzed for Cu(II). All experiments were conducted at ambient temperature (20.0±0.5°C). Similar procedure was performed to investigate sorption of methylene blue onto composite material, wherein the pH of initial solution was adjusted to 8.0.

The concentrations of residual Cu(II) ions in the solution before and after adsorption were determined by using an atomic absorption spectrophotometer (AAS Analyst 300, Perkin Elmer, USA) at the wavelength 324.8 nm. The spectrophotometer was calibrated by a series of standard solutions. The concentrations of residual methylene blue in the solution before and after adsorption were determined by measuring their absorbance at 660 nm on a UV/VIS spectrophotometer Perkin Elmer Lambda 15.

The removal efficiency (RE) of the adsorbent was estimated according to the following equation:

$$RE = \times 100\%$$

where C_0 and C_e are the initial and equilibrium concentrations (mg L^{-1}) of adsorbate in solution, respectively.

RESULTS AND DISCUSSION

The efficiency of CA/Na-MMT composites with various clay content on removal of Cu(II) ions and MB from aqueous solutions is presented in Fig. 1. Also, the results for removal efficiency of Na-MMT under same conditions are given as a comparative system. Na-MMT showed the highest efficiency on removal of Cu(II) ions from aqueous solution. The decrease of clay content in composites (75%, 50%, and 25%)

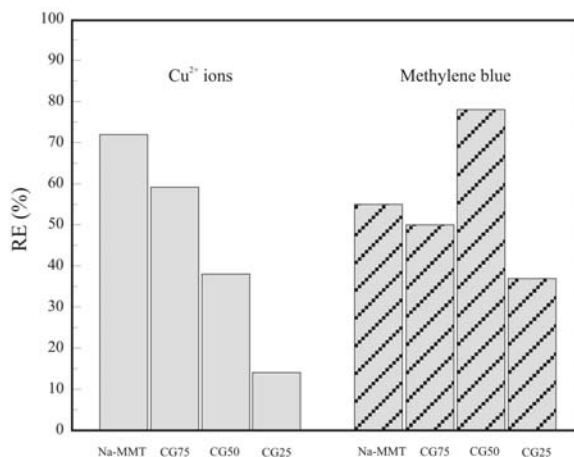


Figure 1. Removal efficiency of Na-MMT and various CA/Na-MMT composites for Cu(II) ions and methylene blue

caused decreasing in the removal efficiency for copper ions (58%, 37%, and 14%, respectively) onto sorbent materials. This suggested that the adsorption of copper ions was majorly attributed to the Na-MMT particles in the composites. On other side, CG50 showed the highest removal efficiency for MB (78%), followed by CG75 (removal of 51% of total MB), and CG25 (removal of 34% of total MB).

CONCLUSION

The results of our investigation demonstrate that the sorbent materials based on cellulose acetate and montmorillonite can be used effectively for the removal of organic dyes from waste waters, but less effective for the removal of copper. The higher clay percentage within composite material leads to improve sorption behavior. Therefore, the adsorption of copper ions and methylene blue was majorly attributed to the Na-MMT particles in the composites.

ACKNOWLEDGEMENT

This work was supported by the Ministry for Science of the Republic of Serbia (Grant no. TR 34008).

REFERENCES

- [1] F. Ji, C. Li, B. Tang, J. Xu, G. Lu, P. Liu, *Chemical Engineering Journal*, 2012, 209, 325-333.
- [2] C.D. Delhom, *Development and thermal characterization of cellulose/clay nanocomposites*, Louisiana State University, 2009.
- [3] S.S. Barton, *Carbon*, 1987, 25, 343–350.

NATURAL RADIOACTIVITY IN THE SOIL SAMPLES OF SUBOTICA, SERBIA

S. Pisanjuk¹, M. Đolić² and Lj. Janković-Mandić²

¹*Faculty of Physical Chemistry, University of Belgrade, Serbia*

²*Vinča Institute of Nuclear Sciences, University of Belgrade, Serbia*

ABSTRACT

The activity concentrations of ^{40}K , ^{226}Ra and ^{232}Th from 23 locations of the territory of Subotica were determined by gamma ray spectrometry. Based on the results obtained the value of absorbed gamma dose rate in air was calculated. Mean values of activity concentrations were found to be 277 Bq kg⁻¹ for ^{40}K , 18 Bq kg⁻¹ for ^{226}Ra and 18 Bq kg⁻¹ for ^{232}Th . The total absorbed gamma dose rate varied between 20 and 44 nGy h⁻¹. The mean value 31 nGy h⁻¹ is lower than the world average value.

INTRODUCTION

Around 90 % of human radiation exposure arises from natural sources such as cosmic radiations, exposure to radon gas, and terrestrial radiations. The naturally occurring radionuclides present in soil include ^{40}K , ^{226}Ra and ^{232}Th [1]. The knowledge of activity concentrations and distributions of the radionuclides in soil are of interest since it provides useful information in the monitoring of environment radioactivity.

The aim of this work to determine the activity concentrations of ^{226}Ra , ^{232}Th and ^{40}K in soil samples collected across the city of Subotica, using gamma ray spectrometry and use the results to calculate absorbed gamma dose rate in air.

EXPERIMENTAL

Subotica is the most northern city in Republic of Serbia. It is located on latitude 46°5'55" North and longitude 19°39'47" East. By census from 2002 it has 99,471 inhabitants and it is the second largest city in Autonomous Province of Vojvodina and sixth in Republic of Serbia. Subotica with its surroundings has continental climate and average annual temperature of 11.4°C. City is located in the Pannonian plane on 1,008 km² [2].

The samples of undisturbed soils (n=23) were collected from 23 locations of Subotica during 2013-2014. From each location, 3-4 subsamples were collected by template method [3], up to depth of 10 cm, and they were mixed (put together) into one composite sample. Samples were dried at

105°C to a constant weight and then homogenized. The homogenized samples were placed in 0.5 L Marinelli beakers. The beakers were sealed hermetically and kept a side for about a month to ensure equilibrium between ^{226}Ra and its daughters before being taken for gamma spectrometric analysis.

The measurements were performed using HPGe gamma-ray spectrometer ORTEC-AMETEK (49% relative efficiency and 1.85 keV FWHM for ^{60}Co at 1.33 MeV, 8192 channels) shielded with 10 cm lead internally lined with 2 mm copper foil. The activity of each sample was measured for 60 000 s. The activity of ^{226}Ra was evaluated from the gamma ray of 609.3 keV of ^{214}Bi peak and 351.9 keV of ^{214}Pb , while 911.2 and 969.1 keV gamma-ray lines emitted by ^{228}Ac and 238.6 keV emitted by ^{212}Pb was used to determine ^{232}Th . The activity of ^{40}K was determined using its 1460.8 keV gamma-ray line. Gamma Vision 32 was used to process the spectra obtained.

The external gamma dose rate in the air at 1 m above ground level was calculated from the measured activity concentrations of ^{226}Ra , ^{232}Th and ^{40}K in soil assuming that other radionuclides, such as ^{137}Cs , ^{90}Sr and the ^{235}U series can be neglected as they contribute very little to the total dose from environmental background [4]. The calculation were performed according to the following equation:

$$D = 0.462A_{\text{Ra}} + 0.604A_{\text{Th}} + 0.042A_{\text{K}} \quad (1)$$

where A_{Ra} , A_{Th} , and A_{K} are activity concentrations (Bq kg^{-1}) of ^{226}Ra , ^{232}Th and ^{40}K , respectively.

RESULTS AND DISCUSSION

Activity concentrations of ^{40}K , ^{226}Ra and ^{232}Th in soil samples collected in Subotica area are presented in Table 1.

It can be seen that activity concentrations of ^{40}K , ^{226}Ra and ^{232}Th ranged from 160 to 390 Bq kg^{-1} , from 12 to 29 Bq kg^{-1} and from 13 to 23 Bq kg^{-1} , respectively. Mean values of activity concentrations were found to be 277 Bq kg^{-1} for ^{40}K , 18 Bq kg^{-1} for ^{226}Ra and 18 Bq kg^{-1} ^{232}Th . These values are lower than the averages in Serbia (^{40}K 607 Bq/kg , ^{226}Ra 34 Bq/kg , ^{232}Th 42 Bq/kg) because of the different geological structures [5], but are similar to those obtained for Palic (^{40}K 310 Bq/kg , ^{226}Ra 19.9 Bq/kg and ^{232}Th 23.5 Bq/kg) [6].

Activity concentrations of analyzed radionuclides in soil are lower than those reported for neighboring Hungary (^{40}K (79-570) Bq/kg , ^{226}Ra (14-76) Bq/kg and ^{232}Th (12-45) Bq/kg) [7]. However, they are similar to the range

of activity concentrations in soil of Csongrad, the city in Southeast Hungary about (130 km far from Subotica) with similar geological substrate (^{40}K (276-453) Bq/kg, ^{226}Ra (14-44) Bq/kg, ^{232}Th (14-35) Bq/kg) [8].

The values of total gamma dose rates varied between 20 and 44 nGy h⁻¹, with the mean value 31 nGy h⁻¹ (52% lower than the world average value of 58 nGy h⁻¹) [9]. The contribution to the total absorbed gamma dose rate by ^{40}K , ^{226}Ra and ^{232}Th was 38%, 27% and 35%, respectively.

Table 1. Activity concentrations of ^{40}K , ^{226}Ra and ^{232}Th in soil samples collected in Subotica (Bq kg⁻¹)

Location	^{40}K	^{226}Ra	^{232}Th
Su-1	310±20	19±3	20±3
Su-2	320±20	18 ±3	19±3
Su-3	280±20	18±2	18±3
Su-4	360±30	20±4	21±2
Su-5	250±20	13±2	15±2
Su-6	390±30	22±3	23±3
Su-7	300±20	21±3	20±2
Su-8	270±20	16±3	18±4
Su-9	200±20	13±2	19±3
Su-10	260±30	17±3	16±3
Su-11	270±20	19±4	17±3
Su-12	230±30	21±3	15±2
Su-13	350±30	22±3	23±4
Su-14	240±20	12±3	13±3
Su-15	280±30	16±2	19±4
Su-16	160±10	29±3	15±3
Su-17	350±20	22±4	22±4
Su-18	220±20	15±3	14±3
Su-19	310±30	20±4	21±3
Su-20	300±30	18±4	20±4
Su-21	240±20	14±3	15±2
Su-22	200±30	12±3	14±3
Su-23	290±20	18±3	20±4

CONCLUSION

The activity concentrations of natural radionuclides ^{40}K , ^{226}Ra and ^{232}Th in 23 soil samples collected from the territory of Subotica were measured by gamma ray spectrometry. Based on these concentrations, the value of absorbed gamma dose rate in air was calculated. The obtained activity

concentrations and total gamma dose rates are lower than the world average values.

The results obtained in this study may be used for preliminary estimation of population exposure due to natural radionuclides. Further investigation is needed before definite conclusions on this issue are drawn.

ACKNOWLEDGEMENT

This work was supported by the Ministry of Education, Science and Technological Development of the Republic of Serbia (Project NoIII43009).

REFERENCES

- [1] Rani, S. Singh, *Atmos. Environ.*, 2005, 39, 6306 - 6314.
- [2] Republički zavod za statistiku, *Stanovništvo, pol i starost, podaci po naseljima*, Beograd, 2003.
- [3] International Atomic Energy Agency, *Soil sampling for environmental contaminants*, IAEA-TECDOC-1415, 2004.
- [4] K.C. Leung, S.Y. Lau, C.B. Poon, *J. Environ. Radioact.*, 1990, 11, 279-290.
- [5] S. Dragović, Lj. Janković, A. Onjia, G. Bačić. *Radiat. Meas.*, 2006, 41, 611-616
- [6] I. Bikit, J. Slivka, Lj. Čonkić, M. Krmar, M. Vesković, N. Žikić-Todorović, E. Varga, S. Čurčić, D. Mrđa *J. Environ. Radioact.*, 1990, 11, 11-19.
- [7] UNSCEAR, *Sources and effects of ionizing radiation. Report to General Assembly, with Scientific Annexes*, United Nations, 2000.
- [8] Z. Papp, *Rad. Prot. Dos.*, 2010, 141, 56-63.
- [9] UNSCEAR, *Sources and effects of ionizing radiation. Report to General Assembly*, United Nations, New York, 2008.

TRAFFIC-RELATED VOC DYNAMICS IN BELGRADE URBAN AREA

A. Šoštarić¹, A. Stojić², S. Stanišić Stojić³ and Z. Mijić²

¹*Institute of Public Health Belgrade, Bulevar Despota Stefana 54, 11000 Belgrade, Serbia (andrej.sostaric@zdravlje.org.rs)*

²*Institute of Physics Belgrade, University of Belgrade, Pregrevica 118, 11080 Belgrade, Serbia*

³*Singidunum University, Danijelova 32, 11010 Belgrade, Serbia*

ABSTRACT

The concentrations of VOCs (obtained by PTR-MS), ethylbenzene, xylene, NO_x, NO, NO₂, SO₂, CO and meteorological parameters were measured at Belgrade (Serbia) urban site during winter 2014. US EPA Unmix receptor model was applied on obtained dataset resolving six emission sources and their contributions to urban air pollution. The dynamics of traffic source contribution and its variation with meteorological parameters were analyzed. The results showed that the urban site is strongly influenced by traffic-related emissions with average contribution of 26%.

INTRODUCTION

Volatile organic compounds (VOCs) include large group of pollutants emitted from biogenic and man-made sources. Anthropogenic sources, estimated to be the major contributors, include traffic-related emission, industrial facilities, solvent usage, refineries, *etc.* [1]. On-line, real time monitoring of pollutant mixtures by means of Proton Transfer Reaction Mass Spectrometry (PTR-MS) allows high time-resolved and ultra-sensitive quantification of VOCs. Identification of daily and seasonal variability of concentrations and accurate determination of emission source profiles are substantial in understanding dynamics driving the VOCs variability and developing of efficient emission abatement strategies.

EXPERIMENTAL

During the campaign from January 22th to March 25th 2014, VOCs, NO_x, NO, NO₂, SO₂ and CO concentrations, and meteorological parameters were measured at the Institute of Public Health in Belgrade (Serbia) urban area. VOC measurements were conducted by Proton Transfer Reaction Mass Spectrometer (PTR-MS, Ionicon Analytik, Austria), while the other data

were obtained from the automatic monitoring station [2]. PTR-MS measuring cycle (24 s) consisted of 34 masses. The E/N parameter, reaction time and mean count rate of H_3O^+ ions were around 145 Td, 90 μs and $5.1 \cdot 10^6$ cps. Normalized sensitivities were calculated according to Taipale *et al.* [3]. For the purpose of source apportionment, US EPA Unmix receptor model [4] was applied on 26 compounds (1-hour averaged concentrations). The Openair software was used for the analysis of measured concentration dynamics, and their dependence on meteorological parameters [5].

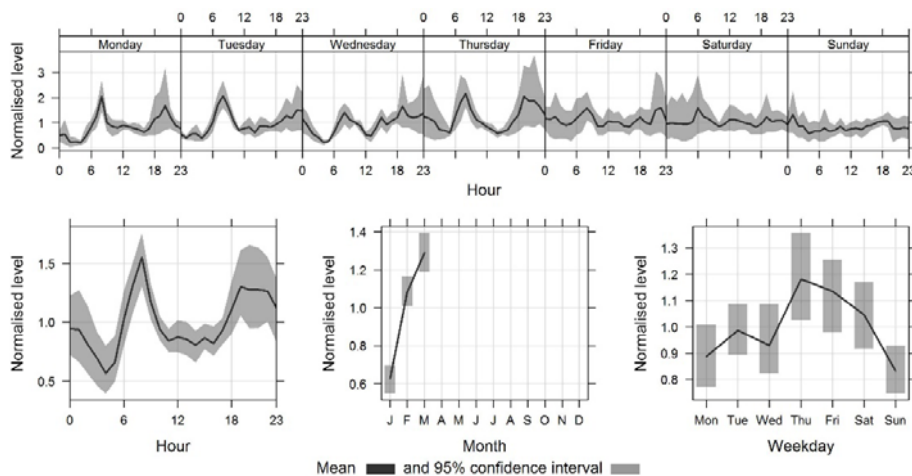
RESULTS AND DISCUSSION

Unmix resolved six source profiles, with the most abundant one accounting for 26% of average contribution. The dominant portions of the total concentrations of benzene (41.3%), NO_x (44.1%), toluene (46.3%), CO (50.6%), NO (56.4%), o-xylene (75.5%), mp-xylene (87.5%), ethylbenzene (80.5%) are apportioned to this source, indicating the profile can be attributed to traffic. Basic statistics regarding traffic-related compounds and meteorological parameters is presented in Table 1.

Apart from emissions, pollutant concentrations are strongly influenced by photochemistry and meteorological conditions. Regarding this, a pronounced diurnal pattern for the traffic-related source is observed in Figure 1. Weekday traffic is characterized by a prominent peak in the morning rush hour (07:00 - 10:00 h) and steady increase in the evening (18:00 - 22:00 h). During the midday (12:00 - 17:00 h), measured levels are decreasing due to the photochemical processes, moderate traffic intensity and pollutant dilution into an expanding daytime boundary layer. The highest contribution of traffic-related compounds is observed on Friday, whereas the weekend traffic load is significantly lower than on weekdays, and does not exhibit clear diurnal patterns. As can be seen in Figure 2, the maximum pollutant contributions coincide with the wind of low speed, which indicates the dominating impact of locally generated traffic emissions in the stagnant zone. The observed hotspot area of significant contribution at this site is enhanced by the specific conditions of a canyon street with low ventilation. The daytime data reveal a moderate contribution (for wind speed of around 3 m s^{-1}) of the emission area located in western sector which can be attributed to the nearest crossroad with heavy, slow traffic.

Table 1. Basic statistics for traffic related compounds VOCs, NO_x, NO [$\mu\text{g m}^{-3}$] and CO [mg m^{-3}], and meteorological parameters.

Species	Mean	Min	Max	St. Dev.
Wind speed [m s^{-1}]	1.69	0	6.15	1.19
Pressure [mbar]	1003.58	986.58	1018.24	7.39
Temperature [$^{\circ}\text{C}$]	8.52	-5.95	22.90	6.02
Relative humidity [%]	63.52	17.80	93.83	17.18
NO _x	149.69	11.24	912.42	116.19
NO	86.76	1.19	673.33	88.32
CO	0.68	0.16	3.42	0.38
Ethylbenzene	2.31	<d.l.	36.93	2.41
mp-Xylene	8.99	<d.l.	124.62	9.52
o-Xylene	1.88	<d.l.	18.52	1.72
m/z 57 (acrolein, MBTE)	1.94	0.26	28.82	1.93
m/z 79 (benzene)	1.35	0.05	6.95	0.90
m/z 93 (toluene)	3.36	0.19	29.66	2.62

**Figure 1.** Daily, weekly and monthly variations of the traffic-related source contribution.

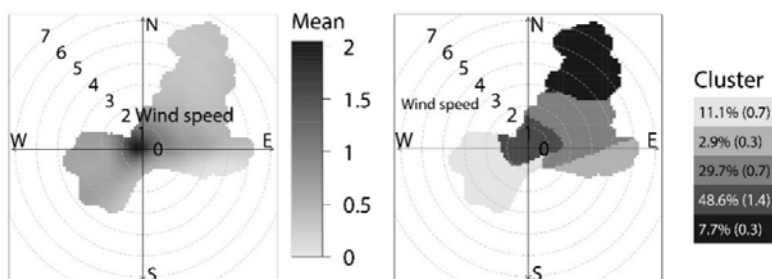


Figure 2. Wind speed and wind direction dependence (left) and cluster plot (right) of the traffic-related source contribution.

CONCLUSION

In this study Unmix receptor model was used in order to resolve emission source profiles and their contribution to urban air pollution. The dominant shares of several compounds were apportioned to traffic-related source profile. The contribution exhibits clear diurnal pattern, weekend/weekday differences, and specific dynamics related to urban site location and canyon street topography. As can be concluded, environmental regulation measures should be targeted on mitigating the pollutant emissions from the traffic-related sources.

ACKNOWLEDGEMENT

This paper was realized as part of projects No III43007 and No III41011 financed by the Ministry of Education, Science and Technological Development of the Republic of Serbia within the framework of integrated and interdisciplinary research for the period 2011-14.

REFERENCES

- [1] M.C. McCarthy, Y.A. Aklilu, S.G. Brown, D.A. Lyder, *Atmospheric Environment*, 2013, 81, 504-516.
- [2] Institute of Public Health Belgrade, Serbia, available from <http://www.beoeko.com/> (in Serbian).
- [3] R. Taipale, T.M. Ruuskanen, J. Rinne, M.K. Kajos, H. Hakola, T. Pohja, M. Kulmala, *Atmospheric Chemistry and Physics*, 2008, 8, 6681-6698.
- [4] U.S. Environmental Protection Agency, 2007. EPA Unmix Version 6.0, available from <http://www.epa.gov/heasd/research/unmix.html>
- [5] D.C. Carslaw, K. Ropkins, *Environmental Modeling & Software*, 2012, 27–28, 52–61.

THE CONTRIBUTION OF CHEMICAL INDUSTRY TO AMBIENT VOC LEVELS IN BELGRADE

S. Stanišić Stojić², A. Šošćarić³, Z. Mijić² and M. Perišić²

¹*Institute of Physics Belgrade, University of Belgrade, Pregrevica 118, 11080 Belgrade, Serbia*

²*Singidunum University, Danijelova 32, 11010 Belgrade, Serbia*

³*Institute of Public Health Belgrade, Bolivars Despota Stefana 54, 11000 Belgrade, Serbia (andrej.sostaric@zdravlje.org.rs)*

ABSTRACT

During a two-month campaign in winter 2014, the concentrations of VOCs were measured by Proton Transfer Reaction Mass Spectrometer (PTR-MS) together with other air pollutants (NO_x, NO, NO₂, SO₂ and CO) and meteorological parameters in Belgrade (Serbia) urban area. US EPA Unmix receptor model was applied resolving six source profiles. The profile with the third largest an average contribution of 12.8% was attributed to chemical industry. The spatio-temporal variations of source contributions and the impact of meteorological parameters were analyzed by Openair software. As shown, the air pollution from petrochemical complex located in Pančevo has a noticeable impact on air quality of Belgrade urban area.

INTRODUCTION

Over the last decade, great emphasis has been placed on anthropogenic emissions of volatile organic compounds (VOCs) due to the clear evidence of an association between short- and long-term exposure to those compounds and adverse health effects [1]. Apart from direct toxic or mutagenic effects, they are important contributors to the generation of ozone and other photochemical oxidants. The chemical industry is recognized as one of the major sources of VOCs originating from the production processes, leakages, loading and unloading operations, and waste treatment. Depending on the level and nature of emitted species, chemical plants pose serious environmental risks, not only on a local, but also on regional scale. The city of Pančevo in Serbia is home to the petrochemical complex (HIP Petrohemija), and is the leading polymer and petrochemical producer in the region with the annual production of more than 650 000 t of ethylene, propylene, methyl tertiary butyl ether (MTBE), synthetic rubber *etc.* [2]. Assessing the impact of petrochemical industry emissions on the Belgrade urban area is presented in this study.

EXPERIMENTAL

The VOC measurements were conducted using the Proton Transfer Reaction Mass Spectrometer (PTR-MS, Ionicon Analytik, Austria) for the two-month period (January 22nd to March 25th 2014) at the Institute of Public Health in Belgrade (Serbia). The concentrations of NO_x, NO, NO₂, SO₂ and CO and meteorological parameters were obtained for the same period from the automatic monitoring station at the same location [3]. PTR-MS measuring cycle (24 s) consisted of 34 masses with the E/N parameter, reaction time and mean count rate of H₃O⁺ ions were around 145 Td, 90 μs and 5.1·10⁶ cps, respectively. Calibration was conducted according to Taipale *et al.* [4]. US EPA Unmix receptor model [5] was applied to the obtained dataset consisting of 1-hour mean concentrations for 26 compounds. The analysis of source contribution dynamics and impact of meteorological conditions was conducted using Openair software [6].

RESULTS AND DISCUSSION

Out of six source profiles resolved by the use of Unmix, one of the sources is shown to have the third largest average contribution of 12.8%. The source contribution coincided with the winds of different speed, from all directions. Still, the highest contribution was associated with the winds coming from the northern and north-eastern direction, whereas winds from the south-western sector were of minor significance. On the basis of the given data, the contribution from the south-western sector was limited only to two isolated incidents that occurred during the night hours on March 2nd and 15th, when the double increase in contribution of several compounds was detected.

As regards weekly variations, the source contribution was highest during weekdays, followed by Saturday, with the maximum observed during working hours (9.00 a.m. - 04.00 p.m.), whereas for Sunday it exhibited a decrease (Figure 1). The decrease is also observed for the period from January to March, which can probably be associated with the prevailing winds blowing from the west in March rather than with the change in source emission. According to meteorological data, the wind speed follows weekly pattern with lowest values recorded on Monday and the average daily speed rising throughout the week. The source contribution follows the same pattern during weekdays; however stronger eastern and north-eastern winds during weekends did not result in higher contribution. On the basis of the observed source contribution dynamics, it can be assumed that the emission originates from the anthropogenic source located in the north-eastern sector which can be related probably to HIP Petrohemija.

The significant shares of the compounds with protonated masses m/z 41 (21.7%), m/z 57 (29.7%), m/z 61 (27.2%), m/z 71 (29.6%), m/z 73 (28.4%), m/z 75 (35.8%), m/z 79 (25.9%), m/z 81 (57.9%), m/z 93 (29.0%), m/z 99 (30.3%), m/z 101 (23.8%), m/z 105 (31.6%) and m/z 137 (63.9%) are apportioned to this source. Four of them are biogenic tracers: peaks m/z 137 and m/z 81 can be attributed to monoterpenes and their fragments, and m/z 99 and 101 to hexenal and hexanal, respectively. It should be taken into consideration that, although apportioned to this source, the last two compounds shown acceptable correlation (over 0.60) only with each other. High loading of monoterpenes and their fragments can be associated with the Botanical garden, located in the vicinity of the sampling site, and in the pathway of air masses coming from the north-eastern sector. As expected, the main part of the source profile comprises compounds that are abundant in petrochemical industry emissions. The two of them are produced in HIP Petrohemija: the most commonly used fuel oxygenate, MTBE (m/z 57), and one of the most important feed stocks in the petrochemical industry, propylene (m/z 41).

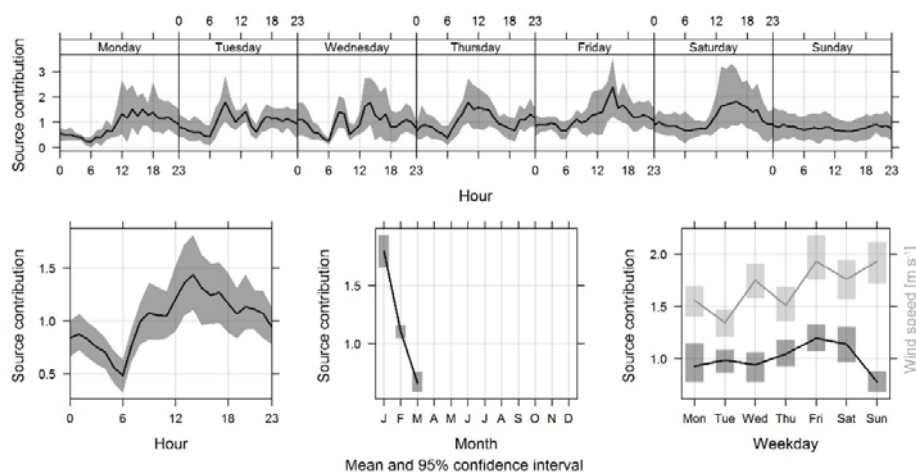


Figure 1. Diurnal, weekly and monthly variations of the source contribution related to petrochemical complex and wind speed [m s^{-1}].

CONCLUSION

In the current study, the Unmix model was applied for the purpose of assessing the effects of petrochemical industry emissions on the urban area of Belgrade. The results have shown that the emissions from petrochemical complex account for 12.8% of the observed pollutant contributions. As diurnal analyses revealed, the source contribution

exhibited a clear daily pattern with the maximum observed during working hours, followed by decrease on Sunday. The significant shares of several compounds which can be related to petrochemical industry, such as benzene, toluene, MTBE and propylene, are apportioned to this source.

The effects of air pollution related to petrochemical industry have to be considered on both local and regional scale and further investigations should be encouraged as they can provide a solid foundation for preparation and implementation of pollution abatement regulations.

ACKNOWLEDGEMENT

This paper was realized as part of projects No III43007 and No III41011 financed by the Ministry of Education, Science and Technological Development of the Republic of Serbia within the framework of integrated and interdisciplinary research for the period 2011-14.

REFERENCES

- [1] X.M. Wu, Z.T. Fan, X. Zhu, K.H. Jung, P. Ohman-Strickland, C.P. Weisel, P.J. Liou, *Atmospheric Environment*, 2012, 57, 72-79.
- [2] HIP-Petrohemija JSC, Pančevo, Serbia, available from <http://www.hip-petrohemija.com/about-us/general-information.130.html>
- [3] Institute of Public Health Belgrade, Serbia, available from <http://www.beoeko.com/> (in Serbian).
- [4] R. Taipale, T.M. Ruuskanen, J. Rinne, M.K. Kajos, H. Hakola, T. Pohja, M. Kulmala, *Atmospheric Chemistry and Physics*, 2008, 8, 6681-6698.
- [5] U.S. Environmental Protection Agency, 2007. EPA Unmix Version 6.0, available from <http://www.epa.gov/head/research/unmix.html>.
- [6] D.C. Carslaw, K. Ropkins, *Environmental Modeling & Software*, 2012, 27-28, 52-61.

DYNAMICS OF GASSEOUS POLLUTANTS IN BELGRADE URBAN AREA

A. Šošćarić¹, M. Perišić², A. Stojić², Z. Mijić² and S. Rajšić²

¹*Institute of Public Health Belgrade, Bulevar Despota Stefana 54, 11000
Belgrade, Serbia (andrej.sostaric@zdravlje.org.rs)*

²*Institute of Physics Belgrade, University of Belgrade, Pregrevica 118,
11080 Belgrade, Serbia*

ABSTRACT

The concentrations of nitrogen oxides, SO₂, CO, and BTEX were measured in an urban area of Belgrade (Serbia) in the period from 2011 to 2013. This paper presents analyses of concentrations and dynamics of measured pollutants on a daily, weekly and annual basis. Daily and seasonal variation indicate a significant impact of anthropogenic activities on pollutant concentrations, primarily traffic and heating. Considering meteorological parameters, predominantly local origin of the air pollution was observed.

INTRODUCTION

High population density, and consequently a high level of air pollution, is one of the main factors that determine the quality of life in urban areas. Production of pollutants characterizes almost all economic and social activities, of which industry and traffic are with the largest contribution [1]. Some of them are known to have adverse effects on human health and the environment. In order to estimate air pollution level in Belgrade urban area, a monitoring network was recently established by the Institute of Public Health of Belgrade [2]. This paper presents the analysis of data obtained at the "Slavija" automatic monitoring station, located in the city center, which is characterized by high traffic density and a large number of individual heating installations.

METHODOLOGY

The analysis were based on a three year (2011-13) data set that includes 1-hour mean concentrations of NO, NO₂, NO_x, SO₂, CO, benzene, toluene, ethylbenzene, xylene (BTEX compounds) and corresponding meteorological parameters. Concentration dependence on wind speed and direction were analyzed with the Openair software [3].

RESULTS AND DISCUSSION

Table 1. Mean, minimum and maximum values for measured pollutants and meteorological parameters from 2011-2013.

Species	Period								
	2011			2012			2013		
	Mean	Min	Max	Mean	Min	Max	Mean	Min	Max
Wind speed [m s ⁻¹]	2.13	0.11	8.39	2.24	0.03	9.02	1.97	0.02	7.71
Pressure [mbar]	1004.44	986.34	1022.32	1000.78	975.87	1020.33	1000.01	969.38	1025.14
Temperature [C°]	16.68	-2.68	38.29	14.38	-14.6	38.95	14.24	-3.72	38.02
Relative humidity [%]	60.48	20.69	100	60.67	12.33	100	65.65	12.98	100
NO [µg m ⁻³]	64.27	< d	801.17	60.6	0.06	915.88	57.39	0.58	1135.29
NO ₂ [µg m ⁻³]	52.4	0.01	1298.23	62.64	< l.d.	288.45	53.9	0.95	247.43
NOx [µg m ⁻³]	74.7	1.13	1067.36	101.65	< l.d.	1655.27	141.5	4.59	1901.39
SO ₂ [µg m ⁻³]	30.82	0.4	841.38	33.21	5.01	470.27	39.59	4.06	645.26
CO [mg m ⁻³]	1.21	0.13	14.66	0.86	0.01	10.75	1.03	0.04	17.8
Benzene [µg m ⁻³]	4.34	< d	42.77	3.49	< l.d.	476.74	2.43	< l.d.	78.87
Toluene [µg m ⁻³]	1.89	< d	51.97	4.49	< l.d.	80.27	5.87	< l.d.	410.74
mp-Xylene [µg m ⁻³]	0.78	< d	13.46	1.95	< l.d.	44.06	2.86	< l.d.	35.59
o-Xylene [µg m ⁻³]	0.25	< d	1.91	0.64	< l.d.	20.7	0.88	< l.d.	11.18
Ethylbenzene [µg m ⁻³]	0.26	< d	2.51	0.64	< l.d.	6.71	1.09	< l.d.	11.98

*l.d. – limit of detection

Mean, minimum and maximum values of the measured concentrations and the corresponding meteorological parameters are shown in Table 1. According to air quality standards [1], limit mean annual value of NO₂ (40 mg m⁻³) was exceeded each year, while the concentrations of SO₂, CO and benzene were within the permissible limits. Meteorological conditions at the end of 2011, low air pressure and wind speed of less intensity, favored the large accumulation of air pollution which was reflected in significant number of NO₂ hourly limit value exceedances (200 µg m⁻³).

Concentrations of all measured pollutants were lower on weekends (Figure 1). Also, the maximum pollutant contributions coincide with the maximum intensity of anthropogenic activities (early morning and afternoon). The nitrogen oxides ratio (NO/NO₂ > 1) point toward the traffic as one of the dominant sources of pollution [4]. The increase in concentration, especially

SO₂ during the heating season, indicates a significant influence of nearby heating plant. For BTEX compounds, there is evident concentration increase at the end of the year caused by intensifying traffic and by meteorological conditions favorable for their accumulation.

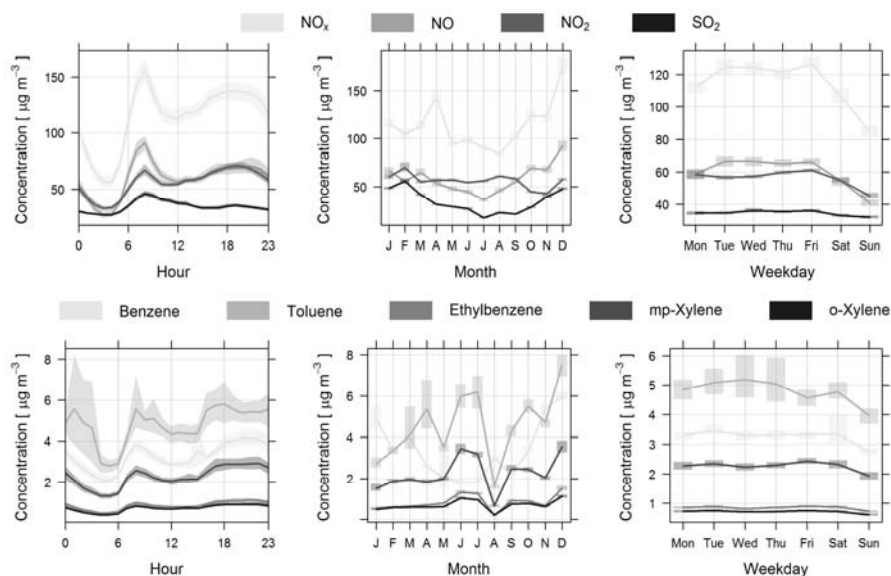


Figure 1. Daily, weekly and monthly variations of NO, NO₂, NO_x, SO₂ and BTEX concentrations (mean and 95th confidence interval).

Figure 2 shows that the pollutant concentrations were highest under the low wind speed conditions, indicating dominant contributions from the local sources. Also, it can be observed that some higher concentrations coincidence with higher wind speeds, indicating the formation of NO₂ in the oxidation process, as well as the existence of additional, weaker source of SO₂ in the vicinity.

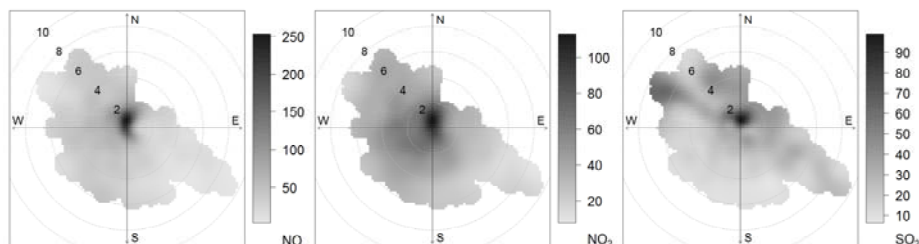


Figure 2. Mean NO, NO₂ and SO₂ [$\mu\text{g m}^{-3}$] concentrations dependence on the wind speed and wind direction.

CONCLUSION

The characteristic dynamics of analyzed pollutants indicates the dominant influence of anthropogenic sources of emission in Belgrade urban area. High concentrations occurrence especially during the winter, as well as the fact that their emission sources are located mainly in the immediate area, point to the need for reduction of traffic density and the number of individual heating installations.

ACKNOWLEDGEMENT

This paper was realized as part of projects No III43007 and No III41011 financed by the Ministry of Education, Science and Technological Development of the Republic of Serbia within the framework of integrated and interdisciplinary research for the period 2011-14.

REFERENCES

- [1] Air quality in Europe — 2013 report
- [2] Institute of Public Health Belgrade, Serbia, information available from <http://www.beoeko.com/> (in Serbian)
- [3] D.C. Carslaw, K. Ropkins, *Environ. Model. Soft.*, 2012, 27–28, 52–61.
- [4] I. Mavroidis, M. Ilija, *Atmos. Environ.*, 2012, 135-147.

DETERMINATION OF TOTAL AND RADIOACTIVE STRONTIUM (^{90}Sr) IN WASTE WATER SAMPLES

N. Sarap¹, M. Milenković², J. Senćanski³ and M. Janković¹

¹*University of Belgrade, Vinča Institute of Nuclear Sciences, Radiation and Environmental Protection Department, Mike Petrovića Alasa 12-14, 11001 Belgrade, Serbia (natasas@vinca.rs)*

²*University of Belgrade, Faculty of Physical Chemistry, Studentski trg 12-16, 11158 Belgrade, Serbia*

³*Institute of General and Physical Chemistry, Studentski trg 12/V, 11158 Belgrade, Serbia*

ABSTRACT

This paper presents the values of concentration of total Sr, as well as the activity concentration of radioactive isotope ^{90}Sr in waste water samples taken around the coal-fired power plant "Nikola Tesla A". Also, conductivity and pH value of these water samples were determined. Concentration of total Sr was determined by atomic absorption spectrometry. Determination of ^{90}Sr content is based on the radiochemical analytical separation of ^{90}Y from the sample and measuring its activity after the establishment of radioactive equilibrium with ^{90}Sr . The obtained results for the concentration of total Sr ranged between 0.1 and 1.3 mg/L. The obtained activity concentration of ^{90}Sr was from 0.015 to 0.037 Bq/L.

INTRODUCTION

Coal-fired power plant "Nikola Tesla A" (TENT A) is the biggest power plant in the Republic of Serbia, consisting of six units with total installed power of 1650 MW. Built on the right bank of the Sava River, near Obrenovac, it is the biggest individual producer of electric power in Serbian electric power system. At the average, more than 8 billion kilowatt hours are produced per year [1].

Coal combustion in power plant may enhance environmental pollution levels in the vicinity of the coal-fired power plant due to fly ash and bottom ash as main solid wastes of coal combustion, which are released into the surrounding environment. Considering that coal-fired power plant TENT A is located in populated area the impact on the environmental impact and the neighboring population can be significant.

Strontium (Sr) is found naturally as a non-radioactive element and has 16 known isotopes. Naturally occurring Sr is found as four stable isotopes: ^{84}Sr ,

^{86}Sr , ^{87}Sr and ^{88}Sr . Other isotopes are radioactive [2]. One of the most important Sr radioactive isotopes in the environment is ^{90}Sr because of its long physical and biological half-lives and similarities with Ca. It has been distributed worldwide since 1945 in fallout from atmospheric weapons testing or as a result of normal or accidental releases related to the nuclear power industry [3].

The aim of this study is to determine the Sr content in waste water samples around the power plant, with special attention to ^{90}Sr .

EXPERIMENTAL

Sampling of five waste water samples was performed in September 2013 at five locations near the power plant TENT A: overflow water (pumping station), drain water at well, drain water between wells, Sava river upstream from the TENT A and Sava river downstream from the TENT A.

Before determination of Sr content, all samples were analyzed for pH and conductivity. For pH measurement pH meter (Hanna Instruments, pH/ $^{\circ}\text{C}$ Tester pHep4) was used. Calibration of the instrument was carried out by 4, 7 and 10 pH standard solutions. The conductivity measurements were done with conductometer (CON 400) with a cell constant of $K=1.0$. The measuring range 0-1999 μS was calibrated at 1411 μS using standard 0.01 M KCl solution at 25 $^{\circ}\text{C}$.

The content of total Sr was determined by atomic absorption spectrometer SENSAA 2G. For measurement of Sr at wavelength of 460.4 nm PHOTRON LAMP was used. Nitrogen as inert gas for the determination of Sr was applied. Determination of total Sr was performed from non-paired water samples.

About 10 L of each water sample was evaporated to a 200 mL under infrared lamp and taken for analytical procedure for radiochemical determination of ^{90}Sr . The method consists from precipitation of calcium and strontium oxalate, firing till oxide and usage of Al collector for ^{90}Y [4]. The samples were stored for 18 days to reach the radioactive equilibrium between ^{90}Sr and ^{90}Y . After 18 days ^{90}Y departs on collector $\text{Al}(\text{OH})_3$, which is then firing till oxide. Measurement was performed on low level proportional counter THERMO EBERLINE FHT 770 T.

RESULTS AND DISCUSSION

The content of total Sr and ^{90}Sr , as well as conductivity and pH value for investigated waste water samples are presented in Table 1.

Table 1. Content of total Sr and ^{90}Sr , conductivity and pH values in investigated waste waters.

Sample	Sr (mg/L)	^{90}Sr (Bq/L)	Conductivity ($\mu\text{S}/\text{cm}$)	pH
Overflow water (pumping station)	0.8	0.036 \pm 0.004	851	8.3
Drain water at well	1.1	0.026 \pm 0.004	1343	8.4
Drain water between wells	1.3	0.027 \pm 0.004	1807	8.4
Sava river upstream from the TENT A	0.1	0.037 \pm 0.004	439	8.5
Sava river downstream from the TENT A	0.2	0.015 \pm 0.004	423	8.5

As can be seen from Table 1, the values for conductivity ranged from 423 to 1807 $\mu\text{S}/\text{cm}$. According to regulation on quality and other requirements for natural mineral water, spring water and bottled drinking water [5] recommended value for conductivity should be up to 2500 $\mu\text{S}/\text{cm}$. Considering the fact that the investigated waters are not drinking waters, this criterion is met anyhow. All waters are alkaline (pH values are from 8.3 to 8.5).

The content of total Sr ranged from 0.1 to 1.3 mg/L, while the activity concentrations of radioactive strontium, ^{90}Sr , ranged between 0.015 and 0.037 Bq/L. The similar results for content of total Sr have been found by Frei and Frei [6] for Denmark surface waters and values ranged between 0.06 and 1.05 mg/L. On the other hand, similar results for ^{90}Sr activity concentrations have been found in river waters Sava and Danube in the Republic of Serbia where values ranged from 0.009 to 0.06 Bq/L [7,8]. Derived activity concentration of ^{90}Sr in drinking water is 4.9 Bq/L [9]. The activity concentrations of ^{90}Sr in water samples analyzed in this paper are less than above mentioned value, even though the analyzed waters are not drinking waters.

CONCLUSION

The concentration of total Sr, the activity concentration of radioactive isotope ^{90}Sr , as well as conductivity and pH value in five waste water samples taken around the coal-fired power plant "Nikola Tesla A" were determined. The obtained values for conductivity meet the limited values according to the Official Gazette [5]. All waters are alkaline, pH values are higher than 7. The concentrations of total Sr and radioactive strontium (^{90}Sr) are similar as values published in literature for river water samples. Determination of ^{90}Sr in the environmental samples is important in the routine environmental radiation monitoring. This is the first study of this type in waste water samples in Republic of Serbia and investigation will be continued in future.

ACKNOWLEDGEMENT

This study has been done in Vinča Institute of Nuclear Sciences, the Faculty of Physical Chemistry and Institute of General and Physical Chemistry in Belgrade. The authors would like to thank to the Ministry of Education, Science and Technological Development of the Republic of Serbia for material support (Grants no. III 43009, 172015, III 45014).

REFERENCES

- [1] <http://www.tent.rs/tent-a>
- [2] M.E.R. Huguet and E. Darre, *Atomic Spectroscopy*, 2006, 27, 80-85.
- [3] R.A. Tinker, J.D. Smith, M.B. Cooper, *Analyst*, 1997, 122, 1313-1317.
- [4] R. Brnović, *Strontium 90 in the Human Environment*, Master's thesis, Faculty of Science, Belgrade, 1972.
- [5] *Official Gazette of Serbia and Montenegro*, 53/05, 2005.
- [6] R. Frei and K.M. Frei, *Applied Geochemistry*, 2013, 38, 147-160.
- [7] N. Sarap, M. Janković, D. Todorović, G. Pantelić, J. Nikolić, V. Stanić in: *Proceedings of the XXVI Symposium of Society for Radiation Protection of Serbia and Montenegro*, M. Kovačević (Ed.), Serbia, 2011.
- [8] N.B. Sarap, M.M. Janković, G.K. Pantelić, *Water Air and Soil Pollution*, 2014, DOI: 10.1007/s11270-014-2003-0.
- [9] *Official Gazette of the Republic of Serbia*, 86/11, 2011.

SIMULTANEOUS REMOVAL OF METHYLENE BLUE AND HEXAVALENT CHROMIUM BY TiO₂/Fe(III)/SUNLIGHT

M.F. Ghorab¹ and R. Djellabi¹

¹*Laboratory of Water Treatment and Valorization of Industrial Wastes,
Chemistry department, Faculty of Sciences, University of Badji-Mokhtar
Annaba, BP12 Annaba 2300, Algeria (fouzi.ghorab@univ-annaba.dz)*

ABSTRACT

Methylene blue and hexavalent chromium are two important toxic pollutants which exist frequently in many categories of industrial wastewaters. For practical reasons, the simultaneous removal of these contaminants is an attractive approach. The results of a simultaneous removal of methylene blue and hexavalent chromium using a combined system TiO₂/Fe(III)/solar are presented. The results show that, only the TiO₂/Fe(III)/solar system ensures a complete simultaneous removal.

INTRODUCTION

Many industrial wastewaters are contaminated by both organic and inorganic pollutants. Therefore, it is of interest to develop methods for simultaneous and efficient removal of both categories of pollutants. Hexavalent chromium (Cr(VI)) is one of the most heavy metals that exists in contaminated wastewater discharges from several industrial activities. The co-existence of both Cr(VI) and organic pollutants namely Methylene blue (MB) in wastewaters is extremely probable. The combination of the (TiO₂/UV) and (Fe(III)/UV) methods gives an efficient synergistic process for simultaneous removal of Cr(VI) and organic dyes [1]. The use of free sunlight to drive these processes is an attractive alternative to artificial UV light, particularly in Algeria where the average sunshine duration is about 2500 hours per year [2]. The comparison of the efficiency of this, i.e., the combined system (TiO₂/Fe(III)/solar) for simultaneous and simple (Cr(VI) or MB) removal cases was investigated.

EXPERIMENTAL

The KRONOS 1077 TiO₂ (Kronos company, Germany) was used as a photocatalyst in this work. It is a pure micro-sized anatase pigment that is particularly suitable for delustering of man-made fibers and pigmentation of paper coatings. The specific surface area of this material is about 12m²/g.

Potassium dichromate and MB solutions were prepared in double-distilled water, adjusting the pH with H₂SO₄. Ferric stock solutions, were prepared by dissolving Fe(NO₃)₃·9H₂O in acidic medium. The photocatalytic experiments were performed using a static batch reactor consisting of 250mL-Pyrex beakers open to air under natural sunlight at sea level and at ambient temperature on sunny days (July). The solution of the substrate (200mL) for the three cases in the presence of catalysts was exposed to natural sunlight under a constant stirring for 5 h. Prior to that all solution were agitated at least 30 minutes in dark in order to achieve adsorption/desorption equilibrium. The catalysts were KRONOS 1077 TiO₂, iron salt or both for the TiO₂ photocatalysis, Iron cycle and the combined system respectively.

The residual concentration of MB was determined colorimetrically using a UV-Vis spectrophotometer and estimated at a wavelength of 662 nm. The intensity of sunlight radiation at 365nm was measured using a VLX-3W radiometer with a cell diameter of 1 cm². The extent of water evaporation during the solar photocatalysis experimental was in average of 6.0% in volume after 5 h of irradiation which is considered to be within the experimental errors. Due to the inherent non reproducibility of solar radiations and in order to minimize the experimental errors, the study of the effects of each parameter was performed simultaneously on a set of experiments along with a blank sample (without TiO₂).

The removal rate of pollutant was calculated using Eq.1

$$R(\%) = \frac{(C_0 - C_t)}{C_0} \times 100 \quad (1)$$

Where C₀ and C_t represent the pollutant concentration

RESULTS AND DISCUSSION

The results of the MB photooxidation alone using TiO₂/solar, Fe(III)/solar and TiO₂/Fe(III)/solar processes are shown in Fig.1. The direct photolysis rate of MB was 9% after 5h. It can be seen from the same figure that, while the oxidation of MB by TiO₂/solar and TiO₂/Fe(III)/solar processes is completely achieved after 2h, it was faster with the latter system. However, the oxidation by the Fe(III)/solar system was only 45% after 5h. The oxidation of MB using TiO₂/solar system occurs by the photogenerated hydroxyl radicals (•OH) during the photoexcitation of TiO₂ by UV part irradiation coming from solar light. The oxidation of MB in the case of Fe(III)/solar system is attributed to the participation of hydroxyl radicals produced by the solar photoexcitation of Fe(III) hydro-complex [3]. As nitrate iron salt was used for making the iron cycle system, it is important to

note that hydroxyl radicals can be produced from the photolysis of nitrate ions at wavelength of 302 nm. However this reaction is negligible since the solar irradiation at this wavelength is very low.

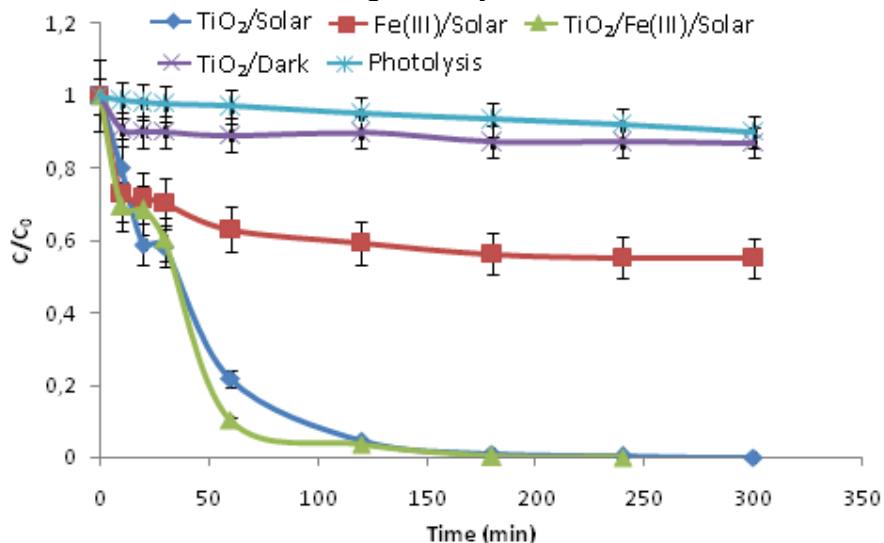


Figure 1. Photooxidation of MB alone under natural sunlight. [MB]: 30ppm, pH: 2.7, [TiO₂]: 0.16g/L, [Fe(III)]: 40ppm

Fig. 2 presents the oxidation of MB using the same processes with the presence of Cr(VI) ions. From this figure, it can be noticed that the presence of Cr(VI) has a negative effect on the MB photooxidation in the system TiO₂/solar since the oxidation rate decreases to 85% from 100% (in the absence of Cr(VI)).

This decrease may be related to the saturation of surface sites by both pollutants. However, in the case of the combined system (TiO₂/Fe(III)/solar), the Cr(VI) ions do not affect the MB oxidation. This may be due to the participation of hydroxyl radicals produced by the Fe(OH)²⁺ photolysis. Furthermore, there is a significant increase in the oxidation rate from 45% to 100% (after 5h) in the case of Fe(III)/solar, where the iron cycle comes into action to oxidize MB and reduce Cr(VI).

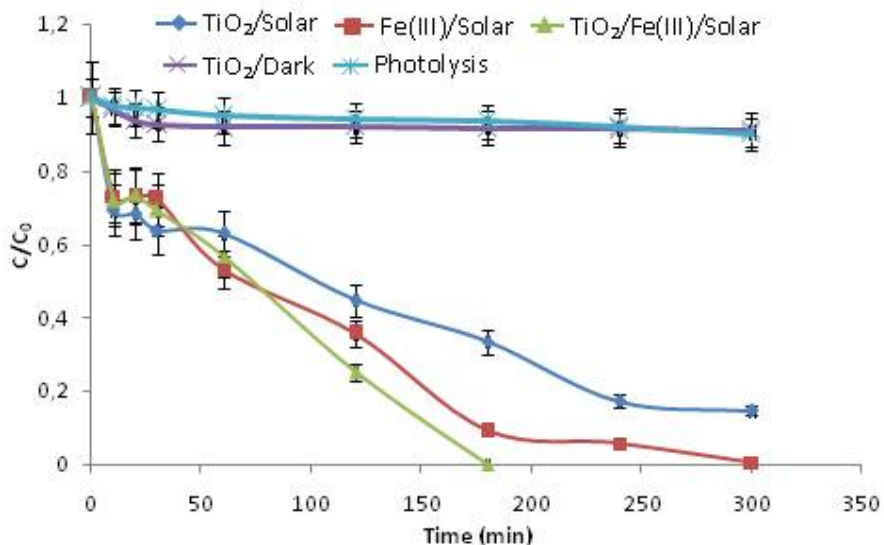


Figure 2. Photooxidation of MB under natural sunlight in the presence of Cr(VI). [MB]: 30ppm, [Cr(VI)]: 30ppm, pH: 2.7, [TiO₂]: 0.16g/L, [Fe(III)]: 40ppm

CONCLUSION

The results of the present study demonstrate that both pollutants Cr(VI) and MB can be efficiently and simultaneously eliminated by the TiO₂/Fe(III)/sunlight process. The synergistic effects of this system obtained by the combination of iron cycle and TiO₂ photocatalytic reactions leads to efficient photoredox pathways.

ACKNOWLEDGEMENT

The authors acknowledge the financial support of the Ministry of Higher Education (Algeria) through the research project grant (E01120/11/0065)

REFERENCES

- [1] S.G. Schrnk and H.J. José, *Journal of Photochemistry and Photobiology A: Chemistry*, 2002, 147, 71–76
- [2] <http://www.sundous.com/Energie.html> (consulted in July 2013)
- [3] N. Brand, G. Mailhot and M. Bolte, *Environmental Science and Technology*, 1998, 32, 2715–2720

SPATIAL DISTRIBUTION OF OZONE AND NITROGEN DIOXIDE IN AN URBAN TRAFFIC SITE IN TIRANA, ALBANIA

S. Mico¹, A. Deda², M. Alushllari³ and A. Deliu⁴

¹*Department of Physics, Faculty of Technical Sciences, University of Vlora, Vlora, Albania silvana.mico@yahoo.com,*

²*Department of Physics, Faculty of Natural Sciences, University of Tirana, Tirana, Albania*

³*Institute of Applied Nuclear Physics, University of Tirana, Tirana, Albania*

⁴*Institute of Public Health, Tirana, Albania*

ABSTRACT

The passive sampling technique is widely used to characterize the spatial and temporal variability in gaseous pollutant concentrations in the ambient air. Kavaja Street in Tirana was selected for mapping spatial distribution of ozone and nitrogen dioxide concentrations. The sampling campaign is carried out during two weeks period using passive diffusion samplers exposed in different positions along and perpendicular to each sides of the street. Estimated regression function between NO₂ and ozone concentrations over entire examined area was discussed.

INTRODUCTION

Air pollutants are being continuously monitored in Albania, and elevated levels of NO₂ and O₃ concentrations are reported during recent years by Institute of Public Health. Combustion sources contribute to the major part of NO₂ and ground level ozone in the ambient air. Nitrogen oxides are traffic related air pollutants emitted by diesel and petroleum vehicles as the predominant contributors. The burning of fuels at high temperatures emit nitrogen oxides NO_x, mostly in the form of nitric oxide NO and a small part of NO₂. In the atmosphere NO is oxidized to NO₂ mainly due to the presence of ozone causing the depletion of ozone [1]. Ground level ozone (GLO) is a secondary air pollutant formed as the result of photochemical reactions between other pollutants, mainly nitrogen oxides and VOCs under strong solar radiation [2]. GLO usually is found to be higher far away from the source areas of the precursor emissions. Since it is a secondary pollutant, cautions taken to manage it in local levels are resulted with low efficiency.

The spatial variability of O₃ and NO₂ concentrations for environments such as roadsides is discrete and very complicated. Understanding of

roadways as emission sources affecting pollutant concentrations has been the focus of many investigations [3], [4], [5]. Diffusive sampling method provides reliable low cost analysis of air quality and useful information on average concentrations during periods of time from one week to a month from traffic emissions which have not large fluctuations from day to day. Diffusive sampling is characterised as an indicative technique which is not very high accuracy technique. It gives the possibility to characterize spatial concentration distribution of gaseous pollutants [6].

EXPERIMENTAL DESIGN

Tirana is the capital and largest city in Albania based on population which has now reached about 760 000. It is characterized by absence of heavy industries, but with a high traffic network which causes problems such as air pollution. At Kavaja Street, for both directions (toward Tirana centre and away from the centre) total daily traffic intensity in the street adds up to about 13 170 vehicles (JICA Project, October 2011, carried out during a normal working day). The percentage of private cars (sedan, van) was 77%. The surrounding environment is characterized by residential houses generally comprised of 4-5 floors. Its axis orientation is in the direction 255° (W-SW to E-NE). The street has two sided building facades and the height to width ratio $<0.3W/H <0.7$ (it is 24 wide and 15m average building height) with two main intersections and several openings. During the examined period of time wind directions were predominantly blowing out from the southwest to northeast, 52% of the time, at an angle 30° relative to the street axis (provided by Meteoalb station). The percentages of calm conditions ($<1\text{m/s}$) and low wind speeds ($<2\text{m/s}$) were 53% and 35% respectively. The highest wind speeds are measured for SW to NW direction. Average O_3 and NO_2 concentrations were measured using passive diffusion tubes. In total 30 sampling points for each pollutant were included in sampling campaign at Kavaja street area. Sampling points were located at 10m, 30m and 60 m distance to the both sides of the street axis (to the south and north side), whereas along the street axis at distances 440m, 1170m, 1600m and 2100m from the first point. Passive samplers were attached to a support 3 m from the ground and far from any obstacle of air flow. The samplers were exposed for two weeks period at the end of the winter, from 20 February 2013 to 4 March 2013. This winter period is relatively drier with no high speed winds which may cause turbulent diffusion leading to significant errors.

RESULTS AND DISCUSSION

Exposed samples were analysed by Saltzman method using a spectrophotometer at 442nm for O₃ and 540nm for NO₂. The detection limit for O₃ and NO₂ passive sampling method were found to be 2.51µg/m³ and 2.17µg/m³, respectively. Over the entire examined area O₃ and NO₂ average concentrations were observed to be 30.08±6.2µg/m³ and 22.2±1.8µg/m³, respectively. Ozone concentrations varied from a maximum 47.4 µg/m³ to a minimum 12.8 µg/m³. NO₂ concentrations varied from a maximum 51.2µg/m³ to a minimum 8.4µg/m³. In Figure 1a and 1b are presented contour plots as the function of distances along and perpendicular to the street axis, to visually compare the horizontal distribution of ozone and NO₂ concentrations. The highest NO₂ concentrations were resulted in the roadside sampling points, while there is a decrease on NO₂ concentrations when the distance from the street axis increases. The ratio between NO₂ roadside average values and backyards values is 2.04. Inside the street canyon NO₂ average levels at leeward side (south side) is 37.18 µg/m³ and NO₂ average levels at windward side (north side) is 30.08 µg/m³. Contrary to NO₂, ozone concentration ratio between roadside and backyards average values is 0.9. Estimated regression function

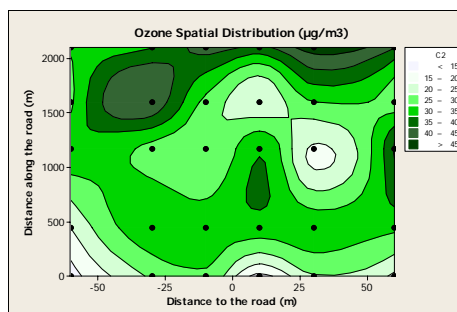
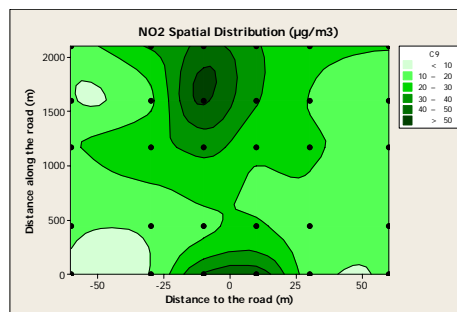


Figure 1. a) Contour plot of NO₂ spatial distribution. b) Contour plot of O₃ spatial distribution.

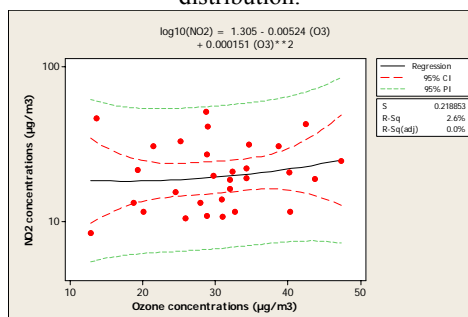


Figure 2. Fitted line plot of quadratic regression between NO₂ and O₃ concentrations.

between NO₂ and ozone concentrations is shown in Figure 2. Very small positive R-squared value of 2.6% and S-value of 0.21 were found between O₃ and NO₂ concentrations. Very poor correlation between O₃ and NO₂ may be result of incomplete photochemical processes due to the short distances of sampling points that fresh air masses have to travel away from the emission source.

CONCLUSIONS

Spatial distribution of O₃ and NO₂ concentrations were investigated using passive sampling method. The measurements were performed at 30 sampling points along and perpendicular to each side of the street, during two weeks period. NO₂ concentrations were found to be very close to the EU Standards limit. Taking into account that campaign was conducted in winter season and sampling points were near the emission sources the ozone concentrations can be considered a concern. Combined effects of O₃ and NO₂ cause poor air quality in Tirana. Ozone concentrations were observed to be less variable within 60m distance from the road axis than NO₂. The highest concentrations of NO₂ occurred at roadside sampling points and a strong negative correlation between NO₂ levels and distance to the road were observed. Statistical analysis using quadratic regression showed very low correlation coefficient between O₃ and NO₂ levels for selected sampling points.

REFERENCES

- [1] G. M. Masters, Introduction to Environmental Engineering and Science, Prentice-Hall, Inc., 1991.
- [2] N. N. Greenwood, A. Earnshaw . Chemistry of the Elements, 2nd edition, Butterworth-Heinemann, 1997.
- [3] S. Vardoulakis, N. Gonzalez-Flesca, B. E. A. Fisher, K. Pericleous, Atmospheric Environment, 2005, 39, 2725–2736.
doi.org/10.1016/j.atmosenv.2004.05.067
- [4] R. W Baldauf, E. Thoma, J Air Waste Manage Assoc, 2008, 58:865–878, doi:10.3155/1047-3289.58.7.865
- [5] F. Palmgren, R. Berkowicz, O. Hertel, E. Vignati, In The Science of the Total Environment., 1996, Volume 189/190, 409-415.
[doi.org/10.1016/0048-9697\(96\)05238-2](https://doi.org/10.1016/0048-9697(96)05238-2)
- [6] F. De Santis, I. Allegrini, M. Fazio, D. Pasella, R. Piredda, Anal Chim Acta, 1997, 346:147-134

MASS TRANSFER KINETICS DURING OSMOTIC DEHYDRATION OF „ABATE FETEL“ PEAR IN SUCROSE SOLUTION

M. P. Petrović¹, T. P. Brdarić¹ and V. M. Pavelkić²

¹ *Institute "Kirilo Savić", Vojvode Stepe 51, 11000 Belgrade, Serbia*

² *IHTM, University of Belgrade, Njegoševa 12, 11000 Belgrade, Serbia*

ABSTRACT

The effects of different concentrations (40%, 60% and 70% w/w) and temperatures (20°C, 35°C and 50 °C) of sucrose solution on mass transfer kinetics during 360 minutes of the osmotic treatment of pear cubes was investigated. Increase in sucrose solution concentration resulted in higher water loss and solid gain values through the osmotic treatment period, due to increase in the osmotic pressure gradients. The applicability of Peleg's model to the experimental data was evaluated. The linearized Arrhenius equation was used for determination of the activation energy for water loss and solid gain.

INTRODUCTION

Pear (variety: *Pyrus communis* L.) is one of the most traditionally consumed fruit, particularly in temperate climate zones. This fruit abounds in saccharides and dietary fiber as well as in nutritionally valuable compounds such as antioxidants. [1]. Osmotic dehydration (OD) is a process of partial removal of water by immersing fruit in hypertonic solution during which the water and small amounts of natural solutes (such as pigments, sugars, organic acids, minerals, vitamins etc.) diffuse from fruit to the solution and the solute is transferred from the osmotic solution to the fruit tissue in a countercurrent mode. According to literature data, temperature and concentration of osmotic solution are the most influencing parameters on mass transfer kinetics during the process of osmotic dehydration [2].

EXPERIMENTAL

„Abate Fetel“ pears were purchased daily from the local market at Belgrade, Serbia. The peeled pears were manually sliced into cubes of 1 cm³. Analytical grade sucrose was purchased from “Merck”. Osmotic solutions were prepared by mixing sucrose with required amount of distilled water to give desired concentration of final solution. The pear cubes were immersed in the glass jars, containing 40%, 60% and 70% mass content of sucrose in

solutions, with a sample to solution ratio of 1:10 (w/w). Temperature uniformity during experiment was assured by placing containers in a constant temperature water bath. Fruits were removed from the containers at a period of 30, 60, 90, 120, 180, 240, 300 and 360 minutes, quickly rinsed with distilled water and gently blotted with tissue paper to remove excess solution from the surface. The mass of the fruits was then measured and the moisture content (dry matter) was gravimetrically determined.

RESULTS AND DISCUSSION

In this study, the kinetics of solid gain (SG) and water loss (WL) during osmotic treatment of pear cubes has been investigated.

Water loss (WL) and solid gain (SG) of the samples were calculated as follows:

$$WL(\%) = \frac{M_o - M_t}{W_o} \cdot 100 \quad (1)$$

and

$$SG(\%) = \frac{S_t - S_o}{W_o} \cdot 100 \quad (2)$$

where M_o is the moisture content in fresh fruit (g); M_t is the moisture content at time "t" of osmotic treatment (g); S_o is the dry matter of fresh fruit (g); S_t is the dry matter after time "t" of osmotic treatment (g); W_o is the mass of fresh fruit before the osmotic treatment (g). Peleg's two parameter equation was used for describing the mass transfer in osmotic treatment of pear's cubes:

$$X = X_o \pm \frac{t}{k_1 + k_2 t} \quad (3)$$

where X is moisture or solid content (g) at time t (h), X_o is initial moisture or solid content (g), k_1 is the Peleg's rate constant that relates to dehydration rate at $t=t_0$ and k_2 , Peleg's capacity constant, which relates to minimum attainable moisture content [2,3,4]. Figure 1 shows the experimental data for SG and WL during osmotic treatment of pear in sucrose solution of 60% (w/w) concentration and at different operating temperatures. As it might be expected, WL and SG increased with immersion time. In all cases, there is an initial rapid rate of mass transfer, followed by slower removal of water and uptake of sugars from fruit tissue in later stages. This trend is due to the large osmotic driving force between fresh fruits' dilute sap and surrounding hypertonic solution at the beginning of the process.

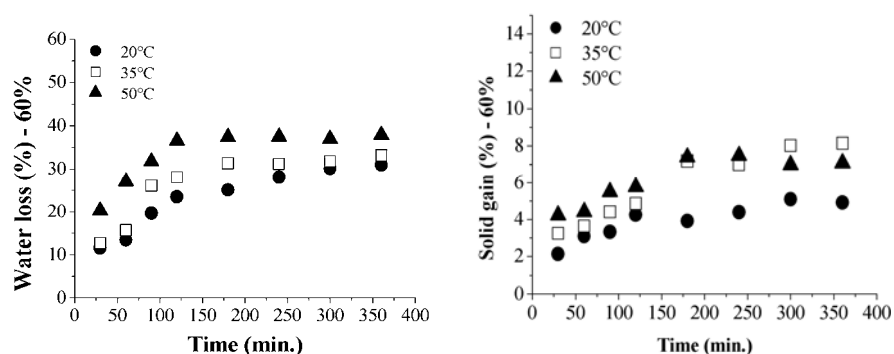


Figure 1. Pear water loss and solid gain versus time at several temperatures.

Table 1. Peleg’s equation parameters and goodness of fit for SG and WL during osmotic treatment of pear

Temp. (°C)	Conc. (%)	Water loss			Solid gain		
		k_1^{WL}	k_2^{WL}	R^2	k_1^{SG}	k_2^{SG}	R^2
20	70	0.51±0.12	0.48±0.03	0.984	3.20±0.51	2.17±0.15	0.986
	60	0.64±0.1	0.51±0.03	0.991	2.89±0.47	3.42±0.25	0.984
	40	1.12±0.23	0.58±0.07	0.962	5.48±2.87	5.50±0.84	0.936
35	70	0.41±0.05	0.34±0.02	0.993	1.58±0.35	2.75±0.11	0.995
	60	0.45±0.09	0.45±0.03	0.990	2.46±0.86	1.67±0.14	0.980
	40	0.58±0.13	0.62±0.04	0.989	4.33±0.58	3.54±0.17	0.993
50	70	0.28±0.07	0.32±0.02	0.987	0.97±0.37	1.85±0.10	0.991
	60	0.15±0.05	0.49±0.02	0.997	1.12±0.36	2.52±0.10	0.995
	40	0.33±0.08	0.54±0.02	0.994	1.70±0.47	3.65±0.14	0.996

At constant solution concentration, k_1^{WL} and k_1^{SG} decreased with increasing temperature of osmotic solution, which indicates an increase in the initial rate of mass transfer. Both k_2^{WL} and k_2^{SG} decrease with increasing concentration, while they do not exhibit particular trend with increasing temperature. The linearized Arrhenius equation represents the temperature dependency of the Peleg’s rate constant:

$$\ln k_1 = \ln k_0 - E_a/RT \tag{4}$$

where k_1 is the Peleg’s rate constant for WL or SG (h g/g); k_0 is the frequency factor (1/s); E_a is the activation energy (kJ/mol). The parameters of Arrhenius equation for the Peleg’s rate constant of SG and WL at different sucrose concentrations were graphically determined and are presented in Table 2.

Table 2 . Parameters of Arrhenius equation for the Peleg rate constant of SG and WL at different sucrose concentrations

Parameter	Concentration (%)		
	70	60	40
Water loss			
ln k_0	-7.15±1.35	-16.19±4.95	-12.97±0.35
E_a (kJ/mol)	15.86±3.46	38.69±12.66	31.88 ±0.89
R^2	0.98	0.95	1.00
Solid gain			
ln k_0	-11.76±0.92	-8.87±4.03	-10.64±4.46
E_a (kJ/mol)	31.45±2.35	24.46±10.30	30.37±11,37
R^2	1.00	0.92	0.94

The linearity of the data ($R^2 > 0.94$) reveals that the k_1 for all the kinetics terms followed an Arrhenius relationship as a function of temperature, regardless of concentration. Higher values of E_a revealed the greater temperature sensitivity of k_1 constant.

CONCLUSION

The SG and WL were increased with increasing sucrose solution concentration and temperature during osmotic treatment of „Abate Fetel“ pear. Peleg's equation presented good fitting to experimental data. The Arrhenius equation was successfully applied to evaluate the temperature dependency of the Peleg's rate constant.

ACKNOWLEDGEMENT

This study was financial supported by Ministry of Education, Science and Technological Development of the Republic of Serbia, project no. TR 31055.

REFERENCES

- [1] D. Komes, A. Belščak-Cvitanović, Z. Domitran, M. Opalić, Journal of Food and Nutrition Research, 2013, 52, 239-250.
- [2] N. M. Mišljenović, G. B. Koprivica, L. L. Pezo, T. A. Kuljanin, M. I. B. Solarov, B. V. Filipčev, Acta Periodica Technologica, 2011, 42, 91-100.
- [3] K. J. Park, A. Bin, F. P. R. Brod, T. H. K. B. Park, Journal of Food Engineering, 2002, 52, 293–298.
- [4] M. Peleg, Journal of Food Science, 1988, 53, 1216–1217.

THERMAL CHARACTERISTICS AND OXIDATIVE STABILITY OF RASPBERRY AND BLACKBERRY SEED OILS FOLLOWED BY DSC

D. Micić¹, S. Ostojić¹, M. Simonović¹ and B. R. Simonović¹

¹University of Belgrade, Institute of General and Physical Chemistry, 11000 Belgrade, Studentski trg 12, Serbia

ABSTRACT

Thermal characteristics and oxidative stability of raspberry (*Rubus idaeus* L., *Willamette cultivar*) and blackberry (*R. fruticosus* L., *Čačak Thornless cultivar*) seed oils have been followed by Differential Scanning Calorimetry (DSC). The raspberry and blackberry seed oils presented a crystallization peak at -66 °C and -61 °C with enthalpy of 25.10 J/g and 29.04 J/g, respectively. Polymorphism was detected in both oils during heating. Blackberry seed oil was shown to be more oxidatively stable than raspberry seed oil because of a lower quantity of linolenic fatty acid, which is less stable in terms of oxidation.

INTRODUCTION

The processing of berry fruit for juices and puree typically removes the seed as a byproduct. The development of a value-added use of seeds could expand the market for berry products and increase grower profit margins. For instance, red raspberry seed was reported to contain 12.2 % protein and 11-23 % oil [1]. High-value vegetable oils (like berry seed oils) are gaining attention owing to the health benefits they may produce, linked to their high content of polyunsaturated fatty acids and antioxidants. All berry seed oils have a high content of polyunsaturated fatty acids in common, thus providing essential fatty acids [2]. The properties of some berry seed oils have been reported in the literature. Parry et al. [3] found significant amounts of linolenic acid, tocopherols, polyphenols and carotenoids in marionberry, boysenberry, red raspberry and blueberry seed oils.

Oxidation of polyunsaturated fatty acids is the main reaction that affects the quality of oil and oil products during storage and use. There are various methods available for measurement of lipid oxidation. Changes in chemical, physical or organoleptic properties of fats and oils during oxidation can be monitored to assess the extent of lipid oxidation. Since oil oxidation is an exothermic reaction, it releases heat that can be measured using Differential Scanning Calorimetry (DSC). Because it is a simple, time saving method

that does not require the use of toxic chemicals, DSC could be used for routine analysis in the oils and fats industry.

The present study was conducted with the aim to investigate raspberry (*Rubus idaeus L., Willamette cultivar*) and blackberry (*R. fruticosus L., Čačak Thornless cultivar*) seed oils for their thermal characteristics and oxidative stability by Differential Scanning Calorimetry.

EXPERIMENTAL

Berry seed oils preparation: Examined oils were obtained by extraction from milled raspberry (*Rubus idaeus L., Willamette cultivar*) and blackberry (*R. fruticosus L., Čačak Thornless cultivar*) seeds using hexane as described in literature [4]. The oil was stored at $-20\text{ }^{\circ}\text{C}$ until analysis. All chemicals and reagents used were of analytical grade (p.a.).

Thermal analysis: All measurements have been performed on TA Instruments DSC Q 1000, Differential Scanning Calorimeter, with TA Universal analysis 2000 software. Oil samples of $3.0 \pm 0.3\text{ mg}$ [5] were weighed into open aluminum pans and were placed in the equipment's sample chamber. An empty open aluminum pan was used as an inert reference to balance the heat capacity of the sample pan. For determining thermal characteristics of berry seed oils DSC scans were conducted in temperature range of 40 to $-90\text{ }^{\circ}\text{C}$, under N_2 purge flow of 50 ml/min . A programmed cycle was followed in which the sample was cooled from 40 to $-90\text{ }^{\circ}\text{C}$ at $2\text{ }^{\circ}\text{C/min}$, maintained at this low temperature for 5 min and heated back to $40\text{ }^{\circ}\text{C}$ with same rate. For determining oxidative stability oils were heated in nitrogen flow (50 ml/min) to $120\text{ }^{\circ}\text{C}$. Then the samples were held isothermal in flow O_2 until the start of the oxidation process. Oxidation induction time, *OIT* (min), was determined from the resulting curve, as the intersection of the extrapolated baseline and the tangent line (leading edge) of the exothermal peak.

RESULTS AND DISCUSSION

On the *Figure 1*. DSC curves of blackberry and raspberry seed oils are presented. These curves are very similar to each other.

The blackberry and raspberry seed oils presented a crystallization peak at $-61\text{ }^{\circ}\text{C}$ and $-66\text{ }^{\circ}\text{C}$ with enthalpy of 29.04 J/g and 25.10 J/g , respectively. Polymorphism was detected in both seed oils: after melting of the low temperature form at $-41\text{ }^{\circ}\text{C}$ (for both oils), an additional form crystallized with an exothermic peak at $-37\text{ }^{\circ}\text{C}$ (for both oils). At $-19\text{ }^{\circ}\text{C}$ and $-22\text{ }^{\circ}\text{C}$ (for blackberry and raspberry seed oils, respectively) this forms melted with an originally existing crystallite of the same kind.

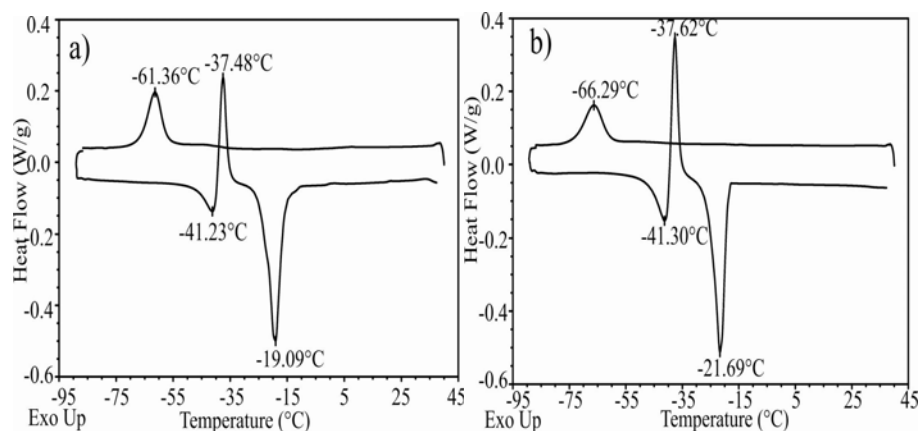


Figure 1. DSC profile of: a) blackberry seed oil; and b) raspberry seed oil.

Similar thermal behavior was observed for grape seed oil by Kaisersberger [6]. These polymorphic changes can be hindered by addition of emulsifiers. According to Garti et al. [7], the first small endothermic peak at $-41\text{ }^{\circ}\text{C}$ represents the melting of the unstable crystal form *a* followed by the crystallization of the more stable form *b* which is characterized by an exothermic peak. The melting enthalpy of blackberry and raspberry seed oils were 72.44 J/g and 63.95 J/g , respectively.

Isothermal DSC oxidation curves of blackberry and raspberry seed oils at $120\text{ }^{\circ}\text{C}$ and the way of determining oxidation induction time (*OIT*) are presented in *Figure 2*. It can be seen that DSC curves have the same shape for both oils. Oxidation induction times were determined from these curves: 165 min for blackberry and 68 min for raspberry seed oil. By comparing *OIT* values, it can clearly be seen that the *OIT* of blackberry seed oil is about 2.5 times higher than that of raspberry seed oil, which indicates that blackberry seed oil is more stable in terms of oxidation.

It can be expected as content of linolenic acid in the raspberry seed oil is higher regarding linoleic acid, as compared to the content of these fatty acids in the blackberry seed oil [2]. Fatemi and Hammond [8] showed earlier that the relative ratio of autoxidation rate of linoleic and linolenic ester was about 1:2, respectively which is in agreement to our results.

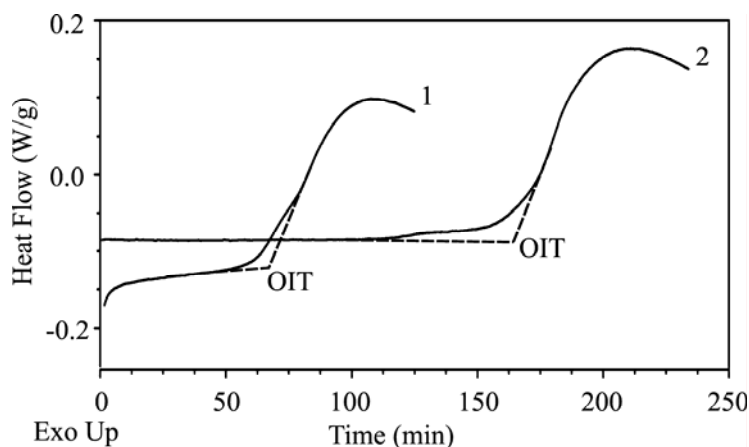


Figure 2. Isothermal DSC oxidation curves of raspberry (1) and blackberry (2) seed oils at 120 °C in O₂ flow 50 ml/min, *OIT* – oxidation induction time.

CONCLUSION

It was shown that in both, blackberry and raspberry seed oils, polymorphism was detected during heating treatment. Blackberry seed oil was shown to be more oxidatively stable than raspberry seed oil because of a lower quantity of linolenic fatty acid, which is less stable in terms of oxidation.

ACKNOWLEDGEMENT

This study was supported by the Ministry of Education, Science and Technological Development of the Republic of Serbia, under the Projects No. TR-31093 and TR-31055.

REFERENCES

- [1] B.S. Bushman, B. Phillips, J. Crane, T. Isbell, B. Ou, S. Knapp, J. Agric. Food Chem., 2004, 52, 7982-7987.
- [2] V. Hoed, N. Clercq, C. Echim, M. Andjelkovic, E. Lebe, K. Dewettinck, R. Verhé, Journal of Food Lipids, 2009, 16, 33 – 49.
- [3] J. Parry, L. Yu, J. Food Sci., 2004, 69, 189–193.
- [4] B.D. Oomah, S. Ladet, D.V. Godfrey, J. Liang, B. Girard, Food Chemistry, 2000, 69, 187-193.
- [5] ASTM E1858 – 08 Standard Test Method for Determining Oxidation Induction Time of Hydrocarbons by Differential Scanning Calorimetry.
- [6] E. Kaisersberger, Analytical Proceedings, 1990, 27, 64-65.
- [7] N. Garti, J. Schlichter, S. Sarig, Fat Science and Technology, 1998, 90, 295-299.
- [8] S.H. Fatemi, E.G. Hammond, Lipids, 1980, 15, 379–385.

OSMOTICALLY DEHYDRATED PORK MEAT- THE GLASS TRANSITION

S. Ostojić¹, D. Micić¹, L. Pezo¹, B.R. Simonović¹ and Lj. Levic²

¹ *University of Belgrade, Institute of General and Physical Chemistry, Studentski trg 12/, P.O. Box 551, 11000 Belgrade, Serbia*

² *University of Novi Sad, Faculty of Technology, Bulevar Cara Lazara 1, 21000 Novi Sad, Serbia*

ABSTRACT

The glass transition temperature (T_g) of osmotically dehydrated pork meat in sugar beat molasses, was determined from the obtained DSC heat flow curves. Samples with low moisture content only showed up the glass transition. T_g decrease with increasing moisture content. T_g decreased from -6.8 °C to -10.3 °C when the moisture content increased from 4% to 6%.

INTRODUCTION

The glass transition temperature (T_g) was used as a parameter for quantifying water mobility and food stability, which became popular in the late 1980s [1]. Biological materials are rigid and brittle below the glass transition temperature. Nevertheless, they are not crystalline with regular structure but retain the disorder of the liquid or amorphous state [2]. The physical state of foodstuffs is very stable below the glass transition temperature because compounds involved in deterioration reactions take many months or even years to diffuse over molecular distances, and approach each other to react [3]. Furthermore, water molecules become kinetically immobilized within the concentrated phase, thus being unable to support or participate in the reactions causing deterioration. Most scientists concur that the glass transition temperature under conditions of maximal freeze concentration, T_g , is the technologically significant transition which has the greatest influence on low-temperature stability [3]. The consequence as far as food products are concerned is that a small change in temperature in the temperature region of the glass transition will result in pronounced changes of texture, other dynamic properties and also in the sensory properties [4, 5]. Glassy and freezing characteristics of pure substances are more commonly reported than that of real foods, which are complex multicomponent mixtures [2]. The intention of this work is to define conditions for glassy state formation and glass temperature (T_g) identification of osmotically dehydrated pork meat.

EXPERIMENTAL

Pork meat, *L. dorsi* muscle, was purchased unfrozen from a local supermarket. Preparation of osmotically dehydrated pork in sugar beat molasses has been described elsewhere [6]. A differential scanning calorimeter (DSC, Q1000, TA Instruments, New Castle, DE) was used to perform DSC experiments. Osmotically dehydrated pork meat samples (7–11 mg) with different water content, were subjected to heating, in Al pans, in the temperature range from -90 °C to 150 °C, with controlled heating rate $Hr= 5\text{ °C/min}$, under the N_2 purge flow of 50 ml/min. The water content was estimated by Thermogravimetric analysis (TGA). TGA measurements were performed on TGA Q 500, (TA Instruments, New Castle, DE) under N_2 purge flow of 60 ml/min, in temperature range from 25 °C to 900 °C, and heating rate $Hr= 5\text{ °C/min}$. Each thermogram was analyzed by TA Advantage Universal analysis 2000 software to obtain the glass transition parameters (onset, T_{onset} ; midpoint, T_g ; final T_{end}) for the onset, mid and end of transition, and also to obtain the percentage of mass loss from TGA curves. The water activity (a_w) has been determined by thermoanalytical techniques as previously described by de Silva et al [7].

RESULTS AND DISCUSSION

Decreased enthalpy and temperature maximum of transition, obtained from DSC curves, which represents meat protein denaturation of osmotically dehydrated pork meat compared to for fresh pork meat suggest that destabilization of meat proteins and conformational changes were induced by the process of osmotic dehydration. Thermodynamic parameters of protein denaturation for osmotically dehydrated and fresh pork meat obtained from DSC and TGA thermograms are presented on Table 1.

Table 1. Thermodynamic parameters of protein denaturation for osmotically dehydrated and fresh pork meat obtained from DSC and TGA thermograms.

Pork meat	Onset temp. $T_o(^{\circ}C)$	Peak temp. $T_m(^{\circ}C)$	Enth ΔH (J/g)	Moisture (%)	Residue at 700 °C (%)	Water activity a_w
Osmotically dehydrated	53.26	89.30	652.3	37.70	5.65	0.745
Fresh meat	27.56	81.92	979.1	70.90	1.45	0.938

These changes of material thermal behavior were consequence of water loss and interaction with molasses components. Further loss of water leads to new changes in the material and the appearance of characteristic thermal

behavior for samples having unfreezible water [3,5,7]. Since much of the water was bound to the solid matrix, samples of dehydrated pork meat with low moisture content (below 20%) only showed up the glass transition Figure 1.

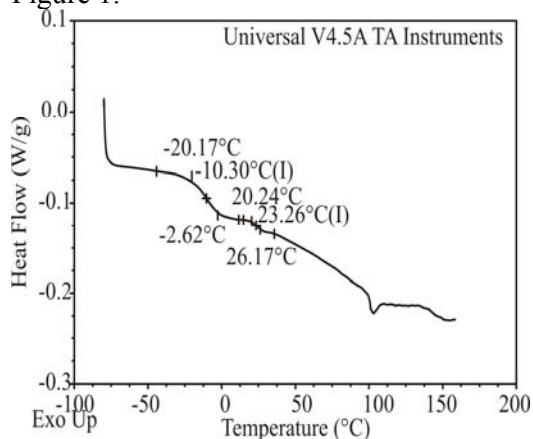


Figure 1. DSC curve of osmotically dehydrated pork meat with low moisture content <20%

As expected T_g decreased with increasing moisture content, as shown in **Table 2**.

Table 2. Water content, glass transition temperature, freezing point and water activity (a_w) of osmotically dehydrated pork meat with freezable and unfreezible water.

Moisture (%)	T_o (°C)	T_g (°C)	T_{end} (°C)	Ice melting (°C)	a_w
38.10	-	-	-	-37.44	0.745
35.02	-	-	-	-33.39	0.732
26.28	-	-	-	-33.67	0.724
20.70	-	-	-	-31.60	0.720
5.90	-20.2±3.0	-10.3±1.1	-2.62±2.5	-	<0.7
3.77	-17.2±3.1	-6.8±1.0	-1.81±2.7	-	<0.7

Transition observed in this work was at a relatively higher temperature which could be due to the initiation of mobility in protein molecules what is agreeable to literature [8] but also results obtained in this work are in agreement with results obtained by Brake and Fennema [9]. It can be suggested that endothermic peaks at ~100 °C and ~150°C correspond to

water evaporation and beginning of material thermal degradation respectively.

CONCLUSION

Since much of the water was linked to the solid matrix, samples with low moisture content (under 20%) only showed up the glass transition. As expected T_g decreased with increasing moisture content: T_g decreased from -6.8°C to -10.3°C when the moisture content increased from 4 to 6%.

It can be proposed that initiation of protein molecules mobility could be induced not only by water loss but also with protein interaction to molasses components.

ACKNOWLEDGEMENT

This work was supported by the Ministry of Education, Science and Technological Development of the Republic of Serbia, under the Project No TR-31055 Project No TR-31093.

REFERENCES

- [1] J. C. Oliveira, P. M. Pereira, J. M. Frias, I.B. Cruz, W. M. MacInnes in: Processing foods quality optimization and process assessment F. A. R. Oliveira, & J. C. Oliveira (Eds.), USA: CRC Press LLC, 1999.
- [2] M. S. Rahman, S. Kasapis, N. Guizani, O.S. Al-Amri., Journal of Food Engineering, 2003, 57, 321–326.
- [3] H. D. Goff, Food Research International, 1994, 27, 187–189.
- [4] Y. H. Roos, Journal of Thermal Analysis and Calorimetry, 2003, 71, 197–203.
- [5] A. E. Delgado, D.W. Sun, Journal of Food Engineering, 2002 55, 1–8.
- [6] D. Šuput, V. Lazić, L. Pezo. Lj. Lević, J. Gubić, N. Hromiš, V. Šojić, Romanian Biotechnological Letters, 2013, 18, 8160-8169.
- [7] V. M. da Silva., L. A. da Silva., J. B. de Andrade, V. da Cunha, G.V. Santos, Quim. Nova, 2008, 31, 901-905.
- [8] S. Qi-Long, Z. Ya, C. Hai-Hua, L. Zhao-Jie, X. Chang-Hu, Thermochemica Acta, 2009, 493, 55–60.
- [9] N.C. Brake, O.R. Fennema, Journal of Food Science, 1999, 64, 10–15.

DETERMINATION OF ANTIOXIDANT ACTIVITY IN STRAWBERRIES, RASPBERRIES AND BLACKBERRIES OF THE WEST-SERBIAN ORIGIN

M. Simonović, M. Dojčinović, S. Hranisavljević and B. Simonović

University of Belgrade, Institute of General and Physical Chemistry, 11000 Belgrade, Studentski trg 12, Serbia

ABSTRACT

The aim of this study is determination of antioxidant activity of berries (strawberry, raspberry and blackberry) of the West-Serbian origin. The antioxidant activity (AO) of the whole berries was determined using the method with DPPH (2,2-diphenyl-1-picrylhydrazyl) and recently reported direct current (DC) polarographic method. It was found, that blackberry showed the strongest AO, having the highest amounts of polyphenols and anthocyanins, followed by raspberry and strawberry. Order of EC50 reciprocal values from DPPH method has been found in correlation with results of AO obtained using DC polarographic assay.

INTRODUCTION

Berry fruits are rich source of phenolic compounds such as phenolic acids, flavonoids, and anthocyanins which possess wide range of bioactive properties including, anticancer, antiinflammatory, antihypertensive, hypoglycemic and antimicrobial activity [1-4]. Number of these health benefit effects can be attributed to high free radical scavenging activity of above mentioned compounds. AO as well as nutrient composition of different berry products has been well documented [1-5], and it varies significantly depending on genetic factors, ripe degree, cultivating and climate conditions [6].

EXPERIMENTAL

Determination of antioxidant activity by DPPH-method

The common method with the stable radical DPPH [7] was used to determine the AO of whole fruits. The amount of 2.2 mg of DPPH dissolved with methanol to 50 ml. Then, the aliquots of 0, 10, 20, 30 and 40 μL of polyphenolic extracts of whole berries in methanol (concentration of stock solution around 300-400 $\mu\text{g}/\text{ml}$) were diluted with methanol to 200 μL , then mixed with 1800 μL of DPPH solution, placed at dark for 30 min and the absorbance was measured at 517 nm. Methanol (1800 μL) mixed with the

sample solution (200 μL) was used as the blank (A_b), while the mixture of DPPH solution (1800 μL) and methanol (200 μL) served as the control (A_c). All determinations were performed in triplicate, and four different dilutions were used for every sample. The DPPH antiradical-scavenging activity, DPPH (%), was determined using following equation:

$\text{DPPH (\%)} = 100 * (1 - (A_s - A_b)/A_c)$ where A_s is the absorbance in the presence of samples in DPPH solution. Quantity of polyphenols needed to decrease absorption of DPPH radical for 50%, EC_{50} , was obtained from the graph $\text{DPPH (\%)} = f(c)$, where c is the value expressed in μg of polyphenols.

Polarographic assay for determination of antioxidant activity

Recently developed DC-polarographic method [8] based on atypical anodic current was performed. This anodic current in form of peak instead of wave was obtained on dropping mercury electrode (DME) in the presence of H_2O_2 in alkaline solution. The peak is attributed to mixed perhydroxyl-hydroxyl complex of Hg(II) formation at potential of anodic dissolution of mercury. The height decrease of this peak in the presence of antioxidants was used as a measure of AO activity. Dependence of anodic current decrease on amount of added sample, during its addition in equal aliquots, was followed and plotted as limiting current intensity (i_l) vs. volume (v) of aliquots added. The slope of the linear part of that plot was considered as measure of AO of that sample. It was expressed as percentage of peak height decrease per volume of complex samples added, or amount of individual compounds. All polarographic current potential (i-E) curves were recorded on Houston Instrument Omnigraphic 2000 X-Y recorder using the Princeton Applied Research (PAR) 174 Polarographic analyzer. The dropping time of DME working electrode was $\tau = 1$ s, while low pass filter for damping current oscillation was 3 s. Saturated calomel electrode (SCE) was used as reference and platinum foil as auxiliary electrode. The initial potential was 0.10 V vs SCE and potential scan rate was 10 mV/s. Clark and Lubs (CL) buffer of pH 9.8 was used. Initial solution was prepared by addition of 0.100 mL of 1.00 M solution of H_2O_2 in 19.9 mL of CL buffer pH 9.8. Before each i-E curve recording (initial solution as well as after addition of every aliquot of investigated sample) solution was deaerated with pure gaseous nitrogen. Inert atmosphere in the electrolytic cell was kept during i-E curve recording.

RESULTS

Determination of antioxidant activity by DPPH-method

The graphs for the AO for the whole fruits using DPPH-method are were constructed (data not shown). On the X-axis, the mass of fruits extracted with methanol in the total volume of 1 ml was given and the values on the Y- axis represented the % for decreasing of DPPH concentration. A good linear dependence of decreasing of DPPH concentration on the mass of extracted fruit entering the reaction was obtained. From these plots the concentration of fruits per ml needed to decrease the DPPH concentration for 50%, i.e. EC50 value, was calculated. Table 1 shows the EC50 values for all three berries together with their reciprocal values ARP (anti radical power).

Table 1. The antioxidant activity of berries obtained by DPPH-method

Sample	EC50 value (conc. of berries)	ARP
Blackberry	4.05 ± 0.22 mg/ml	0.25 ± 0.03
Raspberry	4.50 ± 0.25 mg/ml	0.22 ± 0.03
Strawberry	5.92 ± 0.34 mg/ml	0.17 ± 0.02

Antioxidant activity by DC polarographic assay based on the anodic current analysis Aliquots of methanolic extracts of fruits juice, whole berries and pulp have been gradually added into initial buffered peroxide solution. Prominent difference between anodic limiting current of 5 mmolL⁻¹ solution of H₂O₂ in CL buffer (pH 9.8), recorded before and after the addition of tested samples, has been observed. Remaining anodic limiting current (i_l) obtained upon gradual addition of tested samples has been compared with height of initial limiting current (i_{l0}). Percentage of i_l decrease has been calculated after each addition of tested samples according to eq:

$$i_l \quad \% \text{ scavenged } [H_2O_2] = \left(1 - \frac{i_{lr}}{i_{l0}} \right) \times 100$$

The volume of the linear part of dose-response curves, percentage of i_l decrease calculated upon samples added (%/μL), has been used as criterion of AO activity and is shown in the Table 2.

Table 2. The antioxidant activity of different berry samples using DC-polarographic method

Sample	%/μL
Strawberry	0.042
Raspberry	0.052
Blackberry	0.072

DISCUSSION

In the Table 1 the results for AO of whole fruits of strawberry, raspberry and blackberry are given using DPPH-method. The reciprocal values of EC50, ARP, have higher values for higher AO. The most potent AO showed blackberry, which is in accordance with its total polyphenols and anthocyanins content. These results are in strong correlation with those obtained using DC-polarographic method. The bigger the value %/ μL in the Table 2, the higher AO is to expect. Future studies aiming to follow antioxidant capacity of berries during growth, storage and processing could be facilitated by application of simple, rapid easy-to-handle, low cost and accurate DC polarographic assay.

ACKNOWLEDGMENT

This work was done with financial support by the Ministry of Education, Science and Technological Development of the Republic of Serbia, under the Projects No. TR-31093. Special thanks to Ljiljana Jakić from Bačka Palanka, Serbia, for supplying us with strawberries.

REFERENCES

- [1] S. Tulipani, B. Mezzetti, F. Capocasa, S. Bompadre, J. Beekwilder, C.H. Ric de Vos, E. Capanoglu, A. Bovy, M. Battino. *J. Agric. Food Chem.* 2008, 56, 696-704.
- [2] M. da Silva Pinto, Y-I Kwon, E. Apostolidis, F. Maria Lajolo, M. Ines Genovese, K. Shetty., *J. Agric. Food Chem.* 2008, 56, 4386-4392.
- [3] Gulcin, F. Topal, R. Cakmakci, M. Bilsel, A. Goren, U. Erdogan., *J of food science*, 2011, 76(4), 585-593.
- [4] Z. Juranic, Z. Zizak, S. Tasic, S. Petrovic, S. Nidzovic, A. Lepasovic, T. Stanojkovic. , *Food chemistry* 2005, 93, 39-45.
- [5] P. Zafrilla, F. Ferreres, F.A. Tomas-Barberan, *J. Agric. Food Chem.* 2001, 49, 3651-3655.
- [6] R. Bacchella, A. Testoni, R. Lo Scalzo, *Electronic journal of environmental, agricultural and food chemistry*, 2009, 8(4), 230-242.
- [7] C.M. Liyana-Pathirana, F. Shahidi, *Journal of Agricultural and Food Chemistry*, 2005, 53 2433–2440.
- [8] D. Suznjevic, F. Pastor, S. Gorjanovic., *Talanta*, 2011, 85 (3), 1398-1403.

NUTRITIVE VALUES OF STRAWBERRY, RASPBERRY AND BLACKBERRY OF THE WEST-SERBIAN ORIGIN

M. Simonović, M. Dojčinović, S. Hranisavljević and
B. Simonović

**University of Belgrade, Institute of General and Physical Chemistry,
11000 Belgrade, Studentski trg 12, Serbia*

ABSTRACT

The aim of this study was determination of nutritive properties of berries (strawberry, raspberry and blackberry) of the West-Serbian origin. The content of polyphenols and anthocyanins in the methanolic extracts of berries and their respective parts (pulp and juice) was determined with spectrophotometric methods (previously reported), followed by the determination of the moisture, proteins, sugars and dietary fibers content.

INTRODUCTION

Serbia is known as one of significant producers and exporters of berries, with annual export of over 100000 tons, primarily raspberries and blackberries. Raspberry (*Rubus idaeus*), blackberry (*Eubatus focke*) and strawberry (*Fragaria versa*, *Fragaria ananassa*) are season berries, with attractive odour, color and aroma. These sensory and organoleptic properties come from micronutrients and phytochemicals, which constitute nutritive and bioactive values of berries together with dietary fibers. Berry fruits are rich source of phenolic compounds such as phenolic acids, flavonoids, and anthocyanins which possess wide range of bioactive properties including, anticancer, anti-inflammatory, antihypertensive, antihypoglycemic and antimicrobial activity [1-4]. Because this health promoting effects, especially blackberries have been used since the 16th century in Europe.

The aim of this work was to investigate proximate composition as well as technological quality characteristics of the berries from the West-Serbian origin, to give an indication for quality, and to give some recommendations for the most adequate industrial appliance (dry berries, teas, gelees, juices). Dry matter, total dietary fibers, protein and carbohydrates were subject of investigation.

EXPERIMENTAL

Berries The berries from West Serbia, Čačak and Arilje region, were investigated. Strawberries (*Fragaria L.*, cultivar *Clery*) were from Čačak

region. Raspberries (*Rubus idaeus*, cultivar *Willamette*) were from Arilje region. Blackberries (*Rubus fruticosus* L., cultivar *Čačak Thornless* (*Čačanska bestrna*)) were from Arilje region. All berries were immediately frozen at -20 °C upon arrival. Each time 100 g respectively was defrosted for analysis and kept for 24 h at room temperature (RT).

Spectrophotometric measurements

All spectrophotometric measurements were done at Thermo Fisher Evolution 600 spectrophotometer.

RESULTS

Moisture content of berry fruits

The moisture in fruits was determined by drying 1g of fresh samples at 105 °C for 2 hours, cooling in a desiccator and weighing. The moisture content of the berries is given in the table 1.

Table 1. The moisture content of berries.

Strawberry	Raspberry	Blackberry
89.66 ± 0.54 %	85.03 ± 0.50 %	85.89 ± 0.50 %

Total soluble sugars content

Soluble sugars were extracted from the 1 g of fresh starting material three times for 15 min. with 20 ml 80% ethanol at 60 °C. After centrifugation, the supernatants were combined and the ethanol was evaporated. The total sugar content was determined gravimetrically and expressed in percentages [5].

Table 2. Total soluble sugars in berries.

Sample	Total soluble sugars (%)
Strawberry	6.93 ± 0.18
Raspberry	5.84 ± 0.16
Blackberry	5.13 ± 0.16

Total protein content

The total proteins were determined using the Warburg-Christian method by measuring the absorbance of the solution at 260 and 280 nm [6]. After ethanolic extraction of carbohydrates, residues were mixed with 8M urea to convert all proteins into their soluble form. The subsequent separation of urea extract allowed the determination of the protein content. 8M urea solution was also used as blank. The total protein concentration was expressed in mg/ml using the calculation $1.55 \cdot A_{280} - 0.76 \cdot A_{260}$, where A is

absorbance at given wavelength. In the table 6 the total protein content is given, calculated as percentages in fresh material.

Table 3. Total proteins in berries

Sample	Total proteins (%)
Strawberry	0.89 ± 0.04
Raspberry	1.34 ± 0.06
Blackberry	1.23 ± 0.06

Total dietary fibers content

Total dietary fibers were determined according to the method of AOAC [7]. Briefly, 1 g of fresh samples were weighed with 0.1 mg accuracy and defatted with petroleum ether for 30 min at RT. Samples were then dried and digested with α -amylase, protease and amyloglucosidase to cleave the proteins and starch. 78% ethanol was used to precipitate the soluble dietary fibers. The residue is then filtered and washed with 95% ethanol and acetone. After drying, the residue was weighed, then a half of samples were analyzed for protein content and the other half was ashed. Total dietary fibers were calculated by subtraction of weight of the protein and ash from the weight of the residue and the results were expressed as percentages in table 4.

Table 4. Total dietary fiber content in berries.

Sample	Total dietary fibers (%)
Strawberry	1.78 ± 0.10
Raspberry	5.44 ± 0.33
Blackberry	4.86 ± 0.29

DISCUSSION

As seen from table 1, the moisture content in strawberries, raspberries and blackberries is between 85% and 90%, which is usual for berry fruits.

As seen from table 4, the most dietary fibers were found in raspberry and blackberry, which differs slightly. Strawberry had the smallest content. The protein and carbohydrate content of berries given in the tab. 2 and 3 are almost identical with the available data.

ACKNOWLEDGMENT

This work was done with financial support by the Ministry of Education, Science and Technological Development of the Republic of Serbia, under the Projects No. TR-31093. Special thanks to Ljiljana Jakić from Bačka Palanka, Serbia, for supplying us with strawberries.

REFERENCES

- [1] S. Tulipani, B. Mezzetti, F. Capocasa, S. Bompadre, J. Beekwilder, C.H. Ric de Vos, E. Capanoglu, A. Bovy, M. Battino., *J. Agric. Food Chem.* 2008, 56, 696-704.
- [2] M. da Silva Pinto, Y-I Kwon, E. Apostolidis, F. Maria Lajolo, M. Ines Genovese, K. Shetty., *J. Agric. Food Chem.* 2008, 56, 4386-4392.
- [3] I. Gulcin, F. Topal, R. Cakmakci, M. Bilsel, A. Goren, U. Erdogan., *J of food science*, 2011, 76(4), 585-593.
- [4] Z. Juranic, Z. Zizak, S. Tasic, S. Petrovic, S. Nidzovic, A. Leposavic, T. Stanojkovic., *Food chemistry* 2005, 93, 39-45.
- [5] M. Hall, W. Hoover, J. Jennings, T. Miller Webster., *Journal of the Science of Food and Agriculture*, 11/1999; 79(15):2079 - 2086.
- [6] Warburg O. and Christian W., *Biochem. Z.*, 1942, 310: 384-421.
- [7] Official methods of analysis of AOAC international, 16th edition, volume II, Section 45.4.07, Method 985.29 (1997).

PHASE BOUNDARIES

CHITOSAN-SMECTITE BIOINTERFACES VS. ALKYLAMMONIUM-CLAY INTERFACES IN ADSORPTION PROCESS

N. Jović-Jovičić¹, P. Aranda², M. Darder², E. Ruiz-Hitzky², P. Banković¹,
M. Žunić¹ and A. Milutinović-Nikolić¹

¹*University of Belgrade – IChTM, Center for Catalysis and Chemical
Engineering, Njegoševa 12, 11000 Belgrade, Republic of Serbia*

²*Instituto de Ciencia de Materiales de Madrid, CSIC,
Cantoblanco, 28049 Madrid, Spain*

ABSTRACT

Two series of chitosan-clay nanocomposites were synthesized using commercial (CLOISITE[®] Na⁺) and Na⁺-enriched Serbian clay from seldom investigated locality Mečji Do. The samples were characterized by X-ray diffraction and intercalation of chitosan into bilayer structures was confirmed for particular chitosan/clay ratio in both series of chitosan-clay nanocomposites. Reactivity of chitosan-smectite biointerfaces vs. alkylammonium-clay interfaces in adsorption process was compared using textile dye Reactive Black 5 (RB5) as adsorbate. Chitosan-clay nanocomposites had similar adsorption uptake, being more than three times higher than adsorption uptake of commercial alkylammonium-clay CLOISITE[®] 30B. The Langmuir adsorption model was found to be appropriate for all investigated adsorbents.

INTRODUCTION

Chitosan-clay nanocomposites are promising materials with organic-inorganic hybrid interfaces [1-4]. Since these materials contain a biopolymer such as chitosan they represent a green alternative to conventional alkylammonium organoclays in their applications, i.e. as adsorbents. The intercalation of chitosan into smectite clay can result in monolayer and/or bilayer arrangements. When bilayer structures are formed some free -NH₃⁺ groups are present in the interlamellar region [1,5] making these materials suitable for adsorption of anionic species, i.e. anionic textile dyes.

In this work series of chitosan-clay nanocomposites with different chitosan loading were synthesized using two smectite clays: commercial (CLOISITE[®] Na⁺) and Na⁺-enriched Serbian clay. The XRD was used to confirm the intercalation of chitosan. Only nanocomposites with bilayered intercalation of chitosan were tested as adsorbents. The adsorption of

anionic dye RB5 on the selected samples was tested and compared with the adsorption on CLOISITE[®] 30B.

EXPERIMENTAL

Materials

Two bentonite clays were used for synthesis of nanocomposites: commercial clay CLOISITE[®] Na⁺ (Southern Clay Products Inc., Texas, USA) and Na⁺-enriched Serbian clay, from locality Mečji Do denoted as KB2, both with particle size <2 μm. High molecular weight chitosan (av. $M_w = 342,500 \text{ g mol}^{-1}$) was supplied by Sigma-Aldrich. Organoclay – CLOISITE[®] 30B (Southern Clay Products, Inc., Texas, USA) was used to compare reactivity of chitosan-smectite biointerfaces vs. alkylammonium-clay interfaces in adsorption process. The synthetic textile dye –RB5, was supplied from Sigma Aldrich, and used for adsorption tests.

Synthesis and characterization of chitosan-clay nanocomposites

Chitosan solutions were prepared by the addition of 20, 40, 80, 160, 400 and 640 mg of chitosan to 1% (v/v) acetic acid and stirred until complete dissolution. After the pH was adjusted to 4.6-5, the chitosan solution was added into 2% clay suspension (0.5 g clay/25 cm³ bidistilled water) at room temperature. The suspension was stirred for 48 hours. The obtained samples were centrifuged and then air-dried at 50 °C and ground to powder. The samples were denoted according to initially added chitosan mass and clay designation. The obtained samples were characterized using powder X-ray diffractometer BRUKER D8-ADVANCE equipped with scintillation detector and copper K_α radiation (40 kV and 30 mA).

Adsorption test

The adsorption of RB5 was performed in a batch system at 25°C using thermostated shaker (Memmert WNE 14 and SV 1422). The initial concentrations of RB5 dye were: 20, 30, 40 and 50 mg dm⁻³. The 0.0100 g of the adsorbents were dispersed in 50.00 cm³ of adsorbate solution and shaken for 1440 min. Equilibrium was reached for shorter times, but 1440 min was taken as adsorption time sufficient for all adsorbents to reach maximum of adsorption. After adsorption, solid and liquid phase were separated by centrifugation. The RB5 concentration was estimated by Thermo Electron Nicolet Evolution 500 UV-VIS spectrophotometer at $\lambda_{\text{max}}=599\text{nm}$. All the adsorption experiments were conducted in duplicate, and the mean values were reported.

RESULTS AND DISCUSSION

XRD Analysis

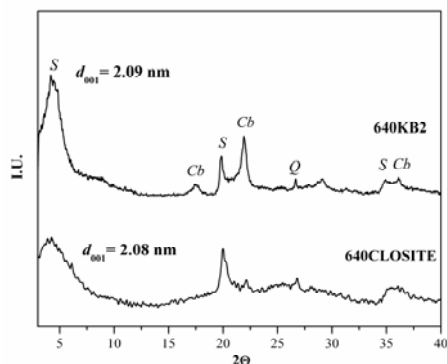


Figure 1. XRD patterns of 640KB2 and 640 CLOISITE; *Cb*–cristobalite, *Q*–quartz, *S*– smectite.

Adsorption test

The adsorption isotherms of RB5 dye on 640 CLOISITE, 640KB2 and CLOISITE[®] 30B are given in Figure 2.

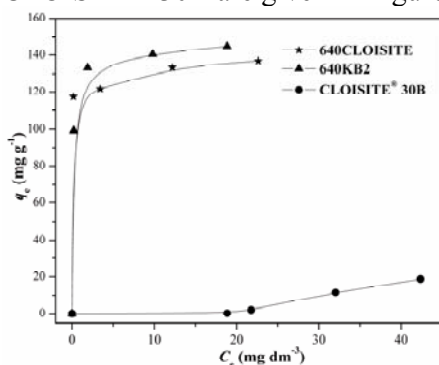


Figure 2. Adsorption isotherms of RB5 removal on 640KB2, 640CLOISITE and CLOISITE[®] 30B.

reported systems [1,4]. These groups can be regarded as active sites that enable interaction with anionic $-\text{SO}_3^-$ groups of RB5 and therefore significantly enhance adsorption capacity.

The adsorption data were fitted with Langmuir and Freundlich models, and corresponding constants were calculated from the intercepts and slopes and given in Table 1.

Loading of 640 mg chitosan per 0.5 g for both clays was needed to obtain solely bilayers of chitosan chains confirmed by characteristic d_{001} values (Fig. 1) [1]. The lower loadings lead to formation of monolayers and mixtures of bi- and mono-layers and these samples were not included in further investigation. Besides smectite in both XRD spectra the associated minerals like cristobalite and quartz are also identified.

The adsorption isotherms showed that the 640KB2 and 640CLOISITE have similar uptake of RB5. The adsorption affinity of CLOISITE[®] 30B was significantly lower. The equilibrium amount of adsorbed RB5 on CLOISITE[®] 30B was approx. 30% of the amount adsorbed on chitosan–clay samples. It can be assumed that 640KB2 and 640CLOISITE with intercalated bilayered chitosan chains possessed the additional cationic sites ($-\text{NH}_3^+$), similarly to previously

Table 1. Langmuir and Freundlich parameters

Samples	Freundlich parameters			Langmuir parameters		
	K_F (dm^3g^{-1})	n	R^2	q_{max} (mg g^{-1})	K_L ($\text{dm}^3\text{mg}^{-1}$)	R^2
640CLOISITE	122.2	32.38	0.775	137.93	3.816	0.999
640KB2	117.2	12.20	0.910	166.67	6.000	0.999
CLOISITE® 30B	9.63	2.64	0.916	54.38	0.062	0.993

The correlation coefficient in Langmuir model is closer to unity and therefore this is the most appropriate model for all adsorbents.

CONCLUSION

The promising chitosan-clay nanocomposites with bilayered structure of incorporated chitosan, a green alternative to conventional alkylammonium organoclays, were synthesized using two different clays as starting materials. These eco-friendly nanocomposites had superior adsorption properties in adsorption of the anionic dye Reactive Black 5 in comparison to commercial alkylammonium organo clay (CLOISITE® 30B) having around three times higher adsorption capacity. The chitosan nanocomposites synthesized using the clay from locality Mečji Do (Serbia) showed somewhat better adsorption properties than nanocomposites obtained with commercial CLOISITE® Na⁺.

ACKNOWLEDGEMENT

The present results were obtained within COST action MP1202. Also the work was partially supported by the Ministry of Education, Science and technological Development of the Republic of Serbia (Project III 45001) and by the CICYT, Spain (Project MAT2012-31759).

REFERENCES

- [1] M. Darder, M. Colilla, E. Ruiz-Hitzky, *Chem. Mater.*, 2003, 15, 3774 – 3780.
- [2] M. Darder, M. López-Blanco, P. Aranda, A. J. Aznar, J. Bravo, E. Ruiz-Hitzky, *Chem. Mater.*, 2006, 18, 1602 – 1610.
- [3] C. M. Futralan, C. C. Kan, M. L. Dalida, K. J. Hsien, C. Pascua, M. W. Wan, *Carbohydr. Polym.*, 2011, 83, 528 – 536.
- [4] M. Darder, P. Aranda, E. Ruiz-Hitzky, "Chitosan-clay bio-nanocomposites" in *Environmental Silicate Nano-Biocomposites*, Eds. L. Avérous and E. Pollet, Springer-Verlag (London), 2012, Ch. 14, pp. 365-391.
- [5] M. Darder, M. Colilla, E. Ruiz-Hitzky, *Appl. Clay Sci.*, 2005, 28, 199 – 208.

DYNAMIC DETERMINATION OF THE COMPLEX DIELECTRIC COEFFICIENT OF THE CHALCOPYRITE NATURAL MINERAL - XANTHATE SOLUTION INTERFACE

R. Todoran, D. Todoran and Zs. Szakacs

Department of Economics And Physics, Technical University of Cluj Napoca, North University Centre of Baia Mare, 62/A, Dr. V. Babes Street, Baia Mare, ROMANIA (szakacsz@yahoo.com)

ABSTRACT

The paper presents the time evolution of the complex dielectric coefficient for the interface formed between the chalcopryrite natural mineral and the potassium ethyl-, isobutyl- respectively amyl-xanthate solution. The work was carried out using differential optical reflectance spectroscopy so the kinetics of the real and imaginary part of the complex dielectric coefficient can be observed over a UV-VIS-NIR spectral domain. The computations were carried out in the framework of the Kramers-Kronig formalism.

INTRODUCTION

Differential reflectance spectroscopy is a useful tool to study “in situ” evolution of froth flotation processes, to determine the optical and electrical properties of interfaces formed at natural mineral – xanthate solution, to detect intermediates and products, because changes in reflectance values can be observed with de aid of this rapid measurement technique. Using UV-VIS reflection spectra in the framework of the Kramers-Kronig formalism, one can evaluate the complex dielectric function for the interface over the specified spectral domain.

EXPERIMENTAL SETUP AND THEORY

Our reflectance determinations were made using the SPECORD M-40 spectrophotometer in the 200-900nm wavelength interval. We did not proceed further in the IR domain not to influence the adsorption process as a catalyst.

The chalcopryrite mineral samples came from the Cavnic mine in our county. The potassium ethyl-, isobutyl- respectively amyl-xanthates were used to prepare the solutions for the “in situ” determinations. Based on our previous work, the solution concentration was fixed to a value of 100mg/l, the pH to 8, and we used a volume of 5ml, because these values led to optimal

adsorption rates and to stable interface layers at industrial temperatures of 18°C [1]. The surface of the mineral was cleaned using chemical and physical methods, minimizing the surface roughness to 0.02µm, and then cleaning any foreign molecule with a spray of argon atoms in a low pressure chamber.

The measurements were carried out at normal radiation incidence angle, over a period of 35 minutes, after which the adsorption-desorption process reached dynamic equilibrium, and the first decomposition products appeared in the solution. A scan of the entire UV-VIS domain, including the time to reset the recorder, took 4.5min. After the determination of 6 successive spectra, we observed no variations in the reflectance, marking the reach of the dynamical equilibrium. The initial values used in our differential reflectance spectroscopy determinations were the reflectance of the polished mineral surface without xanthate solution and then that of the mineral-xanthate solution system at the initial moment.

The complex reflection coefficient r was used in our computations, knowing that $\ln r = \ln \sqrt{R} + i\theta$, where R is the experimental reflectance and θ is the unknown phase shift, determined applying the Kramers-Kronig formalism [2-5]. The complex dielectric function has the form $\varepsilon = \varepsilon_1 + i\varepsilon_2$. The magnetic permeability was taken equal with the unity, as usual in the optical determination, and the spatial dispersions were neglected. Here ε_1 is the dielectric constant (permittivity) and ε_2 is the dielectric loss function. The complex dielectric coefficient was computed using $\varepsilon = (1 - r)^2 / (1 + r)^2$.

Applying the Kramers-Kronig formalism requires that R must be known at all frequencies. Our measurements were made on a sufficiently broad frequency domain so that reliable extrapolations could be done. To determine the phase $\theta(\omega_0) = \theta_1(\omega_0) + \theta_2(\omega_0) + \theta_3(\omega_0)$ we considered three frequency intervals, heaving the experimentally determined data in the middle one, denoted (a,b). We have [4]:

$$\theta_1(\omega_0) = \ln \frac{R(a)}{2\pi} \ln \left(\frac{a + \omega_0}{a - \omega_0} \right), \quad (1)$$

for the low frequency domain,

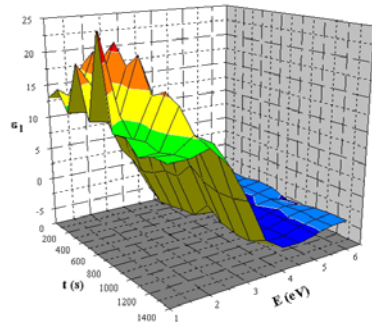
$$\theta_2(\omega_0) = -\frac{\omega_0}{\pi} P \int_a^b \frac{\ln R(\omega)}{\omega^2 - \omega_0^2} d\omega, \quad (2)$$

for the frequency interval (a,b), and for the high frequency domain:

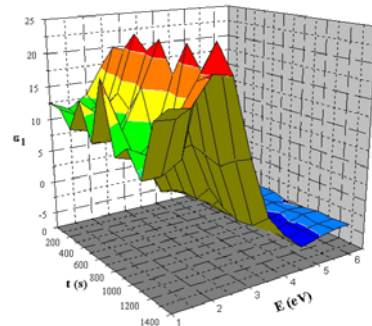
$$\theta_3(\omega_0) = \ln \frac{R(b)}{\pi} \ln \left(\frac{b + \omega_0}{b - \omega_0} \right) + \sum_{n=1} \left(b_n + \frac{1}{\pi} \frac{\ln R(b)}{2n-1} \right) \left(\frac{\omega_0}{b} \right)^{2n-1} \quad (3)$$

where b_n were series expansion coefficients determined numerically.

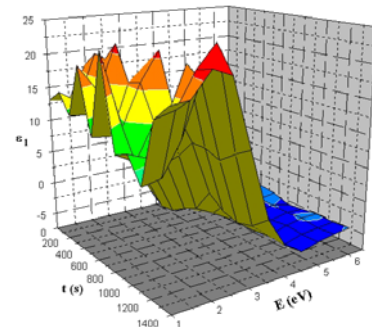
RESULTS AND DISCUSSIONS



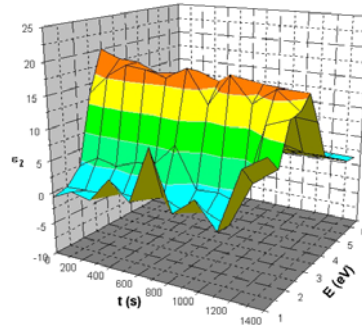
a.) ethyl xanthate



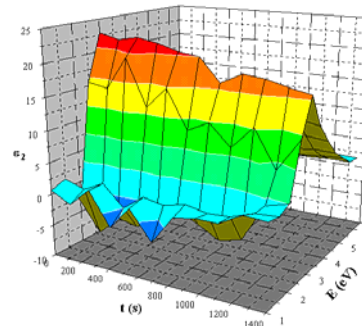
b.) amyl xanthate



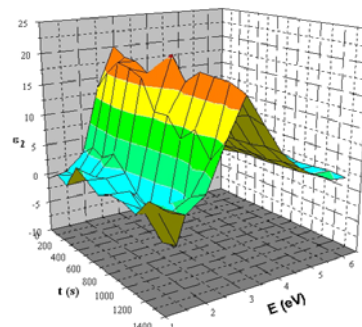
c.) isobutyl xanthate



a.) ethyl xanthate



b.) amyl xanthate



c.) isobutyl xanthate

Figure 1. Time dependence of the spectral distribution of the dielectric constant for the chalcopyrite – xanthate solution interface

Figure 2. Time dependence of the spectral distribution of the dielectric loss function for the chalcopyrite – xanthate solution interface

A program for a personal computer was created to find the coefficients in the series expansion of the reflectivity, to compute the phase shift using the

experimental and extrapolated values, after which the real and imaginary part of the complex valued dielectric constant could be determined.

To have a better overview on the time evolution of the spectral distribution for the real and imaginary part of the complex dielectric constant we used 3D graphs. Figure 1 and 2 presents these graphs for the three xanthate solutions that we used on the chalcopyrite mineral.

The variations of the real dielectric constant exhibit huge initial time dependent oscillations in the 1-1.5eV domain. These oscillations tend to smooth out as the dynamic adsorption equilibrium sets in after 20-25min. After the relatively smooth time dependence of the local minimum found around 1.5eV, the dielectric constant reaches its time oscillating maximum at around 2.5eV, and then an exponential drop follows. At energies over 4.3eV the values of ϵ_1 remain constant.

The same oscillations are present in the behaviour of ϵ_2 at low energies. This quantity reaches its maximum at energies slightly higher than 3eV; a decrease follows to a constant plateau at high energies. One can also observe higher absolute values for amyl-xanthate, lower ones for the isobutyl-xanthate, while ethyl-xanthate produces the lowest ones.

CONCLUSION

In this work we present UV-VIS differential reflectance spectroscopy as a method of determining the “in situ” dynamics of adsorption processes at the chalcopyrite and potassium ethyl-, amyl-, isobutyl-xanthate solution interface. One determined the complex reflection coefficient measuring the differential reflectance of the interface, then computing the phase shift in the Kramers-Kronig formalism. The extrapolation used in the computations is also presented. One could plot the time dependent behaviour of the real and imaginary part of the complex dielectric coefficient over the UV-VIS domain. Initial oscillations in the low energy region are observed, the maximum values are identified, plateaus at high energies are obvious, while a time to reach dynamical adsorption equilibrium of 20-25min can be determined.

REFERENCES

- [1] R. Todoran, D. Todoran, Zs. Szakacs, Phys. Scr., 2013, T157, 014032
- [2] H.A. Kramers, Nature, 1926, 117, 775-778
- [3] R. de Kronig, J. Opt. Soc. Am, 1926, 12, 547-556
- [4] R.K. Ahrenkiel, J. Opt. Soc. Am., 1971, 61, 1651-1655
- [5] K.E. Peiponen and J.J. Saarinen, Rep. Prog. Phys., 2009, 72, 056401
- [6] M. Dressel and G. Gruner, Electrodynamics of Solids, Cambridge University Press, 2002

SOME OPTICAL AND ELECTRICAL PROPERTIES OF THE CHALCOPYRITE NATURAL MINERAL – ETYL XANTHATE SOLUTION INTERFACE

R. Todoran, D. Todoran and Zs. Szakacs

Department of Economics And Physics, Technical University of Cluj Napoca, North University Center of Baia Mare, 62/A, Dr. V. Babes Street, Baia Mare, ROMANIA (szakacs@yaho.com)

ABSTRACT

The paper presents the time evolution of the optical spectral distribution for the attenuation coefficient, refractive index and extinction coefficient, effective valence number and of the electron loss functions for the interface formed between the chalcopyrite natural mineral and the potassium ethyl-xanthate solution. One used the complex dielectric coefficient computed from differential optical reflectance spectroscopy data in the framework of the Kramers-Kronig formalism.

INTRODUCTION

Dynamic “in situ” measurements can be made with the differential reflectance spectroscopy method and, using computer aided data processing, fast access to the variation of the studied microscopic carrier dynamics in strongly correlated electron thin layers can be obtained. One can draw conclusions of the electrical and optical properties of thin films formed at semiconductor-collector reagent interface, determining optical and electrical functions that cannot be measured directly.

EXPERIMENTAL SETUP AND THEORY

Our differential reflectance spectroscopy measurements were made using the SPECORD M-40 spectrophotometer in the domain of 200-900 nm for the chalcopyrite natural mineral in contact with potassium ethyl-xanthate. The Kramers-Kronig formalism with a suitable extrapolation for the reflectance on low and high energy domains was used to determine the phase of the complex reflectance. When complex dielectric coefficient, denoted here by $\varepsilon = \varepsilon_1 + i\varepsilon_2$ [1-3], over the covered optical spectrum was computed, one could proceed to determine time dependence of the spectral distribution of the some electrical and optical parameters of the interface. The complex dielectric constant is directly linked to the complex index of refraction and absorption n^* of the medium by the relation:

$$n^* = \sqrt{\varepsilon} = n + ik, \quad (1)$$

where n is the refractive index and k is the extinction coefficient. These two quantities cannot be measured directly at the same time in optical experiments. We used the following formulas to determine them [4,5]:

$$n = \sqrt{\frac{\sqrt{\varepsilon_1^2 + \varepsilon_2^2} + \varepsilon_1}{2}}, \quad k = \sqrt{\frac{\sqrt{\varepsilon_1^2 + \varepsilon_2^2} - \varepsilon_1}{2}} \quad (2)$$

Using the classical theory of absorption and the Beer-Lambert law, the absorption coefficient α can be computed from the extinction coefficient by the relation:

$$\alpha = 2\omega k, \quad (3)$$

where the speed of light was set to be equal with the unity. The skin depth and the penetration depth, defined as $\delta_{skin} = 2\delta_{pen} = 2/\alpha$, were not studied separately.

The effective valence number n_{eff} can give a numerical estimate of the various physical quantities involved in the cohesion of atomic aggregates. It represents the average valence number of the chemical compound divided by the number of atoms found in that compound.

The characteristic electron loss functions $-Im(1+\varepsilon)^{-1}$ and $-Im \varepsilon^{-1}$ are important in the determination of the energy needed by an electron to jump over the band gap formed between the valence band and conduction band.

RESULTS AND DISCUSSIONS

For a better view over the time evolution of the spectral distribution of the studied properties we have represented the variations using 3D graphs.

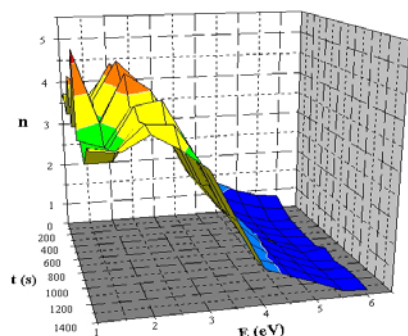


Figure 1. Time and energy dependence of the refractive index n of the interface

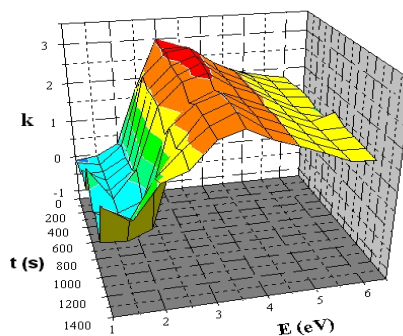


Figure 2. Time and energy dependence of the extinction coefficient k of the interface

The variation of the refractive index is presented in figure 1. At low energies of 1-1.5eV one can see time dependent oscillations of the refractive index

which tend to smooth out, at the onset of the dynamical adsorption-desorption equilibrium, after approximately 20min. The refraction index shows maximum values of around 5 in the 2-3eV (410-620nm) interval. Semiconductors have high refraction indexes in the VIS part of the spectrum. The maximum oscillates in time and has the tendency to shift to higher energies. As the theory predicts, at high energies, above 4eV this quantity tends to reach values slightly higher than 1. The time and energy dependence of the extinction coefficient can be seen in figure 2. It presents a saddle-like behaviour with low extinction in the NIR region and a maximum that shifts with time from 3eV towards 3.5eV. At higher energies one can observe a relatively high extinction that reaches a plateau value of 2.

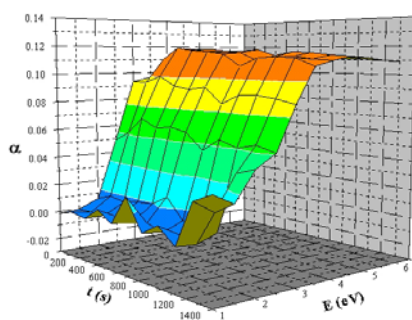


Figure 3. Time and energy dependence of the absorption coefficient α of the interface

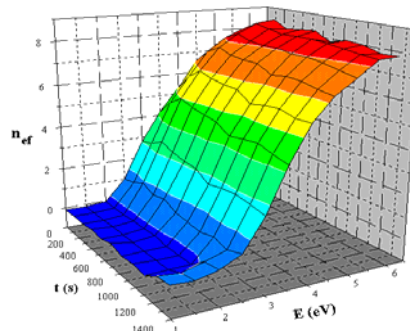


Figure 4. Time and energy dependence of the effective valence number n_{eff} of the interface

The time dependent behaviour of the absorption coefficient α is presented in figure 3. One can observe very low absorption values in the NIR spectrum, a steep increase in the VIS domain until a constant, very high absorption is reached in the UV part of the spectrum. The initial absorption values are the lowest. At the onset of the adsorption dynamic equilibrium the values over the NIR spectrum raise rapidly, as the values of k do. The effective valence number does not exhibit dramatic changes over time. In the spectral dependence one can see that it takes values close to 0 for low energies, a monotonous increase towards in the VIS domain to attain a high positive value on the UV part of the spectrum. The values remain always positive indicating that the interface has an electropositive character, fact that is easily predictable [6]. Studying the representations of the electron energy loss functions in figure 5 one can observe their monotonous increase until reaching the UV part of the spectrum. One cannot observe the van Hove singularities that were so obviously displayed in the case of the mineral, but only on the first measurement near the 6eV value. The presence of valence

band gap is being masked out by the adsorption thin layer interface products.

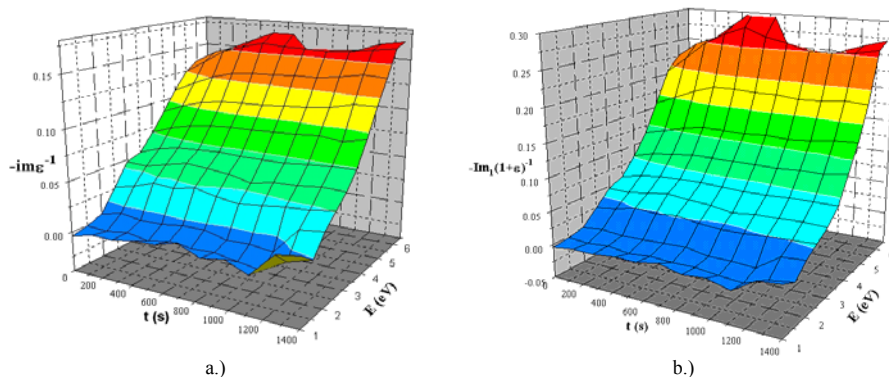


Figure 5. Time evolution of the spectral distribution for the electron energy loss functions a.) $-Im \epsilon^{-1}$ and b.) $-Im(1+\epsilon)^{-1}$ of the interface

CONCLUSION

In the present work we computed and presented the time evolution of the spectral distribution of some optical (refraction index, extinction and absorption coefficient) and electrical (effective valence number and electron energy loss functions) properties of the adsorption interface formed between chalcopyrite natural mineral – potassium ethyl-xanthate. Because these quantities cannot be determined during one experiment, we used differential reflectance data and applied the Kramers-Kronig formalism for the “in situ” dynamical monitoring of the evolution of the adsorption process.

REFERENCES

- [1] M. Dressel and G. Gruner, *Electrodynamics of Solids*, Cambridge University Press, 2002
- [2] F. Wooten, *Optical Properties of Solids*, New York, Academic Press, 1972
- [3] J.D.E. McIntyre and D.E. Aspnes, *Surf. Sci.*, 1971, 24, 417-434
- [4] A.B. Kuzmenko, *Rev. Sci. Instrum.*, 2005, 76, 083108
- [5] J.D. Jackson, *Classical Electrodynamics Third Edition*, John Wiley & Sons, 1998
- [6] J. L. Shay, J.H. Wernick, *Ternary Chalcopyrite Semiconductors*, New York, Pergamon Press, 1975

EXPERIMENTAL TECHNIQUES FOR CHARACTERIZATION OF THE MAGNETITE/AQUEOUS ELECTROLYTE SOLUTION INTERFACE AT ELEVATED TEMPERATURES

S. Vidojković¹, B. Ekmešić¹ and T. Tomković¹

¹*University of Belgrade, Department of Chemistry, Institute of Chemistry,
Technology and Metallurgy, Njegoševa 12, 11001 Belgrade, Serbia
(sonja66yu@yahoo.com)*

ABSTRACT

Enormous efficiency losses and subsequent economic consequences in energy systems, caused by deposition of corrosion products on heat exchange surfaces, created a requisite to study the surface characteristics of deposit components in order to minimize and control its formation. This work treats and summarizes employed experimental techniques for characterization of magnetite/aqueous electrolyte solution interface at high temperatures. Consequently, potentiometric titrations, mass titrations, electrophoresis and streaming potential were considered, their capabilities were highlighted and main features were discussed. It was concluded that potentiometric titrations together with electrophoresis are the most effective techniques for future researches of interest to the power industry and the further work should be focused on improving of experimental techniques in the direction of higher temperature measurement.

INTRODUCTION

Processes at oxide/water interfaces are of utmost importance for deposit formation in water/steam cycles of power plants and other industrial equipment using high temperature water medium. Magnetite (Fe_3O_4) is a predominant deposit compound in all types of power plants and knowledge of its surface and electrokinetic characteristics at high temperatures are highly important for understanding the mechanism of deposition formation. However, there is a deficiency of data on surface properties of magnetite due to lack of experimental techniques and facilities operating at high temperatures. In this paper a succinct review and analysis of existing experimental techniques for magnetite surface characterization at elevated temperatures was presented and directions for their future development and utilization in power industry was given.

EXPERIMENTAL

The following electrochemical techniques were used so far for the study of surface characteristics of magnetite at high temperatures: potentiometric titrations, mass titrations, electrophoresis and streaming potential. The temperatures at which the measurements were performed are presented in Table 1.

The potentiometric titrations are the widely used technique for determining temperature effect on the interface magnetite/aqueous electrolyte solution [1, 2, 3, 4]. This technique represents a useful tool for estimation of surface charge density and the point of zero charge of magnetite particles from the inflection point. The value of the surface charge was derived from the following equations:

$$\sigma = (F/A)(\Gamma_{H^+} - \Gamma_{OH^-}) \quad (1)$$

where σ is surface charge density ($C\ m^{-2}$), F is the Faraday constant ($9.6485 \times 10^4\ C\ mol^{-1}$), A is the specific surface area ($m^2\ g^{-1}$), and Γ_{H^+} and Γ_{OH^-} are the adsorption densities of H^+ and OH^- ($mol\ m^{-2}$), respectively. Amount of H^+ and OH^- at the surface area was calculated as a difference between the amount of acid or base added in suspension and that added in blank. Then, the difference was divided by the surface area of the colloidal magnetite particles. The point of zero charge (pHpzc) is obtained by calculating the surface charge as a function of the concentration of the charge-determining ions (H^+ and OH^-) at various concentrations of the background electrolyte. The common intersection point of surface charge curves is acquired at three or more ionic strengths. For determination of the point of zero charge mass titration was also employed [5] involving the addition of subsequent shares of oxide powder in aqueous electrolyte solution to achieve a constant pH value of equilibrated dispersion, which represents the point of zero charge. In comparison with potentiometric titration this technique is simpler, easier and does not require the utilization of different ionic strengths or blank titrations. A very useful technique for determining the surface characteristics of magnetite is electrophoresis [6] which makes it possible to measure potential at the surface of shear (zeta potential) and provides the plausible data at high temperatures. Electrophoresis is referred to as movement of charged surface spaces under the influence of an external electric field. The zeta potential of magnetite was computed from the experimental particle mobility values using the O'Brien and White (1978) numerical approach. The zeta potential enables the determination of the isoelectric point (pHIEP) representing the condition at which the suspension exhibits the lowest stability. The most obvious advantage of this technique is that, except the

particle-particle interaction, permits the particle-wall interaction comparing the zeta potential of magnetite particles with that of the substrate. Besides electrophoresis, the zeta potential of magnetite at 235°C was measured by streaming potential [7] which is based on measuring the potential drop between two ends of a fine capillary or a powder packed column. However, these measurements showed a lack of reproducibility.

RESULTS AND DISCUSSION

Good agreement was found between the values of the point of zero charge (pHpzc) and isoelectric point of magnetite (pHIEP) obtained by above described techniques (Table 1). Only the results obtained by streaming

Table 1. Techniques used to study the magnetite oxide/electrolyte solution interface at high temperatures and obtained values of pH_{DZC} and pH_{IEP}

Temperature (°C)	pH _{pzc}	pH _{IEP}	Technique	Reference
25	6.55			
35	6.30			
45	6.10		Potentiometric titration and oxide addition	Tewari and McLean (1972)
55	5.90			
60	5.80			
80	5.60			
90	5.40			
25	6.90		Potentiometric titration	Blesa et al. (1984)
30	6.80			
50	6.45			
80	6.00			
235		6.10	Streaming potential	Jayaweera
50	6.50			
100	6.24		Potentiometric titration	Wesolowski et al. (2000)
150	5.65			
200	5.47			
250	5.31			
290	5.55			
5	6.60			
15	6.30			
25	6.20			
35	6.10			
50	6.00		Mass titration	Barale et al. (2008)
50	5.60			
70	5.50			
90	5.50			
125	5.20			
250	5.20			
285	5.90			
320	6.10			
25		6.35		
100		6.00	Electrophoresis	Vidojkovic et al. (2011)
150		5.25		
200		5.05		
100	6.08		Potentiometric titration	Zebardast et al. (2014)
125	5.81			
150	5.44			
175	5.11			

potential show inconsistency with other results. Therefore, some authors do not consider this technique as a suitable for the measurement of magnetite surface properties considering it more appropriate for the study of flat surfaces. It was found in the literature that some authors consider the credibility of point of zero charge obtained by mass titration also limited because of high sensitivity to the minor concentrations of acidic or basic impurities present

on the surface. Consequently, the mass titration can be recommended only for very pure (acid-and base- free) materials. On the other hand, results obtained by potentiometric titration and electrophoresis allowed the reliable characterization of magnetite oxide/electrolyte solution interface at temperatures up to 290°C and 250°C, respectively.

CONCLUSION

Based on the analysis of literature data the conclusion was made that combination of the zeta potential and compatible surface titration data would be the most effective in studying the surface behaviour of magnetite particles at high temperatures. They can enable the establishment of relation between suspended particles and metal substrate, determination of the effect of adsorption of charge determining species on the surface properties of suspended particles and creating mathematical models for predicting the surface behaviour of magnetite particle. Future advancement of these techniques should go towards achievement the temperature ranges over 290°C for potentiometric titration and 250°C for electrophoresis.

ACKNOWLEDGEMENT

This work was supported by the Ministry of Education, Science and Technological Development of the Republic of Serbia (Project No. III 43009).

REFERENCES

- [1] P. H. Tewari, A. W. McLean, *J. Colloid Interf. Sci.*, 1972, 40, 267-272.
- [2] M. A. Blesa, N. M. Figliolia, A. J. G. Maroto, A. E. Regazzoni, *J. Colloid Interf. Sci.*, 1984, 101, 410-418.
- [3] D. J. Wesolowski, M. L. Machesky, D. A. Palmer, L. M. Anovitz, *Chem. Geol.*, 2000, 167, 193-229.
- [4] H. R. Zebardast, M. Pawlik, S. Rogak, E. Asselin, *Colloid Surface A*, 2014, 444, 144-152.
- [5] M. Barale, C. Mansour, F. Carrette, E. M. Pavageau, H. Catalette, G. Lefevre, M. Fedoroff, G. Cote, *J. Nucl. Mater.*, 2008, 381, 302-308.
- [6] S. Vidojkovic, V. Rodriguez-Santiago, M. V. Fedkin, D. J. Wesolowski, S. N. Lvov, *Chem. Eng. Sci.*, 2011, 66, 4029-4035.
- [7] P. Jayaweera, S. Hettiarachchi, H. Ocken, metal oxides, *Colloid Surface A*, 1994, 85, 19-27.

SEPARATION OF YTTRIUM FROM STRONTIUM BY HOLLOW FIBRE SUPPORTED LIQUID MEMBRANE CONTAINING DI(2-ETHYLHEXYL)PHOSPHORIC ACID

K. Kumrić¹, Đ. Petrović², G. Vladisavljević³, M. Stoiljković⁴ and L. Slavković-Beškoski⁵

¹Laboratory of Physics, ²Laboratory of Radioisotopes, ⁴Department of Physical Chemistry, ⁵Laboratory of Chemical Dynamics and Permanent Education, Vinča Institute of Nuclear Sciences, University of Belgrade, P.O. Box 522, Belgrade, Serbia. (kkumric@vinca.rs)

³Loughborough University, Department of Chemical Engineering, Leicestershire LE11 3TU UK.

ABSTRACT

Separation of Y(III) from Sr(II) was performed using the hollow fibre membrane contactor operated in a recirculation mode. The steady-state was established after ~5 h of operation and the maximum removal of Y(III) from the donor to the acceptor was achieved at the donor flow rate of 4.7 cm³ min⁻¹. The investigated system showed promising results as a method which could be potentially applied for the preparation of ⁹⁰Sr/⁹⁰Y generator system.

INTRODUCTION

⁹⁰Sr is an ideal source of carrier-free ⁹⁰Y ($T_{1/2} = 64.1$ h, $E_{\beta, \max} = 2.3$ MeV), which has suitable radionuclidic characteristics for the application in endoradiotherapy of malignant tumors. The separation of carrier-free ⁹⁰Y from ⁹⁰Sr might be achieved by a variety of physicochemical methods [1 - 4], among them is method based on the supported liquid membranes (SLMs).

SLM extraction is based on a three-phase system and involves simultaneous extraction and re-extraction. The pores of a microporous hydrophobic membrane are filled with the organic phase (extractant or liquid membrane) held by the action of capillary forces, while the feed (donor) and the stripping (acceptor) solutions are placed at the opposite sides of the membrane. SLM extraction is performed in a continuous-contact mass transfer devices – membrane contactors, designed as compact units using either flat sheet or hollow fibre (HF) hydrophobic membranes.

The purpose of the present study was to investigate SLM extraction of strontium and yttrium with di(2-ethylhexyl)phosphoric acid (DEHPA) as a carrier in a continuous HF contactor operated in a recirculated mode, with

regard to the potential application of the applied system for the generation of carrier-free ^{90}Y from ^{90}Sr source. The influence of the time of extraction and the donor phase flow rate on the efficiency of separation of Y(III) from Sr(II) was observed.

EXPERIMENTAL

Separation of Y(III) from Sr(II) was carried out in the self-designed membrane contactor containing seven HF polypropylene membranes, ACCUREL 50/280 (Membrana GmbH, Wuppertal, Germany), enclosed in a glass shell. Experimental setup of a recirculating SLM extraction system is shown in Fig. 1. SLM extraction system consisted of a HF membrane contactor (C), two reservoirs for the donor and acceptor solutions (R1 and R2), two peristaltic pumps (P1 and P2) and magnetic stirrer (M).

HF membranes, with the effective length of 119 cm, were impregnated with 15% DEHPA in dodecane. The donor solution (5.5 mM Sr(II) and 0.2 mM Y(III)/0.1 M HCl), 25 cm³, was fed along the shell side of the fibre and recirculated in a closed loop between the module and reservoir R1 using peristaltic pump P1. The flow rate of the donor phase, Q_D , was 0.8-4.7 cm³ min⁻¹. The acceptor solution (3 M HCl), 4 cm³, was pumped through the lumen of the HF using peristaltic pump P2 and recirculated between the module and reservoir R2. The flow rate of the acceptor, Q_A , was 0.8 cm³ min⁻¹. The donor and acceptor solutions flowed co-currently within the module.

Strontium and yttrium concentrations in the donor and acceptor solutions were determined by ICP-OES, Spectroflame model B (Spectro Inc., MA, USA). The efficiency of Sr(II) and Y(III) mass transfer through the liquid membrane was evaluated using the following parameters: the removal efficiency, E_R , (represents the fraction of the respective metal ion removed from the donor phase), the extraction efficiency, E , (represents the fraction of the metal ion initially present in the donor phase that was found in the

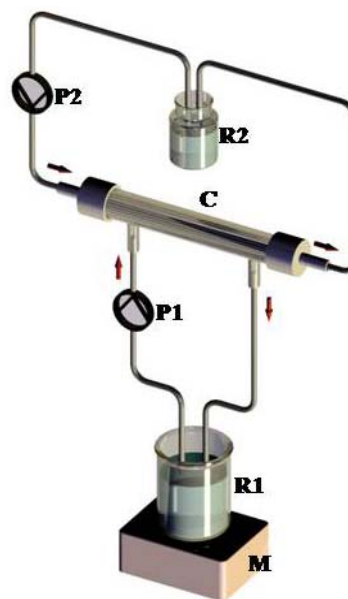


Figure 1. Experimental setup of a recirculating SLM extraction system.

acceptor after extraction) and the memory effect, M , (the fraction of the respective metal ion captured in the organic phase).

RESULTS AND DISCUSSION

Fig. 1 shows time-dependent variations of the Y(III) concentration in the donor and acceptor phase reservoirs at five different donor flow rates. As can be seen, the concentration of Y(III) in the donor reservoir decreased significantly during the first 4 h of operation, and then gradually reached a plateau, whereas its concentration in the acceptor increased nearly in the same manner. The steady state was established after ~ 5 h of operation.

The lowest Y(III) concentration in the donor and the highest Y(III) concentration in the acceptor were achieved at the Q_D of $4.7 \text{ cm}^3 \text{ min}^{-1}$. At the same Q_D , Sr(II) concentration in the donor was reduced by 8% compared to the initial Sr(II) concentration. Despite this fact, re-extraction of Sr(II) in the acceptor was practically negligible ($< 0.03\%$ of its initial concentration). The obtained results suggest that the applied system could be potentially applied as a generator of ^{90}Y for use in nuclear medicine.

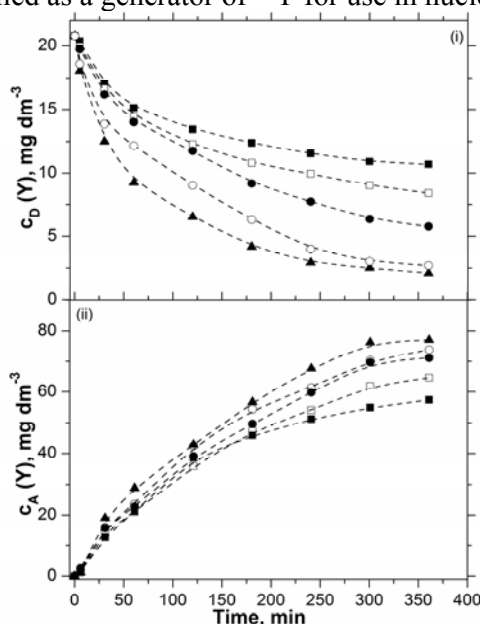


Figure 2. Time dependence of the Y(III) concentration in the donor (c_D) and acceptor (c_A) phase at different Q_D : (\blacksquare) $0.8 \text{ cm}^3 \text{ min}^{-1}$, (\square) $1.6 \text{ cm}^3 \text{ min}^{-1}$, (\bullet) $2.4 \text{ cm}^3 \text{ min}^{-1}$, (\circ) $3.2 \text{ cm}^3 \text{ min}^{-1}$, (\blacktriangle) $4.7 \text{ cm}^3 \text{ min}^{-1}$. Q_A was $0.8 \text{ cm}^3 \text{ min}^{-1}$.

The steady-state values of the extraction parameters (E , E_R and M) are presented in Table 1. It can be seen that the E_R of Y(III) increased

significantly with increasing the Q_D from 0.8 to 3.2 $\text{cm}^3 \text{min}^{-1}$, but the effect was less pronounced with further increase in the Q_D . E of Y(III) was not such affected by increasing the Q_D , indicating that a portion of the extracted Y(III) remained in the organic phase. The reason for the suppressed re-extraction of Y(III) at higher Q_D could be the increased viscosity of the organic phase or insufficient contact area provided for the re-extraction.

Table 1. Efficiency parameters of Y(III) transport through SLM as a function of the donor flow rate.

$Q_D, \text{cm}^3 \text{min}^{-1}$	$E_R, \%$	$E_s, \%$	$M, \%$
0.8	48.6	44.2	4.4
1.6	59.6	49.8	9.8
2.4	72.3	54.8	17.5
3.2	87.0	56.8	30.1
4.7	89.9	59.3	30.6

CONCLUSION

The obtained results indicated that the HF membrane contactor under recirculation mode of operation enabled efficient separation of Y(III) from Sr(II) at all investigated donor flow rates. The maximum removal of Y(III) (~60%) from the donor to the acceptor was achieved after 6 h of operation at the Q_D of 4.7 $\text{cm}^3 \text{min}^{-1}$. However, additional effort is needed to ensure lower degree of Y(III) accumulation in the organic phase.

ACKNOWLEDGEMENT

We acknowledge the support to this work provided by the Ministry of Education and Science of Serbia through the project *Physics and Chemistry with Ion Beams*, No. III 45006.

REFERENCES

- [1] T. B. Hsieh, B. Ting, T. H. Hsieh, H. L. Shen, *Applied Radiation and Isotopes*, 1993, 44, 1473-1480.
- [2] V. P. Achutan, S. P. Dhimi, R. Kannan, V. Gopalakrishnan, A. Ramanujam, *Separation Science and Technology*, 2000, 35, 261-270.
- [3] D. Saha, E. S. Vadivu, R. Kumar, C. R. Venkata Subramani, *Journal of Radioanalytical and Nuclear Chemistry*, 2013, 298, 1309-1314.
- [4] P. Kandwal, S. A. Ansari, P. K. Mohapatra, V. K. Manchanda, *Separation Science and Technology*, 2011, 46, 904-911.

SORPTION OF PERTECHNETATE ONTO ORDERED MESOPOROUS CARBON

Đ. Petrović¹, A. Đukić², K. Kumrić³, I. Milanović², Ž. Rašković-Lovre²
and Lj. Matović²

¹Laboratory for Radioisotopes, ²Laboratory of Materials Sciences,
³Laboratory of Physics, Vinča Institute of Nuclear Sciences, University of
Belgrade, P.O. Box 522, Belgrade, Serbia. (djpetrovic@vin.bg.ac.rs)

ABSTRACT

Ordered mesoporous carbon (OMC) was used as an adsorbent for the removal of pertechnetate (TcO_4^-) anion. Batch experiments were performed to study the effects of pH and ionic strength of the solution. The adsorption of TcO_4^- is almost pH-independent in very wide pH region (from 4.0 to 10.0). Maximum distribution coefficient, K_d , was obtained at pH 2.0. Adsorption of TcO_4^- was not affected by the ionic strength changes.

INTRODUCTION

The presence of the long-lived radionuclide ^{99}Tc ($t_{1/2} = 2.1 \times 10^5$ y) in the environment comes from anthropogenic nuclear activities such as nuclear power plants, nuclear weapons testing facilities, reprocessing of spent nuclear fuel, nuclear accidents and medical application of $^{99\text{m}}\text{Tc}$. The predominant chemical form of the radionuclide ^{99}Tc is the highly soluble and environmentally mobile TcO_4^- anion, that easily penetrates the ecosystems [1]. Because ^{99}Tc is hazardous to the environment, its effective removal from contaminated groundwater and sediments is considered a primary task.

Removal of TcO_4^- by activated carbons is one of the most efficient processes, because of large specific surface area, porous structure and variety of surface functional groups of activated carbons. Ordered mesoporous carbon belongs to a family of porous materials which attracted great attention in recent years due to its unique features such as high surface area and uniform, large and tunable pore channels. These features make OMC attractive for use in the adsorption processes.

The aim of the present paper was to investigate the influence of the solution pH and ionic strength on the TcO_4^- sorption by the OMC.

EXPERIMENTAL

The OMC was synthesized under acidic conditions as previously described by Momčilović et al [2]. Radioactive technetium (in the form of pertechnetate) was obtained from a $^{99}\text{Mo}/^{99\text{m}}\text{Tc}$ generator and its radioactive concentration was determined by a Capintec CRC-15 dose calibrator (Capintec, Inc. Ramsey, USA). The resolution of the instrument is 0.001 MBq, i.e. 0.01 μCi . The measurements of $^{99\text{m}}\text{Tc}$ activity in aliquots were made using vial geometry.

Batch experiments were performed at room temperature by mixing 0.04 g of well powdered OMC adsorbent and 10 cm^3 of working $^{99\text{m}}\text{TcO}_4^-$ solution in closed glass vials. Experimental set-up is presented in Fig. 1. The total $^{99\text{m}}\text{TcO}_4^-$ radioactive concentration in the working solution was 1.4 MBq cm^{-3} (37.8 mCi cm^{-3}). The initial pH was adjusted by using either 0.1 M HCl or NaOH. The samples were shaken on a laboratory shaker for 60 min at a stirring speed of 200 rpm. After that, the liquid phases were separated from the solid phases by filtration through a microporous membrane filter (0.45 μm). The residual radioactive concentration of $^{99\text{m}}\text{TcO}_4^-$ in each aliquot was determined with a Capintec CRC-15 dose calibrator.

The effects of solution pH (2.0-12.0) and ionic strength (0.01 and 0.1 M NaCl) were investigated with respect to the removal efficiency of TcO_4^- . All experiments were carried out in duplicate, and the data obtained were used for analysis.

The removal efficiency (E , %) and the distribution coefficients (K_d , $\text{cm}^3 \text{g}^{-1}$) of $^{99\text{m}}\text{TcO}_4^-$ were calculated using the following equations:

$$E = \frac{(A_i - A_f)}{A_i} \times 100 \quad (1)$$

$$K_d = \frac{(A_i - A_f)}{A_f} \times \frac{V}{m} \quad (2)$$

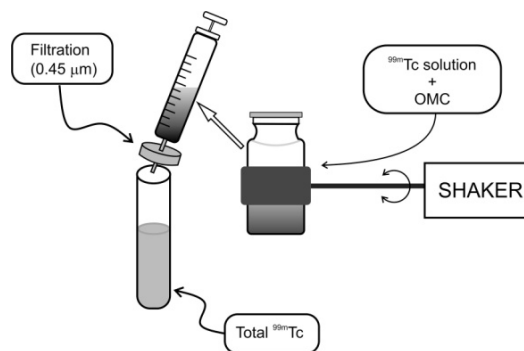


Figure 1. Experimental set-up for the sorption of TcO_4^- onto the OMC.

where A_i and A_f are the initial and the final $^{99m}\text{TcO}_4^-$ radioactive concentrations in the liquid phase (MBq cm^{-3}), V the volume of the solution (cm^3) and m the mass of adsorbent (g).

RESULTS AND DISCUSSION

The effect of the solution pH and ionic strength, I , on the adsorption of TcO_4^- using the OMC was investigated at varying pH values from 2.0 to 12.0. The obtained results are presented in Fig. 2. It is evident that the adsorption of TcO_4^- was pH-dependent, with maximum removal efficiency of 99% at the pH value 2.0. Then, the removal efficiency slightly decreases and reaches the value of 93% at the pH values between 4.0 and 10.0. At the pH values beyond 10.0, the adsorption of TcO_4^- decreased sharply and the removal efficiency of TcO_4^- fell to 72%. The distribution coefficients, presented in the insert in Fig. 2, behaved in a similar manner as a function of solution pH, with the maximum K_d value of 6.6×10^3 at the pH 2.0, plateau with the mean K_d of 2.9×10^3 at the pH range from 4.0 to 10.0, and the K_d value less than 1×10^3 at the pH > 10.0. Under the investigated experimental conditions, E and K_d values are insensitive to ionic strength changes, indicating that the sorption of TcO_4^- was not affected by the presence of competing Cl^- ions.

CONCLUSION

Ordered mesoporous carbon (OMC) was investigated for its sorption capability to remove pertechnetate (TcO_4^-) anions from aqueous solutions.

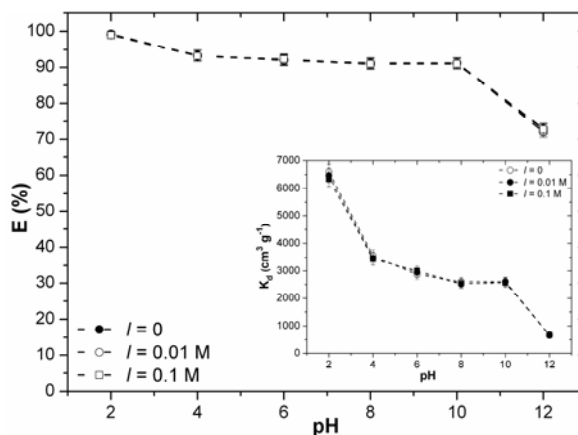


Fig. 2 Effect of pH and ionic strength (0.01 and 0.1 M NaCl) on the sorption of TcO_4^- by the OMC. Insert: Variation of K_d values with pH and ionic strength.

The conclusions are summarized as follows:

- Maximum E and K_d values of 99% and $6.6 \times 10^3 \text{ cm}^3 \text{ g}^{-1}$, respectively, were obtained at the pH 2.0;
- The adsorption of TcO_4^- is almost pH-independent in very wide pH region (from 4.0 to 10.0);
- The sorption of TcO_4^- was not affected by the presence of competing Cl^- ions.

The obtained results indicate that the TcO_4^- sorption by the OMC is well classed compared to other carbon materials (adsorbents). As a material resistant to aging (to the oxidizing conditions and the presence of water), as well as its good sorption properties, the OMC appears to be an efficient adsorbent for the TcO_4^- removal from aqueous solutions.

ACKNOWLEDGEMENT

This work was partially supported by the Ministry of Education and Science of the Republic of Serbia through the project No. III 45012.

REFERENCES

- [1] K. Shi, X. Hou, P. Roos, W. Wu, *Analytica Chimica Acta*, 2012, 709, 1-20.
- [2] M. Momčilović, M. Stojmenović, N. Gavrilov, I. Pašti, S. Mentus, B. Babić, *Electrochimica Acta*, 2014, 125, 606-614.

EFFECT OF GALENA SURFACE OXIDATION ON ETHYLXANTHATE ADSORPTION ON GALENA

D. Vučinić, M. Kostović and P. Lazić

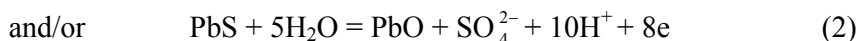
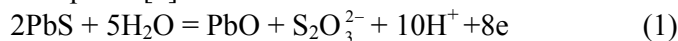
Faculty of Mining and Geology, University of Belgrade, Serbia
(dušica.vucinic@rgf.bg.ac.rs)

ABSTRACT

Zeta and redox potentials and IR data showed that the adsorption of ethylxanthate anions ($C_2H_5CS_2^-$, EX^-) on oxidised galena surface started by ion exchange reaction with sulphate ions from the surface oxidation layers. The next steps are: 1) surface oxidation layers solubility; 2) chemical adsorption of EX^- on -Pb- surface galena sites; 3) formation of physically adsorbed $Pb(EX)_2$.

INTRODUCTION

Many researchers have studied the sulphide minerals surface oxidation as the degree of surface oxidation and thermodynamic and kinetic stability of oxidation products affect surface properties, mechanism of the collector adsorption and thereby the hydrophobic-hydrophilic surface balance and mineral floatability. In the case of the galena (PbS) the metal-deficient surface, metal polysulphide or elemental sulphur are suggested as species responsible for galena surface hydrophobization. A prolonged oxidation lead to the formation of hydrophilic sulphur-oxygen compounds of thiosulphate and sulphate [1] and/or carbonate or basic carbonate of lead:



For each of the above reaction the cathodic balance is an oxygen reduction reaction.

The goal of this study was to investigate the effect of the galena surface oxidation on the mechanism of ethylxanthate adsorption in the pH range from 6.0 to 7.0.

EXPERIMENTAL

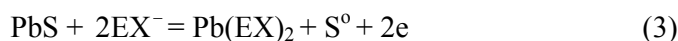
Natural galena (n-type conductivity), was manually selected and ground in an agate mortar several hours. Samples of the mineral used in the test immediately after grinding are referred to as fresh galena. The oxidised galena samples were prepared by being exposed after grinding to air for two

years. The specific surface areas of mineral samples were determined in a Coulter Counter Model D Industrial (fresh galena $2.20 \text{ m}^2/\text{g}$; oxidised galena $2.25 \text{ m}^2/\text{g}$). Commercial grade potassium ethylxanthate (KEX) was purified by multiple recrystallizations from acetone, and then used as flotation collector (surfactant for galena surface hydrophobization). NaNitrate was used to adjust the ionic strength $I=1 \times 10^{-2}$) in zeta potential measurements which were made on a Riddick Zeta-meter using the microelectrophoretic technique. Reflection infrared spectra were recorded using a Perkin Elmer Infrared Spectro-photometer with ATR-attachment. The mineral suspension (0.250 g of the mineral and 0.025 dm^3 of distilled water) was stirred without or with KEX for 15 minutes, except when a different stirring time was selected. After decantation sedimented mineral was placed on the Ge crystal and IR spectrum was recorded. Redox potential expressed in relation to the SHE, was determined in the same IR experimental conditions, using platinum and saturated calomel electrodes. The pH of mineral suspensions was between 6.0 and 7.0.

RESULTS AND DISCUSSION

For fresh galena (Fig.1, curve 1) an increase in KEX concentration provoked the rise in negative values of zeta potential, which indicating EX^- adsorption in the Stern layer of the double electric layer of the mineral. However, the oxidised galena zeta potential remained unchanged up to $1 \times 10^{-4} \text{ mol dm}^{-3}$ of KEX concentration (curve 2). Further increase in KEX concentration led to an increase in negative zeta potential values also confirming EX^- adsorption.

For electrochemical mechanism of xanthate adsorption on galena surface [2]:



redox potential of galena suspension relative to KEX concentration was calculated using the Nernst equation (Fig.2, curve 3) [2]:

$$E_h = 0.139 - 0.059 \log c_{\text{EX}^-} \quad (5)$$

Curve 1 (Fig. 2) shows that the fresh galena suspension redox potential decreases with the increase in KEX concentration. This curve has similar slope as curve 3, but the values were more positive than those obtained according to the Nernst equation (5). The oxidised galena redox potential (Fig. 2, curve 2) is the most positive. The values slowly decrease with increasing of KEX concentration up to $1 \times 10^{-4} \text{ mol dm}^{-3}$, as in the case of zeta potential.

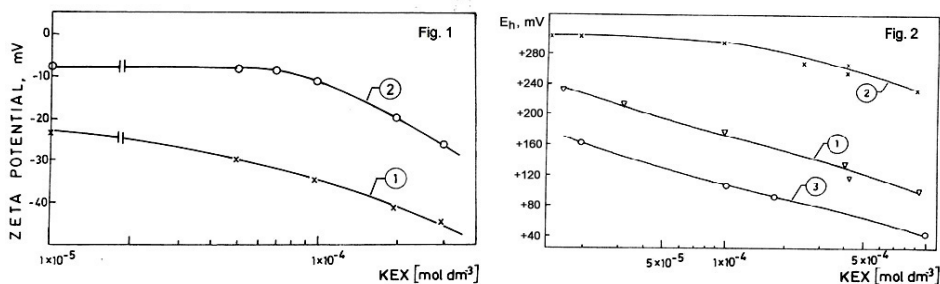


Figure 1. Zeta potential of galena as a function of KEX concentration:
 1) Fresh galena; 2) Oxidised galena.

Figure 2. Redox potential of galena as a function of KEX concentration:
 1) Fresh galena; 2) Oxidised galena; 3) Calculated data using equ.3.

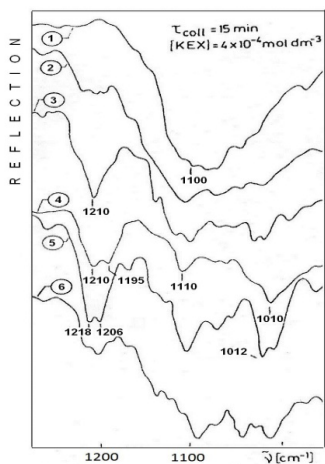


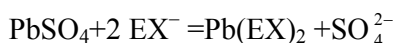
Figure 3. IR spectra of galena: 1) oxidised galena (OG); 2) OG+KEX; 3) OG+KEX (agitated in distilled water 15 minutes and decanted before KEX addition); 4) fresh galena+KEX; 5) OG+KEX ($1 \times 10^{-3} \text{ mol dm}^{-3}$); 6) OG (agitated in distilled water 35 minutes) + KEX.

In any case, according to E_h -pH diagram [1] the measured redox potential of each tested galena sample fell in the region of $\text{Pb}(\text{EX})_2$ stability, under the tested pH conditions and reagent concentrations. The absorption band in the range $1200\text{-}900 \text{ cm}^{-1}$ in the spectrum 1 of oxidised galena (Fig.3) confirms the formation of surface sulphate and/or thiosulphate [3]. In the presence of KEX (Fig. 3 spec. 2) both lead ethylxanthate in a small amount (band about 1210 cm^{-1}), and lead sulphate could be identified in the oxidised galena surface layers. However, the intensive absorption band at 1210 cm^{-1} characteristic for $\text{Pb}(\text{EX})_2$ (Fig.3, spec. 3) was obtained for the same KEX concentration only when the oxidation product was partly removed from mineral surface and aqueous solution decanted before the KEX addition. The position band above 1200 cm^{-1} indicates the prevailing presence of stoichiometric lead ethylxanthate at the mineral surface [4]. The same effect on oxidised galena is accomplished using 2.5 times higher KEX concentration in the solution, without decantation (Fig. 3, spec. 5). In contrast, KEX adsorption layers on fresh galena (Fig.3, spect. 4) contain both, monocoordinated ($-\text{Pb}-\text{EX}$ ($-\text{Pb}-$

surface mineral site), 1195 cm^{-1}) and stoichiometric lead ethylxanthate ($\text{Pb}(\text{EX})_2$, 1210 cm^{-1}), in approximately equal quantities. The prolonged agitation without decantation of the solution did not have any significant effect on the amount or form of the adsorbed ethylxanthate (Fig.3, spectrum 6).

CONCLUSION

The obtained IR results showed that the oxidised galena was covered by multilayers of surface oxidation compounds (lead thiosulphate and sulphate). The prevailing suggested mechanism of the ethylxanthate adsorption is at the beginning the ion exchange reaction between anionic groups at the surface (not deep) of the oxidation layers and EX^- anions from the solution:



(the oxidised galena zeta potential remained unchanged at lower KEX concentrations; IR confirmed $\text{Pb}(\text{EX})_2$ on the surface). But due to the relatively high solubility of oxidations products (solubility products: PbSO_4 1.3×10^{-8} ; PbS 9.3×10^{-29} , at 298 K) physically adsorbed $\text{Pb}(\text{EX})_2$, was then removed from the oxidised galena surface together with several layers of the surface oxidation film, not participating in the galena surface hydrophobization. After this "cleaning" of the surface ethylxanthate anions were chemically adsorbed, forming monocoordinated $-\text{Pb}-\text{EX}$ at galena surface and affecting the zeta potential, and physically, stoichiometric $\text{Pb}(\text{EX})_2$, according to the electrochemical mechanism (reactions 3 and 4). These adsorption species are necessary for the mineral hydrophobization and they are formed on the oxidised galena surface or after aqueous solution decantation before KEX addition or using higher surfactant concentration and longer agitation time.

ACKNOWLEDGEMENT

This work was supported by the Ministry for Science of the Republic of Serbia (Grants no.33007, no. 176010 and no. 33045).

REFERENCES

- [1] M. D. Pritzker, R. H. Yoon, *Int. J. Miner. Process.*, 1987, 12, 95-125.
- [2] P. J. Guy, W. J. Trahar, *Int. J. Miner. Process.*, 1984, 12, 15-38.
- [3] J. A. Gadsden, *Infrared Spectra of Minerals and Related Inorganic Compounds*, Butterworth, London, 1975.
- [4] D. R. Vučinić, P. M. Lazić, A. A. Rosić, *Colloids Surf. A: Physicochem. Eng. Aspects*, 2006, 279, 96-104.

DETERMINATION OF TENSIDE MIXTURES EFFICIENCY: CONDUCTOMETRIC AND STALAGMOMETRIC INVESTIGATION

S. N. Blagojević¹, S. Gajinov¹, N. Potkonjak², S. M. Blagojević³ and N. Pejić³

¹*Institute of General and Physical Chemistry, Studentski trg 12-16,
Belgrade, Serbia*

²*Chemical Dynamics Laboratory, Vinča Institute of Nuclear
Sciences, University of Belgrade, Mike Petrovića Alasa 12-14, Serbia*

³*University of Belgrade – Faculty of Pharmacy, Department of Physical
Chemistry and Instrumental Methods, Vojvode Stepe 450, Belgrade, Serbia*

ABSTRACT

The performances of mixtures of different surfactants: anionic (sodium lauryl ether sulfate (SLES) and α -olefin sulfonates (AOS), amphoteric (coco betaine) and nonionic (coco amide, amine oxide, AO and various etoxylated alcohols, C12-C15-7EO, C10-7EO and C9-C11-7EO), were studied. The parameters measured were critical micelle concentration (CMC) and surface tension of particular tenside mixture. The combination of SLES/AOS/C9-C11-7EO/AO at ratio 75/15/7/3 achieved the lowest both the CMC and surface tension compared to the other examined tenside mixtures (SLES/AOS, SLES/AOS/coco betaine/AO, SLES/AOS/coco amide/AO, SLES/AOS/C12-C15-7EO/AO and SLES/AOS/C10-7EO/AO). This study showed that adding nonionic tenside (alcohol ethoxylate, C9-C11-7EO) improved SLES/AOS foaming properties, synergism in detergency between them. The reduction in the surface tension was obtained, thus indicated that alcohol ethoxylate, C12-C15-7EO, C10-7EO and C9-C11-7EO can be used to produce better cleaning products.

INTRODUCTION

Washing and cleaning in aqueous wash liquor is a complex process involving the cooperative interaction of numerous physical and chemical influences. In the broadest sense, washing can be defined as both the removal by water or aqueous surfactant solution of poorly soluble matter and the dissolution in water (soluble impurities from textile surfaces).

Surfactants (tensides or surface active agents) are amphiphilic molecules that possess both hydrophobic and hydrophilic properties. A typical surfactant molecule consists of a long hydrocarbon “tail” that dissolves in

hydrocarbon and other non-polar solvents, and a hydrophilic "headgroup" that dissolves in polar solvents (typically water) [1]. Because of its dual affinity, an amphiphilic molecule in different solvents show more or less marked tendency to the spontaneous: a) accumulate in the phase boundary surfaces by reducing the surface tension of the solution, and b) form aggregates of molecules (micelles). Namely, when a sufficient amount of surfactant is dissolved in water, several bulk solution properties are significantly changed, particularly the surface tension (which decreases) and the ability of the solution to solubilize hydrocarbons (which increases). These changes do not occur until a minimum bulk surfactant concentration is reached. This concentration is called the critical micelle concentration, CMC. Several experiments, show that below the CMC, the surfactant exists mainly as solvated monomeric species, whereas above the CMC these monomers undergo selfassembly to form roughly spherical structures (having an average diameter of ~5 nm). Micelles are the simplest of all selfassembly structures.

Generally, the main component for cleaner or detergents is a surfactant or mixture of surfactants (anionic and non-ionic) such as in the modern detergent formulations. Synergism between surfactants in detergent formulations will affect the surfactant properties such as detergency, foaming and wetting. For estimating detergency power and detergent concentration of use, it is very important to determine both, the critical micelle concentration and surface tension [2].

In this work, we investigated mixtures of different surfactants: anionic (sodium lauryl ether sulfate, SLES and α -olefin sulfonates, AOS), amphoteric (coco betaine) and nonionic (and coco amide, amine oxide, AO and various etoxylated alcohols, C12-C15-7EO, C10-7EO and C9-C11-7EO). The CMC values and surface tension of various tenside mixtures were obtained from the conductometric and stalagmometric method.

EXPERIMENTAL

The conductivity measurements were applied to determine the CMC in various combinations of surfactant systems. Those measurements were carried out with digital conductivity meter SensION 5 (Hach, USA) with the accuracy ± 0.5 %, and with the 51975 conductivity probe that uses the 4-ring method. The conductometric method is based on the finding of a breaking point on the curve which describes the concentration dependence of electrical conductivity. The value of CMC is the intercept of two linear functions with mutually different slopes.

All the surfactants mixtures were soluble in water. The surfactant mixture solutions were prepared in a standard 100 mL volumetric flask (w/v) and then diluted to desired concentration. The surface tension of each mixed surfactants were measured with a stalagmometer. The determination of the surface tension can be done by the drop-weight method or drop counting method, and we used drop counting method.

RESULTS AND DISCUSSION

In this study, the values of the CMC and surface tension of different tenside mixtures were obtained. We tested following mixture of surfactants: 1) two anionic surfactants (SLES and AOS) – SLES/AOS; 2) two anionic surfactants (SLES and AOS), one amphoteric (coco betaine) and one non-ionic (AO) – SLES/AOS/coco betaine/AO; 3) two anionic (SLES and AOS) and two non-ionic (coco amide and AO) – SLES/AOS/coco amide/AO; 4) two anionic (SLES and AOS) and two non-ionic (C12-C15-7EO and AO) – SLES/AOS/C12-C15-7EO/AO; 5) two anionic (SLES and AOS) and two non-ionic (C10-7EO and AO) – SLES/AOS/C10-7EO/AO; 6) two anionic (SLES and AOS) and two non-ionic (C9-C11-7EO and AO) – SLES/AOS/C9-C11-7EO/AO. The ratio of SLES/AOS is (80/20) and in the other experiment SLES/AOS/tenside/AO (75/15/7/3)

Representative plot of specific conductivity, κ , as a function of the concentration, c , for surfactant mixture SLES/ α -olefin sulfonates (in the ratio of 80/20 at 23 °C is shown in Figure 1.

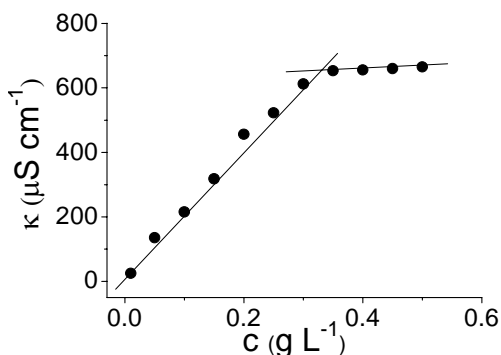


Figure 1.
Conductivity vs concentration
at 23°C for SLES/ α -olefin.

For all examined mixtures of surfactants, each plot shows the single break point. The CMC is obtained from the intersection of the fitting lines of the κ - C plots above and below the break point [3]. For the criterion of the fit, the best correlation coefficient was chosen. The obtained values of the CMC of different tenside mixtures are all summarized in Table 1.

The values of surface tension of 0.1% water solutions of tenside mixtures are presented in Table 1. Using SLES/AOS mixture, the surface tension was found higher (35.3 mNm^{-1}) than with using other examined mixture probably because of the lower polar charge of the latter. Mixing both amphoteric tenside and nonionic tensides in the mixture of anionic surfactants (SLES/AOS), further reduced the surface tension compared by the SLES/AOS. This suggests a mixed micelle formation between anionic and nonionic surfactants. The best detergency was obtained for SLES/AOS/C9-C11-7E/AO from the ratio 75/15/7/3 with surface tension 22.8 mNm^{-1} .

Table 1. The CMC and surface tension of various tenside mixtures

Tenside mixture	CMC (g/L)	γ (mN/m)*
SLES/AOS	0.33	35.3
SLES/AOS/coco betaine/AO	0.28	29.2
SLES/AOS/coco amide/AO	0.25	29.0
SLES/AOS/C12-C15-7EO/AO	0.10	23.2
SLES/AOS/C10-7EO/AO	0.09	23.0
SLES/AOS/ C9-C11-7EO/AO	0.09	22.8

*For 0.1% water solutions of tenside mixture

CONCLUSION

Nonionic tenside have a great influence on the CMC of anionic surfactant mixture. Thus, mixture of tensides (anionic and nonionic) can be used in a lower concentration. Favorable detergency properties of nonionic surfactants derive largely from the following factors: a) low critical micelle concentration, $\text{CMC} = 0.09 \text{ g L}^{-1}$, b) very good detergency performance and c) the low CMC values of nonionic surfactants indicate that they show high detergency performance even at relatively low concentrations.

ACKNOWLEDGEMENT

This work was partially supported by the Ministry for Education, Science and Technological Development of the Republic of Serbia (Grant no. 172015).

REFERENCES

- [1] J. Falbe, *Surfactants in consumer product*, Springer-Verlag, Berlin, 1987.
- [2] X. Yuan, M.J. Rosen, *J. Colloid Interf. Sci.*, 1998, 124, 652–659.
- [3] P. Rodriguez, G. Prieto, C. Rega, L. M. Varela, F. Sarmiento, *Langmuir*, 1998, 14, 4422–4426.

COMPLEX COMPOUNDS

DNA INTERACTION OF BIOLOGICALLY ACTIVE SQUARE-PLANAR Ni(II) COMPLEXES

B. Janović^{1*}, K. Adaila², M. Milenković², B. Čobeljić², K. Anđelković²
and M. Vujčić¹

¹*Institute of Chemistry, Technology and Metallurgy, Department of
Chemistry, University of Belgrade, Njegoševa 12, P.O. Box 815, 11000
Belgrade, Serbia (bjanovic @chem.bg.ac.rs)*

²*Faculty of Chemistry, University of Belgrade, Studentski trg 12–16, 11000
Belgrade, Serbia*

ABSTRACT

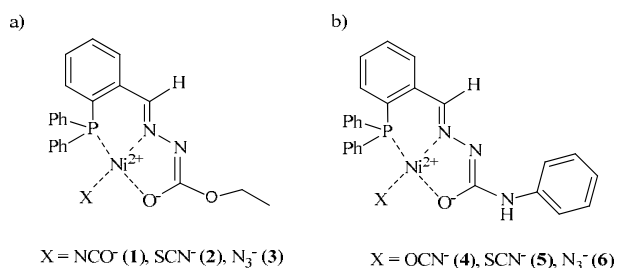
Two series of square-planar Ni(II) complexes with tridentate PNO ligands and monodentate pseudohalides of the general formula [NiLX] and [NiL'X] (**L** = ethyl (2*E*)-2-[2-(diphenylphosphino)benzylidene]hydrazinecarboxylate and **L'** = 2-(diphenylphosphino)benzaldehyde 4-phenylsemicarbazone, X = NCO⁻, NCS⁻ and N₃⁻) were synthesized. In this work DNA-binding and cleavage activity have been studied by fluorescence methods.

INTRODUCTION

Two series of square-planar Ni(II) complexes with tridentate PNO ligands and monodentate pseudohalides of the general formula [NiLX] and [NiL'X] (**L** = ethyl (2*E*)-2-[2-(diphenylphosphino)benzylidene]hydrazine carboxylate and **L'** = 2-(diphenylphosphino) benzaldehyde 4-phenyl semicarbazone, X = NCO⁻ (**1**, **4**), NCS⁻ (**2**, **5**) and N₃⁻ (**3**, **6**) were synthesized (Scheme 1).

The structures of the complexes **1–6** were determined by elemental analysis, IR and NMR spectroscopy and X-ray crystal analysis [1, 2].

Complexes **1–3** showed a significant antifungal activity, while only complex **3** displayed antibacterial activity [1]. Semicarbazonato complexes **4–6** showed moderate antibacterial activity [2].



Scheme 1. a) Complexes of Ni(II) (**1–3**) with **HL**; b) Complexes of Ni(II) (**4–6**) with **HL'**.

All investigated complexes **1–6** exhibited moderate cytotoxic activity to tested tumor cell lines [2]. The activity was, at least in part, a consequence of damage to DNA. The study of the interactions of these Ni(II) complexes with linear calf thymus DNA (CT-DNA) and circular double stranded plasmid DNA (pUC19) would provide information if DNA is the target responsible for biological activity of the complexes.

EXPERIMENTAL

Fluorescence measurements: The competitive interactions of Ni(II) complexes and the fluorescence probe ethidium bromide (EB) or Hoechst 33258 (H) with CT-DNA have been studied by measuring the change of fluorescence intensity of each DNA–complex solution after addition of the probe. Reaction mixtures containing 98 μM of CT-DNA (calculated per phosphate) and different volumes of the complexes (10 mM stock solutions) in 1 mL of bicarbonate buffer (40 mM, pH 8.4) were incubated for 60 min with occasional vortexing at 37°C. 1 μL of 1% EB solution or 1.5 μL of 1.5% H were added to each solution. The incubation was prolonged for 15 min at room temperature. The control was DNA–probe solution. Fluorescence spectra were recorded using a Thermo Scientific Lumina Fluorescence spectrometer (Finland) equipped with a 150W Xenon lamp at room temperature. The slits on the excitation and emission beams were fixed at 10 nm. EB and H were excited at 500 nm and 350 nm, respectively. Fluorescence emission was collected in the range 520–700 nm for EB and 390–650 nm for H.

Agarose gel electrophoresis on 0.8% agarose gel prepared in TAE buffer (pH 8.24) was used to analyze double-stranded closed circular plasmid pUC19 after incubation (at 37°C for 90 min) with different concentrations of investigated compounds in bicarbonate buffer (40 mM, pH 8.4). The gel was stained with ethidium bromide and visualized under UV light.

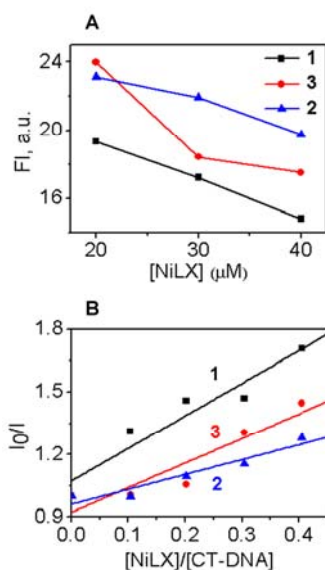


Figure 1. **A** - Changes of fluorescence intensities of EB bound to CT-DNA in presence of **1**, **2** and **3**; **B** - quenching curves of EB bound to CT-DNA in presence of **1**, **2** and **3**.

RESULTS AND DISCUSSION

For the study of the binding mode between the Ni(II) complexes and CT-DNA, the relative binding characteristics such as quenching constant were determined by fluorescence spectroscopy. Complexes had no obvious fluorescence and EB was chosen as a probe to investigate the interactions of CT-DNA with **1**, **2** and **3** and H was probe with **6**. EB is known as a typical DNA intercalator with strong binding affinity. The extent of fluorescence quenching of EB by competitive displacement from DNA is a measure of interaction between the second molecule and DNA [3]. The emission spectra of EB bound to CT-DNA in absence and presence **1**, **2** and **3** were recorded. The fluorescence intensities of the emission band at $\lambda_{\max}=596$ nm for EB-CT-DNA decreased remarkably with the increasing of concentration of the complexes (Fig. 1A). The obtained fluorescence quenching data were analyzed according to the Stern-Volmer equation $I_0/I=1+Kr$ [4], where I_0 and I represent the fluorescence intensities of probe-CT-DNA in absence and presence of the complex, respectively. K is Stern-Volmer quenching constant dependent on the ratio of the bound concentration of the probe to the bound concentration of CT-DNA. r is the ratio of the concentration of the complex to CT-DNA. K was determined by linear regression of a plot of I_0/I against $r=[\text{NiLX}]/[\text{CT-DNA}]$ (Fig 1B). The quenching constants of EB-CT-DNA system by **1**, **2** and **3** were calculated as $K=1.56\pm 0.27$, 0.71 ± 0.12 and 1.18 ± 0.26 , respectively. The results indicate a good agreement of the interactions between Ni(II) complexes and EB-CT-DNA with the model based on Stern-Volmer equation which indicate that quenching process occurred due to fluorophore-quencher complex formation *i.e.* EB-CT-DNA-Ni(II) complex. The K values suggest that the effects of **1** are stronger than those of **2** and **3**. Minor groove binder H binds strongly and selectively with high affinity to double stranded B-DNA structure [5]. The fluorescence intensities of the emission band at $\lambda_{\max}=444$ nm in H-CT-DNA

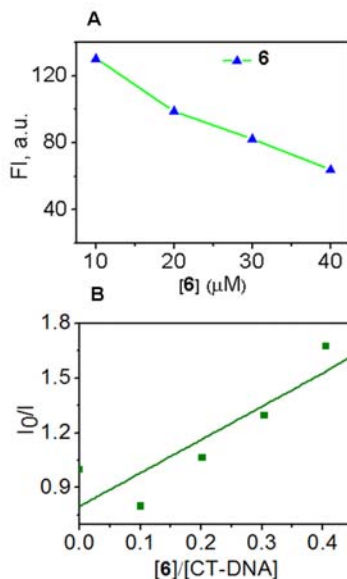


Figure 2. A—Changes of fluorescence intensities of H bound to CT-DNA in presence of 10, 20, 30 and 40 μM of **6**; B—quenching curve of H bound to CT-DNA by complex **6**.

system decreased remarkably with the increasing of concentration of **6** (Fig. 2A). Quenching curve shown in Fig. 2B was applied to determine K by linear regression of a plot I_0/I against $r=[\mathbf{6}]/[\text{CT-DNA}]$. The corresponding quenching constant of H-CT-DNA system by **6** was calculated as $K=1.82\pm 0.59$ (Fig. 2B). Deviation from linearity might be a consequence of other processes such as base modification and/or nicks formation.

The potential of Ni(II) complexes to cleave pUC19 plasmid was studied using agarose gel electrophoresis (Fig. 3). Upon the addition of the complex **1** to the plasmid, the supercoiled DNA converted into nicked form and shorter fragments. **3** had a weaker nuclease activity than other complexes. The maximal cleavage effect was produced by **6**, when the bands of the supercoiled and linear forms almost disappeared with decreasing of the mobility.

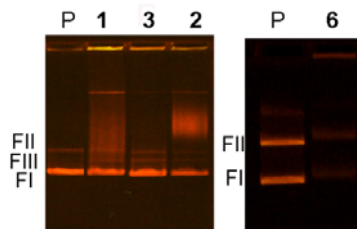


Figure 3. Agarose gel electrophoretic analysis of cleavage pUC19 by Ni(II) complexes **1**, **2**, **3** and **6**. P – control pUC19

CONCLUSION

The present study indicate possible degradation of CT-DNA by square-planar Ni(II) complexes, therefore reducing its interactions with EB (**1-3**) and H (**6**). The result show that DNA cleavage present a mode of action for this Ni(II) complexes.

ACKNOWLEDGEMENT

This work was partially supported by the Ministry for Science of the Republic of Serbia (Grants no. 172055).

REFERENCES

- [1] M. Milenković, A. Bacchi, G. Cantoni, J. Vilipić, D. Sladić, M. Vujčić, N. Gligorijević, K. Jovanović, S. Radulović, K. Anđelković, Eur. J. Med. Chem. 2013, 68, 111–120.
- [2] M. Milenković; A. Pevec, I. Turel, M. Vujčić, M. Milenković, K. Jovanović, N. Gligorijević, S. Radulović, M. Swart, M. Gruden-Pavlović, K. Adaila, B. Čobeljić, K. Andjelković, 2014 (submitted for publication).
- [3] M. Lee, A.L.Rhodes, M.D. Wyatt, S. Forrow. J.A. Hartley, Biochem. 1993, 32, 4237-4245.
- [4] J.R. Lakowitz, G. Weber, Biochemistry, 1973, 12, 4161–4170.
- [5] D.Suh, J.B. Chaires, Bioorg. Med. 1995, 3, 723-728.

EXPLORING THE STACKING OF METAL CHELATES WITH BENZENE BY DISPERSION CORRECTED DFT

D. P. Malenov¹, D. B. Ninković¹, G. V. Janjić² and S. D. Zarić^{3,4}

¹*Innovation center, Department of Chemistry, University of Belgrade, Studentski trg 12-16, Belgrade, Serbia;*

²*Institute of Chemistry, Technology and Metallurgy, University of Belgrade, Njegoševa 12, 11000 Belgrade, Serbia;*

³*Department of Chemistry, University of Belgrade, Studentski trg 12-16, 11000 Belgrade, Serbia;*

⁴*Department of Chemistry, Texas A&M University at Qatar, P. O. Box 23874, Doha, Qatar.*

ABSTRACT

Stacking interactions of metal-chelates with aromatic rings were investigated by performing quantum chemical calculations. Very accurate calculations leading to estimation of CCSD(T)/CBS interaction energies revealed that copper chelate stacks to benzene molecule stronger than nickel chelate. Several Minnesota functionals were shown to be in good agreement with benchmark data and were used to construct the potential energy surface. The most stable stacking interactions of copper and nickel chelates with benzene have the energies of -6.40 and -4.75 kcal/mol, respectively. The described interactions are of great importance in materials science, since the properties of materials can be highly dependent on the stacking interactions of its constituents.

INTRODUCTION

Metal-chelate rings and their interactions with aromatic molecules are of great importance for the process of designing of conducting and magnetic materials and in the areas of crystal engineering and catalysis [1-2]. Their crystal structures are extensively studied [3] and interactions of metal-chelates with aromatic rings are described [4].

However, energies of these interactions have not yet been adequately described, although some attempts have been made [5]. The energies at CCSD(T) level, the golden standard of quantum chemistry which requires considerable computation resources, could not be easily computed. Therefore, noncovalent interactions of metal-chelates and metal systems overall are seriously underrepresented in all databases of energies of noncovalent interactions.

In this work we present our results on energies of stacking interactions of metal-chelates and benzene. We managed to obtain very accurate CCSD(T)/CBS energies of these interactions and found that several dispersion corrected Minnesota DFT functionals as can reproduce the benchmark data and therefore be used for calculation of potential energy curves.

THEORETICAL METHODS

All calculations were performed in Gaussian09 series of programs. As model-systems for metal-chelates we used nickel(II) complex and copper(II) complex that both contain six-membered chelate ring. The most stable geometries for certain offset values at ω B97xD/aug-cc-pVDZ level were used for obtaining the benchmark (CCSD(T)/CBS) data (Figure 1).

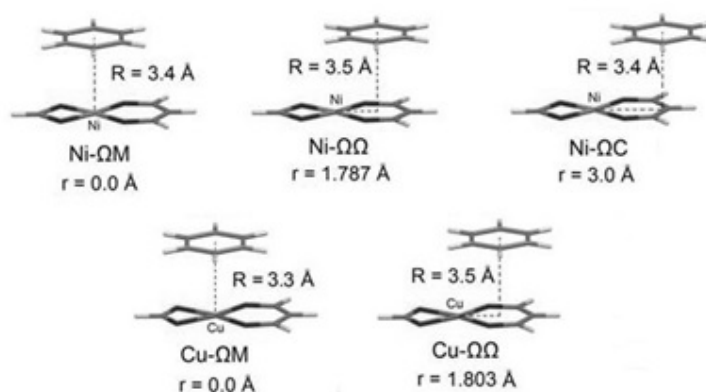


Figure 1. Model systems used for calculation of energies of stacking interactions of metal-chelates with benzene

The CCSD(T)/CBS values for model systems presented in Figure 1 were calculated by using the extrapolation scheme proposed by Mackie and DiLabio [6]. After obtaining these values, Minnesota functionals were tested with aug-cc-pVDZ basis set in order to find considerably less expensive method able to reproduce the benchmark data. All functionals were used with Grimme's D3 version of dispersion correction [7]. Potential energy curves for stacking of metal-chelates with benzene were then calculated using two of the tested functionals.

RESULTS AND DISCUSSION

The values of CCSD(T)/CBS energies (Table 1) indicate that stacking interactions of six-membered copper-chelate with benzene are stronger than those of nickel-chelate (Table 1).

Table 1. Estimated CCSD(T)/CBS energies as benchmark data and calculated energies using dispersion corrected Minnesota functionals with aug-cc-pVDZ basis set for model systems presented at Figure 1; the energies are BSSE corrected and given in kcal/mol

Method	Ni- Ω M	Ni- $\Omega\Omega$	Ni- Ω C	Cu- Ω M	Cu- $\Omega\Omega$
CCSD(T)/CBS	-4.68	-3.98	-4.48	-6.08	-4.71
M05-D3	-4.32	-3.71	-4.03	-5.71	-4.73
M06-D3	-5.20	-4.87	-5.15	-6.50	-5.57
M052X-D3	-4.51	-3.76	-4.37	-6.23	-4.66
M062X-D3	-5.30	-4.05	-4.78	-7.07	-4.93
M06HF-D3	-5.14	-4.44	-5.05	-7.30	-5.49
M06L-D3	-4.87	-3.80	-4.37	-5.92	-4.38

M052X-D3 functional reproduces the benchmark data for both nickel and copper chelates with good accuracy (Table 1). M06L/D3 also gives good agreement with CCSD(T)/CBS values for nearly all model-systems, underestimating only the binding in Cu- $\Omega\Omega$. Other functionals tested in this study are either inconsistent or they over/under-estimate the binding.

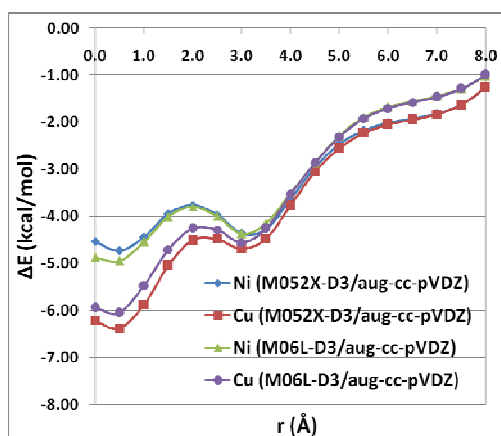


Figure 2. Potential energy curves for stacking interaction of benzene with nickel and copper chelates calculated at two different levels of theory

The most stable interactions for both complexes are at offset value of about 0.5 Å (Figure 2). The calculated energies for stacking of nickel and copper complexes with benzene are -4.75 kcal/mol and -6.40 kcal/mol, respectively, indicating that the type of metal influences interaction energies significantly. After passing through maximum at $r = 2.0$ Å (geometries similar to $\Omega\Omega$), the curves reach second minimum at $r = 3.0$ Å (ΩC geometry), with similar energies of -4.60 and -4.93 kcal/mol, respectively. At this offset value, two curves merge after $r = 3.5$ Å, indicating the loss of dependence on the type of the metal.

CONCLUSION

Energies of stacking interactions of metal-chelates and benzene were calculated at very accurate CCSD(T)/CBS level of theory. Two dispersion corrected Minnesota functionals, namely M052X-D3 and M06L-D3, can reproduce CCSD(T)/CBS energies with satisfying accuracy when used with aug-cc-pVDZ basis set. Potential energy curves calculated with these functionals show that copper chelate forms stronger stacking interactions with benzene than nickel chelate, with energies of -6.40 and -4.75 kcal/mol, respectively. These results can be very important for numerous materials that contain both metal-chelate rings and organic aromatic molecules, whose properties depend on the stacking of these molecules.

ACKNOWLEDGEMENT

This work was supported by the Ministry of Education, Science and Technological Development of Republic of Serbia (grant no. 172065).

REFERENCES

- [1] C. Janiak, J. K. Vieth, *New J. Chem.*, 2010, 34, 2366–2388.
- [2] E. Coronado, P. Day, *Chem. Rev.*, 2004, 104, 5419-5448.
- [3] D. N. Sredojević, G. A. Bogdanović, Z. D. Tomić, S. D. Zarić, *CrystEngComm*, 2007, 9, 793–798..
- [4] Z. D. Tomić, D. N. Sredojević, S. D. Zarić, *Cryst. Growth Des.*, 2006, 6, 29–31.
- [5] D. N. Sredojević, D. B. Ninković, G. V. Janjić, J. Zhou, M. B. Hall, S. D. Zarić, *ChemPhysChem*, 2013, 14, 1797-1800.
- [6] I. D. Mackie, G. A. DiLabio, *J. Chem. Phys.*, 2011, 135, 134318.
- [7] S. Grimme, J. Antony, S. Ehrlich, H. Krieg, *J. Chem. Phys.*, 2010, 132, 154104.

**STABILITY AND VIBRATIONAL SPECTRA OF
DIFFERENT COMPLEXES OF Cu AND Fe IONS WITH
(*E*)-*N*'-[1-(2-HYDROXYPHENYL)ETHYLIDEN]
ISONICOTINOYLHYDRAZIDE)**

D. Dimić and M. Petković

*Faculty of Physical Chemistry, University of Belgrade,
Studentski Trg 12-16, P. O. Box 47, 11158 Belgrade, Serbia*
dimicdusan@gmail.com

ABSTRACT

Complexes of deprotonated form of (*E*)-*N*'-[1-(2-hydroxyphenyl)ethyliden]isonicotinoyl-hydrazide (HAPI) with Cu and Fe in two oxidation states were optimized at CAM-B3LYP/cc-pVTZ level with PCM model for the solvent. Optimized geometries and changes in vibrational spectra due to complex formation are discussed and compared to those of deprotonated HAPI.

INTRODUCTION

Photoinduced isomerization between two conformations, E and Z (where E is a more stable isomer), of arylhydrazones makes them a widely investigated group of molecules as molecular switches. (*E*)-*N*'-[1-(2-hydroxyphenyl)ethyliden]isonicotinoyl-hydrazide (HAPI) behaves as a tridentate ligand with the following metals – Cu, Fe, Al and Ni, by making coordinate bonds through the phenolate O, the imine N and the carbonyl O donor atoms [1]. Some of these complexes were proven to have interesting biological activity and high stability [2]. This paper presents the results of a theoretical study of complexes of deprotonated E form of HAPI and ions with different net charge – Cu⁺ and Cu²⁺, Fe²⁺ and Fe³⁺, with special emphasis on stability and vibrational spectra.

THEORETICAL METHODS

Gaussian 09 package has been used for all calculations [3]. Structures have been optimized using density functional theory (DFT) with CAM-B3LYP functional [4,5] in conjunction with Dunning's correlation-consistent basis set cc-pVTZ [6]. For all structures, solvent effects were modeled with the Polarizable Continuum Model (PCM) in order to investigate the stability of the selected complexes in water. Vibrational frequencies were computed in harmonic approximation.

RESULTS AND DISCUSSION

Structure of deprotonated HAPI was optimized because experiments showed that when dissolved in buffer solution with pH=7.4, HAPI loses one proton. Optimized geometries of deprotonated HAPI and its complexes with Cu^+ , Cu^{2+} , Fe^{2+} and Fe^{3+} ions are shown in Figure 1.a)-e). The stability of complexes is presented as a difference between energy of the complex and sum of energies of separate ions and deprotonated HAPI, and they are shown in Table 1.

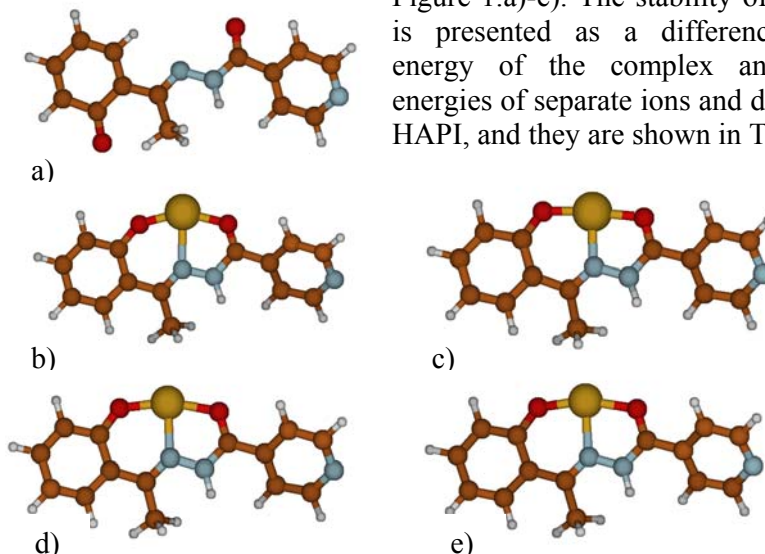


Figure 1. Optimized geometries of a) deprotonated HAPI, b) cuprous complex, c) cupric complex, d) ferrous complex and e) ferric complex

The phenol and pyridine rings of deprotonated HAPI are not coplanar with the N=N bond. Structural changes occur upon complexation: the phenol ring is always in plane with the N=N bond, but the pyridine ring is out-of-plane. The ions with higher net charge are closer to the midpoint between the two oxygen atoms because of the smaller radius and stronger attraction force.

Table 1. Energy difference between energy of complex and sum of energies of separate ions and deprotonated HAPI

Metal ion	Energy difference [kcal/mol]
Cu^+	74
Cu^{2+}	187
Fe^{2+}	75
Fe^{3+}	158

Based on the results shown in Table 1. it was concluded that complexes with the lower charge are less stable in water solution. Energy difference for

cuprous and cupric complexes is larger than 110 kcal/mol, probably because of higher stability of the cupric ion in the polar environment. This difference for ferrous and ferric complexes is lower, about 80 kcal/mol. Cu^{2+} complex is the most stable one because Cu^{2+} needs only one electron for obtaining a configuration with fully occupied d orbitals, which increases its reactivity. Electron configuration of Cu^+ ion is $3d^{10}$, i.e. full-filled d orbitals, which explains formation of weak bonds with HAPI. The electron configuration for ferric ion is $3d^5$, it has half-filled d orbitals and it is attracted towards donor atoms because of the possibility to accept more electrons than Fe^{2+} . Additionally, Coulomb attraction between positively charged ions and deprotonated species is another reason why ions with higher charge are more stable. The analysis of the infrared (IR) spectrum is limited to several vibrations –C=O stretching vibration, C-O stretching vibration and N-H in plane bending vibration. These modes are selected because the corresponding peaks are very intense. The most intense peaks (with relative intensity above 100) are shown in Table 2.

Table 2. Wavenumbers of the most intense vibrations

Metal ion	C=O stretching [cm^{-1}]	N-H bending [cm^{-1}]	(C-O) _{phen} stretching [cm^{-1}]
Deprotonated HAPI	1774	1578, 1316	1534
Cu^+	1702, 1658, 1620	1572, 1547, 1337	1480, 1382
Cu^{2+}	1647, 1601, 1571	1606, 1551, 1341	1254
Fe^{2+}	1679, 1671, 1653, 1613	1613, 1553, 1583, 1351	1484, 1380, 1261
Fe^{3+}	1660, 1620, 1588	1660, 1620, 1588, 1371	1588, 1567

Wave numbers for selected vibrations in the IR spectrum of deprotonated HAPI are given as control numbers for the strength of the coordinate bonds. C=O group has large dipole moment and small changes in dipole moment result in the shift of the corresponding band in the vibrational spectrum. When a metal ion is present, there is a redistribution of electron density in the C=O bond, making it weaker, so a red shift was observed. The most stable complex, the one with the cupric ion, shows the largest red shift. It was also observed that the number of modes increases with the introduction of metal ion and that vibrational modes become more complex, usually

joining several vibrations of groups of atoms in the molecule. That is, due to mode mixing, several normal modes involve change of the C=O bond length. The change in bending vibration of the N-H group is not large comparing to other two vibrations. What can be seen in Table 2. is that when donor-acceptor bonds are formed, there is a mixed mode of vibration that includes C=O stretching and N-H bending vibration, but even with C-O when Fe^{3+} is present, because this metal ion acts like a bridge between the two rings, probably because of its smaller size and larger net charge. As can be seen from Figure 1. all of the complexes are formed between metal ions and the oxygen atoms, as well as with the nitrogen atom closer to the phenol ring. This bonding usually affects the stretching vibrations to a greater extent than the bending ones, and this explains why there is a large red shift between C=O and C-O vibrations in deprotonated HAPI and complexes with Cu and Fe. These spectral changes represent a proof that bonds between the transition metal and the oxygen atoms are formed.

CONCLUSIONS

The results of DFT calculations of the optimized molecular geometries, vibrational spectra and energies of deprotonated HAPI and four of its complexes with Cu^+ and Cu^{2+} , Fe^{2+} and Fe^{3+} ions are presented in this paper. The cupric complex is the most stable one due to both the reactivity and size of the ion, which allows this ion to be centered between two oxygen atoms, forming an almost linear OCuO fragment. Normal mode analysis was limited to the C=O, N-H and C-O vibrations because of the high intensity peaks in the spectra. The largest red shifts of C=O and C-O stretching bands are observed for the Cu^{2+} complex, due to formation of strong bonds and a large change in the electron density distribution.

ACKNOWLEDGMENT

The authors would like to acknowledge the Ministry of Education and Science of the Republic of Serbia for financial support under project No. 172040.

REFERENCES

- [1] K. J. Franz et al, *Inorg. Chem.*, 2014, 53, 1397-1405
- [2] T. Simunek *et al*, *Chem. Res. Toxicol*, 2011, 24, 290-302
- [3] Gaussian 09, Revision A.02, M. J. Frisch et al.
- [4] A. D. Becke, *J. Chem. Phys.*, 1993, 98, 5648
- [5] T. Yanai, D. Tew and N.Handy, *Chem. Phys. Lett.*, 2004, 393, 51-57
- [6] T. H. Dunning, *J. Chem. Phys.*, 1989, 90 1007

ATR-FTIR MICROSPECTROSCOPIC CHARACTERIZATION OF COBALT(II) REDUCED DEXTRAN COMPLEXES

Ž. Mitić¹, M. Cakić², G. Nikolić², I. Savić², G. Nikolić¹, A. Veselinović¹
and Lj. Ilić³

¹*Faculty of Medicine, University of Niš, RS-18000 Niš, Serbia,
(zak_chem2001@yahoo.com)*

²*Faculty of Technology, University of Niš, RS-16000 Leskovac, Serbia*

³*PCI "Zdravlje", RS-16000 Leskovac, Serbia*

ABSTRACT

Synthesized Co(II) complexes with reduced low-molecular dextran (RLMD, $M_w = 5000$ g/mol) were investigated by using Attenuated total reflectance-Fourier transform infrared (ATR-FTIR) spectroscopy and Fourier transform infrared imaging (FTIRI) microscopy. FTIR spectroscopy can get the relatively reliable information about the ligand structure and arrangement in metal complexes. The changes in intensity and width of the IR bands in the region of $1500\text{--}1000\text{ cm}^{-1}$ were related to changes in conformation and short-range interactions of polysaccharide dextran. The IR spectra analysis of polysaccharide dextran indicates the existence of $\alpha\text{-(1}\rightarrow\text{6)}$ and $\alpha\text{-(1}\rightarrow\text{3)}$ O-glycosidic bond. The similarities of the $\gamma\text{(C-H)}$ range in a part of IR spectra from 1000 to 700 cm^{-1} indicate that there is no difference in the conformation of the C₁ glucopyranose units in RLMD and synthesized Co(II)-RLMD complexes.

INTRODUCTION

Polysaccharide dextran is described as a $\alpha\text{-(1}\rightarrow\text{6)}$ linked polymer of $\alpha\text{-D}$ -glucopyranose units. Dextran elaborated by *Leuconostoc mesenteroides* consists of a $\alpha\text{-(1}\rightarrow\text{6)}$ linked glucan with side chains attached to the C3-positions of the backbone glucopyranose units with branching degree approx. 5% [1,2]. The numerous investigations have indicated that the polysaccharide dextran and its reduced derivatives have the extraordinary power to forming the water-soluble complexes with various metal ions [3,4]. It has been established that the degree of metal ion binding within the complex depends primarily on the pH of the solution, as well as on the participation both of the OH groups and the H₂O molecules in the first coordination sphere of Co(II) ion. The emergence of modern structural instrumental methods such as ATR-FTIR microspectroscopy made it

possible to assign the binding OH or other groups, and also to characterize the metal ion coordination of polysaccharides, monitoring the ligand conformation or/and configuration changes forced by the complexation processes [5]. The aim of this work is to use ATR-FTIR microspectroscopy as the main tool to verify the conformation and structure of polysaccharide dextran as ligand around the Co(II) ions in synthesized Co(II)-RLMD complexes.

EXPERIMENTAL

Co(II) ion complex synthesis with RLMD have been described in detail by Mitić et al. [6,7]. FTIR microspectroscopy system, ATR-FTIR spectrometer Bruker Hyperion Tensor-27 in conjunction with a FTIR Bruker Hyperion1000/2000 microscopy attachment equipped with a 15× objective and a 250- μm liquid nitrogen cooled a narrow-band MCT detector (ATR objective GMBH, Germany) with the range of the IR spectrum from 4000 to 400 cm^{-1} , was used in this work. The spectra were measured with 4 cm^{-1} resolution and 50 scans co-addition. In this configuration, each spectral image corresponds to an area of 300 \times 250 μm .

RESULTS AND DISCUSSION

The ATR-FTIR spectra of octahedral pink colored Co(II)-RLMD complexes [8], synthesized at different pH (7.5, 10 and 13) recorded at 298 K and related FTIR microscopy images (250 μm \times 300 μm) are presented on Fig. 1. The differences of the frequencies, intensity and shape of the OH bands implies that in the complexes there is displacement of H₂O molecules by the OH groups in the first coordination sphere of Co(II) ion. The band on the approx. 1645 cm^{-1} is the result of $\delta(\text{HOH})$ vibrations [6]. These results agree with a structural studies of the investigated complexes have been based on the other spectroscopic techniques. [6,7]. The changes in number, frequencies, intensity, and width of the IR bands in the particular region of $\nu(\text{O-H})$ (3400 cm^{-1}), $\delta(\text{C-H})$ (1500–1300 cm^{-1}) and $\nu(\text{C-O})$ vibrations (1200–1000 cm^{-1}) were related to changes in the conformation and short-range interactions of the polysaccharide dextran.

In the 1200–1000 cm^{-1} region, the spectra of RLMD and the Co(II)-RLMD complexes comprise a number of highly fused bands. Special interest in the IR range for structural investigation is from 1000–700 cm^{-1} [9]. Both the number and frequencies of the bands in this IR range depend on the conformation of the D-glucopyranose units [4]. The similarities of the $\gamma(\text{C-H})$ range indicate that there is no difference in the conformation of the glucopyranose unit in the RLMD and complex molecules, and they probably

exhibit C_1 chair conformation (910 and 840 cm^{-1}). Ring deformations and scaffold vibrations were observed at 705 , 668 , 605 , 570 , and 520 cm^{-1} . The IR bands at 765 and 916 cm^{-1} indicates the existence α -($1\rightarrow6$) O-glycosidic bond. The α -($1\rightarrow6$) O-glycosidic bond content is greater than 95%, what points to the high linearity of polysaccharide dextran. In the IR spectra of dextrans were synthesized by different microorganisms, was able to notice the different band intensity from γ (C–H) on the 794 cm^{-1} , indicates presence of α -($1\rightarrow3$)-bond in dextran macromolecules. Measurements of this band intensity on the 794 cm^{-1} , can use for the determining of contents of this bond type by different dextran products [9].

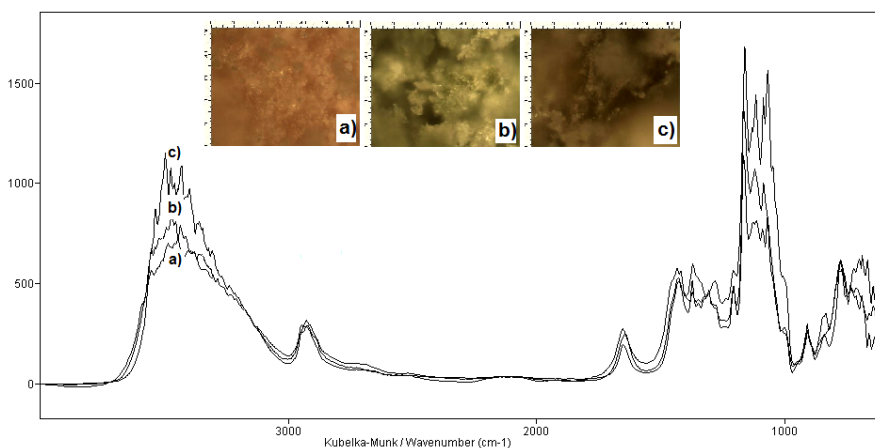


Figure 1. ATR-FTIR spectra with related FTIR microscopic images of Co(II)-RLMD complexes: a) pH 7.5, b) pH 10 and c) pH 13

CONCLUSION

ATR-FTIR spectra of polysaccharide dextran and its Co(II)-RLMD complexes, recorded at room temperature, were analyzed in order to obtain the information about the structure and conformation of ligands. The IR spectra analysis indicates the existence of both α -($1\rightarrow6$) and α -($1\rightarrow3$) O-glycosidic bond in dextran molecule. The differences in the OH region, indicate that complexes originate from the displacement of H_2O molecules by ligand OH groups in the first coordination sphere of Co(II) ions. The similarities of the γ (C–H) range indicate that there is no difference in the C_1 chair conformation of the glucopyranose unit in RLMD and Co(II)-RLMD complexes.

ACKNOWLEDGEMENT

This work was supported by the Ministry of Education, Science and Technological development of the Republic of Serbia (Grant **OI 172044**).

REFERENCES

- [1] A.N. de Belder, *Dextran*, Uppsala, Sweden, Amersham Biosciences AB (Ch. 5), 2003.
- [2] F. Donot, A. Fontana, J.C. Baccou, S. Schorr-Galindo, *Carbohydrate Polymers*, 2012, 87, 951–962.
- [3] B. Gyurcsik, L. Nagy, *Coordination Chemistry Reviews*, 2000, 203, 81–149.
- [4] Ž. Mitić, M. Cakić, G.M. Nikolić, R. Nikolić, G.S. Nikolić, R. Pavlović, E. Santaniello, *Carbohydrate Research*, 2011, 346, 434–441.
- [5] G. Nikolić, M. Cakić, Ž. Mitić, B. Ilić, P. Premović, *Russian Journal of Physical Chemistry A*, 2009, 83, 1520–1525.
- [6] Ž. Mitić, M. Cakić, G. Nikolić, *Spectroscopy Int. J.*, 2010, 24, 269–275.
- [7] Ž.J. Mitić, M.D. Cakić, G.S. Nikolić, R.S. Nikolić, Lj.A. Ilić, *Hemijska Industrija*, 2007, 61, 257–262.
- [8] Ž. Mitić, M. Cakić, G.M. Nikolić, A. Veselinović, Lj. Ilić, *11th International Conference on Fundamental and Applied Aspects of Physical Chemistry*, Belgrade, Serbia, M-05-P, 2012, 695–697.
- [9] K.I. Shingel, *Carbohydrate Research*, 2002, 337, 1445–1451.

INFLUENCE OF THE WEAK INTERACTION ON THE STRUCTURE OF METALLOCYCLE IN BINUCLEAR COPPER(II) COMPLEX

Z. D. Tomić¹, M. Mirković¹, N. Nikolić¹, D. Stanković¹, D. Mijin² and A. Kapor³

¹*Vinča Institute of Nuclear Sciences, University of Belgrade,
P.O.Box 522, 11001 Belgrade, Serbia*

²*Faculty of Technology and Metallurgy, University of Belgrade,
Karnegijeva 4, P.O. Box 3503, 11120 Belgrade, Serbia*

³*Department of Physics, Faculty of Sciences, University of Novi Sad, Trg
Dositeja Obradovića 4, 21000 Novi Sad, Serbia*

ABSTRACT

The structure of binuclear Cu(II) complex containing double oximate bridges was determined by the single-crystal X-ray diffraction analysis. Copper is five-coordinated with perchlorate anion present at the borderline of semi-coordination. Comparison with the structurally related diimine-dioxime Cu(II) complexes revealed the influence of the weak Cu...O(perchlorate) interaction on the geometry of the metallocycle.

INTRODUCTION

Schiff base ligands have been the subject of much research interest owing to their interesting coordination chemistry and a number of established and potential application areas [1,2]. The Schiff base ligands, especially tetradentate, readily form complexes with the transition metals [3]. These studies include development of new Schiff bases containing the diimine-dioxime functionality. Of particular interest is the capability of the deprotonated diimine-dioximes to form bridges between metal ions giving rise to complexes of different nuclearity [4]. Additional interest for complexes with this ligand is connected with the ability of oximate bridges to mediate strong antiferromagnetic interaction between metal centers [5]. Use of copper in the complex synthesis presents a particular problem. Copper is known for its flexible coordination behavior associated with the capability to form weak bonds, a property termed 'plasticity' [6]. This problem becomes more pronounced in the studies of weaker non-bonding interactions [7]. Detailed analysis of the copper environment followed by computational or database studies [8] may provide additional insight into the non-bonding contacts relevant for the properties of copper complexes.

One of the ligands frequently used in the synthesis of copper complexes is perchlorato group. As a ligand the ClO_4^- group may appear in a various bonding arrangements, however its steric properties limit its coordinating ability in the presence of smaller potential ligands [9]. Recently the coordinating properties of the ClO_4^- bonded to Cu were studied [10,11]. However, in most of the crystal structures the ClO_4^- is present as a non-coordinated ion. In the present study the binuclear copper(II) complex of the 4,9-diaza-3,10-diethyl-3,9-dodecadiene-2,11-dione bisoxime ligand (LH) [12] was chosen for study to enable comparison with the previously studied binuclear copper(II) complexes[13-15] of the closely related ligands with a dimethyl group in place of the present diethyl group.

RESULTS AND DISCUSSION

The crystal structure consists of centrosymmetric $[\text{Cu}_2(\text{LH})_2]^{2+}$ cations and perchlorato anions. The copper(II) atom is in a distorted square-pyramidal coordination (Fig. 1). According to the trigonality index $\tau=0.34$, coordination polyhedron can be described as a severely distorted square pyramid. The basal plane is formed by N1, N2, N3 and N4 atoms, and the metal ion deviates by 0.24\AA from this plane, towards the apical positions occupied by oxime oxygen O1 (Fig. 1). Intra-molecular $\text{Cu}\cdots\text{Cu}$ separation is $3.9424(4)\text{\AA}$.

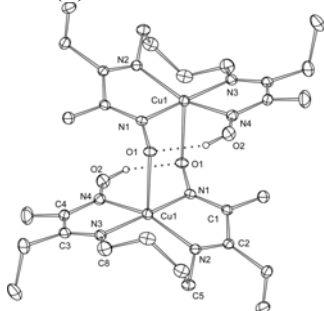


Figure 1. Molecular diagram and atom numbering scheme of $[\text{Cu}_2(\text{LH})_2]^{2+}$. Intramolecular O-H...O hydrogen bonds are depicted by dotted lines.

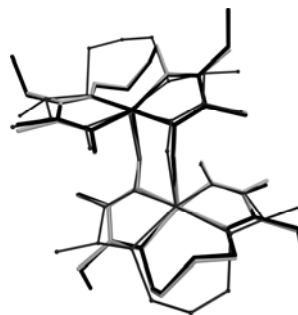


Figure 3. Overlay of the solid state structures of **I** (black), **II** (light grey) and **III** (dark grey, thin line).

This complex exhibits an intramolecular hydrogen bond (Fig. 1) between *cis* oxime groups with an O...O distance of 2.593(3) Å, H...O = 1.83 Å and O-H...O angle of 154°. Different role of O1 and O2 in the nonbonding interactions is associated with different geometry of two N-O bonds. Both, N1-O1 and N1-Cu1 bonds are shorter than N4-O2, and N4-Cu1 bonds, respectively. This finding implies higher multiple bond character in the fragment O1-N1-Cu1, relative to O2-N4-Cu1. Regarding the association of molecules in the solid state, it is interesting to note the lack of strong hydrogen bonding donors. Hence, it was anticipated that intermolecular contacts between the C-H donors and perchlorato oxygen atoms would govern the association of molecules into crystal. Inspection of intermolecular geometry confirms that ClO₄⁻ anion participates in the weak hydrogen bonds to cationic complex through the C-H...O interaction. In order to obtain more insight into the structural features of the title compound **I** we compare obtained results to the crystal structures of similar Cu complexes. Structural formulas of the complexes used for comparison is given in Fig. 2. Three complexes differ in the presence of ethyl instead of methyl substituent at the five-membered chelate ring in **I**, and the presence of six-membered chelate ring, and sulphur instead of nitrogen, in the diimine-dioxime ligand in **III**. Overlay of three solid state structures in Fig. 3 illustrates their overall similarity, confirmed by the examination of geometrical parameters.

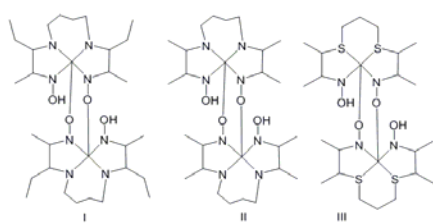


Figure 2. Structural formulas of the cationic complexes used for comparison

Although the overall structures of **I-III** are similar the subtle differences in the geometry of the metallocycle were observed. In **I** and **III** Cu-O bonds are 2.318(2) and 2.293 Å respectively, which is longer than 2.266/2.262 Å found in two polymorphs of **II**. While these differences in the axial Cu-O bonds could be attributed to the 'plasticity' [6] of the copper coordination sphere, it is interesting to examine the possible influence of the closest perchlorato fragment on these bonds. In the crystal structures of **I** and **III** the closest perchlorato oxygen is at the Cu-O distances of 2.947(3) and 2.907 Å, respectively. It is on the borderline of the values which have been reported for the semicoordinated perchlorato group. In the crystal structure

of **II** however, the closest perchlorato oxygen is at a rather larger distance of 3.767/3.766 Å and cannot be considered as semicoordinated to Cu. If the presence of the semicoordinative bond Cu-O(ClO₃) *trans* to Cu-O(oximate) bond is taken into account, the elongation of the Cu-O bonds in **I** and **III**, relative to **II**, could be attributed to the *trans* influence of the weakly coordinated perchlorato oxygen.

CONCLUSION

The crystal structure of complex consist of centrosymmetric [Cu₂(LH)₂]²⁺ cations and perchlorato anions. The copper(II) atom is in a distorted square-pyramidal coordination. During complex formation one oxime proton is lost, and the hydrogen bond between the two oxime groups of the same ligand is formed. Comparison of structurally related dimine-dioxime complexes indicates that geometry of metalocycle is influenced by the presence of weakly coordinated perchlorato anion.

ACKNOWLEDGEMENT: The research work has been financially supported by the Ministry of Education and Science of the Republic of Serbia, Grant No. 45015, No. 172013, No. 172065 and No. 172014.

REFERENCES

- [1] K. C. Gupta, A. K. Sutar, *Coord. Chem. Rev.*, 2008, 252, 1420-1450.
- [2] B. Dede, F. Karipcin, M. Cengiz, *J. Hazard. Mater.*, 2009, 163, 1148-1156.
- [3] S. Choubey, et al., *Polyhedron*, 2013, 55, 1-9.
- [4] P. Chaudhuri, *Coord. Chem. Rev.*, 2003, 243, 143-168.
- [5] B. Cervera, et al., *J. Chem. Soc., Dalton Trans.*, 1997, 395-401.
- [6] B. Murphy, B. Hathaway, *Coord. Chem. Rev.*, 2003, 243, 237-262.
- [7] Z. D. Tomić, V. M. Leovac, S. V. Pokorni, D. Zobel, S. D. Zarić, *Eur. J. Inorg. Chem.*, 2003, 6, 1222-1226.
- [8] Z. D. Tomić, S. B. Novaković, S. D. Zarić, *Eur. J. Inorg. Chem.*, 2004, 11, 2215-2218.
- [9] J. L. Pascal, F. Favier, *Coord. Chem. Rev.*, 1998, 865-902.
- [10] S. Schnitzler, M. –D. Serb, U. Englert, *Acta Cryst.*, 2012, C68, 251-254.
- [11] I. Banerjee, et al., *Cryst. Eng. Comm.*, 2012, 14, 4972-4975.
- [12] M. Mirković, D. Janković, S. Vranješ-Đurić, et. al., *Appl. Organomet. Chem.*, 2012, 26, 347-355.
- [13] J. H. Timmons, et al., *Inorg. Chem.*, 1981, 20, 3056-3060.
- [14] Y. M. Wang, et al., *Acta Cryst.*, 1990, C46, 1770-1772.
- [15] M. J. Prushan, et al., *Inorg. Chim. Acta*, 2005, 358, 3449-3456.

CHARACTERISATION OF CURCUMIN AND BORON-CURCUMIN COMPLEXES BY UV-VIS DIFFUSE REFLECTANCE SPECTROSCOPY

S. Zlatanović¹, O. Kovacević¹, B. Kovacević¹, A. Radulović¹, S. Ostojić¹
and L. Pezo¹

¹ *University of Belgrade, Institute of General and Physical Chemistry,
Studentski trg 12-16, P.O. Box 45, 11158 Belgrade 118, Serbia*

ABSTRACT

In the process of synthesis of two boron complexes with curcumin, rosocyanine – where the stoichiometry of curcumin versus boron is 2:1, and rubrocurcumine – where the stoichiometry of curcumin, boron, and oxalic acid is 1:1:1, when the components are mixed in a stoichiometric ratio in 80 % (v/v) solution of 2-propanol, we have obtained a deep red to brownish-red powder residues. UV-Vis diffuse reflectance (DR) spectra of curcumin, treated in a procedure for the synthesis of the complex, but in the absence of boron, show maxima at 230, 265, 385 and 425 nm. DR spectra of the products from synthesis of boron-curcumin complexes, show additional absorption above 500 nm and a shoulder at 550 nm, which is in accordance with the absorption in UV-Vis spectra of B-curcumin complexes. There are recognizable analogy between positions of maxima in the recorded UV-Vis DR spectra of curcumin and its boron complexes in the solid state, and UV-Vis spectra of these substances in 2-propanol solution. UV-Vis DR spectra of the products show that they are composed of curcumin and the corresponding B-curcumin complex.

INTRODUCTION

Curcumin, 1,7-Bis(4-hydroxy-3-methoxyphenyl)-1,6-heptadiene-3,5-dione, is chelating agent which forms complexes with a set of divalent and trivalent inorganic cation [1-7]. To better understanding of the synthesis of boron-curcumin complexes, rosocyanine and rubrocurcumine, and for their better characterization, there is an interest both in the use of these complexes in the methods for the determination of boron in the water, and in the context of investigation of possibilities for applications of these complexes in medicine. [5-7] Usually, presence of curcumin and its complexes, is examined by UV-Vis spectroscopy, whereby the influence of the environment, the solvent and the pH of the solution, play a large role [1-6,8]. As UV-Vis DR spectroscopy provides the ability to record the spectra

of the solids, the aim of this study was to investigate the possibility of applying this method for the identification and characterization of curcumin and B-curcumin complexes from synthesis, in the solid state without the additional effect of the solvent. We have found support in a few data about UV-Vis DR spectra of curcumin and its complexes available in the literature [4].

EXPERIMENTAL

The synthesis of B-curcumin complex in 2-propanol solution with a stoichiometric ratio of components – Procedure of synthesis of B-curcumin complex: B-curcumine complexes are formed in the plastic containers, in the presence of an aqueous solution of boron and 2-propanol solution which comprising HCl, oxalic acid, and curcumin, by evaporation to dryness on a water bath at 55 ± 2 °C, according to the standard method [8]. In our modification, a solution of boric acid with a boron content of 10 ppm, as well as curcumin, and oxalic acid (for rubrocurcumine) are mixed to achieve stoichiometric ratio for the formation of complex: a) rosocyanine – curcumin:boron = 2:1, and b) rubrocurcumine – curcumin:boron:oxalic acid = 1:1:1. Products from synthesis are stored in the solid state in a dry place.

Chemicals and instrumentation

We used curcumin (Fluka), oxalic acid (Merck), boric acid (Merck), 2-propanol (J.T. Baker), barium sulfate for white standard DIN5033 (Merck) and deionised water Type I (18.2M Ω).

Absorption spectra were recorded on a Thermo, type Evolution 600, ultraviolet-visible spectrophotometer in the range of 220-650 nm. DR spectra were recorded in the range of 220-800 nm using a SPECORD M40 spectrophotometer (Carl Zeiss, Jena, Germany), with an internal diffuse reflectance attachment, in absorbance mode, at the ordinate interval of 0-0.5. Barium sulfate was used as reference material. The values on the ordinate, A_R , absorbances generated on the basis of reflectance data, substantially correlate with the Kubelka-Munk function, as indicated on the presented spectra (Fig. 1).

RESULTS AND DISCUSSION

UV-Vis DR spectra of sample C_F (curcumin Fluka), which was initial component for synthesis of B-curcumin complexes, and sample C_S , which was curcumin treated according to procedure of synthesis of B-curcumin complex, whereby the boron and/or oxalic acid were absent, were shown in Fig. 1. DR spectra of curcumin exhibited maxima: sample C_F at 285, 385 and 420 nm, and sample C_S at 230, 265, 385 and 425 nm. In these spectra, ratios

of peaks of the sample C_F is different from the ratios of corresponding peaks of the sample C_S . Hypsochromic shift from 280 nm in the spectrum of sample C_F to 265 nm in the spectrum of sample C_S is evident. This is a consequence of the substantial effect of the procedure of synthesis of B-curcumin complex (thermal treatment, 2-propanol as a solvent, and acidic medium) on the curcumin [1]. There is accordance between the positions of the peaks in the DR spectrum of the treated curcumin, C_S , and UV-Vis spectrum of the curcumin in 2-propanol solution that has maxima of the absorbance at 230, 265 and 430 nm, as shown in Fig. 2.

Boron-curcumin complexes were formed according to the procedure of synthesis of B-curcumin complex. UV-Vis DR spectra of the products from the synthesis of rosocyanine (RC), and rubrocurcumine (RK), are shown in Fig. 1. DR spectra of the products RC and RK were similar to spectrum of the sample C_S , with additional absorption above 500 nm and a shoulder at 550 nm. Absorption above 500 nm, with a maximum at 550 nm, corresponds to the absorption of the boron-curcumin complexes [5,6,8]. For comparison, UV-Vis absorption spectrum of rubrocurcumine solution in 2-propanol, which was prepared entirely according to the standard method [8] (a large excess of oxalic acid and curcumin), and recorded relative to its blank sample, is shown in Fig. 2. In this spectrum (Fig. 2b), an absorption maximum at 430 nm corresponds to the maximum of absorption in the spectrum of curcumin (Fig. 2a), and well separated peak with the

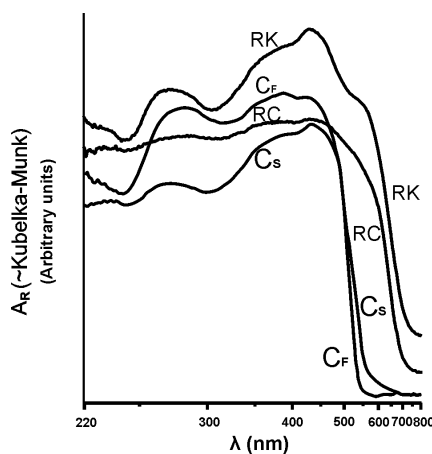


Figure 1. UV-Vis diffuse reflectance spectra of curcumin: C_F – curcumin, Fluka, and C_S – treated curcumin, and spectra of products from B-curcumin complexes synthesis: RC – rosocyanine, and RK – rubrocurcumine.

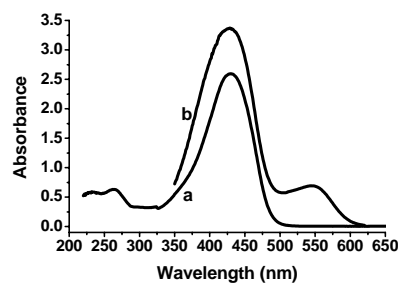


Figure 2. UV-Vis absorption spectra of 2-propanol solution of: a) curcumin, and b) rubrocurcumine.

maximum at 548 nm corresponds to rubrocurcumine [6,8]. Peak positions in the UV-Vis DR spectra of the RC and RK (Fig. 1) correspond to the absorption peaks in the spectrum of the boron-curcumin complex in 2-propanol solution (Fig. 2b). It can be concluded that the synthesis products RC and RK consist of curcumin and B-complex of curcumin.

CONCLUSION

There is recognizable analogy between positions of maxima in UV-Vis DR spectra of curcumin and its boron complexes in the solid state, and absorbance maxima in UV-Vis spectra of these substances in 2-propanol solution. Therefore, UV-Vis DR spectra provide insight into the synthesis of complex and state of each component present in the product. The presented results indicate that the mixing of components in a stoichiometric ratio for boron-curcumin complex, results in the formation of a mixture of curcumin and boron-curcumin complex.

ACKNOWLEDGEMENT

This work was partially supported by the Ministry of Education, Science and Technological Development of the Republic of Serbia, under the Project No TR31055 and TR31093.

REFERENCES

- [1] L. Shen, H.-F. Ji, *Spectrochimica Acta Part A*, 2007, 67, 619–623.
- [2] B.Zebib, Z. Mouloungui, and V. Noirot, *Bioinorg Chem Appl.* 2010, Vol. 2010, Article ID 292760.
- [3] M. Bernabé-Pineda, M. T. Ramirez-Silva, M. A. Romero-Romo, E. González-Vergara, A. Rojas-Hernández, *Spectrochimica Acta Part A* 2004, 60, 1105–1113.
- [4] M. S. Refat, *Spectrochimica Acta Part A: Molecular and Biomolecular Spectroscopy*, 2013, 105, 326–337.
- [5] G.S.Spicer, J.D.H.Strickland, *J. Chem. Soc.*, 1952, 4644-4650.
- [6] G.S.Spicer, J.D.H.Strickland, *J. Chem. Soc.*, 1952, 4650-4653.
- [7] Z. Sui, R. Salto, J. Li, C. Craik and P. R. O. de Montellano, *Bioorganic & Medicinal Chemistry*, 1993, Vol. 1, No. 6, pp. 415-422.
- [8] ASTM D3082-09, ASTM International, *Book of Standards*, 2009, Vol. 11.01.

CHARACTERISATION OF CURCUMIN AND BORON-CURCUMIN COMPLEXES BY IR-SPECTROSCOPY

O.Kovacevic¹, B. Kovacevic¹, S.Zlatanovic¹, A. Radulović¹, L. Pezo¹
and Lj. Lević²

¹ *University of Belgrade, Institute of General and Physical Chemistry,
Studentski trg 12-16, P.O. Box 45, 11158 Belgrade 118, Serbia*

² *University of Novi Sad, Faculty of Technology, Bulevar Cara Lazara 1,
21000 Novi Sad, Serbia*

ABSTRACT

Difference between IR spectrum of curcumin, that has undergone the process of synthesis of the boron-curcumin complex, but in the absence of boron, and the spectrum of untreated curcumin, which is used as a component in the synthesis, show the substantial effect of the treatment (thermal treatment, 2-propanol as a solvent, and an acidic medium) on the curcumin. The similarity of the IR spectra of the products of rosocyanine and rubrocurcumine synthesis, with spectrum of treated curcumin, is a consequence of the effect of the treatment on the curcumin, and of the presence of curcumin, which is not incorporated into the complex. The similarity between the IR spectra of the products from synthesis of rosocyanine and rubrocurcumine reflects the similarity in their composition and structures. IR spectroscopy indicates to the changes that occur in the curcumin, either it was unincorporated, or incorporated in the complex as a chelate. The impact of the complex formation is less visible in these spectra.

INTRODUCTION

Recently, IR spectrum of curcumin has been investigated in detail [1]. Within the growing interest for the curcumin and its complexes, IR and FTIR spectroscopies were used for the investigation of these compounds [2-5]. Spicer and Strickland have been investigated infrared spectra of curcumin and boron-curcumin complexes [6]. Herein, by IR spectroscopy we investigated products of boron-curcumine complexes synthesis. IR spectra of products were compared versus spectrum of initial curcumin samples, which was component in the synthesis, and also versus spectra of curcumin sample which was treated strictly by procedure of boron-curcumin complexes synthesis, but in the absence of boron. This test indicated that for the insight into real physical-chemical characteristics, it is necessary to

compare curcumin and products of synthesis with the same history of the treatment and the same impact of the environment.

EXPERIMENTAL

The synthesis of B-curcumin complex in isopropanol solution with a stoichiometric ratio of components - Procedure 1: B-curcumine complexes are formed in the plastic containers, in the presence of an aqueous solution of boron and 2-propanol solution which comprising HCl, oxalic acid, and curcumin, by evaporation to dryness on a water bath at 55 ± 2 °C, according to the standard method ASTM D 082-79:1981. In our modification, a solution of boric acid with a boron content of 10 ppm, as well as curcumin, and oxalic acid (for rubrocurcumine) are mixed to achieve stoichiometric ratio for the formation of complex: a) rosocyanine – curcumin : boron = 2 : 1, and b) rubrocurcumine – curcumin : boron : oxalic acid = 1 : 1 : 1. Products from synthesis are stored in the solid state in a dry place.

Chemicals and reagents

Curcumin (Fluka), Oxalic acid (Merck), Boric acid (Merck), 2-propanol (J.T. Baker), and other chemicals used were of the highest quality available.. All solutions were prepared using deionised water Type I (18.2M Ω).

The pH readings were obtained using a Consort C533 pH-Meter. Infrared spectra were recorded in the range of 400–4000 cm⁻¹ on KBr pellets using a SPECORD 75 IR spectrometer (Carl Zeiss, Jena, Germany),.

RESULTS AND DISCUSSION

Kolev et al. have done a detailed assignment of the peaks in the spectrum of curcumin [1]. The IR spectrum of the sample of curcumin C_F, which was used in our work as a component in the synthesis of boron-curcumin complexes, is shown in Fig. 1., and corresponds to the assignment [1]. In the area of 400-1700 cm⁻¹ spectrum is characterized by a series of sharp and well-defined peaks. In the literature, spectra of curcumin, which was used as a component in the complex synthesis, are commonly used as the comparative spectra to the spectra of the complexes [2-5]. However, pH and solvent significantly affect the curcumin molecule [7], and therefore it should be expected that their influence is visible in the infrared spectrum of curcumin. The IR spectrum of the sample of curcumin, which is treated in procedure 1, which means that it has gone through the process of the synthesis of boron-curcumin complex, but in the absence of boron, is shown in Fig. 1., as the spectrum of the sample C_S. In the spectrum of treated curcumin, sample C_S, the peaks ratios are significantly different from the corresponding peaks ratios in the spectrum of untreated curcumin, sample

C_F . Therefore, the spectra of samples C_F and C_S are significantly different. These differences indicate a large impact of treatment (thermal treatment, 2-propanol as a solvent, and an acidic medium) on the curcumin molecule.

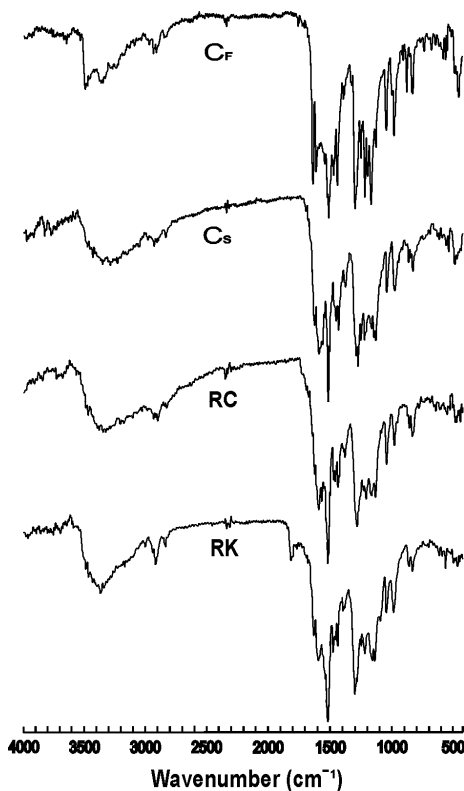


Figure 1. IR spectra of curcumin: C_F – curcumin, Fluka, C_S – curcumin from the procedure of the B-complexes synthesis, but without the boron, and spectra of products of B-curcumin complexes synthesis: RC – rosocyanine, and RK – rubrocurcumine.

the spectrum of treated curcumin C_S (Fig. 1.), we concluded that visible differences in the spectra can be attributed to the changes that occur in the curcumin, either it was unincorporated, or incorporated in the complex as a chelate. Comparison of the spectra in Fig. 1. indicates that the increased

Boron-curcumin complexes were formed according to the procedure 1, when the components were mixed in a stoichiometric ratio in water - 2-propanol solution. IR spectra of the product of the rosocyanine synthesis, sample RC, and the product of the rubrocurcumine synthesis, sample RK, are shown in Fig. 1. IR spectra of these products are markedly similar to spectra of treated curcumin, sample C_S . It indicates that the changes that occur in the curcumin molecule, affected by environment, are fundamental changes that were reflected in the spectrum of curcumin, and in the spectra of the complexes. Investigated spectra of the products of B-curcumin complexes synthesis are very similar to the spectrum of curcumin-lead complex, which was published by Daniel et al [3]. Significant differences between the initial spectrum of curcumin, and the spectra of complexes, the authors attributed to the formation of complexes [3]. Such a behavior is common [2-5]. But taking into account the fact that the spectra of the products of complexes synthesis, RC and RK, resemble to

absorption in the area of $1650\text{-}1850\text{ cm}^{-1}$, probably is dominantly due to the formation of boron-curcumin complexes.

CONCLUSION

IR spectra of curcumin sample which was used as a component in the synthesis, and of curcumin sample that has undergone the process of synthesis of the boron-curcumin complex, but in the absence of boron, are significantly different. Their mutual significant difference indicates to the major impact of the treatment (thermal treatment, 2-propanol as a solvent, and an acidic medium) on molecule of curcumin. There is a great similarity between the IR spectra which correspond to products of the synthesis of boron-curcumin complexes (rosocyanine and rubrocurcumine). These spectra are also similar to the spectrum of the treated curcumin. The similarity may arise from the presence of altered curcumin, either it was unincorporated or incorporated in the complex as a chelate. The existence of certain differences in these spectra indicates that the boron-curcumin complexes are undoubtedly present in the products of synthesis.

ACKNOWLEDGEMENT

This work was partially supported by the Ministry of Education, Science and Technological Development of the Republic of Serbia, under the Project No TR-31055 and No 172018.

REFERENCES

- [1] T. M. Kolev, E. A. Valcheva, B. A. Stamboliyska, and M. Spitteller, *International Journal of Quantum Chemistry*, 2005, 102, 1069-1079.
- [2] B. Tang, L. Ma, H. Wang, and G. Zhang, *Journal of Agricultural and Food Chemistry*, 2002, 50, 1355-1361.
- [3] S. Daniel, J. L. Limson, A. Dairam, G. M. Watkins, and S. Daya, *Journal of Inorganic Biochemistry*, 2004, 98, 266-275.
- [4] M. A. Subhan, K. Alam, M. S. Rahaman, M. A. Rahman, and M. R. Awal, *Journal of Scientific Research*, 2014, 6 (1), 97-109.
- [5] M. S. Refat, *Spectrochimica Acta Part A: Molecular and Biomolecular Spectroscopy*, 2013, 105, 326-337.
- [6] G.S.Spicer, J.D.H.Strickland, *J. Chem. Soc.*, 1952, 4653-4656.
- [7] M. Bernabé-Pineda, M. T. Ramirez-Silva, M. A. Romero-Romo, E. González-Vergara, A. Rojas-Hernández, *Spectrochimica Acta Part A* 2004, 60, 1105-1113.

STACKING INTERACTIONS OF BIPYRIDINE COMPLEXES

G. V. Janjić¹, P. V. Petrović², D. N. Sredojević² and Snežana D. Zarić^{3,4}

¹*ICTM, University of Belgrade, Njegoševa 12, 11001 Belgrade, Serbia;*

³*Innovation center, Department of Chemistry, University of Belgrade, Studentski trg 12-16, Belgrade, Serbia;*

²*Department of Chemistry, University of Belgrade, Studentski trg 12-16, 11000 Belgrade, Serbia;*

⁴*Department of Chemistry, Texas A&M University at Qatar, P. O. Box 23874, Doha, Qatar.*

ABSTRACT

Stacking interactions between *bipyridine* ligands (*bipy*) of square-planar metal complexes are studied by DFT calculations. The calculations were performed on model systems of [Ni(CN)₂bipy] complexes, with geometries based on the data from Cambridge Structural Database (CSD). The energy of the most stable geometry is -29.6 kcal/mol. In this geometry nickel atoms are located above the chelate rings and beside chelate-chelate there are overlaps of CN ligands with chelate and pyridyl rings. Results of calculations show that the energy of interaction decreases by decreasing the overlap area.

INTRODUCTION

Metal-chelate rings and organic aromatic molecules are very often constituents of materials. Their interactions are very responsible for properties of materials, although, their interactions are essential in a number of other biological and chemical systems.

The stacking interactions between aromatic molecules were studied [1-3], but it was shown that other planar systems could also form stacking interactions [4-8]. The stacking interactions between chelate and aromatic rings were identified in the crystal structures from CSD [4]. Analysis of crystal structures has shown that stacking interactions are preferred to CH/ π interactions in these complexes [5]. The energies of stacking interactions of *acac* chelate ring with benzene were calculated [6] and results show that chelate-benzene stacking interactions are remarkably stronger than benzene-benzene interactions [9]. This is accordance with the observation that in crystal structures organic aromatic rings prefer stacking with chelate rings to

other organic aromatic rings [7]. Calculations have shown that the nature of metal ions strongly influences on the strength of stacking. Very accurate calculations at CCSD(T)/CBS level showed that the calculated stacking energies of copper and nickel six-membered chelates with benzene are -6.39 kcal/mol and -4.77 kcal/mol, respectively [8].

Bipyridine (*bipy*) complexes can be used for various applications. To better understand the stacking interactions of *bipy* complexes, geometries of stacked *bipy* ligands in crystal structures from the CSD were analyzed. The results of crystallographic analysis were accompanied by the results of DFT calculations performed on model systems.

THEORETICAL METHODS

To study stacking interactions of *bipy* ligands in crystal structures, CSD search was performed. Two ligands form stacking interaction when the dihedral angle between the mean planes of bipyridines is less than 10° , the distance between centroids of any pyridine fragment is below 4.6 Å, the distance between centroids of pyridine and chelate rings is shorter than 4.4 Å, and the distance between centroids of the chelates is below 4.2 Å.

In order to evaluate the energy of stacking interaction between two *bipy* ligands, the single-point calculations were done on model systems of (2,2'-bipyridyl)dicyanonickel(II) complexes, using the TPSS-D3 method and the def2-TZVP basis set.

RESULTS AND DISCUSSION

In the crystal structures there are 325 stacking interactions of square-planar *bipy* metal complexes. To define the orientation of ligands a torsion angle T has been analysed (Figure 1) [10].

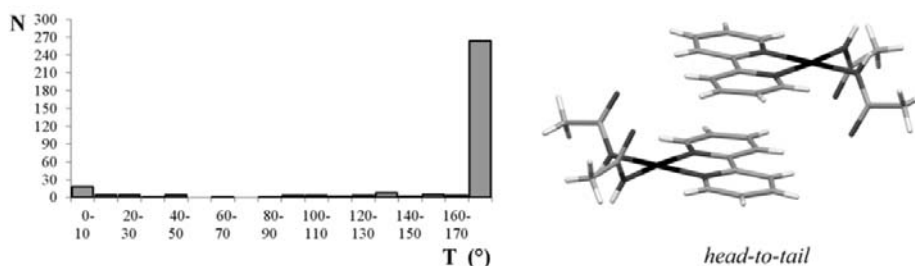


Figure 1. The distributions of torsion angle T for stacking interactions of square-planar *bipy* complexes.

The distribution of T torsion angle values shows preferred orientation with the angle from 170° to 180° (*head-to-tail* orientation) (Figure 1). Several

structures have *head-to-head* orientation (T values from 0° to 10°). The number of interactions with T between 10° and 170° (*twisted* orientation) is quite small.

Starting geometries for calculations (Figure 2) are geometries with *head-to-tail* orientation and *face-to-face* overlap of chelate-chelate (G1), chelate-pyridine (G1), and pyridine-pyridine rings (G1), respectively. Series of calculations were done by systematically varying the normal distances and offset values (in positive and negative directions) starting with face-to-face geometries (values of respective offset of 0.0 \AA) and following the axes that pass through metals and centroids of their respective chelate rings.

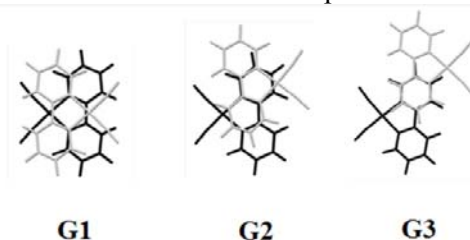


Figure 2. The starting geometries for calculations.

The results of calculation show that the geometries G1 have the strongest interactions between complexes, with energies ranging from -29.6 kcal/mol for the most stable to -12.5 kcal/mol for the least stable geometry. The trend of decrease of interaction energy with increase of offset, toward the positive values, is the consequence of the nature of interactions that occur between complexes. Similar trend is observed for the geometry G2, with range of energy between -29.2 and -7.3 kcal/mol . In the geometry G3, the interaction energy also decreases, but in the range from -20.7 to -3.1 kcal/mol (Figure 3).

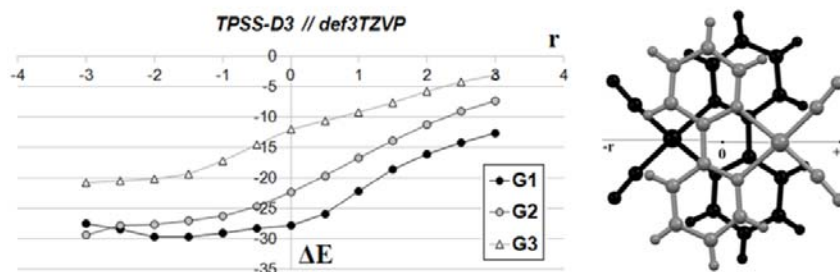


Figure 3. The calculated interaction energies for $[\text{Ni}(\text{CN})_2\text{bipy}]_2$ systems plotted as a function of offset value for three set of geometries.

CONCLUSION

Comparing the interaction energies for model systems G1, G2 and G3, it is evident that chelate-aryl (pyridyl) stacking interactions are stronger than aryl-aryl (pyridyl) stacking interactions and this is in accordance with findings that chelate-benzene stacking interactions are stronger than benzene-benzene stacking interactions [6,8]. Interaction energies in geometry G3 are several times stronger than most stable stacking interactions between pyridine molecules (-4.08 kcal/mol) [3]. This indicates that stacking interactions become far more favorable when pyridyl rings are coordinated to a metal.

These results can be very important for numerous systems that contain metal-chelate rings and organic aromatic molecules, most notably organic-inorganic materials, and in chemical and biological systems.

ACKNOWLEDGEMENT

This work was supported by the Serbian Ministry of Education and Science (grant no. 172065).

REFERENCES

- [1] L. M. Salonen, M. Ellermann, F. Diederich, *Angew. Chem. Int. Edit.*, 2011, 50, 4808-4842.
- [2] D. B. Ninković, G. V. Janjić, S. D. Zarić, *Cryst. Growth Des.*, 2012, 12, 1060-1063.
- [3] D. B. Ninković, G. V. Janjić, D. Ž. Veljković, D. N. Sredojević, S. D. Zarić, *ChemPhysChem*, 2011, 12, 3511-3514.
- [4] Z. D. Tomić, D. Sredojević, S. D. Zarić, *Cryst. Growth Des.*, 2006, 6, 29-31.
- [5] D. Sredojević, G. A. Bogdanović, Z. D. Tomić, S. D. Zarić, *CrystEngComm*, 2007, 9, 793-798.
- [6] D. N. Sredojević, D. B. Ninković, G. V. Janjić, J. Zhou, M. B. Hall, S. D. Zarić, *ChemPhysChem*, 2013, 14, 1-4.
- [7] D. N. Sredojević, D. Z. Vojislavljević, Z. D. Tomić, S. D. Zarić, *Acta Crystallogr. B*, 2012, B68, 261-265.
- [8] D. P. Malenov, D. B. Ninković, D. N. Sredojević, S. D. Zarić, *ChemPhysChem*, 2014, DOI: 10.1002/cphc.201402114R1.
- [9] E. C. Lee, D. Kim, P. Jurecka, P. Tarakeshwar, P. Hobza, K. S. Kim, *J. Phys. Chem. A*, 2007, 111, 3446-3457.
- [10] P. V. Petrović, G. V. Janjić, S. D. Zarić, *Cryst. Growth Des.*, 2014, DOI: 10.1021/cg500447h.

GENERAL
PHYSICAL CHEMISTRY

PHOTOTHERMAL DYNAMIC ELASTIC VIBRATION OF SQUARE MEMBRANE

D. M. Todorović¹, D. V. Jović², K. T. Radulović², D. Markushev³ and M. D. Rabasović³

¹*Institute for Multidisciplinary Research, University of Beograd, P.O.Box33, 11030 Belgrade, Serbia (dmtodor@imsi.rcub.bg.ac.rs)*

²*Institute for Chemistry, Technology and Metallurgy, Njegoseva 12, 11000 Belgrade, Serbia*

³*Institute for Physics, University of Belgrade, Prigrevica 118, 11080 Belgrade-Zemun, Serbia*

ABSTRACT

The plasmaelastic and thermoelastic vibrations in a silicon square membrane (3D geometry), photogenerated by a uniform and intensity-modulated optical excitation, were studied. The theoretical model for the elastic displacements space and frequency distribution by using the Green function method was given. The amplitude and phase of the plasma and thermal wave's assisted elastic displacements in the square membrane were calculated and analysed. These investigations are important for many practical situations (photoacoustic and photothermal experiments, thermal microscopy, thermoelastic microscopy, sensors and actuators, etc).

INTRODUCTION

The photoacoustic (PA) and photothermal (PT) effects can be important as driven mechanisms for micromechanical structures, especially for micro-electro(opto)-mechanical structures (MEMS, OEMS). When a micro-mechanical structure is exposed to optical excitation, the photogenerated carrier-density (the plasma wave) causes a mechanical strain - periodic elastic deformation in the sample – the plasmaelastic (PE) effect. The plasma waves contribute to the generation of thermal wave. The thermal waves produce periodic elastic deformation in the sample – the thermoelastic (TE) effect. The PE and TE mechanisms are main mechanisms of elastic displacement generation in optically driven micromechanical structures [1,2].

In this work, the space and frequency distribution of PT quasi-static and dynamic elastic vibrations, for different thicknesses, in a square membrane, photogenerated by a uniform and intensity-modulated optical excitation, are analyzed.

THEORY OF THE PHOTOTHERMAL ELASTIC VIBRATIONS

The PT elastic vibrations can be written as a vector sum of two components: the thermoelastic (TE) and plasmaelastic (PE) one [3,4]. The TE and PE components of the PT elastic vibrations are the consequence of the thermal and electronic elastic expansion and bending. In the case of periodical excitation, with angular modulating frequency of the incident beam $\omega = 2\pi f$, the theoretical treatment enables quantitative accounts of the carrier density field $N(\mathbf{r};\omega)$, the temperature field $T(\mathbf{r};\omega)$ and the elastic displacement field $\mathbf{U}(\mathbf{r};\omega)$. The photogenerated plasma can directly produce a local strain, which then generates elastic waves in the semiconductor. The electronic strain, $\varepsilon^{PE}(\mathbf{r};\omega)$ can be given vs. the excess carrier density, $\varepsilon^{PE}(\mathbf{r};\omega) \approx \alpha_N N(\mathbf{r};\omega)$, where α_N is the coefficient of electronic elastic deformation. Then, the electronic elastic displacement $\mathbf{U}^{PE}(\mathbf{r};\omega)$, using the strain-stress relations, can be given vs. the electronic deformation. Also, the thermal elastic displacement $\mathbf{U}^{TE}(\mathbf{r};\omega)$, can be given vs. the thermoelastic strain $\varepsilon^{TE}(\mathbf{r};\omega) \approx \alpha_T T(\mathbf{r};\omega)$, where α_T is the coefficient of linear expansion. Then, the elastic displacement $\mathbf{U}(\mathbf{r};\omega)$ can be given as the sum of two components: $\mathbf{U}^{PE}(\mathbf{r};\omega)$ and $\mathbf{U}^{TE}(\mathbf{r};\omega)$. For uniform optical excitation, if the lateral effects are omitted, it is possible to reduce the problem to one-dimensional. i.e. $N(x,y,z;\omega) \approx N(z;\omega)$ and $T(x,y,z;\omega) \approx T(z;\omega)$. The relations for the carrier-density field $N(z;\omega)$ and temperature field $T(z;\omega)$ in Si were given in our previously published paper [4]. The displacement field in a Si square membrane with thickness $L_z = h$, and membrane length L , excited with a uniform and intensity-modulated optical beam is analyzed. When the thickness of the elastic membrane is much smaller than all other dimensions, it is possible to suppose that the elastic deformation is approximately the same along the sample thickness. For that reason, it is possible to use the theory of the elastic thin plate to obtain the elastic bending. The elastic characteristics of the Si chip with square membranes can be simulated as elastic simply supported square plate. In accordance with the elastic theory of thin plate, using the elastic Green function method to solve the elastic equation, the dynamic PT elastic vibrations for square plate, $W_d(x,y; \omega)$, is obtained:

$$W_d(x,y;\omega) = \left(\frac{4}{L}\right)^2 m(\omega) \sum_{m=1,3}^{\infty} \sum_{n=1,3}^{\infty} \frac{e_{mn}}{e_{mn}^2 - k^4(\omega)} \frac{1}{a_m b_n} \varepsilon_m(x) \varepsilon_n(y) \tag{1}$$

$$e_{mn} = a_m^2 + b_n^2, \quad \varepsilon_m(x) = \sin(a_m x), \quad a_m = \frac{m\pi}{L}, \quad \varepsilon_n(y) = \sin(b_n y), \quad b_n = \frac{n\pi}{L}, \quad (m,n=1,3,\dots)$$

$$m(\omega) = m^{TE}(\omega) + m^{PE}(\omega) = (1+\nu) \frac{12}{h^3} \left[\alpha_T \int_0^h (z-z_n) T(z;\omega) dz + \alpha_N \int_0^h (z-z_n) N(z;\omega) dz \right]$$

where the electronic $m^{PE}(\omega)$ and thermal $m^{TE}(\omega)$ elastic moments are the source term from the thermal and plasma waves and $\underline{k}(\omega)$ is the elastic wavenumber. For low frequencies, where the inertia term is neglected, i.e. $\underline{k}(\omega) \approx 0$, the quasi-static elastic vibrations of plate is obtained.

ANALYSIS AND DISCUSSION

The theoretical model, derived in this work, enables to calculate the PT elastic vibrations spectra of Si square membranes.

First we analyzed the quasi-static, W_s , and dynamic, W_d , PT elastic vibrations of the square membrane. Figure 1 shows the quasi-static and dynamic PT amplitude space distribution of the elastic bending at $f = 2$ kHz for Si square membrane (3 mm length, 10 μm thick; n-type, $\langle 100 \rangle$, 5 Ωcm , one surface polished other surface etched). Theoretically calculated curves were obtained for the following Si parameters: the optical absorption coefficient $\alpha = 5 \cdot 10^3 \text{ cm}^{-1}$; the thermal diffusivity $D_T = 0.90 \text{ cm}^2/\text{s}$; the coefficient of thermal expansion $\alpha_T = 3.0 \cdot 10^{-6} \text{ 1/K}$; the carrier diffusivity $D_E = 12 \text{ cm}^2/\text{s}$; the excess carrier lifetime $\tau = 6.0 \cdot 10^{-6} \text{ s}$; the front and back surface recombination velocities; $s_R = 2400 \text{ cm/s}$.

Second we analyzed the PT elastic vibrations of the square membrane for different thicknesses. Figure 2 shows typical amplitude quasi-static and dynamic elastic vibration spectra (the amplitude of elastic bending) for a Si square membrane vs different membrane thicknesses (5, ..., 250 μm). The analysis showed that exist two distinct cases: 1) $h > 60$ and 2) $h < 60 \mu\text{m}$. In the first case, the quasi-static and dynamic spectra are practically the same; it is possible to use the quasi-static approximation. It is interesting that in this case the amplitude of the elastic vibration increase with the thickness.

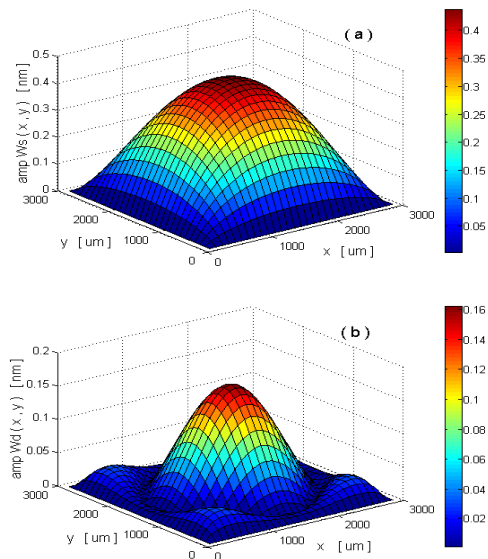


Figure 1. Amplitude space distribution of the elastic bending for Si square membrane (10 μm thick at $f = 2$ kHz): (a) quasi-static, W_s ; (b) dynamic W_d .

In the latter case, the amplitude of the quasi-static and dynamic vibration increases with decreasing thickness. The amplitude of the dynamic vibrations change the character at $h=30 \mu\text{m}$, where there is a maximum (1.10 nm), and then decreases with a decrease in thickness of the sample. In this case, one must use a dynamic model of the PT elastic vibrations, even at relatively low frequencies ($f < 1 \text{ kHz}$).

CONCLUSION

The theoretical dynamic model for the PT elastic vibrations of the square membranes, including the TE and PE effects, were derived and analyzed. We

also analyzed the PT elastic vibration for different membrane thickness. The analysis showed that exist two distinct cases: below and above any critical thickness ($\sim 60 \mu\text{m}$). For the membrane thinner than $50 \mu\text{m}$, one must use a dynamic model of the PT elastic vibrations.

ACKNOWLEDGEMENT

This work was partially supported by the Ministry for Science of the Republic of Serbia (Grants no. ON171016).

REFERENCES

- [1] E. A. Wachter and T. Thundat, Rev. Sci. Instrum. , 1995, 66, 3662-3667.
- [2] D.M.Todorović, Rev. Sci.Instrum., 2003, 74 (1), 578.
- [3] R. G.Stearns, G.S.Kino, Appl. Phys. Lett., 1985, 47, 1048-1050.
- [4] D.M.Todorović, B.Cretin, Y.Song, P.Vairac, J.Appl.Phys, 2010,107, 023516 (9p).

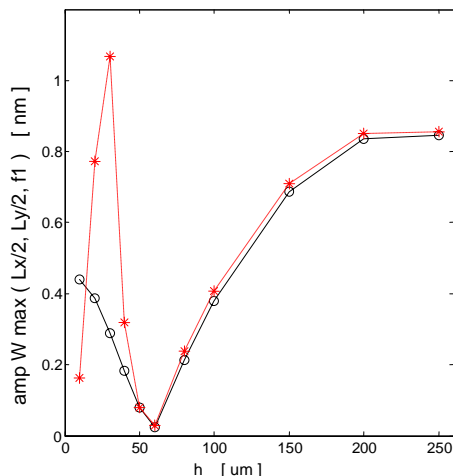


Figure 2. Amplitude of elastic bending at the center of the membrane ($x = L_x/2, y = L_y/2$) at $f = 2 \text{ kHz}$) for different thicknesses ($h = 5, \dots, 250 \mu\text{m}$): (o) quasi-static, W_s ; (*) dynamic W_d .

ANALYSIS OF 4,4'-BIS(2,2'DIPHENYL VINYL)-1,1'-BIPHENYL USING THE ATMOSPHERIC-PRESSURE SOLIDS ANALYSIS PROBE FOR IONIZATION

B. Nastasijević¹, A. Ž. Tomović², V. P. Jovanović², R. Žikić¹ and
S. Veličković¹

¹*Vinča Institute of Nuclear Sciences, University of Belgrade, Belgrade, Serbia (vsuzana@vinca.rs)*

²*Institute of Physics, University of Belgrade, Pregrevica 118, Belgrade, Serbia*

ABSTRACT

An Atmospheric pressure Solids Analysis Probe (ASAP) mass spectrometer are used for investigation the ionization mechanism and fragmentation pathways of 4,4'-bis(2,2'diphenyl vinyl)-1,1'-biphenyl (DPVBi). DPVBi is material used in OLEDs (organic light-emitting diode). Results obtained indicate that by controlling ion source conditions it is possible to optimize forming of desired precursor ion, primarily radical cation and in less content protonated ion of DPVBi. The results presented illustrate the usefulness of ASAP MS in the characterization of DPVBi compounds.

INTRODUCTION

ASAP mass spectrometry is a direct analysis ionization technique derived from atmospheric-pressure chemical ionization (APCI) that was introduced in 2005 [1]. In the ASAP the samples are first vaporized using heated desolvation gas (nitrogen) followed by ionization by electrical discharge at a corona needle [2]. This ionization method belongs to the group of the ambient desorption methods, like as Desorption Electrospray Ionisation (DESI) and Direct Analysis in Real Time (DART) [3 – 5]. The ASAP ionization source is integral part of a commercial electrospray (ESI) or atmospheric pressure chemical ionization mass spectrometer, and this method can be used for rapid qualitative analysis of various materials using only slightly modified commercial ESI-MS. The ASAP method is applied primarily to analysis of volatile and semivolatile solid materials, both polar and non-polar. Due to the significant differences in the mechanism of ionization this method offered the scope for analyzing some compound that do not ionize effectively by the ESI. It should be mentioned that the advantage of ASAP is important for the analysis of non-polar compounds where the ions of interest could not be easily ionized by ESI-MS.

To date, ASAP has facilitated the analysis of steroids, drugs, nucleosides, polymers, and chemicals in food [5 - 7].

In this work, the applicability of the ASAP for characterization 4,4'-bis(2,2'diphenyl vinyl)-1,1'-biphenyl (DPVBi) has been investigated.

DPVBi is material used in OLEDs and it is the particular important to find conditions for its detection [8, 9]. A structure of DPVBi is shown at Figure 1. It should be noted that this compound did not ionized effectively by ESI.

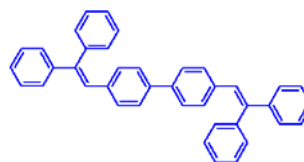


Figure 1.
Structure of 4,4'-bis(2,2'diphenyl vinyl)-1,1'-biphenyl (DPVBi).

EXPERIMENTAL

The ASAP (mass analysis was performed by Acquity Tandem Quadrupole Detector (Waters, USA) – “Vinča“ Institute of Nuclear Sciences) consists of a glass capillary with sealed end onto which solid or liquid sample is deposited.

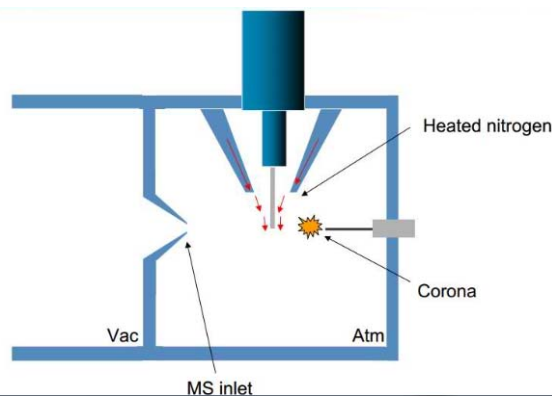


Figure 2. A schematic of the ASAP ion source (Waters corporation)

As can be seen in Figure 2, streams of nitrogen gas introduces into the ASAP source housing e.g. desolvation gas) enabling analyte vaporization. Namely, desorption occurs upon interaction with a hot desolvation nitrogen stream, whereby the solid evaporates from the glass's surface and then ionized at atmospheric pressure by the corona discharge. Typically, the temperature of desolvation gas was set in the range from 200 to 400°C, with the flow rate ranging from 500-800 L/h. Before use, probes should be conditioned (baked) to remove any residual contamination. This is usually achieved by heating the probe at 500 °C for at least 30 s. The ASAP source was operated in positive ion mode with a corona voltage in the range from 2kV to 4.0kV and a cone voltage over the range 10 – 50 V.

RESULTS AND DISCUSSION

In the Figures 3 and 4 are shown positive-ion ASAP mass spectrum of DPVBi obtained at the corona voltage of 4.35kV and under cone voltage in the range from 20 to 40V, respectively.

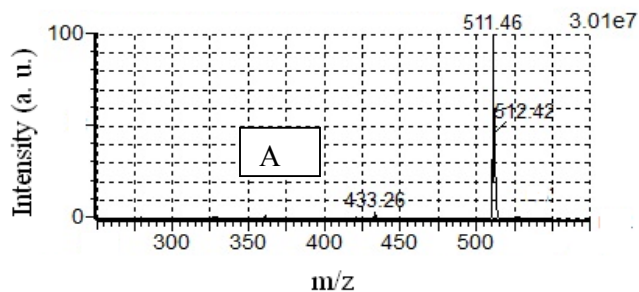
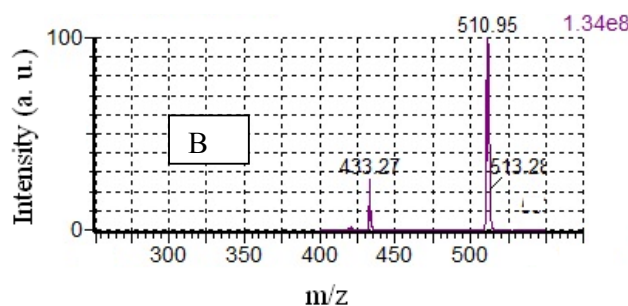


Figure 3. Positive-ion ASAP mass spectrum of DPVBi obtained at the corona voltage of 4.35kV, under cone voltage of 20 V (A), and 30 V (B)



As shown in Figure 3(A) at the cone voltage of 20V the predominant ion was protonated ion of DPVBi.

Otherwise, applying of higher cone voltage above 30V causes formation of predominant, radical cation of DPVBi (m/z 510.95, Fig. 3B). With the enhancement of temperature from 250 to 400 °C, the signal intensity of this radical cation slightly increased. It should be noted that at the corona voltage below 3.0 kV either the radical cation or protonated ion of DPVBi could not be detected. Beside these main molecular ions shown in Fig. 3, it was detected appearance of two other peaks, one observed at m/z 433.27 and another at m/z 356.26 which eventually could be considered as fragments of DPVBi molecule (Fig.4).

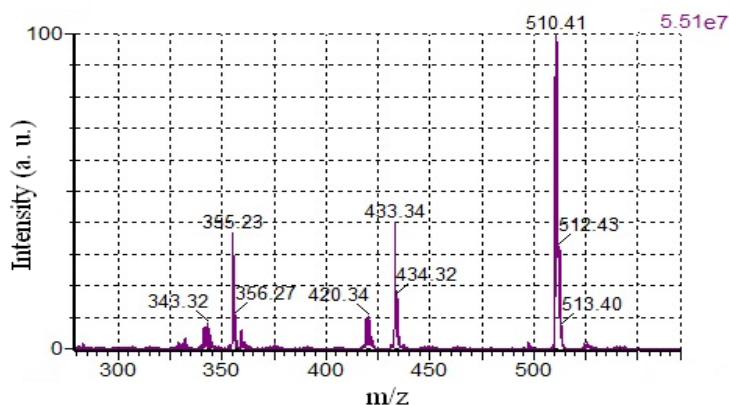


Figure 4. Positive-ion ASAP mass spectrum of DPVBi obtained at the corona voltage of 4.35kV, under cone voltage of 40 V.

Thus, masses with m/z 433.27 and 356.26 could be attributed to fragments of DPVBi molecule after one or two phenyl group loss, respectively. Whether these masses represent DPVBi fragments or they are ions of some other origin has to be additionally established.

CONCLUSION

Work herein demonstrates that ASAP can be used successfully for the characterization of 4,4'-bis(2,2'-diphenyl vinyl)-1,1'-biphenyl. Reliable method for monitoring of this compound and its photo-degradation products could be of importance for further improvements in OLEDs technology.

ACKNOWLEDGEMENT

The authors acknowledge the Ministry of Education and Science Republic of Serbia, for the financial support (under Project No. 172019, 172023 and 171033)

REFERENCES

- [1] C. McEwen, R. McKay and B. Larsen, *Anal. Chem.*, 2005, 77, 7826–7831.
- [2] J. Rozenski, *International Journal of Mass Spectrometry*, 2011, 304, 204–208.
- [3] R. Cody, J. Laramée, H. Durst, *Anal. Chem.*, 2005, 77, 2297 - 2302.
- [4] Z. Takats, J. Wiseman, B. Gologan, R. Cooks, *Science*, 2004, 306, 471 - 473.
- [5] A. Ray, J. Hammond, H. Major, *Eur J Mass Spectrom* 2010, 16, 169–74.
- [6] C. Petucci, J. Diffendal, *J Mass Spectrom* 2008; 43, 1565–8.
- [7] Y. Bennani, *Drug Discov Today* 2011, 16, 779–92.
- [8] X.Zhang, Z.Wu, B.Jiao, D.Wang, D.Wang, X.Hou and W.Huang, *J. Lumin.* 2012, 132, 697–701
- [9] D.Wang, Z.Wu, X.Zhang, B.Jiao, S.Liang, D.Wang, R.He and X.Hou, *Org. Electron.* 2010, 11, 641–648

INVESTIGATION OF SODIUM 3-DEHYDROCHOLATE ASSOCIATION IN AQUEOUS SOLUTION

D.Škorić¹, D. Ćirin², M.Poša² and J. Čanadi¹

¹ *Department of Chemistry, Biochemistry and Environmental Protection, University of Novi Sad Faculty of Sciences, 21000 Novi Sad, R. Serbia*

² *Department of Pharmacy, Faculty of Medicine, University of Novi Sad, Hajduk Veljkova 3, 21000 Novi Sad, R. Serbia*

ABSTRACT

In this paper results of investigation of aggregation of sodium 3-dehydrocholate are presented. Aggregation of title compound was investigated by means of spectrofluoriphotometric measurements using pyrene as the probe molecule. Measurements showed that there are two main micellization areas for this bile acid oxo derivative.

INTRODUCTION

Sodium 3-dehydrocholate (**1**) is a surface active substance with steroidal skeleton. Formally, **1** is an oxo derivative of 7,12-dihydroxy-5 β cholanoic acid (**2**). The convex side of molecule **1** is hydrophobic, while the concave side is hydrophilic, thus sodium 3-dehydrocholate belongs to group of planar surface active substances.

Salts of bile acids usually build micelles having small aggregation number compared to the surfactants of hydrophobic tail – hydrophilic head type [1]. However, longitudinal shape of micelles having specific indentations (fiords) influences interactions with certain drugs (eg. morphine hydrochloride) changing their bioavailability (monomeric form does not interact with the drug). Therefore, the current issue is investigation of aggregation characteristics of different derivatives of bile acids.

Investigation of oxo bile acids is currently very interesting because it is shown that they exhibit lower membrane-toxicity, which is a major drawback in pharmacological application of sodium salts of chenodeoxycholic and ursodeoxycholic acid. There are many pharmacological effects of oxo bile acids described in literature: promotional action on transport on some drugs [2], lowering glucose blood level [3] etc. Many of these effects are due to interaction of oxo bile acid micelles with drug molecules. Because of that there is great importance in determination of critical micellar concentration (CMC) and other parameters of micellization (e.g. aggregation number).

There are lot of techniques that are convenient for determination of CMC values of surfactants. Among them is the spectrofluorimetric measurement wit pyrene as a probe molecule. In general this technique is based on monitoring the influence of change in hydrophobicity of pyren molecule surrounding on it's signal.

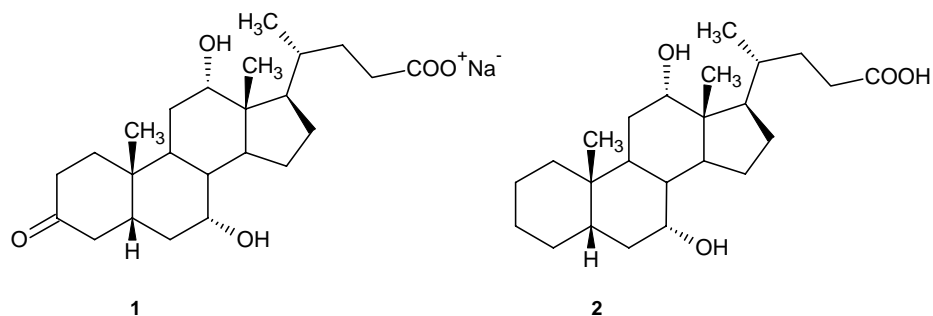


Figure 1. Structure of sodium 3-dehydrocholate (**1**) and 7,12-dihydroxycholanoic acid (**2**)

EXPERIMENTAL

Bile acid oxo derivative was synthesized and converted to sodium salt using known procedures [4,5]. Purity of compound used in measurements was confirmed by NMR. Deionised water was used for all purposes. Accurately weighed quantities of sodium 3-dehydrocholate were dissolved in requisite volumes of pyrene saturated water in order to prepare required solutions for fluorescence measurements.

Spectrofluoriphotometric measurements were carried out in an Agilent Cary Eclipse fluorescence spectrophotometer, using an excitation wavelength of 335 nm. The intensities of first (I_1) and third (I_3) vibrational bands of pyrene emission spectrum were recorded at 373 and 384 nm. Change in the I_1/I_3 ratio was monitored as a function of total surfactant concentration in temperature interval from 0 to 50 °C using spectrofluoriphotometric measurements.

RESULTS AND DISCUSSION

In the investigated temperature interval, the function of the critical micelle concentration (CMC)/temperature does not have a minimum (what is a common characteristic of aliphatic surfactants), but the CMC value continually increases with the temperature rise.

Function $I_1/I_3=f(c)$ shows that in the case of sodium 3-dehydrocholate two micellization areas exist. The first area starts at 9 mM, at 0 °C and has maximum value of 35 mM, at 50 °C. These values correspond to the CMC values which can be obtained by other methods (tensiometry, NMR, etc.) The other area of micellization starts at 100 mM and does not show temperature dependence **Fig 2**.

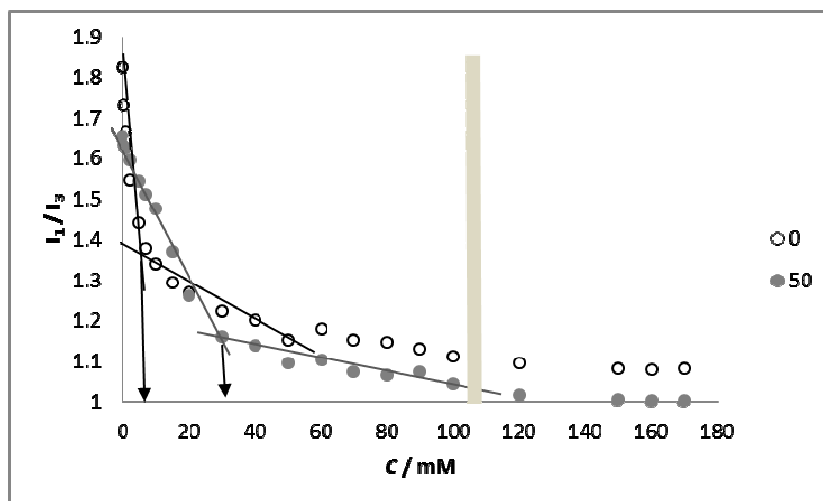


Figure 2. Example of micellization of bile acid derivative **1** at 0 and 50 °C: ratio of the intensity of the pyrene emission as the function of concentration of bile acid derivative.

CONCLUSION

Fact that the function of the critical micelle concentration (CMC)/temperature does not have a minimum (what is a common characteristic of aliphatic surfactants), but the CMC value continually increases with the temperature rise, means that the destabilizing effect due to the thermal mobility of building units is more noticeable (hydration of the hydrophobic micellar domain) than the increase of dehydration of the hydrophobic surface of monomeric sodium 3-dehydrocholate with the

temperature rise. Further, it is obvious that there is no sharp inflexion point on pyrene emission/concentration function which is also characteristic for some other aliphatic surfactants. This is probably due to complex micellization process of bile acid that begins with formation of primary micelles (dimers). These dimers interact with pyrene causing significant change in hydrophobicity of its environment and strong decrease in I_1/I_3 ratio on concentration around 9 mM. Formation of secondary micelles does not change I_1/I_3 ratio dramatically because it's driven by hydrogen bond interactions between primary micelles, according to Small [1]. From results obtained in this study it can be concluded that the micellization of bile acid oxo derivative is a complex process, contains at least two stages, and further investigation with other techniques is needed in order to get more accurate insight in micellization of sodium 3-dehydrocholate.

ACKNOWLEDGEMENT

Financial support of AP of Vojvodina Republic of Serbia, contract No: 114-451-3690/2011-01 for IPA-CBC HUSRB/1002/214/193 project is gratefully acknowledged.

REFERENCES

- [1] D.M. Small, Adv. Chem. Ser., 1968, 84, 31-52.
- [2] M. Poša, J. Čanadi, E.K. Kövér, V. Guzsvány, Gy. Batta, Colloids Surf. B, 2012, 94, 317–323
- [3] H. Al-Salami, G. Butt, I.G. Tucker, M. Mikov, Methods Find. Exp. Clin. Pharmacol., 2008 30 (2), 107–113.
- [4] K. Tserng, Journal of Lipid Research, 1978, 19, 501-504
- [5] A. Roda, A. Hofmann, K. Mysels, The journal of Biological Chemistry, 1983, 258, 6362-6370

INFLUENCE OF HYDROXYCINNAMIC ACIDS ON THE OXY-RADICAL GENERATED IODIDE/HYDROGEN PEROXIDE REACTION SYSTEM

N.I. Potkonjak¹, and S.N. Blagojević²

¹ *Chemical Dynamics Laboratory, Vinča Institute of Nuclear Sciences, University of Belgrade, P.O. Box 522, 11001 Belgrade, Serbia*

² *Institute of General and Physical Chemistry, Studentski trg 12-16, Belgrade, Serbia*

ABSTRACT

The influence of hydroxycinnamic acids (HCA): caffeic acid, chlorogenic acid, and p-coumaric acid, on the potassium iodide/hydrogen peroxide system was investigated. A linear correlation between absorption maximum of triiodide (I_3^-) at 351 nm and HCA concentration was found. In the presence of HCA, reaction yield of I_3^- was found to increase in following order p-coumaric < chlorogenic \leq caffeic acid. This is attributing to their oxy-radical scavenging activity. Results obtained in this study have showed correlation between antioxidant activities of HCA and their ability to enhanced I_3^- production.

INTRODUCTION

Recent investigations have showed that KI/H₂O₂ reaction system abound with free radical species. Namely, the EPR spin-trapping investigation of KI/H₂O₂ reaction system have provided clear evidence on the existence of hydroperoxyl radical (HOO \cdot) and hydroxyl radical (HO \cdot) as intermediary species [1,2]. Thus, KI/H₂O₂ reaction system can be considered as an easy available laboratory source of reactive oxygen species (ROS). It will be of great interest to investigate the effect of most famous antioxidant compounds on the oxy-radicals generated KI/H₂O₂ reaction. It is well-known that the function of antioxidants is to intercept and react with free radicals at a rate faster than substrate [3]. Therefore, antioxidants can be considered as free radical scavengers. Phenolic compounds, widely present in plant kingdom, stand out as the most efficient group of antioxidants [4,5].

EXPERIMENTAL

The chemicals used in this study were: potassium iodide, KI (p.a grade, Merck), hydrogen-peroxide, H₂O₂ (30%, p.a. Merck) and caffeic acid, p-coumaric acid and chlorogenic acid (all used HCA were from Sigma-

Aldrich, p.a. grade). The solutions were prepared with deionised water with resistivity 18.2 M Ω cm (Milli-Q purification system). The stock solutions were: 0.06 mol dm⁻³ KI, 0.125 mol dm⁻³ H₂O₂, and the hydroxycinnamic acids: 1.66 $\times 10^{-4}$ mol dm⁻³ caffeic, 1.97 $\times 10^{-4}$ mol dm⁻³ *p*-coumaric, and 1.47 $\times 10^{-4}$ mol dm⁻³ chlorogenic acid. The reaction mixture is always contained the same concentration of KI and H₂O₂, while the concentration of particular HCA was varied. Volume of reaction mixture was 3 cm³. The characteristic UV/VIS absorption peak was recorded at 351 nm, wavelength of I₃⁻ absorption maximum. The iodide – peroxide – hydroxycinnamic acid system was monitored for 180 s with 10 s step size. All experiments were done at ambient temperature (23 °C).

RESULTS AND DISCUSSION

The UV/VIS absorption spectra of the KI/H₂O₂ reaction system in the presence of *p*-coumaric acid, in various concentrations, are shown in the Fig. 1. The absorption spectra were recorded 180 s after the reaction initiation. The increase of I₃⁻ yield (increase of absorption at 351 nm) with the increasing concentration of caffeic acid can be observed. The same trend is obtained when caffeic or chlorogenic acid are introduced in to the iodide-peroxide system. [5]. Since certain amount of I₃⁻ will be generated even in the absence of HCA, spectra denoted with 0 $\mu\text{mol dm}^{-3}$ concentration in Fig. 1, the absorbance at 351 nm which originate from generated I₃⁻ in the absence of HCA (A_0^{351}) should be taken as background, and subtracted from the measured absorbance value (A_{HCA}^{351}) in the presence of HCA. Therefore, the difference ΔA_{351} , $\Delta A_{351} = A_{HCA}^{351} - A_0^{351}$, will be used in this study As shown in Fig. 2, the linear correlation between ΔA_{351} and concentration of HCA was observed in all cases. It is noteworthy that magnitude of enhanced I₃⁻ production in the system was found to increase in following order *p*-coumaric acid < chlorogenic acid \leq caffeic acid.

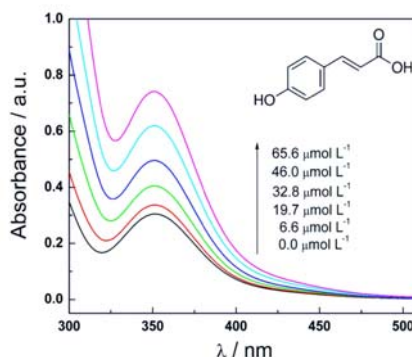


Figure 1. Absorption spectra of the KI/H₂O₂ system, in the presence of different concentrations of *p*-coumaric acid.

Accordingly, it seems to be possible connecting the antioxidant activity of investigated acids with their ability to enhance production of I_3^- . Some rough calculations of the Bond Dissociation Enthalpies (BDE) of O-H bonds in these molecules were complete, using the additivity rules proposed by Wright et al. [6]. As the reaction with radicals and generic antioxidant (ArOH) becomes more exothermic, the energy barrier necessary for reaction occurring should

decrease, and the antioxidant will react faster with the radicals, thus preventing reaction with substrate. Phenolic compounds which contain only one hydroxyl group attached to their aromatic ring are less effective antioxidants if compared with ones that possess second hydroxyl in the ortho or para position [6,7]. Therefore, caffeic and chlorogenic acid, with two OH groups, are a better free-radical scavenger than coumaric acid (one OH group). Due to BDE theory CAFF and CGA acids have a similar antioxidant activity $\Delta BDE = (-9.2-4.7) \text{ kcal/mol} = -13.9 \text{ kcal/mol}$, while *p*-CM is weaker antioxidant $\Delta BDE = -4.7 \text{ kcal/mol}$ [6]. In the calculations we assimilate the side chain has the same effect as $-\text{CH}=\text{CH}_2$ group, since Wright claimed that groups three bonds far from an OH group have little effect on BDE. The results which suggest that CAF is slightly better free radical scavenger than CGA obtained in this study are supported by work Chen et al. [7].

CONCLUSION

The influence of hydroxycinnamic acids on oxy-radical generated iodide-peroxide reaction was investigated. This influence was considered by monitoring the formation of I_3^- as the final product of iodide-peroxide reaction. The linear correlation between I_3^- absorption (ΔA_{352}) and the concentration of hydroxycinnamic acids was found. The different HCA cause the different increases of triiodide production ($p\text{-CM} < \text{CGA} \leq \text{CAF}$). Our preliminary results show that it should be possible to connect the antioxidant activity of these acids with their ability to produce more I_3^- .

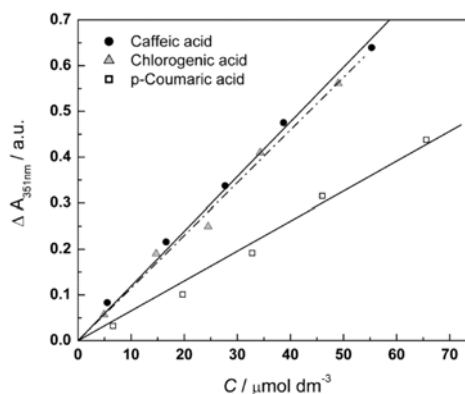


Figure 2. Linear correlation between ΔA_{352} and the concentration of hydroxycinnamic acids.

ACKNOWLEDGEMENT

This study was supported by the Ministry of Education, Science and Technological Development of the Republic of Serbia under the project no. 172015.

REFERENCES

- [1] D. Stanisavljev, M. Milenkovic, M. Mojivic, A. Popovic-Bijelic, *Journal Physical Chemistry A*, 2011, 115, 2247-2249.
- [2] D. Stanisavljev, M. Milenkovic, M. Mojivic, A. Popovic-Bijelic, *Journal of Physical Chemistry A*, 2011, 115, 7955-7958.
- [3] S. Wright, E. Johnson, G. DiLabio, *Journal of American Chemical Society*, 2001, 123, 1173-1183.
- [4] R. Cervellati, C. Renyulli, M. Guerre, E. Speroni, *Journal of Agricultural and Food Chemistry*, 2002, 50, 7504-7509.
- [5] S.Ž. Gorjanović, M.M. Novaković, N.I. Potkonjak, I. Leskošek-Čukalović, D.Ž. Sužnjević, *Journal of Agricultural and Food Chemistry*, 2010, 58, 744-751.
- [6] S. Wright, E. Johnson, G. DiLabio, *Journal of American Chemical Society*, 2001, 123, 1173-1183.
- [7] J. H. Chen, C.-T. Ho, *Journal of Agricultural and Food Chemistry*, 1997, 45, 2374-2378.

GEOPHYSICAL
CHEMISTRY

CRETACEOUS-PALEOGENE BOUNDARY CLAYS: ARSENIC and CRUDE OIL

P. I. Premović

*Laboratory for Geochemistry, Cosmochemistry and Astrochemistry,
University of Niš, P.O. Box 224, 18000 Niš, Serbia*

ABSTRACT

Remarkably high arsenic (As) contents have been reported in numerous Cretaceous-Paleogene boundary (KPB) clays worldwide. The one of many interpretations is that this As was generated by combustion of crude oil near the Chicxulub impact site. This combustion was presumably triggered by the Chicxulub impactor. This report shows that the estimated surface density of As in the KPB clays worldwide strongly contradicts the crude oil hypothesis.

INTRODUCTION

Alvarez et al. [1] reported anomalously high iridium (Ir) in the marine KPB clays at Gubbio (Italy), Højerup (Denmark) and Woodside Creek (New Zealand), Fig. 1. According to them, this enhanced Ir concentration was triggered by an asteroid impact. Later, it has been suggested that the impact site is at Chicxulub (a village at Yucatan Peninsula, southern Mexico, Fig. 1) [2].

Gilmour and Anders [3] estimated that the average abundance of As at the marine KPB clays worldwide is very high about $179 \mu\text{g cm}^{-2}$. These authors examined also the distribution of Ir and As in bulk boundary clays at eight prominent marine sites at Caravaca and Zumaya (Spain) Gubbio, Højerup, Woodside Creek and Flaxbourne River (New Zealand), and Deep Sea Drilling Project 465A (Central Pacific), Fig. 1. These sites are distal (>9000 km) to the proposed Chicxulub impact site. They concluded that, in contrast to Ir which is mainly meteoritic, As predominantly terrestrial in origin and associated in a single, global component of ejecta fallout.

As naturally occurs in crude oil and therefore high temperature processes release As into the atmosphere [4]. For this reason, Gilmour & Anders [5] proposed that combustion (ignited by the Chicxulub impactor) of crude oil was one of possible sources of As in the boundary clays worldwide. Indeed, As is a low-boiling trace element that are volatilized during combustion of fossil fuels and are transferred in the gas phase to the atmosphere.

This short report considers a possibility that As was sourced from combustion of crude oil near Chicxulub.

RESULTS AND DISCUSSION

Most of As generated by the combustion of crude oil ignited by the Chicxulub impact was probably in the elemental form and may be initially present in the gaseous/vapor emission into the atmosphere. This As would be rapidly oxidized to highly soluble oxides and subsequently condensed into the micron and submicron particles (fine dust). However, very coarse particles with mass diameter $>10 \mu\text{m}$ would probably quickly settle in the vicinity of Chicxulub, as particles with diameters $0.1 \mu\text{m}$ and $1 \mu\text{m}$ is particularly suited for long range (stratospheric) transport [6]. Indeed, most of As emitted into the current atmosphere arises from high temperature processes (e. g. crude oil combustion) and occurs only as fine particles (dust) with a mass median diameter of about $1 \mu\text{m}$ [4]. Thus, it is highly likely that mainly the As oxide species associated with submicron particles would rise up to the lower stratosphere and dispersed over the globe. However, a considerable fraction of these oxides would fall to the lower troposphere where they should be mainly removed by the enormous precipitations (probably acid rains). Thus, it appears that only a notably small fraction of As formed by crude oil burned promptly after the impact could reside in the lower stratosphere and be deposited globally.

In the following calculations, f_S is defined as the amount of As dispersed globally through the lower stratosphere to the total As of the crude oil and f_{AS} represents the amount of As distributed over the Earth's surface by the lower stratosphere to the total As emitted by this source into the atmosphere. I will assume that f_S and f_{AS} are equal 1 but this is clearly a high overestimation of their actual values which are probably much lower than 1. The global surface density of As (d_{AS}) derived from crude oil burned promptly after the Chicxulub impact is given by

$$d_{AS} = M_O C_O f_S / A_E$$

where M_O is the mass of crude oil burned, C_O is the average concentration of As in crude oil (0.134 ppm: Piver [7]; Eary et al., [8] and A_E (ca. $5 \times 10^{18} \text{cm}^2$) is the Earth surface area.

Harvey et al. [9] emphasize that the Chicxulub impact crater is located adjacent to the Cantarell very large oil reservoir in the southern Gulf of Mexico, suggesting that abundance of fossil hydrocarbons in the Chicxulub target rocks was likely to have been above global mean crustal abundance. The formation of the Cantarell oil field is a direct consequence of the KPB impact [10] and it belongs to the giant supercharged Pimienta-Tamabra petroleum system, Fig. 1. The crude oil of the Pimienta-Tamabra petroleum

system derives from the Late Jurassic source rock and its expulsion started in the Eocene [11]. This system is the most important in the southern Gulf of Mexico and has a cumulative production and remaining reserves of about 10^{16} g of known petroleum [11]. (The Oil and Gas Journal estimated that as of 2007, there were 12.4 billion barrels of proven oil reserves in Mexico. This corresponds to around 2×10^{15} g of crude oil).



Figure 1. Geographic locations of the marine KPB clays, the Chicxulub impact site, the Pimienta-Tamabra petroleum system and the Cantarell oil field.

The total proven crude oil and natural gas reserves of the world now stand at around 2×10^{17} g; estimates are that there is about 5×10^{17} g of crude oil and natural gas in the Earth's crust. (World Energy Council - Survey of Energy Resources 2010). Of course, oil reserve estimates cited above all refer to "proven", and there may be that much more has not been found.

Let us assume that the amount of crude oil burned during the Chicxulub impact was equal to the crude oil reserves of (ca. 10^{16} g) of the gigantic Pimienta-Tamabra petroleum system. Using these two assumed values, it is estimated that the upper limit of the global surface density (d_{As}) is about 270 pg cm^{-2} compared with the global surface density of As of the Cretaceous-Paleogene boundary clays: ca. $179 \text{ } \mu\text{g cm}^{-2}$. To make matters worse, if all world crude oil ($\sim 2 \times 10^{17}$ g) burns d_{As} would be $< 5.4 \text{ ng cm}^{-2}$.

Another way to estimate d_{As} for crude oil burned is by using the following formula

$$d_{As} = M_O \epsilon_O f_{AS} / A_E$$

where M_O and A_E have the same definition and values as those given above, and ε_O is the As emission factor for crude oil: $160 \times 10^{-6} \text{ g g}^{-1}$ (AP 42, Fifth Edition, Volume I, Chapter 1: External Combustion Sources). Simple calculations then show that the upper estimates of d_{As} are $0.32 \mu\text{g cm}^{-2}$ (for $M_O \sim 10^{16} \text{ g}$, the Pimental-Tamabra petroleum system) and $6.4 \mu\text{g cm}^{-2}$ (for $M_O \sim 2 \times 10^{17} \text{ g}$, all worldwide crude oil).

CONCLUSION

From this study, it appears that the As anomaly in the KPB clays worldwide cannot be attributed to the combustion of the crude oil close to the Chicxulub impact site.

ACKNOWLEDGEMENTS

The author is grateful to Drs. Anil D. Shukla, Emily M. Klein, José M. Grajales-Nishimura and Pete Hollings all those who contributed to this report by providing essential bibliographic material.

REFERENCES

- [1] L. W. Alvarez, W. Alvarez, F. Asaro, H. V. Michel, *Science*, 1980, 208, 1095-1108.
- [2] A. R. Hildebrand, G. T. Penfield, D. A. Kring, M. Pilkington, A. Y. Camargo, S. B. Jacobsen & W. V. Boynton, *Geology*, 1991, 19, 867-871.
- [3] I. Gilmour & E. Anders, *Geochim. Cosmochim. Acta*, 1989, 53, 503-511.
- [4] J. M. Pacyna, *Lead Mercury, Cadmium and Arsenic in the Environment*. Wiley, 1987.
- [5] I. Gilmour I. & E. Anders, *Global Catastrophes in Earth History: An Interdisciplinary Conference on Impacts, Volcanism, and Mass Mortality*, 1988.
- [6] J. Müller, *J. Aerosol Sci.* 1986, 17, 277-282.
- [7] W. T. Piver, *Biological and environmental effects of arsenic*. Elsevier, 1983.
- [8] L. E. Eary, R. Dhanpat, S. V. Mattigod & C. C. Ainsworth, *J. Environ. Qual.*, 1990, 19, 202-214.
- [9] M. C. Harvey, S. C. Brassell, C. M. Belcher, & A. Montanari, *Geology*, 2008, 36, 355-358.
- [10] J. M. Grajales-Nishimura, E. Cedillo-Pardo, C. Rosales-Domínguez, D. J. Morán-Zenteno, W. Alvarez, P. Claeys, J. Ruíz-Morales, J. García-Hernández, P. Padilla-Avila & A. Sánchez-Ríos, *Geology*, 2000, 28, 307-310.
- [11] L. B. Magoon, T. L. Hudson & H. E. Cook, *Mem. Am. Ass. Petrol. Geol.*, 2001, 75, 83-125.

ARSENIC OF CRETACEOUS-PALEOGENE BOUNDARY CLAYS AND DECCAN VOLCANIC EVENT

P. I. Premović

*Laboratory for Geochemistry, Cosmochemistry and Astrochemistry,
University of Niš, P.O. Box 224, 18000 Niš, Serbia*

ABSTRACT

Numerous Cretaceous-Paleogene boundary (KPB) clays worldwide contain anomalously high arsenic (As). The massive volcanism that produced the Deccan Traps of India around the KPB time has been proposed as one of the possible sources of this anomaly. However, the calculations of this brief report indicate that anomalous As in these clays was probably not sourced by the enormous Deccan Traps volcanic emission.

INTRODUCTION

An alternative explanation for the cause of Ir anomaly in the KPB clays worldwide is based on the hypothesis that an unusual large volcanic event of short duration that coincides with the KPB is responsible for this anomaly [1]. One of the largest basaltic provinces in the world the Deccan Traps (Fig. 1) become the most important when considering the volcanic events implied by this hypothesis though no evidence of high Ir in the Deccan volcanic rocks has yet been found [2] (and references therein).



Figure 1. Deccan Traps and Lonar crater.

Deccan Traps (hereinafter Deccan) were created by an enormous volcanic event that originally erupted about 1.2×10^6 km³ of magma [3]. Recent studies indicate three main volcanic stages with the most active phase (hereinafter the phase-2) encompassing about 80 % of the Deccan eruptions and coinciding with the latest Maastrichtian [4, 5] (and references therein). This phase may have occurred in the short time interval of 10,000 years 100,000 years [4, 6].

The current volcanoes are significant sources of As emissions into the atmosphere [7]. Thus enormous volcanic source such as Deccan, in principle, could account for the excess of As at the KPB. This note

considers a possibility that anomalous As in the KPB clays worldwide originated from the Deccan volcanic exhalations.

RESULTS AND DISCUSSION

Adopting the volume of the Deccan magma ($1.2 \times 10^6 \text{ km}^3$) estimated by Keller et al. [3], I calculate that approximately $1 \times 10^6 \text{ km}^3$ or $3 \times 10^{21} \text{ g}$ of basaltic lava (assumed density: 3 g cm^{-3}) erupted during the most active phase-2 of the Deccan eruptions. Osae et al. [8] carried out a geochemical analyses major oxides and trace elements, including As, of a numerous target basalt samples from the Lonar impact crater (Fig. 1) which is escavated in the KPB basalts of Deccan. They reported that an average concentration of As in their samples is 0.58 ppm (Of note, the concentration of As in the continental crust and mantle is, respectfully, 1 ppm and 0.066 ppm [9]). Based on this As concentration, one can calculate that the As content of the phase-2 magma was about $1.75 \times 10^{15} \text{ g}$. The average amount of elemental As at the KPB surface has been estimated as ca. $179 \mu\text{g cm}^{-2}$ [10] implying that the total amount of As at the KPB is about $9 \times 10^{14} \text{ g}$. Thus enormous ~50 % of the total As would have had to be released from the phase-2 magma into the atmosphere (lower stratospheric levels) to account for this amount of As at the KPB.

The global surface density of As (d_{As}) released from the phase-2 magma can be estimated from the following equation:

$$d_{\text{As}} = M_{\text{M}} \epsilon_{\text{M}} f_{\text{AS}} / A_{\text{E}}$$

where M_{M} (ca. $3 \times 10^{21} \text{ g}$) is the mass of the phase-2 magma, ϵ_{M} is the As emission factor for magma ($\sim 1.75 \times 10^{-9} \text{ g g}^{-1}$), A_{E} (ca. $5 \times 10^{18} \text{ cm}^2$) is the Earth surface area; and, f_{AS} represents the amount of As which reaches the lower stratosphere to the total As emitted by this source into the atmosphere. I calculate ϵ_{M} by dividing the above estimated total As released by the phase-2 magma ($\sim 5.25 \times 10^{12} \text{ g}$) with the mass of this magma M_{M} . This value should be considered as an upper limit. I will also assume that f_{AS} is equal 1 but this is clearly a high overestimation of its actual value which is probably much lower than 1. Using these values for ϵ_{M} and f_{AS} , I estimate that the upper limit of d_{As} is about $1 \mu\text{g cm}^{-2}$.

Estimates of the current annual input of volcanic As into the atmosphere vary, ranging from $0.280 \times 10^9 \text{ g per year}$ to $1.72 \times 10^{10} \text{ g per year}$ [7] (and references therein), although values seem to be converging on $\sim 7 \times 10^9 \text{ g per year}$ [11] and this value can be regarded as a minimum amount due to the fact that the volcanic emissions were calculated for a year with no large eruptions [7]. To make matters worse, the Earth's volcanic emission of As

into the atmosphere for the last 100 years could be roughly 10^{12} g As which is about the amount of As emitted by the phase-2 for its assumed duration of 10^4 years up to 10^5 years [4, 6]. As far as is known, there is no report of any marine clayey section in the last about 12,000 years (the Holocene epoch) and which is a few centimeters thick with a thin red basal layer having a sharp anomalous As (or Ir!) spike.

Additional problem is a relatively short time scale of the deposition of the KPB clays which is inconsistent with a relatively long time of the phase-2 event. Indeed, the deposition of the prominent KPB clays occurred for several decades up to a century at most [12, 13] (and references therein) but the duration of the phase-2 far lasted for $10^4 - 10^5$ years [5, 6]. Thus, the deposition time of these clays is difficult to reconcile with a relatively long duration of the phase-2. In addition, Chenet et al. [6] claim (based on their paleomagnetic studies) that the lava pile during the phase-2 was erupted in some 30 single eruptive events each in volume from 1000 to 20,000 km³ and each lasted as short as 100 years. If their claim is correct than we should recognize several lithostratigraphic units with a small As spike at or close the KPB instead only one but anomalous.

CONCLUSION

The estimates of the global surface density of As and other evidence presented here clearly reveal that Deccan volcanism did not contribute appreciable to the high As in the boundary clays worldwide.

ACKNOWLEDGEMENTS

The author is grateful to Drs. Anil D. Shukla, Emily M. Klein, José M. Grajales-Nishimura and Pete Hollings all those who contributed to this report by providing essential bibliographic material.

REFERENCES

- [1] C. B. Officer C.B. & C. L. Drake, *Science*, 1985, 227, 1161-1167.
- [2] P. N. Shukla, N. Bhandari, A. Das A, A. D. Shukla & J. S. Ray, *Proc. Ind. Acad. Sci. Earth Planet. Sci.*, 2001, 110, 103-110.
- [3] G. Keller, T. Adatte, P. K. Bhowmick, H. Upadhyay, A. Dave, A. N. Reddy & B. C. Jaiprakash, *Earth Planet. Sci. Lett.*, 2012, 341-344.
- [4] A. L. Chenet, X. Quidelleur, F. Fluteau & V. Courtillot, *Earth Planet. Sci. Lett.*, 2007, 263, 1-15.
- [5] G. Keller, A. Sahni A. & S. Bajpai, *J. Biosci.*, 2009, 34, 709-728.
- [6] A. L. Chenet, F. Fluteau, V. Courtillot, M. Gérard & S. K. Subbarao, *J. Geophys. Res.*, 2008, 113, B04101.

-
- [7] D. C. Chilvers & P. J. Peterson P. J., Lead, mercury, cadmium and arsenic in the environment, 1987, Wiley, 279-301.
- [8] S. Osae, S. Misra, C. Koeberl, D. Sengupta D. & S. Ghosh, Meteorit. Planet. Sci., 2005, 40, 1473–1492.
- [9] H. Palme H. & H. St. C. O'Neill, Treatise on Geochemistry., 2004, Elsevier, 1-38.
- [10] I. Gilmour & E. Anders, Geochim. Cosmochim. Acta, 1989, 53, 503-511.T. A.
- [11] D. M. Mather, D. M. Pyle & C. Oppenheimer, Volcanism and the Earth's Atmosphere. Geophysical Monograph, 2003, 139, Am. Geophys. Union, 189-212.
- [12] P. I. Premović, Intern. J. Astrobiol., 2009, 8, 193–206.
- [13] P. I. Premović, Geochem. Intern., 2011, 49, 55-65.

EDUCATION,
HISTORY

DOROTHY HODGKIN CROWFOOT AS EXCELLENT PHYSICAL CHEMIST

T. Halaši², S. Kalamković¹ and J. Mandić²

¹Primary School „Prva vojvođanska brigada”, Seljačkih buna 51a, 21000 Novi Sad, Serbia. (kalamkovic@gmail.com)

²Faculty of Science, Department of Chemistry, Biochemistry and Environmental Protection, Methods of Teaching Chemistry, History of Chemistry, University of Novi Sad, Trg Dositeja Obradovića 3, 21000 Novi Sad, Serbia.

ABSTRACT

This paper presents a short biography of Dorothy Crowfoot Hodgkin. The paper said the names of celebrities, Linus Carl Pauling, Margaret Hilda Thatcher, Baroness Thatcher, John Desmond Bernal, Sir Robert Robinson, who helped Dorothy in the development of X-ray, X-ray crystallography. Presents the most important discoveries of Dorothy such as: determined the molecular structures of cholesteryl iodide, penicillin, vitamin B12, vitamin B12 coenzyme and the protein hormone insulin. For his research, Dorothy was awarded the Nobel Prize in chemistry in 1964.

BIOGRAPHY

Dorothy Crowfoot was born in Cairo, in Egypt in 1910. Hodgkins parents were John (*John Winter Crowfoot*, 1873-1959), and Grace (*Grace Mary Crowfoot*, born *Hood*, 1877-1957). Her parents were authorities in archaeology, and she may have followed the family vocation but for a childhood fascination with minerals and crystals. She became interested in chemistry and in crystals at about the age of 10. This interest was encouraged by A.F. Joseph, a friend of her parents in the Sudan, who gave her chemicals and helped her during her stay there to analyse ilmenite. Most of her childhood Dorothy spent with her sisters at Geldeston in Norfolk, from where she went to the *Sir John Leman School*, Beccles, from 1921-28. When she was 15, her mother gave her Sir William Henry Bragg's *Concerning the Nature of Things*, which contained intriguing discussions of how scientists could use X-rays to "see" atoms and molecules. She went to *Oxford* and *Somerville College* from 1928-32 [1]. When she returned to Oxford in 1934, she started to collect money for X-ray. Two things happened on the same day in 1934. First, the name Crowfoot took on a terrible irony. She found she had crippling rheumatoid arthritis. Only hours after, she learned that, people in her lab made the first X-ray photo of a

protein crystal. Three years later, she married a socialist writer Thomas Hodgkin (*Thomas Lionel Hodgkin*, 1910-1982). They have three children (Elizabeth, Luke and Toby) and three grandchildren [2]. Family friends of Dorothy were celebrities, too. Agatha Christie (*Agatha Mary Clarissa Miller*, 1890-1976). Christie had always had an interest in archaeology. Lawrence of Arabia (*Thomas Edward Lawrence*, 1888-1935) was a British archaeologist, adventurer, writer, soldier. He gained international fame as Lawrence of Arabia, thanks to his role in the invasion of the Sinai and Palestine and in the Arab revolt against Ottoman rule from 1916 to 1918. Dorothy Crowfoot Hodgkin died on July 29, 1994.

ASSOCIATES IN THE WORK

Dorothy Crowfoot Hodgkin was a woman who loved working with people. She exchanged personal experience and accepted the suggestions of her closest associates, mentors, as well as students.

Pauling (*Linus Carl Pauling*, 1901-1994) tried to bring Dorothy to America in 1953, but the State Department wouldn't let her in. That was because her husband and John Desmond Bernal, her mentor at Cambridge, were members of the communist party. She was apolitical but strongly sympathetic to a number of socialist causes. Her enduring friendship with Thatcher is all the more remarkable for that. Margaret Thatcher (*Margaret Hilda Thatcher, Baroness Thatcher*, born Roberts, 1925-2013) studied chemistry at Oxford under Dorothy Crowfoot Hodgkin.

John Desmond Bernal (1901-1971) was one of the United Kingdom's most well-known and controversial scientists. Known as "Sage" to friends, Bernal is considered a pioneer in X-ray crystallography in molecular biology. He also worked on the structure of liquid water, showing the boomerang shape of its molecule (1933). It was in Bernal's research group where, following a year working with Tiny Powell at Oxford (*Herbert Marcus Powell*, 1906-1991), Dorothy Hodgkin continued her early research career. Together, in 1934, they took the first X-ray photographs of hydrated protein crystals using the trick of bathing the crystals in their mother liquor, giving one of the first glimpses of the world of molecular structure that underlies living things (Fig. 1) [3].

Sir Robert Robinson (1886-1975) arrived at Oxford in 1943 and graduated in 1947 with Second-Class Honours in the four-year. Robinson's extensive researches in organic chemistry have dealt not only with the structure and synthesis of many organic bodies, but also with the electrochemical mechanism of organic reactions. In terms of women in X-ray crystallography, two women were great contributors. They were Dorothy Hodgkin, of course, and Rosalind Elise Franklin (1920-1958).



Figure 1. *John Desmond Bernal, 1901-1971*

SIGNIFICANT PUBLICATIONS

The molecular structures that she determined include those of cholesteryl iodide, penicillin, vitamin B12, vitamin B12 coenzyme and the protein hormone insulin. Her achievements included not only these structure determinations and the scientific insight they provided, but also the development of methods that made such structure determinations possible.

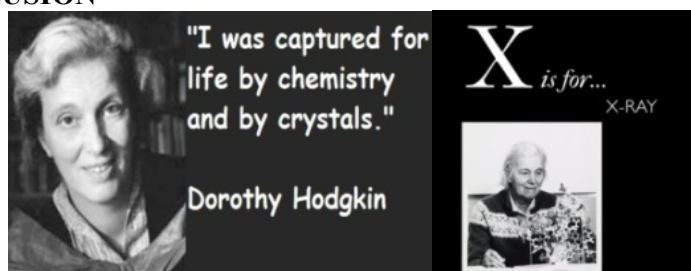
While studying in the department of mineralogy and crystallography, Dorothy Crowfoot employed the physical science of X-ray crystallography (first developed by Bragg (*Sir William Lawrence Bragg, 1890-1971*)) to aid her in determining the structural arrangement of the atoms in simple salts and minerals such as thallium dialkyl halides. This was the first of what would be many X-ray studies. Hodgkin discovered that crystals are a solid composed of atoms arranged in a regular and repeated pattern. She later took this method one step further and used it to analyze more complex molecules. In 1933, Hodgkin began working with Bernal on her doctorate degree. She felt that the scientific world had ceased to know any boundaries while conducting her research with him. Hodgkin stated in a published paper: "...we explored the crystallography of a wide variety of natural products, the structure of liquids and particularly water, Rochelle salt, isomorphous replacement and phase determination, metal and pepsin crystals, and speculated about muscular contraction. By 1946, Dorothy Crowfoot Hodgkin had learned the molecular structure of penicillin. By 1951, she'd figured out the mysterious B12 molecule and for that was given the 1964 Nobel Prize in chemistry. A headline in the *Times* mawkishly cried out: "Nobel Prize for British Wife," and she kept on working. In 1969, she showed how 777 atoms made up the incredibly complex structure of the insulin molecule. It worked, so she resolved to understand this magical lifelike process. A geologist friend gave her a box of reagents and minerals and said, "Buy a proper book on analytical chemistry!" She did. Then she

built a chemistry lab in her attic and set her sights on the male bastion of Oxford University [4].

NOBEL PRICE

There is so much more to tell about Dorothy Crowfoot Hodgkin. She was only the fourth woman ever to win a Nobel Prize, for her determination by X-Ray techniques of the structures of biologically important molecules. She was the first English woman to win the prize. But, before that, at the age of only 36, she became only the third woman to be made a *Fellow of the Royal Society*, in 1965. the *Order of Merit* [5].

CONCLUSION



That, says her biographer, was like drawing plans for a jungle gym when you've seen only its shadow on the ground. Her life was, in fact, one eerie feat of spatial visualization after another.

ACKNOWLEDGEMENT

The authors wish to thank Ministry of Education and Sciences advance of the Republic of Serbia for financial support this work with Project "European Perspective on the Quality of Education in Serbia", No. 179010.

REFERENCES

- [1] G. Ferry, Dorothy Hodgkin, A life, Granta Books, London, 1999.
- [2] G. Dodson, Dorothy Mary Crowfoot Hodgkin, O. M. 12 May 1910 - 29 July 1994, Biographical Memoirs of Fellows of the Royal Society 2002, 48, 179-219.
- [3] D. M. C. Hodgkin, John Desmond Bernal, 10 May 1901-15 September 1971, Biographical Memoirs of Fellows of the Royal Society 1980, 26, 16.
- [4] J. H. Lienhard, The Engines of our Ingenuity, Structure Living in a Built World, VII Crystals, http://www.uh.edu/engines/CD-Structure/_of_our_ingenuity-structure-track7.html [26. IV 2014].
- [5] S. B. McGrayne, Dorothy Crowfoot Hodgkin, May 12, 1910 - Physical Chemist, Nobel Prize in Chemistry 1964, Nobel Prize Women in Science, A Birch Lane Press Book, New York, 2001, Chapter 10.

ARPAD KISS PHYSICAL CHEMIST

T. Halaši¹, M. Mikloš¹ and S. Kalamković²

¹*Faculty of Science, Department of Chemistry, Biochemistry and Environmental Protection, Methods of Teaching Chemistry, History of Chemistry, University of Novi Sad, Trg Dositeja Obradovića 3, 21000 Novi Sad, Serbia. (tibor.halasi@dh.uns.ac.rs)*

²*Primary School „Prva vojvođanska brigada”, Seljačkih buna 51a, 21000 Novi Sad, Serbia.*

ABSTRACT

Arpad Kiss (*Kiss Árpád*, September 16, 1889 - November 10, 1968) was the *Kossuth Prize-winning chemist*, botanist, member of the *Hungarian Academy of Sciences*. His work was very important for the widespread reaction kinetics, electrochemistry and spectroscopy in many areas, in the field of physical chemistry. He was a dominant figure in current chemistry education research on the *University of Szeged*, for nearly four decades,.

BIOGRAPHY

Kiss (*Kiss Árpád*, September 16, 1889 - November 10, 1968) (Fig. 1) continued his studies on the *University of Budapest*, after graduating from *Presbyterian College of Sarospatak*. He was a Buchböck's (*Buchböck Gusztáv*, February 15, 1869 - October 1, 1935) trainee on the *Institute of Chemical III*, in 1912/1913.



Figure 1. *Kiss Árpád*, September 16, 1889 - November 10, 1968.

He was wounded as a Russian prisoner in the World War I in 1914. Kiss stayed on the *Nikolaevsk and State University of Amursk*, in Russian Federation (*Николаевск институт, институт сои Российской академии сельскохозяйственных наук, Амурская область*), over four years. Arpad did experiments and studied the flora of the Far East for two years, on the *Institutions and botanical pathology and wheat breeding*. He was an assistant professor at the *Budapest University Institute* in the 1920-1921, and then inorganic chemistry professor of the physico-chemical in the 1921-1923. on the *Leiden University Institute*. Later, he worked at the Francis Joseph, *University of Szeged*. He was rector of the *University of Szeged* in the 1954-1955. From 1954 to his retirement in 1961, he was head of the *Department of Physical Chemistry* of the *University of Szeged* [1].

WORK

Kiss conducted continuous kinetics of complex chemical, electrochemical and spectroscopic studies in *Leiden University Institute*, and *Physical Research Laboratory* of the *University of Szeged*. In 1896. he discovered the phenomenon of radioactivity. He wrote the first monograph in Hungarian in 1911. Kiss defended doctoral thesis (PhD thesis) in 1913. in which he questioned the topic of nitrogen oxides and chlorine interaction with the investigated homogeneous third-order chemical reactions among the first. In subsequent research, Arpad has studied the role of neutral salt effect kinetics in aqueous solutions and how the non-electrolytes influence the reaction rate. This way the test results contributed to the electrochemical corrosion research in Hungary. In addition, the solutions are thoroughly dealt with Bronsted-Lowry acid-base theory (*Johannes Nicolaus Brønsted*, 1879-1947; *Thomas Martin Lowry*, 1874-1936) and experimental verification possibilities. He conducted an extensive spectroscopic studies on aromatic hydrocarbons, hydrated metal ions and complex salts. He researched the structures of complex compounds based on their spectra and the absorption properties. The experiment proved the chemical and physical properties of the metal complex compounds. Kiss's work was published in textbooks of *German Universities*, and in *Acta Chimica et Physica* between 1924 and 1946. At 1955. he was the journalist at the *Szeged Acta Physica* and editor at the *Chemica*. He researched the flora on the *Far East* and *Zemplen Mountains* and because of that he gained recognition among botanists [2, 3]. He was among the first that dealt with the third-order homogeneous chemical reactions.

MAIN REFERENCES

- *A discussion of the phenomena radioactivitas Chemie perspective*, (Sarospatak 1911);
- *Über die bei Neutralsalzwirkung Ionreaktionen*, *Zeitschrift für Physikalische Chemie*, (Bruckner Gyozo 1927);
- *Zur Lichtabsorption der Kobaltrhodanidlösungen I-II*, *Akademische Verlagsgesellschaft From 1940 to 1941*, Leipzig (Kiss Pal);
- *Cyano-und Thiosulfatokomplexe*, Leipzig, 1941;
- *Colloidics: third-year chemistry students*, University of Szeged, Szeged, 1950; • *General Chemistry*, University of Szeged, Szeged, 1950;
- *Physical Chemistry*, University of Szeged, Szeged, 1951;
- *The effect of the steric hindrance of the opacity*, Department of Chemistry Institute Publications, 1955, 27-35;
- *Beiträge zur Lichtabsorption der Chelan Complex*, *Chimica Acta*, (Csaszar Jozsef, 1957-1958);
- *Theorie der Lichtabsorption*, Budapest, 1958;
- *Lichtabsorption Über die von der Cyanokomplexen Übergangselemente*, *Chimica Acta*, (Miklos Ban, 1964) [6, 7].

Today, in honor of Arpad Kiss, scientist organize a conference titled *Kiss Árpád Emlékkonferencia*.

CORPORATE AFFILIATIONS AND RECOGNITIONS

In 1943: *The London Company Faraday (Faraday Society)*,

In 1945: *The physicochemical German Bunsen Society (Deutsche Physikalische Chemie für Bunsengesellschaft)* and *The American Chemical Society (American Chemical Society)*,

In 1949: *The French Chemical Society (Société de France Chimique)* increased membership,

In 1954: He was elected for a corresponding member of the *Hungarian Academy of Sciences*, and *Medal of Work*,

In 1955: Kossuth Prize, second class, and Soviet Academy of Sciences awarded him a Lomonosov coin (*Михаи́л Васи́льевич Ломоно́сов*, 1711-1765) [8].

ACKNOWLEDGEMENT

The authors wish to thank Ministry of Education and Sciences advance of the Republic of Serbia for financial support this work with Project “European Perspective on the Quality of Education in Serbia”, No. 179010.

REFERENCES

- [1] D. Pal, T. Klement, J. Terjék, State and the Kossuth Prize Laureates Almanac 1948-1985, Academic, Budapest, ISBN 963-05-4420-2, 1988, 238.
- [2] F. Nagy, Hungarian scientist encyclopedia from A to Zs. Spices, Better, MTESZ; OMIKK, Budapest, ISBN 963-85433-5-3, 1997, 461-462.
- [3] F. Glatz, Members of the Hungarian Academy of Sciences 1825-2002 II. (I-P), Spices, Institute for Social Research Centre, Budapest, 2003, 678-679.
- [4] G. Schay, Arpad Kiss, Chemical Communications, 1969.
- [5] G. Schay, Arpad Kiss, Hungarian Science, 1969.
- [6] M. Ban, Arpad Kiss lives and works, Journal of the Hungarian Chemical, 1989.
- [7] G. C. Siberia and Foothills botanical scientist, Remembering the Arpad Kiss academic born 110 years ago, chemist Professor of Szeged, In Szeged XI, 1999, No. 1. p.p. 36-39.
- [8] N. Ban, A consistent research: Remembering Arpad Kiss Academy of Sciences, Szeged scientist chemist, In Szeged XI, 1999, No. 9, 34-37.

CONTRIBUTION OF HENRY CAVENDISH TO THE DEVELOPMENT OF SOME PHYSICAL CHEMISTRY FIELDS

T. Halaši, S. Horvat, J. Mandić, N. Popsavin and S. Vrsajković

¹*Department of chemistry, biochemistry and environmental protection,
University of Novi Sad - Serbia (tibor.halasi@dh.uns.ac.rs)*

ABSTRACT

Henry Cavendish concluded that different gases had the same thermal coefficient of expansion. He developed the concepts of specific heat and enthalpy without establishing them in mathematical terms. Cavendish discovered that when different substances at different temperatures were mixed the final temperature was not determined in the same way as when quantities of the same substance at different temperatures were mixed. Cavendish transformed electricity from a qualitative into a quantitative science.

INTRODUCTION

Henry Cavendish was born on October 10, 1731, in Nice, France. He was an excellent mathematician, electrician, astronomer, meteorologist, geologist, and a chemist equally learned and original. Cavendish died on February 24, 1810 [1].

Cavendish made valuable contributions to physics and chemistry. His work on the combustion of inflammable air (hydrogen) led to the discovery of the composition of water and to the demise of the phlogiston theory [2,3]. He measured the density of several gases with high accuracy [4] and he is also well known for the famous experiment that carries his name for determining the density of the Earth using a torsion balance [5]. In the field of physical chemistry he developed the concepts of specific heat and enthalpy without establishing them in mathematical terms. Together with Coulomb he transformed electricity from a qualitative into a quantitative science [1].

EXPERIMENTS IN PHYSICAL CHEMISTRY

Cavendish measured the vapour pressure of water using the constant volume method and obtained results very close to those that Henri Regnault (*Henri Victor Regnault*, 1810-1878) would obtain almost 50 years later [6]. Afterwards, he proceeded to measure the coefficient of expansion of many gases. Cavendish's method was based on varying the pressure of the gas so

as to maintain the volume constant, a procedure that in 1847 Regnault would claim to be the most accurate [7]. The resulting values of the thermal coefficient of expansion were mostly about $1/370$ for one degree Fahrenheit ($1/205$ in the centigrade scale).

The experiments by which Cavendish was led to the discovery of specific and latent heat appear to have originated in connection with the question as to whether the mixing of equal quantities of water at different temperatures would result in the final temperature being the arithmetical mean of the two. Cavendish was able to show that when known weights of water at different temperature are mixed together, the heat lost by the hotter liquid is strictly equal to the heat gained by the colder one. Here, without realizing it, he was anticipating the concept of enthalpy.

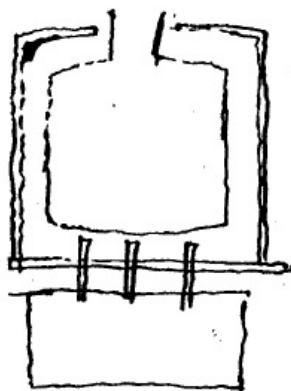


Figure 1. Cavendish's original draft of apparatus for the experiments with latent heat. [8].

In the course of this work Cavendish discovered that when different substances at different temperatures were mixed, the above simple rule no longer held, that is, the final temperature was not determined in the same way as when quantities of the same substance at different temperatures were mixed. Substances accordingly were found to differ as regards their thermal capacity [1].

From his early experiments on latent heats Cavendish was already aware that the temperature remains constant during a change in phase. In the latter publication Cavendish remarked that the cause of the rise in temperature that takes place during freezing is to be thought in the general principle "that all, or almost all, bodies by changing from a fluid to a solid state, or from the state of an elastic to that of an inelastic fluid, generate heat; and that cold is produced by the contrary process" [9].

In the first paper on the subject of electricity Cavendish started from the theory of Aepinus assuming that electricity was caused by an elastic fluid (electric fluid) interspersed between the particles of bodies and surrounding the bodies themselves in the form of an atmosphere. Cavendish gave two fundamental definitions regarding bodies being positively or negatively electrified: (1) the notion of degree of electrification of a conductor, which he later denominated the compression of electricity (today: electric potential); when the fluid within any body was more compressed than in its natural state he called the body positively electrified; when it was less compressed he called it negatively electrified, and (2) when any body contained more of the electric fluid than it did in its natural state, he called it overcharged, and vice versa [10].

In 1771., Cavendish wrote a paper *Thoughts*, that he never published. It contains a lot of interesting material, and is of importance in more than one respect. Cavendish was able to discuss the familiar phenomena of electrostatics - attraction and repulsion, the behaviour of condensers, and induction in general terms - its meaning is precisely what a modern writer would denote by word potential [1].

Further unpublished work (1772-1773) described Cavendish's ingenious experiment to demonstrate that all points inside an electrified hollow sphere are electrically neutral so that the "redundant fluid" (electrical charge) is lodged entirely on its surface. He also provided the definition of electrostatic capacity: the charges of two conductors that are electrified to "the same degree" are proportional to the capacities. The capacity could be measured directly by discharging the conductors by means of a test plane. Cavendish also discovered that the capacity of condensers of equal dimensions varies according to the substance employed to separate the plates. The latter result, which would later be rediscovered by Michael Faraday (1791-1867), would lead to the definition and measurement of the dielectric constant.

A large part of Cavendish's experimental work on electricity was concerned with measurements of the capacity of conductors and a comparison of the electrical conductivities of various bodies [9]. According to his results "iron wire conducts roughly 400 million better than rain or dishwater; that is, the electricity meets no more resistance in passing through a piece of iron wire 400,000,000 inches long, than through a column of water of the same diameter only one inch long. Sea water conducts 100 times, and a saturated solution of sea salt about 720 times, better than rain water." Much of his work was concerned with finding the ratios of the charges of various bodies of different shapes and sizes to that of a sphere 12.1 inches in diameter, all bodies being equally electrified (charged to the same potential). These

findings carried with them the concept, which would later be known as Ohm's law.

CONCLUSION

The influence of Henry Cavendish to the formation of some fields of physics chemistry is obvious. He did a lot of experiments, mainly in the field of heat and electricity.

ACKNOWLEDGEMENT

The authors wish to thank Ministry of Education and Sciences advance of the Republic of Serbia for financial support this work with Project "European Perspective on the Quality of Education in Serbia", No. 179010.

REFERENCES

- [1] A. J. Berry, Henry Cavendish, his Life and Scientific Work, Hutchinson, London, 1960.
- [2] H. Cavendish, Experiments on Air, Phil. Trans. ,1784, 74, 119-173.
- [3] H. Cavendish, Experiments on Air, Phil. Trans., 1785, 75, 372-384.
- [4] H. Cavendish H., Three Papers Containing Experiments of Factitious Air, Part I, Containing Experiments on Inflammable Air, Phil, Trans., 1766, 56,141-184.
- [5] H. Cavendish, Experiments to Determine the Density of the Earth, Phil. Trans.,1798, 88, 469-526.
- [6] V. Regnault, Des Forces Élastiques de la vapeur d'eau aux différents températures, Mém. Acad. Sci., 1847, 21, 465-476.
- [7] J. Wisniak, Henri-Victor Regnault- The Heat Man, Educ. Quím., 2001, 12, 163-174.
- [8] R. McCormach, Speculative Truth Henry Cavendish, Natural Philosophy, and the Rise of Modern Theoretical Science, Charter 5, Henry Cavendish's Research, University press, Oxford, 2004., 116.
- [9] J. C. Maxwell, J. Larmor, T. E Thorpe, The Scientific Papers of the Honourable Henry Cavendish, The University Press, Cambridge,1921.
- [10] H. Cavendish, An Attempt to Explain Some of the Principal Phenomena of Electricity by Means of an Elastic Fluid, Phil. Trans.,1771, 61, 584-677.

PHARMACEUTICAL
PHYSICAL CHEMISTRY

IN VITRO MODELLING OF ANGIOTENSIN- CONVERTING ENZYME INHIBITOR'S ORAL ABSORPTION USING MICELLAR THIN-LAYER CHROMATOGRAPHY

J. Odović¹, B. Marković² and K. Karljiković-Rajić¹

¹Department of Analytical Chemistry, (jodovic@pharmacy.bg.ac.rs)

²Department of Pharmaceutical Chemistry, University of Belgrade - Faculty of Pharmacy, Vojvode Stepe 450, 11221 Belgrade, Serbia

ABSTRACT

Twelve angiotensin-converting enzyme (ACE) inhibitors were studied to evaluate correlation between their literature available absorption data (ABS) and hydrophobicity, k_m parameter, obtained in micellar thin-layer chromatography (MTLC). The theoretical considerations showed that geometric molecular descriptor - volume value (Vol) should be considered, as independent variable, simultaneously with calculated hydrophobicity parameters in multiple linear regression (MLR) analysis to obtain reliable correlation between ACE inhibitor's absorption and lipophilicity (calculated KOWWINlog P) and that captopril should be excluded from further correlations (after its exclusion R^2 was 0.6847). The relationship between literature available and absorption data predicted by MLR, using Vol values besides MTLC hydrophobicity k_m parameter, were studied. It was proved that this parameter accompanied with Vol data is related ($R^2 = 0.6120$) to ACE inhibitors absorption and could be considered for absorption modeling.

INTRODUCTION

Absorption, distribution, metabolism and elimination (ADME) properties has been recognized as critical role in clinical success of drug candidates. The oral drug delivery is the preferred route of administration. The lipophilicity, as a complex physicochemical property is a main determinant of drugs solubility, oral absorption, plasma protein binding, metabolism, elimination and is the most frequently used parameter in quantitative structure-activity relationship (QSAR). The lipophilicity is characterized by the n -octanol/water partition coefficient ($\log P_{O/W}$) and can be determined by traditional technique so-called *shake flask* method [1]. The different chromatographic techniques such as MTLC are also known as well established methods that can yield a significant amount of reproducible retention data for structurally different compounds which can be correlated

with their physicochemical and biological properties at the first place lipophilicity [1]. The main topics of this study were to evaluate experimentally obtained k_m values as measure of ACE inhibitor's lipophilicity through its correlation with calculated hydrophobicity parameters, KOWWINlog P values as well as to model ACE inhibitor's absorption using k_m parameters, including additional independent variable geometric molecular descriptor - volume value (Vol) by MLR analysis.

EXPERIMENTAL

Twelve selected ACE inhibitors were investigated **1.** enalapril maleate, **2.** quinapril hydrochloride, **3.** fosinopril sodium, **4.** lisinopril dihydrate, **5.** cilazapril monohydrate, **6.** ramipril, **7.** benazepril hydrochloride, **8.** perindopril erbumin, **9.** moexipril, **10.** zofenopril calcium, **11.**trandolapril, and **12.** captopril. The study of selected ACE inhibitors was performed on RP-TLC C₁₈ plates, commercially available, (Art. 5559, E. Merck, Germany). The mobile phase was composed of 20% tetrahydrofuran (THF) and 80% phosphate buffer (pH = 6.8) with addition of polyoxyethylene (23) lauryl ether, Brij 35 varied in concentration from 0.01 to 0.06 M. The detection was performed under UV lamp ($\lambda = 254$ nm), after development, by ascending technique. All investigations were performed at room temperature ($25 \pm 2^\circ\text{C}$).

The Excel 2003 from Microsoft Office and Origin 7.0 PRO (Origin Lab Corporation, USA) were used to perform the statistical analysis of the regression. The calculations in regarding to ACE inhibitors lipophilicity descriptors, log P values, as well as their aqueous solubility data, expressed as log S , electronic descriptor - polar surface area (PSA); constitutional parameter - molecular mass (Mr) and geometric descriptor - volume value (Vol) were established using appropriate software packages [2,3]. The calculated KOWWIN log P values were from -0.94 to 6.61; log S values were from -4.70 to -2.35; TPSA values from 95.9 to 132.9 Å²; Mr values from 217.3 to 563.7 and Vol values varied from 356.8 to 538.7. The human intestinal absorption data (ABS) of examined ACE inhibitors were collected from relevant textbook, Clarke's Analysis of Drugs and Poisons [4] and were in the range of 22% to 96%.

RESULTS AND DISCUSSION

The investigated ACE inhibitors were studied to evaluate correlation between their intestinal absorption and MTLC lipophilicity data. According to Foley [5] the following relationship (Eq. 1.) can be established between retention parameter k' and micelle (surfactant) concentration in eluent:

$$\frac{1}{k'} = \frac{1}{k_m} + \frac{K_{AM}}{k_m} [M] \quad (1)$$

where $[M]$ correspond to surfactant concentration in mobile phase, K_{AM} is the constant describing solute-micelle binding and k_m is the solute retention parameter corresponding to surfactant monomer concentration equal to the CMC. The parameters K_{AM} and k_m can be evaluated from the slope and intercept of experimental $1/k'$ versus $[M]$ relationships. The micellar parameter k_m can be considered as analogous to R_M^0 (hydrophobicity parameter) in reversed phase (RP) TLC and different authors [5,6] showed relationship between k_m or $\log k_m$ as a lipophilicity descriptors and $\log P$ values. The hydrophobicity parameter k_m obtained in present MTLC study (Table 1.) showed good correlation ($R^2 = 0.8043$) with calculated KOWWIN $\log P$ values.

Table 1. The MTLC hydrophobicity parameters, calculated molecular descriptors and intestinal absorption data of the selected ACE Inhibitors

ACE I	k_m	ABS	KOWWIN $\log P$	Vol
1	0.262(± 0.005)	60	2.45	356.8
2	0.136(± 0.007)	60	3.72	411.4
3	0.040(± 0.005)	36	6.61	538.7
4	0.668(± 0.013)	25	-0.94	384.4
5	0.138(± 0.008)	60	2.27	392.5
6	0.126(± 0.005)	54	3.32	396.4
7	0.112(± 0.003)	37	3.5	394.8
8	0.289(± 0.004)	70	2.59	358.3
9	0.206(± 0.003)	22	3.36	462.4
10	0.070(± 0.008)	96	3.94	376.1
11	0.123(± 0.006)	70	3.81	413.17
12	0.286(± 0.009)	65	0.84	195.65

As the main topic of the study, possible correlation between MTLC hydrophobicity data, k_m and intestinal absorption data of examined ACE inhibitors was established. The preliminary, theoretical MLR analysis of all 12 studied ACE inhibitors with application of different molecular descriptors and calculated KOWWIN $\log P$ values, as independent variables indicate molecular descriptor, Vol value as suitable for correlation between predicted and literature available ABS. This MLR analysis also confirmed that captopril should be excluded from further correlations since considerably lower correlation coefficients were obtained with captopril ($R^2=0.4632$) than after its exclusion ($R^2=0.6847$). It could be assumed that

captopril was excluded from proposed model since this ACE inhibitor belongs to different group – sulfhydryl group, with different structure and notably lower Vol value in comparison to other investigated drugs.

In further modeling, possible substitution of KOWWIN $\log P$ with MTLC hydrophobicity data, k_m were evaluated. With application of molecular descriptor, Vol value and k_m parameter as independent variables MLR analysis provide following correlation (Eq. 2.) with acceptable probability value ($P < 0.05$):

$$\text{ABS}_{\text{predicted}} = -83.4(\pm 30.0)k_m - 0.31(\pm 0.10)\text{Vol} + 194.7(\pm 43.4)$$
$$n = 11, R^2 = 0.6120, S = 15.353, F = 6.309 \quad (2)$$

The obtained correlation could be evaluated as good as proposed (R^2 range 0.49-0.79) by Asuero et al. 2006 [7].

The results discussed above make it obvious that MTLC lipophilicity data, k_m parameters accompanied with molecular descriptor, Vol values are closely related to ACE inhibitors absorption data and could be considered for their absorption modeling.

CONCLUSION

The results obtained in MTLC showed good correlation ($R^2 = 0.6120$) between predicted and literature available absorption data of ACE inhibitors. The current MTLC study represents another approach, besides other chromatographic techniques (RP-TLC, salting-out TLC), for correlation between absorption and lipophilicity.

ACKNOWLEDGEMENT

This work was partially supported by the Ministry of Education, Science and Technological Development of the Republic of Serbia as a part of Project TR34031.

REFERENCES

- [1] R. Kaliszan, Chem. Rev., 2007, 107, 3212–3246.
- [2] Virtual Computational Chemistry Laboratory: www.vcclab.org
- [3] Molinspiration software: www.molinspiration.com
- [4] A.C. Moffat, M.D. Osselton, B. Widdop (eds), Clarke's Analysis of Drugs and Poisons, 4th ed. Pharmaceutical Press, London, 2011.
- [5] J.P. Foley, Anal. Chim. Acta., 1990, 231, 237-247.
- [6] M. Jnicka, D. Pietras-Ozga, J. Planar Chromat., 2010, 23, 396-399.
- [7] A.G. Asuero, A. Sayago, A.G. Gonzalez, Crit. Rev. Anal. Chem., 2006, 36, 41-59.

**DEVELOPMENT OF REVERSED-PHASE THIN-LAYER
CHROMATOGRAPHY (RP-TLC) ASSAY FOR
LIPOPHILICITY ASSESMENT OF 17 β -CARBOXAMIDE
DERIVATIVES OF PREDNISOLONE AND
DEXAMETHASONE**

V. Dobričić, A. Stanišić, B. Marković, S. Vladimirov and O. Čudina

*Department of Pharmaceutical Chemistry, University of Belgrade-Faculty
of Pharmacy, 11000 Belgrade, Serbia*

ABSTRACT

Reversed-phase thin-layer chromatography (RP-TLC) assay was developed for lipophilicity assessment of 17 β -carboxamide derivatives of prednisolone and dexamethasone. Retention parameters R_M^0 were determined for all tested compounds using four different mixtures of acetonitrile and water as mobile phase, and compared with the octanol-water partition coefficients (logP) determined using the traditional shake-flask method. Good correlation ($r = 0.93$) was obtained between logP and R_M^0 , indicating that RP-TLC could be used as an alternative to the shake-flask method for fast and simple estimation of lipophilicity of newly synthesized 17 β -carboxamide steroids.

INTRODUCTION

Soft glucocorticoids are derivatives with fewer side effects than traditional glucocorticoids. These compounds are synthesized from inactive metabolites using the retrometabolic approach and are usually administered locally near the site of action. Apart from esters, 17 β -carboxamide derivatives of cortienic acids have also been synthesized [1]. Some of these derivatives showed glucocorticoid activity (inhibition of haemagglutinin-mediated proliferation of lymphocytes).

The shake-flask method is a traditional method for determination of lipophilicity, based on the partitioning of a compound between water and octanol. However, this method is time-consuming and requires relatively large amounts of tested compounds and solvents.

The aim of this study was to develop a RP-TLC based assay that could be used for simple and fast estimation of lipophilicity of 17 β -carboxamide steroids. To this aim, octanol/water partition coefficients (logP) of these compounds were determined using the traditional shake-flask method and

correlated with retention parameters (R_M^0) obtained using the proposed RP-TLC method.

EXPERIMENTAL

17 β -carboxamide derivatives of prednisolone and dexamethasone tested in this study have been already synthesized and structurally characterized [2]. These compounds are amides of cortienic acids obtained from prednisolone and dexamethasone with methyl or ethyl esters of amino acids (L-glycine, L-alanine, β -alanine and L-phenylalanine). Structures of these compounds are presented in Table 1.

Saturated water solutions were prepared from all tested compounds. Partitioning between water and n-octanol was performed in 5-ml glass tubes equipped with PTFE screw-caps. 2 ml of saturated water solution of a tested compound and 2 ml of n-octanol were added into a glass tube, which was covered with PTFE screw-caps and stirred at ambient temperature for one hour. Finally, the tube was centrifuged for 15 minutes at 3000 rpm, the aqueous phase was carefully withdrawn and used for further analysis. Concentrations of the tested compound were determined in the saturated water solution (starting solution, C_0 , equation 1) and in the aqueous phase after the shake-flask experiment (C , equation 1).

$$\log P = \log\left(\frac{C_0 - C}{C}\right) \quad (1)$$

Thin-layer chromatography was performed on plates of reversed-phase silica RP-18 F254. Mobile phases consisted of acetonitrile and water in different ratios (4:6; 5:5; 6:4 and 7:3, v/v). All tested compounds were dissolved in methanol (1 mg/ml). The plates were spotted with 1 μ L aliquots of these solutions and developed by the ascending technique in glass TLC chambers with glass lids. After development, the spots were observed under UV light ($\lambda=254$ nm) [3].

RESULTS AND DISCUSSION

Octanol/water partition coefficients ($\log P$) of all tested compounds were calculated and presented in the Table 1.

Retention factors (R_f) were calculated for each compound and each mobile phase according to the equation (2) and used for the calculation of retention parameters R_M (equation (3)):

$$R_f = \frac{l}{l_0} \quad (2)$$

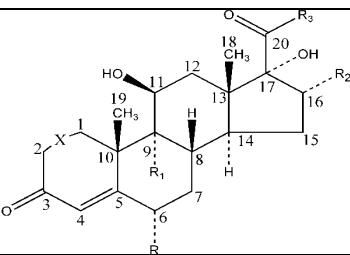
l -Distance from the base line to the center of the spot

l_0 -Distance from the base line to the mobile phase front

$$R_M = \log\left(\frac{l}{l_0} - 1\right) \quad (3)$$

Subsequently, for each compound R_M values were plotted to corresponding percentage of acetonitrile and linear relationships were obtained ($R^2=0.973-0.996$). Finally, R_M^0 values were determined by extrapolation of these lines (R_M^0 represents theoretical R_M value obtained with 100% water (0% acetonitrile) as mobile phase). R_M^0 values of all tested compounds are presented in Table 1.

Table 1. Chemical structures, logP and R_M^0 values of tested compounds



Compound	-X-	R	R ₁	R ₂	R ₃	logP	R_M^0
Prednisolone	-C=C-	H	H	H	CH ₂ OH	1.59	1.73
PG	-C=C-	H	H	H	NHCH ₂ COOCH ₃	1.63	1.78
PA	-C=C-	H	H	H	NH(CH)CH ₃ COOCH ₃	1.96	2.41
PEG	-C=C-	H	H	H	NHCH ₂ COOCH ₂ CH ₃	2.01	1.86
PEA	-C=C-	H	H	H	NHCH ₂ CH ₂ COOCH ₂ CH ₃	2.15	1.97
PF	-C=C-	H	H	H	NH(CH)CH ₂ C ₆ H ₅ COOCH ₃	2.85	3.32
Dexamethasone	-C=C-	H	H	CH ₃	CH ₂ OH	1.92	2.14
DG	-C=C-	H	H	CH ₃	NHCH ₂ COOCH ₃	1.79	2.16
DA	-C=C-	H	H	CH ₃	NH(CH)CH ₃ COOCH ₃	2.07	2.54
DEG	-C=C-	H	H	CH ₃	NHCH ₂ COOCH ₂ CH ₃	2.28	2.68
DEA	-C=C-	H	H	CH ₃	NHCH ₂ CH ₂ COOCH ₂ CH ₃	2.16	2.79
DF	-C=C-	H	H	CH ₃	NH(CH)CH ₂ C ₆ H ₅ COOCH ₃	3.23	3.80

Good correlation obtained between logP and R_M^0 values ($r = 0.93$, Figure 1) indicates that the proposed RP-TLC assay can be used instead of the shake-flask method for fast and simple lipophilicity assessment of newly synthesized 17 β -carboxamide steroids.

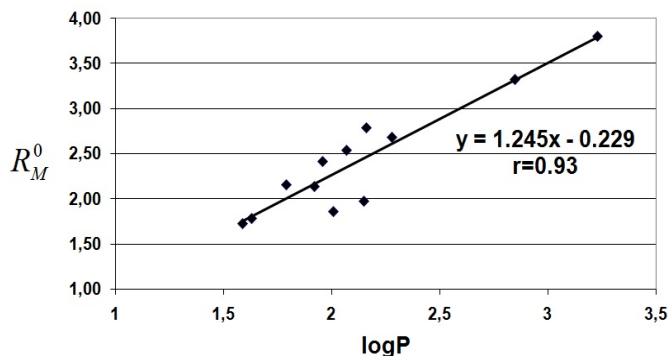


Figure 1. Correlation between logP and R_M^0

CONCLUSION

Octanol-water partition coefficients (logP) of prednisolone, dexamethasone and ten 17 β -carboxamide derivatives of these glucocorticoids were determined using the shake-flask method and compared with retention factors R_M^0 determined using the RP-TLC assay developed herein. Good correlation ($r = 0.93$) between logP and R_M^0 indicates that the proposed RP-TLC assay requires less material, and can be used as a fast and simple alternative to the shake-flask method for lipophilicity assessment of newly synthesized 17 β -carboxamide steroids.

ACKNOWLEDGEMENT

This work was partially supported by the Ministry of Education, Science and Technological development of the Republic of Serbia (Grant no. 172041)

REFERENCES

- [1] B. Manz, M. Rehder, A. Heubner, R. Kreienberg, H.-J. Grill, K. Pollow, *J. Clin. Chem. Clin. Biochem.*, 1984, 22, 209-214.
- [2] V. Dobričić, B. Marković, K. Nikolic, V. Savić, S. Vladimirov, O. Čudina, *Eur. J. Pharm. Sci.*, 2014, 52, 95-108.
- [3] T. Csermely, H. Kalasz, K. Deak, M. Hasan, F. Darvas, G. Petroianu, *J. Liq. Chromatogr. R. T.*, 2008, 31, 2019-2034.

INVESTIGATION OF THE REACTION BETWEEN TETRACYCLINES AND 2,2-DIPHENYL-1-PICRYLHYDRAZYL RADICAL

S. M. Sunarić and N. B. Tatić

*Department of Chemistry, Faculty of Medicine, University of Niš, Bulevar
Zorana Djindjica 81, 18000 Niš, Serbia*

ABSTRACT

In the present work the reactions of oxytetracycline, tetracycline and doxycycline with stable organic nitrogen radical 2,2-diphenyl-1-picrylhydrazyl (DPPH) were investigated. The reactivity of different tetracyclines was compared based on the reaction rates at the selected time and on the percentage of DPPH inhibited. The highest % of inhibition in the first 10 minutes of reaction was achieved by oxytetracycline and tetracycline, while doxycycline was the least active. All of the investigated antibiotics have shown significant DPPH inhibition with concentrations which can be expected by using this drugs in conventional therapy.

INTRODUCTION

Free radicals initiate and promote pathological processes reacting by the specific radical chain reaction mechanism and altering macromolecules. Drug molecules can build chemical complexes and other products with different types of radical species [1]. As a result, active drug concentration can be reduced and its activity can be altered. Changes in cellular activity can also appear [2]. Tetracycline antibiotics (tetracyclines) are used in therapy and prevention of bacterial and protozoal infections. Therefore, it is important to investigate the potential of tetracyclines for reaction with free radicals.

EXPERIMENTAL

The stock solution of DPPH reagent (30 μ M) was prepared by dissolving DPPH standard substance (Sigma-Aldrich) in 95% methanol (Zorka Pharma). The stock solutions of oxytetracycline (100 μ g/mL), tetracycline (100 μ g/mL) and doxycycline (200 μ g/mL) were prepared by dissolving the required amounts of oxytetracycline-hydrochloride, tetracycline-hydrochloride and doxycycline-hydrochloride standard substances (Sigma-Aldrich) in 95% methanol (Zorka Pharma).

The method is based on the decolorization of the violet DPPH solution with addition of antibiotics. The absorbance decrease is proportional to the amount of reduced DPPH [3]. The absorbance change was followed spectrophotometrically by Evolution 60 spectrophotometer (Termo-Fischer Scientific USA). The series of antibiotic reaction solutions were made by mixing x ml of the antibiotic standard solution with $2-x$ ml of methanol and 1 ml of standard DPPH solution. The concentrations of oxytetracycline, tetracycline and doxycycline in the reaction vessels were 0.00, 6.67, 10.00, 20.00, 33.33 and 40.00 $\mu\text{g/mL}$. The tubes were kept in the dark at the room temperature of 20°C . The absorbance was measured at 520 nm against methanol after 10, 30, 60, 90, 120, 150 and 180 minutes from the reaction start. Radical scavenging activity was calculated as % inhibition = $[(A_0 - A_c)/A_0] \cdot 100$, where A_0 is absorption of a referent sample (antibiotic concentration 0.00 $\mu\text{g/mL}$) and A_c is absorption of tested solution.

RESULTS AND DISCUSSION

All of the examined antibiotics have shown notable activity towards DPPH radicals (Table 1). Higher concentrations caused higher DPPH free radical inhibition and the absorbance was decreasing with time in the observed time interval (Figure 1). The highest inhibition percentage was achieved by oxytetracycline for all time intervals and all concentrations (Table 2). Doxycycline was proved to be the least active up to 10 minutes from the reaction start. Further, tetracycline has shown the lowest inhibition percentage after 90 minutes.

Instantaneous rates of the reactions, dA/dt , were determined from the slopes of the tangents to the experimentally obtained absorbance–time curves at selected times [4]. After 10 minutes from the start, oxytetracycline reaction was the fastest, while doxycycline reaction was the slowest. With the progression of time until 30 min all of the three reactions were become slower, but oxytetracycline has shown higher changes in reaction rates between 10 min and 30 min (Table 2).

Difference in radical scavenging activity of investigated tetracyclines against DPPH is the result of structural differences. According to some authors, the reactive site of the tetracycline antibiotics is not just a phenolic -OH group, but all of the -OH groups present in the molecule [1]. Therefore, we can assume that high oxytetracycline activity is due to the presence of six hydroxyl groups bound directly to octahydronaphthacene structure. Containing five hydroxyl groups, tetracycline and doxycycline showed a lower activity against 2,2-diphenyl-1-picrylhydrazyl radical.

Table 1. Activity of examined tetracycline antibiotics against DPPH.

c ($\mu\text{g/mL}$)	% inhibition \pm SD								
	Oxytetracycline			Tetracycline			Doxycycline		
	10 min	90 min	180 min	10 min	90 min	180 min	10 min	90 min	180 min
6.67	20.0	31.0	36.4	7.4	11.7	18.0	1.5	26.3	35.3
	\pm	\pm	\pm	\pm	\pm	\pm	\pm	\pm	\pm
	2.2	2.4	2.0	0.9	1.2	2.1	0.6	2.6	2.3
10.0	26.1	40.5	46.3	13.2	20.0	25.4	3.1	28.6	38.2
	\pm	\pm	\pm	\pm	\pm	\pm	\pm	\pm	\pm
	2.0	1.0	1.9	1.0	2.2	1.8	0.5	2.2	2.4
20.0	46.1	65.5	73.5	23.1	33.3	38.5	10.8	39.8	49.3
	\pm	\pm	\pm	\pm	\pm	\pm	\pm	\pm	\pm
	1.1	1.8	1.8	2.4	2.1	1.6	1.7	2.0	2.1
33.33	61.7	81.0	89.3	31.4	45.0	51.6	12.3	45.9	57.4
	\pm	\pm	\pm	\pm	\pm	\pm	\pm	\pm	\pm
	2.3	2.0	2.5	0.9	2.4	2.3	1.7	2.0	2.7
40.0	67.0	86.2	90.1	33.9	49.2	56.6	15.4	53.4	63.2
	\pm	\pm	\pm	\pm	\pm	\pm	\pm	\pm	\pm
	2.5	2.2	1.1	2.0	2.8	1.7	2.2	1.7	2.1

Table 2. Average instantaneous reaction rates for tetracycline antibiotics obtained for three measurements. Relative standard deviation was $< 8\%$.

c ($\mu\text{g/mL}$)	- dA/dt (min^{-1})					
	Oxytetracycline		Tetracycline		Doxycycline	
	10 min	30 min	10 min	30 min	10 min	30 min
6.67	$1.48 \cdot 10^{-3}$	$1.33 \cdot 10^{-4}$	$4.55 \cdot 10^{-4}$	$1.0 \cdot 10^{-4}$	$4.78 \cdot 10^{-4}$	$2.67 \cdot 10^{-4}$
10.0	$1.88 \cdot 10^{-3}$	$2.00 \cdot 10^{-4}$	$8.05 \cdot 10^{-4}$	$1.5 \cdot 10^{-4}$	$5.28 \cdot 10^{-4}$	$2.67 \cdot 10^{-4}$
20.0	$3.03 \cdot 10^{-3}$	$3.33 \cdot 10^{-4}$	$1.51 \cdot 10^{-3}$	$2.5 \cdot 10^{-4}$	$1.08 \cdot 10^{-3}$	$3.83 \cdot 10^{-4}$
33.33	$3.94 \cdot 10^{-3}$	$3.67 \cdot 10^{-4}$	$2.11 \cdot 10^{-3}$	$2.5 \cdot 10^{-4}$	$1.48 \cdot 10^{-3}$	$4.67 \cdot 10^{-4}$
40.0	$4.23 \cdot 10^{-3}$	$3.83 \cdot 10^{-4}$	$2.36 \cdot 10^{-3}$	$2.5 \cdot 10^{-4}$	$1.63 \cdot 10^{-3}$	$4.83 \cdot 10^{-4}$

CONCLUSION

DPPH method can be applied for the estimation of general radical scavenging capability of tetracycline antibiotics. Overall efficacy of tetracyclines against DPPH radicals can be expressed both as the amount of a substance needed for the free radical inhibition and the time required achieving significant inhibition level. Based on the results in this work, it

can be concluded that examined antibiotics, with their therapeutic concentrations, could show a significant interaction with nitrogen free radicals.

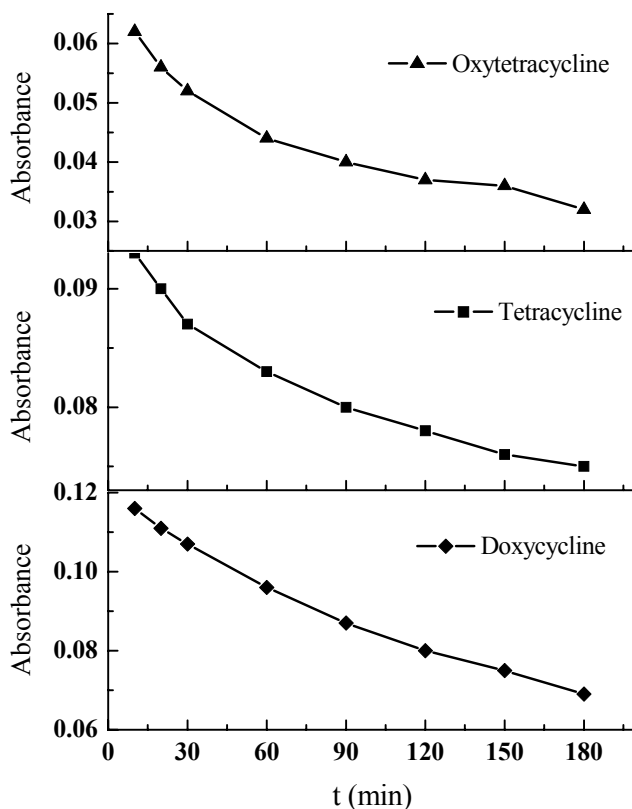


Figure 1. The dependence of the absorbance on the time for the concentration of 20.0 µg/mL for all selected antibiotics.

REFERENCES

- [1] M.O.Griffin, E.Fricovsky, G.Ceballos, F.Villarreal, *Am. J. Physiol. Cell. Physiol.*, 2010, 299(C), 539-548.
- [2] M.E.Huth, A.J.Ricci, A.G.Cheng, *Inter. J. of Otolaryngology*, 2011, volume 2011, Article ID 937861, doi:10.1155/2011/937861.
- [3] P. Molyneux, *J. Sci. Technol.*, 2004, 26 (2), 211-219.
- [4] *Chemical Kinetics and Mechanism*, M. Mortimer, P. Taylor (Eds.), The Open University, Royal Society of Chemistry, Cambridge, UK, 2002.

COMPROMISED GLUTATHIONE-DEPENDENT REDOX SYSTEM OF CHRONICALLY-ISOLATED RATS: A HARMFUL SIDE EFFECT OF CLOZAPINE

M. Bošković, N. Todorović and D. Filipović

Laboratory of Molecular Biology and Endocrinology, Institute of Nuclear Sciences "Vinča", University of Belgrade, Serbia

ABSTRACT

Changes in glutathione (GSH)-related systems are implicated in depressive disorders. Since chronic psychosocial stress contributes to depression, we investigated the effects of 21d of chronic social isolation (CSIS) stress, an animal model of depression, as well as chronic administration of clozapine, an atypical antipsychotic, on GSH content, glutathione peroxidase (GPx) and glutathione reductase (GLR) in the prefrontal cortex of rats. Increased GPx protein expression and its activity in clozapine-treated (controls or chronically-isolated) rats as well as in CSIS group were found. Nonetheless, clozapine administration caused decrease in GSH content but no effects on GLR in controls and CSIS group. Data indicate that CSIS compromises GSH-dependent redox system promoting oxidative stress in rat prefrontal cortex which can't be protected by clozapine. Moreover, clozapine administration in controls has a harmful side effect on this redox system.

INTRODUCTION

Chronic psychosocial stress, as a risk factor of depression, may disturb redox-status in the cell, causing oxidative stress. To maintain redox-homeostasis and counteract to oxidative stress, cells use antioxidant defense system such as glutathione (GSH)-dependent redox system. This system includes GSH, GPx that eliminates peroxides with a concomitant oxidation of GSH to GSSG, and GLR which catalyses reduction of GSSG to GSH. Compromised GSH associated with oxidative stress in the brain has been shown as feature of depression [1]. Based on our previous finding that 21d of chronic social isolation (CSIS) stress on male Wistar rats induces depressive- and anxiolytic-like behaviours [2], we treated chronically-isolated animals with antipsychotic clozapine because recent study has suggested that some atypical antipsychotic drugs may have protective properties against oxidative stress [3]. Clozapine is an atypical antipsychotic effective in treating depressive patients who are resistant to typical antipsychotic drugs [4]. Hence, we investigated the effects of social CSIS,

on GSH content, GPx and GLR protein expression and its activity, in the rat prefrontal cortex and role of clozapine (21d) in rectifying possible changes. The prefrontal cortex was chosen for investigation as it is included in stress response and susceptible to a neurochemical and structural changes under the chronic psychosocial stress as those observed in mental illness.

EXPERIMENTAL

Adult male Wistar rats, 2.5 months old at the onset of the experiment, served as subjects. Control groups consisted of four animals per cage, while rats underwent CSIS were housed individually for 21d. Clozapine was administered daily by intraperitoneal (i.p.) injections of 20 mg/kg during the 21d in both control (Con+Cloz) and chronically-isolated (CSIS+Cloz) groups. We already reported that chronically administration of 20 mg/kg/day of clozapine in rats produces a serum drug level therapeutically relevant in humans [5]. Vehicle-treated rats received daily i.p. injections of 0.9% NaCl (Con+NaCl and CSIS+NaCl groups). Isolated prefrontal cortexes were subcellular fractionated to prepare cytosolic tissue protein extracts. GPx and GLR protein expression was investigated by Western blot, while GSH content was determined by spectrophotometric method [6]. GPx activity was determined using Randox commercial kit [7], while GLR activity was measured by method of Halliwell and Foyer [8]. Results were analyzed by two-way ANOVA followed by Duncan's post-hoc test. The data are expressed as mean \pm S.E.M. of 5-6 animals per group.

RESULTS AND DISCUSSION

The relative changes in GPx and GLR protein expression are presented in Figure 1, while GSH content as well as GPx and GLR activity are presented in Table 1.

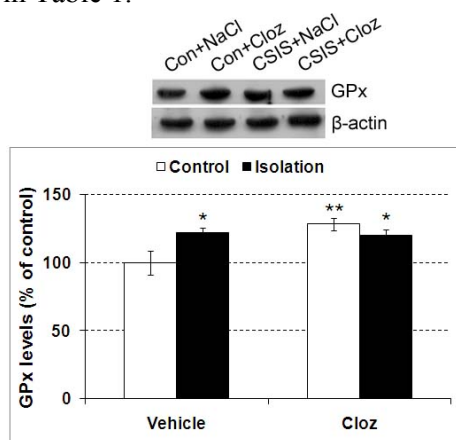
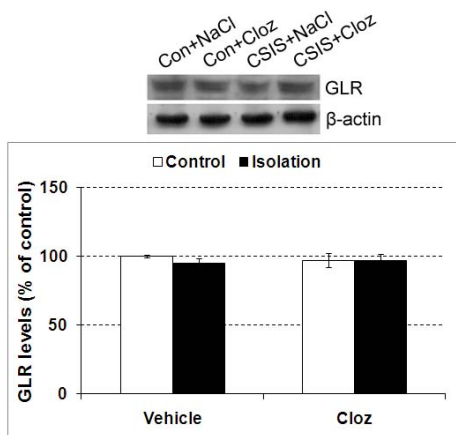


Figure 1. Cytosolic GPx and GLR protein expression in the prefrontal cortex of controls and chronically-isolated male rats treated either with vehicle (0.9% NaCl) or 20 mg/kg/day of clozapine, respectively.



Significant differences are indicated as follows: * $p < 0.05$, ** $p < 0.01$ clozapine treatment or/and isolation vs vehicle-treated controls.

Table 1. Prefrontal cytosolic GSH content, GPx and GLR activity in controls and chronically-isolated rats treated with either 0.9% NaCl or 20 mg/kg/day of clozapine. Asterisks indicate comparison between: clozapine treatment or/and isolation vs vehicle-treated controls, * $p < 0.05$, ** $p < 0.01$

Groups	GSH levels (nmol/mg protein)	GPx activity (mU/mg protein)	GLR activity (mU/mg protein)
Con + NaCl	68.78 ± 3.90	43.48 ± 0.57	24.70 ± 0.45
Con + Cloz	54.95 ± 2.35 **	52.30 ± 2.49 **	24.23 ± 1.35
CSIS + NaCl	60.25 ± 2.89 *	51.42 ± 2.05 **	24.61 ± 1.14
CSIS + Cloz	54.03 ± 0.58 **	51.55 ± 1.54 **	22.59 ± 1.57

Significant decrease of GSH content in CSIS group as compared to controls (* $p < 0.05$) may be consequence of increased oxidative stress as well as increased GPx activity that uses the GSH for the catalytic reduction of hydrogen peroxide. Increased GPx protein expression (* $p < 0.05$) and its activity (** $p < 0.01$) in CSIS rats might contribute to protection of the prefrontal cortex from CSIS-induced oxidative stress. Despite GSH consumption during CSIS, unchanged protein expression and activity of GLR may diminish GSH recycling due to inability of GLR to compensate increased GSH consumption by GPx. Clozapine treatment alone, as well as in combination with CSIS, caused oxidative stress judged by increased GPx protein expression (** $p < 0.01$, * $p < 0.05$) and its activity (** $p < 0.01$) associated with decreased GSH content (** $p < 0.01$) and unaltered GLR protein expression and activity. The present findings concur with previous

obtained results in the liver where clozapine administration used here (21d) reinforce hepatic oxidative stress in chronically-isolated rats, judged by increased nitric oxide and lipid peroxidation, GSH depletion and caused hepatotoxicity [5]. This implies that chronic administration of clozapine, in addition to the liver, also compromises GSH redox system in the prefrontal cortex and failed to protect this structure from oxidative stress following CSIS, moreover it caused the same.

CONCLUSION

Results demonstrate presence of oxidative stress following CSIS in the rat prefrontal cortex, as evidenced by GSH depletion, increased GPx and unchanged GLR protein expression and its activity. Chronic administration (21d) of 20 mg/kg/day of clozapine failed to prevent oxidative stress in chronically-isolated rats and compromised GSH-dependent redox system in controls, as well. Although in terms of efficacy versus typical antipsychotic, clozapine remains an unparalleled choice, our finding together with clozapine study, which demonstrated oxidative cell injury in the brain via increased levels of membrane lipid peroxidation and total protein oxidation [9], confirms that clozapine should be considered as a second choice drug in depressive therapy.

ACKNOWLEDGEMENT

This work was supported by the Ministry of Education, Science and Technological Development of the Republic of Serbia (Grant no. 173023).

REFERENCES

- [1] S.N.Pal, P.C.Dandiya, *Pharmacol.Biochem.Behav.*, 1994, 48, 845-851.
- [2] J.Zlatković, N.Todorović, M.Bošković, S.B.Pajović, M.Demajo, D.Filipović, *Mol.Cell. Biochem.*, 2014, 393, 43-57.
- [3] O.P. Singh, I.Chakraborty, A.Dasgupta, S.Datta, *Indian J.Psychiatry*, 2008, 50, 171-176.
- [4] J.Kane, G.Honigfied, J.Singer, 1989, *Psychopharmacology*, 99, 560-563.
- [5] J.Zlatković, N.Todorović, N.Tomanović, M.Bošković, S.Djordjević, T.Lazarević-Pašti, R.E.Bernardi, A.Djurdjević, D.Filipović, *Eur.J.Pharm. Sci.*, 2014, 59, 20-30.
- [6] P.J.Hissin, R.Hilf, *Anal.Biochem.*, 1976, 74, 214-226.
- [7] D.E.Paglia, W.N.Valentine, *J.Lab.Clin.Med.*, 1967, 70, 158-169.
- [8] B.Halliwel, C.H.Foyer, *Planta*, 1978, 139, 9-17.
- [9] V.E.Barakauskas, A.R.Ypsilanti, A.M.Barr, S.M.Innis, W.G.Honer, C.L.Beasley, *Prog.Neuropsychopharmacol.Biol.Psychiatry*, 2010, 34, 669-673.

OLANZAPINE REVERTS THE ISOLATION-INDUCED ALTERATIONS IN RAT HEPATIC GLUTATHIONE-DEPENDENT DEFENSE SYSTEM

N. Todorović, J. Stevanović and D. Filipović

Laboratory of Molecular Biology and Endocrinology, Institute of Nuclear Sciences Vinča, University of Belgrade, Serbia

ABSTRACT

Chronic psychosocial stress is a risk factor for depression. As the liver is a primary organ for drug activation and detoxification, the effect of chronic administration of olanzapine on rat hepatic glutathione (GSH)-dependent defense system including GSH, glutathione peroxidase (GPx) and glutathione reductase (GLR), following 21d of chronic social isolation stress (CSIS), an animal model of depression, was investigated. Increased GSH content in olanzapine-treated controls was found. Protein levels of GPx were increased in both vehicle- and olanzapine-treated chronically-isolated animals while significant increase in GPx activity was seen only in olanzapine-treated chronically-isolated animals. Reduced activity of GLR in CSIS group that was not in correspondence with its protein level was increased by olanzapine. The results imply that chronic administration of olanzapine reverts the alternations in hepatic GSH-dependent defense of stressed rats caused by CSIS.

INTRODUCTION

Our recent study has shown that chronic social isolation (CSIS) caused oxidative stress in rat liver, measured by compromised superoxide dismutase activity [1]. To neutralize oxidative stress cells use glutathione (GSH)-dependent defense system which includes GSH, glutathione peroxidase (GPx) and glutathione reductase (GLR). GSH acts as co-substrate for GPx, an enzyme catalyzing the reaction of endogenous peroxides reduction that converts GSH to oxidized glutathione (GSSG). GLR is able to reduce GSSG back to GSH and, thus, to maintain reduced state of GSH in the cells. Redox dysregulation via impaired regulation of GSH synthesis or altered function of proteins in GSH-dependent defense may contribute to depression. Olanzapine is an atypical antipsychotic that used in treatment of cognitive deficits observed in mental disorders [2] and may have protective properties against oxidative stress [3]. However, the potential role of chronic psychosocial stress and/or various drugs on GSH-

dependent defense in rat liver is still unrevealed. Since the liver is organ with one of the highest antioxidant enzyme capacity in the body and primary site of drug metabolism, we investigated the effects of chronic administration of atypical antipsychotic olanzapine on hepatic GSH content, activity and protein expression of GPx and GLR, following 21d of CSIS stress, an animal model of depression.

EXPERIMENTAL

Adult male Wistar rats, 2.5 months old, weighting 300 to 350 g, were used at the onset of the experiment. Controls (nonstressed rats) were housed in groups of four animals per cage, while stressed rats were housed individually where rats underwent CSIS stress for 6 weeks. Olanzapine-hydrochloride was administered daily by intraperitoneal injections (i.p.) of 7.5 mg/kg during the last 3 weeks of social isolation to both controls (Con+Olan) and socially isolated (CSIS+Olan) rats. This dose of olanzapine has earlier been shown to produce plasma levels in the rat that correspond to clinically effective concentrations in humans [4]. Vehicle-treated animals (Con+Veh and CSIS+Veh) received daily i.p. injections of normal saline (0.9% NaCl). GSH content was determined in the cytosol of the liver according to Hissin and Hilf [5]. GPx and GLR activity were determined by spectrophotometric assays [6, 7] and protein expression by Western blot. Two way ANOVA followed by Duncan's post hoc test was used for statistical data analysis. The values are mean \pm SEM of 6 animals per group.

RESULTS AND DISCUSSION

The increase of GSH in olanzapine-treated control group as compared to control animals was found ($*p<0.05$) (Table 1).

Table 1. Rat hepatic GSH content, GPx and GLR activity. Con = control; Olan = Olanzapine; CSIS = chronic social isolation stress. Symbols indicate comparison between: treated experimental groups and controls $*p<0.05$, $**p<0.01$, $***p<0.001$; CSIS+Olan and vehicle-treated CSIS group $^{\wedge\wedge}p<0.01$, $^{\wedge\wedge\wedge}p<0.001$.

Groups	GSH content (nmol/mg protein)	GPx activity (U/mg protein)	GLR activity (mU/mg protein)
Con+Veh	74.57 \pm 0.78	3.19 \pm 0.17	57.25 \pm 2.05
Con+Olan	87.45 \pm 2.69 *	3.10 \pm 0.14	57.11 \pm 1.17
CSIS+Veh	79.32 \pm 4.29	3.26 \pm 0.17	48.18 \pm 1.32 **
CSIS+Olan	82.48 \pm 3.66	4.13 \pm 0.20 *** $^{\wedge\wedge\wedge}$	54.64 \pm 2.38 $^{\wedge\wedge}$

The GPx activity was increased in olanzapine-treated chronically-isolated group compared to control ($***p < 0.001$) and vehicle-treated CSIS ($^{\wedge}p < 0.001$) group. In regard to GLR, significantly reduced activity was found following CSIS ($**p < 0.01$), while significant increase was seen in olanzapine-treated chronically-isolated animals compared to vehicle-treated CSIS group ($^{\wedge}p < 0.01$).

Protein expression of GPx and GLR are presented in the Figure 1 and 2, respectively. Increase of GPx protein levels in olanzapine-treated chronically-isolated animals ($*p < 0.05$) and its corresponding enzyme activity indicates protective effect of olanzapine against oxidative stress [1]. Opposite of that, lack of correspondence between GPx protein level and its activity in CSIS group may suggest posttranslational protein modifications affecting activity of GPx.

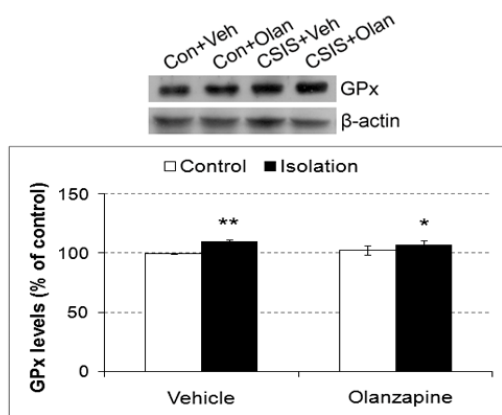


Figure 1. Hepatic GPx protein expression of controls and chronically-isolated rats treated with vehicle (0.9% NaCl) or olanzapine (7.5 mg/kg/day). Asterisks indicate comparison between treated groups and controls $*p < 0.05$; $**p < 0.01$.

Regard to GLR protein expression, Duncan's post hoc test revealed its significant increase only in chronically-isolated rats (Figure 2) that was not in correspondence to its enzyme activity (Table 1). Since GSH content was unchanged despite decreased activity of GLR, enzyme essential for maintaining its reduced state, this tripeptide was probably synthesized *de novo*. Olanzapine had no influence on GLR protein levels in chronically-isolated animals, but it increased GLR activity compared to vehicle-treated isolated animals. Ability of olanzapine to increase GPx and GLR activity in chronically-isolated rats compared to CSIS group may lead to the efficient defense against CSIS-induced oxidative stress.

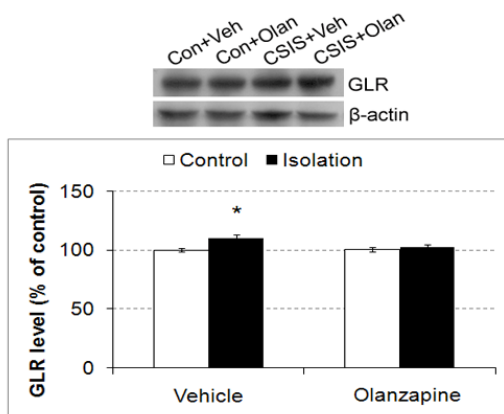


Figure 2. Hepatic GLR protein expression of controls and chronically-isolated rats treated with vehicle (0.9% NaCl), or olanzapine (7.5mg/kg/day). Asterisk indicates comparison between chronically-isolated rats and controls * $p < 0.05$.

CONCLUSION

Despite increased GPx and GLR protein levels in vehicle-treated chronically-isolated animals as response to oxidative stress, lack of consistency between protein levels and their activities may indicate that CSIS stress compromised GSH-dependent defense system. Increased GPx and GLR activity in olanzapine-treated chronically-isolated animals compared to CSIS group alone represents proof of olanzapine effectiveness in defense against CSIS-induced alternation in GSH-dependent defense system.

ACKNOWLEDGEMENT

This work was supported by the Ministry of Education, Science and Technological Development of the Republic of Serbia (Grant no. 173023).

REFERENCES

- [1] J. Zlatković, D. Filipović, *Mol. Cell. Biochem.*, 2011, 357, 143-150.
- [2] H. Y. Meltzer, S. R. McGurk, *Schizophr. Bull.*, 1999, 25, 233-55
- [3] S. W. Parka, C. H. Leea, J. G. Leea, L. W. Kimc, B. S. Shinc, B. J. Lee, Y. H. Kim, *Neurosci. Res.*, 2011, 69, 283-290.
- [4] M. Aravagiri, Y. Teper, S.R. Marder, *Biopharm. Drug Dispos.*, 1999, 20, 369-377.
- [5] P. J. Hissin, R. Hilf, *Anal. Biochem.*, 1976, 74, 214-226.
- [6] D. E. Paglia, W. N. Valentine, *J. Lab. Clin. Med.*, 1967, 70, 158-169.
- [7] B. Halliwell, C. H. Foyer, *Planta*, 1978, 139, 9-17.

FLUOXETINE FAILED TO PREVENT ISOLATION-INDUCED CHANGES OF GLUTATHIONE-DEPENDENT DEFENSE IN RAT HIPPOCAMPUS

N. Todorović, M. Bošković and D. Filipović

Laboratory of Molecular Biology and Endocrinology, Institute of Nuclear Sciences Vinča, University of Belgrade, Serbia

ABSTRACT

Chronic exposure to psychosocial stress is implicated in the pathophysiology of depression. We investigated the effect of 21d of chronic social isolation (CSIS) stress (an animal model of depression) and/or chronic administration of fluoxetine (15 mg/kg/day), an antidepressant, on GSH content, protein expression and activity of glutathione peroxidase (GPx) and glutathione reductase (GLR) in the cytosolic fraction of rat hippocampus. CSIS stress caused reduced GPx and GLR protein expression which was not prevented with fluoxetine treatment. Moreover, fluoxetine administration intensified reduction of these proteins expression. Decreased GSH content, GPx and GLR activity was also found in chronically-isolated animals (vehicle- or fluoxetine treated). Data indicate that fluoxetine not only failed to prevent CSIS-induced changes but itself compromised GSH-dependent defense system in control animals.

INTRODUCTION

Psychosocial stress leads to oxidative stress in the brain that contributes to the development of mental disorders [1]. Chronic social isolation (CSIS) represents a naturalistic type of stress in rodents that has been shown to produce behavioral and structural changes, similar to human depression [2]. Fluoxetine is an antidepressant which belongs to the selective serotonin reuptake inhibitor, a class of drugs used for the treatment of depression [3]. Literature data have shown that fluoxetine protects the hippocampus against the adverse effects of stress-related mental illnesses such as maternal separation followed by social isolation [4]. We have previously published that CSIS causes oxidative stress in rat hippocampus compromising antioxidative activity of MnSOD [5]. Major component of the first line antioxidative defense system is glutathione (GSH) which plays central role in maintaining physiological redox status. GSH is a substrate for glutathione peroxidase (GPx), enzyme which reduces peroxides and converts GSH to its oxidized form (GSSG). Reduction of GSSG back to GSH is catalyzed by

glutathione reductase (GLR). The aim of this study was to examine the influence of CSIS stress on GSH-dependent defense system functioning and possible ability of antidepressant fluoxetine to prevent eventual CSIS-induced detrimental changes.

EXPERIMENTAL

Adult male Wistar rats, 2.5 months old, were divided on control (unstressed) group that was comprised of four animals per cage and chronically-isolated rats that were housed individually for 21d, deprived of any visual or tactile contacts with other animals. Fluoxetine-hydrochloride was administered daily by intraperitoneal (i.p.) injections of 15 mg/kg during the 21d in both control (Cont+Fluox) and chronically-isolated (CSIS+Fluox) rats. This dose of fluoxetine produced serum drug concentrations that correspond to those reported in human patients treated with therapeutically effective doses [6]. Vehicle-treated (Cont+NaCl and CSIS+NaCl) groups received daily i.p. injections of normal saline (0.9% NaCl). Cytosolic fractions of hippocampus were used for determination of biochemical parameters. GSH content was measured according to Ellman's method modified by Hissin and Hilf [7]. GPx and GLR protein expression was monitored by Western blot, while activity of these enzymes was determined by spectrophotometric assay [8, 9]. Data are expressed as mean \pm S.E.M. of 5-6 animals per group and analyzed by two-way ANOVA followed by Duncan's post-hoc test.

RESULTS AND DISCUSSION

The relative changes in GPx and GLR protein expression are presented in Figure 1.

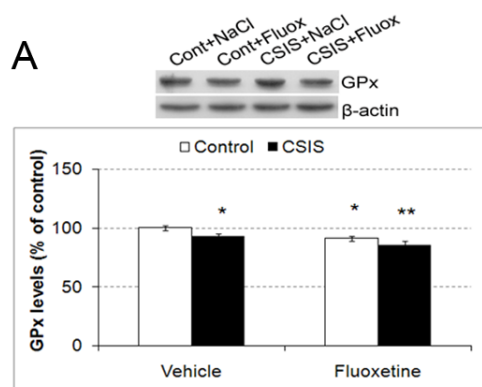
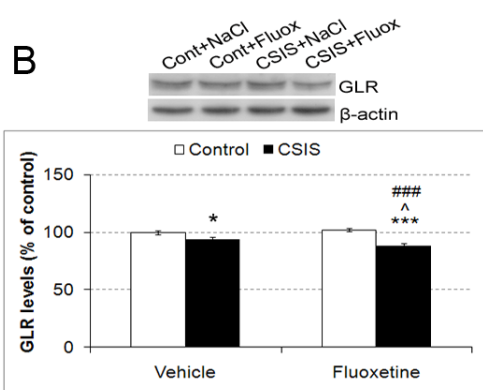


Figure 1. Hippocampal GPx (A) and GLR (B) protein of controls and chronically-isolated rats treated with saline or fluoxetine. Symbols indicate differences between: treated group and Cont+NaCl * p <0.05, ** p <0.01, *** p <0.001; CSIS+Fluox and CSIS+NaCl \hat{p} <0.05; CSIS+Fluox and Cont+Fluox $\hat{\hat{\hat{p}}}$ <0.001.



GPx protein expressions were reduced in fluoxetine-treated rats (both controls and chronically-isolated) (* p<0.05, ** p<0.01) and CSIS group alone (* p<0.05) compared to vehicle-controls (Figure 1A). The levels of GLR were decreased in chronically-isolated rats (vehicle- and fluoxetine-treated) (* p<0.05, *** p<0.001) (Figure 1B).

Although fluoxetine alone didn't cause change in GLR level in controls, its intensified reduction of GLR expression following CSIS, as compared to CSIS stress alone (^ p<0.05). Fluoxetine-induced depletion of GSH content in controls (** p<0.01) may be the result of reduced GLR activity (*** p<0.001) (Table 1). Moreover, decreased GPx activity noted in these animals (* p<0.05) may suggest either enzyme inactivation by reactive oxygen species or already decreased GSH availability. Significantly decreased GSH content, as well as activity of GPx and GLR, which was in accordance with their reduced protein expression in chronically-isolated rats (** p<0.01), suggest that CSIS compromised GSH-dependent defense system in the hippocampus promoting prooxidative state. We already reported that rats exposed to the CSIS used here (21d) (vehicle- or fluoxetine treated) showed a decrease of GSH in the liver whereby fluoxetine caused more pronounced changes in chronically-isolated animals than in controls [6]. These data lead to the conclusion that, in addition to the liver, fluoxetine also compromises GSH regulation in the hippocampus.

Table 1. Hippocampal GSH, GPx and GLR activity in controls and CSIS treated with saline or fluoxetine. Symbols indicate differences between: treated group and Cont+NaCl * p<0.05, ** p<0.01, *** p<0.001; CSIS+Fluox and CSIS+NaCl ^^^ p<0.001; CSIS+Fluox and Cont+Fluox ### p<0.001.

Groups	GSH levels (nmol/mg protein)	GPx activity (mU/mg protein)	GLR activity (mU/mg protein)
Cont+NaCl	67,24 ± 0,95	47,01 ± 1,60	51,96 ± 0,84
Cont+Fluox	58,32 ± 3,93 **	40,71 ± 3,02 *	45,21 ± 0,85 ***
CSIS+NaCl	57,45 ± 0,77 **	38,89 ± 1,89 **	47,28 ± 1,58 **
CSIS+Fluox	56,72 ± 1,13 **	36,36 ± 1,54 **	38,41 ± 0,91 *** ^^^ ###

Moreover, chronic fluoxetine treatment failed to prevent CSIS-induced reduction of abovementioned parameters. In addition, fluoxetine treatment of chronically-isolated rats resulted in even more decreased GLR activity comparing to CSIS alone ($\hat{p}<0.001$), indicating that this antidepressant failed to prevent CSIS-induced compromise of GSH-dependent antioxidative defense but itself has harmful effects on rat hippocampus.

CONCLUSION

CSIS stress increased susceptibility of rat hippocampus to oxidative stress by compromising GSH-dependent defense system. Treatment with antidepressant fluoxetine didn't prevent this detrimental effect, moreover, its administration in controls disturbed functioning of this system as well.

ACKNOWLEDGEMENT

This work was supported by the Ministry of Education, Science and Technological Development of the Republic of Serbia (Grants no. 173023).

REFERENCES

- [1] S. Schiavone, V. Jaquet, S. Sorce, M. Dubois-Dauphin, M. Hultqvist, L. Backdahl, R. Holmdahl, M. Colaianna, V. Cuomo, L. Trabace, K.H. Krause, *Transl Psychiatry*, 2012, 2, e111.
- [2] L.M. Heinrich, E. Gullone, *Clin. Psychol. Rev.*, 2006, 26, 695-718.
- [3] D.T. Wong, F.P. Bymaster, E.A. Engleman, *Life Sci.*, 1995, 57, 411-441
- [4] H.J. Lee, J.W. Kim, S.V. Yim, M.J. Kim, S.A. Kim, Y.J. Kim, C.J. Kim, J.H. Chung, *Mol. Psychiatry*, 2001, 6, 725-728
- [5] D. Filipović, J. Zlatković, D. Inta, I. Bjelobaba, M. Stojiljković, P. Gass, *Journal of Neuroscience Research*, 2011, 89, 1461-1470.
- [6] J. Zlatković, N. Todorović, N. Tomanović, M. Bošković, S. Djordjević, T. Lazarević-Pašti, R.E. Bernardi, A. Djurdjević, D. Filipović, *Eur. J. Pharm. Sci.*, 2014, 59, 20-30.
- [7] P.J. Hissin, R. A. Hilf, *Anal. Biochem.*, 1976, 74, 214-226.
- [8] D.E. Paglia, W.N. Valentine, *J. Lab. Clin. Med.*, 1967, 70, 158-169.
- [9] B. Halliwell, C.H. Foyer, *Planta*, 1978, 139, 9-17.

VALIDATION OF RP-HPLC METHOD FOR DETERMINATION BUTYLATED HYDROXYTOLUENE IN PHARMACEUTICAL DOSAGE FORMS

M. Geđa, B. Ivković and S. Vladimirov

*Department of Pharmaceutical Chemistry, Faculty of Pharmacy, University of Belgrade, Vojvode Stepe 450, Belgrade-Serbia.
(blucic@pharmacy.bg.ac.rs)*

ABSTRACT

A reverse phase liquid chromatographic method was developed for the quantitative determination of antioxidant butylated hydroxy toluene (BHT or 2,6-di-*tert*-butyl-4-methylphenol) in dutasteride soft gelatine capsules. The method was developed by using ReproSil-Pur 120 C4 (150×4.6mm) 3- μ m column under isocratic conditions at 35°C. The optimum conditions for quantitative determination of BHT achieved with the mobile phase: 0.1% *ortho*-phosphoric acid in the water /acetonitrile in the ratio 30/70 (v/v), at a flow rate of 1.5 ml/min and the detection wavelength at 220 nm. The developed method was validated as per ICH guidelines with respect to specificity, linearity, limit of detection (LOD), limit of quantification (LOQ), accuracy, precision and robustness. The limit of detection, limit of quantification are 0.15 μ g/ml and 0.45 μ g/mL, respectively and precision at LOQ level was with 2.2% RSDn. The method was linear over the range of concentrations 0.4 μ g /ml to 6 μ g /mL ($r=0,999$), showed good precision (% RSD was below 2%), accuracy (98.6 % to 101.6%) and robustness.

INTRODUCTION

The synthetic phenolic antioxidant butylated hydroxytoluene (BHT) (Fig. 1) was frequently used to prevent the oxidative rancidity of pharmaceutical, food and other commercial products. The concentration of BHT depends on the amount of sensitive compounds (α -hydroxy acids, ceramides, lipids, vitamins, oils, and so forth) that are susceptible to oxidation by the oxygen in the atmosphere making it possible for the unstable peroxide radicals [1-2]. These additives could have harmful effects on human health. Therefore, many regulations define the permitted percentage of these compounds as well as their concentration limits [3].

BHT is essentially used to prevent oxidative rancidity in pharmaceutical dosage form. BHT is able to inhibit reactions promoted by oxygen, thus avoiding the oxidation and is intended to prevent the appearance of ketones

and aldehydes that can give a product a disagreeable smell and rancidity [2] To prevent formulations from peroxide radicals is must use antioxidant compound which have the ability to neutralize those radicals through the transfer of hydrogen to this radical, stabilizing the antioxidant by resonance [4]. In literature survey there were several publications and research papers focus on separation methods to detect phenolic antioxidants as BHT by RP-HPLC, GC, LC-MS and by electrochemical methods [1-2],[5-8].

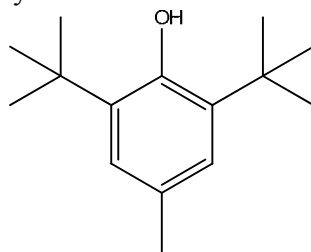


Figure1. The chemical structure of BHT

In these described methods C8 or C18 (modified silica gel with a hydrocarbon chain of 8 or 18 carbon atoms) stationary phases were used. In our work C4 stationary phase was used. Using C4 stationary phase we have developed a method for the quantification of BHT in the dutasterid capsules. The developed method was validated as per ICH guidelines with respect to specificity, linearity, LOD, LOQ, accuracy, precision and robustness.

EXPERIMENTAL

Chemicals All used reagents were of the analytical grade. The mobile phase and the solvents were prepared using acetonitrile (*Lab Scan*, Ireland), *ortho*-phosphoric acid (*Carlo Erba*, Italy) and HPLC grade water.

Chromatographic conditions The experiments were performed on the chromatographic system *Agilent HP1200* with DAD detector. The analytical columns used in this study were *ReproSil-Pur 120 C4* (150×4.6mm) 3- μ m particle size. The mobile phase composition was acetonitrile: 0.1% (v/v) *ortho*-phosphoric acid in the water in the ratio 70: 30. The other chromatographic conditions were: flow rate 1,5 ml/min, column temperature 35°C and UV detection at 220 nm.

Mixture of acetonitrile: water in the ratio 75: 25 v/v was used as solvent.

Standard solutions Stock solution of BHT was prepared by dissolving them in the solvent to obtain the concentration of 200 μ g/mL. The prepared stock solutions were stored at 4 °C. To evaluate the linearity of the developed method, seven solutions of BHT in the concentration range from the 0.4 μ g/ml to 6 μ g/ml were prepared in the solvent using the appropriate standard

solutions. The accuracy of the method was proved by preparing three series of solutions containing appropriate placebo and BHT in three levels: low level 80% (3.2 µg/ml), medium level 100% (4µg/ml) and high level 120% containing 4.8 µg/ml. To prove the precision of the method, six identical solutions of capsules in the solvent was prepared. The appropriate volume of BHT stock solutions was added to all solutions in order to obtain the final concentration of 4 µg/mL.

Sample solutions Sample solution was prepared by dissolving of the 10 intact capsules in the volumetric flask a 100 ml in the 25 ml water to dissolve the capsule shell and release the content solvent, after add 25 ml acetonitrile and again sonication for 10 min. Cool and make up the volume with acetonitrile. Filter through 0.45 µm filter. The concentration of BHT is 3.75 µg/ml.

RESULTS AND DISCUSSION

The proposed method was validated as per ICH guideline. The system suitability was evaluated on the basis of USP tailing factor and theoretical plates of BHT and relative standard deviation (RSD) of five injections of standard solution. A specificity study to establish the interference of placebo was conducted. Chromatograms of placebo had shown no peaks at the retention time of BHT, this indicates that the excipients used in the formulation do not have any interference in estimation of BHT in dutasterid capsules. The precision of method was verified by repeatability and intermediate precision at target concentration level (4 µg/ml). Repeatability was checked by injecting six individual preparations of BHT in dutasterid soft gelatin capsule. %RSD of result for BHT was calculated (1,5%). The intermediate precision of the method was also evaluated using different analyst and different instrument and performing the analysis on different days (2.2%). The LOD and LOQ for BHT were determined at a signal-to-noise ratio of 3:1 and 10:1, respectively, by injecting a series of diluted solutions with known concentrations (LOD is 0,15 µg/mL and LOQ 0,45 µg/ml). Linearity test solutions were prepared by diluting the stock solutions to the required concentrations by covering the range from 0.04 to 0.60 µg/mL of BHT. The correlation coefficient obtained was greater than 0.999. Accuracy of the method BHT were evaluated in triplicate using three concentration levels 80%, 100% and 120%. The percentage recoveries for BHT were calculated and varied from 98.0% to 104.2 %. To determine the robustness of the developed method, experimental conditions (composition of the mobile phase, column temperature and flow rate) were deliberately altered and system suitability parameters for BHT were recorded. To check the application of the method dutasterid soft gelatin capsules was used

where BHT concentration was different. Sample was analyzed three times as and results are found satisfactory (0.036 mg per capsule)

CONCLUSION

It can be concluded that the defined RP-HPLC method is rapid and efficient for determination of BHT in the dosage forms.

ACKNOWLEDGEMENT

This work was partially supported by the Ministry for Science of the Republic of Serbia (Grants no.172041). We are grateful to the HEMOFARM A.D. Vrsac.

REFERENCES

- [1] G Capit'an-Vallvey LF, Valencia MC, Nicolas EA, Anal Lett, 2002, 35, 65-81
- [2] L. F. Capit'an-Vallvey, M. C. Valenciae. E. A., Nicolas., Anal Chim Acta 2004, 503, 179-86
- [3] Y. Guan, Q. Chu Q, L. Fu, J. Ye, J. Chromatogr. A 2005, 1074, 201-204.
- [4] Y. Porat, A. Abramowitz, E. Gazit, Chem Biol Drug Des, 2006, 67, 27-37
- [5] B. Saad, Y.Y. Sing, M.A. Nawi, N.H. Hashim, Ali A.S. Mohamed, M.I. Saleh, Food Chem 2007,105,389-94
- [6] S. Tsuji, M. Nakanoi, H. Terada, Y. Tamura, Y. Tonogai, Shokuhin Eiseigaku Zasshi 2005, 46, 63-71.
- [7] J.F. García-Jiménez, M.C. Valencia, L.F. Capitán-Vallvey, Anal Chim Acta 2007;594:226-33.
- [8] K.H. Garcia Freitas, O. Fatibello-Filh, . Talanta 81 (2010) 1102–1108

RP-TLC IN QUANTITATIVE STRUCTURE-RETENTION RELATIONSHIPS OF SOME ALPHA ADRENERGIC AND IMIDAZOLINE RECEPTOR LIGANDS

S. Filipic, M. Salem M. Shenger, J. Vucicevic, M. Popovic and D. Agbaba

*Department of Pharmaceutical Chemistry, Faculty of Pharmacy, University of Belgrade, Vojvode Stepe 450, Belgrade, Serbia
(sfilipic@pharmacy.bg.ac.rs)*

ABSTRACT

The chromatographic behavior of 16 alpha adrenergic and imidazoline receptor ligands has been studied by reversed-phase thin-layer chromatography (RP-TLC). Retention constant R_M^0 has been determined for all tested compounds in two different chromatographic systems (tetrahydrofuran-ammonia-water/RP-18, and tetrahydrofuran-ammonia-water/CN) and together with computed molecular parameters of the examined compounds further used for the quantitative structure-retention relationship (QSRR) study. The QSRR modeling was performed with use of the partial least squares regression (PLS). Obtained results from leave-one-out cross-validation (Q^2 values: 0.923 and 0.873 for RP-18 and CN stationary phase, respectively) and external test set prediction (root mean square error of prediction, RMSEP: 0.339 and 0.218, for RP-18 and CN stationary phase, respectively) were proved high predictive power of the proposed models.

INTRODUCTION

The concept of non-adrenergic imidazoline receptors (IR) and their ligands was proposed based on a discovery that antihypertensive drug clonidine and its analogues exert their effect on the central nervous system by interaction with both, the α_2 -adrenoreceptors (α_2 -AR) and the imidazoline receptors. Today it is well known that second generation of centrally acting antihypertensives, such as moxonidine and rilmenidine, is more selective for I_1 -IR and have produced less side effects than clonidine and other nonselective imidazoline receptors ligands [1]. Therefore, design and synthesis of novel compounds with diverse activity and selectivity toward I_1 -IR, I_2 -IR, and I_3 -IR, and the α -AR-receptors can instigate the development of promising drug candidates with diverse pharmacological effects and reduced incidence of side effects. Significant interest in

developing of new IR/ α -AR ligands requires fast and reliable methods for estimation of their physicochemical properties and retention behavior.

Application of thin-layer chromatography method in different quantitative structure–retention relationship (QSRR) studies provides valuable data which enable prediction of the retention behavior of the new compounds, understanding of the separation mechanism in a given chromatographic system, identification of important molecular descriptors, estimation of compounds' lipophilicity and prediction of biological activity [2].

The main objectives of this work were to investigate the chromatographic behavior of 16 alpha adrenergic and imidazoline receptor ligands by the RP-TLC and to develop the QSRR models enabling prediction of the retention behavior of the related guanidine and imidazoline derivatives.

EXPERIMENTAL

Chromatography was performed on the commercially available octadecyl silica plates (the TLC Silica gel 60 RP-18 F_{254s} pre-coated aluminium sheets, Merck, Darmstadt, Germany) and CN-modified silica plates (the HPTLC Silica gel 60 CN F_{254s}, Merck, Darmstadt, Germany). Two different mobile phase/stationary phase systems and different contents of organic modifier (ϕ) were used: tetrahydrofuran-ammonia-water/RP-18 ($\phi=0.6-0.8$), and tetrahydrofuran-ammonia-water/CN ($\phi=0.55-0.75$). The content of tetrahydrofuran was changed in the 5% steps, while the content of ammonia was kept constant at 5 vol%. The plates were developed in the ascending mode after 15 min pre-saturation with the mobile phase. Zone detection was performed in the UV light at 254 nm. The R_f values were calculated as an average from the three chromatograms. According to the obtained R_M values, $R_M = \log(1/R_f - 1)$ retention parameter R_M^0 corresponding to pure water was obtained as an extrapolated value to 0% organic modifier in the mobile phase, using following linear equation: $R_M = R_M^0 + m \times \phi$; where m is slope and ϕ is the volume fraction of organic modifier in the mobile phase.

Theoretical studies including calculation of pK_a and selection of a predominant molecular/cationic/anionic form of the analyzed compounds at a given pH value of an aqueous phase, was performed using the Marvin 5.5.1.0 ChemAxon program. Geometry optimizations were performed on the B3LYP/3-21G (d,p) level of the density functional theory in the Gaussian 98 program. The Gaussian 98 (B3LYP/3-21G(d,p) basis set), the Chem3D Ultra 7.0.0, the Molinspiration Cheminformatics, and the Dragon programs were applied for the computation of molecular descriptors. The Soft Independent Modeling of Class Analogy SIMCA P+ 12.0 program was used for the Partial Least Squares (PLS) analysis and the QSRR modeling.

RESULTS AND DISCUSSION

In the QSRR study, experimentally obtained retention parameters (R_M^0) in the two different chromatographic systems were used as dependent variables, while the computed molecular parameters of the examined compounds were used as independent variables. The examined data set of 16 compounds was divided into the training set consisting of 12 compounds (moxonidine, brimonidine, clonidine, amiloride, guanabenz, idazoxan, efaroxan, harmine, naphazoline, tramazoline, oxymetazoline, and xylometazoline), used for building of the models, and the test set consisting of 4 compounds (tizanidine, guanfacine, harmine, and tetrahydrozoline), used for an external validation. The distribution of the studied substances into the training and test set were randomly determined but taking into the account that each chemical group (i.e., the guanidine, 2-aminoimidazoline, 2-arylmethylimidazoline and β -carboline derivatives) has one representative in the test set. The statistical results and PLS-coefficients of the QSRR models are given in Table 1. High values of leave-one-out cross-validation parameter Q^2 ($Q^2 > 0.5$) and low values of the root mean square error of estimation (RMSEE) for the training set and root mean square error of prediction (RMSEP) for the test set indicate good prognostic capacity of the obtained QSRR models (Table 1.). In all devised QSRR models, logarithm of the partition coefficient, $\log P$ is selected as the important property with positive influence on the retention in the tested chromatographic RP-TLC systems. Similar sets of descriptors were selected for both, the RP-18 ($\log P$, nN, P_VSA_e_2) and the CN ($\log P$, nON, P_VSA_e_2) stationary phases and tetrahydrofuran-ammonia-water as mobile phase. The P_VSA-like on Sanderson electronegativity, bin 2 (P_VSA_e_2) descriptor is defined as an amount of the van der Waals surface area (VSA), which in certain range has the P property (Sanderson electronegativity). In the both chromatographic systems, the P_VSA_e_2 descriptor exerts negative influence on the R_M^0 . Therefore the compounds with higher P_VSA_e_2 values have lower retention on the two investigated stationary phases. The number of nitrogen atoms (nN) is a constitutional descriptor and in the tetrahydrofuran-ammonia-water/RP-18 system, it exerts negative influence on the retention constant (R_M^0). Thus the compounds with a higher number of the nitrogen atoms (nN) less efficiently interact with the C18-modified silica stationary phase, which results in a lower retention thereof.

Table 1. Statistical results of the developed PLS-QSRR models

RP-TLC systems	PLS-Coefficients	R ² Y	Q ²	RMSEE	RMSEP
THF-NH ₃ -H ₂ O (RP-18)	Constant: 2.431; log <i>P</i> : 0.953; nN: - 0.375; P_VSA_e_2: -0.364	0.96	0.92	0.171	0.339
THF-NH ₃ -H ₂ O (CN)	Constant: 2.162; log <i>P</i> : 1.078; nON: - 0.116; P_VSA_e_2: - 0.265	0.93	0.87	0.186	0.218

The number of the hydrogen bond acceptors (nON) negatively contributes to the R_M^0 values in the tetrahydrofuran-ammonia-water/CN system, so that the larger number of the nitrogen and oxygen atoms as the hydrogen accepting sites leads to the lower retention on the CN stationary phase.

CONCLUSION

Upon the results of the performed QSRR analysis, the log *P* values were selected in all the devised models as those indicating the importance of lipophilicity for the retention behavior of the investigated compounds. Moreover, constitutional descriptors (nN), P_VSA-like descriptors (P_VSA_e_2), and the number of the hydrogen bond acceptors (nON) contribute to an overall retention mechanism in RP-TLC systems. The developed QSRR models are very useful predictive tools for evaluation of the R_M^0 values for the related guanidine and imidazoline derivatives.

ACKNOWLEDGEMENT

This work was supported by the Ministry of Science and Technological Development of the Republic of Serbia, Contract No. 172033.

REFERENCES

- [1] C. Dardonville, I. Rozas, Medicinal Research Reviews, 2004, 24, 639-661.
- [2] R.Kaliszan, Chemical Reviews, 2007, 107, 3212–3246.

THE EFFECTS OF ANOINIC AND CATIONIC SURFACTANTS ON ACID-BASE EQUILIBRIA OF IRBESARTAN

M. Popović¹, M. Grujić¹, G. Popović² and D. Agbaba¹

¹Department of Pharmaceutical Chemistry Faculty of Pharmacy,

²Department of General and Inorganic Chemistry,

University of Belgrade, Vojvode Stepe 450, 11000 Belgrade, Serbia

(marija.popovic@pharmacy.bg.ac.rs)

ABSTRACT

In this study pK_a values of irbesartan, an angiotensin receptor blocker, were determined by potentiometry and the effects of sodium dodecyl sulfate (SDS) and cetyl trimethyl ammonium bromide (CTAB) on its protolytic equilibria have been investigated. It was observed that shift in pK_a values is a result of complex electrostatic and hydrophobic interactions with the micellar solutions. Based on the obtained results drug interactions with biomolecules can be evaluated.

INTRODUCTION

Irbesartan (IRB), 2-butyl-3-[[2'-(tetrazol-5-yl)biphenyl-4-yl]-methyl]-1,3-diazaspiro[4,4]non-1-en-4-one (Figure 1), is a potent and selective antagonist of angiotensin II at AT₁ receptor. IRB is indicated for use in therapy of hypertension and also for the treatment of renal disease in patients with type 2 diabetes mellitus and nephropathy [1]. Drugs in the sartan class specifically interact with the receptor, in the two-step process which involves incorporating into the membrane and diffusion to the receptor [2]. It is assumed that biological membranes play an important role in the stabilization of the IRB active form.

Chemical structure of IRB contains three ionizable centers, one acidic center (N1 of tetrazole – pK_{a2}) and two basic centers (imidazole – pK_{a3} and N4 of tetrazole – pK_{a1}). Tetrazol ring is a part of the molecule which is required for the pharmacological action because it is analogous to the terminal end of angiotensin II. The overall charge of the drugs under the physiological conditions depends on their pK_a values and

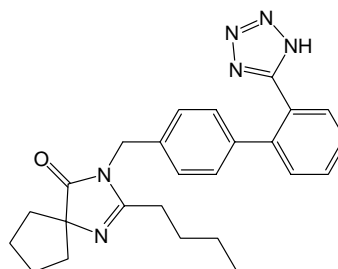


Figure 1. Chemical structure of irbesartan

thereby the bioavailability of the active form which is required for the receptor binding [3]. However, expected ionization extent of the drug can be distinguished in terms of *in vivo* environment as a result of interactions with a variety of biomolecules that may be present on the membrane surface and in body fluids. Since biological membranes are extremely complex structures, much less complex surfactant micelles have been used as a model systems [4].

The main aim of this study was to determine the pK_a values of IRB in the presence of micellar solution of anionic surfactant SDS and cationic surfactant CTAB and compared with the values defined for aqueous solution in order to estimate their effect of the acid-base equilibria of IRB.

EXPERIMENTAL

The pK_a values of IRB in the absence and in the presence of the 10^{-2} M surfactant (SDS and CTAB) were determined by potentiometry. A titration system 798 MPT Titrino with a combined electrode (LL unitrode Pt1000, Metrohm) was used for performing potentiometric titrations. All measurements were carried out at 25 °C and constant ionic strength was adjusted to 0.1 M with NaCl. According to poor water solubility of IRB apparent dissociation constants pK_a^* were obtained in different methanol–water mixtures 40 %, 45 %, 50 %, and 55 %, (w/w). To 40 mL (5×10^{-4} - 10^{-3} M) solutions of IRB in the absence (methanol–water mixtures) and in the presence of surfactants, 1.0 mL of HCl solution (0.10414 M) was added and titrated with standard NaOH solution (0.099564 M). Based on data obtained by potentiometric titrations pK_a values were calculated using a computer program Hyperquad, which enables determination of equilibrium constants in complex systems containing overlapped acid–base equilibria.

RESULTS AND DISCUSSION

Because of a slight IRB solubility, its apparent pK_a values (pK_a^*) in the absence of surfactants were determined in different methanol–water mixtures 40 % to 55 % (w/w). For this purpose, methanol is the solvent of choice because its solvation effect is close to that of pure water [5]. Aqueous pK_a values were calculated by extrapolation of the pK_a^* values to zero cosolvent. (Table 1, Figure 2). Precipitation of the drug did not occur in the presence of micelles formation, because the solubilizing effect of the surfactants acted to increase the IRB solubility.

IRB pK_a values are shifted in the presence of micelles which points out that surfactants affect its acid-base equilibrium. Comparison of the results obtained in the presence and in the absence of surfactants (Table 2) indicates

that the most sensitive to the presence of SDS is acid group of tetrazole ($\Delta pK_{a2} = +1.82$), while CTAB the most prominent affects the ionization of base center in tetrazole ($\Delta pK_{a1} = +1.22$).

Table 1. pK_a^* values of irbesartan determined in different methanol–water mixtures

% Methanol	pK_{a1}	pK_{a2}	pK_{a3}
40	1.91	3.65	4.88
45	2.64	3.65	-
50	2.47	3.59	4.93
55	2.26	3.61	5.02

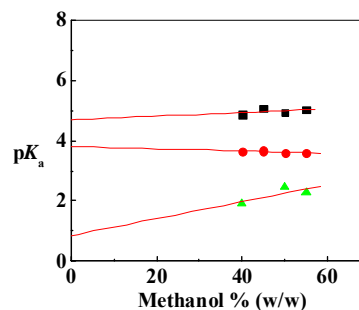


Figure 2. Plots of methanol % (w/w) vs pK_a^*

Table 2. pK_a values of irbesartan with and without of surfactants

	H ₂ O	CTAB	ΔpK_a	SDS	ΔpK_a
pK_{a1}	0.86	2.08	+1.22	-	-
pK_{a2}	3.81	2.60	-1.21	5.63	+1.82
pK_{a3}	4.69	3.55	-1.14	6.23	+1.54

Observed changes in pK_a values can be considered in terms of competing different hydrophobic and electrostatic interactions on the surface of the micelles [6]. Due to repulsion of the same charge, negatively charged surface of SDS micelles can stabilize the nonionized form of the acid center shifting the equilibria by decreasing the acidity. At the same time SDS can stabilize the protonated form of the base group causing an increase in pK_a value and basicity ($\Delta pK_{a3} = +1.54$).

The opposite effect is expected in the case of CTAB micelles whose surface is positively charged. Consequently, the greater stability of the ionized form of the acid group causes an increase in acidity ($\Delta pK_{a2} = -1.21$), while the greater repulsion of the protonated basic center reduces the basicity (ΔpK_{a3}

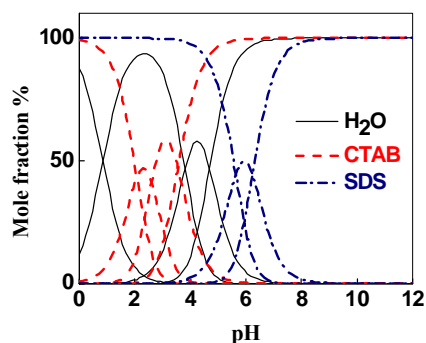


Figure 3. Ionization profiles of irbesartan in water, SDS and CTAB

= -1.14). However, a significant shift of the pK_{a1} value in the presence of CTAB, which is contrary to the expectations, may indicate that the hydrophobic interactions are predominant, with possible insertions into the micelle.

CONCLUSION

Based on obtained results and the shift in pK_a values it can be concluded that the ionisable centers of IRB participate in complex electrostatic and hydrophobic interactions with the SDS and CTAB micelles. The shift in pK_{a2} and pK_{a3} values probably is a consequence of the dominant electrostatic interactions, whereas the predominant hydrophobic interactions with micelles are responsible for a shift in pK_{a3} value. The results obtained in this study can be used for more detailed investigation of the drug behavior in interaction with the membrane and the receptor, particularly if one takes into account that the presence of surfactants affects the ionization of the groups which are required for activity.

ACKNOWLEDGEMENT

This work was supported by the Ministry of Education, Science and Technological Development of the Republic of Serbia, Contract No. 172033.

REFERENCES

- [1] Lemke, T. L.; Williams, D. A.; Roche, V. F.; Zito, S. W. Foye's Principles of Medicinal Chemistry, 7th ed.; Lippincott Williams & Wilkins: Philadelphia, PA, 2013.
- [2] Fotakis, C., Megariotis, G., Christodouleas, D., Kritsi, E., Zoumpoulakis, P., Ntountaniotis, D., Zervou, M., (...), Mavromoustakos, T. *Biochim. Biophys. Acta*, 2012, 1818, 3107-3120
- [3] Manallack, D. T.; Prankerd, R. J.; Yuriev, E.; Opreab, T. I.; Chalmers, D. K. *Chem. Soc. Rev.* 2013, 42, 485–496.
- [4] Fendler, J. H. *Chem. Rev.* 1987, 87, 877–899.
- [5] A. Avdeef, J. E. A. Comer, S. J. Thomson, *Anal. Chem.* 1993, 65, 42.
- [6] M.R. Popović, G.V. Popović, D.A. Agbaba. *J. Chem. Eng. Data*, 2013, 58, 2567–2573

APPLICATION OF PAMPA MODEL TO PREDICT BBB PERMEABILITY OF FORTY COMERCIAL DRUGS

J. Vucicevic, K. Nikolic, V. Dobricic

*Department of Pharmaceutical Chemistry, Faculty of Pharmacy,
University of Belgrade, Vojvode Stepe 450, 11000 Belgrade-SERBIA*

ABSTRACT

The Parallel Artificial Membrane Permeability Assay (PAMPA) has been successfully introduced into pharmaceutical industry to allow useful prediction of blood brain barrier (BBB) penetration. This study estimated the extent of passive uptake for forty commercially available drugs using PAMPA-BBB model. The effective permeabilities (P_e) of the compounds have been calculated taking into account iso-pH condition and their membrane retention. Further, the obtained results will be used to develop new computational models capable of predicting the BBB permeability of novel chemical entities in drug discovery process.

INTRODUCTION

Prediction of ADME (absorption, distribution, metabolism, excretion) processes during the development of new drug candidates is of great importance. The 'poor' pharmacokinetic properties are one of the main reasons for the failure of potential drugs in the pre-clinical and clinical trials. To be effective as therapeutic agent, centrally acting drug must cross blood-brain barrier. For this reason, selecting compounds that have appropriate brain penetration properties is a critical step during drug discovery phase.

Direct measurement of brain permeability is very difficult, time consuming and expensive process. Instead of that, a lot of *in vitro* models have been developed.

The aim of this work was to assess the extent of passive uptake of forty commercially available drugs through blood brain barrier using the parallel artificial membrane permeability assay (PAMPA).

PAMPA, first introduced by Kansy, et al. [1], is rapid and cost effective tool widely used in the pharmaceutical industry.

EXPERIMENTAL

The compounds were dissolved in DMSO at 5mg/ml. Ten microliters of this compound stock solution was diluted 200-fold in physiological phosphate

buffer at pH=7.4 in order to obtain a secondary stock solution of 25 $\mu\text{M}/\text{mL}$. Two hundred microliters of the secondary stock solution was stored in the donor wells. The filter membrane was coated with 4 μL PBL in dodecane (20 mg/mL) and the acceptor well was filled with 200 μL of pH=7.4 buffer. The acceptor filter plate was put on the donor plate with artificial lipid membrane in the middle to form a „sandwich“. Test compounds diffused from the donor well through the lipid membrane and into the acceptor well for eighteen hours [2]. The concentration of drug in the acceptor, the donor, and the reference was determined by standard analytical method-HPLC using UV detector. In cases where UV spectra could not be obtained due to low poor sensitivity, samples were transferred to liquid chromatography mass spectrometry (LC-MS). The measurements have been performed under iso-pH conditions. Samples were analyzed in triplicate and the average of this three runs were reported. The effective permeability (P_e) of compounds has been calculated according to the following equations:

$$VaCa(t) + VdCd(t) = VdCd(0)(1 - R) \quad (1)$$

$$P_e = -\frac{2.303Vd}{A(t - \tau_{lag})} \left(\frac{1}{1 + r_v} \right) \log_{10} \left[1 - \left(\frac{1 + r_v^{-1}}{1 - R} \right) \frac{Ca(t)}{Cd(0)} \right], \quad (2)$$

where Va =acceptor volume (cm^3); Vd =donor volume (cm^3); A =filter area (cm^2); t =permeation time (s); $Ca(t)$ and $Cd(t)$ =the concentration of compound in acceptor and donor wells at time t (μM); $Cd(0)$ =the concentration of compound in donor well at time 0 (μM); τ_{lag} =time needed to saturate the membrane; R =mole fraction of compound retained by membrane; $r_v=Vd/Va$.

RESULTS AND DISCUSSION

The compounds used in this study were imidazoline ligands and CNS drugs with wide range physicochemical properties. The values of effective permeability (P_e) as well as permeability coefficient ($\log P_e$) of those compounds have been reported in Table 1. Depending on the P_e values commercial drugs have been separated into three groups [3]:

- ‘CNS+’ (high BBB permeation predicted); $P_e (10^{-6} \text{ cm s}^{-1}) > 4.0$
- ‘CNS -’ (low BBB permeation predicted); $P_e (10^{-6} \text{ cm s}^{-1}) < 2.0$
- ‘CNS +/-’ (BBB permeation uncertain); $P_e (10^{-6} \text{ cm s}^{-1})$ from 2.0 to 4.0

Table 1. Calculated PAMPA parameters of tested compounds

Compounds	PAMPA-BBB <i>Pe</i> (10^{-6} cm/s)	Log <i>Pe</i>	PAMPA-BBB assay classification
Agmatine	0.0033	-8.48	CNS-
Amiloride	0.000827	-9.08	CNS-
Brimonidine	1.78	-5.75	CNS-
Bromazepam	1.94	-5.71	CNS-
Carbamazepine	3.78	-5.42	CNS+/-
Citalopram	9.45	-5.02	CNS+
Clonazepam	3.98	-5.40	CNS+/-
Closapine	8.34	-5.08	CNS+
Efaroxan	4.92	-5.31	CNS+
Fluoxetine	9.89	-5.00	CNS+
Guanabenz	5.67	-5.25	CNS+
Guanfacine	5.21	-5.28	CNS+
Harman	7.48	-5.13	CNS+
Harmin	7.17	-5.14	CNS+
Idazoxan	5.08	-5.29	CNS+
Clonidine	3.67	-5.44	CNS+/-
Xylometazoline	8.88	-5.05	CNS+
Lamotrigine	0.97	-6.01	CNS-
Levetiracetam	0.06	-7.22	CNS-
Levomepromazine	8.38	-5.08	CNS+
Lorazepam	8.35	-5.08	CNS+
Maprotiline	5.99	-5.22	CNS+
Mianserin	9.08	-5.04	CNS+
Moxonidine	1.86	-5.73	CNS-
Naphazoline	4.31	-5.37	CNS+
Oksazepam	8.23	-5.08	CNS+
Oxymetazoline	2.02	-5.69	CNS+/-
Olanzapine	5.51	-5.26	CNS+
Prazepam	8.61	-5.07	CNS+
Reserpin	2.75	-5.56	CNS+/-
Rilmenidine	7.26	-5.14	CNS+
Risperidone	3.81	-5.42	CNS+/-
Sertraline	6.66	-5.18	CNS+
Tetrahydrozoline	3.23	-5.49	CNS+/-
Tizanidine	3.39	-5.47	CNS+/-
Topiramate	0.54	-6.27	CNS-
Trimazoline	3.92	-5.41	CNS+/-
Venlafaxine	13.35	-4.87	CNS+
Viloxazine	6.47	-5.19	CNS+
Ziprasidone	8.27	-5.08	CNS+

CONCLUSION

The effective BBB permeabilities of forty commercial drugs have been estimated using PAMPA test. According to calculated permeation parameters most compounds have a high or moderate BBB permeation that allows compounds to reach the therapeutic targets in CNS with minimal systemic side effects. Compounds with low permeation were agmatine, amiloride, lamotrigine, levetiracetam and topiramate. Further, obtained results will be used for development of new computational models capable of predicting BBB permeability of novel compounds based on their structures.

ACKNOWLEDGEMENT

This work was supported by the Ministry for Science of the Republic of Serbia (Contract No. 172033).

REFERENCES

- [1] M. Kansy, F. Senner, K. Gubernator, *Journal of Medicinal Chemistry*, 1998, 41, 1007-1010.
- [2] L. Di, E. H. Kerns, K. Fan, O. J. McConnell, G. T. Carter, *European Journal of Medicinal Chemistry*, 2003, 38, 223-232.
- [3] P. Crivori, G. Cruciani, P. Carrupt, B. Testa, *Journal of Medicinal Chemistry*, 2000, 43, 2204-2216.

SYNTHESIS AND CHARACTERIZATION OF LEVAN-AMPHOTERICIN B CONJUGATE

B. Kekez¹, G. Dj. Gojgić-Cvijović², D. M. Jakovljević²
V. P. Beškosi^{1,2}, M. M. Vrvić^{1,2}

¹Faculty of Chemistry, University of Belgrade, 11158 Belgrade, Studentski trg 16, POB 51, Serbia; ²Institute of Chemistry, Technology and Metallurgy, University of Belgrade, 11158, Belgrade, Njegoševa 12, POB 473, Serbia (djakovlj@chem.bg.ac.rs)

ABSTRACT

In this work, microbial polysaccharide levan was functionalized by introducing aldehyde groups in the glycan molecule and coupled with polyene antibiotic amphotericin B. Resulting conjugate was characterized by spectroscopic data (UV-Vis and FT-IR) and by results of elemental analysis.

INTRODUCTION

Levan is nonlinear polyfructan with (2,6)-linked β -fructosyl units and (2,1)-branches (Fig.1). Due to the high molecular mass and solubility in water this polysaccharide has many potential uses in different industries [1]. The selection of levan in the synthesis of drug derivatives is justified on the basis of its blood biocompatibility, solubility and biodegradability. Amphotericin B is a polyene antifungal antibiotic (Fig. 2), macrocyclic lactone, produced by *Streptomyces nodosus*. It is used in medicine intravenously, orally and parenterally, however its insolubility in water leads to undesirable side effects [2].

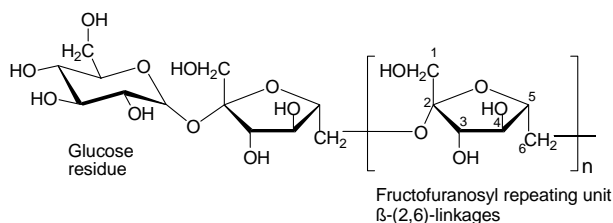


Figure 1. Levan

The aim of the present work was synthesis and spectroscopic characterization of amphotericin B conjugate with activated levan obtained by introducing aldehyde groups in the glycan chain in order to obtain drug with improved solubility in water which would potentially expanded the use of this antibiotic without harmful side effects.

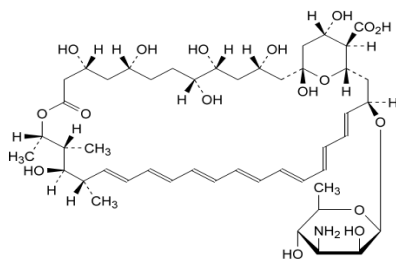


Figure 2. Amphotericin B

EXPERIMENTAL

Levan used in this work was produced by *Bacillus licheniformis* NS032 [3]. Polyaldehyde derivative of this fructan was obtained by reaction with periodate salts in distilled water. Coupling reaction between oxidized levan and amphotericin B was performed in 0.1 M borate buffer (pH 11.0) in the dark, at 40°C, with stirring, during 48 h. Resulting conjugate was purified from unbounded molecules by dialysis (dialysis tubing MWCO 8,000 obtained from Sigma Aldrich Co) against distilled water until negative probe on antibiotic in the surrounding water. Conjugate then was lyophilized (Christ Alpha 2-4 LD plus lyophilizer). Characterization of synthesized product was performed by UV-Vis (GBC Cintra 40 spectrophotometer) and FT-IR (Thermo-Nicolet instrument, Model 6700 equipped with Smart Orbit Diamond ATR accessory) spectral techniques and by the results of elemental analysis, too.

RESULTS AND DISCUSSION

Synthesis of levan-amphotericin B conjugate was done by coupling reaction between aldehyde groups of oxidized polysaccharide and amine groups of antibiotic (Fig. 3).

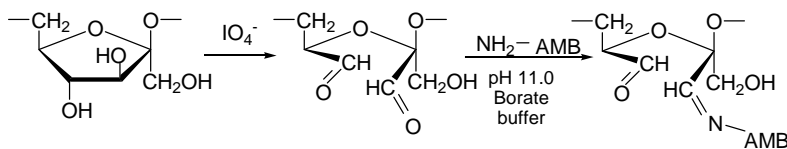


Figure 3. Synthesis of levan-amphotericin B conjugate (AMB-amphotericin B)

In UV-Vis spectrum of oxidized levan no absorption bands were observed (Fig. 4), however, spectrum of synthesized conjugate (Fig. 4) was significantly different, with the typical absorption peaks in the region 340 nm - 430 nm, that characteristic for amphotericin B (Fig. 5). On the basis of

the spectroscopic data it can be concluded that polyaldehyde polymer of levan was successfully coupled with polyene antibiotic amphotericin B.

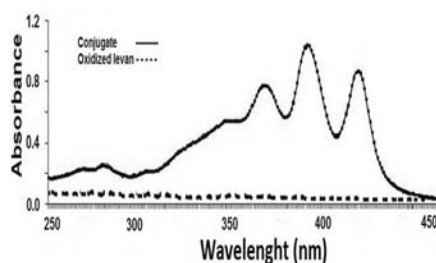


Figure 4.
UV-Vis spectrum of of
conjugate and oxidized levan

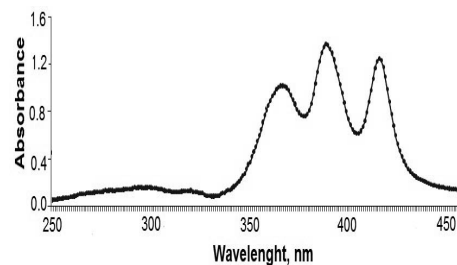


Figure 5.
UV-Vis spectrum of
amphotericin B

Elemental analysis showed the content of nitrogen in the synthesized product, unlike the starting aldehyde-functionalized fructan that did not contain nitrogen. Results of elemental analysis were shown in Table 1.

Table 1. Results of elemental analysis

	% N	% C	% H
Polyaldehyde levan	/	44.40	6.04
Conjugate levan- amphotericin B	3.46	49.12	6.55

The synthesized levan-amphotericin B conjugate was further characterized by FT-IR data (Fig. 6). The FT-IR spectrum of product showed signals specific for polyaldehyde fructan and antibiotic. In the FT-IR spectrum of conjugate among the signals characteristic for levan [4] and band at 1730 cm^{-1} specific for carbonyl group in polyaldehyde glycan, peaks at 1449 cm^{-1} , 1401 cm^{-1} , and 1010 cm^{-1} can be observed relating to $-\text{CH}_3-\text{CH}_2-$, $-\text{COO}^-$ and $-\text{C}-\text{C}-\text{H}$ for chromophore, respectively, characteristic for the peaks of amphotericin B [5]. The strong absorption at 1604 cm^{-1} , relating to imine stretching vibration confirmed that amphotericin B has been covalently coupled to oxidized levan.

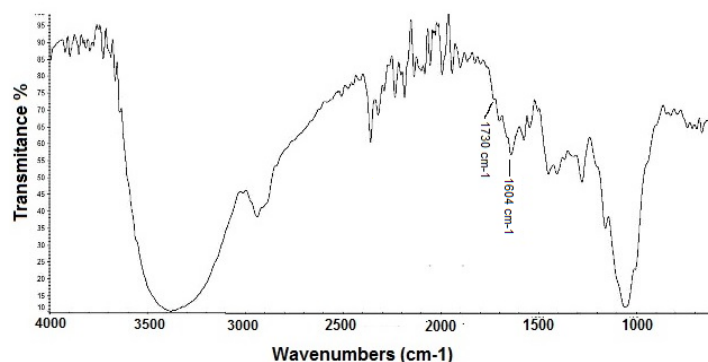


Figure 6. FT-IR spectrum of levan - amphotericin B conjugate

CONCLUSION

In this work a conjugate of aldehyde-functionalized fructan and polyene antibiotic amphotericin B was synthesized by reaction of covalent coupling. Resulting product was characterized by spectroscopic data (UV-Vis and FT-IR) and by the results of elemental analysis.

ACKNOWLEDGEMENT

This work was supported by the Ministry of Education and Science of the Republic of Serbia through Project III 43004.

REFERENCES

- [1] F. Freitas, V. D. Alves, M. A. M. Reis, *Trends Biotechnol.*, 2011, 29, 388-398.
- [2] R. Laniado-Laborín, M.N. Cabrales-Vargas, *Rev. Iberoam. Micol.*, 2009, 223–227.
- [3] G. D. Gojgić-Cvijović, J. S. Milić, T. M. Šolević, V. P. Beškoski, M. V. Ilić, L. S. Djokić, T. M. Narančić, M. M. Vrvic, *Biodegradation*, 2012, 23, 1-14.
- [4] N. L. A. Kee, C. L. Frost, B. I. Pletschke, *Bioresources*, 2012, 7, 4976-4993.
- [5] M. Gagoś, M. Arczewska, *Biochim. Biophys. Acta*, 1798 (2010) 2124–2130.

DETERMINATION OF LOG P OF NEWLY SYNTHETIZED β -HYDROXY- β -ARYL- ALKANOIC ACIDS USING RP-HPLC METHOD

J. Savić¹, J. Brborić¹, S. Dilber² and S. Vladimirov¹

¹ *Department of Pharmaceutical Chemistry, University of Belgrade-Faculty of Pharmacy, Vojvode Stepe 450, 11221 Belgrade, Serbia*

² *Department of Organic Chemistry, University of Belgrade-Faculty of Pharmacy, Vojvode Stepe 450, 11221 Belgrade, Serbia*

ABSTRACT

Lipophilicity expressed via logP of thirteen newly synthesized β -hydroxy- β -arylalkanoic acids was determined using RP-HPLC method. Reported data for five of these acids showed that they exhibit good anti-inflammatory activity which is also expected from remaining eight compounds. In light of this, lipophilicity is very important parameter because of its impact on passive transport of compounds through biological membranes. Classical shake-flask method for logP determination has several disadvantages (emulsion problems, large amount of pure compound required, time consuming), and this is the reason for using RP-HPLC method. In the selection of HPLC method enough low pH value could not be achieved to ensure that all compounds were in their neutral form, so firstly logD was determined, and then log P was calculated. In order to improve chromatographic determination n-octanol was added in mobile phase. The method is based on following the retention times of compounds with known logP values along the newly synthesized compounds in 4 mobile phases with different ratio of methanol and phosphate buffer. LogKw values for all compounds were calculated from the retention times. After plotting a graph of logKw over logD for known compounds, logD for synthesized compounds were interpolated. Because all synthesized compounds are monoprotic acids, logP was calculated from the appropriate equation. LogP of examined compounds was predicted by ChemOffice v8.0 Ultra software package and high correlation was found with experimental logP data ($r=0.8206$).

INTRODUCTION

Thirteen β -hydroxy- β -arylalkanoic acids were synthesized using modified Reformatsky reaction. Synthesis of five acids [**a**: (3-hydroxy-3-(4-

diphenyl)-butanoic acid, **b**: 3-hydroxy-2,2-dimethyl-3-(4-diphenyl)-butanoic acid, **c**: 3-hydroxy-3,3-diphenylpropanoic acid, **d**: 3-hydroxy-2-methyl-3,3-diphenylpropanoic acid, **e**: 3-hydroxy-2,2-dimethyl-3,3-diphenylpropanoic acid] was already reported and their anti-inflammatory activity was documented [1,2]. The impact of substitution of side chain with one or two methyl groups was determined. Remaining eight acids [**f**: 3-phenyl-3-p-tolylpropanoic acid, **g**: 3-hydroxy-3-phenyl-3-m-tolylpropanoic acid, **h**: 3-(4-(trifluoromethyl) phenyl)-3-hydroxy-3-phenylpropanoic acid, **i**: 3-(3-(trifluoromethyl)phenyl)-3-hydroxy-3-phenylpropanoic acid, **j**: 3-(4-chlorophenyl)-3-hydroxy-3-phenylpropanoic acid, **k**: 3-(3-chlorophenyl)-3-hydroxy-3-phenylpropanoic acid, **l**: 3-hydroxy-3,3-bis(4-methoxyphenyl)propanoic acid, **m**: 3,3-bis(4-chlorophenyl)-3-hydroxypropanoic acid] were afterwards synthesized and fully characterized. The aim was to examine their anti-inflammatory activity and to determine the impact of substitution of benzene ring with various substituents which differ in their lipophilicity. Regarding physicochemical descriptors of these compounds it was very important to determine lipophilicity because this descriptor plays a crucial role in pharmacological activity of drugs and organic compounds having influence on passive transport of xenobiotics through biological membranes [3-4]. Lipophilicity is expressed by the log P, which is logarithm of the partition coefficient of a neutral form of a molecule in n-octanol/water system.

The conventional shake-flask method has a few disadvantages such as emulsion problems and the fact that large amounts of pure compounds are required. This is the reason for choosing RP-HPLC method which is shown to be a suitable model for estimating n-octanol/water partition coefficients [5]. The aim was to determine log P values of synthesized compound and to correlate them to predicted values by computer program.

EXPERIMENTAL

The method is based on following the retention times of standard substances (aspirin, ibuprofen, ketoprofen, naproxen and phenanthrene) with known logP values and the newly synthesized compounds in 4 mobile phases consisting of a mixture of phosphate buffer (pH=3) and methanol. Proportion of methanol is 40%, 45%, 50% and 55%. Aqueous phase was previously saturated with n-octanol which also was added to methanol in concentration of 0.25%. BDS Hypersil C18 column 30x4mm, packed with 3 μ m particles was used at mobile phase flow rate 1ml/min and at temperature of 30°C. pKa values were previously determined (around 3.5). All examined compounds were dissolved in appropriate mobile phase. NaNO₃ also dissolved in the mobile phase was injected as the unretained

solute. LogKw values for all compounds were calculated from the retention times of compounds injected in triplicate. After constructing a graph of logKw over logD for known compounds logD for synthesized compounds were interpolated. LogP values for synthesized compounds were calculated from the equation suggested by Scherrer and Howard [6]:

$$\log P = \log D - \log \frac{1}{1 + 10^{\text{pH} - \text{pK}_a}}$$

RESULTS AND DISCUSSION

Experimental results for logP showed in table 1 are in range between 2.321 and 4.043 and that there is high correlation with predicted logP values ($r=0.8206$).

Table 1. Predicted and determined logP values

Compound	Predicted logP values	Determined log P values
a	2.420	2.845
b	4.160	4.043
c	2.610	2.866
d	3.180	2.872
e	3.880	3.062
f	3.100	2.904
g	3.100	2.881
h	3.530	3.127
i	3.530	3.044
j	3.170	2.973
k	3.170	2.970
l	2.360	2.321
m	3.730	3.698

Also, it is important to notice that method is satisfactory due to the time because the longest run, for the compound **b** is 16 minutes in the mobile phase with 40% of methanol. For all the other compounds retention time ranges from couple of minutes in mobile phase with 40% of methanol to about a minute in the mobile phase with 60% of methanol.

Because of pKa values of synthesized compounds ranging around 3.5 it was clear that pH of mobile phase cannot be low enough to ensure neutral form of acids, and in that case only is possible logD determination. However, experimental part is not complicated by this fact, but only one more mathematical step is required which demands that pKa values are known.

The selection of short HPLC column is crucial, because using longer column (100mm) retention times were more 100 minutes.

CONCLUSION

RP-HPLC is a swift method that can be successfully employed in logP determination of synthesized β -hydroxy- β -arylalkanoic acids while taking care of chromatographic conditions especially regarding appropriate column selection. Obtained results show high correlation to calculated logP values in ChemOffice.

ACKNOWLEDGEMENT

This work was partially supported by the Ministry for Science of the Republic of Serbia (Grants No. 34031).

REFERENCES

- [1] S. Dilber, Ž. Žižak, T. Stanojković, Z. Juranić, B. Drakulić, I. Juranić, *Int J Mol Sci*, 2007, 8, 214-228.
- [2] J. Savić, S. Dilber, B. Marković, M. Milenković, S. Vladimirov, I. Juranić, *Molecules*, 2011, 16, 6645-6655.
- [3] T. Hartmann, J. Schmitt, *Drug Discovery Today: Technologies*, 2004, 1, 431-439.
- [4] A. Nasal, D. Siluk, R. Kaliszan, *Curr Med Chem*, 2003, 10, 381-426.
- [5] D. Benhaim, E. Grushka, *J Chrom A*, 2008, 1209, 111-119.
- [6] R. Scherrer, S. Howard, *J Med Chem*, 1977, 20, 53-58.

THE SYNTHESIS OF AMINO ACID ANALOG OF VITAMIN E

Ž. Gagić¹, B. Ivković², J. Vucicević², D. Agbaba² and K. Nikolić²

¹*Faculty of Medicine department of pharmacy, University of Banja Luka, Save Mrkalja 14, Banja Luka, Bosnia and Herzegovina.*

²*Department of Pharmaceutical chemistry, Faculty of Pharmacy, University of Belgrade, Vojvode Stepe 450, Belgrade-Serbia (blucic@pharmacy.bg.ac.rs)*

ABSTRACT

In this study we described the modified synthetic route for esterification of α -tocopherol with amino acid lysine. Using EDC as coupling agent instead of DCC provides an efficient route for preparation of the corresponding di-Cbz-protected tocopheryl lysine ester as an intermediate in synthesis of lysine ester of α -tocopherol.

INTRODUCTION

Vitamin E is a powerful natural antioxidant in the body that controls the peroxidation reactions and the formation of free radicals. Today, special attention is paid to the use of vitamin E and its derivatives in the prevention and treatment of cancer. Specific forms of vitamin E exert a strong apoptotic activity against various types of tumor cells, while not acting, or acting in a small measure, to healthy cells. These data clearly indicate that some natural and synthetic analogs of vitamin E can be effectively used in the therapy of cancer, either alone or in a combination with other anti-cancer drugs, to enhance their effect and reduce the toxicity [1]. Vitamin E derivatives such as α -tocopheryl succinate, which lost their activity against free radicals by the esterification with dicarboxylic acids, act on the growth of many cancer cells and induce apoptosis more efficiently than the α -tocopherol. Structure-activity relationship studies point to a pivotal role of succinyl component in initiating pro-apoptotic cascade of events through a synergistic ways [2-3]. The formation of amino acid esters resulted in a significant increase in antiproliferative activity [4]. The aim of this work is to present enhanced synthetic route for the formation of α -tocopheryl lysine ester.

EXPERIMENTAL

All the solvents and reagents used were analytical grade. For the chemical synthesis and analysis of α -tocopheryl lysine the following compounds were

used: EDC (1-ethyl-3-(3-dimethylaminopropyl) carbodiimide), DMAP (4-dimethylaminopyridine), α -tocopherol and di-Cbz lysine ((2S)-2,6-bis (benzyloxycarbonylamino) hexanoic acid). The purity of the compounds was checked using HPLC and TLC methods. TLC was carried out using silica gel plates (Merck, Germany) and the spots were visualized under UV light at 254 nm or with potassium permanganate / sulfuric acid reagent. HPLC analyses was performed on the Zorbax Eclipse XDS-C18 column with mobile phase methanol : water (97 : 3, v/v) with UV detection at 210 nm. Column chromatography was performed for purification of the compounds on silica gel. The IR spectra were recorded on the Thermo Nicolet 6700 FT-IR spectrophotometer using ATR technique. The NMR spectra were recorded on the Varian Gemini 200 using deuterated chloroform as a solvent. The mass spectra of compound was conducted on a TSQ Quantum Access MAX triple quadrupole spectrometer (Thermo Fisher Scientific) equipped with electrospray ionization (ESI) source operating in positive ion mode.

Synthesis of di-CbZ-Lys- α -tocopherol ester

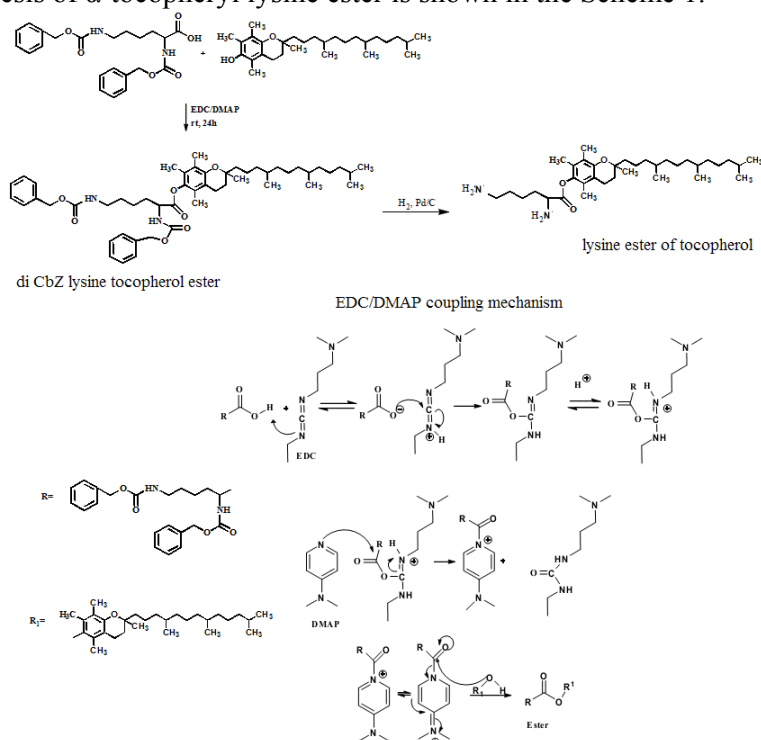
To a stirred solution of 0.904 g α -tocopherol in 80 ml dry CH_2Cl_2 were added 0.062 g DMAP, 0.25 g of EDC and 0.45g of di-CbZ-Lys. The mixture was protected from light and stirred at the room temperature for 27h under nitrogen atmosphere. The reaction mixture was washed three times with 20 ml H_2O and dried over Na_2SO_4 . The solvent was evaporated in vacuo. The resulting yellow oil was purified by flash chromatography with eluent n-hexane: AcOEt (3 : 1.2, v/v) and stored under nitrogen atmosphere at 0-4 °C. (Yield 86%)

Synthesis of α -tocopheryl lysine 450 mg di-CbZ-Lys- α -tocopheryl ester was dissolved in 20 ml absolute ethanol and stirred under nitrogen atmosphere. To this solution was added 90 mg of 10% Pd over activated carbon. The mass was subjected to hydrogenation at ambient temperature with the pressure of 2atm H_2 under mechanical agitation. Once the reaction was completed (TLC monitoring, n-hexane : AcOEt, 3 : 1.2, v/v), the catalyst was filtered over membrane filter and the solvent was evaporated to yield free amine as a yellow oil. Solution of HCL in dry diethyl ether was added and the white precipitate of amine salt was filtered off and dried in a vacuum oven at room temperature for 24h. (Yield=80%). $\text{C}_{35}\text{H}_{63}\text{N}_2\text{O}_3\text{Cl}$: 2,5,7,8-tetramethyl-2-(4,8,12-trimethyltridecyl)-3,4-dihydro-2H-chromen-6-yl 2,6-diaminohexanoate. The albescent solid. Yield=80%; Spectral data for free aminino ester ($\text{C}_{35}\text{H}_{62}\text{N}_2\text{O}_3$), IR (ATR) (cm^{-1}): 3385.2 (- NH_2), 2924.6, 2867.5 and 1377.3 (*as* and *sy* - CH_2 - and - CH_3), 1764.9 (-C=O); 1191.2 (-C-O); ^1H NMR data (CDCl_3 , δ , ppm): 0.80-0.88 (m, 12H - CH_3); 1.58-0.96 (m, 26H, - CH_3 , - CH_2); 1.81-1.70 (m, 6H -CH and CH_2); 1.93-1.90 (m, 6H, - CH_3); 2.03 (m, 3H, - CH_3); 2.11 (s, 2H, - NH_2); 2.63-2.52 (m, 2H, - CH_2); 3.15-3.02 (m, 2H, - CH_2); 3.45 (s, 2H, - NH_2); 3.86 (m, 1H,

-CH-); ^{13}C NMR data (CDCl_3 , δ , ppm): 173.75, 149.47, 140.20, 126.47, 124.79, 123.03, 117.44, 75.01, 53.66, 40.58, 39.75, 39.32, 37.40, 37.23, 32.74, 30.94, 27.91, 24.76, 24.42, 23.42, 22.67, 22.58, 20.99, 20.52, 19.63, 12.93, 12.09, 11.73; LC-MS: $m/z = 559.47$ ($\text{M}^+ + 1$), 84.15, 542.51, 129.06, 56.16.

RESULTS AND DISCUSSION

Synthesis of α -tocopheryl lysine ester is shown in the Scheme 1.



Scheme 1. Synthetic route and structures of investigated di-CBz lysine- α -tocopherol ester and lysine- α -tocopherol ester

The proposed compound was prepared in two steps and the structure has been verified by IR, ^1H -NMR, ^{13}C -NMR and MS spectroscopy. The first step in the synthetic route was the coupling of α -tocopherol with di-CBz-lysine using EDC/DMAP reaction conditions. Di-CBz lysine- α -tocopherol ester was prepared in 86% isolated yield, after purification by column chromatography on silica gel (eluent n -hexane/AcOEt). Hydrogenation of compound with 10% Pd/C as a catalyst gave the corresponding free amine analog that was isolated as the hydrochloride salt after acidification with

HCl solution in dry diethyl ether. The white precipitate of hydrochloride salt thus formed was dried in a vacuum oven (Yield=80%). The mechanism of coupling with EDC (Scheme 1) is similar to nucleophilic catalysis mechanism except that instead of the direct nucleophilic attack of alcohol on acid-urea complex, here the attack comes from DMAP. This reactive amide of DMAP is later attacked by alcohol to form ester. DCC and DMAP in dry CH_2Cl_2 is the most common condition in esterification reaction [6]. However, traces of both DCC and DMAP can be seen in the ^1H NMR of the resultant product. To avoid this, we used EDC, which is water soluble and can easily be removed by washing with water, while DMAP was removed by flash chromatography. The IC and NMR spectra were used to confirm the binding between lysine and α -tocopherol. The IC spectrum of lysine- α -tocopherol indicates that peak at 1764 cm^{-1} was assigned to $-\text{C}=\text{O}$ stretching vibration of carbonyl group (ester band). When compared with α -tocopherol spectra this peak is the new signal. Furthermore, in the ^1H NMR spectrum the newly appeared signals at 0.96-1.70, 3.14-3.02 as well as 3.86 belong to the methene and methylene hydrogen of the lysinyl group.

CONCLUSION

The described synthetic route has the advantage over the literature listed method because the EDC is transformed to the water soluble urea during coupling reactions, which can easily be removed from the reaction mixture by extraction.

ACKNOWLEDGEMENT

This work was partially supported by the Ministry for Science of the Republic of Serbia (Grants No. 172033).

REFERENCES

- [1] B. S. McIntyre, K.P. Briski, M.A. Tirmenstein, M.W. Fariss, A. Gapor, P.W. Sylvester, *Lipids*, 2000, 35(2), 171-80.
- [2] W. Yu, M. Simmons-Menchaca, A. Gapor, B.G. Sanders, K. Kline, *Nutr Cancer*. 1999, 33 (1), 26-32.
- [3] K.M. Nikolić, *J. Mol. Graph. Model*. 2007, 26, 868-873.
- [4] P. Arya, N. Alibhai.; H. Qin, B.W. Burton, *Bioorg. Med. Chem. Lett*. 1998, 8, 2433-2438

DEHP LEACHING FROM MEDICAL DEVICES USED FOR PERITONEAL DIALYSIS DETERMINED BY GC-MS

I. Kostić¹, T. Anđelković¹, D. Anđelković¹, A. Bojić¹, T. Cvetković²
and D. Pavlović²

¹University of Niš, Faculty of Science and Mathematics, Višegradska 33,
18000 Niš, Serbia (ivana.kostic83@gmail.com)

²University of Niš, Faculty of Medicine, Bul. Zorana Đinđića 81, 18000 Niš,
Serbia

ABSTRACT

The presence of di-(2-ethylhexyl) phthalate (DEHP) in the whole peritoneal dialysis set, consisted of peritoneal dialysis PVC bags, PVC tubing and Peritoneal Dialysis Solution is investigated for the first time. Phthalate determination was carried out by gas chromatography-mass spectrometry (GC-MS). The results showed that the PVC dialysis bag in which solution for peritoneal dialysis was stored contains 49-61% DEHP by weight, while tubing material coupled to the bag contains 71-84% DEHP by weight. Concentration of DEHP in Peritoneal Dialysis Solution that was stored in the dialysis bags and tubing was $4.29\mu\text{g L}^{-1}$.

INTRODUCTION

Phthalates are used as plasticizers and additives in plastic materials. Polyvinyl chloride (PVC) materials are widely used in the production of medical and clinical devices, and di-(2-ethylhexyl) phthalate (DEHP) is the most widely used plasticizer in PVC medical devices. PVC medical devices used for the health care industry include: blood bags, dialysis bags and tubing, catheters and gloves.[1]As plasticizer, DEHP is not chemically bound to the PVC polymer. Therefore, DEHP can migrate from plastic to environment and the migration rate is dependent upon its ability to diffuse through the plastic material into the surrounding media.[2] Humans exposed to DEHP showed serious health problems, and DEHP is suspected as endocrine disruptor and carcinogenic to humans. Prenatal exposure of rats to DEHP resulted in teratogenic effects.[3]The standard analysis procedure for phthalates is solvent extraction and GC-MS detection. This technique and procedure is used in this paper.

EXPERIMENTAL

All used reagents were of analytical reagent grade. DEHP and di-butyl adipate (DBA) which was used as internal standard were obtained from Sigma Aldrich (St Louis, MO, US) and hexane was HPLC purity grade (purchased from Merck (USA)). Stock standard solution of DEHP at a concentration of 1000 mg L^{-1} was prepared in hexane in glass-capped volumetric flask and stored at 4°C in refrigerator. Working standard solutions were prepared daily by diluting the stock standard solution. Concentrations of working standard solutions were $0.25 - 50 \text{ } \mu\text{g mL}^{-1}$. Special care was taken to avoid the contamination of sample due to contact of reagents and solvents with plastic laboratory materials during sample preparation. Laboratory glassware was used and usage of plastic consumables during the analysis was avoided.

Samples of dialysis bags and tubing were cut in pieces, each of 1 cm^2 area. A piece of PVC material was extracted with 5 mL hexane and allowed to stand for 6 days. Hexane extracts were analyzed directly after sampling.

Peritoneal dialysis solution samples stored in PVC dialysis bags were collected in glass volumetric flasks and stored at 4°C until analysis. The liquid-liquid extraction method has been applied to the analysis of Dianeal Low Calcium (2.5 meq L^{-1}) Peritoneal Dialysis Solution (contains 1.5% Dextrose), which were stored in PVC bags for 3 years before analysis. Since the usual shelf-life of peritoneal dialysis solutions is three years, migration rates of DEHP from PVC bags can be applied for the period of 3 years. The extraction procedure was carried out with 5 mL of hexane for 500 mL of sample, providing organic to aqueous phase volume ratio equal to 0.01, as minimal for effective extraction.[4] This is justified by the fact that the partition of DEHP for the applied volume ratio is sufficient and that evaporation procedure could cause the analyte loss. Experiments were carried out at room temperature and pH value 6.5. Previous investigations which were performed by spiked solutions of peritoneal dialysis solutions were shown that one-step extraction has recovery more than 95%. Time of extraction was 6 hours. Di-butyl adipate (DBA) was used as an internal standard in all samples, leading to the concentration of DBA to be $1 \mu\text{g mL}^{-1}$ in each sample. Determination of phthalates was performed by Hewlett Packard 6890 Gas Chromatograph equipped with an Agilent 5973 Mass Selective Detector (MSD). A DB-5 MS capillary column ($30 \text{ m} \times 250 \text{ mm} \times 0.25 \text{ mm}$, Agilent, USA) was used for chromatographic separation. The oven is programmed from 60°C (1 min) to 220°C (1 min) at rate of $20^\circ\text{C min}^{-1}$ and after to 280°C (4 min) at rate of 5°C min^{-1} . The gas chromatograph was operated in splitless injection mode. The operating temperature of the MSD was 280°C with the electronic impact at 70 eV. The MSD was used in

the ion-monitoring (SIM) mode at m/z 149. The identification of DEHP was based on the relative retention time, the presence of target ion and its relative abundance. The quantification ion for DEHP is m/z 149. The dwell time was 100 ms. DEHP had high calibration coefficients ($r^2 > 0.9970$). All the samples were quantified in triplicate.

RESULTS AND DISCUSSION

The hexane extraction of solid samples of PVC dialysis bag has been applied for determination of DEHP in solid samples due to high extraction efficiency for phthalates. The yield of extraction showed that more than 80% of the phthalates in solid samples are extracted in the first 3 days. Presented results are obtained after the extraction procedure which was carried out with the time period of 6 days.

The obtained chromatograms of the DEHP from PVC dialysis bag within a running time of 26 minutes. Retention times for DBA and DEHP were 9.945 and 18.266 min, respectively. The results obtained for DEHP from samples of PVC dialysis bag and tubing are given in Table 1. The determined DEHP concentration levels of 49-62% by weight of sample is high although expected bearing in mind the material used for medical device production.

Table 1. Percentage of phthalates in dialysis bag and tubing

Sample	Mass of sample (g)	Concentration of DEHP in hexane extract (mg mL^{-1})	% DEHP
Bag	0.0400	4.91	61.31
	0.0370	4.19	56.67
	0.0341	3.37	49.42
	0.2618	42.01	80.23
Tubing	0.2671	38.11	71.36
	0.2614	43.54	83.29

Analysis of PVC tubing material coupled to the bag was carried out with the same procedure as for dialysis bag. The DEHP concentration levels in tubing were higher than DEHP concentration levels in dialysis bag. Both determined concentrations are higher than expected from literature data.[5] The results obtained by liquid-liquid extraction of DEHP from Peritoneal Dialysis Solution are given in Table 2. Very low amounts were leached by Peritoneal Dialysis Solution from PVC dialysis bag, despite the fact that dialysis bag contains DEHP in high concentration level. Besides, in process of peritoneal dialysis in humans, solution avoids transport path through liver, the majority of an intraperitoneally injected dose of DEHP is not absorbed and a considerable amount of the infused DEHP will be removed upon drainage from the peritoneum.

Table 2. Phthalates concentrations ($\mu\text{g L}^{-1}$) in Peritoneal Dialysis Solution stored in PVC dialysis bag

Peritoneal dialysis solution	DEHP ($\mu\text{g L}^{-1}$)	Mean value DEHP \pm sd ^a
Sample 1	4.33	
Sample 2	4.11	4.29 \pm 0.17
Sample 3	4.44	

^asd – standard deviation (n = 3).

CONCLUSION

A migration of DEHP from dialysis bag and tubing that are made from PVC into dialysis solution that was stored in the PVC bags has been investigated. Phthalates are used as plasticizer, especially in PVC materials and the presence of phthalates in the investigated samples can be attributed to the release of these compounds from the PVC bag. Concentrations of DEHP which are determined in peritoneal dialysis solution were about $4.29 \mu\text{g L}^{-1}$. Even though the determined concentrations in the dialysis set are higher than expected according to literature data, the leached amount of DEHP in the dialysis solution is not significant.

The proposed method can be applied for the determination of DEHP in solid samples of different samples from medical devices and solutions which are stored in plastic containers. Control of material which is used for production of the plastic medical devices is essential to avoid human exposure to phthalates.

ACKNOWLEDGEMENT

This paper was carried out as part of Project III 41018 that was financed by Ministry of Education, Science and Technological Development, Republic of Serbia.

REFERENCES

- [1] M. J. Silva, E. Samandar, J. L. Preau Jr., L. L. Needham, A. M. Calafat, *Toxicology*, 2006, 219, 22–32.
- [2] S. Pradeep, S. Benjamin, *J. Hazard. Mater.*, 2012, 235–236, 69-77.
- [3] C. Perez Feas, M. C. Baricela Alonso, P. Bermejo-Barrera, *J. Chromatogr. A*, 2011, 879, 231-235.
- [4] J. Pawliszyn, *Sampling and Sample Preparation for Field and Laboratory: Fundamentals and New Directions in Sample Preparation*, Elsevier, 2002.
- [5] Australian Government, Department of Health and Ageing, *Human Health Toxicity Risk Assessment of DEHP in Medical Devices*, 2007.

DETERMINATION OF CHLORIDE IN THE PHARMACEUTICAL PREPARATIONS USING FLUORESCENCE QUENCHING METHOD

S.M. Blagojević¹, I. Borić¹, N.Erić¹, A. Janošević Ležaić¹
and R. Daljević²

¹University of Belgrade –Faculty of Pharmacy, Vojvode Stepe 450,
Belgrade ²Institute of General and Physical Chemistry, Studentski trg
12–16, Belgrade Serbia

ABSTRACT

Fluorescence quenching method can give useful kinetic information of the investigated system fluorophore–quencher, but it can be applied for determining the concentration of the quencher in a variety of biological and pharmaceutical samples. In the present paper the influence of chloride ion to the quenching of fluorescence intensity of quinine was investigated. Using fluorescence quenching method, applying the Stern–Volmer kinetics, the concentration of chloride in samples of 0.9 % infusion solution and 2.0 % lidocaine–chloride injection solution was determined.

INTRODUCTION

Fluorescence intensity sensing is an established analytical method due to its high sensitivity and selectivity for a wide variety of analytes. It is generally known that the fluorescence of certain heterocyclic indicators such as those based on quinine and acridine type fluorophores [1] are quenched by halides [2,3]. Decrease in fluorescence intensity or lifetime can be measured and related directly to the halide concentration via different quenching mechanism.

The alkaloid quinine, a well–known anti–malarial drug and muscle relaxant with a bitter taste, is a very strongly fluorescing compound in dilute acid solution which contains a quinolinium ring was sensitive to halide. The chloride ions quench the quinine fluorescence by collisionally deactivating the excited fluorophore (referred to as “dynamic” fluorescence quenching) [4], where both the lifetime and intensity of fluorescence of quinine are reduced in the presence of a quencher. The fluorescence quenching is known to follow Stern–Volmer kinetics [1,4] and has been related to the chloride concentration by the Stern–Volmer equation:

$$I_{oF}/I_F - 1 = K_{SV} c_{Cl^-}$$

where I_{oF} and I_F are the fluorescence intensities before and after adding the quencher (Cl^-), respectively, c_{Cl^-} is the molarity of quencher and K_{SV} is the dynamic Stern–Volmer quenching constant. This equation can be used to obtain values of the Stern–Volmer chloride quenching constant, by plotting $I_{oF}/I_F - 1$ as a function of quencher concentrations and for determination of the chloride ions.

In this paper we describe the dynamic fluorescence quenching of quinine by chloride ions in aqueous media which can be used for chloride concentration determination in sodium chloride infusion solution and lidocaine–chloride injection solution.

EXPERIMENTAL

The series of standard solutions with varying chloride concentrations and a constant quinine concentration will be used to study collisional quenching and determination of chloride ions in both real samples 0.9 % sodium chloride infusion solution (Natrii chloridi infundibile) and 2.0 % lidocaine–chloride injection solution. The quinine (Fluka) solutions were prepared in 0.05 M sulphuric acid (Merck). The quinine concentration in all the standard chloride solutions and real samples was $1.54 \times 10^{-4} \text{ mol L}^{-1}$. Potassium chloride (Sigma–Aldrich) dissolved in deionized water was used to prepare standards of various chloride ion concentrations in the range $2.0 \times 10^{-5} \text{ mol L}^{-1} - 8.0 \times 10^{-3} \text{ mol L}^{-1}$. 1.0 mL of both real samples is transferred to 25 mL volumetric flask and diluted to volume with 0.05 M H_2SO_4 . The fluorescence intensity were measured using a filter fluorimeter Spekol 10 (Carl Zeiss Jena, Germany), with excitation wavelength 365 nm. The results of chloride determination using fluorescence quenching method were compared with those obtained by ion chromatography (IC). Chloride determined by IC using a Dionex ICS–3000 system with suppressed conductivity detection. The column used was an IonPacAS14 with an eluent concentration of 3.5 mM Na_2CO_3 and 1.0 mM $NaHCO_3$ and flow rate is 1.2 mL min^{-1} . All measurements were performed at room temperature.

RESULTS AND DISCUSSION

The results presented in Figure 1a show that fluorescence intensity decreases in the presence of quencher chloride ion, in the frame of applied experimental conditions. A Stern–Volmer plot of a chloride quenching of quinine is presented in Figure 1b. Using the calibration curve method, the linear response obtained for chloride ion in the range $2.5 \times 10^{-4} \text{ mol L}^{-1} - 8.0 \times 10^{-3} \text{ mol L}^{-1}$. The corresponding regression equation was found to be

$I_{0F}/I_F - 1 = 0.00777 + 163.24c_{Cl^-}$ ($r^2 = 0.9993$). Limit of detection (LOD) and limit of quantification (LOQ) were found to be 7.17×10^{-5} and 2.39×10^{-4} , respectively. The accuracy of the method was determined for three different chloride concentrations. Recovery values were in the range 98.4 % – 103.2 % and satisfactory. The value of dynamic Stern–Volmer constant, K_{SV} , for chloride quenching of quinine, determined from the slope of the linear regression curve, is $163.24 \text{ mol}^{-1} \text{ L}$ and it is comparable to the previous results [2,5].

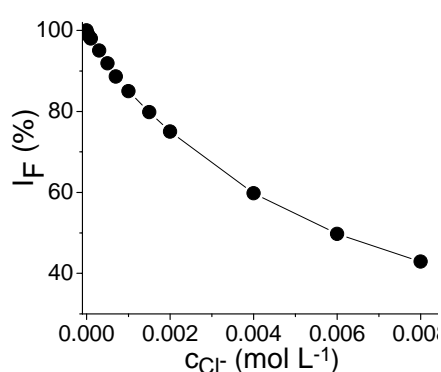


Figure 1a.
Chloride quenching of quinine

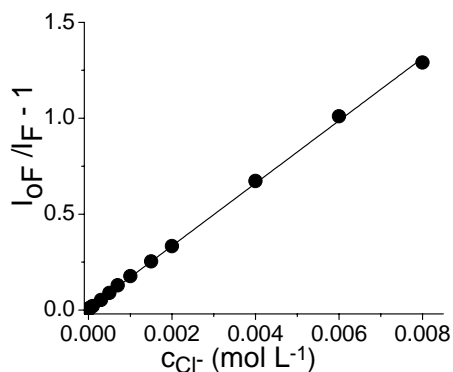


Figure 1b.
The Stern–Volmer plot of
chloride
quenching of quinine

Figure 3 shows a ion chromatogram of 2.0 % lidocaine–chloride injection solution obtained using the IonPac AS14 column.

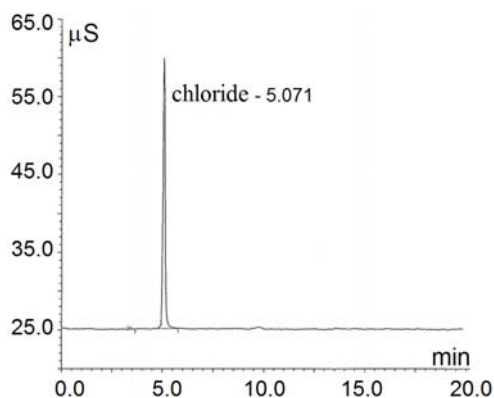


Figure 3.
Ion chromatogram of 2.0 %
lidocaine–chloride solution.

The results for determination of chloride obtained in both samples were summarized and reported as mean value \pm standard deviation (SD) for five replications in Table 1. Measurement uncertainty for IC was determined on the basis of 32 measurements on 100 ppm solution and expressed as relative standard deviation (RSD). RSD was 4.5 %.

Table 1. Chloride ion concentrations in the samples

Sample	Fluorescence quenching method	Ion chromatography
	c (mmol L ⁻¹)	
	(mean \pm SD)	(mean \pm SD)
0.9 % infusion solution*	161.2 \pm 4.2	162.1 \pm 7.3
2.0 % lidocaine–chloride injection solution	162.3 \pm 4.4	163.1 \pm 7.3

*Hydrochloric acid was added as expicent for the adjusting the pH, and by using this method it was determined the total concentration of chloride in the sample.

CONCLUSION

The results show that the influence of chloride ions on fluorescence quenching of quinine can be described by Stern–Volmer kinetics. The simple and sensitive fluorescence quenching method, based in Stern–Volmer equation, was successfully applied to rapid determination of chloride ion in different pharmaceutical preparations. The results obtained by the proposed fluorescence quenching method were in excellent agreement with those obtained by the ion chromatography method.

ACKNOWLEDGEMENT

The present investigations were supported by the Ministry of Education, Science and Technological Development of the Republic of Serbia, Grants no. 172015.

REFERENCES

- [1] J. R. Lakowicz, Principles of Fluorescence Spectroscopy, (Eds.), Plenum Press, New York, 1999.
- [2] A. Martin, R. Narayanaswamy, Sensors and Actuators B, 1997, 38–39, 330–333.
- [3] N. Cheng–Gang, A. Guan, G. Zeng, Y. Liu, G. Huang, P. Gao, X. Gui, Anal. Chim. Acta, 2005, 547, 221–228.
- [4] C. D. Geddes, Meas. Sci. Technol., 2001, 12, 53–88.
- [5] J. H. Gutow, J. Chem. Edu. 2005, 82, 302– 305.

INDEX

Abazović N.	566, 683	Badea M.	399, 403, 631
Adaila K.	1025	Banković P.	260, 407, 991
Adiguzel O.	715	Baranac-Stojanović M.	200
Adnađević B.	296, 312,577	Baskakov A.A.	791
Adžić M.	482, 486, 490	Begović N.	767
Agbaba D.	1129, 1122, 1149	Beloglazkina E.K.	775
Aguado F.	671	Beljanski M.V.	542
Ahrenkiel S.P.	522	Benredjem Z.	411
Ajduković J.	465	Bera O.	608
Aksentijević S.	893	Berdnikova D.V.	558
Aleksić M.M.	422, 430, 426	Beškoski V. P.	514, 687, 1141
Aleksić V.	795	Bilyarska L.	276
Aliyeu T.M.	558	Bjelica L.J.	639
Alleg S.	615	Blagojević S.M.	360, 1019, 1157
Alushllari M.	534, 965	Blagojević S.N.	360, 1071, 1019
Amaral L.	383	Blagojević V.A.	200, 308, 767
Anachkov M.	215	Blanko C.	268, 671
Andelković T.	925, 1153	Blokhina A.G.	81
Andelković D.	1153	Bogdanova Yu. G.	759, 775, 779
Andelković K.	1025	Bogdanović U.	526
Anđus P.R.	554, 550	Bojić A.	937, 1153
Anić S.	336, 360	Borić I.	1157
Anisimov M. P.	31, 77, 600	Bošković M.	1113, 1121
Antić B.	581	Boutabia N.	615
Apostolidou E.	841	Bouteillon J.	434
Aranda P.	991	Bouzabata B.	615
Avramović J.	288	Bowmaker G. A.	651
Avramović N.	461, 538	Božović N.	486, 490
Aydemir T.	845	Brankov M.	477
Aydin E.	164	Brašanac J.	490
Azizoglu A.	192, 188, 196	Brborić J.	1145
Babur Sas E.	115	Brdarić T.P.	969
Bačić G.	546, 550, 554		

Brkić Ž.	490	Daković M.	905
Bubanja I.N.	336	Daljević R.	1157
Budimir M.	526	Darder M.	991
Budinski-Simendić J.	608	David B.	308
Bulanov E.N.	81	Deda A.	965
Bulgakov N.	226	Dekanski A.	707
Caglieri S.C.	124	Delić N. S.	530, 542
Cakić M.	518, 1037	Delimi R.	411
Calatayud P.	581	Deliu A.	965
Can M.	115	Dembska A.	449
Carević M.	683	DEMÍČ S.	115
Cherkezova-Zheleva Z.	230	Dermentzis K.	841
Chernikova E. V.	300, 763, 791	Dilber S.	1145
Chernorukov N.G.	73	Dimić D.	176, 1033
Cholach A.	144, 226	Dimitrić-Marković J.M.	140, 414
Christoforidis A.	841	Dimitrijević A.	109
Cicici N.	534	Dimitrijević S.	526
Ciftci H.	164	Dimkić M.	913
Ciganović J.	172	Dimović S.	901
Crevar Sakač M.	148	Djekoun A.	615
Csanádi Zs.	865	Djellabi R.	961
Cvetičanin J.	152	Djurendić E.	465
Cvetinov M.	733, 737	Djurić D.	461, 538
Cvetković T.	1153	Dobricic V.	1105, 1137
Cvetković V.S.	639	Dojčinović M.	981, 985
Čanadi J.	136, 1067	Dolzhikova V. D.	759, 775, 779
Čobeljić B.	1025	Dominko R.	604
Čolović M.	461, 538	Dostanić J.	180, 239
Čomor M.I.	623, 627, 683	Dragičević V.	473, 477
Čučulović A.	857	Dragović R.	877
Čudina O.	1105	Dragović S.	877, 905
Čupić Ž.	340, 356, 360	Drmanić S.	707
Čirić-Marjanović G.	643	Dujaković N.	913
Čirin D.	1067	Dumanović Z.	473
Čujić M.	877	Džunuzović E. S.	803
		Džunuzović J.V.	526, 803, 811

Đokić M.	877	Gajinov S.	1019
Đolić M.	941	Geđa M.	1125
Đorđević D.	937	Georgieva P.	243
Đorđević J.	675	Gervald A.Yu.	300, 791
Đorđević J.B.	482, 486, 490	Ghorab M.F.	961
Đorđević M.	877	Gizdavic-Nikolaidis M. R.	438, 651
Đorović J.	140	Glebov E.M.	853
Đukić A.	695, 917, 1011	Glumac M.	494, 502
Đurić A.	514	Gluszynska A.	449
Đurović I.	120	Gođevac D.	815
Đurović S.	477	Gojgić-Cvijović G. Dj	514, 687, 1141
Eber N.	733, 737	Gojković S.Lj.	375
Ekmešćić B.	783, 787, 1003	González F.	268, 671
Eliyas A.	230	Gorjanović S.	414, 494, 498
Elokhin V. I.	226, 334	Goronja J.	418
Er C.	164	Goya G. F.	581
Erić N.	1157	Grbović Novaković J.	691, 695, 745
Eronyan M.A.	612	Grinvald I.	128
Fedorov Y.V.	558	Grivin V.P.	853
Fedorova O.A.	558	Grozdanić M.	453
Fekete L.	207	Grozdić T. D.	869, 873
Figueiredo J.L.	383	Grujić A.	591
Filipić S.	1129	Grujić D.	711
Filipović D.	1113, 1117, 1121	Grujić M.	1133
Floroian D.	399, 403, 631	Grujić S. R.	89, 93, 667
Floroian L.	399, 403, 631	Guidetti R.	457
Fodor-Csorba K.	733, 737	Gulakova E.N.	558
Furrow S.D.	12, 320	Güler S.	845
Gabrovska M.	235, 272, 276	Gusarova E.V.	69
Gačić Z.	869	Gutman I.	28
Gadžurić S.	465, 861	Hadač O.	20
Gagić Ž.	1149	Halaši T.	1091, 1097, 1095
		Hedrih K.R.	328
		Hegediš A.	869, 873

Hercigonja R.	819, 823	Jovanović U.	566
Horvat S.	1095	Jovanović V.	562
Hranisavljević S.	981, 985	Jovanović V.P.	1063
İCLİ S.	115	Jovičić M.	608, 799
Ignjatović J.	132	Jović B.	136
Ignjatović N.	518	Jović D. V.	1059
Ikonić B.	795	Jović M.	395, 897
Ilić Lj.	1037	Jovićević J.N.	639
Innocent C.	411	Jović-Jovičić N.	260, 407, 991
ISHIKAWA Y.	248	Jugović D.	604
Ivanović A. T.	395	Juskowiak B.	449, 510
Ivanović-Šašić A.	260, 360, 391	Kačarević-Popović Z.	566, 699, 703
Ivković B.	1125, 1149	Kaji Y	85
Jakovljević D. M.	514, 687, 1141	Kalagaev I.	128
Jakovljević J.K.	647	Kalagasidis Krušić M.	703
Janković D.	581	Kalamković S.	1087. 1091
Janković I.A.	623, 683	Kalgin K.V.	334
Janković M.	957	Kalijadis A.	675, 679, 849
Janković-Mandić Lj.	941	Kapetanović V.	422, 426, 430
Janošević Ležaić A.	418, 1157	Kapor A.	1041
Janović B.	1025	Karaman M.	494, 502
Janjić G. V.	1029, 1053	Karljikovic-Rajic K.	132, 1101
Janjušević Lj.	494, 502	Kecić V.	889, 893
Jelenković B.	711	Kekez B.	687, 1141
Jeremić K. B.	803	Kelarakis A.	39
Jevremovic M.	438, 651	Kishilov S.M.	791
Jevrić L.	465, 861	Kiurski J.	889, 893
Jokić B.	522, 604, 627	Kizilirmak G.M.	741
Jovanovic J.M.	348	Klaus A.	469
Jovanovic M.	348	Knyazev A.V.	57, 69, 81, 729
Jovanović V.	473	Knyazeva S.S.	57, 69, 73
Jovanović D.	215, 230, 272, 387	Kocić G.	925
Jovanović J.	296, 312, 577	Kohout M.	20
Jovanović M.	550	Kokkinos N.	841

Kolar-Anić Lj.	336, 340, 356	Lazić P.	1015
Konstantinović Z.	643, 647	Lazić V.	522, 526
Kordić B.	136	Lević Lj.	977, 1049
Korokin V.J.	81	Lijeskić N.	430
Kosman J.	449	Lončarević D.	180, 239, 272
Kostić I.	1153	Lukić I.	482, 486, 490
Kostina J. V.	763, 779, 791	Lukić-Petrović S.	655
Kostović M.	1015	Lutsyk V.	49, 97, 101, 105
Koturević B.	296	Ljubenović T.	921
Kovačević B.	1045, 1049	Ljubić I.Ž.	352
Kovačević O.	1045, 1049	Macura S.	29
Kovačević S.	465, 861, 913	Maćzka M.	73
Kovalyov E.V.	334	Mačešić S.	356
Krashennnikova O.V.	729	Majouga A. G.	775
Krasnoshchekov S.V.	119	Maksimov G. V.	530, 542
Krstić D.	461, 538	Maksin D.	585, 783, 819
Krstić J.	566, 703	Malenov D. P.	1029
Krstić J.	272, 276, 284	Malenović A.	418
Krstić N. S.	156, 937	Maletić M.	679
Kulesh A.Y.	612	Mamula B.P.	745
Kuljanin-Jakovljević J.	699	Mandić J.	1087, 1095
Kumrić K.	917, 1007, 1011	Mandić-Kovačević N.	506
Kuntić V.	148	Manojlović D.	407, 881, 885
Kurku C.	749, 753	Manyakina M.E.	619
Kurku C.	749	Marinković A. D.	803
Kurko S.	695	Marinković D.	284, 288
Kurt M.	115	Marinković M.	280
Kuzmanoski M.	172, 921	Marinović-Cincović M.	562
Labus N.	659	Marković S.	120
Laušević M.	679, 849, 913	Marković B.	132, 1105, 1101
Laušević Z.	675, 679, 849	Marković D.	823
Lazarević N.	577	Marković D.M.	881, 885
		Marković G.	562

Marković J.	783, 787, 819	Milojković D.	925
Marković S.	252	Milosavljević B. S.	168
Marković V.M.	340	Milošević I.R.	881, 885
Marković Z.	526	Milošević M.	152, 160
Marković Z.S.	120, 140, 414	Milošević S.	691
Markushev D.	1059	Milovanović D.	711
Marmanis D.	841	Milović M.	604
Matijašević S.D.	667	Milutinović S.	819
Matović Lj.	691, 917, 1011	Milutinović-Nikolić A.	387, 407, 991
Matveev A.V.	334	Miljić Z.	949
Mehandjiev D.	243	Minić D.M.	200, 308, 767
Mehellou A.	411	Minić D.M.	308
Mentus S.	438	Mirković M.	585, 1041
Mesaroš G.	869	Mitić A.	937
Meshkovskiy I.K.	612	Mitić M.	482, 486, 490
Micić D.	807, 973, 977	Mitić N.	530
Mico S.	965	Mitić S.S.	304
Mićković M.	869	Mitić Ž. J.	168, 518, 1037
Mijić Z.	945, 949, 953	Mitov I.	230
Mijin D.	1041	Mitrić M.	604, 627, 703
Mikloš M.	1091	Moga M.	403
Miladinović J. M.	89, 93	Mojović M.	457, 550, 554
Miladinović Z. P.	93, 469, 823	Mojović Z.	387, 391, 407
Milanović I.	745, 1011	Molteni M.	434
Milčić M.	184	Momčilović M.	172, 585
Milenković A.	292, 897	Mudrinić T.	260, 387, 391
Milenković D.	140	Murić B.	711
Milenković M.	1025	Najman S.	518
Milenković M.C.	352, 438, 957	Nasrulin E.	105
Milenova K.	230	Nastasijević B.	1063
Milić M.M.	725	Nastasović A.	783, 787, 827
Milićević Z.	477		

Nastović A.	819	Ozturk H.	749, 753
Necib H.	909	Pagnan M.	124
Nedeljković J.M.	280, 522	Pajić-Lijaković I.	849
Nedić Vasiljević B.	288	Pajkić B.	160
Nikčević M.	869	Panić V.	707
Nikolaev A.Yu.	791	Pantelić D.	711
Nikolić B.	473, 477	Pantić J.	422
Nikolić G.	1037	Paskaš Mamula B.	695
Nikolić G. M.	168, 1037	Pasquini L.	691
Nikolić J.	514	Pastor F.	414, 498, 502
Nikolić J.D.	667	Pavelkić V.M.	969
Nikolić K.	426, 1137, 1149	Pavićević A.	546, 550, 457
Nikolić M.	877	Pavličević J.	608
Nikolić M.G.	156	Pavlović D.	1153
Nikolić M.V.	659	Pavlović J.	395
Nikolić N.	1041	Pavlović M. D.	530, 542
Nikolić R.S.	156, 937	Pejić N.	356, 418, 1019
Nikolić Z.S.	635	Pejin B.	414, 498, 502
Nikolova D.	235, 272, 276	Perdigón A.C.	268, 671
Ninković D. B.	1029	Pergal M.V.	807, 811, 815
Novaković N.	695, 745	Perić M.	3
Novaković T.B.	663, 823, 827	Perini D.A.	403
Nur Syuhada binti Che Yob	248	Perišić M.	929, 933, 953
Obadović D.	733, 737	Perišić M.	949
Obradović M.D.	375	Pesquera C.	268, 671
Odovic J.	1101	Petković B. B.	184, 395, 562
Ohishi Y.	85	Petković M.	176, 1033
Okur S.	115	Petrov I.Y.	264
Onjić A.	787, 819	Petrović Đ.	1007, 1011
Oros I.	889, 893	Petrović J.	877
Ortiz B.	268, 671	Petrović M.P.	969
Osawa T.	85	Petrović P. V.	1053
Ostojić S.	973, 977, 1045		
Ostrovskii N.M.	207		

Petrović R.J.	542	Radosavljić A.	566, 699, 703
Petrović S.P.	243, 663	Radosavljević-Mihajlović A.	239
Petuhov A.	128	Radovanović F.	787
Pezo L.	977, 1045, 1049	Radovanović R.	799
Pilić B.	608, 795, 799	Radović M.	581, 585
Pisanjuk S.	941	Radulović K. T.	1059
Plesovskikh A.S.	69	Radulović A.A.	767, 1045, 1049
Plutalova A. V.	763, 779	Radusin T.	795
Plyusnin V.F.	853	Rajczak E.	449
Podunavac-Kuzmanović S.	465, 861	Rajić V.	252
Poleshchuk O.Kh.	256	Rajšić S.	929, 933, 953
Poleti D.	767	Rakić S.	733, 737
Popović D. Ž.	89, 93	Rakić T.	506
Popović G.	1133	Rakovsky S.	215
Popović M.	1129, 1133	Ranković D.	172
Popović-Bijelić A.	435, 506, 554	Ranogajec J.	889
Popsavin N.	1095	Rašeta M.	502
Poreba R.	807	Rašković-Lovre Ž.	691, 1011
Poša M.	1067	Rašović A.	200
Potkonjak N.I.	1019, 1071	Ristić S.I.	795
Pozdnyakov I.P.	853	Rocha R.P.	383
Premović P.I.	1077, 1081	Roglić G.	881, 885
Prokopov N.I.	300, 791	Rožić Lj.S.	663
R. Marković	200	Ruiz-Hitzky E.	991
Rabasović M. D.	1059	Rzepecka P.	449
Radenović Č. N.	530, 542	Salaev M.A.	256
Radetić M.	522	Salem M.	1129
Radetić T.	647	Samaržija-Jovanović S.	562
Radičević R.	795	Samoila C.	399, 631
Radišić M.	913	Samolov A.	905
Radoičić M.	643	Sandić Z.	585, 819, 823
Radoman T. S.	803	Santos D.M.F.	367, 383
Radonjić V.	272, 276, 284	Sarap N.	957
		Savić A.	457
		Savić I.	1037

Savić J.	1145	Spasov L.	235
Savić T.D.	623, 683	Sredojević D. N.	1053
Savić V.	132	Stajić-Trošić J.	591
Savović J.	172	Stamenković S.	550, 554
Schmitz G.	320	Stanciu I.	771
Schreiber I.	20	Stančov D.	573
Scollo A.S.	403	Stanisavljev D. R.	352, 438, 651
Sečanski M. D.	530	Stanišić A.	1105
Sedov I.	65	Stanišić Stojić S.	945, 949
Sen I.	196	Stanković A.	252
Senčanski J.	957	Stanković B.	356
Sequeira C.A.C.	367, 383	Stanković D.	184, 395, 407
Serizawa H.	85	Stanković D.	585, 1041
Serkhacheva N.S.	300	Stanković G. J.	530, 542
Shenger M.S.M.	1129	Stanković M.	272, 284, 288
Shinagawa	635	Stanković M.N.	156, 937
Shodorova S.	97	Stanojević A.	340
Shopska M.	235	Stefanović I.S.	807, 815
Simeonov D.	235	Steinhart M.	807
Simić M.	473	Stepanov N.F.	119
Simionescu B.C.	11	Stevanovic R.	348
Simonović B.	981, 985	Stevanović J.	1117
Simonović B. R.	973, 977	Stoiljković M.	172, 647, 1007
Simonović M.	973, 981, 985	Stojanović A.	383
Slavković-Beškoski L.	1007	Stojanović M.	733, 737
Smara A.	909	Stojanović N.N.	767
Smičiklas I.	292, 897, 901	Stojanović S.	518
Smiljanić S.V.	667	Stojić A.	929, 945, 953
Smirnova N.N.	57	Stojković N.	280
Solomonov B.	65	Stolić A.	518
Sovilj S. P.	184	Stolov M.	65
Spasić A.M.	348	Stoyanova D.	243
Spasojević V.	581	Sunarić S. M.	302, 1109
Spasojević I.	473, 477	Suručić Lj.	827, 585
Spasojević J.	566, 699, 703		

Sužnjević D.	414, 498, 502	Todorović D. M.	1059
Swiatkowska A.	449, 510	Todorović M.	921, 929, 933
Szabó J.	865	Todorović N.	1113, 1117, 1121
Szabó Nagy A.	865	Tolkachev A.V.	300
Szakacs Zs.	721, 955, 999	Tomić Z.D.	1041
Šaponjić Z.V.	627, 643, 647	Tomkovich M.V.	612
Šećerov B.	573	Tomković T.	783, 787, 1003
Šekularac G.	707	Tomović A.Ž.	1063
Šenk N.	913	Topalović V.	667
Šentjurc M.	445	Tošić M.B.	667
Šidanin L.	655	Trajanović M.	518
Škorić D.	136, 1067	Trtica M.	172
Šljivić-Ivanović M.	292, 897, 901	Trtić-Petrović T.	109, 675
Šljukić B.	367, 383	Tryasunov B.G.	264
Šoštarić A.	945, 953, 949	Tukubaev N. T.	77
Špirkova M.	608, 807	Turi A.	457
Štrbac D.	655	Tzvetkov P.	235
Šušnjar S.	546	Uskoković D.	252, 518, 604
Takenaka S.	449	Vajda A.	733, 737
Talevska A.	498	Vasić M.	280
Talevski T.	498	Vasić M.M.	308
Tapilin V.	144	Vasić V.	461, 538
Tatić N. B.	1109	Vasiljević D.	711
Taylor A.	319	Veličković A.V.	288
Tenchev K.	276	Veličković S.	152, 160, 1063
Teofilović V.	608	Veselinović A. M.	168, 1037
Terlecki-Baricevic A.	243	Veselinović D.	857
Tešević V.V.	623, 807, 815	Vidojković S.	783, 787, 1003
Timofeeva M.N.	853	Vladimirov S.	1105, 1125, 1145
Tissaoui H.	434	Vladislavljević G.	1007
Todoran D.	721, 955, 999	Vodnik V. V.	522, 526, 803
Todoran R.	721, 955, 999	Vodyankina O.V.	256

Vorob'eva V.	97, 101	Zarubica A.	280
Vorotyntsev A.	128	Zelenaya A.	105
Vorotyntsev I.	128	Zhang X.	853
Vraneš M.	861	Zlatanović S.	1045, 1049
Vranješ M.	627, 647	Zlatar M.	180
Vranješ-Djurić S.	581	Zolotarev V. M.	612
Vrsajković S.	1095	Zujovic Z. D.	651
Vrvić M. M.	514, 687, 1141	Zyryanov A.	105
Vucicevic J.	1129, 1137, 1149	Žák T.	308
Vučinić D.	1015	Žikić R.	1063
Vučinić Vasić M.	889	Živanović V.D.	667
Vujadinović M.	132	Živković Lj.S.	687
Vujančević J.	659	Živković S.	506
Vujasin R.	695, 691, 745	Žižić M.	469
Vujčić M.	1025	Žunić M.	387, 407, 991
Vujić Z.	148		
Vujković M.	438		
Vujović M. M.	168		
Vukčević M.	679, 849		
Vukelić N.	272, 276, 292		
Vukić N.	795		
Vukićević N.M.	639		
Vukoje I.	522		
Vukojević V.	340, 833		
Vuković Z.M.	663, 827		
Vunduk J.	469		
Waisi H.	477		
Wu F.	853		
Yildiz C.B.	188, 192		
Yulusov V. V.	763, 779		
Zaharieva K.	230		
Zaikov G.E.	215		
Zakrzewska J.	469		
Zanel P.L.	124		
Zarić S. D.	1029, 1053		